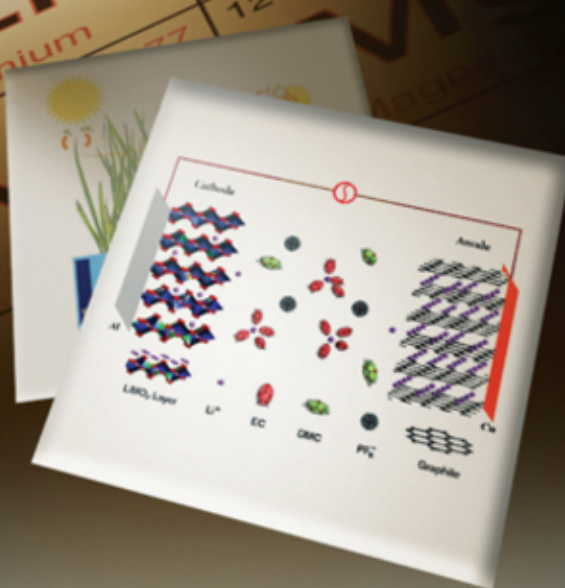


Energy Production and Storage

Inorganic Chemical Strategies for a Warming World



WILEY

Visit the online Encyclopedia of Inorganic Chemistry at
www.mrw.interscience.wiley.com/eic/



EIC Books

ENERGY PRODUCTION AND STORAGE

Inorganic Chemical
Strategies for a
Warming World

EIC Books



EIC Books

Application of Physical Methods to Inorganic and Bioinorganic Chemistry

Edited by Robert A. Scott and Charles M. Lukehart

ISBN 978-0-470-03217-6

Nanomaterials: Inorganic and Bioinorganic Perspectives

Edited by Charles M. Lukehart and Robert A. Scott

ISBN 978-0-470-51644-7

Computational Inorganic and Bioinorganic Chemistry

Edited by Edward I. Solomon, R. Bruce King and Robert A. Scott

ISBN 978-0-470-69997-3

Radionuclides in the Environment

Edited by David A. Atwood

ISBN 978-0-470-71434-8

Energy Production and Storage

Robert H. Crabtree

ISBN 978-0-470-74986-9

Encyclopedia of Inorganic Chemistry

In 1994 John Wiley & Sons published the *Encyclopedia of Inorganic Chemistry* (EIC). This 8-volume work was well received by the community, and has become a standard publication in all libraries serving the inorganic, coordination chemistry, organometallic and bioinorganic communities. The 10-volume Second Edition of the *Encyclopedia* was published in print in 2005, and online in 2006, on the major reference platform Wiley Online Library. The online edition is regularly updated and expanded. For more information see:

<http://www.wileyonlinelibrary/ref/eic>

ENERGY PRODUCTION AND STORAGE

Inorganic Chemical Strategies for a Warming World

Editor

Robert H. Crabtree

Yale University, New Haven, CT, USA



This edition first published 2010
© 2010 John Wiley & Sons Ltd

Registered office

John Wiley & Sons Ltd, The Atrium, Southern Gate, Chichester, West Sussex, PO19 8SQ,
United Kingdom

For details of our global editorial offices, for customer services and for information about how
to apply for permission to reuse the copyright material in this book please see our website at
www.wiley.com.

The right of the authors to be identified as the authors of this work has been asserted in
accordance with the Copyright, Designs and Patents Act 1988.

All rights reserved. No part of this publication may be reproduced, stored in a retrieval system,
or transmitted, in any form or by any means, electronic, mechanical, photocopying, recording or
otherwise, except as permitted by the UK Copyright, Designs and Patents Act 1988, without the
prior permission of the publisher.

Wiley also publishes its books in a variety of electronic formats. Some content that appears in
print may not be available in electronic books.

Designations used by companies to distinguish their products are often claimed as trademarks.
All brand names and product names used in this book are trade names, service marks,
trademarks or registered trademarks of their respective owners. The publisher is not associated
with any product or vendor mentioned in this book. This publication is designed to provide
accurate and authoritative information in regard to the subject matter covered. It is sold on the
understanding that the publisher is not engaged in rendering professional services. If professional
advice or other expert assistance is required, the services of a competent professional should be
sought.

Front cover image credit (back image): This figure was published in the article ‘Green electricity
production with living plants and bacteria in a fuel cell’, Int. J. Energy Res., 2008, 32, 870–876
© John Wiley & Sons, Ltd, 2008.

Library of Congress Cataloging-in-Publication Data

Energy production and storage : inorganic chemical strategies for a warming world / editor,
Robert H. Crabtree.

p. cm.

Includes bibliographical references and index.

ISBN 978-0-470-74986-9 (cloth: alk. paper)

1. Hydrogen as fuel--Research. 2. Water resources development. 3. Renewable energy
sources. 4. Environmental chemistry. 5. Carbon sequestration. I. Crabtree, Robert H., 1948-

TP359.H8E54 2010
621.042--dc22

2010025736

A catalogue record for this book is available from the British Library.

ISBN-13: 978-0-470-74986-9

Set in 9¹/₂ / 11¹/₂ pt TimesNewRomanPS by Laserwords (Private) Limited, Chennai, India.
Printed and bound in Singapore by Markono Print Media Pte Ltd.

Encyclopedia of Inorganic Chemistry

Editorial Board

Editor-in-Chief

Robert H. Crabtree
Yale University, New Haven, CT, USA

Section Editors

David A. Atwood
University of Kentucky, Lexington, KY, USA

R. Bruce King
University of Georgia, Athens, GA, USA

Charles M. Lukehart
Vanderbilt University, Nashville, TN, USA

Robert A. Scott
University of Georgia, Athens, GA, USA

International Advisory Board

Michael Bruce
Adelaide, Australia

Wolfgang Herrmann
Munich, Germany

Fausto Calderazzo
Pisa, Italy

Jean-Marie Lehn
Strasbourg, France

Tristram Chivers
Calgary, Canada

François Mathey
*University of California Riverside,
CA, USA*

Odile Eisenstein
Montpellier, France

Akira Nakamura
Osaka, Japan

C. David Garner
Nottingham, UK

Jan Reedijk
Leiden, The Netherlands

Malcolm Green
Oxford, UK

Vivian Yam
Hong Kong

Contents

Contributors	ix
Series Preface	xiii
Volume Preface	xv
PART 1: ENERGY PRODUCTION	1
H₂ Production from Renewables	3
<i>Rufino M. Navarro, M. Cruz Sanchez-Sanchez, M. Consuelo Alvarez-Galvan, Jose Luis G. Fierro and Saeed M. Al-Zaharani</i>	
Energy Conversion in Photosynthesis	21
<i>Gözde Ulas and Gary W. Brudvig</i>	
Molecular Catalysts for Oxygen Production from Water	35
<i>Antoni Llobet and Sophie Romain</i>	
Dye-Sensitized Solar Cells: an Overview	53
<i>Luisa Andrade, Helena Aguilar Ribeiro and Adélio Mendes</i>	
Enzymes and Microbes for Energy Production by Fuel Cells	73
<i>Frédéric Barrière</i>	
Proton Exchange Membranes for Fuel Cells	89
<i>Ram Devanathan</i>	
Methane-to-Methanol Conversion	101
<i>Brian G. Hashiguchi, Claas H. Hövelmann, Steven M. Bischof, Kapil S. Lokare, Chin Hin Leung and Roy A. Periana</i>	
Photocatalytic Hydrogen Production from Water	143
<i>Shamindri M. Arachchige and Karen J. Brewer</i>	
Intermediate-Temperature Solid Oxide Fuel Cells	173
<i>Alan Atkinson, John Kilner, Stephen Skinner, Nigel P. Brandon and Dan J. L. Brett</i>	
Some Computational Challenges in Energy Research	191
<i>Victor S. Batista</i>	
Toward Solar Fuels Using a Biomimetic Approach: Progress in the Swedish Consortium for Artificial Photosynthesis	199
<i>Sascha Ott, Stenbjörn Styring, Leif Hammarström and Olof Johansson</i>	
Direct Ethanol Fuel Cells	229
<i>Zhi Wen Chia and Jim Yang Lee</i>	

Molecular Catalysis for Fuel Cells <i>Kenichi Oyaizu</i>	253
Recent Advances in Photo-Initiated Electron-Transfer at the Interface between Anatase TiO₂ Nanocrystallites and Transition-Metal Polypyridyl Compounds <i>Shane Ardo and Gerald J. Meyer</i>	265
Electrochemical and Photoelectrochemical Conversion of CO₂ to Alcohols <i>Robert H. Crabtree</i>	301
PART 2: ENERGY STORAGE	307
Hydrogen Economy <i>Stephen A. Wells, Asel Sartbaeva, Vladimir L. Kuznetsov and Peter P. Edwards</i>	309
Thermal Stability of Lithium Ion Battery Electrolytes <i>Brett L. Lucht, Tippawan Markmaitree and Li Yang</i>	333
Supercapacitors: Electrode Materials Aspects <i>Li Li Zhang, Zhibin Lei, Jintao Zhang, Xiaoning Tian and Xiu Song Zhao</i>	341
Thermochemical Water-Splitting <i>Ali T-Raissi</i>	365
Lithium Ion Batteries for Transportation and Electrical Energy Storage Applications: Nuclear Magnetic Resonance Studies of Structure and Function <i>Jordi Cabana and Clare P. Grey</i>	375
Index	393

Contributors

M. Consuelo Alvarez-Galvan

Institute of Catalysis and Petrochemistry, CSIC, Cantoblanco, Madrid, Spain

- H₂ Production from Renewables

Luisa Andrade

Universidade do Porto, Porto, Portugal

- Dye-Sensitized Solar Cells: an Overview

Shamindri M. Arachchige

Virginia Polytechnic Institute and State University, Blacksburg, VA, USA

- Photocatalytic Hydrogen Production from Water

Shane Ardo

Johns Hopkins University, Baltimore, MD, USA

- Recent Advances in Photo-Initiated Electron-Transfer at the Interface between Anatase TiO₂ Nanocrystallites and Transition-Metal Polypyridyl Compounds

Alan Atkinson

Imperial College London, London, UK

- Intermediate-Temperature Solid Oxide Fuel Cells

Saeed M. Al-Zaharani

King Saud University, Riyadh, Saudi Arabia

- H₂ Production from Renewables

Frédéric Barrière

Université de Rennes 1, France

- Enzymes and Microbes for Energy Production by Fuel Cells

Victor S. Batista

Yale University, New Haven, CT, USA

- Some Computational Challenges in Energy Research

Steven M. Bischof

The Scripps Research Institute, Jupiter, FL, USA

- Methane-to-Methanol Conversion

Nigel P. Brandon

Imperial College London, London, UK

- Intermediate-Temperature Solid Oxide Fuel Cells

Dan J. L. Brett

Imperial College London and University College London, London, UK

- Intermediate-Temperature Solid Oxide Fuel Cells

Karen J. Brewer

Virginia Polytechnic Institute and State University, Blacksburg, VA, USA

- Photocatalytic Hydrogen Production from Water

Gary W. Brudvig

Yale University, New Haven, CT, USA

- Energy Conversion in Photosynthesis

Jordi Cabana

Lawrence Berkeley National Laboratory, Berkeley, CA, USA

- Lithium Ion Batteries for Transportation and Electrical Energy Storage Applications: Nuclear Magnetic Resonance Studies of Structure and Function

Zhi Wen Chia

National University of Singapore, Singapore

- Direct Ethanol Fuel Cells

Robert H. Crabtree

Yale University, New Haven, CT, USA

- Electrochemical and Photoelectrochemical Conversion of CO₂ to Alcohols

Ram Devanathan

Pacific Northwest National Laboratory, Richland, WA, USA

- Proton Exchange Membranes for Fuel Cells

Peter P. Edwards	<i>University of Oxford, Oxford, UK</i> • Hydrogen Economy
Jose Luis G. Fierro	<i>Institute of Catalysis and Petrochemistry, CSIC, Cantoblanco, Madrid, Spain</i> • H ₂ Production from Renewables
Clare P. Grey	<i>Stony Brook University, Stony Brook, NY, USA and University of Cambridge, Cambridge, UK</i> • Lithium Ion Batteries for Transportation and Electrical Energy Storage Applications: Nuclear Magnetic Resonance Studies of Structure and Function
Leif Hammarström	<i>Uppsala University, Uppsala, Sweden</i> • Toward Solar Fuels Using a Biomimetic Approach: Progress in the Swedish Consortium for Artificial Photosynthesis
Brian G. Hashiguchi	<i>The Scripps Research Institute, Jupiter, FL, USA</i> • Methane-to-Methanol Conversion
Claas H. Hövelmann	<i>The Scripps Research Institute, Jupiter, FL, USA</i> • Methane-to-Methanol Conversion
Olof Johansson	<i>Uppsala University, Uppsala, Sweden</i> • Toward Solar Fuels Using a Biomimetic Approach: Progress in the Swedish Consortium for Artificial Photosynthesis
John Kilner	<i>Imperial College London, London, UK</i> • Intermediate-Temperature Solid Oxide Fuel Cells
Vladimir L. Kuznetsov	<i>University of Oxford, Oxford, UK</i> • Hydrogen Economy
Jim Yang Lee	<i>National University of Singapore, Singapore</i> • Direct Ethanol Fuel Cells
Zhibin Lei	<i>National University of Singapore, Singapore</i> • Supercapacitors: Electrode Materials Aspects
Chin Hin Leung	<i>The Scripps Research Institute, Jupiter, FL, USA</i> • Methane-to-Methanol Conversion
Antoni Llobet	<i>Institute of Chemical Research of Catalonia (ICIQ) and Universitat Autònoma de Barcelona, Barcelona, Spain</i> • Molecular Catalysts for Oxygen Production from Water
Kapil S. Lokare	<i>The Scripps Research Institute, Jupiter, FL, USA</i> • Methane-to-Methanol Conversion
Brett L. Lucht	<i>University of Rhode Island, Kingston, RI, USA</i> • Thermal Stability of Lithium Ion Battery Electrolytes
Tippawan Markmaitree	<i>University of Rhode Island, Kingston, RI, USA</i> • Thermal Stability of Lithium Ion Battery Electrolytes
Adélio Mendes	<i>Universidade do Porto, Porto, Portugal</i> • Dye-Sensitized Solar Cells: an Overview
Gerald J. Meyer	<i>Johns Hopkins University, Baltimore, MD, USA</i> • Recent Advances in Photo-Initiated Electron-Transfer at the Interface between Anatase TiO ₂ Nanocrystallites and Transition-Metal Polypyridyl Compounds
Rufino M. Navarro	<i>Institute of Catalysis and Petrochemistry, CSIC, Cantoblanco, Madrid, Spain</i> • H ₂ Production from Renewables

Sascha Ott	<i>Uppsala University, Uppsala, Sweden</i> • Toward Solar Fuels Using a Biomimetic Approach: Progress in the Swedish Consortium for Artificial Photosynthesis
Kenichi Oyaizu	<i>Waseda University, Tokyo, Japan</i> • Molecular Catalysis for Fuel Cells
Roy A. Periana	<i>The Scripps Research Institute, Jupiter, FL, USA</i> • Methane-to-Methanol Conversion
Helena Aguilar Ribeiro	<i>Universidade do Porto, Porto, Portugal</i> • Dye-Sensitized Solar Cells: an Overview
Sophie Romain	<i>Institute of Chemical Research of Catalonia (ICIQ), Barcelona, Spain</i> • Molecular Catalysts for Oxygen Production from Water
M. Cruz Sanchez-Sanchez	<i>Institute of Catalysis and Petrochemistry, CSIC, Cantoblanco, Madrid, Spain</i> • H ₂ Production from Renewables
Asel Sartbaeva	<i>University of Oxford, Oxford, UK</i> • Hydrogen Economy
Stephen Skinner	<i>Imperial College London, London, UK</i> • Intermediate-Temperature Solid Oxide Fuel Cells
Stenbjörn Styring	<i>Uppsala University, Uppsala, Sweden</i> • Toward Solar Fuels Using a Biomimetic Approach: Progress in the Swedish Consortium for Artificial Photosynthesis
Ali T-Raissi	<i>University of Central Florida, Orlando, FL, USA</i> • Thermochemical Water-Splitting
Xiaoning Tian	<i>National University of Singapore, Singapore</i> • Supercapacitors: Electrode Materials Aspects
Gözde Ulas	<i>Yale University, New Haven, CT, USA</i> • Energy Conversion in Photosynthesis
Stephen A. Wells	<i>University of Warwick, Coventry, UK</i> • Hydrogen Economy
Li Yang	<i>University of Rhode Island, Kingston, RI, USA</i> • Thermal Stability of Lithium Ion Battery Electrolytes
Jintao Zhang	<i>National University of Singapore, Singapore</i> • Supercapacitors: Electrode Materials Aspects
Li Li Zhang	<i>National University of Singapore, Singapore</i> • Supercapacitors: Electrode Materials Aspects
Xiu Song Zhao	<i>National University of Singapore, Singapore</i> • Supercapacitors: Electrode Materials Aspects

Series Preface

The success of the *Encyclopedia of Inorganic Chemistry* (EIC) has been very gratifying to the editors. We felt, however, that not everyone would necessarily need access to the full ten volumes of EIC. Some readers might prefer to have more concise thematic volumes targeted to their specific area of interest. This idea encouraged us to produce a series of EIC Books, focusing on topics of current interest. These will continue to appear on a regular basis and will feature the leading scholars in their fields. Like the Encyclopedia, we hope that EIC Books will give both the starting research student and the confirmed research worker a critical distillation of the leading concepts and provide a structured entry into the fields covered.

Computer literature searches have become so easy that one could be led into thinking that the problem of efficient access to chemical knowledge is now solved. In fact, these searches often produce such a vast mass of material that the reader is overwhelmed. As Henry Kissinger has remarked, the end result is often a shrinking of one's perspective. From studying the volumes that comprise the EIC Books

series, we hope that readers will find an expanding perspective to furnish ideas for research, and a solid, up-to-date digest of current knowledge to provide a basis for instructors and lecturers.

I take this opportunity of thanking Bruce King, who pioneered the *Encyclopedia of Inorganic Chemistry*, my fellow editors, as well as the Wiley personnel, and, most particularly, the authors of the articles for the tremendous effort required to produce such a series on time. I hope that EIC Books will allow readers to benefit in a more timely way from the insight of the authors and thus contribute to the advance of the field as a whole.

Robert H. Crabtree
Yale University, New Haven, CT, USA

January 2009

Volume Preface

Energy production and storage are central problems for our time and are likely to attract intense public attention during many future decades. One factor will be the gradual decline in world petroleum production, as we pass the moment of peak production at some point in the next few years. The petroleum age is not over, of course, but the era of *cheap* petroleum does seem to be over. Oil wealth can also be associated with political instability, with unpredictable results on supply. A new factor—the economic rise of Asia and her vast population—can only aggravate the situation. Coal, the fossil fuel with the greatest reserves and with the broadest geographical distribution, may be able to fill any future energy supply gap but only at the cost of environmental damage at the mine and more intense CO₂ emissions—coal having the highest CO₂ output per unit of energy produced. Carbon capture and storage is under intense study but its practicality as a low-carbon-footprint means of using coal is still under discussion. Natural gas has been widely acclaimed as the best of the fossil fuels, having the lowest CO₂ output per unit of energy produced. Hopes exist that abundant and widely distributed shale gas, previously considered uneconomic, may become viable with rising energy prices and new production methods.

A key factor that has intensified the growing unease over our current energy production system is the threat of climate change. David King, the UK Government's Chief Science Advisor from 2000 to 2007, has even called climate change “the single biggest challenge our civilization has ever had to face.” Nuclear energy is a potential solution but the problem of waste management has not yet been satisfactorily solved.

This volume is particularly concerned with alternative energy production and storage. Abundant energy is, in principle, available from the sun to run the earth in a sustainable way. Solar energy can be directly harnessed by agricultural and photovoltaic means but the sheer scale of the energy demand poses severe challenges. For example, any major competition between biomass production and food production would simply transfer scarcity from energy to food. Indirect use of solar energy in the form of wind is also promising, especially for those regions not blessed with abundant sunlight. Other modes such as tidal and wave energy may well be niche players.

These are problems in which chemistry can play a decisive role. The present volume covers some promising

modes of alternative energy production and storage that minimize the atmospheric burden of fossil-derived CO₂. No one production or storage mode is likely to dominate, at least at first, and numerous possibilities need to be explored to compare their technical feasibility and economics. This provides the context for a broad exploration of novel ideas that we are likely to see in future years as the field expands.

Water splitting is a central problem in alternative energy work. Only water is a sufficiently cheap and abundant electron source for global exploitation, as Jules Verne foresaw in his 1874 novel, *The Mysterious Island*, “water will be the coal of the future.” Of course, both energy input and suitable catalysts are needed to split water into oxygen and either hydrogen or electrons and protons. In this context, Brudvig and coauthors discuss energy conversion in photosynthesis, Llobet and coauthors cover molecular water splitting catalysts, Brewer and coauthors consider photocatalytic hydrogen production from water and T-Raissi covers thermochemical water splitting. Johannson and coauthors discuss recent progress in the Swedish Consortium for Artificial Photosynthesis. Batista discusses the progress made in computational modeling of energy-related processes including photosynthesis.

Several articles concentrate on hydrogen, notably a key contribution on the hydrogen economy by Edwards and coauthors and on hydrogen production from renewables by Fierro and coauthors.

A number of important chemical conversions are covered, for example reduction of CO₂ to useful fuels either electrochemically or photochemically, as well as conversion of methane to methanol by Periana and coauthors.

Dye-sensitized solar cells for the direct conversion of solar to electrical energy is reviewed by Mendes and coauthors. Related to this problem, Meyer and coauthors discuss photoinitiated electron transfer in such cells.

A number of articles relate to fuel cells. Devanathan discusses the key problem of devising efficient proton exchange membranes, Brett covers intermediate temperature solid oxide fuel cells, Lee considers direct ethanol fuel cells, Oyaizu considers molecular catalysis for fuel cells, and Barrière covers the use of enzymes and microbes in fuel cells.

Batteries are also considered. Lucht and coauthors discuss Li ion batteries, Grey and coauthors cover L-6 MAS NMR studies on battery materials, and Zhao reviews the

area of supercapacitors with special reference to the electrode materials.

It is likely that many more research groups will be moving into the area, attracted not only by the rising funding levels that we are already seeing but also by its major challenges as well as its interdisciplinarity.

Our field will greatly benefit from the current realignment of research priorities and this book provides

an entry point for students and scholars considering a career in the field or needing an up-to-date review.

Robert H. Crabtree
Yale University, New Haven, CT, USA

October 2010

PART 1

Energy Production

H₂ Production from Renewables

Rufino M. Navarro, M. Cruz Sanchez-Sanchez, M. Consuelo Alvarez-Galvan and Jose Luis G. Fierro

Institute of Catalysis and Petrochemistry, CSIC, Cantoblanco, Madrid, Spain

and

Saeed M. Al-Zaharani

King Saud University, Riyadh, Saudi Arabia

1	Introduction	3
2	Hydrogen Production from Biomass	4
3	Hydrogen from Solar Energy	9
4	Conclusions	16
5	Acknowledgments	17
6	Related Articles	17
7	Abbreviations and Acronyms	17
8	Further Reading	17
9	References	17

1 INTRODUCTION

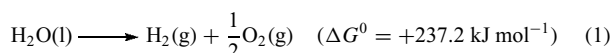
Energy and environmental concerns are among the biggest challenges that the world is facing today, in particular, energy sustainability and carbon emission from the fossil fuels. Hydrogen is considered as one of the few long-term sustainable clean energy carriers, emitting only water vapor as a by-product during its oxidation or combustion. Although hydrogen can be used as a fuel in internal combustion engines (ICEs), the conversion of the chemical energy stored in the H–H bond into electricity in fuel cells is more attractive because of its higher efficiency.¹

Production of H₂ by the currently available technologies consumes greater amounts of natural gas, which in turn emits more greenhouse gas (GHG). However, in spite of using nonrenewable fossil fuel feedstock, the increase in GHG emissions can be reduced through CO₂ sequestration at the production sites. Production of H₂ from renewable sources derived from agricultural or other waste streams offers the possibility to contribute to the production capacity with lower or no net GHG emissions, without carbon sequestration technologies, increasing the flexibility and improving the economics of distributed and semicentralized reforming.

At present, steam reforming of hydrocarbons, i.e., natural gas, is the most commonly used and generally the most economical method for hydrogen production.^{2–5} The use of natural gas, whose major component is methane, fails to provide a solution to deal with the large amount of carbon dioxide emissions (ca 7 kg CO₂/kg H₂) during the reforming processes. In addition, the use of fossil fuels for secondary energy production is nonsustainable. Not only does fossil fuel burning contribute to the GHG pool but the eventual depletion of the world's fossil fuel reserves also threatens sustainable development.^{6,7} However, hydrogen production can be environmentally friendly only if the resource used to extract hydrogen is renewable. Thus, biomass, a product of photosynthesis, is an attractive alternative to fossil feedstocks as it can be considered as a renewable H₂ precursor. CO₂-neutral hydrogen can be produced by the conversion of biomass via gasification,⁸ pyrolysis of bio-oils,⁹ steam reforming of biomass-derived higher alkanes and alcohols,^{2,5,10} and aqueous phase reforming (APR) of oxygenated hydrocarbons.¹¹ Biomass-derived hydrogen can be classified as carbon neutral because the CO₂ released during hydrogen production is further consumed by biomass generation (neglecting the CO₂ produced from the fossil

fuel energy required for operating the hydrogen production unit.¹²

Among the methods for H₂ generation outside the C-cycle, hydrogen production using solar energy also attracts great attention because of the potential to use the abundance of this energy (the maximum direct insolation frequently reaches ca 700 W m⁻² in the sunbelt regions) and water. Thermodynamically, the overall water-splitting reaction is an uphill reaction, with a highly positive change in Gibbs free energy ($\Delta G^0 = +237.2 \text{ kJ mol}^{-1}$):



Solar energy can be used to produce hydrogen in the form of heat (thermochemical), light (photoelectrochemical or photocatalytic), or electricity (electrolysis). Among these, thermochemical, photoelectrochemical, and photocatalytic are the most efficient solar paths to hydrogen since they do not have the inefficiencies associated with the conversion of solar energy to electricity followed by electrolysis.

In this article, we review the recent developments in the conversion involved in hydrogen production from less costly and abundant biomass without net carbon emissions. In addition, this article includes advances in the fully renewable conversion of solar energy into hydrogen via the water-splitting process assisted by thermochemical, photoelectrochemical, and photocatalytic processes. Attention is particularly given to the new materials and strategies reported in the literature over the past years for developing efficient metal oxide redox cycles for a two-step thermochemical water splitting, efficient photoelectrocatalysts under visible light photocatalysts for hydrogen evolution via photoelectrochemical water splitting, and efficient photocatalysts under visible light for the photochemical water splitting.

2 HYDROGEN PRODUCTION FROM BIOMASS

Figure 1 illustrates the different routes that can be adopted to produce hydrogen from biomass, including

gasification to produce syngas, pyrolysis to produce bio-oils, and hydrolysis of cellulose to produce sugar monomers.¹³ Syngas can be converted to hydrogen by water gas shift (WGS) reaction, though any remaining CO must be removed from the gas stream. Pyrolysis bio-oil can be converted to liquid fuel, but the processes are complex and the rate of conversion is low. Hydrogen can be produced from the bio-oil by autothermal reforming with high conversion efficiency, especially with the use of catalytic membrane reactors. APR can be used to convert sugars and sugar alcohols, such as sorbitol, to produce hydrogen. In addition to these, there are other biological (enzymatic and bacterial) routes to produce hydrogen, but the scope of this article is restricted only to the heterogeneous catalytic routes.

2.1 Gasification

Biomass gasification is achieved at temperatures above 1000 K in the presence of oxygen/air and/or steam. A combination of pyrolysis, partial oxidation, and/or steam-reforming reactions of gaseous alkanes and char takes place under these conditions. The presence of oxygen or air in the gasification equipment promotes partial oxidation over pyrolysis reactions. Although gaseous products (H₂ and CO_x) are mainly obtained, the fast pyrolysis reactions can also produce bio-oils, tar (aromatic hydrocarbons), and charcoal. Several parameters such as heating rate, temperature, and residence time can be optimized to maximize the efficiency of gasification with minimum tar formation. Thermal cracking of the tar is possible at temperatures above 1300 K¹⁴ and by using catalytic additives such as dolomite, olivine, and char,¹⁵ with 100% removal of tar by using dolomite as the gasifying agent.¹⁶ Moreover, dolomite and CeO₂/SiO₂-supported Ni, Pt, Pd, Ru, and alkaline metal oxides can be used to catalyze the gasification process to reduce tar formation and improve the product gas purity and conversion efficiency.¹⁷ Although Rh/CeO₂/SiO₂ has been reported to be the most effective catalyst to reduce tar formation, Ni-based catalysts are also highly active for tar destruction. Since Ni-based catalysts are industrially used for steam reforming of methane and naphtha,⁵

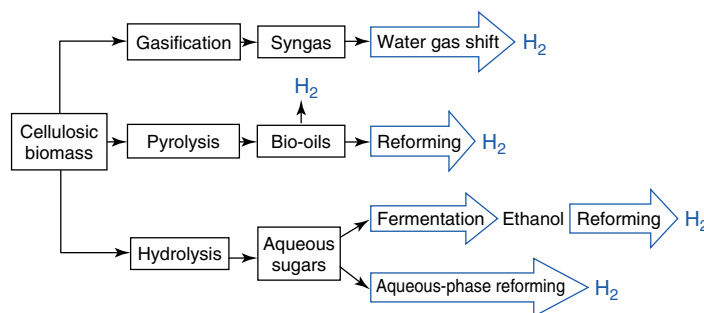


Figure 1 Routes to the production of hydrogen from biomass

they are also expected to catalyze the steam reforming of tars as well as WGS reaction to produce H₂. While alkali metal salts also decrease the tar yield, their use leads to an increase in char and ash content and are therefore not suitable for commercial use.¹⁸

Recent improvements in the gasification technology include the hydrogen production by reaction-integrated novel gasification (HyPr-RING) technology.¹⁹ In this technology, the gasification and WGS reaction are combined in one reactor, with simultaneous absorption of CO₂ and other pollutants to increase the hydrogen yield, while maintaining a relatively low reaction temperature of 900 K. One of the latest developments in gasification technology is the Carbo-V process (CHOREN Technologies GmbH) designed to produce tar-free syngas for H₂ or liquid fuel.²⁰ The advantage of Carbo-V process over the normal gasifier is that it increases efficiency (>80%). A similar two-step process, called *BIOLIQ*, was developed at the Forschungszentrum Karlsruhe, Germany.²¹ High gasification efficiency (70% at 1200 °C operating temperature) and very high carbon conversion (>99%) have been reported with this process.

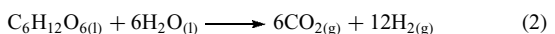
2.1.1 Supercritical Water Gasification

Biomass can be gasified under supercritical water (SCWG) conditions—water above its thermodynamic critical temperature (647 K) and pressure (221.2 bar). Under these conditions, water becomes a fluid with unique properties that can be used in the destruction of hazardous wastes such as PCBs or for the production of H₂,²² although little data for hydrogen via this process are available.

At high-temperature SCWG conditions (800–1000 K), biomass is highly reactive, which increases the gasification efficiency but only at low concentrations. However, the gasification efficiency drops sharply with increasing feed concentration. To solve this problem, high-temperature SCWG is performed in two stages. The first stage involves hydrolysis of biomass to produce water-soluble compounds, followed by gasification in the second stage.²³ The addition of alkalis such as KOH, KHCO₃, and Na₂CO₃ increases the H₂ yield by the gasification of model biomass compounds such as glucose and pryrocatechol.²⁴ To overcome the problem of high recovery costs of the alkali catalysts, zirconia can be used to catalyze high-temperature SCWG reactions; however, the activity of zirconia is lower than that of Na₂CO₃.²⁵

At low temperature, SCWG catalysts are required to achieve high conversions. The catalysts used are generally composed of bimetallic Ru or Ni supported on titania, zirconia, or carbon,²³ which are stable under severe oxidizing and corrosive conditions of the near-critical water. The use of homogeneous alkali solutions²⁴ and heterogeneous alkali metal catalysts²⁶ has also been reported in SCWG, but recovery of such catalysts is a major problem. Metal catalysts such as Ni did not reduce the onset temperature of the hydrolysis reaction but increased the yield of H₂ in the gas

stream. After the hydrolysis of cellulose to produce sugars, the Ni-catalyzed reaction proceeds in a manner similar to the steam-reforming reaction, but in the liquid phase:



However, under these conditions, the methanation reaction is also thermodynamically favorable and therefore some of the hydrogen evolved (equation 1) is consumed to form methane. Ni and many other metal catalysts also suffer from severe corrosion at supercritical water condition, especially at the high temperatures needed for higher H₂ yields. This problem was overcome by using charcoal and other carbons as catalysts for the gasification of tars in supercritical water.²⁷ Carbon may seem to be an unlikely candidate as a catalyst at supercritical water conditions, but the authors showed that in the presence of hydrogen and at the temperatures of supercritical water, carbon catalysts are very stable.²⁸

2.2 Fast Pyrolysis

Pyrolysis of biomass involves the thermal decomposition of the polymeric cellulosic structures in the absence of air or oxygen. This is a slow heating process, with temperatures ranging from 600 to 1200 K, which results mostly in charcoal formation. Therefore, this process is not attractive for producing hydrogen. There is some improvement in H₂ yields using calcium and chromium catalysts,²⁹ but the results are still far from satisfactory.

2.3 Reforming of Biomass-Derived Products

2.3.1 Bio-oils

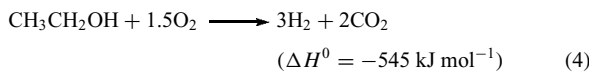
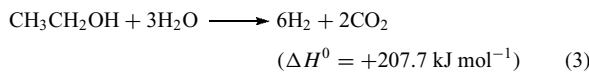
Hydrogen can also be produced from the steam reforming^{30,31} and autothermal reforming of bio-oil products derived from biomass pyrolysis.³² Steam reforming of oxygenated compounds present in bio-oils demonstrated that this reaction competes with the gas-phase thermal decomposition, which may result in coke formation that plugs the reactor and deactivates the catalysts. This problem can be minimized by running the reforming reaction under autothermal conditions. In this latter case, the H₂ yield from these model compounds was found to be 71–78% of the stoichiometric yield, which is comparable to the steam-reforming reaction yields of approximately 80% reported in the literature.³⁰ Recently, H₂ has also been produced from bio-oils using the sequential cracking method.³² Bio-oil sequential cracking is a two-step process, in which catalytic cracking of feed is alternated with a catalyst regeneration step. During the cracking step, the hydrocarbon feed decomposes on a metal catalyst surface (platinum group metals) to produce H₂ and solid carbon on the metal site, which accumulates as

coke. During the regeneration step, the coke deposited on the metal site is combusted or gasified to produce CO₂ and this restores the catalytic activity in the process. This process has an added advantage in that the H₂ and CO₂ are produced in different steps, thereby saving the energy required to purify H₂. Platinum group metals supported on Al₂O₃, ZrO₂, and CeO₂–ZrO₂ have been used for this process.³²

2.3.2 Bioethanol

Among the various feedstocks derived from biomass, bioethanol (a mixture of about 12 wt % ethanol in water) is very attractive because of its relatively high hydrogen content, availability, nontoxicity, and storage and handling safety. More importantly, ethanol can be produced renewably by the fermentation of biomass sources, such as energy plants, agro-food wastes, forestry residues, and urban solid wastes.

Hydrogen can be directly obtained from ethanol by two main processes: steam reforming of ethanol (SRE, equation (3)) and partial oxidation of ethanol (POE, equation (4)). The overall processes are a complex convolution of elementary steps that involve several organic intermediates. Whereas POE offers exothermicity and a rapid response, SRE is endothermic and produces greater amounts of hydrogen, resulting in higher system efficiencies. The third option combines the advantages of both approaches by cofeeding oxygen, steam, and ethanol simultaneously.



Steam Reforming. Ethanol steam reforming is a complex process in which many simultaneous and consecutive reactions are involved, i.e., steam reforming, dehydrogenation, dehydration, decomposition, Boudouard, and WGS.^{33,34} In these reactions, catalysts play a crucial role toward complete conversion of ethanol. Active catalysts should maximize H₂ selectivity and inhibit coke formation as well as CO production. Consistent with this, catalysts for the SRE to produce H₂ selectively must be able to (i) dehydrogenate ethanol, (ii) break the carbon–carbon bonds of surface intermediates to produce CO and CH₄, and (iii) reform these C₁ products to generate hydrogen. On the basis of the influence of the nature of both the metal and the support on the catalytic characteristics of supported metals, the choice of these elements is a key factor in developing supported catalysts that will fulfill the above requirements. Different oxide catalysts,³⁵ metal-based catalysts (Ni, Co, Ni/Cu),^{36,37} and noble metal-based catalysts (Pt, Pd, Rh)^{38,39} have proved to be active in the ethanol-reforming reaction. As a general rule, Rh is generally more effective than other noble metals, such as Pt and Pd, for H₂ production by ethanol steam

reforming. CeO₂, MgO, and La₂O₃ are suitable supports for efficient ethanol reforming on noble metals. The use of Al₂O₃ as support shows significant deactivation of the catalyst after long-term operation. In terms of long-term stability, MgO exhibits the best performance. It is also expected that La₂O₃ may be a suitable support for stable ethanol steam reforming.

Ni is widely used as a low-cost metal catalyst for ethanol reforming. Akande *et al.*⁴⁰ investigated the effects of catalyst synthesis method, Ni loading, and temperature on the catalytic activity of Ni/Al₂O₃ catalysts for ethanol reforming. Three types of preparation methods, namely, coprecipitation, precipitation, and impregnation, were evaluated. Optimal Ni loading of 15% was found for maximum ethanol conversion using Ni/Al₂O₃ catalyst prepared by coprecipitation and precipitation methods. For comparison, Ni loading did not show noticeable effects on Ni/Al₂O₃ activity when the impregnation method was used. Regarding hydrogen production, the catalyst prepared by coprecipitation with Ni loading of 15% showed the best performance. In addition, Ni/Al₂O₃ prepared by coprecipitation also showed the highest selectivity of hydrogen.

Sun *et al.*⁴¹ compared the catalytic activity of Ni catalyst supported on La₂O₃ and Al₂O₃ for H₂ production by ethanol steam reforming at 593 K and atmospheric pressure. The Ni/La₂O₃ catalyst exhibited 99.5% conversion and 48.5% H₂ selectivity and also a high stability due to the formation of a lanthanum oxycarbonate species (La₂O₂CO₃), which could react with surface carbon deposited during the reaction to prevent the deactivation of catalyst.⁴² For comparison, Ni/Al₂O₃ catalyst reached the maximum H₂ selectivity of 47.7% at 573 K.

Besides La₂O₃ and Al₂O₃, other oxides have also been studied as alternative supports for Ni catalyst. Frusteri *et al.*⁴³ reported the effects of alkali addition (Li, Na, and K) on catalytic performance of Ni/MgO. The addition of Li and K was found to enhance the catalyst stability by depressing Ni sintering. Coke formation at Ni/CeO₂ was much faster than that on Ni/MgO.⁴³ This observation could be explained by strong interaction of the CeO₂ support with the adsorbed reaction intermediate species. Their tests also demonstrated that the basic nature of MgO favored ethanol reforming and inhibited coke formation.

Bimetallic or alloy metal catalysts appear quite interesting systems for ethanol steam reforming. Barroso *et al.*⁴⁴ prepared NiZnAl catalysts by citrate sol–gel method for ethanol reforming at 773–873 K. They found that product distribution was very sensitive to the alloy composition. Using Ni loading of 18–25 wt%, a high H₂ selectivity of about 85% was obtained. For CeO₂-supported Ni–Rh bimetallic ethanol-reforming catalyst, it was demonstrated that Ni improves Rh dispersion and smaller CeO₂-support-crystallite size also improves Rh dispersion and leads to strong Rh–CeO₂ interaction.⁴⁵ Marino *et al.* studied catalytic activity of Cu–Ni–K/Al₂O₃ catalysts.⁴⁶ Ethanol dehydrogenation and C–C bond rupture were favored by Cu and Ni, respectively. In

addition, K neutralized the acidic sites of Al₂O₃, minimizing the formation of coke deposits. A series of Cu–Ni–Zn–Al mixed oxide catalysts prepared by the thermal decomposition of Cu_{1-x}Ni_xZnAl-hydrotalcite-like precursors were also tested for ethanol steam reforming.⁴⁷ CuO and NiO were found to distribute on the support ZnO–Al₂O₃. The addition of Cu species facilitated dehydrogenation of ethanol to acetaldehyde, while the presence of Ni led to C–C bond rupture.

Cobalt-based catalysts also exhibited good performance in the ethanol steam-reforming reaction. The ZnO-supported cobalt catalyst exhibited a very high catalytic performance within the temperature range 573–723 K.³⁷ The decomposition of EtOH into acetone occurs to a large extent on Co/ZnO catalysts. Since this reaction results from consecutive reactions, such as dehydrogenation and aldol condensation, activity tests conducted at low contact times have indicated that the reforming reaction is relatively fast, while EtOH decomposition to acetone via aldol condensation of acetaldehyde is depressed. The Co/ZnO catalyst becomes deactivated as a consequence of coke accumulation on the surface of metal particles.

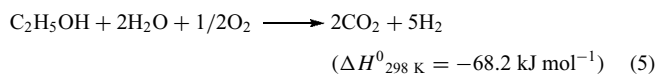
Noble metals supported on porous oxide substrates (Al₂O₃, SiO₂, CeO₂, TiO₂ and MgO)^{39,48–50} are highly active in the steam reforming of ethanol to CO_x and H₂. The nature of the substrate plays a significant role in the SRE over noble metals. When CeO₂–ZrO₂, which has oxygen storage capability, is used as the support of noble metals, ethylene formation is not observed and the order of activity at higher temperature is Pt ≈ Rh > Pd.⁴⁸ Alumina-supported catalysts are very active at low temperatures in the dehydration of ethanol to ethylene. However, at higher temperatures, ethanol is reformed into H₂, CO, CO₂, and CH₄, with an activity order of metals as follows: Rh > Pd > Ni = Pt.⁵¹ Auprêtre *et al.*⁵¹ studied the effect of both the metal and the support in the SRE. They found that at 973 K the hydrogen yield on alumina-supported metal catalysts decreased in the following order: Rh > Pd > Pt > Ru.

In a recent study, Erdohelyi *et al.* reported the performance of Pt, Ir, Pd, Rh, and Ru catalyst supported on Al₂O₃ and CeO₂ in ethanol steam reforming.⁵² By analyzing the surface species in ethanol adsorption on the supported catalysts, it was found that water enhanced the stability of ethoxide surface species, which were formed during the dissociation process of ethanol. Consistent with previous studies, ethylene produced by dehydration of ethanol was observed on Al₂O₃-supported noble metal catalysts, while acetaldehyde derived from dehydrogenation of ethanol was detected on CeO₂-supported catalysts. In addition, hydrogen formation was found to decrease with time on CeO₂-supported noble metal catalysts because of the inhibiting effect of surface acetate species formed on the support.

So far, the development of catalyst for ethanol reforming is basically a trial-and-error approach. Although there exists an important body of work, detailed analyses of reactant species, intermediate product species, and

final product species are lacking. Therefore, the working mechanisms have not been fully understood yet.

Catalytic Partial Oxidation. The POE, (equation (3)) has been investigated with less intensity than in the case of the steam reforming. Partial oxidation is a very interesting process for H₂ production because the catalysts used can be run autothermally, thereby eliminating the need for external heat. It is emphasized that pure POE process is not indicated for bioethanol reforming, since bioethanol is an ethanol–water mixture in which the removal of all the water involves a significant cost. Therefore, for bioethanol partial oxidation, the processes are usually combined with steam reforming in autothermal schemes with the stoichiometry shown in equation (5). Additionally, adding water to the reaction stream is very useful since catalyst stability is improved while coke formation is minimized.



Hydrogen has been produced from ethanol via catalytic autothermal partial oxidation at temperatures of 700–1000 K using noble-metal-based catalysts.^{53,54} Ethanol reforming follows a very complex pathway, including several reaction intermediates. It has been argued that the ethoxy species generated on the metal and on the support can be decomposed on the metal sites, forming CH₄, H₂, and CO, while a part of the ethoxy species generated on the supports is further oxidized to acetate species, which decompose to CH₄ and/or oxidize to CO₂. Thus, supports with redox properties that help the oxidation of ethoxy species and metals with a high capacity to break C–C bonds and to activate C–H bonds are suitable for use in catalysts applied to the POE. Salge *et al.*⁵⁴ studied the effect of the nature of the metal (Rh-, Pd-, Pt-) on the performance of catalysts supported on Al₂O₃ and CeO₂. The yield of H₂ production for catalysts supported on Al₂O₃ followed the order: Rh–Ru > Rh > Pd > Pt. Rh supported on CeO₂ was the most stable and gave higher H₂ selectivity than noble metals supported on Al₂O₃. The better activity and stability associated with the presence of CeO₂ can be related to the capacity of CeO₂ to store oxygen and make it available for reaction via a redox reaction.⁵⁵

2.4 Aqueous Phase Reforming of Biomass-Derived Products

Dumesic *et al.*^{11,56–59} recently developed a catalytic process for the decomposition of oxygenated hydrocarbon into hydrogen. This method involves the conversion of biomass-derived oxygenated hydrocarbons with C:O ratio of 1:1, such as methanol, ethylene glycol, glycerol, glucose, and sorbitol into H₂, CO, CO₂, and light alkanes by the catalytic APR reaction using heterogeneous metal catalysts, within

the temperature range 473–523 K and pressures of 10–50 bar. The principal advantages of this method are as follows: (i) moderate reaction temperature and pressure, which favor the WGS reaction in the same reactor; (ii) low CO level in the gas stream (100–1000 ppm), which is ideal for fuel cell application; and (iii) lower energy requirement compared to that in steam reforming because the oxygenated hydrocarbon feed and water are in the liquid phase. The overall reaction for hydrogen production from oxygenated hydrocarbon with C : O = 1 : 1 by APR is the following:

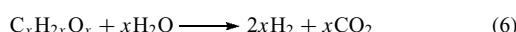


Figure 2 shows the reaction pathways involved in the formation of H₂, CO, CO₂, and alkanes in the aqueous phase ethylene glycol reforming reaction. The reaction pathway for the production of H₂ and CO₂ by APR of oxygenated hydrocarbons involves cleavage of C–C bonds as well as C–H and/or O–H bonds to form adsorbed species on the catalyst surface. Therefore, a good catalyst for the production of H₂ by APR must be highly selective for C–C bond breaking and promote removal of adsorbed CO species by the WGS reaction. However, the catalyst must not catalyze C–O bond cleavage and hydrogenation of CO and CO₂ into CH₄. The C–C bond breaking occurs over Pt and Pd.

Kinetic studies were conducted for the APR of ethylene glycol (a probe molecule for sorbitol) over silica-supported Pd, Ni, Pt, Ir, Ru, and Rh catalysts at moderate temperatures (483–498 K) and pressure (22 bar). The catalytic activity for APR of ethylene glycol, as measured by the rate of CO₂ formation per surface atom at 483 K, followed the order: Pt ~ Ni > Ru > Rh ~ Pd > Ir.⁶⁰ Silica-supported Ni, Ru, and Rh catalysts displayed low selectivity for H₂ production and high selectivity for alkane production. In addition, the Ni/SiO₂ catalyst rapidly deactivated at 498 K. On the contrary, Pt/SiO₂ and Pd/SiO₂ catalysts exhibited higher selectivity for the production of H₂, with lower rates of alkane production. It was also found that both the activity and the selectivity of Pt-based monometallic catalysts can be enhanced by depositing

Pt phase on TiO₂, carbon, and Al₂O₃ substrates⁶¹ or by adding Ni, Co, or Fe to a monometallic Pt/Al₂O₃ catalyst.⁵⁶ Alumina-supported PtNi and PtCo catalysts with Pt/Co or Pt/Ni atomic ratios ranging from 1 : 1 to 1 : 9 had the highest turnover frequencies for H₂ production (moles of H₂ per mole of surface site measured by CO adsorption) with values of 2.8–5.2 min⁻¹ for APR of ethylene glycol solutions at 483 K, compared to a value of 1.9 min⁻¹ for the monometallic Pt/Al₂O₃ under similar reaction conditions.

Nickel catalysts are also active for APR reactions; however, they have low selectivity and stability. The H₂ selectivity of Ni-based catalysts can be enhanced by adding Sn to the Ni catalyst, whereas its stability can be improved by using bulk Ni catalysts, for example, Raney Ni.⁵⁷ The rates of H₂ production by APR of ethylene glycol over an SnNi catalyst with Ni/Sn atomic ratios up to 14 : 1 are comparable to those of a 3 wt % Pt/Al₂O₃ catalyst, based on the reactor volume. Incorporation of Sn to Raney Ni catalysts markedly decreases the rate of methane formation from reactions of CO_x with H₂, while maintaining the high rates of C–C cleavage necessary for the production of H₂. Notwithstanding, the reactor must operate near the bubble-point pressure of the feed and moderate space times to achieve high H₂ selectivities over Raney SnNi catalysts. Remarkably, these Raney SnNi catalysts are stable for more than 250 h on-stream.⁵⁷

2.4.1 Aqueous Phase Reforming of Sugars

Low molecular weight sugars can be directly produced from the hydrolysis of lignocellulosic precursors.^{62,63} However, sugar reforming presents a greater challenge than methanol and ethylene glycol reforming because of the more complex chemical structure of sugars, which determines product selectivity. H₂-selectivity also decreases with increasing number of carbon atoms in the feed molecule. Thus, the H₂-selectivity decreases in the following order: methanol > ethylene glycol > glycerglycerol > sorbitol > glucose.¹¹

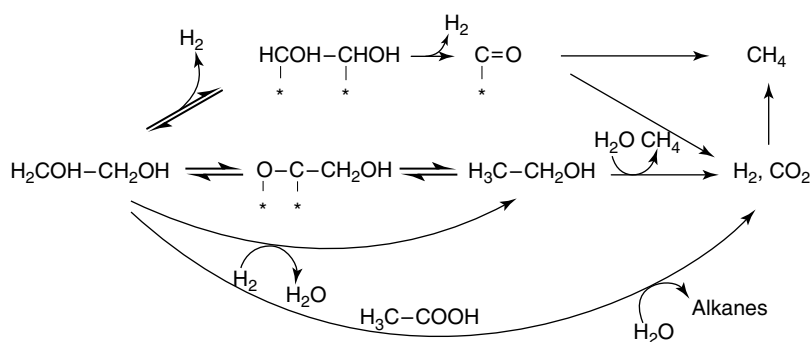


Figure 2 Reaction pathways for ethylene glycol reforming during aqueous phase reforming. The asterisk symbol (*) denotes the adsorption site on a surface metal site. C–C cleavage followed by WGS is the desired pathway whereas the C–O cleavage, dehydration/hydrogenation, and hydrogenation/rearrangement reactions create parallel selectivity issues. (Adapted from Ref. 13. © Elsevier, 2006.)

APR of sugars produces H₂, CO₂, CO, and light alkanes. The reaction pathway of sugar reforming involves cleavage of C–H, C–C, and O–H bonds of sugar molecules to form adsorbed species on the catalyst surface. Adsorbed CO must be removed by the WGS reaction to form CO₂ and additional H₂. Undesired parallel reactions also occur and proceed via C–O bond splitting, followed by hydrogenation to yield alcohols or even acids. Thus, good catalysts for the production of H₂ by APR reactions must be highly active for C–C bond cleavage and also capable of removing adsorbed CO by the WGS reaction, but it must not facilitate C–O bond cleavage and hydrogenation of carbon oxides. H₂ selectivity depends on the feed sugar, the catalyst, and the reaction conditions.

Davda *et al.*⁵⁸ investigated the hydrogenation of glucose to form sorbitol, followed by APR to produce H₂. The hydrogenation of glucose takes place on metal catalysts with high selectivity at low temperature (398 K) and high H₂ pressure (50 bar). However, the APR is H₂-selective at pressures just above the bubble-point pressure of the liquid feed and at moderate space velocities.⁵⁸ Therefore, it may not be practical to operate hydrogenation and APR reactors in series. Recently, an interesting alternative was reported by Fukuoka and Dhepe, whereby cellulose can be directly converted to sorbitol.⁶³ They showed that cellulose hydrolysis to produce glucose can be followed with glucose hydrogenation to yield sorbitol and mannitol in a single reactor. Pt and Ru catalysts supported on Al₂O₃, SiO₂–Al₂O₃, and the ultrastable Y zeolite (HUSY) are active at temperatures ranging from 423 to 473 K and pressure of 50 bar. The maximum yield of 31% (25% sorbitol and 6% mannitol) was obtained with Pt/Al₂O₃ catalyst at 463 K and 50 bar pressure after 24 h reaction. It has been suggested that the acid sites required for the cellulose hydrolysis are produced *in situ* from the dissociation of H₂ on metal sites, in addition to the acidic sites on the support. The dissociated H₂ spills over the support site, and break down the C–O–C bond on Pt and Ru sites to form sorbitol.⁶³

Reforming of sorbitol is more selective for H₂ production compared to sugars because of the lack of an ester group. The APR of sorbitol on alumina nanofiber (ANF)-supported Ni, Pt, Pd, and NiPt bimetallic catalyst was recently investigated.⁵⁹ For an NiPt/ANF catalyst in which the Ni/Pt ratio was 33, the CO bond strength was found to decrease with respect the monometallic Ni/ANF and Pt/ANF catalysts. Such a decrease in CO binding strength results in the removal of adsorbed CO species by WGS reaction and, therefore, a higher fraction of active metal sites is available for the reforming reaction. The turnover frequency (TOF) of H₂ production was found to be maximum for NiPt/ANF, which was 2 and 5 times more than Pt/ANF and Ni/ANF, respectively. The TOF of H₂ production from reforming of 10 wt % sorbitol solution at 473 K and 20 bar using an NiPt/ANF catalyst was found to be 0.074 min⁻¹ at 62.5% sorbitol conversion and 75.6% H₂-selectivity⁵⁹ (Figure 3). This rate of formation compares

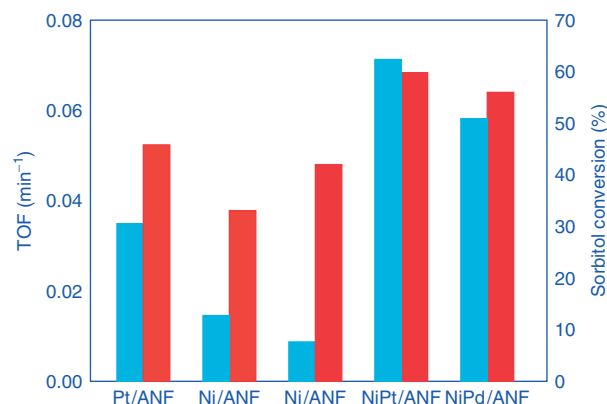


Figure 3 TOF values (blue) and sorbitol conversion levels (red) achieved on several catalysts supported on aluminum nanofibers. (Adapted from Ref. 59. © Elsevier, 2008.)

favorably with the results reported by Cortright *et al.*¹¹ where they achieved H₂ TOF = 1.0 min⁻¹ at 225 °C using a 3% Pt/Al₂O₃ catalyst, but at lower conversion rates. According to Cortright *et al.*,¹¹ the TOF drops sharply with an increase in conversion rate.

3 HYDROGEN FROM SOLAR ENERGY

3.1 Thermochemical Splitting of Water

The most direct method for using solar energy to derive hydrogen from water is the one-step thermolysis of the water molecule. However, the thermodynamics of the thermolysis of water demands very high temperatures to dissociate the molecule (e.g., 3000 K for 64% dissociation at 1 bar).⁶⁴ These temperatures not only require extremely high solar concentrations (38 000 × for 50% efficiency) but material selection for reactor construction at these temperatures also proves challenging. Additionally, direct thermolysis produces a mixture of H₂ and O₂ that requires high-temperature separation based on the use of porous ceramic membranes. Because of material limitations at the high temperatures required, direct water splitting is not expected to be economically viable in the near future.

An alternative to direct thermolysis is the use of a series of processes for the production of hydrogen by multistep thermochemical cycles that bypass the H₂/O₂ separation problem and further allow operating at relatively moderate upper temperatures. Analysis of the most promising thermochemical cycles^{65,66} indicates that two-step water-splitting cycles using metal-oxide redox pair are the most attractive cycles for practical solar applications taking into account its simplicity and efficiency.

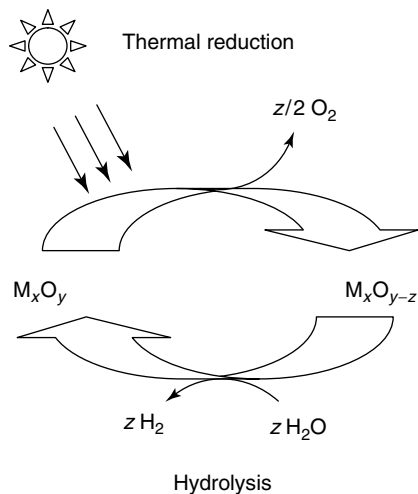
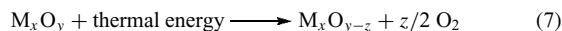


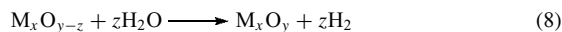
Figure 4 Schematic representation of the two-step water-splitting metal-oxide redox cycle

Two-step metal-oxide redox cycle (Figure 4) proceeds with the endothermic solar thermal dissociation of the metal oxide into the metal or the lower valence oxide (equation (7)), followed by the second, nonsolar, exothermic step corresponding to the hydrolysis of the metal/lower valence oxide to form H_2 and regeneration of the metal oxide (equation (8)). The net reaction is $H_2O + \text{thermal energy} \rightarrow H_2 + 1/2O_2$.

First step (solar):



Second step (nonsolar):



This cycle was originally proposed by Nakamura⁶⁷ using the redox pair Fe_3O_4/FeO . Subsequently, the redox pair ZnO/Zn was also considered as a potential candidate for the two-step thermochemical water splitting.⁶⁸ On the basis of a thermal reduction at 2273 K, the energy efficiency of ZnO/Zn cycle is about 45% and the maximum exergy without heat recovery is 29%.⁶⁹ Consequently, ZnO/Zn is considered as the most favorable cycle given its potential for reaching high energy and exergy efficiencies, but strong technical challenges remain associated with the very high temperature necessary for the thermal reduction of solids. The very high thermal reduction temperature used for the ZnO/Zn (>2235 K) and also for Fe_3O_4/FeO (>2500 K) redox pairs means severe sintering, melting, and vaporization of materials, decreasing the efficiency and durability in the cyclic operation. In addition, in such systems, it is necessary to quench the reduction products (FeO or Zn) in order to avoid reoxidation, introducing irreversibilities and complexities in large-scale utilization. Consequently, the progress in application of material science and engineering to the development of

materials with lower reduction temperature and high water-splitting ability is still a challenge in this scientific area.

3.1.1 Recent Developments in Metal Oxide Redox Pairs Applied to Thermochemical Splitting of Water

With the aim to improve the thermodynamics of the thermal reduction of Fe_3O_4 to FeO , solid solutions between the Fe_3O_4 and M_3O_4 forming ferrites with spinel-type structure have been examined using an approach that involves the possibility of combining the high H_2 yield associated with the Fe_3O_4/FeO redox pair with the high reduction of the M_3O_4/MO pair. Recently, research efforts have focused on various types of ferrites MFe_2O_4 ($M = Co$,^{70,71} Ni ⁷² and Zn).⁷³ These ferrites showed a thermal reduction step that proceeds at lower temperature than in the case of pure Fe_3O_4 : $ZnFe_2O_4 \rightarrow ZnO + 2/3 Fe_3O_4 + 2/3 O_2$ 1800 K⁷³; $NiFe_2O_4 \rightarrow Ni_xFe_{1-y}O + O_2$ 1673 K⁷²; $CoFe_2O_4 \rightarrow CoO + 4/6 Fe_3O_4 + 4/6 O_2$ 1673 K.⁷¹ However, the reduction temperatures of these ferrites are close to their melting points and, therefore, the reduced ferrites sinter after this step, decreasing the H_2 generation in the subsequent hydrolysis cycle. With the aim to prevent the sintering or melting of ferrites during thermal reduction, the supporting of ferrites on monoclinic ZrO_2 that have good sintering resistance in the temperature range from 1273 to 1673 K has been studied.^{70,72} ZrO_2 -supported ferrites showed repeatable two-step water-splitting cycles with hydrogen production rates significantly higher than that with unsupported ferrites. Partially stabilized tetragonal ZrO_2 and yttria-stabilized cubic zirconia (Y CZ) are also studied as supports to suppress the ferrite's high-temperature sintering.⁷⁴ The improvement in the reactivity in repeated cycles observed in the case of ferrites supported on yttria-stabilized zirconia (YSZ) is associated to the formation of an iron-containing YSZ phase by the insertion of Fe^{2+} ions into the YSZ lattice during the thermal reduction. This iron-containing YSZ phase is very reactive in the hydrolysis reaction and also avoids the ferrite sintering because Fe^{2+} ions remains highly dispersed in the YSZ lattice.

Another approach for lowering the reduction temperature of Fe_3O_4 is using the reactivity of the oxygen deficiency of the ferrite with spinel structure. $Ni-Mn$,⁷⁵ $Ni-Zn$, and $Mn-Zn$ ⁷⁶ spinel ferrites can form after reduction at low temperature (1473 K) spinels with oxygen deficiency ($MF_3O_{4-\delta}$) that can decompose H_2O to generate H_2 at 1073 K. In these cycles, the phase transition between ferrite and wustite does not occur in the solid phase and the ferrite retains its spinel-type structure. These cycles require more moderate reduction temperature than those required for Fe_3O_4/FeO cycle, but the amount of hydrogen evolved in this system is very limited because of the small magnitude of nonstoichiometry in the reduced spinel ($\delta < 0.2$) compared to that formed in the normal ferrite process.

To find redox pairs alternative to Fe_3O_4 or ZnO that works at lower temperatures, different metal oxides have

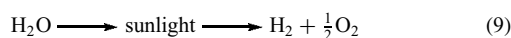
recently been examined. A thermochemical cycle based on CeO₂/Ce₂O₃ has been recently reported by Abanades and Flamant.⁷⁷ Thermodynamic data indicate that CeO₂ may be partially reduced (CeO_{2-δ}) under inert flow at temperatures higher than 1400 K without structural phase transition.⁷⁸ It was estimated that about 3.5% of Ce⁴⁺ was reduced to Ce³⁺ at 1773 K under flowing Ar. The O₂-deficient ceria (CeO_{2-δ}) swiftly decomposes H₂O to generate H₂ at temperatures close to 1273 K. Taking into account that the formation of solid solutions between MO_x (M = Mn, Fe, Ni, Cu, Ca, etc.) and CeO₂ may modify the reducibility of CeO₂,⁷⁹ doped CeO₂ materials (CeO₂–MO_x, M = Mn, Fe, Ni, and Cu) have also been examined as redox pairs for the two-step water splitting.^{78–81} Thermal reduction of these doped CeO₂ solids proceeded at 1573–1773 K, while the subsequent hydrolysis over the reduced phases occurs with the formation of H₂ at 1273 K. Enhancement of H₂ production was observed on these doped CeO₂ solids (at 1773 K: 0.97 cm³H₂ g⁻¹ for Cu–CeO₂, 1.9 cm³H₂ g⁻¹ for Fe–CeO₂, 2.6 cm³H₂ g⁻¹ for Ni–CeO₂, and 3.77 cm³H₂ g⁻¹ for Mn–CeO₂) in comparison with pure CeO₂ (0.7 cm³H₂ g⁻¹) or ferrites supported on YSZ (1.77 cm³H₂ g⁻¹).

Thermochemical cycles based on SnO₂/SnO⁸² and GeO₂/GeO⁸³ are the latest redox pairs studied as alternatives in the water-splitting reaction at low temperatures. The SnO₂/SnO cycle consists of a solar endothermic reduction of SnO₂ into SnO(g) and O₂, followed by a nonsolar exothermic hydrolysis of SnO(s) for H₂ production. According to thermodynamics, the reduction of SnO₂ into SnO is complete at 1873 K under an inert gas flow. The thermal reduction of SnO₂ forms SnO nanoparticles (the reverse reaction between SnO and O₂(g) is noticeable, which requires gas quenching) that can be hydrolyzed in the temperature range 773–873 K, with satisfactory reaction rate and a final yield over 90%. The thermochemical two-step water dissociation based on the SnO₂/SnO redox pair could be considered as an alternative cycle, given its attractive characteristics regarding the low reduction temperature and rapid kinetic. However, it is still necessary to perform further studies to address material stability at high temperature and upon successive cycling. A gallium oxide cycle (GeO₂/GeO redox pair) was the latest two-step thermochemical cycle reported in bibliography.⁸³ Thermal reduction of GeO₂ was demonstrated at low temperature (below 1773 K), but melting of GeO₂ and disproportionation of GeO restricted the practical application of this cycle.

3.2 Photochemical Splitting of Water

One of the most promising renewable energy technologies is the production of hydrogen by water splitting using solar light (equation (3))^{84–86} because the solar energy used as light does not have the inefficiencies associated with thermal transformations or with its conversion to electricity followed by electrolysis. Taking into account that pure water

does not absorb solar radiation, the photochemical splitting of water needs a photocatalyst semiconductor that can absorb sunlight to drive the following reaction:



This reaction has attracted intense research interest since the pioneering work conducted by Honda and Fujishima in 1972 in a photoelectrochemical cell.⁸⁷ This work stimulated the research for overall water-splitting reaction using particulate photocatalysts that was first realized in 1980 by Lehn *et al.*,⁸⁸ Sato and White,⁸⁹ and Domen *et al.*,⁹⁰ which reported stoichiometric evolution of hydrogen and oxygen on particulate photocatalysts suspended on aqueous solutions.

The numerous papers published in the past three decades on the impact of different semiconductor materials on performance in photocatalytic water splitting have clearly proved that the energy conversion efficiency of water splitting is determined principally by the properties of the semiconductors used as photocatalysts. Taking into account the processes involved in the dissociation of water on photocatalysts under visible light irradiation, the materials used as photocatalysts must satisfy several functional requirements with respect to bandgap energy and electrochemical properties: (i) suitable solar visible light absorption capacity and band edge potentials appropriate for overall water splitting; (ii) ability to separate photoexcited electrons from reactive holes; (iii) minimization of energy losses related to charge transport and recombination of photoexcited charges; (iv) chemical stability to corrosion and photocorrosion in aqueous environments; (v) kinetically suitable electron transfer properties from photocatalyst surface to water interface; and (vi) minimum efficiency of solar conversion of 10%. Despite extensive research efforts, no photoactive catalysts have yet been found that fulfill all these requirements. However, the exciting progress made in the field of nanostructured materials during the last few years offers new opportunities for the development of efficient photocatalysts. Among the various approaches undertaken in the search for more efficient and active photocatalysts for water splitting, the following can be mentioned: (i) finding new single-phase materials; (ii) tuning the bandgap energy of UV-active photocatalysts (bandgap engineering); (iii) surface modification of photocatalysts by the deposition of cocatalysts to reduce the activation energy for gas evolution; (iv) sensitization; and (v) nanodesign to control the size, morphology, and defects of photocatalysts.

In the following sections, the advances achieved in the last five years in the photocatalytic water-splitting reaction under visible light are reviewed. Special attention is focused on the formulation of materials as a way to control the electronic energy structure of photocatalysts. Obviously, the formulation of photocatalysts must be combined with appropriate methodologies of synthesis in order to customize the crystallinity, structure defects, and morphology at nanometric

scale since these aspects, as commented previously, have a major impact on the photocatalyst's efficiency for water splitting under visible light.

3.2.1 Development of Photoelectrodes Active under Visible Light for Photoelectrochemical Cells

More than three decades after the initial reports on photoinduced water splitting on semiconductor electrodes,⁸⁷ efficient solar-powered hydrogen production based on this concept remains a challenge. Devices have demonstrated high solar-conversion efficiencies (as high as 12.4%),⁹⁰ but so far no single device has simultaneously satisfied the demands of efficiency, durability, and economic viability.

TiO_2 has been the most extensively investigated material for photoelectrochemical applications because of its excellent chemical stability and low cost. Since TiO_2 absorbs only UV light because of its bandgap of 3.2 eV, most research efforts were aimed at shifting the optical absorption toward the visible part of the solar spectrum. Modifying the band structure of TiO_2 to make it more responsive to visible wavelengths has been an enduring effort, with mixed results. Cationic doping of TiO_2 with metals such as V and Cr has been extensively studied.^{91,92} Although TiO_2 chemically doped with metal ions could, in fact, induce visible light response, these catalysts showed limitations for practical application because the dopant ions introduce defect states in the bandgap that decrease the photocarrier's life time.^{93,94} In 2001, research interest in the sensitization of TiO_2 by anion doping resumed following the work of Asahi *et al.*⁹⁵ This approach consists of the substitution of a nonmetal atom such as N,^{96,97} C,^{98,99} or F¹⁰⁰ for oxygen. The question of whether anionic doping achieves bandgap narrowing in TiO_2 , the extent of any such narrowing and the utility of the resultant materials are a matter of much debate in the scientific literature. A large part of the existing literature agrees that anionic doping produces enhancement in the visible activity. On the other hand, insofar as the photoelectrochemical response of anionically doped TiO_2

is concerned, the improvement of the visible photocurrent response is modest.^{101–103} Therefore, further advances in the structural understanding of these materials are needed to produce a truly viable material.

The morphology and crystallinity of TiO_2 are critical factors in its performance as photoelectrode. Recently, highly structured TiO_2 photoelectrodes (nanowires, nanrods, nanotubes, and nanofibers) attracted more attention since such morphologies enhance the absorption coefficient and provide high surface area and high interfacial charge transfer rate that minimizes the chance for charge trapping and recombination. TiO_2 nanotubes,¹⁰⁴ nanowires,¹⁰⁵ nanofibers,¹⁰⁶ or nanopore arrays¹⁰⁷ (Figure 5) with controlled morphology are reported for the stoichiometric production of H_2 and O_2 by water splitting under visible light. Although efficiency results obtained over these systems are still modest, it allows to illustrate that nanostructure of photoelectrodes is a future way to fabricate photomaterials with faster electron transport and lower recombination rate, which is a key issue for photochemical applications.

In addition to TiO_2 , there are some other traditional metal oxides that have also been investigated extensively in the recent past. Among them, iron oxide ($\alpha\text{-Fe}_2\text{O}_3$, hematite) is especially attractive as a photoanode due to its abundance, stability, and suitable bandgap and valence band edge position. Unfortunately, the reported efficiencies of water oxidation at illuminated hematite electrodes are notoriously low. The poor efficiency of $\alpha\text{-Fe}_2\text{O}_3$ photoanodes has been attributed to a low rate constant of water oxidation by surface-trapped holes¹⁰⁸ and a short hole diffusion length in hematite, which allows only holes created close to the electrolyte interface to oxidize water. It has been proposed to stack several very thin films of $\alpha\text{-Fe}_2\text{O}_3$ in order to minimize hole transfer distances, while still absorbing most of the incident light.^{109,110} Following this proposal, silicon-doped nanocrystalline hematite films synthesized by chemical vapor deposition produce photoanodes that oxidize water under visible light with high efficiency.¹¹¹ The dendritic nanostructure of $\alpha\text{-Fe}_2\text{O}_3$ minimizes the distance

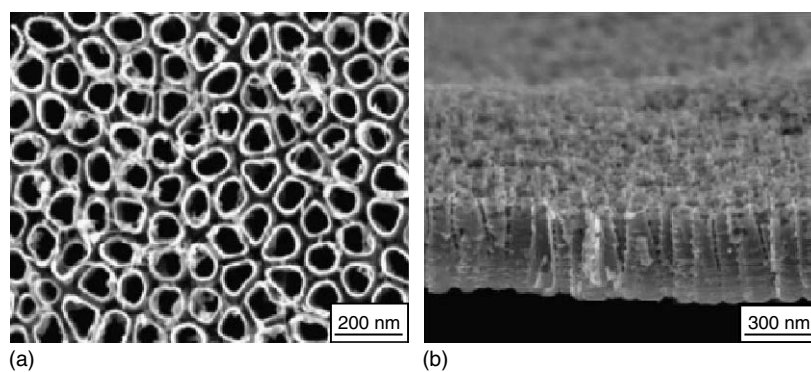


Figure 5 SEM images of TiO_2 nanotube arrays used as photoanode material: (a) top view and (b) cross-sectional view. (Reproduced from Ref. 107. © Elsevier, 2009.)

that photogenerated holes have to diffuse through to the Fe₂O₃/electrolyte interface, increasing the efficiency. The efficiency is further enhanced by the deposition of a thin insulating SiO₂ layer below and a cobalt monolayer on the top of the Fe₂O₃ film. However, the efficiency achieved with these systems remains low (3%) compared to the theoretical value of 16.8% predicted for a material with this bandgap. Higher efficiencies have been obtained in later work¹¹² using a high surface area host (WO₃) to support a thin layer of hematite, allowing photogenerated holes to be produced in high proximity to the semiconductor–liquid junction. Increase in efficiency of ca 20% was observed when using WO₃/Fe₂O₃ host/guest photoanodes when compared to previous development based on dendritic nanostructures.

The photosensitization of wide bandgap semiconductors by adsorbed dyes is also a strategy for populating the conduction band of wide bandgap semiconductors by efficient absorption of visible light by dyes and transfer of electrons from excited dyes to the conduction band of semiconductors. Overall water splitting under visible light has been achieved recently by combining the coumarin-dye-adsorbed Pt/H₄Nb₆O₁₇ with tungsten oxide photocatalysts for O₂ evolution using an I³⁻/I⁻ as redox mediator.¹¹³ A ruthenium polypyridyl dye modified with bidentate carboxylates that serves as both a sensitizer component and a molecular bridge to connect IrO₂ particles to nanoparticulate TiO₂ photocatalysts¹¹⁴ (Figure 6). Although, at present, the quantum efficiency of dye-sensitized H₂ production is still low (e.g., <0.1% for the coumarin-dye-adsorbed Pt/H₄Nb₆O₁₇ systems and 0.9% for ruthenium dye-IrO₂-TiO₂), improvements in efficiency are in progress with the structural design of the dye molecules as well as optimization of the contact between the dye and the semiconductor surfaces.

Another way to obtain stable and active photoelectrodes is the study and the synthesis of new semiconductor phases. In this regard, nitrogen- and carbon-doped In₂O₃ thin

films^{115,116} as well as complicated oxides, such as LaTiO_xN_y thin films,¹¹⁷ have been demonstrated to drive photoelectrochemical reactions for water splitting under irradiation with visible light. However, the activities of the aforementioned photocatalysts are usually low under visible light irradiation because of the relatively large bandgaps.

Stacked high-quality p–n junction cells prepared by the chemical vapor deposition technique were also used as electrodes for high-efficiency solar water splitting.^{118,119} Unfortunately, these electrodes were expensive for practical application. Very recently, several studies have been made on low-cost-oriented composite semiconductor electrodes.^{120,121} A composite semiconductor electrode composed of multiple thin films “n-Si/pCuI/n-pGaP/RuO₂” showed interesting results for full solar water splitting, yielding a solar-to-chemical conversion of 2.3%.¹²¹ The conversion efficiencies for these electrodes are not high enough, yet the electrodes of this type are of much interest because they have the potential ability to achieve high efficiency at low cost.

3.2.2 Development of Particulate Photocatalysts Active under Visible Light

An alternative approach to photoelectrochemical cells is to simply disperse the photocatalysts in water. In particulate photocatalytic systems, the photocatalysts are in the form of particles or powders suspended in aqueous solution in which each particle acts as a microphotoelectrode that performs both the oxidation and the reduction reactions of water on its surface. This eliminates the need for a conducting substrate, enabling the use of conventional synthesis routes, which are therefore much simpler and less expensive to develop and use than photoelectrochemical cells. However, particulate photocatalytic systems have disadvantages when compared to photoelectrochemical cells with regard to the separation of charge carriers, which is not as efficient as with a photoelectrode system, and there are difficulties associated with the effective separation of the stoichiometric mixture of oxygen and hydrogen to avoid the backward reaction.

Many types of semiconductors, with over 130 materials including oxides, nitrides, sulfides, carbides, and phosphides, have been reported to act as efficient particle photocatalysts for hydrogen evolution via water splitting. Unfortunately, most of the photocatalysts are active only under UV light, that is, the materials active under visible light are quite limited. So far, the quantum efficiency for overall water splitting over visible light-driven particle photocatalysts only achieves low values. A 5.9% quantum yield is the maximum value reported over Rh_{2-y}Cr_yO₃/(Ga_{1-x}Zn_x)(N_{1-x}Zn_x) photocatalysts under visible irradiation.¹²² The low quantum yield is still the current “bottleneck” of this photocatalyst process. The efficiency values achieved are still far from the quantum yield of 10%, marked as the initial starting point for practical application. Consequently, progress in application of material science and

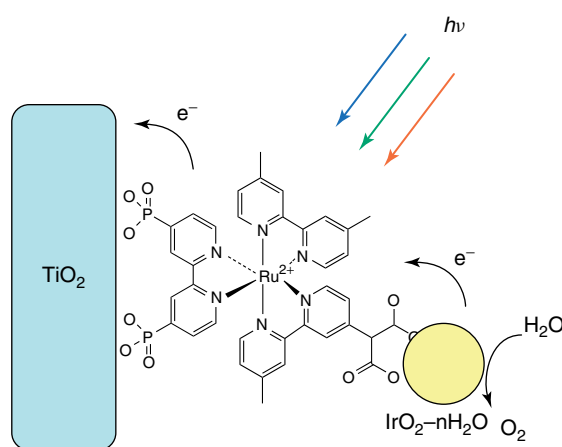


Figure 6 Diagram of dye-sensitized TiO₂ according to Youngblood *et al.* (Reproduced from Ref. 114. © American Chemical Society.)

engineering to the development of efficient semiconductors used as photocatalysts is still a major issue.

Recent Developments in Particulate Photocatalysts

Active under Visible Light Using Sacrificial Reagents. The photocatalytic activities of semiconductors for water splitting are often conducted in the presence of reducing reagents (alcohols, sulfides, sulfites, EDTA, etc.) or oxidizing ones (persulfate, Ag^+ , Fe^{3+} , etc.) to facilitate either water reduction or oxidation. Reactions using sacrificial reagents are regarded as half reactions of water splitting and are not “overall” water-splitting reactions but are often carried out as test reactions for photocatalytic H_2 or O_2 evolution. However, one should note that the results obtained using redox reagents do not guarantee activity for overall water splitting using pure water. In this section, we review the particulate photocatalytic systems recently reported in the literature for H_2 evolution using sacrificial reagents (Table 1). Readers interested in aspects related to photocatalytic systems developed for O_2 evolution are referred to a series of excellent review articles on this subject.^{123,124}

The doping of foreign metal ions into SrTiO_3 and $\text{La}_2\text{Ti}_2\text{O}_7$ is a conventional method for the development of visible-light-driven photocatalysts based on these titanates. A survey of dopants for SrTiO_3 revealed that the codoping of Cr^{3+} – Ta^{5+} or Ni^{2+} – Ta^{5+} was effective in making SrTiO_3 visible light responsive.^{125,126} These doped SrTiO_3 semiconductors loaded with Pt cocatalysts (the cocatalyst improves the efficiency of photocatalysts reducing the

possibility of electron–hole recombination and reducing the activation energy for the reduction/oxidation of water) have shown activity for H_2 production from aqueous methanol solutions under visible light irradiation. On the other hand, doping of $\text{La}_2\text{Ti}_2\text{O}_7$ with Cr^{3+} or Fe^{3+} ions allows visible light absorption above 400 nm.^{127,128} The doped- $\text{La}_2\text{Ti}_2\text{O}_7$ samples are active for H_2 evolution under visible light only in the presence of methanol as a sacrificial electron donor.

Tantalate and niobate oxides with corner-sharing of MO_6 ($\text{M} = \text{Ta}, \text{Nb}$) octahedral structure have been considered as photocatalysts for water splitting. An approach to increase the visible response of photocatalysts based on tantalates and niobates is to form oxynitride compounds to reduce the bandgap of the materials. Following this strategy, MTaO_2N ($\text{M} = \text{Ca}, \text{Sr}, \text{Ba}$), TaON , and $\text{Sr}_2\text{Nb}_2\text{O}_{7-x}\text{N}_x$ ($x = 1.5$ – 2.8) have been studied as photocatalysts for the production of H_2 from aqueous solutions using methanol as a sacrificial reagent under visible light irradiation.^{129,132} BiTaO_4 doped with Cu^{2+} and loaded with RuO_2 cocatalyst was found to have activity in the H_2 production from methanol aqueous solutions.¹³⁰ A new bandgap in the visible light range is obtained by Cu-doped BiTaO_4 , which is attributed to the transition from the donor level resulting from the Cu impurity to the conduction band of BiTaO_4 . Much effort has been devoted to studying the photocatalytic properties of the potassium niobate oxides, $\text{K}_4\text{Nb}_6\text{O}_{17}$,¹⁴⁵ $\text{K}_6\text{Nb}_{10}\text{O}_{30}$,¹⁴⁴ and KNbO_3 ,¹⁴⁶ because of their unique structure. In particular, $\text{K}_4\text{Nb}_6\text{O}_{17}$ with an anisotropic-layered structure has high potential for photocatalytic applications. A series of nickel oxide

Table 1 Overview of particulate photocatalysts reported in literature for H_2 production from aqueous solutions with sacrificial reagents under visible light

Photocatalysts	Cocatalyst	Sacrificial reagent	Activity ($\mu\text{mol h}^{-1} \text{g}^{-1}$)	Reference
SrTiO_3 –Cr–Ta	Pt	CH_3OH (0.1 M)	140	125
SrTiO_3 –Ni–Ta	Pt	CH_3OH (10% vol)	8	126
$\text{La}_2\text{Ti}_2\text{O}_7$ –Cr	Pt	CH_3OH (0.3 M)	30	127
$\text{La}_2\text{Ti}_2\text{O}_7$ –Fe	Pt	CH_3OH (0.3 M)	20	128
CaTaO_2N	Pt	CH_3OH (0.06 M)	37	129
SrTaO_2N	Pt	CH_3OH (0.06 M)	50	129
BaTaO_2N	Pt	CH_3OH (0.06 M)	37	129
$\text{BiTa}_{1-x}\text{Cu}_x\text{O}_4$	RuO_2	CH_3OH (5% vol)	900	130
$\text{K}_4\text{Nb}_6\text{O}_{17}$	NiO	CH_3OH (20% vol)	144	131
$\text{Sr}_2\text{Nb}_2\text{O}_{7-x}\text{N}_x$	Pt	CH_3OH (0.14 M)	80	132
G–C ₃ N ₄	Pt	triethanolamine (10% vol)	108	133
KNbO_3 /CdS	Ni/NiO	isopropanol (30% vol)	150	134
ZnO/CdS	Pt	S^{2-} (0.1 M)/ SO_3^{2-} (0.1 M)	1800	135
MoS ₂ /CdS	—	S^{2-} (0.1 M)/ SO_3^{2-} (0.1 M)	510	136
ZnO/CdO/CdS	—	S^{2-} (0.1 M)/ SO_3^{2-} (0.04 M)	11.6	135
$\text{Cd}_{0.7}\text{Zn}_{0.3}\text{S}$	—	S^{2-} (0.1 M)/ SO_3^{2-} (0.04 M)	350	137
$(\text{Zn}_{0.95}\text{Cu}_{0.05})_x\text{Cd}_{1-x}\text{S}$	Pt	S^{2-} (0.35 M)/ SO_3^{2-} (0.25 M)	3620	138
$(\text{AgIn})_x\text{Zn}_2(1-x)\text{S}_2$	Pt	S^{2-} (0.35 M)/ SO_3^{2-} (0.25 M)	3133	139
$(\text{CuIn})_x\text{Zn}_2(1-x)\text{S}_2$	Ru	S^{2-} (0.35 M)/ SO_3^{2-} (0.25 M)	4000	140
$(\text{CuAg In})_x\text{Zn}_2(1-x)\text{S}_2$	Ru	S^{2-} (0.35 M)/ SO_3^{2-} (0.25 M)	7666	141
$\text{AgGa}_{0.9}\text{Ag}_{0.1}\text{S}_2$	Pt	S^{2-} (0.1 M)/ SO_3^{2-} (0.02 M)	3500	142
$\text{Na}_{14}\text{In}_{17}\text{Cu}_3\text{S}_{35}$	—	S^{2-} (0.5 M)	18	143

intercalated layered K₄Nb₆O₁₇ (Ni/Nb ratio range of 0.8–5%) were reported recently as active systems for the production of H₂ in the presence of methanol as sacrificial electron donor.¹³¹ The high catalytic performance was attributed to the well-dispersed NiO nanoclusters intercalated into the bulk structure of K₄Nb₆O₁₇ that act as very effective cocatalysts.

Recently, carbon nitride (Figure 7) prepared by heating cyanamide to temperatures between 673 and 873 K was prepared and tested in water-splitting reaction.¹³³ The bandgap of the condensed graphitic carbon nitride was found to be 2.7 eV from its UV–visible spectrum, showing an intrinsic semiconductorlike absorption in the blue region of the visible spectrum. The as-prepared g-C₃N₄ achieved steady H₂ production from water containing triethanolamine as a sacrificial electron donor on light illumination ($\lambda > 420$ nm).

Metal sulfide materials are also attractive photocatalysts for the water-splitting reaction because of their small bandgaps that allow for the absorption of visible light. Although the photodegradation is a drawback of the metal sulfide photocatalyst, the photocorrosion may be effectively suppressed by using an Na₂S/Na₂SO₃ salts mixture as an electron donor.

Recent studies have focused on CdS and ZnS and their solid solutions. Changes in CdS photoactivity are also studied by combining the CdS with other semiconductors with different energy levels: KNbO₃,¹³⁴ ZnO,^{135,147} MoS₂,¹³⁶ or CdO.¹³⁵ In these composite systems, the photogenerated electrons move from CdS to the surrounding semiconductors, while photogenerated holes

remain in CdS. This charge–carrier separation stops charge recombination, thereby improving the photocatalytic activity of CdS. The incorporation of Zn^{137,148} or CuZn¹³⁸ in the structure of CdS to make a solid solution is another strategy for improving the photocatalytic properties of CdS. These solid solutions with a narrow bandgap showed high photocatalytic activities for H₂ from aqueous solutions containing sacrificial reagents.

ZnS is another sulfide semiconductor investigated for photochemical water splitting. ZnS cannot split water under visible light because of its wide bandgap (3.66 eV) that restricts light absorption to the UV region. Solid solutions of AgInS₂–ZnS,¹³⁹ CuInS₂–ZnS,¹⁴⁰ and CuInS₂–AgInS₂–ZnS¹⁴¹ are effective strategy for improving the optical absorption of ZnS in the visible range. The optical adsorption of these solid solutions can be adjusted between 400 and 800 nm depending on its composition. Ru loaded on Cu_{0.25}Ag_{0.25}In_{0.5}ZnS₂ showed the highest activity for H₂ evolution, with an apparent quantum yield of 7.4% at 520 nm.¹⁴¹

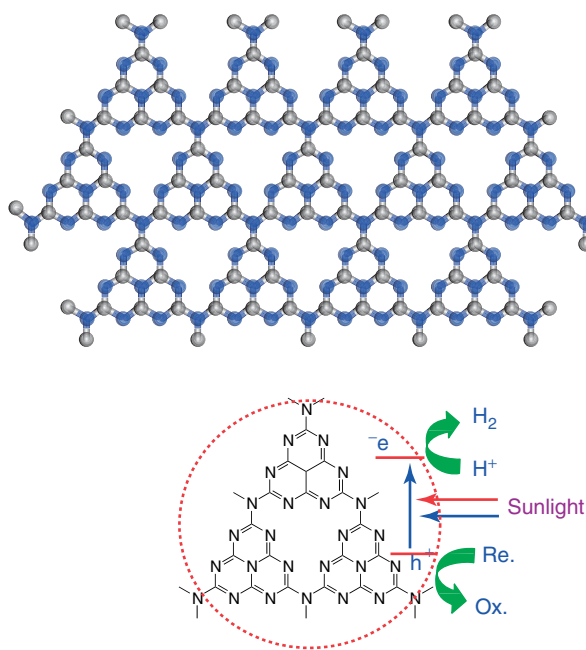
Other ternary sulfides based on solid solutions of In₂S₃–AgGaS₂ have shown activity under visible light.¹⁴² Indium substitution enhanced the visible light absorption of AgGaS₂. Under visible light irradiation, AgGa_{0.9}In_{0.1}S₂ showed the maximum activity for the reduction of H⁺ to H₂ in the presence of a sacrificial electron donor (Na₂S–Na₂SO₃). Other types of sulfides based on open-framework chalcogenides comprising In³⁺ and one type of transition metal cation (Cd²⁺, Zn²⁺, Ag⁺, Cu⁺, Mn²⁺, etc.) have been recently demonstrated to be active photocatalysts for the reduction of water under visible light.¹⁴³ Compared to dense semiconductors, these porous semiconductors showed efficiency (3.7% at 420 nm was reported for the most active Na₁₄In₁₇Cu₃S₃₅ sample) that still requires further improvements. However, the advantages of porous semiconductors, such as high surface area and the easy incorporation of light sensitizers, provide new opportunities that can be explored to maximize photocatalytic efficiency.

Particulate Photocatalysts Active for Overall Water-Splitting under Visible Light. Table 2 presents an overview of recently reported particulate photocatalysts that are able

Table 2 Overview of particulate photocatalysts reported in literature for overall water splitting (without sacrificial reagents) under visible light

Photocatalysts	Cocatalyst	Activity (μmol h ⁻¹ g ⁻¹)			Reference
		H ₂	O ₂		
(Ga _{0.82} Zn _{0.18}) (N _{0.82} O _{0.18})	Rh _{2-y} Cr _y O ₃	3090	1353		122
Zn _{1.44} GeO _{0.38} N ₂	Rh _{2-y} Cr _y O ₃	2075	1010		155
TiS ₂	—	32	<16		156
BYWO ₆	RuO ₂	69	41		157
Bi _{0.5} Dy _{0.5} VO ₄	Pt–Cr ₂ O ₃	17.5	7		158

Figure 7 Schematic diagram of a perfect graphitic carbon nitride sheet constructed from melem units. (Reproduced from Ref. 133. © Nature Publishing Group.)



to split water without the need for any sacrificial agents. Nitrides and oxynitrides of transition metal cations with d¹⁰ electronic configuration (Ga³⁺, Ge⁴⁺) constitute a class of photocatalysts suitable for the water-splitting reaction under visible light illumination without sacrificial reagents. The valence bands of these oxynitride materials are populated by N 2p and O 2p orbitals, resulting in more negative valence band levels and smaller bandgaps compared to those of conventional oxide semiconductors, allowing visible-light-induced H₂ production from water. In the development of oxynitride with d¹⁰ electronic configuration, the solid solution between GaN and ZnO ((Ga_{1-x}Zn_x)(N_{1-x}O_x)) was the first particulate photocatalyst system capable of performing overall water splitting by one-step photoexcitation under visible light.^{122,149–154} The absorption edge of (Ga_{1-x}Zn_x)(N_{1-x}O_x) depends on the concentration of zinc and oxygen, and the highest photocatalytic activity is obtained in a narrow compositional range of about x = 0.18.¹²² For efficient use of solar energy, however, (Ga_{1-x}Zn_x)(N_{1-x}O_x) must be modified by superficial deposition of cocatalyst nanoparticles. Optimized (Ga_{1-x}Zn_x)(N_{1-x}O_x) with Rh_{2-x}Cr_xO₃ cocatalyst achieves 5.9% of quantum yield.¹²²

The solid solution between ZnO and Ge₃N₄ ((Zn_{1+x}Ge)(N₂O_x)) has also been found to be an active oxynitride photocatalyst for pure water splitting under visible light.^{155,159,160} Through optimization of the preparation conditions (nitridation under NH₃ followed by N₂ calcination) and cocatalyst loading (Rh_{2-x}Cr_xO₃), the apparent quantum efficiency of solid solution (Zn_{1-x}Ge_x)(N₂O_x) for overall water splitting under visible light was 2% at 420 nm.¹⁵⁵

A new class of titanium semiconductor, titanium disilicide (TiSi₂), which absorbs a wide range of the solar spectrum, has recently been proposed as a prototype photocatalyst for the water-splitting reaction.¹⁵⁶ A conversion efficiency of 4% has been reported for this system.

Certain class of oxide solid solutions, BiYWO₆¹⁵⁷ and Bi_{0.5}Dy_{0.5}VO₄,¹⁵⁸ have recently been proposed as active photocatalysts for the overall water-splitting reaction under visible light. Solid solution of BiVO₄ and DyVO₄ (Bi_{0.5}Dy_{0.5}VO₄) showed photocatalytic activity to split water into H₂ and O₂ under visible light irradiation. As opposed to other oxides, the valence bands of the solid solution consist of 6s orbitals of Bi mixed with 2p states of O that lead to an increase in valence band potentials and a decrease in bandgap energy. However, the activity so far achieved over this type of photocatalysts is very low (H₂ production of 34.5 μmol h⁻¹ over 0.1 g of Bi_{0.5}Dy_{0.5}VO₄ with Pt–Cr₂O₃ cocatalyst). On the other hand, the solid solution BiYWO₆ responds to visible light up to 470 nm. In this case, the efficiency for water splitting under visible light so far achieved is also very low. For example, a quantum efficiency of only 0.17% at 420 nm was reported for BiYWO₆ solid solution with RuO₂ as a cocatalyst. Nevertheless, the activity of this type of photocatalysts can be expected to be promoted by changing the ratio of Bi/Y/W in the flexible structure of the solid solution.

4 CONCLUSIONS

Methane steam reforming is a standard technology employed in industrial production of H₂, but it produces massive amounts of CO₂, which has an impact on global warming. One approach to reduce CO₂ emissions is to apply reforming methods to alternative renewable precursors. Biomass precursors derived from plant crops, agricultural residues, woody biomass, etc., can be converted to a gas mixture from which hydrogen is extracted. Virtually no net GHG emissions result because a natural cycle is maintained, in which carbon is extracted from the atmosphere during plant growth and is released during hydrogen production, although time constants of the carbon cycle are different. Since these technologies are already advanced from decades of research and development, it is unlikely that there will be a substantial improvement in their performance in future.

Their performance can, however, be improved by new reactor designs such as catalytic membrane reactors, which enhance syngas conversion by shifting the equilibrium of the WGS reaction. The challenge for bioethanol steam reforming is the carbon deposition on the catalyst, which can further cause catalyst deactivation. Despite limited studies in the literature, the design of a novel autothermal reactor with millisecond contact time appears promising for efficient reforming of bioethanol or other forms of hydrocarbons. APR of sugars and sugar alcohols has attracted attention recently because of its several advantages. The most important advantage is that the hydrogen stream contains very low CO concentration, which is ideal for fuel cell application. However, the APR is only at the research and development stage.

There is a need to develop nonconventional processes for H₂ production outside the C-cycle. One of the most promising renewable energy technologies is the production of H₂ by water splitting using solar energy. Two-step metal oxide redox cycles are considered as one of the most attractive cycles for practical solar H₂ production, taking into account its simplicity and potential for reaching high energy and exergy efficiencies, but strong technical challenges remain associated with the very high temperature necessary for the thermal reduction of solids. Consequently, the progress in material science applied to the development of materials with lower reduction temperature and high water-splitting ability is still a challenge in this scientific area. Water-splitting reaction using photonic energy technology on semiconductor surfaces offers the most promising renewable energy technology in the production of H₂. However, more than three decades after the initial reports of photoinduced water splitting on semiconductor electrodes, efficient solar-powered hydrogen production based on this concept remains a challenge. Improving the efficiency of photocatalysts requires developments based on an understanding of the sophisticated factors that determine the photoactivity for the water-splitting reaction: (i) molecular reaction mechanisms involved in the

oxidation and reduction of water on photocatalyst surfaces; (ii) structure and defect chemistry of photocatalyst surfaces; and (iii) charge transfer mechanisms between semiconductor surfaces and cocatalysts. Till date, these factors have not been elucidated in sufficient detail and should be investigated as a means of refining the materials to maximize efficiency. On the other hand, the search for new photocatalytic materials with improved semiconducting and electrochemical properties is still likely to be the key to success. These areas represent significant opportunities for improving water-splitting photocatalysts.

5 ACKNOWLEDGMENTS

We are grateful to many of our colleagues for stimulating discussions and to our research sponsors CICyT and CAM (Spain) under grants ENE2007-67533-C02-01 and S-0505/EN/0404, respectively, and also to King Saud University, Riyadh (Saudi Arabia). One of the authors (MCAG) would also like to acknowledge financial support from the Ministerio de Educación y Ciencia (Spain) through the R&C Program.

6 RELATED ARTICLES

Photocatalytic Hydrogen Production from Water; Thermochemical Water-Splitting.

7 ABBREVIATIONS AND ACRONYMS

ANF = alumina nanofiber; APR = aqueous phase reforming; GHG = greenhouse gas; HyPr-RING = hydrogen production by reaction-integrated novel gasification; ICE = internal combustion engine; POE = partial oxidation of ethanol; SCWG = gasified under supercritical water; SRE = steam reforming of ethanol; TOF = turnover frequency; WGS = water gas shift; YCZ = yttria-stabilized cubic zirconia; YSZ = yttria-stabilized zirconia.

8 FURTHER READING

A. Aboudhei, A. J. Akande, R. O. Idem, and A. K. Dalai, *Int. J. Hydrogen Energy*, 2006, **31**, 752.

9 REFERENCES

- P. Crane and D. S. Scott, *Int. J. Hydrogen Energy*, 1992, **17**, 543.
- M. A. Peña, J. P. Gomez, and J. L. G. Fierro, *Appl. Catal. A: Gen.*, 1996, **144**, 7.
- J. A. Armor, *Appl. Catal. A: Gen.*, 1998, **176**, 159.
- D. L. Trimm and Z. I. Onsan, *Catal. Rev.-Sci. Eng.*, 2001, **43**, 31.
- R. M. Navarro, M. A. Peña, and J. L. G. Fierro, *Chem. Rev.*, 2007, **107**, 3952.
- M. I. Hoffert, K. Caldeira, G. Benford, D. R. Criswell, C. Green, H. Herzog, A. K. Jain, H. S. Kheshgi, K. S. Lackner, J. S. Lewis, H. D. Lightfoot, W. Manheimer, J. C. Mankins, M. E. Mael, L. J. Perkins, M. E. Schlesinger, T. Volk, and T. M. L. Wigley, *Science*, 2002, **298**, 981.
- A. E. Farrell, R. J. Plevin, B. T. Turner, A. D. Jones, M. O'Hare, and D. M. Kammen, *Science*, 2006, **311**, 506.
- G. Chen, J. Andries, H. Spliethoff, M. Fang, and P. J. van de Enden, *Solar Energy*, 2004, **76**, 345.
- G. Taralas and M. G. Kontominas, *J. Anal. Appl. Pyrolysis*, 2006, **76**, 109.
- J. R. Rostrup-Nielsen, *Phys. Chem. Chem. Phys.*, 2001, **3**, 283.
- R. D. Cortright, R. R. Davda, and J. A. Dumesic, *Nature*, 2002, **418**, 964.
- R. M. Navarro, M. C. Sanchez-Sanchez, M. C. Alvarez, F. del Valle, and J. L. G. Fierro, *Energy Env. Sci.*, 2009, **2**, 35. references therein.
- G. W. Huber and J. A. Dumesic, *Catal. Today*, 2006, **111**, 119.
- T. A. Milne, N. Abatzoglou, R. J. Evans, Report No. NREL/TP-570-25357, NREL, Golden, Colorado, 1998.
- J. Corella, M. P. Aznar, J. Gil, and M. A. Caballero, *Energy Fuels*, 1999, **13**, 1122.
- D. Sutton, B. Kelleher, and J. R. H. Ross, *Fuel Process. Technol.*, 2001, **73**, 155.
- K. Tomishige, M. Asadullah, and K. Kunimori, *Catal. Today*, 2004, **89**, 389.
- D. Dayton, Report No. NREL/TP-510-32815, NREL, Golden, Colorado, 2002.
- S. Lin, M. Harada, Y. Suzuki, and H. Hatano, *Fuel*, 2002, **81**, 2079.
- M. Rudloff, 'SYNBIOS-Second Generation Automotive Biofuel Conference', Stockholm, Sweden, 18–20 May, 2005.
- U. Santo, H. Seifert, T. Kolb, L. Krebs, D. Kuhn, and H. J. Wiemer, *Chem. Eng. Technol.*, 2007, **30**, 967.
- D. B. Levin and R. Chahine, *Int. J. Hydrogen Energy*, 2010, **35**(10), 4962.
- Y. Matsumura, T. Minowa, B. Potic, S. R. A. Kersten, W. Prins, and W. P. M. van Swaaij, *Biomass Bioenergy*, 2005, **29**, 269.

24. A. Kruse, D. Meier, P. Rimbrecht, and M. Schacht, *Ind. Eng. Chem. Res.* 2000, **39**, 4842.
25. M. Watanabe, H. Inormata, M. Osada, T. Sato, T. Adschiri, and K. Arai, *Fuel*, 2003, **82**, 545.
26. T. Minowa, F. Zhen, and T. Ogi, *J. Supercrit. Fluids*, 1998, **13**, 253.
27. X. Xu, Y. Matsumura, J. Stenberg, M. J. Antal, Jr, *Ind. Eng. Chem. Res.* 1996, **35**, 2522.
28. M. J. Antal, S. G. Allen, D. Schulman, X. Xu, and R. J. Divilio, *Ind. Eng. Chem. Res.*, 2000, **39**, 4040.
29. G. Chen, J. Andries, and H. Spliethoff, *Energy Convers. Manag.*, 2003, **44**, 2289.
30. S. Czernik, R. Evans, and R. French, *Catal. Today*, 2007, **129**, 265.
31. K. Polychronopoulou, J. L. G. Fierro, and A. Efstathiou, *J. Catal.*, 2004, **228**, 417.
32. E. C. Vagia and A. A. Lemonidou, *Int. J. Hydrogen Energy*, 2008, **33**, 2489.
33. P. D. Vaidya and A. E. Rodrigues, *Chem. Eng. J.*, 2006, **117**, 39.
34. M. Ni, D. Y. C. Leung, and M. K. H. Leung, *Int. J. Hyd. Energy*, 2007, **32**, 3238.
35. J. Llorca, P. R. de la Piscina, J. Sales, and N. Homs, *Chem. Commun.* 2001, 641.
36. A. N. Fatsikostas, D. I. Kondarides, and X. E. Verykios, *Chem. Commun.* 2001, 851.
37. J. Llorca, N. Homs, J. Sales, and P. R. de la Piscina, *J. Catal.*, 2002, **209**, 306.
38. V. Fierro, O. Akdim, and C. Mirodatos, *Green Chem.*, 2003, **5**(1), 20.
39. R. N. Navarro, M. C. Alvarez-Galván, M. C. Sanchez-Sánchez, F. Rosa, and J. L. G. Fierro, *Appl. Catal. B: Environ.*, 2005, **55**(4), 229.
40. A. J. Akande, R. O. Idem, and A. K. Dalai, *Appl. Catal. A: Gen.*, 2005, **287**, 159.
41. J. Sun, X. P. Qiu, F. Wu, and W. T. Zhu, *Int. J. Hydrogen Energy*, 2005, **30**, 437.
42. M. C. Sánchez-Sánchez, R. M. Navarro, and J. L. G. Fierro, *Catal. Today*, 2007, **129**, 336.
43. F. Frusteri, S. Freni, V. Chiodo, L. Spadaro, O. D. Blasi, G. Bonura, and S. Cavallaro, *Appl. Catal. A: Gen.*, 2004, **270**, 1.
44. M. N. Barroso, M. F. Gomez, L. A. Arrua, and M. C. Abello, *Appl. Catal. A: Gen.*, 2006, **304**, 116.
45. J. Kugai, V. Subramani, C. Song, M. H. Engelhard, and Y. H. Chin, *J. Catal.*, 2006, **238**, 430.
46. F. Marino, G. Baronetti, M. Jobbagy, and M. Laborde, *Appl. Catal. A: Gen.*, 2003, **238**, 41.
47. S. Velu, K. Suzuki, M. Vijayaraj, S. Barman, and C. S. Gopinath, *Appl. Catal. B: Environ.*, 2005, **55**, 287.
48. J. P. Breen, R. Burch, and H. M. Coleman, *Appl. Catal. B: Environ.*, 2002, **39**, 65.
49. A. N. Fatsikostas, D. I. Kondarides, and X. E. Verykios, *Catal. Today*, 2002, **75**, 145.
50. S. Freni, S. Cavallaro, N. Mondello, L. Spadaro, and F. Frusteri, *J. Power Sources*, 2002, **108**, 53.
51. G. Auprête, C. Descorme, and D. Duprez, *Catal. Commun.*, 2002, **3**, 263.
52. A. Erdohelyi, J. Rasko, T. Kecskes, M. Toth, M. Domok, and K. Baan, *Catal. Today*, 2006, **116**, 367.
53. L. V. Mattos and F. B. Noronha, *J. Catal.*, 2003, **233**, 453.
54. J. R. Salge, G. A. Deluga, and L. D. Schmidt, *J. Catal.*, 2005, **235**, 69.
55. C. Wheeler, A. Jhalani, E. J. Klein, S. Tummala, and L. D. Schmidt, *J. Catal.*, 2004, **223**, 191.
56. G. W. Huber, J. W. Shabaker, S. T. Evans, and J. A. Dumesic, *Appl. Catal. B: Environ.*, 2006, **62**, 226.
57. J. W. Shabaker, D. A. Simonetti, R. D. Cortright, and J. A. Dumesic, *J. Catal.*, 2005, **231**, 67.
58. R. R. Davda, J. W. Shabaker, G. W. Huber, R. D. Cortright, and J. A. Dumesic, *Appl. Catal. B: Environ.*, 2005, **56**, 171.
59. A. Tanksale, J. N. Beltramini, J. A. Dumesic, and G. Q. Lu, *J. Catal.*, 2008, **258**, 366.
60. R. R. Davda, J. W. Shabaker, G. W. Huber, R. D. Cortright, and J. A. Dumesic, *Appl. Catal. B: Environ.*, 2003, **43**, 13.
61. J. W. Shabaker, G. W. Huber, R. R. Davda, R. D. Cortright, and J. A. Dumesic, *Catal. Lett.*, 2003, **88**, 1.
62. Y. Yu, X. Lou, and H. Wu, *Energy Fuels*, 2008, **22**, 46.
63. A. Fukuoka and P. L. Dhepe, *Angew. Chem.- Int. Ed.*, 2006, **45**, 5161.
64. C. Perkins and A. Weimer, *Int. J. Hydrogen Energy*, 2004, **29**, 1587.
65. T. Perret, Y. Chen, G. Besenbruch, R. Diver, A. Weimer, A. Lewandowski, and E. Miller, ‘Annual Progress Report US DOE IV.I.1 “Solar Hydrogen Generation Research”’, 2005, 377.
66. S. Abanades, P. Charvin, G. Flamant, and P. Neveu, *Energy*, 2006, **31**, 2805.
67. T. Nakamura, *Solar Energy*, 1977, **19**, 467.
68. R. Palumbo, J. Lédé, O. Boutin, E. Elorza Ricart, A. Steinfield, S. Möller, A. Weidenkaff, E. A. Fletcher, and J. Bielicki, *J. Chem. Eng. Sci.*, 1998, **53**(14), 2503.
69. A. Stenfield, *Int. J. Hydrogen Energy*, 2002, **27**(6), 611.
70. T. Kodama, Y. Kondoh, R. Yamamoto, H. Andou, and N. Satou, *Sol. Energy*, 2005, **78**, 623.
71. J. E. Miller, M. D. Allendorf, R. B. Diver, L. R. Evans, N. P. Siegel, and J. N. Stuecker, *J. Mater. Sci.*, 2008, **43**, 4714.
72. T. Kodama, N. Gokon, and R. Yamamoto, *Solar Energy*, 2008, **82**, 73.
73. H. Kaneko, T. Kodama, N. Gokon, Y. Tamaura, K. Lovegrove, and A. Luzzi, *Solar Energy*, 2004, **76**, 317.
74. N. Gokon, T. Mizuno, Y. Nakamuro, and T. Kodama, *J. Solar Energy Eng.*, 2008, **130**(1), 1.

75. T. Tamaura, A. Steinfeld, P. Kuhn, and K. Ehrensberger, *Energy*, 1995, **20**(4), 325.
76. C. Agrifiotis, M. Roeb, A. G. Konstandopoulos, L. Nalbandian, V. T. Zaspalis, C. Sattler, P. Stobbe, and A. M. Steele, *Solar Energy*, 2005, **79**, 409.
77. S. Abanades and G. Flamant, *Solar Energy*, 2006, **80**, 1611.
78. H. Kaneko, T. Miura, H. Ishihara, S. Taku, T. Yokoyama, H. Nakajima, and Y. Tamaura, *Energy*, 2007, **32**, 656.
79. A. Trovarelli, *Catal. Rev. Sci. Eng.*, 1996, **38**, 439.
80. H. Kaneko, H. Ishihara, S. Taku, Y. Naganuma, N. Hasegawa, and Y. Tamaura, *J. Mater. Sci.*, 2008, **43**, 3153.
81. H. Kaneko and Y. Tamaura, *J. Phys. Chem. Sol.*, 2009, **70**, 1008.
82. S. Abanades, P. Charvin, F. Lemont, and G. Flamant, *Int. J. Hydrogen Energy*, 2008, **33**, 6021.
83. K.-S. Kang, C.-H. Kim, W.-C. Cho, K.-K. Bae, S.-H. Kim, and C.-S. Park, *Int. J. Hydrogen Energy*, 2009, **34**, 4283.
84. T. Bak, J. Nowotny, M. Rekas, and C. C. Sorrell, *Int. J. Hydrogen Energy*, 2002, **27**, 991.
85. R. M. Navarro, M. C. Alvarez-Galvan, F. del Valle, J. A. Villoria de la Mano, and J. L. G. Fierro, *ChemSusChem*, 2009, **2**(6), 471.
86. R. M. Navarro, F. del Valle, J. A. Villoria de la Mano, M. C. Álvarez-Galván, and J. L. G. Fierro, *Adv. Chem. Eng.*, 2009, **36**, 111.
87. A. K. Fujishima and K. Honda, *Nature*, 1972, **238**, 37.
88. J. M. Lehn, J. P. Sauvage, and R. Ziessel, *New J. Chem.*, 1980, **4**(11), 623.
89. S. Sato and J. M. White, *Ind. Eng. Chem. Prod. Res. Dev.*, 1980, **19**(4), 542.
90. K. Domen, S. Naito, M. Suma, T. Onishi, and K. Tamaura, *J. Chem. Soc., Chem. Commun.*, 1980, **12**, 543.
91. D. Dvororanova, V. Brezova, M. Mazur, and M. A. Malati, *Appl. Catal. B: Environ.*, 2002, **37**, 91.
92. T. Umebayashi, T. Yamaki, H. Itoh, and K. Asai, *J. Phys. Chem. Solids*, 2002, **63**, 1909.
93. K. Wilke and H. D. Breuer, *Z. Phys. Chem.*, 1999, **213**, 135.
94. M. Anpo, Y. Ichihashi, M. Takeuchi, and H. Yamashita, *Res. Chem. Intermed.*, 1998, **24**, 143.
95. R. Asahi, T. Monrikawa, T. Ohwaki, K. Aoki, and Y. Taga, *Science*, 2001, **293**, 269.
96. S. Sakthivel and H. Kisch, *ChemPhysChem*, 2003, **4**, 487.
97. G. Hitoki, T. Takata, J. N. Kondo, M. Hara, H. Kobayashi, and K. Domen, *Chem. Commun.* 2002, 1698.
98. S. Sakthivel and H. Kisch, *Angew. Chem. Int. Ed.*, 2003, **42**(40), 4908.
99. H. Irie, Y. Watanabe, and K. Hashimoto, *Chem. Lett.*, 2003, **32**, 772.
100. T. Yamaki, T. Umebayashi, T. Sumita, S. Yamamoto, M. Maekawa, Al. Kawasuso, and H. Itoh, *Nucl. Instrum. Methods Phys. Res. Sec. B*, 2003, **206**, 254.
101. K. Shankar, K. Tep, G. Mor, and C. A. Grimes, *J. Phys. D- Appl. Phys.*, 2006, **39**, 2361.
102. R. Nakamura, T. Tanaka, and Y. Nakato, *J. Phys. Chem. B*, 2004, **108**, 10617.
103. G. R. Torres, T. Lindgren, J. Lu, C. G. Granqvist, and S. E. Lindquist, *J. Phys. Chem. B*, 2004, **108**, 5995.
104. M. A. Kam, M. S. Akhtar, S. I. Woo, and O. B. Yang, *Catal. Comm.*, 2008, **10**, 1.
105. J. Jitputti, Y. Suzuki, and S. Yoshikawa, *Catal. Comm.*, 2008, **9**, 1265.
106. C. H. Lin, J. H. Chao, C. H. Liu, J. C. Chang, and F. C. Wang, *Langmuir*, 2008, **24**, 9907.
107. Y. Liu, B. Zhou, J. Bai, J. Li, J. Zhang, Q. Zheng, X. Zhu, and W. Cai, *Appl. Catal. B: Environ.*, 2009, **89**, 142.
108. M. P. D-Edwards, J. B. Goodenough, A. Hamnett, and P. R. Trevellick, *J. Chem. Soc., Faraday Trans. I*, 1983, **79**, 2027.
109. K. Itoh and J. O. Bockris, *Appl. Phys.*, 1984, **56**, 874.
110. K. Itoh and J. O. Bockris, *J. Electrochem. Soc.*, 1984, **131**, 1266.
111. A. Kay, I. Cesar, and M. Grätzel, *J. Am. Chem. Soc.*, 2006, **128**, 15714.
112. K. Sivula, F. Le Formal, and M. Grätzel, *Chem. Mater.*, 2009, **21**(13), 2862.
113. R. Abe, K. Shinmei, K. Hara, and B. Ohtani, *Chem. Commun.* 2009, 3577.
114. W. J. Youngblood, S.-H. A. Lee, Y. Kobayashi, E. A. Hernandez-Pagan, P. G. Hoertz, T. A. Moore, A. L. Moore, D. Gust, and T. E. Mallouk, *J. Am. Chem. Soc.*, 2009, **131**, 926.
115. Y. Sun, C. J. Murphy, K. R. Reyes-Gil, E. A. Reyes-Garcia, J. P. Lilly, and D. Raftery, *Int. J. Hydrogen Energy*, 2008, **33**, 5967.
116. K. R. Reyes-Gil, E. A. Reyes-Garcia, and D. Raftery, *J. Phys. Chem. C*, 2007, **111**, 14579.
117. C. Le Paven-Thivet, A. Ishikawa, A. Ziani, L. Le Gendre, M. Yoshida, J. Kubota, F. Tessier, and K. Domen, *J. Phys. Chem. C*, 2009, **113**, 6156.
118. O. Khaselev and J. A. Turner, *Science*, 1998, **280**, 425.
119. O. Khaselev and J. A. Turner, *Electrochim. Solid-State Lett.*, 1999, **2**, 310.
120. E. L. Miller, B. Marsen, D. Paluselli, and R. Rocheleau, *Electrochim. Solid-State Lett.*, 2005, **8**, A247.
121. S. Yamane, N. Kato, S. Kojima, A. Imanishi, S. Ogawa, N. Yoshida, S. Nonomura, and Y. Nakato, *J. Phys. Chem. C*, 2009, **113**, 14575.
122. K. Maeda, K. Teramura, and K. Domen, *J. Catal.*, 2008, **254**, 198.
123. A. Kudo and Y. Miseki, *Chem. Soc. Rev.*, 2009, **38**, 253.
124. F. E. Osterloh, *Chem. Mater.*, 2008, **20**, 35.
125. R. Niishiro, H. Kato, and A. Kudo, *Phys. Chem. Chem. Phys.*, 2005, **7**, 2241.

126. T. Ishii, H. Kato, and A. Kudo, *J. Photochem. Photobiol. A.*, 2004, **163**, 181.
127. D. W. Hwang, H. G. Kim, J. S. Lee, J. Kim, W. Li, and S. H. Oh, *J. Phys. Chem. B*, 2005, **109**, 2093.
128. D. W. Hwang, H. G. Kim, J. S. Jang, S. W. Bae, S. M. Ji, and J. S. Lee, *Catal. Today*, 2004, **93**, 845.
129. D. Yamashita, T. Takata, M. Hara, J. N. Kondo, and K. Domen, *Solid State Ion.*, 2004, **172**, 591.
130. H. Zhang, G. Chen, X. Li, and Q. Wang, *Int. J. Hydrogen Energy*, 2009, **34**, 3631.
131. H.-Y. Lin, T.-H. Lee, and C.-Y. Sie, *Int. J. Hydrogen Energy*, 2008, **33**, 4055.
132. S. M. Ji, P. H. Borse, H. G. Kim, D. W. Hwang, J. S. Jang, S. W. Bae, and J. S. Lee, *Phys. Chem. Chem. Phys.*, 2005, **7**, 1315.
133. X. Wang, K. Maeda, A. Thomas, K. Takanabe, G. Xin, J. M. Carlsson, K. Domen, and M. Antonietti, *Nature Mater.*, 2009, **8**, 76.
134. J. Chi, S. Y. Ryu, W. Balcerski, T. K. Lee, and M. R. Hoffman, *J. Mater. Chem.*, 2008, **18**, 2371.
135. R. M. Navarro, F. del Valle, and J. L. G. Fierro, *Int. J. Hydrogen Energy*, 2008, **33**, 4265.
136. X. Zong, H. Yan, G. Wu, G. Ma, F. Wen, L. Wang, and C. Li, *J. Am. Chem. Soc.*, 2008, **130**, 7176.
137. F. del Valle, A. Ishikawa, K. Domen, J. A. Villoria de la Mano, M. C. Sánchez-Sánchez, I. D. González, S. Herreras, N. Mota, M. E. Rivas, M. C. Álvarez Galván, J. L. G. Fierro, and R. M. Navarro, *Catal. Today*, 2009, **143**(1–2), 51.
138. W. Zhang, Z. Y. Zhong, Y. S. Wang, and R. Xu, *J. Phys. Chem. C*, 2008, **112**, 17635.
139. I. Tsuji, H. Kato, H. Kobayashi, and A. Kudo, *J. Am. Chem. Soc.*, 2004, **41**, 13406.
140. I. Tsuji, H. Kato, H. Kobayashi, and A. Kudo, *J. Phys. Chem. B*, 2005, **109**, 7323.
141. I. Tsuji, H. Kato, and A. Kudo, *Chem. Mater.*, 2006, **18**, 1969.
142. J.-S. Jang, P. H. Borse, J. S. Lee, S. H. Choi, and H. G. Kim, *J. Chem. Phys.*, 2008, **128**, 154717.
143. N. Zheng, X. Bu, H. Vu, and P. Feng, *Angew. Chem. Int. Ed.*, 2005, **44**, 5299.
144. G. Zhang, X. Zou, J. Gong, F. He, H. Zhang, and Q. Zhang, *J. Alloys Compd.*, 2006, **425**, 76.
145. K. Domen, A. Kudo, A. Tanaka, and T. Onishi, *Catal. Today*, 1990, **8**, 77.
146. M. K. Tian, W. F. Shangguan, J. Yuan, L. Jiang, M. X. Chen, and J. W. Shi, *Appl. Catal. A; Gen.*, 2006, **309**, 76.
147. X. W. Wang, G. Liu, Z. G. Chen, F. Li, L. Z. Wang, G. Q. Lu, and H. M. Chen, *Chem. Commun.*, 2009, **23**, 3452.
148. K. Zhang, D. W. Jing, C. J. Xing, and L. J. Guo, *Int. J. Hydrogen Energy*, 2007, **32**, 4685.
149. K. Maeda, K. Teramura, N. Saito, Y. Inoue, H. Kobayashi, and K. Domen, *Pure Appl. Chem.*, 2006, **78**, 2267.
150. K. Maeda, T. Takata, M. Hara, N. Saito, Y. Inoue, H. Kobayashi, and K. Domen, *J. Am. Chem. Soc.*, 2005, **127**, 8286.
151. K. Maeda, K. Teramura, T. Takata, M. Hara, N. Saito, K. Toda, Y. Inoue, H. Kobayashi, and K. Domen, *J. Phys. Chem. B*, 2005, **109**, 20504.
152. K. Maeda, K. Teramura, D. Lu, T. Takata, N. Saito, Y. Inoue, and K. Domen, *Nature*, 2006, **440**, 295.
153. K. Maeda, K. Teramura, D. Lu, N. Saito, Y. Inoue, and K. Domen, *Angew. Chem., Int. Ed.*, 2006, **45**, 7806.
154. K. Maeda, H. Hashiguchi, H. Masuda, R. Abe, and K. Domen, *J. Phys. Chem. C*, 2008, **112**, 3447.
155. F. Tessier, P. Maillard, Y. Lee, C. Bleugat, and K. Domen, *J. Phys. Chem. C*, 2009, **113**, 8526.
156. P. Ritterskamp, A. Kuklya, M. A. Wüstkamp, K. Kerpen, C. Weidenthaler, and M. Demuth, *Angew. Chem. Int. Ed.*, 2007, **46**, 7770.
157. H. Liu, J. Yuan, W. Shangguan, and Y. Teraoka, *J. Phys. Chem. C*, 2008, **112**(23), 8521.
158. Q. Wang, H. Liu, L. Jiang, J. Yuan, and W. Shangguan, *Catal. Lett.*, 2009, **131**, 160.
159. Y. Lee, H. Terashima, Y. Shimodaira, K. Teramura, M. Hara, H. Kobayashi, K. Domen, and M. Yashima, *J. Phys. Chem. C*, 2007, **111**, 1042.
160. X. Wang, K. Maeda, Y. Lee, and K. Domen, *Chem. Phys. Lett.*, 2008, **457**, 134.

Energy Conversion in Photosynthesis

Gözde Ulas and Gary W. Brudvig

Yale University, New Haven, CT, USA

1 General Overview	21
2 Photocatalytic H ₂ O Oxidation and Photosynthetic Electron Transfer	24
3 Acknowledgments	31
4 Abbreviations and Acronyms	31
5 References	31

1 GENERAL OVERVIEW

1.1 Introduction

Solar water splitting ($2\text{H}_2\text{O} \rightarrow \text{O}_2 + 2\text{H}_2$) is a promising approach for renewable fuel production, but efficient systems have not yet been developed. The natural photosynthetic machinery provides a working example of how this process can be carried out. Moreover, the principles revealed by the natural systems may inform efforts to design artificial systems for water splitting (see *Toward Solar Fuels Using a Biomimetic Approach: Progress in the Swedish Consortium for Artificial Photosynthesis; Molecular Catalysts for Oxygen Production from Water*). Light-driven oxidation of two H₂O molecules into O₂, accompanied by the release of four electrons and four protons, is considered to be the more challenging half reaction in water splitting. In a synthetic system, these electrons, if transferred to a terminal electron acceptor, can be utilized to produce a fuel, such as the green and sustainable fuel H₂ (see *H₂ Production from Renewables*). While a synthetic system, with catalytic oxidation and reduction half reactions that are coupled, would be an ideal solution for the present day energy problem (see *Molecular Catalysis for Fuel Cells; Some Computational Challenges in Energy Research; Photocatalytic Hydrogen Production from Water*), a catalytic system for just the photooxidation of water remains a formidable challenge. The difficulties include (i) the high reduction potential necessary to oxidize H₂O ($E^{\circ'}(\text{pH } 7) = 0.82\text{ V}$), (ii) the need for redox-leveling of cofactors throughout catalysis to avoid excessively high potentials, (iii) the need for efficient removal of H⁺, (iv) avoidance of partially oxidized reactive oxygen species viz. H₂O₂, O₂⁻, etc., and (v) formation of a stable and

highly organized reaction system, with chromophore(s) coupled to catalytic active sites, capable of efficient solar energy absorption and subsequent charge separation.

Nature uses the metalloenzyme photosystem II (PSII) to carry out the challenging water-oxidation half reaction. PSII is found in all oxygenic photosynthetic organisms and does not show any distinct variation among different organisms in its tetranuclear manganese active site, where the water-oxidation chemistry, the first step of the complex process of photosynthesis, is catalyzed. PSII is a part of the photosynthetic machinery, which encompasses all the proteins and cofactors necessary to execute photosynthesis, yet it stands out as the only enzyme with an inorganic core that catalyzes the photoinduced water-oxidation reaction, and thus will be given special attention in this article. Special processes in its mechanism that we currently know of, such as redox-leveling and coupled proton and electron transfers, will be especially considered and elaborated on in Section 2.1.2.

Cyanobacteria, algae, and all green plants carry out oxygenic photosynthesis. In cyanobacteria, the photosynthetic reactions occur in the thylakoid membranes within the cell, whereas in eukaryotes, such as algae and green plants, photosynthesis occurs in specialized organelles called *chloroplasts*. Chloroplasts are compartmentalized to sustain the two parts of photosynthesis, reactions to reduce or “fix” CO₂ (the carbon assimilation or “dark” reactions) and those that generate reducing equivalents in the form of reduced nicotinamide adenine dinucleotide phosphate (NADPH) and energy (adenosine triphosphate, (ATP)) necessary for CO₂ fixation (the photochemical or “light” reactions). (Note that the “dark” reactions only naturally occur in the light when NADPH and ATP are being formed photochemically, but the enzymatic steps of the “dark” reactions do not require light

and will function in the dark as long as NADPH and ATP are available.) The inner membrane of the chloroplast contains flattened vesicles called *thylakoids*, arranged in stacks called *grana*. The “light” reactions, the photooxidation of H₂O to reduce NADP⁺, are catalyzed by enzymes and cofactors mostly embedded in the thylakoid membranes. In these reactions, light energy is converted into chemical potential energy that is used to drive electron transfer (ET). On the other hand, the “dark” reactions are carried out in the aqueous phase that surrounds the thylakoids, the stroma. In the dark reactions, the electrons extracted from H₂O are used to reduce CO₂ and carbohydrates are formed.

The rest of Section 1 briefly introduces the photosynthetic machinery and the processes involved in photosynthesis.

1.2 Energy Capture and Storage

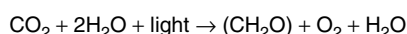
Photosynthesis can be divided into several steps that lead to energy storage: (i) capture of sunlight, (ii) charge separation, (iii) catalysis, (iv) ET to an electron acceptor (NADP⁺), and (v) assimilation of CO₂ into carbohydrates. Steps (i) through (iv) are carried out during the “light” reactions, and step (v) by the “dark” reactions.

The overall reaction of oxygenic photosynthesis is given in Scheme 1, showing how CO₂ fixation in nature relies on energy from sunlight and a constant source of reducing equivalents provided by H₂O. The end product glucose could either be stored in the cell (as starch, or sucrose) or directly used up in glycolysis, where some of the trapped solar energy is conserved in the form of two ATP molecules along with the formation of two NADPH (reducing equivalents) and two pyruvate molecules, which can be consumed in the mitochondrial citric acid cycle to drive ATP synthesis.

1.3 “Light” Reactions: Photooxidation of H₂O to Provide Reducing Equivalents for CO₂ Fixation

The “light” reactions are responsible for providing reducing equivalents to be used in the CO₂ fixation process. Figure 1(a) shows the so-called Z-scheme that summarizes all the cofactors involved in the electron-transport chain, and their relative reduction potentials. Light energy is necessary to oxidize water in the first step of photosynthesis, by PSII, and to drive electron transport in photosystem I (PSI) (Figure 1b).

PSI and PSII are the only two ET complexes in the photosynthetic assembly that directly absorb light energy. The functional cores of PSI and PSII are surrounded by light-harvesting proteins that contain pigments, such as chlorophyll



Scheme 1 Oxygenic photosynthesis. ((CH₂O) denotes carbohydrate)

and carotenoids. These “antennae complexes” are responsible for capturing photons and directing the excitation energy to the site of the primary charge separation by a series of rapid energy-transfer steps.

Primary charge separation occurs between a special group of chlorophyll molecules and a nearby moiety with a suitable redox potential to accept an electron from a chlorophyll molecule upon light excitation. The primary electron donors are called P₆₈₀ in PSII and P₇₀₀ in PSI, and the electron acceptors are a pheophytin molecule in PSII and another chlorophyll molecule in PSI. The chlorophyll cation radicals formed in the charge-separation reactions, P₆₈₀⁺ and P₇₀₀⁺, have reduction potentials of 1.25 V and 0.45 V, respectively. In PSII, such a high potential is necessary to drive the photooxidative “splitting” of H₂O (Scheme 2).

Various cofactors are involved in the ET chain that culminates with NADP⁺ reduction. This process is driven by the spatial positioning of all the cofactors and the alignment of their redox potentials. The ET is, thus, driven by thermodynamics, except for two steps where light energy is necessary (Figure 1a).

1.4 Carbon Fixation in the “Dark” Reactions: Energy Storage in Covalent Bonds

Enzymes that catalyze the carbon-fixing “dark” reactions do not directly absorb light energy, although light activation is necessary for some of them. The catalytic “Calvin–Benson” cycle consists of (i) CO₂ fixation into ribulose 1,5-bisphosphate to afford two 3-phosphoglycerate molecules, (ii) subsequent reduction to give glyceraldehyde-3-phosphate, and (iii) regeneration of ribulose 1,5-bisphosphate.

Ribulose 1,5-bisphosphate carboxylase/oxygenase (rubisco) is the key enzyme that catalyzes the carbon fixation reactions in the cycle. The catalytic mechanism includes (i) activation of CO₂ and ribulose 1,5-bisphosphate by Mg²⁺ in the active site, (ii) C–C bond formation between CO₂ and ribulose 1,5-bisphosphate, and (iii) cleavage of the resulting six-carbon intermediate into two 3-phosphoglycerates. For such a highly demanding catalysis, rubisco’s efficiency is incredibly low, with a turnover of only 3 s⁻¹. Another major problem is that rubisco cannot distinguish between CO₂ and O₂ as substrates. Fixation of O₂ causes the formation of a two-carbon end product (2-phosphoglycolate), which is energetically costly to reincorporate into the cycle (a process called *photorespiration*). Therefore, the oxygenase activity of rubisco is energetically damaging to the organism.

A high concentration of rubisco is required in the chloroplast to compensate for its low efficiency, in order to afford fast catalytic rates. However, the oxygenase activity remains a problem. Most of the plants that live in moderate-temperature climates (10–25 °C), called the *C₃ plants*, survive photorespiration. This is a significant cost, considering how O₂ is more abundant than CO₂ in both the atmosphere and aqueous solutions.

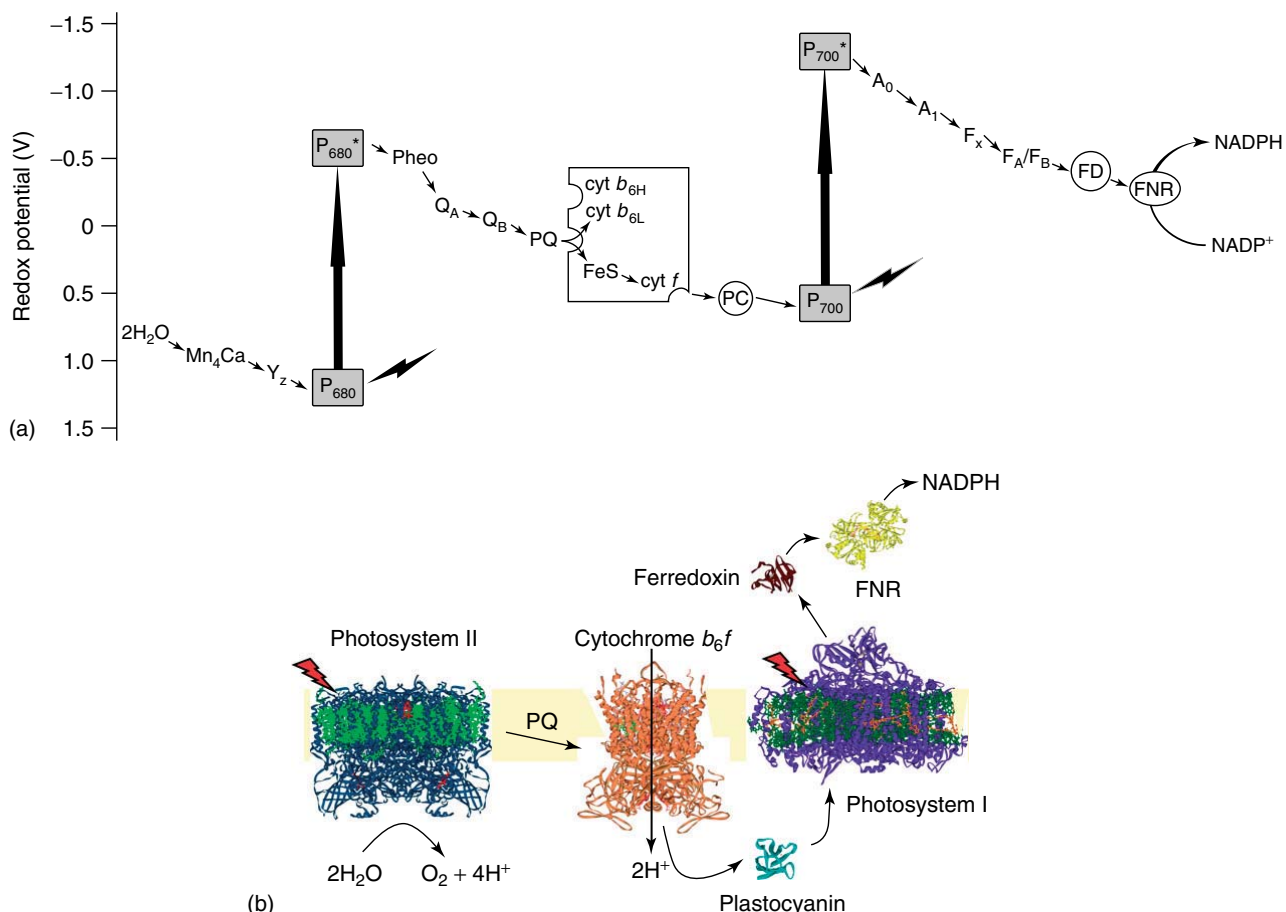


Figure 1 (a) “Z-scheme”, depicting all the cofactors involved in the electron-transfer pathway of the light reactions as a function of their midpoint reduction potentials (y-axis). Light excitation is necessary to thermodynamically favor electron transfer, as the ground states of both P₆₈₀ and P₇₀₀ are not suitable for such a purpose. (b) Structures of all the proteins involved in the ET pathway in the light reactions. The structures were adapted from the respective X-ray crystal structures of each protein, with the following Protein Data Bank ID numbers: 3BZ1 and 3BZ2 for photosystem II, 2E74 for cytochrome b_{6f}, 2Q5B for plastocyanin, 2O01 for photosystem I, 3D89 for ferredoxin, and 3CRZ for ferredoxin:NADP⁺ oxidoreductase



Scheme 2 Photooxidation of H₂O, catalyzed by photosystem II (PSII) (PQ denotes plastoquinone; the stroma and lumen are opposite sides of the thylakoid membrane)

However, an evolutionarily superior mechanism to restrict photorespiration is also known in some plants, named the *C₄* plants. These plants have a more compartmentalized structure, where CO₂ from the atmosphere is temporarily “fixed” into a four-carbon intermediate in one specialized cell, carried into another cell where it is released and then stably fixed by rubisco. Such a system provides rubisco with high concentrations of CO₂ relative to O₂ and results in more efficient carbon fixation. Moreover, less energy is spent on metabolizing products of the oxygenase activity. On the other hand, it is energetically more costly to fix CO₂ due

to the additional steps in the catalytic cycle. These plants, therefore, grow in warmer climates, where energy saved from photorespiration compensates for the energy penalty for CO₂ fixation.

1.5 Concluding Remarks

The total energy conversion in photosynthesis is that of light energy into chemical energy in the form of “fixed carbon”. This article focuses on the details of the energy conversion processes in the “light” reactions, where sunlight is used to create redox potential energy differences in the primary charge-separated states. The site of water oxidation, called the oxygen-evolving complex (OEC), will be discussed in detail. The details of the conversion of chemical potential energy into chemical energy through the formation of carbohydrates, which happens in the course of the “dark” reactions, are beyond the scope of this article, but

comprehensive reviews have been published on this subject,^{1–5} as well as on different CO₂-fixation pathways in plants.^{6–8} Extensive information on the individual ET complexes that function in the “light” reactions, PSII,^{9–14} PSI,^{15–18} and the cytochromes,^{19–22} as well as the whole photosynthetic machinery,^{23–26} is also available.

2 PHOTOCATALYTIC H₂O OXIDATION AND PHOTOSYNTHETIC ELECTRON TRANSFER

2.1 Photosystems I and II

2.1.1 Light Harvesting and Charge Separation: Capture of Photonic Energy and Primary Charge Separation in Photosystems I and II

Besides the chlorophylls and carotenoids required for energy transfer in the core units of PSI and PSII, there are surrounding pigment-containing protein complexes that are used to absorb and transfer light energy to the site of the primary charge separation, yielding, for instance, a total of approximately 250 molecules of chlorophyll per PSII in plants. Some of these “antennae” make up the integral part of the protein (such as the CP47 and CP43 subunits of PSII), and some are peripheral (such as LHCII, the light-harvesting complex associated with PSII). The most commonly found pigments in oxygenic photosynthetic organisms include Chl *a*, Chl *b*, and carotenoids.

The pigments involved in energy capture often exhibit a pattern, where pigments absorbing at higher energy are more on the periphery and those associated with the reaction center core absorb more to the red, thus forming a light-harvesting system that is more efficient.²⁷ The resulting excited-state energy gradient of these pigments then allows the equilibration of excitation transfer to happen on a timescale on the order of picoseconds.²⁷ However, the absolute number of energy-transfer steps seems to be highly dependent on the temperature and the content of the protein preparations, and the rate-determining step (RDS) for the conversion of the excited state into a charge-separated state may be limited by either excitation-energy transfer or charge separation.²⁸ However, in general, the rate of excitation-energy transfer is sufficiently fast to prevent significant loss of excited states during the energy-transfer process. The details of the mechanisms of excitation-energy transfer and trapping in a charge-separated state are still unclear, but several comprehensive reviews describe the current understanding of these processes.^{27,29,30}

Regardless of whether the RDS in the excitation transfer is the transfer step itself or the energy trapping, the chemistry in PSII depends on the establishment of the primary charge separation between a Chl *a* molecule, named *P*₆₈₀, and a pheophytin molecule, to give the charge-separated state,

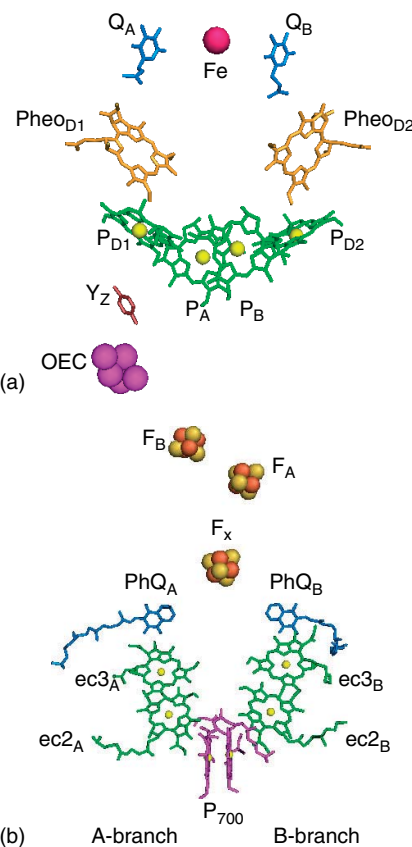


Figure 2 (a) Electron-transfer cofactors in PSII, adapted from a recent 2.9-Å resolution X-ray crystal structure³³ from the thermophilic cyanobacterium, *Thermosynechococcus elongatus*. Long-lived charge separation is established between the chlorophyll *P*_A⁺• (referred to in the text as *P*₆₈₀⁺•) and *Pheo*_{D1}[−]. (b) Electron-transfer cofactors in PSI, adapted from the 3.4-Å resolution plant PSI structure (PDB ID: 2O01)

*P*₆₈₀⁺• *Pheo*[−]. As opposed to bacterial reaction centers, it was found that the actual initial charge separation occurs between an “accessory chlorophyll”, Chl_{D1} (*P*_{D1} in Figure 2a), and Pheo, on a subpicosecond timescale.³¹ Then, on the timescale of a few picoseconds, *P*₆₈₀ is oxidized. Formation of the charge separation marks the energy conversion step in PSII, where excitation energy from sunlight is trapped to yield the excited state *P*₆₈₀^{*} and then converted into chemical potential energy via charge separation. Subsequent forward ET from Pheo[−] to Q_A happens on a timescale of the order of hundreds of picoseconds, in order to establish a stabilized charge-separated state.^{28,32} The electron is then transferred to Q_B, a membrane-soluble quinone that, after accepting two electrons and two protons to form a quinol, diffuses into the thylakoid membrane bilayer and carries the reducing equivalents to the next ET complex in the photosynthetic machinery, cyt *b*₆*f*.

It is worthwhile to look at how efficiently light energy is converted into chemical potential. At 680 nm, *P*₆₈₀ absorbs a photon with the energy equivalent to 1.84 eV. The excited

state, P_{680}^{+*} , decays to form a long-lived charge-separated state $P_{680}^{+•} Q_A^-$; $P_{680}^{+•}$ has an estimated reduction potential of +1.25 V^{34,35} and the reduction potential of Q_A^- is about -0.13 V.²⁸ Hence, we can estimate that out of the total energy absorbed by P_{680} (1.84 eV, (177.5 kJ mol⁻¹), 1.38 eV (133.1 kJ mol⁻¹) is converted into the long-lived charge-separated pair, $P_{680}^{+•} Q_A^-$. This means that the efficiency of energy conversion in PSII to establish a long-lived charge separation is roughly 78%. This is in remarkable contrast with the bacterial photosynthetic reaction centers; *Rhodobacter sphaeroides*, for example, has an efficiency for formation of the analogous charge separation of only 35%,²⁸ which arises from the fact that the primary oxidant is not as oxidizing as $P_{680}^{+•}$.

In comparison to that in PSII, the long-lived charge separation in PSI occurs between P_{700} and an iron–sulfur cluster called F_A to form $P_{700}^{+•}$ ($E_m = 450$ mV) and F_A^- ($E_m = -540$ mV), after the initial and rapid (in picoseconds) charge separation between $P_{700}^{+•}$ and chlorophyll A_0^- ($E_m = -1.05$ mV). The sequential decrease in the redox potential of the ET cofactors is necessary for the efficient relay of the reducing equivalents without charge recombination. The energy conversion from light (1.77 eV for 700 nm, or 170.8 kJ mol⁻¹) into the long-lived charge-separated state (0.99 eV or 95.5 kJ mol⁻¹), yields an efficiency of energy conversion of ~56%, which is somewhat lower than that of PSII.

2.1.2 Photosystem II: Driving H_2O Splitting by Photonic Energy

PSII is the only enzyme in the entire photosynthetic machinery to couple catalysis with photonic energy capture, transfer, and conversion, resulting eventually in the successful relay of reducing equivalents. This section describes the details of this process, with a special interest in its inorganic Mn₄Ca active site, called the *oxygen-evolving complex* (OEC).

Introduction: Overview and Challenges of Water Oxidation. PSII catalyzes the first step of photosynthesis, in which sunlight is used to split water into four protons, four electrons, and O_2 , and two plastoquinones (PQs) are reduced as the terminal electron acceptors within the system (Scheme 2).

Splitting of H_2O is catalyzed by an active site that contains one Ca and four Mn ions (called the *Mn cluster*), a redox-active tyrosine residue (named *Tyrosine Z* (Tyr_Z or Y_Z)) 7 Å away from the inorganic core, and H^+ -accepting basic amino acid residues, thought to be essential in deprotonating substrate H_2O and initiating transport of protons to the lumen (altogether called the oxygen-evolving complex (OEC)). The catalytic mechanism, which will be elaborated in more detail in the following subsections, can be divided into two major processes: (i) accumulation of sufficient potential energy to oxidize H_2O ($E^0 = 0.82$ V at pH 7, but the pH can go as low as 4.2 in the lumen,³⁶ requiring a even higher potential: $E^0 = 0.98$ V at pH 4.2) by single-electron oxidations of the

Mn cluster, along with redox-leveling of the four redox steps in the catalytic cycle, and (ii) catalysis with proton transfer (PT) and ET happening consecutively or simultaneously, depending on the oxidation state of the Mn cluster.

The challenge in coupling these two processes, catalysis to photoinduced ET, is to be able to efficiently carry out a metallic core-based four-electron catalytic oxidation by a photosystem that can only perform single-electron oxidations. This challenge is overcome by oxidizing the Mn cluster in four successive single-electron reactions triggered by the exceptionally oxidizing $P_{680}^{+•}$ via the ET intermediate Y_Z . In the course of these reactions, not only is the Mn cluster's redox potential fine-tuned but also ample time is given for the coordination and activation of both of the substrate H_2O molecules.

Four single-electron oxidations of the Mn cluster are required to accumulate the oxidizing potential necessary to oxidize H_2O to O_2 . Each oxidation state is called an *S-state* (S for “storage”) (Figure 3). Advancement of each S-state requires a photochemical turnover, and four photons are necessary for one complete catalytic cycle. A photon of 680-nm wavelength has about 1.84 eV (177.5 kJ mol⁻¹) of energy. Therefore, a total of 7.36 eV (710.1 kJ mol⁻¹) energy input is required to drive the catalytic process. Oxidation states of Mn in the different S-states are given in Table 1.

It has been suggested that PTs have to be coupled to ET processes for H_2O oxidation to be thermodynamically favorable.^{38,39} This implies that, along with the ET efficiency, proton-extraction and transport efficiency is essential for catalytic turnover. The protons and electrons are thought to be released in a bifurcated mechanism,¹² where electrons are transferred through several cofactors, via $P_{680}^{+•}$, to a final electron acceptor, Q_B , which diffuses into the membrane bilayer, whereas protons are transferred the opposite way;

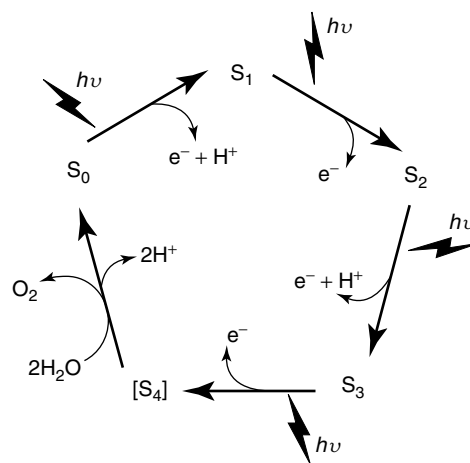


Figure 3 S-state cycle. Halftimes of each transition are as follows: $S_0 \rightarrow S_1$ (30 µs), $S_1 \rightarrow S_2$ (70 µs), $S_2 \rightarrow S_3$ (190 µs), $S_3 \rightarrow [S_4']$ (200 µs, which marks the halftime of a deprotonation), and $[S_4'] \rightarrow [S_4] \rightarrow S_0$ (1.1 ms, halftime of the ET)³⁷

Table 1 Oxidation states of the four Mn in the OEC during the catalytic cycle where O[•] denotes an oxyl radical coordinated to Mn

S-state	Mn oxidation state
S ₀	III/III/III/IV or II/III/IV/IV
S ₁	III/III/IV/IV
S ₂	III/IV/IV/IV
S ₃	IV/IV/IV/IV or III/IV/IV/IV-O [•]
S ₄	IV/IV/IV/IV-O [•] or IV/IV/IV/V

they are eventually released into the bulk solvent in the lumen to establish a proton gradient, used to drive the ATP synthase, which is also embedded in the thylakoid membranes.

Alignment of redox potentials of ET cofactors (spatial orientation shown in Figure 2a) is essential in PSII energy conversion. The midpoint redox potentials of these cofactors were either measured directly or estimated, and are given in Table 2.

Water-Oxidizing Catalytic Mechanism. This section is arranged into various subsections, namely, Redox-active cofactor, Y_Z; S-state transitions: kinetics and thermodynamics; Substrate water exchange and binding; Coordination, Conformational and oxidation state changes in the OEC; O–O bond formation: proposed mechanisms; Computational studies; and Summary.

Redox-active cofactor, Y_Z. P₆₈₀^{+•} is reduced by equivalents extracted from the OEC, even though there is some debate as to whether all the equivalents come from the Mn (see Table 1). A redox-active Tyr_Z (Y_Z) residue (D1-Y161) is essential in the transport of these reducing equivalents from the Mn cluster to P₆₈₀^{+•}.^{44,45} Valuable treatises on Y_Z, including redox kinetics, can be found in previously published reviews.^{12,46,47} However, only the key points concerning what

Table 2 Reduction potentials of the ET cofactors in PSII

Cofactor	E _m (mV)
P ₆₈₀ ^{+•} /P ₆₈₀	+1250 ^{34,35}
Pheo/Pheo [−]	-505 ± 6 ⁴⁰
Q _A /Q _A [−]	-140 ± 2 ⁴¹ or -80 ³⁴
Q _B /Q _B [−]	60 ⁴² higher than Q _A /Q _A [−]
Y _Z [•] /Y _Z	(+1100)–(+1200) ¹²
OEC (average)	~+1050 ³⁷
S ₁ /S ₀	(+760)–(+1020) ⁴³
S ₂ /S ₁	+1020 ³⁵
S ₃ /S ₂	≥+1020 ^(a)

^(a) E_m not experimentally determined, but should have slightly higher potential than the S₂/S₁ couple.

makes this residue special and essential in the water-oxidizing mechanism are discussed here.

Y_Z is found ~7 Å away from the OEC, and ~12.4 Å away from the Mg²⁺ of P₆₈₀; hence, it is in a spatially suitable position for ET (Figure 2a). Another property of Y_Z is that the pK_a of its phenol ring depends greatly on its redox state; when reduced, the phenol is protonated and has a high pK_a of 10, whereas in the oxidized form, the pK_a drops down to -2, preferring to be a neutral tyrosyl radical.⁴⁸ It was found that these pK_a values are very dependent on the proximal basic residue that accepts the H⁺, which is believed to be D1-His190.⁴⁹ A very fast, and pH-independent, kinetic phase of P₆₈₀^{+•} reduction by Y_Z supports the concept of strong H-bonding between Y_Z and D1-His190, allowing this PT to happen very rapidly, on the nanosecond timescale.^{46,47}

Even though Y_Z is no longer believed to play an active part in the water-oxidation catalysis itself, its impact on the turnover is noteworthy. Its reduction potential was estimated to be ~100 mV lower than that of P₆₈₀^{+•}/P₆₈₀,⁴⁵ implying that the potential of Y_Z[•]/Y_Z should be in the 1.1–1.2 V range.¹² The reduction of Y_Z[•] by the OEC shows S-state-dependent kinetics,^{46,47} implying that the potential of the OEC changes relative to that of Y_Z[•]/Y_Z during the catalytic cycle. Therefore, any treatments that lower or increase the Y_Z[•]/Y_Z potential could perturb the catalytic turnover. For example, the action of the acetate anion in the OEC may inhibit O₂ evolution via perturbing the redox potential of Y_Z.⁵⁰ The redox changes of Y_Z may also greatly affect the microscopic electrostatic environment within the OEC (see below).

S-state transitions: kinetics and thermodynamics. Four light-driven single-electron oxidations of the Mn cluster are required to oxidize water, which requires a high redox potential (E^{0'} = 0.82 V, pH 7). There are, thus, five different oxidation states present in each catalytic cycle leading to the final, rate-determining O–O bond-forming step. These oxidation states are called S-states with subscripts that denote the number of electrons by which the cluster has been oxidized, going from the most reduced S₀-state to the most oxidized and highly transient S₄-state that precedes O₂ release.

The S-state cycle turnover frequency (TOF) seems to be organism dependent. For PSII isolated from spinach, the maximal TOF was estimated to be 40 s⁻¹,⁵¹ whereas for PSII isolated from a cyanobacterium, *Synechocystis* PCC 6803, this number is approximately 74 s⁻¹ (assuming 37 mol Chl per mol PSII, and that the maximal PSII activity is 8000 μmol O₂/mg Chl • h). However, there does not seem to be any known variation in the active site or in the cofactors involved in the ET pathways, suggesting that this difference may be due to the differences in protein structure affecting the rate-determining exchange of quinones at the Q_B site. Even though there are X-ray crystal structures of PSII from thermophilic cyanobacteria,^{33,52–54} resolution of this difference between plant and cyanobacterial PSII must wait until a crystal structure of PSII from a higher plant is obtained. This is an important

challenge yet to be overcome in the area of membrane protein crystallography. Nevertheless, based on the fact that there is close analogy in the properties of the OEC in all known PSII complexes, many structural conclusions can be drawn from the available X-ray crystal structures.

The halftime of each S-state transition, taken from Haumann *et al.*,⁵⁵ is given below. The halftimes range from 30–190 µs for the lower S-states to 1.1 ms for the $S_3 \rightarrow [S_4] \rightarrow S_0$ transition. In the $S_3 \rightarrow [S_4] \rightarrow S_0$ transition, Mn oxidation is preceded by a 200-µs lag phase. This lag phase has been attributed to a deprotonation event that precedes the final ET for oxidation of the S_3 -state. The deprotonation was suggested either to involve a substrate water or a nearby basic amino acid residue, believed to be required for efficient PT.⁵⁶ Given the slow rate of ET in the $S_3 \rightarrow [S_4] \rightarrow S_0$ transition, ΔG of reorganization in the OEC must be considered for the RDS. It is likely that a coupled PT/ET process takes place in the O–O bond-forming step, which may plausibly contribute to the high degree of organizational rearrangement in the catalytically active site.

Thermodynamically, a four-electron or rapid two-plus-two-electron mechanism appears to be best suited to oxidize H_2O ; as there is no evidence for partially oxidized products, the intermediate S-states do not seem to have enough oxidizing potential to generate partially oxidized species, such as H_2O_2 . It was proposed that the OEC reduction potential played a role in preventing such partial oxidations of H_2O (0.85 V for S_2/S_0 versus the 1.48 V for H_2O_2/H_2O couples),¹² and that this potential remains approximately constant throughout the whole S-state cycle, ~1.05 V, not much lower than the Y_Z^\bullet/Y_Z potential of ~1.1–1.2 V.³⁷

Krishtalik^{38,39} has proposed a correction to the O_2/H_2O potential within the OEC, considering the possibly high local $[H^+]$ and $[O_2]$, and that the actual potential is higher than in solution. Thus, it is reasonable that proton-coupled electron transfer (PCET) would be required to make the thermodynamics for oxidation of the Mn cluster favorable, especially in higher S-states (past S_1), where electrochromic studies reveal that a +1 charge is accumulated within the OEC.⁵⁷ Sequential release of H^+ from the active site throughout the course of the catalytic cycle has been suggested to contribute greatly in favor of the forward reaction.³⁷ However, the necessity of proton-abstracting moieties to facilitate the reaction is still important. Indeed, it has been suggested, initially from the PSII X-ray crystal structure at 3.5 Å resolution,⁵² that an arginine residue (CP43-R357) is in suitable proximity to the catalytically active face of the OEC (comprising the dangling Mn: Mn(4) in Figure 4(d) and Ca^{2+}), and may act as the “redox-coupled catalytic base”^{12,56} throughout the course of catalysis. This would require Arg-357 to have alternating shifts of pK_a , and to largely deviate from its solution pK_a of 12.48. Such a shift of possibly >6 pH units is not unlikely, considering that the OEC is in a sequestered, hydrophobic environment, and that the *microscopic* pK_a of the amino acid functional groups within the OEC can be

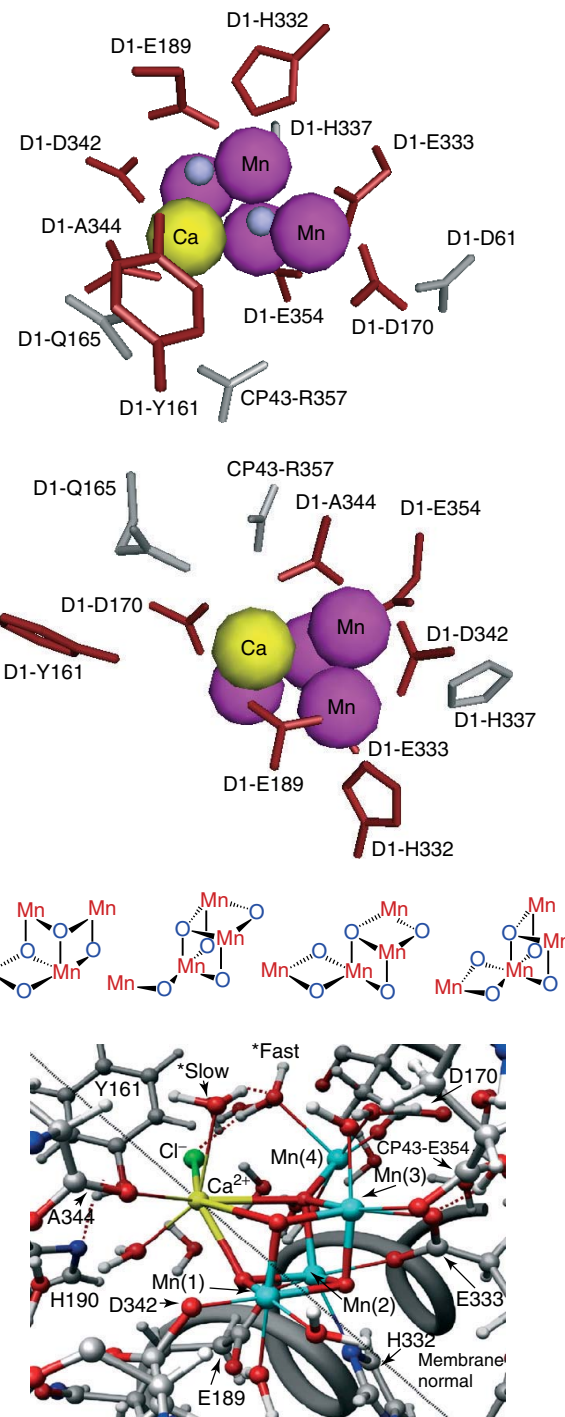


Figure 4 Views of the OEC with the surrounding amino acids. (a) Adapted from the 3.5-Å X-ray crystal structure, with the proposed first shell (in red) and second shell (in gray) ligands (small blue spheres represent bridging oxo ligands), view from the top of the OEC. (b) Adapted from the 2.9-Å structure, with the proposed first shell (in red) and second shell (in gray) ligands, view from the top of the OEC. (c) Reproduced from Ref. 59. © American Chemical Society, 2005, with the proposed coordination geometry of the Mn cluster based on EXAFS spectra. (d) Reproduced from Ref. 60. © Elsevier, 2008, with the proposed structure of the Mn cluster in the S_1 -state based on DFT QM/MM calculations

significantly lower than in bulk solvent. The trigger for deprotonation of CP43-R357 could be the changes in the electrostatic environment within the OEC, possibly brought about by the redox reactions of Y_Z . A positive charge would develop in the $Y_Z^{\bullet\bullet} \cdots H^+ \cdots$ His190 pair when Y_Z is oxidized, and would disappear when Y_Z is reduced. The former state has been suggested to cause CP43-R357 to deprotonate, passing its proton via a PT pathway to the lumen, while the latter redox state of Y_Z would raise the pK_a of CP43-R357, allowing proton abstraction from the OEC. It has to be underlined that this electrostatic change, in addition to the +1 charge present in the S_2 and higher states, makes the guanidinium group of CP43-R357 active as a base in catalysis.⁵⁶ Recent computational models⁵⁸ predict also that a μ -oxo species is formed upon the $S_2 \rightarrow S_3$ transition and could function as a base to accept a proton from water in the O–O bond-forming step (see below).

Another important aspect of the OEC mechanism, which is yet to be completely understood, is “redox leveling”, i.e., the necessity to keep the redox potential of Mn cluster within a narrow range while still oxidizing it by a total of four electrons. It had been shown from manganese-based coordination complexes that the redox potential of the complex remained similar when oxidation is coupled to deprotonation of the ligands.^{61,62} A recent study on manganese-based water-oxidizing catalysts⁶³ further reveals that the pK_a of water terminally bound to a di- μ -oxo Mn_2 (IV/IV) complex is 1.8. Moreover, oxidizing a Mn (III/IV) complex with an open coordination site for water was found to be more favorable than oxidation of a similar complex with no open coordination sites. These results could be related to the OEC redox-leveling processes, and provide a model to explain how the Mn cluster could be oxidized by the same redox-active Y_Z with a set redox potential, throughout several oxidations. The model complex data are also useful to define the pK_a of substrate water molecules, and their protonation states throughout the S-state cycle; it has been suggested that, once the OEC reaches the S_3 -state, where the oxidation states of all the Mn ions are +4, terminally coordinated substrate water bound to Mn would most likely be deprotonated.⁶³

In summary, (i) the midpoint potential of each S-state is aligned so that no partial oxidations of H_2O are favored, and a four-electron or two two-electron reactions are invoked in the catalytic mechanism for oxidation of water to O_2 , (ii) H^+ release is thought to greatly contribute to the driving force for the O–O bond-forming reaction, (iii) PCET seems to be likely, especially in the later S-states, (iv) the presence of a H^+ -accepting basic residue is suggested to facilitate the PT processes, (v) redox leveling within the OEC, analogous to Mn-based model complexes, could be achieved through coupling of oxidation with the deprotonation of a terminally coordinated substrate water molecule bound to Mn, and (vi) the pK_a of substrate water molecules would be significantly lowered by the increased formal charge on high-valent Mn(IV) ions.

Substrate water exchange and binding. Basic biochemical parameters, such as the K_m , cannot be measured for PSII, because its substrate is also its solvent. However, substrate water binding for different S-states has been probed by substrate water-exchange kinetics using $H_2^{18}O$, by mass spectrometry, summarized in a recent review.⁶⁴

Extensive research done in this area has provided valuable insight as to the sites of substrate water binding and the exchange rate upon S-state advancements. Two sites of substrate water binding were identified, one site with slow and the other with fast-exchange kinetics, and both rates change with S-state. The slow-exchange site was associated with Ca^{2+} , and the fast-exchange site with Mn. On the basis of a comparison with the exchange kinetics of model complexes and computational studies, these results are consistent with a mechanism for O–O bond formation involving the coupling of two terminally bound waters, one bound to Ca^{2+} and the other bound to Mn.^{65,66}

These studies, in comparison with work done on synthetic model high-valent Mn–aqua complexes, reveal that the exchange rate is highly affected by (i) the coordination number of the metal, (ii) the oxidation state of the metal, (iii) the coordination environment, and (iv) lastly, one very important piece of information deduced from these studies is that the oxidation of water happens in the final, $S_3 \rightarrow [S_4] \rightarrow S_0$ step, as all the preceding S-states show rapid exchange of the substrate water molecules. The relationship between substrate water exchange and the limitations this puts on the rate of water entry into the OEC through the so-called “ H_2O entry channels” are extensively discussed elsewhere.⁶⁷

Coordination, conformational, and oxidation state changes in the OEC. Information on the coordination environment of the Mn_4Ca cluster has been obtained through various FTIR studies coupled with site-directed mutagenesis,⁶⁸ in addition to the X-ray crystal structures^{33,52–54} and computational modeling.⁶⁰ Although there is still some uncertainty about the exact coordination and structure of the metal ions in the OEC, it is known that the metal ions are bridged by multiple oxo ligands. Such a coordination environment ensures that the metallic core is linked together in a compact manner. In addition, the identities of the ligating amino acid residues have been established. The imidazole N of one histidine residue is a terminal ligand to one of the Mn. All the remaining amino acid ligands to the cluster are carboxylates, but their exact mode of ligation is not established. Both terminal and bridging carboxylate coordination has been invoked. A detailed review of how the amino acids directly coordinating to the Mn cluster have been identified is available.⁶⁹ Some structures based on X-ray crystallography, EXAFS, and theoretical calculations are shown in Figure 4 for comparison.

Essential information on the conformational changes of Mn and Ca^{2+} that occur during the S-state transitions has been gathered over the years, with the use of EPR,

X-ray, and FTIR spectroscopy, overviewed in several references.^{12,37,70} The information gathered from these studies suggests that significant structural changes occur in the $S_0 \rightarrow S_1$ and $S_2 \rightarrow S_3$ transitions. For the $S_2 \rightarrow S_3$ transition, it has been suggested that a new μ -oxo bond is formed between two Mn, bringing them closer together by ~ 0.3 Å, and the coordination number of one Mn goes from 5 to 6 upon a $Mn^{III} \rightarrow Mn^{IV}$ transition. Even though such structural and coordination number changes are very likely to be accompanied by alterations in the protein ligation environment, these changes were not temperature dependent, indicating that the protein scaffold is remarkably robust.⁷¹

Taken together, these studies reveal that the Mn cluster is coordinated by eight amino acid residues, together with μ -oxo ligands, yielding a cuboidal structure. During the course of catalysis, there is evidence for changes in the coordination number and structure of the catalytically active Mn with the formation of a new μ -oxo bridge in the S_3 -state. This indicates that the catalytically active Mn should be able to change its coordination environment without a high energetic barrier and that deprotonation of water or hydroxo ligands upon oxidation of the OEC may give rise to changes in the structure of the Mn_4Ca cluster and the surrounding protein scaffold.⁶⁸

O–O bond formation: proposed mechanisms. Biophysical, biochemical, computational, and synthetic chemistry approaches have been employed to extract more information on the crucial O–O bond-formation step in PSII. However, because the S_4 -state that precedes O_2 evolution is transient and highly reactive, this has proven to be a great challenge. Indeed, the rate-limiting step for formation of the S_4 -state is ET from the S_3 -state of the OEC to Y_Z^\bullet and, as a result, the S_4 -state cannot be observed as an intermediate. Nevertheless, with information gathered from simpler synthetic models (such as dimetallic complexes, namely, $[Mn_2(O)_2(\text{terpy})_2(H_2O)_2]^{3+}$ and $Mn_2(\text{bis-porphyrin})^{72,73}$), a variety of mechanisms have been proposed over the years. Here, we discuss a few representative examples. A more thorough discussion can be found in a recent review.¹²

1. Butterfly and 2 + 2 mechanisms

The “butterfly” mechanism^{74,75} involves the coupling of two μ -oxo ligands forming an O–O bond across the face of a cuboidal Mn cluster. Even though such a mechanism was demonstrated to have a basis in gas-phase experiments where a cube with alternating Mn and O at its vertices evolves O_2 , its validity for the OEC mechanism is questionable, as isotope exchange experiments suggest slow exchange of μ -oxo ligands with the bulk solvent, indicating that such a mechanism would not be fast enough to evolve O_2 at the observed catalytic rate.

The 2 + 2 mechanism⁷⁶ involves a tetranuclear Mn cluster in the form of a “dimer of dimers” with two terminal water ligands held in close proximity to each other. Formation

of a high-valent Mn-bound oxo initiates attack by the second water to form a hydroperoxide intermediate before the final deprotonation and further oxidation results in O_2 formation. This mechanism does not agree with the structural evidence that contradicts the “dimer of dimers” structure. On the other hand, the concept of two terminal waters that are activated to go through a nucleophilic attack mechanism and form a peroxy intermediate has been picked up and formed the basis of the subsequent mechanistic proposals that fit better with the current structural evidence.

2. Coupling of oxyl radicals

Variations of this type of mechanism were postulated by several groups. Oxyl radicals, resulting from possible Mn-bound oxygen-centered oxidations in the latter steps of catalysis, have been proposed on the basis of X-ray absorption spectroscopy and suggested to be involved in reactions to form the O–O bond.⁷⁷ Similar oxyl radical formation in the latter S-states was also suggested on the basis of DFT calculations by Siegbahn.⁷⁸ Finally, a reaction between a free hydroxyl radical and a terminal oxyl radical was proposed as the O–O bond-forming step.⁷⁹

3. Nucleophilic H_2O attacking an electrophilic $Mn(V)=O$ (or $Mn(IV)–O^\bullet$)

Several groups have proposed mechanisms, elaborated in detail in McEvoy and Brudvig,¹² involving two terminal substrate water ligands, one bound to the “dangling” Mn (Mn(4) in Figure 4d), and the other bound to Ca^{2+} . As the oxidation state of Mn(4) increases, the Mn-bound terminal water would be deprotonated and could form either $Mn(V)=O$ or its spin isomer, $Mn(IV)–O^\bullet$. Then, the Ca^{2+} -bound water (or hydroxo) would be spatially proximal to nucleophilically attack the electrophilic oxygen moiety and form the O–O bond. Subsequent deprotonation and further oxidation of the terminally coordinated hydroperoxide intermediate would yield O_2 .

Computational studies. Even though a wide variety of spectroscopic observations have been made and utilized to understand the PSII catalytic mechanism, an understanding at the molecular level could best be complemented using computational methods as a tool. Computational methods employed in current PSII research are molecular dynamics (MD),¹⁴ DFT QM/MM hybrid calculations,⁶⁰ multiconformer continuum electrostatics (MCCE), and DFT calculations.⁸⁰

Recently, a DFT QM/MM study on the catalytic PSII mechanism,⁵⁸ validated through S-state dependent EXAFS studies,^{59,71,81} provided some more insight into the step-by-step mechanism of the water-oxidation catalysis. Simulations of the resulting outcome on the intermediary species agree with the experimental EXAFS data quite well. Highlights from this report are as follows. (i) The change in the coordination environment is S-state dependent, and the $S_1 \rightarrow S_2$ transition lacks any significant structural change, whereas a large conformational change accompanies the $S_0 \rightarrow S_1$ and $S_2 \rightarrow S_3$ transitions. (ii) The necessity of

redox-coupled and S-state-dependent bases are emphasized; in this work, CP43-R357 and a μ -oxo bridge formed in the $S_2 \rightarrow S_3$ act as bases and aid in the efficient deprotonation of the substrate waters. (iii) It is a matter of debate whether all the four oxidations in the OEC were Mn based. The outcome of these calculations suggests that the last oxidation involves the terminally coordinated oxo bound to Mn(4) rather than a Mn-centered oxidation, yielding an S_4 -state with significant oxy radical character. (iv) The formation of a Mn(IV)=O[•] seems to be more favorable than Mn(V)=O.

Further analyses on the pK_a shifts within the microscopic environment of the OEC, on the function and effect of Cl[−] (necessary for complete activity), and the conformers of the Mn cluster (evidenced by electron paramagnetic resonance (EPR)), etc. are necessary for a more thorough understanding of the intricacies of the water-oxidizing mechanism of PSII. More experimental results on these subjects are also highly necessary to aid in benchmarks for the theoretical calculations.

Summary. Even though further experimental and theoretical investigations are necessary to decipher the complete mechanistic details of PSII catalysis, some key points are important for understanding the mechanistic trends.

1. The pK_a of substrate water is significantly decreased during catalysis, because of its coordination with high-valent Mn species.
2. Proximal proton-accepting basic moieties are present to efficiently extract protons in the course of catalysis, and shuttle them away from the OEC, in order to thermodynamically favor water oxidation.
3. Conformational changes in the OEC accompany many of the S-state transitions, pointing to the probability that coordination changes within the Mn cluster are necessary to form the transient base (in the form of a μ -oxo species) and to allow for the coordination of additional water ligands.
4. Not all oxidations are necessarily Mn centered. Especially in higher S-states, the oxidations may be centered on Mn-coordinated oxygens.
5. Redox leveling of the Mn cluster is necessary in order to facilitate the oxidations, and the maximum redox potential should not be more than that of Y_Z (~ 1.1 – 1.2 V); deprotonation of terminal water molecules is suggested to have a significant effect on this process.

2.1.3 Photosystem I (PSI)

PSI employs light-triggered charge separations in order to drive ET toward the terminal electron acceptor in the “light” reactions, NADP⁺. Analogous to PSII, light-harvesting pigment–protein complexes absorb and transfer light energy to the site of the primary charge separation. However, unlike PSII, PSI does not use this trapped energy

for catalysis. Instead, PSI uses light for uphill ET, converting a moderate reductant (plastocyanin, PC) to a strong reductant (ferredoxin, FD).

PSI (Figure 2b) contains a “special pair” of Chl molecules called P_{700} that function as the primary electron donor. Starting from P_{700} , two identical branches of ET cofactors are present. The A- and B-branches (these names come from whether the branch is more associated with the subunit PsaA or PsaB) each contain 2 chlorophyll moieties (called A and A_0 , in order of proximity to P_{700}) and a phylloquinone (PhQ_A or PhQ_B, depending on the branch). After the phylloquinones, both branches terminate at a single 4Fe–4S iron–sulfur cluster called F_X , and all the electrons are then sequentially transferred through two additional 4Fe–4S clusters, F_A and F_B , respectively. P_{700} , which is located on the luminal end of PSI, is in the vicinity of the PC-docking site, which carries the reducing equivalents from cyt *b*₆*f*. On the stromal side of PSI is the terminal 4Fe–4S cluster, F_B , which relays the reducing equivalents to FD.

A very interesting aspect of PSI is the bidirectional ET via its two branches of ET cofactors that are related by an approximate C_2 -symmetry axis. This is in contrast with PSII, where a homologous pair of subunits, D1 and D2, is present, with an analogous pair of branches of ET cofactors related by an approximate C_2 -symmetry axis. However, the PSII constituents do not give rise to bidirectional ET but, rather, form active and inactive branches for ET. The bidirectionality in PSI has been a matter of debate, as the yields vary between plant, algal, and cyanobacterial PSI reaction centers. It is the current general consensus that the directionality of these branches is organism dependent with bidirectional ET pathways in PSI that are not exclusively a 1 : 1 utilization of the A- and B-branches, and various models have been suggested to afford the most efficient ET. An intriguing possibility is that PSI could have a two-branch system in order to ensure that ET can take place even when one of the pathways is damaged. The existence, but the lack of functionality, of these branches in PSII and the purple bacterial photosynthetic reactions center is also quite a puzzling phenomenon.

The midpoint potentials of the redox cofactors in PSI are listed in Table 3. A very thorough treatise of the thermodynamics of these ET processes in light of experimental studies is available.⁸²

Table 3 Experimental midpoint potentials of ET cofactors in PSI⁸²

ET cofactor	Midpoint potential (V)
$P_{700}^{+•}$	+0.45
A_0	−1.05
A_1 (phylloquinone)	−0.85
F_X	−0.7
F_A and F_B	−0.54 and −0.59
Ferredoxin (FD)	−0.4

The efficiency of PSI in transferring reducing equivalents allows it to be applied in processes different from its natural one. Golbeck and coworkers,⁸³ for instance, were successful in wiring PSI to gold nanoparticles on the luminal interface, and to a Ni–Fe H₂ase through a methyl viologen derivative, and demonstrated the use of these hybrid systems in light-driven H₂ formation. This is one of the half reactions of interest in artificial photosynthesis, as well as for green and sustainable fuel production.

2.2 Cytochrome *b*₆*f*

Cyt *b*₆*f* is a four-subunit complex containing the redox cofactors that are involved in ET from plastoquinol to PC: cytochrome *f* (containing one *c*-type heme), cytochrome *b*₆ (containing two *b*-type hemes and one unusual *c*-type heme), a Rieske Fe–S protein, and “subunit IV”. Its function is to oxidize the plastoquinol, which carries the reducing equivalents from water oxidation in PSII, and transfer electrons to PC, which diffuses away and docks into a binding site on PSI.

The Rieske protein’s [2Fe–2S] motif, with a redox potential of about +0.30 V, accepts one electron from plastoquinol. Then, this electron is sequentially relayed to the heme *c* in Cyt *f* (+0.34 V) and then to PC. Meanwhile, the semiquinone is further oxidized by the two heme *b* molecules (about –0.05 and –0.15 V), recycling one of the reducing equivalents from plastoquinol and releasing two protons into the lumen in a process referred to as the *Q*-cycle.⁸⁴ These reactions not only function in the ET chain but are also involved in establishing the transmembrane proton gradient, as two H⁺ are transferred into the lumen per electron from plastoquinol. Reviews on this topic are available,^{19–22} but the details are not covered in this article.

2.3 Plastocyanin, Ferredoxin, and Ferredoxin:NADP⁺ Oxidoreductase

The rest of the cofactors in the photosynthetic light reactions are briefly discussed here. PC is a soluble luminal blue copper protein that is reduced by one electron at the cytochrome *f* subunit of cyt *b*₆*f*, and shuttles electrons to PSI. FD is a soluble stromal protein, containing a [2Fe–2S] cluster, which is reduced by PSI and transfers electrons to ferredoxin:NADP⁺ oxidoreductase (FNR). The electrons are thus carried over to the final protein in the reaction chain, FNR, which catalyzes the reduction of NADP⁺ by one H⁺ and two reducing equivalents shuttled by reduced FD. FNR does not contain any metals to carry out its function, but rather a flavin adenine dinucleotide (FAD) redox center. Finally, reduced FD can also take part in cyclic ET around PSI by passing electrons to cyt *b*₆*f*. This cyclic ET pathway helps to maintain the proper balance of NADPH and ATP needed for the CO₂ fixation process in the Calvin–Benson cycle.

3 ACKNOWLEDGMENTS

This work was supported by grant GM32715 from the National Institutes of Health.

4 ABBREVIATIONS AND ACRONYMS

ATP = adenosine triphosphate; Chl = chlorophyll; Cyt = cytochrome; ET = electron transfer; FAD = flavin adenine dinucleotide; FD = ferredoxin; FNR = ferredoxin:NADP⁺ oxidoreductase; MCCE = multiconformer continuum electrostatics; MD = molecular dynamics; NADPH = reduced nicotinamide adenine dinucleotide phosphate; NADP⁺ = oxidized nicotinamide adenine dinucleotide phosphate; OEC = oxygen-evolving complex; PC = plastocyanin; PCET = proton-coupled electron transfer; Pheo = pheophytin *a*; PQ = plastoquinone; PSI = photosystem I; PSII = photosystem II; PT = proton transfer; Q = quinone; RDS = rate-determining step; TOF = turnover frequency; Rubisco = ribulose 1,5-bisphosphate carboxylase/oxygenase.

5 REFERENCES

1. A. A. Benson, *Photosynth. Res.*, 2002, **73**, 31.
2. D. T. Dennis and S. D. Blakeley, ‘Carbohydrate Metabolism’, in ‘Biochemistry and Molecular Biology of Plants’, eds. B. B. Buchanan, W. Gruissem, and R. L. Jones, American Society of Plant Physiology, Rockville, MD, 2000, p. 630.
3. H. M. Mizorko and G. H. Lorimer, *Annu. Rev. Biochem.*, 1983, **52**, 507.
4. J. N. Siedow and D. A. Day, ‘Respiration and Photorespiration’, in ‘Biochemistry and Molecular Biology of Plants’, eds. B. B. Buchanan, W. Gruissem, and R. L. Jones, American Society of Plant Physiology, Rockville, MD, 2000, p. 676.
5. R. J. Spreitzer and M. E. Salvucci, *Annu. Rev. Plant Biol.*, 2002, **53**, 449.
6. R. Douce and M. Neuberger, *Curr. Opin. Plant Biol.*, 1999, **2**, 214.
7. M. C. Hatch, *Biochim. Biophys. Acta*, 1987, **895**, 81.
8. N. E. Tolbert, *Annu. Rev. Plant Physiol. Plant Mol. Biol.*, 1997, **48**, 1.
9. T. J. Wydrzynski and K. Satoh eds, ‘Photosystem II: The Light-driven Water: Plastoquinone Oxidoreductase’; Springer, Dordrecht, The Netherlands, 2005.
10. J. Barber, K. N. Ferreira, K. Maghlaoui, and S. Iwata, *Phys. Chem. Chem. Phys.*, 2004, **6**, 4737.
11. G. W. Brudvig, *Phil. Trans. R. Soc. B*, 2008, **363**, 1211.
12. J. P. McEvoy and G. W. Brudvig, *Chem. Rev.*, 2006, **106**, 4455.

13. G. Renger and T. Renger, *Photosynth. Res.*, 2008, **98**, 53.
14. S. Vassiliev and D. Bruce, *Photosynth. Res.*, 2008, **97**, 75.
15. J. H. Golbeck ed., ‘Photosystem I: The Light-driven Plasto-cyanin: Ferredoxin Oxidoreductase’; Springer, Dordrecht, The Netherlands, 2006.
16. P. Fromme and P. Mathis, ‘Unraveling the Photosystem I Reaction Center: A History, or the Sum of Many Efforts’, in ‘Discoveries in Photosynthesis’, eds. J. T. Govindjee, H. G. Beatty, and J. F. Allen, Springer, Dordrecht, The Netherlands, 2005, p. 311.
17. P. E. Jensen, R. Bassi, E. J. Boekema, J. P. Dekker, S. Jansson, D. Leister, C. Robinson, and H. V. Scheller, *Biochim. Biophys. Acta*, 2007, **1767**, 335.
18. K. E. Redding, ‘Photosystem I’, in ‘The Chlamydomonas Sourcebook: Organellar and Metabolic Processes’, 2nd edition, ed. D. B. Stern, Academic Press, 2009, Vol. 2.
19. D. Baniulis, E. Yamashita, H. Zhang, S. S. Hasan, and W. A. Cramer, *Photochem. Photobiol.*, 2008, **84**, 1349.
20. W. A. Cramer, H. Zhang, J. Yan, G. Kurisu, and J. L. Smith, *Annu. Rev. Biochem.*, 2006, **75**, 760.
21. G. Hauska and T. Schoedi, ‘Encyclopedia of Biological Chemistry’, 2004, Vol. 1, p. 521.
22. G. Hauska, M. Shchütz, and M. Büttner, ‘The Cytochrome b₆f Complex—Composition, Structure and Function’, in ‘Oxygenic Photosynthesis: The Light Reactions’, in ‘Oxygenic Photosynthesis: the Light Reactions’, eds. D. R. Ort and C. F. Yocum, Kluwer Academic Publishers, Dordrecht, The Netherlands, 1996, p. 377.
23. D. R. Ort and C. F. Yocum eds, ‘Oxygenic Photosynthesis: The Light Reactions’; Kluwer Academic Publishers, Dordrecht, The Netherlands, 1996.
24. B. B. Buchanan, W. Grussem, and R. L. Jones eds, ‘Biochemistry and Molecular Biology of Plants’; American Society of Plant Physiology, Rockville, MD, 2000.
25. R. E. Blankenship, ‘Molecular Mechanisms of Photosynthesis’, Blackwell Science, Oxford, 2002.
26. H.-W. Heldt, ‘Plant Biochemistry and Molecular Biology’, Oxford University Press, Oxford, 1997.
27. R. van Grondelle, J. P. Dekker, T. Gillbro, and V. Sundstrom, *Biochim. Biophys. Acta*, 1994, **1187**, 1.
28. B. A. Diner and G. T. Babcock, ‘Structure, Dynamics, and Energy Conversion Efficiency in Photosystem II’, in ‘Oxygenic Photosynthesis: The Light Reactions’, eds. D. R. Ort, and C. F. Yocum, Kluwer Academic Publishers, Dordrecht, The Netherlands, 1996, p. 213.
29. L. M. C. Barter, D. R. Klug, and R. van Grondelle, ‘Energy Trapping and Equilibration: A Balance of Regulation and Efficiency’, in ‘Photosystem II: The Light-driven Water: Plastoquinone Oxidoreductase’, eds. T. J. Wydrzynski, and K. Satoh, Springer, Dordrecht, The Netherlands, 2005, p. 491.
30. G. Renger and A. R. Holzwarth, ‘Primary Electron Transfer’, in ‘Photosystem II: The Light-driven Water: Plastoquinone Oxidoreductase’, eds. T. J. Wydrzynski, and K. Satoh, Springer, Dordrecht, The Netherlands, 2005, p. 139.
31. M. L. Groot, N. P. Pawłowicz, L. J. G. W. van Wilderen, J. Breton, I. H. M. van Stokkum, and R. van Grondelle, *Proc. Natl. Acad. Sci. USA*, 2005, **102**, 13087.
32. G. Renger, ‘Energy Transfer and Trapping in Photosystem II’, in ‘The Photosystems: Structure, Function and Molecular Biology’, ed. J. Barber, Elsevier Science Publishers, Amsterdam, The Netherlands, 1992, p. 45.
33. A. Guskov, J. Kern, A. Gabdulkhakov, M. Broser, A. Zouni, and W. Saenger, *Nat. Struct. Mol. Biol.*, 2009, **16**, 334.
34. M. Grabolle and H. Dau, *Biochim. Biophys. Acta*, 2005, **1708**, 209.
35. F. Rappaport, M. Guergova-Kuras, P. J. Nixon, B. A. Diner, and J. Lavergne, *Biochemistry*, 2002, **41**, 8518.
36. H. Schiller and H. Dau, *J. Photochem. Photobiol. B: Biol.*, 2000, **55**, 138.
37. H. Dau and M. Haumann, *Coord. Chem. Rev.*, 2008, **252**, 273.
38. L. I. Kristhalik, *Biochim. Biophys. Acta*, 1986, **849**, 162.
39. L. I. Kristhalik, *Bioelectrochem. Bioenerg.*, 1990, **23**, 249.
40. Y. Kato, M. Sugiura, A. Oda, and T. Watanabe, *Proc. Natl. Acad. Sci. USA*, 2009, **106**, 17365.
41. T. Shibamoto, Y. Kato, M. Sugiura, and T. Watanabe, *Biochemistry*, 2009, **48**, 10682.
42. H. H. Robinson and A. R. Crofts, *FEBS Lett.*, 1983, **153**, 221.
43. I. Vass and S. Styring, *Biochemistry*, 1991, **30**, 830.
44. R. J. Debus, B. A. Barry, I. Sithole, G. T. Babcock, and L. McIntosh, *Biochemistry*, 1988, **27**, 9071.
45. J. G. Metz, P. J. Nixon, M. Rögner, G. W. Brudvig, and B. A. Diner, *Biochemistry*, 1989, **28**, 6960.
46. B. A. Diner and R. D. Britt, ‘The Redox-active Tyrosines Y_Z and Y_D’, in ‘Photosystem II: The Light-driven Water: Plastoquinone Oxidoreductase’, eds. T. J. Wydrzynski, and K. Satoh, Springer, Dordrecht, The Netherlands, 2005, p. 207.
47. G. Renger, *Biochim. Biophys. Acta*, 2001, **1503**, 210.
48. C. Tommos and G. T. Babcock, *Biochim. Biophys. Acta*, 2000, **1458**, 199.
49. A.-M. A. Hays, I. R. Vassiliev, J. H. Golbeck, and R. J. Debus, *Biochemistry*, 1999, **38**, 11851.
50. V. A. Szalai, H. Kühne, K. V. Lakshmi, and G. W. Brudvig, *Biochemistry*, 1998, **37**, 13594.
51. C. W. Cady, R. H. Crabtree, and G. W. Brudvig, *Coord. Chem. Rev.*, 2008, **252**, 444.
52. K. N. Ferreira, T. M. Iverson, K. Maghlaoui, J. Barber, and S. Iwata, *Science*, 2004, **303**, 1831.
53. K. Kawakami, Y. Umena, N. Kamiya, and J.-R. Shen, *Proc. Natl. Acad. Sci. USA*, 2009, **106**, 8567.
54. B. Loll, J. Kern, W. Saenger, A. Zouni, and J. Biesiadka, *Nature*, 2005, **438**, 1040.
55. M. Haumann, P. Liebisch, C. Müller, M. Barra, M. Grabolle, and H. Dau, *Science*, 2005, **310**, 1019.

56. J. P. McEvoy and G. W. Brudvig, *Phys. Chem. Chem. Phys.*, 2004, **6**, 4754.
57. E. Schlodder and H. T. Witt, *J. Biol. Chem.*, 1999, **274**, 30387.
58. E. M. Sproviero, J. A. Gascón, J. P. McEvoy, G. W. Brudvig, and V. S. Batista, *J. Am. Chem. Soc.*, 2008, **130**, 3428.
59. J. Yano, Y. Pushkar, P. Glatzel, A. Lewis, K. Sauer, J. Messinger, U. Bergmann, and V. K. Yachandra, *J. Am. Chem. Soc.*, 2005, **127**, 14974.
60. E. M. Sproviero, J. A. Gascón, J. P. McEvoy, G. W. Brudvig, and V. S. Batista, *Coord. Chem. Rev.*, 2008, **252**, 395.
61. M. T. Caudle and V. L. Pecoraro, *J. Am. Chem. Soc.*, 1997, **119**, 3415.
62. H. H. Thorp, J. E. Sarneski, G. W. Brudvig, and R. H. Crabtree, *J. Am. Chem. Soc.*, 1989, **111**, 9249.
63. C. W. Cady, K. Shinopoulos, R. H. Crabtree, and G. W. Brudvig, *Dalton Trans.*, 2010, **39**, 3985.
64. W. Hillier and T. J. Wydrzynski, *Coord. Chem. Rev.*, 2008, **252**, 306.
65. E. M. Sproviero, K. Shinopoulos, J. A. Gascón, J. P. McEvoy, G. W. Brudvig, and V. S. Batista, *Phil. Trans. R. Soc. B*, 2008, **363**, 1149.
66. R. Tagore, H. Chen, R. H. Crabtree, and G. W. Brudvig, *J. Am. Chem. Soc.*, 2006, **128**, 9547.
67. F. M. Ho, *Photosynth. Res.*, 2008, **98**, 503.
68. T. Noguchi, *Coord. Chem. Rev.*, 2008, **252**, 336.
69. R. J. Debus, *Coord. Chem. Rev.*, 2008, **252**, 244.
70. K. Sauer, J. Yano, and V. K. Yachandra, *Coord. Chem. Rev.*, 2008, **252**, 318.
71. M. Haumann, C. Müller, P. Liebisch, L. Iuzzolino, J. Dittmer, M. Grabolle, T. Neisius, W. Meyer-Klaucke, and H. Dau, *Biochemistry*, 2005, **44**, 1894.
72. J. Limburg, J. S. Vrettos, L. M. Liable-Sands, A. L. Rheingold, R. H. Crabtree, and G. W. Brudvig, *Science*, 1999, **283**, 1524.
73. Y. Shimazaki, T. Nagano, H. Takesue, B.-H. Ye, F. Tani, and Y. Naruta, *Angew. Chem. Int'l. Ed.*, 2004, **43**, 98.
74. W. Ruettger, M. Yagi, K. Wolf, S. Bernasek, and G. C. Dismukes, *J. Am. Chem. Soc.*, 2000, **122**, 10353.
75. J. B. Vincent and G. Christou, *Inorg. Chim. Acta*, 1987, **136**, L41.
76. C. W. Hoganson and G. T. Babcock, *Science*, 1997, **277**, 1953.
77. V. K. Yachandra, in ‘Photosystem II: Light-driven Water: Plastoquinone Oxidoreductase’, eds. T. J. Wydrzynski and K. Satoh, Springer-Verlag, Dordrecht, The Netherlands, 2005.
78. P. E. M. Siegbahn, *Inorg. Chem.*, 2000, **39**, 2923.
79. H. Dau, L. Iuzzolino, and J. Dittmer, *Biochim. Biophys. Acta*, 2001, **1503**, 24.
80. P. E. M. Siegbahn and M. R. A. Blomberg, *Dalton Trans.*, 2009, 5832.
81. H. Dau, P. Liebisch, and M. Haumann, *Phys. Chem. Chem. Phys.*, 2004, **6**, 4781.
82. D. Mauzerall, ‘Thermodynamics of Photosystem I’, in ‘Photosystem I: The Light-driven Plastocyanin:Ferredoxin Oxidoreductase’, ed. J. H. Golbeck, Springer, Dordrecht, The Netherlands, 2006, p. 571.
83. C. E. Lubner, R. Grimme, D. A. Bryant, and J. H. Golbeck *Biochemistry*, 2010, **49**, 404.
84. P. Mitchell, *J. Theor. Biol.*, 1976, **62**, 327.

Molecular Catalysts for Oxygen Production from Water

Antoni Llobet

Institute of Chemical Research of Catalonia (ICIQ) and Universitat Autònoma de Barcelona, Barcelona, Spain

and

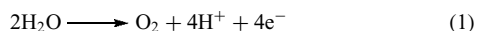
Sophie Romain

Institute of Chemical Research of Catalonia (ICIQ), Barcelona, Spain

1	Introduction	35
2	Water Oxidation at a Molecular Level	37
3	O–O Bond Formation Promoted by Ru Complexes	38
4	Polynuclear Ru Complexes	39
5	Mononuclear Ru Complexes	47
6	Ir Complexes	49
7	Mn and Co Complexes and Oxides	49
8	Conclusions	50
9	Complex Numbering	50
10	Acknowledgments	50
11	Related Articles	50
12	Abbreviations and Acronyms	51
13	References	51

1 INTRODUCTION

The oxidation of water to molecular oxygen is a reaction that takes place in the dark in the oxygen-evolving complex of photosystem II, OEC-PSII.^{1,2}



It is a very interesting reaction to be modeled from a bioinorganic perspective, since it can give insight into the mechanism that operates in this natural system. It is of still greater importance from an energetic perspective, since water oxidation has been recognized as the bottleneck in the development of commercial light-harvesting devices for the photoproduction of H₂ from water.^{3,4}

Actually, for solar energy conversion schemes, a good catalyst capable of oxidizing water to dioxygen and its assembly into a cell for the photoproduction of hydrogen are

seen as one of the most promising solutions for maintaining our lifestyle in the near future. Potential schemes for the use of sunlight to split water into H₂ and O₂ have currently been presented, but so far have never been put into practice. An example is shown in Figure 1.

This device is based on a modification of the so-called Grätzel cell,⁵ where, instead of simply generating a photocurrent, the cell is modified to use the electron flow to prepare and store a chemical fuel, in this particular case, molecular hydrogen. The cell contains two compartments physically separated by a proton exchange membrane, and it consists of three components. The first component is the light-harvesting antenna ore photosensitizer, P (typically a Ru(bpy)₃²⁺ type of complex; bpy is 2,2'-bipyridine; the ligands described in this work are depicted in Scheme 1), which, upon irradiation generate an excited state that in turn transfers an electron to the conduction band of a TiO₂ photoanode semiconductor (TiO₂(cb)). A very important feature of this Grätzel cell is

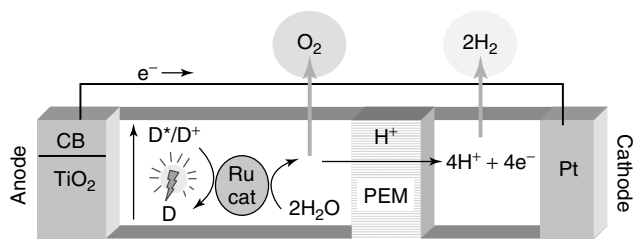
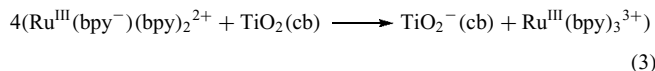
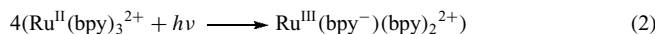


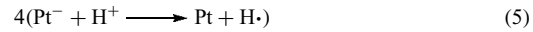
Figure 1 Schematic drawing of a water-splitting photochemical cell with three components: a light-harvesting device attached to a semiconductor photoanode, a Ru water oxidation catalyst, and a Pt cathode where hydrogen is evolved. See text for further details

the fact that upon excitation by light, the electron-transfer (ET) process from the bpy-based excited state to the $\text{TiO}_2(\text{cb})$ surface takes place at the pico- to femto-second timescale and the quantum yield of charge injection exceeds 90%. These two processes are shown in equations (2) and (3) below:

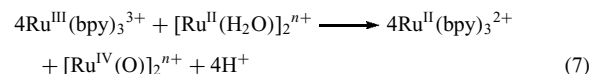


where $\text{TiO}_2^-(\text{cb})$ represents the conduction band of the TiO_2 containing a transferred electron. The reaction is indicated four times for stoichiometric reasons, vide infra. Then, TiO_2 photoanode sends electrons to the second component, that

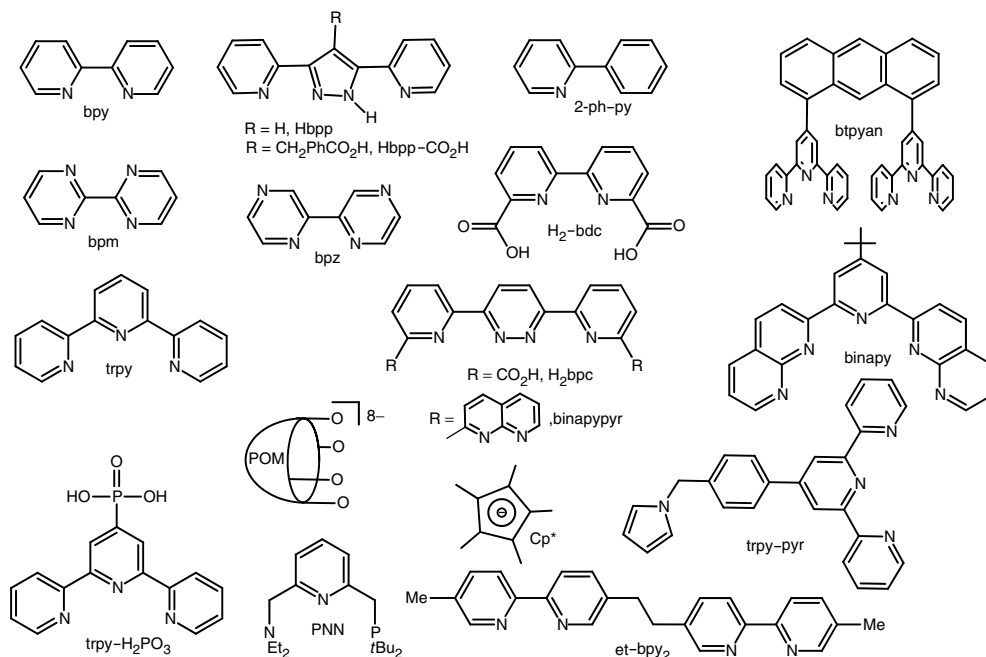
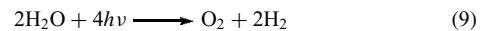
is, a Pt cathode, where the electron reduction takes place as indicated in equations (4)–(6), and the process ends with the production of molecular hydrogen in the right compartment of the cell (Figure 1):



The third component contains the water oxidation catalyst, represented here by $[\text{Ru}^{\text{II}}(\text{H}_2\text{O})]_2^{n+}$, that is, for instance, a diruthenium–diaquo complex similar to the ones that are described in this paper and whose auxiliary ligands are not shown. The oxidized photosensitizer, $\text{Ru}^{\text{III}}(\text{bpy})_3^{3+}$ type of complex, is now used to oxidize the water oxidation catalyst to its higher oxidation states, and the process ends up in the production of molecular oxygen in the left compartment, as shown in Figure 1, as illustrated in equations (7) and (8):



The overall reaction after adding up equations (2)–(8) corresponds to water splitting by visible light:



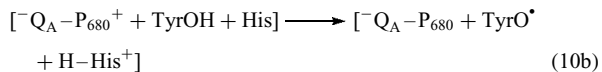
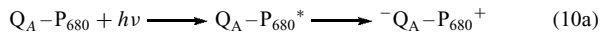
Scheme 1 The ligands used

The combination of all the reactions carried out by the device just described has a synthetic origin, and thus this solar energy conversion strategy can be named “the materials science way”. However, the same concepts and reactions can be potentially carried out partially⁶ or totally⁷ by natural systems, leading to “the hybrid way” and “the biological way”, respectively.

The topic is so appealing that many research groups have started to work in this field, and as a result very important contributions have recently appeared in the literature. The objective of this article is to give an overview of the elements that constitute the pillars of the field and to describe and discuss the new aspects of selected recent contributions that are reshaping the way we think about this field.

2 WATER OXIDATION AT A MOLECULAR LEVEL

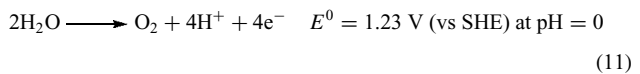
Nature takes advantage of PCET (proton-coupled electron transfer) in a variety of enzymatic processes, involving vitamin B₁₂, cytochromes P₄₅₀, and lipoxygenases.⁸ An example for this key transfer is the activation of PSII toward water oxidation. Oxidative quenching of a chlorophyll excited state P₆₈₀^{*} by a bound Q_A plastoquinone generates ⁻Q_A–P₆₈₀⁺ complex with charge separation. This is followed by fast electron transfer (ET) in the timescale of microseconds to nanoseconds, from Tyr161 (Tyrosine-161 or Y_z) to P₆₈₀⁺, which are separated by ca 10 Å, to give the neutral species P₆₈₀ and the tyrosine radical TyrO[•] (Y_z[•]), together with the release of a proton. This process is energetically favored thanks to a proximal histidine residue, His190, which picks up the above-mentioned proton. Thus, this constitutes an example of multiple-site concerted proton-coupled electron transfer (MS-EPT).⁹



The process shown in equation (10b) is thermodynamically favorable since $\Delta G^0 = -8.4 \text{ kcal mol}^{-1}$. It is important to realize here that stepwise processes in which the proton followed by the electron is transferred (ET-PT) or vice versa (PT-ET) incur serious energy penalties of 6.0 and 1.8 kcal mol⁻¹, respectively.

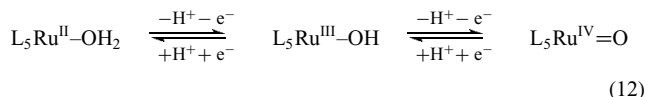
In the following step, the Y_z[•] radical species oxidizes the OEC tetranuclear Mn complex to its higher oxidation states through a series of electron and proton transfer processes, finally releasing molecular oxygen; this sequence of redox reactions is known as the Kok cycle and is the subject of intense research at the moment.¹⁰ Thus, the tetranuclear Mn complex acts as a catalyst in the process of oxidation of water, a photochemically induced reaction that occurs in the dark.

The water oxidation reaction is a thermodynamically demanding reaction and constitutes an example of PCET as shown below:



This reaction is of enormous molecular complexity from a mechanistic perspective, since formally it involves the removal of four protons and four electrons from two water molecules, together with the formation of an oxygen–oxygen bond. It is thus an important reaction to be modeled since efficient low-molecular-weight models can lead to a first step toward creating a clean renewable energy source. Recently, substantial efforts have been directed toward the elucidation of the structure and mechanisms of oxidation of water that takes place in the oxygen-evolving complex (OEC) of PSII,^{1,2,11,12} constituting fundamental information to inspire future research in the field of low-molecular-weight structural and functional models.

Most of the Ru complexes described here, which are capable of oxidizing water to molecular dioxygen, are based on, or are precursors of, the so-called Ru–OH₂/Ru=O system discovered by Meyer’s group about three decades ago.¹³ The capacity of Ru–aquo polypyridyl complexes to lose protons and electrons and easily reach higher oxidation states is exemplified in the following equation (L₅ = polypyridyl ligands)



The higher oxidation states are accessible within a narrow potential range mainly because of the σ and π donating nature of the oxo group. In addition, the simultaneous loss of protons and electrons precludes an otherwise highly destabilized scenario with highly charged species. Thus proton-coupled electron transfer (PCET) again provides energetically reasonable reaction pathways that avoid high-energy intermediates. For instance, for the comproportion reaction of LRu^{II}–OH₂ (L=(bpy)₂(py)) and LRu^{IV}=O to give two molecules of LRu^{III}–OH, the energy penalty for a stepwise process with regard to the PCET is higher than 12.6 kcal mol⁻¹ for the ET-PT and higher than 13.6 kcal mol⁻¹ for the PT-ET, whereas the concerted pathway is downhill by $-2.5 \text{ kcal mol}^{-1}$. Furthermore, the energy of activation for the concerted proton–electron transfer process EPT is 10.1 kcal mol⁻¹ and is lower than the thermodynamic value of any of the stepwise pathways.¹⁴

A large amount of literature has emerged related to these type of systems, mainly because of the rich oxidative properties of the Ru^{IV}=O species. Reaction mechanisms for the oxidation of several substrates by Ru^{IV}=O have been established and catalytic oxidation systems described.¹³

The Ru–OH₂/Ru=O system provides low-energy oxidation pathways for a 2H⁺, 2e[−] loss; it follows that the design of complexes capable of performing the above-mentioned process twice with the adequate redox potentials should be able to provide low-energy pathways for the oxidation of water to O₂ as shown in equation (1). Finally, for the production of oxygen, another inevitable requirement is obviously the formation of an oxygen–oxygen bond.

3 O–O BOND FORMATION PROMOTED BY Ru COMPLEXES

A fundamental piece of knowledge that is needed to further develop this field and design an efficient and rugged catalyst is the understanding of the mechanism through which the water oxidation reaction can proceed, promoted by transition metal complexes.

The oxidation of water leads to a range of species depending on the number of electrons removed, whose thermodynamics are summarized in Table 1, together with interesting features of the oxidized species. As can be observed from the Table, the more the electrons transferred the lower the thermodynamic potential. Thus, a one-electron oxidation process has a prohibitive thermodynamic barrier of 2.5 V vs SSCE at pH = 1.0, whereas the four-electron transfer, as it happens in the OEC-PSII,¹⁵ has the lowest barrier (equation (1)).

This lowering of thermodynamics contrasts with the increase in molecular complexity. In the four-electron process, 4O–H bonds from two water molecules need to be broken and an O–O bond needs to be formed. Thus, the potential transition metal complexes that can be considered as candidates to carry out this reaction in a catalytic manner are required to deal with multiple-electron transfer processes accompanying proton transfer management. These requirements are met by Ru–OH₂ polypyridyl complexes mentioned in the previous section.

There are several issues that make mechanistic determinations challenging and that have been hampering its development. One is the intrinsic complexity of the reaction, where the catalyst is likely to cycle among five different

oxidation states, whether metal or ligand based or both.¹⁶ This imposes a requirement for transition metal complexes that need to be sufficiently long lived to be able to perform the reaction and also to be spectroscopically detectable. Another fundamental problem is the unavoidable use of water as solvent, which is a problematic issue because of the limited temperature range in which reactions can be studied, and its high absorptivity prevents the proper use of techniques such as UV-vis-near-IR, EPR, etc., that could provide otherwise valuable information. One more problem associated with this reaction is the limited solubility of the catalysts or catalyst precursors in water; some are completely insoluble. This leads to inherent difficulties in measuring physical properties at low concentrations and, in some cases, the difficulty in separating the kinetics of the reactions involved with the solubilization of the starting complex and/or its intermediates. In some instances, organic solvents like acetonitrile have been added to permit the reaction to proceed, but this introduces an increase in mechanistic complexity due to the potential coordination of MeCN with the active species.¹⁷ An additional problem is that the high thermodynamic redox potential needed for the oxidation of water permits the catalyst to oxidize a broad range of organic and inorganic substrates, and thus the presence of organic solvents can lead to undesirable deactivation pathways.¹⁸

For simplicity, the oxidation state of the Ru metal is considered formally, keeping in mind that electron distribution depends on the rest of the auxiliary ligands. As an example, the bonding is represented as a combination of two extreme resonance forms, such as Ru(IV)=O \longleftrightarrow Ru(III)–O[−].

Formally, from a mechanistic perspective, the formation of an oxygen–oxygen bond promoted by transition metal complexes can be classified on the basis of whether an unbound free water molecule participates in the formation of the aforementioned bond. From this perspective, two possibilities exist:

1. Solvent water nucleophilic attack (WNA) on an M–O as depicted in Scheme 2.

As depicted in the scheme, there is a 4-ET demand for the complex, which is quite stringent for a mononuclear

Table 1 Redox potentials for the oxidation of water at pH 1.0 and 7.0 together with key features of the water oxidized species

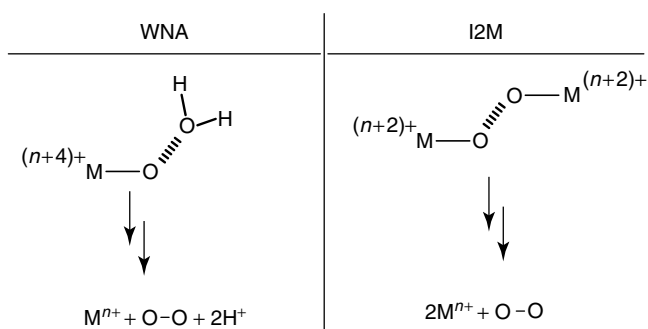
Redox couple	E ⁰ , V (vs SSCE)		H ₂ O-oxidized species			
	pH = 1.0	pH = 7.0	BO ^(a)	n ^(b)	freq ^(c)	Dist ^(d)
•OH + 1H ⁺ + 1e [−] → H ₂ O	2.50	2.15	—	—	—	—
HO–OH + 2H ⁺ + 2e [−] → 2H ₂ O	1.48	1.13	1	0	740–850	1.49
HO–O [·] + 3H ⁺ + 3e [−] → 2H ₂ O	1.37	1.02	1.5	1	1100–1150	1.28
O=O + 4H ⁺ + 4e [−] → 2H ₂ O	0.94	0.58	2	2	1560	1.21

^(a) BO: O–O bond order.

^(b) n is the number of unpaired electrons.

^(c) freq is the range of vibrational frequencies for the O–O bond in cm^{−1}.

^(d) dist refers to the range of O–O bond distance in Å.



Scheme 2 Potential metal-based O–O bond formation pathways

complex. A solution to this is to share the burden with more metal centers in a cooperative manner, provided there is a bridging ligand (BL) that couples them electronically. Another option for a metal complex is to cycle up and down in similar oxidation states of different species as is shown in the following section. It is interesting to point out here that WNA is one of the favored mechanisms nowadays for the OEC-PSII,¹⁹ and it is also the mechanism proposed for the inverse reaction, the reduction of dioxygen in the HIP Cyt-P450.²⁰ Furthermore, this mechanism has recently been shown to occur in a Mn–porphyrin model complex.²¹ As discussed in the following section, the complex can be mononuclear or polynuclear and it can have one or several Ru–O groups. In the case of the latter, the role of each Ru–O group is radically different. While one of them will be responsible for the O–O bond formation, the other center/s will be responsible for facilitating electron trafficking so that the four-electron acceptance process can be shared among the different metal centers.

2. The interaction of two M–O entities (I2M), displayed in Scheme 2.

In the scheme, this reaction is described as a reductive elimination, but depending on the oxidation states of both the metal center and the oxygen atoms, the O–O bond-forming step could also be a radical–radical coupling reaction. As with the previous mechanism, the nuclearity of the complex can also be variable. The interaction of two Ru–O units can potentially take place both in an intramolecular manner with complexes containing two Ru–O units linked by a BL and through a bimolecular process with complexes containing only one Ru–O unit.

4 POLYNUCLEAR Ru COMPLEXES

Polynuclear complexes are, in general, more difficult to prepare and characterize than the corresponding mononuclear complexes, and the nature and properties of the complex are strongly dependent on the BL. The BL is responsible for

the degree of electronic coupling between the metal centers,²² and thus can strongly influence the electronic structure of the metal. Furthermore, the BL can also have control on the potential to a certain extent through space interactions of the putative active groups. From a mechanistic perspective, the presence of two or more metal centers in the complex adds to the complexity since even for symmetrical complexes, the roles of metals in the catalytic cycle might be different.

4.1 The Blue Dimer and Analogs

In 1982, Meyer's group reported the synthesis, structure, and electrochemical properties of a dinuclear complex, *cis,cis*-{[Ru^{III}(bpy)₂(H₂O)]₂(μ-O)}⁴⁺, 1, shown in Figure 2(a), commonly known as *the blue dimer* ($\lambda_{\text{max}} = 637 \text{ nm}$; $\varepsilon = 21\,100$ at pH = 1.0).^{23,24} In this dimer, each metal center contains a Ru–OH₂ group in oxidation state III, bridged by a dianionic oxido ligand; the rest of the available positions for an octahedral type of coordination are occupied by ancillary bpy ligands. The bridging oxido ligand is responsible for the electronic coupling between the metal centers, which is manifested by its unique magnetic, spectroscopic, and electrochemical properties.²⁵ This, in turn, is responsible for its redox properties and, by extension, for its catalytic behavior. It is important to note here that the aquo ligands are *cis* with regard to the oxido-bridging ligand, their relative torsion angle is 65.7°, and the Ru–OH₂ oxygen are situated at a distance of 4.72 Å. A thorough thermodynamic picture of the zones of stability of the different oxidation states of the blue dimer is offered by its Pourbaix diagram shown in Figure 2(b). At lower oxidation states such as III,II, the complex undergoes reductive cleavage of the Ru–O–Ru bond within the cyclic voltammetry timescale, leading to the corresponding mononuclear complexes—a chemistry typical for this type of oxide-bridge compounds²⁶—which are not shown in the Pourbaix diagram.

For the blue dimer at pH = 1.0, in which most of the catalytic water oxidation has been carried out, it is interesting to observe that it shows two redox processes: one at $E^{\circ} = 0.79 \text{ V}$, which involves the removal of one electron from III,III to give the III,IV oxidation state, and the other at $E^{\circ} = 1.22 \text{ V}$, which involves the removal of three electrons from III,IV to give the V,V oxidation state. Overall, the E° for the four-electron process, V,V to III,III, appears at 1.12 V, that is, 180 mV above the thermodynamic value for the oxidation of water to molecular oxygen at pH = 1.0 ($E^{\circ} = 0.94 \text{ V}$, see Table 1: redox potentials at pH 1 and 7).

In the presence of excess Ce^{IV}, the blue dimer is capable of oxidizing water to molecular oxygen, yielding at least 13.2 turnover cycles.²⁷ It is assumed that one of the major handicaps for this catalytic cycle is anation that deactivates the catalytic species. Over the last 20 years, there have been a few mechanistic studies that have been carried out in order to understand how the reaction proceeds. In this article, we describe a simplified version that contains the

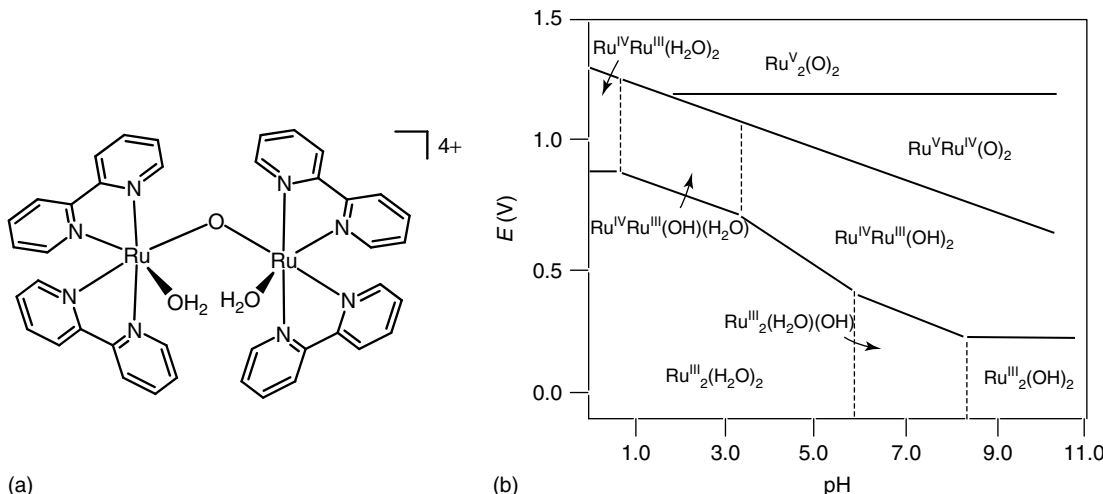
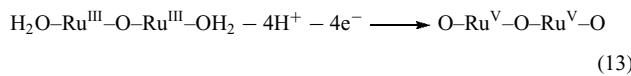


Figure 2 (a) Drawn structure of the *cis,cis*-[$\text{Ru}^{\text{III}}(\text{bpy})_2(\text{H}_2\text{O})$] $_2(\mu\text{-O})$ $^{4+}$, **1**, complex. (b) Pourbaix diagram. The zones of stability of the different species generated by proton and electron loss or gain are indicated. The bpy and O^{2-} ligands are not indicated in the diagram. Redox potentials are referenced vs SSCE

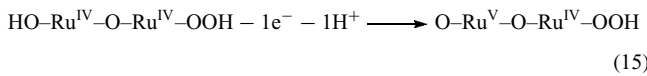
latest contributions reflecting the present state of knowledge on this system.^{28,29} Figure 3(a) shows the mechanism proposed for this reaction using both a stoichiometric amount and an excess of the Ce^{IV} oxidant. For both cases, a series of one-electron oxidations are proposed, which in some cases are also accompanied by proton transfer, wherein the initial $\text{Ru}^{\text{III}}-\text{O}-\text{Ru}^{\text{III}}$ complex is oxidized to its $\text{Ru}^{\text{V}}-\text{O}-\text{Ru}^{\text{V}}$ oxidation state as summarized in the following equation, where the bpy ligands and overall charge of the complex have been omitted:



The individual rate constants have also been calculated (Figure 3a) and show the last ET process as the slowest process. Once generated, this species suffers a nucleophilic attack from the solvent, water, to generate a potential $\text{OH}-\text{Ru}^{\text{IV}}-\text{O}-\text{Ru}^{\text{IV}}-\text{OOH}$ intermediate,



In the absence of excess oxidant (Ce^{IV}), this intermediate releases molecular oxygen and generates the initial blue dimer in its III,III oxidation state in a “volcano” type of mechanism, as illustrated in Figure 3(b). In the presence of an excess of oxidant, it is proposed that the $\text{OH}-\text{Ru}^{\text{IV}}-\text{O}-\text{Ru}^{\text{IV}}-\text{OOH}$ intermediate is further oxidized to the IV,V oxidation state:



Now this V,IV species rapidly releases molecular oxygen with generation of the III,IV species; in this case, it represents a “rollercoaster” type of mechanism as depicted in Figure 3(c).

As mentioned before, in polynuclear complexes, the role of the BL is critical since it is responsible among other issues for establishing the degree of communication between metal centers. The *blue dimer* is a good example of the importance of this influence, which can be clearly observed in equation (14), where the species with oxidation state V,V reacts with water oxidized by two electrons to form hydroperoxidic intermediate with oxidation state IV,IV, where the two-electron oxidation is shared by the two metals. This description of the mechanism raises another important issue, that is, the role of the two metal centers is clearly different, even if the complex possesses C_2 symmetry. While one of the metal centers is responsible for the O–O bond formation through WNA, the other one mainly acts as an electron shuttle. This cooperative effect allows sharing of the burden of multiple-electron transfer between the two metal centers and occurs thanks to the electronic coupling of the oxido-bridging ligand.

For the *blue dimer*, Hurst’s group³⁰ proposed mechanisms different than the ones just described. In particular, they proposed that, besides the WNA mechanism described above, there is a part of the oxidation process that involves the bpy ligands in the formation of the O–O bond as is depicted in Figure 3(d). This mechanism is proposed to occur when the dimer in its $\text{Ru}^{\text{V}}=\text{O}$ form reacts with a solvent, water, that adds to one of the pyridyl ring of a bpy forming a coordinated bpy radical that further adds one more water forming a *cis*-dihydroxyl-bpy, which is responsible for the formation of the O–O bond that finally produces molecular oxygen and the initial Ru complex, closing the catalytic cycle.

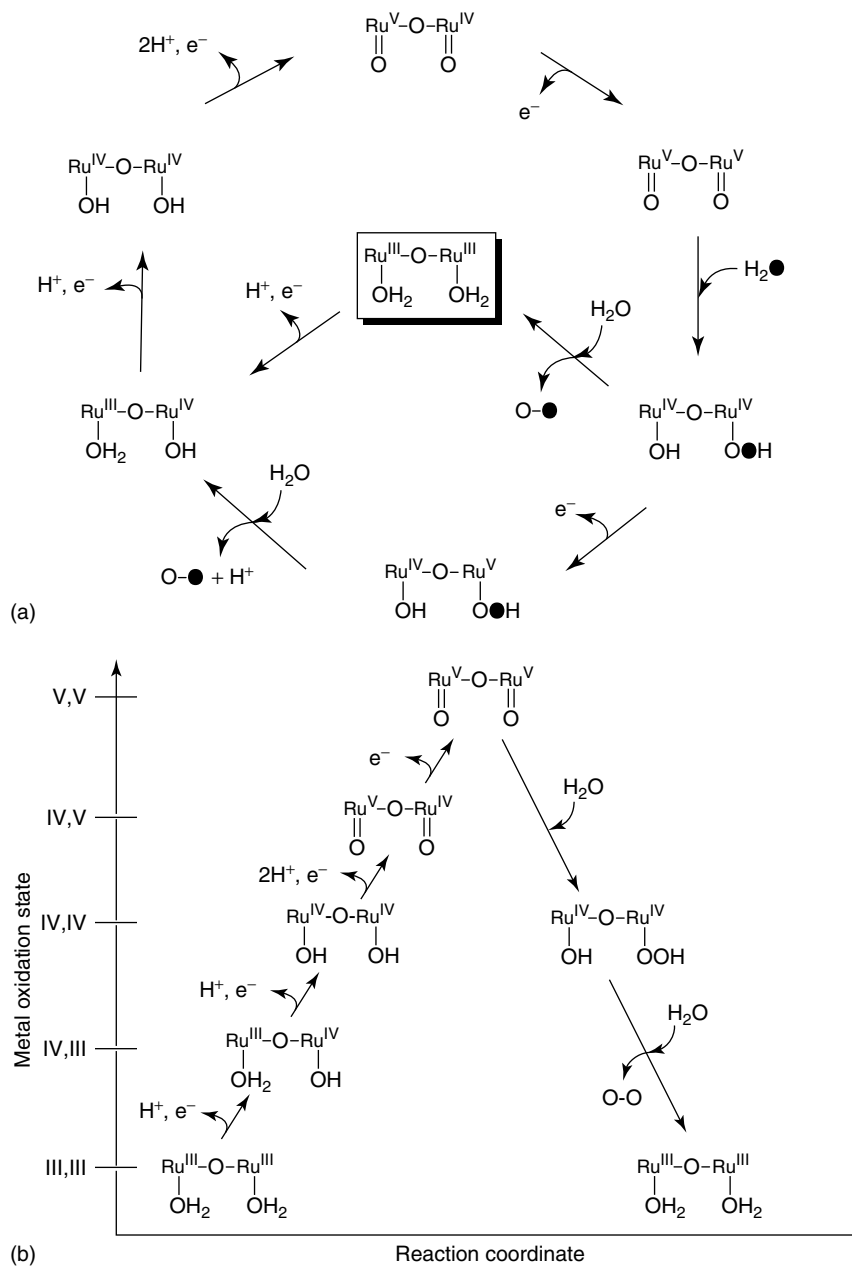
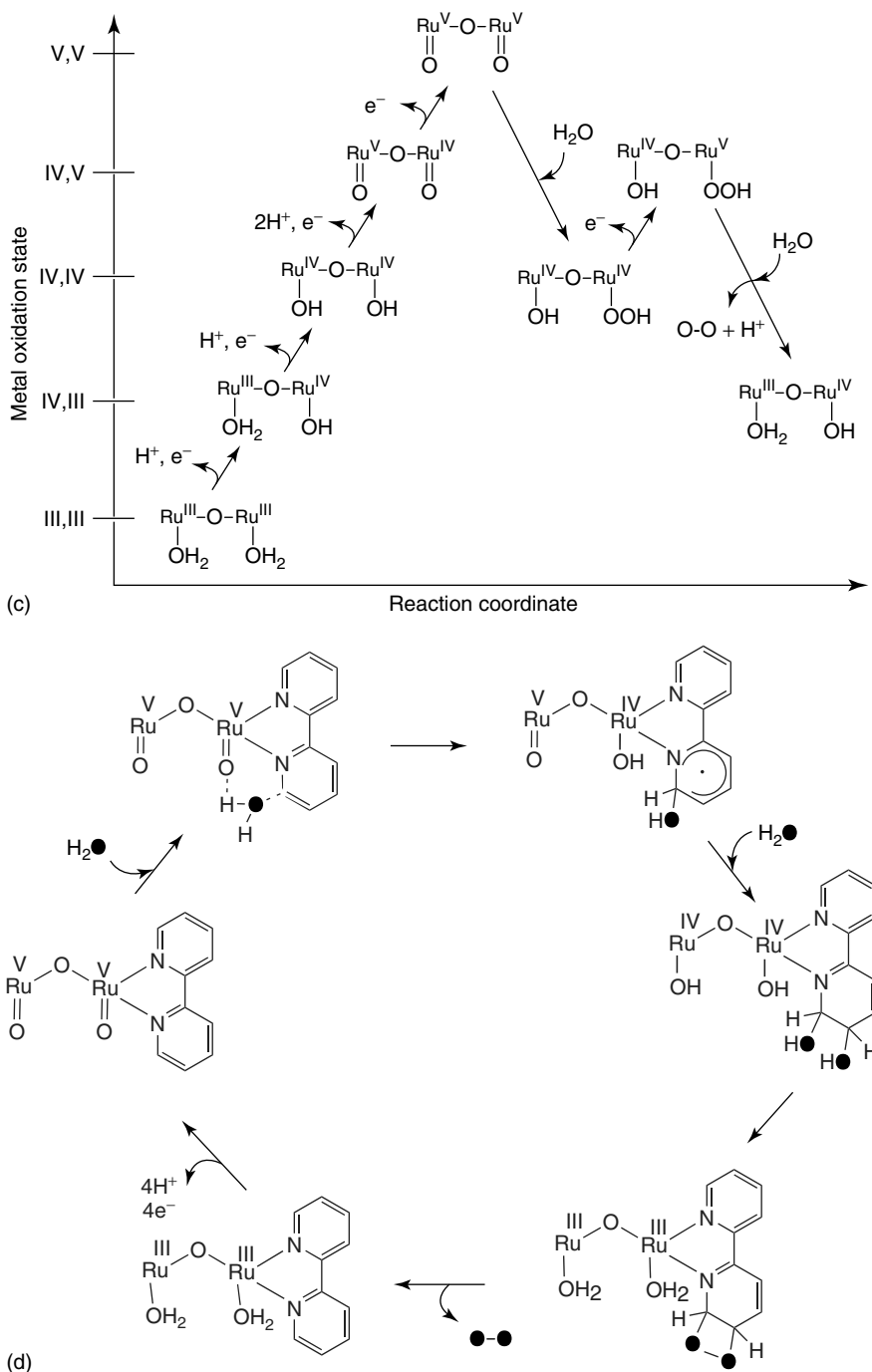


Figure 3 (a) Proposed WNA water oxidation mechanisms by the blue dimer, **1**. Black filled O represent labeled oxygen atoms. (b) metal oxidation state vs reaction coordinate representation showing a “volcano-type” mechanism. (c) “Roller coaster-type” mechanism. (d) Ligand-based mechanism. Overall complex coulombic charges are omitted

A number of blue dimer analogs based on the Ru–O–Ru framework and using different polypyridylic type of ligands have been reported in the literature. Their redox and catalytic properties are relatively similar to those of the blue dimer, and have been described in a recent review,³¹ and have thus not been discussed further here. The blue dimer constitutes a landmark in water splitting because it is the first molecularly well-characterized complex that has been shown to be capable of oxidizing water to molecular oxygen.

Besides the intrinsic advantages of heterogeneous catalysis versus homogeneous catalysis, the anchoring of a molecular water oxidation catalyst onto solid supports is of interest mainly for two reasons: one is that the reduced translational mobility can furnish a deeper insight into the potential catalyst deactivation pathways, and the second is that it can demonstrate the viability of a water oxidation catalyst in the solid state. These would allow incorporation of the catalyst into complex devices for harvesting solar energy based on splitting of water.⁵ The availability of these

**Figure 3** (continued.)

solid-state materials would greatly facilitate the handling and assembling, from a practical point of view, of devices based on energy conversion schemes such as the one shown in Figure 1.

An attempt to heterogenize the blue dimer into Nafion polymer films was made by Kaneko *et al.*³² through simple cationic exchange. Addition of Ce^{IV}, another cation, generated molecular oxygen, but with a much lower efficiency than that of the same catalyst in homogeneous phase. Another example

for immobilization of a water oxidation catalyst onto solid supports has recently been reported by Meyer *et al.*³³ In this case, a pseudo-analog of blue dimer, containing a tpy ligand functionalized with a phosphonate group (see scheme 1), [Ru^{III}₂(μ-O)(H₂PO₃-trpy)₂(H₂O)₄]⁴⁺, has been anchored onto solid oxide-conductive surfaces, ITO (Sn^{IV}-doped In₂O₃) and FTO (fluorine-doped tin oxide). In the homogeneous phase, this trpy-Ru complex generates a turnover number (TN) of

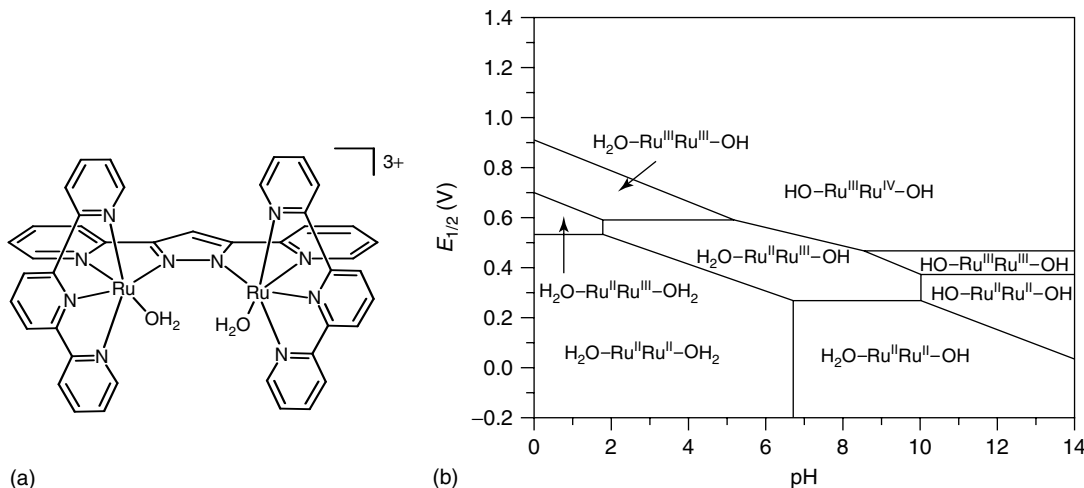


Figure 4 (a) Drawn structure of the *in,in*-{{[Ru^{II}(trpy)(H₂O)]₂(μ-bpp)}³⁺, 2, complex. (b) Pourbaix diagram. The zones of stability of the different species generated by proton and electron loss or gain are indicated. The trpy and bpp ligands are not indicated in the diagram, nor are their overall coulombic charges. Redox potentials are referenced vs SSCE

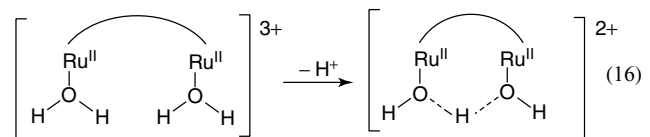
nearly 1 and, when anchored onto the above-mentioned solid surfaces, can reach a maximum value of 3.³⁴

4.2 The Ru-Hbpp and Analogs

A new synthetic approach for the design of four-electron water oxidation catalysts was adopted by our group.³⁵ In order to improve the stability of the blue dimer type of complexes, we envisioned the replacement of the oxido-BL by a more robust and rigid chelating BL, to avoid the known reductive cleavage deactivation pathways of the oxido-BL as well as to avoid the potential cis-trans isomerization of the bis oxo-group active sites that are known to take place, for instance, in the *cis*-[Ru^{VI}(bpy)₂(O₂)]²⁺.³⁶ We prepared the complex *in,in*-{{[Ru^{II}(trpy)(H₂O)]₂(μ-bpp)}³⁺, 2; the process consisted of dinucleating 3,5-bis(2-pyridyl)pyrazolate anionic ligand (bpp⁻) that acts as a backbone (see Scheme 1) for the Ru metal centers, placing them in close proximity and further providing a route for electronic coupling between them as shown in Figure 4(a). In addition, the ancillary trpy ligands occupy three meridional positions in such a way that the sixth coordination is occupied by oxygen atoms of aquo groups. This arrangement places the two O atoms at a distance of 2.48 Å (sum of the van der waals radii is 3.04 Å), producing a through-space supramolecular interaction. Thus, geometrically the Hbpp bridging ligand allows (i) the two aquo/oxo groups to be placed sufficiently far from each other, so that an oxide bridge, Ru=O–Ru, cannot be formed, since this would kill the catalyst and (ii) the two aquo groups to be placed sufficiently close to each, so that they can have significant through-space intramolecular interaction in a supramolecular manner. Thus, when higher oxidation states are reached, the corresponding Ru=O groups are properly

oriented and situated so that they can reductively couple to generate dioxygen.³⁷

The interaction between the two aquo groups in 2, at oxidation state II, is clearly manifested by the acidity increase of 4 orders of magnitude with regard to the corresponding mononuclear complex, owing to the formation of a very stable [H₃O₂]⁻ entity, as shown in equation (16).



Furthermore, this interaction between the two active groups is manifested in the fluxional behavior of the molecule, as evidenced by NMR spectroscopy, wherein it undergoes a very fast process that interconverts the C_2 enantiomeric forms associated with the aquo positions above and below the plane of the pyrazolate moiety. This process is so fast at room temperature that the NMR spectrum looks similar to that for a molecule having C_{2v} symmetry.³⁸

The electronic coupling between the metal centers that takes place through the bpp⁻ bridging ligand is also manifested through their redox potentials which are entirely different from those of their mononuclear counterparts.³⁹ The Pourbaix diagram of 2, illustrated in Figure 4(b), is significantly different from that of the blue dimer, mainly because of the absence of the oxido group linking the Ru metal centers. In the latter, the highest oxidation state that can be reached is Ru^{VRu^V}, which is responsible for the formation of O₂, whereas in the former the highest oxidation state that can be reached is the Ru^{IV}Ru^{IV}. On the other hand for 2, both Ru^{II}Ru^{II} and Ru^{II}Ru^{III} oxidation states are stable, whereas for the blue dimer oxidation states lower than Ru^{III}Ru^{III}, as

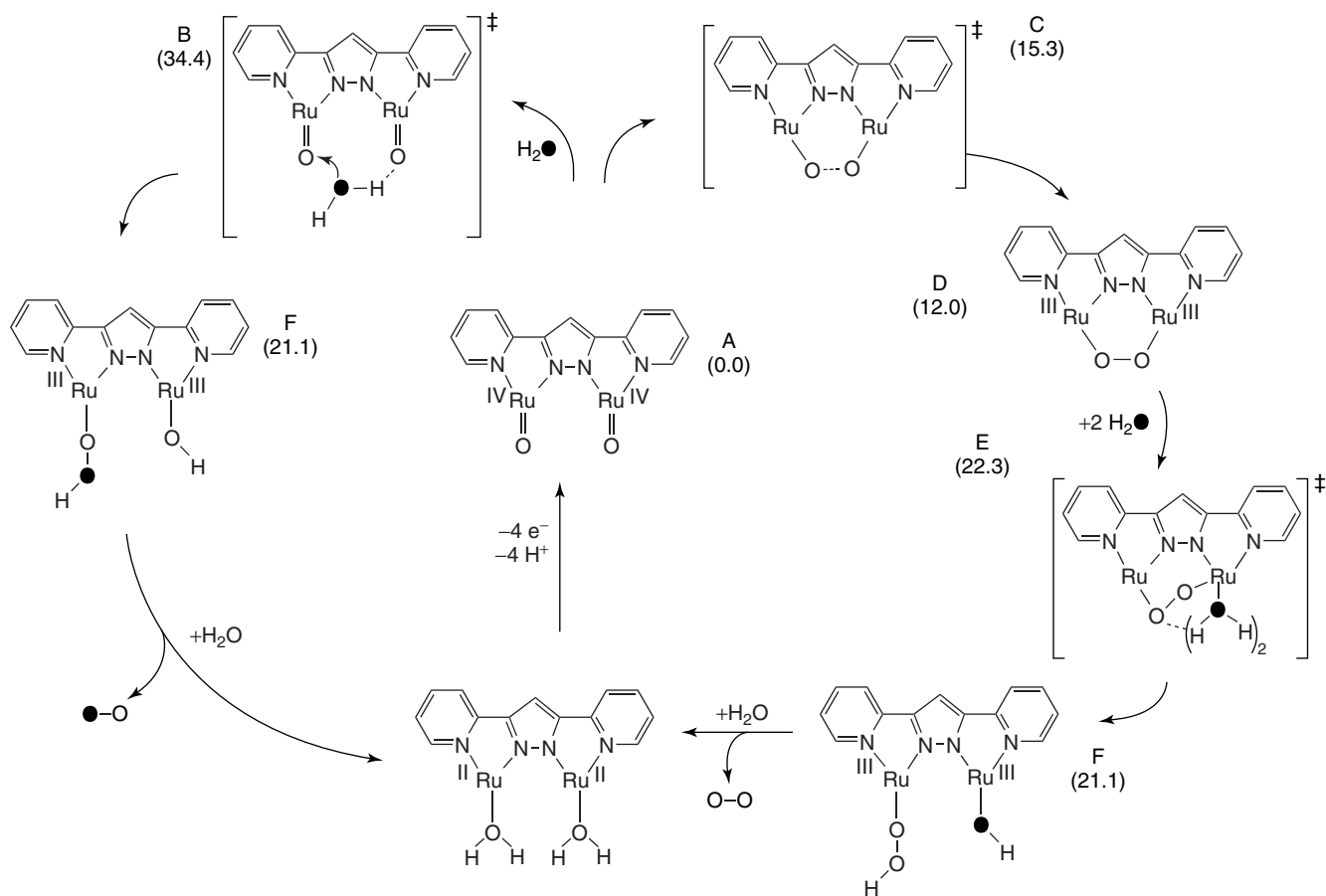


Figure 5 Proposed water oxidation mechanisms for the Ru–Hbpp complex, **2**: (left) WNA mechanism and (right) I2M mechanism. Black filled O represent labeled oxygen atoms. Coulombic charges are not shown

mentioned before, cause the cleavage of the oxido bridge. A TN up to 512 has been achieved with this catalyst using Ce^{IV} as the oxidant, at pH = 1.0 in 0.1 M triflic acid at 25 °C.

Mechanistic studies with **2** were carried out by means of kinetics monitored by UV-vis spectroscopy together with O-18 labeling experiments. The II,II species is sequentially oxidized by one-electron process with Ce^{IV} up to the IV,IV oxidation state. At this stage, the complex advances to an intermediate that later on evolves molecular oxygen. Initially, two “volcano” type of mechanisms with cooperative effects were considered, namely, (i) WNA (Figure 5, left) with the formation of hydroperoxidic intermediate that later progresses toward the generation of molecular oxygen and the formation of the initial catalyst and (ii) an I2M process (Figure 5, right) that forms a μ-1,2-peroxy intermediate, which is followed by the formation of a hydroperoxidic intermediate that finally generates oxygen. Oxygen-labeling experiments with H₂¹⁸O unambiguously show that the only mechanism occurring in this system is the intramolecular process. The mechanistic proposal is further supported by a thorough theoretical analysis of intermediates and transition states based on DFT and CASPT2 calculations.⁴⁰ A bimolecular process was discarded

on the basis of the first-order kinetics found for the formation of the intermediate and on the basis of the 18-O labeling results.

The exceptional performance of **2** as a water oxidation catalyst is attributed to (i) a favorable disposition of the Ru=O groups that rigidly face each other, (ii) the absence of the oxide bridge, avoiding decomposition by reductive cleavage and by the strong thermodynamic driving force to *trans*-dioxo formation, and (iii) the competing anion side reaction that deactivates complex **1** takes place in a lower degree in **2**, since the overall charge of the active complex as well as that of the Ru oxidation states are lower.

The catalyst **2** was anchored onto conducting solid surfaces (vitreous carbon sponges and FTO) via anodic electropolymerization of *N*-substituted pyrroles utilizing the modified trpy ligand 4'-(*para*-pyrrolylmethyl-phenyl)-2,2':6',2''-terpyridine (trpy-pyr; see Scheme 1).⁴¹ Under sufficient anodic potentials the pyrrol group of the trpy-pyr polymerizes, generating a material that remains firmly attached to the surface of the electrode termed FTO–poly-**2'** as depicted in Figure 6 (the prime denotes anchored catalyst). The performance of the water oxidation catalyst is dramatically

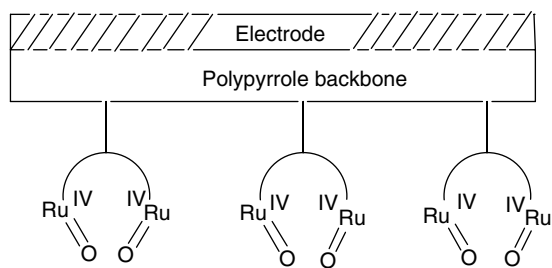


Figure 6 Schematic drawing of the water oxidation species obtained from the oxidative treatment of *FTO/poly-2'* anchored via anodic electropolymerization

improved compared to that of the same catalyst in homogeneous phase, presumably due to the minimization of catalyst–catalyst interactions. This work demonstrates the feasibility to build a solid-state device for the oxidation of water to molecular dioxygen, which could be integrated, via a modular assembly, into a larger device for the photoproduction of H₂, and thus it also constitutes a step forward in this field. We have also heterogenized catalyst **2**, by anchoring it onto TiO₂-anatase by using the Hbpp–CO₂H ligand¹⁸ (see Scheme 1). This ligand can be considered as a functionalized Hbpp, where the intrinsic N4 coordination properties have not been modified. Addition of Ce^{IV} to the new dinuclear Ru complex, which is attached to the surface of TiO₂-anatase, generates molecular oxygen, but it also produces significant amounts of CO₂. These results manifest the need for careful choice of ligands when dealing with powerful water oxidation catalysts.

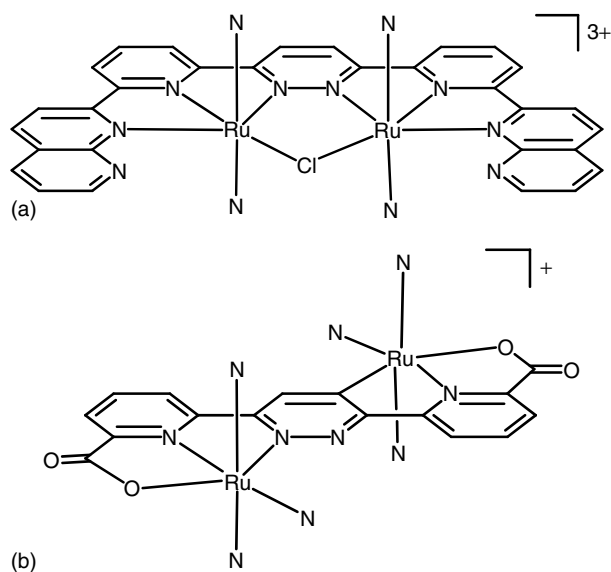


Figure 7 Structures of pyridazine-bridged complexes: (a) *trans,trans*-[Ru₂(μ-Cl)(μ-binapypyrr)(4-pic)₄]³⁺, **3** and (b) [Ru₂(μ-bpc)(4-Me-pic)₆]³⁺, **4**. The N in the drawing represent the 4-picoline ligand

4.3 Pyridazine-Bridged Dinuclear Ru Complexes

Following a similar strategy as in the Ru–Hbpp case, Thummel and coworkers prepared an octadentate (that acts as hexadentate) dinucleating neutral ligand binapypyrr (see Scheme 1) that contains two naphthyridyl groups coupled to a bispyridylpyridazine unit. This ligand, together with four monosubstituted pyridines, coordinates to two Ru metal centers to generate the corresponding μ-Cl complex, *trans,trans*-[Ru₂(μ-Cl)(μ-binapypyrr)(4-Me-py)₄]³⁺, **3**, whose preliminary X-ray structure has been reported and is depicted in Figure 7(a).⁴² Addition of Ce^{IV} to a solution of **3** dissolved in a mixture of MeCN/1.0 M triflic acid (1/30) generates a enormous amount of molecular oxygen, giving a TN of 538 with an efficiency of 23.6% compared to the Ce^{IV} oxidant. For this complex, the substitution of the chloro-bridging ligand could generate the corresponding diaquo complex, which in turn could be responsible for the catalytic activity. However, attempts to prepare this complex have not succeeded, and thus the mechanism for the formation of this complex remains unknown to date. A series of related dinuclear complexes have also been prepared by the same author by slightly modifying the bridging ligand and the monodentate ligands that allow the performance of the complexes to be fine tuned with regard to their capacity to oxidize water to dioxygen.⁴³ In cases where the aquo ligands are involved, all ligands bonded to Ru are neutral and therefore should generate a rather different thermodynamic scenario compared to that of **1** and/or **2**. It is thus very important to study the electrochemical properties of this series of complexes, in order to understand the potential pathways through which they bring about the oxidation of water.

Recently, Sun *et al.* have prepared a new dinuclear complex based also on the pyridazine motif, but containing two pyridylcarboxylate units (see Scheme 1)—[Ru^{II}₂(μ-bpc)(4-pic)₆]³⁺, **4**.⁴⁴ The bpc²⁻ symmetric ligand coordinates to Ru in an unsymmetrical manner, generating an organometallic dinuclear Ru complex with one of the C-atoms of the pyridazine group bonded to the Ru center as shown in Figure 7(b). It is reported that addition of Ce^{IV} to this complex generates molecular oxygen with a TN of 1700 and an efficiency of 16.3% compared to the oxidant together with a catalytic amount of CO₂, whose origin is not known. In this case, it is interesting to realize that the Ru center has a saturated octahedral type of coordination with no labile ligands. Thus, the catalyst can be a seven coordinated Ru–aquo, or a six coordinate with either decoordination of a monodentate ligand or a potential partial decoordination of the carboxylate ligand. Again as in the previous case, further studies are essential to understand the active species involved in the mechanism of water oxidation that takes place with this complex.

4.4 Anthracene-Bridged Ru Dinuclear Complexes

Tanaka and coworkers designed and prepared a dinucleating ligand, btpyan, where two trpy groups are attached in

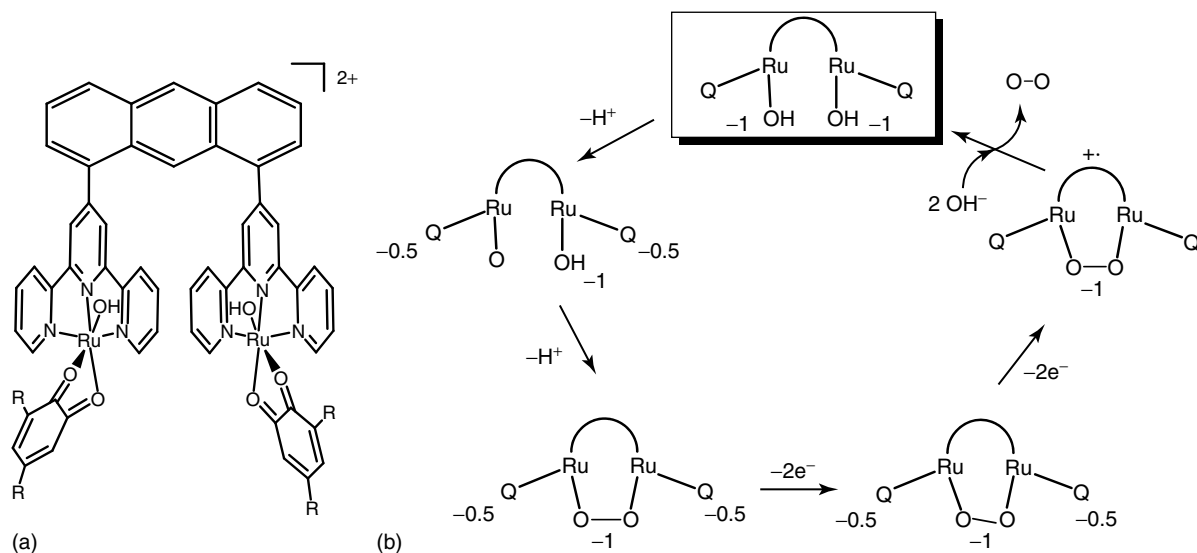


Figure 8 (a) Structure for the $\{[\text{Ru}^{\text{II}}(\text{H}_2\text{O})(\text{quinone})_2]_2(\mu\text{-btpyan})\}^{4+}$, **5**, complex. (b) Proposed ligand-based water oxidation mechanism. The arcs represent the anthracene-based bridging ligand, btpyan, and the bidentate quinoline ligand is represented as Q. The oxidation states of the Ru atoms remain unchanged at II. Formal charges for the ligands are indicated for the proposed species in the catalytic cycle. Overall coulombic charges for the complex are not indicated

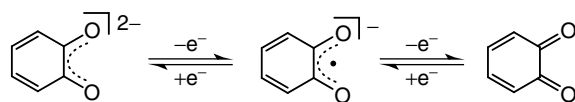
an anthracene unit as shown in Scheme 1 and Figure 8(a).⁴⁵ The derived dinuclear Ru complexes— $\{[\text{Ru}^{\text{II}}(\text{H}_2\text{O})(\text{L})_2]_2(\mu\text{-btpyan})\}^{4+}$, (L = quinone, **5**)—are also bonded to a bidentate chelating quinone ligand and finally to a monodentate ligand, that is, $\text{H}_2\text{O}/\text{OH}^-$, depending on the pH. Even though there is no X-ray structure, modeling studies show that the btpyan ligand has the virtue of placing two Ru metal centers in close proximity, while the σ bond nature of the anthracene-trpy unit confers a certain degree of flexibility. Furthermore, these modeling studies also indicate that the two monodentate aquo ligands are juxtaposed to one another.

Catechols are known to be relatively easily oxidized by a sequential one-electron loss to form the corresponding semiquinones and quinones, as shown in Scheme 3. The combination of Ru–OH₂ groups and redox-active ligands like catechols makes the system complex, but it is particularly interesting for multiple ET redox transformation such as the oxidation of water to molecular dioxygen. The redox properties of these complexes have been thoroughly characterized mainly by CV in organic solvents with and without added water, given their insolubility in neat aqueous solutions, and manifest the rich electrochemistry of this complex. Further, at an applied potential of 1.70 V vs

Ag/AgCl, it has been reported that complex **5** is capable of oxidizing water to molecular dioxygen in homogeneous phase in $\text{CF}_3\text{CH}_2\text{OH}$ with added water (10% in volume), giving a turnover number (TN) of 21 with a current efficiency of 91%. In sharp contrast, the process, through which the catalyst is deposited on the surface of an ITO electrode at pH = 4.0 (phosphate buffer), also generates molecular oxygen at 1.70 V, giving a spectacular TN of 33.500.⁴⁶ It is not reported whether this catalyst is active or not with chemical oxidants such as Ce^{IV} . Recently, a mechanistic study based on DFT calculations, made in collaboration with the group of Muckerman,⁴⁷ has been performed and the main results are depicted in Figure 8(b). It is interesting to realize the redox inactivity of the Ru centers; in other words, all the electron-transfer processes that are proposed to lead to the formation of O_2 from water are based on the quinone ligand. It is also interesting to highlight here that the O–O bond formation takes place via an I2M mechanism between a $\text{Ru}^{\text{II}}\text{–O}\cdot$ (oxyl) and a $\text{Ru}^{\text{II}}\text{–OH}$ to form a superoxide concomitant with an one-electron reduction of each Q to Q^- .

4.5 POM-Bridged Tetranuclear Ru Complex

In 2008, the groups of Bonchio and Hill^{48,49} reported the water oxidation activity of a beautiful complex, $[\text{Ru}^{\text{IV}}_4(\mu\text{-O})_4(\mu\text{-OH})_2(\text{H}_2\text{O})_4(\gamma\text{-SiW}_{10}\text{O}_{36})_2]^{10-}$, **6**, ($\text{Ru}_4\text{–POM}$; POM is the polyoxometalate ligand $\gamma\text{-SiW}_{10}\text{O}_{36}^{8-}$) whose structure is shown in Figure 9; the structure consists of a tetranuclear complex containing four $\text{Ru}^{\text{IV}}\text{–OH}_2$ groups, with the POM and bridging OH⁻ and O²⁻ ligands in the first coordination sphere of the metal centers. For this complex, it



Scheme 3 Redox states of the quinone ligand

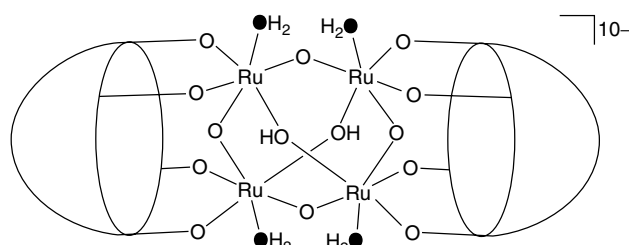


Figure 9 Structure of the tetranuclear Ru-POM complex, $[\text{Ru}^{\text{IV}}_4(\mu\text{-O})_4(\mu\text{-OH})_2(\text{H}_2\text{O})_4(\gamma\text{-SiW}_{10}\text{O}_{36})]^{10-}$, **6**, where each polyoxometalate unit acts as an O₄ anionic tetradeятate bridging ligand. Oxygen atoms for Ru-OH₂ groups are represented as black filled O

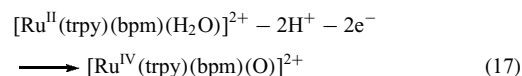
has been shown that the initial $[\text{Ru}^{\text{IV}}\text{-OH}_2]_4$ core is oxidized by four successive steps to form the $[\text{Ru}^{\text{V}}\text{-OH}]_4$ species. The latter reactive species, on the basis of kinetics and DFT calculations, is proposed to undergo a WNA to form a hydroperoxidic intermediate, which later on evolves molecular oxygen in a “volcano” type of mechanism. The mechanistic proposal relies on the fact that the oxygen evolution is a first-order process with regard to the catalysts and the unlikelihood that a deca-anionic species could undergo a bimolecular process. This complex constitutes another example of a cooperative effect, in this case shared by four metal centers, and manifests the enormous possibilities available for designing water oxidation catalysts containing a wide range of bridging and ancillary ligands. Interestingly, complex **5** has also been reported to be able to oxidize water in the homogeneous phase with a light-driven strategy that involves $\text{Ru}^{\text{II}}(\text{bpy})_3^{2+}$ as the photosensitizer and $\text{S}_2\text{O}_8^{2-}$ as the sacrificial oxidant.⁵⁰

5 MONONUCLEAR Ru COMPLEXES

5.1 Mononuclear N₅Ru-OH₂ Type of Complexes

Recently, Sakai and Masaoka⁵¹ and Meyer’s group⁵² have reported mononuclear octahedral $\text{Ru}^{\text{II}}\text{-H}_2\text{O}$ complexes of the general formula: $[\text{Ru}^{\text{II}}(\text{trpy})(\text{B})(\text{H}_2\text{O})]^{2+}$, containing the meridional trpy ligand and a bidentate chelating ligand (B = bpy, **7**; B = bpm (2,2'-bipyrimidine), **8**; B = bpz (2,2'-bipyrazine), **9**. See Scheme 1 and Figure 10(a)). For the $[\text{Ru}(\text{trpy})(\text{bpy})(\text{H}_2\text{O})]^{2+}$ complex, it is reported that it is capable of generating oxygen, giving a TN of 178, when dissolved in 20 : 1 water/acetonitrile mixture followed by the addition of Ce^{IV} , with an impressive 89.2% efficiency with regard to the latter. Complexes **8** and **9** have been reported to perform even better than **7**, and more importantly their mechanisms have been studied with certain detail.

Whereas in most $\text{Ru}^{\text{II}}\text{-OH}_2$ complexes the removal of protons and electrons takes place in a sequential manner, as in the case of **7**, ($\Delta E_{\text{IV}/\text{III}-\text{III}/\text{II}} = 130 \text{ mV}$ at pH = 7), in the case of **8**, oxidation state III is not stable and the oxidation takes places directly by a two-electron process:



This is a phenomenon that has been previously reported for other $\text{Ru}^{\text{II}}\text{-OH}_2$ complexes, and it is strongly dependent on the electronic nature of the ligands bonded to the Ru center.⁵³ Further oxidation to even higher oxidation states is clearly observed and occurs at a reasonable potential

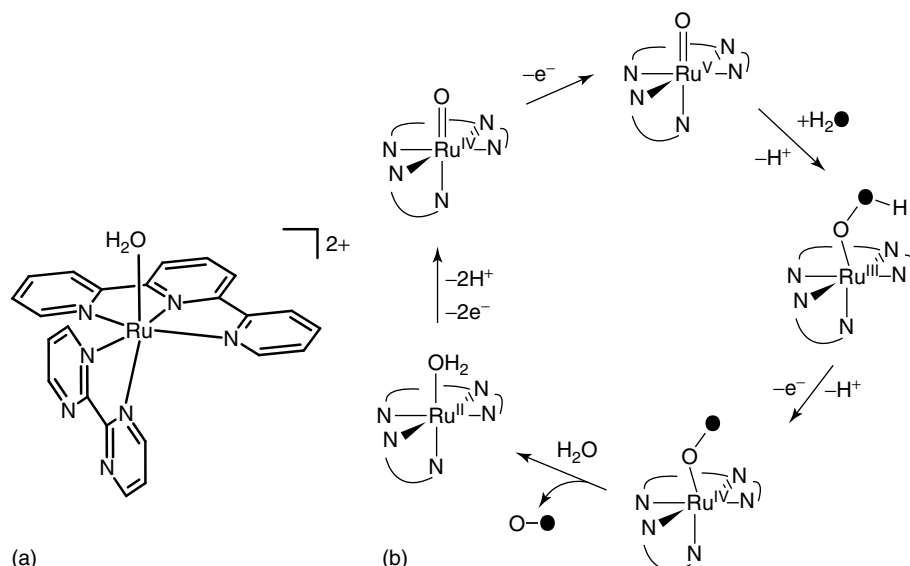
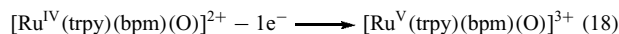


Figure 10 (a) Structure for the $[\text{Ru}^{\text{II}}(\text{trpy})(\text{bpm})(\text{H}_2\text{O})]^{2+}$, **8**, complex. (b) Proposed water oxidation mechanism based on WNA. Black filled O represent labeled oxygen atoms

as shown in the following equation:



Once the oxidation state V is reached, this species becomes highly reactive and suffers a nucleophilic attack by water that generates the O–O bond, forming a Ru^{III}–OOH intermediate, as shown in Figure 10(b), where the proposed mechanism for water oxidation is represented. Then, the Ru^{III}–OOH intermediate undergoes a rapid one-electron oxidation accompanied by proton loss to form a Ru^{IV}–OO that finally generates molecular oxygen, the latter being the rate-determining step. This “rollercoaster” type of mechanism has been elucidated by means of a detailed kinetic analysis, monitored by UV-vis spectroscopy. A dinuclear version of 7 has been reported by Sakai using the flexible bridging ligand ethyl-bis-bpy (See Scheme 1),—{[Ru^{II}(trpy)(H₂O)]₂(μ-ethyl-bpy)₂}⁴⁺, and it is striking to realize that even though it is capable of catalytically oxidizing water to oxygen, its performance is really poor.

Other mononuclear Ru complexes based on the meridional ligands bis-naphthyridine-pyridine (binapy) and trpy have been reported by Thummel’s group, and their catalytic water oxidation performances upon addition of Ce^{IV} have been disclosed.^{42,54}

5.2 Mononuclear N₆Ru Type of Complexes

Thummel *et al.* have also reported a couple of N₆Ru complexes, namely, the [Ru^{II}(trpy)(4-pic)₃]²⁺, **10**, and the [Ru^{II}(trpy)(bpy)(4-pic)]²⁺, **11**,⁵⁴ (where 4-pic is the 4-methylpyridine ligand). These complexes are interesting, given the absence of an aquo group and the saturated first coordination sphere of a d⁶ N₆Ru^{II} type of complex. Even though there is no detailed experimental mechanistic information available, it is proposed that the water oxidation mechanism proceeds via a metal coordination expansion. That is the coordination of a water molecule generates a seven coordination around the metal center as shown in Figure 11. The critical O–O bond formation step is proposed to involve a water molecule in addition to the generated higher oxidation state [Ru^{VI}(trpy)(4-pic)₃(O)]⁴⁺, which generates an Ru–OOH intermediate that finally yields dioxygen and the initial Ru^{II} species in a “volcano” type of mechanism. The mechanistic proposal is supported by DFT calculations that yield reasonable energies for the proposed intermediate species. The seven coordination proposed is further supported by the fact that after the catalytic reaction, the first coordination sphere of the complex remains intact, and by the need to have reactive Ru–OH₂ groups that lower potential and which, upon reaching higher oxidation states, can form O–O bonds. It is important here to bear in mind that N₆Ru type of complexes such as Ru(trpy)₂²⁺ and Ru(bpy)₃²⁺ have redox potentials in the range of 1.1–1.3 V vs SSCE for their Ru^{III}/Ru^{II} couple,

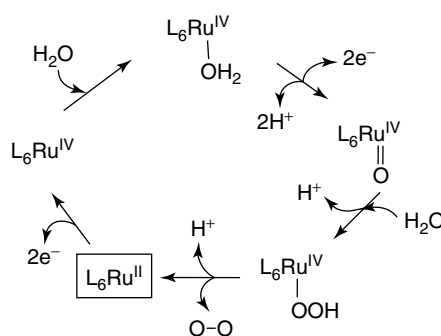


Figure 11 Proposed water oxidation mechanism based on seven coordination expansion for complexes [Ru^{II}(trpy)(4-pic)₃]²⁺, **10**, and [Ru^{II}(trpy)(bpy)(4-pic)]²⁺, **11**. The pyridyllic ligands are represented by L₆

and that the oxidation state of the Ru^{IV}/Ru^{III} couple is beyond the solvent oxidation limits.

5.3 A Mononuclear N₄O₂Ru Complex

Very recently, Sun’s group⁵⁵ has prepared an octahedrally distorted Ru complex—[Ru^{II}(bdc)(4-pic)₂]⁻, **12**—containing a tetradentate N₂O₂ dianionic ligand (bdc²⁻ is the 2,2'-bipyridine-6,6'-dicarboxylato anionic ligand, see Scheme 1) that constrains the equatorial coordination around the metal center, while the two axial positions are occupied by 4-picoline ligands, as shown in Figure 12(a). Treatment of this complex with excess Ce^{IV} generates molecular oxygen in a catalytic manner. During the course of water oxidation, a seven coordinate Ru^{IV}–OH₂ dimer intermediate, {[Ru^{IV}(bdc)(4-pic)₂]₂(μ-(HOHOH))}³⁺, **13**, with a pentagonal bipyramidal type of geometry was obtained and characterized; the hydroxo groups of the intermediate were found to be situated in the equatorial plane and were part of the HOHOH⁻ bridging ligand. The water molecules interact with the HOHOH group via hydrogen bonding, as can be observed from Figure 12(b). This complex is interesting since, even though a detailed mechanistic work has not been carried out, it seems that it is situated at the crossroads of the WNA and the I2M mechanisms. As indicated in Figure 12(b), slight modifications of key O–H bonds will drive the intermediate to one or the other pathway.

5.4 A Mononuclear Ru Pincer Complex

Recently, the Milstein group reported a mononuclear Ru complex, [Ru^{II}(PNN)(CO)(OH)₂]⁻, **14**, containing an unsymmetric tridentate meridional ligand 2-(di-*tert*-butyl phosphino-methyl)-6-diethylaminomethylpyridine (PNN, see Scheme 1), two OH⁻ groups in a *cis* fashion, and a carbonyl complex completing the octahedral type of coordination; see Figure 13.⁵⁶ Irradiation of this complex in the

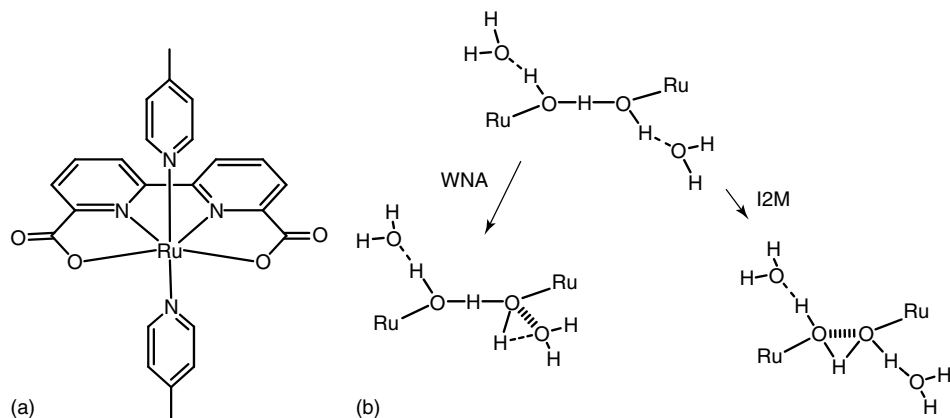


Figure 12 (a) Structure for the $[\text{Ru}^{\text{II}}(\text{bdc})(\text{4-pic})_2]$, **12**, complex. (b) Two potential evolution pathways that can generate the O–O bond, for the seven coordinate reactive intermediate $([\text{Ru}^{\text{IV}}(\text{bdc})(\text{4-pic})_2]_2(\mu\text{-(HOHOH)}))^{3+}$, **13**. The bdc and 4-pic ligands are not shown

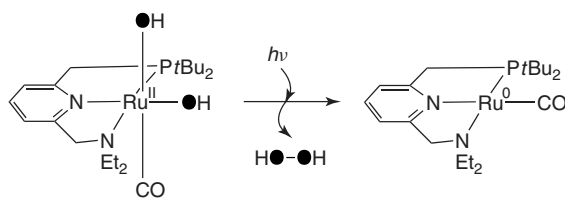


Figure 13 Structure of the neutral complex $[\text{Ru}^{\text{II}}(\text{OH})_2(\text{PNN})(\text{CO})]$ and its evolution under light irradiation. Black filled O represent labeled oxygen atoms

320–420 nm range produces HOOH, which later on catalytically disproportionates to molecular oxygen and water. Even though in this system HOOH is released, and thus the thermodynamic demands are higher than those for the four-electron oxidation to generate O_2 , the process is mechanistically very interesting. Oxygen-labeling experiments with ¹⁸O, together with kinetic analysis, clearly indicates that the formation of the O–O bond proceeds in an intramolecular manner involving a reductive elimination process, where the Ru metal changes oxidation state from II to 0.

6 Ir COMPLEXES

Bernhard *et al.* have prepared a series of iridium organometallic complexes with the general formula *cis*- $[\text{Ir}^{\text{III}}(\text{L})_2(\text{H}_2\text{O})_2]^+$ ($\text{L} = 2\text{-phenyl-pyridine anion}$, **15**; also with other related ligands; see Scheme 1),⁵⁷ which constitute the first Ir complexes reported in the literature capable of catalytically oxidizing water to molecular oxygen. The TNs reported are impressive and are in the order of 2500 with efficiencies in the order of 66% with regard to the Ce^{IV} oxidant, although the kinetics are slower than those of their Ru counterparts. Crabtree *et al.*⁵⁸ have very recently reported mononuclear Ir–Cl complexes, such

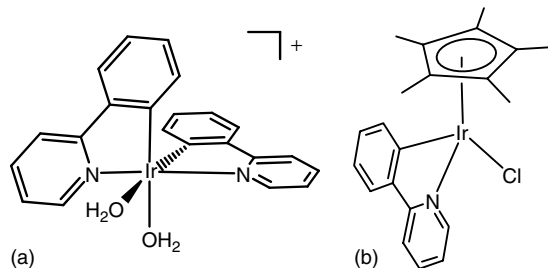


Figure 14 (a) Structure of *cis*- $[\text{Ir}^{\text{III}}(2\text{-ph-py})_2(\text{H}_2\text{O})_2]^+$, **15**. (b) Structure of $[\text{Ir}^{\text{III}}(\text{Cp}^*)(2\text{-ph-py})(\text{Cl})]$, **16**

as $[\text{Ir}^{\text{III}}(\text{Cp}^*)(2\text{-ph-py})(\text{Cl})]^+$, **16**, containing the facial Cp* (1,2,3,4,5-pentamethylcyclopentadienyl anion) and 2-ph-py ligands, and also with other related ligands. These new Ir complexes, depicted in Figure 14, are robust water oxidation catalysts, which, upon addition of Ce^{IV} as the primary oxidant, are highly active. In the case of **16**, it is capable of achieving initial rates of 54 TN min⁻¹ while being active for several hours.

While these series of Ir complexes are the first structurally relatively well-characterized non-Ru complexes that oxidize water to molecular dioxygen, their spectroscopic and electrochemical characterization needs to be studied in more detail. In particular, the characterization of their corresponding higher oxidation states should be performed together with a thorough kinetic analysis, in order to be able to address their potential mechanisms. A DFT calculation has been carried out, which is consistent with the involvement of an Ir^V–O species, $[(\text{Cp}^*)(2\text{-ph-py})\text{Ir}(\text{O})]^+$, as an active intermediate that is proposed to suffer a nucleophilic water attack.

7 Mn AND Co COMPLEXES AND OXIDES

There are several Mn complexes that have been described in the literature that are capable of oxidizing

water to molecular dioxygen, notably $[\text{Mn}^{\text{III}}\text{Mn}_2^{\text{IV}}(\text{trpy})_2(\mu-\text{O})_2(\text{H}_2\text{O})_2](\text{NO}_3)_3$, **17**,⁵⁹ and related dinuclear Mn complexes containing pentadentate pyridyl carboxylate type of ligands such as *N*-methyl-*N'*-carboxymethyl-*N*, *N'*-bis(2-pyridylmethyl)ethane-1,2-diamine.^{60,61} Those complexes are discussed in *Toward Solar Fuels Using a Biomimetic Approach: Progress in the Swedish Consortium for Artificial Photosynthesis* by the Swedish Consortium and hence they will not be further discussed here.

In 1937, Noyes *et al.*⁶² reported the kinetics of oxidation of water to dioxygen by Co^{III} species in acidic solutions. A few years later, in 1966 Pecht *et al.*⁶³ undertook a thorough kinetic study and proposed a mechanism in which $[\text{Co}^{\text{III}}(\text{H}_2\text{O})_6]^{3+}$ in solution is in equilibrium with a dinuclear species doubly bridged by hydroxo ligands $\{[\text{Co}^{\text{III}}(\text{H}_2\text{O})_4]_2(\mu-\text{OH})_2\}^{4+}$, **18**. Calculations indicate that even at pH = 1.0, about 3.1% of the dinuclear species is available. This dinuclear species can then undergo an intramolecular ET to form the peroxy species, $\{[\text{Co}^{\text{II}}(\text{H}_2\text{O})_4]_2(\eta_2 : \eta_2-\text{O}_2\text{H}_2)\}^{4+}$, releasing HOOH or can react with a molecule of $[\text{Co}^{\text{III}}(\text{H}_2\text{O})_6]^{3+}$ to form a Co-superoxide species releasing HO_2 . The released molecules are proposed to be further oxidized with Co^{III} to finally generate O_2 .

Cobalt oxides have been known for a long time to be capable of oxidizing water to dioxygen.⁶⁴ Even though oxides are beyond the scope of this article, it is interesting to mention here recent publications that use IrO_2 ⁶⁵ and Co_3O_4 type of oxides^{66,67} to carry out the water oxidation at relatively small overpotentials and thus constitute very promising alternative materials.

8 CONCLUSIONS

In 1982, the blue dimer, the first water oxidation catalyst that was well characterized at a molecular level was reported.²³ It took more than 20 years, from 1982 to 2004, to report another water oxidation catalyst with a significantly different molecular structure.³⁵ The latter led to the development of new families of transition metal complexes that were capable of acting as a catalyst for this important reaction. This molecular development had been further stimulated by the universal realization by our society of the urgent need for a C-neutral renewable energy source, since, as mentioned in the Introduction, a rugged and efficient water oxidation catalyst is seen as one of the bottlenecks in the development of new sustainable energy conversion schemes. The combination of impetus has produced a spectacular revolution in the field, where many new important breakthroughs have been achieved during the last three years. The discovery that mononuclear complexes can also perform the water oxidation reaction in a catalytic and efficient manner^{52,54} is one of the main achievements of this revolution, because it simplifies access to a whole new family of complexes that are generally easier

to prepare, purify, and isolate than dinuclear or polynuclear complexes.

In spite of the new and important achievements, there are a couple of related challenging issues that still need to be solved and studied in detail. One concerns the mechanism through which the water oxidation reactions take place. This is an inherently difficult topic, given the molecular complexity of the water oxidation reaction and the intrinsic experimental difficulties associated with the characterization of reactive intermediates in water. The second issue concerns coupling of the water oxidation catalyst to the cell proposed in Figure 1 and making it work in a harmonious manner.

9 COMPLEX NUMBERING

1	<i>cis,cis</i> - $\{[\text{Ru}^{\text{III}}(\text{bpy})_2(\text{H}_2\text{O})_2](\mu-\text{O})\}^{4+}$, blue dimer
2	<i>In,in</i> - $\{[\text{Ru}^{\text{II}}(\text{trpy})(\text{H}_2\text{O})_2](\mu-\text{bpp})\}^{3+}$, Ru-Hbpp,
3	<i>trans,trans</i> - $[\text{Ru}^{\text{II}}_2(\mu-\text{Cl})(\mu\text{-binapypyrr})_2(4\text{-pic})_4]^{3+}$
4	$[\text{Ru}^{\text{II}}_2(\mu\text{-bpc})(4\text{-pic})_6]^{+}$
5	$\{[\text{Ru}^{\text{II}}(\text{H}_2\text{O})(\text{quinone})_2](\mu\text{-btpyan})\}^{4+}$
6	$[\text{Ru}^{\text{IV}}_4(\mu\text{-O})_4(\mu\text{-OH})_2(\text{H}_2\text{O})_4(\gamma\text{-SiW}_{10}\text{O}_{36})_2]^{10-}$
7	$[\text{Ru}^{\text{II}}(\text{trpy})(\text{bpy})(\text{H}_2\text{O})]^{2+}$
8	$[\text{Ru}^{\text{II}}(\text{trpy})(\text{bpm})(\text{H}_2\text{O})]^{2+}$
9	$[\text{Ru}^{\text{II}}(\text{trpy})(\text{bpz})(\text{H}_2\text{O})]^{2+}$
10	$[\text{Ru}^{\text{II}}(\text{trpy})(4\text{-pic})_3]^{2+}$
11	$[\text{Ru}^{\text{II}}(\text{trpy})(\text{bpy})(4\text{-pic})]^{2+}$
12	$[\text{Ru}^{\text{II}}(\text{bdc})(4\text{-pic})_2]$
13	$\{[\text{Ru}^{\text{IV}}(\text{bdc})(4\text{-pic})_2](\mu\text{-}(\text{HOHO}))\}^{3+}$
14	$[\text{Ru}^{\text{II}}(\text{PNN})(\text{CO})(\text{OH})_2]$
15	<i>cis</i> - $[\text{Ir}^{\text{III}}(2\text{-ph-py})_2(\text{H}_2\text{O})_2]^{+}$
16	$[\text{Ir}^{\text{III}}(\text{Cp}^*)(2\text{-ph-py})(\text{Cl})]^{+}$
17	$[\text{Mn}^{\text{III}}\text{Mn}_2^{\text{IV}}(\text{trpy})_2(\mu\text{-O})_2(\text{H}_2\text{O})_2]^{3+}$
18	$\{[\text{Co}^{\text{III}}(\text{H}_2\text{O})_4](\mu\text{-OH})_2\}^{4+}$

10 ACKNOWLEDGMENTS

Funding support for this research by SOLAR-H2 (EU 212508) and the MICINN (Consolider Ingenio 2010 (CSD2006-0003), CTQ2007-67918) is gratefully acknowledged.

11 RELATED ARTICLES

Molecular Catalysis for Fuel Cells; Toward Solar Fuels Using a Biomimetic Approach: Progress in the Swedish Consortium for Artificial Photosynthesis.

12 ABBREVIATIONS AND ACRONYMS

2-ph-py = 2-phenyl-pyridine; 4-pic = 4-methyl-pyridine; bdc²⁻ = 2,2'-bipyridine-6,6'-dicarboxylato anion; binapypyrr = 3,6-bis-[6'-(1",8"-naphthyrid-2"-yl)-pyrid-2'-yl]pyridazine; BL = bridging ligand; bpc = 3,6-bis-(6'-carboxypyrid-2'-yl)-pyridazine; bpy = 2,2'-bipyridine; bpm = 2,2'-bipyrimidine; bpz = 2,2'-bipyrazine; btpyan = 1,8-bis(2,2':6',2"-terpyridine)anthracene; CASPT2 = complete active space with second-order perturbation theory; cb = conduction band; Cp* = pentamethylcyclopentadienyl anion; Cyt-P₄₅₀ = cytochromes P₄₅₀ DFT = density functional theory; EPT = concerted proton-coupled electron transfer; ET = electron transfer; et-bpy₂ = ethyl-bis-bpy; ET-PT = stepwise first electron then proton transfer; Hbpp = 3,5-bis(2-pyridyl)pyrazole; His = histidine; I2M = interaction of two M-O entities; ITO = indium tin oxide; FTO = fluorine-doped tin oxide; MS-EPT = multiple site concerted proton-coupled electron transfer; OEC-PSII = oxygen evolving complex of photosystem II; OSET = outer sphere electron transfer; P = photosensitizer; PC-ET = proton-coupled electron transfer; PNN = 2-(di-*tert*-butylphosphino-methyl)-6-diethylaminomethyl)pyridine; POM = γ-SiW₁₀O₃₆⁸⁻; PT-ET = stepwise first proton then electron transfer; py = pyridine; Q_A = plastoquinone; SSCE = sodium-saturated calomel electrode; TN = turnover number; trpy = 2,2':6',2"-terpyridine; trpy-pyr = 4'-(*para*-pyrrolylmethyl-phenyl)-2,2':6',2"-terpyridine; Tyr = tyrosine; WNA = solvent water nucleophilic attack.

13 REFERENCES

- J. Yano, J. Kern, K. Sauer, M. J. Latimer, Y. Pushkar, J. Biesiadka, B. Loll, W. Saenger, J. Messinger, A. Zouni, and V. K. Yachandra, *Science*, 2006, **314**, 821.
- M. Haumann, P. Liebisch, C. Müller, M. Barra, M. Grabolle, and H. Dau, *Science*, 2005, **310**, 1019.
- V. Balzani, A. Credi, and M. Ventura, *Chem. Sus. Chem.*, 2008, **1**, 26.
- K. Sanderson, *Nature*, 2008, **452**, 400.
- M. Grätzel, *Nature*, 2001, **414**, 338.
- L. de la Garza, G. Jeong, P. A. Liddell, T. Sotomura, T. A. Moore, A. L. Moore, and D. Gust, *J. Phys. Chem. B*, 2003, **107**, 10252.
- W. Lubitz, E. J. Reijerse, and J. Messinger, *Energy Environ. Sci.*, 2008, **1**, 15.
- J. M. Mayer, *Annu. Rev. Phys. Chem.*, 2004, **55**, 363.
- M. H. B. Huynh and T. J. Meyer, *Chem. Rev.*, 2007, **107**, 5004.
- M. Haumann and H. Dau, *Biochim. Biophys. Acta*, 2007, **1767**, 472.
- K. N. Ferreira, T. M. Iverson, K. Maghlaoui, J. Barber, and S. Iwata, *Science*, 2004, **303**, 1831.
- B. Loll, J. Kern, W. Saenger, A. Zouni, and J. Biesiadka, *Nature*, 2005, **438**, 1040.
- T. J. Meyer and M. H. V. Huynh, *Inorg. Chem.*, 2003, **42**, 8140.
- T. J. Meyer, M. H. V. Huynh, and H. H. Thorp, *Angew. Chem. Int. Ed.*, 2007, **46**, 5284.
- J. Barber, *Chem. Soc. Rev.*, 2009, **38**, 185.
- M. K. Tsai, J. Rochford, D. E. Polyansky, T. Wada, K. Tanaka, E. Fujita, and J. T. Muckerman, *Inorg. Chem.*, 2009, **48**, 4372.
- M. J. Collins, K. Ray, and L. Que, *Inorg. Chem.*, 2006, **45**, 8009.
- L. Francas, X. Sala, J. Benet-Buchholz, L. Escriche, and A. Llobet, *Chem. Sus. Chem.*, 2009, **2**, 321.
- G. Renger and T. Renger, *Photosynth. Res.*, 2008, **98**, 53.
- J. Zheng, D. Wang, W. Thiel, and S. Shaik, *J. Am. Chem. Soc.*, 2006, **128**, 13204.
- Y. Gao, T. Åkermark, J. Liu, L. Sun, and B. Åkermark, *J. Am. Chem. Soc.*, 2009, **131**, 8726.
- V. Balzani, A. Juris, M. Venturi, S. Campagna, and S. Serroni, *Chem. Rev.*, 1996, **96**, 759.
- S. W. Gestern, G. J. Samuels, and T. J. Meyer, *J. Am. Chem. Soc.*, 1982, **104**, 4029.
- J. A. Gilbert, D. S. Eggleston Jr., W. R. Murphy, D. A. Geselowitz, S. W. Gestern, D. J. Hodgson, and T. J. Meyer, *Am. Chem. Soc.*, 1985, **107**, 3855.
- E. R. Batista and R. L. Martin, *J. Am. Chem. Soc.*, 2007, **129**, 7224.
- A. Llobet, M. E. Curry, H. T. Evans, and T. J. Meyer, *Inorg. Chem.*, 1989, **28**, 3131.
- J. P. Collin and J. P. Sauvage, *Inorg. Chem.*, 1986, **25**, 135.
- F. Liu, J. J. Concepcion, J. W. Jurss, T. Cardolaccia, J. L. Templeton, and T. J. Meyer, *Inorg. Chem.*, 2008, **47**, 1727.
- J. J. Concepcion, J. W. Jurss, J. L. Templeton, and T. J. Meyer, *Proc. Nat. Acad. Sci. U.S.A.*, 2008, **105**, 17632.
- J. L. Cape and J. K. Hurst, *J. Am. Chem. Soc.*, 2008, **130**, 827.
- I. Romero, M. Rodriguez, C. Sens, J. Mola, M. R. Kollipara, L. Francas, E. Mas-Marza, L. Escriche, and A. Llobet, *Inorg. Chem.*, 2008, **47**, 1824.
- M. Yagi and M. Kaneko, *Chem. Rev.*, 2001, **101**, 21.
- E. L. Lebeau, S. A. Adeyemi, and T. J. Meyer, *Inorg. Chem.*, 1998, **37**, 6476.
- F. Liu, T. Cardolaccia, B. J. Hornstein, J. R. Schoonover, and T. J. Meyer, *J. Am. Chem. Soc.*, 2007, **129**, 2446.
- C. Sens, I. Romero, M. Rodríguez, A. Llobet, T. Parella, and J. Benet-Buchholz, *J. Am. Chem. Soc.*, 2004, **126**, 7798.
- J. C. Dobson and T. J. Meyer, *Inorg. Chem.*, 1988, **27**, 3283.
- C. Sens, M. Rodriguez, I. Romero, A. Llobet, T. Parella, B. P. Sullivan, and J. Benet-Buchholz, *Inorg. Chem.*, 2003, **42**, 2040.
- A. Llobet *et al.*, work in progress.

39. C. Sens, M. Rodríguez, I. Romero, A. Llobet, T. Parella, and J. Benet-Buchholz, *Inorg. Chem.*, 2003, **42**, 8385.
40. F. Bozoglian, S. Romain, M. Z. Ertem, T. K. Todorova, C. Sens, J. Mola, M. Rodríguez, I. Romero, J. Benet-Buchholz, X. Fontrodona, C. J. Cramer, L. Gagliardi, and A. Llobet, *J. Am. Chem. Soc.*, 2009, **131**, 15176.
41. J. Mola, E. Mas-Marza, X. Sala, I. Romero, M. Rodríguez, C. Viñas, T. Parella, and A. Llobet, *Angew. Chem. Int. Ed.*, 2008, **47**, 5830.
42. R. Zong and P. Thummel, *J. Am. Chem. Soc.*, 2005, **127**, 12802.
43. Z. Deng, H. W. Tseng, R. Zong, D. Wang, and R. A. Thummel, *Inorg. Chem.*, 2008, **47**, 1835.
44. Y. Xu, T. Åkermark, V. Gyollai, D. Zou, L. Eriksson, L. Duan, R. Zhang, B. Åkermark, and L. Sun, *Inorg. Chem.*, 2009, **48**, 2717.
45. T. Wada, K. Tsuge, and K. Tanaka, *Inorg. Chem.*, 2001, **40**, 329.
46. T. Wada, K. Tsuge, and K. Tanaka, *Angew. Chem. Int. Ed.*, 2000, **39**, 1479.
47. J. T. Muckerman, D. E. Polyansky, T. Wada, K. Tanaka, and E. Fujita, *Inorg. Chem.*, 2008, **47**, 1787.
48. A. Sartorel, M. Carraro, G. Scorrano, R. De Zorzi, S. Geremia, N. D. McDaniel, S. Bernhard, and M. Bonchio, *J. Am. Chem. Soc.*, 2008, **130**, 5006.
49. Y. V. Geletii, B. Botar, P. Kögerler, D. A. Hillesheim, D. G. Musaev, and C. L. Hill, *Angew. Chem. Int. Ed.*, 2008, **47**, 3896.
50. Y. V. Geletii, Z. Huang, Y. Hou, D. G. Musaev, T. Lian, and C. L. Hill, *J. Am. Chem. Soc.*, 2009, **131**, 7522.
51. S. Masaoka and K. Sakai, *Chem. Lett.*, 2009, **38**, 182.
52. J. J. Concepcion, J. W. Jurss, J. L. Templeton, and T. J. Meyer, *J. Am. Chem. Soc.*, 2008, **130**, 16462.
53. E. Masllorens, M. Rodríguez, I. Romero, A. Roglans, T. Parella, J. Benet-Buchholz, M. Poyatos, and A. Llobet, *J. Am. Chem. Soc.*, 2006, **128**(16), 5306.
54. H. W. Tseng, R. Zong, J. T. Muckerman, and R. Thummel, *Inorg. Chem.*, 2008, **47**, 11763.
55. L. Duan, A. Fischer, Y. Xu, and L. Sun, *J. Am. Chem. Soc.*, 2009, **131**, 10397.
56. S. W. Kohl, L. Weiner, L. Schwartsburg, L. Konstantinovski, L. J. W. Shimon, Y. Ben-David, M. A. Iron, and D. Milstein, *Science*, 2009, **324**, 74.
57. N. D. McDaniel, F. J. Coughlin, L. L. Tinker, and S. Bernhard, *J. Am. Chem. Soc.*, 2008, **130**, 210.
58. J. F. Hull, D. Balcells, J. B. Blakemore, C. D. Incarvito, O. Eisenstein, G. W. Brudvig, and R. H. Crabtree, *J. Am. Chem. Soc.*, 2009, **131**, 8730.
59. J. Limburg, J. S. Vrettos, L. M. Liable-Sands, A. L. Rheingold, R. H. Crabtree, and G. W. Brudvig, *Science*, 1999, **283**, 1524.
60. P. Kurz, G. Berggren, M. F. Anderlund and S. Styring, *Dalton Trans.*, 2007, **38**, 4258.
61. A. K. Poulsen, A. Rompel, and C. J. McKenzie, *Angew. Chem. Int. Ed.*, 2005, **44**, 6916.
62. A. A. Noyes and T. J. Deahl, *J. Am. Chem. Soc.*, 1937, **59**, 1337.
63. M. Anbar and I. Pecht, *J. Am. Chem. Soc.*, 1967, **89**, 2553.
64. A. C. C. Tseung and S. Jasem, *Electrochim. Acta*, 1977, **22**, 31.
65. T. Nakagawa, N. S. Bjorge, and R. W. Murray, *J. Am. Chem. Soc.*, 2009, **131**, 15578.
66. F. Jiao and H. Frei, *Angew. Chem. Int. Ed.*, 2009, **48**, 1841.
67. M. Risch, V. Khare, I. Zaharieva, L. Gerencser, P. Chernev, and H. Dau, *J. Am. Chem. Soc.*, 2009, **131**, 6936.

Dye-Sensitized Solar Cells: an Overview

Luísa Andrade, Helena Aguilar Ribeiro and Adélio Mendes

Universidade do Porto, Porto, Portugal

1	Introduction	53
2	Structure and Working Principles	53
3	Overview of Materials in DSC Devices	56
4	EIS Characterization	58
5	Phenomenological Modeling	64
6	DSC Bottlenecks and New Developments	70
7	Related Articles	70
8	Abbreviations and Acronyms	70
9	References	70

1 INTRODUCTION

The world power consumption is currently about 13 TW (terawatts) and it is expected that an additional 10 TW will be required in 2050.¹ Moreover, the *Gas Crisis* at the beginning of 2006 has demonstrated that the world, and in particular Europe, is still highly vulnerable with respect to its total energy supply. On the other hand, this energetic paradigm is also being hastened by severe climatic consequences of the greenhouse effect caused by combustion of fossil fuels. A possible solution is the diversification of energy sources including renewable energies, such as thermal solar energy and photovoltaics (PV). In fact, the solar resource in Europe and the world over is abundant, offering the only prospect of cost reduction in the future. The year 2008 was a record year for solar PV sales, with an increase in installed capacity of 5.7 GW. Actually, since 2003, the total PV production grew on average by almost 50%, whereas the thin-film PV segment grew on average by over 80%, reaching 400 MW, i.e., 10% of the total PV production in 2007. The high growth rate of thin-film production clearly shows that this technology is gaining more and more acceptance in the PV worldwide market.² Dye-sensitized solar cells (DSCs) are an important type of thin-film photovoltaics because of their potential for low-cost fabrication and versatile applications as flexible or light-weight products.³ State-of-the-art lab DSCs achieve more than 11% energy conversion on small-area devices.⁴

2 STRUCTURE AND WORKING PRINCIPLES

In a conventional p–n junction photovoltaic cell, the semiconductor assumes simultaneously the functions of harvesting sunlight to create an electron-hole pair and the transport of charge carriers (Figure 1a). On the other hand, in dye-sensitized solar cells the dye is the element responsible for light absorption and charge generation, while charge transport occurs both in the semiconductor and in the electrolyte (Figure 1b).

In DSCs, the semiconductor (also named *photoelectrode* or *working electrode* (WE)) is a mesoporous oxide layer composed of nanometer-sized particles that have been sintered together to allow electronic conduction. Attached to the surface of the oxide is a monolayer of dye molecules (sensitizer), which, upon light absorption, are promoted into an excited state. As a result, electrons from the valence band (VB) are injected into the conduction band (CB) of the semiconductor, giving rise to formation of excitons (excited electrons) and subsequent charge separation. The free electrons in the conduction band diffuse across the semiconductor toward the external circuit, performing electrical work. Once electrons reach the counterelectrode (CE), typically a thin layer of platinum, they react with the electrolyte that fills the space between the two electrodes, usually a solution of an ionic liquid solvent containing a triiodide/iodide redox system. The original state of the oxidized dye is subsequently restored by electron

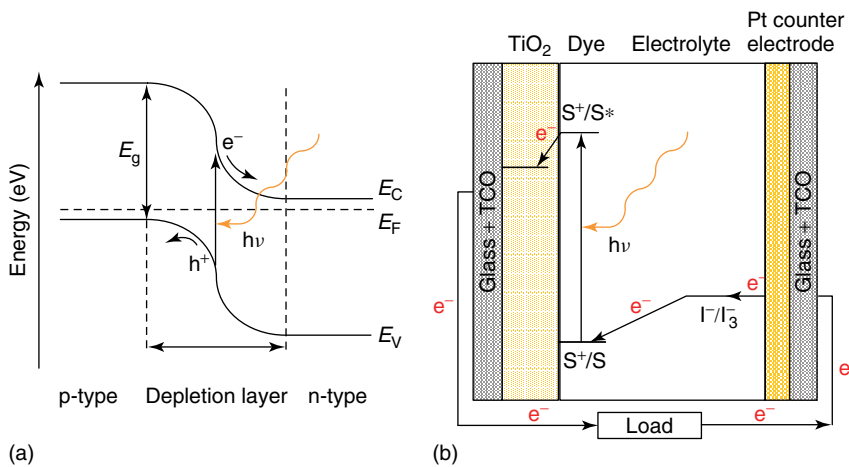


Figure 1 (a) Energy band scheme of a p–n junction solar cell; (b) principle of operation of a dye-sensitized solar cell. E_g , band gap energy; E_V , valence band energy; E_C , conduction band energy; E_F , semiconductor Fermi energy; e^- , electrons; h^+ , holes; S, ground state of the sensitizer; S^* , excited state of the sensitizer; S^+ , oxidized sensitizer

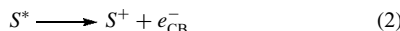
donation from the electrolyte, which is itself regenerated at the platinum CE by reduction of the triiodide.^{5–8} The redox electrolyte therefore allows the transport of electrical charge between the two electrodes of the DSC, closing the cycle.

The efficiency of a DSC is strongly determined by the electronic energy levels of the excited state (lowest unoccupied molecular orbital, LUMO) and the ground state (highest occupied molecular orbital, HOMO) of the dye, by the electron Fermi level of the semiconductor and by the redox potential of the electrolyte. Moreover, an operating DSC is largely governed by the relative kinetic rates of several charge-transfer processes. Figure 2 shows the following sequence of charge-transfer processes responsible for the operation of a DSC⁹:

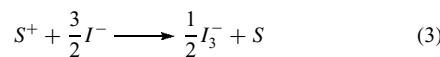
1. The photosensitizer, adsorbed on the surface of the semiconductor, absorbs incident sunlight becoming excited from the ground state (S) to the excited state (S^*).



2. Excited electrons are injected into the conduction band of the semiconductor, resulting in the oxidation of the sensitizer (S^+).



3. The oxidized sensitizer (S^+) is regenerated by accepting electrons from the iodide ion.



4. The triiodide redox mediator diffuses toward the CE and is reduced to iodide.

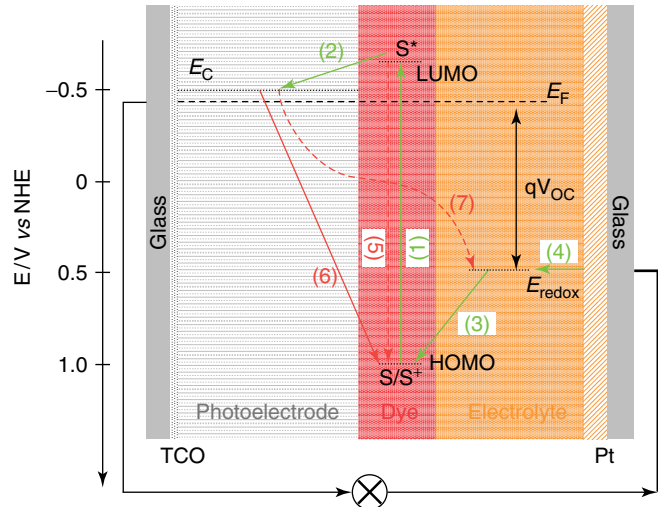
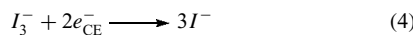


Figure 2 Schematic diagram of the operation kinetics of DSCs: forward electron transfer and electron loss pathways. The photovoltage, V_{OC} , of the system corresponds to the difference between the TiO₂ Fermi energy, E_F , and the redox energy of the electrolyte, E_{redox}

In addition to the forward electron transfer and ionic transport processes, several competing electron loss pathways should be considered:

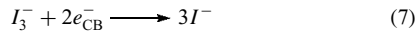
5. Decay of the dye excited state to ground state.



6. Recombination of injected electrons with dye cations.



7. Recombination of injected electrons with the triiodide redox mediator.



For efficient photoconversion of solar energy into electric current, the charge injection must occur with unit quantum yield (the parameter that denotes the fraction of photons absorbed by the dye that is converted into conduction band electrons). Thus, the excited state of the dye must energetically lie above the conduction band edge of the semiconductor to guarantee fast electron injection into the semiconductor, before it can fall back to its ground state (reaction in equation 5). The rate of electron injection depends on the electronic coupling between the dye LUMO and the accepting states in the semiconductor.^{10–12} Time-resolved laser spectroscopy measurements are used to study the kinetics of electron injection from sensitizers into the conduction band of the semiconductor. Since typical rates of decay of dye excited state to ground state are in the range 10^7 – 10^{10} s⁻¹ and electron injection rates higher than 10^{12} s⁻¹ have already been reported,^{13,14} efficient electron injection is therefore achieved (Figure 3). On the other hand, the oxidized dye must have a more positive potential than the redox couple in the electrolyte. Thus, the regeneration of the dye by the redox electrolyte must be fast in order to prevent recombination of the injected electrons with the oxidized dye (reaction in equation 6). This recombination reaction strongly depends on the electron density in the semiconductor and is naturally undesirable because, instead of electrical current, it simply generates heat. The regeneration reaction is dependent on the iodide concentration, electrolyte viscosity, and dye structure.¹⁵

The redox electrolyte is responsible for the regeneration of the dye, which becomes oxidized by electron injection to the TiO₂ conduction band, and conducts the positive charges (holes) to the CE, where the redox couple itself is regenerated. Consequently, for these processes to take place, several requirements must be fulfilled. Since the photovoltage of the system corresponds to the difference between the redox potential of the electrolyte and the TiO₂

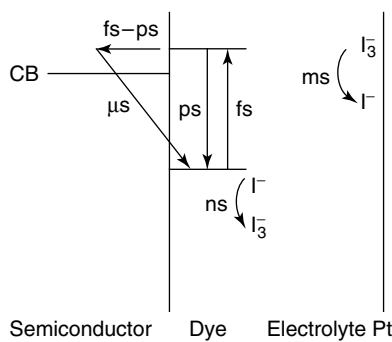


Figure 3 Kinetics of the electron transfer processes at the different interfaces in DSCs. CB labels the conduction band edge

Fermi level, the redox potential must be as positive as possible in order to guarantee high photovoltages (Figure 2). In contrast, the overvoltage required for triiodide reduction at the CE should be small, since it represents a loss in the photovoltage of the cell. Moreover, to overcome the problem related with possible slow charge-transfer reaction at the CE, a platinum-based catalyst is usually employed.

An efficient DSC also requires that the time constant for electron transport within the mesoporous semiconductor has to be faster than charge recombination of injected electrons with the redox couple (reaction in equation 7). In fact, this is the most predominant loss pathway to be considered in DSCs, which enables achieving higher efficiencies—dark current. Dark current often occurs at the semiconductor/electrolyte interface where the sensitizer is not adsorbed. To avoid this phenomenon, pyridine derivatives, for example, *tert*-butylpyridine (TBP), are used as coadsorbates on the TiO₂ surface, resulting in the improvement of photovoltaic.

In order to describe the kinetic competition between charge transport in the semiconductor and charge recombination at the semiconductor/electrolyte interface, the parameter electron diffusion length is defined as

$$L_n = \sqrt{D_n \tau_n} \quad (8)$$

where D_n is the diffusion coefficient and τ_n is the electron lifetime due to the charge recombination with triiodide. When $L_n \gg L$, L being the thickness of the semiconductor layer, electrons have time to cross the entire length before recombining with the electrolyte, which is an essential requirement for efficient cells. By contrast, in the case of high reactivity $L_n \ll L$, electrons tend to recombine at the TiO₂/electrolyte interface. As a result, the number of free electrons close to the conductive substrate ($x = 0$) decays rapidly (Figure 4).¹⁶

An experimental I – V curve is shown in Figure 5, together with the respective power curve. The overall conversion efficiency of the dye-sensitized cell is determined by the photocurrent density measured under short-circuit conditions (I_{sc}), the open-circuit photovoltage (V_{oc}), the fill factor (FF) of the cell, and the intensity of incident light (I_s):

$$\eta_{\text{global}} = \frac{I_{sc} V_{oc}}{I_s} \text{FF} \quad (9)$$

Under full sunlight (1 sun, air mass 1.5 global) the incident light intensity I_s is 100 mW cm^{-2} . The power curve is calculated as the product of current density and voltage, and the maximum-power point (MPP) is labeled with a dot in Figure 5. At this point, the device delivers the highest power output with voltage V_{MPP} and current I_{MPP} . The FF is the ratio of solar cell's actual power to that obtained from its I_{sc} and V_{oc} :

$$\text{FF} = \frac{I_{MPP} V_{MPP}}{I_{sc} V_{oc}} \quad (10)$$

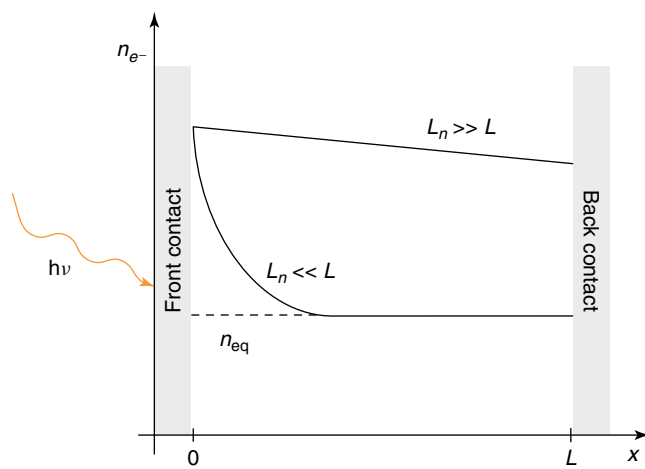


Figure 4 Density profile of injected electrons in the semiconductor film for the case when the diffusion length is much higher than the film thickness, $L_n \gg L$, and for the opposite situation, $L_n \ll L$; n_{eq} is the equilibrium concentration

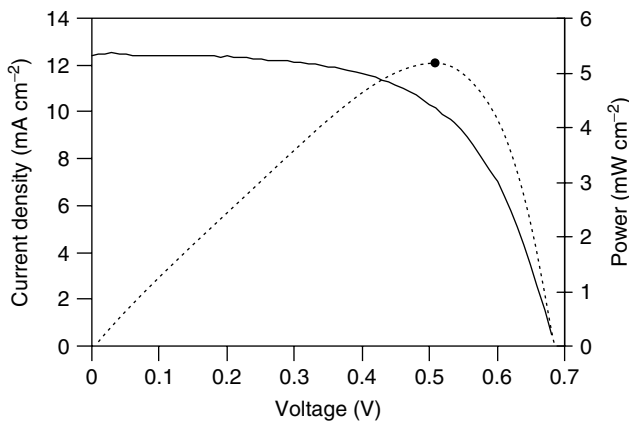


Figure 5 Typical $I-V$ curve (solid line) and respective power curve that shows the cell's power output at different bias (dashed line). The full dot in the power curve indicates the maximum-power point

Finally, it is important to understand the behavior of the cell under operating conditions, usually at maximum-power point, in dark equilibrium and at open-circuit conditions. The power output from a DSC operating at maximum-power point requires not only efficient charge collection and subsequent electric current generation but also setting up a photovoltage corresponding to the difference between the quasi-Fermi level of electrons in the semiconductor and the redox energy of the electrolyte. On the other hand, in the dark, there is neither voltage nor current generation. The Fermi level energy of electrons in the conduction band equilibrates with the redox energy of the electrolyte. Under illumination and at open-circuit conditions, there is no current flowing through the external circuit. The

injection and recombination rates are in equilibrium in the TiO_2 mesoporous structure. Consequently, all the injected electrons are recaptured by triiodide, the oxidized dye is regenerated by iodide, and there is no electron transfer to the triiodide at the platinum CE.¹⁷

3 OVERVIEW OF MATERIALS IN DSC DEVICES

3.1 Semiconductor

The semiconductor, typically a metal oxide, is responsible for providing the surface for dye adsorption, for accepting the electrons from the excited dye and for conducting the electrons toward the external circuit. This semiconductor layer is typically obtained by applying a paste of metal oxide nanocrystalline particles over a conducting substrate by screen printing or doctor blading.¹⁸ Its structure plays a crucial role in harvesting sunlight. The use of high surface area films of nanocrystalline oxide particles, with an average size of about 20 nm, leads to a significant surface area being available for dye adsorption, responsible for the absorption of a high percentage of the incident light. In contrast, flat electrodes promote very low light-harvesting levels due to the small absorption cross section of a monolayer of dye, which results in quite low photovoltaic efficiencies. A suitable degree of porosity is also needed to promote good contact between the dye molecules adsorbed onto the semiconductor nanoparticles and the electrolyte species, ultimately assuring the regeneration of the dye. Moreover, the porous film must form an interconnected network to allow the percolation of the injected electrons. In addition, the position of the conduction band edge is also important and must allow charge injection from the excited state of the dye.

TiO_2 is the preferred semiconductor for application in DSCs. Although some promising properties are exhibited by other semiconducting oxides, like ZnO or SnO_2 , TiO_2 is still the cornerstone semiconductor for the electrodes of DSCs.¹⁹ Two crystalline forms of TiO_2 are normally considered: anatase and rutile. However, the former is preferable since it has a wide band gap energy of about 3.2 eV and an absorption edge that makes it insensitive to the visible light. In fact, this prevents the generation of holes by band gap excitation which would act as oxidants. In what concerns rutile, it has a lower band gap (~ 3.0 eV) and a higher dark current, and absorbs part of the near-UV region, making rutile less chemically stable.^{20,21} Furthermore, anatase is nontoxic, thermally stable, chemically inert, readily available, and cheap.^{22,23}

Bearing in mind that the main loss pathway is the dark current due to the reaction of injected electrons with triiodide ions, researchers are developing modified nanocrystalline TiO_2 structures that avoid the recombination path. This fact leads to the growing of an emergent and interesting field in DSCs: incorporation of nanotubes,^{24–27} nanowires,²⁸

nanorods,^{29,30} and inverse opals^{31,32} in conventional dye solar cells. These ordered and oriented structures enhance the electrical conductivity in TiO₂ electrodes, increasing the electron percolation through the film.³³ In addition, highly ordered nanostructures seem to induce stronger internal light-scattering effects, resulting in higher light-harvesting efficiencies. It should be noted, however, that defect-mediated recombination may also be promoted in these nanostructures, which means that high crystal quality must be ensured to yield a better performance of the photovoltaic device. A way to prevent the recapture of photojected electrons by triiodide is the use of a “blocking layer”, made of semiconductors that have a more negative conduction band, e.g., Al₂O₃³⁴ or MgO.³⁵ The idea is to block the surface with an insulator layer that allows electron injection but diminishes the interfacial recombination kinetics that limits the overall performance.³ Several surface treatments are also being considered in order to control the unfavorable dark current and increase the photocurrent output. Ito *et al.*³⁶ observed that these treatments improve the J_{SC} by enlarging the surface area of the mesoscopic film. Finally, the use of a light-scattering layer is also quite common. It consists of larger titania particles (between 100 and 400 nm) that work as a photo-trapping system.^{36,37} In fact, when using light-scattering particles, Koo *et al.*³⁸ observed efficiency increments of about 15%.

3.2 Dye

Since in DSCs the function of light absorption is separated from the charge carrier transport, the dye should have a broad absorption spectrum in order to capture solar radiation as much as possible: the ideal dye should absorb light at wavelengths up to 920 nm (equivalent to a semiconductor with a band gap of approximately 1.4 eV).³⁹ To prevent energy losses and to maximize the cell photovoltage, the excited state should be only slightly above the conduction band of the semiconductor but sufficiently above to produce an energetic driving force that ensures electron injection (Figure 2). In the same way, the dye’s ground state should be only slightly below the redox potential of the electrolyte to ensure an efficient regeneration process.⁴⁰ In addition, the dye should present long stability (it must endure at least 10⁸ redox turnovers, corresponding to about 20 years of operation), good adsorption to the semiconductor’s surface, high solubility in the corresponding solvent, and no toxicity.^{5,23}

Till date, sensitizers based on bipyridyl complexes of ruthenium have been widely used due to their advantageous spectral properties, photostability in the final device, and high energy conversion efficiencies.^{41–44} An example of high-performance ruthenium polypyridine complexes is the *cis*-dithiocyanatobis (4, 4'-dicarboxylic acid - 2, 2'-bipyridine)ruthenium(II), commonly known as the *N3 dye*. The carboxylate groups in N3 dye confer a strong binding to the TiO₂ surface, explaining its excellent stability, while

the thiocyanate groups (NCS) enhance its response to visible light. For an N3 dye-sensitized solar cell, the measured incident photon-to-current conversion efficiency (IPCE) values exceeds 80% in the wavelength range between 480 and 600 nm, reaching 85–90% between 510 and 570 nm.^{28,45–47} Since the development of the N3 dye in 1993,⁴⁵ its tetrabutylammonium salt N719 has been used as the standard red dye because of its unmatched performance.⁴ This dye is derived from the N3 form by substituting two protons with two TBA (tetrabutylammonium) cations. On the basis of intensive efforts to enhance spectral response in the red and near infrared (NIR) region, the dye tris(cyanato)-2,2',2'-terpyridyl-4,4',4"-tricarboxylate Ru(II), also called *black dye*, was developed. TiO₂/black-dye-based DSCs show IPCE values around 80% over a broad wavelength range extending from 400 to 700 nm.⁴⁸ More recently, the amphiphilic ruthenium dye Z907⁴⁹ and the high molar extinction coefficient dye K19⁵⁰ have attracted researchers’ attention.

Although high efficiency and stability have been achieved with ruthenium-based dyes, alternatives should also be considered. In fact, due to its scarcity, ruthenium is a very expensive metal. Organic dyes, such as porphyrins, phthalocyanines, cyanines, and merocyanines, can be a promising alternative since they are much cheaper than ruthenium compounds.^{51,52} However, the efficiency and stability achieved with these compounds is still very low.⁵³

Semiconductor quantum dots are another attractive option. Quantum dots are a nontraditional type of semiconductor with limitless applications because of their particle sizes that are small enough to produce quantum confinement effects. By changing the particle size, different absorption spectra are obtained. Furthermore, quantum dots have a very high extinction coefficient when compared with conventional dyes, allowing the use of thinner mesoporous oxide films. The main disadvantage is the possibility of photocorrosion when the junction contact is a liquid electrolyte, mainly due to the aggressive nature of the electrolyte employed.⁵⁴

Despite all efforts made till date concerning the improvement on photovoltaic performance and stability, it is still mandatory to find novel efficient and stable sensitizers.

3.3 Electrolyte

The redox couple in the electrolyte has the function of regenerating the dye after electron injection into the conduction band of the semiconductor, as well as to transport the positive charges (holes) toward the CE. The most used liquid electrolyte in DSCs is based on the charge mediator I₃[–]/I[–] redox couple in acetonitrile, a low-viscosity volatile solvent. In fact, its redox potential is energetically favorable with respect to redox potential of several oxidized ruthenium-based dyes and fully organic sensitizers, which contributes to maximizing the cell voltage.⁵⁵ The electrolyte mediator should not absorb in the visible range to prevent competition with the sensitizer. Since the maximum photovoltage of the cell is

determined by the redox potential edge of the electrolyte, it should be as positive as possible to provide high photovoltages. While in the CE the redox couple must be reversible, in the semiconductor it should be inert. The redox couple should be highly soluble in the solvent to ensure high concentration of charge carriers in the electrolyte. Additionally, the solvent should allow fast diffusion of the charge carriers and should not contribute to desorption of the dye from the surface of the semiconductor.

The electrolyte characteristics strongly affect the overall operation of the DSC mainly because of its influence in the mass transport of the charge carriers. In fact, the electrolyte participates in the electron transfer kinetics at the CE (the maximum current density is normally achieved when the reduction of I_3^- occurs as fast as it can be supplied by diffusion to the CE), strongly controls the dark current reactions, and determines the charge transport in the film semiconductor and in solution (dependent not only on the viscosity of the electrolyte but also on the structure of the semiconductor). The photovoltage can also be affected by nonelectroactive species in the electrolyte, particularly by cations that can adsorb onto the surface of the TiO_2 electrode, shifting its conduction band edge to a lower energy level. This can lower the photovoltage but enhance the efficiency of interfacial charge injection, increasing the photocurrent and the efficiency of the DSC.⁵⁶

Despite solid and quasi-solid-state electrolytes being developed and improved, liquid electrolytes are still the most commonly used. However, the latter require efficient encapsulation of the DSC, necessary to prevent the loss of electrolyte by leakage and/or evaporation of the solvent. This is, in fact, a major drawback for the long-term stability of DSCs, with important consequences to the market implementation of the technology. Bearing this in mind, several efforts have been developed in order to overcome this problem: TiO_2 DSCs assembled with nonvolatile electrolytes based on ionic liquids (commonly known as *robust electrolytes*) instead of the typical organic solvents seem to be a good solution. In fact, ionic liquids have good chemical and thermal stability, negligible vapor pressure, nonflammability, high ionic conductivity, and high solubility for organic or inorganic materials.⁸ Despite the recent advancements,^{57–59} their high viscosities limit their applications, ultimately reducing the efficiency of the cells.

3.4 Counterelectrode

At the CE the reduction of triiodide to iodide takes place (reaction in equation 4). However, to ensure fast reaction kinetics and to overcome the high activation energy of the two-electrons transfer, a catalyst is needed. Platinum is traditionally used as the most efficient catalyst not only because it provides high exchange current densities, but also because it is transparent. The deposition method of the platinum catalyst onto the transparent conducting oxide

(TCO) substrate influences its performance. In fact, it has been found that platinum becomes unstable in the presence of the iodide electrolyte when coated electrochemically or by vapor deposition.^{60,61} Since platinum is very expensive, some other cheaper alternatives were also studied. Among other materials, carbon,⁶² carbon black,⁶³ graphite,⁶⁴ activated carbon⁶⁵ or single-wall carbon nanotubes,⁶⁶ and conductive polymers⁶⁵ have been used as CEs in DSCs. Moreover, the CE is normally chosen bearing in mind the final application of the DSC. For instance, for DSCs incorporated in power-producing windows, a transparent CE should be employed; for inexpensive DSCs, a low-cost material as a carbon catalyst should be used; or for very efficient cells, a material with the lowest possible sheet resistance and with high rate of redox electrolyte reduction should be considered.⁶³

4 EIS CHARACTERIZATION

The steady-state $I-V$ characteristic gives the performance parameters of the cell, such as the short-circuit current (I_{sc}), open-circuit potential (V_{oc}), and FF. Nevertheless, more detailed properties cannot be extracted from steady-state measurements, and so dynamic techniques should be considered. These techniques allow the interpretation of the charge-transfer kinetics, mainly characterized by diffusion coefficients and lifetime of the different charge carriers. One of the most powerful characterization techniques of DSCs involving transient probing is electrochemical impedance spectroscopy (EIS).

EIS is a dynamic technique that has many advantages, not only because it is user-friendly but also because of its sensitivity and ability to separate different complex processes, such as those occurring in a DSC.^{67–69} However, working in the linear response range of the system has to be ensured.

Despite being a relatively easy method to apply to the study of electrochemical systems, the results may sometimes be difficult to interpret. The use of equivalent electrical analogs to fit the EIS experimental data is a useful tool in this respect, as it helps to identify and interpret some of the characteristic parameters of the system, such as, for instance, the internal resistances of a DSC.

4.1 EIS Fundamentals

EIS is a technique widely used for characterizing the electrical behavior of systems in which the overall performance is determined by a number of strongly coupled processes, each proceeding at a different rate. The most common and standard procedure in impedance measurements consists of applying a small voltage sinusoidal perturbation and monitoring the resulting current response of the system at the corresponding frequency. An EIS measurement can be performed under any bias illumination and at any working

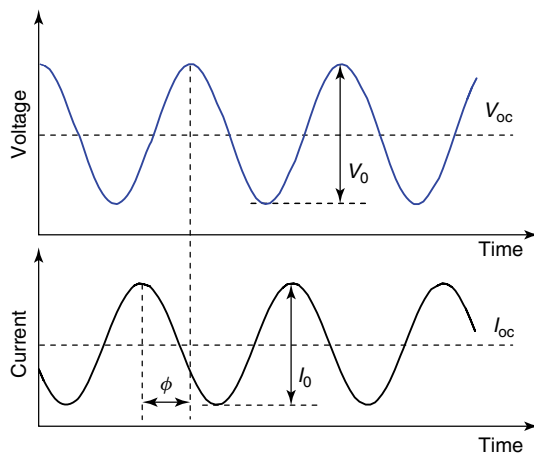


Figure 6 Sinusoidal voltage perturbation and resulting sinusoidal current response, phase-shifted by ϕ . V_0 , amplitude of the voltage signal; I_0 , amplitude of the current signal; V_{oc} , open-circuit voltage; I_{oc} , open-circuit current

condition of the solar cell. Nevertheless, the single-frequency voltage perturbation is usually done under open-circuit conditions with a modulation signal of magnitude V_0 (see Figure 6):

$$V(t) = V_{oc} + V_0 \cos(\omega t) \quad (11)$$

The response in current has the same period as the voltage perturbation but will be phase-shifted by ϕ :

$$I(t) = I_{oc} + I_0 \cos(\omega t - \phi) \quad (12)$$

V_0 and I_0 are the amplitudes of the voltage and current signals, respectively, and $\omega (= 2\pi f)$ is the radial frequency in radians per second; the open-circuit current I_{oc} is zero.

Similar to resistance, impedance is a measure of the ability of a system to impede the flow of electrical current.

Thus, impedance is the ratio of a time-dependent voltage and a time-dependent current as defined by equations (11) and (12):

$$Z = \frac{V_0 \cos(\omega t)}{I_0 \cos(\omega t - \phi)} = Z_0 \frac{\cos(\omega t)}{\cos(\omega t - \phi)} \quad (13)$$

The impedance is therefore expressed in terms of a magnitude, Z_0 , and a phase shift, ϕ . Applying complex notation, the impedance response of a system can be described in terms of real and imaginary components, as follows⁷⁰:

$$Z = Z_0 \frac{\exp(j\omega t)}{\exp(j\omega t - j\phi)} = Z_0 (\cos \phi + j \sin \phi) \quad (14)$$

Knowing the values of $Z_{real} = Z_0 \cos \phi$ (also denoted as Z'), $Z_{imag} = Z_0 \sin \phi$ (also denoted as Z'') and the phase angle ϕ , the Nyquist and Bode diagrams can be plotted. The former is the representation of the $-Z_{imag}$ versus Z_{real} , while the Bode diagram is the representation in a semilogarithmic plot of the symmetric of the phase angle ϕ versus frequency.

A typical EIS spectrum for a DSC under illumination exhibits three semicircles in the Nyquist plot and three frequency peaks in the Bode phase diagram (Figure 7). The phenomena involved at these characteristic frequencies, from low to high frequencies (from right to left in Figure 7b), are Nernst diffusion within the electrolyte, electron transfer at the TiO₂/electrolyte interface, and redox reaction at the platinum CE. In some cases, two peaks might overlap, in particular, the low-frequency peak often vanishes underneath the mid-frequency peak.⁷¹

It is important to emphasize that impedance analysis is based on the assumption that the system under study behaves linearly. Since linear systems typically exhibit features and properties that are much simpler than the general nonlinear cases, the analysis becomes less complex. A system is linear if it complies with both homogeneity and additivity principles, which state that (i) when a perturbation is imposed to a system, the response will be proportional and of the same

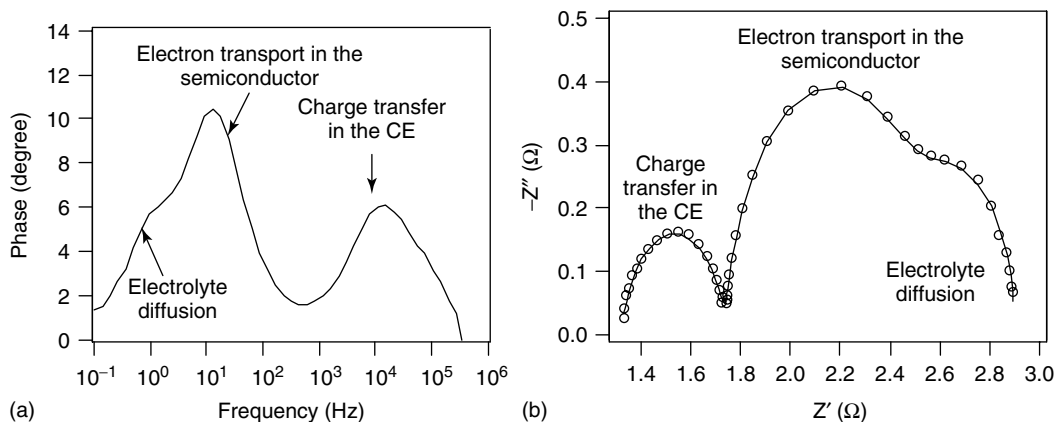


Figure 7 Typical (a) Bode and (b) Nyquist diagrams for a DSC

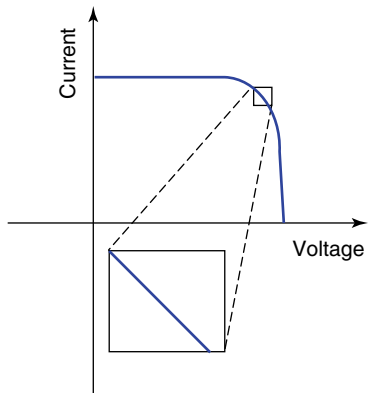


Figure 8 Current versus voltage curve showing pseudolinearity

type as the input signal (for instance, if a tensile strength applied to a sample increases twofold, the corresponding strain will double) and (ii) if the perturbation imposed to a system consists of the weighted sum of several signals, then, the output is simply the weighted sum of the system's responses to each input signal. Mathematically, let us consider $y_1(t)$ as the response of a continuous time system $x_1(t)$ and $y_2(t)$ as the output corresponding to the input $x_2(t)$. Then the system is linear under the following conditions:

1. **Principle of homogeneity:** The response to $a \cdot x_1(t)$ is $a \cdot y_1(t)$
2. **Principle of additivity:** The response to $x_1(t) + x_2(t)$ is $y_1(t) + y_2(t)$

Applying this on the system under study, i.e. a dye-sensitized solar cell and its $I-V$ characteristic (Figure 5), it is clear that the response to a voltage input signal is not linear. The way to circumvent this situation is to consider only a small portion of the cell's current *versus* voltage curve, which appears to be linear (Figure 8). In practice, for EIS measurements a small voltage perturbation (1–20 mV) is applied to the cell, ensuring that the response is in the pseudolinear range.⁷²

4.2 Electrical Analogs

General EIS data are commonly analyzed by means of equivalent electrical circuit models, which may consist of resistors, capacitors, inductors, and more complex elements, assembled in series or in parallel. In particular, fitting the experimental data to specific arrangements of electrical elements can provide relevant information concerning reaction kinetics, ohmic conduction processes, and even mass transfer phenomena occurring in electrochemical systems such as DSCs. The most common circuit elements used to describe electrochemical cell behavior are briefly described hereafter. However, complementary knowledge about standard circuit elements is strongly encouraged.⁷⁰

4.2.1 Ohmic Resistance

The equivalent analog for an ohmic conduction process is a simple resistor, which, according to the Ohm's law, represents the resistance to electric charge transfer. The impedance of an ohmic resistance is simply defined as

$$Z_R = R \quad (15)$$

Notice that the impedance of a resistor is independent of frequency and has no imaginary component.

4.2.2 Double-Layer Capacitance

An electrical double layer exists at the interface between an electrode and its surrounding electrolyte. This double layer is formed because of the charge separation that occurs across the interface: an excess of ions of charge opposite to that on the electrode will be found on the electrolyte phase boundary. A simple way of understanding the double-layer behavior is to imagine that ions at each side of the interface approach the electrode surface as closely as possible, originating two parallel layers of equal and opposite charge, one on the electrode side and the other on the electrolyte side (Figure 9). This double layer will act as a charge storage,⁷³ i.e., a capacitor with an impedance response, defined as follows:

$$Z_C = \frac{1}{j\omega C} \quad (16)$$

In real cells, formed by nanoporous semiconductors, the double-layer capacitor does not behave ideally. Instead, it acts like a constant phase element (CPE), a nonideal capacitance with a nonuniform distribution of current in the heterogeneous material. In this case, the impedance of the double-layer capacitance is defined as

$$Z_{CPE} = \frac{1}{j\omega C^n} \quad (17)$$

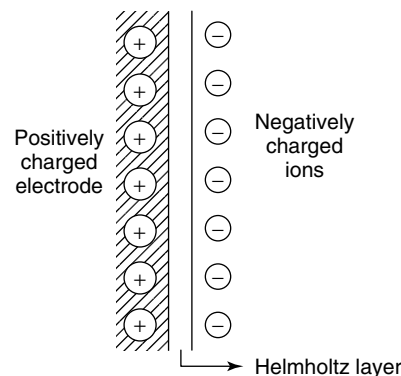


Figure 9 Helmholtz double layer

where n ($0 < n < 1$) is an empirical constant with no real physical meaning; for ideal capacitors $n = 1$.⁷⁰

4.2.3 Electrochemical Reaction

The impedance behavior of an electrochemical reaction can be well represented by a parallel assembling of a resistor, R , and a capacitor, C . While the resistor models the kinetics of the electrochemical reaction, the capacitor describes the charge separation across the interface.⁷⁴

Components of an electrical circuit can be connected in series or in parallel. The net impedance of a system with elements assembled in series is the sum of the impedances of the circuit elements, whereas the total impedance combined in parallel is given by

$$\frac{1}{Z_{\text{parallel}}} = \frac{1}{Z_1} + \dots + \frac{1}{Z_i} \quad (18)$$

i being the number of circuit elements. Thus, for an electrochemical reaction the total impedance may be defined as

$$Z = \frac{1}{1/R + j\omega C} \quad (19)$$

The corresponding Nyquist diagram, presented in Figure 10, shows a semicircle with diameter R . The extension of the semicircle, therefore, provides useful information concerning the reaction kinetics of the system: facile reaction kinetics will show a small diameter, while a blocking electrode will be characterized by a huge semicircle. Finally, the time constant of the reaction kinetics, τ , is given by

$$\omega_{\text{max}} = \frac{1}{\tau} = \frac{1}{RC} \quad (20)$$

where ω_{max} is the radial frequency at the semicircle maximum (Figure 10).

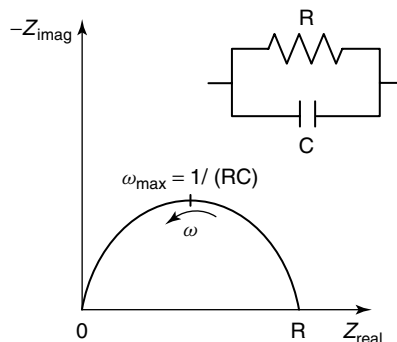


Figure 10 Circuit diagram and Nyquist plot representing the impedance behavior of an electrochemical reaction; ω is the radial frequency

4.2.4 Mass Transport

In most electrochemical systems, mass transport is based on diffusion processes that can be modeled by a Warburg circuit element. At high frequencies, the Warburg impedance is small since diffusing reactants do not have to move very far. At low frequencies, the reactants have to diffuse farther, increasing the Warburg impedance. In this case, an infinite thickness diffusion layer may be assumed, which leads to the definition of the “infinite” Warburg impedance, Z_W :

$$Z_W = \frac{\sigma_i}{\sqrt{\omega}} (1 - j) \quad (21)$$

where σ_i is the Warburg coefficient for species i and is given by

$$\sigma_i = \frac{RT}{(nF)^2 A \sqrt{2}} \left(\frac{1}{c_i \sqrt{D_i}} \right) \quad (22)$$

A is the electrode area, n is the number of electrons transferred in the electrode reaction (see equation (4)), c_i is the bulk concentration of the reactant specie i , and D_i is the respective diffusion coefficient. On a Nyquist plot, the Warburg impedance appears as a 45° diagonal line (Figure 11).

4.2.5 Transmission Line Model

After this brief description of the most common and simple electrical elements, the following section will discuss more complex analogs, namely, those used in the analysis of DSCs. Recently, several models based on electrical analogs have been developed in an effort to understand all the complex charge-transfer phenomena that take place at the interfaces of DSCs.^{67,68,75–78} However, the interpretation of these phenomena in terms of resistive and capacitive elements is not straightforward because of the complexity inherent to these photoelectrochemical cells. The electron transport,

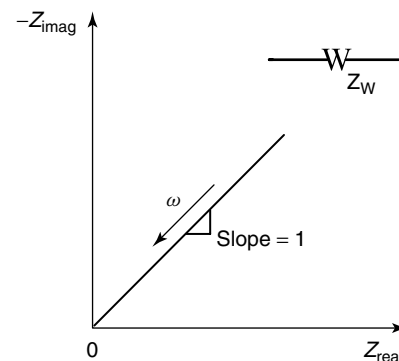


Figure 11 Circuit diagram and Nyquist plot for a Warburg element used to model diffusion-like mass transport phenomena; ω is the radial frequency

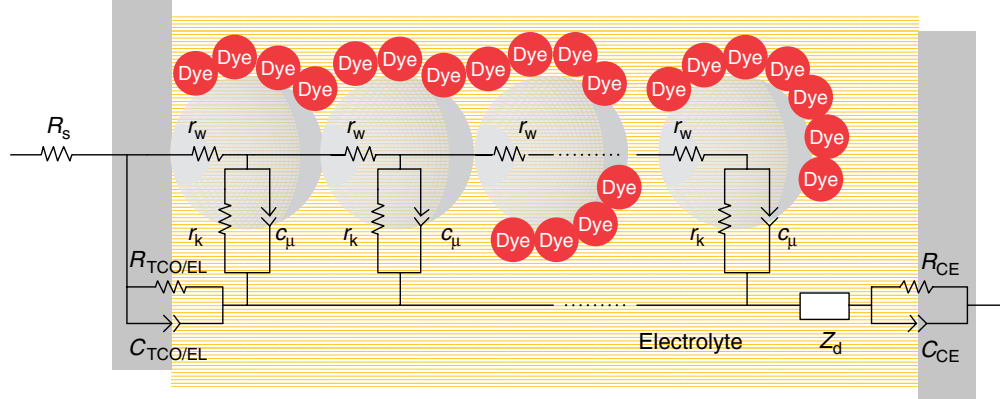


Figure 12 Transmission line model used to fit EIS experimental data.^{75,80} R_s , series resistance; $R_{\text{TCO/EL}}$, charge-transfer resistance at exposed TCO/electrolyte interface; $C_{\text{TCO/EL}}$, double-layer capacitance at exposed TCO/electrolyte interface; r_k , recombination resistance; r_w , transport resistance; c_μ , chemical capacitance; Z_d , Nernst diffusion within electrolyte; R_{CE} , charge-transfer resistance at the platinized TCO; C_{CE} , double-layer capacitance at the platinized TCO

accumulation, and charge recombination in nanocrystalline TiO_2 films have been widely studied by Bisquert *et al.*,⁷⁹ who suggested an infinite transmission line model based on the diffusion–recombination theory (Figure 12).

This model describes the whole mesoscopic TiO_2 film as an interconnected network of nanoparticles. In an EIS measurement, under forward bias, electrons are injected from the TCO substrate into the TiO_2 film, which, in its turn, is charged by electron percolation through the individual particles of the film. This charge-transfer process is characterized by a resistance R_w . Then, some of the injected electrons may recombine with the oxidized species in the electrolyte and the remaining electrons are then recaptured by the TCO current collector during the opposite phase of the sinusoidal voltage modulation (see Figure 6). The recombination phenomenon is characterized by a charge-transfer resistance, R_k , and a capacitance, C_μ . If L is the thickness of the mesoscopic TiO_2 film, the electron transport resistance is defined as $R_w = r_w L$, while the interfacial charge recombination resistance is $R_k = r_k / L$. Note that the lowercase letters refer to the circuit element properties per unit length L since they are distributed in a repetitive arrangement throughout the entire semiconductor of thickness L . The chemical capacitance, $C_\mu = c_\mu L$, reflects the change of electron density at the TiO_2 /electrolyte interface upon a small variation of the chemical potential. This $r_w(r_k c_\mu)$ electrical analog, representing the two pathways for electron transfer at the semiconductor, is assembled in series with a diffusion-like element Z_d , which characterizes the Nernst diffusion impedance of I_3^- ions in the electrolyte. Regeneration of I_3^- at the CE is characterized by R_{CE} and C_{CE} , which are the charge-transfer resistance and double-layer capacitance at the platinized TCO, respectively. R_s is the series resistance, including the sheet resistance of the TCO glass and the contacts resistance of the cell.⁶⁹ $R_{\text{TCO/EL}}$ and $C_{\text{TCO/EL}}$ stand for the charge-transfer resistance

and the corresponding double-layer capacitance at exposed TCO/electrolyte interface.

Fitting EIS experimental data of the DSC to the transmission line model described above, parameters R_k , R_w , and C_μ allow the calculation of the electron lifetime, τ_n , and the effective electron diffusion length, L_n :

$$\tau_n = R_k C_\mu \quad (23)$$

$$L_n = L \sqrt{R_k / R_w} \quad (24)$$

Combining equations (8), (23), and (24) the effective diffusion coefficient of electrons in the TiO_2 semiconductor, D_n ($D_n = L_n^2 / \tau_n$), can also be obtained.⁸¹

The impedance model described above is valid for a homogeneous distribution of electrons in the semiconductor, yielding to constant resistive and capacitive elements in the transmission lines model (Figure 12). The impedance function of the diffusion–recombination model in nanostructured electrodes is described by the following equation⁷⁹:

$$Z = \left(\frac{R_w R_k}{1 + j\omega/\omega_k} \right)^{1/2} \coth \left[\left(\frac{\omega_k}{\omega_d} \right)^{1/2} \left(1 + \frac{j\omega}{\omega_k} \right)^{1/2} \right] \quad (25)$$

where ω_d is the characteristic frequency of diffusion; ω_k is the characteristic frequency of recombination; ω is the angular frequency of the perturbation and j is the imaginary number. Note that ω_d and ω_k are related to the transit time τ_{tr} and lifetime τ_n , as defined in equation (20):

$$\omega_d = \frac{D_n}{L^2} = \tau_{\text{tr}} \quad (26)$$

$$\omega_k = \frac{1}{R_k C_\mu} = \frac{1}{\tau_n} \quad (27)$$

From this diffusion–recombination model, three particular physical situations should be considered, as

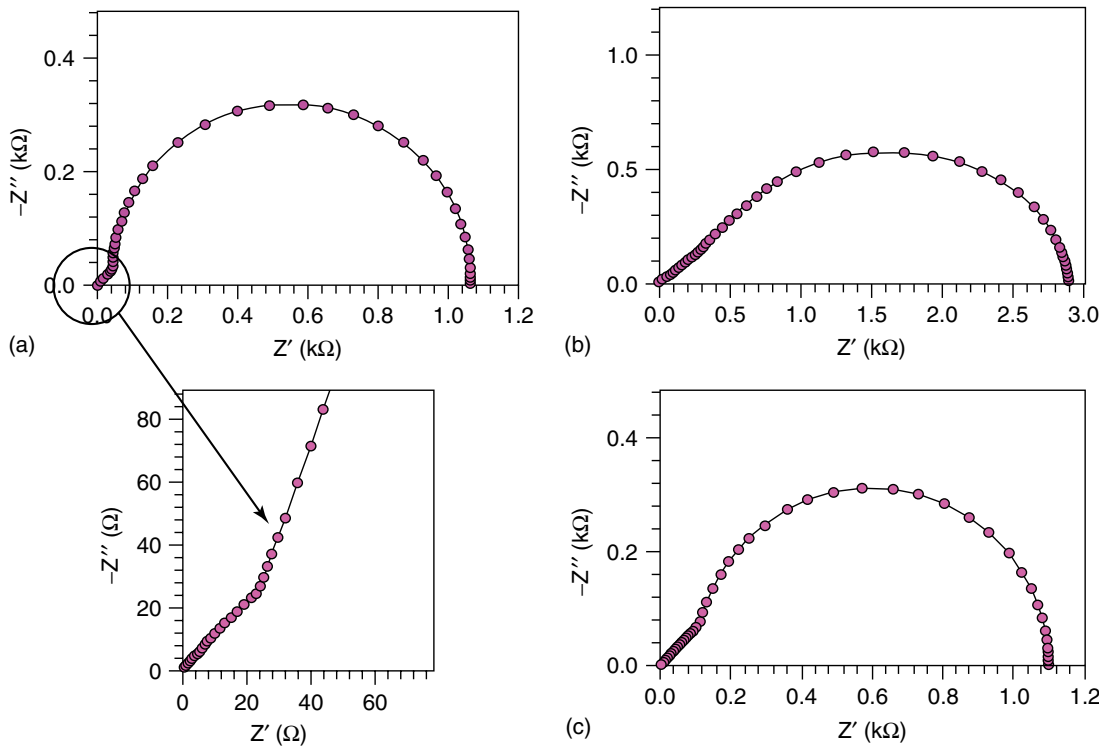


Figure 13 Impedance spectra obtained for the diffusion–recombination model when (a) $R_k \gg R_w$; (b) $R_w \gg R_k$; (c) $R_k \approx R_w$

illustrated in Figure 13.⁷⁵ The first case corresponds to the situation where the charge-transfer resistance associated with recombination of electrons at the TiO₂/electrolyte interface is much higher than the electron transport resistance through the semiconductor ($R_k \gg R_w$). This means that the electron lifetime is much higher than the transit time and the respective diffusion length will be larger than the thickness of the cell, an essential requirement for efficient cells ($L_n \gg L$). At low frequencies, equation (25) reduces to the expression of a semicircle defined as

$$Z = \frac{1}{3} R_w + \frac{R_k}{1 + j\omega/\omega_k} \quad (28)$$

while at high frequencies the impedance function is defined by a straight line with slope 1:

$$Z = R_w \left(\frac{j\omega}{\omega_d} \right)^{1/2} \quad (29)$$

As a result, the impedance spectrum in Figure 13(a) shows a small Warburg diffusion impedance at high frequencies, i.e., a straight line with slope 1, followed by a large arc with characteristic frequency ω_k due to the recombination process. The total impedance is in fact largely dominated by the high recombination resistance, the second term in equation (28). On the other hand, if electrons tend to recombine with the I_3^- ions in the electrolyte, a low

recombination resistance will be observed, together with a high resistance to electron diffusion through the semiconductor film ($R_w \gg R_k$). As a consequence, $L_n \ll L$, and the impedance spectrum in Figure 13(b) exhibits a Gerisher impedance at low frequencies:

$$Z = \left(\frac{R_w R_k}{1 + j\omega/\omega_k} \right)^{1/2} \quad (30)$$

As in the previous case, at high frequencies the impedance spectrum shows a diffusion line with slope 1, defined by equation (29). Finally, Figure 13(c) illustrates the intermediate situation, where $R_w \approx R_k$. In this case, the time constants are similar and thus $L_n \approx L$.

Note that the model defined by equation (25), illustrated in Figure 13 and based on the considerations made so far, describes only the behavior of the semiconductor and does not take into account the effects of the TCO layer, the platinum CE, or the diffusion of the redox species in the electrolyte.

The shape of the impedance spectra is also strongly affected by the light intensity and the potential applied to the system, and therefore this should be taken into account when performing impedance measurements. Increasing the illumination at constant voltage, the recombination resistance decreases significantly with respect to its value measured in the dark. In what concerns the applied voltage, varying its value implies a variation in the electron Fermi level of the

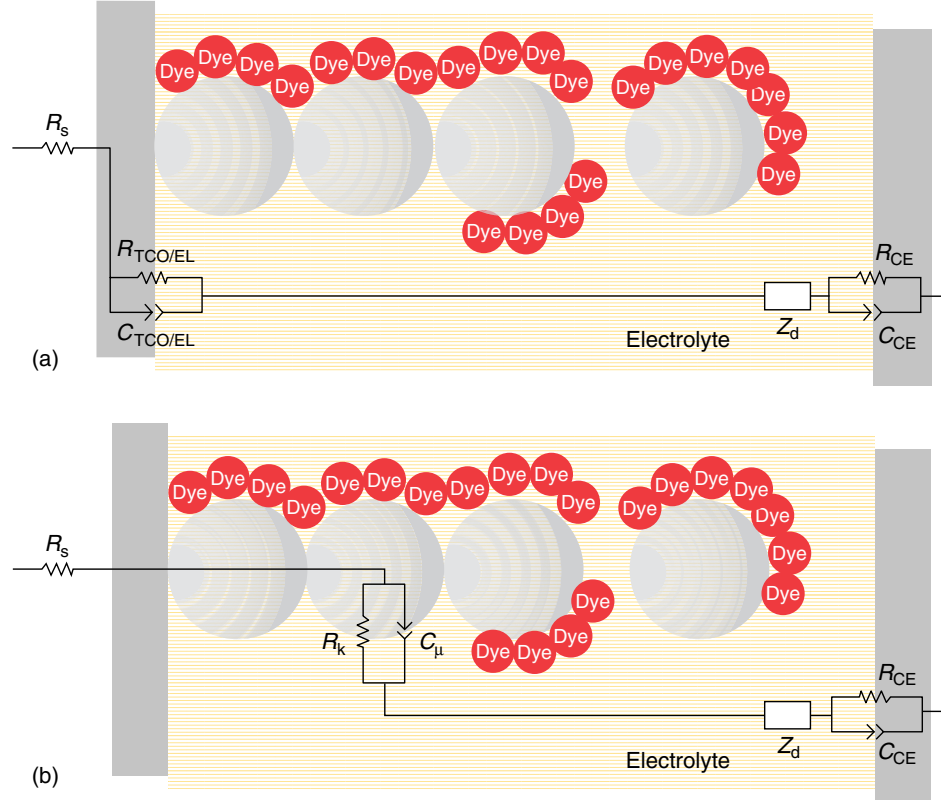


Figure 14 Simplified circuits of the model presented in Figure 13: (a) at very low applied potentials (insulating TiO_2); (b) at high applied potentials (conductive TiO_2)⁷⁵

injected electrons in the semiconductor, and consequently a variation in the capacitance. Changing the operating conditions may therefore allow the extraction of important information about the processes occurring in DSCs. In fact, at very low applied potentials, the impedance spectrum has only one semicircle displaced from the origin by R_s . Since at low potentials the TiO_2 behaves like an insulator, this semicircle is due to the parallel contributions of the charge-transfer resistance and the corresponding double-layer capacitance at exposed TCO/electrolyte interface, $R_{\text{TCO/EL}}$ and $C_{\text{TCO/EL}}$, respectively. At high frequencies, a smooth deformation in this single semicircle can be detected, arising from the contribution of the platinized CE (R_{CE} in parallel with C_{CE}). Moreover, as the current flow at these potentials is very low the diffusion element in the electrolyte, Z_d , can be neglected, and the corresponding electric analog is reduced to that shown in Figure 14(a). As the voltage increases, the TiO_2 becomes more conductive and the transport resistance becomes negligible. At very high potentials, the chemical capacitance C_μ , which reflects the change of electron density, dominates over the double-layer capacitance at the TCO/electrolyte interface ($C_\mu \gg C_{\text{TCO/EL}}$), and the impedance spectrum assumes the typical shape of a DSC Nyquist plot as shown in Figure 7. The transmission line model reduces to that shown in Figure 14(b) where a single parallel arrangement of R_k and

C_μ is assembled in series with an ohmic resistance R_s , the CE contribution (R_{CE} and C_{CE}), and the diffusion in the electrolyte (Z_d).

5 PHENOMENOLOGICAL MODELING

The phenomena occurring at the TCO layer, at the CE/electrolyte interface and at the TiO_2 /dye/electrolyte interfaces have been extensively studied by means of equivalent electrical analogs and impedance measurements, following the approach described in the previous section. However, due to the limitations of the EIS technology and in order to get a deeper understanding of the charge transport processes at those interfaces, a phenomenological model is required. In the literature, one can find several phenomenological studies describing the functioning of the DSCs. Sodergren *et al.*⁸² developed a steady-state phenomenological model based on electron diffusion through the porous semiconductor and considered a constant diffusion length, L_n . The presented $I-V$ characteristic equation was similar to the expression for a p-n junction solar cell, but the properties of the electrolyte were not taken into account.

Later on, Papageorgiou *et al.*⁸³ presented a comprehensive analysis of the relevance of mass transport in the steady-state operation of nanocrystalline photoelectrochemical solar cells. This work was intended to provide a better understanding of the role of the electrolyte species and not to predict $I-V$ characteristics or energy conversion parameters. Ferber *et al.*⁸⁴ suggested an electrical model for DSCs, allowing the calculation of the internal properties of the cell as well as the charge carriers' density distributions. On the basis of this complex electrical model, a complete $I-V$ characteristic was simulated and a simplified electric model of a DSC was published in the same year.⁸⁵ In that work, the authors used the experimentally obtained external current as input to the model. In 2001, Ferber *et al.*⁸⁶ extended their previous work⁸⁴ by developing a two-dimensional steady-state model. Here, the electric fields within the TiO_2 semiconductor and the redox electrolyte were distinguished, and the numerical calculations specifically addressed the spatial distribution of the electric and electrochemical potential in the cell. Other studies concerning several specific phenomena occurring in DSCs have been widely developed, but a global integrated model has never been presented. Peter⁹ and many other authors^{9,87-89} also contributed to a deeper understanding of the physical and chemical processes taking place in DSCs. Their works evidence the roles of the different components of the DSC (semiconductor, sensitizer, redox electrolyte, and CE) concerning the overall performance of the system. The routes that can lead to loss of DSC performance are also analyzed, considering the electron transport, interfacial electron transfer processes, and trapping in the mesoporous oxide.

The following sections are dedicated to the description of an integrated phenomenological model for dye-sensitized solar cells. The continuity and transport governing equations are defined for the mobile species involved: the electrons in the TiO_2 conduction band and the I^-/I_3^- ions in the electrolyte.⁹⁰ They also provide a brief description of the physics of semiconductors and the main characteristics of a metal–semiconductor contact, semiconductor–electrolyte junction, and electrolyte–platinized TCO contact.

5.1 Semiconductor

Solid materials can be categorized as conductors, insulators, or semiconductors, depending on their ability to transport electrical current. A conductor carries electrical current, whereas an insulator cannot carry current. Semiconductors have intermediate electric properties. To understand the fundamental concepts of semiconductors, one must consider the energy band structure theory. Here, two important considerations are relevant: first, it is necessary to know how many fixed and mobile charges are present in the material; second, the transport of the mobile carriers through the semiconductor should be analyzed. Two carriers transport

mechanisms can be considered: the drift of carriers in an electric field and the diffusion of carriers due to a carrier density gradient. Recombination mechanisms are also considered at this point. All these aspects are combined in the continuity equation for the photo-injected electrons, together with the respective boundary conditions.

5.1.1 Energy Band Structure

Electrons in semiconductors can have energies only within certain bands between the energy of the ground state, corresponding to electrons tightly bound to the atomic nuclei of the material, and the free electron energy, which is the energy required for an electron to escape. Between these two bands there is a band gap with energy E_g . A simplified energy band structure is illustrated in Figure 15. The energy range below the gap, called *valence band*, is the highest energy band nearly occupied with electrons. The energy range above the gap, called the *conduction band*, is the lowest energy band that, by contrast, is nearly empty. The photoexcitation of an electron in the valence band requires that the energy of the photon must at least equal the energy of the band gap:

$$E_g = h\nu \quad (31)$$

where h is the Planck constant and ν is the radiation frequency. In the valence band, electrons fill the energy states from bottom to top. A successful electron injection into the conduction band of the semiconductor will partially or even totally empty the energy states near the top of the valence band. These empty states can be regarded as positively charged carriers, commonly designated as holes. The top of the valence band and the bottom of the conduction band are approximately parabolic in shape and therefore the conduction band energy, E_C , and the valence band energy, E_V , can be considered constant (Figure 15). This is a very practical assumption that greatly simplifies the analysis of semiconductors.⁹¹

5.1.2 Electron Distribution in Semiconductors

The number of electrons n_{e^-} per unit of volume occupying levels in the conduction band is the integral of the product between the density of states in the conduction band and the Fermi–Dirac distribution over all energies in the conduction band:

$$n_{e^-} = \int_{E_c}^{\infty} n(E) f(E) dE \quad (32)$$

where $n(E)$ is the density of states in the conduction band and $f(E)$ is the Fermi–Dirac distribution. At an energy E near the conduction band, $n(E)$ is given by

$$n(E) = \frac{8\pi\sqrt{2}m_e^{*3/2}}{h^3}(E - E_C)^{1/2} \quad (33)$$

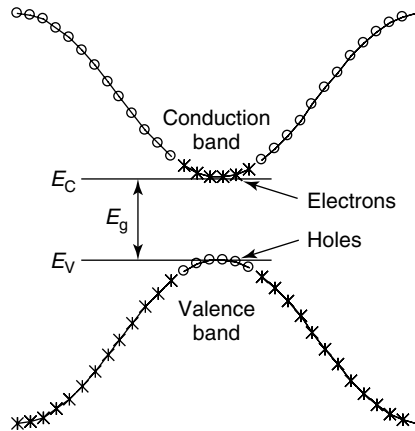


Figure 15 Simplified energy band diagram for a direct semiconductor. E_g , band gap energy; E_V , valence band energy; E_C , conduction band energy

with m_e^* being the electron effective mass. This effective mass is introduced here since the mass of an electron in a crystal lattice differs from that of an electron in free space. The Fermi–Dirac distribution function, also called *Fermi function*, provides the probability of occupancy by an electron at energy level E and in thermal equilibrium (at a constant temperature with no external injection or generation of carriers). The Fermi function is given by

$$f(E) = \frac{1}{1 + \exp\left(\frac{E - E_F}{k_B T}\right)} \quad (34)$$

The system is characterized by its temperature, T , and its Fermi energy, E_F ; k_B is the Boltzmann constant. However, for energies well above E_F , the exponential term of equation (34) is quite higher than unity and it reduces to the Boltzmann equation ($E - E_F \gg k_B T$):

$$f(E) \approx \exp\left(-\frac{E - E_F}{k_B T}\right) \quad (35)$$

This is the case at the energy level of the conduction band, $E = E_C$. The corresponding electron density is given by

$$n_{e^-} = 2 \left(\frac{2\pi m_e^* k_B T}{h^2} \right)^{3/2} \exp\left(-\frac{E_C - E_F}{k_B T}\right) = N_c \exp\left(-\frac{E_C - E_F}{k_B T}\right) \quad (36)$$

where N_c is the effective density of states of the conduction band, which takes the value $N_c = 2 \times 10^{19} \text{ cm}^{-3}$ assuming that $m_e^* = m_e$. A similar approach can be held for holes, resulting in a density of holes n_h defined as

$$n_h = N_V \exp\left(-\frac{E_F - E_V}{k_B T}\right) \quad (37)$$

where $N_V = 2(2\pi m_h^* k_B T / h^2)^{3/2}$ is the effective density of states of the valence band.

In an undoped (intrinsic) semiconductor in thermal equilibrium, the number of electrons in the conduction band equals the number of holes in the valence band: $n_{e^-} = n_h = n_i$ (n_i is the intrinsic carrier concentration). Considering equations (36) and (37), the intrinsic carrier concentration is given by

$$\begin{aligned} n_i &= \sqrt{n_{e^-} n_h} = \sqrt{N_c N_V} \exp\left(\frac{E_V - E_C}{2k_B T}\right) \\ &= \sqrt{N_c N_V} \exp\left(\frac{-E_g}{2k_B T}\right) \end{aligned} \quad (38)$$

The Fermi energy in an intrinsic semiconductor is⁹¹

$$E_F = \frac{E_V + E_C}{2} + \frac{k_B T}{2} \ln\left(\frac{N_V}{N_c}\right) \quad (39)$$

On the other hand, doping semiconductors means the introduction of deliberate impurity atoms in its structure. A semiconductor can be either n-doped or p-doped by the introduction of donor (D) or acceptor (A) states, respectively. All impurities introduce additional localized electronic states into the energy band structure, often within the forbidden band between E_C and E_V (Figure 16). If the energy of the state, E_D , introduced by a donor atom is sufficiently close to the conduction band, there will be sufficient thermal energy to allow the extra electron to occupy a state in the conduction band. The donor state will be then positively charged (ionized). Similarly, an acceptor atom will introduce a negatively charged (ionized) state at energy E_A . Assuming that all donors and acceptors are completely ionized, in n-type material $n_{e^-} \approx n_D = N_c e^{-(E_C - E_F)/(k_B T)}$ and in p-type material $n_h \approx n_A = N_V e^{-(E_F - E_V)/(k_B T)}$. Thus, the Fermi energy can then be written as

$$E_F = E_C + k_B T \ln\left(\frac{n_{e^-}}{N_c}\right) \quad (40)$$

for an n-type semiconductor and as

$$E_F = E_V + k_B T \ln\left(\frac{N_V}{n_h}\right) \quad (41)$$

for a p-type semiconductor.^{91,92}

5.1.3 Continuity Equation

In a semiconductor, such as TiO₂ in the case of DSCs, electrons in the conduction band and holes in the valence band are the charge carriers. Considering a phenomenological approach for DSCs, then a general one-dimensional equation for electron density, comprising the continuity and transport

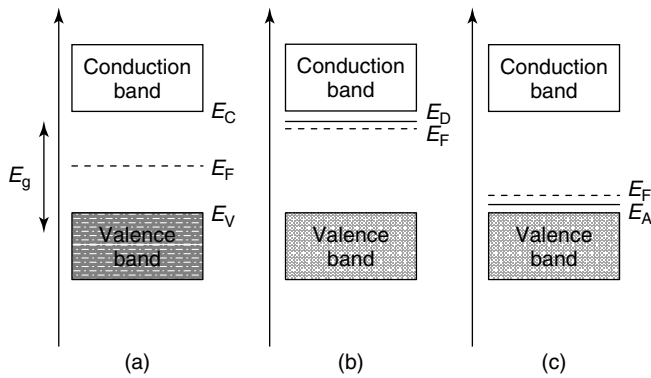


Figure 16 Energy level diagrams for (a) intrinsic; (b) n-type and (c) p-type semiconductors. E_g , band gap energy; E_V , valence band energy; E_C , conduction band energy; E_F , semiconductor Fermi energy; E_D , donor state energy; E_A , acceptor state energy

equations in unsteady state and isothermal conditions, can be expressed as

$$-\frac{\partial j_{e^-}}{\partial x} + G_{e^-}(x) - R_{e^-}(x) = \frac{\partial n_{e^-}}{\partial t} \quad (42)$$

The first term on the left-hand side of the equation represents the electron flux. The second and third terms are the rate of electron injection resulting from the photoexcitation process and the electron recombination rate at the electrolyte interface, respectively. Both reaction kinetics are characterized by a time constant. The term on the right-hand side of the equation corresponds to the accumulation of electrons.

Concerning the charge transport within the semiconductor, it can take place via diffusion and migration. However, due to the small dimension of the titania particles, no significant electrical potential gradient is generated, resulting only in a diffusive charge transport.⁹³ Equation (43) relates the electron flux j_{e^-} to the gradient of electron concentration across the TiO₂ layer by means of the electron coefficient of diffusion, D_{e^-} — Fick's law⁶⁸:

$$j_{e^-} = -D_{e^-} \frac{\partial n_{e^-}}{\partial x} \quad (43)$$

The absorption of each photon by a dye molecule is assumed to result in the injection of one electron into the TiO₂ conduction band and the consequent oxidation of the I⁻ to I₃⁻. The electron generation term in equation (42) is given by the Beer–Lambert law, which relates the absorption of light to the properties of the material through which the light is traveling⁹¹:

$$G_{e^-} = \eta_{\text{inj}} \alpha(\lambda) I_0 e^{-\alpha(\lambda)x} \quad (44)$$

The wavelength-dependent absorption coefficient of the dye, $\alpha(\lambda)$, is a function of its optical cross section and

the density of active molecules of dye adsorbed in the TiO₂ surface. The proposed model considers a uniform distribution of dye molecules throughout the TiO₂ film. The incident photon flux, I_0 , is corrected for reflection losses of the TCO glass and can be changed according to the incident radiation intensity.

Finally, the recombination of electrons with triiodide species is assumed to follow first-order kinetics:

$$R_{e^-} = \frac{n_{e^-}(x, t) - n_{\text{eq}}}{\tau_{e^-}} \quad (45)$$

The dark equilibrium electron density, n_{eq} , is given by equation (36), where the Fermi level in the TiO₂ is that of the redox potential. Bringing all these considerations together, the continuity equation becomes

$$\begin{aligned} D_{e^-} \frac{\partial^2 n_{e^-}(x, t)}{\partial x^2} + \eta_{\text{inj}} \alpha(\lambda) I_0 e^{-\alpha(\lambda)x} - \frac{n_{e^-}(x, t) - n_{\text{eq}}}{\tau_{e^-}} \\ = \frac{\partial n_{e^-}(x, t)}{\partial t} \end{aligned} \quad (46)$$

5.2 Electrolyte

The oxidation of iodide ions, as well as the reduction of triiodide, occurs in the electrolyte that fills the interstitial space among the TiO₂ nanoparticles. Taking into account the stoichiometry of reactions (3) and (4), the terms of generation and recombination of triiodide and iodide species must be affected by the corresponding coefficients, $\frac{1}{2}$ and $-\frac{3}{2}$, respectively:

$$\begin{aligned} D_{I_3^-} \frac{\partial^2 n_{I_3^-}(x, t)}{\partial x^2} \\ + \frac{1}{2\varepsilon_p} \left[\eta_{\text{inj}} \alpha(\lambda) I_0 e^{-\alpha(\lambda)x} - \frac{n_{e^-}(x, t) - n_{\text{eq}}}{\tau_{e^-}} - \frac{\partial n_{e^-}(x, t)}{\partial t} \right] \\ = \frac{\partial n_{I_3^-}(x, t)}{\partial t} \end{aligned} \quad (47)$$

$$\begin{aligned} D_{I^-} \frac{\partial^2 n_{I^-}(x, t)}{\partial x^2} \\ - \frac{3}{2\varepsilon_p} \left[\eta_{\text{inj}} \alpha(\lambda) I_0 e^{-\alpha(\lambda)x} - \frac{n_{e^-}(x, t) - n_{\text{eq}}}{\tau_{e^-}} - \frac{\partial n_{e^-}(x, t)}{\partial t} \right] \\ = \frac{\partial n_{I^-}(x, t)}{\partial t} \end{aligned} \quad (48)$$

Note that, in unsteady state, the accumulated electrons do not participate in the redox reactions and therefore must be discounted from the ions' generation term:

$$\underbrace{\eta_{\text{inj}} \alpha(\lambda) I_0 e^{-\alpha(\lambda)x}}_{\text{generation}} - \underbrace{\frac{\partial n_{e^-}(x, t)}{\partial t}}_{\text{electron accumulation}} \quad (49)$$

5.3 Boundary Conditions

5.3.1 Electrons

Metal–Semiconductor Contact. Metal contacts allow charge transport between the solar cell and the external load. The metal is only characterized by the chemical potential of its electrons, whose absolute value is known as the *work function* of the metal. Work function is the energy that must be expended in order to remove an electron from a solid to a point immediately outside the solid surface (immediately outside means that the final electron position is far from the surface on the atomic scale, but still close to the solid on the macroscopic scale). When the semiconductor and the metal get into contact, an electrical potential difference arises. Assuming that there is no charge at the contact interface other than the surface charge of the metal, the electrical potential is continuous across the interface—metal–semiconductor ohmic contact (a contact with voltage independent of the resistance). In this case, the carriers are free to flow out of the semiconductor so that there is a minimal resistance across the contact. For an n-type semiconductor, this means that the work function of the metal must be close to or smaller than the electron affinity of the semiconductor. According to equation (50), a charge balance at the TiO₂ and the TCO interface ($x = 0$) determines that the current density at $x = 0^-$, $j_{e^-}^{0^-}$ equals the current density at $x = 0^+$, $j_{e^-}^{0^+}$:

$$j_{e^-}^{0^-} = j_{e^-}^{0^+} \quad (50)$$

where

$$j_{e^-}^{0^-} = j_{\text{cell}} \quad (51)$$

and

$$j_{e^-}^{0^+} = -q D_{e^-} \frac{\partial n_{e^-}}{\partial x} \Big|_{x=0^+} \quad (52)$$

The current density flowing across $x = 0^+$ results from the diffusive electrons that percolated through the semiconductor—equation (52)—which, in steady-state conditions, corresponds to the net current density, j_{cell} , generated by the cell under operation. The j_{cell} value is determined by the applied voltage and calculated as explained in the section “*Electrolyte–Platinized TCO Contact*”.

Semiconductor–Electrolyte Junction. When a semiconductor comes into contact with an electrolyte containing a redox couple, a space charge layer arises in the semiconductor adjacent to the interface with the electrolyte. If the initial Fermi level in an n-type semiconductor is above the initial Fermi level in the electrolyte, then equilibration of the two Fermi levels occurs by transfer of electrons from the semiconductor to the electrolyte. This produces a positive space

charge layer in the semiconductor, also called a *depletion layer* since the region is depleted of majority charge carriers. Nevertheless, a charged layer also exists in the electrolyte adjacent to the interface with the solid electrode—Helmholtz layer. This layer consists of charged ions from the electrolyte adsorbed on the solid electrode surface. Figure 17 shows a diagram for a semiconductor–electrolyte junction.⁹⁴

To relate the energy levels of the electrolyte and the semiconductor, it is necessary to consider the flat-band potential, V_{fb} . This is the electrode potential at which the semiconductor’s bands are flat (zero space charge in the semiconductor).⁹⁴ The classical method to experimentally determine flat-band potentials is based on the Schottky–Mott equation⁹⁵:

$$\frac{1}{C_{\text{sc}}^2} = \frac{2}{\varepsilon \varepsilon_0 N_c q} \left(V - V_{\text{fb}} - \frac{k_B T}{q} \right) \quad (53)$$

Measuring the space-charge capacitance C_{SC} of the semiconductor electrode as a function of applied voltage, a plot of $1/C_{\text{sc}}^2$ versus V yields a straight line that intercepts the x -axis at V_{fb} .⁹⁵ However, for the present system, band bending within a TiO₂ nanoparticle should be negligible due to its small size, and so is the presence of Helmholtz layers.⁹³

Electrolyte–Platinized TCO Contact. At this interface ($x = L$), there are no electrons flowing from the electrolyte to the platinized CE. The presence of a layer of electrolyte (with thickness specified by the spacer ring used to seal the cell) in contact with the cathode ensures that there is no contact between the TiO₂ and the CE. Electrons are thus returned back and diffuse into the inner layers of the TiO₂ film.⁸² The corresponding boundary condition can be written as follows:

$$\frac{\partial n_{e^-}(L, t)}{\partial x} = 0 \quad (54)$$

As mentioned before, additional information is required to calculate the electron flux at $x = 0$. Assuming

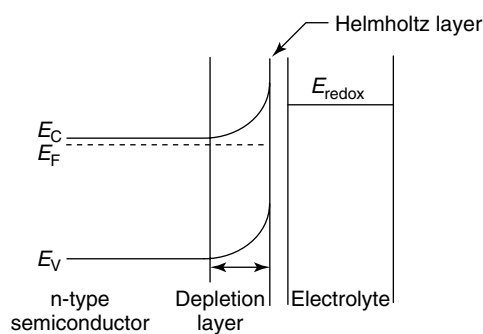


Figure 17 Energy levels for a semiconductor–electrolyte junction. E_g , band gap energy; E_V , valence band energy; E_C , conduction band energy; E_F , semiconductor Fermi energy; E_{redox} , electrolyte redox energy

that there are no resistances in the external circuit load, the flux j_{cell} at $x = 0$ equals the current density that is returned to the cell via the CE. Here, electrons take part in the iodide/triiodide redox reaction catalyzed by the platinum layer coated onto the TCO. Consequently, the electrolyte/platinized TCO interface can be treated as an electrochemical half-cell.⁸⁴ A Butler–Volmer approach is therefore considered to describe the electrochemical kinetics⁷⁷:

$$j_{\text{cell}} = j_0 \left[\frac{n_{I_3^-}(L)}{n_{I_3^-}^{\text{OC}}(L)} e^{\frac{\beta q \eta_{\text{Pt}}}{k_B T}} - \frac{n_{I^-}(L)}{n_{I^-}^{\text{OC}}(L)} e^{\frac{-(1-\beta)q \eta_{\text{Pt}}}{k_B T}} \right] \quad (55)$$

Equation (55) states that the current generated by the electrochemical reaction at $x = L$ increases exponentially with the activation overvoltage η_{Pt} . It is important to hold that this overvoltage is the voltage sacrificed or lost to overcome the energy activation barrier.⁷³ If the current density value is zero, which corresponds to open-circuit conditions, equation (55) reduces to the Nernst equation. In this case, the concentration of triiodide and iodide under open-circuit conditions can be calculated.

At this stage, the only value in equation (55) that is unknown is the overvoltage in the platinum layer η_{Pt} . The internal voltage of a DSC is defined as the difference in electrochemical potentials between the boundaries $x = 0$ and $x = L$. Bearing in mind that the TCO/TiO₂ interface behaves as an ohmic contact, the respective electrochemical potential is assumed to be continuous and equals the electron Fermi level at $x = 0$. On the other hand, the electrochemical potential of the platinum electrode at $x = L$ equals the electrolyte redox energy. The value of the internal voltage can then be calculated as

$$\Delta V_{\text{int}} = [E_F(x = 0) - E_{\text{redox}}]/q \quad (56)$$

where $E_F(x = 0)$ is given by equation (40). The redox energy of the electrolyte has two contributions: the redox energy under open-circuit conditions and the platinum overvoltage. Considering this fact and the Nernst's equation to define $E_{\text{redox}}^{\text{OC}}$, equations (57) and (58) can be written as

$$E_{\text{redox}} = E_{\text{redox}}^{\text{OC}} + q \eta_{\text{Pt}} \quad (57)$$

$$E_{\text{redox}}^{\text{OC}} = E_{\text{redox}}^\circ - \frac{k_B T}{2} \ln \frac{n_{I_3^-}^{\text{OC}}(L)}{\left[n_{I^-}^{\text{OC}}(L) \right]^3} \quad (58)$$

Substituting these two equations into equation (56) and solving in order to η_{Pt} :

$$\begin{aligned} \eta_{\text{Pt}} &= \frac{1}{q} (E_C - E_{\text{redox}}^\circ) + \frac{k_B T}{2q} \ln \frac{n_{I_3^-}^{\text{OC}}(L)}{\left[n_{I^-}^{\text{OC}}(L) \right]^3} \\ &\quad + \frac{k_B T}{q} \ln \frac{n_{e^-}(x = 0)}{N_C} - \Delta V_{\text{int}} \end{aligned} \quad (59)$$

Equation (59) should now be included in the Butler–Volmer equation (equation (55)). By analyzing equations (51) and (59) it can be concluded that the flux of electrons at $x = 0$, and consequently the electron concentration profiles are a function of the internal voltage of the cell.

Up to this point, the model does not account for external resistances, which have to be considered for real systems. Ferber *et al.*⁸⁴ proposed an electrical analog able to describe additional external series (R_{TCO}) and shunt resistances (R_p). A correlation between the internal and external voltages can be established applying the Kirchhoff's and Ohm's laws⁸⁴:

$$\Delta V_{\text{int}} = (R_{\text{TCO}} + R_{\text{ext}}) \left(\frac{R_p}{R_{\text{ext}} + R_{\text{TCO}} + R_p} \right) A \cdot j_{\text{cell}} \quad (60)$$

$$V_{\text{ext}} = R_{\text{ext}} \left(\frac{R_p}{R_{\text{ext}} + R_{\text{TCO}} + R_p} \right) A \cdot j_{\text{cell}} \quad (61)$$

Imposing a certain external resistance, R_{ext} , and substituting equation (60) into equation (59), the overvoltage at the platinum CE is then determined. The corresponding current, j_{cell} , is obtained by substituting equation (59) into equation (55), which then allows the calculation of V_{ext} by means of equation (61). This procedure defines a single point in the I – V characteristic curve. For different values of R_{ext} , a complete I – V curve is then obtained.

5.3.2 Triiodide/Iodide Ions

At $x = 0$, only the photojected electrons are able to flow across the interface. The net flux of I^- and I_3^- is zero:

$$\frac{\partial n_{I_3^-}(0, t)}{\partial x} = 0 \quad (62)$$

$$\frac{\partial n_{I^-}(0, t)}{\partial x} = 0 \quad (63)$$

The total amount of the redox species contained in the TiO₂ nanopores remains constant during the DSC operation. This may be described as integral boundaries for $x = L$ ⁸³:

$$\int_0^L n_{I_3^-}(x) dx = n_{I_3^-}^{\text{init}} L; \quad \int_0^L n_{I^-}(x) dx = n_{I^-}^{\text{init}} L \quad (64)$$

5.4 Experimental and Simulation Results

To simulate a DSC, it is necessary to solve equations (46), (47), and (48) with the respective boundary conditions. In order to apply the boundary condition at $x = 0$ for electrons, equation (60) should be substituted in equation (59); the result should then be inserted into equation (55) to obtain the current density in the external circuit. The partial

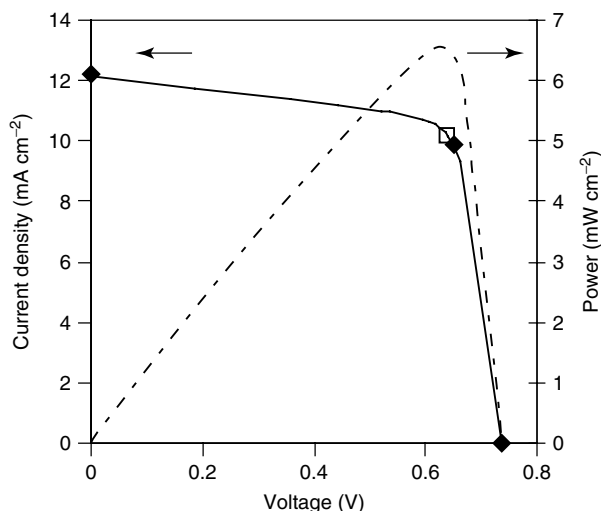


Figure 18 Experimental and simulated I – V characteristic, under 1 sun illumination.⁹⁰ (◆) Experimental performance parameters taken from Ref. 67; (□) Simulated maximum-power point. Solid and dashed lines correspond to the simulated I – V curve and power output, respectively, for the system described in Ref. 90

differential equations can be spatially discretized using the finite differences method. For the calculation of theoretical I – V curves, the equations should be solved for steady-state (Figure 18) conditions.

6 DSC BOTTLENECKS AND NEW DEVELOPMENTS

In the last years, research on DSC technology has been growing quite fast, and remarkable developments on various aspects have been achieved. Nevertheless, many other improvements should be considered in the various fields that concern DSCs in order to surpass the record efficiency of approximately 11% obtained in laboratory-scale cells. Developments in the area of sensitizers should include some new dyes able to absorb across the visible and NIR light spectrum and with enhanced molar absorption coefficient leading to higher efficiencies; in this respect, the production costs and sustainability are also relevant. In fact, the advent of nanotechnology has opened a window of opportunity for the development of more efficient and environment-friendly materials at considerably lower costs. For instance, the application of nanotechnology at the electrolyte level within recent developments of nanostructured semiconductors with enhanced electric conductivity and more accessible pores has been especially important for solid-state DSCs, which are typically more stable but less efficient. For liquid-based electrolytes, the development of new additives that suppress electron recombination with the redox mediator is of extreme importance. Moreover, the replacement of volatile solvents

by additives will increase not only the cell efficiency but also its stability. This is, in fact, a basic requirement for all solar cell technologies, and for DSCs in particular. Despite all the efforts to enhance the performance of DSCs, long-term stability is still a major issue that limits market implementation of this technology. As an example, for building integrated applications, it should be reasonable and expectable that the performance of DSCs remained stable for at least 20 years. State-of-the-art knowledge in long-term stability suggests that apart from the intrinsic stability of the materials that constitute a DSC, efficient encapsulation of the cell must be guaranteed to avoid degradation induced by atmospheric conditions. Current materials used to encapsulate DSCs do not ensure hermetic sealing of the cell, as they typically degrade at temperatures around 60–80 °C. New sealing materials and methodologies are now being developed in an effort to foster the dissemination and commercialization of DSCs. This approach is based on inert, stable, and environment-friendly materials such as lead-free glass frits and derivatives.^{96–99} The use of new materials and sealing processes will certainly require optimization in terms of operating conditions such as the temperature of sealing and cell design (including the size and shape of the active layers). Here, both the empirical and phenomenological models described in the previous sections may play an important role in the identification of the most promising approach to get an optimized DSC.

7 RELATED ARTICLES

Energy Conversion in Photosynthesis.

8 ABBREVIATIONS AND ACRONYMS

CB = conduction band; CE = counterelectrode; CPE = constant phase element; DSCs = dye-sensitized solar cells; EIS = electrochemical impedance spectroscopy; FF = fill factor; HOMO = highest occupied molecular orbital; IPCE = incident photon-to-current conversion efficiency; LUMO = lowest unoccupied molecular orbital; MPP = maximum-power point; NCS = thiocyanate; NIR = near infrared; PV = photovoltaics; TBA = tetrabutylamm onium; TBP = tert-butylpyridine; TCO = transparent conducting oxide; VB = valence band; WE = working electrode.

9 REFERENCES

1. International Energy Agency, ‘Key World Energy Statistics’, Report, International Energy Agency, 2008.
2. A. Jäger-Waldau, ‘PV Status Report 2008: Research, Solar Cell Production and Market Implementation of Photovoltaics’, Report, 2008.

3. F. O. Lenzmann and J. M. Kroon, *Adv. OptoElectron.*, 2007, ID 65073.
4. M. Nazeeruddin, F. DeAngelis, S. Fantacci, A. Selloni, G. Viscardi, P. Liska, S. Ito, B. Takeru, and M. Grätzel, *J. Am. Chem. Soc.*, 2005, **127**, 16835.
5. A. Hagfeldt and M. Grätzel, *Acc. Chem. Res.*, 2000, **33**, 269.
6. M. Grätzel, *C. R. Chim.*, 2006, **9**, 578.
7. M. Grätzel, *J. Photochem. Photobiol. A: Chem.*, 2004, **164**, 3.
8. F. Kong, S. Dai, and K. Wang, *Adv. OptoElectron.*, 2007, 75384.
9. L. Peter, *J. Electroanal. Chem.*, 2007, **599**, 233.
10. Y. Tachibana, J. E. Moser, M. Gratzel, D. R. Klug, and J. R. Durrant, *J. Phys. Chem.*, 1996, **100**, 20056.
11. N. Cherepy, G. Smestad, M. Grätzel, and J. Zhang, *J. Phys. Chem. B*, 1997, **101**, 9342.
12. R. L. Willis, C. Olson, B. O'Regan, T. Lutz, J. Nelson, and J. R. Durrant, *J. Phys. Chem. B*, 2002, **106**, 7605.
13. N. Anderson and T. Lian, *Annu. Rev. Phys. Chem.*, 2005, **56**, 491.
14. J. R. Durrant, S. A. Haque and E. Palomares, *Chem. Commun.*, 2006, 3279.
15. M. Grätzel and J. R. Durrant, 'Nanostructured and Photoelectrochemical Systems for Solar Photon Conversion', Imperial College Press, London, 2008, Chapter 8.
16. M. Grätzel, *Inorg. Chem.*, 2005, **44**, 6841.
17. J. A. Rodriguez and M. Fernández, 'Synthesis, Properties, and Applications of Oxide Nanomaterials', John Wiley & Sons, Inc, 2007.
18. Y. Li, J. Hagen, W. Schaffrath, P. Otschik, and D. Haarer, *Sol. Energy Mater. Sol. Cells*, 1998, **56**, 167.
19. K. Sayama, H. Sugihara, and H. Arakawa, *Chem. Mater.*, 1998, **10**, 3825.
20. S. Deb, *Sol. Energy Mater. Sol. Cells*, 2005, **88**, 1.
21. N. Park, J. Lagemaat, and A. Frank, *J. Phys. Chem. B*, 2000, **104**, 8989.
22. K. Kalyanasundaram and M. Grätzel, *Coord. Chem. Rev.*, 1998, **177**, 347.
23. L. M. Goncalves, Vd. Z. Bermudez, H. A. Ribeiro, and A. M. Mendes, *Energy Environ. Sci.*, 2008, **1**, 655.
24. G. K. Mor, K. Shankar, M. Paulose, O. K. Varghese, and C. A. Grimes, *Nano Lett.*, 2006, **6**, 215.
25. K. Zhu, N. Neale, A. Miedaner, and A. Frank, *Nano Lett.*, 2007, **7**, 69.
26. M. Wei, Y. Konishi, H. Zhou, H. Sugihara, and H. Arakawa, *J. Electrochem. Soc.*, 2006, **153**, A1232.
27. J. Park, T. Lee and M. Kang, *Chem. Commun.*, 2008, 2867.
28. M. Adachi, Y. Murata, J. Takao, J. Jiu, M. Sakamoto, and F. Wang, *J. Am. Chem. Soc.*, 2004, **126**, 14943.
29. J. Jiu, S. Isoda, F. Wang, and M. Adachi, *J. Phys. Chem. B*, 2006, **110**, 2087.
30. L. Greene, B. Yuhas, M. Law, D. Zitoun, and P. Yang, *Inorg. Chem.*, 2006, **45**, 7535.
31. C. Huisman, J. Schoonman, and A. Goossens, *Sol. Energy Mater. Sol. Cells*, 2005, **85**, 115.
32. C. Kuo and S. Lu, *Nanotechnology*, 2008, **19**, 095705.
33. C. Longo and M. Paoli, *J. Braz. Chem. Soc.*, 2003, **14**, 889.
34. E. Palomares, J. N. Clifford, S. A. Haque, T. Lutz, and J. R. Durrant, *Chem. Commun.*, 2002, 1464.
35. A. Kay and M. Gratzel, *Chem. Mater.*, 2002, **14**, 2930.
36. S. Ito, T. Murakami, P. Comte, P. Liska, C. Grätzel, M. Nazeeruddin, and M. Grätzel, *Thin Solid Films*, 2008, **516**, 4613.
37. Z. Wang, H. Kawauchi, T. Kashima, and H. Arakawa, *Coord. Chem. Rev.*, 2004, **248**, 1381.
38. H. Koo, J. Park, B. Yoo, K. Yoo, K. Kim, and N. Park, *Inorg. Chim. Acta*, 2008, **361**, 677.
39. M. Grätzel, *Prog. Photovoltaics: Res. Appl.*, 2000, **8**, 171.
40. C. Kelly and G. Meyer, *Coord. Chem. Rev.*, 2001, **211**, 295.
41. J. Desilvestro, M. Grätzel, L. Kavan, J. Moser, and J. Augustynski, *J. Am. Chem. Soc.*, 1985, **107**, 2988.
42. N. Vlachopoulos, P. Liska, J. Augustynski, and M. Grätzel, *J. Am. Chem. Soc.*, 1988, **110**, 1216.
43. R. Argazzi, C. A. Bignozzi, T. A. Heimer, F. N. Castellano, and G. J. Meyer, *Inorg. Chem.*, 1994, **33**, 5741.
44. O. Kohle, S. Ruile, and M. Gratzel, *Inorg. Chem.*, 1996, **35**, 4779.
45. M. Nazeeruddin, A. Kay, I. Rodicio, R. Humphry-Baker, E. Mueller, P. Liska, N. Vlachopoulos, and M. Grätzel, *J. Am. Chem. Soc.*, 1993, **115**, 6382.
46. T. Horiuchi, H. Miura, K. Sumioka, and S. Uchida, *J. Am. Chem. Soc.*, 2004, **126**, 12218.
47. Z.-S. Wang, T. Yamaguchi, H. Sugihara, and H. Arakawa, *Langmuir*, 2005, **21**, 4272.
48. M. Nazeeruddin, P. Péchy, and M. Grätzel, *Chem. Commun.*, 1997, 1705.
49. P. Wang, S. Zakeeruddin, J. Moser, M. Nazeeruddin, T. Sekiguchi, and M. Grätzel, *Nat. Mater.*, 2003, **2**, 402.
50. P. Wang, C. Klein, R. Humphry-Baker, M. Zakeeruddin, and M. Grätzel, *Appl. Phys. Lett.*, 2005, **86**, 123508.
51. G. Zhang, H. Bala, Y. Cheng, D. Shi, X. Lv, Q. Yu and P. Wang, *Chem. Commun.*, 2009, 2198.
52. M. Wang, M. Xu, D. Shi, R. Li, F. Gao, G. Zhang, Z. Yi, R. Humphry-Baker, P. Wang, S. M. Zakeeruddin, and M. Grätzel, *Adv. Mater.*, 2008, **20**, 4460.
53. H. Choi, J. Lee, K. Song, S. Kang, and J. Ko, *Tetrahedron*, 2007, **63**, 3115.
54. R. Plass, S. Pelet, J. Krueger, M. Grätzel, and U. Bach, *J. Phys. Chem. B*, 2002, **106**, 7578.
55. G. Wolfbauer, A. M. Bond, J. C. Eklund, and D. R. MacFarlane, *Sol. Energy Mater. Sol. Cells*, 2001, **70**, 85.

56. G. P. Kalaignan and Y. S. Kang, *J. Photochem. Photobiol. C: Photochem. Rev.*, 2006, **7**, 17.
57. Y. Bai, Y. Cao, J. Zhang, M. Wang, R. Li, P. Wang, S. Zakeeruddin, and M. Grätzel, *Nat. Mater.*, 2008, **7**, 626.
58. D. Kuang, S. Ito, B. Wenger, C. Klein, J.-E. Moser, R. Humphry-Baker, S. M. Zakeeruddin, and M. Grätzel, *J. Am. Chem. Soc.*, 2006, **128**, 4146.
59. D. Kuang, C. Klein, Z. Zhang, S. Ito, J. Moser, S. Zakeeruddin, and M. Grätzel, *Small*, 2007, **3**, 2094.
60. N. Papageorgiou, W. Maier, and M. Grätzel, *J. Electrochem. Soc.*, 1997, **144**, 876.
61. E. Olsen, G. Hagen, and S. Lindquist, *Sol. Energy Mater. Sol. Cells*, 2000, **63**, 267.
62. T. Kitamura, M. Maitani, M. Matsuda, Y. Wada, and S. Yanagida, *Chem. Lett.*, 2001, **30**, 1054.
63. T. Murakami and M. Grätzel, *Inorg. Chim. Acta*, 2008, **361**, 572.
64. A. Kay and M. Grätzel, *Sol. Energy Mater. Sol. Cells*, 1996, **44**, 99.
65. K. Imoto, K. Takahashi, T. Yamaguchi, T. Komura, J. Nakamura, and K. Murata, *Sol. Energy Mater. Sol. Cells*, 2003, **79**, 459.
66. K. Suzuki, M. Yamaguchi, M. Kumagai, and S. Yanagida, *Chem. Lett.*, 2003, **32**, 28.
67. Q. Wang, J.-E. Moser, and M. Grätzel, *J. Phys. Chem. B*, 2005, **109**, 14945.
68. J. Bisquert, *J. Phys. Chem. B*, 2002, **106**, 325.
69. F. Fabregat-Santiago, G. Garcia-Belmonte, J. Bisquert, A. Zaban, and P. Salvador, *J. Phys. Chem. B*, 2002, **106**, 334.
70. E. Barsoukov and J. R. Macdonald, ‘Impedance Spectroscopy: Theory, Experiment and Applications’, 2nd edition, John Wiley & Sons, 2005.
71. R. Kern, R. Sastrawan, J. Ferber, R. Stangl, and J. Luther, *Electrochim. Acta*, 2002, **47**, PII S0013-4686(0002)00444-00449.
72. B. E. Conway, J.O’m. Bockris, and Ralph E. White, ‘Modern Aspects of Electrochemistry, No. 32’, Kluwer Academic Publishers, 2002.
73. A. J. Bard and L. R. Faulkner, ‘Electrochemical Methods: Fundamentals and Applications’, 2nd edition, John Wiley & Sons, Inc., USA, 2001.
74. R. O’Hayre, S.-W. Cha, W. Colella, and F. B. Prinz, ‘Fuel Cells Fundamentals’, John Wiley & Sons, Inc., New York, 2006.
75. F. Fabregat-Santiago, J. Bisquert, G. Garcia-Belmonte, G. Boschloo, and A. Hagfeldt, *Sol. Energy Mater. Sol. Cells*, 2005, **87**, 117.
76. J. Bisquert, A. Zaban, M. Greenshtein, and I. Mora-Sero, *J. Am. Chem. Soc.*, 2004, **126**, 13550.
77. J. Bisquert, *Phys. Chem. Chem. Phys.*, 2003, **5**, 5360.
78. J. Lagemaat, N. G. Park, and A. J. Frank, *J. Phys. Chem. B*, 2000, **104**, 2044.
79. J. Bisquert, G. Garcia-Belmonte, F. Fabregat-Santiago, N. S. Ferriols, P. Bogdanoff, and E. C. Pereira, *J. Phys. Chem. B*, 2000, **104**, 2287.
80. L. Andrade, S. M. Zakeeruddin, M. K. Nazeeruddin, H. A. Ribeiro, A. Mendes, and M. Grätzel, *ChemPhysChem*, 2009, **10**, 1117.
81. Q. Wang, S. Ito, M. Grätzel, F. Fabregat-Santiago, I. Mora-Sero, J. Bisquert, T. Bessho, and H. Imai, *J. Phys. Chem. B*, 2006, **110**, 25210.
82. S. Soedergren, A. Hagfeldt, J. Olsson, and S.-E. Lindquist, *J. Phys. Chem.*, 1994, **98**, 5552.
83. N. Papageorgiou, M. Grätzel, and P. P. Infelta, *Sol. Energy Mater. Sol. Cells*, 1996, **44**, 405.
84. J. Ferber, R. Stangl, and J. Luther, *Sol. Energy Mater. Sol. Cells*, 1998, **53**, 29.
85. R. Stangl, J. Ferber, and J. Luther, *Sol. Energy Mater. Sol. Cells*, 1998, **54**, 255.
86. J. Ferber and J. Luther, *J. Phys. Chem. B*, 2001, **105**, 4895.
87. A. C. Fisher, L. M. Peter, E. A. Ponomarev, A. B. Walker, and K. G. U. Wijayantha, *J. Phys. Chem. B*, 2000, **104**, 949.
88. S. Y. Huang, G. Schlichthorl, A. J. Nozik, M. Gratzel, and A. J. Frank, *J. Phys. Chem. B*, 1997, **101**, 2576.
89. L. Dloczik, O. Illeperuma, I. Lauermann, L. M. Peter, E. A. Ponomarev, G. Redmond, N. J. Shaw, and I. Uhendorf, *J. Phys. Chem. B*, 1997, **101**, 10281.
90. L. Andrade, J. Sousa, H. A. Ribeiro, and A. Mendes, Phenomenological modeling of dye-sensitized solar cells under transient conditions. 2009, submitted.
91. J. L. Gray, in ‘Handbook of Photovoltaic Science and Engineering’, ed. S. H. Antonio Luque, editon, 2003, p. 61.
92. P. Würfel, ‘Physics of Solar Cells: From Principles to New Concepts’, Weinheim, 2005.
93. A. Hagfeldt and M. Graetzel, *Chem. Rev.*, 1995, **95**, 49.
94. A. J. Nozik, *Annu. Rev. Phys. Chem.*, 1978, **29**, 189.
95. A. J. Nozik and R. Memming, *J. Phys. Chem.*, 1996, **100**, 13061.
96. A. Hinsch, S. Behrens, M. Berginc, H. Bonnemann, H. Brandt, A. Drewitz, F. Einsele, D. Fassler, D. Gerhard, H. Gores, R. Haag, T. Herzig, S. Himmler, G. Khelashvili, D. Koch, G. Nazmutdinova, U. Opara-Krasovec, P. Putyra, U. Rau, R. Sastrawan, T. Schauer, C. Schreiner, S. Sensfuss, C. Siegers, K. Skupien, P. Wachter, J. Walter, P. Wasserscheid, U. Wurfel, and M. Zistler, *Prog. Photovoltaics*, 2008, **16**, 489.
97. R. Sastrawan, J. Beier, U. Belledin, S. Hemming, A. Hinsch, R. Kern, C. Vetter, F. M. Petrat, A. Prodi-Schwab, P. Lechner, and W. Hoffmann, *Sol. Energy Mater. Sol. Cells*, 2006, **90**, 1680.
98. W. J. Lee, E. Ramasamy, D. Y. Lee, and J. S. Song, *J. Photochem. Photobiol. A: Chem.*, 2006, **183**, 133.
99. A. Mendes, J. Mendes, H. A. Ribeiro, M. Grätzel, L. Andrade, L. M. Gonçalves, and C. V. Costa, ‘Processo de Selagem com Vidro de Células Solares DSC’, PT 104282, 2008.

Enzymes and Microbes for Energy Production by Fuel Cells

Frédéric Barrière

Université de Rennes 1, France

1	Introduction	73
2	Enzymatic Catalysis in Biofuel Cells	74
3	Microbial Catalysis in Microbial Fuel Cells	80
4	Transformation and Production Roles of Enzymes, Microbes, and Higher Organisms in Biological Fuel Cells	84
5	Conclusions	85
6	Glossary	86
7	Acknowledgments	86
8	Related Articles	86
9	Abbreviation and Acronyms	86
10	References	86

1 INTRODUCTION

A fuel cell is a simple electrochemical system that converts the chemical energy of molecules into electrical current.¹ The system contains two electrodes: an anode at which the fuel is oxidized and a cathode at which the oxidant is reduced. Ideally, the fuel must be oxidized at a low potential and the oxidant must be reduced at a high potential, both reactions occurring with high rates, in order to maximize the cell voltage (U) and current (I), and consequently the power output. The two electrodes are plunged into an electrolyte (a medium allowing ionic current), and the anodic and cathodic compartments are usually separated with a membrane. The system is fitted in a case equipped with tubing, allowing the input of fuel and oxidant to their respective electrodes and the exhaust of the waste/product resulting from the global redox reaction. The two electrodes are connected through an external circuit containing a load (e.g. a heating resistor, a light bulb, an electrical motor, etc.) in which the current flows. Figure 1 shows a schematic of such a system, using, as an example, dihydrogen, H_2 , as the fuel and dioxygen, O_2 , as the oxidant. In this system, water is produced as the waste/reaction product.

In a fuel cell, the power ($P = U \times I$, in watt) depends on the potential difference between the electrodes (U , in volt) and on the current intensity (I , in ampère).

At zero current (open circuit potential, OCP), U is ideally close to the difference between the normal redox potentials (E^0) of the redox couples involved at both electrodes. In the H_2/O_2 fuel cell, at zero pH, $E^0(H^+/H_2) = 0\text{ V}$ and $E^0(O_2/H_2O) = 1.23\text{ V}$ (versus NHE), and hence the cell voltage at OCP is $U \sim 1.23\text{ V}$ at most. When the fuel cell is connected through an external load, then the value of U decreases as a function of the current intensity, at a rate depending on the overpotentials of the electrodes' redox reactions (kinetic losses), notwithstanding ohmic losses due to the resistivity of the electrolyte between the electrodes. In order to diminish the kinetic losses, catalytic electrode materials are sought. For example, the oxidation of H_2 ($H_2 \rightarrow 2H^+ + 2e^-$) is usually rather slow at most electrode materials, except, for example, at platinum, palladium, rhodium, rhenium, iridium, and their alloys on which this oxidation is relatively fast, which explains the extensive use of these precious metals in such fuel cells.

A biological fuel cell follows the same principles as discussed above.² The main specificity of biological fuel cells lies in the nature of the catalysts that originate from the living world. These biocatalysts can be either enzymes or living microorganisms. Such biological catalysts may be found at both electrodes and are represented as dashed circles in Figure 2. Because of the biological nature of the

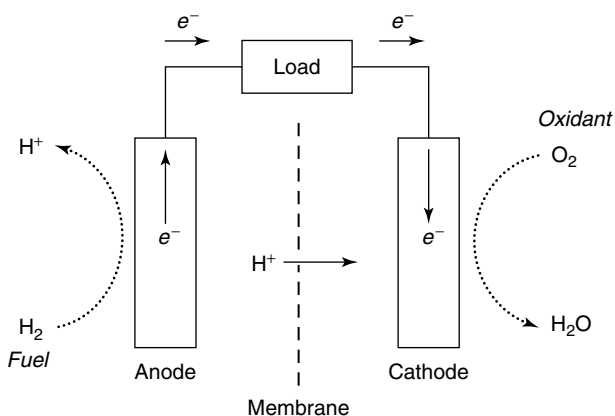


Figure 1 Scheme of the H_2/O_2 fuel cell

catalyst, there is also a restraint on the nature of the fuel and oxidant that must obviously be compatible with the enzyme or the microbe. Hence, the reactant found in a biological fuel cell will for the most part originate from the living world, or at least be biocompatible. The enzyme or microbe, or even higher organisms like fungi or plants, may also play the role of transforming a substrate for its further use by the biological catalysts at the electrodes. They could also play a role in producing the catalysts themselves. This transformation/production role is symbolized by the dashed ellipses (Prod.) in Figure 2.

In this article, we first discuss the use of enzymes, followed by that of microorganisms, as catalysts in biological fuel cells. In each section, we successively consider the anodic and cathodic biocatalyses, and the performance of assembled devices. The specific contribution of inorganic chemistry is also highlighted, although it becomes apparent throughout this article that research in biological fuel cells requires a truly multidisciplinary approach encompassing electrochemistry, biochemistry, microbiology, and materials, organic, and inorganic chemistry. The following section is

devoted to the transformation/production role of enzymes, microbes, and higher organisms, as defined above. The article is organized to present the main concepts and issues related to these special classes of fuel cells, with developments and references up to 2009 to which the reader is referred for more focused or comprehensive accounts on these topics.

2 ENZYMATIC CATALYSIS IN BIOFUEL CELLS

2.1 Introduction

Enzymatic biofuel cells were introduced in 1964 in a device relying on glucose and dioxygen,³ but were developed, however, more recently^{4–6} concurrent to the progresses made in the field of electrochemical biosensors, and specifically the electrical linking of redox enzymes to electrodes.⁷ Enzymes are proteins, biological macromolecules based on a polymer of natural amino acids in a sequence coded in the genes borne by DNA.⁸ These macromolecules are involved in different physiological functions such as catalysis (in this case they are called *enzymes*), transport, and electron transfer. Among the enzyme classes, oxido-reductases are the ones of potential interest for biofuel cells. Indeed, these enzymes catalyze redox reactions that are otherwise very slow in the absence of a catalyst. For example, the oxidation of β -D-glucose to D-gluconolactone is catalyzed by glucose oxidase, one of the most studied and used oxido-reductase. The natural electron acceptor of glucose oxidase, dioxygen, is reduced to hydrogen peroxide in the process. Hence, glucose oxidase may be used as a catalyst and glucose as a fuel at the anode of a biofuel cell, as shown schematically in Figure 3 (cf. development in the next section).

At this biocatalytic anode, the enzyme uses the electrode as the electron acceptor, while at the cathode, a complementary process with an appropriate enzyme, reaction, and redox potential should occur. Because the redox potential

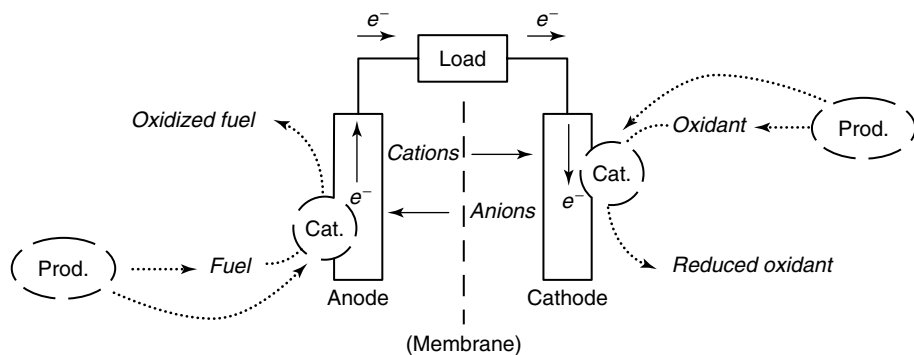


Figure 2 Roles of enzymes and microbes in biological fuel cell. Cat.: Catalysts at the electrodes. Prod.: transformation of a substrate into a usable fuel or oxidant, or production of the biological catalyst itself. Resorting to a membrane can be avoided in some cases (see text)

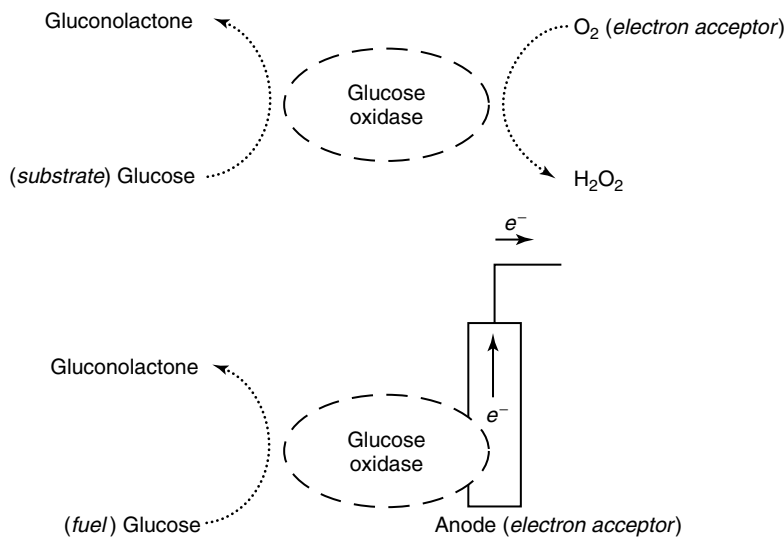


Figure 3 Natural activity of glucose oxidase and its use at a biocatalytic anode

for the oxidation of glucose and the redox potential of the glucose oxidase enzyme are rather low, the use of glucose as the fuel and of glucose oxidase as the biocatalyst is appropriate at the anode of biofuel cells, as discussed in the next section. Suitable enzymes, substrates, and electrodes for anodic and cathodic biocatalyses are discussed in the subsections below. This section ends with a focus on inorganic aspects of the topic and consideration of the performance and applications of assembled biofuel cells.

2.2 Anodic Enzymatic Biocatalysis

Many substrates have been considered as fuels in biofuel cells, such as, carbohydrates (sugars), alcohols, and dihydrogen. For the purpose of concision and illustration, we focus here on β -D-glucose, certainly the most studied fuel in this context. As mentioned above in the introduction, glucose oxidase may specifically oxidize this carbohydrate in the presence of a suitable electron acceptor. The active site of this enzyme is made of a redox-active organic cofactor, FAD/FADH₂, wrapped within the protein matrix. The oxidation of glucose and the reduction of dioxygen occur at this active site. Because of the relative burial of the enzyme-active site within the polypeptide, direct electron transfer to an electrode is very often difficult and slow. For this reason, a redox mediator is usually needed in order to maximize the rate of anodic glucose oxidation by glucose oxidase. A redox mediator is a sufficiently small electroactive molecule that is also stable in two interconvertible redox states. It can thus easily diffuse into and out of protein channels and efficiently shuttle electrons between the enzyme-active site and the electrode surface. The redox potential of the mediator is also critical for the biofuel cell's performance. To allow for a high electron-transfer rate, a large enough driving force

must be secured; in other words, for an anodic redox mediator, its redox potential must be at least ca. 50 mV more positive than that of the redox enzyme-active site. At the same time, the redox potential of the mediator should also be close enough to that of the redox enzyme-active site in order to maximize the cell voltage and consequently the power output of the fuel cell. Hence, a reasonably good compromise to satisfy both demands is to target a redox potential of around 50–100 mV more positive than that of the enzyme-active site for the anodic redox mediator. The electron-transfer sequence between glucose and the anode of a biofuel cell is shown in Figure 4, together with indications of the redox potentials of the different redox couples. Note that ultimately, it is the redox potential of the redox mediator that dictates the potential at which the anodic reaction occurs, and consequently, in part, the cell voltage.

Resorting to soluble redox mediators implies that the two compartments of the fuel cell will be separated by a membrane to avoid unwanted cross reactions with the anodic biocatalysis. It is possible, however, to immobilize the mediator and the enzyme within a matrix at the surface of the electrode. This strategy then alleviates the use of the membrane since the specificity of the enzyme to a given substrate and its immobilization at the surface of the electrode together with the redox mediator avoids the cross reaction problem. The biofuel cell may then simply consist of two modified electrodes directly linked to the external load. Examples of efficient and popular redox mediators are shown in Figure 5. Indeed, coordination complexes of osmium⁹ III/II with bipy-like ligands are known for their relative stability in water and photostability compared to their analogs of iron and ruthenium. A refinement approach of the redox mediator potential and structure is shown in Figure 5. The complex, *cis*-Os(bipy)Cl₂ with $E^0 = 0.00$ V is efficient as a soluble redox mediator

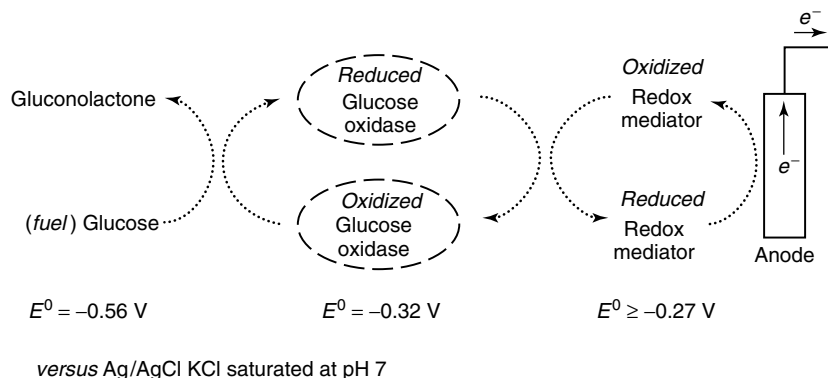


Figure 4 Mediated electron transfer between glucose oxidase and an anode

for the biocatalytic oxidation of glucose by glucose oxidase. Nevertheless, since it has to be used in solution, the biofuel cell should contain a membrane to separate the two electrode compartments. In addition, a large amount of potentially recoverable energy is lost because of its rather high redox potential compared to that of the enzyme. A first refinement step consists of coordinating the redox-active mediator to a polymer backbone. For example, *cis*-Os(bipy)Cl₂ reacts with PVI to yield a redox polymer, where the metal is coordinated through an imidazole group of the polymer backbone. This allows the crosslinking of the polymer with the enzyme and its deposition onto an electrode surface, and hence removes the need for a membrane in the biofuel cell.¹⁰ The resulting redox potential ($E^0 = 0.20 \text{ V}$) is, however, higher than that of *cis*-Os(bipy)Cl₂ and is therefore less interesting in this respect. Classical coordination chemistry permits a fine tuning of the redox potential through the careful choice of the donor–acceptor properties of the ligands. Hence, with electron-donating *para*-amino-substituted bipy,¹¹ the resulting redox polymer ($E^0 = -0.11 \text{ V}$) nearly satisfies the two criteria defined above: a low redox potential but positive enough from that of the enzyme. A further refinement step involves the introduction of a tether between the polymer backbone and the redox-active moiety. This is important, first, to bring a larger flexibility to the immobilized redox mediator that must move in and out of the enzyme and, second, to improve the hopping mechanism (collision and electron transfer with neighboring redox-active groups) responsible for the transfer of electrons to the electrode.¹² The redox polymer based on PVP ($E^0 = -0.19 \text{ V}$)¹³ can then be considered as one of the most nicely refined anodic redox mediators of this type according to the demands of a membraneless enzymatic biofuel cell. Note that some of the pyridine groups of PVP in this polymer are quaternized to allow a good hydration of the material.

2.3 Cathodic Enzymatic Biocatalysis

The cathode of an enzymatic biofuel cell follows the same principles as detailed above for the anode. The oxidant

of choice to be reduced at the enzymatic cathode is dioxygen, since it is widely available and may be reduced with the transfer of four electrons and four protons down to harmless water. Oxidases that use O₂ as their natural electron acceptor may then be considered as catalysts at enzymatic cathodes. Alternative substrate and enzymes can be, for example, hydrogen peroxide and peroxidases.

An interesting oxidase for application in biofuel cells is laccase extracted from the white-rot fungus *Trametes versicolor*. This fungus uses laccase to oxidize and destroy the lignin polymer of rotting wood to access layers of cellulose on which it thrives. While oxidizing the phenolic groups of lignin, it also reduces its natural electron acceptor, dioxygen, to water. Figure 6 (the cathodic symmetric of Figure 4) shows the electron-transfer sequence for a laccase-catalyzed cathodic dioxygen reduction. The redox mediator structure and potential can be refined as already detailed for the anode above. Here, the redox mediators sketched in Figure 5 with E^0 of 0.00, 0.20, 0.40, and 0.55 V, respectively, represent an example of a potential/structure refinement for such an enzymatic cathode.^{9,10,14,15} Similar to the anode discussion, crosslinking and deposition onto the electrode as an hydrogel are possible.¹² Many laccase sources exist with various redox potentials and pH optima. Laccase from *T. versicolor* is peculiar because of its very high redox potential, which is very close to that of dioxygen reduction at pH 7. Nevertheless, this enzyme has an optimum pH of around 5 and has a low activity at neutral pH, which precludes its use in physiological fluids, e.g., blood, where pH is ca. 7.4.

More relevant to the inorganic themes of this article is the fact that laccase belongs to the blue copper oxidase class. The active site of laccase is indeed made up of two copper sites: A single copper site named Type 1, responsible for the blue color of the enzyme and where the substrate (phenolic groups in the wild, or the redox mediator in a biofuel cell) is oxidized, and a trinuclear copper site (of Type 2 and 3) where the sequential reduction of dioxygen to water occurs, Figure 7.¹⁶

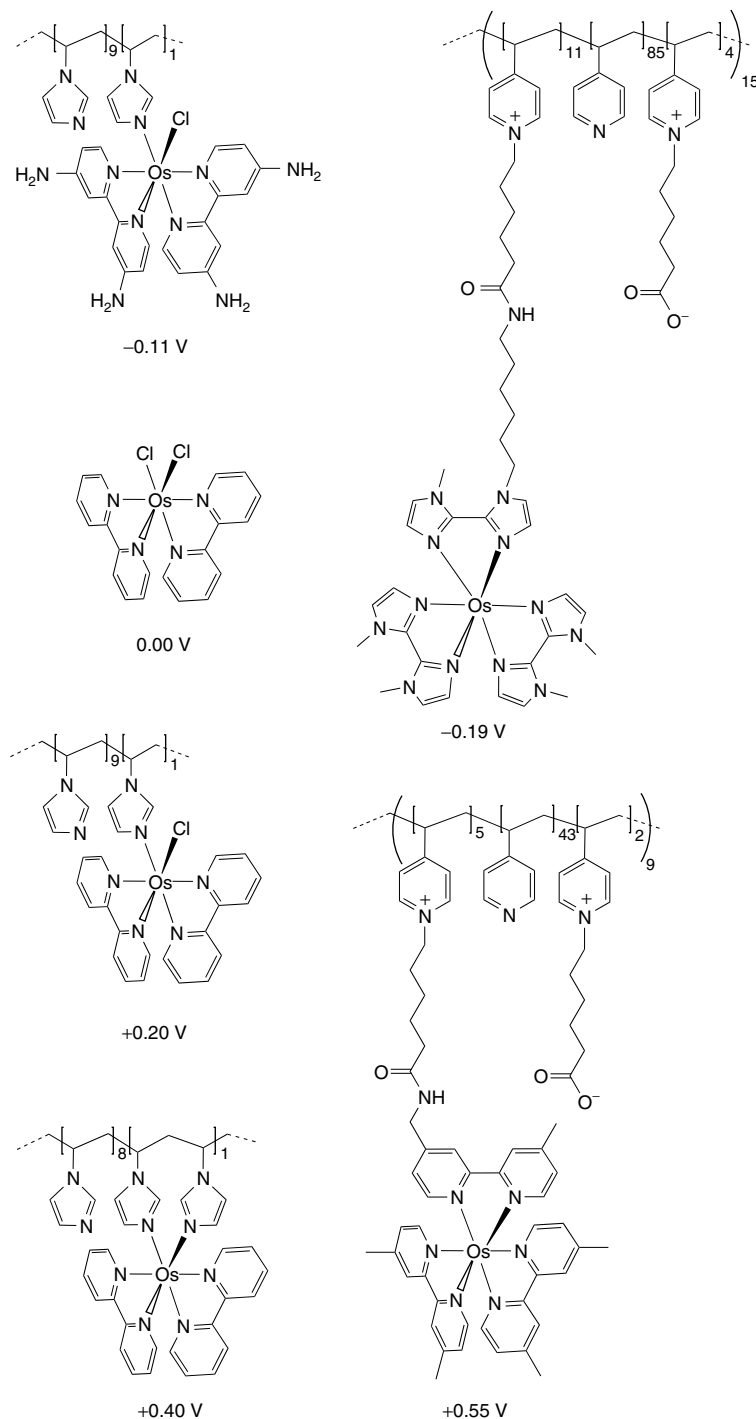


Figure 5 Refinement in the design of redox mediators based on osmium coordination complexes. The redox potentials for the Os(III)/Os(II) couples are given versus Ag/AgCl. The counteranion for the positive charge borne by the metal complex (not shown), or for some of the quaternized pyridinium, is usually chloride

As for other metallo-oxido-reductases, bioinorganic chemistry serves two purposes, namely, the synthesis and study of small coordination complexes of structural and/or functional relevance to the enzyme-active site. The first and most successful approach of bioinorganic chemistry

consists of providing an array of compounds with structural features similar to those found in the enzyme-active site. These small coordination complexes have the advantage of being structurally better characterized and of allowing more facile spectroscopic studies than on the whole enzyme.

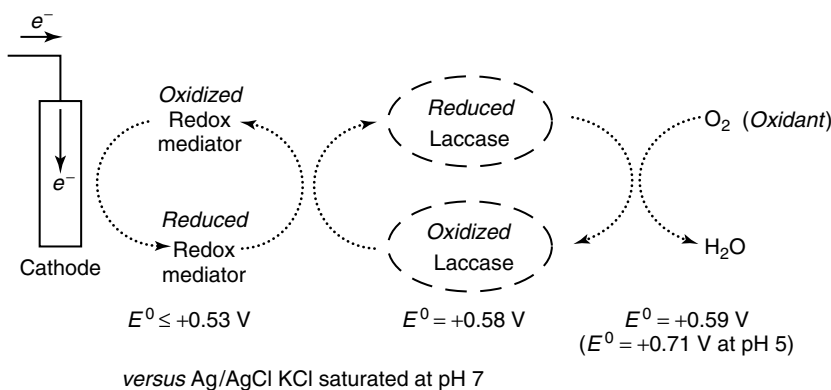


Figure 6 Mediated electron transfer between dioxygen and laccase (laccase redox potential is from fungus *T. versicolor*)

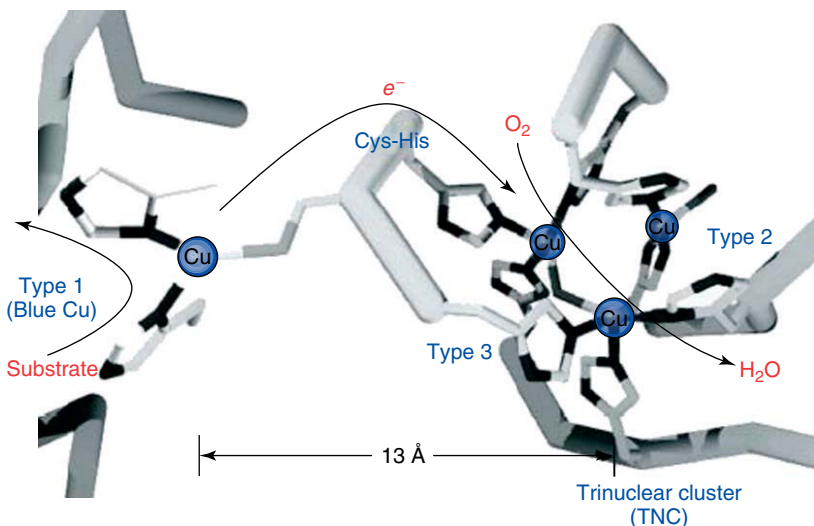


Figure 7 Structure and function of the active site of blue copper oxidases. (Reproduced from Ref. 16. © Royal Society of Chemistry, 2008.)

These synthetic models may also be amenable to changes in ligand types, oxidation states, charge, etc. In conjunction with enzymatic studies, this approach is very useful in precisely defining the structure (and function) of the metallic enzyme's active site at different stages of catalysis. In the context of biofuel cells, however, the contribution of bioinorganic chemistry can only be weighed when embodied in the complete array of techniques and fields required for the understanding of enzymes, e.g., protein crystallography, biochemistry, and spectroscopy. In addition, not all oxidoreductases are metalloenzymes; this can be seen, for instance, in the above discussion on glucose oxidase that bears the organic FAD/FADH₂ cofactor. The second approach of bioinorganic chemistry is the pursuit of the reproduction of the high specificity and catalytic activity of enzymes through the synthesis of the essential known features of their active sites.^{17–19} So far, this approach has, however, contributed more to the understanding of enzymatic catalysis rather than to the

design of competitive artificial catalysts. Indeed, modeling the active site of enzymes with small inorganic complexes often results in the absence of catalytic activity and makes one realize the crucial importance of the supramolecular proteic framework around the enzyme-active site. As far as oxygen reduction is concerned, no competitive synthetic copper complexes are available. However, molecular compounds based on cobalt or iron porphyrins and phthalocyanines, deposited on electrodes, have been used as efficient catalysts for the cathodic reduction of oxygen, in particular, in association with a microbial anode.^{20,21} Another contribution of inorganic chemistry in this context is that of optimizing the nature of efficient oxygen-reducing cathodes based on precious metals or alloys. These studies can now be efficiently supported by a theoretical selection of potentially stable and active alloys. Indeed, examples of theoretically selected platinum alloys, i.e., Pt₃Y and Pt₃Sc, have been confirmed experimentally to display catalytic activity higher than that of

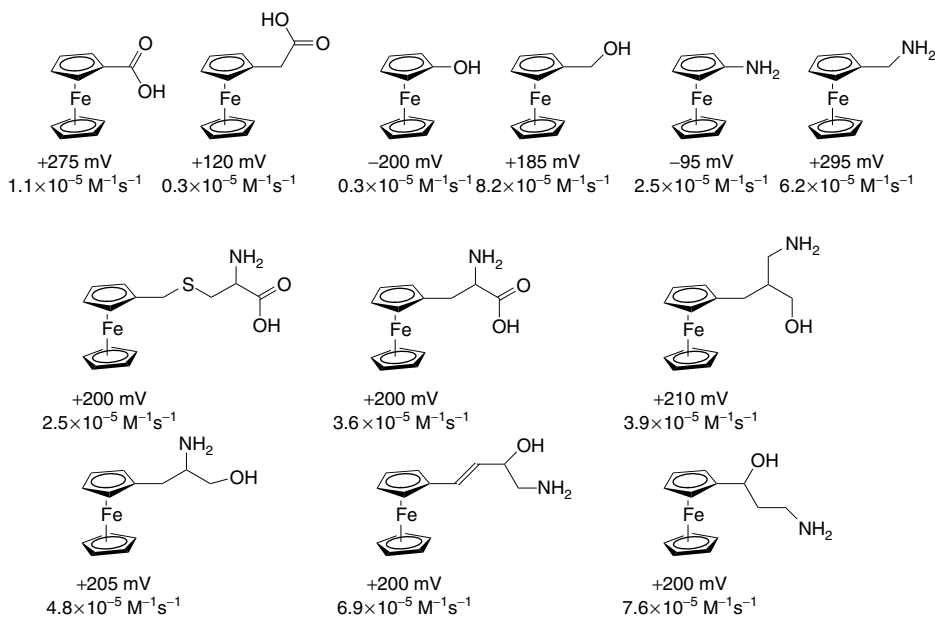


Figure 8 Rate constants reported by Forrow *et al.* for the oxidation of glucose by glucose oxidase, mediated by Ferrocenyls. Redox potentials are given versus SCE²⁷

pure Pt.²² Other ways of reducing the amount of precious metal while maintaining high activity is to use smaller metal particles. A recent approach involves the use of a macromolecular template for the aggregation of Pt(IV) clusters, the reduction of which yields subnanometer Pt(0) particles that have been shown to be very efficient for the electroreduction of O₂ to H₂O.²³ A recurrent problem with small metal particles, however, is often their low physical stability on surfaces, so that significant metal loss occurs through leaching with time, which also reduces the catalytic activity of the electrode. Resorting to precious metals or their alloys, even in small quantities, is not the only alternative, as it has been shown recently that an air cathode based on an organic conductive polymer (PEDOT) displays high rates of oxygen reduction.²⁴ Hence, the important reduction of dioxygen can be addressed in many ways, including enzymatic, molecular, and materials approaches, all with different levels of inorganic contents.²⁵

2.4 Inorganic Perspective of Biofuel Cells

In this section, the contribution of inorganic chemistry to the field of biofuel cells is summarized. One obvious contribution through the synthesis of redox mediators is utilitarian and crucial: these small electroactive complexes allow a fast electrical connection between redox enzymes and electrodes. The nature of the redox mediator, however, is not necessarily inorganic, as organic dyes, for example, can be very efficient as well, as is ABTS for laccase.²⁶ Redox mediators can also be used to probe the properties of the enzyme-active sites' environment. An eloquent illustration of

such a study is that of Forrow and colleagues who considered the rate of anodic glucose oxidation by glucose oxidase mediated by ferrocenyls.²⁷ Selection of data from Forrow *et al.*,²⁷ is presented in Figure 8 and shows the intricate effect of both redox potentials and structure (including size, charge, lipo/hydrophilicity, acid/base properties, etc.). Hence, systematic alteration of the substituent of one of the cyclopentadienyl rings shows that the observed oxidation rate of glucose almost spans 1 order of magnitude even when the redox potential of the mediator is kept constant.

Note that ideally, avoiding the use of redox mediators altogether would simplify the design of biocatalytic electrodes. This can be attempted through genetic engineering in order to expose the active site on the surface of the protein, so that direct electron transfer to an electrode at significant rates can be reached. The enzyme can also be chemically modified to achieve this goal. Recently, glucose oxidase has been chemically stripped from its glycosilated surrounding: efficient direct electron transfer has been demonstrated with the “naked” or “more exposed” enzyme.²⁸ An important fundamental contribution of inorganic chemistry is that of modeling of the enzyme-active sites with the different approaches of bioinorganic chemistry. This improves our understanding of metallo-redox enzymes and may provide simpler, more efficient, and specific synthetic-molecule-based catalysts for the reaction currently carried out by enzymes. Perhaps, other more realistic, inorganic catalytic alternatives of enzymatic reactions may come from the refinement of electrode materials, assisted by theoretical chemistry, or from molecular species that have, in the end, little to do with any of the enzyme-active sites. In any case, catalysts

alternative to redox enzymes could then be implemented in a hybrid fuel cell, where only one of the two electrodes is biocatalytic.

One drawback of enzymes is often their limited physical and/or functional lifetime on electrode surfaces, as they can detach and leach out, undergo denaturation, become inactivated by inhibitors, or are clogged by the medium. One way to overcome this limitation is to develop surface science approaches to strongly attach the enzyme to the surface through covalent bonds.^{29–31} Here again small metallic particles or porous metallic materials can be interesting, as are nonmetallic conducting materials such as carbon.

It is therefore apparent that the contribution of inorganic chemistry to this field has to be apprehended in a larger context, where all branches of chemistry are required to understand and improve biofuel cells. This will then be beneficial to both fields.

2.5 Performance of Assembled Biofuel Cells and their Applications

The best available cells can now operate at a voltage close to 1 V, which is very near to the thermodynamically achievable maximum. In terms of power output, power densities of electrode surface of about 1 mW cm^{-2} can be reached.¹⁵ Such values are modest but sufficient for powering small and low-energy-consuming electronic devices, which is the realistic target of these fuel cells, as demonstrated recently. Indeed, a high-power glucose/O₂ biofuel cell has been designed with the NADH-dependent glucose dehydrogenase–diaphorase–VK3 system at the anode and a blue copper oxidase, namely bilirubin oxidase, at the cathode, with Fe(CN)₆^{3-/4-} as the redox mediator.³² The fuel cell operates at 0.3 V and generates power of over 100 mW for a volume of 80 cm³. It can be used in series and has been shown to power a small radio-controlled toy car or a Walkman®. One long-term goal of membraneless enzymatic biofuel cells could be their implementation in the human body (e.g., in blood vessels where glucose and O₂ are available) coupled with their ability to power small biomedical electronics. The level of glucose could be monitored in situ, and if needed, the delivery of insulin to patients with diabetes could be triggered. The stability of these fuel cells with time (a few months at best) precludes this kind of application for the moment. In addition to the problem of physical stability of the biocatalytic films on electrode surfaces, the issue of their functional stability with time must be addressed as well. For example,³³ in complex biological media like serum, even small amounts of transition-metal ions like Fe²⁺ or Zn²⁺ will compromise the flexibility of redox polymers based on PVI or PVP (cf. Figure 5) by coordination to the polymer backbone, and consequently decrease the efficiency of biocatalysis.

2.6 Conclusion

Biofuel cells have now found demonstrative applications with refinement of their different constituents: catalysts, mediators, electrodes, and fuel cell design, yielding usable power outputs. There is more than a single approach for improving biofuel cells, because these devices depend on the many possible substrates, redox enzymes, electrodes, and targeted applications. Inorganic chemistry has an important role to play in designing functional biofuel cells and in the fundamental studies related to the structure and function of metallo-redox enzymes. Alternative materials or molecular catalysts can also be provided by inorganic chemistry, especially aimed at the important reduction of dioxygen to water. The major drawback of biofuel cells, however, is their relatively poor stability with time when used in continuous operation. This issue is being addressed through surface science of active enzyme layers, which aims to improve their physical and functional stabilities without compromising the relatively high current densities at the electrodes. Irrespective of significant improvements in this matter, the inherent limited lifetime of the biological macromolecules will always be a concern for biofuel cells, when they are required to be stable and to have long lifetimes (over a year). An attractive alternative to the unavoidable fugacity of enzyme functionality is to take advantage of living organisms, in which redox enzymes are naturally at work, get destroyed when not functional, and are replaced by new ones. This is discussed in the next section.

3 MICROBIAL CATALYSIS IN MICROBIAL FUEL CELLS

3.1 Introduction

The demonstration that electrical power can be produced in a fuel cell containing living organisms at the anode was reported at the beginning of the twentieth century by Potter.³⁴ Two microbial fuel-cell prototypes were studied, and they contained either bacteria (*Escherichia coli*) or yeast (*Saccharomyces cerevisiae*) in their anolyte. This simple and fascinating observation has only recently been revisited in order to understand how this could happen and what applications could be derived from the improved microbial fuel cells.^{2,35,36} The basic principle of a microbial fuel cell is shown in Figure 9, with a schematic of a microbial anode.^{2,35,36}

The fuel may be any organic molecule that can be metabolized by the microbe, e.g., sugars, alcohols, and carboxylic acids. The substrate is degraded at different stages of microbial metabolism (glycolysis and Krebs cycle),⁸ eventually producing carbon dioxide and reducing equivalents in the form the electron carriers NADH and FADH₂.⁸ In the absence of their natural electron acceptor (often, but not exclusively, dioxygen) some species of bacteria, called the

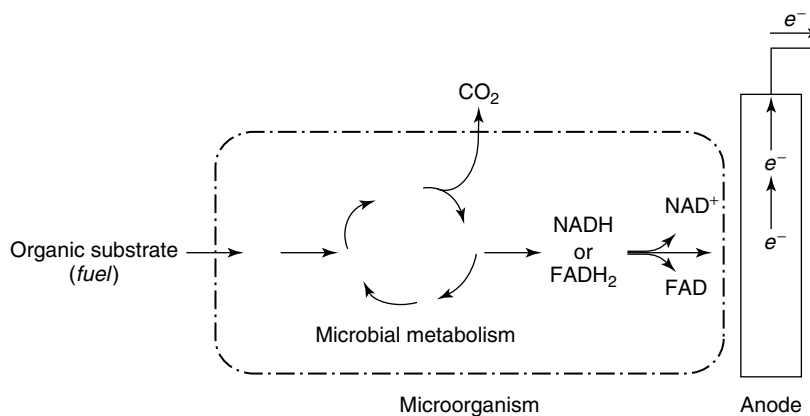


Figure 9 Principle of an anaerobic anode of a microbial fuel cell

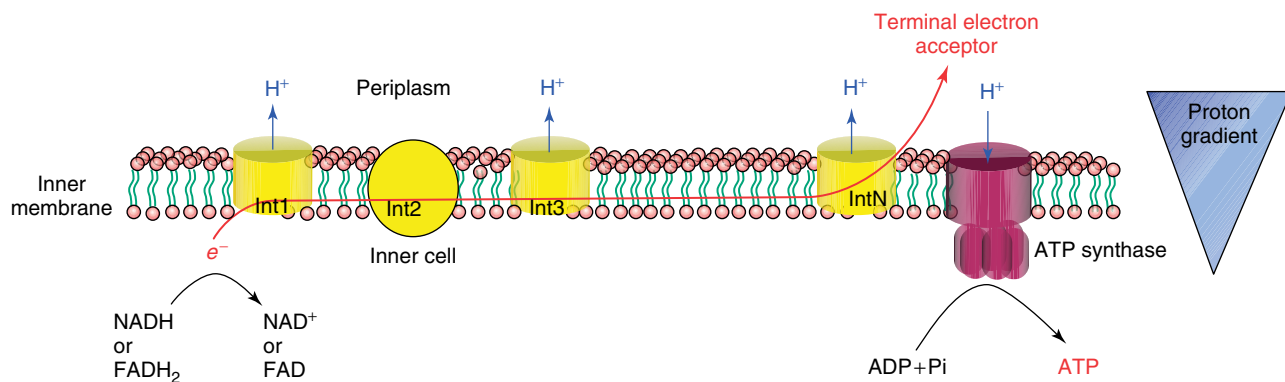


Figure 10 Schematic of the membrane-based respiration electron-transfer chain of bacteria. Intermediaries are redox enzymes, and their number and nature depend on the bacterial species. The natural electron acceptor may be either dioxygen or, in an anaerobic medium, the anode of the fuel cell. (Reproduced from Ref. 36. © Royal Society of Chemistry, 2008.)

anodophiles, are able to transfer electrons to the anode of a fuel cell. The electrons then flow to the cathode of the fuel cell, where any oxidant with a sufficiently high redox potential is reduced. Here again dioxygen is the oxidant of choice because of its wide availability. Hence, in a microbial fuel cell the decoupling of microbial respiration (i.e., substrate oxidation) across the two electrodes allows the extraction of a large part of the free energy of the redox reaction. Electron transfer between a bacterium and an electrode implies some kind of interaction between the membrane-based electron-transfer chains of the microbe and the electrode surface. This is really surprising considering the difficult anodic/cathodic electron transfer from/to redox enzymes, as discussed in the earlier section. Indeed, in addition to the insulation of their active site by the protein scaffold, the enzymes themselves are more or less embedded in the bacterial membrane structure (Figure 10), which should preclude any interaction between the membrane redox enzymes and the electrode surface. This initial surprise turns to perplexity when considering the case of yeasts: these unicellular eukaryotes possess by

definition an organelle called *mitochondria* in the cytoplasm where respiration occurs. The cytoplasm and the yeast's outer membrane constitute additional hurdles toward the electrode surface. The reader interested in yeast biofuel cells is referred to Schaetzel *et al.*³⁶ which includes a perspective on this topic and a review of different possible electron-transfer mechanisms. Recently, a biofuel cell has been designed by immobilization of the mitochondria at a carbon electrode surface using pyruvate as the fuel,³⁷ which provides another illustration of the interaction of the membrane electron-transfer chain and an electrode. Experiments carried out under O₂ resulted in decreased current densities, explained by competition for electrons between the anode and dioxygen. Accordingly, in the presence of cyanide, a known inhibitor of cytochrome c oxidase, current density increased, pointing to the involvement of this enzyme at some stage of exo-cellular electron transfer.

The next section focuses on bacterial fuel cells, because they are the most widely studied and interesting for energy production. First, we consider anodic biocatalysis

followed by cathodic biocatalysis. Next, we focus on inorganic aspects of the research and end the section with a discussion on the performance and applications of microbial fuel cells.

3.2 Anodic Microbial Biocatalysis

Among the many different species of bacteria that have been found on anodes of microbial fuel cells, some strains, from the *Shewanella* and *Geobacter* genera, for example, are known to use solid metal oxides or hydroxides (e.g., of iron or manganese) as electron acceptors. This suggests that some species of bacteria have evolved to allow a favorable interaction between their outer membrane and reducible solids. This could explain the efficient direct electron transfer between bacteria and the electrode surface in microbial fuel cells. This mechanism alone, even if possible, seems insufficient to account for the current densities found in such devices, especially when considering that only a small fraction of the relatively thick three-dimensional biofilms can interact directly with the electrode. There must exist other ways for interaction with the electrode, or between organisms themselves within the biofilms. In this context, the discovery that some bacteria can grow exo-cellular fibrous protein structures, also called *biological “nanowires”*, could explain the facilitated exo-cellular electron transfer to electrodes and between bacteria.³⁸ From the discussion on enzymatic fuel cells above, the presence of redox mediators might also be suspected. Indeed, evidence has been provided in some cases that naturally excreted organic compounds, for example, flavins and quinones, are involved in redox mediation between the bacterial respiratory redox enzymes and the electrode surface.³⁹ Accordingly, addition of artificial redox mediators to the microbial fuel cells’ anolyte, with redox potentials of about 0.0 to 0.3V vs NHE, enhances current densities. There is a large diversity of bacterial species that have been found to be electroactive. Gram-negative bacteria, like those from the genera *Shewanella* and *Geobacter*, possess an outer membrane and can support the different electron-transfer mechanisms discussed above. Gram-positive bacteria, however, usually require soluble redox mediators to be electrically connected to electrode surface, although this has been challenged recently.⁴⁰

3.3 Cathodic Microbial Biocatalysis

Bacteria may also be found or grown at cathodes or in the catholytes of microbial fuel cells.⁴¹ One interesting case is that of biological cathodes that reduce dioxygen to water. The bacteria must accept electrons from the cathode at some point in their outer membrane’s electron-transfer chain, where dioxygen is reduced as the natural electron acceptor. At first sight, this seems to be less energetically favorable for the fuel cell power output. However, one should recall that the overpotential for O₂ reduction to H₂O is high at most electrode surfaces so that microbial assistance may be

beneficial, if the reduction of the oxidant occurs at high rates, even if the effective reduction potential is significantly lower than the thermodynamic limit. The benefit to the bacterial metabolism may be a cheaper biosynthesis of ATP through the input of “free” electrical energy. The catholyte should nevertheless contain a continuous supply of substrates for the bacterial metabolism, so as to provide a minimum of matter necessary to sustain the long-term viability of the biofilm. A general trend found in these kinds of cathodic biofilms is that they are usually more fragile than those found at the anode. In the presence of dioxygen in the catholyte, some bacteria may be used indirectly to regenerate the reduced oxidant at the cathode. Hence, oxidants reduced at the cathode, like MnO₂ or Fe³⁺, may be regenerated biologically as Mn²⁺ or Fe²⁺, respectively, with bacteria using O₂ as their electron acceptor. In the absence of dioxygen, other substrates may be considered as electron acceptors, such as carbon dioxide, sulfate, and nitrate. It is significant to note that biological nitrate reduction to dinitrogen is quite efficient despite the required successive proton-coupled electron transfer and intermediates such as nitrite, NO, and NO₂ on the path to dinitrogen.⁴² In addition, the succession of denitrifying enzymes integrated in the living machinery of bacteria is advantageous compared to the handling of isolated enzymes or the designing of simple molecular catalysts.

3.4 Inorganic Perspective of Biofuel Cells

The use of abiological cathodes in microbial fuel cells often relies on inorganic redox couples with high redox potentials, like permanganate/manganese dioxide (1.18 V vs NHE at pH 7) or ferricyanide/ferrocyanide (0.42 V vs NHE). However, this represents more of a convenient approach to study the microbial anode while securing a high potential at the cathode rather than the design of sustainable devices. The reason for this originates from the poor performance of cathodes relying on direct dioxygen reduction. Alternative dioxygen-reducing cathodes have already been discussed in the enzymatic section of this article and must now be completed with the biological cathode approach discussed above.

Perhaps the most obvious relevance to inorganic chemistry of microbial fuel cell research is that of the coupling of simple inorganic redox couples to bacterial activity. As discussed above, the oxidants used at the cathode, like MnO₂ and Fe³⁺, may be biologically regenerated by bacteria that use dioxygen in the process. In other words, it is an inorganic redox-species-mediated bacterial reduction of dioxygen. This regeneration of the oxidant permits, in principle, the sustainability of the device. Direct reoxidation of these oxidants by O₂ may be considered as well, but it is usually either not possible or too slow. Addition of redox mediators to the anolyte of microbial fuel cells is also possible. These species have, however, been mostly organic redox molecules inspired by the naturally occurring species such as quinones or flavins.

Sulfates, sulfites, and thiosulfates may be reduced by *Desulfovibrio desulfuricans* to sulfides, which in turn may be anodically oxidized to sulfur. Complete denitrification (reduction to dinitrogen) is possible using microorganisms accepting electrons from the cathode.⁴²

The most fundamental issue of relevance to bioinorganic chemistry is certainly the interaction of the electron-transfer-chain redox enzymes with electrodes. Contrary to the study of isolated enzymes or synthetic models of their active sites, the macromolecules are here part of a redox series that is structurally organized in the membrane of a living organism. This presents challenges for the study of electron transfer between a large microbe and an electrode, and the characterization of the redox species involved. An example of such a study on *Geobacter sulfurreducens* involved a thin-film gold electrode in order to combine electrochemical study with ATR-SEIRAS. The authors demonstrated electron transfer between the polarized gold electrode (0.2 V vs Ag/AgCl), and the infrared adsorption band that was concomitantly detected was assigned to proteins and lipids connecting the electrode surface. A new band at 1600 cm⁻¹ was assigned to the c-type cytochromes known to be involved in exocellular electron transfer. The change in adsorption spectra was followed as the electrode was polarized from -0.1 to +0.4 V. A midpoint potential from the spectroelectrochemical measurement was calculated to be 0.17 V and was consistent with the electrochemical measurement.⁴³ This study confirms not only that these proteins are located at the surface of the outer bacterial membrane, but also that their active sites are accessible to establish electrical contact with the electrode surface. It is known that cytochrome-type proteins are found at the outer membrane of bacteria, for example, *Shewanella*, and this raises many questions related to the number of different redox enzymes that are effectively addressed electrochemically,⁴⁴ either directly or through the mediation of small redox molecules or complexes. The derived bioenergetic implications are not immediately realized by the classical inorganic chemist, ideally working with pure species in a controlled environment. Addressing the electrochemistry of inorganic sites of functional enzymes in their natural and dynamic environment presents challenges to which inorganic chemistry can contribute, and at the same time, it stresses on the need for a multidisciplinary approach. The dynamic and plastic nature of the subject of study, i.e., the microbe, might also be destabilizing for the hardcore inorganic chemist, new to this field. For example, the nature and number of expressed proteins at the outer membrane may depend on the conditions of growth, like pH, dioxygen concentration, and polarization of electrode. In some cases, strains grown under dioxygen will not need these exposed surface proteins for respiration, but will express them only in the absence of O₂ in order to be able to reach an alternative solid electron acceptor. In addition, one must keep in mind that it is not necessarily a redox metalloenzyme such as cytochrome-type proteins that may be addressed electrochemically but, in some instances, even an organic

cofactor such as the quinone pool of the respiratory chain, may be addressed, as it has been proposed in the biological nitrate reduction at the cathode of a microbial fuel cell.⁴² The modest power output of microbial fuel cells allows the implementation of cheaper electrode materials like carbon even if their absolute catalytic performance is not optimal. Inorganic materials like tungsten carbide may equally be revisited, and they find applications as, for example, electrocatalysts in the production of dihydrogen by soil bacteria.⁴⁵

3.5 Performance of Assembled Microbial Fuel Cells and their Applications

Microbial fuel cells have been considered as a profitable way of cleaning up wastewaters, by removing their organic content (pollutants), while also producing and selling electrical power. Other pollutants as well could, in principle, be removed at the anode, such as sulfur contaminants. An ideal combination from the perspective of wastewaters treatment would be the association of a biological anode to a biological cathode that would also remove nitrates from the effluents. Reported power densities for the best microbial fuel cells, ca. 100 W m⁻³ for the whole fuel cell volume, remain about 1 order of magnitude low to be interesting economically. Real-world niche applications have, however, been reported, such as the powering of a meteorological buoy set in the river bed of an estuary.⁴⁶ The noncorrosive cathode floats on the dioxygen-rich water surface while the biological anode is buried in the sediment of the river, which provides a medium that is both rich in organic substrates (fuel) and poor in dioxygen (thus favoring the growth of anodophiles on the electrode). The performance of this device is enough to power the buoy (100 mW) and hence to avoid the burden of the regular changing of batteries, since the system has also been shown to be stable over time (over two years). Pending improvements in the design of microbial fuel cells,^{47,48} the technology has been partly reoriented toward other kinds of bioelectrochemical systems, viz., bioelectrolyzers. In these systems, rather than electricity production, there is an input of electrical energy in order to electrosynthesize valuable products. For example, H₂ can be generated at the cathode of the electrolyzer, while organic substrates are oxidized at the microbial anode. Because the oxidation of organic substrates at the microbial anode occurs at rather low potentials, the amount of electrical energy needed to produce dihydrogen is lessened. In addition, these electrolyzers are also considered as a wastewater treatment technology, since organic substrates are oxidized.

3.6 Conclusion

The electrical linking of bacteria at the electrodes of a fuel cell permits the recovery (or the saving) of some electrical energy. Despite their current insufficient performance in terms of power output, there are recent research and developments

that provide interesting avenues for the refinement of these systems. Hence, bioelectrochemical systems may find applications beyond niches and especially in the wastewater treatment plants and in the electrosynthesis of value-added products. The contribution of inorganic chemistry to microbial fuel cell research is somewhat similar to its contribution to the enzymatic fuel cells' field, because the same functional units are at work, viz., redox enzymes. However, the nature and size of the catalyst, bacteria interacting with others within a biofilm, provide specific challenges for characterizing the interplay between the functionality of redox enzymes, metabolism and bioenergetics, and exocellular electron transfer.

4 TRANSFORMATION AND PRODUCTION ROLES OF ENZYMES, MICROBES, AND HIGHER ORGANISMS IN BIOLOGICAL FUEL CELLS

In addition to their biocatalytic function at electrodes, enzymes or living organisms may be integrated in fuel cells as entities dedicated to the production or transformation of the

fuel or oxidant, and even to the production of the electrode catalyst.

In enzymatic fuel cells, the coupling of only one substrate and one enzyme is often not viable. For example, the biofuel cell designed by Kano and coworkers³² relies on the two-electron oxidation of glucose by glucose dehydrogenase. This enzyme is interesting, because it is NAD dependent and does not produce hydrogen peroxide. The redox potential of NAD^+/NADH is quite low (-0.32 V vs NHE at pH 7). The oxidation of NADH is, however, slow at most electrode surfaces, so that regeneration of the glucose dehydrogenase cofactor is not possible directly. A second enzyme/mediator system is then needed for high rate anodic oxidation of glucose, i.e., diaphorase, efficient for the oxidation of NADH to NAD^+ , and VK3, an established and suitable redox mediator of diaphorase.

An interesting electron-transfer mechanism between a microbe and an electrode in the context of microbial fuel cells, and complementary to the other direct, mediated, and pili-assisted mechanisms, is the direct anodic oxidation of a secondary substrate, biologically excreted, such as formate or dihydrogen.⁴⁵ This, of course, may also be applied in

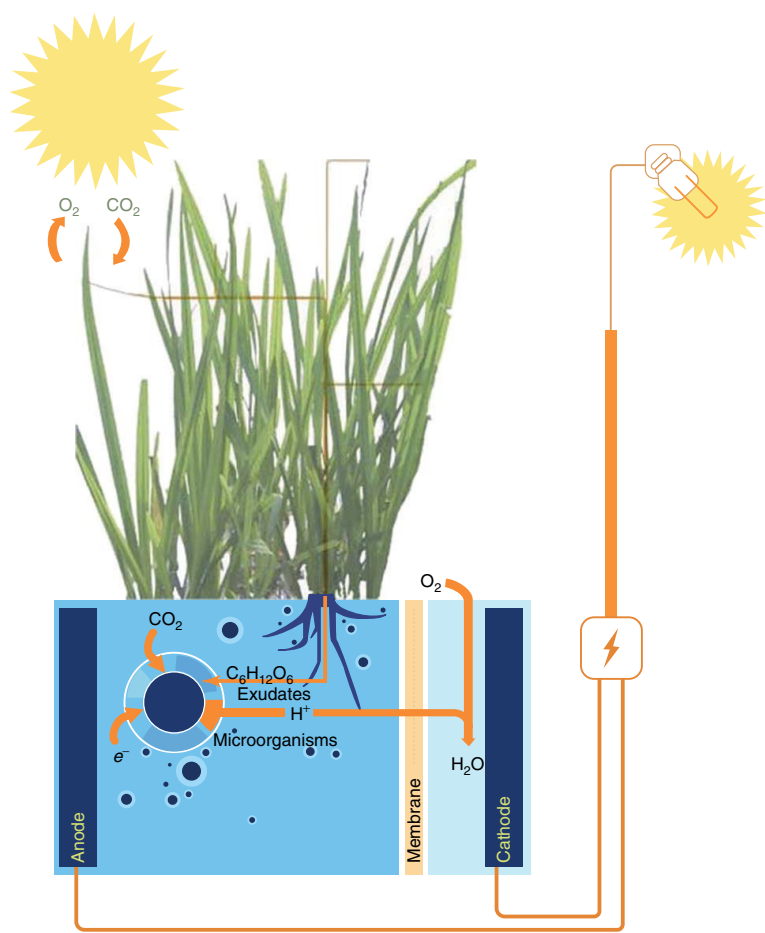


Figure 11 Principle of a plant-microbial fuel cell. (Reproduced from Ref. 49. © John Wiley & Sons, Ltd, 2008.)

enzymatic fuel cells, where a suitable enzyme would transform a substrate into a product directly oxidizable at the anode.

At the cathodic side of the fuel cell, a recurrent problem with dioxygen cathodes working in quiescent conditions is the rapid depletion of O₂ in the vicinity of the electrode surface that limits current densities and eventually the cell power output. Growing photosynthetic algae on the surface of the catholyte may be an interesting way of enriching the medium in dioxygen under light irradiation.⁴¹

The secretion of redox enzymes by microorganisms or higher organisms could solve the problem of the limited lifetime of enzymes operating in self-sustainable fuel cells. For example, since laccase is naturally produced by some species of fungi,²⁶ having a culture of these organisms near the cathode would secure a constant leaching of the catalyst into the catholyte. A suitable redox mediator would, nevertheless, still be needed. We have seen, however, that some microorganisms do excrete redox-active molecules. One may therefore foresee an ideal combination of living organisms and electrode materials that would reach a balanced energetic steady state, where the fuel, oxidant, and catalysts would be naturally and continuously delivered to the electrode. To the author's knowledge, this dream biological fuel cell is not a possibility in the near future. In 2008, however, three papers have appeared demonstrating that if plants were grown in the anolyte of microbial fuel cells, organic substrate exudation by the roots could then be used as the fuel at the biological anode (Figure 11).^{49–51} This concept is appealing on many counts: (i) the fuel cell is carbon neutral since organic substrates that are oxidized up to CO₂ at the microbial anode have been photosynthesized by the plant through the light induced fixation of atmospheric CO₂; (ii) this device may be implemented in wetlands that are otherwise not used for food production so that there is no competition for arable land; and (iii) the plant itself may be cropped and sold for its biomass and/or nutritive value, e.g., rice. Strik *et al.* estimated the energy potential of this technology in Europe to be 21 GJ per hectare per year.⁴⁹ It would be a shame not to try to tap even a fraction of this energy.

5 CONCLUSIONS

Enzymatic and microbial fuel cells have been shown to produce significant amounts of electrical energy, sufficient for powering low-energy-consuming devices. Despite the modest performance of these bioelectrochemical systems, there are many perspectives for their refinement and for the widening of their applications. Inorganic chemistry has been part of the development of this multidisciplinary research and can contribute to the current challenges facing these bioenergy-producing systems. Indeed, inorganic chemistry has provided inorganic redox mediators of controlled shape, size, charge, and potential that are essential for the electrical

linking electrodes to redox enzymes (considered either as isolated macromolecules or part of the living machinery of microorganisms). Libraries of consistently altered redox mediators are also of interest for the more fundamental approach of probing and understanding the intimate function of redox enzymes. When these redox enzymes contain a metal-active site, bioinorganic chemistry contributes to the understanding of their structure and function.

Simpler inorganic redox couples are also being used in biological fuel cells, which at first sight may not fascinate the inorganic chemists. However, realizing that these simple species, sometimes in their solid state, can transfer electron to/from a microorganisms should raise their interest. This should even widen the perspectives of any chemist, with the linking of molecular inorganic chemistry, to microbiology and even geochemistry.⁵²

In microbial fuel cells, the use of simple inorganic redox couples has been shown to be either utilitarian (redox mediators) or applicative (removal of sulfur- or nitrogen-containing pollutants). In both cases, this involves fascinating microbial inorganic redox chemistry.

The critical cathodic dioxygen reduction reaction has been the focus of research in almost every kind of fuel cell, not only because of its advantages like the wide availability of O₂, the high redox potential of the O₂/H₂O couple, and the innocuous reduction product in the form of water, but most of all because the kinetics of this reaction are slow at most electrodes, which is a major drawback to overcome. Here again inorganic chemistry contributes through a molecular approach in providing small metal complexes for the activation of oxygen that may be immobilized at electrode surfaces. The biomacromolecular approach contains an inorganic contribution as well, because of the metallic nature of the oxidases' active sites. These enzymes may indeed be used as efficient biocatalysts at the oxygen-reducing cathodes of fuel cells. Mimicking these redox metalloenzymes with bioinspired functional and stable inorganic complexes also provides an endeavor for the inorganic chemist. In terms of materials chemistry, reducing the amount of precious metals like platinum at these cathodes is important, as is the search for cheaper substitutes that also display high catalytic activity. In this context, the methods of theoretical chemistry may now valuably assist the experimentalist.

Finally, the traditional inorganic chemists, away from their comfort zone, may be rightly found a bit lost and puzzled, when considering the network of biomacromolecules organized as functional units in living organisms which are themselves organized in a dynamic consortium and integrated in a working electrochemical device that may also contain higher organisms like plants, algae, or fungi. Biological fuel cell research, however, needs the contribution of different scientists encompassing microbiologists, geneticists and biochemists, environmental engineers, electrochemists and fuel cell specialists, surface and materials scientists, and even organic and inorganic chemists. If the prospect of an integrated

and self-sustained plant-microbial fuel cell still dazzles the inorganic chemists, they should realize that they are in fact contemplating the manganese cluster of photosystem II,⁵³ the iron–molybdenum cofactor of nitrogenase,⁵⁴ the copper sites of oxidases,¹⁶ enzymes involved in denitrification,⁵⁵ and, among other redox metalloenzymes, the cytochrome c oxidase of the respiratory chain,¹⁸ working as elementary catalytic units of a macroscopic energy-transformation device.

It is hoped that this article provided a useful overview and introduction to the multidisciplinary perspectives of biological fuel cells and particularly the inorganic chemistry issues related to these energy producing devices.

6 GLOSSARY

Biofuel cell: a biological fuel cell with redox enzymes as catalysts

Microbial fuel cell: a biological fuel cell with living microorganisms as catalysts

7 ACKNOWLEDGMENTS

The European Community's Seventh Framework Programme FP7/2007-2011 is thanked for funding the Plant-Power project (www.plantpower.eu).

8 RELATED ARTICLES

Energy Conversion in Photosynthesis; Molecular Catalysis for Fuel Cells; Proton Exchange Membranes for Fuel Cells.

9 ABBREVIATION AND ACRONYMS

ABTS = 2,2'-azino-bis(3-ethylbenzo-thiazoline-6-sulfonic acid) diammonium salt; ATP = adenosine triphosphate; ATR-SEIRAS = attenuated total reflection surface enhanced infrared absorption spectroscopy; Bipy = bipyridine; DNA = deoxy ribonucleic acid; FAD = flavin adenine dinucleotide (oxidized); FADH₂ = flavin adenine dinucleotide (reduced, by two electrons and two protons); NAD⁺ = nicotinamide adenine dinucleotide (oxidized); NADH = nicotinamide adenine dinucleotide (reduced, by two electrons and one proton); NHE = normal hydrogen electrode; PVI = polyvinylimidazole; PVP = polyvinylpyridine;

PEDOT = poly(3,4-ethylenedioxythiophene); VK₃ = 2-methyl-1,4-naphthoquinone, vitamin K₃.

10 REFERENCES

1. M. Winter and R. J. Brodd, *Chem. Rev.*, 2004, **104**, 4245.
2. G. T. R. Palmore and G. M. Whitesides, 'Microbial and Enzymatic Biofuel Cells', in 'Enzymatic Conversion of Biomass for Fuels Production', eds. M. E. Himmel, J. O. Baker, and R. P. Overend, ACS Symposium Series American Chemical Society, Washington, DC, 1994, Vol. 566, p. 271.
3. A. T. Yahiro, S. M. Lee, and D. O. Kimble, *Biochim. Biophys. Acta*, 1964, **88**, 375.
4. D. Leech, M. Pellissier, and F. Barrière, 'Biopowering Fuel Cells Through Biocatalysis', in 'Electrochemical Sensors, Biosensors and their Biomedical Applications', eds. X. Zhang, H. Ju, and J. Wang, Elsevier, 2008, p. 385.
5. A. Heller, *Phys. Chem. Chem. Phys.*, 2004, **6**, 209.
6. S. C. Barton, J. Gallaway, and P. Atanassov, *Chem. Rev.*, 2004, **104**, 4867.
7. A. Heller, *Acc. Chem. Res.*, 1990, **23**, 128.
8. J. M. Berg, J. L. Tymoczko, and L. Stryer, 'Biochemistry', 5th edition, W.H. Freeman and Company, 2001.
9. E. M. Kober, J. V. Casper, B. P. Sullivan, and T. J. Meyer, *Inorg. Chem.*, 1988, **27**, 4587.
10. F. Barrière, Y. Ferry, D. Rochefort, and D. Leech, *Electrochim. Comm.*, 2004, **6**, 237.
11. H.-H. Kim, N. Mano, Y. C. Zhang, and A. Heller, *J. Electrochem. Soc.*, 2003, **150**, A209.
12. A. Heller, *Curr. Opin. Chem. Biol.*, 2006, **10**, 664.
13. N. Mano, F. Mao, and A. Heller, *J. Am. Chem. Soc.*, 2002, **124**, 12962.
14. F. Barrière, P. Kavanagh, and D. Leech, *Electrochim. Acta*, 2006, **51**, 5187.
15. V. Soukarev, N. Mano, and A. Heller, *J. Am. Chem. Soc.*, 2004, **126**, 8368.
16. E. I. Solomon, A. J. Augustine, and J. Yoon, *Dalton Trans.*, 2008, 3921.
17. Y. Wang, J. L. DuBois, B. Hedman, K. O. Hodgson, and T. D. P. Stack, *Science*, 1998, **279**, 537.
18. J. P. Collman and R. A. Decréau, *Chem. Commun.*, 2008, 5065.
19. C. Tard and C. J. Pickett, *Chem. Rev.*, 2009, **109**, 2245.
20. F. Zhao, F. Harnisch, U. Schröder, F. Scholz, I. Bogdanoff, and I. Herrmann, *Environ. Sci. Technol.*, 2006, **40**, 5193.
21. M. Bron, J. Radnik, M. Fieber-Erdmann, P. Bogdanoff, and S. Fiechter, *J. Electroanal. Chem.*, 2002, **535**, 113.
22. J. Greeley, I. E. L. Stephens, A. S. Bondarenko, T. P. Johansson, H. A. Hansen, T. F. Jaramillo, J. Rossmeisl, I. Chorkendorff, and J. K. Nørskov, *Nat. Chem.*, 2009, **1**, 552.

23. K. Yamamoto, T. Imaoka, W.-J. Chun, O. Enoki, H. Katoh, M. Takenaga, and A. Sonoi, *Nat. Chem.*, 2009, **1**, 397.
24. B. Winther-Jensen, O. Winther-Jensen, M. Forsyth, and D. R. MacFarlane, *Science*, 2008, **321**, 671.
25. M. L'Her, 'Redox Properties, Electrochemistry of Oxygen', in 'Encyclopedia of Electrochemistry', eds. A. J. Bard, M. Stratman, F. Scholz, and C. J. Pickett, Inorganic Electrochemistry, Wiley-VCH, Weinheim, 2006, Vol. 7a, p. 119.
26. O. Schaetzle, F. Barrière, and U. Schröder, *Energy Environ. Sci.*, 2009, **2**, 96.
27. N. J. Forrow, G. S. Sanghera, and S. J. Walters, *J. Chem. Soc., Dalton Trans.*, 2002, 3187.
28. O. Courjean, F. Gao, and N. Mano, *Angew. Chem. Int. Ed.*, 2009, **48**, 5897.
29. M. Pellissier, F. Barrière, A. J. Downard, and D. Leech, *Electrochim. Comm.*, 2008, **10**, 835.
30. M. J. Moehlenbrock and S. D. Minteer, *Chem. Soc. Rev.*, 2008, **37**, 1188.
31. M. J. Cooney, V. Svoboda, C. Lau, G. Martin, and S. D. Minteer, *Energy Environ. Sci.*, 2008, **1**, 320.
32. H. Sakai, T. Nakagawa, Y. Tokita, T. Hatazawa, T. Ikeda, S. Tsujimura, and K. Kano, *Energy Environ. Sci.*, 2009, **2**, 133.
33. G. Binyamin, T. Chen, and A. Heller, *J. Electroanal. Chem.*, 2001, **500**, 604.
34. M. C. Potter, *Proc. R. Soc. London, Ser. B*, 1912, **84**, 260.
35. B. E. Logan, 'Microbial Fuel Cells', John Wiley & Sons, New York, 2008.
36. O. Schaetzle, F. Barrière, and K. Baronian, *Energy Environ. Sci.*, 2008, **1**, 607.
37. R. L. Arechedarra, K. Boehm, and S. D. Minteer, *Electrochim. Acta*, 2009, **54**, 7268.
38. Y. A. Gorby, S. Yanina, J. S. McLean, K. M. Rosso, D. Moyles, A. Dohnalkova, T. J. Beveridge, I. S. Chang, B. H. Kim, K. S. Kim, D. E. Culley, S. B. Reed, M. F. Romine, D. A. Saffarini, E. A. Hill, L. Shi, D. A. Elias, D. W. Kennedy, G. Pinchuk, K. Watanabe, S. Ishii, B. Logan, K. H. Nealson, and J. K. Fredrickson, *Proc. Natl. Acad. Sci. U.S.A.*, 2006, **103**, 11358.
39. E. Marsili, D. B. Baron, I. D. Shikhare, D. Coursolle, J. A. Gralnick, and D. R. Bond, *Proc. Natl. Acad. Sci. U.S.A.*, 2008, **105**, 3968.
40. C. W. Marshall and H. D. May, *Energy Environ. Sci.*, 2009, **2**, 699.
41. Z. He and L. T. Angenent, *Electroanalysis*, 2006, **18**, 2009.
42. P. Clauwaert, K. Rabaey, P. Aelterman, L. de Schampheleire, T. H. Pham, P. Boeckx, N. Boon, and W. Verstraete, *Environ. Sci. Technol.*, 2007, **41**, 3354.
43. J. P. Busalmen, A. Esteve-Núñez, A. Berná, and J. M. Feliu, *Angew. Chem. Int. Ed.*, 2008, **47**, 4874.
44. M. Firer-Sherwood, G. S. Pulcu, and S. J. Elliot, *J. Biol. Inorg. Chem.*, 2008, **13**, 849.
45. M. Rosenbaum, F. Zhao, U. Schröder, and F. Scholz, *Angew. Chem. Int. Ed.*, 2006, **45**, 6658.
46. L. M. Tender, S. A. Gray, E. Grovesman, D. A. Lowy, P. Kauffman, J. Melhado, R. C. Tyce, D. Flynn, R. Petrecca, and J. Dobarro, *J. Power Sources*, 2008, **179**, 571.
47. B. E. Logan and J. M. Regan, *Environ. Sci. Technol.*, 2006, **40**, 5172.
48. B. E. Logan, B. Hamelers, R. Rozendal, U. Schröder, J. Keller, S. Freguia, P. Aelterman, W. Verstraete, and K. Rabaey, *Environ. Sci. Technol.*, 2006, **40**, 5181.
49. D. P. B. T. B. Strik, H. V. M. Hamelers, J. F. H. Snel, and C. J. N. Buisman, *Int. J. Energy Res.*, 2008, **32**, 870.
50. L. De Schampheleire, L. Van den Bossche, H. S. Dang, M. Hoefte, N. Boon, K. Rabaey, and W. Verstraete, *Environ. Sci. Technol.*, 2008, **42**, 3053.
51. N. Kaku, N. Yonezawa, Y. Kodama, and K. Watanabe, *Appl. Microbiol. Biotechnol.*, 2008, **79**, 43.
52. D. K. Newman, *ChemSusChem*, 2009, **2**, 380.
53. B. Loll, J. Kern, W. Saenger, A. Zouni, and J. Biesadka, *Nature*, 2005, **438**, 1040.
54. O. Kuhl, *ChemBioChem*, 2009, **10**, 809.
55. I. Moura and J. J. G. Moura, *Curr. Opin. Chem. Biol.*, 2001, **5**, 168.

Proton Exchange Membranes for Fuel Cells

Ram Devanathan

Pacific Northwest National Laboratory, Richland, WA, USA

1	Introduction	89
2	Perfluorinated Sulfonic Acid Membranes	91
3	Novel Proton Exchange Membranes	96
4	Degradation of Proton Exchange Membranes	98
5	Summary	99
6	Acknowledgments	99
7	Abbreviations and Acronyms	99
8	References	100

1 INTRODUCTION

Inexpensive energy obtained from readily available fossil fuels has served as the engine of industrialization and improvement in quality of life for people in the industrialized world over the last three centuries. It is widely acknowledged¹ that increased per capita energy use provides the easiest path to achieve prosperity and uplift large segments of the population out of poverty. Today, rapid growth in developing nations, such as China and India, is manifesting itself in the form of steadily increasing consumption of energy and materials. In 2008, the United States used about 100 quadrillion British thermal units (BtU) of energy of which about 83% came from fossil fuels as shown in Figure 1.² This dependence on fossil fuels is causing global concern about the adequacy of energy supplies, increasing cost of energy, excessive reliance on energy sources located in politically unstable regions, and the environmental impact of the use of fossil fuels.

In order to achieve sustainable development, there is a pressing need to ensure the reliability and adequacy of energy supplies while at the same time reducing pollution in general and the emission of greenhouse gases, such as CO₂ and CH₄, in particular. In this regard, a hydrogen-based economy has been proposed (*see Hydrogen Economy*) as an alternative to our current economy based on the combustion of fossil fuels. Hydrogen is envisaged as an efficient, low-pollution, and possibly sustainable energy carrier that can reduce the carbon footprint and energy cost of energy-intensive sectors of the economy, such as transportation. The final and key

link in the hydrogen economy is the conversion of the chemical energy of the hydrogen fuel to electrical energy using fuel cells (FCs). The electricity generated can be used to provide power for stationary applications, portable power for electronics in consumer devices as well as battlefield applications, and automotive power when combined with high-efficiency electric motors.

There are several types of FCs, such as molten carbonate, phosphoric acid, alkaline, solid oxide (*see Intermediate-Temperature Solid Oxide Fuel Cells*), and proton exchange membrane (PEM). Of these, polymer electrolyte membrane fuel cells (PEMFCs) are preferred for portable power and electrical power for transportation applications, because they are well suited for quick start-up and start-stop cycling, operate at lower temperatures (~85 °C), are compact and have high power density. PEMFCs can use hydrogen, methanol, ethanol (*see Direct Ethanol Fuel Cells*), or formic acid as fuel and produce only water and heat as by-products when using hydrogen as fuel. PEMFC technology has been used to power laptop computers, cars, sports utility vehicles, scooters, rickshaws, forklifts, buses, boats, submarines, and aircraft.³ However, significant reductions in cost and improvements in durability are needed to achieve widespread commercialization of fuel cell technology.

Figure 2 shows a schematic cross-sectional view of a PEMFC operating on hydrogen. The core of the fuel cell is the PEM that is sandwiched between the anode or fuel electrode and cathode or air electrode. Each electrode consists of an electrocatalyst layer, which is typically Pt catalyst on

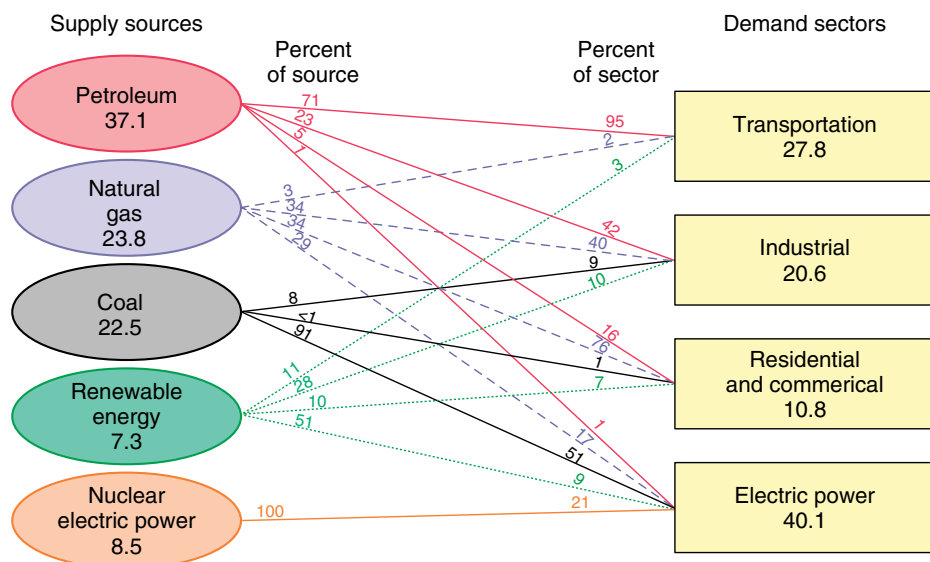


Figure 1 Energy use in the United States of America in 2008

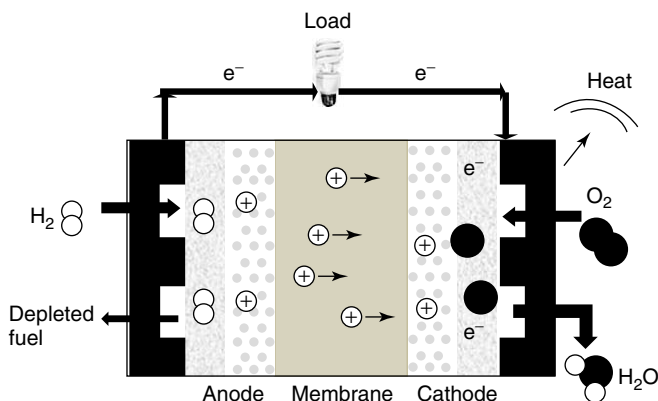


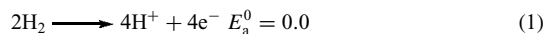
Figure 2 Schematic cross section of a fuel cell showing bipolar plates with flow fields, gas diffusion layers, catalyst layers in the electrodes, and the membrane in the center

carbon support, and a gas diffusion layer (GDL). The GDL is porous to permit gas permeation and water flow while at the same time conducting electrical current. The fuel on the anode side and oxygen on the cathode side flow through channels in bipolar plates that also serve as electrical conductors. Several such cells are connected in series to produce a fuel cell stack. Besides the reliable generation of electricity from chemical energy, water management and heat extraction are important concerns in designing a fuel cell stack.

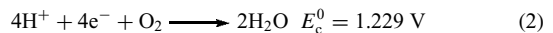
The membrane and electrodes are collectively known as the *membrane-electrode assembly (MEA)* and constitute the key component of the PEMFC that has a major influence on cost and durability. Hydrogen dissociates into protons and electrons on the anode side. The protons travel through the PEM, while the electrons are conducted by an external

circuit through a load to produce the current output of the fuel cell. At the cathode side, the relatively inefficient oxygen reduction reaction takes place. The half-cell reactions are as follows:

Anode:



Cathode:



The overall reaction is



Here, E_a^0 and E_c^0 are the standard anode and cathode potentials. The reversible open circuit voltage of the fuel cell, also known as the *Nernst voltage*, is 1.229 V. A typical PEMFC produces about 0.6–0.7 V under load with the voltage decreasing as current increases due to activation losses in the catalysts layer, ohmic losses, and mass transport inefficiencies.

The membrane has to perform reliably at elevated temperature, in a highly acidic environment, with oxidizing conditions on one side and highly reducing conditions on the other, and under a potential gradient. Several recent reviews have examined the current state of PEM development, transport properties, and durability of membranes.^{4–9} Ideally, the PEM should have excellent proton conductivity and poor electron conductivity. In addition, it should act as a barrier for the reactant gases and must not allow fuel, such as methanol, to cross over from one side of the cell to the other. The PEM must be compatible with electrode materials and must maintain dimensional stability during operation despite significant changes in humidity

levels. Good mechanical strength and chemical stability are needed to ensure durability for at least 5000 h of operation. Low membrane cost is essential for commercial viability. According to a recent cost analysis, the MEA accounts for about 83% of the cost of the stack and nearly 50% of the overall system cost for an 80-kW PEMFC unit for transportation.¹⁰ Assuming high-volume production of 500 000 units, the system cost is projected to be \$108 per kW, which is well above the United States Department of Energy (DOE) target of \$30 per kW for the year 2015. There is a need to develop durable and inexpensive membranes, because none of the known PEMs meets all the requirements listed above.

2 PERFLUORINATED SULFONIC ACID MEMBRANES

2.1 Nafion® Membrane Characteristics and Challenges

PEM technology was developed initially by Thomas Grubb and coworkers at the General Electric Company in 1959. Sulfonated polystyrene membrane was initially used as the electrolyte. This was replaced by Nafion®, which has since become the most extensively studied PEM. This polymer, developed by DuPont Inc, has a tetrafluoroethylene (Teflon) backbone and a pendant of perfluorovinyl ether groups terminated with sulfonate groups. The chemical structure of Nafion is shown in Figure 3. By varying x , y , and z one can change the structure and properties of Nafion. Typical values of x and y are 7 and 1, respectively, while z , which is typically 1, can be varied to control the side-chain length. The molecular weight of Nafion is not well known and membranes are described by the thickness and equivalent weight (EW), i.e., weight of the polymer per mole of sulfonate. Thus, Nafion 115 stands for 1100 g EW and thickness of 0.005 in. (127 µm).

Nafion is an excellent proton conductor at 75 °C and 100% relative humidity (RH) and has good chemical and mechanical stability. However, it is expensive, performs poorly at temperatures above 80 °C and low relative humidity (80% RH), requires water to conduct protons, and allows methanol to cross over in direct methanol fuel cells (DMFCs). Moreover, physical and chemical degradation is a performance-limiting factor in perfluorinated sulfonic acid

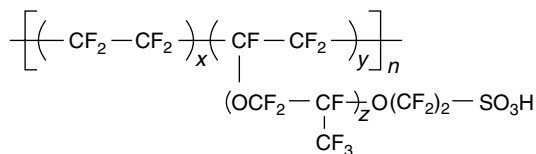


Figure 3 Chemical structure of Nafion

(PFSA) membranes, especially under dry conditions and load cycling.⁹

The indispensable role of water in PFSA membranes is due to the fact that water molecules help dissociate the proton from the SO₃H groups and also enable proton transport through the membrane. The H₂O molecules can act as shuttles for vehicular proton transport and at high RH they can form a water wire along which the proton can hop by the Grotthuss mechanism of structural diffusion.¹¹ Proton hopping between water molecules is illustrated in Figure 4 using the rather simple case of the Zundel ion (H₂O···H···OH₂)⁺ as intermediary. It is known that even in bulk water, the transport of protons by structural diffusion is a complex process that involves solvent fluctuations leading to an interconversion between the limiting structures of the Eigen ion, H₃O⁺, (H₂O)₃, and the Zundel cation.¹² Since structural diffusion that is enabled by high hydration levels is a much more

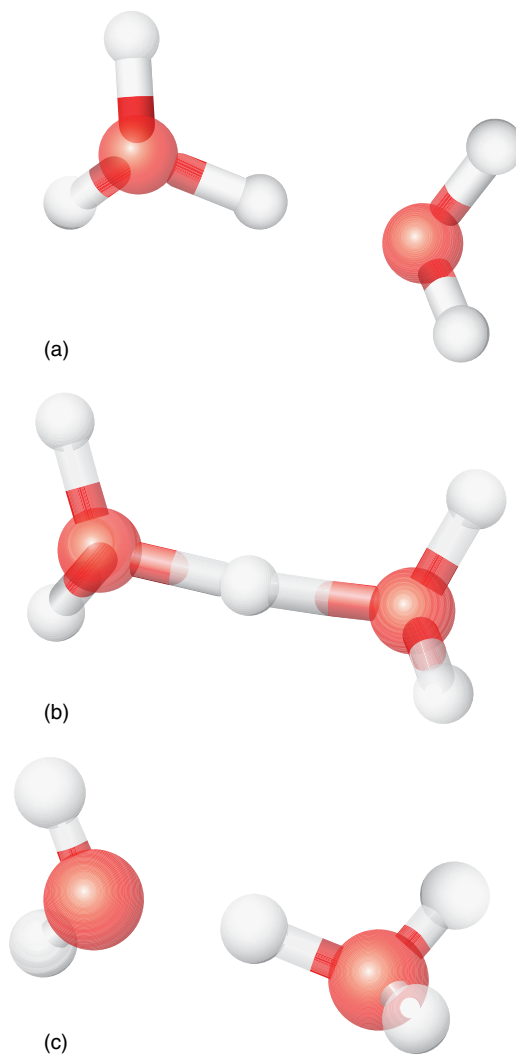


Figure 4 A sequence of configurations showing proton hopping from left (a) to right (c) by formation of a Zundel ion (b)

Table 1 United States Department of Energy technical targets for PEMs for the year 2010. (Reproduced from Ref. 14. © Elsevier, 2007.)

Properties	Target
Operating temperature	$\leq 120\text{ }^{\circ}\text{C}$
Inlet water vapor partial pressure	$\leq 1.5\text{ kPa}$
Membrane conductivity at operating temperature	$—$
at room temperature	0.10 S cm^{-1}
at $-20\text{ }^{\circ}\text{C}$	0.07 S cm^{-1}
Oxygen crossover	2 mA cm^{-2}
Hydrogen crossover	2 mA cm^{-2}
Cost of membrane	\$20 per m^2
Durability with cycling for operation below $80\text{ }^{\circ}\text{C}$	$—$
For operation above $80\text{ }^{\circ}\text{C}$	5000 h
Minimum unassisted start temperature	$-40\text{ }^{\circ}\text{C}$
Thermal cycling in presence of condensed water	Yes

effective proton-transport mechanism than vehicular diffusion and the protons are likely to be bound to the sulfonate group at low RH,⁷ proton conductivity of PFSA membranes increases appreciably with hydration level.¹³

The dependence of Nafion membrane performance on the presence of water creates operational challenges. First, the operating temperature is restricted to be below $100\text{ }^{\circ}\text{C}$. Higher temperature operation has the potential to bring down cost by enhancing electrochemical reactions and minimizing catalyst poisoning (see *Molecular Catalysis for Fuel Cells*). Second, the H_2O molecules are dragged by the protons as they travel across the membrane. This phenomenon, known as *electroosmotic drag*, floods the cathode and blocks the pores in the GDL. At the same time, the anode becomes dry with a detrimental effect on conductivity. In addition to degradation of membrane performance, the membrane is also subjected to mechanical stresses as a result of swelling and shrinkage. The use of an external water management system to regulate membrane hydration increases system volume, weight, complexity, and cost, and decreases efficiency. In an effort to overcome these limitations, the DOE has set stringent technical targets for PEMs as shown in Table 1.¹⁴ Of these targets, performance at elevated temperature and low humidity, and durability with cycling at elevated temperatures are the most elusive.

2.2 Morphology of Nafion and Molecular Transport

Considerable experimental effort has been devoted to the study of Nafion membrane morphology, proton and water transport, mechanical behavior, and durability. The experimental techniques employed include nuclear magnetic resonance (NMR), infrared (IR) spectroscopy, dielectric relaxation spectroscopy, electron spin resonance spectroscopy, alternating current impedance spectroscopy, small-angle neutron scattering (SANS), small-angle X-ray scattering

(SAXS), transmission and scanning electron microscopy, atomic force microscopy, differential scanning calorimetry, and dynamic mechanical analysis. The task of characterizing PEMs is challenging, because there is a hierarchy of scales in the hydrated membrane starting with the molecular level of proton transfer to the macroscopic scale, and the membrane morphology is influenced by processing conditions, thermal history of the membrane, and hydration level.

Data from SANS and SAXS experiments have been used as the basis to develop models of hydrated PEM morphology. Nafion has a phase-separated structure that consists of nanoscale hydrophilic domains that enable proton transport and hydrophobic regions that offer mechanical support and contribute to durability. One of the most widely cited models of Nafion is the cluster network model.¹⁵ It considers the hydrophilic region of Nafion to be made of spherical ionic clusters of 3–5-nm diameter with an inverse micelle structure. These clusters are assumed to be periodically repeated and interconnected by narrow water channels of 1-nm width. Changes in the relative humidity cause changes in the cluster size and the water content of clusters. The assumption of periodic clusters is simplistic, and models based on elongated structures, as opposed to spherical clusters, provide a better fit to the SAXS data. The original authors did not propose this as the definitive model of Nafion and recognized the need for refinement. Periodicity was assumed for ease of calculation and the 1-nm channels were included to account for the percolation of water through the membrane.⁶

Several other models of Nafion have been discussed in detail by Mauritz and Moore.⁶ In order to reconcile with experimental evidence in favor of elongated structures, cylindrical or ribbonlike polymer aggregates and layered structures with hydrophilic domains sandwiched between hydrophobic regions have been proposed. Recently, it has been shown that none of these elongated models can provide a reasonable match to experimental SAXS data.¹⁶ On the basis of a detailed analysis of published SAXS data, a new model of hydrated Nafion based on parallel cylindrical water channels has been proposed.¹⁶ This model considers cylindrical water channels with diameter of 1.8–3.5 nm and persistence length of more than 20 nm as shown in Figure 5(a). The cylinders have an inverted micelle structure and are stabilized by the stiff polymer backbone. Hydrophilic groups line the cylinders, which are considered to be packed as shown in Figure 5(b). Crystallites are included in the model and considered to run parallel to the water channels as shown in Figure 5(c). The model can account for methanol permeation and electroosmotic drag of water in Nafion. While this model can explain the behavior of fully hydrated Nafion, it may not provide a good representation of Nafion under low-humidity conditions.

One of the successes of the parallel cylindrical model of Nafion is that it can explain the occurrence of water diffusion and proton conduction in Nafion even at subfreezing temperatures, because water in the narrow channel is unlikely

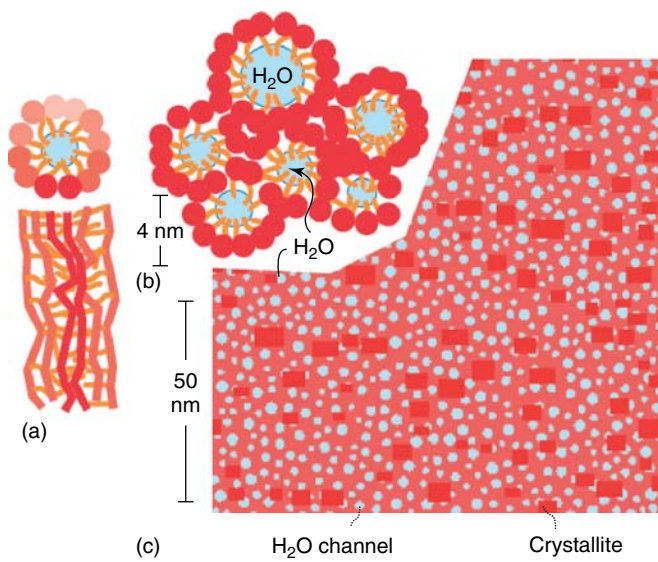


Figure 5 Parallel cylindrical water channel model¹⁶ showing (a) a cylindrical channel, (b) packing of cylinders, and (c) distribution of water channels and crystallites. (Reproduced from Ref. 16. © Nature Publishing Group, 2008.)

to freeze. In fact, only a fraction of the water that exists in Nafion freezes like bulk water. It is difficult to experimentally quantify this fraction, especially as it varies with hydration level. This is where realistic molecular modeling can aid in the interpretation of experiments. Devanathan *et al.*¹⁷ have performed molecular dynamics simulations of hydrated Nafion at 300 K and identified three classes of water molecules whose relative proportions as a function of hydration level are shown in Figure 6. The hydration level (λ) is defined as the ratio of the number of water molecules to the number of sulfonate groups. The bound or nonfreezing water is associated with sulfonate groups, while the freezing water has a coordination environment that is similar to that of bulk water. The weakly bound water does not fall into either of these classes. At all hydration levels, more than a third of the water present in Nafion is nonfreezing. Although the proportion of nonfreezing water declines with increasing hydration level, the number of nonfreezing water molecules increases with increasing hydration, because the total number of water molecules is more at higher hydration levels.

The changes that take place in the distribution of water in Nafion with hydration level are shown in Figure 7 based on molecular dynamics simulations. The polymer is shown in gray and water molecules are illustrated in red. At a low hydration level of $\lambda = 3$, small isolated water clusters are present and they are mostly located in close proximity to the sulfonate groups as shown in Figure 7(a). As the hydration level increases, these clusters increase in spatial extent and some of the water molecules are also free to migrate from cluster to cluster. At a critical hydration level, the water molecules form a percolating network that

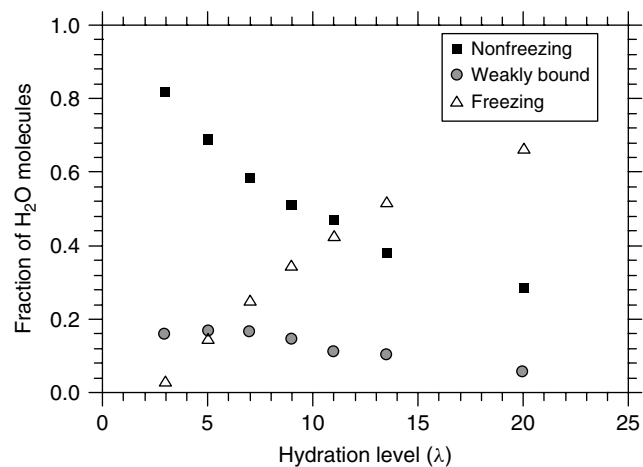


Figure 6 Relative fractions of water molecules in the nonfreezing, weakly bound and freezing states in Nafion as a function of hydration level

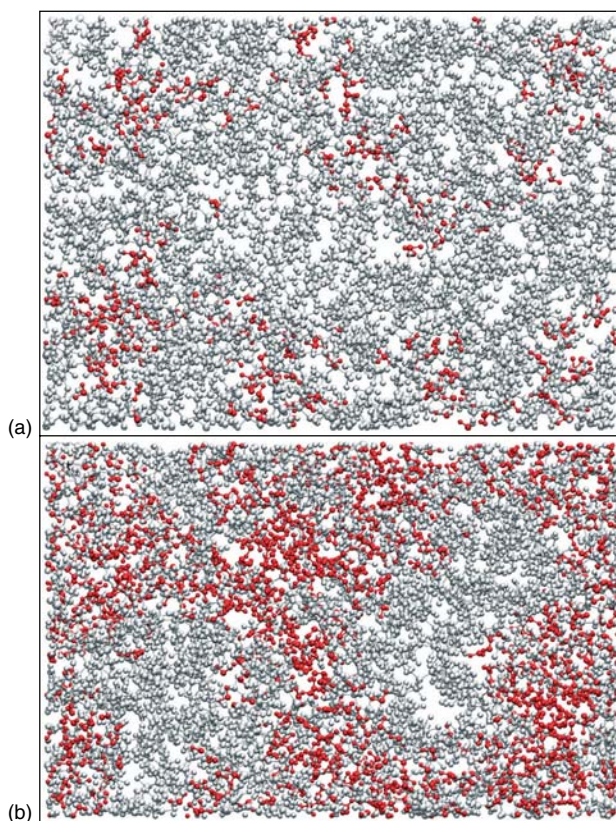


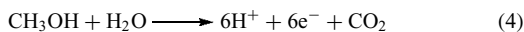
Figure 7 Simulated structure of Nafion for hydration levels of (a) $\lambda = 3$ and (b) $\lambda = 11$. The water molecules are shown in red, while the membrane is shown in gray. Percolation of water clusters is evident at the higher hydration level

spans the membrane. In Figure 7(b), the network of water molecules is quite evident at a hydration level of $\lambda = 11$.

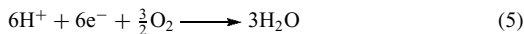
The water network is not a static wire, but a dynamic entity whose shape can change as the water molecules migrate. It is easy to see how protons can hop across such a network in a manner similar to the transport of a bucket along a bucket brigade. The formation of this network can drastically improve conductivity as seen from experimental measurements of conductivity as a function of hydration level.¹³ The picture of water clustering obtained from molecular modeling is quite consistent with experimental findings. IR spectroscopy studies¹⁸ of Nafion show that an abrupt structural change takes place in Nafion membrane around $\lambda = 5$. But the nature of this structural transition is not clear from experiments. By using molecular modeling in conjunction with experiments, one can infer that this transition corresponds to the coalescence of isolated water clusters to form a proton-transport network.

In addition to water transport through Nafion, methanol crossover is also of great interest for DMFCs. In a DMFC, liquid methanol is oxidized at the anode and oxygen reduction takes place at the cathode. The half-cell reactions are as follows:

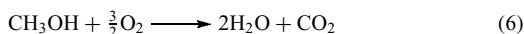
Anode:



Cathode:



The overall reaction is



The Nernst voltage for the DMFC is 1.18 V. The cell efficiency is decreased by the slow kinetics of catalytic oxidation of methanol and by fuel crossover. One strategy to minimize crossover is to use low concentrations of methanol (1–2 M and 4–8 vol %), but this has the undesirable consequence of limiting cell potential.¹⁹ These issues have led to the development of the direct formic acid fuel cell (DFAFC) with Pd supported on porous carbon as anode catalyst. Formic acid is nontoxic, has lower crossover through Nafion compared to the crossover of methanol, and offers a high Nernst voltage of 1.45 V. Owing to low crossover, higher formic acid concentrations (15 M) and thinner membranes can be used and high power densities can be achieved. Much work remains to be done in evaluating the long-term performance characteristics of membranes in DFAFCs. Membrane dehydration is a concern when a high concentration of formic acid is used.

It is known from experiment and molecular modeling studies⁷ that proton conduction in hydrated PEMs is governed by phenomena that occur over multiple length and timescales. At the molecular level, conductivity originates from proton dissociation from the acidic group, which is sulfonic acid in Nafion, and subsequent proton transfer to water molecules. At the nanoscale, hydrogen bonds form dynamically between water molecules to create a

percolating network for proton transport. At a larger scale, the flexibility of the polymer backbone and motion of side chains influence water uptake, methanol permeability, fuel crossover, and mechanical behavior. Most efforts to improve on the performance of the benchmark set by Nafion membrane have involved control of these processes to achieve the desired results. For instance, a recent study¹⁶ suggested that polymers with flexible backbones and stiff side chains, such as aromatic polymer membranes, would have narrower water channels resulting in lower methanol permeation.

2.3 Short Side-Chain PFSA Membranes

One of the simplest modifications of Nafion is to shorten the length of the side chain by setting $z = 0$ in Figure 3. This results in a decrease in the EW of the membrane. A membrane with lower EW has a higher density of acidic groups, which is desirable strictly from the proton-conductivity standpoint. However, low-EW membranes have higher swelling and lower durability. A PEMFC using a short side-chain (SSC) membrane with an EW of 800–900, compared to 1100 for Nafion, developed by the Dow Chemical Company has produced 4 times the power as Nafion membrane at the same operating voltage.²⁰ Owing to the high density of sulfonic acid groups, the Dow membrane has lower membrane resistance. This permits operation at higher voltage and lower current densities (0.1–0.5 A cm⁻²). A similar membrane of about 850 EW, Hyflon, has been developed by Solvay Solexis Inc.²¹ Other Nafion-like membranes include Flemion® (Asahi Glass Co. Ltd), Aciplex® (Asahi Chemical Co. Ltd.), and 3M membrane (3M Inc.). Aciplex has a longer side chain than Nafion. A comparison of the side-chain structure of various Nafion-like membranes is shown in Figure 8. For a given EW, SSC membranes possess higher crystallinity and a higher glass transition temperature compared to Nafion. These characteristics can lead to higher operating temperature and better mechanical properties for SSC membranes. PEMFCs with SSC membranes could potentially operate in the 80–100 °C temperature range.

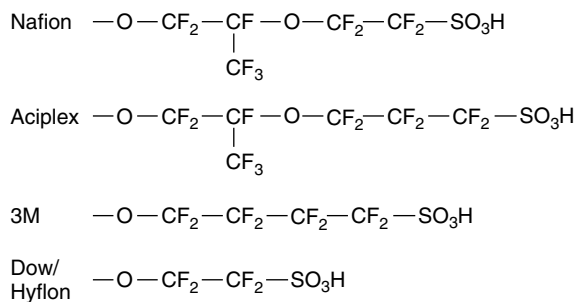


Figure 8 Comparison of the side chains of Nafion-like membranes

A recent study²² has systematically compared proton conductivity, water sorption, diffusion and electroosmotic drag, morphology, and viscoelastic properties of Dow 858 (EW 858 and thickness ~80 µm), Dow 1084 (EW 1084 and thickness ~90 µm), and Nafion 117 (EW 1100 and thickness ~175 µm) membranes. While the water diffusion coefficient is comparable for all the membranes at a high hydration level ($\lambda > 15$), it is higher for the Nafion membrane at low hydration due to the greater flexibility of the long side chain of Nafion. The proton conductivity also follows a similar trend with Nafion showing better proton conductivity at low hydration levels ($\lambda < 5$) and Dow 858 showing better conductivity than Nafion 117 at high hydration levels. No significant differences were seen in electroosmotic drag and methanol crossover. Since the Nafion membrane was thicker than the Dow membranes in this study, it is not clear what role thickness plays in the observed differences. The relationship between side-chain length and membrane performance is not well established and requires further study.

2.4 Composite PFSA Membranes

Composite PFSA membranes contain reinforcements for mechanical strength or inorganic fillers in the polymer matrix for improved water retention at elevated temperatures. The use of reinforcements can improve durability and hygroscopic fillers can help improve conductivity for operation at low humidity. The operation of a DMFC at 145 °C with power density of 0.24 W cm⁻² has been demonstrated using a Nafion–silica composite membrane.²³ The use of a composite in place of a regular Nafion membrane was observed to improve water retention and reduce methanol crossover. It is believed that the hydroxyl groups attached to the surface of silica particles bind water molecules and help form a hydrogen-bonded network for proton transport. PEMFC operation at 130 °C has been sustained for 50 h without performance loss using a Nafion 115–silica composite membrane with 6 wt % silica loading.²⁴ Under similar conditions, PEMFC operation with a Nafion 115 membrane resulted in failure in less than 1 h. The hydration level in the composite membrane at 130 °C and 3 atm was comparable to that in Nafion 115 at 80 °C and 1 atm. By using a composite membrane, there is the potential to raise the operating temperature by 50 °C without significant decrease in current density. This can speed up electrochemical reactions and minimize CO poisoning of the catalyst from impurities in the fuel.

It is important to note that filler size can have a major influence on the performance of composite membranes. Small silica nanoparticles of average size around 3 nm have been found to be effective in forming a hydrogen-bonded network.²⁵ Much larger silica particles were found to disrupt the formation of a hydrogen-bonded network and thus impede proton transport through the membrane. In addition to silica particles, mesoporous silica containing sulfonic acid groups have also been incorporated in Nafion membranes to reduce swelling

and improve proton conductivity at elevated temperature. The key characteristic appears to be high surface area to improve water uptake and retention.

Since water retention at elevated temperature and water management at low temperature are key challenges, it would be worthwhile to develop durable self-humidifying PEMS. This concept has been demonstrated²⁶ using a composite membrane consisting of Nafion 112 with a uniform distribution of TiO₂ and Pt nanoparticles produced by *in situ* reactions. The Pt nanoparticles suppress fuel crossover by catalytic recombination of H₂ and O₂, while TiO₂ nanoparticles adsorb the water produced by the cathode reaction and by Pt nanoparticles. A PEMFC based on this membrane has been operated to produce peak power of 0.78 W cm⁻² at 80 °C and ambient pressure in dry H₂ and O₂ after drying the cell overnight with dry N₂. No external humidification was used. Water balance between the cathode and anode was achieved owing to enhanced back-diffusion of H₂O molecules generated at the cathode.

Nafion/sulfated zirconia nanocomposites have shown improved water uptake and proton conductivity compared to Nafion membrane. Composites of Nafion with alumina, zeolites, and RuO₂ have also been studied. Nanoparticles of superacidic inorganic oxides, such as 12-phosphotungstic acid (H₃PW₁₂O₄₀ or PTA) and 12-silicotungstic acid (H₄SiW₁₂O₄₀ or STA), can be incorporated as nanoparticles in Nafion to improve proton conductivity. MEAs with Nafion–PTA composite membranes have been tested at 120 °C at 35% RH.²⁷ The influence of heteropolyacids on proton transport is not well understood. There is a need to understand the fundamental mechanisms governing the interaction of fillers with the membrane and water to optimize filler particle size, composition, and loading. Zirconium phosphate has been used as a reinforcing filler in Nafion. These particles do not directly influence proton transport but serve as mechanical supports that maintain dimensional stability when the humidity level changes drastically. The use of such scaffolds can help improve membrane durability with load cycling.

Since mechanical strength appears to hold the key to enhanced durability, there is growing interest in reinforced membranes. Gore Select is a commercially available reinforced membrane developed by W. L. Gore and Associates. It is made of Nafion reinforced with a layer of polytetrafluoroethylene (PTFE). The micreinforcement concept is employed in that microporous PTFE sheets are impregnated with Nafion. These membranes offer better dimensional stability, mechanical strength, and water management than unreinforced Nafion. Nafion XL is a new reinforced and chemically stabilized membrane from DuPont Fuel Cells that offers much improved tensile strength, dimensional stability and lifetime, and reduced fluoride emissions during operation compared to unreinforced Nafion. Composite membranes made by impregnating Solupor®, a microporous ultrahigh-molecular weight polyethylene film, with Nafion 117 have been tested in DMFCs.²⁸ The advantages

of this membrane are good dimensional stability, low methanol crossover, and the ability to use a thinner membrane. By reducing thickness, one can improve performance and efficiency of the fuel cell.

Impregnation of Nafion with ionic liquids (ILs) is a novel strategy to use Nafion above 100 °C.²⁹ 1-Hexyl-3-methylimidazolium tris(pentafluoroethyl) trifluorophosphate (HMI-FAP), HMI-bis trifluromethylsulfonyl imide (BTSI), 1-butyl-3-methylimidazolium tetrafluoroborate (BMI-BF₄), 1-butyl-1-methylpyrrolidinium-FAP (BMPyr-FAP), and BMPyr-BTSI are some of the ILs that have been studied. ILs with hydrophobic anions such as FAP appear to penetrate the Nafion membrane better and are shielded effectively from water, thereby minimizing the washout of IL by water generated at the cathode. The impregnated membranes show lower swelling, higher breaking strain, and higher proton conductivity at 120 °C compared to Nafion 117. ILs based on bulky and hydrophobic anions such as FAP, (CF₂CF₃)₃F₃P⁻, seem to show the most promising performance improvements when incorporated into Nafion.

3 NOVEL PROTON EXCHANGE MEMBRANES

3.1 Polystyrene Sulfonic Acid-Based Membranes

Polystyrene sulfonic acid (PSSA) membranes have been developed as less expensive alternatives to PFSA membranes. Fuel cells have been operated using a partially fluorinated PEM based on trifluorostyrene and the durability of the membranes has been demonstrated. The chemical structure of a PSSA membrane, known as BAM3G (*Ballard Advanced Materials 3rd Generation*), is shown in Figure 9. Unlike PFSA membranes or the composite membranes with oxide or heteropoly acid fillers, very little information is available about the chemical composition, morphology, conductivity, and chemical stability of BAM membranes.

A recent study³⁰ has compared the performance of BAM membranes with EW of 407, 436, 455, 509, 542, and 735 with the performance of Nafion 117 membrane. BAM membrane with EW of 509 offers optimum conductivity of 0.17 S cm⁻¹ at 30 °C at a water content of 55.9 vol % ($\lambda = 33$). The EW influences water uptake, which in turn

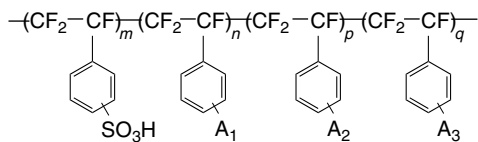


Figure 9 Chemical structure of α,β,β -trifluorostyrene membrane. A₁, A₂ and A₃ are chosen from the following groups: FC=CF₂, CN, NO₂, OH, O—C_xH_yF_z (where $x > 3$ and $y + z = 2x + 1$) and aryls

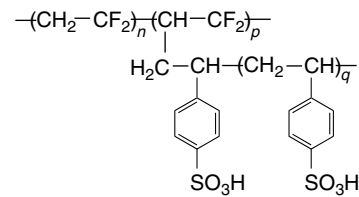


Figure 10 Chemical structure of radiation-grafted PVDF-g-PSSA membrane

affects membrane performance. BAM membranes with EW lower than 509 have large uptake (up to $\lambda \sim 100$), which results in lower conductivity because of the dilution of acidic groups. At higher EW, the water uptake is poor and there are not enough water molecules to form a proton-conducting network. The styrenic side chains of BAM membranes, shown in Figure 9, are more rigid than Nafion side chains, which inhibits the aggregation of ionic sites. Phase separation into hydrophilic and hydrophobic domains is also not as well developed in BAM membranes as in Nafion membranes. The proton-conductivity mechanism in BAM membranes is not well understood and much of the water may not be associated with ionic aggregates.

Novel PEMs based on PSSA have been prepared by the radiation grafting technique. γ -Radiation has been used to graft PSSA to polyvinylidene fluoride (PVDF).³¹ The chemical structure of the PVDF-g-PSSA membrane is shown in Figure 10. At low hydration level, the hydrophilic network is not well developed, leading to poor proton conductivity. Increasing the density of the hydrophilic pendants by increasing the ion exchange capacity enhances the hydrophilic network and increases the content of free water. The proton conductivity increases, but the methanol crossover also increases. In general, graft copolymers are considered to have more highly concentrated, isotropically connected ionic domains and a more cohesive hydrophobic matrix that resists swelling compared to diblock polymers of the same composition.

3.2 Hydrocarbon Membranes

Aromatic hydrocarbon-based membranes have been proposed as alternatives to PFSA-based membranes for elevated temperature use. Hydrocarbon membranes offer the advantages of low cost, ease of processing, ability to tune the chemistry, and mechanical, thermal, and oxidative stability. Rigid polymers unsuited for PEM applications are produced by linked benzene rings. Ether links are added to benzene rings to obtain flexibility and oxidative stability. Poly(ether ether ketone) (PEEK), poly(ether sulfone) (PES), sulfonated polyimide, and poly(benzimidazole) (PBI)-based membranes are some of the leading candidates among hydrocarbon membranes to replace Nafion. Sulfonation of the hydrocarbons serves to improve proton conductivity.

Kreuer³² has compared the morphology of Nafion and sulfonated poly(ether ether ketone) (SPEEK) by analyzing data from SAXS experiments. SPEEK has a more rigid backbone and the water channels are expected to be narrower with many dead-end channels compared to the case of Nafion. The combination of poorer connectivity of water clusters and larger distance between sulfonate groups results in lower proton conductivity in SPEEK than in Nafion. The proton conductivity of SPEEK also falls off drastically as the humidity level is lowered. One can attain proton conductivity on par with Nafion by increasing the ion exchange capacity, but this results in excessive swelling due to water uptake and poor mechanical stability. Blending with other polymers and cross-linking are some of the strategies to overcome the shortcomings of the SPEEK membrane.

Low-cost sulfonated poly(ether ketone)s (SPEKs) have been synthesized with phenyl, methylphenyl, trifluoromethylphenyl, and phenoxyphenyl groups.³³ The sulfonic acid group can be attached to the main chain or a side group. Postsulfonation of polymers is simple, but lacks good control over degree of sulfonation (DS) and produces random location of sulfonic acid groups in the polymer chain. Direct copolymerization of sulfonated monomers with nonsulfonated monomers yields better control over DS and the location of sulfonic acid groups. For instance, the DS can be varied by polymerization of bisphenol monomer with phenyl ketone monomers of different lengths. In other words, one can vary the DS by changing the ratios of segments that are sulfonated and segments that are not sulfonated. One of the promising PEEK membranes is phenylated sulfonated poly(ether ether ketone diphenyl ketone) or Ph-SPEEKDK. The chemical structure is shown in Figure 11. Ph-SPEEKDK has higher tensile strength than Nafion 117 in both wet and dry conditions, is flexible, and has good oxidative stability, dimensional stability, and conductivity. The conductivity was improved and methanol permeability reduced further by choosing a methylphenylated version of the above PEEK, Me-SPEEKDK, which is shown in Figure 12. The methanol permeability of Me-SPEEKDK is less than that of Nafion 117 by a factor of about 16. The proton conductivity of Me-SPEEKDK was roughly 60% of that of Nafion 117 at 100 °C. Extensive fuel cell performance tests are needed to thoroughly evaluate these membranes.

Since conductivity and mechanical strength are two desired properties, there is considerable ongoing research in the area of synthesis of thermally stable hydrophilic–hydrophobic multiblock copolymers.³⁴ These copolymers have a hydrophilic block with sulfonic acid

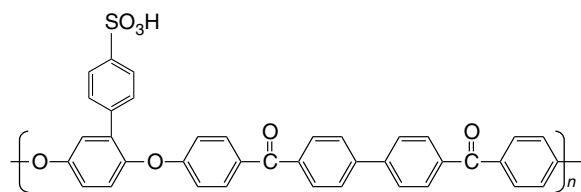


Figure 11 Chemical structure of Ph-SPEEKDK

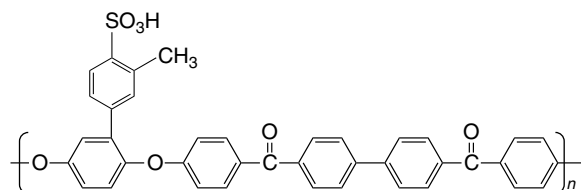


Figure 12 Chemical structure of Me-SPEEKDK

groups to facilitate proton conductivity and a hydrophobic block to offer mechanical strength and thermal stability. The characteristics of the membrane can be varied by controlling the chemistry and relative lengths of the blocks. BPSH-XX, shown in Figure 13, is a copolymer that is made of bisphenol-based wholly aromatic random poly(arylene ether disulfonated sulfone)/poly(arylene ether sulfone). The notation XX refers to the mole fraction of disulfonated monomer. The DS can be increased by increasing XX, and this increases water uptake and conductivity at the expense of mechanical stability. Composite membranes of BPSH-40 have been prepared by this group with zirconium hydrogen phosphate filler by in situ precipitation. The effect of including the filler was to stabilize membrane swelling and reduce methanol permeability. The addition of phosphotungstic acid to BPSH membranes has also been observed to reduce swelling without detrimental effect on proton conductivity. Composite membranes have been synthesized with proton conductivity of 0.15 S cm⁻¹ at 130 °C.

The McGrath group has recently synthesized a multiblock copolymer, 6FK-BPSH, with tailored backbone structure.³⁵ The chemical structure of 6FK-BPSH is based on a hydrophobic fluorine-terminated poly(arylene ether ketone) block and a hydrophilic disulfonated poly(arylene ether sulfone) block as shown in Figure 14. The molecular weight of the two blocks is nearly the same to establish good connectivity between hydrophilic domains even at low

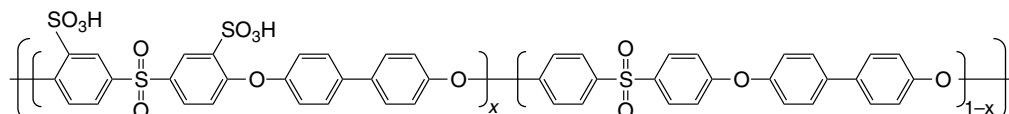


Figure 13 Chemical structure of BPSH-xx

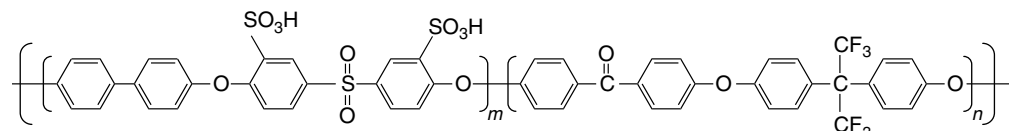


Figure 14 Chemical structure of 6FK-BPSH

hydration levels. While the proton conductivity of 6FK-BPSH was comparable to that of Nafion 112 over a wide range of RH and temperature, there is a need to develop compatible electrode materials to enhance the fuel cell performance of these novel membranes.

3.3 Anhydrous Membranes

Water-free membranes that operate reliably at about 120 °C can revolutionize PEMFC technology by alleviating concerns about catalyst poisoning and water management. Anhydrous membranes may contain some water as a by-product from fuel cell operation, but are expected to function above 100 °C without external humidification. Initial efforts to develop anhydrous membranes focused on using a proton solvent that has a higher boiling point than water. Such solvents include imidazole and phosphoric acid. Fuel cells based on membranes containing imidazole were not successful because of Pt catalyst poisoning by imidazole. Polymers with imidazole tethered to a polysiloxane backbone have been examined, but the proton conductivity is poor ($\sim 1.5 \times 10^{-3}$ S cm $^{-1}$ at 160 °C).³⁶

PBI doped with phosphoric acid (H₃PO₄) has been studied for PEMFC operation above 120 °C. The weak acid forms a proton-transport network to provide conductivity in the absence of water. Basic polymers infused with acids suffer from a host of problems including acid leaching from the membrane, adsorption of anions on catalysts, and corrosion of cell components. One has to make a compromise between poor conductivity at low acid doping levels and poor mechanical strength at high doping levels. The presence of water produced at the cathode can help proton transport by enhancing the acid dissociation. Durability of the MEA is a key challenge for the PBI–H₃PO₄ system.

A second approach to develop anhydrous membranes is based on a protic ion liquid (PIL)/polymer matrix gel membranes. PILs are low-melting analogs of molten salts and feature proton transfer from a Brønsted acid to a Brønsted base. They are of great interest from the point of view of green chemistry. PILs generally melt below 100 °C, are nonvolatile, and environmentally benign. Some of the PILs being studied include 1-methyl-3-propyl-methylimidazolium dihydrogen phosphate, trifluoroacetic propylamine (TFAPA), and diethylmethyl amine-trifluoromethane sulfonic acid (dema-TfOH), which is one of the most promising PILs for anhydrous membranes.³⁷ Proton transport in dema-TfOH

is believed to occur by vehicular transport of the dema. Dema-TfOH remains in the liquid state over a wide temperature range and has good thermal stability. Rigorous fuel cell performance tests are needed to evaluate the true potential of PIL-based membranes.

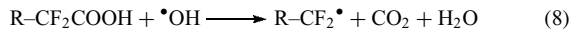
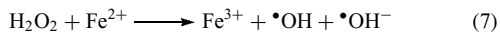
Nonpolymeric electrolytes have also been investigated for use as anhydrous PEMs that can operate in the temperature range 200–300 °C. Cesium dihydrogen phosphate, CsH₂PO₄, is a solid acid that conducts protons above the superprotic transition temperature (230 °C). Solid acid fuel cells with 25-μm-thick CsH₂PO₄ membrane have been fabricated and operated at 240 °C with a peak power density of 0.41 W cm $^{-2}$.³⁸ Cells with 260-μm-thick membranes have been tested for 100 h. Solid acid fuel cells have the advantage that they require a smaller loading of precious metal catalysts compared to conventional polymer membrane fuel cells.

4 DEGRADATION OF PROTON EXCHANGE MEMBRANES

Degradation of PEMFC components has been thoroughly reviewed by Borup *et al.*⁹ Most fuel cell life tests have been performed under steady-state conditions typically at a temperature of about 80 °C. Both Nafion 117 and BAM3G have survived such fuel cell tests for over 10 000 h of operation. PSSA membranes other than BAM3G have been shown to have shorter lifetime and radiation-grafted membranes also show limited durability. Sulfonated polyimides, SPEEK membranes, and phosphoric acid-doped PBI membranes have all been demonstrated to have a lifetime of at least 1000 h.⁹ The lifetime is dependent on the membrane thickness and the fuel cell operating conditions, such as temperature, pressure, and relative humidity. Operation at temperatures above 100 °C and at low humidity limits membrane lifetime. Membrane thinning, increased fuel and gas crossover, pinhole formation, chemical decomposition, embrittlement, creep, fatigue, and microcracking are some of the failure modes observed in PEMs.

Oxygen molecules diffusing through the membrane can form hydrogen peroxide at the anode catalyst layer, which in turn gives rise to hydroperoxy ($\bullet\text{OOH}$) and hydroxyl ($\bullet\text{OH}$) radicals that can attack the polymer membrane. The presence of Fe²⁺ from the end plates is known to greatly enhance the degradation of the membrane.⁹ In PFSA membranes, radical

attack at the end sites initiates decomposition into HF, CO₂ and low-molecular-weight compounds. This attack is especially enhanced if the backbone is incompletely fluorinated or contains the carboxylic end group.³⁹ The reactions that occur are^{9,39}



As we proceed from reaction (8) to (11), we note that R-COOH is regenerated so that reaction (8) can start all over again in the presence of ·OH radical. This depolymerization is referred to as the *unzipping mechanism*.⁹ For this reason, a common accelerated ex situ durability test for membranes is the Fenton's reagent test (H₂O₂ containing a few parts per million of Fe²⁺). However, it is not clear how the results of Fenton's reagent test relate to lifetime under fuel cell operation, and how the tests are to be interpreted across different membrane classes, especially non-PFSA membranes. While the test is a good measure of chemical degradation of PFSA membranes, it must be remembered that it does not include mechanical and thermal effects on degradation.

Strategies to improve chemical durability of membranes include dispersion of Pt nanoparticles in the membrane²⁶ to convert permeating H₂ and O₂ to H₂O, incorporation of heteropoly acids in the membrane⁴⁰ to decompose peroxide to water, and the incorporation of CeO₂ nanoparticles⁴¹ in the membrane to scavenge free radicals. Incorporation of Pt nanoparticles along with hygroscopic TiO₂ nanoparticles have been shown to self-humidify Nafion at 80 °C.²⁶ A 10 wt % loading of α-H₃P₂W₁₈O₆₂ or H₆P₂W₂₁O₇₁ or 20 wt % loading of H₄SiW₁₂O₄₀ in 3M PFSA membrane can drastically decrease the F⁻-ion release rate in fuel cell testing at 90 °C.⁴⁰ The fluoride emission rate in Nafion was found to be lowered by an order of magnitude without loss of performance after incorporation of ceria nanoparticles with an agglomerate size of 200 nm. The reduction in fluoride ion emission has been attributed to the known ability of ceria nanoparticles to scavenge free radicals.

In addition to chemical effects, mechanical stresses also play an important role in membrane degradation. The MEA operates under compressive stress,⁹ which can cause creep deformation, local thinning, and eventual pinhole formation, especially when combined with hydroxyl radical attack. Changes in humidity level can cause local stress concentrations that can result in microcracking. Membrane swelling and shrinking in response to changes in humidity can result in stress cycles leading to fatigue. Chemical degradation may increase the susceptibility of the membrane to creep and

fatigue. At elevated temperature, tensile strength is reduced and the synergistic thermal, chemical, and mechanical effects can accelerate membrane failure. It is not surprising that development efforts are moving toward reinforced membranes to enhance durability.

5 SUMMARY

The proton exchange membrane is the heart of PEM fuel cells, and the MEA holds the key to cost reduction and durability improvement needed to make this exciting technology viable. Important considerations in choosing membranes are proton conductivity, fuel crossover, dimensional stability, mechanical properties, resistance to degradation upon prolonged operation at elevated temperature and low humidity, behavior under load cycling, processability, compatibility with electrode materials, and cost. Nafion, despite its high cost and hydration requirement that restricts operation to 80 °C, continues to be the most widely studied membrane for fuel cells. Several promising candidates to replace Nafion, such as the BAM3G membrane, are being developed and deployed, while hydrocarbon membranes are being actively studied. At the same time, strategies based on mechanical reinforcement and nanoparticle dispersions to ward off chemical attack are being developed to enhance existing membranes. IL-based gel membranes are a futuristic technology that holds the promise of environmentally friendly, low-cost materials for fuel cells. With continuing improvements in durability and cost reduction, one can be optimistic about the commercialization of PEM fuel cell technology for stationary and transportation applications.

6 ACKNOWLEDGMENTS

This work was supported by the United States Department of Energy's (DOE) Office of Basic Energy Sciences, Chemical Sciences program under the Hydrogen Fuel Initiative at Pacific Northwest National Laboratory (PNNL). PNNL is operated by Battelle for DOE.

7 ABBREVIATIONS AND ACRONYMS

BAM3G = Ballard Advanced Materials 3rd Generation; BtU = British thermal unit; dema-TfOH = diethylmethyl amine-trifluoromethane sulfonic acid; DFAFC = direct formic acid fuel cell; DMFCs = direct methanol fuel cell; DOE = United States Department of Energy; DS = degree of sulfonation; EW = equivalent weight; FCs = fuel cells; GDL = gas diffusion layer; ILs = ionic liquids; IR = infrared; MEA = membrane-electrode assembly;

NMR = nuclear magnetic resonance; PBI = poly(benzimidazole); PEEK = poly(ether ether ketone); PEM = proton exchange membrane; PEMFCs = polymer electrolyte membrane fuel cells; PES = poly(ether sulfone); PFSA = perfluorinated sulfonic acid; Ph-SPEEKDK = phenylated sulfonated poly(ether ether ketone diphenyl ketone); PIL = protic ion liquid; PSSA = polystyrene sulfonic acid; PTFE = poly tetra fluoro ethylene; PVDF = polyvinylidene fluoride; RH = relative humidity; SANS = small-angle neutron scattering; SAXS = small-angle X-ray scattering; SPEEK = sulfonated poly (ether ether ketone); SPEKs = sulfonated poly (ether ketone)s; SSC = short side-chain; TFAPA = trifluoroacetic propylamine.

8 REFERENCES

1. G. W. Crabtree and M. S. Dresselhaus, *MRS Bull.*, 2008, **33**, 421.
2. Energy Information Administration, United States Department of Energy, <http://www.eia.doe.gov/aer/pdf/aer.pdf> (accessed in 2010).
3. F. Barbir, 'PEM Fuel Cells: Theory and Practice', Elsevier Academic Press, New York, 2005.
4. R. Devanathan, *Energy Environ. Sci.*, 2008, **1**, 101.
5. F. A. de Bruijn, V. A. T. Dam, and G. M. Janssen, *Fuel Cells*, 2008, **8**, 3.
6. K. A. Mauritz and R. B. Moore, *Chem. Rev.*, 2004, **104**, 4535.
7. S. J. Paddison, *Annu. Rev. Mater. Res.*, 2003, **33**, 289.
8. J. Roziere and D. J. Jones, *Annu. Rev. Mater. Res.*, 2003, **33**, 503.
9. R. Borup, J. Meyers, B. Pivovar, Y. S. Kim, R. Mukundan, N. Garland, D. Myers, M. Wilson, F. Garzon, D. Wood, P. Zelenay, K. More, K. Stroh, T. Zawodzinski, J. Boncella, J. E. McGrath, M. Inaba, K. Miyatake, M. Hori, K. Ota, Z. Ogumi, S. Miyata, A. Nishikata, Z. Siroma, Y. Uchimoto, K. Yasuda, K. Kimijima and N. Iwashita, *Chem. Rev.*, 2007, **107**, 3904.
10. E. J. Carlson, P. Kopf, J. Sinha, S. Sriramulu, and Y. Yang, National Renewable Energy Laboratory Subcontract Report, NREL/SR-560-39104, 2005, <http://www.nrel.gov/hydrogen/pdfs/39104.pdf>.
11. S. Cukierman, *Biochim. Biophys. Acta*, 2006, **1757**, 876.
12. D. Marx, M. E. Tuckerman, J. Hutter, and M. Parrinello, *Nature*, 1999, **397**, 601.
13. T. A. Zawodzinski Jr, M. Neeman, L. O. Sillerud, and S. Gottesfeld, *J. Phys. Chem.*, 1991, **95**, 6040.
14. N. L. Garland and J. P. Kopasz, *J. Power Sources*, 2007, **172**, 94.
15. W. Y. Hsu and T. D. Gierke, *Macromolecules*, 1982, **15**, 101.
16. K. Schmidt-Rohr and Q. Chen, *Nature Mater.*, 2008, **7**, 75.
17. R. Devanathan, A. Venkatnathan, and M. Dupuis, *J. Phys. Chem. B*, 2007, **111**, 8069.
18. D. E. Moilanen, E. R. Piletic, and M. D. Fayer, *J. Phys. Chem. A*, 2006, **110**, 9084.
19. N. W. Deluca and Y. A. Elabd, *J. Poly. Sci.: B*, 2006, **44**, 2201.
20. G. A. Eisman, *J. Power Sources*, 1990, **29**, 389.
21. V. Arcella, C. Troglia, and A. Ghielmi, *Ind. Eng. Chem. Res.*, 2005, **44**, 7646.
22. K. D. Kreuer, M. Schuster, B. Obliers, O. Diat, U. Traub, A. Fuchs, U. Klock, S. J. Paddison, and J. Maier, *J. Power Sources*, 2008, **178**, 499.
23. P. L. Antonucci, A. S. Aricò, P. Creti, E. Ramunni, and V. Antonucci, *Solid State Ionics*, 1999, **125**, 431.
24. K. T. Adjemian, S. J. Lee, S. Srinivasan, J. Benziger, and A. B. Bocarsly, *J. Electrochem. Soc.*, 2002, **149**(3), A256.
25. G. Ye, C. A. Hayden, and G. R. Goward, *Macromolecules*, 2007, **40**, 1529.
26. H. Uchida, Y. Ueno, H. Haghara, and M. Watanabe, *J. Electrochem. Soc.*, 2003, **150**(1), A57.
27. V. Ramani, H. R. Kunz, and J. M. Fenton, *J. Power Sources*, 2005, **152**, 182.
28. M. H. Yildirim, D. Stamatialis, and M. Wessling, *J. Membr. Sci.*, 2008, **321**, 364.
29. C. Schmidt, T. Glück, and G. Schmidt-Naake, *Chem. Eng. Technol.*, 2008, **31**, 13.
30. P. D. Beattie, F. P. Orfino, V. I. Basura, K. Zychowska, J. Ding, C. Chuy, J. Schmeisser, and S. Holdcroft, *J. Electroanal. Chem.*, 2001, **503**, 45.
31. A. Siu, B. Pivovar, J. Horsfall, K. V. Lovell, and S. Holdcroft, *J. Polym. Sci. Part B: Polym. Phys.*, 2006, **44**, 2240.
32. K. D. Kreuer, *J. Membr. Sci.*, 2001, **185**, 29.
33. B. Liu, G. P. Robertson, D.-S. Kim, M. D. Giver, W. Hu, and Z. Jiang, *Macromolecules*, 2007, **40**, 1934.
34. M. A. Hickner, H. Ghassemi, Y. S. Kim, B. R. Einsla, and J. E. McGrath, *Chem. Rev.*, 2004, **104**, 4587.
35. Y. Li, A. Roy, A. S. Badami, M. Hall, J. Yang, S. Dunn, and J. E. McGrath, *J. Power Sources*, 2007, **172**, 30.
36. G. Scharfenberger, W. H. Meyer, G. Wegner, M. Schuster, K.-D. Kreuer, and J. Maier, *Fuel Cells*, 2006, **6**, 237.
37. H. Nakamoto and M. Watanabe, *Chem. Commun.*, 2007, **24**, 2539.
38. T. Uda and S. M. Haile, *Electrochem. Solid State Lett.*, 2005, **8**, A245.
39. D. Curtin, R. Lousenberg, T. Henry, P. Tangeman, and M. Tisack, *J. Power Sources*, 2004, **131**, 41.
40. G. M. Haugen, F. Meng, N. V. Aieta, J. L. Horan, M.-C. Kuo, M. H. Frey, S. J. Hamrock, and A. M. Herring, *Electrochem. Solid State Lett.*, 2007, **10**, B51.
41. P. Trogadas, J. Parrondo, and V. Ramani, *Electrochem. Solid State Lett.*, 2008, **11**, B113.

Methane-to-Methanol Conversion

Brian G. Hashiguchi, Claas H. Hövelmann, Steven M. Bischof, Kapil S. Lokare, Chin Hin Leung and Roy A. Periana

The Scripps Research Institute, Jupiter, FL, USA

1	Introduction	101
2	Methane Functionalization by Coordination Catalysis	104
3	Methane Functionalization by Chain Reactions	129
4	Conclusion	135
5	Related Articles	137
6	Abbreviations and Acronyms	137
7	References	137

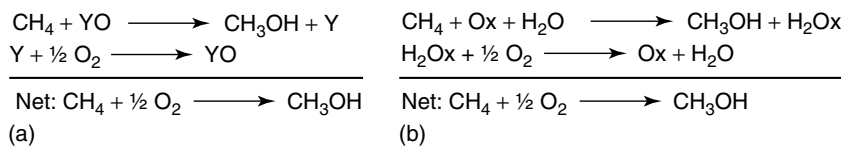
1 INTRODUCTION

Methane (CH_4) is the smallest saturated hydrocarbon and one of the most abundantly available carbon-based feedstocks.^{1–5} It is the main component of natural gas, which is widely available around the world and is just as abundant as oil on a per energy content basis.⁶ If efficient, inexpensive technology can be developed, natural gas can be converted into liquids that could be used as precursors to chemical and fuels that would provide an alternative to dwindling petroleum reserves. In addition to augmenting petroleum, an important immediate need for lower cost methane to liquid (MTL) technology is with respect to the so-called “associated gas” in remote locations.⁷ Associated gas is the natural gas that accompanies liquid hydrocarbon products during petroleum drilling operations. Methane is typically associated with petroleum reserves and currently no cost-effective method is in place to convert the associated gas that is obtained from oil production to a transportable liquid. It is estimated that worldwide methane flaring (i.e., combusted without utilizing the produced energy) could provide 25% of the US’ liquid fuel needs. Minimizing such flaring is important both for economic reasons and in light of the growing realization that emissions can influence climate change.⁸ These concerns are particularly timely, given that in the short term (likely the next 30 years) we will likely continue to depend on fossil fuels for much of our energy and materials needs.

Efficient utilization of abundant methane from remote locations, as a source of transportation fuels or chemical feedstocks, requires its chemical transformation

into a liquid product because of the high costs associated with transportation of a gas. The most desirable liquid products, such as methanol, dimethyl ether, or longer alkanes, would retain most of the energy content of methane and would also serve as an efficient, flexible chemical feedstock. Methane is, in general, quite unreactive with commercially available hydrocarbon conversion catalysts and requires high temperatures to induce reactivity. Unfortunately, the conditions required for methane reactivity are also applicable to the generated products, which are often substantially more reactive than methane itself.^{9,10} This often leads to overoxidized products such as CO_2 or coke as the dominant product at higher conversions of methane (>10%) required for practical processes. As a result, no commercial process exists for the economical, direct conversion of methane to desired liquid products such as methanol or higher alkanes.

The only commercial technologies available for methane to liquid (MTL) conversion products are *indirect* and based on high-temperature (>800 °C) syngas chemistry. As a result of the complex equipment required to manage such extreme conditions, these processes are capital intensive, and the products are too expensive to compete with liquid products generated from oil.^{1–5,11,12} Thus, the key to developing new, lower cost MTL technology is to develop *lower temperature* (<250 °C) chemistry that allows the *direct* (non-syngas), *selective* functionalization of methane. If the capital for such processes can be substantially reduced relative to that required for the existing MTL processes, this could help to reduce the world’s dependence on petroleum by augmenting oil with liquids produced from natural gas (i.e., methane).^{13–19}

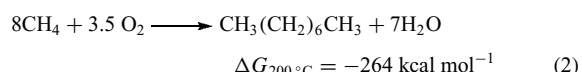
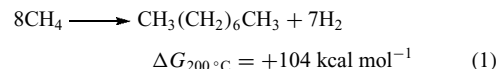


Scheme 1 Functionalization of methane to methanol by a two-step, air-regenerable, O-atom donor, YO (a) and electron acceptor Ox (b)

This article focuses on studies directed toward the net conversion of methane to a stable *functionalized* and *useful* derivative by means of homogeneous organometallic and/or inorganic complexes. The term homogeneous is used loosely, since methane is a gas at normal temperatures and pressures and most systems involve both liquid and gas phases. This article is limited in scope to only gas–liquid systems in which all reactants exist in either the gaseous or the liquid phase. Systems that involve solids (so-called heterogeneous systems, e.g., based on supported metals, metal oxides, nanotubes, etc.) as reagents, catalysts, or initiators are not covered. In addition, methane oxidation in biological systems has been previously reviewed^{20–24} and will not be covered.

While most of the recent reviews on C–H activation provided a broad survey of the field,^{13–19,25} some more specialized reviews have focused on late transition metals,^{26,27} selective radical functionalization,²⁸ heterogeneous methane oxidation,²⁹ and aqueous chemistry.³⁰ To the best of our knowledge, there have been no reviews devoted solely to homogeneous methane functionalization since Crabtree's review in 1995 on aspects of methane chemistry,^{9,10} which covered both the activation and functionalization of methane. This article focuses on reactions that result in the net functionalization of the methane C–H bond, with an emphasis on developments since 1995.

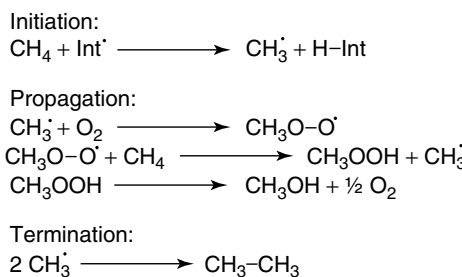
Since the existing high-temperature, commercialized syngas-based MTL processes can be considered the baseline for any new large-scale chemical conversion process for conversion of methane to liquids, it is important to consider that (i) these commercial MTL processes are chemical conversion processes that utilize only O₂ as the co-reactant. This is because O₂ is the only economically viable co-reactant for the large-scale chemical conversion of methane.³¹ A co-reactant is required in the chemical conversion of methane to liquid products in order to provide a thermodynamic driving force for the reaction (e.g., the idealized conversion of methane through dehydrogenative coupling to give long-chain alkanes and H₂ (equation (1)), which is not thermodynamically feasible without the use of a co-reactant such as dioxygen (equation (2)). (ii) The carbon yield of the existing commercial processes is relatively high (~70–75%),³¹ and therefore any new low-temperature, MTL chemistry to replace current technologies should have a minimum reaction selectivity of ~70% (since the reaction selectivity determines the maximum overall yield).



Given the pivotal importance of whether a methane conversion process utilizes dioxygen, this article is subdivided to distinguish between systems that consume dioxygen as the ultimate co-reactant (referred to as *air-regenerable*, i.e., use O₂ directly or are regenerated from direct reaction with O₂) from those that do not (referred to as *non-air-regenerable*). In examples of systems that use O₂ indirectly, as shown in Scheme 1, O-atom donor reagent (YO) or electron acceptors (Ox) can operate as functionalization reagents for the direct, thermodynamically favorable functionalization of methane in one step, and the reduced forms are regenerated from O₂ in a second step.

In addition to the practical considerations of air regenerability, methane functionalization systems are also classified in this article on the basis of the reaction mechanism. Two general mechanistic strategies have emerged: (i) the use of coordination catalysts that coordinate and cleave the CH bond of methane (defined as CH activation, see below) or that coordinate and activate the oxidizing reagent (oxidant activation), and (ii) the use of chain reactions with reactive species such as free radicals or other chain-carrying species.

Systems that operate by catalytic methane functionalization are distinct from those that operate by chain reactions. In chain reactions, some species, e.g., hydrogen peroxide or persulfate, are consumed to generate a chain-carrying species, such as a methyl radical. This species reacts with O₂ or another reagent through a propagation sequence to generate the desired functionalized product and regenerate the chain-carrying species. Termination reactions halt the propagation sequence by quenching the radical. A possible sequence of reactions in a chain-reaction process is shown in Scheme 2. Although these systems may seem to show “catalysis,” in the sense that more moles of product are generated per mole of initiator consumed, they are not catalytic. The amount of product generated per molecule of initiator consumed is dependent on the number of propagation reactions that occur before termination stops the propagating species.



Scheme 2 Methane functionalization by O_2 in chain-reaction process with initiation, propagation, and termination steps

In contrast, coordination catalysts operate by activation of one or more reactants, through direct coordination to facilitate the formation of the desired product and regeneration of the catalyst. It has become apparent when examining the literature that the catalytic functionalization of methane involves either (i) CH activation of methane followed by functionalization or (ii) oxidant activation (e.g., $\text{Y}-\text{"O"}^\cdot$) by the catalyst and functionalization of methane. In the first case, the catalyst precursor (e.g., L_nMX) coordinates methane and cleaves the CH bond to generate a discrete $\text{L}_n\text{M-CH}_3$ “activated” intermediate that undergoes reaction with the oxidizing reagent (e.g. $\text{Y}-\text{"O"}^\cdot$) to generate the desired functionalized product and regenerate the catalyst precursor (Scheme 3).

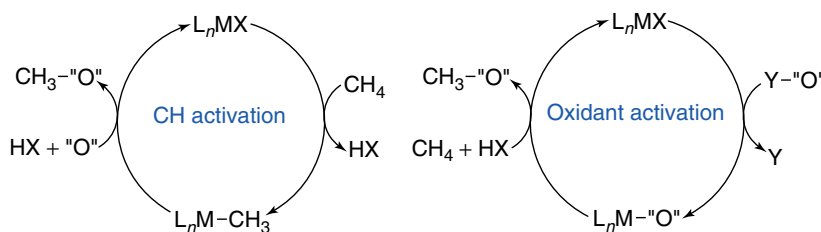
In contrast to coordination catalysts that operate by activation of the CH bond, some catalysts operate by the initial coordination and activation of the oxidizing reagent (e.g., $\text{Y}-\text{"O"}^\cdot$) followed by methane functionalization. In these systems, the functionalization agent, generalized in this scheme as $\text{Y}-\text{"O"}^\cdot$, coordinates to the catalyst to generate an activated intermediate (e.g. $\text{L}_n\text{M-CH}_3$) that reacts with the CH bond to directly generate the product or reactive fragments such as free radicals that can rapidly form the functionalized product.

Although much of the discussion thus far has been centered on the conversion of methane into products such as methanol or higher alkanes that can function as transportation fuels and chemical feedstocks, the conversion of methane to smaller volume products such as acetic acid (HOAc) or

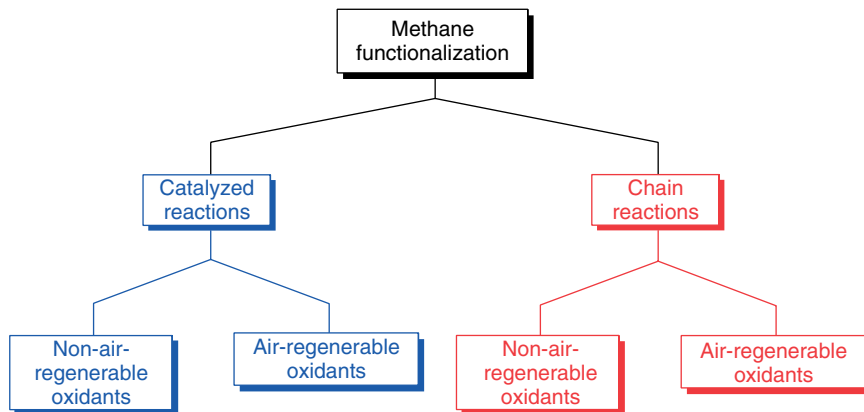
methanesulfonic acid (MSA) is also an important challenge. It is possible that with smaller volume, higher value-added products such as MSA, the reagents other than dioxygen, e.g., H_2O_2 , which cannot be regenerated from O_2 alone, can be completely consumed in potentially economical processes. Other possible liquid products such as aromatics or olefins could also be considered as desirable products.

The word functionalization is used throughout this article to describe the substitution (replacement) of a methane hydrogen atom with a functional group (e.g., hydroxyl, sulfonyl, etc.) to give a stable product. If hydrogen is substituted by a metal–ligand fragment, L_nMX , to generate a discrete $\text{L}_n\text{M-C}$ intermediate, this is referred to as *CH activation* rather than *CH functionalization*. CH activation is meant to convey Shilov and other early investigators’ original meaning, where the CH bond is “activated” in order to facilitate a second functionalization step. Therefore, it is inconsistent with these definitions to simply refer to the overall substitution of hydrogen from a CH bond to generate a functionalized product, such as an alcohol or halide, as CH activation. Within the context of the above general definitions of CH activation and CH functionalization, this article does not focus on systems that only activate methane via $\text{L}_n\text{M-CH}_3$ complexes but rather focuses on systems that lead to the overall conversion of methane to stable functionalized molecules through the use of homogeneous (gas–liquid), catalyzed (Section 2), and chain reactions (Section 3).

In summary, this article uses two major categories to classify the presented systems: those that involve catalytic methane functionalization and those that undergo functionalization via chain reactions. Each of these categories has been subdivided into systems that consume only oxygen (air-regenerable or potentially so) as the terminal oxidant and those that consume reagents that cannot be regenerated with oxygen (non-air-regenerable). This overall classification is summarized in Scheme 4. Given the focus on functionalization, every attempt is made to show in the various subdivisions the reagents utilized and the functionalized products generated. We hope that this will provide the reader with an efficient method to quickly find or classify (by mechanism and use of O_2) the various systems for methane conversion that have been reported.



Scheme 3 Catalytic functionalization of methane with an oxidizing reagent (“O”) that proceeds by CH activation followed by oxidation (left) and oxidant activation followed by methane oxidation (right)



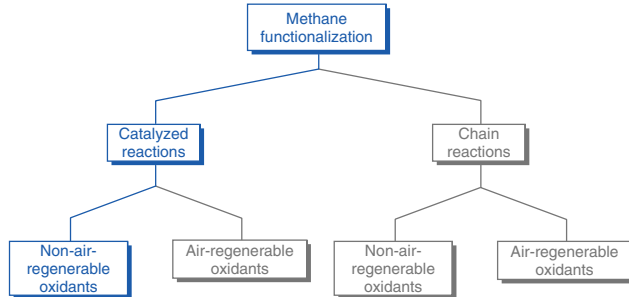
Scheme 4 General classification of methane functionalization into catalyzed and chain reactions containing both non-air-regenerable and air-regenerable oxidants

2 METHANE FUNCTIONALIZATION BY COORDINATION CATALYSIS

In this section, we will review the various systems for methane functionalization that utilize coordination catalysis. This type of catalysis typically involves the inner-sphere (or direct) coordination of the substrate to the central atom of the catalyst, typically followed by cleavage of one or more bonds to generate reactive intermediates. The catalyst has a well-defined, stable composition that is retained throughout the catalytic cycles and involved in the conversion of reactants to products. Of the two possible modes of coordination catalysis, activation of the CH bond and activation of the oxidant, the bulk of the systems reported for methane functionalization involving a coordination catalyst primarily operate by CH activation of methane.

Today, the principal challenge in the field of alkane functionalization is not the activation of CH bonds, but finding examples of CH-activation catalysts that also functionalize methane. The primary reasons for this to be challenging are that (i) most systems capable of CH activation are not compatible with the reaction conditions required for functionalization due to decomposition or inhibition under the reaction conditions; (ii) there is no facile pathway for the functionalization of the M–R intermediates generated from the CH activation; (iii) many of the conditions utilized for functionalization employ reagents that cannot be regenerated with air and can be impractically expensive; and (iv) the reaction selectivity to products is not sufficiently high. Of course, CH activation is not the only basis for developing catalytic reactions for methane functionalization. As discussed in Section 3, other pathways include noncatalytic pathways (e.g., chain reactions) as well as pathways based on activation of the functionalizing reagent. These various categories for functionalization and the reagents and products generated form the basis for this article.

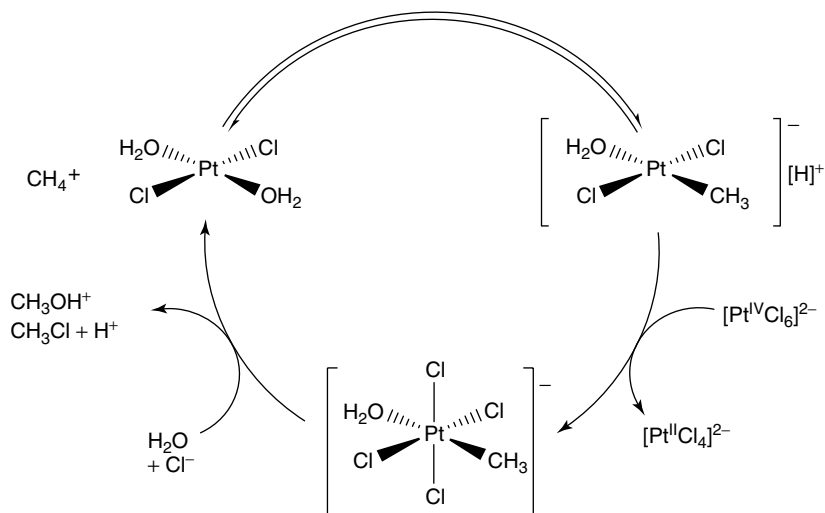
2.1 Catalysis Using Non-Air-Regenerable Oxidants via CH Activation



Systems that utilize catalysts to facilitate the functionalization of methane by CH activation with functionalization reagents that cannot be regenerated by air are covered in this section. While many of these systems involve separate catalysts and stoichiometric oxidizing reagents, some CH activation catalysts can activate methane and act as the stoichiometric oxidizing reagents.

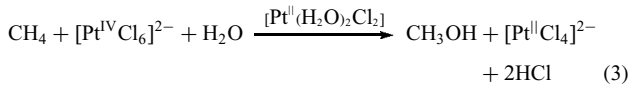
2.1.1 Platinum-Catalyzed Functionalization Using Pt(IV) to Produce CH_3OH

The first examples of methane functionalization under relatively mild conditions were reported by Shilov and coworkers in the early 1980s.^{32,33} They showed that K_2PtCl_4 in the presence of stoichiometric amounts of K_2PtCl_6 catalyzed the functionalization of methane to methanol and methyl chloride (equation (3)). Scheme 5 shows the proposed reaction mechanism, which consists of three fundamental steps: (i) CH activation of methane by Pt(II) to generate a Pt(II)– CH_3 intermediate, (ii) oxidation of the Pt(II)– CH_3 intermediate by inorganic Pt(IV) to generate a Pt(IV)– CH_3 species, and (iii) reductive functionalization



Scheme 5 Platinum-catalyzed oxidation of methane to methanol with Pt(IV)

of the $\text{Pt(IV)}-\text{CH}_3$ to generate the functionalized product CH_3X , where $\text{X} = \text{OH}, \text{Cl}$, and the Pt(II) catalyst.^{34–37} Unfortunately, detailed study of this mechanism is difficult in the actual Shilov system because of its relative complexity and interference from side reactions. Therefore, several model systems have been designed to investigate the proposed mechanism.^{38–50}



The most important characteristics of the Shilov system that were behind its success and design of related systems were (i) the relatively mild reaction conditions ($<100^\circ\text{C}$ in acidic water); (ii) the formation of potentially useful functionalized products, CH_3OH and CH_3Cl ; (iii) involved well-defined, soluble species instead of ill-defined, heterogeneous species such as Pt black that could be amenable to rational design; and (iv) exhibited good selectivity for the generation of the functionalized products, CH_3OH and CH_3Cl , relative to the more overoxidized products such as CH_2O , CO_2 , and CH_2Cl_2 . Significantly, these important and rather unique reaction characteristics implicated that a then new reaction mechanism, so-called “CH activation,” was operating in the mild and selective cleavage of the CH bonds of methane by soluble Pt(II) species.

The key disadvantages of the Shilov system were that (i) the system was not very active, with a catalyst turnover frequency (TOF) of $<10^{-5}\text{ s}^{-1}$ at $<100^\circ\text{C}$, which led to an impractically low volumetric productivity for the conversion of methane to methyl products; (ii) the catalyst was short lived, with a turnover number (TON) of <20 , due to decomposition to Pt black; and (iii) perhaps most significantly, the system utilized Pt(IV) as the stoichiometric oxidant and since this

material could not be regenerated with air, the system could not be commercialized. However, the Shilov system served to illustrate the important potential of the CH-activation reaction when incorporated into catalytic cycles that could generate functionalized products, and substantial effort has been directed at addressing the deficiencies of the system as well as developing new methane-functionalization systems based on the CH-activation reaction with Pt.

2.1.2 Platinum-Catalyzed Functionalization Using Cl_2 to Produce CH_3Cl

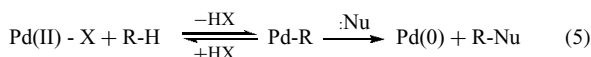
Chlorination is potentially an important process for the functionalization of methane because the chlorinated products can be used as solvents or chemical intermediates. Methane is usually chlorinated at high temperatures or under ultraviolet radiation to afford a mixture of four chloromethanes. Horváth and coworkers reported the first oxidation of methane by Cl_2 mediated by platinum salts in aqueous solution at 125°C .^{51,52} The methyl chloride is partially hydrolyzed to methanol in situ. A typical experiment involves the reaction of Na_2PtCl_4 (0.16 mmol) and Na_2PtCl_6 (1.2 mmol) in D_2O (3 mL), pressurized with 5.0 bar of Cl_2 and 26.6 bar of $^{13}\text{CH}_4$ at 125°C for 1 h. The reaction was monitored by NMR and shows selective conversion of methane to methyl chloride and methanol, with no formation of metallic platinum. At longer reaction times (3 h), overoxidation products such as CH_2Cl_2 , $\text{CH}_2(\text{OD})_2$, HCO_2D , and CO were observed. ^{195}Pt NMR of the reaction mixture showed a strong signal at 0 ppm $[\text{PtCl}_6]^{2-}$ and a low-intensity signal at -1625 ppm $[\text{PtCl}_4]^{2-}$, thus indicating the equilibrium shown below:



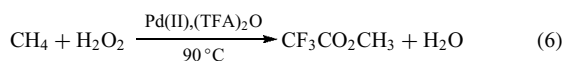
The hydrolysis of methyl chloride to methanol can be significantly slowed down by performing the above experiment at 100 °C for 12 h.

2.1.3 Palladium-Catalyzed Functionalization Using H_2O_2 to Produce $CF_3CO_2CH_3$

In 1987, Sen and coworkers reported the first stoichiometric CH activation and functionalization of alkanes with palladium in acetic acid.^{53,54} $Pd(OAc)_2$ was shown to react with various alkanes (e.g. methane, adamantane, toluene, *p*-xylene,⁵³ and *p*-dimethoxybenzene⁵⁴) to give the corresponding alkyl and aryl trifluoroacetates (equation (5)). Trifluoroacetic acid was used as the solvent because it lacks C–H bonds, is an ideal solvent for a variety of organic substrates, and facilitates the generation of highly electrophilic metal ions. Therefore, the CH activation step was proposed to follow an electrophilic substitution mechanism.



The functionalization of methane (55.2 bar) in HTFA with $Pd(OAc)_2$ resulted in a 60% yield of methyl trifluoroester based on added Pd(II), which acts as a stoichiometric oxidant. Aryl substrates showed a higher selectivity for functionalization of the aromatic CH bonds and were catalytic in Pd(II) when $K_2S_2O_8$ was used as the oxidant.⁵⁴ In addition, H_2O_2 was later found to be a viable oxidant for palladium-catalyzed reactions in trifluoroacetic anhydride to convert methane to methyltrifluoroacetate with a TON of 5.3 after 2 h (equation (6)).⁵⁵



Prolonged reaction times resulted in significantly lower yields of methyl trifluoroacetate. This was attributed to hydrolysis of the ester and subsequent overoxidation of methanol. Initial mechanistic investigations implicated that peroxytrifluoroacetic acid was the active oxidant in one of two electrophilic mechanisms. Pd(II) cations could promote C–H bond cleavage by coordination to the α -oxygen atom of peroxytrifluoroacetic acid, thereby polarizing the O–O bond to enable an electrophilic O-atom attack on the methane CH bond (Figure 1). Alternatively, Pd(II) could activate methane by an electrophilic substitution similar to the stoichiometric system where it is reduced to Pd(0) in the functionalization step. Pd(0) is then reoxidized by CF_3COOOH to Pd(II) to complete the catalytic cycle.

Ingrosso *et al.*⁵⁶ used palladium or copper complexes with hexafluoroacetylacetone ligands (Figure 2) under similar conditions. Optimized conditions for palladium gave a TON of 50 for the conversion of methane to

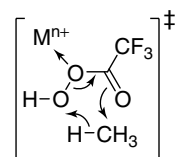


Figure 1 Proposed Pd(II)-promoted methane activation with peroxytrifluoroacetic acid

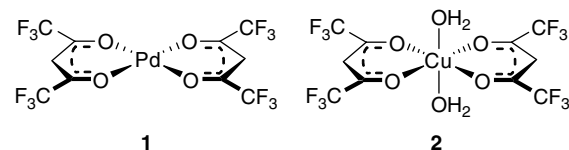


Figure 2 Palladium and copper complexes for methane functionalization

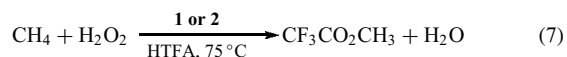
Table 1 Palladium- and copper-catalyzed methane functionalization to methyltrifluoroacetate with H_2O_2

Entry	Catalyst	TON
1 ^(a)	$Pd(hfaca)_2$	50
2 ^(b)	$Cu(hfaca)_2(H_2O)_2$	12

^(a) Conditions: CH_4 (16.8 mmol), HTFA (1.8 mL), 35% H_2O_2 (0.2 mL, 2.3 mmol), 50 °C, 4 h, catalyst loading 8.7×10^{-6} mol.

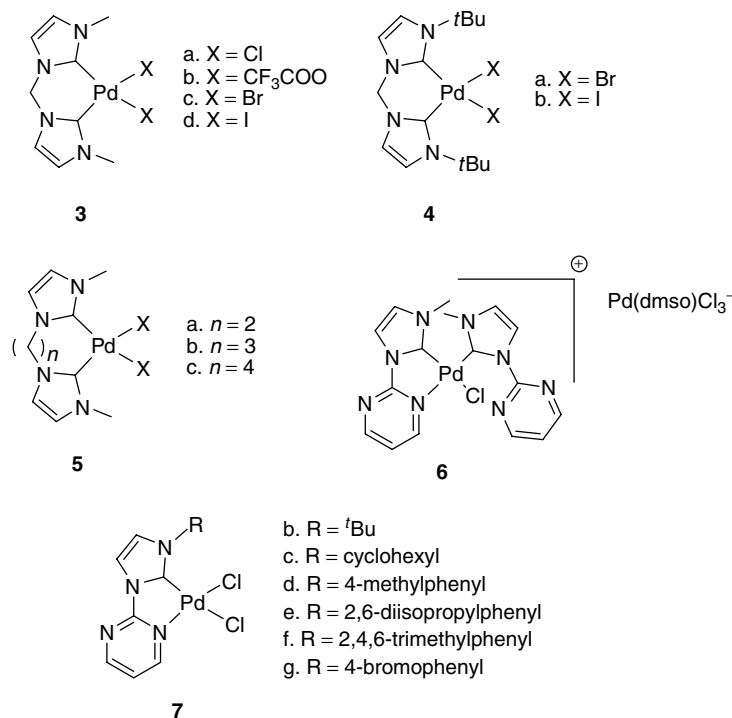
^(b) Conditions as mentioned above, but 75 °C and catalyst loading 7.7×10^{-6} mol. hfaca = hexafluoroacetylacetone.

methyltrifluoroacetate, while with the copper catalyst only up to 12 turnovers were achieved within 4 h (Table 1). It is likely that the Cu systems operate by activation of the peracid as shown in Figure 1 above. Longer reaction times led to increased overoxidation to carbon dioxide and overall diminished yields of the methyl ester.

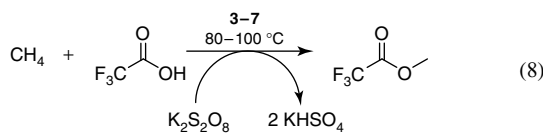


2.1.4 Palladium-Catalyzed Functionalization Using $S_2O_8^{2-}$ to Produce $CF_3CO_2CH_3$

Initially, Muehlhofer *et al.*⁵⁷ and later Stassner and coworkers^{58–61} investigated a series of Pd–carbene complexes (Chart 1) for the functionalization of methane in HTFA with $K_2S_2O_8$ as an oxidant (equation 8 and Table 2). In the initial communication involving **3a,b** and **4a,b**, reported the best results were observed with **4a**, as a TON of 20 after 7 h at 90 °C.⁵⁷ The advantage of the Pd–carbene complexes over the palladium carboxylates lies in the enhanced stabilization

**Chart 1** Palladium-carbene complexes for methane functionalization

of the catalyst toward formation of Pd black.



The reactions with Pd-biscarbene catalysts are highly dependent on the halide anion. While Palladium -Cl, -Br, and -TFA complexes showed high activity, the corresponding iodide complexes exhibited no methane oxidation. (Table 3) Addition of KBr to the LPdBr₂-catalyzed reactions similarly led to the inhibition of

Table 2 Palladium-biscarbene-catalyzed methane functionalization to methyltrifluoroacetate with K₂S₂O₈^(a)

Entry	Catalyst	Yield ^(b) (mmol)
1	3c	1.07
2	3d	0
3	4a	2.06
4	4b	0
5	4a	6.30 ^(c)
6	Pd(OAc) ₂	0.80

^(a) Conditions: catalyst (0.21 mmol); CF₃COOH (60 mL); (CF₃CO)₂O (10 mL); K₂S₂O₈ (5.7 g, 21 mmol); CH₄ (20 bar); 80 °C; 24 h.

^(b) Yield based on GC-MS analysis.

^(c) T = 90 °C; 14 h; CH₄ (30 bar).

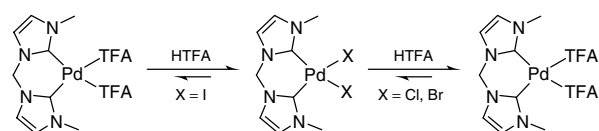
Table 3 Comparison of anion effect in palladium-biscarbene-catalyzed methane functionalization to methyltrifluoroacetate with K₂S₂O₈^(a)

Entry	Catalyst	TON ^(b)
1	3a	24
2	3b	21
3	3c	24
4	3c + KBr ^(c)	0
5	3d	0

^(a) Conditions: catalyst (0.21 mmol); CF₃COOH (40 mL); CF₃CO₂)₂ O (30 mL); K₂S₂O₈ (5.7 g, 21 mmol); CH₄ (30 bar); 90 °C; 20 h.

^(b) Yield based on GC-MS analysis.

^(c) 10 equivalents of KBr.

**Scheme 6** Proposed equilibrium of **3** in HTFA

methyl trifluoroacetate formation.⁵⁸ Strassner concluded that LPd(TFA)₂ might be the active catalyst that is generated in situ from the bromide and chloride complexes while the iodide complexes do not undergo ion exchange (Scheme 6).

However, density functional theory (DFT) calculations showed that the free energy for replacement of I^- by TFA^- is higher than for the other halides (overall reaction energies: $Cl^- = 14.7 \text{ kcal mol}^{-1}$, $Br^- = 20.4 \text{ kcal mol}^{-1}$, $I^- = 26.0 \text{ kcal mol}^{-1}$), but can still proceed under the reaction conditions.

Strassner further explored the effect of bite-angle in bis-chelating carbene ligands on the oxidation yield. Palladium complexes with $(CH_2)_n$ ($n = 1-4$) linkers were examined (**3a**, **5b-d**).⁵⁹ The catalyst activity was slightly improved (4.5% conversion, TON of 33 after 17 h) when Pd complex **5b** with an ethylene linker ($n = 2$) in the N-heterocyclic (NHC) ligand was used instead of the previously used **3a**.

More recently, Strassner and coworkers described the development of another series of Pd–NHC complexes (**7**).^{60,61} One of the NHC moieties in the previous ligands was changed to pyrimidine, in order to combine the stability of the bisNHC ligands with the versatility of the bipyrimidine ligands. Use of the *N*-methyl-carbene ligands led to the formation of complex **7a**, which contains two C,N ligands in different coordination modes and $Pd(dmso)Cl_3^-$ as the anion. Complex **7a** was the only entity (Table 4 entry 1) that showed increased reactivity (TON = 41 vs 33 after 17 h) compared to the previously reported bisNHC complexes (**3–5**). It was not discussed if the higher activity was caused by the new ligand structure or the Pd anion.

Table 4 Palladium–carbene-catalyzed methane functionalization to methyltrifluoroacetate with $K_2S_2O_8^{(a)}$

Entry	Catalyst	Quantity of catalyst (mmol)	Time (h)	TON ^(b)
1	7a	0.084	17	41
2	7b	0.168	17	14
3	7c	0.168	17	13
4	7d	0.168	17	19
5	7e	0.168	17	11
6	7f	0.168	17	18
7	7g	0.168	17	16

^(a) Conditions: $K_2S_2O_8$ (16.8 mmol); CF_3COOH (32 mL); $(CF_3CO)_2O$ (24 mL); 90°C ; CH_4 (30 bar).

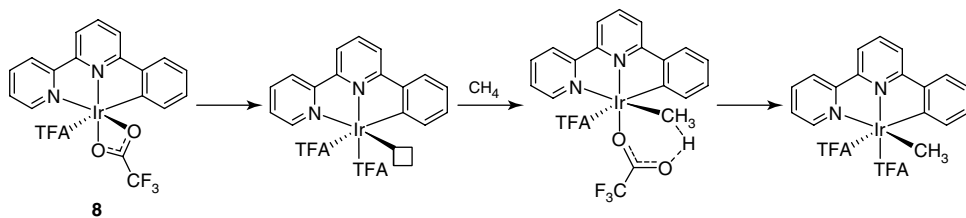
^(b) Product analysis was calculated by GC-MS analysis of an aliquot of reaction solution with an added internal standard.

2.1.5 Iridium-Catalyzed Functionalization Using IO_4^- to Produce $CF_3CO_2CH_3$

Goddard and coworkers used quantum mechanical rapid prototyping (QMRP) to sample different catalytic conditions (ligand, metal, solvent, and oxidation state) to arrive at an $Ir(NNC)(TFA)_2(HTFA)$ complex, **8**, for the hydroxylation of methane.⁶² Experimental rate data between 105°C and 135°C gave a $24 \pm 3 \text{ kcal mol}^{-1}$ barrier for H/D exchange between CH_4 and $TFA-d_1$. However, at temperatures above 150°C , slow loss of catalytic activity was observed, and at 180°C , catalysis stopped after ~ 6 h. In acetic acid (a more coordinating acid), H/D exchange was not observed at 180°C . Methane oxidation to MeTFA was observed when catalyst **8** was heated with methane (35.5 bar) and KIO_4 at 180°C for 3 h to yield MeTFA (TON = 6.3). The use of isotope-labeled $^{13}CH_4$ led to full incorporation into the product (i.e., $^{13}CH_3OC(O)CF_3$). Through DFT calculations, it was determined that the lowest energy transition state is an electrophilic substitution via intramolecular deprotonation of methane by trifluoroacetate (Scheme 7).

2.1.6 Scandium-Catalyzed Functionalization

Thompson *et al.* reported the stoichiometric reaction of $Cp^*Sc(CH_3)$ with propene to yield isobutane.⁶³ Building on those results, the Tilley group successfully incorporated the chemistry into the catalytic functionalization of methane.^{64,65} The reaction of propene and methane catalyzed by $Cp^*Sc(CH_3)$ proceeded over three days at room temperature and yielded three equivalents of isobutene versus $Cp^*Sc(CH_3)$. However, multiple $Cp^*Sc(X)$ products were also observed, which accounts for the low turnover numbers. Additional experiments with other alkenes (*cis/trans*-2-butene, 1-hexene, 1-butene, 2-methylpropene, norbornylene, and 2-butyne) did not yield hydromethylated products. DFT analysis revealed that the turnover-limiting step ($\Delta G^\ddagger = 31 \text{ kcal mol}^{-1}$) is the CH activation of methane via σ -bond metathesis with the coordinated isobutyl group (Figure 3(a)). Surprisingly, methane incorporation into the isobutyl group has a lower activation barrier than that of isobutene ($\Delta G^\ddagger = 30$ versus 31 kcal mol^{-1} , respectively); only methane insertion



Scheme 7 Calculated mechanism for CH activation of methane

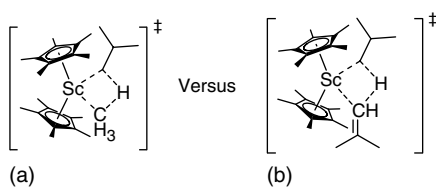


Figure 3 Transition states of σ -bond metathesis between isobutyl and methane (a) and isobutene (b)

regenerates the catalyst, whereas isobutene insertion leads to unproductive scandium species (Figure 3(b)).

Catalytic dehydrogenative silylation of methane with Ph₂SiH₂ to Ph₂MeSiH by Cp*Sc(Me) was also explored by Sadow and Tilley.^{66,67} At 80 °C and with excess Ph₂SiH₂, 5 equivalents of CH₄ were converted in 7 days to Ph₂CH₃SiH with Cp*Sc(Me). The catalytic cycle (Scheme 8) is proposed to proceed through (i) direct reaction of the Cp*Sc(Me) with Ph₂SiH₂ to give the product (Ph₂CH₃SiH) and Cp*Sc-H; (ii) internal C-H activation of a methyl group of the cyclopentadiene ring and elimination of H₂ from Sc-H; and (iii) C-H activation of CH₄ to regenerate Cp*Sc(CH₃). Although the overall reactions are relatively slow (TOF = 1.2×10^{-5} s⁻¹ for hydromethylation and TOF = 8.3×10^{-6} s⁻¹ for silylation), this work is significant because it is a rare example of early metal-catalyzed and nonradical methane functionalization.

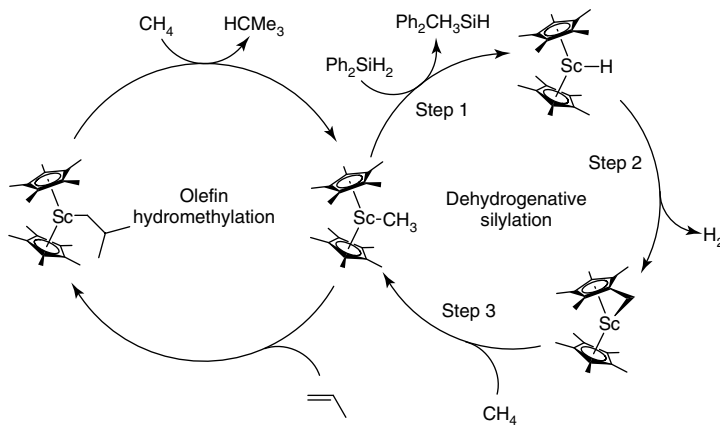
2.2 Catalytic Functionalization Using Non-air-regenerable Oxidants via Oxidant Activation

In this section, we discuss catalytic systems that generate functionalized products from methane via oxidant activation. In this activation approach, reaction of the catalyst with the oxidant generates an activated L_nM-“O” species (see Scheme 3). The activated L_nM-“O” complex in turn

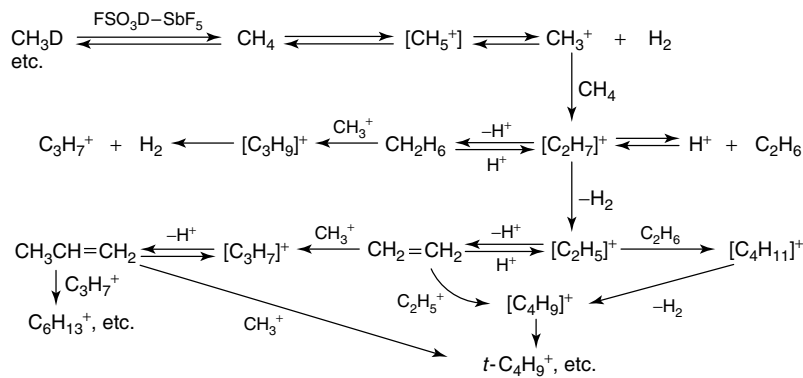
reacts directly with methane to yield the functionalized products. This section covers catalytic systems such as superacids, heteropolyacids, and complexes of osmium, europium, and vanadium that use non-air-regenerable oxidants to functionalize methane.

2.2.1 Superacid-Catalyzed Functionalization

Over four decades ago, Olah and coworkers began an elegant series of studies on the activation and functionalization of methane by superacids.^{68–71} They found that the reaction of alkanes in neat superacids (FSO₃H-SbF₅ or HF-SbF₅) produced alkylcarbonium ions. Reactions of methane in superacids did not ionize at room temperature and only reacted at more than 140 °C to yield unidentified products. Significant amounts of H₂ are produced in the reaction of alkanes with FSO₃H-SbF₅, so-called “magic acid.” It is proposed that methane acts as a base and generates CH₅⁺ cations, which can lose H₂ to form the highly reactive CH₃⁺ ion. The carbonium ion reacts with another molecule of methane to start “polycondensation” that gives a mixture of different carbonium ions with varying chain lengths and branching (Scheme 9). While these reactions can be considered organic reactions, these are examples of catalytic activation of hydrocarbons by coordination and cleavage of the CH bond to generate reactive intermediates, postulated to be CH₅⁺ or CH₃⁺ (or more likely some carbon species coordinated to SbF₆⁻). Treatment of methyl fluoride with SbF₅ in the presence of methane resulted in *t*-butyl cations and some *t*-hexyl cations. Theoretical calculations were used to determine the mechanism and structural characteristics of the CH₅⁺ ion. Three mechanisms for the protonation of methane were examined: backside (**1**), frontside (**2**), and direct protonation (**3**) of the methane CH bond (Scheme 10). Both frontside and backside attacks were considered to be reasonable (-5.48 eV and -5.84 eV, respectively), whereas direct reaction with the hydrogen atom was higher in energy. The energy difference between frontside and backside attacks is too small



Scheme 8 Olefin hydromethylation and dehydrogenative silylation catalytic cycles for scandium-catalyzed methane functionalization

**Scheme 9** Polycondensation of methane with superacids

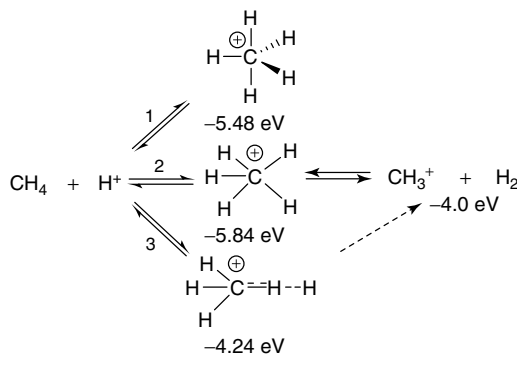
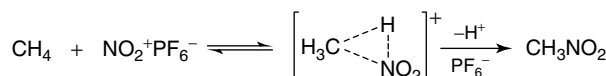
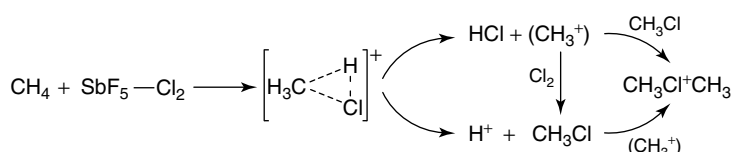
to distinguish between the two mechanisms because of the solvation energies associated with various systems.

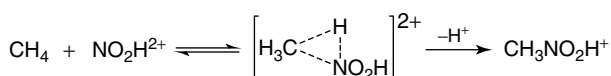
Chlorination. In addition to reactions with superacids, methane also reacts with $\text{SbF}_5\text{--Cl}_2$ in SO_2ClF at -78°C to yield the dimethylchloronium ion (Scheme 11).^{72,73} However, without added chlorine (i.e., only SbF_5 in SO_2ClF), the chlorination reaction does not proceed. It is believed that the superacid solvent results in the activation of the Cl_2 to generate a postulated Cl^+ species (or adducts of SbF_5 and Cl_2) that can attack the C–H bond through a three-center, two-electron-bonded carbonium ion transition state to give either (CH_3^+) and HCl or H^+ and CH_3Cl . A radical mechanism

was discounted because reactions of toluene under identical conditions showed only aromatic and no benzylic chlorination. Catalytic chlorination of methane to methylchloride with $\text{Cl}_2\text{--AlCl}_3$ was also tested, but the reaction was very slow ($\sim 1\%$ yield based on chlorine at 25°C after 17 h).

Nitration. Functionalization of methane to nitromethane was observed when methane was reacted with $\text{NO}_2^+\text{PF}_6^-$ in a CH_2Cl_2 –sulfolane solution to give only 0.1% yield of nitromethane at 25°C with no reported reaction time.⁷⁴ With strong acid (HF/SbF_5) as a solvent, approximately a 10-fold increase ($\sim 1\%$) in the yield of nitromethane is observed. Again, akin to the protonation and chlorination mechanisms, the superacid solvent facilitates the generation of the poorly coordinated NO_2^+ , which is believed to undergo reaction with methane via a three-center/two-electron transition state (Scheme 12).

Higher nitration yields were observed in the reaction of methane with $\text{NO}_2^+\text{PF}_6^-$ in a boron tris(triflate)/triflic acid mixture in 1,1,2-trichlorotrifluoroethane (Scheme 13).⁷⁵ After 4 days at 60°C , approximately 3% yield of nitromethane was obtained based on the nitronium salt used.

**Scheme 10** Theoretical study of backside (1), frontside (2), and direct protonation of the CH bond (3) for methane protonation with superacids**Scheme 12** Nitration of methane to nitromethane with $\text{NO}_2^+\text{PF}_6^-$ in HF/SbF_5 **Scheme 11** Superacid-catalyzed chlorination of methane to methylchloride



Scheme 13 Nitration of methane to nitromethane with $\text{NO}_2^+ \text{PF}_6^-$

Hydroxylation. Direct oxidation of methane to methanol and formaldehyde with hydrogen peroxide (H_2O_2) or ozone (O_3) in the presence of magic acid was also reported by Olah and coworkers (Scheme 14).^{76,77} One likely mechanism outlined by these authors is the protonation of the oxidizing reagent (H_2O_2 or O_3) followed by subsequent reaction with methane. For H_2O_2 , protonated methanol was almost exclusively formed, while O_3 yielded almost exclusively protonated formaldehyde with a minor amount (no exact yield was reported) of protonated methanol.

Carboxylation. Functionalization of methane to acetic acid or methyl acetate was achieved with CO under strongly acidic conditions (Scheme 15).⁷⁸ It was postulated that SbF_5 reacts directly with methane to form the SbF_5H^- anion and CH_3^+ . The CH_3^+ ion then reacts with CO to form the CH_3CO^+ ion, which is quenched with either methanol (to form 20–30% methyl acetate based on methane) or H_2O (to form acetic acid).

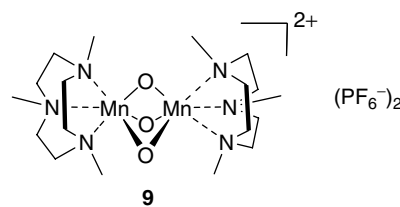
Similarly, carboxylation of methane to acetic acid took place with CO under strongly acidic conditions (HF/SbF_5 or $\text{HSO}_3\text{F/SbF}_5$).⁷⁹ Initially, HC(O)F and HCO^+ are formed, which react with methane at 80°C over a period of 80 h to selectively convert methane to CH_3CO^+ , which can be quenched with water to exclusively form acetic acid.

2.2.2 Functionalization to Produce CH_3OH

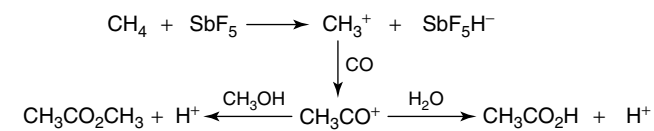
Shul'pin and coworkers reported the use of OsCl_3 with added pyridine to catalyze methane oxidation to methanol by H_2O_2 . In 1.5 h at 80°C , methanol (TON = 17) was the major product with small amounts of formaldehyde.⁸⁰ On the basis of observed selectivities for higher alkane oxidations, the authors suggested the generation of an activated Os=O species that directly reacted with methane to generate a free radical that undergoes rapid conversion to methanol. Wang and coworkers reported in a more detailed study⁸¹ the

functionalization of methane to methanol (TON = 12) without added ligand in 1 h at 90°C . Overoxidation to much higher quantities of CO_2 was observed at elevated temperatures (e.g., from 90°C to 100°C , CO_2 production increases threefold from ca. 100 to 300 μmol under otherwise identical conditions). Methanol and formaldehyde were formed in parallel, at approximately the same rate. An Os(IV) complex was suggested as the active catalyst through the use of UV spectroscopy. Na_2OsCl_6 was shown to be less active, but a similar product distribution was achieved. Replacement of H_2O_2 with *t*-butylhydroperoxide showed lower activity and no activity occurred when OsCl_3 , NaClO , NaClO_4 or NaIO_4 were used. A free radical mechanism was proposed as reaction inhibition was observed upon the addition of hydroquinone.

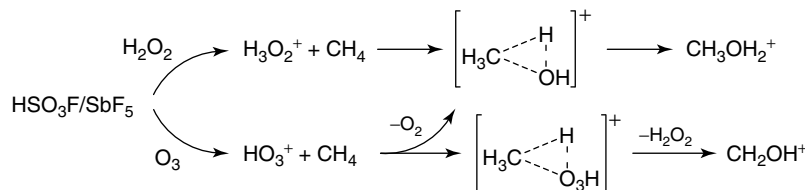
A dimanganese complex, **9**, was also shown to catalyze methane oxidation by H_2O_2 in aqueous solution in the presence of oxalic acid, producing a mixture of methanol and formaldehyde (in a 7:2 ratio, TON = 4.5 in 1 h at 50°C).⁸² The authors did not elaborate on the mechanism, but noted that for higher alkanes, the systems showed reactivity patterns different from those of systems involving hydroxyl radical generation.



Yamanaka and coworkers reported $\text{Eu}(\text{III})/\text{Zn}(0)$ -catalyzed oxidation of methane in TFA to methanol (after work-up with NaOH) using molecular oxygen as the terminal oxidant, with a TON of 5.3 in 1 h at 50°C .^{83,84} There was significant CO_2 (TON = 2 in 1 h) formation, presumably



Scheme 15 Superacid-catalyzed carboxylation of methane to acetic acid



Scheme 14 Superacid-catalyzed methane hydroxylation to methanol or formaldehyde

caused by oxidation of the solvent. Addition of Ti(IV) in the form of TiO_2 or $(\text{acac})_2\text{TiO}$ increased the TON to ca. 10 in 1 h, but also increased CO_2 production.⁸⁵ This is presumably due to the enhancing effect of Ti(IV) on the electron transfer between Eu(III) and Zn(0) to generate the active Eu(II) species. Kinetic studies of the catalytic system comparing cyclopentane and cyclohexane oxidations suggested proton abstraction as a key step in the oxidation, which is further confirmed by loss of stereochemistry when *cis*- or *trans*-1,2-dimethylcyclohexane was oxidized by the same system.⁸⁶ The authors did not comment on whether the radical reaction proceeds by chain or nonchain mechanism. Based on the fact that oxygen is used as the sole oxidant in the system, the system is unlikely to proceed by a chain mechanism. (For further discussion on role of oxygen in a chain mechanism, see introduction to Section 3.1.)

2.2.3 Functionalization to Produce Methylformate

Fujiwara and coworkers used $\text{H}_5\text{PV}_2\text{Mo}_{10}\text{O}_{40}$ as a catalyst to oxidize methane to methyl formate and formic acid with $\text{K}_2\text{S}_2\text{O}_8$ in HTFA, achieving a TON as high as 241 and a yield as high as 95%, based on methane after 20 h at 80 °C.⁸⁷ The authors suggested a mechanism in which an oxidant-activated species, $\text{V(V)} = \text{O}$, directly reacts with methane to generate methyl radicals that are converted to methyl formate.

Mizuno and coworkers showed $\text{H}_4\text{PV}_1\text{Mo}_{11}\text{O}_{40}$ as a catalyst precursor for methane functionalization to methyl formate and MeTFA using H_2O_2 as the initiator. Methyl formate was formed with 72% selectivity and 5% conversion (based on methane) at 80 °C, 24 h, and 50 atm CH_4 . Under optimized conditions, with various compositions of $\text{H}_{3+x}\text{PV}_x\text{Mo}_{12-x}\text{O}_{40}$, a TON of 164 as achieved after 24 h. Earlier studies^{88,89} suggested that $\text{VO(O}_2^+\text{)}$ is formed in situ from $\text{H}_4\text{PV}_1\text{Mo}_{11}\text{O}_{40}$ under similar conditions to generate the active species.

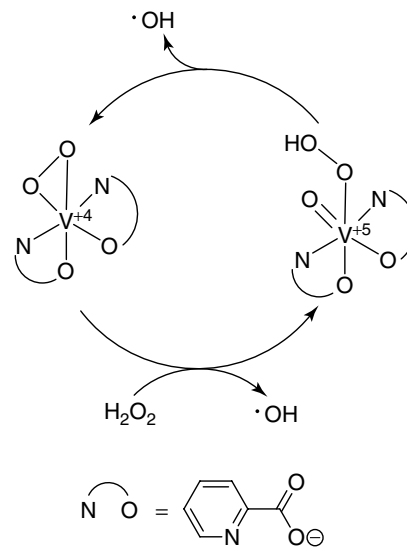
Mizuno and coworkers also observed catalytic activity of a water-soluble potassium salt of di-iron-substituted silicotungstates $\mu\text{-SiW}_{10}[\text{Fe}(\text{OH}_2)]\text{O}_{6-38}$ in methane oxidation by H_2O_2 in an aqueous solution.⁹⁰ Methyl formate was produced with a TON of 2.1 in 48 h at 80 °C. Overoxidation to CO_2 is prominent, and the ratio of CO_2 to HCOOCH_3 is 17 : 10. The authors noted that $\text{H}_4\text{PVMo}_{11}\text{O}_{40}$ was not active under the reported conditions.

2.2.4 Functionalization to Produce CH_3OOH

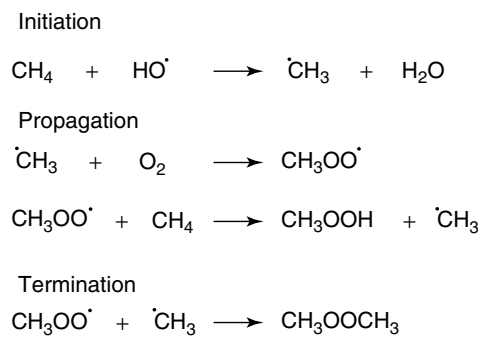
Shul'pin and coworkers have presented systems in which methyl hydroperoxide (CH_3OOH) was produced from methane in the presence of excess H_2O_2 , air, and catalytic amounts of vanadium compounds. While it was initially argued that oxygen acts as the only terminal oxidant in these reactions, hydrogen peroxide is needed in excess.

First reported in 1997, the oxidation of methane to methyl hydroperoxide was successful with a $\text{VO}_3\text{-PCA}$ (PCA = pyrazine-2-carboxylic acid) in the presence of H_2O_2 and O_2 in acetonitrile.^{91,92} However, a later publication⁹³ showed significant oxidation of the solvent (acetonitrile), and the initial publications did not take the background reaction into account. In aqueous media, without acetonitrile, no background oxidation was observed and CH_3OOH was the major product (TON = 480) in 24 h at 50 °C. Vanadium systems have been shown to work without added ligand. For example, when Shul'pin and coworkers replaced H_2O_2 with peroxyacetic acid, $n\text{Bu}_4\text{NVO}_3$ and other similar vanadium salts showed catalytic activity on par with those with ligands such as $[\text{VO(O}_2\text{)(PCA)}]^-$.⁹⁴ In addition, Shul'pin and Pompeiro reported similar activity with NaVO_3 , H_2O_2 , and H_2SO_4 for methane oxidation to methyl hydroperoxide in acetonitrile.⁹⁵

Both $[\text{VO}_2\text{(PCA)}_2]^-$ and $[\text{VO(O}_2\text{)(PCA)}_2]^-$ were isolated under reaction conditions and characterized by X-ray crystallography.⁹⁶ Each showed identical activity for cyclohexane oxidation as the precursor $\text{VO}_3\text{-PCA}$.⁹⁷ The authors propose that the role of the vanadium catalyst is to activate H_2O_2 and generate OH radicals that can directly react with methane to produce methyl radicals (Scheme 16). Reaction of the methyl radicals with dioxygen then generates methyl hydroperoxide radicals, which presumably abstract a hydrogen from another methane to propagate the free radical chain (Scheme 17). In this scenario, only substoichiometric amounts of H_2O_2 would be necessary to provide the initial OH radicals as well as activate the catalyst precursor. However, this and all subsequent studies have shown H_2O_2 to be necessary in excess amounts (at least 2 equivalents compared to an equivalent of products formed).⁹² As is discussed in Section 3.1, the second



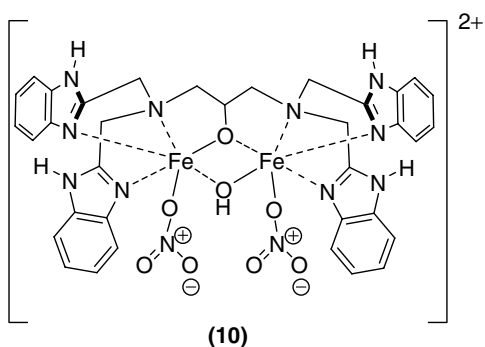
Scheme 16 V^{4+} as a “catalytic pump”



Scheme 17 Proposed chain reaction

propagation step in the proposed mechanism is probably unfavorable, which explains the need for excess initiator (H_2O_2). As suggested in later publications,^{94,95} catalytic activation of the H_2O_2 oxidant followed by functionalization by addition to O_2 is most likely. Further optimization of the system showed that increased acidity can further improve efficiency in aqueous medium, presumably by increasing catalyst stability.⁹⁸

With the hope of extending the vanadium chemistry to a less expensive metal, Shul'pin and coworkers demonstrated that a diiron(III) complex (**10**) with added PCA catalyzed the formation of methyl hydroperoxide and formic acid (3 : 1) from methane and $\text{H}_2\text{O}_2/\text{O}_2$ in acetonitrile.⁹⁹ A total TON of 4 was obtained in 6 h at 25 °C. On the basis of the conditions and selectivities observed for cyclohexane, the authors suggested a mechanism involving generation of hydroxyl radicals similar to the related vanadium systems.



Park *et al.* reported methane functionalization to methanol by copper or vanadium compounds, with H_2O_2 generated *in situ* from H_2 , O_2 , and Pd/C ^{100,101} at 80°C .¹⁰² Copper salts were generally more active, requiring lower loading. There is no notable correlation between the oxidation state of copper and its activity; the reactive species reported are $\text{Cu}(\text{OAc})_2$, Cu_2O , and Cu. Regardless of the Cu precursor, Cu(II) is the dominant species in the postreaction solution, as indicated by X-ray near edge absorption spectroscopy (XANES). The authors claimed a nonradical mechanism based on experiments with radical scavengers.

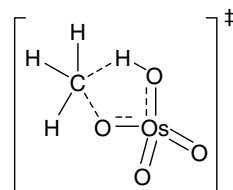
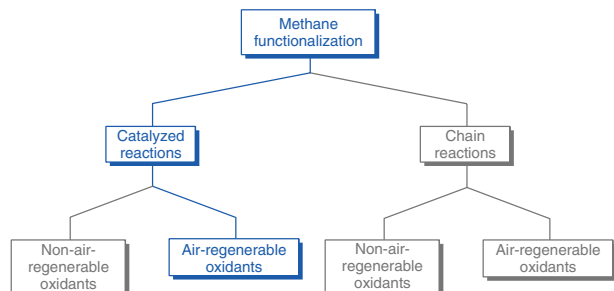


Figure 4 Hydroxylation of methane with OsO₄

2.2.5 Functionalization with OsO_4 and IO_4^-

Mayer and coworkers observed an interesting example of oxidant activation using OsO₄ in the presence of IO₄⁻ for the stoichiometric functionalization of methane to methanol in D₂O. They propose that some uniquely reactive oxidant, presumably a M=O species, is generated from reactions between IO₄⁻ and OsO₄ and that this species likely reacts with methane via a [3 + 2] type transition state as shown in Figure 4. In addition to this novel pathway for methane functionalization by oxidant activation, an unusual and unprecedented protection of the methanol product from overoxidation by the OsO₄/NaIO₄ mixture in D₂O is observed when low pressures of methane (5 bar) are introduced.¹⁰³ Methanol was observed only when both OsO₄ and NaIO₄ were present. Most interestingly, the authors showed that background oxidation of methanol by OsO₄/IO₄⁻ was slowed by ca. 1000-fold in the presence of methane. Methanol oxidation by OsO₄ alone was not inhibited by methane, while methanol oxidation by IO₄⁻ alone was only slightly inhibited (4×). The authors did not observe optical/NMR spectroscopic evidence for any methane interaction with OsO₄ or IO₄. However, a [3 + 2] addition between the C–H bond and two oxo groups has been suggested computationally¹⁰⁴ in the analogous reaction between RuO₄ and CH₄ and further suggested by the authors.

2.3 Catalytic Functionalization Using O₂ or Air-Regenerable Reagents



As discussed above, methane-functionalization reactions that consume only O₂ as the co-reactant have the unique economic potential to be used on large scale to potentially augment the use of petroleum and mitigate the flaring of associated

gas. As shown above in Scheme 3, there are two general schemes for the use of O_2 as the only other reagent for methane functionalization: (i) direct, reactions with air or O_2 and (ii) indirect—use of air or O_2 —which employs O_2 -regenerable reagents. In general, the catalytic functionalization of methane that involves direct reaction between methane and O_2 is relatively rare, and most reported systems operate by the two-step, indirect scheme. The key disadvantage of using an air-regenerable reagent is that such a process involves two steps versus one for direct reactions with O_2 and could potentially lead to increased costs. However, these considerations are balanced by several key advantages: (i) in such a two-step scheme, gaseous O_2 and methane are never mixed and explosive mixtures can be avoided; (ii) since air-regenerable functionalization reagents are generally singlet species that can act as O-donors ($Y-O$) or electron-pair acceptors (Ox), as shown in Scheme 1, there is less propensity for the involvement of free radicals and greater control of reaction selectivities can be attained; (iii) since the air-regenerable functionalization reagent and the reduced forms can be liquids with low vapor pressure, e.g., aqueous Cu(II)/Cu(I), there is little issue with methane separation from other gaseous species and there is no requirement to consume all methane in the reactor zone; and (iv) importantly, air, instead of more expensive pure O_2 , can be used to regenerate the reduced form of the air-recyclable oxidant as long as the oxidized form is nonvolatile, e.g., Cu(II), or easily separable, e.g., SO_3 , which can be removed by scrubbing with water. In fact, such a two-step, air-recyclable oxidant scheme has been commercialized and is used in the Wacker process for the oxidation of ethylene to acetaldehyde.

2.3.1 Catalytic Functionalization by Direct Reaction with O_2

Systems that operate with methane and dioxygen in the same reaction vessel are rare and the mechanisms in most of the systems are largely speculative (with exception of that mentioned in Section 2.2.5). The convenient methodology of a single reaction makes these systems favorable from the standpoint of simplicity; however, as outlined above, there could be induced complications due to the mixture of methane and dioxygen. Nonetheless, the inherent elegance in the direct reaction between methane and dioxygen to facilitate catalytic reaction is highlighted in these examples.

Ruthenium-Catalyzed Formation of CH_3OH . Jasra and coworkers reported methane hydroxylation catalyzed by a Ru³⁺ salen dimer [(HSalen)₂Ru₂(μ -O)(μ -CH₃COO)₂], **11**, where one of the Hsalen ligands remains tridentate with a dangling phenol group (Figure 5).¹⁰⁵ They achieved a TON of 54 at 30 °C with an oxygen pressure of 5 bar (the study did not report on CO₂ and other oxygenate formation in the gas chromatography analysis). The authors proposed that this system operates by a nonradical mechanism based on radical scavenger studies. It is possible that this system involves

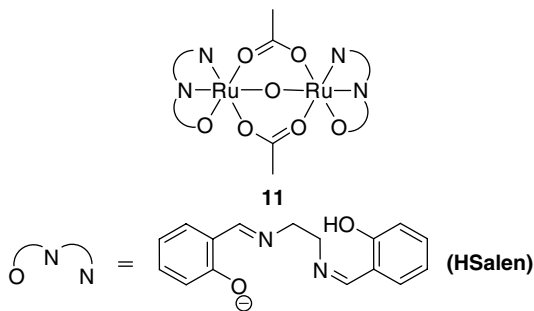


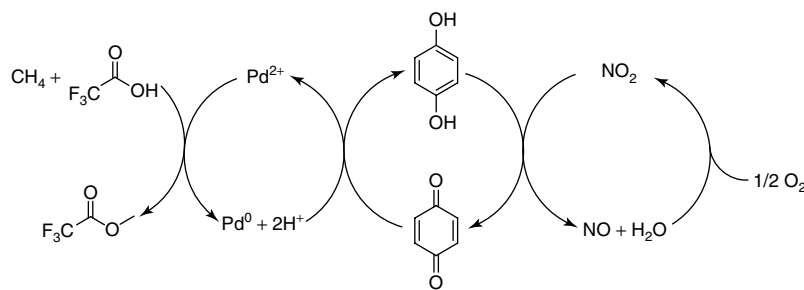
Figure 5 Ruthenium dimer for methane functionalization

activation of O_2 (oxidant activation) by the Ru complex to generate the reactive Ru–O–Ru intermediate that reacts with methane to generate methanol.

Manganese-Catalyzed Formation of CH_3OH . In another example of oxidant activation, Chen *et al.* showed that Mn₂O₃ dissolved in HTFA is capable of stoichiometric oxidation of methane at 180 °C. The metal oxide could then be completely regenerated by treating with NaOH in air. When air is fed into the system, a TON of 8.5 was achieved with 36% yield based on methane. The catalyst turnover was limited by catalyst deactivation by formation of MnF₂. On the basis of UV-spectroscopic studies, the authors suggested Mn(TFA)₃ as the active catalyst.¹⁰⁶

Cobalt-Catalyzed Formation of $CF_3CO_2CH_3$. In a related study, Moiseev and coworkers reported that the trifluoroacetate salts of Mn(III), Pb(IV), and Co(III) showed significant activity in stoichiometric oxidations of methane to methyl trifluoroacetate (MeTFA) in trifluoroacetic acid (HTFA) at 180 °C. Co(III) was the most active and catalysis was observed when oxygen was used as the terminal oxidant (TON = 4 after 4 h).¹⁰⁷

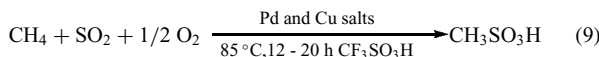
Palladium-Catalyzed Formation of $CF_3CO_2CH_3$ Mediated by Benzoquinone and NO_2 . Bao and coworkers recently used combined redox couples to achieve regeneration of the Pd(OAc)₂ catalyst.¹⁰⁸ Initial studies integrated a *p*-benzoquinone (Q)/hydrobenzoquinone (H₂Q) oxidant cycle for the selective oxidation of methane in trifluoroacetic acid. Quantitative regeneration of the Pd(II) catalyst was obtained using this strategy. Attempts for direct coupling of the Q/H₂Q system with dioxygen as the terminal oxidant led only to slightly increased CF₃COOCH₃ yields, but showed precipitation of Pd(0) during the reaction. The oxidation of H₂Q by dioxygen seems to be too slow to prevent irreversible Pd black formation. An improved oxidation cycle was found using NO/NO₂ by coupling three redox cycles: Pd(0)/Pd(II), Q/H₂Q, and NO/NO₂/O₂ (Scheme 18). This improved redox chain led to methyl trifluoroacetate yields of up to 106 μmol



Scheme 18 Regeneration of the Pd(II) catalyst by redox-couple-mediated oxidation

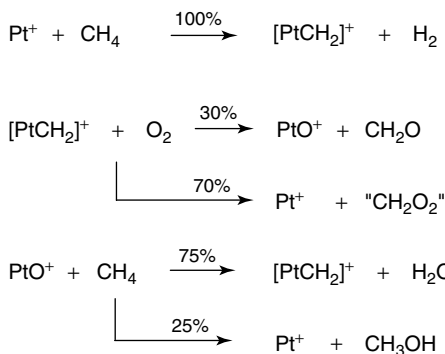
after 10 h at 80 °C with a TOF of $1.9 \times 10^{-4} \text{ s}^{-1}$ and high selectivity.

Palladium-Catalyzed Functionalization to Produce CH₃SO₃H. Mukhopadhyay and Bell showed that the sulfonation of methane to CH₃SO₃H using Pd and Cu salts in the presence of SO₂ and O₂ in triflic acid (equation (9)) proceeds cleanly.¹⁰⁹ Both Pd and Cu were required to generate high yields of product and it was postulated that the role of copper is to mediate the oxidation of the Pd catalyst by oxygen. Yields of CH₃SO₃H (based on SO₂) up to 20% were obtained when the reaction was carried out at 85 °C for 40 h under pressures of 82.7 bar and 2.1 bar of methane and SO₂, respectively. However, the TOF of this system is rather low (8×10^{-5} s⁻¹). The mechanism for this oxidation is not well understood.



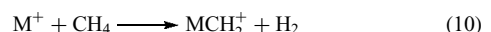
Basickes *et al.*^{110,111} showed the oxidation of methane to methylbisulfate by PdSO₄ in fuming sulfuric acid (H₂SO₄ containing 30 % SO₃, 160 °C, 24 h). In contrast to radical reactions, which mainly form methanesulfonic acid under these conditions (see Section 3.2.1), the Pd(II) reaction showed selective oxy-functionalization with a TON of up to 15.

Platinum-Catalyzed Gas-Phase Functionalization. Metal ions are well known to react with methane in the gas phase. This can be conveniently studied by ion beam mass spectroscopy or by ion cyclotron resonance. In these cases, only products still carrying charge are observed, and only their mass fragmentation patterns are reported.^{112,113} Oxidative addition of the C–H bond occurs in the first step of the process. Müller and Goll were the first to report the formation of organometallic species from alkanes in this way.¹¹⁴ With no ligands, “naked” metals directly insert into C–H bonds by formal oxidative addition. The formed alkyl hydride (or dialkyl derivative) then undergoes further transformations. For example, naked Pt ions reacted



Scheme 19 Reactions of Pt^+ , $[\text{PtCH}_2]^+$, and PtO^+ with CH_4 or O_2

efficiently with methane and are well studied by Schwarz and coworkers.^{115–118} The common intermediate in all these systems was found to be the cationic platinum carbene $\text{Pt}(\text{CH}_2)^+$ species that was first observed by Irikura and Beauchamp (equation (10)).^{119,120}



where M = Ta, W, Os, Ir, and Pt.

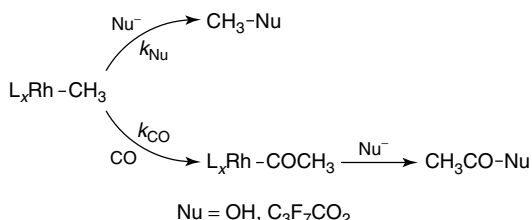
In the case of Pt, a catalytic variant with O₂ leading to the formation of CH₃OH, HCHO, and HCO₂H was also studied by Schwarz and coworkers.¹²¹⁻¹²⁴ Scheme 19 shows the proposed pathway for the formation of these oxidized products. The naked metal first reacts with methane to generate a cationic platinum carbene species. Subsequent direct reaction with oxygen generates CH₂O and CH₂O₂. If only one oxygen is used in this step, the cationic PtO is generated, which can also react with methane to generate either water or methanol. Analogous to the naked metals, platinum chloride and platinum bromide cations, Pt(X_n)⁺, where X = Cl or Br and n = 1, 2, are also capable of methane activation under thermal conditions. All platinum halides are known to generate similar methane oxidation products.

2.3.2 Catalytic Functionalization with CO and O₂ to Produce CH₃CO₂H and RCO₂CH₃

The functionalization of methane to acetic acid is thermodynamically favorable in reactions with CO and O₂. These reactions operate by activation of methane, CO insertion to form the acyl intermediate, followed by hydroxylation.

Rhodium-Catalyzed Functionalization to CH₃CO₂H and RCO₂CH₃. The Monsanto acetic acid process has been used for the conversion of methanol to acetic acid. However, this requires the initial conversion of methane to methanol using the syngas process. Direct conversion of methane to acetic acid using CO and O₂ could be a desirable process that was first reported by Sen and coworkers using RhCl₃ in D₂O.¹²⁵ The reaction is proposed to proceed through the CH activation of CH₄ with a Rh catalyst to generate Rh—CH₃ intermediates. CO insertion to generate Rh—COCH₃ followed by reaction with water generates acetic acid. Addition of Cl[−] and I[−] (in the form of HCl, and HI or KI) shows significant rate acceleration (Table 5). To discover the source of the Rh—CH₃ fragment (in the catalytic cycle), ¹³CH₃OH was added to the reaction mixture and no ¹³CH₃CO₂H was observed. These data provide evidence that (i) the Rh—CH₃ species is exclusively formed from methane (and not methanol or methyl iodide via CH₃OH + HI → CH₃I + H₂O) and (ii) the catalyst has significantly different reactivity than the Monsanto acetic acid process. In the case of the Monsanto process, the formation of methyl iodide is crucial because it has been proposed that the reaction proceeds via oxidative addition of methyl iodide to the rhodium catalyst.¹²⁶

The Rh-catalyzed reaction of methane with CO and O₂ was later shown to have profound solvent effects (on both catalytic rate and product distribution).¹²⁷ Upon addition of a strong acid (i.e., 6:1 mixture of perfluorobutyric acid and water), the preference for methanol-derived products (C₃F₇CO₂CH₃ and CH₃OH) versus acetic acid was greatly increased. The authors postulate that the observed increase in catalytic rate is caused by the increased nucleophilicity of the perfluorobutyrate ion compared to water. The



Scheme 20 Proposed origin for reaction selectivity observed in rhodium-catalyzed methane functionalization

perfluorobutyrate ion readily captures the Rh—CH₃ to form the methyl ester (Scheme 20).

Similar to the previous system (without added acid), ¹³CH₃OH and ¹²CH₄ were added to the reaction mixture to reveal that methyl products (¹²CH₃OH, C₃F₇CO₂¹²CH₃, and ¹²CH₃CO₂H) are almost exclusively derived from methane. This information further indicates that methane is significantly more reactive than methanol (or its ester) despite the fact that the homolytic bond strength of the latter is 10 kcal mol^{−1} lower. Preference of product selectivity was switched back to acetic acid from methanol-derived products (2.4 : 1 with propanol additive versus 1 : 5 without) by adding 1,1,1,3,3-hexafluoro-2-propanol to the reaction mixture. When acetic acid was used as a solvent, the reaction rate was drastically reduced (<10% of the rate in perfluorobutyric acid) presumably because of much stronger coordination of the acetate ion to the metal center. Addition of radical sources (K₂S₂O₈ and ¹³CH₃I) did not change the catalyst activity or product distribution.

The acid dependence of the RhCl₃/NaCl/KI system was further investigated by Chepaikin and coworkers, which revealed that both CH₃CO₂H and CF₃CO₂H accelerate the reaction (when compared to the system without added acid).^{128–132} When the less coordinating CF₃CO₂H was used, faster catalytic rates and equally less selective product distribution were observed (when compared to the Sen perfluorobutyric acid system). In addition, selectivity for methanol-derived products (CH₃OH and CF₃CO₂CH₃) was increased upon addition of CuO.^{128–132} The authors attribute

Table 5 Catalytic conversion of methane to acetic acid^(a) (Reproduced from Ref. 105. © Elsevier, 2009.)

Promoter	[H+] (M)	[Cl] (M)	Temperature (°C)	Time (h)	Yields ^(b) (M)		
					CH ₃ CO ₂ H	CH ₃ OH	HCO ₂ H
None ^(c)	0.1	0.13	140	72	0.014	0.005	0.0252
5% Pd/C ^(d)	0.1	0.13	150	108	0.088	0.0046	0.0592
HI (0.025 M)	0.125	0.13	95	420	0.276	Trace	0.01
KI (0.025 M)	0.0005	1.13	95	352	0.275	0.0065	0.105

^(a) Typical conditions: RhCl₃ (0.01 M) + HCl + promoter in 5 ml D₂O in 120-mL stainless-steel bomb equipped with glass liners.

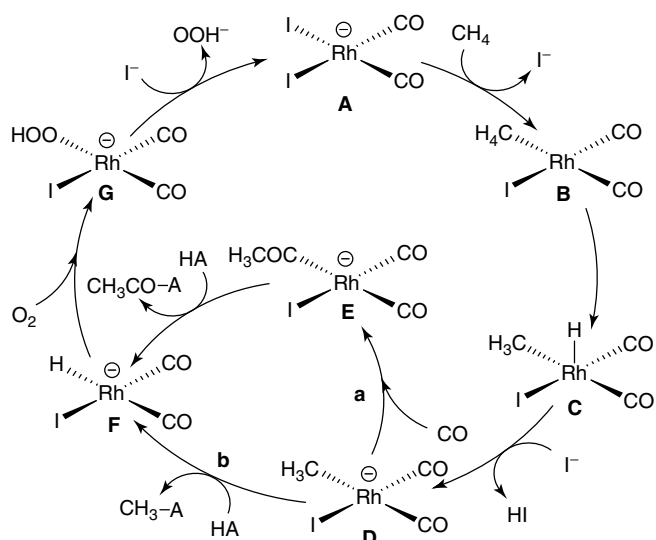
^(b) Yields determined by ¹H-NMR spectroscopy.

^(c) CH₄ (55.2 bar), CO (13.8 bar), O₂ (6.89 bar).

^(d) CH₄ (68.94 bar), CO (10.3 bar), O₂ (3.4 bar).

this improved reactivity to the formation of CuCl–OOH (via $2\text{Cu}^{\text{II}}\text{Cl} + \text{O}_2 + \text{H}^+ \rightarrow \text{Cu}^{\text{II}}\text{Cl}-\text{OOH} + \text{Cu}^{\text{II}}\text{Cl}^+$), which facilitates the oxidation of the Rh complex. Though the yields of $\text{CH}_3\text{CO}_2\text{H}$ and HCO_2H were fairly consistent regardless of the reaction conditions, the correct ratio of Rh(III) : Cu(II) : Cl[−] (1 : 20 : 6) was crucial to yield higher levels of methanol and $\text{CF}_3\text{CO}_2\text{CH}_3$. A kinetic isotope effect (KIE) study comparing the reactivity of CH_4 versus CD_4 with both $\text{RhCl}_3/\text{NaCl}/\text{KI}$ and $\text{RhCl}_3/\text{CuO}/\text{NaCl}$ catalytic systems in trifluoroacetic acid gave a k_{H} and k_{D} of 4.34 ± 0.16 and 3.93 ± 0.18 , respectively. This is indicative of a CH activation mechanism and is unlikely to involve free radicals. Studies with isotopically labeled $^{18}\text{O}_2$, H_2^{18}O , and $\text{CF}_3\text{CO}^{18}\text{OH}$ imply that the methane oxidation involves an O-atom transfer from the oxygen molecule to Rh–CH₃. This can proceed through two possible mechanisms: (i) direct insertion of O_2 into the Rh–CH₃ bond (which has been observed with Pt complexes¹³³ but not with Rh complexes) and (ii) formation of an Rh–CH₃–peroxy complex and migration of the methyl group to one of the O-atoms of the peroxy complex (which seems more likely). Indeed, upon addition of titanium (which is used as a test for two-electron oxidizing agents such as H_2O_2), oxidation is observed under reaction conditions.

The Rh-catalyzed selective oxidation of methane with CO and O_2 was studied by Ziegler and coworkers using DFT techniques.¹³⁴ Four stages are presumed for the functionalization of methane to acetic acid (or three steps if methanol is the product, because the CO insertion step is excluded): (i) C–H activation, (ii) CO insertion, (iii) reductive elimination, and (iv) metal hydride oxidation (Scheme 21). After examining both CH activation mechanisms, oxidative addition (OA) and σ -bond metathesis, it was determined that the OA mechanism had a significantly lower barrier



Scheme 21 The catalytic cycle for rhodium-catalyzed methane functionalization with CO and O_2

(24.8 kcal mol^{−1} versus 29.8 kcal mol^{−1}). The OA of methane forms the 5-coordinate complex C (rather than the 6-coordinated $[\text{Ru}(\text{CO})_2(\text{CH}_3)(\text{H})\text{I}_2]^-$), and with added I[−], HI is eliminated to yield D. The Rh complex, D, can react in two different ways: (i) coordination of CO and insertion into the Rh–CH₃ bond to form E and (ii) reaction of the Rh–CH₃ directly with the anion of perfluorobutyric acid to form the corresponding elimination products ($\text{C}_3\text{H}_7\text{CO}_2\text{CH}_3$) and the Rh(I)–hydrido, F. This step is responsible for the distribution of products and with a more acidic solvent (i.e., perfluorobutyric acid), attack by the anion is favored (methyl ester formation) over CO insertion (acetic acid formation). The low nucleophilicity of water explains why acetic acid is the preferred product when water alone is used as solvent (i.e., CO insertion is favored). However, when a mixture of perfluorobutyric acid is used, methanol products are preferred. To complete the cycle, if CO insertion occurs, the anion of perfluorobutyric acid reacts with the Rh–acetyl complex to yield the product and Rh–H complex, G. Reaction with O_2 yields the Rh–OOH complex H, which reacts with I[−] to regenerate A, upon loss of OOH[−].

Rhodium-based CH activation of methane has not received the same notoriety as other systems. However, products derived from methane (methanol, its ester, and acetic acid) can be obtained in nearly 1.2 M quantities in 80 h at 80 °C. Though this is not nearly as fast as some of the other systems, the system developed by Sen's group and further investigated by Chepaikin and coworkers is an important discovery in the area of CH activation and functionalization chemistry.

Palladium-Catalyzed Functionalization to $\text{CH}_3\text{CO}_2\text{H}$. Fujiwara and coworkers^{135–138} reported studies using Pd(II) and/or Cu(II) catalysts for the conversion of methane to acetic acid in the presence of CO and O_2 or $\text{K}_2\text{S}_2\text{O}_8$ (Tables 6 and 7). The authors suggest that the addition of Cu alters the catalytic mechanism. Palladium-containing systems generally operate by an electrophilic substitution mechanism for CH activation, while the use of only Cu(II) leads to radical reactions (see Section “Chain Reactions with $\text{S}_2\text{O}_8^{2-}$ ”). The rate enhancement found in the Pd/Cu mixed system was attributed to the formation of a 1 : 1 Pd(II)–Cu(II) complex with enhanced electrophilicity. The use of CO_2 instead of CO (equation (11)) decreased the reaction rate but still retained a TON of 10–15 after 20 h at 80 °C. (Table 6).

Table 6 Comparison of methane functionalization to acetic acid with Pd(II), Cu(II), and both^(a)

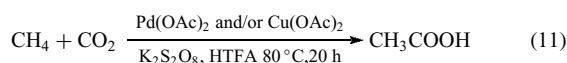
Alkane	Product	Catalyst and yield (mmol)		
		Pd(II)–Cu(II)	Pd(II)	Cu(II)
CH ₄	CH ₃ COOH	0.4	0.03	0.9

^(a) Conditions: reactor was loaded with $\text{K}_2\text{S}_2\text{O}_8$ (9 mmol); CF_3COOH (5 mL); 80 °C; CH_4 (40 bar); CO (20 bar); $\text{Pd}(\text{OAc})_2$, and $\text{Cu}(\text{OAc})_2$ (0.05 mmol).

Table 7 Comparison of methane functionalization to acetic acid using O₂ versus K₂S₂O₈^(a)

Entry	Oxidant	Time (h)	Yield (mmol)
1	O ₂	20	0.14
2	K ₂ S ₂ O ₈	20	0.07

^(a) Conditions: reactor was loaded with O₂ (15 bar) or K₂S₂O₈ (9 mmol); CF₃COOH (5 mL); 80 °C; CH₄ (20 bar); CO (15 bar); Pd(OAc)₂; and Cu(OAc)₂ (0.05 mmol).



Platinum-Catalyzed Functionalization to CH₃CO₂H.

Research by Maitlis, Souma, and coworkers has shown that Pt(II) can catalyze the carboxylation of alcohols to carboxylic acids. However, Pt(II) salts were found to be less effective than Pd(II) salts.^{139,140} Bell and Zerella¹⁴¹ also reported that the oxidative carbonylation of methane mediated by platinum salts such as PtCl₂, (NH₃)₄PtCl₂, (bpy)PtCl₂, and Pt(acac)₂ with the use of co-catalysts such as CuCl₂ and VO(acac)₂ together with O₂ increases the yields of acetic acid and, more dramatically, the yield of methyl bisulfate. A typical experiment involved 3 mL of 96 wt % H₂SO₄, 20 mM Pt salt, pressures of 27.6 bar and 27.6 bar of CH₄ and CO, respectively, 180 °C, 4 h. Further, the more soluble Pt salt, Pt(acac)₂, with CuCl₂ and O₂ increases the acetic acid formation to 42.0 mM, corresponding to a TOF of 1.5 × 10⁻⁴ s⁻¹. In the absence of CO, the sole product was methyl bisulfate, but only in the presence of CO, the product undergoes carbonylation to acetic acid. CO functions as a reducing agent and can reduce the active Pt(II)

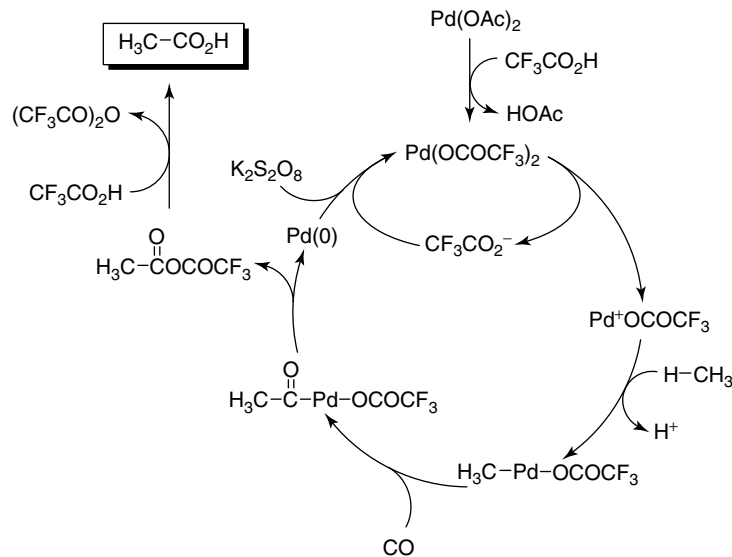
species to inactive Pt(0). The reoxidation can be achieved by the use of a co-catalyst, such as CuCl₂ and O₂.

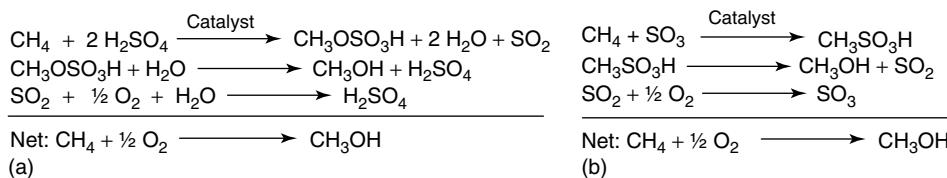
2.3.3 Catalytic Functionalization Using SO₃ or Concentrated H₂SO₄

A particularly widely utilized, air-regenerable functionalization reagent is SO₃ or the hydrated form, H₂SO₄. SO₃ (as sulfuric acid or oleum) is one of the world's largest commodity chemicals and is manufactured and handled on massive scale.¹⁴² Since it is generated from the air oxidation of SO₂, it meets the requirement for a regenerable reagent. Given the relative inertness of methane to typical organic reagents, even reactions with these rather harsh functionalization agents (hot SO₃ or concentrated H₂SO₄) must be catalyzed at below ~300 °C to obtain appreciable reactions.

The most common functionalization products generated from SO₃ or concentrated H₂SO₄ are CH₃OSO₃H and CH₃SO₃H. The oxidation of methane to methanol could be accomplished with either SO₃ or H₂SO₄ and regeneration of the oxidant utilizing O₂ as the ultimate oxidant (Scheme 23).

Significantly, both of the immediate products generated from reactions of methane with H₂SO₄ and SO₃, CH₃OSO₃H and CH₃SO₃H, are relatively thermally stable to neat SO₃ or concentrated H₂SO₄. However, a major issue that can limit the use of these reagents for methane functionalization is separation of the products from the reaction system. Thus, while methanol can be readily generated from mixtures of CH₃OSO₃H in sulfuric acid solvent by the simple addition of several volume equivalents of water, the subsequent removal of the excess water to concentrate the sulfuric acid can be expensive and energy

**Scheme 22** Palladium-catalyzed methane functionalization to acetic acid with CO and O₂, or K₂S₂O₈ in CF₃CO₂H

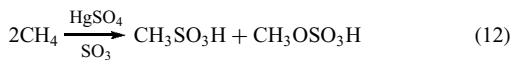


Scheme 23 Methane oxidation and oxidant regeneration using H_2SO_4 (a) and SO_3 (b) with O_2

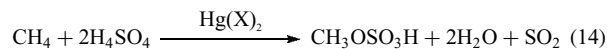
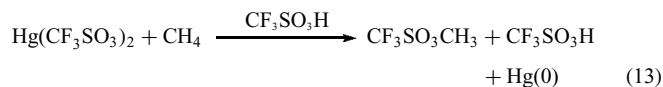
intensive. In the case of $\text{CH}_3\text{SO}_3\text{H}$, this material has a relatively high boiling point (167°C at 0.013 bar) and cannot be easily separated in pure form from liquid sulfuric acid.¹⁴³ Products that could potentially result from higher hydrocarbons are relatively more reactive and separation is likely more problematic. Consequently, there is limited extension of the SO_3 or concentrated H_2SO_4 chemistry to the functionalization of higher hydrocarbons.

Mercury Catalysis Using SO_3 and H_2SO_4 to $\text{CH}_3\text{OSO}_3\text{H}$ and $\text{CH}_3\text{SO}_3\text{H}$. It has long been known that Hg(II) dissolved in acidic solvents such as acetic acid (HOAc) or trifluoroacetic acid (HTFA) will react with benzene by aromatic electrophilic substitution to generate stable Ph-Hg(II) species.¹⁴⁴ While methane, a much weaker nucleophile than benzene, does not react with Hg(II) salts dissolved in these organic acids, facile CH activation can be observed in stronger, less coordinating “hard” oxy-acids such as concentrated sulfuric acid or triflic acid to generate XHgCH_3 intermediates. In strongly acidic media, these resulting species are highly positively polarized on the carbon. This, along with the strong electron affinity of Hg(II) , means that even attack of the weak nucleophiles in strongly acidic solvents on the carbon can readily lead to the formation of functionalized R-heteroatom species and reduced Hg(0) . In a strongly oxidizing acid such as hot H_2SO_4 , both oxidation of the methyl fragment and reoxidation of the Hg(0) can be accomplished.

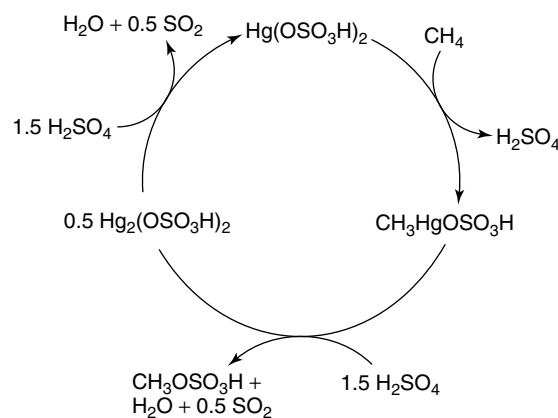
The earliest reported homogeneous catalytic system for methane functionalization was accomplished with mercury salts in 1950 (equation (12)).¹⁴⁵ In this initial publication, reaction between methane and SO_3 , with catalytic HgSO_4 between 100 and 450°C , yielded a mixture of oxidized products (predominately $\text{CH}_3\text{OSO}_3\text{H}$, $\text{CH}_3\text{SO}_3\text{H}$, and $\text{CH}_2(\text{SO}_3\text{H})_2$). The ratio of CH_4 to SO_3 and the reaction temperature were critical in determining the mixture of products and ratios. Under optimized conditions (300°C , $\text{SO}_3 : \text{CH}_4 = 6.9$, $P_{\text{CH}_4} = 93.1$ bar, no catalyst loading information given), total methane conversion to liquid organic products was 45% in a 1.65 : 1 ratio of $\text{CH}_3\text{OSO}_3\text{H}$ to $\text{CH}_3\text{SO}_3\text{H}$. It was proposed that $\text{CH}_3\text{SO}_3\text{H}$ is initially formed with subsequent oxidation to $\text{CH}_3\text{OSO}_3\text{H}$. No other mechanistic details were reported at the time.



Mercury-catalyzed functionalization with SO_3 and H_2SO_4 to $\text{CH}_3\text{OSO}_3\text{H}$ and $\text{CH}_3\text{SO}_3\text{H}$. Highly selective catalytic oxidation of methane to methanol derivatives with high conversion was first reported by Periana *et al.* using strongly acidic conditions and a Hg(II) catalyst.¹⁴⁶ Preliminary experiments showed that stoichiometric mercuric triflate was quantitatively converted to methyl triflate in triflic acid (equation (13)). Since triflic acid is not strongly oxidizing, in this case, mercuric triflate acted as both the catalyst and the stoichiometric oxidant. Switching to more oxidizing sulfuric acid, reactions of methane with $\text{Hg}(\text{SO}_4)_2$ in sulfuric acid (100%) produced methylbisulfate with 85% selectivity (major by-product is CO_2) and a single-pass yield of 50% (based on methane) (equation (14)). Sulfuric acid plays a triple role in this system: (i) solvent, (ii) in situ protecting agent, and (iii) oxidant.



Periana *et al.* postulated that the reaction proceeds by electrophilic activation of methane (Scheme 24) by mercury bisulfate [$\text{Hg}(\text{OSO}_3\text{H})_2$] to produce methylmercurybisulfate [$\text{CH}_3\text{Hg}(\text{OSO}_3\text{H})$], which decomposes to methyl bisulfate [$\text{CH}_3\text{OSO}_3\text{H}$] and 0.5 equivalent of the reduced mercurous bisulfate [$\text{Hg}_2(\text{OSO}_3\text{H})_2$]. Subsequent oxidation with sulfuric



Scheme 24 Catalytic cycle for the electrophilic CH activation of methane with $\text{Hg}(\text{OSO}_3\text{H})_2$ to generate $\text{CH}_3\text{OSO}_3\text{H}$ and $\text{CH}_3\text{SO}_3\text{H}$

acid regenerates $\text{Hg}(\text{OSO}_3\text{H})_2$ to complete the catalytic cycle. A study of different mercuric salts revealed that weakly coordinating anions (e.g., triflate and bisulfate) gave much higher activities than strongly coordinating anions (e.g., acetate).

Several key experiments have provided evidence for an electrophilic activation mechanism: (i) observation of the reaction mixture by ^{13}C and ^{199}Hg NMR showed $\text{CH}_3\text{HgOSO}_3\text{H}$ as an intermediate; (ii) H/D exchange of methane with the mercury catalysts in D_2SO_4 yielded CH_3D ; (iii) direct reaction of $\text{CH}_3\text{HgOSO}_3\text{H}$ with H_2SO_4 yielded methane (the microscopic reverse of activation) and methylbisulfate at 180°C ; (iv) stoichiometric decomposition of $\text{CH}_3\text{HgOSO}_3\text{H}$ to methyl bisulfate, sulfur dioxide, mercurous bisulfate, and methane matches the observed rates in the catalysis.

Further research into mercury(II)-catalyzed methane CH activation focused on optimization through modification of reaction conditions, such as SO_3^- concentration, methane pressure, and temperature. The Hg(II) system for the oxidation of methane in sulfuric acid was studied by Kataja *et al.* under a variety of supercritical and noncritical conditions to show that temperature had the greatest effect and the reaction rate was slightly increased under supercritical conditions.¹⁴⁷ In a different study, Bjerrum and coworkers showed that in the catalytic system, the reaction reaches equilibrium after 1 h with a final $\text{CH}_3\text{OSO}_3\text{H}$ concentration independent of HgSO_4 concentration.¹⁴⁸ The reaction was determined to be largely effected by stirring rates up to 720 rpm, and only minimally at higher stirring rates, which, the authors report, result from an increase of gas (methane) to liquid contact (catalyst). In addition, reaction rates were found to be dependent only on HgSO_4 concentration, with the maximum being attained at 0.8 wt % HgSO_4 in 65% oleum. Surprisingly, temperature change has no effect on the overall rate of catalysis. The authors postulate that as the temperature increases, the catalyst activity does increase but this effect is negated by a decrease in HgSO_4 solubility caused by an increased SO_3^- concentration in H_2SO_4 at higher temperatures.

Computational work by Cundari and coworkers on the mechanism of methane CH activation by Hg(II) revealed that activation barriers and reaction enthalpies are highly dependent on the exact ligands coordinated to Hg.^{149,150} The transition structure located by Cundari involves displacement of a bisulfate ligand with concomitant methane deprotonation and Hg– CH_3 bond formation (Figure 6). The authors report that electronegative “activating ligands” assist in CH activation of methane (both kinetically and thermodynamically) and electron-donor groups on the “spectator ligand” help stabilize interactions between mercury and methane in the transition state to significantly lower the activation barrier (between 6 and 12 kcal mol⁻¹). Such an effect could influence the activation barrier in the case of an $\text{Hg}(\text{OSO}_3\text{H})_2$ catalyst.

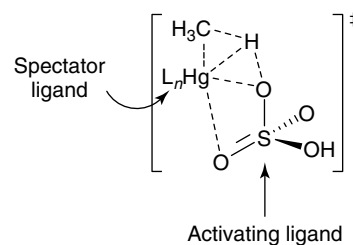
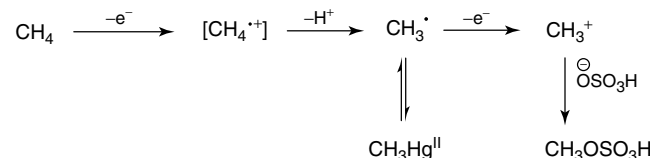


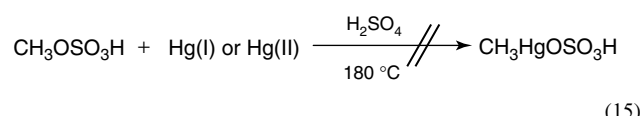
Figure 6 Ligand effects in electrophilic CH activation with mercury



Scheme 25 Radical mechanism for the Hg(II)-initiated functionalization of methane

Is mercury catalytic or chain? Sen and coworkers reported^{110,111} Hg reactions under conditions similar to those reported in the work by Periana *et al.*¹⁴⁶ Using stoichiometric amounts of known radical initiators and metal salts, they reported the functionalization of methane and ethane in fuming sulfuric acid and proposed that the functionalization follows a chain mechanism initiated by Hg(II). In this scenario (Scheme 25), the acidic solvent and poor donor ligands enable the mercury salt to act as a one-electron oxidant and generate a methyl radical by outer-sphere electron transfer followed by proton loss. The observed methylmercury bisulfate is formed by reversible recombination of the methyl radical and Hg(I) but plays no role in the propagation of the mechanism. Further oxidation of the methyl radical and combination with bisulfate lead to the product methylbisulfate.

Sen proposed a different reaction mechanism than that proposed by Periana, based on several points: (i) similar product yields are obtained with known radical initiators under conditions where mercury is not reoxidized in the reaction medium. (ii) Attempts to synthesize $\text{CH}_3\text{HgOSO}_3\text{H}$ in sulfuric acid from Hg(I) or Hg(II) (the reverse of the functionalization step in Periana’s mechanism) failed (equation 15).



(iii) The use of ethane in the reaction leads to cleavage of the C–C bond (up to 25% $\text{CH}_3\text{OSO}_3\text{H}$ relative to the oxidant). Similar yields of methyl product from ethane are observed with known radical initiators such as $\text{K}_2\text{S}_2\text{O}_8$ and $\text{Ce}(\text{SO}_4)_2$, and the authors reference precedence for such

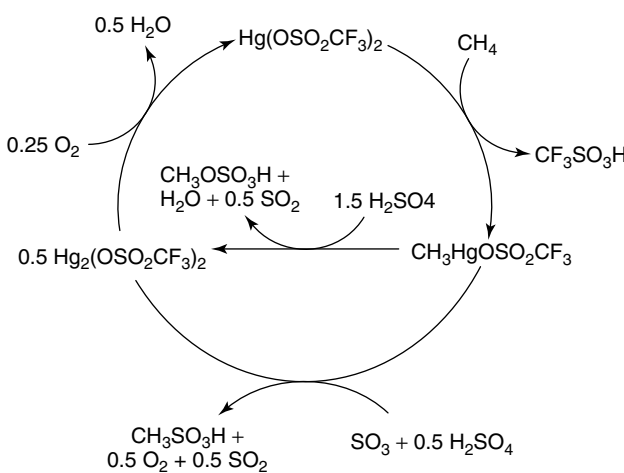
a step by Olah and Lin in the reaction of ethane with NO_2PF_6 .⁷⁴ Given the significant differences in the two reaction mechanisms proposed by Periana and Sen for these Hg(II)-catalyzed reactions of methane and H_2SO_4 (or SO_3), it would be useful to have additional data to determine whether both mechanisms operate or only one does. Such a comparison will have to await further study of the system.

Mercury-catalyzed functionalization using SO_3 to $\text{CH}_3\text{SO}_3\text{H}$. In addition to $\text{CH}_3\text{OSO}_3\text{H}$ formed by reductive functionalization of the $\text{CH}_3\text{HgOSO}_3\text{H}$ intermediate, $\text{CH}_3\text{SO}_3\text{H}$ can be generated if free SO_3 is present in the system (Scheme 23). A selective and high-yielding route to methanesulfonic acid ($\text{CH}_3\text{SO}_3\text{H}$) from methane would be more economical than existing processes. In addition, it has been shown that $\text{CH}_3\text{SO}_3\text{H}$ can rearrange to generate CH_3OH (or overoxidation to $\text{CH}_3\text{OSO}_3\text{H}$ in strong sulfuric acid solvent) and SO_2 . As discussed above, key challenges will be to (i) prevent rearrangement of the $\text{CH}_3\text{SO}_3\text{H}$ (if this is the desired end product) to $\text{CH}_3\text{OSO}_3\text{H}$ and (ii) isolate $\text{CH}_3\text{SO}_3\text{H}$ from sulfuric acid mixtures that are invariably formed even if SO_3 is utilized, given the strong dehydrating properties of this material.

Selective mercury-catalyzed methane oxidation with oxygen to methanesulfonic acid (MSA) in fuming sulfuric acid was performed by Mukhopadhyay and Bell.¹⁵¹ Reactions were conducted at 130 °C with the addition of O_2 as the oxidant in order to prevent overoxidation of MSA to $\text{CH}_3\text{OSO}_3\text{H}$. The most active catalyst was $\text{Hg}(\text{CF}_3\text{SO}_3)_2$ (92% selectivity for MSA with TON = 60). Examination of other Hg catalysts showed higher activities (TON of up to 104 for HgTe) but lower selectivities. In addition, MSA yield increases rapidly with increasing SO_3 concentration up to 40 wt %; however, concentrations greater than 30 wt % also led to an increased overoxidation to $\text{CH}_3\text{OSO}_3\text{H}$.

In the absence of O_2 , the selectivity of SO_3 decreased from 21% to 14% for MSA, giving higher yields of $\text{CH}_3\text{OSO}_3\text{H}$ (~2% to 10%). Lower pressures of O_2 (1.4 bar) lowered the overall rate but increased the selectivity for MSA, whereas higher O_2 pressure up to 4.1 bar gave higher activity but lowered selectivity. These results led to the proposal of two competing mechanisms for the sulfonation of methane, an electrophilic substitution mechanism and a radical mechanism. In the presence of oxygen, the radical mechanism is suppressed and the electrophilic CH activation mechanism dominates (Scheme 26).

Cerium-Catalyzed Functionalization Using SO_3 to $\text{CH}_3\text{OSO}_3\text{H}$ and $\text{CH}_3\text{SO}_3\text{H}$. Cerium sulfate has also been successfully employed for the functionalization of methane to MSA,^{110,111,152} and to acetone.¹⁵³ Sen and coworkers first reported a reaction of CH_4 with $\text{Ce}(\text{SO}_4)_2$ at 180 °C in H_2SO_4 that resulted in 39% conversion (based on $\text{Ce}(\text{IV}) \rightarrow \text{Ce}(\text{II})$).¹¹⁰ Sen and coworkers proposed that it was generated by a free radical mechanism giving the same evidence provided



Scheme 26 Catalytic cycle of the functionalization of methane to methylbisulfate and methanesulfonic acid with $\text{Hg}(\text{OSO}_2\text{CF}_3)_2$

in the mercury chemistry (Scheme 25). After this initial report, 4 equivalents of methane were sulfonated to MSA in fuming sulfuric acid (27–33% oleum) with $\text{Ce}(\text{SO}_4)_2$ in fuming sulfuric acid (27–33% oleum).¹¹¹ Sen's sulfonation chemistry was expanded upon by Mukhopadhyay and Bell through the use of O_2 and $\text{Ce}(\text{SO}_4)_2$ in fuming sulfuric acid (Table 8).¹⁵² In attempts to optimize reaction conditions, different components of the reaction were varied. However, the results from the initial screen gave the highest yield and selectivity of MSA. In particular, higher O_2 pressure (>2.8 bar), higher catalyst loading (>0.09 mmol), higher temperatures (>130 °C), and higher $[\text{SO}_3]$ (>30 wt %) all yielded higher quantities of $\text{CH}_3\text{OSO}_3\text{H}$ (and lower quantities of MSA). In addition, this reaction slows down with extended reaction time. Contrary to the suggested free radical mechanism proposed by Sen and coworkers, Mukhopadhyay and Bell showed that with higher catalyst activity attained with added O_2 (versus the original Sen system) a free radical mechanism is unlikely.

The only other use of cerium for methane functionalization was made by Peng and Deng, who demonstrated catalytic conversion of methane to acetone in a molten salt mixture of $\text{AgNO}_3-\text{KNO}_3$ with $\text{Ce}(\text{SO}_4)_2$.¹⁵³ Peng and Deng did not report any mechanistic data, but did determine that after 5 h at 160 °C, the reaction gave 1.4% conversion of methane with a TON of 4.9, with $\text{Ce}(\text{SO}_4)_2$.

Platinum-Catalyzed Functionalization Using SO_3 and H_2SO_4 to $\text{CH}_3\text{OSO}_3\text{H}$. As summarized above, the key challenges with the early Shilov system were (i) low reaction rates; (ii) short catalyst life; and (iii) the use of stoichiometric amounts of Pt(IV) as the functionalization reagent. One possible replacement for Pt(IV) could be species such as Cu(II), SO_3 , or H_2SO_4 , or other air-regenerable functionalization reagents as has been utilized with Hg(II). However, a key challenge in using solvents such

Table 8 Effect of different catalytic parameters on the Ce(SO₄)₂-catalyzed methane sulfonation to MSA^(a) (Reproduced from Ref. 152. © Wiley-VCH, 2004.)

Entry	Parameter	t(h)	% Conversion of SO ₃ to MSA	% Conversion of SO ₃ to CH ₃ OSO ₃ H	MSA (mmol)	% Selectivity to MSA
1	N/A	6	11	0.01	2.34	99.9
2	O ₂ , 0 bar	6	8	7	1.7	53
3	4.1 bar	6	12	0.1	2.55	88
4	Ce(SO ₄) ₂ , 0 mmol	6	0	0	0	—
5	0.12 mmol	6	12	0.5	2.55	96
6	Temp, 95 °C	6	4	0	0.85	100
7	150 °C	6	16	9	3.4	61
8	SO ₃ , 56 wt %	6	9	7	1.91	53

^(a) General reaction conditions unless otherwise stated: P_{CH₄} = 24.8 bar (101 mmol); P_{O₂} = 2.8 bar; Ce(SO₄)₂ = 0.09 mmol; fuming sulfuric acid (30 wt % SO₃) = 5.67 g; T = 130 °C.

as concentrated sulfuric acid is that unlike HgSO₄, simple inorganic Pt salts are not readily soluble or stable in such a solvent.

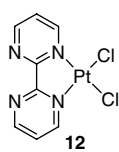
Nitrogen-ligated platinum catalysis. To overcome these limitation, several researchers have utilized novel ligands to allow Pt(II) to be utilized for CH activation and functionalization in strongly acidic solvents. The first example of such a system was reported by Periana with the use of complex **12** (Figure 7), κ^2 -{2,2'-bipyrimidyl}platinum(II)dichloride, also known as the “Catalytica system.” Selective oxidation of methane in fuming sulfuric acid to give CH₃OSO₃H is catalyzed by **12** as shown in equation (16).¹⁵⁴



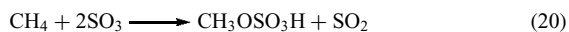
The system utilized concentrated sulfuric acid as both the solvent and the oxidizing reagent. The oxy-functionalized products varied from methyl bisulfate, protonated methanol to methanol depending on the concentration of sulfuric acid, which decreases with reaction time. When utilizing concentrated sulfuric acid with added SO₃, (oleum 102% = 9% SO₃ dissolved in H₂SO₄), relatively high conversions of methane (80%) to methanol derivatives (a mixture of CH₃OSO₃H, CH₂OH⁺, and CH₃OH) with high selectivity (~90%) could be achieved. The only observable by-product was gaseous CO₂. The volumetric productivity of the system after a reaction time of 3 h at 220 °C, 34.4-bar pressure of CH₄, and in a 1 : 1 gas to liquid batch reactor is ~10⁻⁷ mol cm⁻³ s⁻¹. Under these conditions, the turnover frequency of the catalyst

is ~10⁻³ s⁻¹. The characteristics are similar to those observed with the Hg(II)/96% H₂SO₄ system with the key differences being that (i) the Pt(II) system gives the same performance at higher temperatures (220 °C versus 180 °C) and (ii) the Pt(II) system gives higher yields (~70% versus 40%). The primary reason for the higher yield with the Pt(II) system is that this system can utilize oleum (102% sulfuric acid) as the solvent without the generation of by-product CH₃SO₃H. In the Hg(II) system, any significant concentrations of free SO₃ led to the formation of large amounts of this by-product. By starting at higher concentrations of sulfuric acid, the drop in concentration of sulfuric acid as the reaction products (CH₃OH and H₂O) build up can be minimized.

There has been substantial interest in the Catalytica system since its publication in 1998. The primary reasons for this are (i) the relatively high reaction rates, volumetric productivity, and selectivity; (ii) the reaction system and catalyst are stable (up to 300 turnovers have been observed without decomposition) at a temperature range of ~200–250 °C, and (iii) the system is potentially practical since the SO₃ generated can be regenerated by the well-known, commercialized oxidation of SO₂ to SO₃. The primary disadvantages of the system are the relatively high cost of the catalyst and separation of the products from the reaction mixture. These disadvantages are all related to the severe sensitivity of the catalyst to reversible inhibition by nucleophiles (or bases) such as H₂O and CH₃OH. Consequently, the catalyst is very sensitive to the presence of water and requires strongly acidic conditions (conditions under which the concentrations of bases such as H₂O and CH₃OH are negligible due to protonation) to operate at useful rates. Thus, as the acidity of the solvent drops due to water and methanol buildup from the reaction, catalytic activity decreases such that the reaction effectively stops (TOF < 10⁻⁵ s⁻¹) when the acid concentration is <90% H₂SO₄ concentration. Two key disadvantages result from this catalyst inhibition and the requirement for strongly acidic solvents: (i) the integrated catalyst rate over the 3-h reaction period is ~10⁻³ s⁻¹ and (ii) given the low volatility of CH₃OH⁺ or CH₃OSO₃H and

**Figure 7** (κ^2 -{2,2'-bipyrimidyl}) platinum(II) dichloride

the low concentration of free, volatile CH_3OH above 90% H_2SO_4 , the efficient separation of methanol from the reaction mixture requires excess water (1–3 volume equivalents) to be added to the reaction mixture. However, since the catalyst is not sufficiently active below 90% sulfuric acid concentrations, the excess water has to be removed before the system can again be utilized for reaction with methane. Given the high affinity of concentrated sulfuric acid for water, the removal of this excess water is sufficiently expensive, which reduces the advantages of this process over the syngas-based processes.



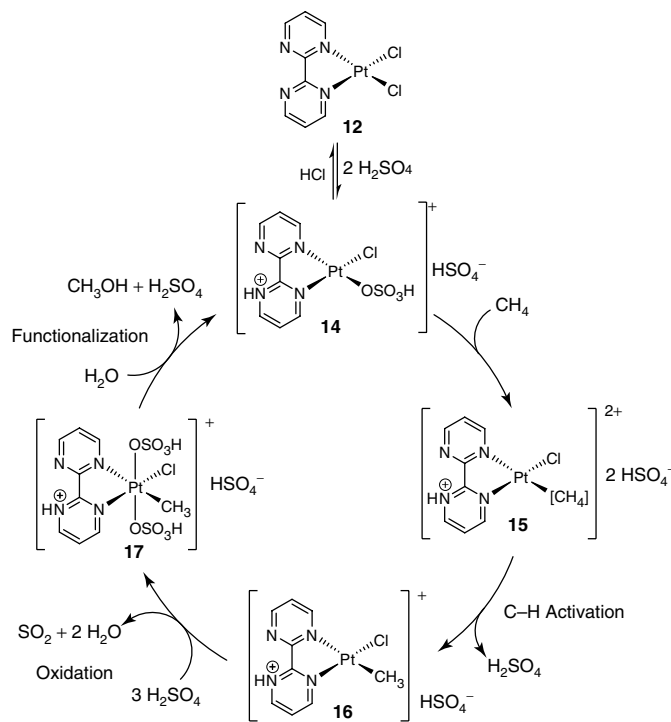
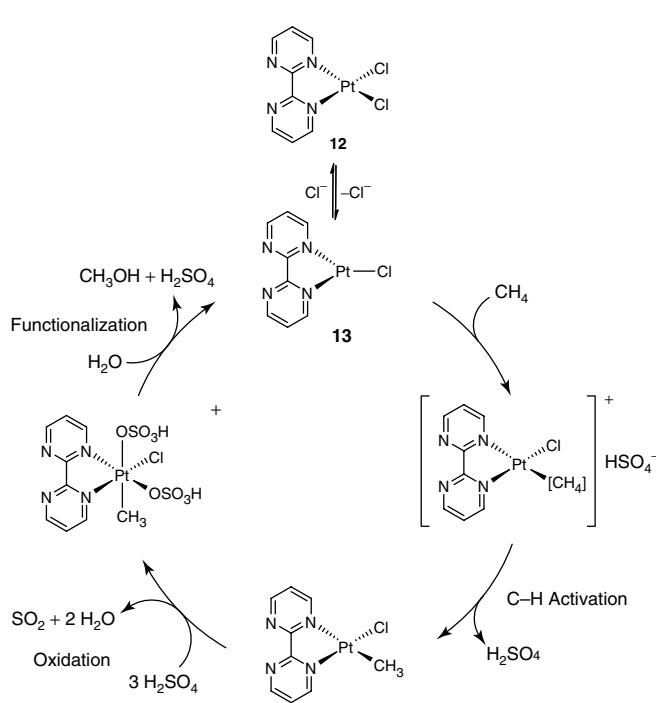
The Catalytica system generates large amounts of sulfuric acid (via equation (17)), which suppresses the amount of methanol formed through the reaction depicted in equation (18).¹⁵⁵ Therefore, to achieve 100% yield of methanol, sulfuric acid has to be diluted up to 50%. Michalkiewicz and coworkers highlighted a novel method for the extraction of the methyl ester formed in the Catalytica system without the usual hydrolysis of ester to methanol. This is done by utilizing low-pressure membrane distillation (LPMD) in the conversion of methane to methanol (via equation 20). The authors have shown that only the unreacted

SO_3 is passed through the membrane because of its high vapor pressure compared to that of H_2SO_4 . The depletion of SO_3 helps in the separation of methyl bisulfate from the mixture. Thus, the sulfuric acid produced and the amount of water added can be reduced. The efficiency of the ester separation was 100%. The ester was hydrolyzed after LPMD to obtain methanol, and the SO_3 was absorbed in H_2SO_4 to regenerate oleum.

Oxidative addition or electrophilic substitution?

The high efficiency of the Catalytica system has led to several theoretical studies to determine the mechanism of methane oxidation.^{156–160} All of the studies agree that the reaction proceeds in three steps: (i) coordination and CH activation of methane, (ii) catalyst oxidation, and (iii) functionalization of the Pt–CH₃ to methylbisulfate (Scheme 27). The catalyst is then oxidized from Pt(II) to Pt(IV), and the reaction between bisulfate (either coordinated to Pt or in solution) and the methyl group results in functionalization. A major difference between these various reports is the conclusion on the identity of the catalyst and on how the catalyst activates the methane molecule.

Ziegler and coworkers^{156,159} found that **12** is not protonated in sulfuric acid (6.9 kcal mol⁻¹ higher in energy) and that one of the chlorides can be displaced with a bisulfate group. The Pt complex then loses Cl^- or HSO_4^- to form a 3-coordinate, **13**, (where X is Cl^- or HSO_4^-), which

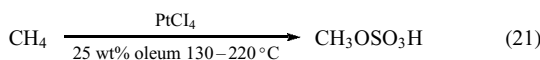


Scheme 27 Proposed CH-activation mechanism for the $\text{Pt}(\text{bpym})\text{Cl}_2/\text{H}_2\text{SO}_4$ system for methane oxidation to methanol by Ziegler (a) and by Goddard and Musgrave (b)

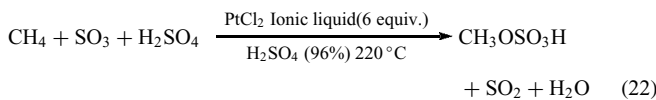
efficiently undergoes oxidative addition of methane to form the Pt–CH₃ complex.

In contrast, the Goddard^{157,160} and Musgrave¹⁵⁸ groups determined that the ground state structure is **14**, where the bipyrimidine ligand is protonated and a chloride is displaced with a bisulfate group. This imparts both thermal stability and acid stability by the active Pt(II) oxidation state to prevent the irreversible formation of insoluble (PtCl₂)_n. In support of this argument, theoretical and experimental studies showed that the replacement of the bipyrimidine ligand with simpler NH₃ ligands leads to systems that are active for catalytic oxidation of methane to methanol but are unstable.^{161,162} Initially, both Goddard and Musgrave determined that **14** promotes an electrophilic substitution mechanism for the activation of methane. However, a recent publication by Ahlquist *et al.* suggests that protonation of the coordinated bisulfate by sulfuric acid prior to methane coordination lowers the activation barrier for the oxidative addition of methane by 11 kcal mol⁻¹.¹⁶³

Alternative platinum catalysis. In a recent report,^{164,165} Michalkiewicz and Kobowski studied the selective catalytic oxidation of methane in 25 wt % oleum to methyl bisulfate at ambient pressure and in the presence of PtCl₄ (equation (21)). The study was directed toward methane esterification at ambient pressure. The authors addressed the mass transfer issue by the use of an absorption reactor. It was shown that it is possible to functionalize methane at 0.1 MPa with the use of a large surface area that was shown to facilitate liquid–gas contact.



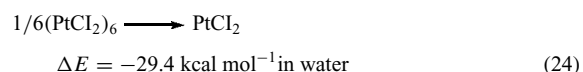
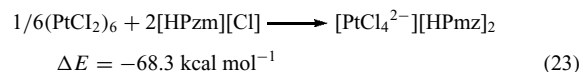
Tang and coworkers have shown the use of highly active ternary systems that involve ionic liquids, Pt(II) compounds [PtCl₂, K₂PtCl₄, PtO₂, (bpym)PtCl₂], and sulfuric acid (98%) to activate and functionalize methane (equation (22)).¹⁶⁶ These ternary systems are more water tolerant than previous systems. However, the activity of these systems is 50% lower than that of the Catalytica system. The reagents of the Shilov chemistry (i.e., K₂PtCl₄ and H₂PtCl₆) that are insoluble in water and not compatible with sulfuric acid readily dissolve in ionic liquids upon heating. The only products derived from methane were methanol and methylbisulfate. A maximum turnover of 3.5 was observed.



Quantum mechanical studies by Goddard and coworkers on the activation of methane by PtCl₂ in H₂SO₄

and ionic liquids show that the ionic liquid enables Shilov-like chemistry in oxidizing media.¹⁶⁷

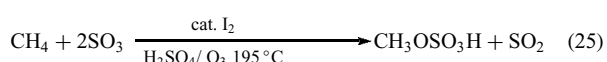
The ionic liquid enables solvation of PtCl₂ catalyst, through the formation of an ion pair as the CH₄ migrates associatively into the first solvation shell and is activated to form the M–C bond. Consequently, it appears that the function of the ionic liquids is to shift the Shilov C–H activation process from water to the oxidizing media characteristic of the Catalytica system.



The study of the Catalytica and related systems suggests that if catalysts could be developed, which operate at commercially viable rates (TOF of ~0.1–1 s⁻¹) in 50% to 75% sulfuric acid (where methanol removal requires less addition of water and the removal of water is less energy intensive), then a process based on regeneration of sulfuric acid by air (Scheme 23) could be economically viable. Engineering considerations show that to minimize capital costs the volumetric productivity of reactor systems should be approximately 10⁻⁶ mol cm⁻³ s⁻¹. With typical residence times in commercial reactors of ~1000 s (~17 min), this would readily result in required methanol (the other functionalized product) of ~1 M concentration. Since the carbon yield of the commercial methane to methanol or diesel conversion processes is ~70%, the selectivity of any new process must be above 70% to achieve comparable or higher yields. Kinetic analyses show that to achieve >70% selectivity with solubilities of methane in the millimolar range while the concentration of methyl-functionalized product is in the molar range, it will require a catalyst that reacts with methane with a rate constant that is 100–1000 times greater than that for the functionalized product. As was discussed for the (bpym)Pt(II) system in concentrated sulfuric acid, this was achieved through a combination of the electrophilic character of the CH-activation mechanism and the effect of the strong acid solvent to convert the hydroxyl group in CH₃OH through protonation or esterification to an electron-withdrawing group that “protected” the product. Ironically, it was this very efficient protection (that required high acidity) that also reduced the economic advantage of the system. As efforts to develop improved methane-functionalization systems continue, a key emphasis will have to be laid on developing new mechanisms and methods of minimizing reaction of the functionalized products.

Iodine-Catalyzed Functionalization Using SO₃ to CH₃OSO₃H. Following the success of cationic electrophiles, Periana and coworkers discovered that elemental iodine

dissolved in $\text{H}_2\text{SO}_4/\text{SO}_3$ catalyzed the oxidation of methane to methyl bisulfate (equation (25)).¹⁶⁸ It was shown that a $\text{H}_2\text{SO}_4/\text{oleum}$ mixture (2–3%) was critical for catalytic oxidation. Without SO_3 or in less than 98% H_2SO_4 , no methyl bisulfate was observed. At 195 °C, methane is oxidized with 53% conversion and with greater than 95% selectivity. Methyl bisulfate was obtained up to a concentration of 1 M with a turnover frequency of $3.3 \times 10^{-2} \text{ s}^{-1}$ and a volumetric productivity of $\sim 10^{-7} \text{ mol cm}^{-3} \text{ s}^{-1}$. Importantly, no CH_3OH , CH_3I , or $\text{CH}_3\text{SO}_3\text{H}$ was observed and only SO_2 and very low levels of CO_2 were detected in the gas phase.

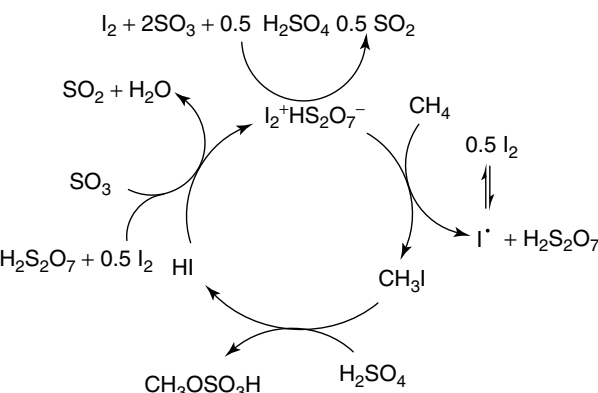


Periana and coworkers originally reported that rates and product selectivities gave first-order dependence on both methane and iodine. However, a recent study by Jarosińska *et al.* has shown the reaction to be of 1/2 order in iodine.¹⁶⁹

Bjerrum and coworkers have shown that beyond I_2 , KI , CH_3I , and I_2O_5 , KIO_3 and KIO_4 also catalyze the oxidation of methane to methyl bisulfate with similar yields and selectivity.¹⁷⁰ This led the authors to suggest that a common active intermediate is generated from all of these sources of iodine. This work also established an optimal temperature of ~ 180 °C. Catalysis conducted at higher temperatures leads to significant overoxidation. The total yield of methanol is only slightly higher (57%) in this optimized system, but a final methanol concentration up to 6 M could be generated with essentially total consumption of SO_3 .

It is well known that extensive hydrogen–deuterium (H/D) exchange ($\sim 50\%$) between gas-phase methane and $\text{D}_2\text{SO}_4/\text{SO}_3$ occurs in just 30 min.¹⁷¹ Olah and coworkers have suggested that CH_4D^+ is a plausible intermediate in this process. However, addition of I_2 suppressed this H/D exchange process, and the methyl bisulfate obtained under the same conditions using D_2SO_4 shows essentially no deuterium incorporation. This indicates that CH_5^+ is an unlikely catalytic intermediate, and on the basis of this knowledge, Periana and coworkers proposed that the $\text{I}_2^+\text{HS}_2\text{O}_7^-$ complex, generated from the combination of I_2 , SO_3 , and H_2SO_4 , is the active catalyst (Scheme 28). To bolster evidence for this catalytic complex, stoichiometric reactions between methane and $\text{I}_2^+[\text{Sb}_2\text{F}_{11}]^-$ in oleum were shown to give 30% methyl bisulfate at 50 °C. Without SO_3 , this stoichiometric reaction too does not give methyl bisulfate. Other cationic species of iodine such as IOHSO_4 , IO_2HSO_4 , and $\text{I}(\text{HSO}_4)_3$ fail to undergo stoichiometric reaction with methane.

As outlined in Scheme 28, the catalytic cycle begins with the reaction of methane with the $\text{I}_2^+\text{HS}_2\text{O}_7^-$ complex to give methyl iodide, which further reacts with H_2SO_4 to give methyl bisulfate and HI . Regeneration of the $\text{I}_2^+\text{HS}_2\text{O}_7^-$ complex then requires SO_3 oxidizing I_2 and $\text{H}_2\text{S}_2\text{O}_7$ to give SO_2 and water. To probe the intermediacy of methyl iodide,



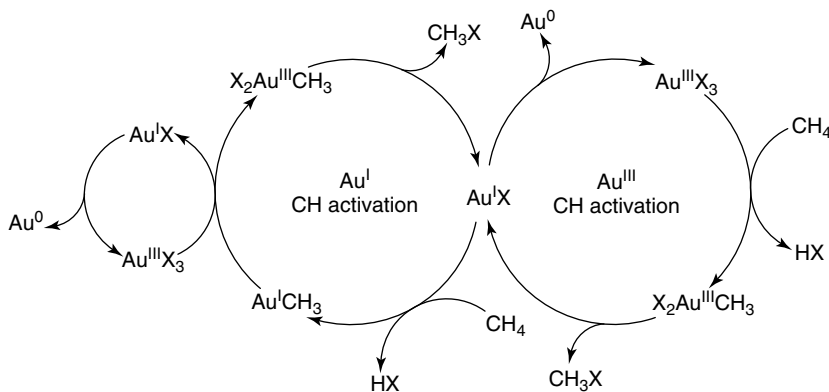
Scheme 28 Proposed catalytic cycle for methane oxidation by iodine in $\text{H}_2\text{SO}_4/\text{SO}_3$

addition of CH_3I to oleum at 150 °C showed quantitative formation of methyl bisulfate and a characteristic blue color species that was ascribed to I_2^+ .

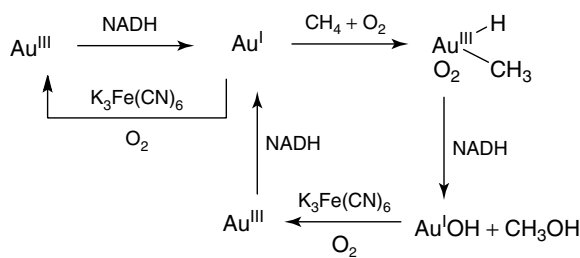
In contrast to the I_2^+ complex proposed by Periana and coworkers, Davico has postulated that an I^+ cation may be the catalyst.¹⁷² Davico carried out gas-phase reactions and ab initio calculations on the reactions of I_2^+ and I^+ with methane. It was shown that I_2^+ did not react with methane at a measurable rate, and computationally, all products generated from the addition of I_2^+ to methane are energetically not accessible. In contrast, I^+ was found to react with methane quite rapidly. On the basis of this evidence, Davico postulated that I^+ directly inserts into the methane CH bond to give CH_3IH^+ . The rest of the proposed catalytic cycle is essentially the same as that proposed by Periana and coworkers. It is important to note that Davico's results have no direct relevance to the catalytic system run in a highly polar sulfuric acid medium with oleum. This postulate is also in disagreement with the successful stoichiometric reaction of $\text{I}_2^+[\text{Sb}_2\text{F}_{11}]^-$ and methane in sulfuric acid and oleum. However, the 1/2 order dependency on iodine concentration found by Jarosińska *et al.* may indicate that a more extensive study is needed to rule out an I^+ catalytic complex.

Although $\text{I}_2\text{HS}_2\text{O}_7$ may have radical character, Periana and coworkers showed that addition of O_2 and $\text{K}_2\text{S}_2\text{O}_8$ had no appreciable effect on the reaction rate and selectivity.^{161,162} In contrast, using elemental bromine and chlorine under the same conditions, polyhalogenated methane derivatives were obtained, which are postulated to be the products of a radical process.

Gold-Catalyzed Functionalization Using SO_3 and H_2SO_4 to $\text{CH}_3\text{OSO}_3\text{H}$. In 2004, Periana, Goddard, and coworkers reported the first example of methane oxy-functionalization by a gold catalyst.¹⁷³ They showed that Au(III) (Au_2O_3) promotes stoichiometric methane activation and functionalization to yield metallic gold. The addition



Scheme 29 Possible Au(I) and Au(III) mechanisms for the Au-catalyzed functionalization of methane

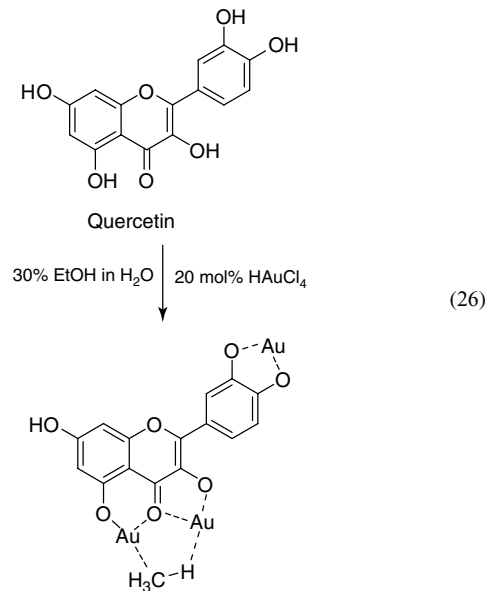


Scheme 30 Proposed catalytic cycle for gold-catalyzed methane functionalization with $K_3Fe(CN)_6$ and O_2

of H_2SeO_4 (a stronger oxidant than H_2SO_4) was shown to reoxidize elemental gold and render the system catalytic (Scheme 29). The use of metallic gold as a catalyst precursor in a 3 M H_2SeO_4 / H_2SO_4 solution as oxidant leads to a TON of up to 32 in 2 h and CH_4 conversions of 11% with 81% selectivity to CH_3OSO_3H . The addition of 2 wt % SO_3 increases both the conversion and selectivity. Methane conversion of up to 28% at 94% selectivity was ultimately reached under these optimized conditions. Introduction of O_2 (6 bar) did not alter the reaction rate, which likely excludes a radical mechanism. Instead, DFT calculations showed that electrophilic CH activation by Au(III) or Au(I) species is possible. If CH activation occurs by a substitution Au(III) pathway, subsequent reductive functionalization to methyl bisulfate and inorganic Au(I) species occurs, which is reoxidized by Se(VI). Alternatively, CH activation by au Au(I) pathway cannot directly yield functionalized products. Instead, oxidation to Au(III) is required for the functionalization step.

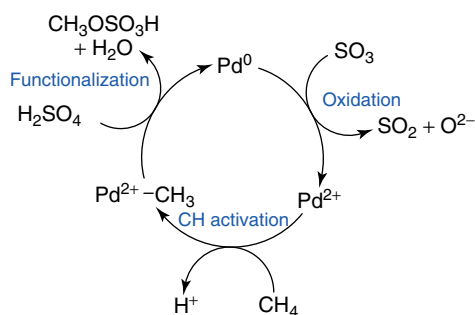
Auophilic microbes *Micrococcus luteus* can accumulate gold from the environment. This was found to be incorporated into a membrane-bound NADH oxidase called ‘Au-protein,’¹⁷⁴ which is capable of oxidizing methane to form methanol and other organic products in the presence of NADH, $K_3Fe(CN)_6$, and oxygen (Scheme 30). Gold is bound

to a rutin cofactor of the protein, which inspired Shilov and coworkers to investigate the methane oxidation of mixtures of gold and several bioflavonoids.^{175,176}



A mixture of 0.2 μM $HAuCl_4$ and 1 μM quercetin in 30% EtOH in water showed up to 60 turnovers based on added gold within 48 h at room temperature. A quercetin–gold complex that contains Au in three different coordination modes is proposed to be the catalytically active species (equation (26)). The fact that NADH, Fe(III), and oxygen are required for the functionalization of methane was explained by the following mechanism without further explanation of the single reaction steps.

Several theoretical studies of methane oxidation by gold complexes with simpler O-containing ligands^{177–179} showed that the activation barriers for methane in aqueous solvents are usually $>35\text{ kcal mol}^{-1}$. Only cationic Au(III) complexes showed lower activation energies.



Scheme 31 The catalytic cycle for palladium-catalyzed methane functionalization to methylbisulfate with SO_3 and H_2SO_4

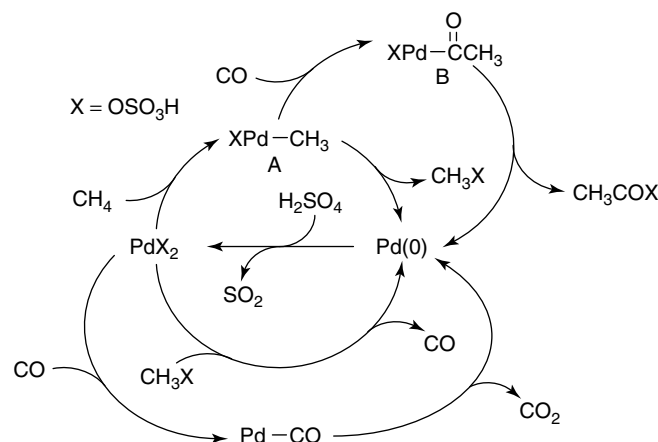
Palladium-Catalyzed Functionalization Using SO_3 to $\text{CH}_3\text{OSO}_3\text{H}$. Sen and coworkers^{110,111} showed the oxidation of methane to methylbisulfate by PdSO_4 in fuming sulfuric acid (H_2SO_4 containing 30% SO_3 , 160 °C, 1 day). In contrast to radical reactions that mainly form methanesulfonic acid under similar conditions (see Section 3.2.1), the Pd(II) reaction showed selective oxy-functionalization with a TON of up to 15 (Scheme 31). Palladium sulfate was replaced by metallic palladium in a later study by Michalkiewicz *et al.*¹⁸⁰ With 0.1–0.2 g of metallic palladium, up to 47 turnovers were achieved at 160 °C in just 2 h. Recycling of the catalyst was successful up to five times without loss of the catalyst's activity. The selectivity to methylbisulfate was found to be dependent on the SO_3 content of the solvent. At 30% SO_3 , significant amounts of CO_2 (~7–8% of added CH_4) were observed.

Palladium-Catalyzed Functionalization Using H_2SO_4 to $\text{CH}_3\text{CO}_2\text{H}$. In 2003, Periana, Taube, and coworkers¹⁸¹ reported the use of $\text{Pd}(\text{SO}_4)_2$ as a catalyst for the direct oxidative coupling of methane to acetic acid in 96% sulfuric acid (equation (27)). ^{13}C labeling studies showed that this process results remarkably in oxidative condensation of two molecules of methane to form acetic acid. The reaction occurs at greater than 90% selectivity and ~10% yield of acetic acid based on methane. On monitoring catalysis at 180 °C, one observed

up to 18 turnovers with a $\text{TOF} = \sim 10^{-3} \text{ s}^{-1}$, leading to a combined methanol and acetic acid yield of ~12% (Table 9). Sulfuric acid acts as both a solvent and an oxidant (8-electron oxidation process).



Periana *et al.* proposed a nonradical, two-step oxidation reaction shown in Scheme 32. Pd(II)-mediated CH activation of methane by an electrophilic substitution mechanism forms the $\text{Pd}(\text{II})-\text{CH}_3$ intermediate A. This species partially forms methylbisulfate, via a reductive elimination mechanism, which is further oxidized to CO by inorganic Pd(II). Insertion of CO into a $\text{Pd}(\text{II})-\text{C}$ bond of A forms the $\text{Pd}(\text{II})$ -acyl intermediate B, which, by reductive elimination, gives acetic acid and Pd(0). Importantly, this reaction proceeds by efficient carboxylation of the $\text{Pd}-\text{Me}$ species by CO generated *in situ* from methanol oxidation without excessive overoxidation to CO_2 . The formation of acetic acid is dependent on CO concentration, but increased CO concentration led to inhibition of catalysis. It was proposed



Scheme 32 Catalytic cycle for palladium-catalyzed methane functionalization to acetic acid in H_2SO_4

Table 9 Palladium-catalyzed methane functionalization^(a)

Entry	Time (h)	TON	CH_3OH (mM)	$\text{CH}_3\text{CO}_2\text{H}$ (mM)	CO_2 (mmol)	Yield (%)	% Carbon Selectivity			Additive
							CH_3OH	$\text{CH}_3\text{CO}_2\text{H}$	CO_2	
1	1	5	35	15	0.01	4 (93)	54	39	7	—
2	3	8	44	30	0.02	6 (91)	39	52	9	—
3	3	9	40	35	0.02	7 (92)	33	59	8	10% O_2
4	7	18	38	82	0.05	12 (89)	17	72	11	—
5	3	<1	0	8	0.16	~1	0	17	83	5% CO

^(a)TONs were calculated as $\{(4 \times [\text{CH}_3\text{CO}_2\text{H}] + [\text{CH}_3\text{OH}])/\text{[PdSO}_4\text{]}\}$. The % carbon yield of CH_3OH plus $\text{CH}_3\text{CO}_2\text{H}$ is based on amount of added CH_4 . The % carbon selectivity is relative to the total CH_3OH , $\text{CH}_3\text{CO}_2\text{H}$, and CO_2 produced. Values in parentheses are the combined selectivity for CH_3OH and $\text{CH}_3\text{CO}_2\text{H}$. Dashed entries indicate no additives.

Table 10 Comparison of palladium sources and additives for methane functionalization to $\text{CH}_3\text{CO}_2\text{H}$ and $\text{CH}_3\text{OH}^{(a)}$

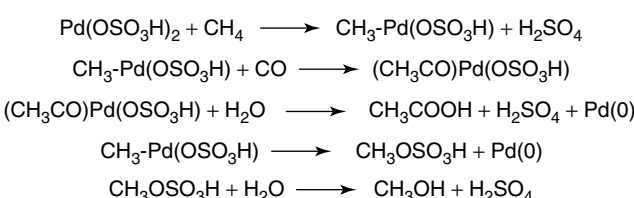
Entry	Catalyst	Co-catalyst	HOAc (mM)	CH_3OH (mM)
1	PdCl_2	—	10	8
2	PdSO_4	—	9	7
3	PdSO_4	CuCl_2	49	4

(a) Conditions: 3 mL of 96% H_2SO_4 ; 20 mM catalyst and co-catalyst; CH_4 (27.6 bar); O_2 (2.1 bar, when co-catalyst is present); 180 °C; 4 h.

that more acetic acid is produced with only methane as reactant versus methane and CO because of catalyst stability.

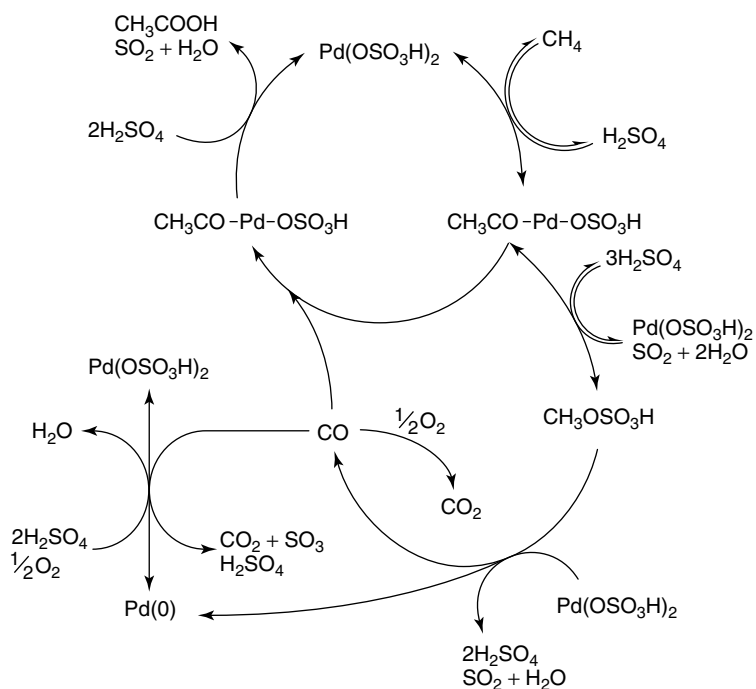
Bell and coworkers recently extended this work by utilizing O_2 as the final oxidant.^{182,183} Initial work¹⁸² used CuCl_2 as a co-catalyst in 96% sulfuric acid under a CH_4/O_2 atmosphere and resulted in a carbon selectivity of 47% to $\text{CH}_3\text{CO}_2\text{H}$ (9 mmol L⁻¹) and CH_3OH (7 mmol L⁻¹) after 4 h at 180 °C (Table 10). Analogous to Periana's report, Bell confirmed that CO is an intermediate and a by-product in the process. The authors proposed a stepwise mechanism for the functionalization of methane to acetic acid (Scheme 33).

In their initial publication, Bell and coworkers claimed that they could not reproduce the reported yields of acetic acid and methanol that Periana *et al.*¹⁸¹ reported, albeit they utilized different-sized reactors than those used by the Periana group. However, in a recent publication,¹⁸³ Bell and coworkers investigated similar reactions without the use of Cu as co-catalyst and reported yields similar to that of the Periana system in the absence of oxygen. When oxygen was present,

**Scheme 33** Stepwise mechanism for palladium-catalyzed methane functionalization to acetic acid with H_2SO_4

the yield of acetic acid was found to be strongly dependent on the ratio and pressure of CH_4 and O_2 . Higher O_2/CH_4 ratio and higher total pressure showed that higher yields of acetic acid and TON of up to ~14 (versus TON = 2.5 with Cu/O_2) could be obtained. By-products of this reaction include CO_x , $\text{CH}_3\text{SO}_3\text{H}$, $\text{CH}_3\text{OSO}_3\text{H}$, and $\text{CH}_2(\text{SO}_3\text{H})_2$, and the selectivity of acetic acid can be maximized up to 82% by lowering the reaction temperature to 160 °C. Bell's postulated mechanism is consistent with Periana's original proposal, except for the use of O_2 instead of SO_3 for Pd reoxidation (Scheme 34).

The formation of palladium black was found to be the major problem in the original Periana system. High CO concentrations led to reduction of the Pd catalyst and formation of Pd(0) that is only slowly reoxidized by SO_3 . The use of O_2 or $\text{O}_2/\text{Cu}(\text{II})$ increases the reoxidation rate and leads to higher TOF and product concentrations. In accordance with this proposal, the concentrations of Pd(II) found after the catalysis were increased when oxygen was used.

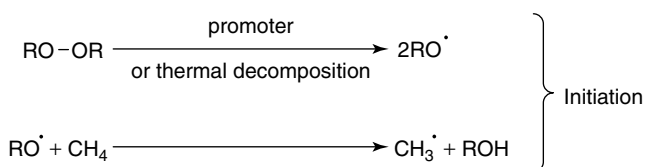
**Scheme 34** The catalytic cycle for palladium-catalyzed methane functionalization to acetic acid with O_2 and H_2SO_4

Bell and Chempath¹⁸⁴ systematically studied the mechanism of this Pd(II)-catalyzed methane oxidation to acetic acid by DFT methods. Their results agreed with previous mechanistic proposals. Cleavage of the methane CH bond takes place through electrophilic substitution by $\text{Pd}(\eta^2\text{-HSO}_4)(\text{HSO}_4)(\text{H}_2\text{SO}_4)$. Subsequent insertion of CO to the Pd–C bond of $\text{Pd}(\text{Me})(\text{HSO}_4)(\text{H}_2\text{SO}_4)_2$ to give $\text{Pd}(\text{CH}_3\text{CO})(\text{HSO}_4)(\text{HSO}_4)_2$ is thermodynamically favorable ($\Delta G^\circ = -14.4 \text{ kcal mol}^{-1}$). The formation of acetic acid via a direct reductive elimination from this Pd(II)–acyl intermediate was deemed to have too high a barrier. Instead, oxidation of $\text{Pd}^{\text{II}}(\text{CH}_3\text{CO})(\text{HSO}_4)(\text{HSO}_4)_2$ to the octahedral complex $\text{Pd}^{\text{IV}}(\text{HSO}_4)_3(\text{H}_2\text{SO}_4)_2(\text{CH}_3\text{CO})$ followed by subsequent reductive elimination of $\text{CH}_3\text{CO}(\text{HSO}_4)$ was proposed.

3 METHANE FUNCTIONALIZATION BY CHAIN REACTIONS

A widely employed method for the functionalization of methane, besides metal-catalyzed CH bond activation, is the use of radicals in stoichiometric or chain reactions. A typical free radical reaction uses a radical initiator, sometimes accompanied by a promoter^{185,186} to initiate a reaction (Scheme 35).¹⁸⁷ These can undergo free radical substitutions with CH_4 in the initiation step to yield methyl radicals.

Propagation of the chain generally occurs in two different modes (Scheme 36): propagation by addition of the

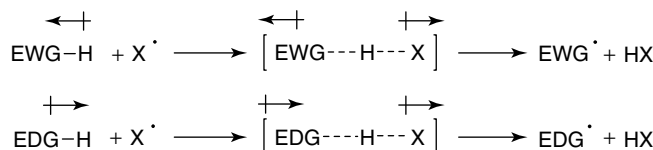


Scheme 35 Initiation of free radical chain reactions for methane functionalization by a peroxide initiator

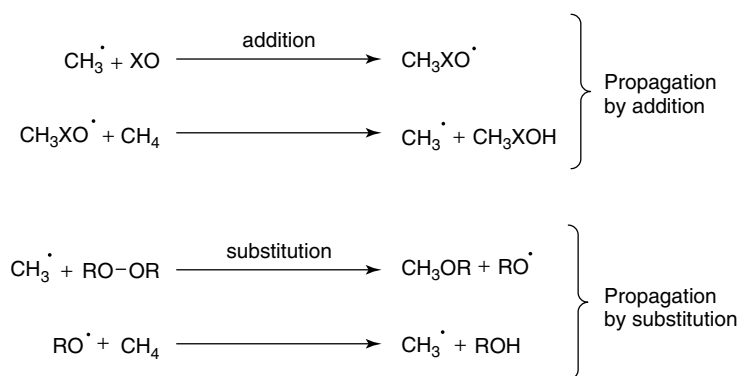
methyl radical to a double (or triple) bond and propagation by substitution of single bond (usually an O–O bond). Functionalization by addition of methyl radicals to double bonds (SO_2 , SO_3 , CO, CO_2 , or O_2) leads to O-centered radicals, CH_3XO , which in turn abstract H atoms from CH_4 to propagate the chain reaction. However, substitution of an O–O bond directly generates the oxy-functionalized product CH_3OR ; it also generates a new O-centered radical that propagates the chain reaction.

The use of free radical reactions for the functionalization of methane seems problematic at first sight owing to the difference in homolytic bond strength of the starting material (methane) and the products (e.g., methanol, methylsulfonic acid, or acetic acid). Nonetheless, a number of reactions that involve free radicals show a surprisingly high selectivity for functionalization of methane. This is usually attributed to the so-called “polar effect”^{188–192} or “polarity effect.”^{193,194} The activation energy of a radical transfer reaction can be influenced by polar forces in the transition state. The attack of an electrophilic radical (e.g., halogen radical, RO radical) on a CH bond can lead to a polar transition state, in which the electrophilic radical induces a positive charge on the carbon atom of the CH bond. Adjacent electron-withdrawing groups destabilize this transition state, while electron donation groups stabilize it.

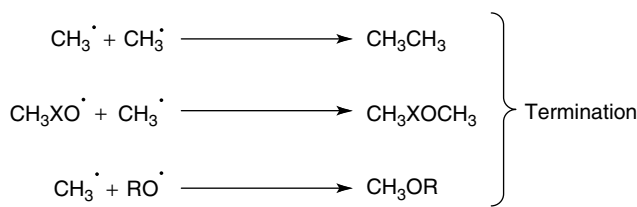
An example of this protection is the functionalization of methyl radicals by addition to SO_3 . The resulting methylsulfonic acid is protected against H-atom abstraction by the electron-withdrawing effect of the sulfonyl group and the



Scheme 37 Polar effect in radical transfer reactions. X^\cdot = electrophilic radical, EWG = electron-withdrawing group, EDG = electron-donating group



Scheme 36 General mechanism for methane functionalization by free radical chain reactions ($\text{X} = \text{C}, \text{CO}, \text{SO}, \text{SO}_2$, or O)



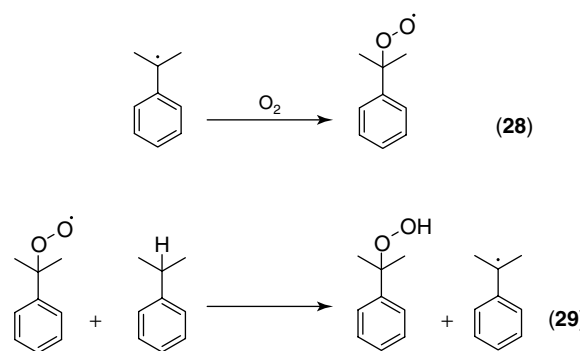
Scheme 38 Termination of free radical chain reactions for methane functionalization

formation of electrophilic CH_3SO_3 radicals. Less electrophilic or nucleophilic radicals will show less protection toward free radical substitution of methanesulfonic acid.¹⁹⁵

A key challenge in chain reactions is to maximize the number of times the propagation sequence (chain reactions that produce the product and the chain-carrying species) is repeated relative to the initiation or termination reactions (Scheme 38), so as to maximize the amount of product generated per mole of initiator consumed. In the context of methane functionalization, where the typical product is of relatively low value per mole (e.g., CH_3OH or $\text{CH}_3\text{SO}_3\text{H}$) and good economics requires large volumes, this can be a key challenge since most initiators are much more expensive than the reaction products on a molar basis.

3.1 Direct Use of Dioxygen for the Functionalization of Methane by Radical-Chain Reactions

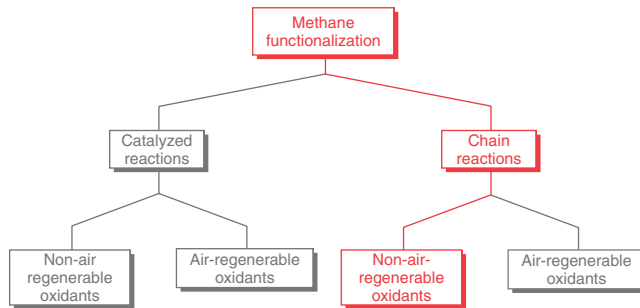
Alkanes can be functionalized directly with dioxygen by radical autoxidation processes. The most prominent example for the use of autoxidation in industrial syntheses is the cumene process, which produces phenol and acetone by oxidation of cumene with oxygen and subsequent rearrangement.¹⁹⁶ Homolysis of the benzylic CH bond in cumene forms a radical that can add to dioxygen to form a peroxy-radical (Scheme 39, equation (28)). The chain reaction propagates by abstraction of an H atom of another cumene molecule by the cumylperoxy radical to form a cumene radical and cumyl hydroperoxide (equation (29)).



Scheme 39 Propagation steps in the cumene process

It would be desirable to design a similar process for the functionalization of methane to methylhydroperoxide, and a related reaction is in fact already proposed (see Section 2.2.4). However, thermodynamic analysis shows that autoxidation analogous to the cumene process is not viable for methane. While the benzylic CH bond in cumene is relatively weak ($\text{BDE} \sim 83 \text{ kcal mol}^{-1}$),¹⁹⁷ which enables H-atom abstraction by the cumylperoxy radical ($\text{BDE} \sim 85\text{--}90 \text{ kcal mol}^{-1}$),¹⁹⁸ the CH bond in methane is considerably stronger ($\text{BDE} 104 \text{ kcal mol}^{-1}$) and further chain propagation by H-atom extraction of methane will be slow compared to known deactivation mechanisms.¹⁹⁹ This also seems to be the reason why several radical reactions with methane show severe inhibition in the presence of oxygen.^{111,200}

3.2 Chain Reactions with Reagents That Are Not Regenerable with O_2



Highlighted in this section are systems that involve free-radical-initiated chain reactions with methane using oxidants that cannot be regenerated by reaction with dioxygen. These systems are characterized by generation of a methyl radical via hydrogen atom abstraction. The methyl radical then undergoes functionalization and subsequently reacts with another equivalent of methane to generate the propagated methyl radical and the desired products.

3.2.1 Chain Reactions with $\text{S}_2\text{O}_8^{2-}$ and SO_2 to Produce $\text{CH}_3\text{SO}_3\text{H}$

Sulfonylation of methane to methanesulfonic acid (MSA) with SO_2 , Ca salts, and $\text{K}_2\text{S}_2\text{O}_8$ was reported by Bell and coworkers.²⁰¹ CaCl_2 and CaO_2 were the only promoters found to yield significant amounts of MSA. Screening of different reaction conditions showed that small changes in the catalyst system resulted in large changes in MSA yield (Table 11). Without addition of SO_2 , $\text{K}_2\text{S}_2\text{O}_8$, and CaCl_2 , or at too low reaction temperatures ($<45^\circ\text{C}$), no MSA formation was observed. Under optimized conditions, 2.89 mmol of MSA (22% yield based on SO_3) was produced in 10 h at 65°C . The authors believe that the reaction proceeds through

Table 11 Effect of reaction conditions on the sulfonation of methane to MSA^(a)

Entry	CH ₄ (mmol)	SO ₂ pressure (bar)	K ₂ S ₂ O ₈ (mmol)	CaCl ₂ (mmol)	T (°C)	MSA (mmol)	% conversion of SO ₂ to MSA
1	1000	2.4	5	0.6	65	1.84	14
2 ^(b)	1000	2.4	5	0.6	65	2.89	14
3	1000	2.4	5	0	65	Trace	Trace
4	1000	2.4	5	0.9	65	1.57	12
5	1000	2.4	0	0.6	65	0	0
6	1000	2.4	6.3	0.6	65	0.91	7
7	1000	2.4	5	0.6	45	Trace	Trace
8	1000	2.4	5	0.6	85	1.18	9
9 ^(c)	200	2.4	5	0.6	65	0.92	7
10	600	2.4	5	0.6	65	0.26	2
11	1200	2.4	5	0.6	65	2.1	16

(a) General reaction conditions: time, 10 h; solvent, triflic acid, 5 mL.

(b) Time, 26 h.

(c) Time, 72 h.

Ca²⁺-promoted formation of KSO₄[•], OH[•], or Cl[•], which then reacts with methane to form CH₃[•].

3.2.2 Chain Reactions Using S₂O₈²⁻ and CO₂

In an early report by Fujiwara and coworkers, CO₂ was suggested to be capable of functionalizing methane to form acetic acid in HTFA.²⁰² However, Spivey and coworkers have since doubted the validity of the claim based on thermodynamic considerations (Scheme 40).^{203,204}

Bell and coworkers suggested that carboxylation could be made thermodynamically favorable by using an anhydrous acid (Scheme 41).²⁰⁵ In anhydrous acid, the energy from the solvation of water provides the driving force for the reaction.

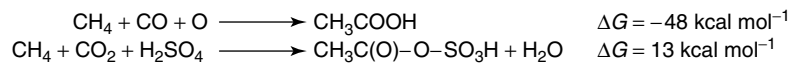
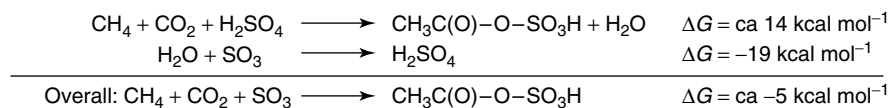
To prove this theory, triflic acid, sulfuric acid (oleum), and trifluoroacetic acid (HTFA) were tested as solvents for the functionalization of methane with CO₂. In a HTFA/TFAA solution, reaction of methane with potassium persulfate catalyzed by VO(acac)₂ yielded 40% CH₃CO₂H and 3.6% CF₃CO₂CH₃, (based on CH₄) in 17 h at 80 °C. Other anhydrous solvents were examined (H₂SO₄/SO₃ and triflic acid/triflic anhydride), but they gave lower yields of acetic

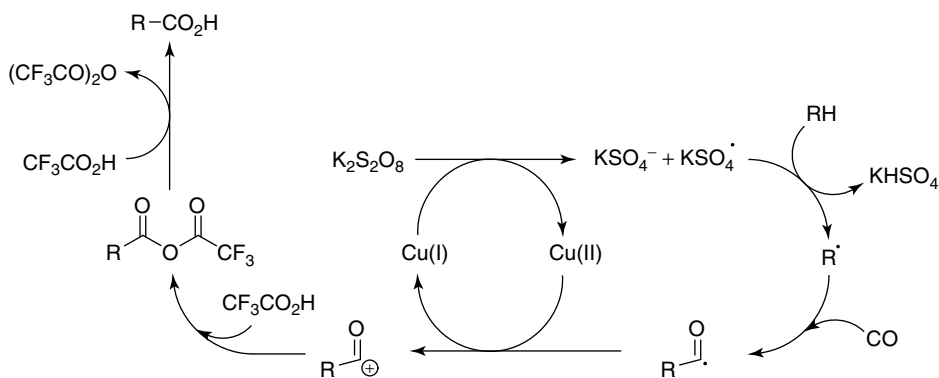
acid (7% and 13%, respectively). An in situ study (using NMR spectroscopy) of the H₂SO₄/SO₃ system shows the mixed acid anhydride CH₃C(O)-O-SO₃H as the immediate product, which is then hydrolyzed to acetic acid in the work-up.

3.2.3 Chain Reactions Using CO to Produce CH₃CO₂H

Originally reported by Sen and coworkers, though stoichiometric and nonmetal mediated, the reaction of K₂S₂O₈ and methane with CO produced acetic acid in good yields (48.6% yield based on K₂S₂O₈) at 105–115 °C after 10–16 h. Addition of metal salts by Fujiwara and Pombeiro^{207,208} expanded the previous work by facilitating the oxidation of the acyl radical (formed by the reaction of a methyl radical and CO) to form acetic acid as a product. Shul'pin's work with VO₃/H₂O₂/CO, described in Section 3.1.2, also falls under this category.

Chain Reactions with S₂O₈²⁻. A catalytic carboxylation of methane with CO and K₂S₂O₈ by a Pd/Cu catalyst was previously mentioned. The use of Cu(OAc)₂ under the same conditions (trifluoroacetic acid, K₂S₂O₈, 40-atm CO, 20-atm CH₄, 80 °C, 20 h) showed higher acetic acid yields (TON

**Scheme 40** Free-energy values for the carboxylation of methane with CO₂**Scheme 41** Free-energy values for the carboxylation of methane with CO₂, with SO₃ as the dehydrating agent



Scheme 42 Proposed copper-catalyzed methane functionalization to produce acetic acid

of 30). Reactions of xylene showed functionalization of the aromatic CH bonds with Pd or Pd/Cu, but showed dimerization when only Cu(II) was present. This led to the proposal of a radical-chain mechanism with the Cu salt in a dual role as promoter and $1-e^-$ oxidant (Scheme 42).

The Fujiwara group later reported $\text{VO}(\text{acac})_2$ as an efficient catalyst for methane carboxylation in the presence of CO and $\text{K}_2\text{S}_2\text{O}_8$ in HTFA to form acetic acid.²⁰⁶ After 20 h at 80 °C, acetic acid (TON = 27.5) is produced in a 93% yield (based on CH_4). Other simple vanadium complexes and vanadium-containing heteropolyacids such as $\text{H}_7\text{PV}_4\text{Mo}_8\text{O}_{40}\cdot30\text{H}_2\text{O}$ and $\text{H}_5\text{SiVW}_{11}\text{O}_{40}\cdot29\text{H}_2\text{O}$ also produced acetic acid with $\text{K}_2\text{S}_2\text{O}_8$, but the heteropolyacids were not dissolved under such conditions (see Section 2.2.3). Using other oxidants such as $t\text{-BuOOH}$ and NaOCl , the group obtained lower TON (<10) for the reaction. Utilization of $^{13}\text{CH}_4$ and ^{13}CO confirmed that the methyl group in acetic acid originated from methane and the carbonyl from carbon monoxide.

Pombeiro and coworkers described the role of amavadine (**18**) and related systems (V^{IV} , V^{V} , and V^{VI} complexes with N,O ligands) in catalyzing the conversion of methane and CO into acetic acid using $\text{K}_2\text{S}_2\text{O}_8$ as the oxidant (Chart 2).²⁰⁷ Amavadine derivatives, $\text{Ca}[\text{V}(\text{ON}(\text{CH}_2\text{COO})_2)_2]$ (**19**) and $[\text{VO}(\text{N}(\text{CH}_2\text{CH}_2\text{O})_3)]$ (**20**), were among the best systems, giving 25.4% (TON = 27.9) and 25.6% (TON = 28.2) yield, respectively (based on methane), after 20 h at 80 °C in TFA. In the absence of CO, the solvent also acted as the source of the

carbonyl. High CO pressures were shown to inhibit reactivity, whereas sufficiently low (15 bar) CO pressure enhanced the carboxylation of methane to yield acetic acid.

The Pombeiro group further optimized the catalytic system using **19** and **20**.²⁰⁸ The amavadine analogs were very efficient for the production of acetic acids (21.1% yield based on CH_4 ; TON = 5.39×10^3 in 20 h). Screening of possible oxidants ($\text{K}_2\text{S}_2\text{O}_8$, $(\text{NH}_4)_2\text{S}_2\text{O}_8$, H_2O_2 , oxone, $\text{K}_2\text{Cr}_2\text{O}_7$, KMnO_4 , or MnO_2) under catalytic conditions revealed that only persulfates were successful in initiating the reaction with methane. Ta and Mo compounds analogous to **19** showed very low activity and the Ca^{2+} counterion in some of the catalysts had no significant effect, as switching to an ammonium counterion showed no variance in reactivity. DFT calculations proposed a mechanism in which the vanadium complexes are oxidized by persulfate to a vanadium peroxy species, which then functionalizes an acyl radical (Scheme 43).

In a later study, the same group also showed methane carboxylation with the simple salts V_2O_4 (19% yield, TON 10), V_2O_5 (33% yield, TON 17), $\text{K}[\text{ReO}_4]$ (16% yield, TON 12), with CO and $\text{K}_2\text{S}_2\text{O}_8$ (as an oxidant), in HTFA at 80 °C in 20 h. Finally, under optimized conditions, the V_2O_4 system yielded 30.8% acetic acid (based on CH_4).²⁰⁹

Low-temperature catalysis by CaCl_2 to form acetic acid from methanol and CO, using $\text{K}_2\text{S}_2\text{O}_8$ as an oxidant, was reported by Fujiwara and coworkers.²¹⁰ Only 2–3 catalytic turnovers were observed, but acetic acid yield based on methane could be as high as 94% when a relative small

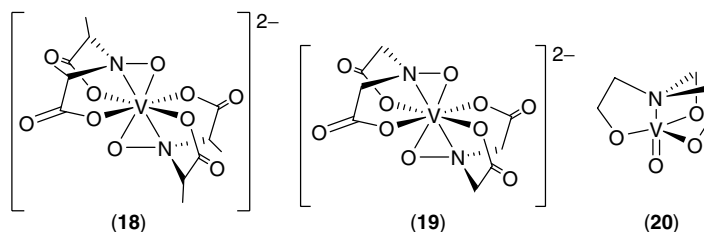
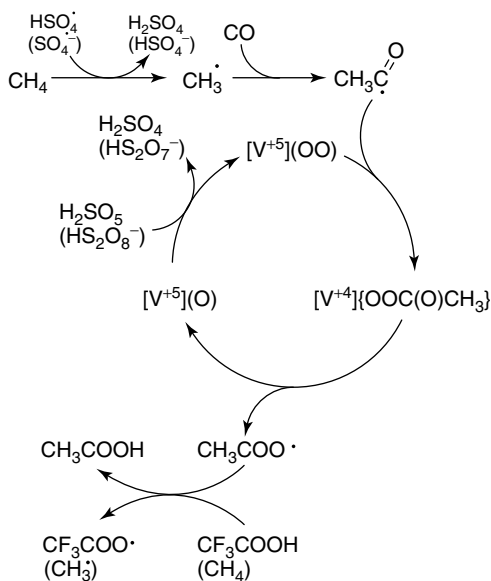


Chart 2 Amavadine (**18**) and analogs (**19**, **20**) for methane functionalization



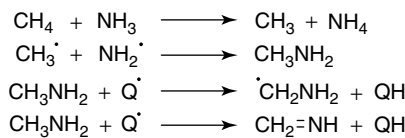
Scheme 43 The proposed mechanism for the vanadium-catalyzed methane carboxylation with CO and HS_2O_8^-

amount of methane (2 bar) was used. Using $^{13}\text{CH}_4$ and ^{13}CO , it was confirmed that the methyl group in acetic acid originated from methane and the carbonyl from carbon monoxide.

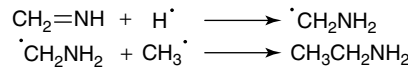
Chain Reactions with OCl^- . In a multiple-component system, Fujiwara and coworkers showed that Mn(III) and Yb(III) acetates (in 1 : 10 ratio) form an effective catalytic system for methane oxidation by NaClO.²¹¹ This aqueous-based system could achieve TONs as high as 69.1 (based on Yb) in 20 h at 40 °C. Using Mn(III) acetate alone, they obtained only trace activity, and using Yb(III) acetate, they achieved only 30% of the yield compared to that of the combined system. The authors proposed that a high-oxidation-state ytterbium-oxo species, generated from oxidation by Mn(III) and NaClO, was the active species in producing methyl radicals.

3.2.4 Chain Reactions That Produce $\text{CF}_3\text{CO}_2\text{CH}_3$

Fujiwara and coworkers found that Fe(II), Cr(II), or Mn(OAc)₂ oxidized methane using K₂S₂O₈ to an equal mixture of MeOAc and MetTFA.²¹² However, Cu(OAc)₂ yielded primarily MetTFA (98 : 2 of MeOAc) with TONs as high as 151 after 20 h at 100 °C. The reaction of methyl radicals and CO (from decomposition of the TFA) was suggested as the source of acetate. The authors attributed the high selectivity of Cu(II) to the oxidation of methyl radical to a methyl cation, which selectively forms MetTFA.



Scheme 44 Methane functionalization with ammonia by the photosensitized mercury



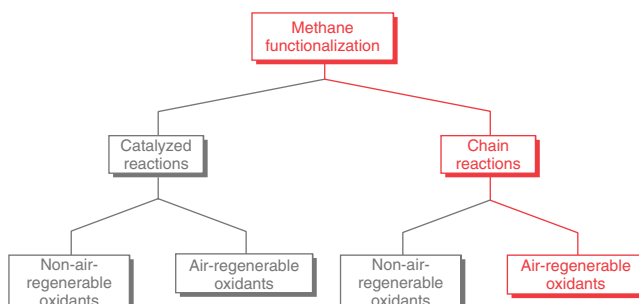
Scheme 45 Chain-reaction homologization of methylimine to ethylamine

3.2.5 Functionalization by Photolysis

Mercury vapor mediates the reaction of methane with ammonia upon irradiation at 254 nm.^{213,214} The photosensitized mercury alone did not react efficiently with simple alkanes (CH_4 , C_3H_6), while in the presence of NH_3 , facile functionalization was observed (Scheme 44). This is attributed to the formation of a Hg^*NH_3 exciplex that leads to a homolysis of the NH bond of the ammonia ligand. The exciplex formation was previously observed and showed a heat of formation of 17 kcal mol⁻¹.²¹⁵ The NH bond strength in ammonia is 107 kcal mol⁻¹, strong enough to form a radical that will functionalize both methane and ethane.

In a static reactor, an oligomeric liquid mixture containing C, H, and N was obtained. If the reaction was conducted under a constant gas flow and the products were collected in a -20 °C cold trap, the alkanes were functionalized to the corresponding imines. At low gas flow rates, even further functionalization to $\text{CH}_3\text{CH}=\text{NH}$ was observed. A possible mechanism for this reaction includes addition of a hydrogen radical to the N–H bond of the imine and reaction of the intermediate with another CH_3 radical to form the homologized amine, which is again converted to the imine (Scheme 45).

3.3 Chain Reactions with O_2 or Air-Regenerable Reagents



Chain reactions with methane using oxidants that can be regenerated by direct reaction with dioxygen are described below. These systems are characterized by generation of a methyl radical via hydrogen atom abstraction. The methyl radical then undergoes functionalization and subsequently reacts with another equivalent of methane to generate the propagated methyl radical and the desired products.

3.3.1 Peroxide-Initiated Functionalization with SO_3

In a series of publications by Mukhopadhyay and Bell, the researchers demonstrated the functionalization of methane to methanesulfonic acid (MSA) by SO_3 in the presence of free radical initiators.^{216–220} These reports usually included an initial screen of a set of initiators and, in some cases, promoters. An optimization study of the system was then performed to determine the highest yield of MSA.

Calcium-Peroxide-Initiated Functionalization to $\text{CH}_3\text{SO}_3\text{H}$. Screening of strontium, lead, sodium, lithium, barium, magnesium, and calcium peroxides as free radical initiators for sulfonation of methane to methanesulfonic acid (MSA) with SO_3 was performed.^{216–220} Calcium and barium were both identified as good candidates as initiators for MSA synthesis. By changing the methane pressure, $[\text{SO}_3]$, [initiator], and temperature, it was observed that the best conditions were $\text{CH}_4 = 44.8$ bar, 30 wt % SO_3 , and 0.6-mmol CaO_2 for 5 h at 65 °C, which yielded 91% conversion of SO_3 to MSA. In addition, HTFA, H_2SO_4 , and $\text{CF}_3\text{SO}_3\text{H}$ were screened as solvents for the reaction, and H_2SO_4 was determined as the best solvent. Lower conversions were observed when more than 0.6 mmol of the metal peroxide was used (presumably due to decomposition of H_2O_2 to O_2 , which can act as a free radical scavenger).

Table 12 Direct free-radical-initiated methane sulfonation with $\text{SO}_3^{(a)}$

Entry	Parameters	% conversion of SO_3 to MSA
1	N/A	0
2	0.052 mmol	14
3	0.104 mmol	21
4	0.208 mmol	16
5	Temperature, 85 °C	7
6	Temperature, 105 °C	14
7	5.5 bar	6
8	SO_3 , 15 wt %	11
9	SO_3 , 38 wt %	26
10	SO_3 , 52 wt %	19

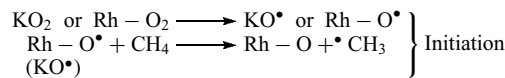
^(a) General reaction conditions unless otherwise stated: methane, 13.8 bar (58 mmol); SO_3 , 30 wt % (21.4 mmol); initiator, 0.104 mmol; temperature, 95 °C; H_2SO_4 (SO_3), 5.7 g.

Peroxydiphosphate-Initiated Functionalization to $\text{CH}_3\text{SO}_3\text{H}$.



The sulfonation of methane to methanesulfonic acid (MSA) with SO_3 was initiated with $\text{K}_4\text{P}_2\text{O}_8$ to test lower methane pressures (i.e., 13.8 bar vs 68.9 bar).^{216–220} Different initiators ($\text{K}_4\text{P}_2\text{O}_8$, $\text{K}_2\text{S}_2\text{O}_8$, Oxone, and H_2O_2) were screened, and $\text{K}_4\text{P}_2\text{O}_8$ showed the highest MSA yield (21% based on SO_3) (Table 12). Slightly higher SO_3 concentrations (i.e., 38% versus 30%) gave up to 26% conversion of SO_3 to MSA.

Potassium-Peroxide-Initiated, Rh-Mediated Functionalization to $\text{CH}_3\text{SO}_3\text{H}$. The sulfonation of methane to methanesulfonic acid (MSA) with SO_3 in the presence of a peroxide (KO_2 in this case) and promoters (metal salts) was performed in fuming sulfuric acid.^{216–220} The examination of metal salts as promoters revealed that RhCl_3 functions as the most efficient radical promoter. Under optimum conditions, 24% conversion of SO_3 to MSA was achieved. The authors propose that a rhodium-peroxy or -hydroperoxy species is formed in situ, which is a more effective free radical initiator than KO_2 .



Urea-Peroxide-Initiated, Rh-Mediated Functionalization with SO_3 . The sulfonation of methane to methanesulfonic acid (MSA) with SO_3 initiated by urea/ H_2O_2 was screened with different promoters (i.e., metal salts).^{216–220} The highest selectivity and conversion to MSA was observed with RhCl_3 as the radical promoter. The catalyst system is very sensitive to changes in catalytic conditions such as [$\text{urea}/\text{H}_2\text{O}_2$], [RhCl_3], CH_4 pressure, identity of initiator, and temperature (Table 13).

In a subsequent report,^{216–220} a stepwise conversion of methane to methanol via MSA and $\text{CH}_3\text{OSO}_3\text{H}$ was examined by Bell and coworkers (Scheme 46). RhCl_3 and SO_3 were used for the conversion of MSA to $\text{CH}_3\text{OSO}_3\text{H}$ and $\text{CH}_3\text{SO}_3\text{CH}_3$ in neat MSA. Increase in the added SO_3 showed an increase not only in the conversion of MSA but also in $\text{CH}_3\text{SO}_3\text{CH}_3$ yields. However, when sulfuric acid was used as a solvent, MSA was almost quantitatively (96%) converted to $\text{CH}_3\text{OSO}_3\text{H}$. Hydrolysis of $\text{CH}_3\text{OSO}_3\text{H}$ to methanol in a biphasic system of H_2O and chlorinated solvents (CH_2Cl_2 , CHCl_3 , $\text{C}_2\text{H}_4\text{Cl}_2$) revealed a single-pass conversion of 63% in $\text{C}_2\text{H}_4\text{Cl}_2$ with a molar ratio of 5 : 1 (H_2O : MSA) at 83 °C in 2 h.

3.3.2 Chain Reactions Using O_2 and CO or CO_2

Shul'pin and coworkers reported NaVO_3 to be an effective catalyst for methane functionalization with added

Table 13 Effect of process parameters on the sulfonation of methane^(a)

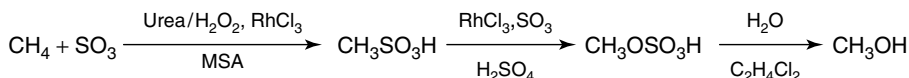
Entry	CH ₄ (bar),	<i>t</i> (h)	Initiator (mmol)	RhCl ₃ (mmol)	<i>T</i> (°C)	MSA (mmol)	SO ₃ conversion ^(b) (%), (CH ₄ conversion ^(c) (%))
1	44.8	3	urea/H ₂ O ₂ , 0.74	0.33	65	16.8	79 (13)
2	44.8	3	urea/H ₂ O ₂ , 0	0.33	65	0.06	0.3 (–)
3	44.8	3	urea/H ₂ O ₂ , 0.16	0.33	65	14.5	68 (8)
4	44.8	3	urea/H ₂ O ₂ , 0.96	0.33	65	14.7	69 (8)
5	44.8	3	urea/H ₂ O ₂ , 0.74	0	65	4.9	23 (3)
6	44.8	3	urea/H ₂ O ₂ , 0.74	0.14	65	20.2	95 (11)
7	5.52	3	urea/H ₂ O ₂ , 0.74	0.33	160	0.5	2 (24)
8	44.8	3	CaO ₂ , 0.74	0.33	65	13.3	63 (7)
9 ^(d)	44.8	3	CaO ₂ , 0.74	0.24	65	32	75 (18)

^(a) General reaction conditions: SO₃ (1.7 g, 21.26 mmol), urea/H₂O₂ as radical initiator, RhCl₃ as promoter, fuming sulfuric acid (30 wt % SO₃, 5.67 g) as solvent.

^(b) Moles of SO₃ converted to MSA/total moles of SO₃ in the autoclave.

^(c) Moles of methane converted/moles of methane in the autoclave.

^(d) Amount of fuming sulfuric acid used, 11.34 g (initial SO₃ amount, 42.52 mmol).

**Scheme 46** Conversion of methane to methanol

CO or CO₂ and O₂ or H₂O₂ to give a mixture of acetic acid, methanol, methyl hydroperoxide, and formaldehyde.²²¹ Depending on the identity of the oxidant, a variety of products were observed (equation (30) vs (31)).



In the presence of air, CO and sodium vanadate yield a mixture of acetic acid, MeOH, and formaldehyde in a ratio of 20:9:6 (TON = 35 in 6 h). However, in the presence of H₂O₂, CO, and pyrazine-2-carboxylic acid as co-catalysts, acetic acid is the only product (TON = 12 in 8 h). Interestingly, no methyl hydroperoxide was reported in the reaction with air, and it was only observed as a by-product in reactions with low CO pressure. Two different reaction mechanisms operate this system depending on the added oxidant, as characterized by the varied product distributions. The H₂O₂/CO functionalization could proceed in a manner similar to those of K₂S₂O₈/CO functionalization reactions (See Section 3.1.3). The use of H₂O₂ as the oxidant in the presence of CO₂ also led to highly selective formation of acetic acid (TON = 20 in 30 h). The authors explain a similar selectivity with reductive formation of CO from CO₂ in the latter reactions.

4 CONCLUSION

To augment oil and mitigate the flaring of associated gas, a low-cost process for the conversion of methane to liquid products is urgently needed today. To maximize utility as liquid fuels and flexible chemical feedstocks, the ideal products are either oxygenates (such as methanol or dimethyl ether) or higher hydrocarbons (such as long-chain alkanes). Other products such as methanesulfonic acid, acetic acid, or aromatics can play an important role in potentially replacing existing chemical processes, but are unlikely to meet the economic requirements for use as precursors to liquid fuels or flexible chemical feedstocks. The current commercial processes that carry out the transformations to these desired liquid products, such as the methanol and Fischer–Tropsch processes, are too capital intensive, given the high temperature and indirect syngas processes utilized. Consequently, the goal of new methane-functionalization chemistry is to reduce the capital costs while meeting or surpassing the high carbon yield (~70%) of the existing processes. This goal leads to guidelines for new methane-functionalization chemistry: (i) operate at 200–250 °C in order to minimize the cost of reactors and heat management; (ii) directly convert methane into a functionalized product in order to minimize the number of process steps; (iii) utilize O₂ (ideally low-pressure air) as the ultimate oxidant since this is the only co-reagent that can be economically used on the immense scale required to produce fuels and chemical feedstocks; (iv) operate at a space–time

yield (STY) of $\sim 10^{-6}$ mol cm $^{-3} \cdot$ s $^{-1}$ in order to maximize the efficiency of the reactor systems and minimize capital costs; and (5) attain a minimum overall carbon yield of $\sim 70\%$ in order to compete with the existing commercial processes.

As can be seen from the diverse range of systems reported in this article, substantial progress has been made on the development of low-temperature, selective functionalization of methane to liquid products. However, no chemistry has emerged yet that provides a substantial reduction in costs relative to the commercially available high-temperature, syngas-based processes to justify aggressive commercial development. Consequently, the rapid search for new methane chemistry must continue in order to allow methane to augment oil in the medium term and to minimize flaring of “associated gas” in the short term. In this article, we have attempted to categorize the broad range of “homogeneous, metal-mediated methane-functionalization” systems based on whether O₂ is the only terminal oxidant and whether the chemistry operates via a catalytic or a chain mechanism.

Within the systems that utilize O₂ as the ultimate oxidant, two distinct approaches have emerged: systems that use O₂ directly and systems that utilize O₂ indirectly via a two-step process. From the perspective of simplicity, there seems to be an inherent advantage of the direct use of O₂. However, the indirect use of O₂ may be advantageous because of safety and cost issues. It is thus important to explore both types of systems in order to expand the range of possible solutions.

The reported approaches follow two distinct mechanistic strategies: those based on homogeneous catalysts and those based on chain reactions. A survey of the literature shows that the most efficient systems to date (based on STY) utilize catalysis as opposed to chain reactions. However, it can be argued that such a survey is not the appropriate method of comparing the relative merits of the approaches and that the chemistries are not yet fully developed. From a consideration of the fundamental chemistry, it could be appealing to consider that catalytic reactions could allow greater control, be more selective, and be less expensive. However, chain reactions can also utilize catalysts in metal-mediated chain reactions that can allow the desired control; the data shows that by employing the concept of “product protection,” high selectivities are possible in chain reactions, and in some cases the amount of product generated per mole of initiator can rival the TON obtained in catalyzed reactions. Consequently, it is not clear that any strong recommendation can be made regarding the merits of a chain reaction mechanism versus a catalyzed reaction mechanism. However, if one projects the “ideal” requirements for a commercial solution, this could allow some greater degree of discrimination between the approaches. Thus far, no chemical system has been developed that can generate methanol or long-chain hydrocarbons directly in a one-step process. All the high-yield systems reviewed utilized the concept of “product protection,” which, as was noted in the Catalytica system,

comes at an economic penalty that has prevented that system from being commercialized. In the “ideal” case, no product protection would be required, and methanol or long-chain hydrocarbons would be directly produced by some system that shows, as discussed above, selectivities of $\sim 70\%$. There is little precedent to show that chain reactions that operate by radical mechanism can produce the desired products with overall yields of $\sim 70\%$. This is because it is well-established that the relative rates of free radical reactions strongly correlate with the homolytic bond strengths and as such free radicals would tend to react faster with the CH bonds of methanol or long-chain alkanes than with methane. However, there are reports that show that catalyzed reactions of methane that proceed by both CH activation and oxidant activation (Mayer) can be slower with methanol and higher alkanes compared to methane. This may suggest that catalyzed processes allow higher selectivities that are required for the eventual “ideal” process. However, an important challenge that needs to be addressed in developing catalytic systems based on the CH activation reaction is that many systems that are active for the CH activation reaction are inhibited by oxidants that are required for the overall oxidation of methane to alcohols or long-chain-hydrocarbon liquid products.

Clearly from a practical point of view, the focus needs to be on the use of O₂ or air-regenerable reagents. As discussed, given practical issues such as the possibility for explosion and the need for pure O₂ to minimize CH₄/N₂ separations, coupled with the potential challenges with likely free radical chemistry in the preferred temperature range, the inherent elegance of direct reactions of CH₄ and O₂ loses out to the slightly more complicated two-step processes that utilize air-regenerable reagents. Within the area of air-regenerable functionalization reagents, the most commonly utilized were H₂SO₄, SO₃, Cu(II), and HPAs. As noted above, the use of SO₃ and H₂SO₄ leads to product separation issues, unless very high conversion of these materials can be attained and the use of anhydrous H₂SO₄ or SO₃ likely will not lead to practical processes. Given the stringent need to maintain low costs, the most likely practical systems would utilize some low-molecular-weight, nonvolatile, air-regenerable electron acceptors such as Cu(II)/Cu(I) couple or O-atom donors such as a NO₃/NO₂⁻ couple.

In addition to the functionalization reagent, another important consideration is the solvent. From an economic perspective, water is the ideal solvent, given the cost and relative ease of separation from desired products. However, as noted systems that operate by CH activation are often inhibited by water and this could provide a basis for preferring the chain reaction systems that do not operate by coordination reactions.

In summary, significant progress has been made in developing new, low-temperature chemistry for the selective conversion of methane to liquid products that could eventually lead to low-cost practical processes. However, none of these systems developed to date are close to commercialization, and it is likely that significant advances in methane chemistry

will be required before practical processes can be developed. Given the potential for converting the vast reserves of natural gas to liquid products and minimizing emissions that could mitigate concerns of global warming, it is imperative that we resolutely continue to develop the chemistry that will enable such a vision.

5 RELATED ARTICLES

Electrochemical and Photoelectrochemical Conversion of CO₂ to Alcohols; Molecular Catalysis for Fuel Cells; Molecular Catalysts for Oxygen Production from Water; Photocatalytic Hydrogen Production from Water; Some Computational Challenges in Energy Research.

6 ABBREVIATIONS AND ACRONYMS

acac = acetylacetone; BDE = bond disassociation energy; bpym = bipyrimidine; im = imidazolium; hfacac = 1,1,5,5,5-hexafluoropentane-2,4-dione; HOAc = acetic acid; HTFA = trifluoroacetic acid; MBS = Methyl bisulfate; 1-mim = 1-methylimidazolium; MeCN = acetonitrile; MeTFA = methyl trifluoroacetate; MSA = methanesulfonic acid; MTL = methanol to liquids; NHC = N-heterocyclic carbene; NNC = 6-phenyl-2,2'-bipyridine; OAc = acetate; Ox = electron acceptor; PCA = pyrazine-2-carboxylic acid; STY = space-time yield (mol/cc/s); TFA = trifluoroacetate; TFAA = trifluoroacetic anhydride; TMTACN = 1,4,7-trimethyl-1,4,7-triazacyclononane; TOF = turnover frequency (s⁻¹); TON = turnover number; UV = ultraviolet; YO = O-atom donor.

7 REFERENCES

- G. A. Olah and Á. Molnár, 'Hydrocarbon Chemistry Ed. II', Wiley Interscience, 2003.
- G. A. Olah, A. Goeppert, and G. K. S. Prakash, 'Beyond Oil and Gas: The Methanol Economy', Wiley-VCH, 2006.
- E. E. Wolf. Ed. 'Methane Conversion by Oxidative Processes', Van Nostrand Reinhold; New York, 1992.
- R. A. Periana, *C E News*, 2001, **79**, 287.
- H. E. Curry-Hyde and R. F. Howe Eds. 'Natural Gas Conversion II', Elsevier, New York, 1994.
- US Department of Energy, 'International Energy Annual', 2007.
- C. D. Elvidge, E. H. Erwin, K. E. Baugh, B. T. Tuttle, A. T. Howard, D. W. Pack, and C. Milesi, *Oil Gas J.*, 2007, **105**, 50. World Bank Issue Brief / GGFR2006.
- S. Solomon, D. Qin, M. Manning, Z. Chen, M. Marquis, K. B. Averyt, M. Tignor, and H. L. Miller, 'Contribution of Working Group I to the Fourth Assessment Report of the Intergovernmental Panel on Climate Change', Cambridge University Press, Cambridge, United Kingdom and New York, NY, USA, 2007, Chap. 2.
- R. H. Crabtree, *Chem. Rev.*, 1985, **95**, 987.
- R. H. Crabtree, *Chem. Rev.*, 1995, **85**, 245.
- J. H. Lunsford, *Catal. Today*, 2000, **63**, 165.
- E. G. Derouane, J. Haber, F. Lemos, F. R. Ribeiro, M. Guisnet eds., 'Catalytic Activation and Functionalization of Light Alkanes', in 'Advances and Challenges', Nato ASI Series, Kluwer Academic Publishers; Dordrecht, The Netherlands, 1997.
- B. A. Arndtsen, R. G. Bergman, T. A. Mobley, and T. H. Peterson, *Acc. Chem. Res.*, 1995, **28**, 154.
- A. E. Shilov and G. B. Shul'pin, 'Activation and Catalytic Reactions of Saturated Hydrocarbons in the Presence of Metal Complexes', Kluwer Academic, Dordrecht, 2000.
- C. G. Jia, T. Kitamura, and Y. Fujiwara, *Acc. Chem. Res.*, 2001, **38**, 633.
- W. D. Jones, *Acc. Chem. Res.*, 2003, **36**, 140.
- R. H. Crabtree, *Dalton Trans.*, 2001, **19**, 2437.
- J. A. Labinger and J. E. Bercaw, *Nature*, 2002, **417**, 507.
- R. A. Periana, G. Bhalla, W. J. Tenn III, K. J. H. Young, X. Y. Liu, O. Mironov, C. Jones, and V. R. Ziatdinov, *J. Mol. Catal. A: Chem.* 2004, **220**, 7.
- M.-H. Baik, M. Newcomb, R. A. Friesner, and S. J. Lippard, *Chem. Rev.*, 2003, **103**, 2385. For Recent Reviews on Biological Methane Oxidation.
- M. Strous and M. S. M. Jetten, *Annu. Rev. Microbiol.*, 2004, **58**, 99.
- S. J. Lippard, *Phil. Trans. R. Soc. A.*, 2005, **363**, 861.
- R. Balasubramanian and A. C. Rosenzweig, *Acc. Chem. Res.*, 2007, **40**, 573.
- A. S. Hakemian and A. C. Rosenzweig, *Annu. Rev. Biochem.*, 2007, **76**, 223.
- A. E. Shilov and G. B. Shul'pin, *Chem. Rev.*, 1997, **97**, 2879.
- S. S. Stahl, J. A. Labinger, and J. E. Bercaw, *Angew. Chem., Int. Ed.*, 1998, **37**, 2180.
- M. Lersch and M. Tilset, *Chem. Rev.*, 2005, **105**, 2471.
- A. A. Fokin and P. R. Schreiner, *Chem. Rev.*, 2002, **102**, 1551.
- T. J. Hall, J. S. J. Hargreaves, G. J. Hutchings, R. W. Joyner, and S. H. Taylor, *Fuel Process. Technol.*, 1995, **42**, 151.
- C. I. Herreras, X. Yao, Z. Li, and C.-J. Li, *Chem. Rev.*, 2007, **107**, 2546.
- J. H. Edwards and N. R. Foster, *Fuel Sci. Technol. Int.*, 1986, **4**, 365.
- A. E. Shilov, 'Activation of Saturated Hydrocarbons by Transition Metal Complexes', Riedel, Dordrecht, 1984.
- J. A. Labinger and J. E. Bercaw, *Nature*, 2002, **417**, 507.

34. A. E. Shilov and G. B. Shul'pin, 'Activation and Catalytic Reactions of Saturated Hydrocarbons in the Presence of Metal Complexes', Kluwer Academic, Dordrecht, 2000.
35. A. E. Shilov and A. A. Shteinman, *Coord. Chem. Rev.*, 1977, **24**, 97.
36. G. S. Chen, J. A. Labinger, and J. E. Bercaw, *Proc. Natl. Acad. Sci. U.S.A.*, 2007, **104**, 6915.
37. U. Fekl and K. Goldberg, *Adv. Inorg. Chem.*, 2003, **54**, 259.
38. M.-H. Baik, M. Newcomb, R. A. Friesner, and S. J. Lippard, *Chem. Rev.* 2003, **103**, 2385.
39. R. L. Lieberman and A. C. Rosenzwig, *Crit. Rev. Biochem. Mol.*, 2004, **39**, 147.
40. A. Sen, *Acc. Chem. Res.*, 1998, **31**, 550.
41. V. V. Rostovtsev, J. A. Labinger, J. E. Bercaw, T. Lasseter, and K. I. Goldberg, *Organometallics*, 1998, **17**, 4530.
42. D. D. Wick and K. I. Goldberg, *J. Am. Chem. Soc.*, 1999, **121**, 11900.
43. V. V. Rostovtsev, L. Henling, J. A. Labinger, and J. E. Bercaw, *Inorg. Chem.*, 2002, **41**, 3608.
44. A. N. Vedernikov, S. A. Binfield, P. Y. Zavalij, and J. R. Khusnutdinova, *J. Am. Chem. Soc.*, 2005, **128**, 83.
45. J. L. Butikofer, T. G. Parson, and D. M. Roddick, *Organometallics*, 2006, **25**, 6108.
46. J. R. Khusnutdinova, P. Y. Zavalij, and A. N. Vedernikov, *Organometallics*, 2007, **26**, 3466.
47. A. V. Pawlikowski, A. D. Getty, and K. I. Goldberg, *J. Am. Chem. Soc.*, 2007, **129**, 10382.
48. A. N. Vedernikov, *Curr. Org. Chem.*, 2007, **11**, 1401. For a recent review on platinum mediated C-H bond functionalization.
49. A. Yahav-Levi, I. Goldberg, A. Vigalok, and A. N. Vedernikov, *J. Am. Chem. Soc.*, 2008, **130**, 724.
50. K. A. Grice and K. I. Goldberg, *Organometallics*, 2009, **28**, 953.
51. I. T. Horváth, R. A. Cook, J. M. Millar, and G. Kiss, *Organometallics*, 1993, **12**, 8.
52. I. T. Horváth and J. M. Millar, *Chem. Rev.*, 1991, **91**, 1339.
53. E. Gretz, T. F. Oliver, and A. Sen, *J. Am. Chem. Soc.*, 1987, **109**, 8109.
54. A. Sen, E. Gretz, T. F. Oliver, and Z. Jiang, *New J. Chem.*, 1989, **13**, 755.
55. L. C. Kao, A. C. Hutson, and A. Sen, *J. Am. Chem. Soc.*, 1991, **113**, 700.
56. G. Ingrosso and N. Midollini, *J. Mol. Catal. A: Chem.*, 2003, **204–205**, 425.
57. M. Muehlhofer, T. Strassner, and W. A. Herrmann, *Angew. Chem., Int. Ed.*, 2002, **41**, 1745.
58. T. Strassner, M. Muehlhofer, A. Zeller, E. Herdtweck, and W. A. Herrmann, *J. Organomet. Chem.*, 2004, **689**, 1481.
59. S. Ahrens, A. Zeller, Z. Taige, and T. Strassner, *Organometallics*, 2006, **25**, 5409.
60. D. Meyer, M. A. Taige, A. Zeller, K. Hohlfeld, S. Ahrens, and T. Strassner, *Organometallics*, 2009, **28**, 2142.
61. T. Strassner, S. Ahrens, and A. Zeller, WO 2006058535, A2, 2006.
62. K. J. H. Young, J. Osgaard, D. H. Ess, S. K. Meier, T. Stewart, W. A. Goddard, and R. A. Periana, *Chem. Commun.* 2009, 3270.
63. M. E. Thompson, S. M. Baxter, A. R. Bulls, B. J. Burger, M. C. Nolan, B. D. Santarsiero, W. P. Schaefer, and J. E. Bercaw, *J. Am. Chem. Soc.*, 1987, **109**, 203.
64. A. D. Sadow and T. D. Tilley, *J. Am. Chem. Soc.*, 2003, **125**(26), 7971.
65. N. Barros, O. Eisenstein, L. Maron, and T. D. Tilley, *Organometallics*, 2006, **25**, 5699.
66. A. D. Sadow and T. D. Tilley, *Angew. Chem., Int. Ed.*, 2003, **42**(7), 803.
67. A. D. Sadow and T. D. Tilley, *J. Am. Chem. Soc.*, 2005, **127**(2), 643.
68. G. A. Olah and R. H. Schlosberg, *J. Am. Chem. Soc.*, 1967, **89**, 2227.
69. G. A. Olah and J. Lukas, *J. Am. Chem. Soc.*, 1967, **89**, 4739.
70. G. A. Olah and R. H. Schlosberg, *J. Am. Chem. Soc.*, 1968, **90**, 2726.
71. G. A. Olah, G. Klopman, and R. H. Schlosberg, *J. Am. Chem. Soc.*, 1969, **91**, 3261.
72. G. A. Olah and Y. K. Mo, *J. Am. Chem. Soc.*, 1972, **94**, 6864.
73. G. A. Olah, R. Renner, P. Schilling, and Y. K. Mo, *J. Am. Chem. Soc.*, 1973, **95**, 7686.
74. G. A. Olah and H. C. Lin, *J. Am. Chem. Soc.*, 1971, **93**, 1259.
75. G. A. Olah, P. Ramaiah, and G. K. S. Prakash, *Proc. Natl. Acad. Sci. USA*, 1997, **94**, 11783.
76. G. A. Olah, N. Yoneda, and D. G. Parker, *J. Am. Chem. Soc.*, 1976, **116**, 5261.
77. G. A. Olah, N. Yoneda, and D. G. Parker, *J. Am. Chem. Soc.*, 1977, **117**, 483.
78. H. Hogeveen, J. Lukas, and C. F. Roobek, *Chem. Commun.* 1969, 920.
79. P. J. F. de Rege, J. A. Gladysz, and I. T. Horvath, *Adv. Synth. Catal.*, 2002, **344**, 1059.
80. G. B. Shul'pin, G. Shul'pin, and L. S. Shul'pina, *Chem. Commun.* 2000, 1131.
81. Q. Yuan, W. P. Deng, Q. H. Zhang, and Y. Wang, *Adv. Synth. Catal.*, 2007, **349**(7), 1199.
82. G. B. Shul'pin, G. V. Nizova, Y. N. Kozlov, V. S. Arutyunov, A. C. M. dos Santos, A. C. T. Ferreira, and D. Mandelli, *J. Organometal. Chem.*, 2005, **690**(20), 4498.
83. I. Yamanaka, M. Soma, and K. Otsuka, *Chem. Commun.* 1995, 2235.
84. I. Yamanaka, *Catal. Surv. Jpn.*, 2002, **6**(1–2), 63.
85. I. Yamanaka, M. Soma, and K. Otsuka, *Chem. Lett.*, 1996, **7**, 565.

86. I. Yamanaka, K. Nakagaki, T. Akimoto, and K. Otsuka, *J. Chem. Soc. Perk. T. 2.*, 1996, **11**, 2511.
87. D. Piao, K. Inoue, H. Shibasaki, Y. Taniguchi, T. Kitamura, and Y. Fujiwara, *J. Organomet. Chem.*, 1999, **574**(1), 116.
88. Y. Seki, N. Mizuno, and M. Misono, *Chem. Lett.*, 1998, **12**, 1195.
89. Y. Seki, N. Mizuno, and M. Misono, *Appl. Catal. A-Gen.*, 2000, **194**, 13.
90. N. Mizuno, Y. Seki, Y. Nishiyama, I. Kiyoto, and M. Misono, *J. Catal.*, 1999, **184**(2), 550.
91. G. V. Nizova, G. Süss-Fink, and G. B. Shul'pin, *Chem. Commun.*, 1997, **4**, 397.
92. G. V. Nizova, G. Süss-Fink, and G. B. Shul'pin, *Tetrahedron*, 1997, **53**(10), 3603.
93. G. Süss-Fink, G. V. Nizova, S. Stanislas, and G. B. Shul'pin, *J. Mol. Catal. A-Chem.*, 1998, **130**(1–2), 163.
94. L. G. Cuervo, Y. N. Kozlov, G. Süss-Fink, and G. B. Shul'pin, *J. Mol. Catal. A-Chem.*, 2004, **218**(2), 171.
95. L. S. Shul'pina, M. V. Kirillova, A. J. L. Pombeiro, and G. B. Shul'pin, *Tetrahedron*, 2009, **65**(12), 2424.
96. G. Süss-Fink, S. Stanislas, G. B. Shul'pin, G. V. Nizova, H. Stoeckli-Evans, A. Neels, C. Bobillier, and S. Claude, *J. Chem. Soc.-Dalton.*, 1999, **18**, 3169.
97. G. Süss-Fink, S. Stanislas, G. B. Shul'pin, and G. V. Nizova, *Appl. Organomet. Chem.*, 2000, **14**(10), 623.
98. V. B. Romakh, G. Süss-Fink, and G. B. Shul'pin, *Petrol. Chem.*, 2008, **48**(6), 440.
99. G. V. Nizova, B. Krebs, G. Süss-Fink, S. Schindler, L. Westerheide, L. G. Cuervo, and G. B. Shul'pin, *Tetrahedron*, 2002, **58**(45), 9231.
100. M. Lin, T. Hogan, and A. Sen, *J. Am. Chem. Soc.*, 1997, **119**, 6048.
101. C. Shen, E. A. Garcia-Zayas, and A. Sen, *J. Am. Chem. Soc.*, 2000, **122**, 4029.
102. E. D. Park, Y. S. Hwang, C. W. Lee, and J. S. Lee, *Appl. Catal. A-Gen.*, 2003, **247**(2), 269.
103. T. Osako, E. J. Watson, A. Dehestani, B. C. Bales, and J. M. Mayer, *Angew. Chem., Int. Ed.*, 2006, **45**, 7433.
104. M. Drees and T. Stassner, *J. Org. Chem.*, 2006, **71**, 1755.
105. M. D. Khokhar, R. S. Shukla, and R. V. Jasra, *J. Mol. Catal. A-Chem.*, 2009, **299**(1–2), 108.
106. W. S. Chen, J. A. Kocal, T. A. Brandvold, M. L. Bricker, S. R. Bare, R. W. Broach, N. Greenlay, K. Popp, J. T. Walenga, S. S. Yang, and J. J. Low, *Catal. Today*, 2009, **140**(3–4), 157.
107. M. N. Vargaftik, I. P. Stolarov, and I. I. Moiseev, *J. Chem. Soc. Chem. Comm.*, 1990, **15**, 1049.
108. Z. An, X. Pan, X. Liu, X. Han, and X. Bao, *J. Am. Chem. Soc.*, 2006, **128**, 16028.
109. S. Mukhopadhyay and A. T. Bell, *Chem. Commun.* 2003, 1590.
110. A. Sen, M. A. Benvenuto, M. Lin, A. C. Hutson, and N. Basickes, *J. Am. Chem. Soc.*, 1994, **116**, 998.
111. N. Basickes, T. E. Hogan, and A. Sen, *J. Am. Chem. Soc.*, 1996, **118**, 13111.
112. J. L. Beauchamp, *Annu. Rev. Phys. Chem.*, 1971, **22**, 527.
113. J. Allison, R. B. Freas, and D. P. Ridge, *J. Am. Chem. Soc.*, 1979, **101**, 1332.
114. J. Müller and W. Goll, *Chem. Ber.*, 1973, **106**, 1129.
115. D. Schröder and H. Schwarz, *Can. J. Chem.*, 2005, **83**, 1936.
116. H. Schwarz, *Angew. Chem. Int. Ed.*, 1991, **30**, 820.
117. H. Schwarz and D. Schröder, *Pure Appl. Chem.*, 2000, **72**(12), 2319.
118. D. Schröder and H. Schwarz, *Proc. Natl. Acad. Sci. U.S.A.*, 2008, **105**, 18114.
119. K. K. Irikura and J. L. Beauchamp, *J. Am. Chem. Soc.*, 1991, **113**, 2769.
120. K. K. Irikura and J. L. Beauchamp, *J. Phys. Chem.*, 1991, **95**, 8344.
121. R. Wesendrup, D. Schröder, and H. Schwarz, *Angew. Chem. Int. Ed.*, 1994, **33**, 1174.
122. M. Pavlov, M. R. A. Blomberg, and P. E. M. Siegbahn, *J. Phys. Chem. A.*, 1997, **101**, 1567.
123. R. Wesendrup and H. Schwarz, *Angew. Chem. Int. Ed.*, 1995, **34**, 2033. For a stoichiometric coupling of methane and CO₂ to afford a ketene using TaCH²⁺.
124. N. Sandig and W. Koch, *Organometallics*, 1998, **17**, 2344.
125. M. Lin and A. Sen, *Nature*, 1994, **368**, 613.
126. D. Forster, *Adv. Organomet. Chem.*, 1979, **17**, 255.
127. M. Lin, T. E. Hogan, and A. Sen, *J. Am. Chem. Soc.*, 1996, **118**, 4574.
128. E. G. Chepaikin, G. N. Boyko, A. P. Bezruchenko, A. A. Leshcheva, and E. H. Grigoryan, *J. Mol. Cat. A: Chem.*, 1998, **129**, 15.
129. E. G. Chepaikin, A. P. Bezruchenko, A. A. Leshcheva, G. N. Boyko, E. H. Grigoryan, and A. E. Shilov, *J. Mol. Cat. A: Chem.*, 2001, **169**, 89.
130. E. G. Chepaikin, A. P. Bezruchenko, and A. A. Leshcheva, *Kinet. Catal.*, 2002, **43**, 507.
131. E. G. Chepaikin, *Kinet. Catal.*, 2004, **45**, 307.
132. E. G. Chepaikin, A. P. Bezruchenko, G. N. Boyko, A. E. Gekhman, and I. I. Moiseev, *Kinet. Catal.*, 2006, **47**, 12.
133. K. A. Grice and K. I. Goldberg, *Organometallics*, 2009, **28**, 953.
134. I. H. Hristov and T. Ziegler, *Organometallics*, 2003, **22**, 3513.
135. Y. Fujiwara, K. Takaki, and Y. Taniguchi, *Synlett*, 1996, **7**, 591.
136. T. Nishiguchi, K. Nakata, K. Takaki, and Y. Fujiwara, *Chem. Lett.* 1992, **7**, 1141.

137. K. Nakata, T. Miyata, T. Jintoku, A. Kitani, Y. Taniguchi, K. Takaki, and Y. Fujiwara, *Bull. Chem. Soc. Jpn.*, 1993, **66**, 3755.
138. K. Nakata, Y. Yamaoka, T. Miyata, Y. Taniguchi, K. Takaki, and Y. Fujiwara, *J. Organomet. Chem.*, 1994, **473**, 329.
139. J. Yang, A. Haynes, and P. Maitlis, *Chem. Commun.* 1999, 179.
140. Y. Souma, N. Tsumori, H. Willner, Q. Xu, H. Mori, and Y. Morisaki, *J. Mol. Catal. A: Chem.*, 2002, **189**, 67.
141. M. Zerella and A. T. Bell, *J. Mol. Cat.: A*, 2006, **259**, 296.
142. Hermann Müller, ‘Ullmann’s Encyclopedia of Industrial Chemistry’, 6th edition Wiley-VCH, 2002.
143. D. R. Lide, ‘CRC Handbook of Chemistry and Physics’, 88th edition, CRC Press, Boca Raton, 2007.
144. O. Dimroth, *Chem. Ber.*, 1902, **35**, 2032.
145. J. C. Snyder, and A. V. Grosse, US Patent 2493038, 1950.
146. R. A. Periana, D. J. Taube, E. R. Evitt, D. G. Löfller, P. R. Wentzcek, G. Voss, and T. Masuda, *Science*, 1993, **259**, 340.
147. K. Kataja, X. M. Song, and M. Huuska, *Catal. Today*, 1994, **21**, 513.
148. X. Gang, H. Birch, Y. Zhu, H. A. Hjuler, and N. J. Bjerrum, *J. Catal.*, 2000, **196**, 287.
149. T. R. Cundari, L. A. Snyder, and A. Yoshikawa, *J. Mol. Struc.-Theochem.*, 1998, **425**, 13.
150. T. R. Cundari and A. Yoshikawa, *J. Comput. Chem.*, 1998, **19**, 902.
151. S. Mukhopadhyay and A. T. Bell, *J. Mol. Cat. A*, 2004, **211**, 59.
152. S. Mukhopadhyay and A. T. Bell, *Adv. Synth. Catal.*, 2004, **346**, 913.
153. J. Peng and Y. Deng, *App. Catal. A-Gen*, 2000, **201**, L155.
154. R. A. Periana, D. J. Taube, S. Gamble, H. Taube, T. Satoh, and H. Fujii, *Science*, 1998, **280**, 560.
155. B. Michalkiewicz, J. Ziebro, and M. Tomaszewska, *J. Mem. Sci.*, 2006, **286**, 223.
156. T. M. Gilbert, I. Hristov, and T. Ziegler, *Organometallics*, 2001, **20**, 1183.
157. J. Kua, X. Xu, R. A. Periana, and W. A. Goddard III, *Organometallics* 2002, **21**, 511.
158. A. Paul and C. B. Musgrave, *Organometallics*, 2007, **26**, 793.
159. I. H. Hristov and T. Ziegler, *Organometallics*, 2003, **22**, 1668.
160. X. Xu, J. Kua, R. A. Periana, and W. A. Goddard, *Organometallics*, 2003, **22**, 2057.
161. J. Kua, X. Xu, R. A. Periana, and W. A. Goddard, *Organometallics*, 2002, **21**, 511.
162. X. Xu, J. Kua, R. A. Periana, and W. A. Goddard III, *Organometallics* 2003, **22**, 2057.
163. M. Ahlquist, R. A. Periana, and W. A. Goddard III, *Chem. Commun.* 2009, 2373.
164. B. Michalkiewicz and P. Kosowski, *Catal. Commun.*, 2007, **8**, 1939.
165. B. Michalkiewicz, *Appl. Catal.*, 2006, **307**, 270.
166. J. Cheng, Z. Li, M. Haught, and Y. Tang, *Chem. Commun.* 2006, 4617.
167. Z. Xu, J. Oxgaard, and W. A. Goddard III, *Organometallics*, 2008, **27**, 3770.
168. R. A. Periana, O. Mirinov, D. J. Taube, and S. Gamble, *Chem. Commun.* 2002, 2376.
169. M. Jarosińska, K. Lubkowski, J. G. Soonicki, and B. Michalkiewicz, *Catal. Lett.*, 2008, **126**, 407.
170. X. Gang, M. Zhu, H. Birch, H. A. Hjuler, and N. Bjerrum, *Appl. Catal., A*, 2004, **261**, 91.
171. G. A. Olah, G. K. S. Prakash, and J. Sommer, ‘Superacids’, Wiley-Interscience, New York, 1985.
172. G. E. Davico, *J. Phys. Chem. A*, 2005, **109**, 3433.
173. C. Jones, D. Taube, V. R. Ziatdinov, R. A. Periana, R. J. Nielsen, J. Oxgaard, and W. A. Goddard III, *Angew. Chem. Int. Ed.* 2004, **43**, 4626.
174. L. A. Levchenko, A. P. Sadkov, N. V. Lariontseva, E. M. Koldasheva, A. K. Shilova, and A. E. Shilov, *J. Inorg. Biochem.*, 2002, **88**, 251.
175. L. A. Levchenko, A. P. Sadkov, N. V. Lariontseva, V. S. Kulikova, A. K. Shilova, and A. E. Shilov, *Doklady Biochem. Biophys.*, 2004, **394**, 33; Translated from *Dokl. Akad. Nauk.* **394**(2), 2004, 272. Original Russian Text Copyright © 2004 by Levchenko, Sadkov, Lariontseva, Kulikova, Shilova, Shilov.
176. L. A. Levchenko, B. G. Kartsev, A. P. Sadkov, A. F. Shestakov, A. K. Shilova, and A. E. Shilov, *Dokl. Akad. Nauk.*, 2007, **412**, 35.
177. D. A. Pichugina, A. F. Shestakov, and N. E. Kuz’menko, *Russ. Chem. Bull. Int. Ed.* 2006, **55**, 195, Published in Russian in *Izvestiya Akad. Nauk. Seriya Khimicheskaya*, 2006, 2, 191.
178. D. A. Pichugina, N. E. Kuz’menko, and A. F. Shestakov, *Gold Bull.*, 2007, **40**, 115.
179. D. A. Pichugina, A. F. Shestakov, and N. E. Kuz’menko, *Russ. J. Phys. Chem. A*, 2007, **81**, 883; Original Russian Text © D. A. Pichugina, A. F. Shestakov, and N. E. Kuz’menko, published in *Zh. Fiz. Khim.*, 2007, 81, 1015.
180. B. Michalkiewicz, K. Kalucki, and J. G. Soonicki, *J. Catal.*, 2003, **215**, 14.
181. R. A. Periana, O. Mironov, D. Taube, G. Bhalla, and C. J. Jones, *Science*, 2003, **301**, 814.
182. M. Zerella, S. Mukhopadhyay, and A. T. Bell, *Chem. Commun.*, 2004, 1948.
183. M. Zerella, A. Kahros, and A. T. Bell, *J. Catal.*, 2006, **237**, 111.
184. S. Chempah and A. T. Bell, *J. Am. Chem. Soc.*, 2006, **128**, 4650.
185. Keith J. Laidler, *PAC*, 1996, **68**, 149, 170.
186. J. K. Fink, ‘Reactive Polymers Fundamentals and Application’, William Andrew, 2006, p. 34.
187. J. McMurry, ‘Organic Chemistry’, Brooks/Cole-Thompson Learning, 2004, p. 138.

188. G. A. Russell and H. C. Brown, *J. Am. Chem. Soc.*, 1955, **77**, 4578.
189. G. A. Russell and R. C. Williamson, *J. Am. Chem. Soc.*, 1964, **86**, 2357.
190. G. A. Russell and R. C. Williamson, *J. Am. Chem. Soc.*, 1964, **86**, 2364.
191. J. L. Heidbrink, L. E. Ramirez-Arizmendi, K. K. Thoen, L. Guler, H. I. Kenttämaa *J. Phys. Chem.* 2001, **105**, 7875.
192. A. A. Zavitsas and J. A. Pinto, *J. Am. Chem. Soc.*, 1971, **94**, 7390. For a critical discussion of the polar effect as change in homolytic bond strength.
193. J. M. Tedder, *Angew. Chem. Int. Ed. Engl.*, 1982, **21**, 401. For a comprehensive summary of influences on the rate of free radical transfer reactions.
194. A. F. Parsons, in 'An Introduction to Free-Radical Chemistry', Wiley-Blackwell, 2000,, p. 90.
195. I. Fleming, 'Frontier Orbitals and Organic Chemical Reactions', John Wiley & Sons, Chichester, 1976, p. 186. For an explanation of the polar effect using frontier orbital theory.
196. V. M. Zakoshansky, *Petrol. Chem.*, 2007, **47**, 273. Original Russian Text © V. M. Zakoshansky, published in *Neftekhimiya*, 2007, **47**, 301.
197. P. Peter Mulder, S. Hemmink, M. I. De Heer, M. Lupo, D. Santoro, and H.-G. Korth, *J. Org. Chem.*, 2001, **66**, 6611.
198. N. Sebbar, J. W. Bozzelli, and H. Bockhorn, *J. Phys. Chem.*, 2004, **108**, 8353.
199. J. A. Howard and J. E. Bennett, *Can. J. Chem.*, 1972, **50**, 2374.
200. S. Mukhopadhyay and A. T. Bell, *Ind. Eng. Chem. Res.*, 2002, **41**, 5901.
201. S. Mukhopadhyay and A. T. Bell, *J. Am. Chem. Soc.*, 2003, **125**, 4406.
202. Y. Taniguchi, T. Hayashida, T. Kitamura, Y. Fujiwara, T. Inui, M. Anpo, K. Izui, S. Yanagida, and T. Yamaguchi, *Stud. Surf. Sci. Catal.*, 1998, **114**, 439.
203. E. M. Wilcox, M. R. Gogate, J. J. Spivey, G. W. Roberts, E. Iglesia, and T. H. Fleisch, *Stud. Surf. Sci. Catal.*, 2001, **136**, 259.
204. E. M. Wilcox, G. W. Roberts, and J. J. Spivey, *Appl. Catal. A: General*, 2002, **226**(1–2), 317.
205. M. Zerella, S. Mukhopadhyay, and A. T. Bell, *Org. Lett.*, 2003, **5**(18), 3193.
206. Y. Taniguchi, T. Hayashida, H. Shibasaki, D. G. Piao, T. Kitamura, T. Yamaji, and Y. Fujiwara, *Org. Lett.*, 1999, **1**(4), 557.
207. P. M. Reis, J. A. L. Silva, A. F. Palavra, J. da Silva, T. Kitamura, Y. Fujiwara, and A. J. L. Pombeiro, *Angew. Chem.-Int. Edit.*, 2003, **42**(7), 821.
208. M. V. Kirillova, M. L. Kuznetsov, P. M. Reis, J. A. L. da Silva, J. da Silva, and A. J. L. Pombeiro, *J. Am. Chem. Soc.*, 2007, **129**(34), 10531.
209. M. V. Kirillova, A. M. Kirillov, P. M. Reis, J. A. L. Silva, J. J. R. F. da Silva, and A. J. L. Pombeiro, *J. Catal.*, 2007, **248**, 130.
210. M. Asadullah, T. Kitamura, and Y. Fujiwara, *Angew. Chem.-Int. Edit.*, 2000, **39**(14), 2475.
211. M. Asadullah, Y. Taniguchi, T. Kitamura, and Y. Fujiwara, *Appl. Organomet. Chem.*, 1998, **12**(4), 277.
212. G. C. Yin, D. G. Piao, T. Kitamura, and Y. Fujiwara, *Appl. Organomet. Chem.*, 2000, **14**(8), 438.
213. P. Krajnik, D. Michos, and R. H. Crabtree, *New J. Chem.*, 1993, **17**, 805.
214. D. Michos, C. A. Sassano, P. Krajnik, and R. H. Crabtree, *Angew. Chem. Int. Ed.*, 1993, **32**, 1491.
215. M. C. Duval, B. Soep, and W. H. Breckenridge, *J. Phys. Chem.*, 1991., **95**, 7145.
216. S. Mukhopadhyay and A. T. Bell, *Angew. Chem. Int. Ed.*, 2003, **42**, 1019.
217. S. Mukhopadhyay and A. T. Bell, *Org. Process Res. Dev.*, 2003, **7**, 754.
218. S. Mukhopadhyay and A. T. Bell, *Org. Process Res. Dev.*, 2003, **7**, 161.
219. S. Mukhopadhyay and A. T. Bell, *Angew. Chem. Int. Ed.*, 2003, **42**, 2990.
220. S. Mukhopadhyay, M. Zerella, and A. T. Bell, *Adv. Synth. Catal.*, 2005, **347**, 1203.
221. G. V. Nizova, G. Süss-Fink, S. Stanislas, and G. B. Shul'pin, *Chem. Commun.*, 1998, **17**, 1885.

Photocatalytic Hydrogen Production from Water

Shamindri M. Arachchige and Karen J. Brewer

Virginia Polytechnic Institute and State University, Blacksburg, VA, USA

1	Introduction	143
2	Photocatalytic Hydrogen Production	146
3	Conclusions	166
4	Glossary	169
5	Acknowledgments	169
6	Related Articles	170
7	Abbreviations and Acronyms	170
8	References	170

1 INTRODUCTION

Solar energy is an abundant and underutilized source of energy. Solar radiation that reaches the southern United States has an instantaneous maximum intensity of 1 kW m^{-2} and an average 24-h intensity of 250 W m^{-2} in a year.¹ In the Basic Energy Sciences report on solar utilization, sunlight is recognized as the largest of all carbon-neutral energy sources with $4.3 \times 10^{20}\text{ J h}^{-1}$ reaching the earth's surface, representing more energy than that consumed on the planet in a year.² Solar energy is harnessed by plants through photosynthesis, which is then consumed by animals as biomass or degrades to produce carboniferous fossil fuels that are currently used to supply much of the global energy needs. The rate of depletion of fossil fuels with growing energy demands has stimulated research on exploring alternative means to harness solar energy and alternative energy sources. Capturing and harnessing solar energy for sustainable use in a scale that is economically viable remains a challenge. Artificial photosynthesis in which solar energy is converted to fuels without the use of plants has appeal. The significance of the development and study of systems for the conversion of solar energy to fuels for storage and distribution is a topic that has received much recognition.^{1–4} Hydrogen has been proposed as an energy solution for the future because of its high energy content per gram (120 kJ g^{-1}), its ability to be used in fuel cells, and low environmental impact.^{1–4} Hydrogen production through water splitting using solar energy would provide the ultimate clean, renewable energy solution.

1.1 Scope and Limitations

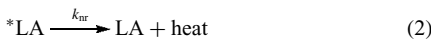
This article highlights the recent progress in the use of large molecular systems that are applicable in water reduction to produce hydrogen fuel. These supramolecular systems are composed of multiple subunits that together allow for the complicated functions required to facilitate the light induced multielectron photochemistry needed for solar water splitting. Some of the systems use proton sources other than water but are discussed in this article as the conceptual design considerations are relevant for the construction of systems that are applicable in water reduction to produce hydrogen fuel. The focus is on supramolecular complexes that couple a light-harvesting unit to a catalytic site that is typically a reactive metal center. This design allows the light-absorbing properties to be coupled in an intramolecular manner with favorable catalytic properties of reactive metals, providing structural motifs that display unique functions. Illustrative examples of different molecular architectures are provided and the basic chemical and photophysical properties are discussed. The understanding of the basic ground and excited state properties of these systems is important in the design and development of efficient devices in solar hydrogen production schemes. It is important to note that the pioneering work on intermolecular electron transfer of smaller light-absorbing systems and catalytic development on monometallic systems laid the foundation needed to make this rapidly evolving area of supramolecular multielectron photochemistry possible.^{5–7}

1.2 Light Absorption

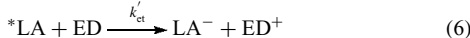
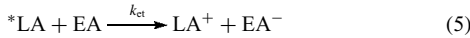
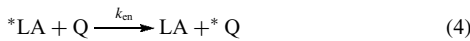
Efficient light absorption is key for efficient solar energy conversion. Optical excitation of a light absorber (LA) forms an electronically excited state, ${}^*\text{LA}$ (equation 1), that possesses properties unique compared to the electronic ground state, often able to undergo electron or energy transfer.



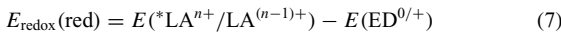
Relaxation of the ${}^*\text{LA}$ can occur in a nonradiative manner (equation 2) or in a radiative manner (equation 3; k_{nr} and k_r are rate constants for nonradiative and radiative decay, respectively).



It is well accepted that optical excitation to generate an electronic excited state increases both the oxidizing and the reducing powers of a molecule. The ${}^*\text{LA}$ can undergo energy and/or electron transfer reactions to a quencher (Q), an electron donor (ED), or electron acceptor (EA), providing a means to use this absorbed light energy in solar energy conversion schemes (equations 4–6; k_{en} , k_{et} , and k'_{et} are rate constants for energy transfer quenching, oxidative quenching, and reductive quenching, respectively).



The thermodynamic driving force (E_{redox}) of an excited state electron transfer process depends on the excited state reduction potential of the LA ($E({}^*\text{LA}^{n+}/\text{LA}^{(n-1)+})$) and the ground state oxidation potential of the ED ($E(\text{ED}^{0/+})$) for excited state reduction (equation 7) or the excited state oxidation potential of the LA ($E({}^*\text{LA}^{n+}/\text{LA}^{(n+1)+})$) and the ground state reduction potential of the EA ($E(\text{EA}^{0/-})$) for excited state oxidation (equation 8). The excited state redox potentials, $E({}^*\text{LA}^{n+}/\text{LA}^{(n-1)+})$ and $E({}^*\text{LA}^{n+}/\text{LA}^{(n+1)+})$, differ significantly from the ground state potentials as electronic excited states are simultaneously better oxidizing and reducing agents than their respective ground states. The excited state redox potentials are calculated based on the ground state reduction and oxidation potential of the LA, respectively, and the energy gap between the ground vibronic state of the electronic ground and excited states (E^{0-0}) (equations 9 and 10).



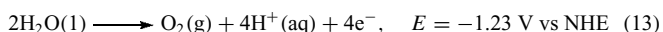
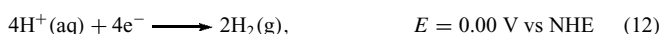
$$E_{\text{redox}}(\text{oxd}) = E({}^*\text{LA}^{n+}/\text{LA}^{(n+1)+}) - E(\text{EA}^{0/-}) \quad (8)$$

$$E({}^*\text{LA}^{n+}/\text{LA}^{(n-1)+}) = E(\text{LA}^{n+}/\text{LA}^{(n-1)+}) + E^{0-0} \quad (9)$$

$$E({}^*\text{LA}^{n+}/\text{LA}^{(n+1)+}) = E(\text{LA}^{n+}/\text{LA}^{(n+1)+}) - E^{0-0} \quad (10)$$

1.3 Thermodynamics of Photochemical Water Splitting

Water splitting using sunlight to produce clean, environmentally friendly energy is a very attractive but challenging means to harvest and store a renewable energy source. The reactions involved in water splitting are complex and require bond breaking, bond formation, and multielectron transfer reactions (equations 11–13).



The relevant reduction and oxidation half reactions provide insight into the mechanism for water splitting. The redox potentials of these half reactions are strongly pH dependent. The redox potentials listed in equations (12) and (13) apply for acidic condition when $\text{pH} = 0$. The reduction potential of water reduction shifts to more negative potentials with increasing pH, while the opposite is true for water oxidation. At $\text{pH} = 7$, the reduction of water to produce hydrogen requires -0.41 V and the oxidation of water to produce oxygen requires -0.82 V . Multielectron chemistry is key as water splitting through multiple electrons is energetically much more favorable (1.23 V vs NHE)¹ than water splitting through single-electron reactions (5 V vs NHE).⁷ Most of the solar spectrum has energies $> 1.23 \text{ eV}$ and can be used for the multielectron splitting of water. Figure 1 displays the solar spectrum demonstrating the variation of solar energy with spectral irradiance.⁸

However, water does not absorb solar energy efficiently, and reactions to produce hydrogen and oxygen are complex. Developing systems that absorb solar energy efficiently and promote multielectron photocatalysis remain one of the major challenges to efficient water splitting to produce fuels.^{7,9–13} Many chromophoric systems absorb UV and visible light to form excited states with sufficient energy to cleave water; yet this process remains illusive.^{5,6} It has long been known that $[\text{Ru}(\text{bpy})_3]^{2+}$ possesses a long-lived metal-to-ligand charge-transfer (${}^3\text{MLCT}$) excited state with sufficient energy to split water; yet direct photocatalysis does not occur. In a landmark monograph, Balzani eluded to the power of supramolecular design to address this challenge, proposing orbital energetics needed for photoinitiated electron collection (PEC) in 1987.¹⁴ Despite detailed studies of numerous supramolecular systems,¹⁵ the first functioning photoinitiated electron collector (EC) was not reported until 1994.¹⁶

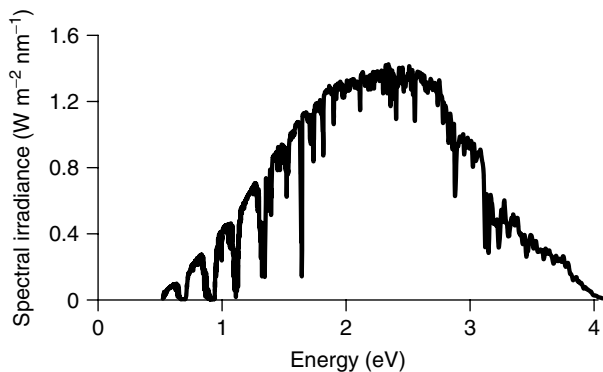


Figure 1 Plot demonstrating the variation of the direct and circumsolar spectral irradiance as a function of energy. Direct radiation is the amount of solar radiation from the direct sun and circumsolar radiation is the solar radiation coming from a circle in the sky centered on the sun from a radius between 2.5 and 3.5°. Figure 1 is based on data in Ref. 8

Although systems that split water to produce fuel using ultraviolet light are known, development of systems that split water in the visible region has received much focus, as a large fraction of solar energy is in the visible region of the spectrum.^{9,10} Current technologies for photolytic water splitting to produce hydrogen employ photobiological processes,¹¹ photoelectrochemical processes using semiconductors,¹⁰ and molecular photocatalysis.^{12,13}

1.4 Evaluation of Light Absorption and Photophysical Properties of Supramolecular Complexes

Ruthenium polyazine chromophores are broadly applicable LAs with good spectral coverage, emissive charge-transfer excited states, and long excited state lifetimes.^{5,6,15} Ruthenium polyazine LAs display $\pi \rightarrow \pi^*$ ligand-based transitions with high extinction coefficients in the UV region of the electronic absorption spectrum. They also possess lower energy transitions involving charge transfer from a ruthenium-based highest occupied molecular orbital (HOMO) to a ligand-based lowest unoccupied molecular orbital (LUMO) ${}^1\text{MLCT}$ (metal-to-ligand charge-transfer) transition. The absorption maximum is located in the visible region of the spectrum. The orbitals involved in an electronic transition must be electronically coupled to allow for observation of an intense electronic transition. The symmetry selection rule for the intensity of an electronic transition is expressed in equation (14):

$$f \propto \left| \int \psi_{\text{el}}^{\text{ES}} \mu \psi_{\text{el}}^{\text{GS}} dv \right|^2 \quad (14)$$

The oscillator strength, f , is reflective of the predicted integrated intensity and proportional to the integral of the product of the ground and excited state wavefunctions, Ψ , and the electronic dipole moment operator, μ . The spin selection rule predicts that an electronic transition is allowed only if the spin multiplicity of the ground state and excited state are the same. In ruthenium polyazine LA systems, the molecules in the ${}^1\text{MLCT}$ state rapidly intersystem cross (k_{isc} is the rate constant for intersystem crossing) to populate an ${}^3\text{MLCT}$ state typically with unit efficiency. The ${}^3\text{MLCT}$ state can radiatively (k_r is the rate constant for radiative decay) or nonradiatively (k_{nr} is the rate constant for nonradiative decay) decay to the ground state (GS) or undergo energy/electron transfer quenching. The emission from the ${}^3\text{MLCT}$ state provides a probe into the photoreactivity of the molecules. Transitions between ground and electronic excited states are typically represented with state or Jablonski diagrams (Figure 2). Radiative processes are typically represented as straight arrows (\rightarrow) and nonradiative processes are presented as wavy arrows (\rightsquigarrow). Radiative decay with a change in spin state is *phosphorescence* while radiative decay without change in spin is *fluorescence*. Typically ruthenium polyazine chromophores display phosphorescence from their emitting ${}^3\text{MLCT}$ states and have significant spin-orbit coupling.

The quantum yield, Φ , of an excited state process provides a means to understand the efficiencies of a particular pathway to decay to the ground state. For example, Φ for emission resulting from radiative decay from the ${}^3\text{MLCT}$ state, represented in equation (15), is defined as k_r divided by the sum of the rate constants of all pathways depopulating that state, Σk ($\Sigma k = k_r + k_{\text{nr}} + k_{\text{rxn}}$; equation 15) times the quantum yield for population of that state, $\Phi_{{}^3\text{MLCT}}$.

$$\Phi = \Phi_{{}^3\text{MLCT}} \frac{k_r}{\sum k} \quad (15)$$

For many ruthenium polyazine LAs, the $\Phi_{{}^3\text{MLCT}}$ is unity and omitted from these equations. The excited state lifetime of the ${}^3\text{MLCT}$ state, τ , is the inverse of the sum of the

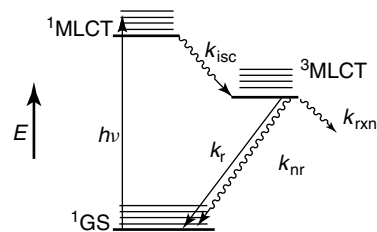


Figure 2 Representative state diagram for ruthenium–polyazine complexes of the type $[\text{Ru}(\text{TL})_3]^{2+}$ (TL, terminal polyazine ligand; GS, ground state; MLCT, metal-to-ligand charge transfer; k_r , rate constant for radiative decay; k_{nr} , rate constant for nonradiative decay; k_{isc} , rate constant for intersystem crossing; and k_{rxn} , rate constant of reaction)

rate constants of all pathways depopulating that state, Σk^{-1} (equation 16):

$$\tau = \frac{1}{k_r + k_{nr} + k_{rxn}} \quad (16)$$

The efficiency of excited state reactions can be described by probing Φ for that reaction as a function of quencher concentration using the Stern–Volmer kinetic relationship (equation 17). Φ^0 and Φ are quantum yields in the absence and the presence of Q , respectively; k_q is the overall quenching rate constant and τ is the excited state lifetime of the ${}^3\text{MLCT}$ state. The Stern–Volmer relationship, which plots Φ^0/Φ as a function of the quencher concentration, provides a linear relationship with a slope of τk_q , denoted as K_{sv} . The value of k_q provides the rate of quenching by Q .

$$\frac{\Phi^0}{\Phi} = 1 + \tau k_q [Q] \quad (17)$$

2 PHOTOCATALYTIC HYDROGEN PRODUCTION

A few approaches to light-driven hydrogen production through water reduction provide a background for the supramolecular systems described herein.

2.1 Photobiological Water Splitting

Photobiological water splitting employs sunlight and microorganisms such as microalgae and cyanobacteria to produce hydrogen from water.¹¹ Photobiological water splitting is not extensively discussed here. In these systems, electrons and protons generated through solar water splitting are transported to the hydrogen-producing enzymes, hydrogenase or nitrogenase, which catalyze the production of hydrogen fuel. Hydrogenase activity is impeded by the sensitivity to oxygen generated, limiting the efficiency of these systems. Photobiological water splitting is still at its infancy and research on enhancing hydrogen production efficiency through modification of the microorganisms and identifying other naturally occurring microbes is ongoing. Despite often low efficiencies, hydrogenase engineering efforts show much promise as analysis projects to show that overcoming oxygen inhibition could lead to hydrogen production with 10 % efficiency in the conversion of solar energy. Achieving this efficiency would allow photobiological systems to replace gasoline in the United States when cultivated in sealed reactors in an area of less than 5000 square miles.¹⁷

A recent report introduces the concept of using carbon nanotubes as electron relays (ERs) to electrically wire hydrogenases¹⁸ to electrodes to be used in hydrogen production technologies.¹⁹ This method provides a facile way of incorporating an electrical connection between

the hydrogenases and a single-walled carbon nanotube that displays excellent electronic conductivity without compromising the catalytic activity of the hydrogenase site. Establishing an electric connection between hydrogenase and a support without compromising the catalytic activity is often difficult, impeding the use of these systems in hydrogen production schemes. This study provides insight into the use of these carbon nanotube/hydrogenase hybrids in hydrogen production schemes.

2.2 Photoelectrochemical Water Splitting

Photoelectrochemical water splitting employs light and semiconductors to split water. This area has been recently reviewed¹⁰ and is not discussed in detail in this article. These systems typically employ semiconductors, catalysts, and more recently LAs.^{10,20–27}

2.2.1 Direct Semiconductor Excitation for Photoelectrochemical Water Splitting

The type of semiconductor, the nature of the catalyst, as well as interfacial electron transfer processes impact the efficiency of water splitting to produce fuel. TiO_2 was used as a semiconductor for UV-based photoelectrochemical water splitting in 1972 by Honda and Fujishima.²¹ This system used UV light at wavelengths <415 nm. Irradiation of the surface of a TiO_2 electrode coupled to a platinum black electrode through an external load resulted in hydrogen production at the platinum electrode. In the presence of more reducing species, for example, Fe^{3+} , at the platinum compartment, hydrogen production occurred with quantum efficiency of 0.1.²¹ There is much recent focus on development of efficient photoelectrochemical systems that utilize visible light to split water for fuel production.^{10,22}

The electronic structure of the semiconductor is key to efficient photocatalysis. An ideal semiconductor should have a band gap, E_g , that constitutes the energy difference between the conduction band (CB) and the valence band (VB) with sufficient energy to drive the water splitting reaction. For the production of hydrogen, the CB should be more negative than the redox potential of H^+/H_2 (0 V vs NHE). For the production of oxygen, the VB should be more positive than $\text{O}_2/\text{H}_2\text{O}$ (1.23 V vs NHE). Thus, the semiconductor should have an E_g minimum of 1.23 eV. Optical excitation promotes an electron from the VB to the CB to create an electron–hole pair. The water is reduced by promoted electrons to form hydrogen and oxidized by the holes to produce oxygen. Figure 3 represents the principles of water splitting using semiconductor photocatalysts.

Many factors are critical to efficient light-to-fuel conversion in this semiconductor-promoted water splitting. Rapid charge recombination in the electron–hole pair is a serious concern, which impedes catalytic activity. In this

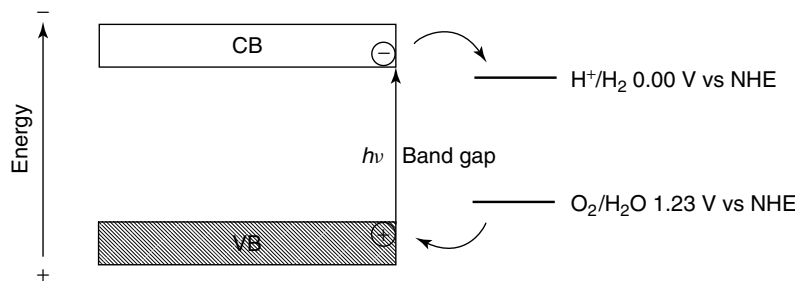


Figure 3 Schematic representing photocatalytic water splitting using semiconductors

regard, suitable band engineering is required when designing systems that would be catalytically active in the visible region that do not undergo rapid electron–hole recombination. The addition of sacrificial agents has been studied and provides a method to evaluate whether the photocatalyst satisfies the thermodynamic and kinetic potentials for hydrogen and oxygen production.^{10,22} The level of crystallinity and particle size are factors that are considered during the engineering process. Enhancement of photocatalytic efficiency has been achieved through metal ion doping, anion doping, and dye sensitization.^{10,22} A recent report describes the use of metal-free polymeric carbon nitride that produces hydrogen from water under visible irradiation in the presence of a sacrificial ED.²³ This system provides a promising first step toward water reduction, using commonly available materials in the absence of metals.

The use of semiconductor materials in solid/liquid junctions provides efficient systems for solar energy technology.²⁴ Charge carrier generation, transport, and recombination at semiconductor/liquid interfaces impact the efficiency of solar energy conversion. Fundamental understanding of the energetics and kinetic processes at the semiconductor/liquid junction is needed to allow the use of these systems as an economically viable solar energy tool. Studies on factors controlling the charge transfer and recombination at the semiconductor/liquid junction, impact by the type of semiconductor material and liquid, and the surface properties of the semiconductor provide information to enhance system function.²⁴

2.2.2 Dye-Sensitized Semiconductor Photoelectrochemical Water Splitting

The use of dye-sensitized colloidal semiconductor films is an attractive solar energy conversion method. The Grätzel cell employing this technology was first reported in 1991 and attracted much attention because of its stability, low cost, and device efficiency.²⁵ In this system, an optically transparent film of nanometer scale TiO₂ particles were coated with a dye, $[(L)_2Ru(\mu-(CN)Ru(CN)(bpy)_2)_2]^{2-}$ (L , 2'-bipyridine-4,4' carboxylic acid). The high surface area

of the TiO₂ film and the favorable light-absorbing properties of the dye allow a high proportion of the incident light to be absorbed. Optical excitation of the dye at $\lambda > 400$ nm affords an electron injection into the CB of the semiconductor. The dye is regenerated by electron transfer from a species in solution that is regenerated at the counter electrode. Overall light-to-electric-energy conversion efficiencies of 12% in diffused solar light has been achieved in this system.²⁵ Studies are in progress to enhance system efficiency and focus on the impact by the essential components within the system including the conductive mechanical support, semiconductor film, sensitizer, electrolyte, and counter electrode.²⁶ A system consisting of ruthenium-dye-sensitized TiO₂ nanoparticles loaded with a thin coating of Al₂O₃ and platinum (Al₂O₃/TiO₂/Pt) has been prepared.²⁷ This dye-sensitized Al₂O₃/TiO₂/Pt system shows enhanced hydrogen production activity to the corresponding dye-sensitized TiO₂/Pt system when an aqueous solution was irradiated at $\lambda > 420$ nm in the presence of the ethylenediaminetetraacetic acid (EDTA) ED. Up to 390 turnovers in 3 h was achieved with respect to the dye. No hydrogen was produced in the absence of the dye or platinum loading. The enhanced photocatalytic efficiency in the dye-sensitized Al₂O₃/TiO₂/Pt system is attributed to the impact by platinum, which completely scavenges the electrons to reduce protons, and the Al₂O₃ barrier, slowing down the charge recombination processes.

2.3 Multicomponent Molecular-Based Photocatalysis for Hydrogen Production

The use of molecular species for photocatalytic water splitting has some appeal over heterogeneous systems as heterogeneous systems depend on a number of parameters that are difficult to control and are more complicated to study. Molecular catalysis offers unique advantage as their basic chemical, redox, and photophysical properties can be tuned to understand system function at the molecular level and are more amenable to study by traditional methods. Many systems are multicomponent and comprise an LA, ER, ED, and a transition metal catalyst (CAT).^{9,12}

The complex $[Ru(bpy)_3]^{2+}$ (bpy, 2,2'-bipyridine) is a prototypical LA, which has been used in solar

hydrogen production schemes. This complex relies on the ${}^3\text{MLCT}$ excited state, containing a formally oxidized ruthenium, Ru^{III} , and a reduced bipyridine, bpy^- , that is relatively long lived ($\lambda_{\text{max}}^{\text{em}} = 605 \text{ nm}$, $\tau = 860 \text{ ns}$ at room temperature (RT) in acetonitrile), has sufficient driving force to split water, and can undergo electron and energy transfer quenching.²⁸ Early studies demonstrate the use of the multicomponent system, $[\text{Ru}(\text{bpy})_3]^{2+}$ LA, $\text{Co}^{\text{II}}\text{L}$ ($\text{Co}^{\text{II}}\text{L}=\text{Co}^{\text{II}}(\text{Me}_6[14]\text{dieneN}_4)(\text{H}_2\text{O})_2^{2+}$) CAT, and Eu^{2+} or ascorbate ED for the production of hydrogen from water under visible light.²⁹ Optical excitation of a system containing $[\text{Ru}(\text{bpy})_3]^{2+}$, $\text{Co}^{\text{II}}\text{L}$ ($\text{Co}^{\text{II}}\text{L}=\text{Co}^{\text{II}}(\text{Me}_6[14]\text{dieneN}_4)(\text{H}_2\text{O})_2^{2+}$), and Eu^{2+} at $\lambda = 450 \text{ nm}$ afforded hydrogen production, providing 10 turnovers with respect to $[\text{Ru}(\text{bpy})_3]^{2+}$ and 1 turnover with respect to $\text{Co}^{\text{II}}\text{L}$ ($\text{Co}^{\text{II}}\text{L}=\text{Co}^{\text{II}}(\text{Me}_6[14]\text{dieneN}_4)(\text{H}_2\text{O})_2^{2+}$), with $\Phi = 0.04$. Optical excitation of the LA leads to intermolecular electron transfer, generating a Co^{I} species that reduces water

to produce hydrogen (see Figure 4 for mechanism of solar hydrogen production).²⁹

$[\text{Rh}(\text{bpy})_3]^{3+}$ has been used as an EA in solar hydrogen production schemes using $[\text{Ru}(\text{bpy})_3]^{2+}$ as the LA and triethanolamine (TEOA) ED.³⁰ Photocatalytic hydrogen production from water occurs in the presence of a heterogeneous platinum catalyst (see Figure 5 for the mechanism of solar hydrogen production) with $\Phi = 0.11$ when irradiated at $\lambda = 450 \text{ nm}$. In the excited state, $[\text{Ru}(\text{bpy})_3]^{2+}$ undergoes electron transfer to $[\text{Rh}(\text{bpy})_3]^{3+}$ to produce $[\text{Ru}(\text{bpy})_3]^{3+}$ and $[\text{Rh}(\text{bpy})_3]^{2+}$. The photogenerated $[\text{Rh}(\text{bpy})_3]^{2+}$ can rapidly disproportionate to $[\text{Rh}^{\text{I}}(\text{bpy})_2]^+$ and $[\text{Rh}^{\text{III}}(\text{bpy})_3]^{3+}$, which deactivates the system. Alternatively, the Pt catalyst can accept an electron from the reduced rhodium species to catalyze the reduction of water to hydrogen. Creutz and Sutin have done detailed studies on $[\text{Rh}^{\text{I}}(\text{bpy})_2]^+$.^{31,32} At low concentrations in alkaline solutions $[\text{Rh}^{\text{I}}(\text{bpy})_2]^+$ predominates, while at higher $[\text{Rh}^{\text{I}}(\text{bpy})_2]^+$ concentration

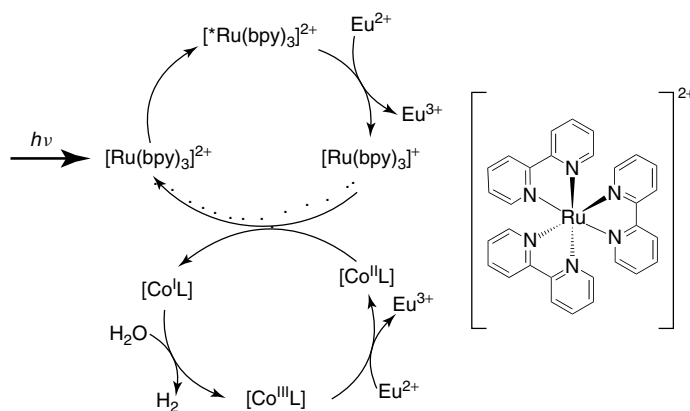


Figure 4 Proposed reaction mechanism for photocatalytic hydrogen production from water in an $[\text{Ru}(\text{bpy})_3]^{2+}/\text{Co}^{\text{II}}\text{L}/\text{Eu}^{2+}$ system (bpy, 2,2'-bipyridine)

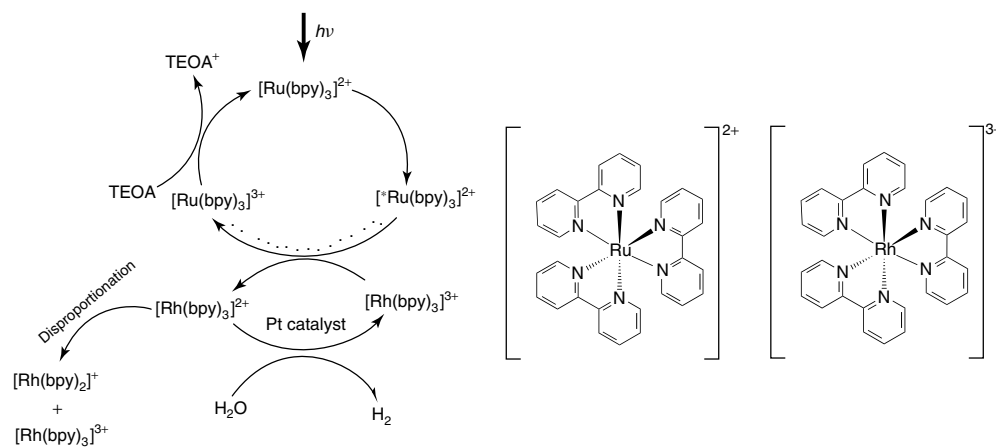


Figure 5 Proposed reaction mechanism for photocatalytic hydrogen production from water in an $[\text{Ru}(\text{bpy})_3]^{2+}/[\text{Rh}(\text{bpy})_3]^{3+}/\text{triethanolamine}/\text{Pt catalyst}$ system (bpy, 2,2'-bipyridine)

association occurs, generating the dimer, $[\text{Rh}^{\text{I}}(\text{bpy})_2]_2^{2+}$. Lowering the pH at low $[\text{Rh}^{\text{I}}(\text{bpy})_2]^+$ concentration leads to oxidative addition of H_3O^+ to $[\text{Rh}^{\text{I}}(\text{bpy})_2]^+$ affording $[\text{Rh}^{\text{III}}(\text{bpy})_2(\text{H})(\text{H}_2\text{O})]^{2+}$, while increasing the $[\text{Rh}^{\text{I}}(\text{bpy})_2]^+$ concentration affords $[\text{Rh}^{\text{I}}(\text{bpy})_2]_2(\text{H})^{3+}$. Creutz, Sutin, and Fujita have studied thermodynamic and kinetic parameters for the oxidative addition of hydrogen to $[\text{Rh}^{\text{I}}(\text{bpy})_2]^+$ and photoinduced reductive elimination of hydrogen.³³

2.4 Supramolecular Charge-Transfer Complexes

Energy and electron transfer efficiency in multi-component systems is limited by the need for diffusional contact during the excited state lifetime of the LA. Excited state lifetimes typically decrease with decreasing energy of the excited states due to the energy gap law.³⁴ This makes utilization of the full solar spectrum with multicomponent systems challenging. The inherent inefficiencies associated with the needed intermolecular electron or energy transfer processes have been circumvented by constructing complex molecular assemblies that incorporate multiple subunits covalently attached within the molecular architecture. Each subunit performs a specific function and provides a unique function to the molecular assembly. Such molecular assemblies are referred to as *supramolecular complexes*.¹⁴ This article focuses largely on supramolecular systems that photocatalyze the production of hydrogen fuel from water. These systems typically couple an LA to a CAT through coordinate covalent bridges. The redox, optical, and photophysical properties of the supramolecular complexes are discussed. The photochemistry associated with the hydrogen production schemes is also highlighted. The electrochemical potentials are listed in Table 1 and the optical and photophysical properties are listed in Table 2. Supramolecular complexes whose functions

are initiated by light are referred to as *photochemical molecular devices (PMDs)* as introduced in 1987 by Balzani.¹⁴ Some common subunits used to construct PMDs are LAs that harvest light, bridging ligands (BLs) that act as connectors, EDs that supply electrons, ECs that collect reducing equivalents, and CATs that deliver these electrons to substrates. Absorption of light initiates the function of a PMD, so the choice of the LA is critical to design and engineering constraints. Reviews on emissive polynuclear transition metal complexes¹⁵ and electron transfer in ruthenium/osmium complexes³⁵ provide comprehensive discussions of these topics.

The redox and excited state properties of ruthenium polyazine type LAs can be modulated by variation of the coordinated ligands.⁶ Replacing one or more of the bpy of $[\text{Ru}(\text{bpy})_3]^{2+}$ with polyazine BLs allows the expansion of the molecular architecture and the construction of polymetallic supramolecular systems. In this regard, $[(\text{bpy})_2\text{Ru}(\text{dpp})]^{2+}$, in which a bpy is replaced by a dpp (dpp, 2,3-bis(2-pyridyl)pyrazine) (Figure 6), is well studied. The lowest lying excited state of $[(\text{bpy})_2\text{Ru}(\text{dpp})]^{2+}$ is a $\text{Ru}(\text{d}\pi) \rightarrow \text{dpp}(\pi^*)$ CT state with a $\lambda_{\text{max}}^{\text{abs}} = 475 \text{ nm}$ with an emission maximum at 691 nm and an excited state lifetime of 240 ns.^{48,49} In the MLCT excited state, charge is transferred from the ruthenium to the dpp, the site of attachment of additional metal centers. Polymetallic complexes including $[(\text{bpy})_2\text{Ru}]_2(\text{dpp})]^{4+}$ display dpp^{0/-} couple shifted to more positive potential relative to monometallic systems. The ${}^1\text{MLCT}$ absorption red shifts to 526 nm with an emission at 744 nm,⁵⁰ exhibiting a shortened ${}^3\text{MLCT}$ excited lifetime of ca. 140 ns.⁵¹ The change in the electrochemical and optical properties in the multimetallic system is consistent with the stabilization of the dpp(π^*) orbital with coordination of the second metal center.

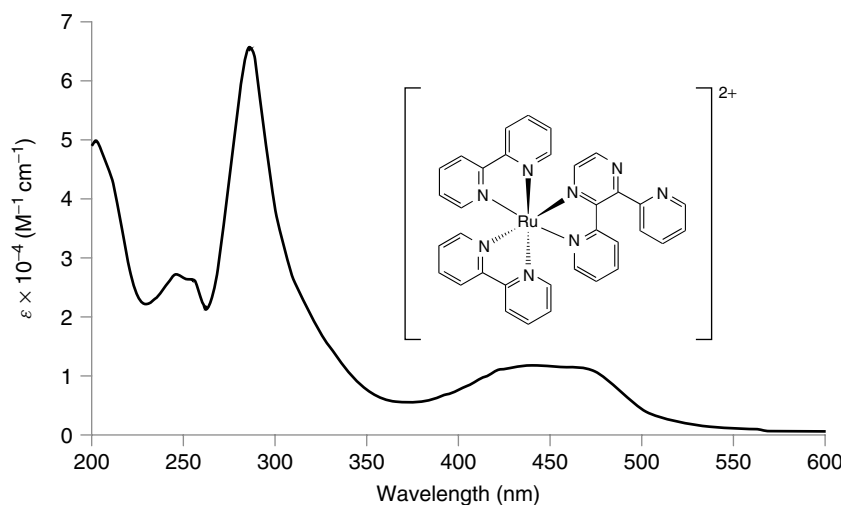


Figure 6 Electronic absorption spectrum of $[(\text{bpy})_2\text{Ru}(\text{dpp})](\text{PF}_6)_2$ in acetonitrile at RT (bpy, 2,2'-bipyridine, dpp, 2,3-bis(2-pyridyl)pyrazine)

Table 1 Electrochemical properties of complexes of interest in the development of hydrogen production photocatalysts

Complex ^(a)	$E_{1/2}^{\text{ox}}$ (V vs SCE)	$E_{1/2}^{\text{red}}$ (V vs SCE)		Ref.
		CAT	$\text{L}^{0/-}$	
$[(\text{bpy})_2\text{Ru}(\text{MebpyCONHPhCOO}(\text{Fe}_2\{\mu-\text{S}_2(\text{CH}_2)_2\text{CH}\}\{\text{CO}_6\}))]^{2+}$ ^(b)	1.20 Ep ^a 1.30 ($\text{Ru}^{\text{II/III}}$)	-1.20(Fe ₂ -site) Ep ^c		36
$[(\text{tpy})\text{Ru}(\text{tpyC}_2\text{Ph}(\text{Fe}_2\{\mu-\text{S}_2(\text{CH}_2)_2\text{N}\}\{\text{CO}_6\}))]^{2+}$ ^(c)	1.08 Ep ^a 1.34 ($\text{Ru}^{\text{II/III}}$)	-1.06(Fe ₂ -site) Ep ^c	-1.24(tpy ^{0/-}) -1.46(tpy ^{0/-})	37
$[(\text{bpy})_2\text{Ru}(\text{bpyC}_2\text{Ph}(\text{Ph}_2)\text{P}(\text{Fe}_2\{\mu-\text{S}_2(\text{CH}_2)_3\}\{\text{CO}_5\}))]^{2+}$ ^(c)	0.83 Ep ^a 1.08 Ep ^a 1.34 ($\text{Ru}^{\text{II/III}}$)	-1.33(Fe ₂ -site) Ep ^c	-1.08(bpy ^{0/-}) -1.58(bpy ^{0/-})	38
$[(\text{bpy})_2\text{Ru}(\text{L-pyr})\text{Co}(\text{dmgBF}_2)_2(\text{OH}_2)]^{2+}$ ^(d)		-0.51($\text{Co}^{\text{II/I}}$)		39
$[(\text{bpy})_2\text{Ru}(\text{L-pyr})\text{Co}(\text{dmgH})_2\text{Cl}]^{2+}$ ^(d)		-0.69($\text{Co}^{\text{III/II}-\text{Cl}}$) -0.95($\text{Co}^{\text{II/I}}$) -0.24($\text{Co}^{\text{II/I}}$)		39
$[(\text{bpy})_2\text{Ru}(\text{L-pyr})\text{Co}(\text{dpgBF}_2)_2(\text{OH}_2)]^{2+}$ ^(d)		-0.48($\text{Co}^{\text{II/I}}$)		39
$[(\text{Me}_2\text{phen})_2\text{Ru}(\text{L-pyr})\text{Co}(\text{dmgBF}_2)_2(\text{OH}_2)]^{2+}$ ^(d)		-0.47($\text{Co}^{\text{II/I}}$)		40
$[(\text{ppy})_2\text{Ir}(\text{L-pyr})\text{Co}(\text{dmgBF}_2)_2(\text{OH}_2)]^{+}$ ^(e)		-0.45($\text{Co}^{\text{II/I}}$)		40
$[(\text{bpy})_2\text{Ru}(\text{bpy-4-CH}_3, 4'\text{-CONH-4-py})\text{Co}(\text{dmgBF}_2)_2(\text{OH}_2)]^{2+}$ ^(b)		-0.42($\text{Co}^{\text{II/I}}$)	-1.33(bpy ^{0/-}) -1.52(bpy ^{0/-}) -1.80(bpy ^{0/-})	41
$[(\text{bpy})_2\text{Ru}(\text{bpy-4-CH}_3, 4'\text{-CONHCH}_2\text{-4-py})\text{Co}(\text{dmgBF}_2)_2(\text{OH}_2)]^{2+}$ ^(b)		-0.42($\text{Co}^{\text{II/I}}$)	-1.32(bpy ^{0/-}) -1.52(bpy ^{0/-}) -1.78(bpy ^{0/-})	41
$[(\text{bpy})_2\text{Ru}(\text{dpp})_2\text{RhCl}_2]^{5+}$ ^(f)	1.60 ($2\text{Ru}^{\text{II/III}}$)	-0.40($\text{Rh}^{\text{III/I}}$)	-0.79(dpp ^{0/-}) -1.03(dpp ^{0/-})	42
$[(\text{bpy})_2\text{Ru}(\text{dpp})_2\text{RhBr}_2]^{5+}$ ^(f)	1.56 ($2\text{Ru}^{\text{II/III}}$)	-0.36($\text{Rh}^{\text{III/I}}$)	-0.75(dpp ^{0/-}) -1.05(dpp ^{0/-})	42
$[(\text{phen})_2\text{Ru}(\text{dpp})_2\text{RhCl}_2]^{5+}$ ^(f)	1.54 ($2\text{Ru}^{\text{II/III}}$)	-0.42($\text{Rh}^{\text{III/I}}$)	-0.83(dpp ^{0/-}) -1.09(dpp ^{0/-})	42
$[(\text{bpy})_2\text{Os}(\text{dpp})_2\text{RhCl}_2]^{5+}$ ^(f)	1.17 ($2\text{Os}^{\text{II/III}}$)	-0.42($\text{Rh}^{\text{III/I}}$)	-0.79(dpp ^{0/-}) -1.03(dpp ^{0/-})	42
$[(\text{tpy})\text{RuCl}(\text{dpp})_2\text{RhCl}_2]^{3+}$ ^(f)	1.09 ($2\text{Ru}^{\text{II/III}}$)	-0.51($\text{Rh}^{\text{III/I}}$)	-0.91(dpp ^{0/-}) -1.24(dpp ^{0/-})	42
$[(\text{tpy})\text{OsCl}(\text{dpp})_2\text{RhCl}_2]^{3+}$ ^(f)	0.81 ($2\text{Os}^{\text{II/III}}$)	-0.54($\text{Rh}^{\text{III/I}}$)	-0.89(dpp ^{0/-}) -1.23(dpp ^{0/-})	42
$[(\text{bpy})_2\text{Ru}(\text{dpb})_2\text{IrCl}_2]^{5+}$ ^(f)	1.53 ($2\text{Ru}^{\text{II/III}}$)		-0.005(dp ^{b0/-}) -0.16(dp ^{b0/-})	42
$[(\text{tpyPh}(\text{Ph}_2\text{P}))_2\text{Os}]\text{RhCl}(\text{CO})]^{2+}$ ^(g)	0.92 ($\text{Os}^{\text{II/III}}$)		-1.11(tpy ^{0/-}) -1.34(tpy ^{-/-2})	43
$[({}^t\text{Bu}_2\text{bpy})_2\text{Ru}(\text{tpphz})\text{PdCl}_2]^{2+}$ ^(h)		-0.82($\text{Pd}^{\text{II/0}}$)	-0.63(tpphz ^{0/-})	44
$[(\text{bpy})_2\text{Ru}(\text{Mebpy}(\text{CH}_2)_2\text{C}_6\text{H}_2\text{-}(\text{OCH}_3)_2(\text{CH}_2)_2\text{Mebpy})\text{PdCl}_2]^{2+}$ ^(c)	1.27 ($\text{Ru}^{\text{II/III}}$) 1.46 ($\text{DMB}^{0/+}$) Ep ^a	-0.92($\text{Pd}^{\text{II/0}}$)		45
$[(\text{bpy})_2\text{Ru}(\text{dpp})_2\text{Ru}(\text{dpq})\text{PtCl}_2]^{6+}$ ^(h)	1.56 ($2\text{Ru}^{\text{II/III}}$)		-0.12(dpq ^{0/-}) -0.49(dpp ^{0/-}) -0.66(dpp ^{0/-})	46

(a) Potential reported vs SCE, Ep^a or Ep^c demonstrates that only the anodic or cathodic potential was observed.

(b) In acetonitrile with 0.01 AgNO₃, Ag/Ag⁺ is converted to SCE by adding 0.30 V to the Ag/Ag⁺ potential.

(c) In acetonitrile with 0.1 M NBu₄PF₆, Fc/Fc⁺ is converted to SCE by adding 0.430 V to the Fc/Fc⁺ potential.

(d) In DMF with 0.1 M NBu₄BF₄.

(e) In acetonitrile with 0.1 M NBu₄BF₄.

(f) In acetonitrile with 0.1 M NBu₄PF₆, NHE is converted to SCE by subtracting 0.244 V from the NHE potential.

(g) In acetonitrile containing 0.1 M Bu₄NClO₄.

(h) In acetonitrile with 0.1 M NBu₄PF₆, converted Ag/AgCl to SCE by subtracting 35 mV from the Ag/AgCl potential.

2.5 Photoinitiated Charge Separation: Molecular Design

Photoinduced charge separation is a key component in photocatalytic water splitting, and molecules displaying

this function are termed *molecular photovoltaics*. A charge-separated state formed upon absorption of a photon of light by an LA can undergo facile intramolecular electron transfer. A simple device for photoinitiated charge separation may

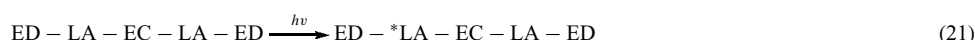
Table 2 Spectroscopic and photophysical properties of complexes of interest in the development of hydrogen production photocatalysts

Complex	$\lambda_{\text{max}}^{\text{abs}}$ (nm)	$\lambda_{\text{max}}^{\text{em}}$ (nm)	Φ^{em} (RT)	τ (RT, ns)	Ref.
$[(\text{bpy})_2\text{Ru}(\text{MebpyCONHPhCOO}(\text{Fe}_2\{\mu\text{-S}_2(\text{CH}_2)_2\text{CH}\}(\text{CO})_6))^{2+}$ ^(a)	460			234, 1190	36
$[(\text{tpy})\text{Ru}(\text{tpyC}_2\text{Ph}(\text{Fe}_2\{\mu\text{-S}_2(\text{CH}_2)_2\text{N}\}(\text{CO})_6))^{2+}$ ^(b)	500	674	2×10^{-5}	6.5	37
$[(\text{bpy})_2\text{Ru}(\text{bpyC}_2\text{Ph}(\text{Ph}_2)\text{P}(\text{Fe}_2\{\mu\text{-S}_2(\text{CH}_2)_3\}(\text{CO})_5))^{2+}$ ^(a)	400–500	670		770	38
$[(\text{bpy})_2\text{Ru}(\text{L-pyr})\text{Co}(\text{dmgBF}_2)_2(\text{OH}_2)]^{2+}$	454 ^(c)	ca. 625 ^(d)		1630	39
$[(\text{bpy})_2\text{Ru}(\text{L-pyr})\text{Co}(\text{dmgH}_2\text{Cl})^{2+}$	460 ^(c)	ca. 625 ^(d)		1170	39
$[(\text{bpy})_2\text{Ru}(\text{L-pyr})\text{Co}(\text{dpqBF}_2)_2(\text{OH}_2)]^{2+}$	453 ^(c)	ca. 625 ^(d)		1720	39
$[(\text{bpy})_2\text{Ru}(\text{bpy-4-CH}_3, 4'\text{-CONH-4-py})\text{Co}(\text{dmgBF}_2)_2(\text{OH}_2)]^{2+}$ ^(d)	400–500	650			41
$[(\text{bpy})_2\text{Ru}(\text{bpy-4-CH}_3, 4'\text{-CONH}(\text{CH}_2)\text{-4-py})\text{Co}(\text{dmgBF}_2)_2(\text{OH}_2)]^{2+}$ ^(d)	400–500	650			41
$[(\text{bpy})_2\text{Ru}(\text{dpp})_2\text{RhCl}_2]^{5+}$ ^(a)	520	760	7.3×10^{-5}	32	42
$[(\text{bpy})_2\text{Ru}(\text{dpp})_2\text{RhBr}_2]^{5+}$ ^(a)	520	760	1.5×10^{-4}	26	42
$[(\text{phen})_2\text{Ru}(\text{dpp})_2\text{RhCl}_2]^{5+}$ ^(a)	520	746	1.8×10^{-4}	27	42
$[(\text{bpy})_2\text{Os}(\text{dpp})_2\text{RhCl}_2]^{5+}$ ^(a)	530				42
$[(\text{tpy})\text{RuCl}(\text{dpp})_2\text{RhCl}_2]^{3+}$ ^(a)	540				42
$[(\text{tpy})\text{OsCl}(\text{dpp})_2\text{RhCl}_2]^{3+}$ ^(a)	538				42
$[(\text{bpy})_2\text{Ru}(\text{dpb})_2\text{IrCl}_2]^{5+}$ ^(a)	666				42
$[(\text{tpyPh}(\text{Ph}_2\text{P}))_2\text{Os}]\text{RhCl}(\text{CO})]^{2+}$ ^(e)	482, 655	728	0.52		43
$[(\text{bpy})_2\text{Ru}(\text{phenNHCO}(\text{COOHbpy}))\text{PtCl}_2]^{2+}$ ^(f)	ca. 450	610			47
$[(^t\text{Bu}_2\text{bpy})_2\text{Ru}(\text{tpphz})\text{PdCl}_2]^{2+}$	445 ^(a)	650 ^(a)		27 ^(g)	44
$[(\text{bpy})_2\text{Ru}(\text{Mebpy}(\text{CH}_2)_2\text{C}_6\text{H}_2(\text{OCH}_3)_2(\text{CH}_2)_2\text{Mebpy})\text{PdCl}_2]^{2+}$ ^(a)	455				45
$[(\text{bpy})_2\text{Ru}(\text{dpp})_2\text{Ru}(\text{dpq})\text{PtCl}_2]^{6+}$ ^(a)	542	745	2.5×10^{-4}	92	46

^(a) Room temperature spectra obtained in deoxygenated acetonitrile.^(b) In dichloromethane.^(c) In DMF.^(d) In acetone.^(e) In acetonitrile:water (1 : 1) prepared in situ.^(f) In water.^(g) In air-saturated acetonitrile.

be constructed by covalent attachment of ED, LA, and EA subunits generating an ED–LA–EA structural motif. In an ideal system, absorption of a photon of light would lead to a series of intramolecular electron transfer processes to generate a spatially separated, charge-separated state, $\text{ED}^+ - \text{LA}^- - \text{EA}^-$ (equations 18–20). An extended τ of the charge-separated state is desirable for efficient exploration of this charge separation. This can be modulated by component modification to tune electronic coupling, relative orbital energies, and the distance between the ED and EA.

The coupling of two ED–LA units with an EA that can accept multiple electrons provides a device for PEC. In such a situation, the EA can be referred to as an *electron collector* (EC), generating supramolecular complexes having the general architecture ED–LA–EC–LA–ED. Electronic isolation between the LA subunits is needed for PEC. Excitation of an LA followed by intramolecular electron transfer leads to a singly reduced EC (equations 21–23). Subsequent excitation of the second LA unit followed by intramolecular electron transfer (equations 24–26) provides PEC.



The discovery of the desirable redox and photophysical properties of $[\text{Ru}(\text{bpy})_3]^{2+}$ and related chromophores has led to the development of complicated supramolecular assemblies that can absorb light and participate in solar energy conversion schemes.¹⁵ In supramolecular systems, electron or energy transfer quenching is facilitated through intramolecular pathways. Coupling a CAT to a charge-transfer LA provides an alternative means for the conversion of solar energy to transportable fuels. The recent progress in the use of supramolecular PMDs as photocatalysts applicable in the production of hydrogen fuel from water and other proton sources in homogeneous systems is discussed, with focus on systems that contain iron, cobalt, rhodium, platinum, or palladium as the CAT.

2.6 Iron-Based Biomimetic Supramolecular Systems and Photocatalysts

Biomimetic systems that mimic the iron–hydrogenase active site for photochemical water reduction to produce hydrogen has been a topic of recent interest.¹⁸ The active site of the iron hydrogenase is known to consist of two iron atoms linked by a dithiolate bridge.⁵² The biomimetic diiron model, $[\text{Fe}_2\{\mu\text{-S}_2(\text{CH}_2)_3\}(\text{CN})(\text{CO})_4(\text{PMe}_3)]^-$ (Figure 7), has been shown to serve as a catalyst for electrochemical hydrogen production.⁵³

Sun and coworkers have constructed a series of supramolecular dyads, $[(\text{bpy})_2\text{Ru}(\text{MebpyCONHPhCOO}(\text{Fe}_2\{\mu\text{-S}_2(\text{CH}_2)_2\text{CH}\}(\text{CO})_6))]^{2+}$, $[(\text{tpy})\text{Ru}(\text{tpyC}_2\text{Ph}(\text{Fe}_2\{\mu\text{-S}_2(\text{CH}_2)_2\text{N}\}(\text{CO})_6))]^{2+}$, $[(\text{bpy})_2\text{Ru}(\text{MebpyCONHPh}(\text{Fe}_2\{\mu\text{-S}_2(\text{CH}_2)_2\text{N}\}(\text{CO})_6))]^{2+}$, and $[(\text{bpy})_2\text{Ru}(\text{bpyC}_2\text{Ph}(\text{Ph}_2)\text{P}(\text{Fe}_2\{\mu\text{-S}_2(\text{CH}_2)_3\}(\text{CO})_5))]^{2+}$, where a model iron–hydrogenase active site is attached to $[\text{Ru}(\text{bpy})_3]^{2+}$ -type chromophores (Figure 8).^{12,36–38,54} These systems were developed to couple the favorable optical properties of the Ru-based chromophore to the catalytic properties of the diiron-active site. It was anticipated that in the presence of an ED, the optically excited ruthenium chromophore would be oxidatively quenched by the dinuclear iron site, which when repeated twice would create a doubly reduced diiron species that could photocatalyze water reduction to produce hydrogen. The oxidative electrochemistry displays an irreversible oxidation of the iron component, followed by

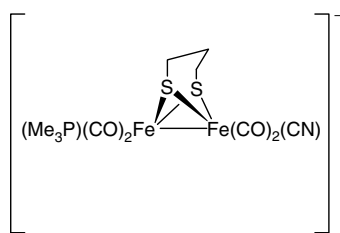


Figure 7 Biomimetic model for $[\text{Fe}_2\{\mu\text{-S}_2(\text{CH}_2)_3\}(\text{CN})(\text{CO})_4(\text{PMe}_3)]^-$

reversible $\text{Ru}^{\text{II}/\text{III}}$ oxidation. The reductive electrochemistry displays reductions of the iron component, followed by the ligand-based reductions. The complexes absorb light throughout the ultraviolet and visible regions of the solar spectrum. The lowest energy absorptions in the visible region are MLCT transitions, while the UV region is dominated by $\pi \rightarrow \pi^*$ -ligand-based transitions. The electrochemical and spectroscopic properties of $[(\text{bpy})_2\text{Ru}(\text{MebpyCONHPhCOO}(\text{Fe}_2\{\mu\text{-S}_2(\text{CH}_2)_2\text{CH}\}(\text{CO})_6))]^{2+}$, $[(\text{tpy})\text{Ru}(\text{tpyC}_2\text{Ph}(\text{Fe}_2\{\mu\text{-S}_2(\text{CH}_2)_2\text{N}\}(\text{CO})_6))]^{2+}$, and $[(\text{bpy})_2\text{Ru}(\text{MebpyCONHPh}(\text{Fe}_2\{\mu\text{-S}_2(\text{CH}_2)_2\text{N}\}(\text{CO})_6))]^{2+}$ are very similar to their subunits, indicating negligible electronic interaction between the chromophoric counterpart and the diiron unit, while the properties were perturbed in $[(\text{bpy})_2\text{Ru}(\text{bpyC}_2\text{Ph}(\text{Ph}_2)\text{P}(\text{Fe}_2\{\mu\text{-S}_2(\text{CH}_2)_3\}(\text{CO})_5))]^{2+}$, suggesting electronic coupling in this system.^{36–38,54}

All complexes display an emission from the ${}^3\text{MLCT}$ state of the chromophoric unit, quenched relative to the monomeric chromophore. Emission quenching of the ${}^3\text{MLCT}$ states is a characteristic of intramolecular electron or energy transfer.^{36–38,54} However, the excited state reduction potentials of the dyads indicate that the electron transfer from the ruthenium chromophore to the diiron component is energetically uphill. The driving force for reductive quenching of the ${}^3\text{MLCT}$ excited state is, however, favorable with the formation of a transiently oxidized diiron portion and a reduced ruthenium LA unit.^{36–38,54} The diiron dyads cannot be directly reduced by the excited photosensitizer within this framework. Although not applicable in hydrogen photocatalysis, this study provides an insight into system design considerations. Component modification at the diiron center to facilitate electron transfer from the ${}^3\text{MLCT}$ excited state of the photosensitizer and/or photogeneration of a ${}^3\text{MLCT}$ excited state with a higher energy acceptor orbital has been suggested as a means to promote excited state electron transfer from the ruthenium LA to the diiron core.^{36–38,54}

Sun and coworkers recently used a pyridyl-functionalized hydrogenase-active site model complex bound to a zinc tetraphenylporphyrin [ZnTPP] unit for photochemical hydrogen production, $[\text{ZnTPP}(\text{pyridylCOO}(\text{CH}_2)_2(\text{Fe}_2\{\mu\text{-S}_2(\text{CH}_2)_2\text{N}\}(\text{CO})_6))]^{2+}$ (Figure 9).⁵⁵ Two main strategies were employed in system design. The first was to take advantage of the weak coordination of pyridine to zinc to limit back electron transfer through complex dissociation after the reduction of the diiron center. The second strategy was to make use of the ability of the system to self-assemble to mediate intramolecular electron transfer. The mechanism for electron transfer was studied by transient absorption spectroscopy in the presence of ZnTPP and $[\text{pyridylCOO}(\text{CH}_2)_2(\text{Fe}_2\{\mu\text{-S}_2(\text{CH}_2)_2\text{N}\}(\text{CO})_6)]$ (Figure 9) or noncoordinating $[\text{OH}(\text{CH}_2)_2(\text{Fe}_2\{\mu\text{-S}_2(\text{CH}_2)_2\text{N}\}(\text{CO})_6)]$ (Figure 9).

ZnTPP displays a strong emission from the singlet excited state (${}^1\text{ZnTPP}^*$), providing a probe to excited state dynamics. The emission from ZnTPP is

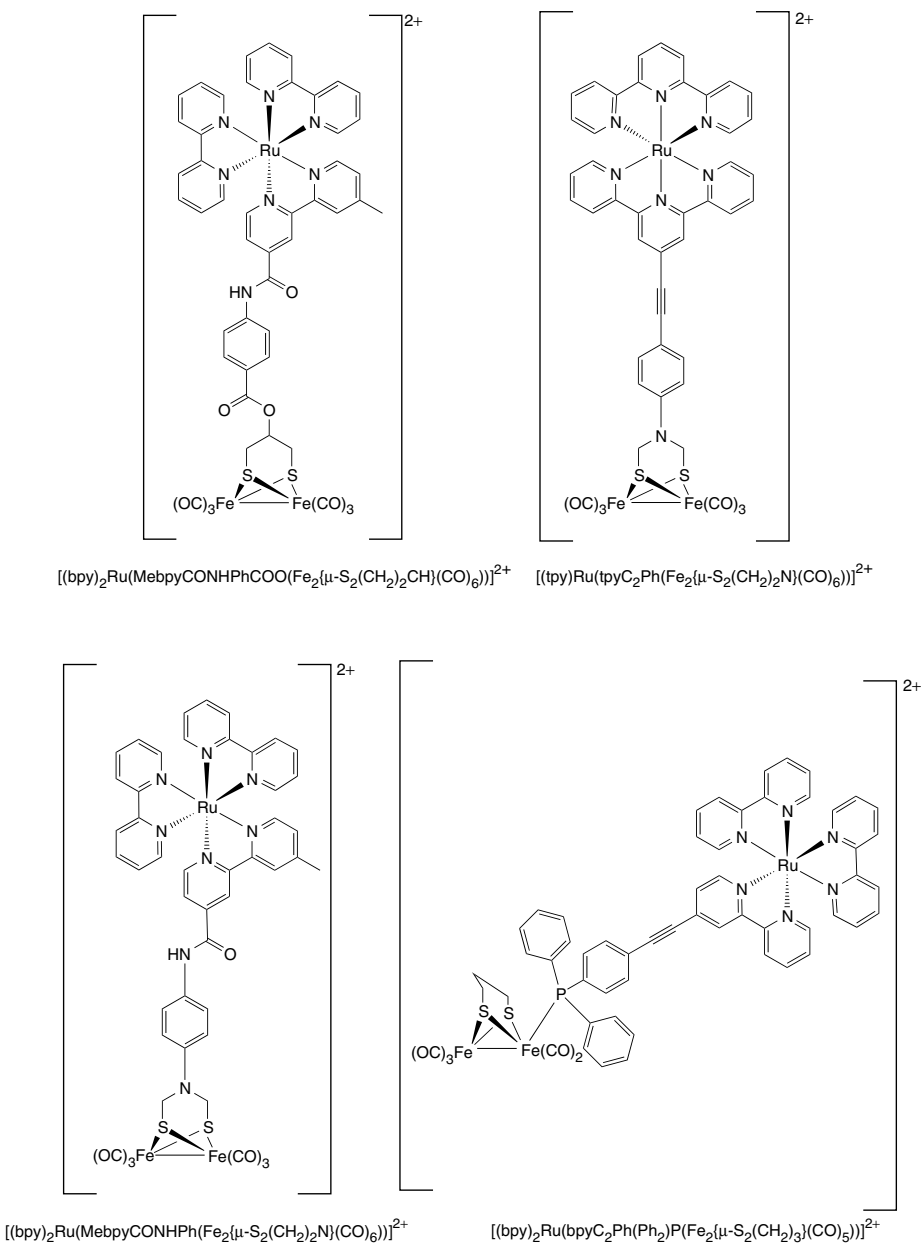


Figure 8 Systems that couple a ruthenium chromophore to an iron-based catalyst (bpy, 2,2'-bipyridine)

quenched by 50–60% in the presence of a 20-fold excess of $[\text{pyridylCOO}(\text{CH}_2)_2(\text{Fe}_2\{\mu\text{-S}_2(\text{CH}_2)_2\text{N}\})(\text{CO})_6]$ with a reduction in the singlet excited state lifetime, not observed in the presence of the noncoordinating $[\text{OH}(\text{CH}_2)_2(\text{Fe}_2\{\mu\text{-S}_2(\text{CH}_2)_2\text{N}\})(\text{CO})_6]$.⁵⁵ This emission quenching is consistent with a static absorption titration measurement under similar conditions. These both suggest the necessity for the formation of a supramolecular species through zinc coordination to pyridine, coupling the $^1\text{ZnTPP}^*$ and the diiron moiety, promoting excited state electron quenching. The high energy of the $^1\text{ZnTPP}^*$ singlet excited state allows electron or energy transfer to the diiron unit. Photoexcitation of ZnTPP using

a nanosecond flash photolysis technique in the presence of $[\text{OH}(\text{CH}_2)_2(\text{Fe}_2\{\mu\text{-S}_2(\text{CH}_2)_2\text{N}\})(\text{CO})_6]$ resulted in a spectral change in the transient absorption spectrum consistent only with the formation of a triplet excited state ($^3\text{ZnTPP}^*$) with bleaching of the ground state. An identical spectral change occurs when a solution of only ZnTPP is photoexcited, implying that no quenching of the $^1\text{ZnTPP}^*$ occurs in the presence of $[\text{pyridylCOO}(\text{CH}_2)_2(\text{Fe}_2\{\mu\text{-S}_2(\text{CH}_2)_2\text{N}\})(\text{CO})_6]$. In the presence of $[\text{pyridylCOO}(\text{CH}_2)_2(\text{Fe}_2\{\mu\text{-S}_2(\text{CH}_2)_2\text{N}\})(\text{CO})_6]$, a new species is observed using transient absorbance spectroscopy.⁵⁵ This is attributed to intramolecular electron transfer to form a charge-separated species, $([\text{ZnTPP}^+\text{ pyridyl}]^-)$

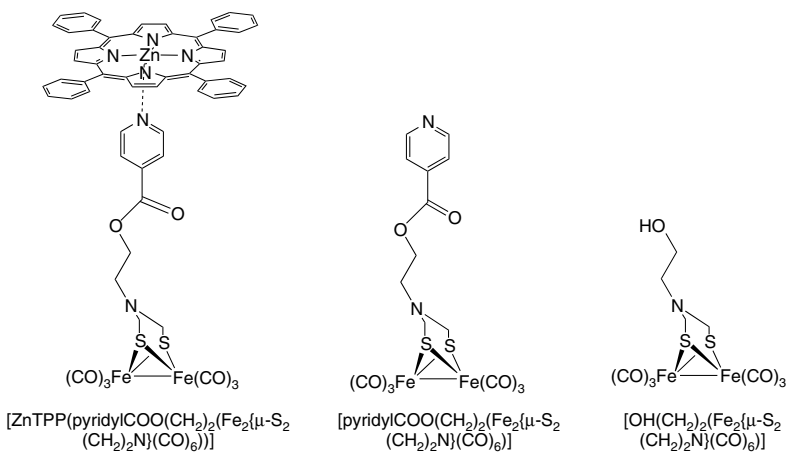


Figure 9 Representations of ZnFe self-assembling system and the FeFe subunits

$\text{COO}(\text{CH}_2)_2(\text{Fe}_2\{\mu\text{-S}_2(\text{CH}_2)_2\text{N}\}(\text{CO})_6)^-$], which could dissociate to ZnTPP^+ and $[\text{pyridylCOO}(\text{CH}_2)_2(\text{Fe}_2\{\mu\text{-S}_2(\text{CH}_2)_2\text{N}\}(\text{CO})_6)]^-$. Photolysis of ZnTPP , $[\text{pyridylCOO}(\text{CH}_2)_2(\text{Fe}_2\{\mu\text{-S}_2(\text{CH}_2)_2\text{N}\}(\text{CO})_6)]$, and the ED 2-mercaptopbenzoic acid in the presence of CF_3COOH as the proton source in methylene chloride at $\lambda > 400 \text{ nm}$ resulted in photochemical hydrogen production with 0.16 turnovers based on $[\text{pyridylCOO}(\text{CH}_2)_2(\text{Fe}_2\{\mu\text{-S}_2(\text{CH}_2)_2\text{N}\}(\text{CO})_6)]$ and 16 turnovers based on $[\text{ZnTPP}]$. Hydrogen production does not occur when $[\text{pyridylCOO}(\text{CH}_2)_2(\text{Fe}_2\{\mu\text{-S}_2(\text{CH}_2)_2\text{N}\}(\text{CO})_6)]$ is replaced by $[\text{OH}(\text{CH}_2)_2(\text{Fe}_2\{\mu\text{-S}_2(\text{CH}_2)_2\text{N}\}(\text{CO})_6)]$. It is proposed that $[\text{ZnTPP}^+\text{pyridylCOO}(\text{CH}_2)_2(\text{Fe}_2\{\mu\text{-S}_2(\text{CH}_2)_2\text{N}\}(\text{CO})_6)^-]$ may undergo dissociation to form $[\text{ZnTPP}^+]$, which is reductively quenched by the ED, and $[\text{pyridylCOO}(\text{CH}_2)_2(\text{Fe}_2\{\mu\text{-S}_2(\text{CH}_2)_2\text{N}\}(\text{CO})_6)]^-$, which gets protonated. Protonation of the radical anion renders the reduction potential more positive, facilitating the second electron transfer event, which is followed by further protonation and hydrogen release. This represents an interesting system for hydrogen production using intramolecular excited state electron transfer in a self-assembled system.⁵⁵

2.7 Cobalt-Based Supramolecular Photocatalysts

The use of $[\text{Co}(\text{bpy})_3]^{2+}$ as a CAT in photochemical hydrogen production schemes has inspired research on the use of cobaloximes.^{29,56} Recent efforts have been directed toward the construction of supramolecular complexes that couple the light-absorbing properties of Ru^{II} or Ir^{III} chromophores to the reactive properties of cobaloxime CATs in solar hydrogen production schemes.^{39,40} Fontecave and coworkers have constructed a series of supramolecular dyads $[(\text{bpy})_2\text{Ru}(\text{L-pyr})\text{Co}(\text{dmgBF}_2)_2(\text{OH}_2)]^{2+}$, $[(\text{bpy})_2\text{Ru}(\text{L-pyr})\text{Co}(\text{dmgH})_2\text{Cl}]^{2+}$, $[(\text{bpy})_2\text{Ru}(\text{L-pyr})\text{Co}(\text{dpgBF}_2)_2(\text{OH}_2)]^{2+}$,³⁹ $[(\text{Me}_2\text{phen})_2\text{Ru}(\text{L-pyr})\text{Co}(\text{dmgBF}_2)_2(\text{OH}_2)]^{2+}$, and $[(\text{ppy})_2\text{Ir}(\text{L-pyr})\text{Co}(\text{dmgBF}_2)_2(\text{OH}_2)]^+$ (L-pyr , $[(4\text{-pyridine})\text{oxazolo}$

(4,5-f)phenanthroline]⁴⁰; dmgH , dimethylglyoximate; dmgBF_2 , (difluoroboryl)dimethylglyoximate; dpgBF_2 , (difluoroboryl)diphenylglyoximate; Me_2phen , 4,7-dimethylphenanthroline; ppy , 2-phenylpyridine; Figure 10) as photocatalysts for solar hydrogen production.

2.7.1 Cobalt-Based Photocatalysts: Redox Properties

The electrochemical properties of these supramolecular dyads were investigated by cyclic voltammetry. In the ruthenium-based systems, $[(\text{bpy})_2\text{Ru}(\text{L-pyr})\text{Co}(\text{dmgBF}_2)_2(\text{OH}_2)]^{2+}$ and $[(\text{bpy})_2\text{Ru}(\text{L-pyr})\text{Co}(\text{dpgBF}_2)_2(\text{OH}_2)]^{2+}$, the $\text{Co}^{II/III}$ reductions were observed at -0.51 and -0.24 V vs SCE as reversible couples in DMF using $0.1 \text{ M } \text{Bu}_4\text{NBF}_4$ as the electrolyte. The cyclic voltammogram of $[(\text{bpy})_2\text{Ru}(\text{L-pyr})\text{Co}(\text{dmgH})_2\text{Cl}]^{2+}$ in DMF showed the two irreversible $\text{Co}^{III/II}$ reductions, attributed to reduction of Co^{III} -DMF and Co^{III} -Cl at -0.38 and -0.69 V vs SCE, respectively, followed by the reversible $\text{Co}^{II/III}$ couple at -0.95 V vs SCE.³⁹ The cyclic voltammograms of $[(\text{Me}_2\text{phen})_2\text{Ru}(\text{L-pyr})\text{Co}(\text{dmgBF}_2)_2(\text{OH}_2)]^{2+}$, in which the two bpy ligands are replaced by Me_2phen ligands, and $[(\text{ppy})_2\text{Ir}(\text{L-pyr})\text{Co}(\text{dmgBF}_2)_2(\text{OH}_2)]^+$ display reversible $\text{Co}^{II/III}$ couples at -0.48 V vs SCE in DMF.⁴⁰ The $\text{Co}^{II/III}$ couple occurs slightly more positive than the parent cobaloximes, whereas no significant redox changes are observed in the ruthenium-centered ligand-based processes upon dyad formation.^{39,40} The ability of cobalt to access the Co^{III} , Co^{II} , and Co^{I} oxidation states provides a means for multielectron catalysis. The functioning of these systems as electrocatalysts for proton reduction was probed by electrochemical methods. An electrocatalytic wave attributed to proton reduction was observed in an acetonitrile solution of $[(\text{bpy})_2\text{Ru}(\text{L-pyr})\text{Co}(\text{dmgBF}_2)_2(\text{OH}_2)]^{2+}$ at -0.49 V vs SCE with the addition of *p*-cyanoanilinium tetrafluoroborate, $[(\text{bpy})_2\text{Ru}(\text{L-pyr})\text{Co}(\text{dmgH})_2\text{Cl}]^{2+}$, at -0.94 V

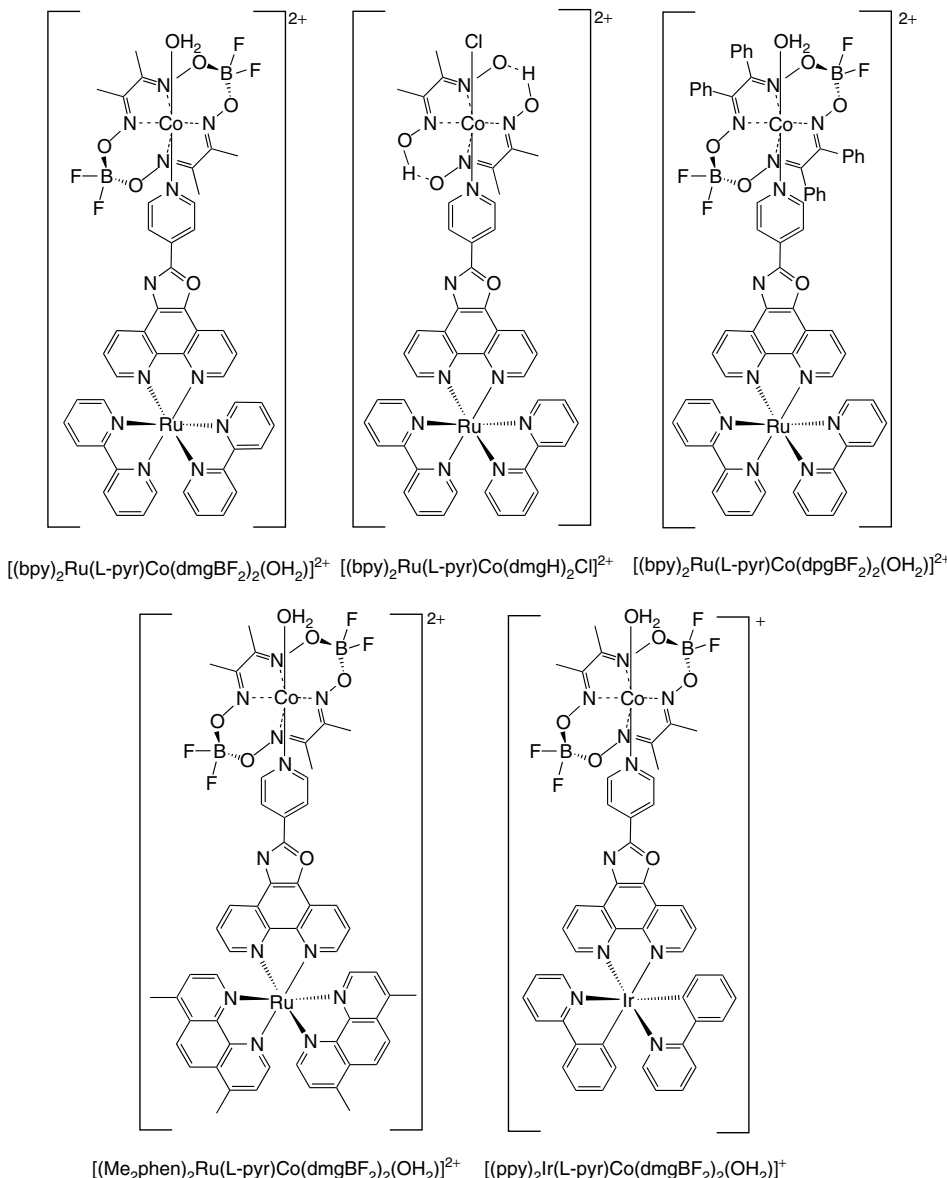


Figure 10 Representations of cobalt-based supramolecular dyads (L-pyr, [(4-pyridine)oxazolo(4,5-f)phenanthroline]; dmgh, dimethylglyoximate; $dmgBF_2$, (difluoroboryl)dimethylglyoximate; $dpgBF_2$, (difluoroboryl)diphenylglyoximate; Me_2phen , 4,7-dimethylphenanthroline; ppy, 2-phenylpyridine)

vs SCE in the presence of Et_3NHCl , and $[(bpy)_2Ru(L\text{-}pyr)Co(dpgBF_2)_2(OH_2)]^{2+}$ at -0.69 V vs SCE in the presence of *p*-cyanoanilinium tetrafluoroborate.³⁹ The cyclic voltammogram of $[(Me_2phen)_2Ru(L\text{-}pyr)Co(dmgBF_2)_2(OH_2)]^{2+}$ also demonstrated a catalytic wave attributed to proton reduction at -0.54 V vs SCE in the presence of *p*-cyanoanilinium tetrafluoroborate.⁴⁰

2.7.2 Cobalt-Based Photocatalysts: Photophysics

The complexes are potent LAs in the UV and visible regions of the spectrum, with the lowest energy transition

being MLCT in nature with $\lambda_{max}^{abs} = ca. 450$ nm in dimethylformamide (DMF). $[(bpy)_2Ru(L\text{-}pyr)Co(dmgBF_2)_2(OH_2)]^{2+}$, $[(bpy)_2Ru(L\text{-}pyr)Co(dmgH)_2Cl]^{2+}$, and $[(bpy)_2Ru(L\text{-}pyr)Co(dpgBF_2)_2(OH_2)]^{2+}$ display emissions from the 3 MLCT states with excited state lifetimes of 1.63, 1.17, and $1.72\ \mu s$ in deaerated acetone, respectively, at RT. The emission from the 3 MLCT state of the dyads is slightly quenched relative to $[(bpy)_2Ru(L\text{-}pyr)]^{2+}$ ($\tau = 1.72\ \mu s$), and intrinsic time constants for electron transfer of 30, 4, and $>300\ \mu s$ are estimated for $[(bpy)_2Ru(L\text{-}pyr)Co(dmgBF_2)_2(OH_2)]^{2+}$, $[(bpy)_2Ru(L\text{-}pyr)Co(dmgH)_2Cl]^{2+}$, and $[(bpy)_2Ru(L\text{-}pyr)Co(dpgBF_2)_2(OH_2)]^{2+}$, respectively.³⁹

2.7.3 Cobalt-Based Photocatalysts: Photocatalytic Production of H_2

Photolysis of $[(bpy)_2 Ru(L\text{-}pyr) Co(dmgBF_2)_2(OH_2)]^{2+}$, $[(bpy)_2 Ru(L\text{-}pyr)Co(dmgH)_2Cl]^{2+}$, or $[(bpy)_2 Ru(L\text{-}pyr)Co(dpgBF_2)_2(OH_2)]^{2+}$ in acetone, using a CdI-doped Hg light source, in the presence of a 100-fold excess of the ED, triethylamine (TEA), and a 100-fold excess of the proton source, $[Et_3NH]^+$, resulted in photochemical hydrogen production. Turnover numbers of 56, 17, and 12, respectively, over 4 h were seen. The impact of solvent on photocatalytic efficiency of $[(bpy)_2 Ru(L\text{-}pyr)Co(dmgBF_2)_2(OH_2)]^{2+}$ was investigated.³⁹ Lower turnover numbers in acetonitrile (turnover number = 10), methanol (turnover number = 9), DMF (turnover number = 3), and 1,2-dichloroethane (turnover number = 0) were observed. The low turnover numbers in DMF and 1,2-dichloroethane are attributed to decomplexation of the photocatalyst in these solvents. When the proton source was changed to water, a lower turnover number, 22 in 4 h, was obtained. This lower turnover number is attributed to the high pH of the solution under the conditions investigated.³⁹ Photocatalyst function was maintained under visible light when irradiated at $\lambda > 350$ nm with over 100 turnovers over 15 h of photolysis. Lower turnovers obtained when a UV cut-off filter was used suggest that both UV and visible light impact the catalyst function. Photolysis of $[(Me_2phen)_2 Ru(L\text{-}pyr)Co(dmgBF_2)_2(OH_2)]^{2+}$ or $[(ppy)_2 Ir(L\text{-}pyr)Co(dmgBF_2)_2(OH_2)]^+$ at $\lambda > 380$ nm in the presence of 300 equivalents of Et_3N and $[Et_3NH]^+$ in acetone yielded 9 and 90 turnovers, respectively, over 4 h.⁴⁰ The iridium-based system demonstrated enhanced photocatalytic efficiency to the ruthenium-based system, with 200 turnovers

over 15 h in the presence of 600 equivalents of ED and proton source.⁴⁰

The ruthenium-based dyads demonstrate superior photocatalytic efficiency to the multicomponent $[Ru(bpy)_3]^{2+}$ /cobaloxime system.^{39,40} By contrast, the iridium-based dyad shows similar catalytic efficiency to the multicomponent $[Ir(ppy)_2(phen)]^+$ /cobaloxime system, but the supramolecular dyad shows greater stability. It is predicted that intramolecular electron transfer affords a Co^{II} species, which is protonated to yield a $Co^{III}\text{-}H$ intermediate that can be further protonated to generate hydrogen. A favorable driving force for oxidative quenching of the chromophore by the attached Co^{II} site is predicted as the observed electrocatalytic potentials are more positive than the standard potentials of the excited state reduction potential for $[Ru(bpy)_3]^{2+}$.⁵⁷ Thus, the mechanism for photochemical hydrogen production by the ruthenium-based systems is predicted to proceed through intramolecular electron transfer to the cobalt center from a photoexcited ruthenium chromophore. The resistivity of the cobaloxime CAT to acid hydrolysis and hydrogenation reactions, the presence of a more reducible Co^{II} species in systems that incorporate a BF_2 to bridge, and the supramolecular nature of the dyads that favor more efficient intramolecular electron transfer events have been suggested as means for higher photocatalytic efficiency.³⁹

Sun and coworkers reported two other heterobinuclear complexes $[(bpy)_2 Ru(bpy\text{-}4\text{-}CH}_3, 4'\text{-CONH}\text{-}4\text{-py})Co(dmgBF_2)_2(OH_2)]^{2+}$, in which the ruthenium chromophore and the cobaloxime catalyst are connected by a conjugated bridge, and $[(bpy)_2 Ru(bpy\text{-}4\text{-}CH}_3, 4'\text{-CONH(CH}_2\text{-}4\text{-py})Co(dmgBF_2)_2(OH_2)]^{2+}$, in which the two components are connected by an unconjugated bridge (Figure 11).⁴¹ Electrochemically, a reversible couple for

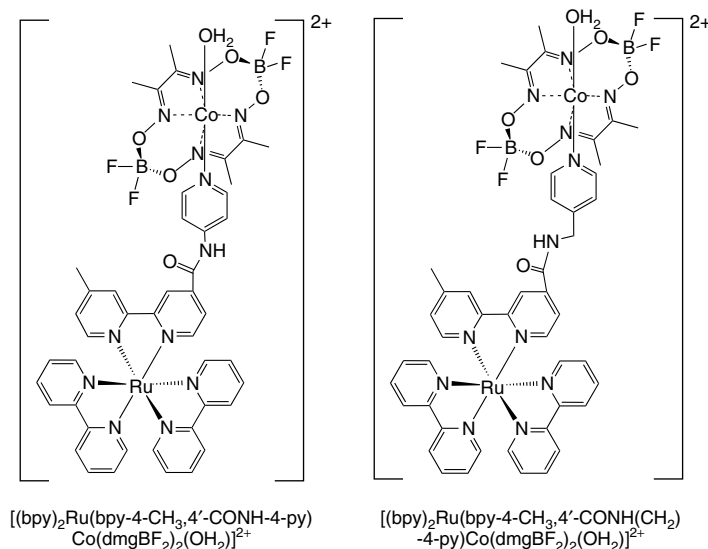


Figure 11 Representations of $[(bpy)_2 Ru(bpy\text{-}4\text{-}CH}_3, 4'\text{-CONH}\text{-}4\text{-py})Co(dmgBF_2)_2(OH_2)]^{2+}$ and $[(bpy)_2 Ru(bpy\text{-}4\text{-}CH}_3, 4'\text{-CONH(CH}_2\text{-}4\text{-py})Co(dmgBF_2)_2(OH_2)]^{2+}$ (dmgboryl, (difluoroboryl)dimethylglyoximate; bpy, 2,2'-bipyridine)

the $\text{Co}^{\text{II}/\text{I}}$ reduction is observed at -0.45 and -0.42 V vs SCE in acetonitrile for $[(\text{bpy})_2\text{Ru}(\text{bpy}-4\text{-CH}_3, 4'\text{-CONH-4-py})\text{Co}(\text{dmgBF}_2)_2(\text{OH}_2)]^{2+}$ and $[(\text{bpy})_2\text{Ru}(\text{bpy}-4\text{-CH}_3, 4'\text{-CONH}(\text{CH}_2)\text{-4-py})\text{Co}(\text{dmgBF}_2)_2(\text{OH}_2)]^{2+}$, respectively. This $\text{Co}^{\text{II}/\text{I}}$ couple is followed by bpy-based reductions. Both complexes display an emission from the ${}^3\text{MLCT}$ charge-transfer state, providing a probe to excited state dynamics. The emission intensity of $[(\text{bpy})_2\text{Ru}(\text{bpy}-4\text{-CH}_3, 4'\text{-CONH-4-py})\text{Co}(\text{dmgBF}_2)_2(\text{OH}_2)]^{2+}$ is quenched to 35% the intensity of the parent system, $[(\text{bpy})_2\text{Ru}(\text{bpy}-4\text{-CH}_3, 4'\text{-CONH-4-py})]^{2+}$, while the emission intensity of $[(\text{bpy})_2\text{Ru}(\text{bpy}-4\text{-CH}_3, 4'\text{-CONH}(\text{CH}_2)\text{-4-py})\text{Co}(\text{dmgBF}_2)_2(\text{OH}_2)]^{2+}$ is quenched to 25% the intensity of the parent system, $[(\text{bpy})_2\text{Ru}(\text{bpy}-4\text{-CH}_3, 4'\text{-CONHCH}_2\text{-4-py})]^{2+}$.⁴¹ The lower emission intensity in the dyad containing the conjugated bridge is attributed to the shorter distance between the chromophoric unit and the cobaloxime impacting the deactivation pathways. Photolysis of $[(\text{bpy})_2\text{Ru}(\text{bpy}-4\text{-CH}_3, 4'\text{-CONH-4-py})\text{Co}(\text{dmgBF}_2)_2(\text{OH}_2)]^{2+}$ or $[(\text{bpy})_2\text{Ru}(\text{bpy}-4\text{-CH}_3, 4'\text{-CONH}(\text{CH}_2)\text{-4-py})\text{Co}(\text{dmgBF}_2)_2(\text{OH}_2)]^{2+}$ at $\lambda = 400$ nm in the presence of 300 equivalents of Et_3N ED and $[\text{Et}_3\text{NH}]^+$ proton source in acetone resulted in hydrogen production with 38 and 49 turnovers in over 8 h for $[(\text{bpy})_2\text{Ru}(\text{bpy}-4\text{-CH}_3, 4'\text{-CONH-4-py})\text{Co}(\text{dmgBF}_2)_2(\text{OH}_2)]^{2+}$ and $[(\text{bpy})_2\text{Ru}(\text{bpy}-4\text{-CH}_3, 4'\text{-CONH}(\text{CH}_2)\text{-4-py})\text{Co}(\text{dmgBF}_2)_2(\text{OH}_2)]^{2+}$, respectively. Lower turnover numbers were obtained when DMF or acetonitrile was used as the solvent. The complex $[(\text{bpy})_2\text{Ru}(\text{bpy}-4\text{-CH}_3, 4'\text{-CONH-4-py})\text{Co}(\text{dmgBF}_2)_2(\text{OH}_2)]^{2+}$ with a conjugated bridge shows similar photocatalytic efficiency to $[(\text{bpy})_2\text{Ru}(\text{L-pyr})\text{Co}(\text{dmgBF}_2)_2(\text{OH}_2)]^{2+}$. The higher catalytic function in the system with an unconjugated bridge implies that unwanted deactivation pathways through the bridge may be limited in the unconjugated system, favoring hydrogen production schemes. In $[(\text{bpy})_2\text{Ru}(\text{bpy}-4\text{-CH}_3, 4'\text{-CONH-4-py})\text{Co}(\text{dmgBF}_2)_2(\text{OH}_2)]^{2+}$ and $[(\text{bpy})_2\text{Ru}(\text{bpy}-4\text{-CH}_3, 4'\text{-CONH}(\text{CH}_2)\text{-4-py})\text{Co}(\text{dmgBF}_2)_2(\text{OH}_2)]^{2+}$, oxidative quenching of the excited ruthenium chromophore by the Co^{II} through intramolecular electron transfer has been suggested as the dominant quenching process based on the favorable driving forces ($E = -0.79$ V vs SCE for ${}^*\text{Ru}^{2+}/\text{Ru}^{3+}$ and -0.55 V vs SCE in CH_3CN for the $[\text{Co}^{\text{II}}/\text{Co}^{\text{I}}]$) and the fact that the excited states of the parent chromophores are not quenched efficiently with Et_3N .⁴¹

2.8 Photoinitiated Electron Collectors: Functioning Systems

Light can be used to promote multielectron catalysis through PEC. PEC employs light energy to promote collection of at least two reducing equivalents to a central site. This process is significant in solar hydrogen production schemes as multielectron chemistry is important in water splitting to produce hydrogen fuel. The development of supramolecular assemblies that function as photoinitiated ECs allows the use of such systems in solar hydrogen production schemes.

The complexity of multielectron photochemistry has retarded the development of supramolecular PMDs that display PEC. The ability to tune the orbital energetics through component modification in supramolecular chemistry allows construction of complex molecular assemblies. In this regard, construction of supramolecular devices coupling multiple LAs to a single EA that can accept multiple electrons to provide an EC is feasible. Such devices would lead to PEC if the proper orbital energetic requirements are satisfied and there exists electronic isolation between the LA subunits. These systems represent two photoinitiated charge separation devices coupled to a common EA that functions as an EC.

2.8.1 Early Photoinitiated Electron Collectors: Ligand-Based Electron Collection

Brewer and coworkers reported the first functioning photoinitiated EC in a molecular system, $[(\text{bpy})_2\text{Ru}(\text{dpb})_2\text{IrCl}_2]^{5+}$ (dpb, 2,3-bis(2-pyridyl)benzoquinoxaline; Figure 12), in 1994.¹⁶ This supramolecular assembly separates two ruthenium LA units by an iridium core. Visible light irradiation in the presence of the ED, *N,N*-dimethylaniline (DMA), affords the two-electron-reduced product, $[(\text{bpy})_2\text{Ru}(\text{dpb}^-)_2\text{IrCl}_2]^{3+}$.

Bimetallic systems reported by MacDonnell and Campagna, $[(\text{phen})_2\text{Ru}(\text{BL})\text{Ru}(\text{phen})_2]^{4+}$ (BL, phenanthroline-pyrazine-benzene-pyrazine-phenanthroline (tatpp) or phenanthroline-pyrazine-quinone-pyrazine-phenanthroline (tatpq)), photochemically collect up to four electrons on the BL in the presence of TEA as the ED. These systems separate two ruthenium phenanthroline LA units through an extended aromatic BL.⁵⁸ These first photoinitiated ECs do not reduce water to produce hydrogen photochemically.

2.8.2 Early Photoinitiated Electron Collectors: Metal-Based Electron Collection

Brewer and coworkers reported the first photoinitiated EC that collects electrons on a metal with the supramolecular architecture remaining intact, $[(\text{bpy})_2\text{Ru}(\text{dpp})_2\text{RhCl}_2]^{5+}$ (Figure 12).^{50,59} This system has been modified from the initial iridium-based system by replacing the iridium with rhodium and the dpb BLs with dpp. $[(\text{bpy})_2\text{Ru}(\text{dpp})_2\text{RhCl}_2]^{5+}$ is a photocatalyst for water reduction to produce hydrogen.⁵⁹ Details of the redox and photophysical properties of this and other systems having a similar molecular architecture are discussed in detail in Section 2.4.

2.9 Mixed-Valence Systems for Multielectron Photochemistry to Produce H₂

Dinuclear mixed-valence complexes for multielectron photochemistry capable of reducing hydrohalic

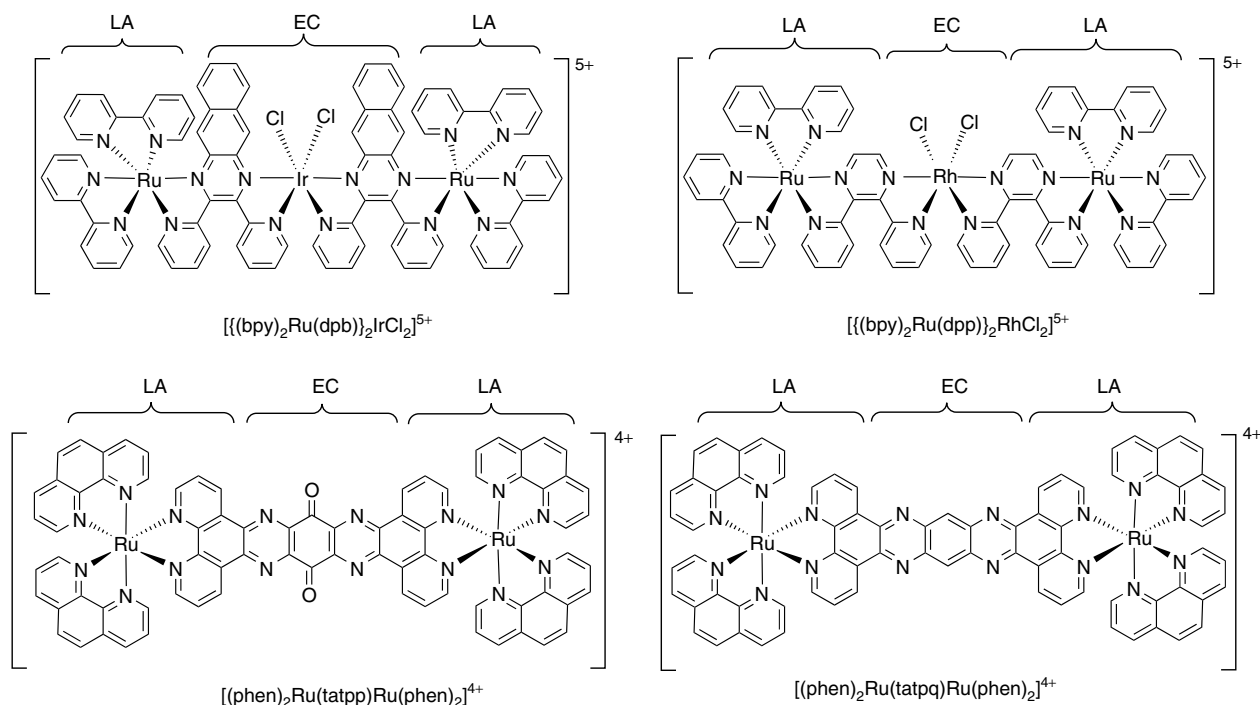
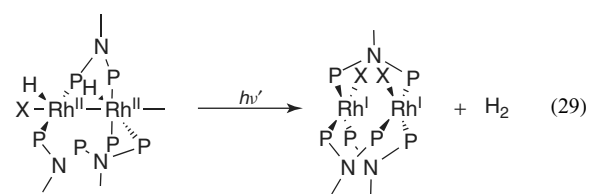
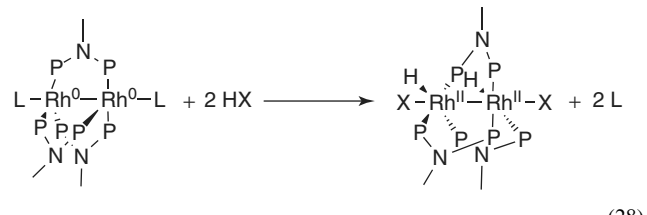
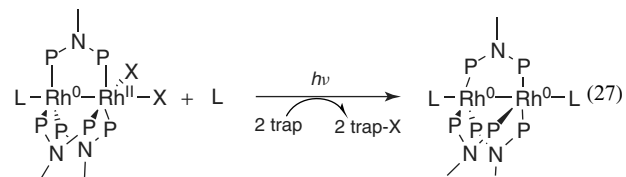
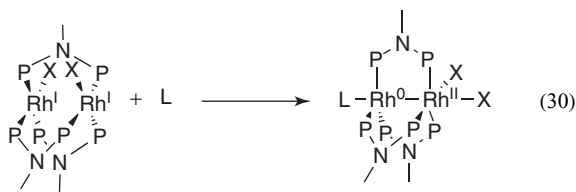


Figure 12 Representations of initial photoinitiated electron collectors (bpy, 2,2'-bipyridine, 2,3-bis(2-pyridyl)pyrazine; dpb, 2,3-bis(2-pyridyl)benzoquinoline)

acids to hydrogen, with $\Phi = 0.01$, in the presence of a halogen trap have been reported by Nocera and coworkers.^{13,60,61} Mixed-valence compounds of the form $M^{n+}\cdots M^{n+2}$ are employed to drive multielectron chemistry. Rhodium bimetallics, $[Rh_2(dfpm)_3X_4]$, when ligated by three dfpma ligands, transform to a two-electron mixed-valence state, $[Rh_2^{0,II}(dfpm)_3X_2(L)]$ (dfpma, $MeN(P(OCH_2CF_3)_2)_2$, X, Cl or Br; L, CO, PR_3 , or CNR) when irradiated at excitation wavelengths between 300 and 400 nm in the presence of excess L and a halogen-atom trap. The dfpma ligand is unique in the fact that it can act as both a π -acceptor and a π -donor, stabilizing the mixed-valence oxidation state of $[Rh_2^{0,II}(dfpm)_3X_2(L)]$. Further irradiation activates a $Rh^{II}-X$ to generate a doubly reduced form, $[Rh_2^{0,0}(dfpm)_3L_2]$ (see equations 27–30 for the reaction mechanism). This $Rh^{II}-X$ bond activation is the rate-determining step in the hydrogen production scheme. Photolysis of $[Rh_2^{0,0}(dfpm)_3L_2]$ in the presence of HCl results in an intermediate Rh^{II},Rh^{II} dihydride, dihalide, $[Rh_2^{II,II}(dfpm)_3Cl_2H_2]$, which, on photolysis, produces hydrogen with the generation of $[Rh_2^{1,I}(dfpm)_3Cl_2]$. This $Rh_2^{1,I}$ species undergoes internal disproportionation, leading to regeneration of $[Rh_2^{0,II}(dfpm)_3X_2(L)]$. Since activation of the $Rh-X$ bond is the rate-determining step for solar hydrogen production, studies have focused on systems that undergo more efficient rate of $M-X$ bond activation. In this regard, heterobimetallic complexes, $[Rh^I Au^I(tfepma)_2(CN^tBu)_2]^{2+}$

and $[Pt^{II}Au^I(dfpm)_2PhCl]^+$ (tfepma, $MeN(P(OCH_2CF_3)_2)_2$ and dfpma, $CH_2(PPh_2)_2$), have been synthesized.^{62,63} The $Pt^{III}-Au^{II}$ species, $[Pt^{III}Au^{II}(dfpm)_2PhCl_3]^+$, formed by photooxidation displays enhanced efficiency of metal–halide bond activation with respect to the dirhodium complexes.⁶²





2.10 Rhodium-Based Supramolecular Photocatalysts for H₂ Production

Since the initial discovery of $\{(\text{bpy})_2\text{Ru}(\text{dpp})\}_2\text{RhCl}_2^{5+}$ as a photoinitiated EC for solar hydrogen production from water, other systems incorporating a similar architecture that are also photoinitiated ECs have been reported by Brewer and coworkers.^{42,50,59,64} These systems separate two Ru^{II} or Os^{II} LAs through a single Rh^{III} acceptor. The metal components are connected to each other through polyazine BLs. These systems are unusual in that the rhodium coordination site has potentially labile monodentate halide ligands that allow photoreactivity within the molecule. The supramolecular assemblies provide an LA–BL–RhX₂–BL–LA structural motif (LA, Ru^{II} or Os^{II} polyazine chromophore; X, Cl⁻ or Br⁻; BL, dpp). Visible light irradiation affords PEC resulting in rhodium reduction, followed by loss of the labile ligands (Figure 13). Studies have established $\{(\text{bpy})_2\text{Ru}(\text{dpp})\}_2\text{RhX}_2^{5+}$ (X, Cl⁻ or Br⁻) and $\{(\text{phen})_2\text{Ru}(\text{dpp})\}_2\text{RhCl}_2^{5+}$ as PMDs for electron collection at a metal center and photocatalysts for solar hydrogen production from water with a hydrogen yield of $\Phi \approx 0.01$.^{42,50,59,64} Modification of the LA to osmium and/or the TL to tpy destabilizes the LA metal-d π orbitals, imparting distinctive properties in such systems. The complexes $\{(\text{bpy})_2\text{Os}(\text{dpp})\}_2\text{RhCl}_2^{5+}$, $\{(\text{tpy})\text{OsCl}(\text{dpp})\}_2\text{RhCl}_2^{3+}$, and $\{(\text{tpy})\text{RuCl}(\text{dpp})\}_2\text{RhCl}_2^{3+}$ have been synthesized and their photocatalytic activity evaluated. The complexes $\{(\text{bpy})_2\text{Os}(\text{dpp})\}_2\text{RhCl}_2^{5+}$ and $\{(\text{tpy})\text{RuCl}(\text{dpp})\}_2\text{RhCl}_2^{3+}$ also photocatalyze hydrogen production through water reduction, but with lower quantum efficiencies. Factors that impact photocatalytic efficiency have been evaluated by studying the redox and photophysical properties of these systems as discussed below.⁴²

2.10.1 Rhodium-Based Supramolecular Photocatalysts: Redox Properties

Electrochemistry was used to determine the redox potentials of the supramolecular species and identify the redox sites for addition or removal of electrons. Cyclic voltammetry was used to evaluate the electrochemical properties of the LA–BL–RhX₂–BL–LA molecular architectures. Electrochemistry provides a good estimation of the energy of the HOMO and the lowest unoccupied molecular orbital (LUMO), providing deep insight into the orbital energetics within a molecule. Electrochemically the trimetallic complexes of the general formula $\{(\text{TL})_2\text{M}(\text{dpp})\}_2\text{RhX}_2^{5+}$ (TL, bpy or phen; M, Ru or Os; X, Cl or Br) and $\{(\text{tpy})\text{MCl}(\text{dpp})\}_2\text{RhCl}_2^{3+}$ (M, Ru or Os) demonstrate reversible metal-based oxidations and irreversible rhodium- and reversible ligand-based reductions that are tuned over a large potential range by subunit identity.⁴² All the trimetallics show overlapping Ru^{II/III}- or Os^{II/III}-based oxidations for the two-terminal ligands, indicating minimal electronic interaction between the two ruthenium or osmium LA subunits, an important requirement for photoinitiated ECs. By contrast, the RuRu bimetallic systems that lack a rhodium EC, $\{(\text{bpy})_2\text{Ru}\}_2(\text{dpp})^{4+}$ and $\{(\text{phen})_2\text{Ru}\}_2(\text{dpp})^{4+}$, show two distinct Ru^{II/III} oxidation events at ca. +1.47 and +1.66 V vs SCE, indicating coupling of the metals in the bimetallic system.⁵¹ These bimetallic systems do not display PEC. The oxidative electrochemistry of $\{(\text{bpy})_2\text{Ru}(\text{dpp})\}_2\text{RhX}_2^{5+}$ (X, Cl or Br) or $\{(\text{phen})_2\text{Ru}(\text{dpp})\}_2\text{RhCl}_2^{5+}$ shows overlapping Ru^{II/III} couples at ca. 1.60 V vs SCE. The reductive electrochemistry shows irreversible Rh^{III/II/I} reductions, followed by two reversible dpp^{0/-} reductions. The Rh^{III/II/I} reduction is followed by the loss of halides, consistent with previously reported $[\text{Rh}(\text{bpy})_2\text{Cl}_2]^+$.⁶⁵ The halides on the rhodium center impact the redox properties as evidenced by a slightly more positive Rh^{III/II/I} reduction, -0.36 V vs SCE for $\{(\text{bpy})_2\text{Ru}(\text{dpp})\}_2\text{RhBr}_2^{5+}$ relative to $\{(\text{bpy})_2\text{Ru}(\text{dpp})\}_2\text{RhCl}_2^{5+}$, -0.40 V vs SCE.⁴² This positive shift is consistent with a rhodium coordination environment, resulting in a more electron-deficient metal, making it easier to reduce when the weaker σ -donor Br⁻ is the halide. When the LA metal is osmium, a destabilized Os(d π) orbital is observed with the Os^{II/III} couple occurring at 1.17 V vs SCE.

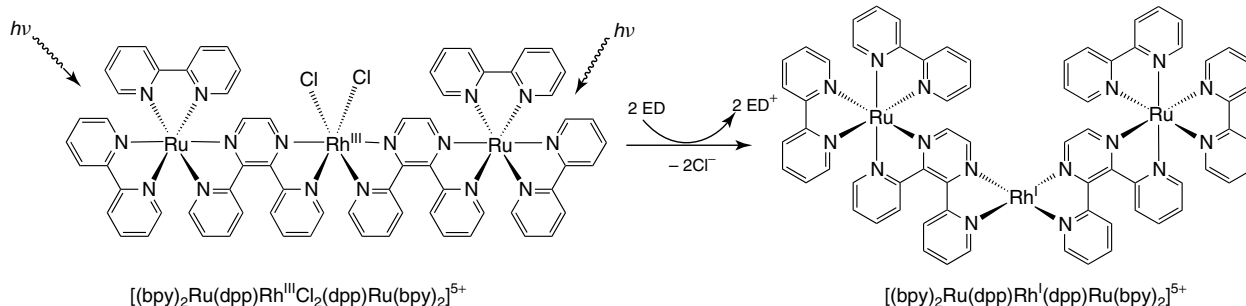


Figure 13 Photoinitiated electron collection on a metal center (bpy, 2,2'-bipyridine; dpp, 2,3-bis(2-pyridyl)pyrazine)

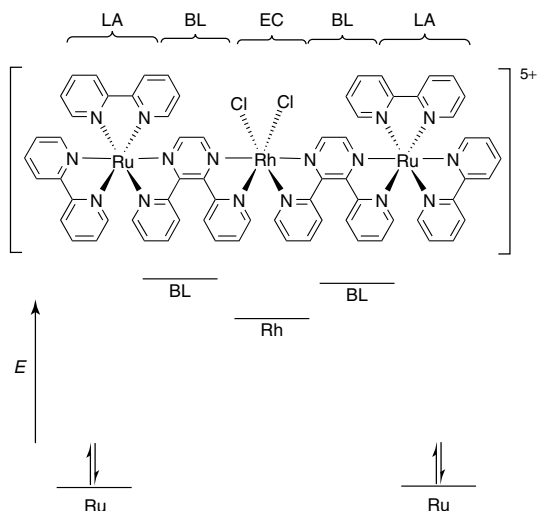


Figure 14 Orbital energy diagram of Rh-centered photoinitiated electron collection of the form LA–BL–RhX₂–BL–LA (LA, bpy or phen; BL, dpp; X, Cl or Br)

in $\{(\text{bpy})_2\text{Os}(\text{dpp})\}_2\text{RhCl}_2\}^{5+}$. The tpy-based systems can have stereochemical advantages over the bpy-based systems because of reduced isomers through the elimination of Δ and Λ isomeric mixtures associated with the tris(bidentate) metal centers. The Ru^{II/III} oxidation of $\{(\text{tpy})\text{RuCl}(\text{dpp})\}_2\text{RhCl}_2\}^{3+}$ occurs at 1.09 V vs SCE, more positive than the Ru^{II/III} oxidations of the analogous bpy-based systems consistent with a more electron-rich ruthenium center due to Cl⁻ coordination in place of a pyridine ring. The Os^{II/III} couple in $\{(\text{tpy})\text{OsCl}(\text{dpp})\}_2\text{RhCl}_2\}^{3+}$ occurs at 0.81 V vs SCE, consistent with even more destabilized Os(dπ) orbitals. The reductive electrochemistry of $\{(\text{tpy})\text{MCl}(\text{dpp})\}_2\text{RhCl}_2\}^{3+}$ shows irreversible Rh^{III/II/I} reductions at -0.51 and -0.55 V vs SCE (M, Ru or Os), respectively, followed by dpp^{0/-} couples for each dpp.⁴² The lower cationic charge and the presence of more electron-rich TLs in the tpy-based systems shifts the Rh^{III/II/I} reduction to more negative potentials. The electrochemistry of the trimetallic supramolecular complexes predicts an Ru(dπ)- or Os(dπ)-HOMO with energy tuned by the TL or LA metal and an Rh(dσ^{*})-based LUMO with energy tuned by the halides. The electrochemistry also predicts the lowest lying metal-to-metal charge-transfer (MMCT) state with an oxidized ruthenium and a reduced rhodium. These systems can function as photoinitiated ECs with electrons being collected on low lying rhodium(dσ^{*}) orbitals (Figure 14).

2.10.2 Rhodium-Based Supramolecular Photocatalysts: Spectroscopic Properties

Electronic absorption spectroscopy is a powerful technique that is easy to perform and provides information about the optical and electronic properties of molecules. Electronic absorption spectroscopy

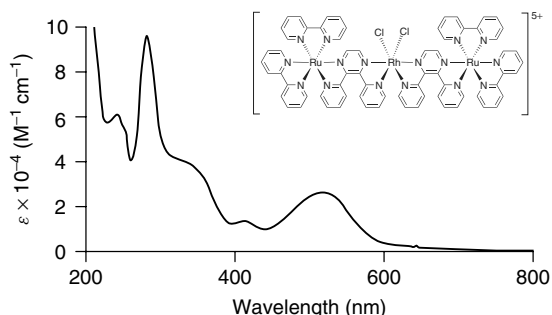


Figure 15 Electronic absorption spectrum of $\{(\text{bpy})_2\text{Ru}(\text{dpp})\}_2\text{RhCl}_2\}(\text{PF}_6)_5$ in acetonitrile (bpy, 2,2'-bipyridine; dpp, 2,3-bis(2-pyridyl)pyrazine)

demonstrates the trimetallic supramolecular assemblies, LA–BL–RhX₂–BL–LA LA, as efficient LAs throughout the UV and visible regions of the spectrum with transitions characteristic of each subunit of the LA–BL unit. The electronic absorption spectra of $\{(\text{bpy})_2\text{Ru}(\text{dpp})\}_2\text{RhX}_2\}^{5+}$ (X, Cl or Br) and $\{(\text{phen})_2\text{Ru}(\text{dpp})\}_2\text{RhCl}_2\}^{5+}$ are similar, exhibiting intense π → π* TL and dpp transitions in the UV, Ru(dπ) → TL(π*) (TL, bpy or phen) CT transitions between 410 and 420 nm, and Ru(dπ) → dpp(π*) CT transitions at $\lambda_{\text{max}}^{\text{abs}} = 520$ nm ($\epsilon = 2.6 \times 10^4 \text{ M}^{-1} \text{ cm}^{-1}$).^{42,50,59} For comparison, the lowest energy Ru(dπ) → dpp(π*) CT transition for $\{(\text{bpy})_2\text{Ru}\}_2\text{(dpp)}^{4+}$ and $\{(\text{phen})_2\text{Ru}\}_2\text{(dpp)}^{4+}$, which lack a rhodium acceptor, occurs at $\lambda_{\text{max}}^{\text{abs}} = 526$ nm.⁵¹ The electronic absorption spectrum of $\{(\text{bpy})_2\text{Ru}(\text{dpp})\}_2\text{RhCl}_2\}^{5+}$ is shown in Figure 15 and can be used as a representative spectrum for systems having this structural motif. The variation of the halide from Cl⁻ to Br⁻ does not significantly impact the optical properties as evidenced by the nearly identical electronic absorption spectra of $\{(\text{bpy})_2\text{Ru}(\text{dpp})\}_2\text{RhCl}_2\}^{5+}$ and $\{(\text{bpy})_2\text{Ru}(\text{dpp})\}_2\text{RhBr}_2\}^{5+}$. The electronic absorption spectra for the tpy-based systems are similar to the bpy analogs, showing changes consistent with the decreased HOMO–LUMO gap with the Ru(dπ) → dpp(π*) CT transitions at $\lambda_{\text{max}}^{\text{abs}} = 540$ nm.⁴² For the osmium analogs, $\{(\text{bpy})_2\text{Os}(\text{dpp})\}_2\text{RhCl}_2\}^{5+}$ and $\{(\text{tpy})\text{OsCl}(\text{dpp})\}_2\text{RhCl}_2\}^{3+}$, the Os(dπ) → dpp(π*) CT transitions occur at slightly lower energies relative to the ruthenium-based systems, consistent with the destabilized Os(dπ) orbitals that provide a decreased HOMO–LUMO gap. A unique feature in the electronic absorption spectra of the osmium-based systems is the intense ³MLCT absorption in the low-energy region. The enhanced spin–orbit coupling in osmium-based systems provides for enhanced intensity of the ³MLCT absorption.

2.10.3 Rhodium-Based Supramolecular Photocatalysts: Photophysics

Many of the rhodium-based supramolecular photoinitiated ECs display observable emissions at RT, allowing

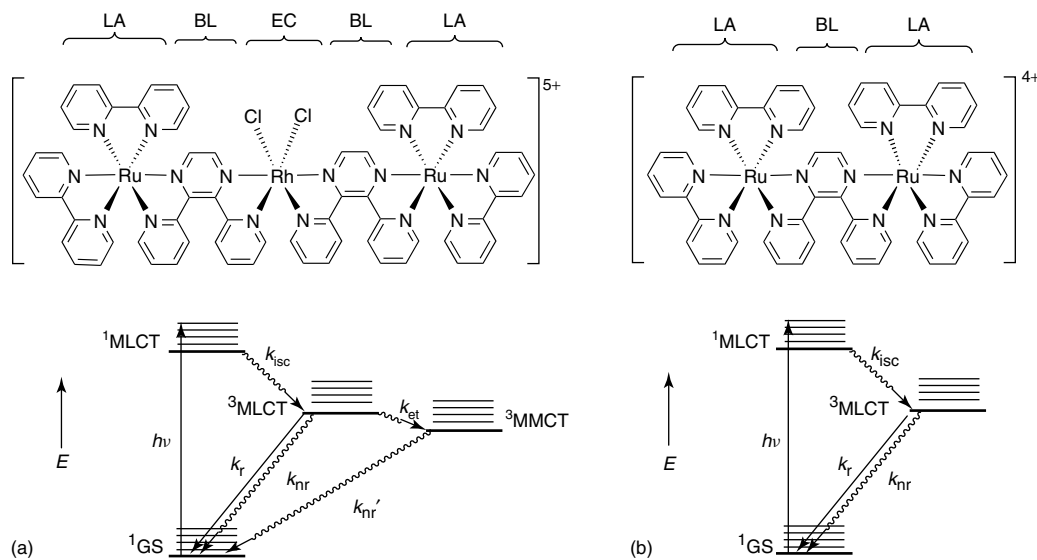


Figure 16 State diagrams for $\{[(\text{bpy})_2\text{Ru}(\text{dpp})_2\text{RhX}_2]\}^{5+}$ (X, Cl^- or Br^-) and $\{[(\text{phen})_2\text{Ru}(\text{dpp})_2\text{RhCl}_2]\}^{5+}$ (a) and $\{[(\text{bpy})_2\text{Ru}]_2(\text{dpp})\}^{4+}$ (b) (bpy , 2,2'-bipyridine; dpp , 2,3-bis(2-pyridyl)pyrazine)

the study of the excited state dynamics. The optically excited $^1\text{MLCT}$ state populates a $^3\text{MLCT}$ state that is quenched by intramolecular electron transfer to populate a low lying $^3\text{MMCT}$ state (Figure 16). The complexes $\{[(\text{bpy})_2\text{Ru}(\text{dpp})_2\text{RhCl}_2]\}^{5+}$, $\{[(\text{bpy})_2\text{Ru}(\text{dpp})_2\text{RhBr}_2]\}^{5+}$, and $\{[(\text{phen})_2\text{Ru}(\text{dpp})_2\text{RhCl}_2]\}^{5+}$ display weak emissions from the $\text{Ru}(\text{d}\pi) \rightarrow \text{dpp}(\pi^*)$ $^3\text{MLCT}$ state at $\lambda_{\max}^{\text{em}} = 760 \text{ nm}$ for $\{[(\text{bpy})_2\text{Ru}(\text{dpp})_2\text{RhCl}_2]\}^{5+}$ and $\{[(\text{bpy})_2\text{Ru}(\text{dpp})_2\text{RhBr}_2]\}^{5+}$ and $\lambda_{\max}^{\text{em}} = 746 \text{ nm}$ for $\{[(\text{phen})_2\text{Ru}(\text{dpp})_2\text{RhCl}_2]\}^{5+}$ with $\Phi^{\text{em}} = 7.3 \times 10^{-5}$, 1.5×10^{-4} , and 1.8×10^{-4} , respectively, at RT in deoxygenated acetonitrile solutions following excitation at 520 nm .^{42,50} The emission from the $^3\text{MLCT}$ state is ca. 10–15% as intense as $\{[(\text{bpy})_2\text{Ru}]_2(\text{dpp})\}^{4+}$ ($\lambda_{\max}^{\text{em}} = 744 \text{ nm}$, $\Phi^{\text{em}} = 1.38 \times 10^{-3}$) used as a model complex to evaluate the rate of electron transfer (k_{et}) to populate the $^3\text{MMCT}$ state. The similarities of the nature ($\text{Ru}(\text{d}\pi) \rightarrow \text{dpp}(\pi^*)$ CT) and energies of the $^1\text{MLCT}$ state and the $^3\text{MLCT}$ state between $\{[(\text{bpy})_2\text{Ru}]_2(\text{dpp})\}^{4+}$ and the trimetallic systems make $\{[(\text{bpy})_2\text{Ru}]_2(\text{dpp})\}^{4+}$ an acceptable model for these studies. The state diagrams for $\{[(\text{bpy})_2\text{Ru}(\text{dpp})_2\text{RhCl}_2]\}^{5+}$ (a) and $\{[(\text{bpy})_2\text{Ru}]_2(\text{dpp})\}^{4+}$ (b) are shown in Figure 16. The τ of the $^3\text{MLCT}$ state was determined on a nanosecond timescale by monitoring the emission decay profile after excitation with a pulsed nitrogen excited dye laser. The excited state lifetimes of the $^3\text{MLCT}$ state in deoxygenated acetonitrile solution at RT for $\{[(\text{bpy})_2\text{Ru}(\text{dpp})_2\text{RhCl}_2]\}^{5+}$, $\{[(\text{bpy})_2\text{Ru}(\text{dpp})_2\text{RhBr}_2]\}^{5+}$, and $\{[(\text{phen})_2\text{Ru}(\text{dpp})_2\text{RhCl}_2]\}^{5+}$ are 32, 26, and 27 ns, respectively,^{42,50} reduced relative to the τ of $\{[(\text{bpy})_2\text{Ru}]_2(\text{dpp})\}^{4+}$, 140 ns.⁵¹ The k_{et} to populate the $^3\text{MMCT}$ states, estimated by assuming k_r and k_{nr} of the trimetallic systems to be similar to $\{[(\text{bpy})_2\text{Ru}]_2(\text{dpp})\}^{4+}$, is comparable with $k_{\text{et}} = 1.2 \times 10^8 \text{ s}^{-1}$, $5.2 \times 10^7 \text{ s}^{-1}$, and $4.4 \times 10^7 \text{ s}^{-1}$

for $\{[(\text{bpy})_2\text{Ru}(\text{dpp})_2\text{RhCl}_2]\}^{5+}$, $\{[(\text{bpy})_2\text{Ru}(\text{dpp})_2\text{RhBr}_2]\}^{5+}$, and $\{[(\text{phen})_2\text{Ru}(\text{dpp})_2\text{RhCl}_2]\}^{5+}$, respectively. The other trimetallic systems do not display an observable emission, which was anticipated due to the significantly lower energy of the $^3\text{MLCT}$ states arising from the decreased HOMO–LUMO gap.

2.10.4 Rhodium-Based Supramolecular Photocatalysts: Photochemical Production of H_2

Supramolecular complexes of the general form LA–BL–RhX₂–BL–LA have been evaluated as photoinitiated ECs.^{42,50} Spectroelectrochemical and photolysis experiments were used to investigate PEC in this structural motif. Electrochemical reduction of $\{[(\text{bpy})_2\text{Ru}(\text{dpp})_2\text{RhCl}_2]\}^{5+}$ by two electrons just past the $\text{Rh}^{\text{III}/\text{II}/\text{I}}$ couple leads to a spectroscopic shift with the $\text{Ru}(\text{d}\pi) \rightarrow \text{dpp}(\pi^*)$ CT shifting to higher energy. The formation of an electron-rich Rh^{I} species, $\{[(\text{bpy})_2\text{Ru}(\text{dpp})_2\text{Rh}^{\text{I}}]\}^{5+}$, destabilizes the $\text{dpp}(\pi^*)$ orbitals, shifting the $\text{Ru}(\text{d}\pi) \rightarrow \text{dpp}(\pi^*)$ to higher energy. Photolysis of $\{[(\text{bpy})_2\text{Ru}(\text{dpp})_2\text{RhCl}_2]\}^{5+}$ at 520 nm in the presence of DMA leads to similar spectroscopic changes, suggesting the formation of the same reduced species, $\{[(\text{bpy})_2\text{Ru}(\text{dpp})_2\text{Rh}^{\text{I}}]\}^{5+}$. This photolysis study combined with the spectroelectrochemical study established $\{[(\text{bpy})_2\text{Ru}(\text{dpp})_2\text{RhCl}_2]\}^{5+}$ as a photoinitiated EC.⁵⁹ Photoreduction of $\{[(\text{bpy})_2\text{Ru}(\text{dpp})_2\text{RhBr}_2]\}^{5+}$ or $\{[(\text{phen})_2\text{Ru}(\text{dpp})_2\text{RhCl}_2]\}^{5+}$ in the presence of DMA affords spectroscopic shifts consistent with the formation of $\{[(\text{TL})_2\text{Ru}(\text{dpp})_2\text{Rh}^{\text{I}}]\}^{5+}$ (TL, bpy or phen), establishing them as photoinitiated ECs.⁴² The reduced $\{[(\text{bpy})_2\text{Ru}(\text{dpp})_2\text{Rh}^{\text{I}}]\}^{5+}$ species is formed by the excited

trimetallic molecule using a sacrificial ED and passes through an intermediate Rh^{II} species. Reductive quenching of both the ³MLCT and ³MMCT states to form [{(bpy)₂Ru(dpp)}₂Rh^I]⁵⁺ is potentially feasible. A Stern–Volmer kinetic investigation on emission quenching as well as product formation was performed to probe the photoreduction mechanism of [{(bpy)₂Ru(dpp)}₂RhCl₂]⁵⁺ in the presence of DMA. For simplification purposes, only the initial photochemical steps leading to the singly reduced Rh^{II} species were considered for the kinetic investigation.⁵⁰ The rate of reductive quenching to generate the Rh^{II} species from the ³MLCT excited state was found to be $1.9 \times 10^9 \text{ M}^{-1} \text{ s}^{-1}$. A Stern–Volmer quenching analysis showed the ³MLCT excited state to be efficiently quenched by DMA, $k_q = 2 \times 10^{10} \text{ M}^{-1} \text{ s}^{-1}$. The excited state reduction potentials of the ³MLCT and ³MMCT excited states of the trimetallic complexes were estimated using equation (9). The E^{0-0} was estimated using the emission energy. The estimated excited state reduction potentials of the ³MLCT and ³MMCT states for [{(bpy)₂Ru(dpp)}₂RhCl₂]⁵⁺ are 1.23 and 0.84 V vs SCE, respectively. On the basis of these potentials and the oxidation potential of DMA, $E_{1/2} = 0.81$ V vs SCE, the driving force for reductive quenching can be calculated using equation (7). The positive driving forces predict that DMA can reductively quench both the ³MLCT and ³MMCT excited states. The excited state reduction potentials of the ³MLCT and ³MMCT states for [{(bpy)₂Ru(dpp)}₂RhBr₂]⁵⁺ and [{(phen)₂Ru(dpp)}₂RhCl₂]⁵⁺ are also similar to [{(bpy)₂Ru(dpp)}₂RhCl₂]⁵⁺, predicting similar driving forces for reductive quenching of the excited states by DMA.

The trimetallic complexes [{(bpy)₂Ru(dpp)}₂RhCl₂]⁵⁺, [{(bpy)₂Ru(dpp)}₂RhBr₂]⁵⁺, [{(phen)₂Ru(dpp)}₂RhCl₂]⁵⁺, [{(bpy)₂Os(dpp)}₂RhCl₂]⁵⁺, [{(tpy)RuCl(dpp)}₂RhCl₂]³⁺, and [{(tpy)OsCl(dpp)}₂RhCl₂]³⁺, and the first photoinitiated EC [{(bpy)₂Ru(dp^b)₂IrCl₂}]⁵⁺ were evaluated with respect to their functioning as hydrogen photocatalysts in the presence of water and an ED.⁴² All complexes demonstrate photocatalytic activity with the exceptions of [{(bpy)₂Ru(dp^b)₂IrCl₂}]⁵⁺ and [{(tpy)OsCl(dpp)}₂RhCl₂]³⁺. The functioning systems possess a rhodium-localized LUMO for electron collection and a ³MLCT and/or ³MMCT states/state with sufficient driving forces for excited state reduction by the ED. The photochemistry of [{(bpy)₂Ru(dpp)}₂RhCl₂]⁵⁺, [{(bpy)₂Ru(dpp)}₂RhBr₂]⁵⁺, or [{(phen)₂Ru(dpp)}₂RhCl₂]⁵⁺ in the presence of DMA suggests the formation [{(TL)₂Ru(dpp)}₂Rh^I]⁵⁺ (TL, bpy or phen) following halide loss. The Rh^I coordination geometry is d⁸, square planar, and coordinately unsaturated, making it reactive and susceptible to interaction with substrates such as water. Photolysis of acetonitrile solutions of [{(bpy)₂Ru(dpp)}₂RhX₂]⁵⁺ (X, Cl⁻ or Br⁻) or [{(phen)₂Ru(dpp)}₂RhCl₂]⁵⁺ in the presence of DMA and water at $\lambda = 470$ nm leads to water reduction to produce hydrogen with $\Phi = 0.01$ with ca. 30–38 turnovers in 4 h.^{50,59,64} Comparatively higher hydrogen yields are obtained for [{(bpy)₂Ru(dpp)}₂RhBr₂]⁵⁺, implying that the

type of halide on the rhodium impacts the photochemistry. The increased ease of Br⁻ loss due to its weaker ligating ability may account for the enhanced photocatalytic activity of [{(bpy)₂Ru(dpp)}₂RhBr₂]⁵⁺. The complexes [{(bpy)₂Os(dpp)}₂RhCl₂]⁵⁺ and [{(tpy)RuCl(dpp)}₂RhCl₂]³⁺ yield similar amounts of hydrogen when irradiated at 470 nm in the presence of DMA and water, but with much lower efficiency than [{(bpy)₂Ru(dpp)}₂RhCl₂]⁵⁺. The excited state reduction potentials of the ³MLCT and ³MMCT were predicted to be 0.91 and 0.54 V vs SCE, respectively, for [{(bpy)₂Os(dpp)}₂RhCl₂]⁵⁺ and 1.01 and 0.61 V, respectively, for [{(tpy)RuCl(dpp)}₂RhCl₂]³⁺, making quenching of the ³MMCT excited state by DMA unlikely. The production of hydrogen despite this suggests that the ³MLCT excited state can be quenched by DMA and lead to hydrogen production. The lower driving force for reductive quenching of the ³MLCT and the lower τ may be accountable for the lower photocatalytic efficiency of these complexes. [{(tpy)OsCl(dpp)}₂RhCl₂]³⁺ does not function as a photocatalyst under the conditions investigated. On the basis of the excited state reduction potentials of the ³MLCT and ³MMCT states, 0.71 and 0.37 V vs SCE, respectively, the reductive quenching of both excited states by DMA are thermodynamically unfavorable. This, combined with a short τ may explain the lack of photocatalytic activity of this system. Addition of mercury to the photocatalytic systems does not impair hydrogen production.^{66,67}

The first photoinitiated EC [{(bpy)₂Ru(dp^b)₂IrCl₂}]⁵⁺ that collects electrons on the BL was evaluated as a photocatalyst.⁴² A thermodynamically favorable driving force for reductive quenching of the ³MLCT state by DMA exists for [{(bpy)₂Ru(dp^b)₂IrCl₂}]⁵⁺, as the excited state reduction potential of the ³MLCT is 1.13 V vs SCE. This iridium-based complex is not a photocatalyst under the conditions studied for the other systems. The lack of photocatalytic activity by this system implies that other factors in addition to multi-electron photochemistry and favorable thermodynamics for reductive quenching should be considered in the photochemical scheme. Electron collection on the rhodium center is a key for the photochemical reduction of water to hydrogen.

The impact of the ED on the most efficient photocatalysts [{(bpy)₂Ru(dpp)}₂RhCl₂]⁵⁺, [{(bpy)₂Ru(dpp)}₂RhBr₂]⁵⁺, and [{(phen)₂Ru(dpp)}₂RhCl₂]⁵⁺ was investigated. Photocatalysis is seen using EDs DMA, TEA, and TEOA.⁴² The hydrogen production efficiency varied in the order DMA > TEA > TEOA.⁴² TEOA has a slightly higher driving force for reductive quenching than TEA, but results in lower hydrogen yields. This further supports the notation that factors other than the driving force and multielectron chemistry should be considered in efficient solar hydrogen production schemes. An important factor to be considered is the solution pH. The effective pH values of the photolysis solutions using DMA, TEA, and TEOA were estimated to be ca. 9.1, 14.7, and 11.8, respectively, on the assumption that the pK_a values of their conjugated acids remain

unchanged in the photocatalytic solutions relative to aqueous conditions ($pK_a = 5.07$ (DMAH $^+$), 10.75 (TEAH $^+$), and 7.76 (TEOA $^+$)).⁶⁸ It is known that water reduction is pH dependent and energetically more feasible at lower pH. Thus, the lower catalyst function when TEOA is the ED may be attributed to the higher effective pH of the solution rendering water reduction energetically more difficult. In addition, the ability of DMA to form donor-chromophore π -stacking interactions may be advantageous for more efficient reductive quenching of the excited states, affording the highest hydrogen yields compared to that of the aliphatic EDs.

Photochemical properties of $[(bpy)_2Ru(dpp)]_2RhBr_2]Br_5$ in aqueous medium have been investigated.⁶⁹ Studies have established this complex to function as a photoinitiated EC in water, the first system shown to display this function in aqueous medium. $[(bpy)_2Ru(dpp)]_2RhBr_2]Br_5$ functions as a photocatalyst for the production of hydrogen in the presence of TEOA with added triflic acid, hydrobromic acid, or phosphoric acid. The photocatalytic efficiency is lower in the aqueous medium possibly because of the lower lifetimes of the excited states of ruthenium polyazine chromophores in water and additional quenching mechanisms.

2.11 Osmium, Rhodium Supramolecular Photocatalysts for the Production of H₂

Nishibayashi and coworkers have used diphosphine ligands attached to an $[Os(tpy)_2]^{2+}$ moiety to coordinate a rhodium center (Figure 17) and used this system for photochemical hydrogen production.⁴³ Their approach allows the use of a $Os(tpy)_2$ -based chromophore in photocatalytic schemes. The OsRh diad has been synthesized and analyzed in situ by treatment of the osmium-based chromophore with $[RhCl(CO)_2]_2$. The electrochemistry displays a reversible $Os^{II/III}$ couple at 0.92 V vs SCE and $tpy^{0/-}$ reductions at -1.11 and -1.34 V vs SCE.⁴³ The dyad absorbs in the UV and visible regions of the spectrum, displaying 1MLCT and 3MLCT absorptions at 482 and 655 nm, respectively.⁴³ An emission is observed at 728 nm ($\Phi^{em} = 0.52$ in an acetonitrile/water mixture) with reduced intensity than the parent chromophore ($\Phi^{em} = 0.73$ in an acetonitrile/water mixture).⁴³ Irradiation of catalytic amounts of the dyad generated in situ at $\lambda > 380$ nm

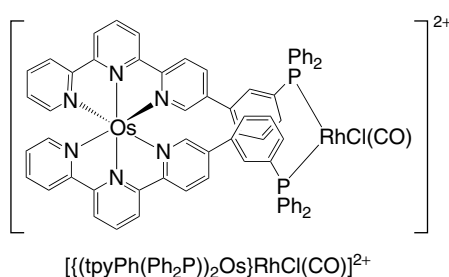


Figure 17 OsRh dyad systems for solar hydrogen production

in a trifluoromethanesulfonic acid/sodium ascorbate mixture at pH = 5.2 for 18 h affords hydrogen with 36 turnovers. The use of $RhCl_3$ instead of $[RhCl(CO)_2]_2$ yielded 87 turnovers with $\Phi = 0.007$. It is suggested that intramolecular electron transfer to rhodium upon optical excitation by two electrons leads to a reduced rhodium that can react with a proton to form a rhodium hydride, which generates hydrogen.

2.12 Platinum- and Palladium-Based Supramolecular Photocatalysts

Systems that couple polyazine LAs to reactive Pt or Pd CATs that photocatalyze water reduction are known.^{9,12,44,47,70,71} The use of a supramolecular design allows component modification to enhance device function and light-absorbing properties. The systems use rigid and flexible spacer between the chromophore and the CAT. Follow-up studies in other laboratories suggest that colloids may be produced by these systems as discussed below.^{45,72}

2.12.1 Ruthenium–Platinum-Based Supramolecular Photocatalysts

Sakai and coworkers reported an Ru–Pt bimetallic system, $[(bpy)_2Ru(phenNHCO(COOHbpy))PtCl_2]^{2+}$, in which the platinum component is linked to the ruthenium LA through an amide linkage on the phenanthroline ligand (Figure 18).⁴⁷ This complex is capable of producing hydrogen from water in the presence of the ED, EDTA, with a $\Phi = 0.01$ and 5 turnovers in 10 h when illuminated at $\lambda > 350$ nm. The bimetallic complex is a good LA and displays typical ligand $\pi \rightarrow \pi^*$ transitions in the UV region and MLCT transitions in the visible region of the solar spectrum. The light-absorbing properties are very similar to the parent monometallic synthon, $[(bpy)_2Ru(phenNHCO(COOHbpy))]^{2+}$. The lowest energy transition occurs at ca. 450 nm in water in the monometallic and bimetallic systems. $[(bpy)_2Ru(phenNHCO(COOHbpy))PtCl_2]^{2+}$ displays an emission from the 3MLCT state at $\lambda_{max}^{em} = 610$ nm in an aqueous solution with its intensity quenched by 67% relative to the parent $[(bpy)_2Ru(phenNHCO(COOHbpy))]^{2+}$. Emission quenching is suggestive of some intramolecular electron transfer process occurring in $[(bpy)_2Ru(phenNHCO(COOHbpy))PtCl_2]^{2+}$.⁴⁷ For comparison, photolysis of a mixture of precursor molecules, which consists of $[PtCl_2((COOH)_2bpy)]$ and $[Ru(bpy)_3]^{2+}$, under the same conditions does not lead to hydrogen production, demonstrating that an intramolecular electron transfer step is important in the photochemical hydrogen production scheme. Since the initial finding, other Ru–Pt systems, $[(bpy)_2Ru(bpy)(CONH(CH_2)_3NH_2)_2]PtCl_2]^{2+}$ and $[(bpy)_2Ru(bpy)(CONH(CH_2)bpy)_2]PtCl_2]^{2+}$ (py, pyridyl; Figure 19), having similar structural motifs have been reported by this group.⁷¹ These systems incorporate aliphatic linkages to connect the chromophore to the CAT.

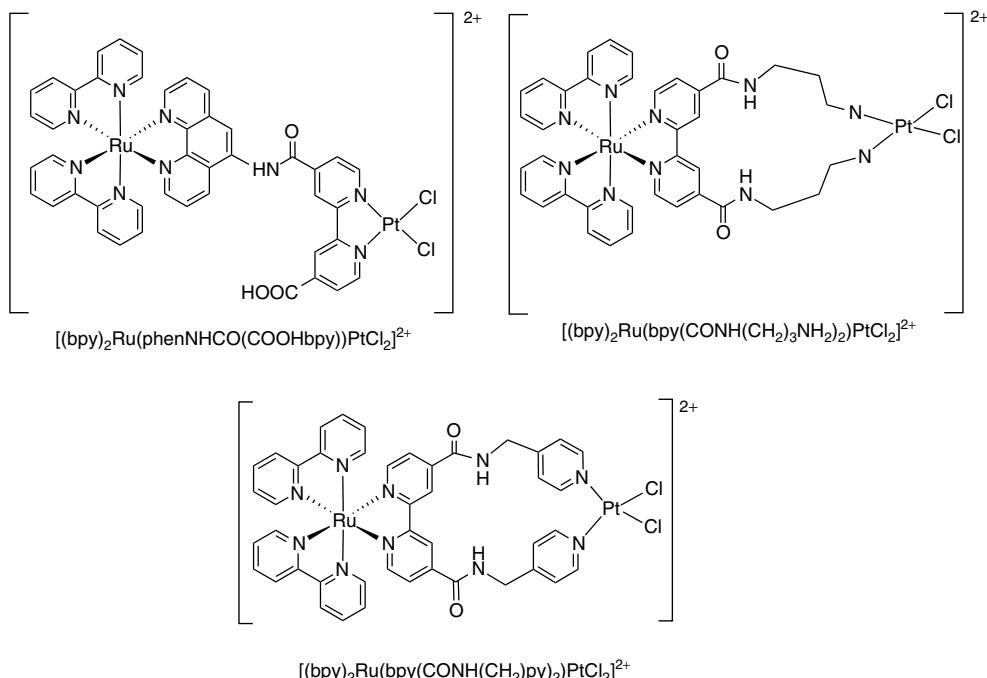


Figure 18 RuPt supramolecular systems for solar energy conversion (bpy, 2,2'-bipyridine)

Interestingly, these systems do not display photocatalytic activity. This implies that aromaticity of the bridge connecting the chromophore and the CAT is important in $[(bpy)_2Ru(phenNHCO(COOHbpy))PtCl_2]^{2+}$.

2.12.2 Ruthenium–Palladium-Based Supramolecular Photocatalysts

Rau and coworkers reported a Ru–Pd bimetallic system $[(^t\text{Bu}_2\text{bpy})_2\text{Ru}(\text{tpphz})\text{PdCl}_2]^{2+}$ (^tBu , tertiary butyl; tpphz, tetrapyridophenazine; Figure 19) that photochemically produces hydrogen, with turnover number = 56, in the presence of the ED, TEA, in acetonitrile when optically excited

at $\lambda = 470\text{ nm}$.⁴⁴ TEA also acts as the proton source in this system. The tpphz connects the LA and a catalytically active Pd through a conjugated reducible π -electron system. Electrochemically, $[(^t\text{Bu}_2\text{bpy})_2\text{Ru}(\text{tpphz})\text{PdCl}_2]^{2+}$ displays a reversible phenazine-based reduction at -0.63 V vs SCE, an irreversible Pd(II) reduction at -0.82 V vs SCE, and reversible bpy-based reductions between -1.09 and -1.43 V vs SCE. The phenazine-based reduction occurs at a slightly less negative potential in $[(^t\text{Bu}_2\text{bpy})_2\text{Ru}(\text{tpphz})\text{PdCl}_2]^{2+}$ relative to $[(^t\text{Bu}_2\text{bpy})_2\text{Ru}(\text{tpphz})]^{2+}$, consistent with the stabilization of the tpphz(π^*) orbitals upon palladium coordination. $[(^t\text{Bu}_2\text{bpy})_2\text{Ru}(\text{tpphz})\text{PdCl}_2]^{2+}$ displays the typical ligand-based transitions in the UV region and MLCT transitions in the visible regions in the electronic absorption spectrum with the lowest energy MLCT transition at $\lambda_{\max}^{\text{abs}} = 445\text{ nm}$ in acetonitrile. A weak emission at $\lambda_{\max}^{\text{em}} = 650\text{ nm}$ with $\tau = 27\text{ ns}$ that is significantly quenched relative to the parent $[(^t\text{Bu}_2\text{bpy})_2\text{Ru}(\text{tpphz})]^{2+}$ ($\lambda_{\max}^{\text{em}} = 638\text{ nm}$, $\tau = 154\text{ ns}$) is observed in an air-saturated acetonitrile solution. The authors assume that the Ru^{II}–phenazine[–]–Pd^{II} radical that is photogenerated in the presence of TEA is involved in the photochemical hydrogen generation step. This species initiates chloride loss from palladium and intramolecular electron transfer to Pd^{II} to generate a Pd⁰. It is assumed that the palladium center acts as an electron storage site as well as a CAT, leading to photochemical proton reduction to produce hydrogen. The photoinduced electron transfer processes have been verified by resonance Raman and ultrafast time-resolved spectroscopy.⁷³

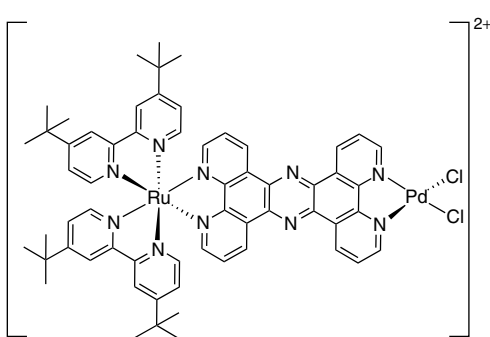


Figure 19 Representation of $[(^t\text{Bu}_2\text{bpy})_2\text{Ru}(\text{tpphz})\text{PdCl}_2]^{2+}$ (^tBu , tertiary butyl; bpy, 2,2'-bipyridine; tpphz, tetrapyridophenazine)

2.12.3 Mechanistic Studies of Platinum- and Palladium-Based Supramolecular Photocatalysts

Recent studies by Eisenberg and coworkers⁷² and Hammarström and coworkers⁴⁵ have shown that metal decomplexation of similar systems incorporating reactive metals generates metal colloids, which act as the hydrogen generation catalysts. Their studies imply that in some of the systems discussed, the active catalytic species may be colloidal metal that is formed by decomplexation of the CAT. Hammarström and coworkers have studied the stability, redox properties, and spectroscopic properties of $[(bpy)_2Ru(Mebpy(CH_2)_2C_6H_2(OCH_3)_2(CH_2)_2Mebpy)PdCl_2]^{2+}$ (Figure 20).⁴⁵ The oxidative electrochemistry displays an Ru^{II/III} oxidation, 1.27 V vs SCE, followed by an irreversible oxidation attributed to the BL^{0/+}, 1.46 V vs SCE. The reductive electrochemistry displays an irreversible reduction attributed to Pd^{II} reduction at -0.92 V vs SCE. The electronic absorption spectrum revealed the typical absorptions observed for ruthenium polyazine complexes with the lowest energy MLCT transition at $\lambda_{max}^{abs} = 455$ in acetonitrile. In the presence of TEA, $[(bpy)_2Ru(Mebpy(CH_2)_2C_6H_2(OCH_3)_2(CH_2)_2Mebpy)PdCl_2]^{2+}$ photocatalyzes proton reduction to produce hydrogen. A control experiment using the LAs $[(bpy)_2Ru(Mebpy(CH_2)_2C_6H_2(OCH_3)_2(CH_2)_2Mebpy)]^{2+}$ or $[Ru(bpy)_3]^{2+}$ in the presence of $[Pd(Me_2bpy)Cl_2]$ and TEA also afforded comparable amounts of hydrogen to the dyad, suggesting that hydrogen production may not be an intramolecular process in $[(bpy)_2Ru(Mebpy(CH_2)_2C_6H_2(OCH_3)_2(CH_2)_2Mebpy)PdCl_2]^{2+}$. XPS and TEM measurements of the evaporated reaction mixture revealed colloidal palladium, which suggested that decomplexation of $[(bpy)_2Ru(Mebpy(CH_2)_2C_6H_2(OCH_3)_2(CH_2)_2Mebpy)PdCl_2]^{2+}$ afforded metallic palladium, which is the catalytically active species for proton reduction.⁴⁵ The impact of concentration on the reaction solution or resulting reactions upon evaporation on a surface are not discussed. A Hg test has been proposed as a means of eliminating factors arising from colloidal particles. Hg can extract colloidal particles from the reaction medium via formation of an inactive alloy to eliminate the impact of the colloid on photochemical activity.^{66,67} Reduced polyazine complexes are sometimes known to adsorb on electrodes or metal surfaces. The formation of potentially more efficient catalytically active colloidal particles should be considered in these systems, but it is a complicated issue to address. Care must be taken when analyzing reaction mixtures through solvent evaporation and/or the Hg test. Evaporation of solvents to study solids may alter the system, leading to decomplexation resulting in metallic solids. In addition to colloids, mercury is also known to adsorb many electrochemically reduced metal complexes including ruthenium polyazine complexes.⁵ These important studies by Eisenberg and coworkers⁷² and Hammarström and coworkers⁴⁵ point out the complexity of studying multistep photocatalytic processes and the need for detailed and careful analysis of the results of such studies.

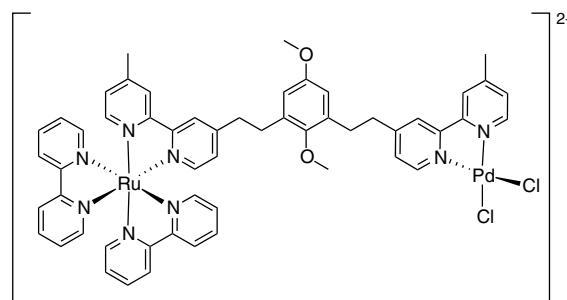


Figure 20 Representation of $[(bpy)_2Ru(Mebpy(CH_2)_2C_6H_2(OCH_3)_2(CH_2)_2Mebpy)PdCl_2]^{2+}$ (bpy, 2,2'-bipyridine)

2.12.4 Platinum-Based Single-Component Systems for Photocatalytic Production of H_2

Sakai and coworkers recently described the use of $[PtCl(tpy)]Cl$ as a single-component photocatalyst for hydrogen production from water.⁷⁴ Although this system deviates from the “conventional” supramolecular systems, it functions in a bifunctional manner, promoting both photosensitization and hydrogen production. Photolysis of this system using light of wavelength between 350 and 550 nm in the presence of EDTA and water affords 3 turnovers over 7 h with a $\Phi = 0.02$. It is suggested that photochemical hydrogen production proceeds through a bimolecular mechanism. Photosensitization process is thought to occur through a 3MMLCT state (MMLCT, metal–metal-to-ligand charge transfer) facilitated by Pt···Pt interactions in assembled dimers of this complex and/or photoproducts.

2.12.5 Tetrametallic Ruthenium–Platinum Supramolecular Photocatalysts for H_2 Production

Brewer and coworkers have investigated the redox, photophysical, and photochemical properties of $\{[(bpy)_2Ru(dpp)\}_2Ru(dpq)PtCl_2\}^{6+}$ and related systems as photoinitiated ECs (dpq, 2,3-bis(2-pyridyl)quinoxaline), which photocatalyze the production of hydrogen from water with $\Phi = 0.01$.^{46,75} These systems couple two-terminal $(bpy)_2Ru^{II}(dpp)$ LA units to a central ruthenium that is connected to a reactive platinum component through a dpq bridge (Figure 21).

The redox properties of $\{[(bpy)_2Ru(dpp)\}_2Ru(dpq)PtCl_2\}^{6+}$ are dictated by subunit components. A reversible oxidative couple that represents overlapping terminal Ru^{II/III} processes is observed at 1.56 V vs SCE, indicating minimal electronic interaction between the terminal LA units. The first reduction at -0.12 V vs SCE is indicative of a $\mu\text{-}dpq^{0/-}$ couple, consistent with the stabilized $dpq(\pi^*)$ orbital when coordinated to Ru^{II} and Pt^{II}. The $dpq^{0/-}$ couple is followed by two dpp^{0/-} reductions at -0.49 and -0.66 V vs SCE. The electrochemical properties predict a low-energy charge-separated (CS) state with an

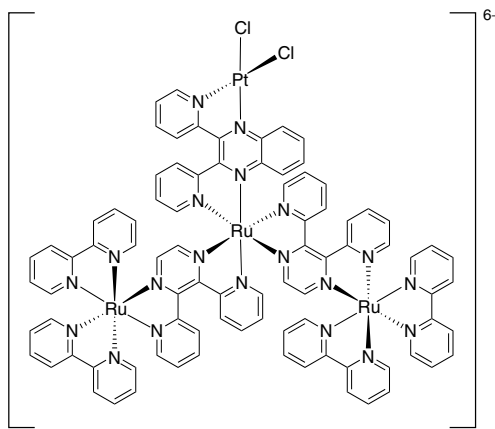


Figure 21 Representation of $[{(bpy)_2Ru(dpp)}_2Ru(dpq)PtCl_2]^{6+}$ (bpy, 2,2'-bipyridine; dpp, 2,3-bis(2-pyridyl)pyrazine; dpq, 2,3-bis(2-pyridyl)quinoxaline)

oxidized terminal ruthenium center and a reduced dpq ligand that are spatially separated. The electrochemical properties suggest an Ru($d\pi$)-based HOMO and a dpq(π^*)-based LUMO in this structural motif. For comparison, the electrochemistry of the trimetallic system that lacks the reactive platinum component, $[{(bpy)_2Ru(dpp)}_2Ru(dpq)]^{6+}$, indicates a Ru($d\pi$)-based HOMO and a dpq(π^*)-based LUMO with the $dpq^{0/-}$ couple occurring at -0.86 V vs SCE. Upon reduction of $[{(bpy)_2Ru(dpp)}_2Ru(dpq)PtCl_2]^{6+}$, an electron is localized on a dpq ligand bound to platinum, allowing facile electron transfer to substrates.

The tetrametallic complex, $[{(bpy)_2Ru(dpp)}_2Ru(dpq)PtCl_2]^{6+}$, is a potent LA displaying ligand-based $\pi \rightarrow \pi^*$ transitions in the UV region and Ru($d\pi$) \rightarrow BL(π^*) CT transitions in the visible region of the spectrum.⁴⁶ The spectral profiles of the tetrametallic and trimetallic systems are very similar, with the Ru($d\pi$) \rightarrow bpy(π^*) CT transitions at 416 nm and Ru($d\pi$) \rightarrow μ -dpp(π^*) and Ru($d\pi$) \rightarrow μ -dpq(π^*) CT transitions at ca. 500–580 nm ($\varepsilon = 3.3 \times 10^4$ M $^{-1}$ cm $^{-1}$ for the $\lambda_{\max}^{\text{abs}} = 540$ nm). The tetrametallic system, $[{(bpy)_2Ru(dpp)}_2Ru(dpq)PtCl_2]^{6+}$, displays an emission from the $^3\text{MLCT}$ state $\lambda_{\max}^{\text{em}} = 745$ nm and $\Phi^{\text{em}} = 2.5 \times 10^{-4}$ with reduced intensity relative to $[{(bpy)_2Ru(dpp)}_2Ru(dpq)]^{6+}$ ($\lambda_{\max}^{\text{em}} = 745$ nm and $\Phi^{\text{em}} = 6.0 \times 10^{-4}$) in acetonitrile. The τ of $[{(bpy)_2Ru(dpp)}_2Ru(dpq)PtCl_2]^{6+}$ is 92 ns, which is reduced relative to that of $[{(bpy)_2Ru(dpp)}_2Ru(dpq)]^{6+}$, 133 ns. The reductions in the Φ^{em} and τ are characteristic of intramolecular electron transfer in $[{(bpy)_2Ru(dpp)}_2Ru(dpq)PtCl_2]^{6+}$, populating the lowest energy CS state with $k_{\text{et}} = 3.4 \times 10^6$ s $^{-1}$ (see Figure 22 for the state diagram). Intramolecular electron transfer is hindered at 77 K in a solid glass matrix with $\tau = 1.7$ K in both tetrametallic and trimetallic systems. The emission of $[{(bpy)_2Ru(dpp)}_2Ru(dpq)PtCl_2]^{6+}$ is quenched efficiently by DMA with k_q of 5.4×10^9 M $^{-1}$ s $^{-1}$.

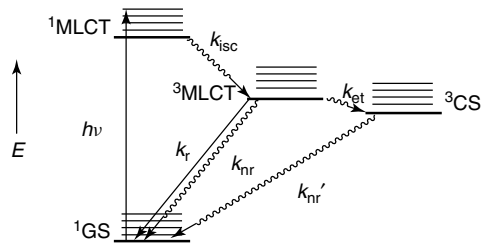


Figure 22 Representative state diagram for ruthenium polyazine complexes of the type $[{(bpy)_2Ru(dpp)}_2Ru(dpq)PtCl_2]^{6+}$ (GS, ground state; MLCT, metal-to-ligand charge transfer; CS, charge-separated state; k_r , rate constant for radiative decay; k_{nr} , rate constant for nonradiative decay; k_{isc} , rate constant for intersystem crossing; k_{et} , rate constant for electron transfer)

$[{(bpy)_2Ru(dpp)}_2Ru(dpq)PtCl_2]^{6+}$ is a photoinitiated EC with electrons being collected on the molecular orbitals of the central ruthenium and the surrounding BLs. Photochemical reduction of $[{(bpy)_2Ru(dpp)}_2Ru(dpq)PtCl_2]^{6+}$ in the presence of DMA at 530 nm yields spectroscopic shifts mirroring that of the two-electron-reduced product obtained by electrochemical reduction. Photochemical hydrogen production occurs in the presence of DMA and water when photoexcited at $\lambda = 530$ nm with $\Phi = 0.01$, representing 40 turnovers in 3 h. The amount of hydrogen produced by $[{(bpy)_2Ru(dpp)}_2Ru(dpq)PtCl_2]^{6+}$ is much higher than that produced by $[{(bpy)_2Ru(dpp)}_2Ru(dpq)]^{6+}$ and Pt colloid. The Hg test has a little impact on the photocatalytic activity of $[{(bpy)_2Ru(dpp)}_2Ru(dpq)PtCl_2]^{6+}$, while it completely quenches the much less efficient $[{(bpy)_2Ru(dpp)}_2Ru(dpq)]^{6+}$ and Pt colloid system. Interestingly, recent studies have shown that the identity of the BL bound to the central ruthenium and catalytic platinum site is important for photocatalysis. Substitution of dpq with dpp produces much lower hydrogen yields, even though the platinum decomplexed systems, $[{(bpy)_2Ru(dpp)}_2Ru(dpq)]^{6+}$ and $[{(bpy)_2Ru(dpp)}_2Ru(dpp)]^{6+}$, have very similar photophysical properties and the same Ru($d\pi$) \rightarrow μ -dpp(π^*) CT lowest lying $^3\text{MLCT}$ states. The complex $[{(bpy)_2Ru(dpp)}_2Ru(dpq)PtCl_2]^{6+}$ represents one of only a handful of photoinitiated ECs that can reduce water to hydrogen. Studies to understand the impact of component modification to modulate the redox, photophysical, and photochemical properties are in progress.⁷⁵ Studies demonstrate that the redox and excited state properties and photocatalytic activity are modulated by the type of BL connected to the platinum as well as the terminal LAs.

3 CONCLUSIONS

The conversion of solar energy to a transportable fuel remains a challenge and is vital to meeting our

planet's increasing energy needs. The production of hydrogen fuel via solar water splitting is an attractive approach to alternative energy conversion and storage. The amount of energy reaching the Earth's surface from the sun in one hour is sufficient to power our planet for more than a year. Solar energy remains one of the most widely available and environmentally sound sources of energy. Conversion of solar energy to hydrogen fuel is a complicated task involving the separation of charge to generate a potential (even if on a molecular scale), the collection of multiple reducing equivalents to provide for energetically feasible reactions, and the breaking and making of multiple chemical bonds. These processes by themselves are challenging and together require long-term interest and research funding to assemble the fundamental chemical knowledge needed to establish efficient solar hydrogen production schemes. Despite the complexity of these processes, functioning photocatalysts for the reduction of water to produce hydrogen fuel are rapidly emerging with increasing awareness of the need for the development of efficient solar energy conversion processes.

The development of solar energy conversion schemes has focused in a number of arenas, including the direct conversion of light energy to electricity via photovoltaics, the application of biological-based systems to produce biomass that can be used as fuels, and the direct conversion of light energy into chemical energy via molecular photocatalysis to produce transportable fuels. The latter process is typically addressed in two arenas, the conversion of solar energy into electrochemical potentials coupled to catalysts to produce fuels and the conversion of light energy directly to fuels using complex supramolecular assemblies. In this article, we have highlighted the direct conversion of solar energy to the high-energy-content fuel, hydrogen. Hydrogen is an ideal fuel in that it possesses the highest energy content per gram of any nonnuclear fuel and produces only water when it is used as a fuel. The splitting of water using sunlight has been a topic of long-term interest. The work described in this field has been built on basic studies of multicomponent systems that provide the intellectual backdrop for these studies. A few examples of these multicomponent studies are provided to place the context for which the research described has been carried out.

The redox, photophysical, and photochemical properties of supramolecular complexes that couple LAs to reactive metals and are applicable in solar hydrogen production schemes have been discussed. An array of structurally diverse systems is available, and most systems couple ruthenium polyazine LAs to a reactive metal center that is the catalyst. Incorporation of chromophores within the molecular architecture that absorb in the visible region provides systems that can use more of the solar spectrum for the photochemical activity. The application of typical Ru(II) tris(chelate) systems with ligands such as bpy or phen provides for absorption to ca. 450 nm. The addition of polyazine BLs with typically stabilized π^* orbitals provides for longer wavelength excitation often to ca. 550–650 nm. Covalently binding the photosensitizer to the

catalyst allows for efficient intramolecular electron transfer from the LA to the catalytic site. In addition, factors that impact intramolecular electron transfer can be studied and modulated within molecular systems. The ability to modulate the electrochemical and photochemical properties by component modification is an attractive feature of supramolecular chemistry. The study and understanding of the basic chemical and photophysical properties are important in the future engineering of efficient systems for solar water splitting. The application of large molecular systems to this problem allows for the study of these photocatalytic systems using conventional molecular characterization methods, allowing for the ability to probe the processes involved in the photocatalytic process.

Systems that couple polyazine LAs to noble metals including rhodium, platinum, and palladium are known photocatalysts for solar hydrogen production. The use of first row transition metals, including iron and cobalt, as the catalytic site provides means for the design and construction of systems that are proposed as economically viable, although the cost of the system must be counterbalanced by the typically increased stability of second and third row transition metal complexes. Multielectron chemistry is key to efficient solar water splitting. The field of multielectron chemistry is still in its infancy and only a handful of systems that display this important property are available. Supramolecular assemblies that use light to store reducing equivalents afford PMDs that are referred to as *photoinitiated ECs*. A system for PEC must efficiently absorb light and undergo multiple electron transfers to form a stable multielectron-reduced form. The stored electrons could be used for the reduction of a substrate to generate a fuel. The process of PEC typically draws upon the more highly studied process of photoinitiated charge separation or molecular photovoltaics. The coupling of two molecular photovoltaics to one EC can theoretically produce a photoinitiated EC and this approach is attractive as it draws on the extensive research in the field of molecular photovoltaics. Using single molecular photovoltaics that cycle twice to yield PEC is another popular means described in this article. The knowledge base developed previously in the field of molecular photovoltaics is extensively exploited in the area of photocatalysis of water reduction to produce hydrogen.

Rhodium-centered photoinitiated ECs are known to catalyze water reduction to hydrogen. $[(bpy)_2Ru(dpp)]_2RhCl_2]^{5+}$, $[(bpy)_2Ru(dpp)]_2RhBr_2]^{5+}$, and $[(phen)_2Ru(dpp)]_2RhCl_2]^{5+}$ are the lead photocatalysts in this area, demonstrating higher hydrogen yields and turnover capacities. These systems have an Ru or Os($d\pi$)-based HOMO and an Rh($d\sigma^*$)-based LUMO. The spectroscopic and photophysical properties display population of the emissive 3MLCT excited state, followed by intramolecular electron transfer to populate the 3MMCT excited state. Optical excitation in the presence of an ED leads to at least two intramolecular electron transfer steps, affording a coordinatively unsaturated Rh^I species that can interact with and reduce a substrate such as

water. These systems couple two charge-transfer LAs to a single EC. Studies on the design considerations for a functioning system for optical multielectron reduction of water to produce hydrogen have shown that this general structural motif is applicable in solar hydrogen production schemes.

Studies have shown that PEC alone is not sufficient for hydrogen photocatalysis. This is demonstrated by the lack of photocatalytic activity by $\{[(bpy)_2Ru(dpb)\}_2IrCl_2\}^{5+}$, which is also a photoinitiated EC. This highlights the complexity of the water splitting process, involving not only the multielectron reduction of the water substrate but also the breaking and making of covalent bonds. The lack of photocatalytic activity by $\{[(bpy)_2Ru(dpb)\}_2IrCl_2\}^{5+}$ implies that the $^3\text{MMCT}$ state and/or the rhodium metal center are important in the catalyst function. The Ru,Ru-photoinitiated ECs with tatpp and tatpq BLs are effective in collecting reducing equivalents but do not produce hydrogen from water.

The coordination environment on the rhodium center impacts the photocatalytic activity as evidenced by the greater hydrogen yields when weaker σ -donors are present on rhodium, further implying that the reactive rhodium center and/or the $^3\text{MMCT}$ excited state may be important. $\{[(bpy)_2Ru(dpp)\}_2RhBr_2\}^{5+}$ provides a system with a lower lying Rh($d\sigma^*$) acceptor orbital with a larger driving force for intramolecular electron transfer to produce the $^3\text{MMCT}$ state and/or promotes halide loss to generate the Rh 1 system.

Factors such as the driving force for reductive quenching of the excited states by the ED, excited state lifetime of the photocatalyst, effective pH of the solution, and ED–catalyst interactions must also be considered in efficient systems for multielectron catalysis. $\{[(tpy)RuCl(dpp)\}_2RhCl_2\}^{3+}$ and $\{[(bpy)_2Os(dpp)\}_2RhCl_2\}^{5+}$ function as supramolecular photocatalysts but at lower efficiency, consistent with the lower driving force for reductive quenching of the $^3\text{MLCT}$ excited state by DMA. The impact of the pH and the effect of ED–catalyst interactions are evidenced by the variation of the photocatalytic activity with varying EDs and the ability of DMA to provide the best efficiency to the system. Ideally, the oxidizing equivalents formed by the reaction between the ED and the photosensitizer can be used for the water oxidation process leading to oxygen evolution. In this case, water will formally play the role of ED. Studies that address the development of devices capable of overall water splitting to produce hydrogen and oxygen remain an important and open area of research.

The work on the reduction of HX by mixed-valence dirhodium complexes highlights another insightful approach for driving important multielectron processes. These systems utilize ligand design to provide bidentate ligands that simultaneously stabilize low and high oxidation states of the same metal to provide for facile two-electron processes. These systems use a halogen atom trap to facilitate turnover. Systems that undergo more efficient M–X bond activation are investigated as means to enhance hydrogen production efficiency. This mixed-valence chemistry is a unique approach

to multielectron photochemistry that should be applicable with a number of structural motifs.

The coupling of cobalt reactive metals to ruthenium, charge-transfer LAs, is a new area of research. These systems follow up on the promising multicomponent systems in which the ability of cobalt to reduce from Co III to Co II and Co I can facilitate multielectron chemistry. These studies are similar to those of the rhodium-based complexes, exploiting the three easily accessible oxidation states of the reactive metal site and a potentially labile ligand. The often substitutionally labile cobalt centers are stabilized by the use of cobaloximes. These cobaloximes use two bidentate chelating ligands bound to the cobalt site with hydrogen bonding between the two chelates, producing a macrocyclic-like coordination environment. Alternatively, the boron-modified versions of these ligands that close the macrocycle are employed. Either coordination environment appears to provide stability of the cobalt coordination during the redox cycling of this center.

The use of iron-based catalytic sites has been a topic of recent interest as a result of the biologically based systems that exploit the ability of iron-based hydrogenases to catalyze water reduction to produce hydrogen. Interesting biomimetic assemblies have been produced that couple ruthenium to diiron catalytic centers, but these complexes have not shown applicability to solar hydrogen photocatalysis. The diiron systems are electrocatalysts for the reduction of water to hydrogen. The diiron-linked ruthenium supramolecules have redox and photophysical properties, whereby the excited state electron transfer from the ruthenium LA unit to the diiron core is energetically uphill and PEC is not observed in current systems.

The coupling of alternative ZnTPP LA units to these diiron cores has provided for photocatalytic systems. The ZnTPP LA unit possesses a higher energy singlet excited state. These supramolecular assemblies reduce acidic solutions of 2-mercaptopbenzoic acid to produce hydrogen following optical excitation with low turnovers for the diiron site. These systems are intriguing in their use of weak coordination of a pyridine linker for covalent assembly of the diiron, the ZnTPP supramolecular construct that can dissociate following reduction of the diiron center.

Recent studies have focused on the coupling of Pd- and Pt-reactive metal centers to Ru charge-transfer LAs. These systems are generally proposed to function through excitation of the LA unit, followed by electron transfer and quenching by an ED. This process is repeated, yielding the multielectron reduction of the complex. This can then facilitate the reduction of water to produce hydrogen. There have been conflicting reports on these systems with follow-up studies showing that in the RuPt and RuPd systems the reduction of the complex may lead to colloidal Pd or Pt that is an active catalyst for hydrogen generation. These conclusions followed from analysis of evaporated solutions or addition of Hg(l) to produce alloys with Pd(s) or Pt(s) that are formed. The study of the mechanism of photocatalytic reactions can

be a daunting process. In photocatalytic systems of this type producing hydrogen from water in multicomponent systems with multielectron chemistry involved, mechanistic studies are even more complex. Careful analysis of these catalytic systems is needed to provide insight into the function of these photocatalysts and the optimization of future generation of catalysts.

The area of solar hydrogen production through the use of photocatalysts that collect and deliver reducing equivalents is an active area of current research in inorganic photochemistry. The ability to couple multiple components into a large supramolecular assembly with predictable properties that can be exploited is paramount to the success of this endeavor. The fundamental understanding of the perturbations of LA, EC and catalyst properties upon incorporation into complex assemblies is critical to the successful development of efficient and stable photocatalysts for the reduction of water to produce hydrogen fuel. A number of promising systems have been discovered to carry out this complex task. The factors that limit the functioning of these systems can be uncovered through detailed mechanistic studies of these supramolecular photocatalytic systems. Such mechanistic studies are important to the design of more promising molecular architectures that carry out this complicated photocatalytic reaction. The development of commercial systems requires this understanding and optimization. The balance of cost of production and functioning of these photocatalysts is important in the design of the molecular devices that will carry out this chemistry on a large scale to contribute to the availability of renewable, clean energy in future. Key insights have been provided in a relatively short timeframe on the factors that provide for functioning photocatalysts for the production of hydrogen fuel. Sustained and focused research is needed to bring these systems to fruition.

4 GLOSSARY

bpy: 2,2'-Bipyridine

CAT: Catalyst

dmgH: Dimethylglyoximate

dmgBF₂: (Difluoroboryl)dimethylglyoximate

dpgBF₂: (Difluoroboryl)diphenylglyoximate

dpp: 2,3-Bis(2-pyridyl)pyrazine

dpq: 2,3-Bis(2-pyridyl)quinoxaline

dpb: 2,3-Bis(2-pyridyl)benzoquinoxaline

et: Excited state electron transfer

GS: Ground state

I_a: Intensity

ic: Internal conversion

isc: Intersystem crossing

k_x: Rate constant of process "x"

LA: Ground state light absorber

**LA*: Excited state light absorber

Me₂bpy: 4,4'-Dimethyl-2,2'-bipyridine

Me₂phen: 4,7-Dimethylphenanthroline

L-pyr: [(4-Pyridine)oxazolo(4,5-f) phenanthroline]

nr: Nonradiative decay

phen: 1,10-Phenanthroline

ppy: 2-Phenylpyridine

py: Pyridyl

q: Bimolecular deactivation

Q: Quencher

rxn: Photochemical reaction

tpy: 2, 2' : 6', 2''-terpyridine

Φ^{em}: Quantum yield of emission

Φ: Quantum yield

λ_{max}^{abs}: Absorption maximum

λ_{max}^{em}: Emission maximum

5 ACKNOWLEDGMENTS

We acknowledge all the students and research scientists who have worked in this area in the Brewer Group. Our special thanks go to Ms Joan Zapiter, Dr Baburam Sedai, and Mr Travis White for their help with the article. We also acknowledge the Chemical Sciences, Geosciences and Biosciences Division, Office of Basic Energy Sciences, Office of Sciences, US Department of Energy for their generous support of our research. We also thank the financial collaboration of Phoenix Canada Oil Company,

which holds long-term license rights to commercialize our Rh-based technology.

6 RELATED ARTICLES

Energy Conversion in Photosynthesis; Hydrogen Economy; Molecular Catalysis for Fuel Cells; Molecular Catalysts for Oxygen Production from Water; Toward Solar Fuels Using a Biomimetic Approach: Progress in the Swedish Consortium for Artificial Photosynthesis.

7 ABBREVIATIONS AND ACRONYMS

BL = bridging ligand; CB = conduction band; CS = charge separated; DMA = *N,N*-dimethylaniline; EA = electron acceptor; ED = electron donor; ER = electron relay; HOMO = highest occupied molecular orbital; LUMO = lowest unoccupied molecular orbital; MLCT = metal-to-ligand charge transfer; MMCT = metal-to-metal charge transfer; PEC = photoinitiated electron collection; PMD = photochemical molecular device; RT = room temperature; TEA = triethylamine; TEOA = triethanolamine; TL = terminal ligand; VB = valence band.

8 REFERENCES

1. A. J. Bard, and M. A. Fox, *Acc. Chem. Res.*, 1995, **28**, 141.
2. DOE Report of the Basic Energy Sciences Workshop on Solar Utilization, Department of Energy, April 2005.
3. N. S. Lewis, *ChemSusChem.*, 2009, **2**, 383.
4. D. G. Nocera, *Chem. Soc. Rev.*, 2009, **38**, 13.
5. K. Kalyanasundaram, *Coord. Chem. Rev.*, 1982, **46**, 159.
6. A. Juris, V. Balzani, F. Barigelletti, S. Campagna, P. Belser, and A. Von Zelewsky, *Coord. Chem. Rev.*, 1988, **84**, 85.
7. M. Kirch, J.-M. Lehn, and J.-P. Sauvage, *Helv. Chim. Acta*, 1979, **62**, 1345.
8. National Renewable Energy, <http://rredc.nrel.gov/solar/spectra/am1.5/ASTMG173/ASTMG173.html>.
9. L. L. Tinker, N. D. McDaniel, and S. Bernhard, *J. Mater. Chem.*, 2009, **19**, 3328.
10. A. Kudo and Y. Miseki, *Chem. Soc. Rev.*, 2009, **38**, 253.
11. M. L. Ghirardi, A. Dubini, J. Yu, and P.-C. Maness, *Chem. Soc. Rev.*, 2009, **38**, 52.
12. M. Wang, Y. Na, M. Gorlov, and L. Sun, *Dalton Trans.*, 2009, 6458.
13. A. J. Esswein and D. Nocera, *Chem. Rev.*, 2007, **107**, 4022.
14. V. Balzani, L. Moggi, and F. Scandola, in 'Supramolecular Photochemistry', ed. V. Balzani, D. Reidel, Dordrecht, 1987, p. 1.
15. V. Balzani, A. Juris, M. Venturi, S. Campagna, and S. Serroni, *Chem. Rev.*, 1996, **96**, 759.
16. S. M. Molnar, G. Nallas, J. S. Bridgewater, and K. J. Brewer, *J. Am. Chem. Soc.*, 1994, **116**, 5206.
17. M. L. Ghirardi, M. C. Posewitz, P.-C. Maness, A. Dubini, J. Yu, and M. Seibert, *Annu. Rev. Plant Biol.*, 2007, **58**, 71.
18. M. Y. Dahrensbourg, E. J. Lyon, and J. J. Smee, *Coord. Chem. Rev.*, 2000, **206–207**, 533.
19. T. J. McDonald, D. Svedruzic, Y.-H. Kim, J. L. Blackburn, S. B. Zhang, P. W. King, and M. J. Heben, *Nano Lett.*, 2007, **7**, 3528.
20. S. Ardo and G. J. Meyer, *Chem. Soc. Rev.*, 2009, **38**, 115.
21. A. Fujishima and K. Honda, *Nature*, 1972, **238**, 37.
22. M. Ni, M. K. H. Leung, D. Y. C. Leung, and K. Sumathy, *Renewable and Sustainable Energy Rev.*, 2007, **11**, 401.
23. X. Wang, K. Maeda, A. Thomas, K. Takanabe, G. Xin, J. M. Carlsson, K. Domen, and M. Antonietti, *Nat. Mater.*, 2009, **8**, 76.
24. N. S. Lewis, *Inorg. Chem.*, 2005, **44**, 6900.
25. B. O'Regan and M. Grätzel, *Nature*, 1991, **353**, 737.
26. J.-H. Yum, P. Chen, Michael. Grätzel, and M. K. Nazeeruddin, *ChemSusChem.*, 2008, **1**, 699.
27. W. Kim, T. Tachikawa, T. Majima, and W. Choi, *J. Phys. Chem. C*, 2009, **113**, 10603.
28. B. Durham, J. V. Caspar, J. K. Nagle, and T. J. Meyer, *J. Am. Chem. Soc.*, 1982, **104**, 4803.
29. G. M. Brown, B. S. Brunschwig, C. Creutz, J. F. Endicott, and N. Sutin, *J. Am. Chem. Soc.*, 1979, **101**, 1298.
30. G. M. Brown, S.-F. Chan, C. Creutz, H. A. Schwarz, and N. Sutin, *J. Am. Chem. Soc.*, 1979, **101**, 7638.
31. M. Chou, C. Creutz, D. Mahajan, N. Sutin, and A. P. Zipp, *Inorg. Chem.*, 1982, **21**, 3989.
32. H. A. Schwarz and C. Creutz, *Inorg. Chem.*, 1983, **22**, 707.
33. E. Fujita, B. S. Brunschwig, C. Creutz, J. T. Muckerman, N. Sutin, D. Szalda, and R. van Eldik, *Inorg. Chem.*, 2006, **45**, 1595.
34. J. V. Caspar, E. M. Kober, B. P. Sullivan, and T. J. Meyer, *J. Am. Chem. Soc.*, 1982, **104**, 630.
35. L. De Cola and P. Belser, *Coord. Chem. Rev.*, 1998, **177**, 301.
36. H. Wolpher, M. Borgström, L. Hammarström, J. Bergquist, V. Sundström, S. Styring, L. Sun, and B. Åkermark, *Inorg. Chem. Commun.*, 2003, **6**, 989.
37. S. Ott, M. Borgström, M. Kritikos, R. Lomoth, J. Bergquist, B. Åkermark, L. Hammarström, and L. Sun, *Inorg. Chem.*, 2004, **43**, 4683.
38. J. Ekström, M. Abrahamsson, C. Olson, J. Bergquist, F. B. Kaynak, L. Eriksson, L. Sun, H.-C. Becker, B. Åkermark, L. Hammarström, and S. Ott, *Dalton Trans.*, 2006, 4599.

39. A. Fihri, V. Artero, M. Razavet, C. Baffert, W. Leibl, and M. Fontecave, *Angew. Chem. Int. Ed.*, 2008, **47**, 564.
40. A. Fihri, V. Artero, A. Pereira, and M. Fontecave, *Dalton Trans.*, 2008, 5567.
41. C. Li, M. Wang, J. Pan, P. Zhang, R. Zhang, and L. Sun, *J. Organomet. Chem.*, 2009, **694**, 2814.
42. S. M. Arachchige, J. R. Brown, E. Chang, A. Jain, D. F. Zigler, K. Rangan, and K. J. Brewer, *Inorg. Chem.*, 2009, **48**, 1989.
43. Y. Miyake, K. Nakajima, K. Sasaki, R. Saito, H. Nakanishi, and Y. Nishibayashi, *Organometallics*, 2009, **28**, 5240.
44. S. Rau, B. Schäfer, D. Gleich, E. Anders, M. Rudolph, M. Friedrich, H. Görls, W. Henry, and J. G. Vos, *Angew. Chem. Int. Ed.*, 2006, **45**, 6215.
45. P. Lei, M. Hedlund, R. Lomoth, H. Rensmo, O. Johansson, and L. Hammarström, *J. Am. Chem. Soc.*, 2008, **130**, 26.
46. R. Miao, D. F. Zigler, and K. J. Brewer, manuscript to be submitted to *Inorg. Chem.*
47. H. Ozawa, M.-A. Haga, and K. Sakai, *J. Am. Chem. Soc.*, 2006, **128**, 4926.
48. C. H. Braunstein, A. D. Baker, T. C. Strekas, and H. D. Gafney, *Inorg. Chem.*, 1984, **23**, 857.
49. G. Denti, S. Campagna, L. Sabatino, S. Serroni, M. Ciano, and V. Balzani, *Inorg. Chem.*, 1990, **29**, 4750.
50. M. Elvington and K. J. Brewer, *Inorg. Chem.*, 2006, **45**, 5242.
51. K. Kalyanasundaram and M. K. Nazeeruddin, *Inorg. Chem.*, 1990, **29**, 1888.
52. J. W. Peters, W. N. Lanzilotta, B. J. Lemon, and L. C. Seefeldt, *Science*, 1998, **282**, 1853.
53. F. Gloaguen, J. D. Lawrence, and T. B. Rauchfuss, *J. Am. Chem. Soc.*, 2001, **123**, 9476.
54. S. Ott, M. Kritikos, B. Åkermark, and L. Sun, *Angew. Chem. Int. Ed.*, 2003, **42**, 3285.
55. X. Li, M. Wang, S. Zhang, J. Pan, Y. Na, J. Liu, B. Åkermark, and L. Sun, *J. Phys. Chem. B.*, 2008, **112**, 8198.
56. P. Du, K. Knowles, and R. Eisenberg, *J. Am. Chem. Soc.*, 2008, **130**, 12576.
57. U. Kölle, *New J. Chem.*, 1992, **16**, 157.
58. R. Konduri, H. Ye, F. M. MacDonnell, S. Serroni, S. Campagna, and K. Rajeshwar, *Angew. Chem. Int. Ed.*, 2002, **41**, 3185.
59. M. Elvington, J. Brown, S. M. Arachchige, and K. J. Brewer, *J. Am. Chem. Soc.*, 2007, **129**, 10644.
60. A. F. Heyduk and D. G. Nocera, *Science*, 2001, **293**, 1639.
61. A. J. Esswein, A. S. Veige, and D. G. Nocera, *J. Am. Chem. Soc.*, 2005, **127**, 16641.
62. A. J. Esswein, J. L. Dempsey, and D. G. Nocera, *Inorg. Chem.*, 2007, **46**, 2362.
63. T. R. Cook, A. J. Esswein, and D. G. Nocera, *J. Am. Chem. Soc.*, 2007, **129**, 10094.
64. S. M. Arachchige, J. Brown, and K. J. Brewer, *J. Photochem. Photobiol. A: Chem.*, 2008, **197**, 13.
65. G. Kew, K. DeArmond, and K. Hanck, *J. Phys. Chem.*, 1974, **78**, 727.
66. D. R. Anton and R. H. Crabtree, *Organometallics*, 1983, **2**, 855.
67. R. Baba, S. Nakabayashi, A. Fujishima, and K. Honda, *J. Phys. Chem.*, 1985, **89**, 1902.
68. D. R. Lide, ed., ‘CRC Handbook of Chemistry and Physics’, 88th edition (Internet Version 2008), CRC Press/Taylor and Francis, Boca Raton, 2008.
69. K. Rangan, S. M. Arachchige, J. R. Brown, and K. J. Brewer, *J. Energy Environ. Sci.*, 2009, **2**, 410.
70. K. Sakai and H. Ozawa, *Coord. Chem. Rev.*, 2007, **251**, 2753.
71. H. Ozawa, Y. Yokoyama, M.-A. Haga, and K. Sakai, *Dalton Trans.*, 2007, 1197.
72. P. Du, J. Schneider, F. Li, W. Zhao, U. Patel, F. N. Castellano, and R. Eisenberg, *J. Am. Chem. Soc.*, 2008, **130**, 5056.
73. S. Tscherlei, M. Presselt, C. Kuhnt, A. Yartsev, T. Pascher, V. Sundström, M. Karnahl, M. Schwalbe, B. Schäfer, S. Rau, M. Schmitt, B. Dietzek, and J. Popp, *Chem. Eur. J.*, 2009, **15**, 7678.
74. R. Okazaki, S. Masaoka, and K. Sakai, *Dalton Trans.*, 2009, 6127.
75. G. Wang, J. D. Knoll, S. M. Arachchige, and K. J. Brewer, manuscript to be submitted to *Inorg. Chem.*.

Intermediate-Temperature Solid Oxide Fuel Cells

Alan Atkinson, John Kilner, Stephen Skinner and Nigel P. Brandon

Imperial College London, London, UK

and

Dan J. L. Brett

Imperial College London and University College London, London, UK

1	Introduction	173
2	Materials Selection and Processing for IT-SOFCS	176
3	IT-SOFC Performance Durability	186
4	Conclusions	187
5	Related Articles	187
6	Abbreviations and Acronyms	187
7	References	187

1 INTRODUCTION

Fuel cells are electrochemical energy conversion devices that convert chemical energy in a fuel directly into electricity (and heat), without involving the process of combustion. A fuel cell can be considered to be a battery/engine hybrid. Chemical energy is directly converted into electrical energy, akin to a battery, while air and fuel are continuously supplied to the device, as in a heat engine.

A number of different fuel cell technologies exist, each with its own set of materials and application focus. However, they all share the characteristics of high efficiency, few moving parts, quiet operation, and low or zero emissions at the point of use. The range of fuel cell applications is vast and includes areas such as portable electronic devices, prime movers and/or auxiliary power units (APUs) in vehicles, residential combined heat and power (CHP), and large-scale electrical power generation. Widespread adoption of fuel cell technology is anticipated to contribute to a reduced dependence on fossil fuels, lessen noxious pollutant and CO₂ emissions, improve security of electricity supply, and enable the development of a “hydrogen economy”.

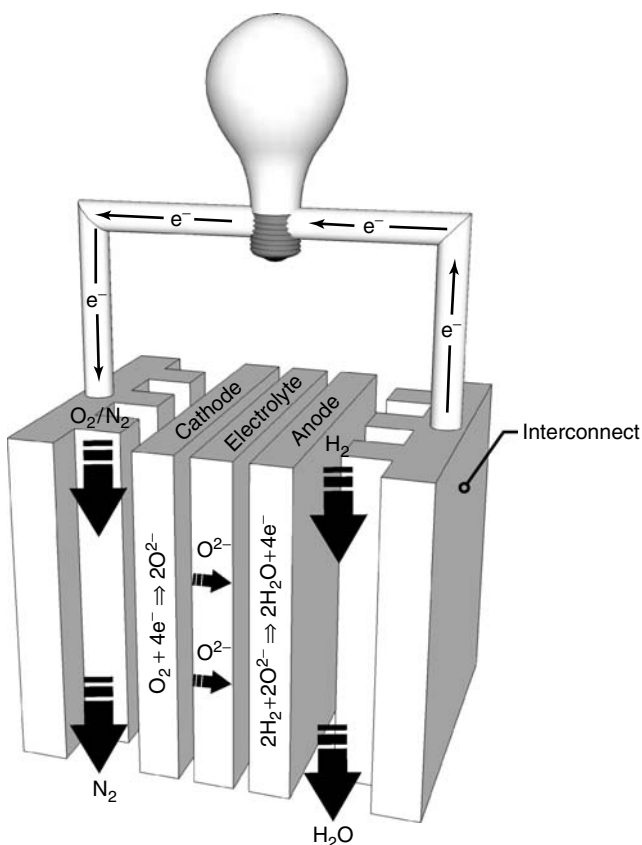
Figure 1 shows the generic fuel cell mode of operation, using a solid oxide fuel cell (SOFC)¹ as an example. Fuel cells come in a range of architectures (planar,

tubular, etc.), but central to all is the electrolyte. This may be solid (polymer or ceramic) or liquid (aqueous or molten salt) and must have a high ionic conductivity and low electronic conductivity for efficient operation. The electrolyte in an SOFC is an oxide ion conductor; however, the electrolyte may also be a proton, carbonate, or hydroxide ion conductor depending on the type of fuel cell.

On each side of the electrolyte is an electrode/electrocatalyst. Oxidant is fed to the cathode (positive electrode), typically oxygen in the form of air, and fuel is supplied to the anode (negative electrode) where it is electrochemically oxidized. Oxygen is reduced at the cathode, producing oxide ions (O²⁻) which migrate through the electrolyte and react with the fuel at the anode. If the fuel is hydrogen, water is liberated as shown in equations (1)–(3).



Viewed from a superficial level, fuel cells appear to be uncomplicated devices. The lack of moving parts and simple positive–electrolyte–negative (PEN) composite structure makes them, ostensibly, a much less complex device than an internal combustion engine, for example.



However, closer inspection brings an appreciation of the various processes occurring during operation and the materials challenges involved. The processes that occur in a fuel cell are distributed over a range of scales, as illustrated in Figure 2. In practice, the power and voltage of the fuel cell are increased by connecting individual cells in series to form a “stack”, analogous to the chain of cells in a battery, with each cell connected to its adjacent cell using an electrically conducting interconnect, which also serves to distribute reactant across the surface of the electrodes using integrated flow channels. At this scale, factors such as heat management (cooling and the effective withdrawal of heat for practical use), mechanical forces on the stack components, sealing, manifold flow, hardware materials, and design for the reduction of mass and volume are of greatest relevance. At the cell level, electrical contact resistance, flow-field plate design, reactant and temperature distribution, chemical compatibility of materials under operational conditions, and the manufacture of cells are of primary concern. Moving into the internal structure of the cell and the individual anode, cathode, and electrolyte, processes occurring at the nano- to micrometer scale are of relevance, and include ionic charge transport, electron conduction, microporosity, and electrocatalysis.

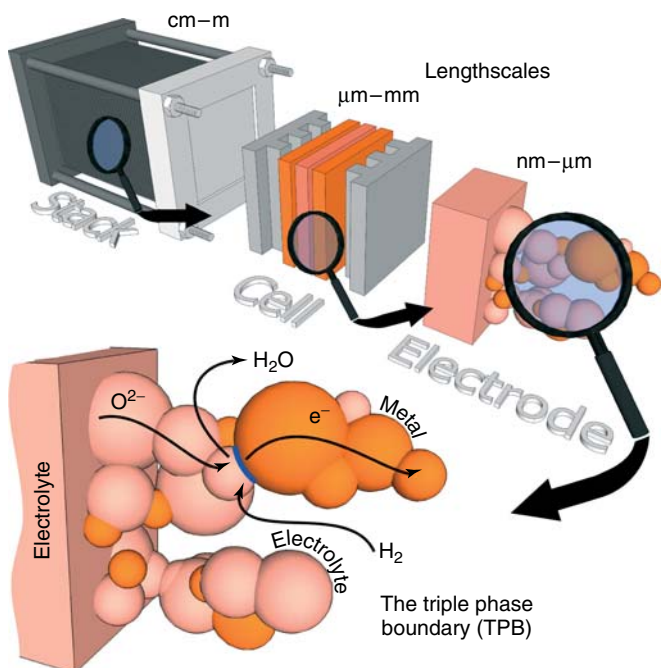


Figure 2 Scales of operation in a fuel cell (using the SOFC as an example), and illustration of an active anode triple-phase-boundary (TPB) line at which electrochemical reaction takes place

Within the electrodes themselves, reaction occurs (in the majority of electrodes used at present) at the so-called triple phase boundary (TPB), which is the line interface between the open pores in the electrode, and the electronic and ionic conducting phases.² It is the extent of the fully percolated TPB (i.e., the TPB that has a contiguous pore path to the source of reactant, electronic path to the current collector, and ionic path to the electrolyte), along with the inherent ability of the materials used to catalyze the electrode reaction, that determines the electrochemical activity of the electrode.

The example given in Figure 2 is for a SOFC; however, as noted previously, there are a number of fuel cell technologies, operating over a range of temperatures from ambient to over 1000 °C and using a diverse range of materials. Figure 3 summarizes the main fuel cell types; note the different ion transport mechanisms in the electrolyte. Each fuel cell is named according to its electrolyte type, and it is primarily the electrolyte used that determines the temperature range of operation. The “low” temperature fuel cell technologies, namely, alkaline fuel cells (AFC), polymer electrolyte fuel cells (PEFC), and phosphoric acid fuel cells (PAFC), require relatively pure hydrogen to maintain stable performance. This is because in low-temperature operation there is a need for precious metal electrocatalysts (i.e., platinum) to ensure adequate electrode reaction kinetics; these catalysts are deactivated by carbon monoxide, which is a product of hydrocarbon reforming for the production of hydrogen.

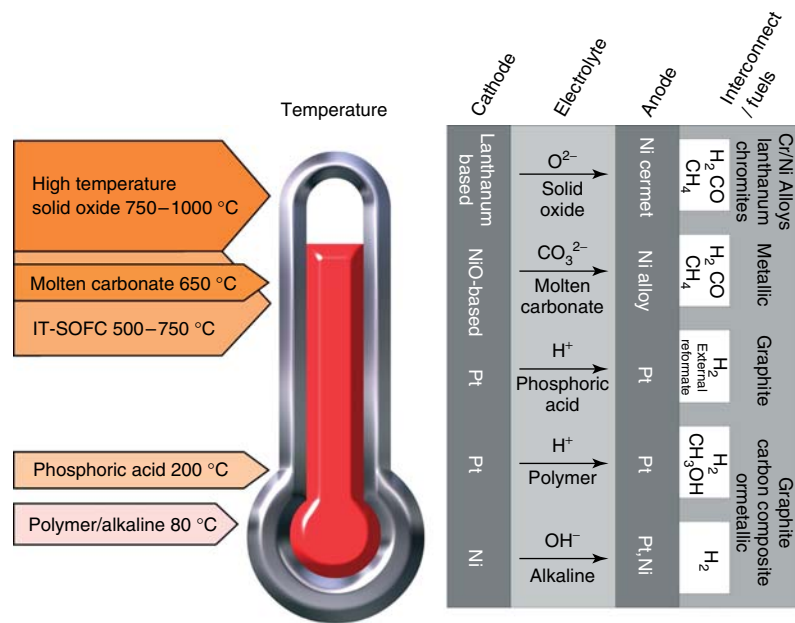


Figure 3 Illustration of the range of fuel cell types, and examples of typical materials of construction and their operating temperatures

If hydrocarbons (such as natural gas) are to be used as fuels for low-temperature fuel cells, a fuel processor must be used to convert the fuel into hydrogen and carbon dioxide containing very low levels of carbon monoxide. The fuel processor may be composed of a reformer reactor, shift reactor, and gas cleanup stage, all adding to the cost and complexity of the system and eroding the efficiency.

Of the various fuel cell technologies, the PEFC (low temperature) and SOFC (high temperature) are currently attracting most attention. It is the SOFC and its trend to move to lower temperature operation that is the subject of this article.

There is no consensus as to the optimal operating temperature of fuel cells per se. The preferred temperature of operation will depend to a large extent on the application. However, there is currently significant effort to raise the operating temperature of PEFCs and reduce that of SOFCs for certain applications. PEFCs operating at temperatures as high as 200 °C are being developed to facilitate water and thermal management, which are key challenges for automotive applications. Higher temperature facilitates stack cooling since heat rejection is easier from higher temperature systems, thus avoiding the need for large radiators and reducing parasitic losses from cooling fans and pumps. Increased temperature also significantly reduces the poisoning effect of CO on the electrocatalyst. In contrast, the operating temperature of SOFCs is being lowered to better address small-scale applications such as residential micro-CHP,³ APUs, and even hybrid fuel cell/battery vehicles.

High-temperature solid oxide fuel cells (HT-SOFCs), typified by developers such as Siemens Westinghouse and Rolls-Royce, operate up to 1000 °C. For such systems, high efficiencies can be achieved from integration with

gas turbines for large-scale stationary applications. High-temperature operation means that the components of the stack need to be mainly ceramic, and a tubular or box section design is commonly used, which results in low volumetric power density. For smaller scale applications, such as micro-CHP, APUs, and small electrical generators, there is a trend to move to lower temperatures of operation, into the so-called intermediate-temperature (IT) range of 500–750 °C, as defined by Steele.⁴

By lowering the temperature of operation, a wider range of materials that allow cheaper fabrication can be used, particularly in relation to interconnects and balance-of-plant (BoP) components. Lower temperature operation also affords more rapid start-up and shutdown, reduced corrosion rate of metallic components, improved durability (sintering and component interdiffusion are accelerated at higher temperatures), more robust construction through the use of compressive seals and metallic interconnects, as well as the advantage of greatly simplified system requirements.⁵

There are two main routes by which SOFCs can be operated at lower temperatures, while still attaining performance comparable to that of the higher temperature technology. The dimensional thickness of the electrolyte can be reduced, thereby reducing the area-specific resistance (ASR) of the fuel cell, and/or materials development can bring about the same result by improving the ionic conductivity of the electrolyte at lower temperatures as well as improving the performance of electrodes.

Since metallic interconnects and nonceramic seals can be used at lower temperatures, IT-SOFCs are more conducive to planar stack architectures than HT-SOFCs. As can be seen in Figure 4, a number of cell configurations

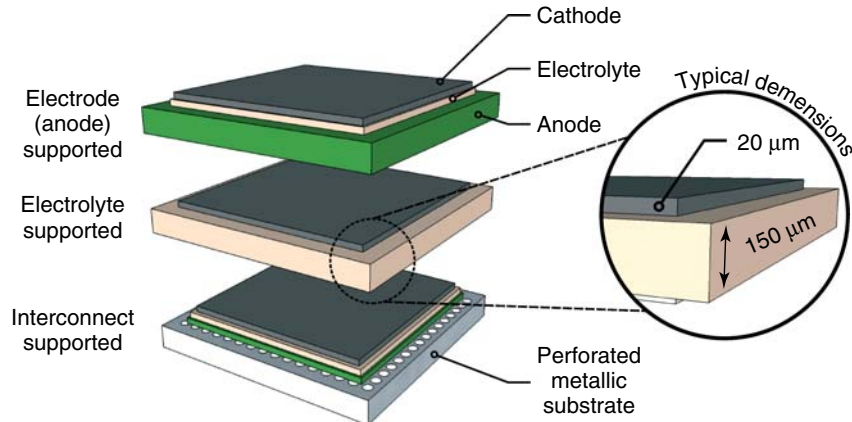


Figure 4 Illustration of the different types of cell support architectures for SOFCs

exist, each classified according to the layer that mechanically supports the cell. These include individual support by each of the cell components (anode, cathode, and electrolyte) as well as distinct structural components such as porous substrates or perforated metallic supports. As a general indicator of the thickness scale of these assemblies, the supporting component will typically have a thickness $>150\text{ }\mu\text{m}$ and the supported layers will have a thickness of tens of microns.

1.1 Applications of IT-SOFCs

Lowering the temperature of operation opens up a new realm of applications for SOFCs. While HT-SOFCs dominate development for applications in the hundreds of kilowatts_e to megawatts_e power range, using combined-cycle technology that is most efficient with a fuel cell of $>850\text{ }^{\circ}\text{C}$, the IT-SOFC particularly suits a power range of $\sim 1\text{ kW}_e$ to a few tens of kilowatts_e, with the majority of applications being in the sub-10 kW_e range. Faster start-up and shutdown times, and more rugged construction due to compliant seals and metallic interconnects, make IT-SOFCs a viable technology for mobile applications. IT-SOFCs have even been demonstrated for use as APUs and traction power in vehicles.⁶

Of all of the potential applications, it is the small-scale CHP market where the IT-SOFC is seen to be particularly well suited. Micro-CHP is the generation of zero or low-carbon heat and power by individuals, small businesses, and communities to meet their own needs. In many situations, local generation has the potential to provide operational cost and/or CO₂ savings via utilizing a renewable primary energy source, or capturing otherwise discarded heat in the case of micro-CHP. This approach avoids the losses associated with delivering electrical power via the grid over long distances and enables both the heat and power to be utilized at the point of generation. Operating on natural gas, and with a heat-to-power ratio around unity, IT-SOFCs are being developed for

residential-scale CHP, and are seen as having the potential for significant market penetration.³

The performance and cost requirements for IT-SOFCs will largely depend on the specific application. A micro-CHP unit will require in excess of 40 000 h of operation at a near-constant load with few start/stop cycles, whereas a prime mover for a vehicle will require 5000 h of operation but will be subjected to dynamic load variation and large numbers of start/stop cycles. As a general indication of targets for IT-SOFC technology, the following are reasonable values (but not universal across all applications): stack cost $<\$400\text{--}800\text{ kW}_e^{-1}$; net system electrical efficiency 35–50% (LHV); stack energy density $>0.5\text{ kW}_e\text{ L}^{-1}$; stack power density $>0.25\text{--}0.5\text{ W cm}^{-2}$; stack fuel utilization $>80\%$; stack degradation rate $<0.5\%$ per 1000 h.⁵ For all of these targets, the materials used for construction coupled with the duty cycle will dictate if and when they are reached.

Having introduced fuel cell technology and detailed the benefits and applications of IT-SOFCs, we now turn our attention to the materials and processes used to manufacture these devices.

2 MATERIALS SELECTION AND PROCESSING FOR IT-SOFCs

It is reasonable to say that most of the major improvements in fuel cell performance have been a consequence of materials and processing innovation. For the SOFC, this is firmly rooted in the area of solid-state inorganic chemistry, since high-temperature operation precludes the use of organic ion-conducting polymers (ionomers) and aqueous electrolytes. The following discussion describes the role of inorganic materials in each of the components that make up the SOFC, with a particular emphasis on improving performance so as to make lower temperature (IT) operation possible.

2.1 Electrolytes

The properties of the electrolyte have a major impact on fuel cell performance through the electrolyte's contribution to the ohmic internal resistance. The following summarize the ideal properties of an SOFC electrolyte: (i) high oxide ion conductivity (typically $>10^{-3} \text{ S cm}^{-1}$) and low electronic conductivity, that is, to say that the electrolyte should have an ionic transference number close to unity. If a significant electronic conductivity exists, then an internal short circuit between the anode and the cathode will result, with a resultant consumption of some of the reactant, increased generation of heat, and reduction in useful electrical current delivered. (ii) Good thermal and chemical stability in relation to the reactant environment and materials in physical contact: the electrolyte will be exposed to both high and low $p\text{O}_2$ environments on each of its sides and will be in contact with electrode materials. (iii) Closely matched thermal expansion coefficient (TEC) with the electrodes and contacting components. (iv) Dense structure to maximize conductivity and minimize reactant crossover. The ability to make thin (few tens of micrometers) and dense electrolyte layers via a simple formation route is a major challenge for SOFC developers. (v) Low cost and environmentally benign.

2.1.1 Oxide Ion Conduction

The oxide ion transport mechanism in ceramic electrolytes is thermally activated and the conductivity is

therefore a strong function of temperature. High temperatures ($>500^\circ\text{C}$) are typically required to achieve technologically useful performance in SOFCs; this is because the oxide ion is large and thermal energy is needed to overcome the substantial barriers to migration into vacant lattice sites. Goodenough has described in detail the conduction mechanism in oxide ion electrolytes.⁷

Figure 5 shows how the specific ionic conductivity of different solid oxide electrolytes varies with temperature. Note that these are representative values of the total conductivity for each of the electrolytes; actual values will depend on the microstructure, exact level of doping, fabrication, and sintering processes. Ionic conductivity exhibits an Arrhenius-like dependence on temperature, which is the reason for the graph being plotted as the logarithm of conductivity vs reciprocal of temperature.

The trade-off between electrolyte conductivity and thickness, in order to give a suitable power density, has been described by Steele.^{4,9} A commonly adopted performance target for an SOFC electrolyte is an ASR $<0.15 \Omega \text{ cm}^2$. Hence, if the thinnest dense impermeable electrolyte layer that can be reliably produced using low-cost processing routes is $15 \mu\text{m}$ thick (as shown by the dashed line in Figure 5), then the specific ionic conductivity (σ) required to achieve the target ASR is ($\sigma = \text{thickness}/\text{ASR}$) $10^{-2} \text{ S cm}^{-1}$ ($\log_{10} \sigma = -2$). So, ceria–gadolinia solid solutions (CGO), for example, would attain the required ASR at a temperature of above $\sim 500^\circ\text{C}$, whereas yttria-stabilized zirconia (YSZ) would require over 700°C . If the cell is to be electrolyte supported, calling for a

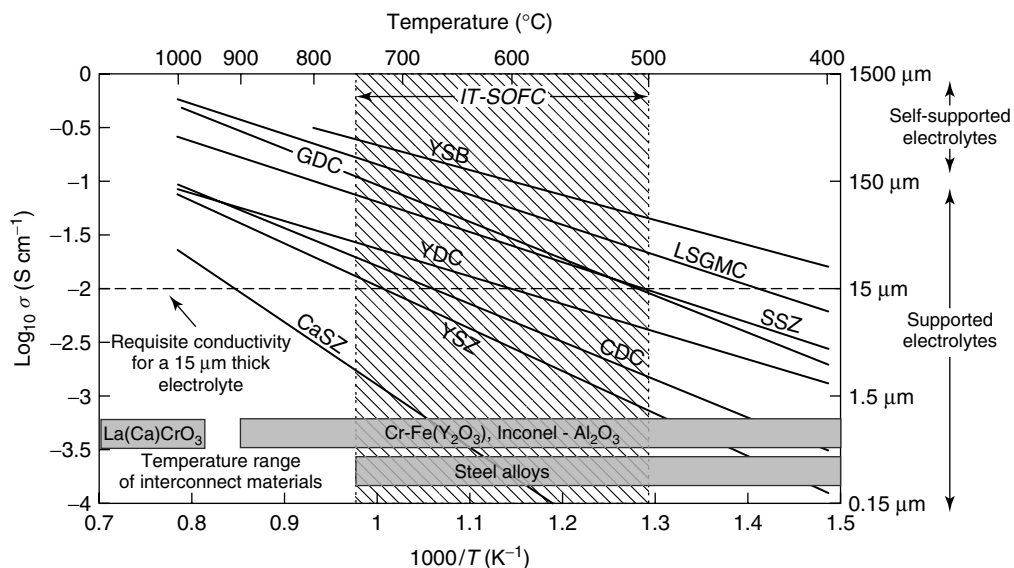


Figure 5 Total conductivity as a function of reciprocal temperature of selected solid oxide fuel cell electrolytes and operational range of different interconnect materials. Conductivity data are from Wincewicz and Cooper and references therein.⁸ Note that the exact conductivity will depend on the electrolyte microstructure, doping level, and fabrication process. YSB ($(\text{Bi}_2\text{O}_3)_{0.75}(\text{Y}_2\text{O}_3)_{0.25}$); LSGMC ($(\text{La}_x\text{Sr}_{1-x}\text{Ga}_y\text{Mg}_{1-y-z}\text{Co}_z\text{O}_3$; $x \sim 0.8$, $y \sim 0.8$, $z \sim 0.085$); CGO ($\text{Ce}_{0.9}\text{Gd}_{0.1}\text{O}_{1.95}$); SSZ ($(\text{ZrO}_2)_{0.8}(\text{Sc}_2\text{O}_3)_{0.2}$); YDC ($\text{Ce}_{0.8}\text{Y}_{0.2}\text{O}_{1.96}$); CDC ($\text{Ce}_{0.9}\text{Ca}_{0.1}\text{O}_{1.8}$); YSZ ($(\text{ZrO}_2)_{0.92}(\text{Y}_2\text{O}_3)_{0.08}$); CaSZ ($\text{Zr}_{0.85}\text{Ca}_{0.15}\text{O}_{1.85}$). Also note that certain advanced steel alloys are being employed, which are capable of withstanding temperatures in excess of the IT-SOFC range

thickness of say 150 µm, then a YSZ electrolyte would require an operating temperature >950 °C.

The thickness of the electrolyte that can be tolerated on this basis dictates the supporting configuration of the cell. Even for electrolytes with superior low-temperature conductivity, electrolyte-supported geometries lead to high ohmic resistance in the IT regime of operation, and therefore configurations other than electrolyte supported tend to be the route taken for IT-SOFCs.

2.1.2 Fluorite-Based Electrolytes

Electrolytes based on the fluorite lattice structure are the most common class of SOFC electrolytes.¹⁰ Fluorite has a face centred cubic (FCC) crystal structure with the generic formula MO₂. Oxygen ion conductivity is achieved by the oxygen ions migrating via a vacancy mechanism through the fluorite lattice. Of the fluorites, zirconia (ZrO₂)-based materials have been the most extensively studied materials as electrolytes for SOFCs. By substitution with lower oxidation state (allovalent) cations, such as Y³⁺, zirconia is stabilized in its cubic form. The addition of aliovalent cations also has the effect of producing oxygen vacancies, hence increasing the oxide ion conductivity. YSZ is the most widely used electrolyte for SOFCs and boasts good chemical and physical stability as well as a wide operating range of temperature and pO₂, without suffering from electronic conductivity. Addition of ~8 mol% of yttria, i.e., (ZrO₂)_{0.92}(Y₂O₃)_{0.08} (8 YSZ—the number prefix representing the mole percentage of substitution), leads to the highest oxide ion conductivity, although higher levels (i.e., 10 YSZ) produce a better stabilized cubic phase. A range of substitutional aliovalent cations have been investigated, including Y³⁺, Eu³⁺, Gd³⁺, Yb³⁺, Er³⁺, Dy³⁺, Sc³⁺, Ca²⁺, and Mg²⁺. Scandia-stabilized zirconia (SSZ) is a particularly promising combination, although Sc₂O₃ is significantly more expensive than Y₂O₃. However, the quantity used in a thin supported electrolyte is small and hence there is currently much interest in this material.

Although YSZ has a lower ionic conductivity than many of the materials being developed for IT operation, suitable oxide ion conductance can be achieved by fabricating the electrolyte film with a thickness of 10 µm or less. The challenge is then to produce a homogeneous, leak-free layer on a porous substrate by a process that is amenable to volume manufacture.

Ceria solid solutions are considered to be promising electrolytes for IT operation.^{4,9,11} Ceria (CeO₂) has a fluorite structure, and oxygen vacancies are introduced by substituting Ce⁴⁺ with divalent alkaline earth or trivalent rare earth ions. The oxide ion conductivity is a function of temperature, the nature of the substituted ion, and its concentration, with the maximum ionic conductivity occurring at ~10–20 mol% substitution. It is generally found everywhere, and in the case of ceria- and zirconia-based electrolytes, the highest oxygen ion conductivity is observed when the aliovalent cation is

closest to the ionic radius of the host cation. In the case of Zr⁴⁺, it is Sc³⁺ and in the case of Ce⁴⁺, it is Sm³⁺ or Gd³⁺. Gadolinium-doped ceria Ce_{0.9}Gd_{0.1}O_{1.95} (10 CGO) is the most extensively studied ceria-based electrolyte.^{12,13}

Ceria-based electrolytes suffer from the partial reduction of Ce⁴⁺ to Ce³⁺ when exposed to a combination of low pO₂ (as low as 10⁻¹⁹ atm) and high temperature (>600 °C), with the reduction process taking place at the anode side of the fuel cell and affecting a significant volume fraction of the electrolyte. The consequence of this chemical reaction is that (i) there is a volume expansion of the lattice, which can result in mechanical failure of the electrolyte; (ii) electronic (n-type) conductivity is introduced that reduces performance due to electronic leakage currents between the anode and cathode. The mechanism of reduction and mixed ionic–electronic conduction (MIEC) of ceria-based electrolytes has been studied and reviewed in depth.^{11,14}

Figure 6 shows how the performance of a 10 CGO-based fuel cell is affected by electronic leakage current as a function of temperature. Using a model developed by Godickemeier *et al.*,¹⁵ the presence of partial short circuiting electronic currents, due to the mixed conducting properties of CGO, can be estimated. Area-specific resistances for both the anode and the cathode are taken to be 0.5 Ω cm² and independent of temperature, and an electrolyte thickness of 15 µm is chosen as typical for an electrode- or metal-supported cell; the fuel composition is 50% H₂, 3% H₂O with N₂ balance. Increasing temperature promotes the reduction of Ce⁴⁺ and leads to higher electronic leakage current and lower open circuit voltage (OCV). Since cell voltage is a direct measure of fuel cell electrochemical efficiency, it can be concluded that leakage current can become a significant source of efficiency loss. However, when the cell is put under electrical load, the electronic current is reduced (i.e., the oxide ion transport number increases), as can be seen in Figure 6 (inset); this is because Ce⁴⁺ reduction is suppressed by oxide ion flux. Under practical operating cell voltages of ~0.65 V, the loss in efficiency is negligible for operation at less than 600 °C, but is significant at (or above) 650 °C. It can be seen that in the high-current-density regime, decreasing temperature results in a steeper polarization curve because of decreasing oxide ion conductivity. It is for this combination of factors that the operation of SOFCs with CGO electrolyte is considered most effective in the 500–600 °C temperature range.

2.1.3 Perovskites

Work by Ishihara *et al.* has shown that Sr- and Mg-doped LaGaO₃ (LSMG) exhibit high ionic conductivity (comparable to that of CGO) and low electronic conductivity, even at low pO₂ levels.¹⁶ This class of material potentially offers adequate performance at temperatures as low as 400 °C. However, LSMG is substantially more expensive than ceria-based electrolytes, and durability problems have been reported with electrode materials.

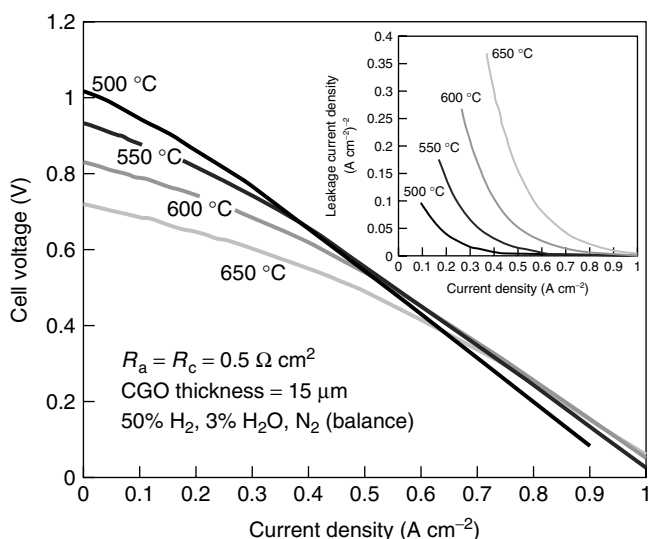


Figure 6 Model prediction of the polarization profile for a CGO-based fuel cell at temperatures from 500 to 650 °C; the variation in electronic leakage current with electronic current density and temperature is given in the inset. R_a and R_c are the area-specific resistances of the anode and cathode, respectively

2.1.4 $\text{Ln}_{10}(\text{XO}_4)_6\text{O}_{2\pm y}$ Systems and $\text{La}_2\text{Mo}_2\text{O}_9$ -Based Materials

Relatively few structure types have been identified as potential oxide-ion-conducting electrolytes. Fast ion conductivity has been reported in two novel systems: apatite-based $\text{Ln}_{10}(\text{XO}_4)_6\text{O}_{2\pm y}$ systems¹⁷ and the $\text{La}_2\text{Mo}_2\text{O}_9$ -based materials.¹⁸ For the apatite-type materials, significant ionic conductivity has been reported in systems where the lanthanide is either La, Pr, or Nd and X = Ge or Si. A number of substitutions on both cation sites have been reported with significant effects on the oxide ion conductivity, with three-orders-of-magnitude difference reported for substitution with Bi and Ga on the La and Si sites, respectively.¹⁷ In one study, a conductivity as high as 0.05 S cm⁻¹ at 800 °C for the $\text{La}_9\text{Ba}(\text{SiO}_4)_6\text{O}_{2.5}$ composition was reported.¹⁹ It is also of interest to note that these materials have a novel interstitial conduction pathway, as revealed by atomistic simulation, and a degree of anisotropy. Each of these features offers opportunities to develop new devices with enhanced performance.

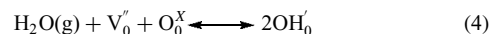
An alternative material, $\text{La}_2\text{Mo}_2\text{O}_9$, was reported as having oxide ion conductivity comparable with that of YSZ, CGO, and LSGM. There are some concerns over the stability of the material, but the synthesis of this and related compositions requires relatively low temperatures, and hence in the longer term it may be seen as an advantage in producing devices with reduced processing temperatures.

These new materials are not likely to replace the conventional electrolytes in the near future, but as has been seen with the ceria-based systems, with substantial

dedication and control of the chemistry and morphology of the ceramic, successful devices may be prepared in the medium to long term. As is common with all SOFC materials, developers have to address concerns over durability, compatibility, and synthesis conditions before technologically relevant cells can be produced. Initial studies have, however, demonstrated successful operation of a fuel cell based on a $\text{La}_{9.6}\text{Si}_{5.7}\text{Mg}_{0.3}\text{O}_{26.1}$ electrolyte and operating between 600 and 800 °C.²⁰

2.1.5 Proton-Conducting Electrolytes

The electrolyte materials discussed so far are all oxide ion conductors; however, alternative proton-conducting ceramics have been suggested as the basis for IT applications. Since the size of a proton is much smaller than that of an oxide ion, higher conduction at lower temperature is envisaged. In this instance, protons are incorporated into the oxide via the following reaction:



where oxygen vacancies combine with H₂O to produce OH₀⁻ defects in the lattice. A number of potential steps are possible in this process, but they generally result in materials with significant proton conduction at temperatures below 600 °C. As the temperature increases, it is normally the case that oxide ion conduction increases and eventually dominates, restricting the operating regime of ceramic proton conductors to relatively low temperatures. However, this is clearly an advantage when the objective is IT operation.

Iwahara *et al.* observed appreciable proton conductivity at high temperatures ($\sim 10^{-2}$ S cm⁻¹ at 1000 °C) in BaCeO₃-based oxides, which is improved by substituting with rare earth cations on the Ce site.²¹ Other barium-based perovskite-type structures, such as BaZr_{0.9}Y_{0.1}O_{2.95}, have shown protonic conductivity approaching that of the best oxide ion conductors at the low-temperature end of IT-SOFC operation. However, the chemical stability of these materials is not suitable for long-term fuel cell operation, particularly with regard to exposure to CO₂ resulting in the formation of surface carbonate species that block ion conduction. Proton-conducting systems also have the disadvantage that a proton cannot oxidize CO in the fuel stream, as an oxide ion can at the anode of a SOFC, and therefore they require full reforming (and shift reaction) processors for operation with hydrocarbon fuels.

As the Ba- and Sr-based perovskites have some problems with processing and stability, attention has been focused on the discovery of new materials. Haugsrud *et al.* have suggested that the divalent substituted LaNbO_4 and LaTaO_4 series of materials are attractive candidates,^{22,23} with Ca-doped LaNbO_4 identified as having a conductivity of 10^{-3} S cm⁻¹ at 800 °C.²³ These materials indicate that there is considerable scope for solid proton fuel cell (SPFC)

development, which could offer a viable lower temperature alternative to conventional oxide-ion-conducting IT-SOFCs. Ishihara *et al.*¹⁶ and Kreuer²⁴ have both reviewed proton-conducting ceramics for the development of SPFCs.

2.1.6 Nanostructured Electrolytes

Santamaria and coworkers have reported that nanostructured materials, specifically thin epitaxial heterostructures, can greatly enhance the oxide ion conductivity of materials potentially suitable for SOFC electrolytes.²⁵ By fabricating epitaxial heterostructures formed from thin layers of YSZ (two unit cells thick) between much thicker layers of strontium titanate, SrTiO₃ (STO), the conductivities of the YSZ layers were increased by *eight orders* of magnitude, suggesting that devices based on YSZ could operate at temperatures close to the room temperature.

The origin of the enormous increase in conductivity in the epitaxial YSZ/STO heterostructures reported by Santamaria *et al.* is intriguing; however, it remains to be demonstrated that the observed conductivity is due to the oxide ion.²⁶ To achieve such significant increases, the authors suggest that the strain at the YSZ/STO interface, imposed by the epitaxial relationship, is critical and allows facile oxygen diffusion pathways to open along this nanostructured interface.

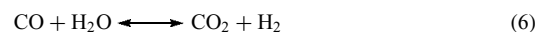
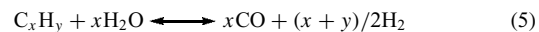
A similar effect has been identified, but to a lesser degree, in heterostructured YSZ, where the magnitude of the conductivity has been increased as a function of the number of layers of the electrolyte.²⁷ Again, these data were obtained from conductivity measurements, and hence there is no direct measure of the ionic mobility within these structures; however, these two studies, along with other works on oxide-ion-conducting superlattices,²⁸ indicate that nanostructured layers might enhance SOFC performance. If the “colossal” electrolyte conductivity enhancement reported can be verified and then realized in working fuel cell devices, this could represent a step change in SOFC performance and define a new “low-temperature” regime of operation—LT-SOFCs.

2.2 Anodes

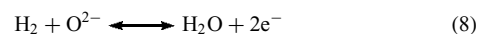
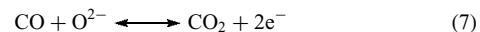
2.2.1 Fueling IT-SOFCs

Hydrogen is the best fuel for all fuel cell types in terms of electrochemical performance and materials durability; this also holds for SOFCs. However, given the lack of a supply infrastructure and difficulties in storing hydrogen, the ability of SOFCs to operate at high efficiency on hydrocarbon fuels is seen as a major advantage over low-temperature technologies; consequently, hydrocarbons are considered as the preferred fuel for SOFCs. Natural gas (primarily methane) is seen as an ideal fuel because of its abundance, existing distribution infrastructure (particularly in Western Europe), and low cost. Lighter (shorter chain) hydrocarbons are also easier to reform

than heavier ones. The reforming and shift reactions can be written as



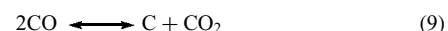
and the anode electrochemical reactions as



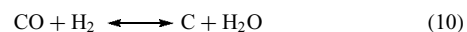
Issues relating to fueling of fuel cells are highly dependent on the temperature of operation and electrode materials used. Lowering the temperature from the HT to IT regime has an impact on the efficiency of internal reforming, the propensity of carbon formation to occur, and the extent to which impurities such as sulfur interact with the anode.²⁹

The steam reforming (oxygenolysis) of hydrocarbons is a well-established process used on an industrial scale for the production of hydrogen. The reaction is shown in equation (5) and results in the formation of a mixture of CO and H₂ (syngas). Further reaction via the water–gas shift (WGS) reaction (equation (6)) converts CO and steam into greater quantities of H₂. During internal reforming, these two reactions occur simultaneously, with the equilibrium composition of the gas being dictated by temperature and pressure.

The CO and H₂ produced are subsequently electrochemically oxidized by the O²⁻ ions at the anode (equations (7) and (8)). Figure 7 shows the thermodynamically predicted composition of a system supplied with methane over a range of temperatures for three different steam-to-carbon (S/C) ratios. Although the thermodynamically predicted composition may not be realized for lower temperatures due to kinetic limitations, at higher temperatures, relevant to IT-SOFC operation, kinetics are fast and the equilibrium predictions are a reasonable indicator of the actual fuel composition. The amount of solid-phase carbon expected to form is also shown. Carbon formation (coking) can occur via disproportionation of CO (Boudouard reaction):



or through the reduction of CO, the reverse of which under conditions of high steam-to-methane ratios acts to suppress carbon formation at higher temperatures:



Notice that in the HT region, the various reactions go to completion and the fuel composition is relatively stable with temperature. In contrast, in the IT region the fuel composition is highly sensitive to temperature, with a relatively small change in operating temperature having a significant effect on fuel composition.

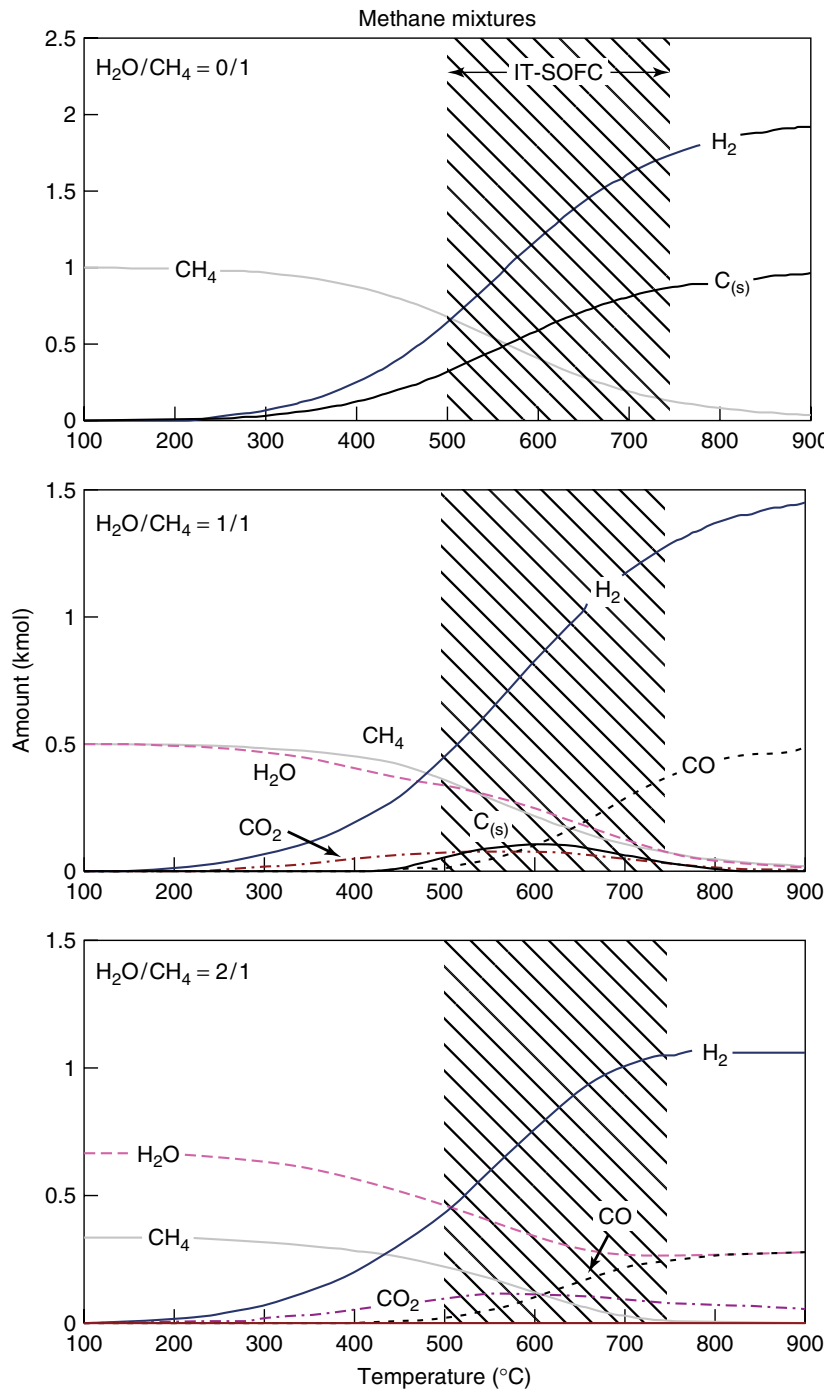


Figure 7 Thermodynamic predictions of the equilibrium composition for methane fed at different temperatures and steam-to-carbon ratios. The combined $\text{CH}_4 + \text{H}_2\text{O}$ input amount is 1 kmol in each case

It can be seen from Figure 7 (the thermodynamically predicted fuel composition with temperature) that temperature and steam content have a strong effect on the formation of carbon. Operating dry (i.e., with no initially added steam), carbon formation becomes progressively worse with increasing temperature, whereas an S/C of 2 or more results in

complete suppression of carbon. Between these bounds (e.g., S/C = 1), carbon formation is predicted to be the greatest in the IT range. In practice, an S/C ratio between 2 and 3 is used to safely avoid carbon deposition; however, excessive addition of steam can lower the system efficiency due to fuel dilution and the energy required to raise the steam.

The lowest temperature at which an SOFC can effectively achieve internal reforming is contentious. The reforming reaction will occur at an appreciable rate over an appropriate catalyst, given an ample supply of steam at temperatures above ~500 °C.⁵ Direct coupling of the reforming reaction to the anode of the IT-SOFC then allows oxidation of the hydrogen-rich reformate at the anode, shifting the equilibrium of the reforming reaction such that a high conversion of hydrocarbon fuels can be achieved, even at operating temperatures down to 500 °C. Furthermore, since the reforming reaction is strongly endothermic ($\Delta H^\circ = +206 \text{ kJ mol}^{-1}$) cooling of the cell will occur, lowering the requirement for additional air cooling, reducing the parasitic air blower load and increasing net system efficiency. A small external pre-reformer may also be needed to convert higher hydrocarbons to methane before the fuel enters the stack.

SOFC performance can be degraded by interaction of various contaminants in the fuel. Sulfur is a “poison” of nickel-containing anodes even at very low (ppm) concentrations.²⁹ Desulfurizers are therefore commonly used to remove sulfur, though this adds to the complexity, cost, and maintenance burden of the system. The interaction of sulfur (typically in the form of H₂S) with the anode is complex.³⁰ Increasing temperature tends to lessen the degrading effect of sulfur on performance. However, steam and hydrogen content, oxide ion flux to the anode surface, and the metallic and electrolyte material composition all have an effect.

2.2.2 Anode Materials—Cermets

The anode must perform electro-oxidation of fuel by catalyzing the reaction and facilitating fuel access and product removal; it must also have sufficient electronic conductivity (typically 100 S cm⁻¹, although this depends on the cell design) to efficiently transport electrons to the current collector. Most anodes are porous cermets (a composite of ceramic and metal), the microstructure of which is optimized

to have a fully percolated metallic component that allows conduction of electrons through the structure, while optimizing the active TPB length, as shown in Figure 2. Optimization of the microstructure to maximize the effective TPB length is a major research effort in such cermets. However, the use of MIEC ceramic materials is also being exploited, where the electrochemical reaction zone can be extended from a one-dimensional TPB to a two-dimensional surface, as shown in Figure 8.

The cermet approach to anode design provides sintering compatibility with the electrolyte and helps match the TEC between the electrolyte and the current collector; cermets can also be used as the structural support for a cell (cf. the anode-supported IT-SOFC in Figure 4).

The most commonly used anode cermet material is Ni-YSZ, with a nickel volumetric content typically in the range of 40–70%. Substantial work has been done to replace zirconia with ceria, and Ni with Cu. Nickel is an excellent electrocatalyst for the oxidation of hydrogen; unfortunately, it also promotes the formation of carbon from hydrocarbon fuel.²⁹ Copper is being explored as a replacement since it does not significantly catalyze the carbon formation reaction, the copper simply acting as an electron-conducting matrix with ceria performing the electro-oxidation catalyst role.^{31,32}

Lowering the temperature of operation means that it is easier to use materials together that have a mismatch in TEC without compromising the mechanical integrity of the electrode during temperature transients. It also means that Cu, which is highly mobile at HT-SOFC temperatures, can be used without suffering degradation caused by sintering.

Many different methods have been used to make ceramic powders for the manufacture of cermet anodes; these include solid-state reactions, spray pyrolysis, solgel, dip coating, microwave hydrothermal syntheses, synthesis in supercritical CO₂, coprecipitation routes, hydrothermal syntheses, and solution combustion routes. Materials processing

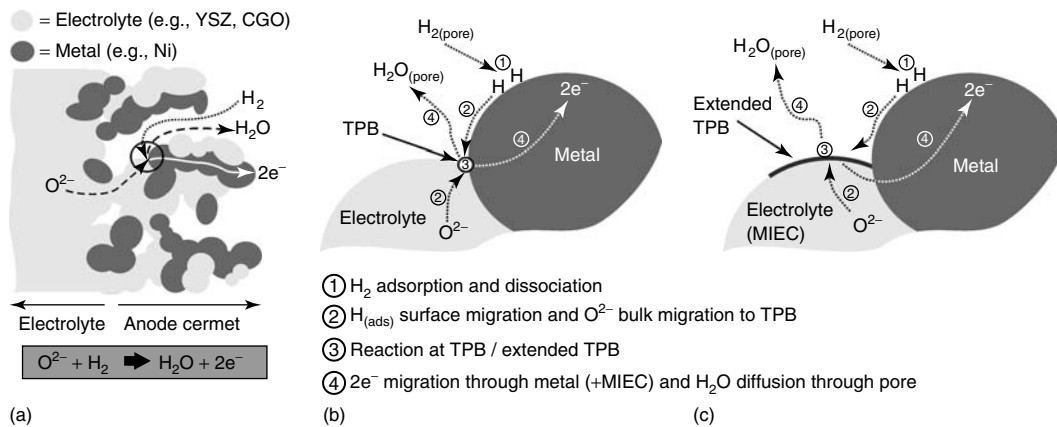


Figure 8 Illustration of the effect of extending the anode reaction region using an MIEC electrolyte. (a) Electrolyte/cermet anode with active TPB circled; (b) mechanism of reaction at the TPB; (c) mechanism of reaction at the extended TPB

routes for the production of anode cermets are discussed in detail in the literature.³³

The syntheses of Ni-YSZ cermets are most commonly achieved by physically mixing micron-sized powders of NiO and YSZ; multiple or complex steps ensue, often involving high temperatures and lengthy processing times that are energy intensive and do not allow much direct control over powder or cermet properties. Moreover, the substitution of yttria into the zirconia lattice via these methods is sometimes inhomogeneous as a result of batch-to-batch variations. This has led workers to investigate alternative methods, including nanostructured cermet anodes.

2.2.3 Nanoceramic Cermet Anodes

Nickel content has a crucial effect on the microstructural and mechanical stability of Ni-YSZ cermets. For example, the most predominant microstructural change that facilitates the degradation of Ni-YSZ anodes is the agglomeration and coarsening of the Ni phase. Consequently, if one could retain sufficient electrical conductivity at reduced nickel content, this may reduce the deleterious effects of thermal mismatch and coarsening of the Ni phase. However, reducing the Ni content below 35–40 vol % normally results in a large increase in electrical resistance of Ni-YSZ anodes as the electrical percolation network is lost.¹ Recent advances in nanoparticle preparation methods have led to novel fabrication routes for metalloceramic materials that can be used as electrodes for SOFCs. One of the main beneficial characteristics of these materials is that Ni-ceria cermets can exhibit high electronic conductivity with low Ni content.³⁴

Another major cause of SOFC degradation is the change in the microstructural properties of the anode caused by redox cycling of the Ni component.³⁵ Dimensional changes associated with redox cycling (oxidation of Ni to NiO is accompanied by an increase of ~70% in solid volume) can also compromise the mechanical integrity of the entire cell, manifested by electrode cracking and delamination from the electrolyte. By reducing the amount of Ni in the cermet, the stress induced by redox cycling is minimized; therefore the degradative effect on performance is reduced.

2.2.4 Ceramic Anodes

There is growing interest in the use of ceramic anodes as alternatives to cermets.³⁶ Using an anode that is not Ni based avoids the problem of coke formation when operating on hydrocarbon fuels, intolerance to sulfur impurity, and large volume changes associated with redox cycling. Both oxygen stoichiometric and substoichiometric perovskites have been investigated. Atkinson *et al.* have reviewed the recent advances in anode technology for SOFCs, which include development of single-phase oxides with MIEC properties, such as ceria and transition-metal perovskites.³⁶

2.3 Cathodes

Cathodes in SOFCs carry out several functions within the cell: reduction of molecular oxygen, transport of charged species to the electrolyte, and distribution of the electrical current associated with the oxygen reduction reaction. At high operating temperatures, the kinetics associated with cathode reactions are sufficiently rapid that cell losses are relatively minor. Decreasing operating temperature, however, increases the polarization losses of the cell as the kinetics associated with the oxygen reduction reaction and charge transport are much slower at these low temperatures. Development of alternative cathode compositions that function effectively at lower temperatures is therefore an important step in the realization of technologically viable IT-SOFCs.

In high-temperature SOFCs, the cathodes that are commonly used operate via a TPB mechanism (gas, electrode, and electrolyte) similar to that described for anodes. These cells therefore feature a largely electronic conductor as the cathode (or electronic component in a composite with the electrolyte material), typically a perovskite (ABO_3)-structured material. A typical choice is slightly A-site deficient $(\text{La}_{1-x}\text{Sr}_x)_{1-y}\text{MnO}_{3\pm\delta}$ (LSM). These materials work well with the YSZ-based electrolytes, but care is required in the production of cells as reaction between the materials to form $\text{La}_2\text{Zr}_2\text{O}_7$ insulating phases at high temperatures can result in cell degradation. Further enhancements in cathode performance can be achieved through the use of composite materials, and YSZ–LSM composites have been extensively investigated.

On reducing the temperature of cell operation to the IT range, there are significant challenges presented in materials selection. Key processes in the cathode such as the reduction of oxygen and its incorporation and transport to the electrolyte mean that LSM-based cathodes are no longer effective. Materials with increased oxygen transport properties (oxygen reduction, surface exchange, and diffusion) are required, leading to the use of MIECs; $\text{La}_{1-x}\text{Sr}_x\text{CoO}_3$ (LSC) materials with high strontium substitutions have been identified as possessing perhaps the best transport properties in terms of both ionic conductivity and electronic conductivity. However, these materials have a high apparent TEC and are difficult to use with electrolytes such as CGO. Substituting iron for cobalt to give $\text{La}_{1-x}\text{Sr}_x\text{Co}_{1-y}\text{Fe}_y\text{O}_{3-\delta}$ (LSCF) results in a group of compounds with fast ion transport, good oxygen reduction kinetics, lower TEC, and acceptable electronic conduction. However, to produce a suitably active cathode, it has again been found advantageous to develop composites with the electrolyte material. For these materials, the phase fraction of electrolyte to cathode is critical as there is clearly a percolation threshold for both components.³⁷

The performance of IT cathodes is still an area of intense research activity, and there are a number of new materials that have been proposed. These include perovskite-type materials $\text{Sm}_{1-x}\text{Sr}_x\text{CoO}_{3-\delta}$ (SSC), $\text{Ba}_{0.5}\text{Sr}_{0.5}\text{Co}_{0.8}\text{Fe}_{0.2}\text{O}_{3-\delta}$ (BSCF), layered perovskite-related Ruddlesden–Popper

structures ($\text{La}_{n+1}\text{Ni}_n\text{O}_{3n+1}$), and double perovskites ($\text{GdBaCo}_2\text{O}_{5+\delta}$), all of which have shown encouraging performance at lower temperatures.³⁸

2.3.1 Barium Strontium Cobalt Ferrite (BSCF)

$\text{Ba}_{0.5}\text{Sr}_{0.5}\text{Co}_{0.8}\text{Fe}_{0.2}\text{O}_{3-\delta}$ is a cubic perovskite material in the $\text{BaCo}_{3-\delta}-\text{SrCo}_{3-\delta}$ system, which was originally developed for high-temperature oxygen-permeation-membrane applications. Shao and Haile³⁹ proposed this material for IT-SOFC applications and reported high power densities of $\sim 1 \text{ W cm}^{-2}$ at 600°C and 0.4 W cm^{-2} at 500°C for a BSCF/SDC/Ni-SDC cell, operated with humidified hydrogen and air. Wang *et al.*⁴⁰ calculated the TEC for the $\text{Ba}_{0.5}\text{Sr}_{0.5}\text{Co}_{0.8}\text{Fe}_{0.2}\text{O}_{3-\delta}$ composition from high-temperature XRD data and obtained a value of $11.5 \times 10^{-6} \text{ K}^{-1}$, which is comparable with those of most of the electrolytes used in SOFCs. Higher values for the TEC have been reported, with Zhu *et al.* recording TEC values over the range $19.2-22.9 \times 10^{-6} \text{ K}^{-1}$.⁴¹ In this work, they also reported on the chemical compatibility of BSCF with 8 YSZ and 20 GDC. They found no reaction up to 800°C , although severe reactions were detected above this temperature. BSCF cathodes have, however, also been tested with LSGM as the electrolyte, with no apparent reaction between these materials.⁴² Nevertheless, the best results were found when using the BSCF cathode with GDC as the electrolyte. For example, Liu *et al.* obtained $\sim 1.3 \text{ W cm}^{-2}$ at 600°C for a BSCF-GDC-Ni/GDC cell.⁴³

Li *et al.* showed by means of AC impedance spectroscopy that Nd-substituted BSCF presents higher electrical conductivity than BSCF. It also presents better electrochemical performance than the BSCF cathode; this is probably determined by a combination of the high electrical conductivity and the amount of oxide ion vacancies in the cathode.⁴⁴ However, a major drawback with BSCF is the reactivity of the Ba with atmospheric CO_2 that gradually degrades its performance.⁴⁵

2.3.2 Double Perovskites, $A_2B_2\text{O}_{6-\delta}$

$\text{GdBaCo}_2\text{O}_{5+\delta}$ (GBCO) adopts the double perovskite structure with orthorhombic symmetry, in which Co ions are coordinated in square pyramids (CoO_5) and octahedra (CoO_6), which alternate along the b -axis. The Ba cations are ordered in alternating (001) layers with oxygen vacancies mainly located along (100), in the $[\text{GdO}]_x$ planes.⁴⁶ (see Figure 9). This material was reported to have rapid oxygen transport kinetics at low temperatures and was first proposed for IT-SOFC cathode applications by Chang *et al.*⁴⁷ Using AC impedance spectroscopy, they found that GBCO cathode materials exhibit good performance at low temperatures with CGO electrolytes. Furthermore, high oxygen surface exchange ($k^* = 2.8 \times 10^{-7} \text{ cm s}^{-1}$) and reasonable oxide ion diffusivity ($D^* = 4.8 \times 10^{-10} \text{ cm}^2 \text{ s}^{-1}$) were obtained for

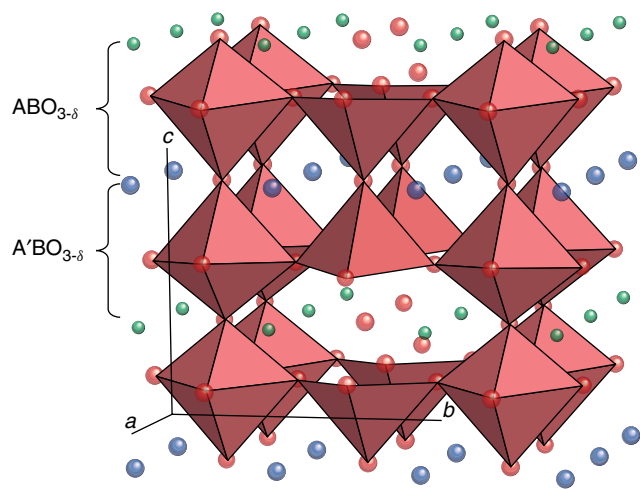


Figure 9 Representation of the double perovskite structure adopted by the generic compound $\text{AA}'\text{B}_2\text{O}_{5+\delta}$, A, blue; A', green; O, red

GBCO at 575°C .⁴⁸ These authors reported an area-specific resistance of $0.25 \Omega \text{ cm}^2$ at 625°C for a GBCO/CGO/GBCO cell. Peña-Martínez *et al.*⁴⁹ also reported no reactivity and good electrochemical performance of the GBCO cathode with an LSGM electrolyte, indicating that this is one of the most exciting alternatives to the ABO_3 cathodes discussed earlier.

The effect of substituting Sr for Ba in the GBCO material on the structural chemistry has been investigated.⁵⁰ The $\text{GdB}_{1-x}\text{Sr}_x\text{Co}_2\text{O}_{5+\delta}$ system exhibits a structural change from an orthorhombic $Pmmm$ ($x = 0$) to tetragonal $P4/mmm$ ($x = 0.2-0.6$) to a further orthorhombic $Pnma$ ($x = 1$) structure. The $x = 0.2$ and 0.6 samples exhibit higher power density than either the $x = 0$ or $x = 1$ samples when tested as an SOFC cathode, partly due to faster oxygen transport within the tetragonal structure. While the parent $\text{GdBaCo}_2\text{O}_{5+\delta}$ sample suffers from interfacial reaction with LSGM and CGO electrolytes at 1100°C , substituting Sr for Ba greatly improves the chemical stability of $\text{GdB}_{1-x}\text{Sr}_x\text{Co}_2\text{O}_{5+\delta}$.

The analogous material $\text{PrBaCo}_2\text{O}_{5+\delta}$ (PBCO) has also been suggested as an SOFC cathode because of its unusually rapid oxygen transport kinetics at low temperatures ($300-500^\circ\text{C}$).⁵¹ Zhu *et al.*⁵² demonstrated the suitability of PBCO for IT-SOFC applications. They performed electrochemical measurements on a PBCG/SDC/Ni-SDC single cell, obtaining a maximum power density of $\sim 850 \text{ mW cm}^{-2}$ at 650°C . Moreover, the samarium derivative ($\text{SmBaCo}_2\text{O}_{5+\delta}$) presents good electrochemical properties and has also been proposed as a cathode material for IT-SOFCs.⁵³

2.3.3 Mixed Conducting Composites

Composite cathodes generally include an electronically conducting material and a solid electrolyte. By the introduction of the solid electrolyte, the electrochemical reaction zone is enlarged, and the microstructural stability and

adherence to the electrolyte are therefore enhanced. The incorporation of crystalline nanocatalysts onto the cathode could also improve the performance of the electrodes.⁵⁴

The most studied composite cathode to date is LSM–YSZ.^{55–58} The connectivity of the electronically conducting LSM and ionically conducting YSZ phases is crucial to produce a mixed conducting composite, because the ionic conductivity of LSM and the electronic conductivity of YSZ are negligible under normal SOFC operating conditions. Results from electrochemical measurements performed by Haanappel *et al.*⁵⁹ showed the highest performance when using an LSM/YSZ mass ratio of 50/50. Princivalle and Djurado reported on the fabrication of LSM–YSZ composite films prepared by electrostatic spray deposition (ESD), with various compositions and microstructures.⁶⁰ By this technique, they prepared LSM–YSZ composites with simultaneous graded composition and porosity by adjusting the YSZ content and nozzle-to-substrate distance at a constant substrate temperature. Electrical and electrochemical properties of these promising composites are still unknown. Huang *et al.* also reported an improvement on the performance of LSM-based cathodes through B-site substitution with Co, forming a La_{0.8}Sr_{0.2}Mn_{0.75}Co_{0.25}O₃–YSZ composite.⁶¹

Composites of LSM with other electrolyte materials such as scandia-stabilized zirconia (ScSZ),^{62,63} CGO,⁶⁴ Ce_{0.7}Bi_{0.3}O₂ (CBO),⁶⁵ or yttria-stabilized bismuth oxide (YSB)⁶⁶ have also been shown to improve the cathode performance. Another interesting manganite-based composite is the La_{0.8}Sr_{0.2}Sc_{0.1}Mn_{0.9}O_{3–δ}–ScSZ. Using a mass ratio of 80/20, Zheng *et al.* showed high power densities of about 1.2 W cm⁻² at 800 °C for an anode-supported Ni–ScSZ/ScSZ/La_{0.8}Sr_{0.2}Sc_{0.1}Mn_{0.9}O_{3–δ}–ScSZ cell.⁶⁷

MIEC used in combination with the electrolyte material (usually SDC or GDC) to form a composite also present superior performance in comparison with the pure MIEC, as shown, for example, in the Sm_{0.5}Sr_{0.5}CoO₃–Sm_{0.2}Ce_{0.8}O_{1.9} (75/25 wt %)⁶⁸ and SrCo_{0.8}Fe_{0.2}O_{3–δ}–La_{0.45}Ce_{0.55}O_{2–δ} (50/50 wt %)⁶⁹ composites. Adding an ionic conducting phase to the LSCF electrode also reduces the cathode polarization.³⁷

Camaratta *et al.* reported on the Bi₂Ru₂O₇–Bi_{1.6}Er_{0.4}O₃ composite, applying pure Bi₂Ru₂O₇, a pyrochlore oxide, as a current collector to the electrode surfaces.⁷⁰ The lowest values of ASR they obtained were 0.73 Ω cm² at 500 °C and 0.03 Ω cm² at 700 °C, two of the lowest SOFC electrode ASR values reported to date, making this composite a good candidate for IT-SOFCs.

Concerning the Ruddlesden–Popper series, Laberty *et al.* reported on the performance of SOFC cathodes with lanthanum-nickelate-based composites.⁷¹ They showed that lanthanum nickelate performs poorly when used as a single-phase cathode in yttria-stabilized zirconia-based air–H₂ button cells at 800 °C. However, high power densities of up to 2.2 W cm⁻² were measured using a La₂NiO_{4+δ}–SDC composite bilayer cathode.

2.4 Interconnects

The interconnect (also referred to as the *bipolar plate*) in planar fuel cells performs the vital role of separating the fuel from air, collecting the current from the electrodes, conducting the electrical current between each layer of the stack, distributing reactant gas evenly across the face of each electrode, and providing mechanical support to the cell and stack structure. The component should have high bulk electrical conductivity (several orders of magnitude greater conductivity than that of the electrolyte); low contact resistance with the electrodes, the formation of scales on metallic interconnects being a particular issue; good thermal conductivity—efficient removal of heat from the electrodes is vital for maintaining an even temperature distribution; adequate chemical and thermal stability: the range of oxygen partial pressures that interconnects are exposed to is particularly wide and leads to a large oxygen partial pressure gradient between the two sides, which can range from 0.21 atm on the cathode side (in air) to as low as 10⁻¹⁹ atm at the anode; very low permeability to reactant gases; good mechanical strength; corrosion and creep resistance; thin and lightweight construction; easy manufacturability; and low cost. These requirements are a challenge for any class of material and are made more difficult due to the temperature of operation. Figure 5 shows the temperature range of operation for the three main classes of interconnect materials: ceramics (i.e., La(Ca)CrO₃), high-performance alloys, and ferritic stainless steels.

For HT-SOFCs, the interconnect must be either a ceramic or a special high-Cr alloy; both options can make the interconnect the most expensive component of the stack on a materials value basis. The most popular ceramic option is based on the perovskite-structured LaCrO₃, which is typically doped with Sr or Ca in order to reduce its sintering temperature and increase conductivity.⁷² These materials do not possess sufficiently high electrical conductivity for operation in the IT-SOFC temperature range.

Metallic interconnects are more robust and can withstand rapid temperature change associated with fast start-up; they also make it easier to incorporate internal structure such as internal manifolding, flow-field geometries, or sealing wells into the stack. Examples include the chromium-based alloy, Ducrolloy, from Plansee (Cr–5Fe–1Y₂O₃) and the nickel-based alloy, Inconel 600. In large part, it is the ability of metallic interconnects to form conducting chromia (Cr₂O₃) containing scales at the surface upon oxidation that protects the metal from further corrosion, as opposed to the insulating Al₂O₃ and SiO₂ phases that can also form. However, Cr-containing alloys have the disadvantage that volatile chromium compounds (CrO₃ or CrO₂(OH)₂) can form, which accelerate degradation of the interconnect, and more importantly degrade cell performance by forming phases at the surface of electrodes, and particularly the cathode, which block the cathodic reaction sites. Coating interconnects significantly retards corrosion and vaporization

of chromium species. Coating materials include $\text{La}(\text{Ni},\text{Fe})\text{O}_3$, $(\text{La},\text{Sr}/\text{Ca})\text{CrO}_3$, $(\text{La},\text{Sr}/\text{Ca})\text{MnO}_3$, $(\text{Y},\text{Ca})\text{MnO}_3$, and CeO_2 .⁷³

Alternatively, advanced alloys specially designed for SOFC applications can be used. Incorporation of Mn in Fe–Cr alloys can lead to the formation of double-layer oxide scale, composed of a top layer of $(\text{Mn},\text{Cr})_3\text{O}_4$ and underlayer of Cr_2O_3 .⁷⁴ This retards Cr evaporation and improves electrical conductivity and contact resistance. Incorporation of elements such as Y, La, and Zr can improve oxidation resistance, conductivity, and scale adherence,⁷⁵ while the addition of Ti has been shown to form better conducting phases such as Ti-doped Cr_2O_3 and TiO_2 .⁷⁶

IT-SOFC operation allows relatively low-cost ferritic (low TEC) stainless steel alloys to be used. These steels also owe their corrosion resistance to the formation of chromia at the surface; however, at these temperatures Cr vaporization is not as extreme as that for HT-SOFCs, although it is still a notable source of performance deactivation. Ferritic steel has the advantage of high strength, machinability, closely matched TEC with the electrolyte material (i.e., both ferritic stainless steel and CGO have a TEC of 12.5×10^{-6} K), and low cost. Ferritic stainless steel has also been used as the mechanical support for IT-SOFCs, where a perforated (porous) ferritic stainless steel foil acts as the support for thin anode, electrolyte, and cathode layers (cf configuration in Figure 4). The range of metallic alloys that have been investigated for SOFC interconnects is substantial and has been extensively reviewed.⁷³

2.5 Seals

Seals are necessary to stop fuel and air mixing within a fuel cell as well as to avoid leakage from the edges of cells; in certain circumstances they also act to help bond the stack together. Seals come in two main varieties: (i) bonded seals, which do not require a load during operation and (ii) compressive seals, which require a load to be applied during operation. In either case, the seal should be an electrical insulator that is chemically compatible with the gaseous environment and materials with which it is in contact, and should have a TEC that is compatible with the adjacent components. The last requirement is particularly important for achieving fast start-up and shutdown rates since thermally induced stresses are the greatest in seals during rapid temperature transients.

Bonded seals tend to be glass (silicates, borosilicates, boroaluminosilicates, etc.), or glass–ceramic materials, and effectively “glue” the stack components together. These materials are inherently brittle and prone to cracking if the TEC is not carefully matched to that of the adjacent components. In order to operate as an effective seal, the fuel cell must operate above the glass transition temperature, T_g . For most glasses, T_g is above $\sim 625^\circ\text{C}$, precluding the use of bonded seals below this temperature.

Compressive seals act like a conventional gasket and do not bond to the interconnect or cell. To maintain a gastight seal, a compressive force must be applied at all times and the stack components must be able to withstand this force. This means that a load frame needs to be incorporated into the stack design. Use of compliant compressive seals means that components are free to expand and contract during thermal cycling; there is therefore much more scope for allowing differences in TEC, which provides a wider choice in materials selection.

One approach is to use metal gaskets such as gold; however, establishing the correct balance between strength and ductility is difficult and the materials are expensive. An alternative is to use mica-based (phyllosilicate) sealants.⁷⁷ These inorganic compounds (general formula $\text{AB}_{2-3}(\text{X},\text{Si})_4\text{O}_{10}(\text{O},\text{F},\text{OH})_2$) are composed of sheets of silicate tetrahedrons and exhibit very high electrical resistivity. Common examples include muscovite ($\text{KAl}_2-(\text{AlSi}_3\text{O}_{10})(\text{F},\text{OH})_2$), phlogopite ($\text{KMg}_3(\text{AlSi}_3\text{O}_{10})(\text{OH})_2$), and vermiculite ($(\text{MgFe},\text{Al})_3(\text{Al},\text{Si}_4\text{O}_{10})(\text{OH})_2$) such as the commercially available Thermiculite 815, which incorporates a stainless steel inlay. Although mica-based seals can operate in the HT-SOFC temperature regime, their compliant nature requires constant force to be applied throughout the course of operation. Active compression, using tie bolts, for example, is much less of an issue for IT-SOFCs where metallic structural components can be used; however, above 650°C , bolts may still creep.

Extensive work by Chou and coworkers (for example, Refs. 78 and 79) has advanced the development of mica-based compressive seals by investigating factors such as compressive force, pre-compression, durability, glass volume fraction, thermal cycling, mica thickness, interfacial contact, and interaction (with Cr and NiO).

Arguably, the most difficult engineering challenge in developing planar SOFC stacks involves ensuring gastight operation. The IT-SOFC regime of operation reduces the stresses within the stack and opens the way to a broader range of materials. A comprehensive review of sealants for SOFCs has been compiled by Fergus.⁸⁰

3 IT-SOFC PERFORMANCE DURABILITY

Section 2 described the range of materials that have been applied in the development of each component of the IT-SOFC. Probably, more important than the absolute properties and performance of each of these components is the way in which they interact with each other when operating as a working device on a technologically relevant scale. While impressive performance ($> 1 \text{ W cm}^{-2}$) is routinely reported for lab-scale IT-SOFC devices, achieving this on a practical

scale for thousands of hours without appreciable performance degradation is a much greater challenge.

Performance degradation originates from various mechanisms; it may involve all of the main components of the stack (i.e., electrolyte, electrodes, and interconnects) and may be exacerbated or remedied by excursions from steady-state operation, such as the cycling of temperature, electrical load, fuel steam content, and electrode oxidation state. Degradation occurs through mechanisms explicit to each component, as well as through the interaction between components. It is likely that several degradation mechanisms will be contributing to the overall decline in performance; these mechanisms may also be coupled.

Lower temperature operation has the potential to improve durability, since many of the degradation mechanisms that affect SOFCs are antagonized by high temperatures. TEC mismatch between components becomes an increasing problem with temperature, as is creep, which can lead to adverse stresses in the stack, resulting in delamination and cracking. Volatilization of Cr species from interconnects, seal degradation, corrosion, and Ni coarsening are likely to worsen with increasing temperature, while degradation associated with each thermal cycle and the likelihood of catastrophic failure with cycling are greater at higher temperatures.

While lower temperature SOFC operation is, in general, expected to improve performance durability, certain factors, such as the effect of sulfur poisoning from impurities in the fuel and coke formation management, are likely to be more of a challenge, and require further study.

4 CONCLUSIONS

The future of fuel cells and the emergence of a “hydrogen economy” are often viewed as intimately associated. Significant advancements in hydrogen storage technologies and huge investment in hydrogen distribution infrastructure are necessary in order to realize a hydrogen economy. In order for fuel cells not to be bound by the uncertain future of “hydrogen”, fuel cells need to be able to operate effectively on alternative fuels such as natural gas, alcohols, biofuels, LPG, and military logistic fuels. Advances in the chemistry and processing of inorganic materials are allowing the operating temperature of SOFCs to be lowered into the so-called IT region of 500–750 °C. The IT-SOFC offers an attractive fuel cell option that is much more fuel flexible than low-temperature fuel cells, suitable for a wide range of applications, and which can also be used in any future hydrogen economy, should one emerge. Maintaining the ability to operate on hydrocarbon fuels, either directly or with a minimum of fuel processing, and producing high-quality heat, the IT-SOFC opens up a new range of applications and opportunities for SOFCs. IT-SOFCs have the potential to be the fuel cell technology with the simplest overall system,

and are a contender to be the first fuel cell technology to reach mass market.

As with all fuel cells, cost must be reduced to compete in the market with incumbent technologies. Use of less, and lower cost, material is necessary; moving to lower temperature operation represents a significant step in this direction. Technical challenges still to be addressed are largely focussed on demonstrating commercially meaningful levels of cell, stack, and systems durability, under realistic operating conditions for a range of applications. This is being supported by fundamental studies to improve our understanding of processes, such as electrode sintering, anode–fuel interaction, and electrocatalyst poisoning, and the mechanical properties of electrolytes and support structures.

5 RELATED ARTICLES

H₂ Production from Renewables; Enzymes and Microbes for Energy Production by Fuel Cells; Proton Exchange Membranes for Fuel Cells; Direct Ethanol Fuel Cells; Molecular Catalysis for Fuel Cells.

6 ABBREVIATIONS AND ACRONYMS

APU = auxiliary power unit; AFC = alkaline fuel cells; ASR = area-specific resistance; BoP = balance-of-plant; CHP = combined heat and power; ESD = electrostatic spray deposition; FCC = face centred cubic; HT-SOFC = High-temperature solid oxide fuel cell; IT = intermediate-temperature; MIEC = mixed ionic–electronic conduction/conductor/conducting; MIEC = mixed ionic–electronic conduction; OCV = open circuit voltage; PAFC = phosphoric acid fuel cells; PEFC = polymer electrolyte fuel cells; PEN = positive–electrolyte–negative; SOFC = solid oxide fuel cell; SPFC = solid proton fuel cell; SSZ = Scandia-stabilized zirconia; TEC = thermal expansion coefficient; TPB = triple phase boundary; WGS = water–gas shift; YSZ = yttria-stabilized zirconia.

7 REFERENCES

1. R. M. Ormerod, *Chem. Soc. Rev.*, 2003, **32**, 17.
2. N. P. Brandon and D. J. Brett, *Phil. Trans. R. Soc. A*, 2006, **364**, 147.
3. A. D. Hawkes, I. Staffell, D. L. Brett, and N. P. Brandon, *Energy Environ. Sci.*, 2009, **2**, 729.
4. B. C. H. Steele, *J. Mater. Sci.*, 2001, **36**, 1053.

5. D. J. L. Brett, A. Atkinson, N. P. Brandon, and S. J. Skinner, *Chem. Soc. Rev.*, 2008, **37**, 1568.
6. D. J. L. Brett, P. Aguiar, N. P. Brandon, R. Bull, R. C. Galloway, G. W. Hayes, K. Lillie, C. Mellors, C. Smith, and A. R. Tilley, *J. Power Sources*, 2006, **157**, 782.
7. J. B. Goodenough, *Annu. Rev. Mater. Res.*, 2003, **33**, 91.
8. K. C. Wincewicz and J. S. Cooper, *J. Power Sources*, 2005, **140**, 280.
9. B. C. H. Steele, *Solid State Ionics*, 1995, **75**, 157.
10. T. Kawada and J. Mizusaki, 'Current Electrolytes and Catalysts', in 'Handbook of Fuel Cells—Fundamentals, Technology and Applications', eds. W. Vielstich, H. A. Gasteiger, and A. Lamm, John Wiley & Sons, New York, 2003, Vol. 4, p. 987.
11. B. C. H. Steele, *Solid State Ionics*, 2000, **134**, 3.
12. J. A. Kilner, *Chem. Lett.*, 2008, **37**, 1012.
13. J. A. Kilner, *Solid State Ionics*, 2000, **129**, 13.
14. S. Wang, H. Inaba, H. Tagawa, M. Dokiya, and T. Hashimoto, *Solid State Ionics*, 1998, **107**, 73.
15. M. Godickemeier, K. Sasaki, L. J. Gauckler, and I. Riess, *Solid State Ionics*, 1996, **86**, 691.
16. T. Ishihara, H. Matsuda, and Y. Takata, *J. Am. Chem. Soc.*, 1994, **116**, 3801.
17. E. Kendrick, M. S. Islam, and P. R. Slater, *J. Mater. Chem.*, 2007, **17**, 3104.
18. P. Lacorre, F. Goutenoire, O. Bohnke, R. Retoux, and Y. Laligant, *Nature*, 2000, **404**, 856.
19. J. E. H. Sansom, J. R. Tolchard, M. S. Islam, D. Apperley, and P. R. Slater, *J. Mater. Chem.*, 2006, **16**, 1410.
20. H. Yoshioka and S. Tanase, *Solid State Ionics*, 2005, **176**, 2395.
21. H. Iwahara, H. Uchida, K. Ono, and K. Ogaki, *J. Electrochem. Soc.*, 1988, **135**, 529.
22. R. Haugsrud and T. Norby, *J. Am. Ceram. Soc.*, 2007, **90**, 1116.
23. R. Haugsrud and T. Norby, *Nat. Mater.*, 2006, **5**, 193.
24. K. D. Kreuer, *Annu. Rev. Mater. Res.*, 2003, **33**, 333.
25. J. Garcia-Barriocanal, A. Rivera-Calzada, M. Varela, Z. Sefrioui, E. Iborra, C. Leon, S. J. Pennycook, and J. Santamaría, *Science*, 2008, **321**, 676.
26. J. A. Kilner, *Nat. Mater.*, 2008, **7**, 838.
27. I. Kosacki, C. M. Rouleau, P. F. Becher, J. Bentley, and D. H. Lowndes, *Solid State Ionics*, 2005, **176**, 1319.
28. C. Korte, A. Peters, J. Janek, D. Hesse, and N. Kazharov, *Phys. Chem. Chem. Phys.*, 2008, **10**, 4623.
29. G. J. Offer, J. Mermelstein, E. Brightman, and N. P. Brandon, *J. Am. Ceram. Soc.*, 2009, **92**, 763.
30. M. Y. Gong, X. B. Liu, J. Trembly, and C. Johnson, *J. Power Sources*, 2007, **168**, 289.
31. D. J. L. Brett, A. Atkinson, D. Cumming, E. Ramirez-Cabrera, R. Rudkin, and N. P. Brandon, *Chem. Eng. Sci.*, 2005, **60**, 5649.
32. S. McIntosh and R. J. Gorte, *Chem. Rev.*, 2004, **104**, 4845.
33. Z. Cheng, J. H. Wang, and M. Liu, 'Anodes', in 'Solid Oxide Fuel Cells—Materials, Properties and Performance', eds. J. Fergus, R. Hui, X. Li, D. P. Wilkinson, J. Zhang, and S. Lee, CRC Press, 2008, Vol. 2, p. 74.
34. P. Jasinski, T. Sukuki, T. V. Petrovsky, and H. U. Anderson, *Electrochim. Solid-State Lett.*, 2005, **8**, A219.
35. D. Sarantidis and A. Atkinson, *Fuel Cells*, 2007, **7**, 246.
36. A. Atkinson, S. Barnett, R. J. Gorte, J. T. S. Irvine, A. J. McEvoy, M. Mogensen, S. C. Singhal, and J. Vohs, *Nat. Mater.*, 2004, **3**, 17.
37. V. Dusastre and J. A. Kilner, *Solid State Ionics*, 1999, **126**, 163.
38. A. Tarancón, M. Burriel, J. Santiso, S. J. Skinner, and J. A. Kilner, *J. Mater. Chem.*, (accepted). DOI:10.1039/b922430k.
39. Z. P. Shao and S. M. Haile, *Nature*, 2004, **431**, 170.
40. H. H. Wang, C. Tablet, A. Feldhoff, and J. Caro, *J. Membrane Sci.*, 2005, **262**, 20.
41. Q. S. Zhu, T. A. Jin, and Y. Wang, *Solid State Ionics*, 2006, **177**, 1199.
42. J. Pena-Martinez, D. Marrero-Lopez, J. C. Ruiz-Morales, B. E. Buergler, P. Nunez, and L. J. Gauckler, *Solid State Ionics*, 2006, **177**, 2143.
43. Q. L. Liu, K. A. Khor, and S. H. Chan, *J. Power Sources*, 2006, **161**, 123.
44. S. Y. Li, Z. Lu, X. Q. Huang, and W. H. Su, *Solid State Ionics*, 2008, **178**, 1853.
45. Z. Yáng, A. S. Harvey, and L. J. Gauckler, *Scr. Mater.*, 2009, **61**, 1083.
46. A. Maignan, C. Martin, D. Pelloquin, N. Nguyen, and B. Raveau, *J. Solid State Chem.*, 1999, **142**, 247.
47. A. M. Chang, S. J. Skinner, and J. A. Kilner, *Solid State Ionics*, 2006, **177**, 2009.
48. A. Tarancón, S. J. Skinner, R. J. Chater, F. Hernández-Ramírez, and J. A. Kilner, *J. Mat. Chem.*, 2007, **17**, 3175.
49. J. Peña-Martínez, A. Tarancón, D. Marrero-López, J. C. Ruiz-Morales, and P. Núñez, *Fuel Cells*, 2008, **8**, 351.
50. J. H. Kim, F. Prado, and A. Manthiram, *J. Electrochem. Soc.*, 2008, **155**, B1023.
51. G. Kim, S. Wang, A. J. Jacobson, L. Reimus, P. Brodersen, and C. A. Mims, *J. Mat. Chem.*, 2007, **17**, 2500.
52. C. J. Zhu, X. Liu, C. Yi, D. Yan, and W. Su, *J. Power Sources*, 2008, **185**, 193.
53. Q. J. Zhou, T. M. He, and Y. Ji, *J. Power Sources*, 2008, **185**, 754.
54. T. Z. Sholklapper, V. Radmilovic, C. P. Jacobson, S. J. Visco, and L. C. De Jonghe, *J. Power Sources*, 2008, **175**, 206.
55. S. McIntosh, S. B. Adler, J. M. Vohs, and R. J. Gorte, *Electrochim. Solid-State Lett.*, 2004, **7**, A111.
56. M. J. L. Østergård, C. Clausen, C. Bagger, and M. Mogensen, *Electrochim. Acta*, 1995, **40**, 1971.
57. M. Juhl, S. Primdahl, C. Manon, and M. Mogensen, *J. Power Sources*, 1996, **61**, 173.

58. E. P. Murray, T. Tsai, and S. A. Barnett, *Solid State Ionics*, 1998, **110**, 235.
59. V. A. C. Haanappel, J. Mertens, D. Rutenbeck, C. Tropatz, W. Herzhof, D. Sebold, and F. Tietz, *J. Power Sources*, 2005, **141**, 216.
60. A. Princivalle and E. Djurado, *Solid State Ionics*, 2008, **179**, 1921.
61. Y. Y. Huang, J. M. Vohs, and R. J. Gorte, *J. Electrochem. Soc.*, 2006, **153**, A951.
62. Z. W. Wang, M. Cheng, Y. Dong, M. Zhang, and H. Zhang, *Solid State Ionics*, 2005, **176**, 2555.
63. A. Hagiwara, N. Hobara, K. Takizawa, K. Sato, H. Abe, and M. Naito, *Solid State Ionics*, 2006, **177**, 2967.
64. N. T. Hart, N. P. Brandon, M. J. Day, and N. Lapeña-Rey, *J. Power Sources*, 2002, **106**, 42.
65. H. Zhao, L. H. Huo, and S. Gao, *J. Power Sources*, 2004, **125**, 149.
66. Z. Y. Jiang, L. Zhang, K. Feng, and C. Xia, *J. Power Sources*, 2008, **185**, 40.
67. Y. Zheng, R. Ran, H. Gu, R. Cai, and Z. Shao, *J. Power Sources*, 2008, **185**, 641.
68. X. Zhang, M. Robertson, S. Yick, C. Deces-Petit, E. Styles, W. Qu, Y. Xie, R. Hui, J. Roller, O. Kesler, R. Maric, and D. Ghosh, *J. Power Sources*, 2006, **160**, 1211.
69. X. D. Zhu, K. N. Sun, N. Q. Zhang, X. B. Chen, L. J. Wu, and C. Jiad, *Electrochim. Commun.*, 2007, **9**, 431.
70. M. Camaratta and E. Wachsman, *J. Electrochem. Soc.*, 2008, **155**, B135.
71. C. Laberty, F. Zhao, K. E. Swider-Lyons, and A. V. Virkar, *Electrochim. Solid-State Lett.*, 2007, **10**, B170.
72. W. Z. Zhu and S. C. Deevi, *Mater. Sci. Eng.*, 2003, **348**, 227.
73. J. W. Fergus, *Mater. Sci. Eng.*, 2005, **397**, 271.
74. Z. Yang, J. S. Hardy, M. S. Walker, G. Xia, S. P. Simner, and J. W. Stevenson, *J. Electrochem. Soc.*, 2004, **151**, A1825.
75. W. Qu, J. Li, D. G. Ivey, and J. M. Hill, *J. Power Sources*, 2006, **157**, 335.
76. S. J. Geng and J. H. Zhu, *J. Power Sources*, 2006, **160**, 1009.
77. S. P. Simner and J. W. Stevenson, *J. Power Sources*, 2001, **102**, 310.
78. Y. S. Chou, J. W. Stevenson, and R. N. Gow, *J. Power Sources*, 2007, **168**, 426.
79. Y. S. Chou, J. W. Stevenson, and R. N. Gow, *J. Power Sources*, 2007, **170**, 395.
80. J. W. Fergus, *J. Power Sources*, 2005, **147**, 46.

Some Computational Challenges in Energy Research

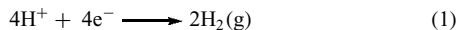
Victor S. Batista

Yale University, New Haven, CT, USA

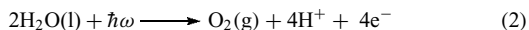
1	Introduction	191
2	Functionalization of Semiconductor Surfaces	192
3	Proton-Coupled Electron Transfer	194
4	Rectification of Interfacial Electron Transfer	195
5	Fuel Formation	196
6	Conclusions	197
7	Related Articles	197
8	Abbreviations and Acronyms	197
9	References	197

1 INTRODUCTION

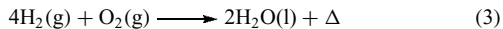
The development of cheap, robust, and efficient photocatalytic cells for water oxidation would allow the sustainable production of fuel from renewable resources.^{1–4} An example of such a cell is shown in Figure 1, where hydrogen evolution at the cathode



is thermodynamically driven by photoanodic water oxidation:



The underlying photocatalytic process generates fuel (e.g., hydrogen) from water by using solar light to extract cheap electrons and protons from a renewable resource (e.g., water). The generated fuel is environmentally benign since, upon combustion, it generates only heat and water as follows:



The development of such type of photocatalytic solar cells based on inexpensive (e.g., earth-abundant) materials has been a long-standing challenge in photoelectrochemistry research,⁵ and significant effort has been invested since the discovery of ultraviolet (UV) water oxidation on *n*-TiO₂ electrodes.⁶ However, for many years, progress in the field has

been hindered by the lack of efficient catalytic materials as well as by the lack of fundamental understanding of the processes that limit the efficiency of the conversion mechanisms.

The main challenge has been to identify catalysts able to carry out the necessary multielectron transformations at energies and rates consistent with solar irradiance. This implies designing surface-bound complexes for catalyst turnover where solar irradiance is rate limiting, activating these catalysts by multiple single-electron injection events, designing cells with redox potentials sufficiently high as to drive the desired half-reactions, and designing and assembling robust molecular components. Such a design problem requires fundamental understanding of the factors affecting the elementary steps (numbered in Figure 1), including (1) photoexcitation; (2) interfacial electron transfer (IET) and surface charge separation; (3) charge transport; (4) storage of oxidizing equivalents for catalysis; and (5) irreversible carrier collection by sacrificial acceptors, or fuel-forming reactions at the cathode. The characterization of all these processes clearly surpasses the limits of traditional disciplines and therefore calls upon researchers to establish collaborative research programs combining synthesis, computational modeling, electrochemistry, and spectroscopy.

In recent years, we have witnessed a flurry of interest in the development of catalysts for water oxidation^{7–22} as well as on the development of fundamental studies of photocatalysis based on semiconductor surfaces.^{23,24} Current efforts are focused on the development of more efficient catalysts based on earth-abundant materials and on molecular

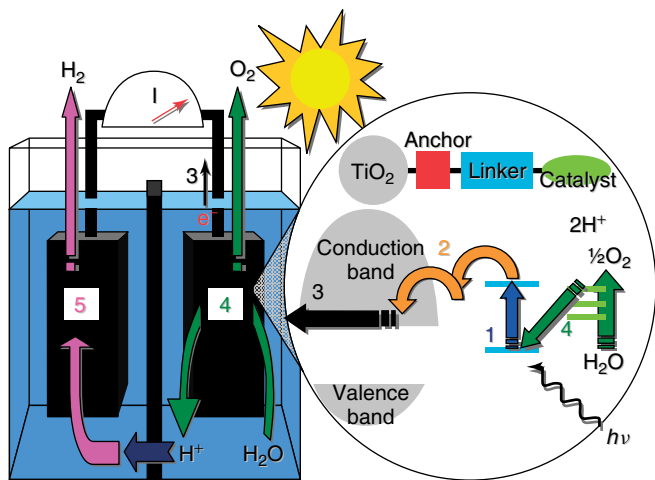


Figure 1 Photocatalytic cell for water oxidation and hydrogen evolution with schematic of elementary photoanodic processes

assemblies to efficiently couple multielectron photoanodic processes to fuel production cathodic processes. This article reviews recent advances in the field, with emphasis on computational work for the development and characterization of catalytic surfaces based on nanoporous TiO₂ thin films sensitized with manganese catalysts. The reviewed studies have been integrated with synthesis, electrochemistry, and spectroscopy in an interdisciplinary effort to advance our understanding of structure/function relationships in catalytic materials. The main aim has been to provide understanding of the fundamental processes that limit the efficiency of the reaction mechanisms and to develop guidelines for the design of novel photocatalytic materials for fuel production.

2 FUNCTIONALIZATION OF SEMICONDUCTOR SURFACES

Surface functionalization of nanoporous TiO₂ thin films is used in dye-sensitized solar cells (DSSCs) to maximize light harvesting.²⁵ Dye molecules on TiO₂ shift the absorption spectrum of the semiconductor to the visible region, leading to the efficient injection of electrons into the TiO₂ conduction band upon visible light absorption. The holes h^+ left behind usually have limited redox potentials since they are localized in the oxidized adsorbate molecule, rather than in the semiconductor valence band. Therefore, while efficient for light harvesting, such an approach has not led to photocatalysis.

Achieving photocatalysis with maximal light harvesting, requires sophisticated *surface catalysts* for IET. Recent studies have focused on the functionalization of TiO₂ surfaces by covalent attachment of biomimetic high-valent oxo-Mn complexes (Figure 2). These are known to be efficient catalysts

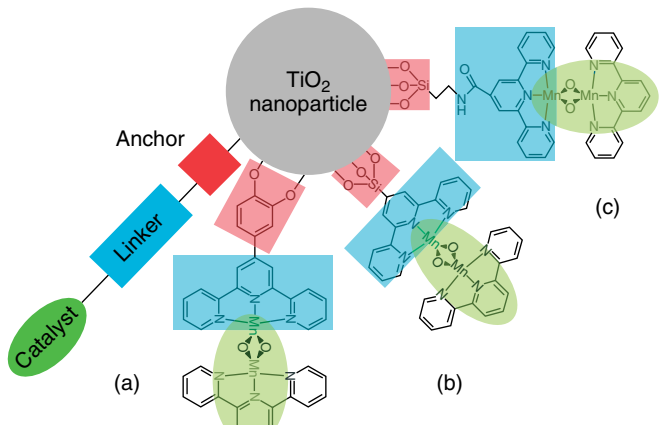
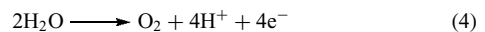
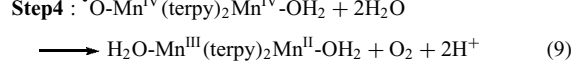
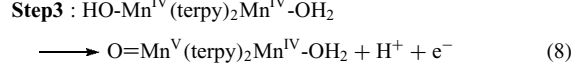
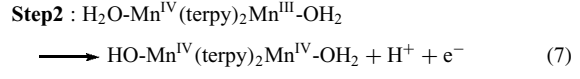
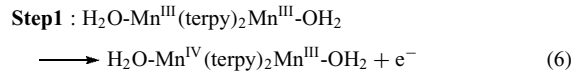
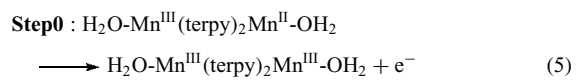


Figure 2 TiO₂ NP functionalized with Mn dimers by using various linkers including catechol (a) and siloxane-based (b and c) linkers

for selective C–H oxygenation,²⁶ and water splitting to O₂.¹⁰ Manganese catalysts are inspired by Nature, where only oxo-Mn complexes achieve redox potentials high enough to form O₂ at the oxygen-evolving complex (OEC) of photosystem II, as follows:^{27–30}



The following mechanism illustrates the underlying catalytic process of water oxidation by formation of high-valent Mn^{IV}Mn^{IV}–O[•] species, as illustrated for the complex [H₂O(terpy)Mn^{III}(O)₂Mn^{IV}(terpy)H₂O]³⁺ (terpy, 2,2':6,2''-terpyridine):



The Mn^{IV}Mn^{IV}–O[•] species is thought to be the activated form of the catalyst, normally formed by reaction of the Mn dimer with a primary oxidant (e.g., oxone), storing the four oxidizing equivalents that are necessary to oxidize water. In the photocatalytic case (Figure 1), however, such a species is formed through multiple one-electron injection processes and electron collection by the TiO₂ anode. The activation process thus avoids the use of a primary oxidant, yielding

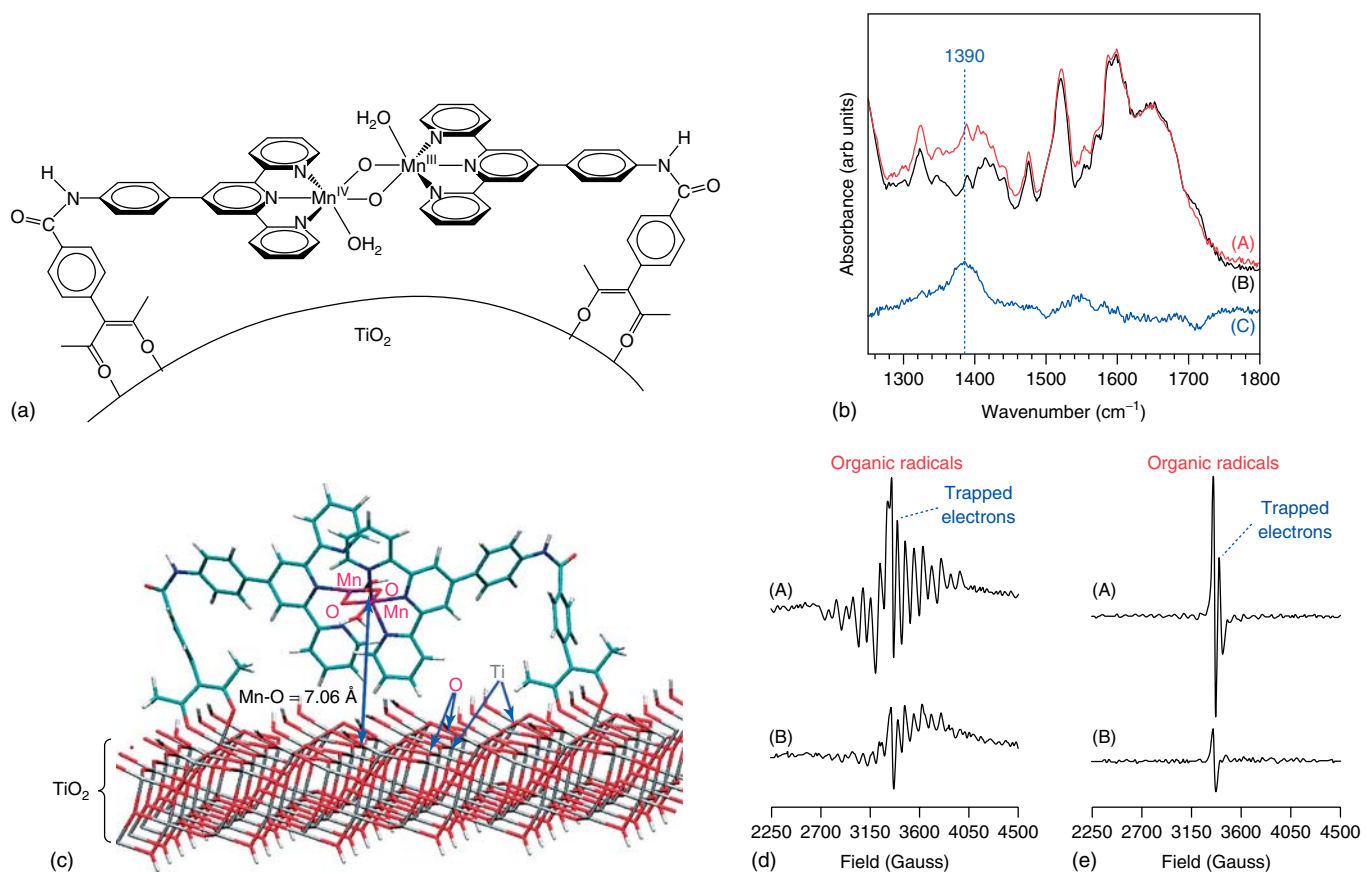


Figure 3 (a) DFT QM/MM configuration of **Mn-L-TiO₂**. (b) attenuated total reflection infrared (ATR-IR) spectra of (A) **Mn-L-P25**; (B) **Mn^{II}-L-P25**; and (C) shows the difference between spectra (A) and (B). (c) Resonances of organic radicals and TiO₂ lattice-trapped electrons (Ti³⁺) are labeled. (d,e) EPR difference spectra of (A) **Mn-L-P25** and (B) **Mn-L-D70**. (d) Light-minus-dark EPR spectra. (e) Postillumination dark minus preillumination dark EPR spectra. (Reproduced from Ref. 31. © American Chemical Society.)

a general approach for green oxidation chemistry driven by solar light.

Recent work has been focused on the direct deposition⁹ as well as on the covalent attachment³¹ of the Mn dimer [H₂O(terpy)Mn^{III}(μ-O)₂Mn^{IV}(terpy)H₂O]^{](NO₃)₃, (terpy, 2,2':6',2''-terpyridine) onto nanoporous semiconductor surfaces by using a robust chromophoric linker **L**, a phenylterpy ligand attached to a 3-phenyl-acetylacetone anchoring moiety via an amide bond (Figure 3). The resulting covalent binding to the semiconductor surface has been characterized by using quantum mechanics/molecular mechanics (QM/MM) hybrid methods in conjunction with UV-visible, IR (infrared), and EPR (electron paramagnetic resonance) spectroscopy. In addition, these studies have shown that **L** absorbs visible light, leading to photoinduced interfacial electron transfer into the semiconductor conduction band, reversibly advancing the Mn complex to the Mn(IV,IV) state. The reported work also showed that, in the absence of electron scavengers, the injected electron recombines back to form the Mn(III,IV) state in the dark.}

2.1 Simulations of Interfacial Electron Transfer

Ab initio DFT (density functional theory) molecular dynamics simulations have been combined with quantum dynamics calculations of electronic relaxation to investigate IET in sensitized semiconductor nanostructures, providing fundamental understanding of IET at the detailed molecular level.^{9,31–39} The characteristic times for the excited-state IET from adsorbate complexes have been shown to be consistent with terahertz experiments and with ultrafast measurements in TiO₂ sensitized by small organic molecules, including bisisonicotinic acid on rutile and alizarin on TiO₂.^{40,41}

2.2 Interfacial Electron Transfer

Quantum dynamics simulations have provided valuable insights on the nature of interfacial electron transfer processes leading to the activation of Mn catalysts anchored onto TiO₂ surfaces. For example, Figure 4 shows a series of snapshots for the distribution of electron density as it evolves

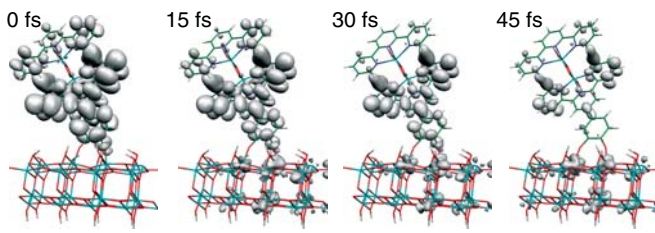


Figure 4 Snapshots, at 15-fs intervals, of the electronic charge distribution corresponding to IET after visible excitation (508 nm) of the catalyst surface complex depicted in Figure 2(a). Only the center semiconductor block is shown to allow a detailed view of the time-dependent charge distribution

during the early time dynamics of interfacial electron injection following photoexcitation of Mn dimer adsorbate. These simulations indicate that the interfacial electron injection is typically complete within an ultrafast, subpicosecond timescale when the initially populated electronic state localized in the adsorbate chromophore has suitable energy match with electronic states in the conduction band of the semiconductor surface.

Quantum dynamics simulations of interfacial electron transfer solve the time-dependent Schrödinger equation, yielding a detailed description of the time-dependent charge distribution after photoexcitation of the adsorbate. The resulting charge distribution provides information on the electronic orbitals responsible for hosting the injected electron in the semiconductor host substrate as well as the evolution of the spatial distribution of electronic population as it relaxes in the semiconductor conduction band. This type of atomistic simulations have also provided a description of the influence of thermal fluctuations on the underlying relaxation pathways.³³ Simulation studies beyond the low-temperature analysis have analyzed room-temperature conditions typical of photocatalytic cells, showing that thermal nuclear fluctuations can speed up the underlying interfacial electron transfer dynamics. The molecular/electronic origin of such effects has been traced to fluctuations that break the symmetry of otherwise orthogonal electronic states, creating additional relaxation pathways for carrier diffusion. Analogous computer simulations have also allowed the detailed analysis of the relaxation dynamics of holes, localized the monolayer of adsorbate molecules, created upon photoexcitation and interfacial electron transfer of sensitized TiO₂ nanoparticles (NPs) under cryogenic temperature conditions.^{34,42}

3 PROTON-COUPLED ELECTRON TRANSFER

Proton-coupled electron transfer (PCET) is often essential to achieve high catalytic turnovers of multielectron redox processes. Protonation/deprotonation processes can

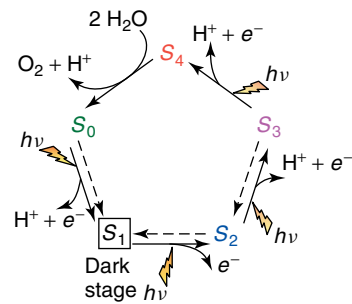


Figure 5 Catalytic cycle proposed by Joliot and Kok for water splitting into dioxygen, protons, and electrons at the OEC in PSII [1,2]. Dashed arrows indicate spontaneous interconversion processes in the dark. The steps for substrate water attachment and proton release are only tentatively proposed and might change with pH

facilitate reduction/oxidation state transitions, preventing charge buildup during the accumulation of multiple reducing (or oxidizing) equivalents. For example, PCET is thought to play an important role in keeping all of the redox steps in the Kok's catalytic cycle of water oxidation (Figure 5),^{43,44} over a narrow range of potential at ~1 V. The resulting “redox-leveling” effect prevents the accumulation of charge in the catalytic complex, allowing for the accumulation of four oxidizing equivalents in the OEC, embedded in the low dielectric environment of photosystem II (PSII).

The design of efficient catalysts for water oxidation often aims to develop molecular frameworks where the reactivity mimics the catalytic functionality of the OEC, leading to reaction pathways where the redox-leveling effect is induced by PCET. However, general design principles for efficient PCET mechanisms are still lacking. Computational modeling can play an important role in understanding catalytic processes of natural systems (e.g., photosystem II),^{11,12,45–51} as well as on the design and characterization of catalysts with similar functionality, by guiding the selection of suitable ligands for transition metal complexes that lead to redox-leveling mechanisms based on PCET. Recent studies of biomimetic oxomanganese complexes have been based on rigorous quantum chemistry calculations of redox potentials and pK_a values and direct comparisons with electrochemical measurements.⁵²

Figure 6 shows results of calculations of free energy changes associated with the oxidation state transition (III,III) → (III,IV) in the mixed-valent Mn complex [(bpy)₂Mn^{III}(μ-O)₂Mn^{IV}(bpy)₂]³⁺ (bpy, 2,2'-bipyridyl), as obtained at the DFT B3LYP/cc-pVTZ(-f) level by using the standard thermodynamic cycle formalism applied in conjunction with continuum solvation models.⁵² It is shown that the pK_a values of the oxo-ligands depend strongly on the oxidation states of the complex, changing by approximately 10 pH units (i.e., from pH ~ 2 to pH ~ 12) upon III,IV → III,III reduction of the Mn complex. These results are in good agreement with the experimental pK_a values determined by solution

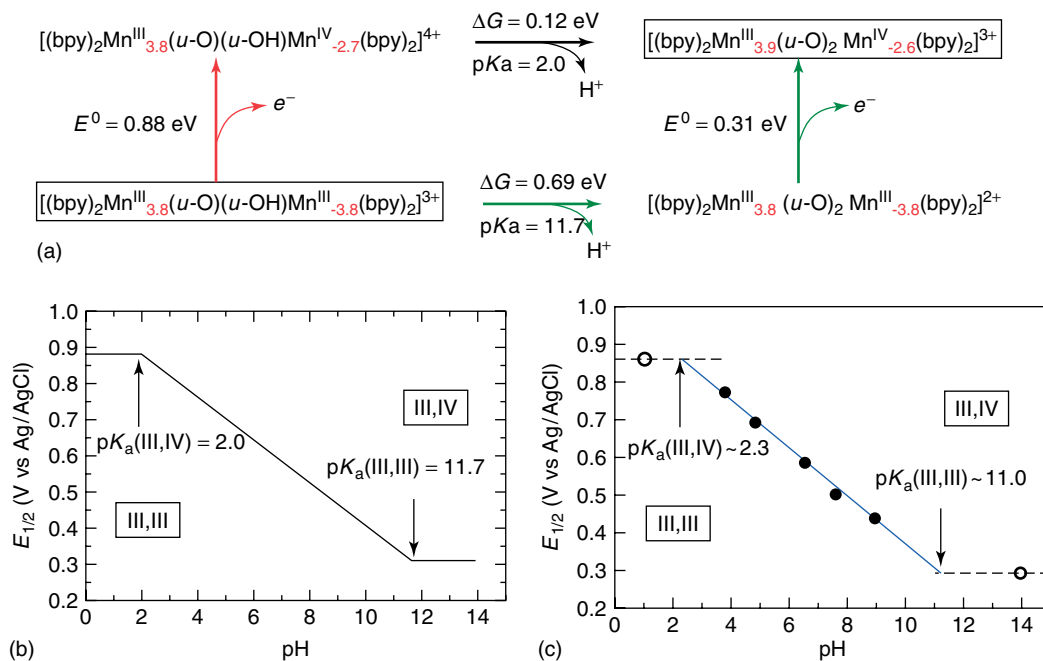


Figure 6 (a) Thermodynamic energy diagram of PCET for complex **1** in aqueous solutions at pH = 0, as described by DFT B3LYP/cc-pVTZ(-f) free energy calculations of redox potentials and pK_a values based on the Haber-Born cycle method applied in conjunction with a continuum solvation model. Formal oxidation numbers are indicated as superscripts in Roman numbers and the spin populations obtained according to the Mulliken population analysis are indicated as subscripts in red. (b) Pourbaix diagram for complex **1** in aqueous solutions, obtained (b) from free energy calculations of redox potentials at the DFT B3LYP/cc-pVTZ(-f) level of theory, and (c) experimental data (the circles). (Reproduced from Ref. 54. © American Chemical Society.)

magnetic susceptibility and near-IR spectroscopy,⁵³ as well as with the pH dependence of the redox potential previously reported by cyclic voltammogram (CV) measurements,⁵⁴ and provide fundamental understanding of the underlying changes in protonation and oxidation states leading to the pH dependence of redox potentials.

Figure 6(a) shows that the protonated reduced species $\mathbf{1}_{\text{red}} [(\text{bpy})_2\text{Mn}^{\text{III}}(\mu\text{-O})(\mu\text{-OH})\text{Mn}^{\text{III}}(\text{bpy})_2]^{3+}$ can be oxidized via two possible pathways, including oxidation by a direct ionization process requiring a rather high free energy change of 0.88 eV (red arrow), or oxidation by the concerted removal of an electron from the complex and a proton from the μ -hydroxo bridge (green arrow). These results indicate that the underlying oxidation is strongly coupled to deprotonation of the $\mu\text{-OH}$ bridge for a wide range of values of pH (i.e., pH = 2.0–11.7). For $\mathbf{1}_{\text{red}}$, the oxidation free energy is constant ($\sim 0.88 \text{ V}$) at pH < 2.0 (oxidation takes the red path). Within the $2.0 < \text{pH} < 11.7$ range, the overall free energy requirement consists of two parts, including 0.69–0.059*pH eV for the deprotonation step and an extra 0.31 eV for the oxidation of the deprotonated species. Finally, at pH > 11.7, the oxidation free energy becomes constant since the green path dominates with spontaneous deprotonation.

Figure 6(b,c) shows the comparison of Pourbaix diagrams, illustrating the pH dependence of $E_{1/2}$, as computed at the DFT B3LYP/cc-pVTZ(-f) level of theory and directly

compared to CV measurements.⁵⁴ The agreement shows that theory can provide accurate descriptions of the regulatory effect of reduction state transitions on the pK_a values of the ligands and the effect of protonation of oxo-ligands on the redox potentials of metal centers. Therefore, it is natural to expect that analogous calculations and direct comparisons to experimental data will allow the study of PCET along the catalytic cycle of multielectron reactions catalyzed by other transition metal complexes.

4 RECTIFICATION OF INTERFACIAL ELECTRON TRANSFER

A common problem to any scheme where photoexcitation creates an electron-hole pair state is electron-hole pair recombination. In PSII, recombination is suppressed by an arrangement of redox cofactors that induce directionality of electron transfer after the initial charge separation. Molecular diodes can also induce directionality of electron transfer⁵⁵ and have been recently explored in the design of semiconductor materials where the covalent attachment of molecular linkers induces rectification of interfacial electron transfer (Figure 7). The electronic rectification properties of molecular linkers that covalently bind Mn catalysts to TiO₂ surfaces, including

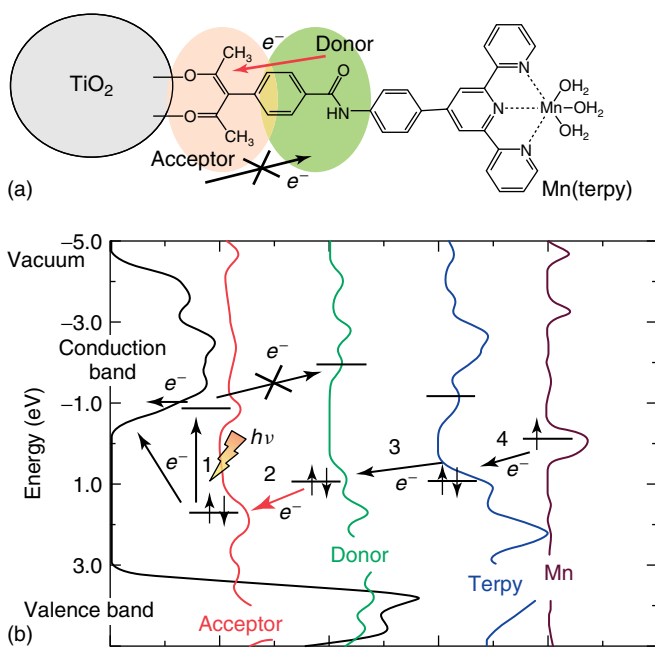


Figure 7 (a) Schematic diagram of a TiO_2 NP functionalized with $[\text{Mn}^{\text{II}}(\text{H}_2\text{O})_3]^{2+}$, where the Mn complex is covalently attached to the TiO_2 surface by the phenyl-acac anchor. (b) Density of electronic states and arrows indicating the electron transfer pathway, induced by photoexcitation and electron injection, leading to Mn oxidation. Favorable directionality of electron transfer is due to the positioning of electronic energy levels in the electron donor and acceptor parts of the ligand-linker chromophore. (Reproduced from Ref. 36. © American Chemical Society.)

Mn-complexes with phenylterpyridine ligands attached to 3-phenyl-acetylacetone anchors via amide bonds, have been characterized by calculations of current–voltage characteristics at metallic junctions.⁵⁶ It was found that a suitable choice of the amide linkage can induce directionality of interfacial electron transfer. These findings were consistent with EPR measurements, confirming an asymmetry of electron transfer rates for linkers with significant rectification.⁵⁶ These studies are particularly relevant for the development of photovoltaic or photocatalytic devices based on functionalized TiO_2 thin films where the overall performance is often affected by recombination processes competing with interfacial electron injection.

Calculations of current–voltage (I – V) characteristics were performed with the software package SMEAGOL,^{57,58} integrating the nonequilibrium Green’s function (NEGF) method^{59,60} with DFT⁶¹ as implemented in the SIESTA package for electronic structure calculations.⁶² The systems were modeled in the usual three-subsystem segmentation with the molecular diode of interest in between metallic electrodes.⁵⁶ The surface Green’s functions, describing the current–voltage probes, were obtained as a direct summation of both open and closed scattering channels together with a regularization procedure of the Hamiltonian that provides a significant improvement over standard recursive methods.

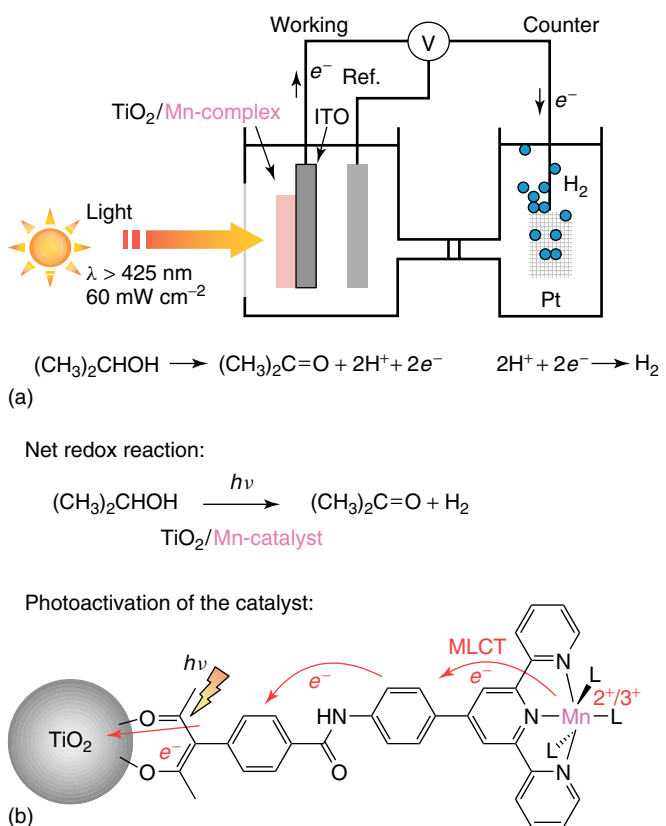


Figure 8 Photocatalytic cell for visible-light-driven oxidation chemistry and H_2 evolution (a), based on TiO_2 thin-film photoanodes functionalized with Mn catalysts covalently attached via chromophoric linkers (b)

5 FUEL FORMATION

Recent work on photocatalytic cells based on TiO_2 thin-film photoanodes functionalized with Mn-complexes has focused on coupling H_2 evolution driven to photoanodic oxidation reactions. Figure 8 shows a schematic diagram of a specific photocatalytic cell based on TiO_2 electrodes functionalized with Mn-terpy catalysts that can couple hydrogen evolution with oxidation of isopropanol to acetone. The reaction is catalyzed by the Mn-terpy complex adsorbate, activated by interfacial electron injection into the TiO_2 host substrate, upon absorption of visible light ($\lambda > 425 \text{ nm}$).⁶³ The activation process induces the oxidation-state transition $\text{Mn}(\text{II}) \rightarrow \text{Mn}(\text{III})$ in the metal center, generating $\text{Mn}(\text{III})$ with sufficient oxidizing power to transform isopropanol in acetone. The injected electrons are combined with protons in the counter-electrode to produce hydrogen. It has been shown that such a mechanism, involving photoexcitation, interfacial electron injection, charge carrier collection, and irreversible hydrogen evolution, can be accomplished when the Mn-terpy catalysts are covalently attached to the TiO_2 surface by using robust chromophoric linkers that are stable in aqueous solutions under oxidative conditions.

Similar results have been reported for other “proof-of-concept” visible-light-driven photocatalytic cells, including cells based on other (although more expensive) transition metal catalysts,^{13,24} indicating that the functionalization of semiconductor surfaces by covalent attachment of transition metal complexes yields a general approach for the development of photocatalytic solar cells.

6 CONCLUSIONS

The emergence of photocatalytic solar cells based on semiconductor materials functionalized with earth-abundant transition metal complexes represent a promising development for the sustainable production of fuel from renewable resources (e.g., water). Recent advances in the study of fundamental aspects that affect the overall efficiency of the underlying catalytic mechanisms suggest that control over photoabsorption, PCET, and IET can be achieved by implementing the ligand design methodology that has been so successful for many years in the development of homogeneous catalysts. When fundamentally informed by structural and mechanistic characterization based on computational modeling, high-resolution spectroscopy, and electrochemistry, in conjunction with the comparative analysis of analogous catalytic processes in nature, the resulting methodology constitutes a powerful “bottom-up” synthetic tool for the development of new catalytic materials. These emerging methods are thus expected to continue making significant contributions in the development of novel semiconductor materials for photocatalytic solar cells.

7 RELATED ARTICLES

Dye-Sensitized Solar Cells: an Overview; Energy Conversion in Photosynthesis; Hydrogen Economy; Molecular Catalysis for Fuel Cells; Molecular Catalysts for Oxygen Production from Water; Photocatalytic Hydrogen Production from Water; Toward Solar Fuels Using a Biomimetic Approach: Progress in the Swedish Consortium for Artificial Photosynthesis; Recent Advances in Photo-Initiated Electron-Transfer at the Interface between Anatase TiO₂ Nanocrystals and Transition-Metal Polypyridyl Compounds.

8 ABBREVIATIONS AND ACRONYMS

CV = cyclic voltammogram; DFT = density functional theory; DSSC = dye-sensitized solar cells; EPR = electron paramagnetic resonance; IET = interfacial electron transfer; IR = infrared; NEGF = nonequilibrium green’s

function; NP = nanoparticle; OEC = oxygen-evolving complex; PCET = proton coupled to electron transfer; QM/MM = quantum mechanics/molecular mechanics; UV = ultraviolet.

9 REFERENCES

1. A. J. Bard and M. A. Fox, *Acc. Chem. Res.*, 1995, **28**, 141.
2. E. E. Benson, C. P. Kubiak, A. J. Sathrum, and J. M. Smieja, *Chem. Soc. Rev.*, 2009, **38**, 89.
3. A. J. Morris, G. J. Meyer, and E. Fujita, *Acc. Chem. Res.*, 2009, **42**, 1983.
4. M. Rakowski-Dubois and D. L. Dubois, *Acc. Chem. Res.*, 2009, **42**(12), 1974.
5. A. J. Bard and M. A. Fox, *Acc. Chem. Res.*, 1995, **28**, 141.
6. A. Fujishima and K. Honda, *Nature*, 1972, **238**, 37.
7. N. D. McDaniel, F. J. Coughlin, L. L. Tinker, and S. Bernhard, *J. Am. Chem. Soc.*, 2008, **130**, 210.
8. J. F. Hull, D. Balcells, J. D. Blakemore, C. D. Incarvito, O. Eisenstein, G. W. Brudvig, and R. H. Crabtree, *J. Am. Chem. Soc.*, 2009, **131**, 8730.
9. G. H. Li, E. M. Sproviero, R. C. Snoeberger, N. Iguchi, J. D. Blakemore, R. H. Crabtree, G. W. Brudvig, and V. S. Batista, *Energy Environ. Sci.*, 2009, **2**, 230.
10. J. Limburg, J. S. Vrettos, L. M. Liable-Sands, A. L. Rheingold, R. H. Crabtree, and G. W. Brudvig, *Science*, 1999, **283**, 1524.
11. E. M. Sproviero, J. A. Gascon, J. P. McEvoy, G. W. Brudvig, and V. S. Batista, *Curr. Opin. Struct. Biol.*, 2007, **17**, 173.
12. E. M. Sproviero, J. A. Gascon, J. P. McEvoy, G. W. Brudvig, and V. S. Batista, *Coord. Chem. Rev.*, 2008, **252**, 395.
13. W. J. Youngblood, S. H. A. Lee, K. Maeda, and T. E. Mallouk, *Acc. Chem. Res.*, 2009, **42**, 1966.
14. M. W. Kanan and D. G. Nocera, *Science*, 2008, **321**, 1072.
15. M. W. Kanan, Y. Surendranath, and D. G. Nocera, *Chem. Soc. Rev.*, 2009, **38**, 109.
16. Z. F. Chen, J. J. Concepcion, J. W. Jurss, and T. J. Meyer, *J. Am. Chem. Soc.*, 2009, **131**, 15580.
17. J. J. Concepcion, J. W. Jurss, M. K. Brennaman, P. G. Hoertz, A. O. T. Patrocinio, N. Y. M. Iha, J. L. Templeton, and T. J. Meyer, *Acc. Chem. Res.*, 2009, **42**, 1954.
18. J. J. Concepcion, J. W. Jurss, M. R. Norris, Z. F. Chen, J. L. Templeton, and T. J. Meyer, *Inorg. Chem.*, 2010, **49**, 1277.
19. S. W. Gersten, G. J. Samuels, and T. J. Meyer, *J. Am. Chem. Soc.*, 1982, **104**, 4029.
20. R. Brimblecombe, A. M. Bond, G. C. Dismukes, G. F. Swiegers, and L. Spiccia, *PCCP*, 2009, **11**, 6441.
21. R. Brimblecombe, G. F. Swiegers, G. C. Dismukes, and L. Spiccia, *Angew. Chem.-Int. Ed.*, 2008, **47**, 7335.

22. G. C. Dismukes, R. Brimblecombe, G. A. N. Felton, R. S. Pryadun, J. E. Sheats, L. Spiccia, and G. F. Swiegers, *Acc. Chem. Res.*, 2009, **42**, 1935.
23. A. Mills and S. Le Hunte, *J. Photochem. Photobiol.*, 1997, **108**, 1.
24. J. A. Treadway, J. A. Moss, and T. J. Meyer, *Inorg. Chem.*, 1999, **38**, 4386.
25. B. ORegan and M. Gratzel, *Nature*, 1991, **353**, 737.
26. S. Das, C. D. Incarvito, R. H. Crabtree, and G. W. Brudvig, *Science*, 2006, **312**, 1941.
27. R. Manchanda, G. W. Brudvig, and R. H. Crabtree, *Coord. Chem. Rev.*, 1995, **144**, 1.
28. E. M. Sproviero, J. A. Gascon, J. P. McEvoy, G. W. Brudvig, and V. S. Batista, *J. Chem. Theory Comput.*, 2006, **2**, 1119.
29. J. Limburg, J. S. Vrettos, H. Y. Chen, J. C. de Paula, R. H. Crabtree, and G. W. Brudvig, *J. Am. Chem. Soc.*, 2001, **123**, 423.
30. E. M. Sproviero, J. A. Gascon, J. P. McEvoy, G. W. Brudvig, and V. S. Batista, *J. Inorg. Biochem.*, 2006, **100**, 786.
31. G. Li, E. M. Sproviero, W. R. McNamara, R. C. Snoeberger, R. H. Crabtree, G. W. Brudvig, and V. S. Batista, *J. Phys. Chem. B*, 2010, DOI: 10.1021/jp908925z (Submitted).
32. L. G. C. Rego and V. S. Batista, *J. Am. Chem. Soc.*, 2003, **125**, 7989.
33. S. G. Abuabara, L. G. C. Rego, and V. S. Batista, *J. Am. Chem. Soc.*, 2005, **127**, 18234.
34. L. G. C. Rego, S. G. Abuabara, and V. S. Batista, *J. Chem. Phys.*, 2005, **122**(15), 122.
35. S. Jin, R. C. Snoeberger, A. Issac, V. S. Batista, and T. Lian, *J. Phys. Chem. B*, 2010, DOI: 10.1021/jp911662g (Submitted).
36. W. R. McNamara, R. C. Snoeberger, G. Li, J. M. Schleicher, C. W. Cady, M. Poyatos, C. A. Schmuttenmaer, R. H. Crabtree, G. W. Brudvig, and V. S. Batista, *J. Am. Chem. Soc.*, 2008, **130**, 14329.
37. W. R. McNamara, R. C. Snoeberger, G. H. Li, C. Richter, L. J. Allen, R. L. Milot, C. A. Schmuttenmaer, R. H. Crabtree, G. W. Brudvig, and V. S. Batista, *Energy Environ. Sci.*, 2009, **2**, 1173.
38. L. G. C. Rego, R. da Silva, J. A. Freire, R. C. Snoeberger, and V. S. Batista, *J. Phys. Chem. C*, 2010, **114**, 1317.
39. R. C. Snoeberger, T. Lian, and V. S. Batista, *Proc. SPIE*, 2010, **7396**, 739604.
40. R. Huber, J. E. Moser, M. Gratzel, and J. Wachtveitl, *J. Phys. Chem. B*, 2002, **106**, 6494.
41. J. Schnadt, P. A. Bruhwiler, L. Patthey, J. N. O'Shea, S. Sodergren, M. Odelius, R. Ahuja, O. Karis, M. Bassler, P. Persson, H. Siegbahn, S. Lunell, and N. Martensson, *Nature*, 2002, **418**, 620.
42. L. G. C. Rego, S. G. Abuabara, and V. S. Batista, *Quantum Inf. Comput.*, 2005, **5**, 318.
43. P. Joliot, G. Barbieri, and R. Chabaud, *Photochem. Photobiol.*, 1969, **10**, 309.
44. B. Kok, B. Forbush, and M. McGloin, *Photochem. Photobiol.*, 1970, **11**, 457.
45. E. M. Sproviero, J. A. Gascon, J. P. McEvoy, G. W. Brudvig, and V. S. Batista, *J. Chem. Theory Comput.*, 2006, **2**, 1119.
46. E. M. Sproviero, J. A. Gascon, J. P. McEvoy, G. W. Brudvig, and V. S. Batista, *J. Inorg. Biochem.*, 2006, **100**, 786.
47. E. M. Sproviero, J. A. Gascon, J. P. McEvoy, G. W. Brudvig, and V. S. Batista, *J. Am. Chem. Soc.*, 2008, **130**, 6728.
48. E. M. Sproviero, J. A. Gascon, J. P. McEvoy, G. W. Brudvig, and V. S. Batista, *J. Am. Chem. Soc.*, 2008, **130**, 3428.
49. E. M. Sproviero, J. P. McEvoy, J. A. Gascon, G. W. Brudvig, and V. S. Batista, *Photosynth. Res.*, 2008, **97**, 91.
50. E. M. Sproviero, M. B. Newcomer, J. A. Gascon, E. R. Batista, G. W. Brudvig, and V. S. Batista, *Photosynth. Res.*, 2009, **102**, 455.
51. E. M. Sproviero, K. Shinopoulos, J. A. Gascon, J. P. McEvoy, G. W. Brudvig, and V. S. Batista, *Philos. Transa. R. Soc. B-Biol. Sci.*, 2008, **363**, 1149.
52. T. Wang, G. Brudvig, and V. S. Batista, *J. Chem. Theory Comput.*, 2010, **6**, 755.
53. S. R. Cooper and M. Calvin, *J. Am. Chem. Soc.*, 1977, **99**, 6623.
54. H. H. Thorp, J. E. Sarneski, G. W. Brudvig, and R. H. Crabtree, *J. Am. Chem. Soc.*, 1989, **111**, 9249.
55. M. Elbing, R. Ochs, M. Koentopp, M. Fischer, C. von Hanisch, F. Weigend, F. Evers, H. B. Weber, and M. Mayor, *Proc. Natl. Acad. Sci. U.S.A.*, 2005, **102**, 8815.
56. J. A. Palma, W. R. McNamara, R. C. Snoeberger, C. Richter, R. L. Milot, C. A. Schmuttenmaer, R. H. Crabtree, G. W. Brudvig, and V. S. Batista, *J. Am. Chem. Soc.*, 2010, submitted.
57. A. R. Rocha, V. Garcia-Suarez, S. W. Bailey, C. J. Lambert, and J. S. S. Ferrer, *J. Chem. Phys.*, 2005, **4**, 335.
58. A. R. Rocha, V. Garcia-Suarez, S. W. Bailey, C. J. Lambert, J. Ferrer, and S. Sanvito, *Phys. Rev. B*, 2006, **73**, 085414.
59. L. V. Keldysh, *Sov. Phys. JETP*, 1965, **20**, 1018.
60. S. Datta, 'Electronic Transport in Mesoscopic Systems', Cambridge University Press, Cambridge, 1997.
61. W. Kohn and L. J. Sham, *Phys. Rev. A*, 1965, **140**(4A), 1133.
62. J. M. Soler, E. Artacho, J. D. Gale, A. Garcia, J. Junquera, P. Ordejon, and D. Sanchez-Portal, *J. Phys. Cond. Matt.*, 2002, **14**, 2745.
63. G. Li, W. R. McNamara, R. C. Snoeberger, R. H. Crabtree, G. W. Brudvig, and V. S. Batista, *J. Am. Chem. Soc.*, 2010, submitted.

Toward Solar Fuels Using a Biomimetic Approach: Progress in the Swedish Consortium for Artificial Photosynthesis

Sascha Ott, Stenbjörn Styring, Leif Hammarström and Olof Johansson

Uppsala University, Uppsala, Sweden

1	Introduction	199
2	Ruthenium(II) Polypyridyl Photosensitizers	202
3	Mimicking the Electron Donor Side in Photosystem II	208
4	[FeFe] Hydrogenase Active Site Models in Light-Driven Proton Reduction Schemes	218
5	Concluding Remarks	225
6	Acknowledgments	225
7	Abbreviations and Acronyms	225
8	Related Articles	225
9	References	225

1 INTRODUCTION

Decreasing reserves of fossil fuels and the effect of CO₂ on global warming have led to an urgent need to develop clean and sustainable energy resources. The global energy consumption is projected to increase by 50% in the next 20 years,¹ which, using existing carbon-based fuels, would lead to a continued increase in atmospheric CO₂ concentrations to levels far higher than it has ever been the last 650 000 years. To satisfy the projected energy demands without relying on fossil fuels, new technologies need to be developed, in particular, those based on renewable energy. Solar energy has great potential to be the dominant energy source for the future as it is clean and abundant; solar energy received by the Earth in 1 h is more than the energy needed in one year. However, solar energy has to be captured and converted to an energy form that can be efficiently utilized. Both solar thermal conversion and solar electricity are existing technologies, which are of much current interest, but the realization of a solar fuel that can be stored and transported has several advantages.² Integrated light-to-fuel systems that can use solar energy for direct synthesis of energy-rich compounds, where the energy is stored in the chemical bonds, is thus highly desirable. The choice of a raw material for the solar fuel is equally important

as the energy source. It must be cheap, available everywhere, sustainable, and possible to use in an environmentally benign way. Water is an ideal raw material and can be oxidized in a four-electron process requiring, 4.92 eV (474.7 kJ mol⁻¹) or 1.23 eV per electron transferred (equation 1), to produce oxygen and hydrogen. Hydrogen has evolved as a promising candidate as the dominant energy carrier of the future and can be combined with oxygen in a fuel cell to generate electricity and form water as byproduct, thereby completing a cyclic process. However, as water does not absorb sunlight, some means to affect this endergonic reaction is necessary:



Initial photoinduced charge separation is an efficient approach to convert solar energy into chemical energy, where the incident light is stored as electrochemical potential energy. The captured energy can be subsequently used to drive endergonic reactions such as the production of hydrogen and oxygen from water. In natural photosynthesis, such charge-separation processes constitute the initial events of the solar energy conversion process, eventually leading to the production of adenosine triphosphate (ATP), the energy carrier in nature. Photosystem II (PSII) in green plants, algae,

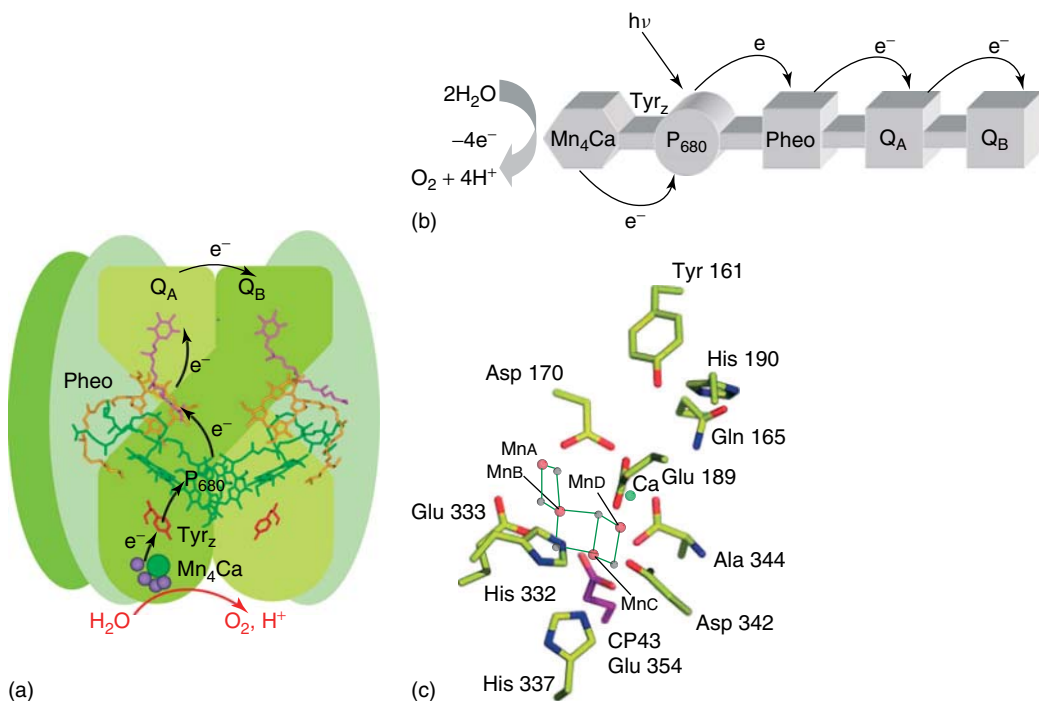


Figure 1 (a) and (b) Photoinduced charge separation in PSII involving several redox cofactors is coupled to water splitting at the Mn₄Ca cluster. (c) Recent model of the Mn₄Ca cluster based on EXAFS on single crystals of PSII. (Reproduced from Ref. 3. © American Association for the Advancement of Science, 2006.)

and cyanobacteria couples the charge-separation process to water splitting through the oxygen-evolving Mn₄Ca complex (OEC). The reducing equivalents are subsequently transferred to a second light-driven charge-separation process in PSI, followed by reduction of NADP⁺ to NADPH. The use of water as substrate in PSII allowed photosynthetic organisms to exploit an unlimited supply of electrons and, as a consequence, introduced an oxygenic atmosphere on earth. In this regard, OEC plays an essential role as it catalyzes water splitting by a sequence of single-electron transfers, which accumulate oxidizing equivalents at the Mn₄Ca cluster. Four consecutive stepwise oxidations, coupled to the release of protons, cycle the OEC through five redox states (S₀–S₄), referred to as the *Kok cycle*, where the S₄ state oxidizes water to dioxygen and the OEC returns to the S₀ state, the most reduced intermediate.

PSII is a large protein complex located in the thylakoid membranes and is composed of more than 25 protein subunits, which hold the cofactors involved in the initial charge-separation process (Figure 1). An intrinsic feature of this protein complex is the precise location of these cofactors, which directly influences the thermodynamics and kinetics of the photoinduced charge separation, ensuring rapid forward electron transfer while minimizing wasteful charge recombination reactions. Light energy is initially captured by antenna molecules and transferred to the reaction center, P₆₈₀, a multimer of chlorophylls. Excited P₆₈₀, now a strong reductant, transfers an electron to a nearby pheophytin and subsequently

to the secondary quinone acceptors Q_A and Q_B, while P₆₈₀⁺ is re-reduced by a nearby tyrosine residue. Although this sequence of events reduces the amount of stored redox energy, it efficiently stabilizes the charge-separated state across the thylakoid membrane and allows for subsequent reactions.

The primary electron donor to oxidized P₆₈₀ is a redox-active tyrosine (Tyr_z), hydrogen bonded to a nearby histidine (D1-His190) and situated close (ca. 5 Å) to the Mn₄Ca cluster. P₆₈₀⁺ is one of the strongest oxidants found in biology and oxidizes Tyr_z in a proton-coupled electron transfer (PCET) reaction, where the proton is transferred to the nearby His190 in an exceptionally well-tuned hydrogen bond. Tyr_z[•] subsequently oxidizes the Mn₄Ca cluster in reactions that also involve PCET steps and that are dependent on the intermediate state of the OEC. The exact details of these complex proton and electron equilibria are under extensive study and an extended model of the Kok cycle was recently put forward.⁴

The structure of the Mn₄Ca cluster is still not known in molecular detail. On the basis of spectroscopic studies by extended X-ray absorption fine structure (EXAFS) and electron paramagnetic resonance (EPR), a number of structural proposals have been put forward.⁵ The recent crystal structures of PSII at 3.5 Å⁶ and 3.0 Å⁷ identify many of the cofactors and amino acid side chains, but the structural resolution is insufficient to determine the exact positions of the metal ions of OEC. However, the data were modeled as a 3 + 1 arrangement of the Mn ions with one distinctly different Mn ion. The Mn

ions and the neighboring Ca^{II} ions are held together by, mainly, di- μ -oxo-bridges and most of the coordinating amino acid side chains have been identified. It is of concern that the cluster may suffer from damage by the X-ray radiation used. However, recent polarized EXAFS on single crystals of PSII combined with the crystal structures proposed new possible structures that may also be viewed as 3 + 1 clusters (Figure 1).³ During catalysis, the Mn ions in the OEC cycle between Mn^{III} , Mn^{IV} and maybe even Mn^V oxidation states. It is important to note that structural rearrangements of the ligand sphere around Mn ions and changes in the protonation state of one di- μ -oxo bridge are known to occur at the OEC during S-state advancements as a consequence of substrate binding and oxidation state changes.⁸

On the electron acceptor side, plastoquinone (Q_B) leaves PSII at the hydroquinone redox level. The reductive equivalents are transferred via the photosynthetic electron transfer chain to PSI and then to NADP^+ and are used for the reduction of CO_2 to produce carbohydrates. While the production of biomass is fundamental to natural photosynthesis, a more attractive option is to use the electrons to provide a more versatile and easy-to-transport fuel with high-energy content. Molecular hydrogen fulfills these requirements and, perhaps not surprising, is also involved in the metabolism of certain cyanobacteria and green algae. The enzymes that nature has devised to catalyze the reversible interconversion of protons to molecular hydrogen are termed *hydrogenases* (H_2ases). These biocatalysts can be classified into three different types, depending on the nature and the number of transition metals in their active sites. Despite certain similarities, [NiFe] H_2ases , [FeFe] H_2ases , and [Fe] H_2ases (earlier known as FeS —cluster-free H_2ases) have evolved independently and differ in their preference to catalyze the reduction of protons or the oxidation of hydrogen. Here, the focus is on [FeFe] H_2ases and biomimetic models of this enzyme.

The catalytically active portion of the [FeFe] H_2ase is a part of the so-called H-cluster: an arrangement of six iron cations held together mostly by seven sulphur-based ligands (Figure 2). The H-cluster has spectroscopically been studied for many years and the structure has been characterized by X-ray crystallography.^{9,10} It can be divided in two parts, one of which is a [4Fe–4S] cubane that is the final cluster in the chain of similar clusters that provide the electron transfer path from the surface of the enzyme to the active site that is deeply buried inside the enzyme. The catalytic unit of the H-cluster is connected to the FeS cubane by a cysteine residue of the protein. It is composed of two iron centers that are coordinated by biologically very unusual cyanide and carbon monoxide ligands. The two iron centers are held together by two bridging thiolates that flank the ends of a chain of three light atoms. There is still a debate on whether the central atom of this chain is carbon, nitrogen, or oxygen. Apart from the cysteine that links the FeS cubane to the active site subcluster, the latter is held in the protein matrix only by hydrogen bonds, in particular, to the cyanide ligands by nearby lysine residues.

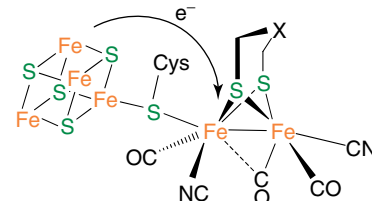


Figure 2 H-cluster of the [FeFe] H_2ase -active site. X can be CH_2 , NH , or O

Given the efficiency of natural enzymes to split water using the energy in light and to produce hydrogen, an attractive option for solar energy conversion is biomimetic chemistry. Artificial photosynthesis is concerned with the design and the realization of molecular and/or supramolecular assemblies where key principles from nature are mimicked.¹¹ It is important to note that the entire machinery of the enzymes or organisms need not be mimicked. After all, the organisms have evolved to sustain life, and not to produce valuable fuels for mankind. Figure 3 shows a potential assembly for photoinduced water splitting, involving a photosensitizer (P), electron donor(s) and acceptor(s), and catalysts where oxidizing and reducing equivalents are stored and subsequently used for water oxidation and reduction. A light-harvesting antenna may also be incorporated to compensate for the rather low photon density of sunlight (not shown). All components are organized in space, analogous to PSII, where one achieves vectorial separation of the photoproduced oxidant/reductant pair and where the undesirable charge recombination reaction can be controlled.

In the article, the progress within the Swedish Consortium for Artificial Photosynthesis in the last five years is discussed. Our research includes many of the key aspects in the field, with an emphasis on a homogeneous approach to artificial photosynthesis. This includes Ru^{II} polypyridyl complexes, a family of photosensitizers that has played a pivotal role in solar-energy-related research in the last 30–40 years, and photoinduced charge separation and

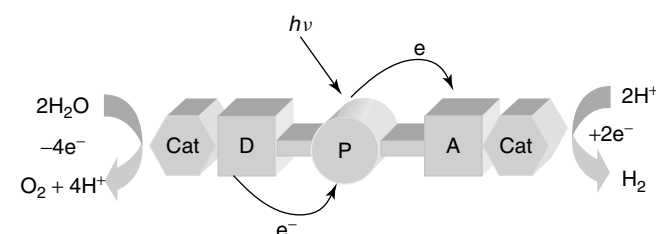


Figure 3 A supramolecular approach to artificial photosynthesis where a photosensitizer is combined with electron donors (D)/acceptors (A) and biomimetic catalysts for water oxidation and reduction

charge accumulation at potential catalytic sites. Also, the development and the optimization of biomimetic Mn and Fe catalysts for water oxidation and reduction, respectively, are discussed. Where necessary, a summary of previous work is included.

2 RUTHENIUM(II) POLYPYRIDYL PHOTOSENSITIZERS

Since the first reports in the 1970s, which state that the metal-to-ligand charge transfer (MLCT) excited state of $[\text{Ru}(\text{bpy})_3]^{2+}$ (bpy is 2,2'-bipyridine) undergoes efficient electron transfer quenching in bimolecular reactions, this class of chromophores has received much attention as potential mediators for photoinduced water splitting. Ruthenium(II) polypyridyl complexes are synthetically versatile, and they show both chemical and photochemical (in most cases) stability, which has stimulated their use in many branches of chemistry. Here, an overview of the properties of Ru^{II} polypyridyl complexes is given; more detailed reviews are found elsewhere.^{12,13}

2.1 Classical Trisbidentate and Bistridentate Ru^{II} Complexes

2.1.1 Structure and Photophysical Properties

The classical $[\text{Ru}(\text{bpy})_3]^{2+}$ complex depicted in Figure 4 contains a d^6 metal ion surrounded by three bpy ligands and exhibits D_3 symmetry and is therefore chiral. The complex shows intense absorptions in the UV and visible regions, the former due to ligand-centered (LC) transitions and the latter originating from $^1\text{MLCT}$ absorptions, where an electron has been promoted from a π_M metal orbital to ligand-based π^* orbitals. The different transitions may be described in a molecular orbital diagram such as the one shown in Figure 4, simplified for octahedral symmetry. Excitation in any of the absorption bands leads to, within 100 fs and with unity efficiency, an emissive $^3\text{MLCT}$ state ($\phi = 0.09$) with an energy of 2.12 eV that lives for around 1.0 μs at room temperature (MeCN). As shown by different techniques (e.g., time-resolved resonance raman spectroscopy), the relaxed $^3\text{MLCT}$ state is best described as $[\text{Ru}^{\text{III}}(\text{bpy})_2(\text{bpy}^{\bullet-})]^{2+}$ with the electron localized on a single bpy ligand. A question of particular interest for photoinduced electron transfer in supramolecular chromophore–quecher assemblies relates to the rate of interligand hopping. A time scale of 40 ps has been inferred from various techniques, but recent results suggest that it is considerably faster.¹⁴

Deactivation of the $^3\text{MLCT}$ state occurs via radiative (k_r) and nonradiative (k_{nr}) pathways (Figure 4c) and its lifetime, τ , is given by equation (2). At room temperature,

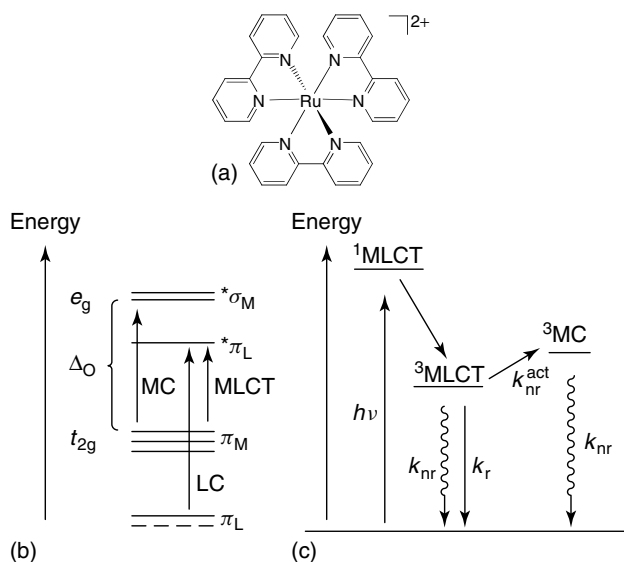


Figure 4 (a) The $[\text{Ru}(\text{bpy})_3]^{2+}$ ion. (b) Molecular orbital diagram simplified for octahedral geometry. The state diagram (c) shows all possible deactivation pathways of the $^3\text{MLCT}$ state for a typical Ru^{II} polypyridyl complex

the excited state decay occurs to a large extent by thermal population of higher lying metal-centered (^3MC) states ($k_{\text{nr}}^{\text{act}}$), while direct radiative and nonradiative decays to the ground state (the latter governed by the energy gap law) dominate at lower temperatures. The assignment of ^3MC states is based on photosubstitution reactions on account of the metal–ligand antibonding character of the ^3MC states. Evaluation of the temperature dependence of the luminescent lifetime by a simple Arrhenius plot above the solvent-melting region allows one to estimate the ΔE for activated decay via ^3MC states (equation 3). (A more comprehensive treatment of the temperature dependence of τ can be found in References¹² and¹³.) A large energy separation (Δ_O) between the t_{2g} metal orbitals (in an octahedral field) and the e_g orbitals, which depends on the ligand-field strength, is therefore crucial to obtain long-lived excited states. This is evident in the related $[\text{Ru}(\text{tpy})_2]^{2+}$ (tpy is 2,2':6',2''-terpyridine) where the poor bite angle of the tpy ligands (158°) leads to a weak ligand field and the complex, therefore, undergoes rapid nonradiative decay via ^3MC states at room temperature with $\tau = 0.25\text{ ns}$.¹⁵

$$\tau = \frac{1}{(k_r + \sum k_{\text{nr}})} \quad (2)$$

$$\tau = \frac{1}{(k_r + k_{\text{nr}} + Ae^{-\Delta E/RT})} \quad (3)$$

Excited $[\text{Ru}(\text{bpy})_3]^{2+}$ is both a strong oxidant and reductant, making electron transfer quenching feasible. The excited state redox potentials are related to the ground-state redox potentials through the 2.12 eV excited state energy

(E_{00}) according to equations (4) and (5) (Ru^{I} refers to a singly reduced species with the electron localized on a polypyridyl ligand; e is the elementary charge).

$$E^0(\text{Ru}^{\text{III}/\text{II}*}) = E^0(\text{Ru}^{\text{III}/\text{II}}) - (E_{00}/e) \quad (4)$$

$$E^0(\text{Ru}^{\text{II}*/\text{I}}) = E^0(\text{Ru}^{\text{II}/\text{I}}) + (E_{00}/e) \quad (5)$$

Based on the ground-state redox potentials, +0.85 and −1.76 V (all potentials in this article are referenced vs $\text{Fc}^{+/0}$ in MeCN solution; Fc is ferrocene), the excited state redox potentials are, therefore, shifted to −1.27 and +0.36 V for oxidation and reduction, respectively. Comparing the first reduction at −1.76 V with the −1.27 V for the excited state redox potential, it is evident that a stronger reductant is generated if an initial reductive quenching pathway is possible for the excited photosensitizer. This increases the driving force for electron transfer to a potential catalyst and ultimately hydrogen evolution by approximately 500 mV.

2.1.2 Synthesis Strategies and Stereochemical Outcomes

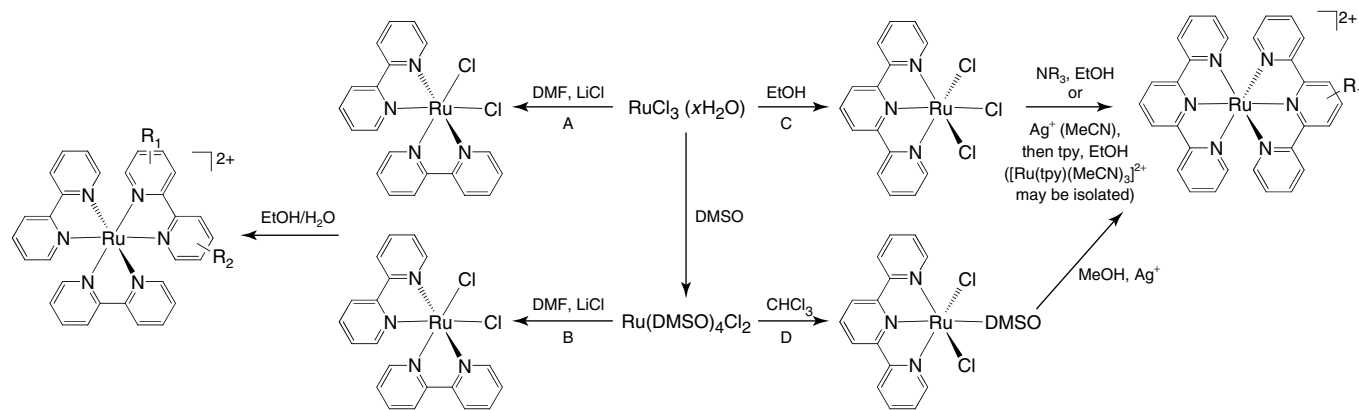
An extensive set of strategies to form the $[\text{Ru}(\text{bpy})_3]^{2+}$ - or $[\text{Ru}(\text{tpy})_2]^{2+}$ -based complexes is now available to the synthetic chemist. The most important ones are summarized in Scheme 1. Most strategies rely on the preassembly of functionalized polypyridyl ligands, prepared via well-established methods, although a “chemistry on the complex” strategy has opened up new exciting opportunities.

Homoleptic trisbidentate Ru^{II} complexes are conveniently prepared by reacting $\text{RuCl}_3 \cdot x\text{H}_2\text{O}$ or $\text{Ru}(\text{DMSO})_4\text{Cl}_2$ with three equivalents of a bpy ligand, using either conventional heating or microwave-assisted heating, which is becoming increasingly popular. Using $\text{RuCl}_3 \cdot x\text{H}_2\text{O}$ as a substrate, reducing equivalents may be provided by the solvent or some added reductant, e.g., tertiary amines. The desire to tune the redox and spectroscopic properties of Ru^{II} polypyridyl

complexes led to the development of synthetic methods to both bisheteroleptic and trisheteroleptic complexes. A frequently used method for bisheteroleptic complexes is route A, or route B for ligands susceptible to oxidation, with the third bpy ligand being introduced typically using protic solvents. The synthesis of trisheteroleptic complexes relies on the sequential coordination of the bpy ligands, using either $\text{Ru}(\text{DMSO})_4\text{Cl}_2$ or $[\text{Ru}(\text{CO})_2\text{Cl}_2]_n$ as a Ru source, and is usually achieved in a multistep sequence relying on different solvents (not discussed).¹⁶

Similar to trisbidentate complexes, homoleptic bistridentate Ru^{II} complexes can be obtained in a one-step reaction using $\text{RuCl}_3 \cdot x\text{H}_2\text{O}$ or $\text{Ru}(\text{DMSO})_4\text{Cl}_2$, while heteroleptic complexes are conveniently prepared in a stepwise manner using route C. Introducing the second tpy ligand may involve initial dechlorination using Ag^+ to facilitate coordination; an intermediate solvate species can be isolated but is usually prepared in situ. An important contribution was recently made by Ziessel and coworkers, who prepared heteroleptic complexes under mild conditions using *cis*- $\text{Ru}(\text{tpy})(\text{DMSO})\text{Cl}_2$ as a precursor (D).¹⁷

The stereochemical outcome for trisbidentate complexes containing unsymmetrical bpy ligands is rich. Apart from being chiral, a number of geometric isomers may result in complicating characterization. The issue of stereoisomerism has been addressed in recent years and is not treated in detail in this article.¹⁸ The D–P–A assembly shown in Figure 5 based on bpy ligands substituted in the versatile 4-positions exemplifies the possible formation of isomers. Importantly, only one isomer adopts the ideal trans-arrangement of the donor and the acceptor. This is in contrast to achiral $[\text{Ru}(\text{tpy})_2]^{2+}$ -based complexes where a linear arrangement can be selectively obtained when substituents are introduced along the C_2 axis, i.e., in the 4'-position of the central pyridines (Figure 5). However, because of the much longer excited state lifetime of $[\text{Ru}(\text{bpy})_3]^{2+}$ compared to $[\text{Ru}(\text{tpy})_2]^{2+}$, most chromophore–quencher assemblies have been based on trisbidentate Ru^{II} chromophores.



Scheme 1 Common synthetic strategies for the preparation of homoleptic and heteroleptic Ru^{II} complexes

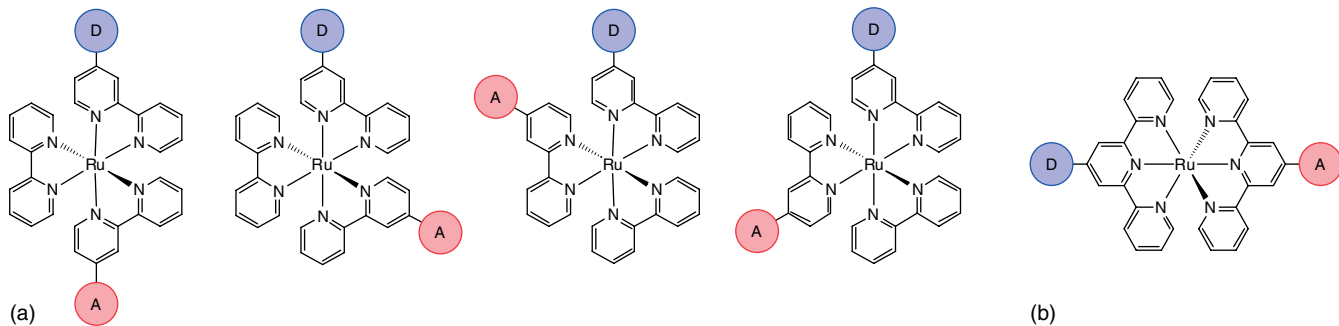


Figure 5 (a) Geometric isomers in a D–P–A assembly based on $[\text{Ru}(\text{bpy})_3]^{2+}$. (b) Linear arrangement of a D–P–A assembly based on $[\text{Ru}(\text{tpy})_2]^{2+}$

2.1.3 Intramolecular Charge Separation in Chromophore–Quencher Assemblies

Photoinduced charge separation on a single electron level in chromophore–quencher multiunit assemblies has been demonstrated in a large number of systems, many of them based on Ru^{II} polypyridyl photosensitizers. The charge-separation event is one of the central themes in artificial photosynthesis and continues to be of great interest to the field, in particular, with the aim to produce long-lived charge-separation lifetimes, which ultimately can be coupled with catalytic reactions.

The P–A complexes **1** and **2** shown in Figure 6 containing either a $[\text{Ru}(\text{bpy})_3]^{2+}$ - or $[\text{Ru}(\text{tpy})_2]^{2+}$ -based photosensitizer linked to a naphthalenediimide (NDI) electron acceptor were prepared by refluxing one equivalent of an NDI-functionalized polypyridyl ligand with a Ru precursor according to routes A and C (Scheme 1), respectively.¹⁹ The complexes are two examples in a series of Ru^{II} -NDI dyads studied to optimize the primary photoinduced charge separation, where the NDI acceptor was chosen due to its suitable redox potentials ($E_{1/2} = -0.97 \text{ V}$) and spectroscopic signature in the reduced state. The free energies for the charge separation and the recombination reaction (equations 6 and 7), as well as competing energy-transfer processes, can be calculated from electrochemical data and excited state energies.

$$\Delta G^\circ(\text{CS}) = e(E_{1/2}(\text{Ru}^{\text{III}/\text{II}}) - E_{1/2}(\text{NDI}^{0/-})) - E_{00}(^3\text{MLCT}) \quad (6)$$

$$\Delta G^\circ(\text{CR}) = e(E_{1/2}(\text{NDI}^{0/-}) - E_{1/2}(\text{Ru}^{\text{III}/\text{II}})) \quad (7)$$

Efficient quenching of the excited state was observed in **1**, attributed to competing energy-transfer quenching and electron transfer to the NDI moiety. Both pathways, however, lead to the same $\text{Ru}^{\text{III}}\text{-NDI}^{\bullet-}$ state (~100% charge-separation yield), where the excitation energy is transiently stored as redox energy. In contrast, no oxidative quenching was observed in **2** due to the short excited state lifetime of the Ru^{II} chromophore.

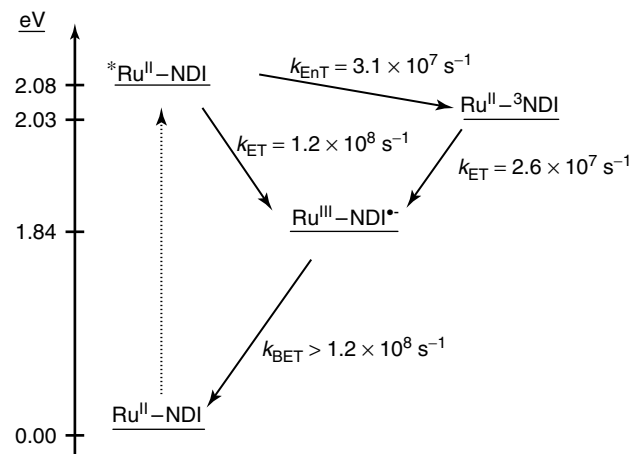
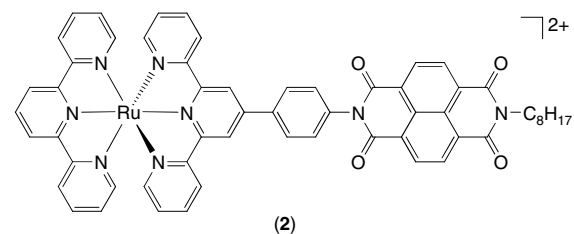
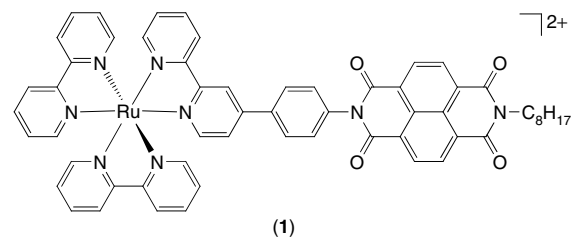


Figure 6 Two Ru^{II} -NDI dyads: complex **1**; complex **2** and the reaction scheme and rate constants determined for complex **1**. The triplet excited state energies are those for the chromophore (³MLCT) and electron acceptor (³NDI), respectively

Ru^{II} polypyridyl complexes almost always have excited state energies around 2.0 eV, while the thermodynamic

limit for water splitting is 1.23 eV. Considering energy losses in charge-separation devices and in catalytic reactions, the use of a single chromophore in artificial photosynthetic systems may be difficult to achieve. One way to solve this problem is to mimic nature by dividing the system in two separated half-reactions, each driven by its own chromophore. Alternatively, the use of other chromophores with higher energy excited states, or the use of two chromophores in the same charge-separation device, may be plausible. In an attempt to obtain high-energy charge-separated states using the latter strategy, triad **3** was prepared, which contains a cyclometalated unit ($\text{Ru}^{\text{II}}_{\text{C}}$) where a nitrogen donor has been replaced by an anionic carbon donor (Figure 7).²⁰ The $\text{Ru}^{\text{II}}_{\text{C}}$ unit is a strong excited state reductant (with sufficient excited state lifetime, cf. Section 2.2.1), capable of reducing a pyromellitimide (PI) electron acceptor ($E_{1/2} = -1.2$ V). The complex was prepared via selective coordination of $\text{Ru}(\text{bpy})_2\text{Cl}_2 \cdot 2\text{H}_2\text{O}$ to a ditopic bridging ligand, followed by a cyclometalation reaction with a PI-functionalized $\text{Ru}(\text{PI-tpy})\text{Cl}_3$ precursor. By subsequent two-photon excitation, the $\text{Ru}^{\text{III}}-\text{Ru}^{\text{II}}_{\text{C}}-\text{PI}^{\bullet-}$ fully charge-separated state (2.1 eV, based on electrochemical data) can be possibly formed. Excitation of either Ru^{II} unit leads to the formation of the $\text{Ru}^{\text{II}}-\text{Ru}^{\text{III}}_{\text{C}}-\text{PI}^{\bullet-}$ state, which relies on rapid energy transfer to the lowest excited state localized on the cyclometalated unit.²¹ The system, therefore, functions as an efficient antenna/charge-separation device. However, excitation of the Ru^{II} unit within the lifetime of the primary charge-separated state did not lead to any detection of $\text{Ru}^{\text{III}}-\text{Ru}^{\text{II}}_{\text{C}}-\text{PI}^{\bullet-}$. Further work on double-chromophoric systems would most likely have to rely on more weakly coupled chromophores for success, possibly in conjunction with efficient antenna systems to compensate for the low photon density of sunlight.

2.2 Increasing the Bite Angle in Bistridentate Ru^{II} Complexes

2.2.1 First Generation Complexes

The short excited state lifetime of bistridentate Ru^{II} chromophore has limited their use in chromophore–quencher complexes, and the development of bistridentate Ru^{II} complexes with prolonged excited state lifetimes has, therefore, been a long-standing goal in artificial photosynthetic research.²² One approach to prolong the excited state lifetime in $[\text{Ru}(\text{tpy})_2]^{2+}$ derivatives is by functionalization in the 4'-positions of the tpy ligands with electron-donating/electron-withdrawing substituents. Other strategies include the introduction of tridentate ligands with extended π^* orbitals or the introduction of strong field ligands with the aim to increase the energy of the ${}^3\text{MC}$ states. The latter approach includes cyclometalating ligands, carbenes, anionic triazole ligands, and cyanides; strong field ligands that are high in the spectrochemical series. Most, if not all, of these approaches, however, lead to a decreased energy of the ${}^3\text{MLCT}$ state.

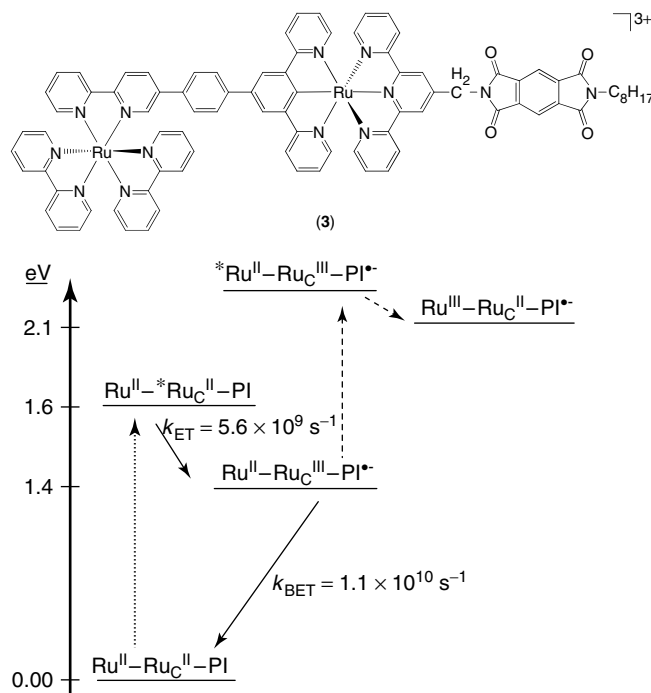


Figure 7 A $\text{Ru}^{\text{II}}-\text{Ru}^{\text{II}}_{\text{C}}-\text{PI}$ (3) triad. The reaction scheme is reminiscent of a Z scheme due to the possibility of subsequent two-photon excitation. However, no evidence for the second excitation (dashed line) was observed. The energy levels and rate constants are those determined in CH_2Cl_2

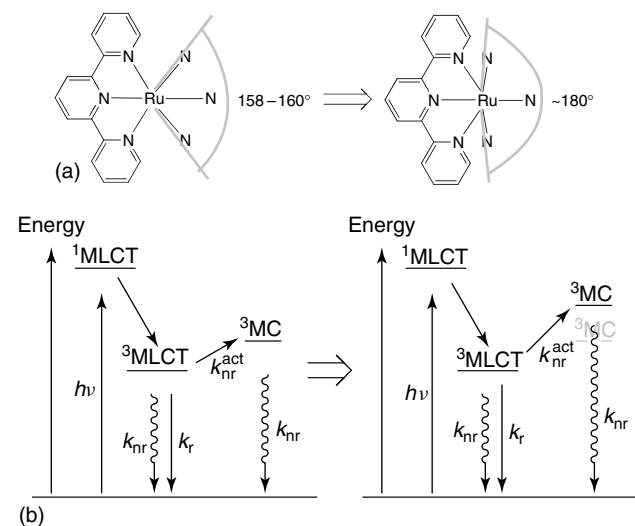


Figure 8 (a) Increasing the bite angle in bistridentate Ru^{II} complexes and (b) the proposed effect in the state energy diagram

A different approach that specifically aims at destabilizing the ${}^3\text{MC}$ states by increasing the ligand field is to introduce tridentate ligands that provide a more octahedral coordination (Figure 8). Such an approach can, in principle,

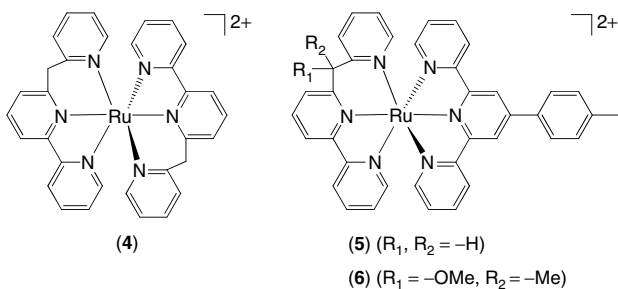


Figure 9 Ru^{II} complexes based on bipyridyl–pyridyl tridentate ligands

leave the energy of the ${}^3\text{MLCT}$ excited state unaffected, while keeping the valuable 4'-positions available for further functionalization. Following this strategy, a first series of complexes where a saturated carbon was introduced between two pyridines was synthesized, three of which are shown in Figure 9.^{23,24} Although a pyridine ligand is lower in the spectrochemical series than, e.g., a bpy ligand, it was believed that the tridentate bipyridyl–pyridyl ligands as a whole would exert a stronger ligand field than the pivotal tpy ligand. The complexes were prepared by reacting the ligands with common Ru^{II} precursors, either $\text{Ru}(\text{tpy})(\text{DMSO})\text{Cl}_2$ or $\text{Ru}(\text{DMSO})_4\text{Cl}_2$, with one or two equivalents of the ligands in refluxing alcohol solutions.

The X-ray crystal structure of the homoleptic complex **4** indeed shows a less distorted structure due to the formation of one six-membered chelate within each tridentate ligand (Figure 10). While complexes **5** and **6** display similar ${}^3\text{MLCT}$ excited state lifetimes as $[\text{Ru}(\text{tpy})_2]^{2+}$, complex **4** is considerably more long lived ($\tau = 15 \text{ ns}$ in degassed EtOH/MeOH solutions) and the excited state energy is similar as that for $[\text{Ru}(\text{tpy})_2]^{2+}$. Temperature-dependent emission measurements further confirmed that the deactivation rate via thermal population of higher lying ligand-field states ($k_{\text{nr}}^{\text{act}}$) is greatly reduced in **4** compared to $[\text{Ru}(\text{tpy})_2]^{2+}$ due to an increased energy difference between the ${}^3\text{MLCT}$ and ${}^3\text{MC}$ states.

2.2.2 Introducing 2,6-Di(quinolin-8-yl)pyridine, Second Generation Complexes

The insertion of a saturated carbon between two pyridines to increase the N–Ru–N bite angle proved to be a viable approach to luminescent bistridentate Ru^{II} complexes, but complex **4** was photolabile probably due to pyridine decoordination. The 2,6-di(quinolin-8-yl)pyridine (dqp) ligand, the second generation ligands, which upon coordination gives only six-membered chelates, was expected to be less flexible than the previous ligands. Initial DFT (B3LYP/LANL2DZ) calculations on the homoleptic complex $[\text{Ru}(\text{dqp})_2]^{2+}$ (**7**) predicted an almost perfect octahedral coordination with N–Ru–N bite angles close to 180° .^{25,26}

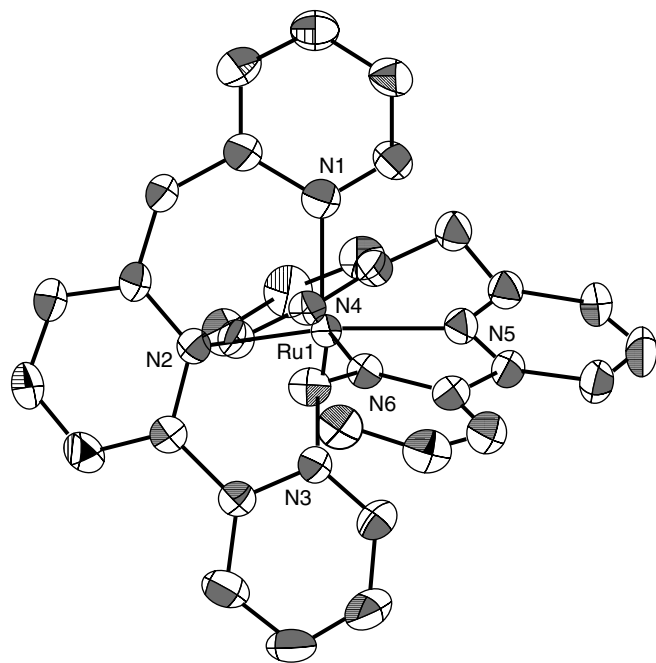
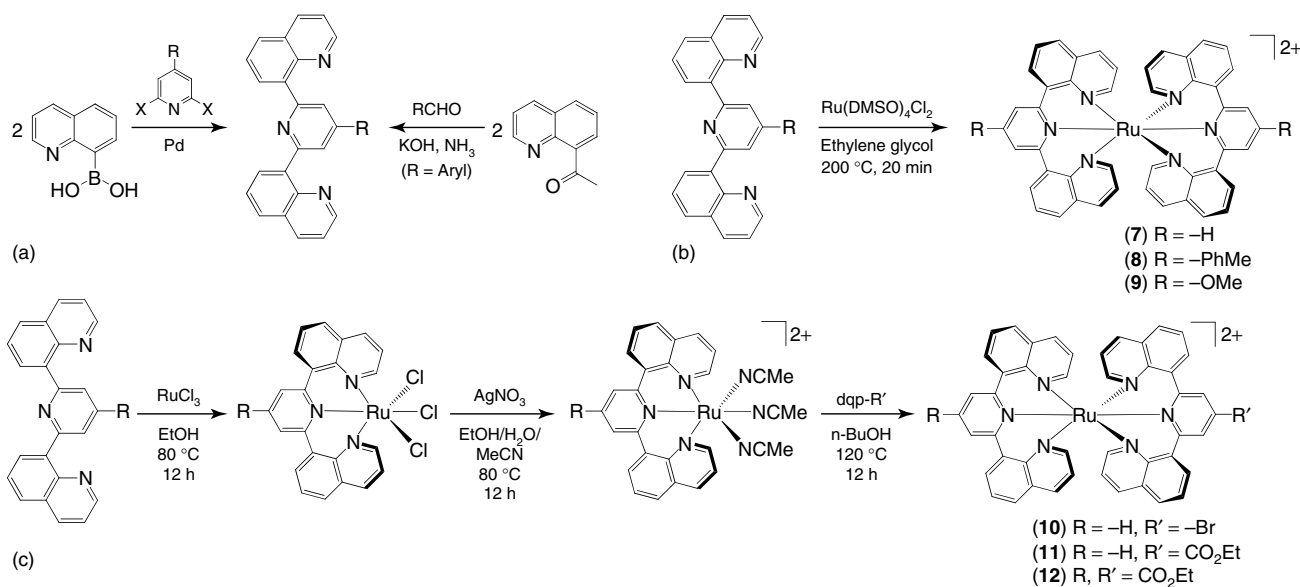


Figure 10 ORTEP view of **4** at 30% probability ellipsoids. The N1–Ru1–N3 and N4–Ru1–N6 bite angles are $\sim 168^\circ$. (Reproduced from Ref. 23. © Elsevier, 2004.)

The synthesis relied on the established procedures for $[\text{Ru}(\text{tpy})_2]^{2+}$. Once the ligands were obtained, either via Pd-catalyzed cross-coupling of the different heterocycles or via a one-step ring-forming methodology generating the central pyridine ring (Scheme 2),²⁷ homoleptic complexes **7–9** were prepared in a straightforward manner in 50–90% yields by refluxing two equivalents of the ligand with one equivalent $\text{Ru}(\text{DMSO})_4\text{Cl}_2$ in ethylene glycol using microwave heating (Scheme 2).²⁸ A synthetic strategy toward homoleptic and heteroleptic complexes containing more sensitive groups (e.g. complexes **10–12** in Scheme 2) was developed and relied on the isolation of an intermediate $[\text{Ru}(\text{dqp})(\text{MeCN})_3]^{2+}$ species, analogous to route C in Scheme 1. In contrast to Ru-tpy chemistry, the $\text{Ru}(\text{dqp})\text{Cl}_3$ precursor mostly gives $\text{Ru}(N^{\wedge}N^{\wedge}N\text{-dqp})(N^{\wedge}N\text{-dqp})\text{Cl}^+$ species with a noncoordinated quinoline unit, while $[\text{Ru}(\text{dqp})(\text{MeCN})_3]^{2+}$ reacts smoothly with a range of dqp ligands to give the products normally in high yields (60–80%). Slightly higher reaction temperatures (120°C) than normally used for Ru-tpy chemistry are needed in the second coordination step, which indicates a larger steric barrier for the formation of $[\text{Ru}(\text{dqp})_2]^{2+}$ complexes compared to $[\text{Ru}(\text{tpy})_2]^{2+}$.

X-ray analysis of $[\text{Ru}(\text{dqp})_2]^{2+}$ (**7**) confirmed meridional coordination of the dqp ligands with a very close to ideal geometry, similar to the calculated geometry (Figure 11). The ligands adopt twisted arrangements with dihedral angles between the central pyridine and quinoline units that are $35\text{--}39^\circ$, an arrangement that leads to intramolecular stacking between quinoline units. Such interligand $\pi\text{--}\pi$ interactions



Scheme 2 Synthesis of dqp ligands (a), and synthesis of $[\text{Ru}(\text{dqp})_2]^{2+}$ complexes, either in a one-step reaction (b) or via a stepwise sequence with isolation of a $[\text{Ru}(\text{dqp})(\text{MeCN})_3]^{2+}$ intermediate (c)

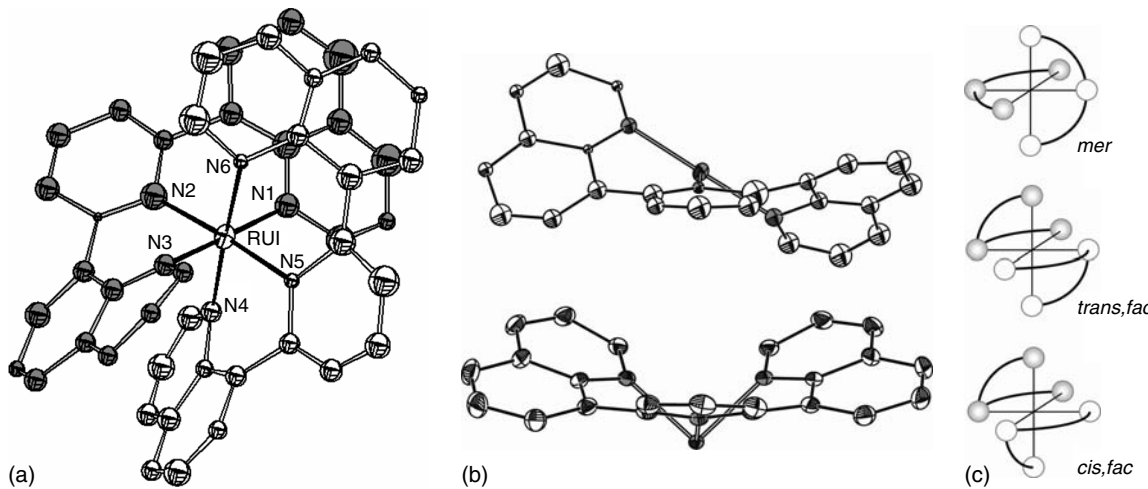


Figure 11 (a) ORTEP view of 7 at 30% probability ellipsoids, showing almost ideal bite angles (N1–Ru1–N3 and N4–Ru1–N6 bite angles are $\sim 178^\circ$). (Reproduced from Ref. 25. © American Chemical Society, 2006.) (b) Ligand orientations in the mer isomer (top) and trans, fac isomer (bottom); one dqp ligand is omitted for clarity. (Reproduced from Ref. 28. © American Chemical Society, 2009.) (c) Schematic representations of the three isomers where the trans/cis notation refers to the relative positions of the pyridine units

are also observed by ¹H NMR in solution, but it has most likely a minor role in stabilizing the structure since the dqp ligand adopts a similar helical twist in $[\text{Ru}(\text{dqp})(\text{MeCN})_3]^{2+}$.²⁸ The induced helical arrangement of the ligands makes the complex chiral (best described by symmetry label D_2) where one ligand sets the conformation of the other (either λ,λ or δ,δ conformations). Two kinetic facial products are also formed in small quantities, identified as the trans, fac and cis, fac isomers by X-ray analysis (Figure 11), which illustrates the rich coordination chemistry of the dqp ligands.

The photophysical properties of the $[\text{Ru}(\text{dqp})_2]^{2+}$ -based complexes exceeded expectations, with 7 displaying a 3 μ s luminescent ($\phi = 0.02$) ³MLCT excited state lifetime at room temperature in EtOH/MeOH mixtures (Figure 12). This is the longest lifetime ever reported for a trisubstrate Ru^{II} polypyridyl complex and is even longer than those obtained in most trisubstrate Ru^{II} complexes. The excited state energy for 7, $E_{00} = 1.84$ eV, is slightly lower than that for complex 4, as discussed above, but in contrast to complex 4, complex 7 is remarkably photostable and it has a long lifetime even at

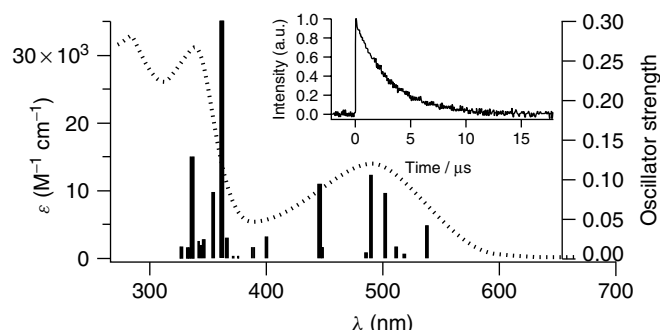


Figure 12 Measured (dotted line, MeCN) and calculated (bars, EtOH) absorption spectrum of 7. Inset: Emission decay at room temperature in oxygen-free EtOH/MeOH. (Reproduced from Ref. 25. © American Chemical Society, 2006.)

363 K (1.3 μs), where $[\text{Ru}(\text{bpy})_3]^{2+}$ shows a lifetime of only ca. 100 ns. This property is important as high temperatures may be encountered in future solar conversion systems. The long lifetime, even at high temperatures, again points to an increased energy difference between the ${}^3\text{MLCT}$ and ${}^3\text{MC}$ states due to a more octahedral coordination of the dqp ligands to Ru^{II} . The long lifetimes are maintained with only small variations in substituted complexes (1.2–5.5 μs for 7–12), which make these complexes promising candidates for elaboration along the principal axis for vectorial photoinduced charge separation.

Analysis of the emission decay in 7 revealed a radiative decay rate, which is a magnitude lower than usually observed for ${}^3\text{MLCT}$ emitters ($k_r = 7 \times 10^3 \text{ s}^{-1}$). In addition, the nonradiative rate constant (k_{nr}) was found to be lower than expected based on energy gap law arguments. This accounts for the long excited state lifetimes of this class of chromophores, and efforts are currently being made to explain these observations.

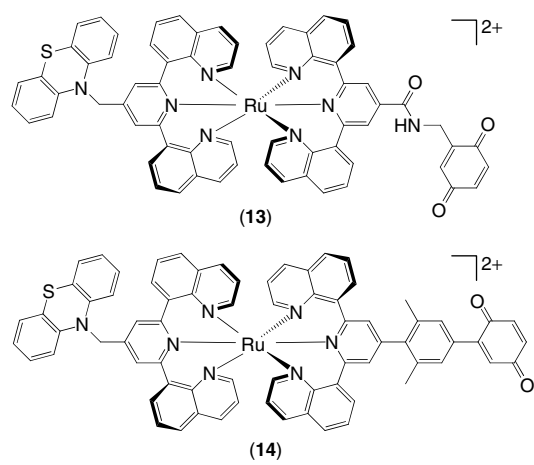


Figure 13 PTZ– Ru^{II} –Q triads 13 and 14 based on $[\text{Ru}(\text{dqp})_2]^{2+}$ units

2.2.3 $[\text{Ru}(\text{dqp})_2]^{2+}$ in Chromophore–Quencher Assemblies

The excited state of complex 7 was shown to be efficiently quenched in bimolecular photoinduced electron transfer and energy-transfer reactions. Triads 13 and 14 depicted in Figure 13, which contain a phenothiazine (PTZ) electron donor and a benzoquinone (Q) electron acceptor, were prepared to demonstrate the utility of the $[\text{Ru}(\text{dqp})_2]^{2+}$ complexes in linear D–P–A arrays for vectorial electron transfer.²⁹ The complexes were synthesized in a stepwise method with initial coordination of the acceptor-functionalized dqp ligand at the dimethoxybenzene oxidation level. Subsequent deprotection/oxidation gave the final triads. On the basis of electrochemical data and equations (6) and (7), the reaction scheme in Figure 14 was constructed.

The electron transfer products following excitation of the $[\text{Ru}(\text{dqp})_2]^{2+}$ unit was followed by transient absorption spectroscopy (Figure 14), monitoring the changes in absorption at different times after excitation. The charge-separated states are formed via oxidative quenching ($\text{PTZ}^-\text{Ru}^{II}\text{-Q} \rightarrow \text{PTZ}-\text{Ru}^{III}\text{-Q}^\bullet-$), followed by a rapid charge shift to generate the fully charge-separated state ($\text{PTZ}-\text{Ru}^{III}\text{-Q}^\bullet- \rightarrow \text{PTZ}^+\text{-Ru}^{II}\text{-Q}^\bullet-$) in high total quantum yield ($\phi \geq 95\%$ for 13). In the charge-separated state, an energy of approximately 1.2 eV is stored, and the state subsequently recombines to the ground state with $k = 5.0 \times 10^6 \text{ s}^{-1}$. The unusually high charge-separation yield is attributed to the long excited state lifetime of the $[\text{Ru}(\text{dqp})_2]^{2+}$ unit as well as the fast electron transfer from the donor moiety following the initial charge separation.

3 MIMICKING THE ELECTRON DONOR SIDE IN PHOTOSYSTEM II

Charge separation at the single-electron level is important as it mimics some key features of natural photosynthesis. However, to successfully use water as an electron source in the production of a sustainable fuel, the photoinduced single-electron transfer steps need to be coupled with charge accumulation at a single catalytic site. Four consecutive electron transfer events with a concomitant build up of redox equivalents at the catalyst must occur before water gets oxidized and molecular oxygen is released. The realization of charge accumulation leads to new thermodynamic and kinetic challenges to control. At first, each successive electron removal from the catalytic site will be increasingly difficult unless it is coupled to a charge-compensating reaction (e.g., deprotonation or ligand-exchange reactions). Without a charge-compensating reaction, each successive oxidation can be expected to increase by 0.5–1 V as a result of the increase in charge at the catalytic site. Such charge-compensating reactions occur in PSII, for example, at the intermediate Tyr_Z donor where deprotonation

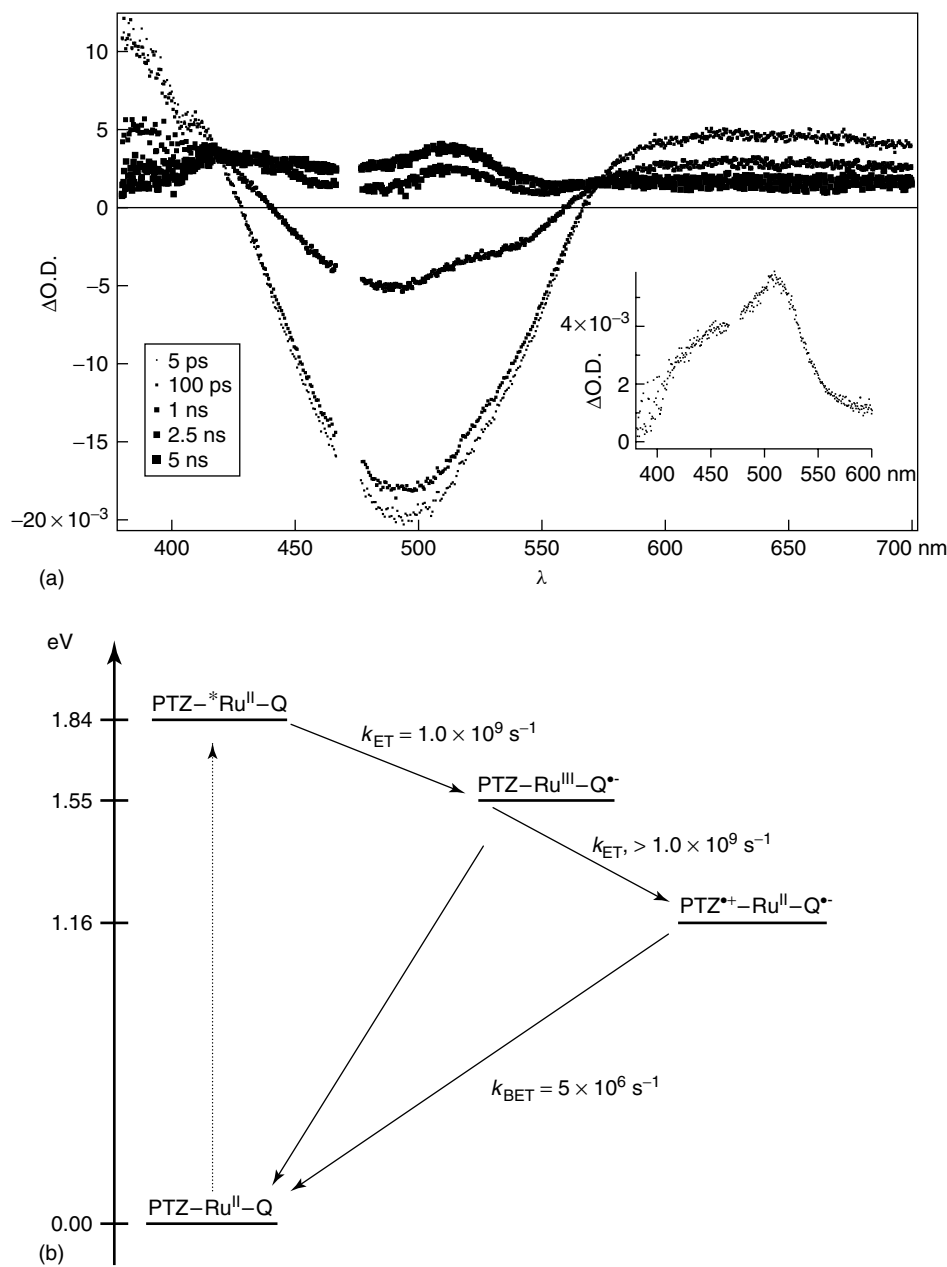


Figure 14 (a) Transient absorption spectra at different times after the initial excitation (MeCN, 298 K). Inset shows the spectrum after 5 ns, after subtraction of excited state features due to unreactive $[\text{Ru}(\text{dqp})_2]^{2+}$, showing both $\text{Q}^{\bullet-}$ (at 440 nm) and $\text{PTZ}^{\bullet+}$ (at 510 nm). (b) Reaction scheme and rate constants determined for complex **14**

occurs upon oxidation in a PCET reaction, which ensures enough driving force for reduction of P_{680}^+ . In addition, at the Mn_4Ca cluster, deprotonation and/or ligand-exchange reactions keep the potential within a narrow range and close to the thermodynamic limit for water oxidation. Similar redox contractions in synthetic systems have been thoroughly examined.³⁰

Secondly, the desired electron transfer reaction must successfully compete with undesired competing reactions such as energy transfer or reverse electron transfer quenching. As

excited chromophores are often both strong excited state oxidants and reductants, there is often considerable driving force for, e.g., competing oxidative quenching by electron transfer to an already oxidized catalyst. In addition, low-energy excited states of the oxidized electron donor or reduced electron acceptor may provide efficient quenching pathways. In PSII, efficient forward electron transfer from excited P_{680} is ensured by rapid forward electron transfer to a nearby pheophytin, while the intermediate Tyr_Z allows considerable distance between P_{680} the Mn_4Ca cluster.

3.1 Chromophore–Quencher Assemblies Involving Mn and Tyrosine Electron Donors

3.1.1 Marcus Theory and Mn Complexes as Electron Donors

Electron transfer rates can be analyzed using nonadiabatic Marcus theory, which expresses the rate of electron transfer as a function of temperature and three additional parameters (equations 8 and 9): the electronic coupling (H_{tp}), driving force (ΔG^0), and reorganization energy (λ).

$$k_{\text{ET}} = \frac{2\pi}{\hbar} |H_{\text{tp}}|^2 \frac{1}{\sqrt{4\pi\lambda k_b T}} \exp\left(\frac{-\Delta G^*}{k_b T}\right) \quad (8)$$

$$\Delta G^* = \frac{(\Delta G^0 + \lambda)}{4\lambda} \quad (9)$$

where H_{tp} depends on the electronic orbital overlap between reactant and product states, while λ is the energy needed to change the nuclear configuration of the equilibrated reactant state to the geometry of the equilibrated product state. The main contribution to λ in polar solvents using Ru^{II} polypyridyl complexes and organic electron donors and acceptors usually comes from reorganization of the surrounding medium in response to the charge redistribution (λ_{solv} typically ~ 1.0 eV).

An important conclusion from Marcus theory relates to the activation energy, ΔG^* . As evident from equation (9), when $-\Delta G^0 \geq \lambda$, a further increase in the driving force is predicted to lead to a decrease in electron transfer rate (Marcus inverted region). To rely on the inverted region is a common strategy to obtain rather long-lived charge-separated states in simple chromophore–quencher assemblies, but the lifetimes rarely exceed some hundred picoseconds to several nanoseconds. Instead, increasing the distance between the oxidant/reductant pair to obtain weak electronic coupling may also lead to slow recombination reactions. The latter strategy has successfully been used in, e.g., triads, tetrads, and pentads where efficient forward electron transfer steps are ensured by the close proximity between the redox-active components in each successive electron transfer step, while the final oxidant/reductant pair is separated over a long distance.

The Swedish Consortium for Artificial Photosynthesis has been mimicking the donor side of PSII using Ru^{II}-Tyr and Ru^{II}-Mn supramolecular chemistry, most of which has been reviewed elsewhere.^{31–34} The first studies on Ru–Mn complexes focused on mononuclear Mn^{II} complexes covalently linked to a Ru^{II} polypyridyl chromophore.^{35,36} Electron transfer from the Mn^{II} donors to photogenerated Ru^{III} was studied by laser flash photolysis in the presence of methyl viologen (MV²⁺) as an external quencher (Figure 15). The temperature dependence of electron transfer was studied and λ was determined. It was found that $\lambda = 1.4 – 2.0$ eV for all complexes studied, which suggest significant inner reorganization of the Mn complex attributed to a substantial compression of the Mn–L bond lengths in Mn^{III} compared to Mn^{II}. In

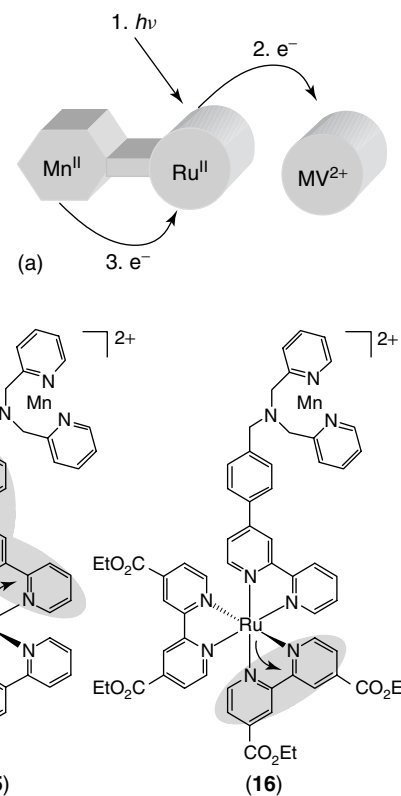


Figure 15 (a) Bimolecular oxidative quenching using MV²⁺ as quencher generates Ru^{III}, which subsequently undergoes reduction in an intramolecular electron transfer reaction. (b) Different excited state localization depending on ligand substituents

addition, undesired energy-transfer quenching of the ³MLCT excited state of the Ru^{II} chromophore by the appended Mn^{II} unit is significant but can be controlled by design that specifically takes into account excited state localization. As discussed above, the excited state of [Ru(bpy)₃]²⁺ derivatives is best described as $[(\text{bpy})_2\text{Ru}^{\text{III}}(\text{bpy}^{\bullet-})]^{\text{2}+}$ with the electron localized on a single bpy ligand. Complexes **15** and **16** differ only in the electron-withdrawing ethyl carboxylate substituents on the peripheral bpy ligands in **16**, leading to an excited state that is localized at a greater distance from the Mn^{II} unit (Figure 15). This results in a much longer Ru^{II} excited state lifetime in **16**, i.e., a smaller energy-transfer quenching rate than for **15**. In fact, the energy-transfer rate for **16** is reduced by a factor ~ 600 , similar to that predicted by the Boltzmann equilibrium of ³MLCT states (over the remote and bridging bpy ligands) based on the determined reduction potentials.

3.1.2 Proton-Coupled Electron Transfer Involving Hydrogen-Bonded Tyrosine

To model the PCET from tyrosine in PSII, intramolecular PCET was studied in the Ru^{II}-Tyr complex **17** (Figure 16).³⁷ The Ru^{II} unit was photooxidized using

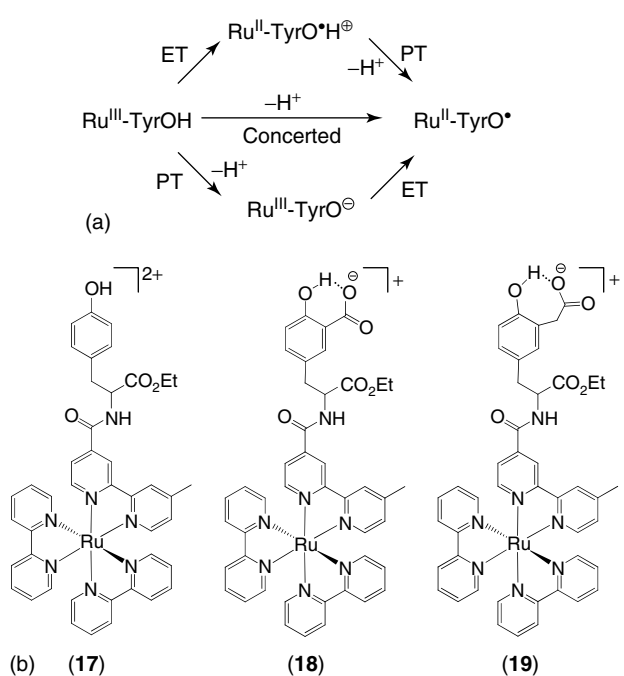


Figure 16 (a) Mechanisms of proton-coupled electron transfer. (b) Ru^{II}-Tyr complexes **17–19** studied, where **18** and **19** involve internal hydrogen bonds. The synthesis of the complexes relied on an initial preparation of the functionalized ligand, followed by the reaction with one equivalent of Ru(bpy)₂Cl₂·2H₂O according to route A in Scheme 1

external quenchers in analogy to Figure 15 and the subsequent intramolecular PCET from tyrosine was studied. The electron is transferred to Ru^{III} and the proton to the external aqueous solution. Thus, the reaction is a bidirectional PCET, which is often found in radical enzymes such as PSII but more rarely in model systems.^{38,39} It was concluded that the reaction occurs via concerted electron–proton (CEP) transfer, in which the reaction coordinates for the electron and proton are evolved to a common transition state (Figure 16). The reaction is pH dependent at pH < 10, with a slope of 0.4–0.5 in a plot of log (rate) vs pH. Neither stepwise PCET mechanisms—proton transfer followed by electron transfer (PTET) or electron transfer followed by proton transfer (ETPT)—nor CEP to OH[−] or buffer species would show this pH dependence. This behavior has been much discussed as it was believed that a CEP with proton release to the aqueous solution should not show a pH dependence.⁴⁰

Although the bidirectional CEP reaction may be expected to have larger reorganization energy than a pure electron transfer due to proton release, it can outcompete a pH-independent ETPT mechanism because it uses all available free energy in a single reaction step. However, a switch in the mechanism to ETPT was established at low pH by increasing the oxidant strength of the Ru^{III} unit or by changing the pK_a of the oxidized amino acid (tryptophan instead of tyrosine).⁴¹

The results for complex **17** show similarities to data for Tyr_Z oxidation in Mn-depleted PSII,⁴² at pH < 7, the Tyr_Z reaction shows a weak pH dependence and it was also suggested that this reaction occurs via a CEP mechanism with proton release to the bulk. At pH > 7, the Tyr_Z reaction is pH independent because of an internal hydrogen bond to His190. More recent studies of complexes **18** and **19** (Figures 16 and 17) with internal hydrogen bonds to the phenol showed similar pH-independent CEP reactions when the proton is transferred to a carboxylic base.⁴³ In a pH region between the pK_a values of the carboxylic base and the phenol, these groups form an internal hydrogen bond. The rate is then independent of pH and much higher than that in complex **17**, which may be attributed to the combined effect of a smaller reorganisation energy and better proton vibrational wave function overlap due to the stronger hydrogen bond.^{44,45} At lower pH, the base is protonated and the rate is again lower and pH dependent.

There are several interesting features of the data. One concerns the “gating” behavior shown by **19** in the low-pH region, but not by **18**. For **19** the observed PCET rate is proportional to the fraction of deprotonated carboxylic groups (pK_a = 4.3). This also shows that, at low pH, all complexes react via the fraction of deprotonated complexes forming an internal hydrogen bond, i.e., PCET is gated by the formation

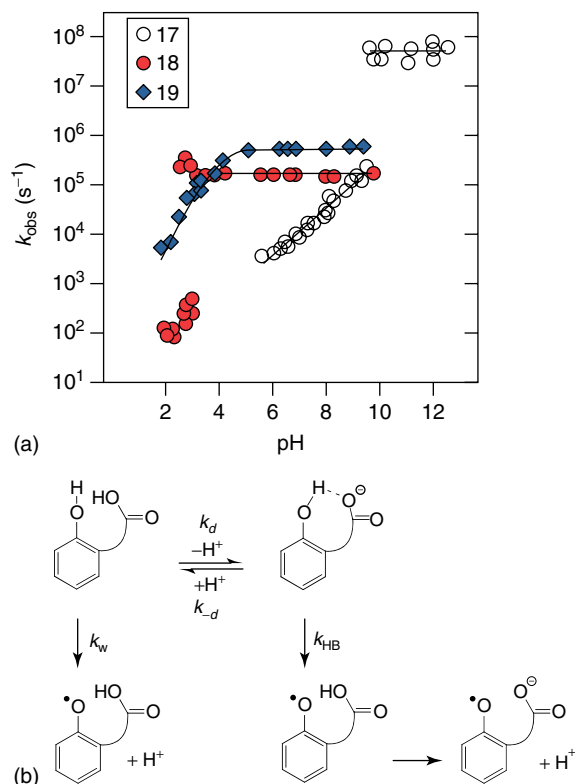


Figure 17 (a) The rate constants as a function of pH for the Ru^{II}-Tyr complexes **17–19**. (b) Mechanism of gating with an internal hydrogen bond. (Reproduced from Ref. 43. © American Chemical Society, 2008.)

of the hydrogen bond (Figure 17). The kinetics of **18** is instead biexponential at pH around the carboxylic pK_a ($= 3.1$). The faster phase, which decreases with decreasing pH, is the fraction of complexes with an internal hydrogen bond. Concomitantly, there is a larger contribution from the slow phase where the carboxylic acid is protonated. The equilibrium of deprotonation and hydrogen bond formation (k_d and k_{-d}) is faster than PCET from the nonhydrogen-bonded form (k_w) in **19**. For **18**, the opposite situation is true, as deprotonation and formation of the hydrogen bond is apparently very slow in this complex. Dynamic gating via hydrogen bond formation is frequently discussed for oxidation of Tyr_Z and Tyr_D in PSII.

In native PSII, the hydrogen bond between Tyr_Z and His190 is believed to be stronger than that in the manganese-depleted system and the rate then is even higher. It is interesting that oxidation of Tyr_Z in PSII can occur at 5 K. This low-temperature oxidation occurs only in a pH region where the Tyr_Z-His190 hydrogen bond is assumed to be set. At pH 5 when the hydrogen bond is not present, low-temperature oxidation of Tyr_Z does not occur.⁴⁶

The second feature of the data given in Figure 17 is that the intramolecular PCET rates span nearly six orders of magnitude, even though electron transfer occurs through the same Ru^{II}-Tyr structure. The rate is modulated by internal hydrogen bonds or deprotonation of the tyrosine, which shows the large impact that proton coupling may have on the kinetics of electron transfer. Thus, the data form a “rate ladder”, where the slowest step is pH dependant with the aqueous solution being the proton acceptor. With an internal hydrogen bond to a proton-accepting base, the rate is instead independent of pH and is typically faster. Finally, when the tyrosine is already deprotonated, the rate is even higher and also pH independent. Overall, the data constitute model reactions for amino acid oxidations under different conditions, and underscore the large effects proton coupling may have on electron transfer kinetics.^{45,47}

The effects of internal hydrogen bonds were studied in quantitative detail using theoretical simulation of experimental data. Temperature-dependent rate constants were determined for *intramolecular* PCET both in **18** and **19**, using H₂O and D₂O solutions to exchange the phenolic proton before the experiment.⁴⁸ A quantum mechanical model⁴⁹ was used to simulate the data, supported by DFT estimates of, e.g., proton tunneling distances and inner reorganization energies. It was found that it was necessary to include “promoting vibrations” of the heavier nuclei to simulate the experimental data. These vibrations modify the distance between the phenolic and the carboxylate oxygen atoms and thus the proton tunneling distance. The promoting vibrations greatly increase the PCET rate, as tunneling at much shorter than equilibrium distances dominates the reaction. They also reduce the kinetic isotope effect (KIE) from the hypothetical value of ca. 40—for proton tunneling fixed at the equilibrium distance—to the experimentally observed values of ca. 2 and 3 for **18** and **19**, respectively. Because of its larger

mass, the proton tunneling probability is much more distant dependent than electron tunneling, which is why, similarly, low-amplitude vibrations of donor–acceptor pairs—merely tenths of Ångströms—have no noticeable effect on electron transfer. It was noted that at low temperatures, PCET reactions approach the case of a fixed tunneling distance. This may lead to large isotope effects and very small rates, unless the hydrogen bond is short already at equilibrium. Promoting vibrations have been discussed and analyzed for reactions in proteins,⁵⁰ and often believed to involve motion of large protein regions. Our results were the first clear example of promoting vibrations impacting a PCET reaction in a small molecular system.

In addition to demonstrating the effect of promoting vibrations, it was shown that λ is higher for PCET than for a pure electron transfer from phenolate. Interestingly, the hydrogen bond in **18** is weaker and less stiff than in **19**, because it is less linear. Nevertheless, the hydrogen bond is shorter in **18**, and these effects contribute to give rates that are nearly as large as that in **19**, in spite of the ca. 25 kJ mol⁻¹ larger driving force in the latter.

3.1.3 Charge Accumulation at a Dinuclear Mn Unit

Light-induced charge accumulation at a potential catalytic site was studied in a binuclear Mn₂^{II,II}–Ru^{II} complex (**20**, Figure 18), which contains the same tyrosine link used for PCET reactions discussed in the previous section. However, dipicolylamine (dpa) units are linked in the ortho positions of the central phenol, generating the Hbpmp ligand with a N₆O donor set, studied by Hendrickson and coworkers.⁵¹ The Ru^{II} complex with the linked Hbpmp unit was prepared via an amide condensation of known [Ru(bpy)₂(4-Me-4'-CO₂H-bpy)]²⁺ with dpa-functionalized tyrosine using SOCl₂ activation. In **20**, the Mn₂^{II,II} unit contains bridging acetate ligands and the final complex was prepared by stirring the precursor with two equivalents Mn(OAc)₂ in EtOH, followed by precipitation as the PF₆⁻ salt.

Electrochemical characterization in MeCN revealed two Mn-based oxidations, to Mn₂^{III,II} and to Mn₂^{III,III}, below the reduction potential of the Ru unit. Initial experiments in MeCN established that photogenerated Ru^{III} rapidly oxidizes the Mn₂^{II,II} dimer, generating Ru^{II}–Mn₂^{III,II}, with a rate of electron transfer that is limited by the initial oxidative quenching to the sacrificial electron acceptor.⁵² Subsequent laser flash photolysis studies in 10% water in the presence of [Co(NH₃)₅Cl]²⁺ as sacrificial electron acceptor showed (by EPR) the eventual formation of Mn₂^{IV,III}, formed by oxidation in three steps by photogenerated Ru^{III}.⁵³ Although the oxidation from Mn^{III,II} → Mn^{IV,III} by photogenerated Ru^{III} is thermodynamically not favorable in MeCN, ligand-exchange reactions and subsequent charge-compensating reactions occur in aqueous solution. This is supported by extensive solution FTIR experiments and ESI mass spectrometry,⁵⁴ and

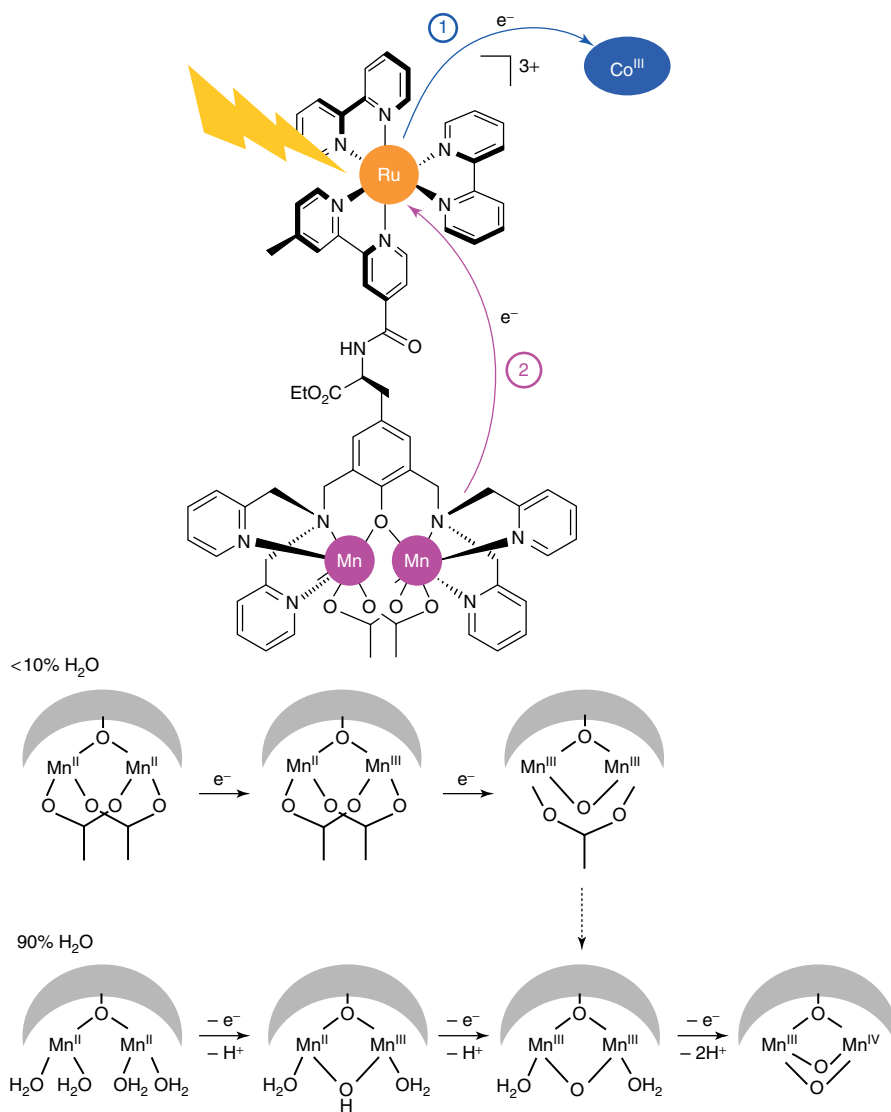


Figure 18 Water-dependent charge accumulation reactions at the Mn_2 site in the $\text{Ru}^{\text{II}}\text{--}\text{Mn}_2^{\text{II},\text{II}}$ complex **20** following bimolecular quenching with $[\text{Co}(\text{NH}_3)_5\text{Cl}]^{2+}$. A di- μ -oxo-bridged dimer was the only $\text{Mn}_2^{\text{IV},\text{III}}$ species observed by ESI mass spectrometry after online electrolysis in 10% water solution and was generated at a potential only slightly higher than the $\text{Mn}_2^{\text{II},\text{II}}/\text{Mn}_2^{\text{III},\text{II}}$ redox couple in dry MeCN

EXAFS measurements in different oxidation states of the isolated Mn_2 -bpmp complex.⁵⁵

On the basis of these studies, the simplified scheme shown in Figure 18 was constructed. Ligand-exchange reactions occur already at low water content, ca. 90% acetate remains bound in the $\text{Mn}_2^{\text{III},\text{II}}$ state at <10% water content, while less than 10% acetate remains coordinated in the $\text{Mn}_2^{\text{II},\text{II}}$ state at high water content (90%). Although the substitution of acetate ligands to aqua ligands initially leads to an increase in positive charge, the ligand exchange allows for charge-compensating deprotonation reactions of coordinated aqua ligands. This leads to a redox contraction, already at a low water concentration (<10%), where three oxidation states can be reached within ca. 0.2 V.

The yield of Mn_2 oxidation for each flash was found to be low. This is attributed to rapid quenching of the Ru^{II} excited state, in particular for higher oxidation states of the Mn_2 unit. Evidence for such competing reactions comes from the measurements on electrochemically generated $\text{Ru}^{\text{II}}\text{--}\text{Mn}_2^{\text{III},\text{II}}$ (unpublished results) and from analogous complexes based on Ru_2 electron donors where rapid quenching was observed in all oxidation states ($\text{Ru}^{\text{II}}\text{--}\text{Ru}_2^{\text{II},\text{II}}$, $\text{Ru}^{\text{II}}\text{--}\text{Ru}_2^{\text{III},\text{II}}$, and $\text{Ru}^{\text{II}}\text{--}\text{Ru}_2^{\text{III},\text{III}}$).⁵⁶ Excited state localization on remote bpy ligands, similar to Figure 15, was again shown to considerably decrease quenching rates. These results demonstrate that undesired competing quenching reactions most likely have to be taken into account in accumulative electron transfer.

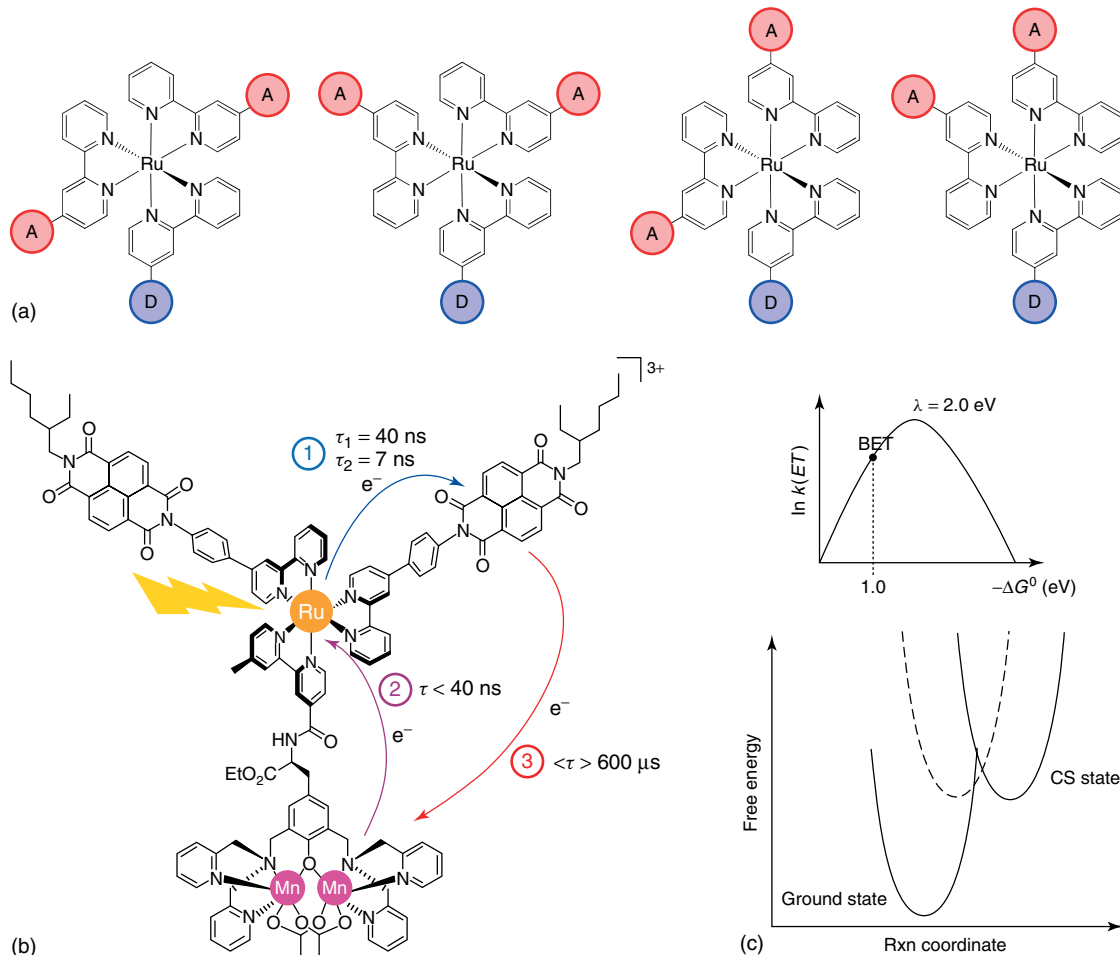


Figure 19 (a) Geometrical isomers in the $\text{Mn}_2^{\text{II},\text{II}}\text{-Ru}^{\text{II}}\text{-NDI}$ complex **21**. (b) Structure of **21**. (c) (top) The back electron transfer lies in the Marcus normal region ($-\Delta G^0 < \lambda$) in spite of the large driving force, which explains the high activation energy; (bottom) corresponding Marcus-free energy surfaces. The dashed surface represents a typical system with moderate reorganization energy

3.1.4 Long-Lived Charge Separation in a $\text{Mn}_2^{\text{II},\text{II}}\text{-Ru}^{\text{II}}\text{-NDI}$ Triad

The light-induced charge accumulation at a potential catalytic site, such as that demonstrated in complex **20**, constitutes an important step toward a functional supramolecular complex for photoinduced water splitting. The system was further elaborated by incorporating NDI electron acceptor units in a first attempt to further study the intramolecular $\text{Mn}_2^{\text{II},\text{II}} \rightarrow \text{Ru}^{\text{III}}$ electron transfer reaction. The $\text{Mn}_2^{\text{II},\text{II}}\text{-Ru}^{\text{II}}\text{-NDI}$ triad **21** (Figure 19) was synthesized in a stepwise protocol using a well-established protocol for the synthesis of heteroleptic Ru^{II} polypyridyl complexes (route B, Scheme 1).⁵⁷ The NDI-linked bpy (bpy-NDI) is identical to that used previously (in complex **1**) and was coordinated to Ru(DMSO)₄Cl₂ to give (bpy-NDI)₂RuCl₂; the latter intermediate was subsequently converted to **21** in analogy to the preparation of **20**. The material obtained is a mixture of geometrical isomers, in addition to the optical isomers, as a consequence of the unsymmetrical bpy ligands.

Time-resolved optical and EPR spectroscopies in MeCN and butyronitrile demonstrated the formation of a long-lived charge-separated state ($\text{Mn}_2^{\text{III},\text{II}}\text{-Ru}^{\text{II}}\text{-NDI}^{\bullet-}$) with an electron at an NDI unit and a hole at the Mn₂ unit. The initial quenching to form $\text{Mn}_2^{\text{II},\text{II}}\text{-Ru}^{\text{III}}\text{-NDI}^{\bullet-}$ shows biexponential kinetics ($k_1 = 2.5 \times 10^7 \text{ s}^{-1}$ (0.75) and $k_2 = 1.4 \times 10^8 \text{ s}^{-1}$ (0.25) in MeCN) and may occur partly via triplet energy transfer in analogy to complex **1**, although the driving force for electron transfer quenching is considerably larger (Figure 20). A subsequent electron transfer from the Mn₂ unit to Ru^{III} generates the charge-separated state in 20% yield (butyronitrile) at room temperature (40% yield at 140 K). The recombination reaction at both the acceptor and the donor units was monitored and found to decay in a 1 : 1 ratio with an average lifetime of 600 μs at room temperature and ca. 0.5 s at 140 K, which is the longest lifetime ever reported for an intramolecular charge-separated state involving Ru^{II} polypyridyl complexes. Both the generation of NDI^{•-} and the oxidation of Mn^{II,II} to Mn^{III,II} were followed, and it was demonstrated that each

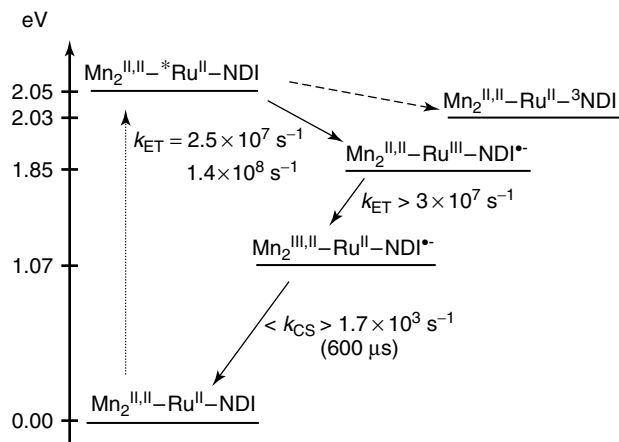


Figure 20 Reaction scheme and rate constants determined for complex **21**. The energy levels were determined using equations (6) and (7)

molecule can undergo several cycles of charge separation without noticeable degradation, which proves that a genuine charge-separated state is formed.

Analysis of the temperature dependence according to equation (8) on the initial forward electron transfer and recombination reaction rates provides insight into the unusually slow charge recombination. While the initial electron transfer, which involves only the Ru and an NDI unit, shows normal reorganization energy ($\lambda \sim 0.8$ eV), it is remarkably high for the charge recombination reaction that involves the Mn₂ unit ($\lambda \sim 2.0$ eV). Analysis of the published X-ray structures for the Mn₂^{II,II}- and Mn₂^{III,II}-bpm complexes reveals considerable bond length contractions, on an average 0.2 Å per metal–ligand bond, which can account for the large inner reorganization energy. As $-\Delta G^0 < \lambda$, the charge recombination reaction therefore occurs far down in the Marcus normal region ($\Delta G^0 \sim -1.1$ eV) and is highly activated, accounting for the long lifetime. It is also important to realize that the charge shift reaction, Mn₂^{II,II}-Ru^{III}-NDI^{•-} → Mn₂^{III,II}-Ru^{II}-NDI^{•-} ($\Delta G^0 \sim -0.8$ eV), is expected to show large inner reorganization energy, but it is not possible to verify this due to the rate-limiting initial charge separation. However, the oxidation of Mn₂^{II,II} is considerably faster than the recombination reaction in the Mn₂^{III,II}-Ru^{II}-NDI^{•-} state and can be explained by the shorter distance between the Mn₂ and Ru units.

The multiexponential kinetics, observed both in the forward electron transfer reaction (Mn₂^{II,II}-*Ru^{II}-NDI → Mn₂^{II,II}-Ru^{III}-NDI^{•-}) and the recombination reaction (Mn₂^{III,II}-Ru^{II}-NDI^{•-} → Mn₂^{II,II}-Ru^{II}-NDI), is attributed to the mixture of geometrical isomers. The biexponential kinetics in the forward reaction is particularly intriguing since a similar reference complex, [Ru(bpy-NDI)₂(4,4'-Me₂-bpy)]²⁺, shows single-exponential quenching of the Ru chromophore (unpublished results). The latter complex has an excited state mainly localized towards the NDI unit due to conjugation

with the phenyl substituents, while in **21**, because of the electron-withdrawing amide substituent, the excited state is mainly localized toward the Mn₂^{II,II} unit. A rapid Boltzmann equilibrium in the excited state as discussed for **16** above cannot explain the observations as that would show single-exponential kinetics. An alternative scenario of slow interligand hopping with the 75%/25% amplitudes from the kinetic measurements representing excited state localization toward the Mn₂^{II,II} unit and NDI unit, respectively, is interesting but would rely on improbably slow hopping kinetics on the nanosecond timescale. Instead, it is speculated that the different geometrical isomers show small variations in the Ru–NDI electronic couplings as a result of trans influence of the various pyridine donors.

3.2 Synthetic Mn Complexes for Homogeneous Water Oxidation

The mechanism of water oxidation at the OEC is still poorly understood, but based on spectroscopy, the crystal structures of PSII, and recent computational work, a number of proposals have been put forward which have been recently reviewed.^{5,58} In essence, three mechanisms are currently discussed including (i) radical mechanisms, (ii) coupling of two di- μ -oxo ligands, and (iii) nucleophilic attack on a terminal high-valent Mn-oxo (Figure 21). The proposed radical mechanisms are based on the notion that the S₂–S₃ transition might involve oxidation of another unit than Mn, e.g., a μ -oxo unit, while the S₃–S₄ transition may involve oxidation of a second μ -oxo unit or oxidation of a terminal oxygen. The second proposal invokes coupling of two μ -oxo ligands, a mechanism that has been suggested to occur in tetranuclear Mn model complexes. The third category involves nucleophilic attack of a water or hydroxide, potentially coordinated to calcium or manganese, on a high-valent Mn^V-oxo (or Mn^{IV}-oxyl) species. The latter mechanism has found support both from the proposed

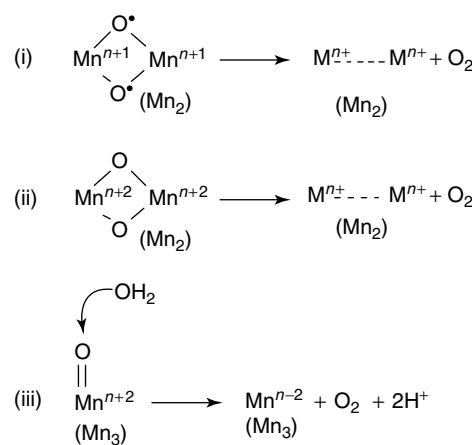


Figure 21 Summary of proposed mechanisms for the oxygen–oxygen bond formation at the OEC

$3+1$ arrangements of the Mn ions with the dangling Mn ion acting as the catalytic center and from small synthetic models.

The rational design of molecular catalysts for water oxidation relies on an understanding of the factors that govern the reactivity of high-valent metal-oxo species. Current efforts on developing catalysts for water oxidation are focusing on biomimetic Mn-based catalysts, and on Ru- and Ir-based catalysts (see *Molecular Catalysts for Oxygen Production from Water*). Although further studies on Ru- and Ir-based systems are important to establish potential mechanisms for the crucial oxygen–oxygen bond formation mechanism, more efforts using different catalysts based on more abundant and less toxic metals such as Mn are clearly desirable. The switch to Mn-based catalysts, however, imposes new challenges due to the lability of low-valent Mn ions. Although desired for rapid catalytic turnover, this can lead to the decomposition of the complexes and the formation of unknown species that may complicate analysis.

Numerous mono- and multinuclear Mn complexes have been prepared and thoroughly characterized as models for the OEC in PSII.⁵⁹ However, until recently, only two of these complexes have been shown to catalytically generate oxygen (using oxygen-containing oxidants) in solution with several turnovers: $[(\text{tpy})(\text{H}_2\text{O})\text{Mn}(\text{O})_2\text{Mn}(\text{H}_2\text{O})(\text{tpy})]^{3+}$ (**22**), studied by Brudvig and coworkers,⁶⁰ and $[\text{Mn}_{2}^{\text{II}}(\text{mcbpen})_2(\text{H}_2\text{O})_2]^{2+}$ (**23**), reported by McKenzie and coworkers.⁶¹ In these experiments, chemical oxidants are used to probe catalysis, which, together with electrochemical methods, are complementary to the desired goal of photochemical oxidation in a future artificial photosynthetic system. Brudvig and Crabtree report >50 turnovers using oxone (HSO_5^-) as oxidant and propose an oxygen–oxygen bond formation via a nucleophilic attack on a high-valent Mn^{V} -oxo species. Recent findings on oxygen–oxygen bond formation via nucleophilic attack of hydroxide in a corrole-based Mn^{V} -oxo complex support such a mechanistic model.⁶² McKenzie and coworkers in turn report 10–20 turnovers using *tert*-butyl hydroperoxide (TBHP) as oxidant and propose coupling of a di- μ -oxo $\text{Mn}_2^{\text{IV},\text{IV}}$ intermediate of complex **23**. It is important to note that only oxygen-containing oxidants were shown to efficiently generate oxygen in these systems, with one oxygen atom originating from the oxidant. This is in contrast to the much studied Ru polypyridyl aqua systems, where one-electron oxidants such as Ce^{IV} are functional (see *Molecular Catalysts for Oxygen Production from Water*). Oxidation by Ce^{IV} more closely mimics the multiple light-induced oxidations (single-photon/single-electron events) needed for charge accumulation at a potential catalytic site.

Oxygen-evolving experiments with potential catalysts have been performed using a range of different oxidants and conditions. To make a direct comparison of the performance of different catalysts, the reaction conditions and detection methods must be the same. A systematic screening of different catalysts demonstrated that Mn complexes **22–25** (Figure 22) evolved oxygen using oxygen atom transfer

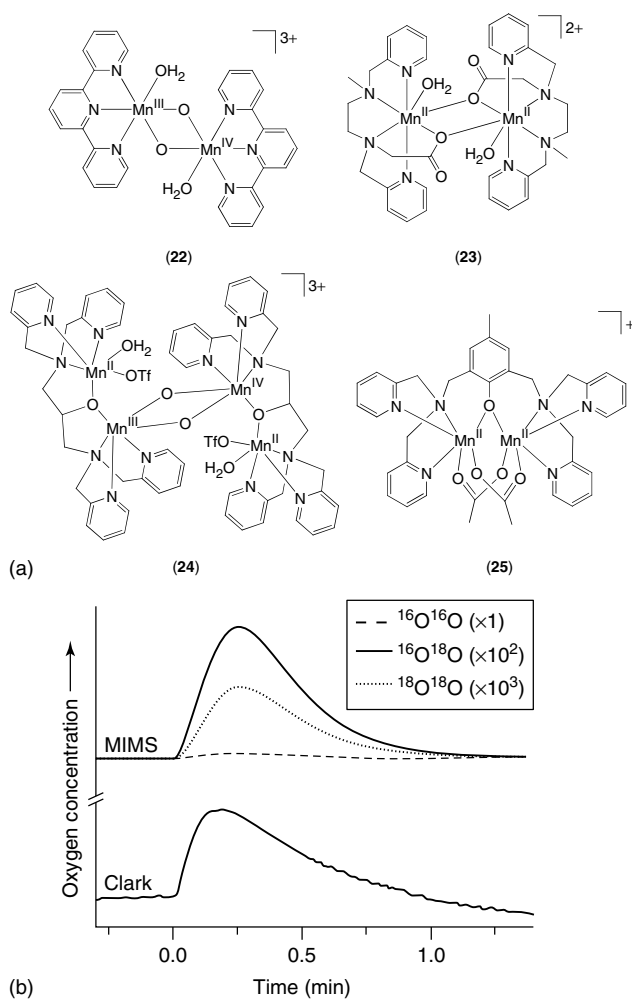


Figure 22 (a) Four complexes that promoted oxygen evolution in the presence of oxone. Only **25** was found to yield O_2 where both oxygen atoms were derived from water. (b) Oxygen evolution traces for **25** recorded by mass spectrometry (MIMS, top) and by a Clark electrode (bottom). The water in the aqueous phase contained 10% ^{18}O -labeled water, and the evolved oxygen of $^{18}\text{O}_2$, $^{16}\text{O}^{18}\text{O}$, and $^{16}\text{O}_2$, at ratios that can be expected if all oxygen atoms originated from the solvent water. (Reproduced from Ref. 64. © Royal Society of Chemistry, 2008.)

agents.⁶³ In particular, not only previous published results for **22** and **23** were reproduced using HSO_5^- and TBHP, respectively but also a more efficient oxidant (HSO_5^-) for complex **23** was discovered. Oxygen evolution was also observed for the first time for complex **25** using HSO_5^- as the oxidant, the same Mn unit used in **20** and **21** for the intramolecular light-induced reactions discussed above. This is interesting since three electrons were successfully removed from the Mn_2 unit in **20** (generating $\text{Mn}_2^{\text{IV},\text{III}}$) in reactions using photoproduced Ru^{III} as oxidant (Section 3.1.3). The origin of the oxygen atoms in **22–25** was determined using mass spectrometry with ^{18}O -labeled H_2O .⁶⁴ Complexes **22–24** showed oxygen evolution consistent with only one oxygen atom, at most,

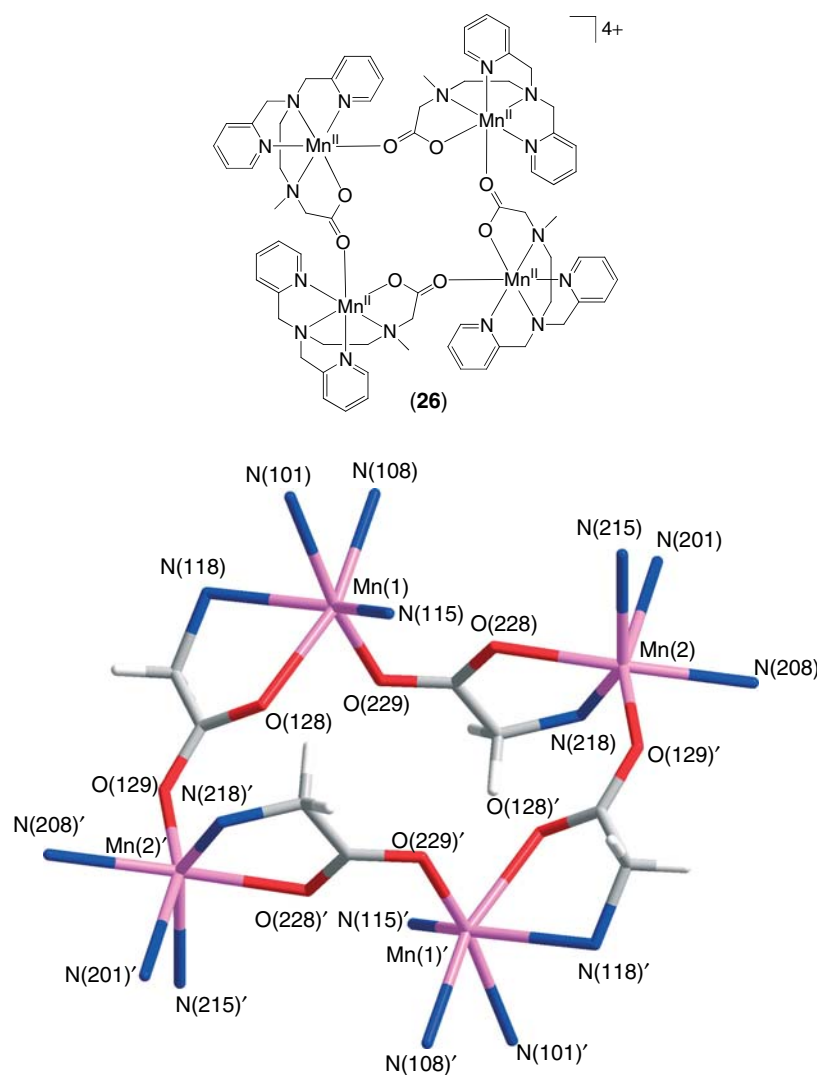


Figure 23 The metallamacrocyclic tetranuclear complex **26**. (Reproduced from Ref. 65. © Royal Society of Chemistry, 2009.)

originating from water, while the other came from the oxidant. In contrast, complex **25** gave $^{18}\text{O}_2$ -labeled oxygen where both oxygen atoms originate from water. As no oxygen was detected using Ce^{IV} , the formation of $^{18}\text{O}_2$ for **25** using oxone without incorporation of an oxygen atom from the oxidant may be explained by the potential for oxone to act as a two-electron oxidant. Similar experiments using $\text{Pb}^{\text{IV}}(\text{OAc})_4$, a well-known two-electron oxidant that has not been reported to act as an oxygen atom donor reagent, also gave $^{18}\text{O}_2$, similar to oxone, implicating the importance of two-electron oxidation. Although the reaction is not catalytic (<1 turnover), it is interesting to note that **25** is one of very few synthetic Mn complexes that homogeneously oxidizes water where two water molecules are oxidized to O_2 .

For complex **23**, a di- μ -oxo $\text{Mn}_2^{\text{IV},\text{IV}}$ intermediate was proposed as the active species that liberates oxygen similar to path (ii) in Figure 21. As the carboxylate arm was suggested

to play a key role in this process, a study was initiated where the position of this moiety was changed by repositioning one pyridyl unit and the carboxylate arm.⁶⁵ Reacting the ligand with one equivalent $\text{Mn}(\text{ClO}_4)_2$ gave a metallamacrocyclic tetranuclear complex **26** (Figure 23), with alternating μ -1,3-carboxylate and Mn ions. The complex was found to oxidize water both with HSO_5^- and Ce^{IV} as oxidants, the latter, however, in substoichiometric amounts. An important finding in this study concerned its reactivity toward $[\text{Ru}(\text{bpy})_3]^{3+}$. In the presence of lutidine as a base, a dimeric di- μ -oxo $\text{Mn}_2^{\text{IV},\text{IV}}$ intermediate forms, analogous to the reactive intermediate postulated for **23**. This species slowly reverts back to Mn^{II} , with no oxygen detected, suggesting that the di- μ -oxo $\text{Mn}_2^{\text{IV},\text{IV}}$ species is not an intermediate in the catalytic cycle. However, given the capacity of **26** to reversibly generate two oxidizing equivalents per Mn ion, current efforts focus on the isolation of the $\text{Mn}_2^{\text{IV},\text{IV}}$ species to further explore its reactivity.

4 [FeFe] HYDROGENASE ACTIVE SITE MODELS IN LIGHT-DRIVEN PROTON REDUCTION SCHEMES

4.1 [FeFe] Hydrogenase Active Site Models as Proton Reduction Catalysts

4.1.1 Mechanism of the [FeFe] H₂ases

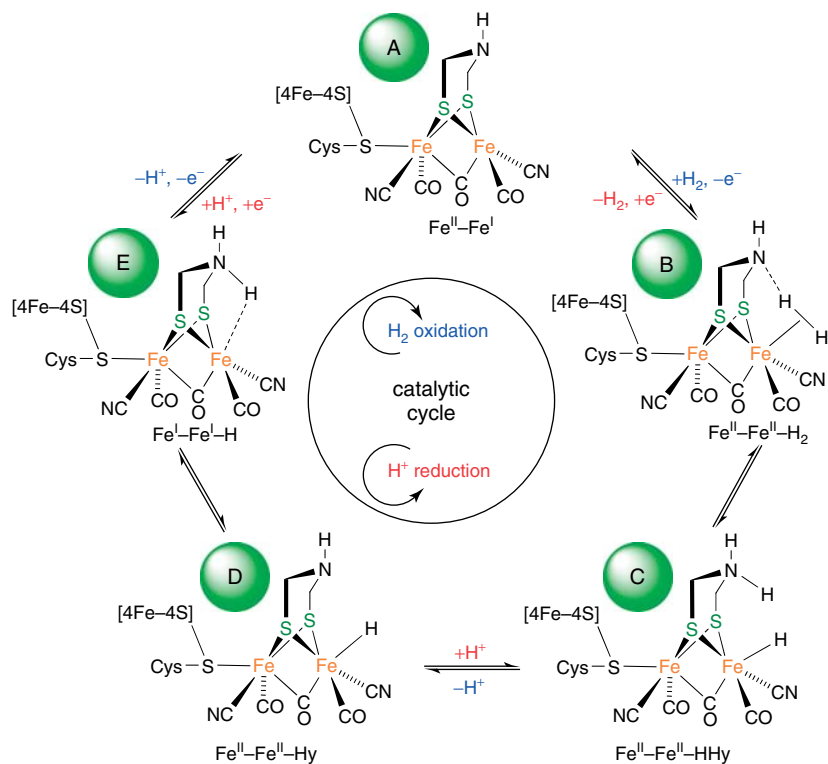
The interconversion of protons and hydrogen that is catalyzed by [FeFe] H₂ases is understood in considerable detail.⁶⁶ The reaction follows an ionic mechanism and the catalytic effect arises from the stabilization of the hydride intermediate by binding to the distal Fe (Fe^d), i.e., the Fe that is not connected to the [4Fe–4S] cluster. Available mechanistic proposals (which are typically based on DFT calculations) differ to some extent, especially in the location of the proton after heterolytic splitting of H₂. These differences result mostly from the uncertainty of the nature of the three atoms that constitute the bridge between the two thiolate ligands. A nitrogen in the dithiolate bridge offers a basic site that can accept a proton in the heterolytic splitting of hydrogen, with the hydride being accepted by Fe^d, which presumably is in an Fe^{II} oxidation state (Scheme 3).

After reductive activation (step not shown), the catalytic site is in a mixed-valent Fe₂^{II,I} oxidation state, with an intriguing arrangement of its ligands (state A). One of

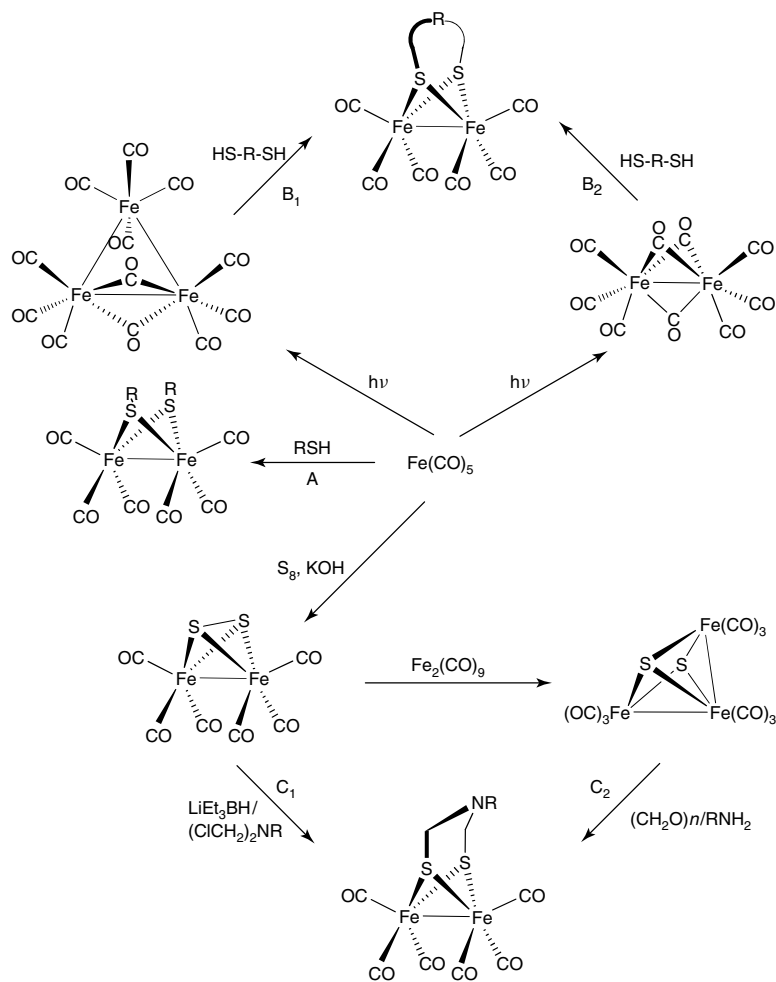
the CO ligands is in the bridging position, exposing a free coordination site of Fe^d. This ligand geometry is often referred to as the *inverted structure* to express the inversion of the square pyramidal coordination of Fe^d compared to that of the proximal Fe. The substrate H₂ binds to the free coordination site, a hypothesis that is well accepted as exogenously added CO binds to exactly this site and thereby inhibits the catalyst. Hydrogen binding in a η^2 manner is accompanied by a one-electron oxidation, either in a concerted reaction or as two discrete steps, and subsequent heterolytic splitting of H₂ leads to an iron hydride and protonation of the bridge-N (state C). In mechanistic proposals that assume the absence of a bridge-N, protonation occurs at an alternative site, for example, at the thiolate ligands or proximate amino acids. Either way, the proton is subsequently expelled to liberate the basic site. Intramolecular proton shift of the Fe^d-bound hydride to the bridge-N produces a formally reduced Fe^d, which has to be reoxidized. Finally, removal of the second proton will close the catalytic cycle. In the last steps, the order of events is again slightly unclear and concerted reactions may be beneficial.

4.1.2 Synthesis of Model Complexes

Synthetic Fe₂ complexes that are structural analogs of the active site of [FeFe] H₂ases have been known for more than 80 years when Reihlen and coworkers reacted Fe(CO)₅ with thiols (route A in Scheme 4). In the 1980s,



Scheme 3 Proposed enzymatic catalytic cycle for the oxidation of hydrogen (blue) and the reduction of protons (red)



Scheme 4 Common synthetic strategies to $[(\mu\text{-SRS})\text{Fe}_2(\text{CO})_6]$ complexes pertinent to the $[\text{FeFe}] \text{ H}_2\text{ase}$ active site

Seydel and coworkers systematically explored the chemistry of FeS carbonyl complexes, which was thus well established by the time the first crystal structure of $[\text{FeFe}] \text{ H}_2\text{ases}$ appeared in the late 1990s.^{9,10} A number of different synthetic routes toward $[\text{Fe}_2(\text{SR})_2(\text{CO})_6]$ complexes are available, some of which are depicted in Scheme 4.⁶⁷ Many routes utilize iron(0)carbonyl precursors, namely, $[\text{Fe}_3(\text{CO})_{12}]$ and $[\text{Fe}_2(\text{CO})_9]$. When dithiols are employed, complexes including the prototypic $[\text{Fe}_2(\mu\text{-pdt})(\text{CO})_6]$ with a bridging propanedithiolate (pdt) ligand can be synthesized (routes B₁ and B₂). One of the most widely used iron-carbonyl precursor is $[\text{Fe}_2\text{S}_2(\text{CO})_6]$, which can be converted to the lithium salt, $\text{Li}_2[\text{Fe}_2\text{S}_2(\text{CO})_6]$, by treatment with super-hydride (LiEt_3BH). This dianion can be alkylated, either with alkyl dihalides to form $[\text{Fe}_2(\mu\text{-}(S_2\text{R}))(\text{CO})_6]$ complexes or with bis(chloromethyl)amines to afford $[\text{Fe}_2(\mu\text{-}(\text{SCH}_2)_2\text{NR})(\text{CO})_6]$, containing the mechanistically interesting azadithiolate (adt) bridging unit (route C₁). If a substituent at the amine is not compatible with the harsh basic conditions, an alternative protocol has been developed, which relies on

a reaction of $[\text{Fe}_3\text{S}_2(\text{CO})_9]$ with formaldehyde and the amine (route C₂).

The hexacarbonyl complexes in Scheme 4 are obtained in the $\text{Fe}_2^{\text{II},\text{I}}$ oxidation state and may be used as starting materials in subsequent ligand-exchange reactions, for example, with biomimetic cyanide ligands. Other electron-donating ligands such as phosphines or carbenes can be introduced similarly. Apart from a few special cases, higher oxidation states such as $\text{Fe}_2^{\text{II},\text{I}}$ or $\text{Fe}_2^{\text{II},\text{II}}$ are not attainable in the presence of the ligand set of the initial $\text{Fe}_2^{\text{I},\text{I}}$ precursors. Higher oxidation states can, however, be stabilized by electron-donating ligands. It is in these $\text{Fe}_2^{\text{II},\text{I}}$ and $\text{Fe}_2^{\text{II},\text{II}}$ oxidation states that structural features of the isolated $[\text{FeFe}] \text{ H}_2\text{ase}$ active sites such as the semibridging CO and the inverted structure of Fe^{d} can be modeled.^{67,68}

4.1.3 Azadithiolate-Bridged Fe_2 Complexes

Structural features of the natural active site can be modeled in synthetic complexes and their function examined

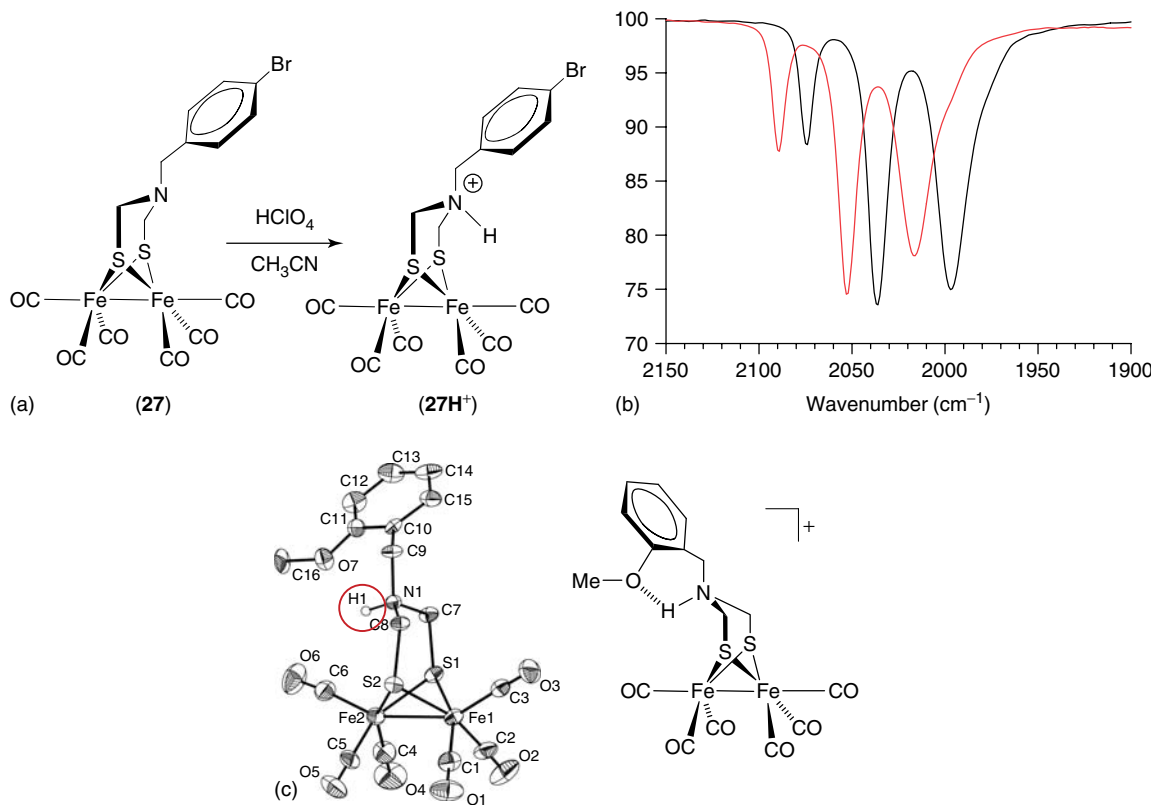


Figure 24 (a) Protonation of the adt-bridged $\text{Fe}_2^{I,I}$ complex **27** by HClO_4 , verified by IR spectroscopy (b), complex **27** (black trace) and **27H⁺** (red trace). (c) X-ray structure of a related complex with an ortho-methoxy substituent, ORTEP view 30% probability ellipsoids

by spectroscopic and electrochemical techniques. In particular, the role of the potential N-atom at the center of an adt-bridged complex is interesting from a mechanistic viewpoint, and complex **27** was thus prepared following route C₁ of Scheme 4.⁶⁹ Unexpectedly, the adt-N was found to be a very weak base. In fact, its basicity is so low that complexes where the adt-N is part of aniline cannot be protonated at all (complexes not shown). Solutions of **27** in MeCN are not affected by acetic (pK_a (MeCN) = 22) or trifluoroacetic acid (12.65), and require stronger triflic acid (2.60) or HClO_4 (≤ 2.0) for their protonation.

IR spectroscopy is a very valuable tool to probe changes of the electronic structure at the Fe_2 site as the CO ligands give strong signals in an exclusive region of the IR spectrum around 2000 cm^{-1} . The strength of the CO bond is largely determined by the degree of back-bonding from the metal into CO-based π^* -orbitals, and their stretching frequencies are thus a reliable messenger of the electron density at the metal. Protonation of **27** results in a shift of the CO stretching frequencies by ca. 15 cm^{-1} , and the structure of a similar protonated complex was verified by X-ray crystallography (Figure 24).

N-protonated **27H⁺** is a model of species E in Scheme 3 and can thus be regarded as a first intermediate on the way to catalytic proton reduction. The ability of **27** to function as

a catalyst for electrochemical proton reduction was studied by differential pulse voltammetry (Figure 25). In the absence of any acid, **27** is reduced at -1.56 V (MeCN). Addition of HClO_4 results in the protonation of the adt-N to give **27H⁺**, which is reduced already at -1.15 V . N-protonation thus shifts the reduction potential of the complex by 0.4 V toward lower values, an effect that the natural enzyme may also exploit. The addition of more acid results in the appearance of a new wave around -1.4 V , the current height of which increases with an increase in acid concentration, indicative of electrocatalytic proton reduction. Gas-chromatographic examination of the gas bubbles formed at the electrode surface unambiguously demonstrated that H_2 is produced. On the basis of these observations, a catalytic cycle was proposed that bears some resemblance to that of the enzyme active site (Figure 25). It commences with protonation of the adt-N, followed by reduction to form **27H**. After at least one more protonation and reduction, H_2 is expelled and the catalytic cycle closed. In the presence of acid and a sufficiently reducing electrode potential, catalysis is too fast to accumulate a sufficient concentration of later intermediates of the catalytic cycle that would permit their spectroscopic characterization. The chemistry of the second reduction and protonation steps, potential structural rearrangements to allow for the formation of terminal hydrides and other mechanistic details of the catalytic cycle, therefore

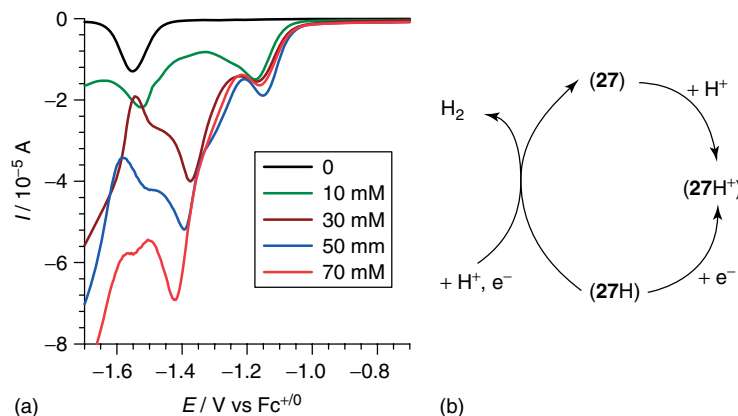


Figure 25 (a) Differential pulse voltammograms of **27** (1 mM) in the presence of 0 (black), 10 (green), 30 (brown), 50 (blue), and 70 mM (red) HClO_4 . (b) Proposed cycle for the electrocatalytic reduction of protons: initial protonation is followed by reduction. A second proton and electron uptake results in the formation of H_2 that closes the catalytic cycle

remains elusive. Although not explicitly investigated, controlled potential electrolysis of a solution of **27** in the presence of HClO_4 gave turnover numbers in the order of 100.

Electron-donating phosphines that mimic the biological cyanide ligands were introduced to increase the electron density and favor initial protonation at the $\text{Fe}_2^{\text{I},\text{I}}$ site. Similar to the natural active site, complex **28** (Figure 26) thus contains two basic sites. Addition of one equivalent of acid to a solution of **28** in MeCN affords the N-protonated species as verified by a shift of the CO vibrations in the IR spectrum of 16 cm^{-1} toward higher energy (Figure 26), reminiscent of the observed shift observed upon protonation of **27**. Excess acid leads to the formation of a new species that features only two CO stretching frequencies, shifted to higher energy by an average of 80 cm^{-1} . This shift reflects a substantial decrease in electron density as expected for a formal oxidation to an $\text{Fe}_2^{\text{II},\text{II}}$ valence state, and the species was identified as the doubly protonated hydride complex $[\text{Fe}_2(\mu\text{-Hadt})(\mu\text{-H})(\text{CO})_4(\text{PMe}_3)_2]^{2+}$, **28HHy**²⁺. Complex **28HHy**²⁺ was the first [FeFe] H₂ase-active site mimic, which carries a proton at the adt-N as well as a hydride at the Fe_2 core and, thus, resembles many features of species C in the enzymatic catalytic cycle as shown in Scheme 3, including the correct $\text{Fe}_2^{\text{II},\text{II}}$ oxidation state. Treating **28HHy**²⁺ with an excess of organic base (triethanolamine) selectively deprotonates the adt-N. The resulting **28Hy**⁺ exhibits an IR spectrum that is similar in shape to that of **28HHy**²⁺, but shifted by $\tilde{\nu}_{\text{CO}} \approx 16 \text{ cm}^{-1}$ toward lower frequencies. The hydride can be removed and **28** recovered quantitatively by the addition of an anionic inorganic base such as chloride. Of the two monoprotonated products, N-protonated **28H**⁺ is the kinetic and **28Hy**⁺ the thermodynamic product. This is supported by DFT calculations and by the experimental finding that **28H**⁺ can be transformed into **28Hy**⁺ by the addition of chloride.^{70,71}

As a result of the electron-donating PMe_3 ligands, **28** is reduced at -2.18 V . Protonation at the adt-N shifts the

reduction potential by ca. 600 mV , whereas hydride formation leads to an even more significant shift of 1 V . The two effects are not additive; the reduction of **28HHy**²⁺ proceeds at -1.00 V , but this is still one of the mildest reduction potentials ever reported for an [FeFe] H₂ase-active site mimic. However, hydride formation in **28Hy**⁺ and **28HHy**²⁺ is very slow, with bimolecular rate constants below $1 \text{ M}^{-1} \text{ s}^{-1}$ in some instances. Catalysis involving hydride species of **28** is therefore slow, and voltammetric experiments could unambiguously only establish catalysis that involves **28H**⁺. EXAFS and DFT studies on **28** in its four protonation states revealed that the largest elongation of the Fe–Fe bond distance occurs already in the transition from **28** to **28H**⁺, and that hydride formation inflicts little changes in this respect.⁷² Thus, this structural rearrangement upon protonation may explain the unusual behavior of **28**.

4.1.4 Unconventional Bridging Motifs

Over the years, a large number of Fe_2S_2 complexes have been reported, in which one or more CO ligands have been replaced by other ligands. Variations of the dithiolate, in contrast, have been underexplored. This shortcoming is somewhat surprising, considering that dithiolates can be used to electronically tune appended metal centers. Electron-withdrawing groups decrease the electron density at the Fe_2 site, render the reduction of the complex more facile, and potentially also shift the potential required for the catalytic reduction of protons to milder values. With this approach in mind, complexes with slightly unusual bridging motifs were synthesized and their properties investigated (Figure 27).

The thiolate donor strengths in **29–32** are all weaker than in **27** or **28**. The carborane in **29** is electron deficient, while the S lone pairs in **30–32** are delocalized into the aromatic ligands, both strategies leading to decreased electron density at the Fe_2 site.⁷³ As a result, the first reduction potentials of

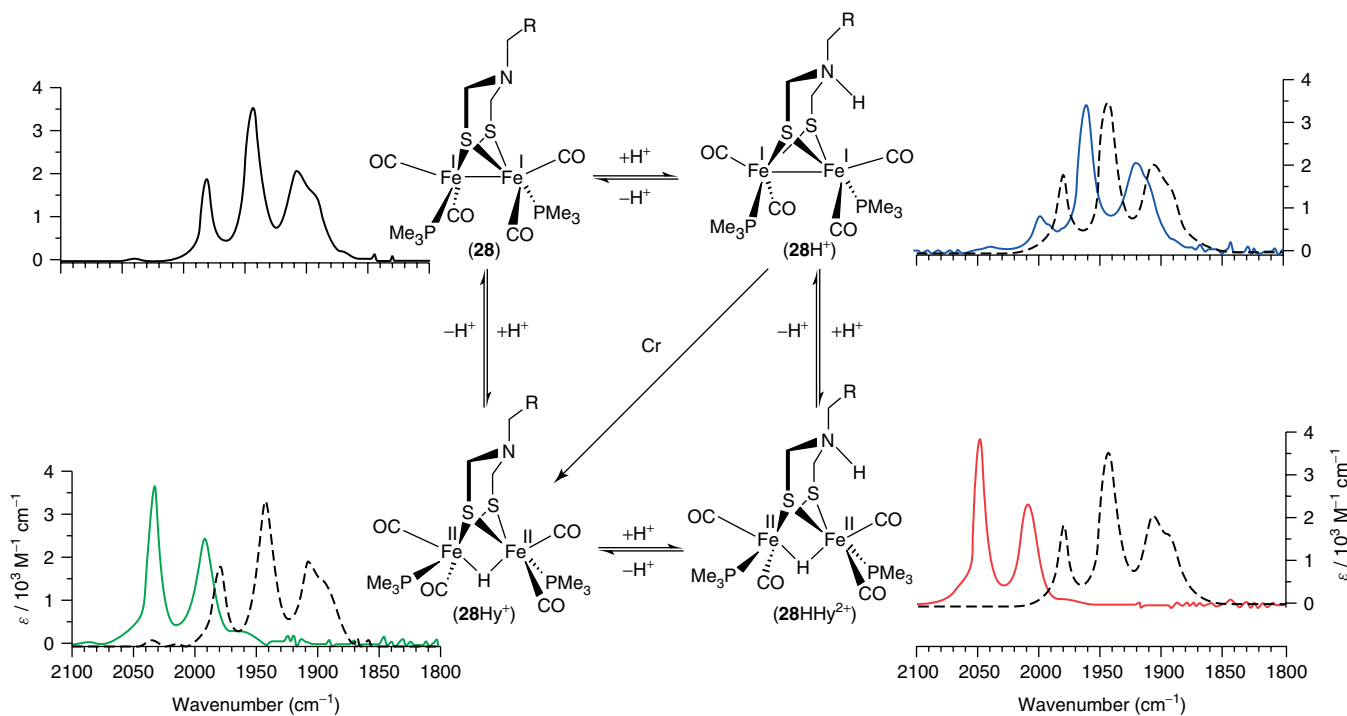


Figure 26 Protonation states of complex **28** (black) and their respective IR spectra: bridge-N protonated **28H⁺** (blue), double protonated **28HHy²⁺** (red), and hydride species **28Hy⁺** (green)

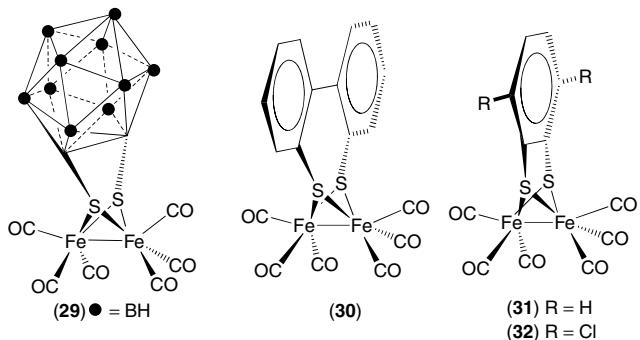


Figure 27 Fe₂ complexes with unusual dithiolate bridging motifs: carborane (**29**) and aromatics: biphenyl-2,2'-dithiolate (**30**) and benzene-1,2-dithiolate (**31** and **32**)

29–32 ($E_{1/2} = -0.88, -1.09, -1.31, -1.20$ V, respectively) are substantially anodically shifted compared to that of the pdt prototype ($E_{pc} = -1.67$ V).

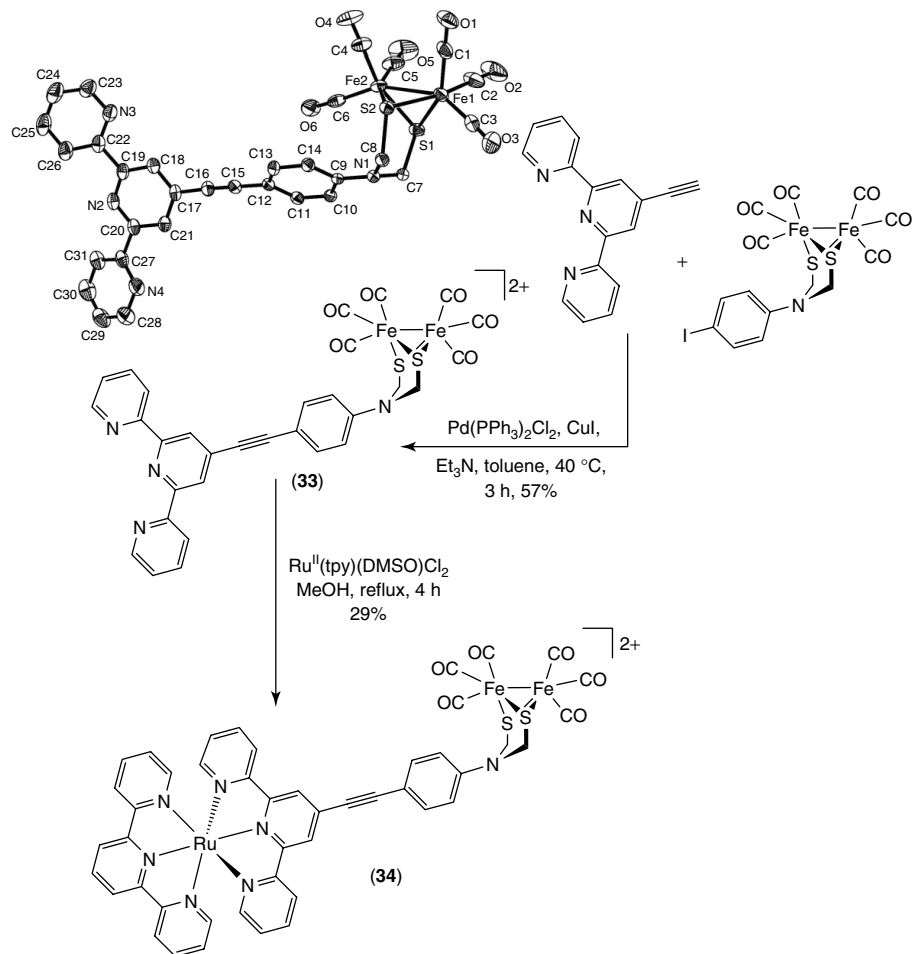
Complexes **29–32** exhibit reversible reductions in their cyclic voltammograms, which is in contrast to pdt and adt complexes, the irreversible electrochemical reductions of which are associated with CO loss and dimerization. The radical anion of **30** was isolated and characterized by FTIR and EPR spectroscopy. Aided by DFT calculations, the structure was assigned to a species that is largely similar to the parent complex, but features one broken Fe–S bond.⁷⁴ In

contrast to the two separated reversible reductions observed for **30**, the reductions of **31** and **32** are two-electron processes. This potential inversion phenomenon is facilitated by a structural rearrangement of the radical anion intermediate, which features one broken Fe–S bond and a bridging CO ligand, allowing the system to compensate for the introduced charge. A second reduction is thus enabled at the same or even milder potential, leading to an overall two-electron process. The dianions of **31** and **32** are capable to catalytically reduce protons at the potential of their electrochemical formation.^{75,76}

4.1.5 Concluding Remarks on Catalysis

Since the first reports of electrochemical proton reduction catalyzed by models of the [FeFe] H₂ase-active site by Rauchfuss⁷⁷ and the authors⁶⁹ in 2001 and 2004, respectively, the field has developed significantly. A recent review summarized the electrochemical studies performed on almost 250 complexes over the last 5 years.⁷⁵ Almost all of these catalyze the electrochemical reduction of protons, although none of them as fast and at similarly mild potential as the enzymes.

In analogy to the charge compensation reactions discussed in Section 3, the reduction potential of an Fe₂ complex and its basicity are interconnected. Reduction of the complex will increase its basicity and the reactivity of the hydride intermediates toward protons. In turn, initial protonation will lead to a decrease in the potential required for



Scheme 5 Synthetic route to Ru^{II}-Fe₂^{I,I} dyad 34. ORTEP view of 33 at 30% probability ellipsoids

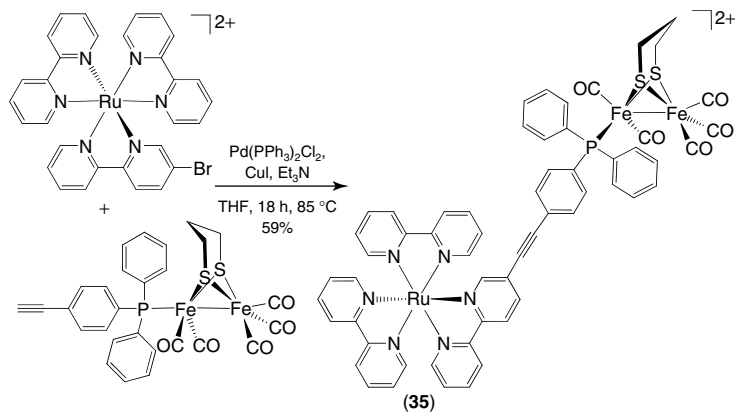
reduction. Complexes with strong donor ligands (cyanides, phosphines) such as in **28** are initially difficult to reduce but can be protonated before reduction, at least with stronger acids. On the other hand, complexes without particular donor ligands or complexes that contain even electron-withdrawing ligands such as **29–32** are reduced at a mild potential, but can be protonated only after initial reduction. The sequence of reduction and protonation events in the catalytic cycle thus strongly depends on the ligand set of the Fe₂ site, the proton activity of the medium, and the available electrode potential. Alterations of the latter two can lead to a situation where the same complex may engage in different catalytic cycles.^{75,78,79}

4.2 Ruthenium-[FeFe] Systems for Photochemical Hydrogen Production

Covalently linked Ru^{II}-Fe₂^{I,I} dyads were prepared to study the interaction between the Ru^{II} polypyridyl unit and the Fe₂^{I,I} catalyst in a defined environment at a fixed distance. The two units can be connected either through the organic part of the Fe₂^{I,I} complex, i.e., the dithiolate bridge or through

a ligand to the Fe₂^{I,I} unit. An example of the first strategy was presented already in 2003.⁸⁰ The synthesis relied on a Sonogashira cross-coupling reaction between an iodoarene-substituted [(adt)Fe₂(CO)₆] complex and an acetylenic tpy to afford complex **33** (Scheme 5). A Ru^{II} fragment was subsequently introduced using standard conditions (route D in Scheme 1) to give **34**. In the preparation of **33** and **34**, it is vital to avoid the use of strong nucleophiles once the [(\mu-SRS)Fe₂(CO)₆] unit is present. These easily attack the CO ligands, ultimately leading to ligand-substitution reactions. In addition, uncoordinated polypyridyl ligands may coordinate to the Fe₂ site. However, it was found that complex **33** was stable enough to be isolated presumably due to an unfavorable geometry for the coordination of the tpy ligand, although it is rapidly decomposed under ambient light.

The synthetic sequence for the second strategy also relied on a Sonogashira reaction but used fully assembled Ru^{II} polypyridyl and Fe₂^{I,I} subunits (Scheme 6).⁸¹ Although some of the synthetic flexibility is lost in such a convergent approach, it is necessary in order to avoid undesired decomposition of the Fe₂ site caused by uncoordinated bpy.



Scheme 6 Synthetic route to $\text{Ru}^{\text{II}}\text{-}\text{Fe}_2^{\text{I},\text{I}}$ dyad **35**

Excited state quenching of the Ru^{II} polypyridyl chromophores by the appended $\text{Fe}_2^{\text{I},\text{I}}$ units was demonstrated by time-resolved optical spectroscopy. In **34**, the ${}^3\text{MLCT}$ emission is quenched by 70% compared to a reference complex lacking the $\text{Fe}_2^{\text{I},\text{I}}$ unit, which was attributed to energy-transfer quenching by the Förster mechanism.⁸² Electron transfer quenching is thermodynamically not favored as the reduction potential of the $\text{Fe}_2^{\text{I},\text{I}}$ moiety is too negative with respect to the excited state reduction potential of the Ru^{II} chromophore. Light-induced electron transfer from the chromophore to the $\text{Fe}_2^{\text{I},\text{I}}$ unit may still be feasible, however, using a reductive quenching pathway with an external electron donor. As discussed in Section 2.1.1, photoreduced Ru^{l} is 500 mV more reducing than that of the excited state (${}^*\text{Ru}^{\text{II}}$) and would thus provide sufficient driving force to reduce the Fe_2 site. For complex **35**, oxidative quenching is even more unfavorable due to the electron-donating phosphine ligand in the coordination sphere of the Fe_2 site. Instead, reductive quenching by reverse electron transfer from the $\text{Fe}_2^{\text{I},\text{I}}$ unit to ${}^*\text{Ru}^{\text{II}}$ is thermodynamically favorable.⁸¹ This may explain the relatively high light sensitivity of **35** as the transiently oxidized Fe_2 complex ($\text{Fe}_2^{\text{II},\text{l}}$) is known to be unstable.

To establish photocatalytic proton reduction by models of the $[\text{FeFe}] \text{H}_2\text{ase}$ -active site, it is not imperative to use covalently linked dyads. Although spatial control is lost

in bimolecular systems, the screening of many potential Fe_2 catalysts without the need for industrious dyad syntheses is enabled. A further advantage of the bimolecular approach lies in the option to alter the ratio between the catalyst and the photosensitizer, which may be advantageous in cases where the availability of one or the other is limiting. However, models of the $[\text{FeFe}] \text{H}_2\text{ase}$ -active site have long been believed to be unqualified as catalytic units in photochemical schemes, with the first published attempts giving less than five equivalents of H_2 per catalyst.⁷⁸ One of the major reasons for this poor performance arises presumably from the known instability of reduced Fe_2 species, which, compared to electrocatalytic experiments, need to exhibit a longer lifetime in photocatalytic schemes where the next reducing equivalent may not be available immediately.

The reversible reductive electrochemistry and its capacity to reduce protons to molecular hydrogen electrocatalytically at a relatively mild potential (-1.2 V) made complex **32** a promising candidate for photochemical hydrogen evolution.⁷⁶ Using ascorbic acid as both an electron and a proton donor and $[\text{Ru}(\text{bpy})_3]^{2+}$ as a photosensitizer, hydrogen was detected in a $\text{DMF}/\text{H}_2\text{O}$ solution and identified by gas chromatography (Figure 28).⁸³ Experiments at varying pH revealed that reductive quenching of the Ru^{II} excited state is rate limiting. Increasing the pH from 3.5 to 5.5 increases the

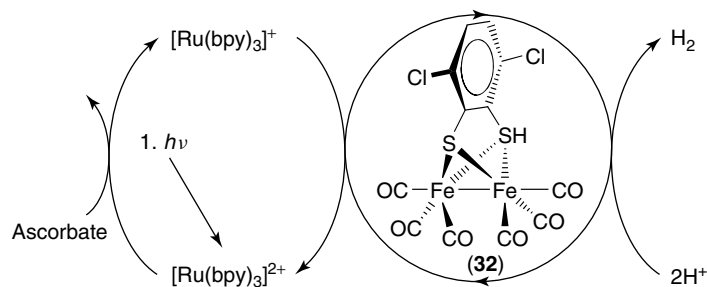


Figure 28 Proposed catalytic cycle for the photochemical reduction of protons catalyzed by **32** in 1 : 1 $\text{H}_2\text{O}/\text{DMF}$ at near neutral pH

ascorbate fraction, which gives rise to larger amounts of Ru¹. Under these conditions, up to 200 turnovers per catalyst were reproducibly obtained at a maximum rate of 2.4 turnovers per minute.⁸³ This behavior was interpreted by the presence of an intermediate in the catalytic cycle that decomposes in the absence of a proximate electron donor, but can be kept in the catalytic cycle when electron transfer is sufficiently fast. After H₂ evolution leveled out, an FTIR spectroscopic investigation of the reaction mixture indicated that all Fe₂ catalyst was consumed. It is remarkable that the near neutral pH of 5.5 is still sufficient to protonate the reduced Fe₂ intermediate to form a hydride and to protonate this hydride to form hydrogen and thus close the catalytic cycle.

5 CONCLUDING REMARKS

In this article, much of the research on biomimetic systems relevant for the light-driven splitting of water performed within the Swedish Consortium for Artificial Photosynthesis has been described. While the exact detail of the water-oxidizing mechanism and the structure of OEC remains elusive, the structure of the [FeFe] H₂ase-active sites has led to an impressive progress within the field to develop cheap and sustainable homogeneous catalysts for the production of hydrogen. A similar development within biomimetic Mn-based catalysts for water oxidation will hopefully become reality as we learn more about the natural system. Inorganic chemistry plays a central role in this process, developing metal complexes that are based on abundant elements and are capable to perform the multielectron catalytic processes needed for small molecule activation. The realization of a solar fuel using a biomimetic approach, however, requires that these multielectron processes are coupled to single-photon/single-electron events involving chromophores and electron acceptors/donors. This calls for a strong interdisciplinary research involving many branches of chemistry.

While photoinduced charge separation at a single-electron level can be controlled to a large extent, more research on charge accumulation at a catalytic site involving consecutive single-electron transfer steps is needed. Much has been learned about these processes, e.g., charge-compensating reactions such as PCET, studying multimolecular systems or supramolecular assemblies with spatial control of the components. This knowledge has led to new insights in the design of next generation of biomimetic systems. Self-organization and self-repair are of particular concern for future energy conversion systems using molecular approaches. The multielectron processes of water oxidation and reduction inevitably place high demands on the systems, requiring many different components that have to be assembled into a single device. Relying on supramolecular structures that can self-assemble would be advantageous and may allow for a mechanism of self-repair/replacement to be built into the

system. Alternatively, more robust systems may be developed that would allow catalytic turnovers that fulfill those needed for the production of sustainable solar fuel in the future.

6 ACKNOWLEDGMENTS

We thank all present and past collaborators and coworkers in the Swedish Consortium for Artificial Photosynthesis who have contributed to this work. Financial support from the Swedish Research Council (VR), the Swedish Energy Agency, the Knut and Alice Wallenberg Foundation, and EU (NEST-STRP 516510 “SOLAR-H”; FP7 Energy 212508 “SOLAR-H2”) is gratefully acknowledged. L.H. gratefully acknowledges a Research fellow position during 2002–2007 from the Royal Swedish Academy of Science, and a generous grant from the Swedish Foundation for Strategic Research.

7 ABBREVIATIONS AND ACRONYMS

ATP = adenosine triphosphate; CEP = concerted electron–proton; DFT = density functional theory; EPR = electron paramagnetic resonance; ESI = electrospray ionisation; ET = electron transfer; ETPT = electron transfer followed by proton transfer; EXAFS = extended X-ray absorption fine structure; KIE = kinetic isotope effect; LC = ligand-centered; MC = metal centered; MLCT = metal-to-ligand charge transfer; NDI = naphthalenediimide; OEC = oxygen-evolving Mn₄Ca complex; PI = pyromellitimide; PCET = proton-coupled electron transfer; PSII = photosystem II; PT = proton transfer; PTET = proton transfer followed by electron transfer; PTZ = phenothiazine; TBHP = *tert*-butyl hydroperoxide.

8 RELATED ARTICLES

Electrochemical and Photoelectrochemical Conversion of CO₂ to Alcohols; Energy Conversion in Photosynthesis; H₂ Production from Renewables; Molecular Catalysts for Oxygen Production from Water; Photocatalytic Hydrogen Production from Water.

9 REFERENCES

- N. S. Lewis and D. G. Nocera, *Proc. Natl. Acad. Sci. U. S. A.*, 2006, **103**, 15729.

2. V. Balzani, A. Credi, and M. Venturi, *ChemSusChem*, 2008, **1**, 26.
3. J. Yano, J. Kern, K. Sauer, M. J. Latimer, Y. Pushkar, J. Biesiadka, B. Loll, W. Saenger, J. Messinger, A. Zouni, and V. K. Yachandra, *Science*, 2006, **314**, 821.
4. H. Dau and M. Haumann, *Science*, 2006, **312**, 1471.
5. J. P. McEvoy and G. W. Brudvig, *Chem. Rev.*, 2006, **106**, 4455.
6. K. N. Ferreira, T. M. Iverson, K. Maghlaoui, J. Barber, and S. Iwata, *Science*, 2004, **303**, 1831.
7. B. Loll, J. Kern, W. Saenger, A. Zouni, and J. Biesiadka, *Nature*, 2005, **438**, 1040.
8. M. Haumann, C. Müller, P. Liebisch, L. Iuzzolino, J. Dittmer, M. Grabolle, T. Neisius, W. Meyer-Klaucke, and H. Dau, *Biochemistry*, 2005, **44**, 1894.
9. J. W. Peters, W. N. Lanzilotta, B. J. Lemon, and L. C. Seefeldt, *Science*, 1998, **282**, 1853.
10. Y. Nicolet, C. Piras, P. Legrand, E. C. Hatchikian, and J. C. Fontecilla-Camps, *Structure*, 1999, **7**, 13.
11. J. H. Alstrum-Acevedo, M. K. Brennaman, and T. J. Meyer, *Inorg. Chem.*, 2005, **44**, 6802.
12. A. Juris, V. Balzani, F. Barigelli, S. Campagna, P. Belser, and A. von Zelewsky, *Coord. Chem. Rev.*, 1988, **84**, 85.
13. S. Campagna, F. Puntiliero, F. Nastasi, G. Bergamini, and V. Balzani, *Top. Curr. Chem.*, 2007, **280**, 117.
14. S. Wallin, J. Davidsson, J. Modin, and L. Hammarström, *J. Phys. Chem. A*, 2005, **109**, 4697.
15. J. M. Calvert, J. V. Caspar, R. A. Binstead, T. D. Westmoreland, and T. J. Meyer, *J. Am. Chem. Soc.*, 1982, **104**, 6620.
16. L. Spiccia, G. B. Deacon, and C. M. Kepert, *Coord. Chem. Rev.*, 2004, **248**, 1329.
17. R. Ziessel, V. Grosshenny, M. Hissler, and C. Stroh, *Inorg. Chem.*, 2004, **43**, 4262.
18. F. R. Keene, *Coord. Chem. Rev.*, 1997, **166**, 121.
19. O. Johansson, M. Borgström, R. Lomoth, M. Palmlund, J. Bergquist, L. Hammarström, L. Sun, and B. Åkermark, *Inorg. Chem.*, 2003, **42**, 2908.
20. M. Borgström, S. Ott, R. Lomoth, J. Bergquist, L. Hammarström, and O. Johansson, *Inorg. Chem.*, 2006, **45**, 4820.
21. S. Ott, M. Borgström, L. Hammarström, and O. Johansson, *Dalton Trans.*, 2006, **11**, 1434.
22. E. A. Medlycott and G. S. Hanan, *Coord. Chem. Rev.*, 2006, **250**, 1763.
23. H. Wolpher, O. Johansson, M. Abrahamsson, M. Kritikos, L. Sun, and B. Åkermark, *Inorg. Chem. Commun.*, 2004, **7**, 337.
24. M. Abrahamsson, H. Wolpher, O. Johansson, J. Larsson, M. Kritikos, L. Eriksson, P.-O. Norrby, J. Bergquist, L. Sun, B. Åkermark, and L. Hammarström, *Inorg. Chem.*, 2005, **44**, 3215.
25. M. Abrahamsson, M. Jäger, T. Österman, L. Eriksson, P. Persson, H.-C. Becker, O. Johansson, and L. Hammarström, *J. Am. Chem. Soc.*, 2006, **128**, 12616.
26. M. Abrahamsson, M. Jäger, R. J. Kumar, T. Österman, P. Persson, H.-C. Becker, O. Johansson, and L. Hammarström, *J. Am. Chem. Soc.*, 2008, **130**, 15533.
27. M. Jäger, L. Eriksson, J. Bergquist, and O. Johansson, *J. Org. Chem.*, 2007, **72**, 10227.
28. M. Jäger, R. J. Kumar, H. Görts, J. Bergquist, and O. Johansson, *Inorg. Chem.*, 2009, **48**, 3228.
29. R. J. Kumar, S. Karlsson, D. Streich, A. Rolandini Jensen, M. Jäger, H.-C. Becker, J. Bergquist, O. Johansson, and L. Hammarström, *Chem. Eur. J.*, 2010, **16**, 2830.
30. M. H. V. Huynh and T. J. Meyer, *Chem. Rev.*, 2007, **107**, 5004.
31. L. Sun, L. Hammarström, B. Åkermark, and S. Styring, *Chem. Soc. Rev.*, 2001, **30**, 36.
32. R. Lomoth, A. Magnuson, M. Sjödin, P. Huang, S. Styring, and L. Hammarström, *Photosynth. Res.*, 2006, **87**, 25.
33. L. Hammarström and S. Styring, *Phil. Trans. R. Soc. B*, 2008, **363**, 1283.
34. A. Magnuson, M. Anderlund, O. Johansson, P. Lindblad, R. Lomoth, T. Polivka, S. Ott, K. Stensjö, S. Styring, V. Sundström, and L. Hammarström, *Acc. Chem. Res.*, 2009, **113**, 1899.
35. L. Sun, H. Berglund, R. Davydov, T. Norrby, L. Hammarström, P. Korall, A. Börje, C. Philouze, K. Berg, A. Tran, M. Andersson, G. Stenhammar, J. Mårtensson, M. Almgren, S. Styring, and B. Åkermark, *J. Am. Chem. Soc.*, 1997, **119**, 6996.
36. M. L. A. Abrahamsson, H. Berglund Baudin, A. Tran, C. Philouze, K. E. Berg, M. K. Raymond-Johansson, L. Sun, B. Åkermark, S. Styring, and L. Hammarström, *Inorg. Chem.*, 2002, **41**, 1534.
37. M. Sjödin, S. Styring, B. Åkermark, L. Sun, and L. Hammarström, *J. Am. Chem. Soc.*, 2000, **122**, 3932.
38. C. J. Chang, M. C. Y. Chang, N. H. Damrauer, and D. G. Nocera, *Biochim. Biophys. Acta—Bioenerg.*, 2004, **1655**, 13.
39. J. M. Mayer, *Ann. Rev. Phys. Chem.*, 2004, **55**, 363.
40. L. I. Krishtalik, *Biochim. Biophys. Acta—Bioenerg.*, 2003, **1604**, 13.
41. M. Sjödin, S. Styring, H. Wolpher, Y. Xu, L. Sun, and L. Hammarström, *J. Am. Chem. Soc.*, 2005, **127**, 3855.
42. R. Ahlbrink, M. Haumann, D. Cherepanov, O. Bögerhausen, A. Mulkidjanian, and W. Junge, *Biochemistry*, 1998, **37**, 1131.
43. T. Irebo, O. Johansson, and L. Hammarström, *J. Am. Chem. Soc.*, 2008, **130**, 9194.
44. M. Sjödin, T. Irebo, J. E. Utas, J. Lind, G. Merényi, B. Åkermark, and L. Hammarström, *J. Am. Chem. Soc.*, 2006, **128**, 13076.
45. S. Hammes-Schiffer and A. V. Soudackov, *J. Phys. Chem. B*, 2008, **112**, 14108.
46. K. G. V. Havelius, J.-H. Su, Y. Feyziyev, F. Mamedov, and S. Styring, *Biochemistry*, 2006, **45**, 9279.
47. T. F. Markle and J. M. Mayer, *Angew. Chem. Int. Ed.*, 2008, **47**, 738.

48. L. O. Johannissen, T. Irebo, M. Sjödin, O. Johansson, and L. Hammarström, *J. Phys. Chem. B*, 2009, **113**, 16214.
49. A. M. Kutznetzov and J. Ulstrup, *Can. J. Chem.*, 1999, **77**, 1085.
50. M. J. Knapp and J. P. Klinman, *Eur. J. Biochem.*, 2002, **269**, 3113.
51. H. Diril, H.-R. Chang, X. Zhang, S. K. Larsen, J. A. Potenza, C. G. Pierpont, H. J. Schugar, S. S. Isied, and D. N. Hendrickson, *J. Am. Chem. Soc.*, 1987, **109**, 6207.
52. L. Sun, M. K. Raymond, A. Magnuson, D. LeGourriérec, M. Tamm, M. Abrahamsson, P. Huang Kenéz, J. Mårtensson, G. Stenhamn, L. Hammarström, S. Styring, and B. Åkermark, *J. Inorg. Biochem.*, 2000, **78**, 15.
53. P. Huang, A. Magnuson, R. Lomoth, M. Abrahamsson, M. Tamm, L. Sun, B. van Rotterdam, J. Park, L. Hammarström, B. Åkermark, and S. Styring, *J. Inorg. Biochem.*, 2002, **91**, 159.
54. G. Eilers, C. Zettersten, L. Nyholm, L. Hammarström, and R. Lomoth, *Dalton Trans.*, 2005, **6**, 1033.
55. A. Magnuson, P. Liebisch, J. Höglblom, M. F. Anderlund, R. Lomoth, W. Meyer-Klaucke, M. Haumann, and H. Dau, *J. Inorg. Biochem.*, 2006, **100**, 1234.
56. Y. Xu, G. Eilers, M. Borgström, J. Pan, M. Abrahamsson, A. Magnuson, R. Lomoth, J. Bergquist, T. Polívka, L. Sun, V. Sundström, S. Styring, L. Hammarström, and B. Åkermark, *Chem. Eur. J.*, 2005, **11**, 7305.
57. M. Borgström, N. Shaikh, O. Johansson, M. F. Anderlund, S. Styring, B. Åkermark, A. Magnuson, and L. Hammarström, *J. Am. Chem. Soc.*, 2005, **127**, 17504.
58. R. Eisenberg and H. B. Gray, *Inorg. Chem.*, 2008, **47**, 1697. and subsequent review articles in the *Inorganic Chemistry Forum*, p. 1700.
59. S. Mukhopadhyay, S. K. Mandal, S. Bhaduri, and W. H. Armstrong, *Chem. Rev.*, 2004, **104**, 3981.
60. J. Limburg, J. S. Vrettos, L. M. Liable-Sands, A. L. Rheingold, R. H. Crabtree, and G. W. Brudwig, *Science*, 1999, **283**, 1524.
61. A. K. Poulsen, A. Rompel, and C. J. McKenzie, *Angew. Chem. Int. Ed.*, 2005, **44**, 6916.
62. Y. Gao, T. Åkermark, J. Liu, L. Sun, and B. Åkermark, *J. Am. Chem. Soc.*, 2009, **131**, 8726.
63. P. Kurz, G. Berggren, M. F. Anderlund, and S. Styring, *Dalton Trans.*, 2007, **38**, 4258.
64. K. Beckmann, H. Uchtenhagen, G. Berggren, M. F. Anderlund, A. Thapper, J. Messinger, S. Styring, and P. Kurz, *Energy Environ. Sci.*, 2008, **1**, 668.
65. G. Berggren, A. Thapper, P. Huang, P. Kurz, L. Eriksson, S. Styring, and M. F. Anderlund, *Dalton Trans.*, 2009, 10044, DOI: 10.1039/b906175d.
66. P. E. M. Siegbahn, J. W. Tye, and M. B. Hall, *Chem. Rev.*, 2007, **107**, 4414.
67. C. Tard and C. J. Pickett, *Chem. Rev.*, 2009, **109**, 2245.
68. F. Gloaguen and T. B. Rauchfuss, *Chem. Soc. Rev.*, 2009, **38**, 100.
69. S. Ott, M. Kritikos, B. Åkermark, L. Sun, and R. Lomoth, *Angew. Chem. Int. Ed.*, 2004, **43**, 1006.
70. G. Eilers, L. Schwartz, M. Stein, G. Zampella, L. D. Gioia, S. Ott, and R. Lomoth, *Chem. Eur. J.*, 2007, **13**, 7075.
71. L. Schwartz, G. Eilers, L. Eriksson, A. Gogoll, R. Lomoth, and S. Ott, *Chem. Commun.*, 2006,, 520.
72. S. Löscher, L. Schwartz, M. Stein, S. Ott, and M. Haumann, *Inorg. Chem.*, 2007, **46**, 11094.
73. L. Schwartz, L. Eriksson, R. Lomoth, F. Teixidor, C. Viñas, and S. Ott, *Dalton Trans.*, 2008,, 2379.
74. P. S. Singh, H.-C. Rudbeck, P. Huang, S. Ezzaher, L. Eriksson, M. Stein, S. Ott, and R. Lomoth, *Inorg. Chem.*, 2009, **48**, 10883.
75. G. A. N. Felton, C. A. Mebi, B. J. Petro, A. K. Vannucci, D. H. Evans, R. S. Glass, and D. L. Lichtenberger, *J. Organomet. Chem.*, 2009, **694**, 2681.
76. L. Schwartz, P. S. Singh, L. Eriksson, R. Lomoth, and S. Ott, *C. R. Chim.*, 2008, **11**, 875.
77. F. Gloaguen, J. D. Lawrence, and T. B. Rauchfuss, *J. Am. Chem. Soc.*, 2001, **123**, 9476.
78. R. Lomoth and S. Ott, *Dalton Trans.*, 2009, 9952, DOI: 10.1039/b911129h.
79. J.-F. Capon, F. Gloaguen, F. Y. Pétillon, P. Schollhammer, and J. Talarmin, *Coord. Chem. Rev.*, 2009, **253**, 1476.
80. S. Ott, M. Kritikos, B. Åkermark, and L. Sun, *Angew. Chem. Int. Ed.*, 2003, **42**, 3285.
81. J. Ekström, M. Abrahamsson, C. Olson, J. Bergquist, F. B. Kaynak, L. Eriksson, L. Sun, H.-C. Becker, B. Åkermark, L. Hammarström, and S. Ott, *Dalton Trans.*, 2006,, 4599.
82. S. Ott, M. Borgström, M. Kritikos, R. Lomoth, J. Bergquist, B. Åkermark, L. Hammarström, and L. Sun, *Inorg. Chem.*, 2004, **43**, 4683.
83. D. Streich, Y. Astuti, L. Schwartz, R. Lomoth, L. Hammarström, and S. Ott, *Chem. Eur. J.*, 2010, **16**, 60.

Direct Ethanol Fuel Cells

Zhi Wen Chia and Jim Yang Lee

National University of Singapore, Singapore

1	Introduction	229
2	Anode Catalysts	230
3	Cathode Catalysts	243
4	Conclusions	243
5	End Notes	250
6	Related Articles	250
7	Abbreviations and Acronyms	250
8	References	250

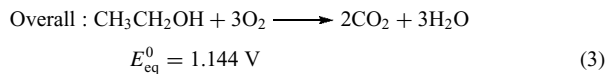
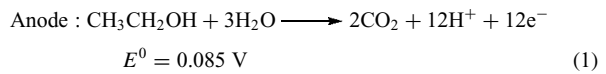
1 INTRODUCTION

Fuel cells operate by oxidizing a fuel electrochemically with air (oxygen) to produce direct current electricity without the classical combustion process (and hence are not subjected to the Carnot cycle limitation in energy conversion). In hydrogen fuel cells, for example, hydrogen is oxidized to water in a process which is the reverse of water electrolysis.¹ The catalytic oxidation of hydrogen at the anode and the reduction of oxygen at the cathode create a potential difference between the electrodes. This potential difference generates current flow by electrons in the external circuit and current flow by ionic species in the fuel cell electrolyte. The product of this reaction is clean water, and the energy from the chemical reaction is liberated as electricity amidst some heat. For low-to-moderate temperature applications such as mobile power sources, the polymer electrolyte membrane fuel cells (PEMFCs), where an ionically conducting polymer membrane is used in lieu of a liquid electrolyte, have drawn the most interest. A fuel other than hydrogen may be used directly (direct fuel cells) or reformed into hydrogen for use in a hydrogen fuel cell (indirect fuel cells). The direct fuel cells have the salient advantage of operating without a reformer, and are therefore simpler in construction. However, the direct oxidation of fuel at the anode without any additional treatment depends on the availability of an effective catalyst, and is not always possible.

Alcohols, and in particular methanol, have been extensively studied as the fuel for direct fuel cells for mobile applications.^{2–4} Methanol is preferred to hydrogen because it

is a liquid and thus its transport, storage, and handling are much easier than hydrogen. However, methanol is a neurotoxin and its large miscibility with water⁵ could lead to potential environmental issues. The fuel cell community is now looking at ethanol as an alternative to methanol. Compared to methanol, ethanol has a number of salient advantages: (i) a higher energy density (24 MJ L^{-1}) that compares favorably with methanol (15.6 MJ L^{-1}) and even compressed hydrogen (5.6 MJ L^{-1} at 700 bar)⁶; (ii) ethanol can be produced from biomass through fermentation processes. A variety of renewable resources may be used, such as sugar cane, wheat, corn, and straw.^{7,8} In principle, the use of ethanol as a fuel would not alter much of the natural balance of carbon dioxide in the atmosphere, as the carbon dioxide released from the fuel cell is reused by the biomass.

In a direct ethanol fuel cell (DEFC), the typical reactions occurring at the electrodes and the overall reaction are the following (the electrode potentials are given with respect to the standard hydrogen electrode, or SHE):



The theoretical open-circuit potential of a DEFC is about 1.144 V, which is comparable to that of a direct methanol fuel cell (DMFC).² However, due to a myriad

of irreversibilities in fuel cell operation (such as mixed potential at electrodes, activation losses, ohmic losses, and mass transport losses), this reversible cell voltage is not realized even under the open-circuit condition. The typical potential of a DEFC is about 0.79–0.82 V at 50 °C depending on the ethanol feed concentration.⁹ In addition, the DEFC has several significant technical issues, in particular the slow anode kinetics which results in poor fuel cell performance. The oxidation of fuel requires the use of an effective catalyst in order to deliver the current density expected of a commercially viable mobile power source. Platinum-based catalysts are most commonly used for the oxidation of small organic molecules, but the low operating temperature of the DEFC requires catalysts that are more active than Pt. The current anode catalysts do not prove to be very effective in achieving high current densities or sufficiently high conversions.^{7,8} Consequently, the typical anode Pt catalyst loadings for the hydrogen PEMFC, the DMFC, and the DEFC are about 0.05–0.1, 2, and 1.5–2 mg cm⁻² respectively.^a The anode activation overpotential increases to about 600 mV¹⁰ at a cell current density of about 100 mA cm⁻². Thus, there is a need to improve existing catalysts or to develop new catalysts that can oxidize the ethanol molecules more effectively and more completely.

In addition, it is also known that the ethanol fed to the anode compartment of a DEFC can permeate through the polymer electrolyte membrane into the cathode compartment. This is similar to the case of methanol crossover in DMFCs. However, due to both its lower permeability through the Nafion membrane and its slower electrochemical oxidation kinetics on the Pt/C cathode, ethanol crossover affects the cell performance less severely than methanol crossover.¹¹ Nonetheless, due to the low activity of the oxygen reduction reaction (ORR) on Pt, there is still strong interest to look for alternatives to pure Pt for the cathode. A suitable cathode material for the DEFC should therefore have a high tolerance to ethanol besides good ORR activity.

There have been a few previous reviews on the DEFCs,^{7,8} and this article aims to build upon those reviews as well as give a more recent outlook on the developments in the field. It provides a succinct account of the catalysts currently in use at the anode and cathode of a DEFC. More emphasis is placed on the discussion of anode catalysts that operate under the common acidic environment. The use of cocatalysts, promoters, supports, as well as catalysts developed for ethanol oxidation in alkaline media is also briefly mentioned.

2 ANODE CATALYSTS

Pt-based catalysts are commonly used for the oxidation of fuel in hydrogen PEMFCs and DMFCs, but pure Pt catalysts exhibit a rather lower catalytic activity when ethanol is used as the fuel.⁷ The oxidation of ethanol on

polycrystalline Pt surfaces generates a mixture of products including acetaldehyde, acetic acid, and carbon dioxide.¹² This is an indication that ethanol is not completely oxidized to carbon dioxide to release its full count of 12 electrons (via reaction (1)). Instead, a significant portion of ethanol is partially oxidized to intermediate products. The oxidation of ethanol to acetaldehyde results in the release of only two electrons:



and the oxidation of ethanol to acetic acid releases four electrons:



The electrooxidation of ethanol generally involves a network of series and parallel reactions, and only the direct route to carbon dioxide releases the full count of 12 electrons. Figure 1 is a schematic representation of the major reaction pathways for ethanol electrooxidation, along with the number of electrons released.

The efficiency of ethanol oxidation is very different from that of methanol. Contrary to methanol oxidation where over 90% of the products is CO₂, the formation of CO₂ is limited to 20–40% and is dependent on the catalyst used.¹⁴ In most of the reactions with the catalysts developed so far, the main products of ethanol electrooxidation are acetaldehyde and acetic acid, both containing an intact C–C bond. This implies that a lot of the latent energy in the ethanol molecule cannot be fully released. Also, the typical power density of a DEFC is about 6–80 mW cm⁻², which is substantially lower than the power density of 250 mW cm⁻² that can be obtained from a DMFC working at a cell voltage of 0.2–0.3 V. This is in spite of the higher energy density of ethanol compared with methanol.

Several mechanisms have been proposed to explain the formation of various reaction products on platinum electrodes.^{2,15,16} The reaction mechanism in Figure 2 is the one most generally accepted and is consistent with electrochemical

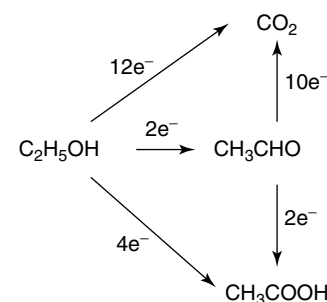


Figure 1 Schematic representation of the parallel pathways for ethanol oxidation¹⁷. (Reproduced from Ref. 13. © Elsevier, 2005.)

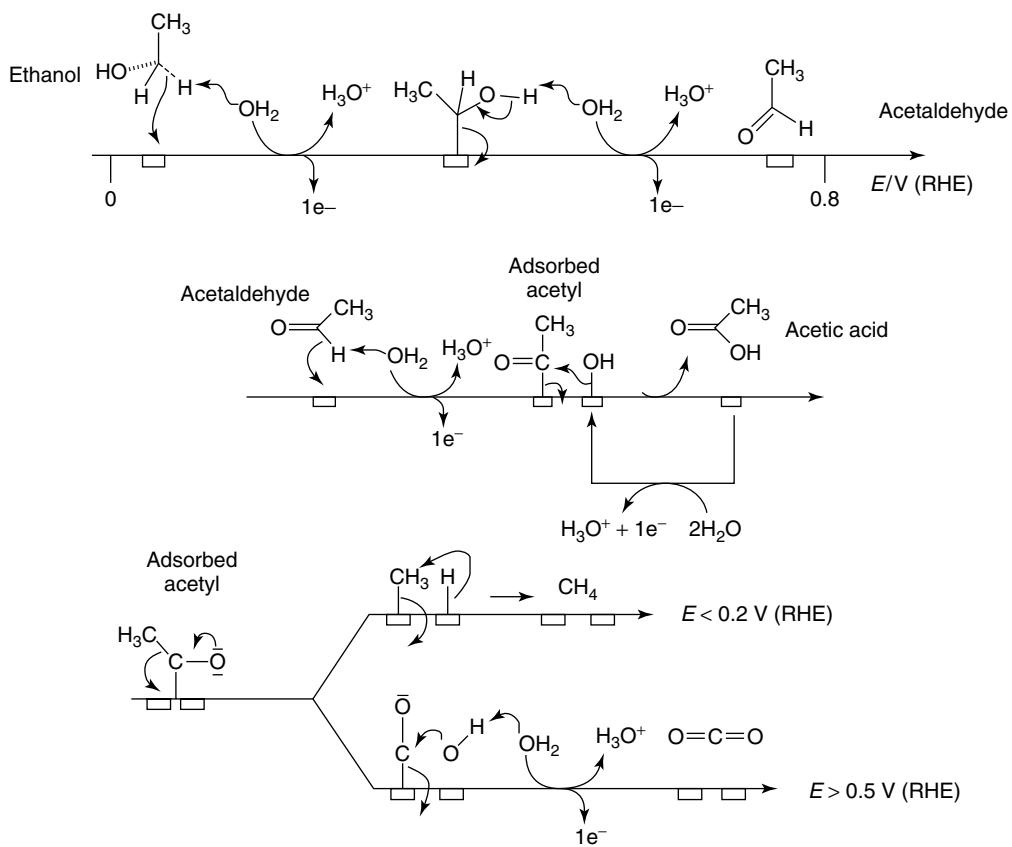


Figure 2 Mechanism of ethanol electrooxidation at platinum surface in acidic medium. (Reproduced from Ref. 18. © Springer, 2006.)

in situ infrared reflectance spectroscopic measurements.¹⁸ According to this mechanism, ethanol first adsorbs on the surface of the catalyst followed by the cleavage of the α -C–H bond. The O–H bond of the adsorbed ethanol is cleaved next to form acetaldehyde, releasing two electrons per ethanol molecule. Acetaldehyde then has to readsorb on the catalyst surface to undergo further oxidation to either acetic acid or carbon dioxide with methane production a possibility at low potentials ($E < 0.2$ V versus SHE). An extra oxygen atom is needed in order to further the oxidation reaction leading to these species and this is provided by an activated adsorbed water molecule on the platinum surface. The oxidation from acetaldehyde to acetic acid results in the release of a further two electrons, whereas the oxidation from acetaldehyde to carbon dioxide results in the release of a further 10 electrons.

It can be seen from the mechanism that the dissociative adsorption of ethanol also produces strongly adsorbed species, which can deactivate the surface of pure Pt.¹² Thus there is a need to modify the Pt catalysts for sustainable catalytic activity, and efforts in this regard are mostly based on the addition of cocatalysts such as ruthenium and tin to platinum.⁸

Lai and Koper¹⁹ investigated the surface structure dependence of the ethanol oxidation reaction (EOR) using

single-crystal Pt electrodes. On the basis of their results and the results in the electrochemistry and ultrahigh vacuum literature reported earlier, the authors suggested a detailed reaction scheme for ethanol oxidation. According to this mechanism, ethanol initially adsorbs weakly on the Pt surface through the lone pair electrons on the oxygen. Once adsorbed, the ethanol can then be oxidized to (weakly) adsorbed acetaldehyde. This reaction requires two dehydrogenation steps, and it is suggested that the first bond to be broken under electrochemical conditions is the α -C–H bond. The cleavage of the O–H bond is the other dehydrogenation step. It is also proposed that C–C bond breaking occurs mainly in acetaldehyde, especially in the potential range where ethanol is readily oxidized to acetaldehyde. However, C–C bond breaking may also occur in ethanol or ethoxy at low potentials ($E < 0.3$ V), especially on the step sites. The authors also concluded that the oxidation of ethanol to acetaldehyde is a surface-sensitive reaction which occurs preferentially at or near step sites. The direct oxidation of acetaldehyde, however, shows the opposite trend of a decreasing overall activity with increasing step density. The authors explained this by hypothesizing that the current observed for ethanol oxidation at high ethanol concentrations is mainly the result of the oxidation of ethanol to acetaldehyde. This reaction

has preference for the step sites and thus the overall activity increases with increasing step density. In the case of acetaldehyde oxidation to acetic acid at potentials above 0.7 V, the steps sites are also used for C–C bond breaking. It is the blockage of these sites by the partial products of the C–C bond-breaking reaction that resulted in the observed decrease in the overall activity with increasing step density.

The structure sensitivity of ethanol oxidation on Pt was also investigated by Wang and Liu²⁰ using density functional theory calculations. The authors examined the reaction network of ethanol oxidation on three common Pt surfaces, namely the close-packed Pt{111} faces, the stepped Pt{211} faces, and the open Pt{100} faces, and reported a strong dependence of the oxidation products of ethanol oxidation on the Pt surface crystallography. The open Pt{100} surface was found to be the best facet to fully oxidize ethanol at low coverages, a conclusion similar to that of Lai and Kopper.¹⁹ This was attributed to the effectiveness of this facet for two important reaction steps, namely the initial dehydrogenation of ethanol and the oxidation of acetyl. The authors also showed that CO₂ and acetic acid originate from the same surface intermediate (acetyl), but acetaldehyde comes directly from ethanol. C–C bond breaking occurs through strongly chemisorbed precursors such as CH₂CO or CHCO only at low-coordinated surface sites, whereas acetaldehyde formation proceeds via the one-step concerted dehydrogenation of ethanol which prefers the close-packed Pt{111} faces. This could explain why commercial Pt catalysts and polycrystalline Pt, with their preponderance of low energy {111} faces, all have poor CO₂ selectivity in ethanol electrooxidation. Han *et al.*²¹ also reported enhanced ethanol electrooxidation activities on Pt nanocubes with dominant {100} faces, and attributed this to preferential C–C bond breaking on the edges of the {100} stepped sites.

2.1 Binary Catalysts

Some of the more extensively researched binary anode catalysts for DEFCs are based on the Pt–Ru^{7,8,13,15,22–37} and Pt–Sn^{4,5,7,8,28–30,36,38–58} bimetallics. The better performance of these binary catalysts for ethanol oxidation relative to Pt-only catalysts has been credited to a bifunctional mechanism^{29,41,46,59} and to the electronic interaction^{29,60} between Pt and the adjuvant metal, similar to the case of methanol oxidation. According to the bifunctional mechanism, Ru or Sn can activate water at potentials lower than that on pure Pt, and the presence of Ru oxides or Sn oxides is able to provide labile oxygen atoms to the neighboring Pt sites for the oxidation of strongly adsorbed oxygen-containing species there, consequently lowering the inhibiting effect of the latter in anode catalysis. The mechanism in Figure 2 shows that an extra oxygen atom is needed in order to oxidize acetaldehyde to acetic acid and carbon dioxide. The electronic effect theorizes that the adsorption of oxygen-containing species such as acetyl and CO is altered by the presence of Ru or Sn because of the

modification of the electronic structure of Pt. Besides Pt–Ru and Pt–Sn, Pt–Rh,^{37,61–64} Pt–W,^{33,53} Pt–Pd,^{53,65} Pt–Ce,⁶⁶ and Pt–Mo^{26,67} have also been investigated as potential binary catalysts.

2.1.1 Pt–Ru Catalysts

The alloys of Pt and Ru have been extensively studied and used as electrocatalysts for fuel cells, due to the belief that alloying Pt with the more oxophilic Ru could help raise the CO-tolerance of the platinum electrocatalysts.⁷ Pt–Ru catalysts have indeed shown enhanced activities for methanol oxidation in DMFCs, and were thus among the first to be considered for DEFC anode catalysis.

Pure Pt has a face-centered cubic (fcc) crystal structure, while Ru is hexagonal close-packed (hcp). Pt and Ru can form solid solutions with the Pt atoms on the lattice points of the fcc structure replaced by Ru atoms up to about 0.7 atomic fraction of Ru.⁶⁸ There is a decrease in the Pt lattice parameter as more Ru is added. Above 0.7 atomic fraction of Ru, the Pt atoms replace the Ru atoms in the hcp structure to form solid solutions of Pt in Ru. It should be mentioned that while unsupported Pt–Ru alloys could be prepared over a wide range of composition, the current method of preparation of supported Pt–Ru catalysts (i.e., via the concurrent deposition of Pt and Ru precursors on the carbon support followed by metal precursor coreduction) makes it difficult to obtain Pt : Ru atomic ratios comparable to those in the unsupported bulk Pt–Ru alloys.⁶⁹

With regard to the electrooxidation of ethanol, Liu *et al.*²² observed that the addition of Ru to Pt improves the catalyst's tolerance to the accumulation of carbonaceous species. From the ratios of the forward anodic peak current density to the reverse anodic peak current density, the authors found that a large quantity of intermediate carbonaceous species is not oxidized to CO₂ in the forward scan, and this gives rise to catalyst poisoning. The presence of Ru facilitates the oxidation of chemisorbed species such as CH₃–COOH and Pt–CO_{ads} from the partial oxidation of ethanol in the forward scan and the activity for ethanol electrooxidation increases. These findings are in agreement with the results of Fujiwara *et al.*²³ where the promoter action of Ru in the oxidation of strongly bound chemisorbed intermediates may be used to explain the higher CO₂ yield compared with Pt/C. On the other hand, Camara *et al.*²⁴ reported that Ru addition could inhibit the dissociative adsorption of ethanol. This is probably due to the reduction in the number of neighboring Pt sites, which are necessary for the scission of the C–C bond. This is consistent with the findings of Chatterjee *et al.*,²⁵ who studied the kinetics of ethanol electrooxidation on Pt and Pt–Ru catalysts of various compositions in the temperature range of 25–45 °C, and observed a minimum in the apparent activation energy for ethanol oxidation at around 15–20 atom % of Ru in the Pt–Ru alloy catalysts. The minimum could be explained by a geometric model, which supposes an ensemble

of three Pt atoms with an adjacent Ru atom is required for the efficient electrooxidation of ethanol. The calculated probability distribution of such an ensemble also shows a high occurrence (~84% of the maximum probability) at around 15–20 atom % of Ru in the Pt–Ru alloys.

The importance of the amount of Ru in the Pt–Ru/C alloy catalysts is also reported by others. Camara *et al.*²⁴ found that ethanol oxidation rate is high only in a relatively narrow range of Pt–Ru composition. At low Ru concentrations (less than 20 atom %), there are not enough Ru sites to effectively assist in the oxidation of the adsorbed residues and the oxidation current remains almost at the same level as that of pure Pt. At high Ru concentrations (more than 40 atom %), there is a dilution of the Pt sites which results in decreased ethanol adsorption and consequently a reduction in the oxidation current. Neto *et al.*²⁶ investigated the cyclic voltammetric response of Pt–Ru catalysts up to 40 atom % of Ru and concluded that the ethanol electrooxidation activity of Pt–Ru/C increases with the Ru content. However, in the study of Spinacé *et al.*²⁷ on ethanol electrooxidation on Pt–Ru/C up to 75 atom % of Ru, a monotonically increasing relationship was reported between ethanol oxidation activity and Ru content for all compositions. The authors attributed this to the presence of more ruthenium oxide species on the nanoparticles surface. Liu *et al.*²² also found from single-stack fuel cell tests that the power density of the fuel cell follows a volcano curve with increasing Ru content of the Pt–Ru/C catalyst, and a maximum power density was found at 48 atom % of Ru. Hence, while the Ru content is undeniably an important factor in the Pt–Ru catalyst design, there is no consensus on the optimal Ru content.

The results from fuel cell tests also confirmed Pt–Ru/C as a more effective anode catalyst than Pt/C.^{5,28,29} Figure 3 shows the dependence of the maximum power density on cell temperature in the temperature range of 70–100 °C for single cells with Pt/C, Pt–Sn/C (3 : 1), and Pt–Ru/C (1 : 1) anode electrocatalysts. The figure clearly shows the superiority of the alloy catalysts in providing a higher power density at all the temperatures studied.

Table 1 Summary of performance of single fuel cell tests using different anode catalysts at 90 °C. (Reproduced from Ref. 29. © Elsevier, 2003.)

Anode catalysts	Open-circuit voltage (mV)	At 30 mA cm ⁻²		At 60 mA cm ⁻²		Maximum power density (mW cm ⁻²)	Current density at maximum power density (mA cm ⁻²)
		Output voltage (mV)	Corresponding power density (mA cm ⁻²)	Output voltage (mV)	Corresponding power density (mA cm ⁻²)		
Pt/C	547	275	8.25	177	10.62	10.85	75.1
Pt ₁ Pd ₁ /C	500	285	8.55	193	11.58	11.97	75.1
Pt ₁ W ₁ /C	540	312	9.36	232	13.92	15.88	86.4
Pt ₁ Ru ₁ /C	677	461	13.83	368	22.08	28.54	120.3
Pt ₁ Sn ₁ /C	811	662	19.86	576	34.56	52.22	135.55
Pt ₁ Ru ₁ W ₁ /C	698	503	15.09	425	25.50	38.54	142.2
Pt ₁ Ru ₁ Mo ₁ /C	720	486	14.58	389	23.34	31.19	120.5

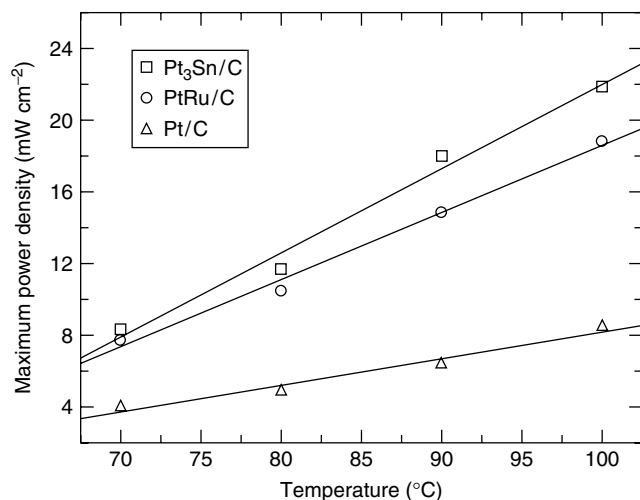


Figure 3 Dependence of the maximum power density on cell temperature for single cells with Pt/C, Pt–Sn/C (3 : 1) and Pt–Ru/C (1 : 1) anode electrocatalysts at 3 atm O₂ pressure using 1 mol L⁻¹ ethanol solution. Anode metal loading: 1 mg cm⁻². Cathode 20 wt % Pt/C, Pt loading: 1 mg cm⁻². (Reproduced from Ref. 28. © Elsevier, 2006.)

2.1.2 Pt–Sn Catalysts

The fcc Pt can form five intermetallic phases with tetragonal Sn, namely PtSn₄, PtSn₂, Pt₂Sn₃, PtSn, and Pt₃Sn, of which PtSn and Pt₃Sn are congruently melting compositions.⁸ These intermetallic phases can be differentiated by their X-ray diffraction (XRD) patterns due to their dissimilar crystal structures. Sn is incorporated into the fcc structure of Pt and forms a solid solution, as can be seen from the shifts of the fcc Pt peaks in Pt–Sn catalysts to Bragg angles higher than those of fcc Pt₃Sn (the most stable phase) but lower than those of pure Pt.

For DMFCs, Pt–Ru/C is generally recognized as the best performing anode electrocatalysts. However, for DEFCs, the Pt–Sn/C catalysts have been shown to outperform the best of Pt–Ru/C catalysts,^{5,28,29} as can be seen in Figure 3 and Table 1.

Song *et al.*³⁰ have compared the performance of DEFCs using various Pt–Ru/C (1 : 1) and Pt–Sn/C (2 : 1) anode electrocatalysts. As can be seen from Figure 4, the fuel cells using Pt–Sn/C anode electrocatalysts outperformed those using commercial and in-house prepared Pt–Ru/C catalysts.

Rousseau *et al.*³⁸ found that the addition of Sn to Pt not only increases the activity of the catalyst toward the oxidation of ethanol but also alters the product distribution. For Pt–Sn/C catalysts, the formation of acetic acid is increased, whereas the formation of CO₂ and acetaldehyde is decreased. This was explained by the ability of Sn to activate water dissociation at a potential lower than that on Pt, leading to the formation of OH species necessary for the oxidative removal of adsorbed acetaldehyde by the bifunctional mechanism. The difference in CO₂ yields was explained by the requirement to have contiguous platinum sites to dissociatively adsorb

the ethanol molecule and to break the C–C bond. The incorporation of Sn atoms between the platinum atoms interrupts the C–C bond scission. Similarly, Song *et al.*³⁰ compared the product distributions between DEFCs using Pt–Sn/C (2 : 1) and Pt–Ru/C (1 : 1) anode electrocatalysts and found that more acetic acid and less acetaldehyde are formed when ethanol is electrooxidized over Pt–Sn/C than Pt–Ru/C. The authors attributed this to the ability of Sn to oxidize ethanol to a larger extent than Ru, and also proposed a mechanism for the promoting effect of Sn in Pt catalysts for ethanol electrooxidation, as shown in Figure 5.

Using on-line differential electrochemical mass spectrometry (DEMS) measurements, Wang *et al.*³⁹ evaluated the selectivity of Pt–Sn/C (3 : 1), Pt–Ru/C (1 : 1), and Pt/C catalysts for the oxidation of ethanol and obtained different results. The authors found that the acetaldehyde to acetic acid ratios are about the same for the Pt/C and Pt–Sn/C catalysts and are significantly lower in the Pt–Ru/C catalyst. The addition of Sn in binary Pt–Sn catalyst only lowers the onset potential for ethanol electrooxidation and CO_{ads} oxidation but does not increase the selectivity for the complete oxidation to CO₂. Li *et al.*⁴⁰ also have a different proposition: the enhancement of ethanol oxidation on Pt–Sn/C is mainly a structural effect associated with crystal structure changes and not due to a bifunctional mechanism which is the case for Pt–Ru/C. This is in partial agreement with the studies of Vigier *et al.*⁴¹ who investigated the EOR on Pt/C and Pt–Sn/C (5 : 1) catalysts by in situ IR reflectance spectroscopy. Vigier *et al.*⁴¹ proposed that in the case of methanol oxidation on Pt–Ru/C, in addition to the bifunctional mechanism, the electronic interaction between Pt and Sn results in a change in the electronic structure of Pt that weakens the Pt–CO bond,

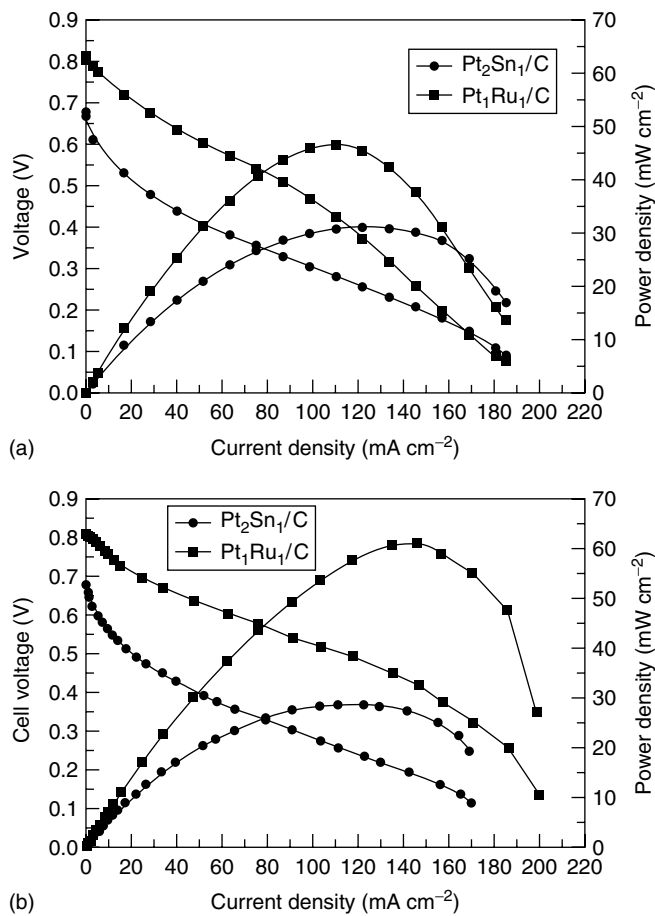


Figure 4 Performance comparison of DEFCs using various Pt-based catalysts. (a) PtSn/C-a and commercial Pt–Ru/C; (b) PtSn/C-b and in-house Pt–Ru/C. $T_{\text{cell}} = 90^\circ\text{C}$. Anode: PtSn/C or Pt–Ru/C with a loading of 1.3 mgPt cm^{-2} , $C_{\text{ethanol}} = 1.0 \text{ mol L}^{-1}$, flow rate: 1.0 mL min^{-1} . Cathode: Pt/C (20 wt %, Johnson Matthey Corporation), metal loading: 1.0 mgPt cm^{-2} , $\text{PO}_2 = 2 \text{ atm}$. Electrolyte: Nafion-115 membrane. (Reproduced with permission from Ref. 30. © International Association for Hydrogen Energy, 2005.)

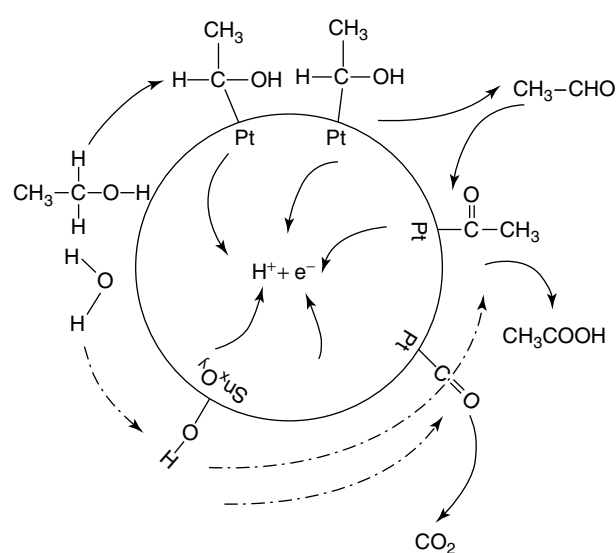


Figure 5 Proposed mechanism for ethanol electrooxidation on Pt–Sn/C catalyst. (Reproduced with permission from Ref. 30. © International Association for Hydrogen Energy, 2005.)

easing the CO diffusion from Pt to Ru sites and allowing the formation of CO_2 at lower potentials. Similar behavior can occur on Pt–Sn/C for the adsorbed CO formed in ethanol electrooxidation.

There are also disagreements on the optimal Sn content for the Pt–Sn catalysts.^{5,29,42–44} Zhou *et al.*⁴² investigated the EOR on carbon-supported Pt–Sn catalysts prepared by the ethylene glycol reduction method and found that Pt–Sn/C electrocatalysts with higher Pt:Sn ratios of 3:2, 2:1, and 1:1 outperform those with lower Pt–Sn ratios of 4:1 and 3:1. The authors reported the optimum Pt:Sn composition to be 3:2 at 60 °C and 2:1 at 90 °C, and no significant difference between the two at 75 °C. This result agrees well with the findings of Tsiakaras⁴³ shown in Figure 6. A volcano curve exists between the fuel cell maximum power density and the corresponding atomic percentage of Sn, with optimal Pt:Sn ratios of 3:2 and 2:1 depending on the operational temperature. Tsiakaras⁴³ also observed a linear increase in the lattice parameter with the Sn content. Hence, the existence of the volcano relationship implies the existence of an optimal lattice parameter which can be reasoned as follows. The increase in the lattice parameter enhances ethanol adsorption and favors the cleavage of the C–C bond, improving the fuel utilization and, consequently, the performance of the cell. Beyond the optimal Sn content, a decrease in the anode electronic conductivity occurs due to the poor electronic conductivity of tin oxide and, as a consequence, the internal resistance of the catalyst increases. Furthermore, the presence of a high Sn-content could partially block the Pt-active sites, thus hindering the ethanol adsorption.

The work by Kim *et al.*⁴⁴ also showed an optimal Pt:Sn atomic ratio of 2:1 for Pt–Sn/C catalysts prepared by the borohydride reduction method. However, Lamy *et al.*⁵ prepared Pt–Sn/C catalysts with Pt:Sn atomic ratios varying

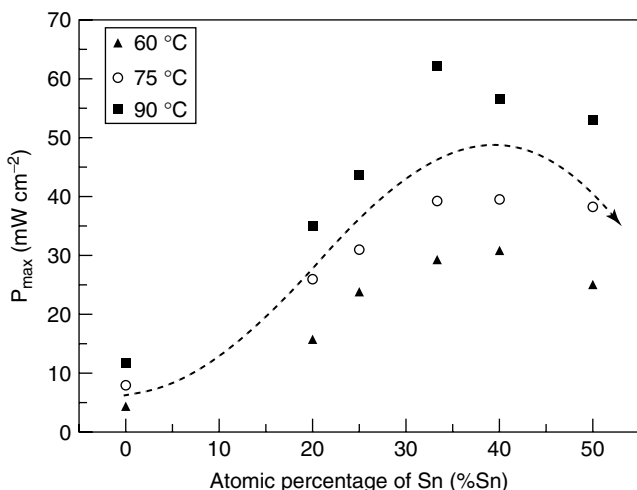


Figure 6 Relationship between maximum power density and the atomic percentage of Sn in a $\text{Pt}_x\text{Sn}_y/\text{C}$ catalyst at different operating temperatures. (Reproduced from Ref. 43. © Elsevier, 2007.)

from 1:1 to 9:1 via the Bönneman method and found that although the overall electrocatalytic activity is greatly enhanced at low potentials for all the Pt–Sn/C catalysts, the optimal composition for tin is in the range 10–20 atom %. With this composition, it was demonstrated that catalyst deactivation by adsorbed CO resulting from ethanol dissociative chemisorption is greatly reduced, leading to a substantial improvement of the catalyst activity. Thus it was suggested that the preparation method has a significant impact on the performance of the Pt–Sn catalysts.^{30,45} The importance of the preparation method was investigated by Jiang *et al.*⁴⁵ The authors prepared carbon-supported Pt–Sn catalysts for DEFCs by three different methods, namely reduction by ethylene glycol, reduction by formaldehyde, and reduction by NaBH_4 . Figure 7 shows the performance of the catalysts in single-stack fuel cells. It was found that while all three Pt–Sn/C catalysts are improvements over commercial Pt/C catalysts, the Pt–Sn/C catalyst prepared via reduction with ethylene glycol has the best performance and the other two have comparable performance. The authors attributed the better performance to the smaller particle size, an appropriate dilation of the Pt crystal lattice, and the supply of OH species at a lower potential on SnO_2 . The two catalysts not prepared by the ethylene glycol reduction method were also found to contain less tin oxide.

Song *et al.*³⁰ also investigated the effect of the preparation method on DEFC performance. The authors prepared carbon-supported Pt–Sn catalysts by the commonly used polyol method, with some variations in the preparative details. One catalyst was prepared by the deposition of the Sn precursor on presynthesized Pt/C (denoted by PtSn/C-a), while the other was prepared by the simultaneous deposition of Pt and Sn precursors on the carbon support (denoted by PtSn/C-b). The authors found marked differences in the

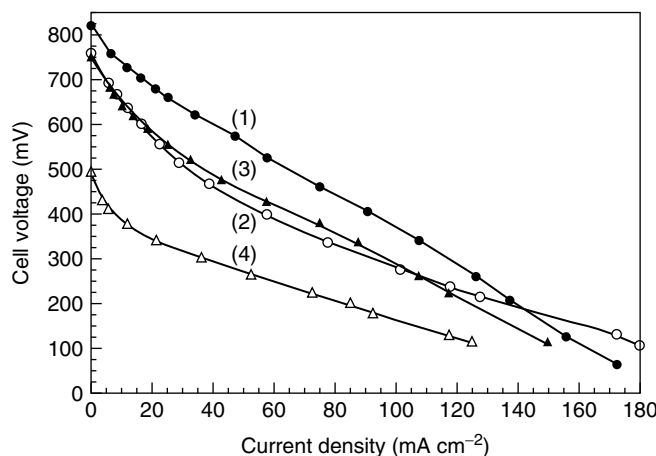


Figure 7 Performance of single direct fuel cells with different anode catalysts: (1) PtSn/C(EG), (2) PtSn/C(HCHO), (3) PtSn/C(NaBH_4), (4) Pt/C(Johnson Matthey). (Reproduced from Ref. 45. © Elsevier, 2006.)

catalyst composition due to the preparation methods. Only SnO_2 is found when the tin precursor is deposited onto Pt/C, whereas a mixture of tin in various oxidation states (zero valent, divalent, and quadrivalent) is formed when Pt and Sn precursors are simultaneously deposited on carbon. It is apparent from the comparison between Figure 4(a) and (b) that the fuel cells with Pt–Sn/C prepared differently behave similarly in the low current density region. However, as the current density increases, the cell with PtSn/C-a lags behind that of PtSn/C-b in performance and the difference widens as the current density increases. The authors attributed this to a higher content of oxidized Sn in PtSn/C-a than in PtSn/C-b, resulting in a higher internal cell resistance, which impacts the cell performance negatively. Also, the direct deposition of Sn onto Pt/C could partially cover the Pt surface, thus decreasing the number of platinum active sites available for ethanol adsorption, dissociation, and oxidation, leading to a poorer performance of the PtSn/C-a catalyst in the high current density region.

Siné *et al.*⁴⁶ investigated the ethanol oxidation activity of bimetallic Pt–Sn nanoparticles of different compositions synthesized by the microemulsion method and deposited on boron-doped diamond (BDD) electrodes. The authors found that the synthesis produces Sn-decorated Pt nanoparticles instead of true alloys, and those nanoparticles with a richer Pt content are more electrocatalytically active for ethanol electrooxidation and have a higher tolerance for CO poisoning, due to their excellent alcohol adsorption properties at room temperature. The authors also observed that the current density of EOR can be higher than that of methanol electrooxidation on Pt–Sn surfaces and this was attributed to several factors, such as the activation of the ethanol C–C bond breaking or an increase in the turnover frequency of acetaldehyde and/or acetic acid formation. Similarly, Salazar-Banda *et al.*⁴⁷ investigated the electrooxidation of ethanol on Pt– SnO_2 sol–gel-modified BDD surfaces. They also observed the addition of SnO_2 to Pt produces a very reactive electrocatalyst that can adsorb and/or dissociate ethanol more effectively than pure Pt. The authors believed that the addition of SnO_2 inhibits catalyst deactivation caused by strongly adsorbed intermediate species and that SnO_2 could also facilitate the cleavage of the C–C bond of the adsorbed intermediates in the reaction.

There are some contentious results regarding the effect of alloying extent on the catalytic activity for ethanol electrooxidation. Zhu *et al.*⁴⁸ investigated this by synthesizing three Pt–Sn/C samples with varying alloying degrees by different preparation methods using a fixed atomic ratio of Pt:Sn = 3:1. Briefly, the catalysts were prepared by successive reduction of Sn precursors followed by Pt precursors in ethylene glycol (denoted by PtSnO₂/C), by coreduction of Sn and Pt precursors in ethylene glycol (denoted by PtSn/C-EG), and by coreduction with NaBH₄ in ethylene glycol (denoted by PtSn/C-B). From the XRD characterizations, it was seen that PtSn/C-B has the highest

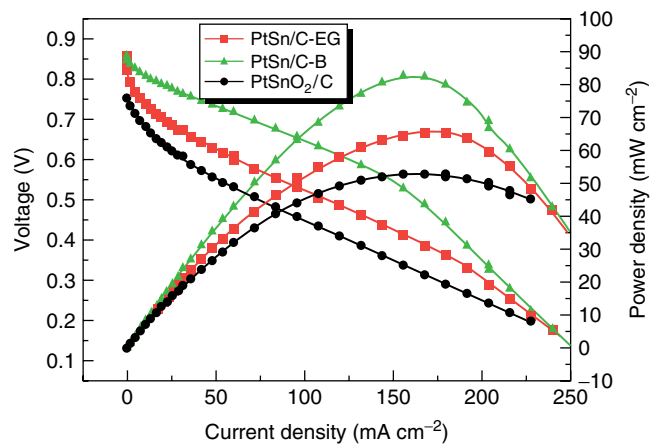


Figure 8 Polarization and power density curves of DEFCs with PtSnO₂/C, PtSn/C-EG and PtSn/C-B anode catalysts, respectively. Metal loading: 2 mg cm⁻² at anode, 1 mg cm⁻² at cathode (Pt/C-40% from JM). Anode fuel feed: 1.5 mol L⁻¹ ethanol at 1 mL min⁻¹. Pressure at cathode: 0.2 MPa. Cell temperature: 90 °C. (Reproduced from Ref. 48. © Elsevier, 2009.)

alloying degree, while PtSnO₂/C has the lowest. Cyclic voltammetry showed that catalysts with lower alloying degrees and higher SnO_2 contents have lower onset potentials for EOR and higher current densities at low potentials (<0.6 V versus SHE). This was attributed to the bifunctional mechanism wherein SnO_2 provides the OH species necessary for the oxidation of acetaldehyde to acetic acid. At high potentials (>0.6 V versus SHE), however, catalysts with lower SnO_2 contents exhibit higher current densities. This was attributed to the fact that at higher potentials, the adjacent Pt atom is able to provide the OH species to remove the CO-like intermediates and the adsorption of ethanol on the Pt surface of the catalyst becomes the rate-determining step in EOR. However, this performance at high potentials may not be very useful since the anode needs to be operated at as low a potential as possible to deliver an acceptable cell voltage from the DEFC. Additionally, Pt–Sn alloying changes the geometric and electronic structures of Pt by expanding the Pt lattice parameter, thus promoting the adsorption of ethanol. In single-cell tests, the catalyst with the least amount of SnO_2 also exhibited the highest power density, as can be seen in Figure 8. In order to explain the excellent ethanol oxidation activity of the Pt–Sn/C catalyst with the highest alloying degree, the authors measured the anode polarization curves and Tafel plots. From the results, the authors concluded that the mechanism for ethanol oxidation is the same for all three catalysts despite their differences in alloying degrees. They have also extrapolated the Tafel lines to obtain the exchange current densities indicative of the intrinsic activities of the catalysts and found the PtSn/C-B catalyst to be the most active. According to the authors, although the process of EOR involves many complex reactions, the first step of α -C–H dissociation from ethanol is the rate-determining step with

high anodic transfer coefficient. The Pt–Sn alloy can facilitate this step, thus improving the overall EOR activity of the catalyst.

On the other hand, Sen Gupta *et al.*⁴⁹ reported that alloying of Pt with Sn actually lowers the activity of the Pt–Sn catalysts and that Pt–Sn catalysts with a Pt-rich phase and Sn and/or Sn oxides in a dispersed and unalloyed state generate the most-pronounced enhancements in ethanol electrooxidation relative to pure Pt. This was attributed to the inhibition of ethanol adsorption/dehydrogenation on the alloyed Pt–Sn catalysts and to the presence of Sn oxide particles closely associated with the Pt particles in poorly alloyed Pt-rich Pt–Sn catalysts. It appears that the copresence of SnO_2 and Sn atoms on the catalyst surface can exert a catalytically synergistic effect toward the oxidation of adsorbed CO on Pt resulting from ethanol electrooxidation. Similarly, Antolini *et al.*⁵⁰ evaluated the effect of Pt–Sn alloy phases in carbon-supported $(\text{Pt–Sn})_{\text{alloy}}/\text{SnO}_2$ and $(\text{Pt–Sn–Pd})_{\text{alloy}}/\text{SnO}_2$ catalysts with a fixed Pt/ SnO_2 ratio. From the XRD results, it was suggested that the Sn atoms partially alloy, while the Pd atoms almost fully alloy with the Pt atoms, thus altering the Pt–Sn alloying degree while maintaining the same Pt/ SnO_2 ratio. The steady-state current density in EOR measured by chronoamperometry is higher for the binary PtSn catalyst than the ternary PtSnPd catalysts. This was attributed to the increase in the nonactive atoms different from Pt in the crystal lattice. The adsorption of ethanol requires the existence of several adjacent Pt atoms and the presence of heteroatoms around Pt-active sites could block ethanol adsorption on Pt due to dilution effects. Thus it was concluded that at a fixed $(\text{PtSn})_{\text{alloy}}/\text{SnO}_2$ ratio, it is not possible to increase the EOR activity of the catalysts by alloying a third metal, owing to the suppression of ethanol adsorption by the ensemble effect. As a consequence, the only way to increase the EOR activity of $(\text{PtSn})_{\text{alloy}}/\text{SnO}_2$ is to add a third metal in the oxide form, such as $(\text{PtSn})_{\text{alloy}}/\text{SnO}_2/\text{RuO}_x$.

Colmati *et al.*⁵¹ studied the EOR on Pt–Sn/C catalysts synthesized by the formic acid method and found that the activity depends on the amounts of both alloyed and unalloyed Sn. The authors proposed that the rate-determining step for the EOR is dependent on the reaction temperature and determines the optimal distribution of Sn between the alloyed and unalloyed states. At low current densities and/or at low temperatures when the electrooxidation of ethanol is slow, the oxidation of adsorbed CO and CH_3CO species determines the rate of the overall process. In this case, the oxidation of ethanol is enhanced by the presence of tin oxides. On the other hand, at high current densities and high temperatures, the rate-determining step is the dissociative adsorption of ethanol and/or the oxidation of acetaldehyde to acetic acid. In this case, a larger lattice parameter consequent upon the formation of a Pt–Sn solid solution should benefit the cleavage of the C–C bond. The increase in the lattice parameter is also associated with an increased number of Pt–Sn pairs that are necessary for the oxidation of adsorbed acetaldehyde to acetic acid.

To summarize, while the Sn content is undeniably an important factor in the Pt–Sn catalyst design, there is no consensus on the optimal Sn content. The situation is made more complex by the fact that the degree of alloying as well as the amount of unalloyed SnO_2 in the catalyst could also affect the ethanol electrooxidation activity, and all these factors vary to different extents depending on the synthesis methods employed.

2.1.3 Pt–Rh Catalysts

Analyses of the reaction products^{38,39,41} have shown that the addition of Ru or Sn to pure Pt not only significantly increases the activity of the catalyst for ethanol oxidation but also changes the product distribution. However, incomplete oxidation to acetaldehyde and acetic acid still prevails, suggesting that the catalyst ability for C–C bond breaking rather than its activity for the oxidation of adsorbed reaction intermediates (e.g., CO_{ads} or $\text{CH}_{x,\text{ad}}$) is limiting the catalyst performance.^{38,39} Rh, which has a marked tendency for the hydrogenolytic splitting of C–C bonds,⁷⁰ is therefore a promising candidate for splitting the C–C bond in ethanol electrooxidation.

De Souza *et al.*⁶¹ investigated the electrooxidation of ethanol on Pt–Rh bimetallic catalysts using on-line DEMS and in situ Fourier transform infrared (FTIR), and found that the Pt–Rh catalysts produce less acetaldehyde compared to a pure Pt electrode. The CO_2 yield is improved relative to pure Pt for Pt–Rh electrodes in the atomic ratios of 73 : 27 and 55 : 45, with the best being the 73 : 27 composition. While the selectivity for CO_2 over acetaldehyde production improves, the Pt–Rh catalysts are generally less active than the Pt electrode. The authors attributed this to the innate ability of the Pt–Rh catalysts to break the C–C bond. The role of Rh seems to relate more to its intrinsic property as an electrocatalyst rather than to provide more accessible oxygen for the oxidation of CO-like species. Bergamaski *et al.*⁶² explained the improved selectivity activity for CO_2 formation on the Pt–Rh/C catalysts in terms of a ligand effect: Rh modifies the electronic properties of Pt in such a way that the Pt-adsorbate interaction is weakened, consequently lowering the energy barrier for the oxidation of adsorbates. The better efficiency is however not accompanied by higher faradic current densities for ethanol electrooxidation because of the decreases in the Pt content of the bimetallic catalyst, or Rh segregation on the nanoparticle surface.

Sen Gupta and Datta⁶³ obtained slightly different results from their comparative study on the EOR activities of electrodeposited Pt and Pt–Rh using cyclic voltammetry, polarization curves, and electrochemical impedance spectroscopy. The authors found that some Pt–Rh/C catalysts performed better than Pt, and the optimal catalyst composition for ethanol oxidation is a Pt–Rh electrode with an atomic ratio of 74 : 26. The difference in activity as compared to that obtained by De Souza *et al.*⁶¹ may be attributed to

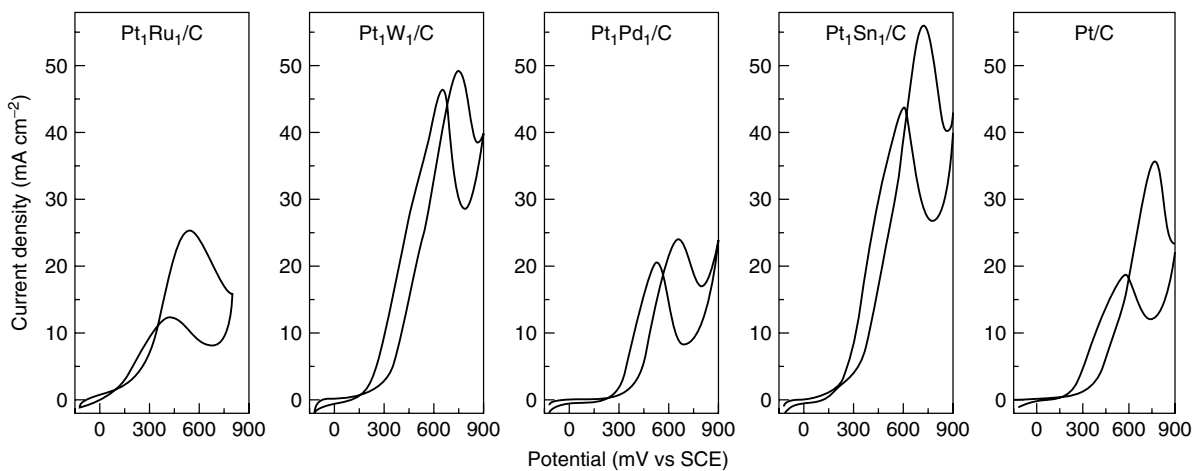


Figure 9 Cyclic voltammograms of carbon-supported bimetallic catalysts at 25 °C. Electrolyte is 0.5 M H₂SO₄ solution containing 1.0 M ethanol. The scan rate was 10 mV s⁻¹. (Reproduced from Ref. 29. © Elsevier, 2003.)

the differences in the electrolyte concentration. The authors proposed that the enhanced activity for ethanol oxidation over Pt is due to the improvement in C–C bond breaking rather than due to a bifunctional mechanism, and that the approximately Pt₃Rh composition has the right balance between the number of Rh sites for C–C bond dissociation and the number of Pt sites for ethanol dissociative adsorption. At significantly higher Rh compositions, the adsorption of ethanol is suppressed by the reduction in the number of Pt sites, whereas at low Rh compositions, there are possibly not sufficient Rh sites to effectively cleave the C–C bond.

Lima *et al.*⁶⁴ studied the effect of crystallite size of carbon-supported Pt–Rh nanoparticles for EOR using cyclic voltammetry, *in situ* FTIR, and DEMS. The authors found that CO-oxidation on the Pt–Rh/C electrocatalysts is shifted to lower potentials compared to Pt/C, and this could be attributed to the bifunctional mechanism and the electronic effect. Faster CO-electrooxidation is more pronounced on catalysts with larger crystallite sizes, and this was attributed to a lower Pt–CO adsorption strength and/or higher water activation, which facilitates the CO–O coupling. The higher electrochemical conversion efficiencies (i.e., higher CO₂/acetaldehyde production ratios) of the Pt–Rh/C catalysts were attributed to the facilitation of C–C bond breaking by the Rh atoms, an effect which is more pronounced in catalysts with a smaller crystallite size.

2.1.4 Other Binary Pt-Based Catalysts

Binary Pt-based catalysts other than Pt–Ru, Pt–Sn, and Pt–Rh have also been investigated for the EOR, such as Pt–W, Pt–Pd, Pt–Mo, and Pt–Ta. Most of the time, the activities of these catalysts are between that of Pt (lowest) and Pt–Sn (highest).

Zhou *et al.*²⁹ investigated a number of Pt-based binary catalysts, and found that other than Ru and Sn, W and Pd could also be used to improve the activity of Pt toward ethanol electrooxidation. As shown in Figure 9, the enhancement in ethanol oxidation activity increases in the following order: Pt/C < Pt–Pd/C < Pt–W/C < Pt–Ru/C < Pt–Sn/C. In Table 1, it is seen the improvements in maximum power density from the Pt–W and Pt–Pd catalysts are clearly lower than the Pt–Sn and Pt–Ru catalysts.

Pt–Pd/C catalysts prepared by the polyol process were investigated by Kadırgan *et al.* for EOR.⁶⁵ The authors attributed the improvement in EOR activity to the presence of Pd changing the electron density of states of Pt. This electronic effect leads to a weakening of the CO–Pt bond or a decrease in catalyst poisoning and the overall reaction rate increases as a result. However, the improvement in overall reaction rate is not as significant as that for methanol oxidation because other oxidation products such as acetaldehyde and acetic acid are also adsorbed on the catalyst surface.

Salazar-Banda *et al.*⁴⁷ investigated the ethanol electrooxidation on Pt–Ta₂O₅ sol–gel-modified BDD surfaces. They found that the addition of Ta₂O₅ to Pt produces a more reactive electrocatalyst than Pt for the EOR. The authors hypothesized that the adsorption of CO is inhibited by the presence of TaO_x, which weakens the Pt–CO bond. Furthermore, OH generation on TaO_x neighboring the Pt sites could contribute to CO removal by means of a bifunctional mechanism. The improvements in the electrocatalysis of Pt for the CO-oxidation could also be due to a ligand effect, which reduces the accumulation of surface CO. However, the activity of the Pt–Ta₂O₅ catalyst is still not comparable to the Pt–SnO₂ catalyst and the authors attributed this to the poorer ability of tantalum oxide in cleaving the C–C bond of the adsorbed reaction intermediates.

Dos Anjos *et al.*⁶⁷ prepared Pt–Mo alloy electrocatalysts by arc-melting and investigated the origin of their activity

in ethanol oxidation. Two Mo compositions were chosen in the binary phase diagram to form alloys with the atomic compositions of Pt–Mo (50 : 50) and Pt–Mo (80 : 20). It was found that the Pt–Mo alloy catalysts are more active than Pt alone. Gradual Mo dissolution at the electrode surface was detected after voltammetric and chronoamperometric measurements. The authors proposed that the dissolved Mo contributed to the EOR catalysis as underpotentially deposited (upd) ad-atoms on the electrode. The resulting changes in the electrode surface roughness together with the upd Mo atoms and the electronic modifications to the Pt catalyst topmost layer are cited as the reasons for the enhancement of EOR activity compared to Pt alone.

2.2 Ternary Catalysts

Even though Pt–Ru and Pt–Sn catalysts provide the most notable improvements among the binary Pt-based catalysts for ethanol oxidation, the bulk of their oxidation products still contain the C–C bond. The inability to extract the full count of 12 electrons per ethanol molecule greatly lowers the fuel cell efficiency in utilizing the fuel. Although the Pt–Rh catalysts are more capable of cleaving the C–C bond, their activity for ethanol electrooxidation is lower than that of Pt–Sn. There is therefore a continuing need to look for more effective EOR catalysts. One of the strategies is to modify the existing binary catalysts into ternary or quaternary catalyst systems.

2.2.1 Pt–Ru-Based Catalysts

Zhou *et al.*^{29,53} evaluated the Mo, W, and Sn modifications of Pt–Ru catalysts by cyclic voltammetry and single-cell tests. The catalysts were all synthesized by a modified polyol process and it was found that the addition of Mo and W to the binary Pt–Ru/C catalyst produces no apparent changes in the XRD patterns, indicating that the crystal structures of the Pt–Ru/C catalysts are not significantly modified by Mo or W addition. The addition of Sn, however, expands the lattice parameter of the Pt–Ru/C (1 : 1) catalyst. From single-cell tests, the authors determined that Pt–Ru–W/C (1 : 1 : 1) and Pt–Ru–Mo/C (1 : 1 : 1) catalysts have improved upon the performance of the Pt–Ru/C (1 : 1) catalyst, increasing both the open-circuit voltage (OCV) and the maximum power density. As shown in Figure 10 and Table 1, the addition of Mo is more effective in raising the OCV but has a smaller effect on the increase in maximum power density. Single-cell tests with the Pt–Ru–Sn/C (1 : 1 : 1) anode also showed improvement similar to that of Pt–Ru–W/C. Indeed the former outperformed the latter in the resistance-controlled and activation-controlled regions. Although these ternary catalysts constitute an improvement of the Pt–Ru/C (1 : 1) binary catalyst in terms of power density, they still perform below the level of the Pt–Sn/C (1 : 1) binary catalyst under the same operating conditions. Since the performance

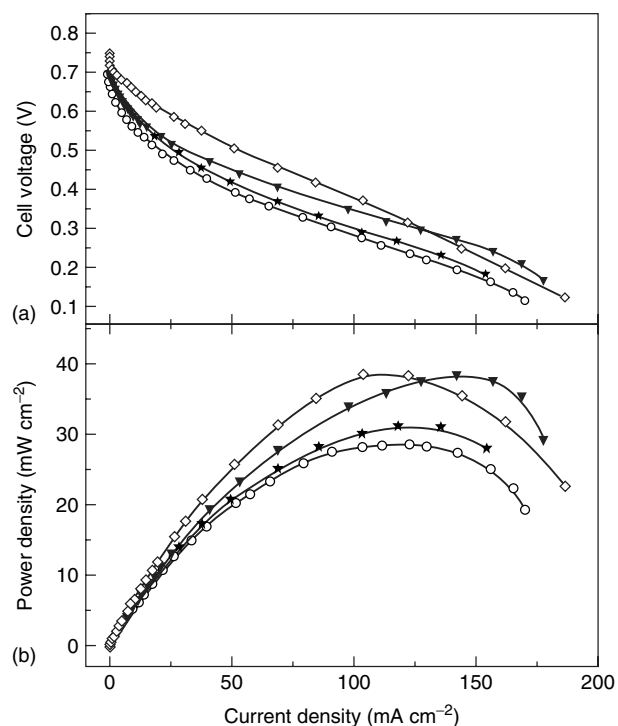


Figure 10 Comparison of the cell voltage (a) and power density (b) of a direct ethanol fuel cell with different anode catalysts operating at 90 °C. Anode catalyst: (○) Pt–Ru/C (1 : 1); (▽) Pt–Ru–W/C (1 : 1 : 1); (★) Pt–Ru–Mo/C (1 : 1 : 1); (◇) Pt–Ru–Sn/C (1 : 1 : 1). The metal loading in anode is always 1.3 mg Pt cm². Nafion®-115 was used as electrolyte; ethanol concentration and flow rate: 1 M and 1.0 mL min⁻¹; cathode catalyst and metal loading: 1.0 mg Pt cm² (20 wt % Pt, Johnson Matthey Co.). (Reproduced from Ref. 53. © Elsevier, 2004.)

of the single cell with Pt–Ru–Sn/C (1 : 1 : 1) is higher than that of the cell with Pt–Ru/C (1 : 1) while still inferior to that of the cell with Pt–Sn/C (1 : 1), the authors concluded that the addition of Sn to Pt–Ru/C helps to bring up the catalytic activity for ethanol electrooxidation. This was attributed to the increase in the lattice parameter.

Wang *et al.*⁵⁹ also investigated the effect of Mo addition to Pt–Ru/C on EOR activity. Pt–Ru–Mo/C (6 : 3 : 1) and Pt–Ru/C (1 : 1) were prepared by a chemical reduction method and evaluated by cyclic voltammetry, chronoamperometry, and amperometric current–time measurements. Similar to the results of Zhou *et al.*,^{29,53} the peak current density is higher in the case of Pt–Ru–Mo/C than the Pt–Ru/C binary catalyst. In addition, CO-tolerance and catalyst durability in the acidic fuel cell environment are also better. The authors attributed the improved performance to three main causes: the bifunctional mechanism in which MoO_x promotes water activation and improves CO-oxidation activity; the “hydrogen spillover” effect in which the transfer of hydrogen from Pt to MoO_x liberates the Pt active sites for the oxidation of ethanol; and the modification of Pt electronic states which changes the catalytic activity of Pt in the EOR.

Wang *et al.*⁷¹ also investigated the performance of Pt–Ru–Ni/C (6 : 3 : 1) ternary catalyst relative to the Pt–Ru/C (1 : 1) binary catalyst. In this case, there are no significant differences between the onset potentials for ethanol electrooxidation, and the electrochemically active surface areas of the Pt–Ru–Ni/C and Pt–Ru/C catalysts are almost the same. Yet the catalytic activity of the Pt–Ru–Ni/C catalyst is still noticeably higher than that of the Pt–Ru/C catalyst. The authors attributed this to the improved CO-tolerance of the ternary catalyst. The promoting effect of Ni addition to Pt–Ru/C on the electrooxidation of ethanol is more noticeable at low potentials, reaching a maximum at a potential of about 0.3 V versus SHE. Another study on the Ni modification of Pt–Ru/C catalysts was performed by Ribadeneira and Hoyos,⁷² and again higher ethanol oxidation activities were reported for the ternary catalyst. The best ternary catalyst measured under their experimental conditions was found to be Pt : Ru : Ni = 75 : 15 : 10.

2.2.2 Pt–Sn-Based Catalysts

Given that both the binary Pt–Ru/C and Pt–Sn/C catalysts exhibit significantly improved behavior for ethanol electrooxidation, it is no surprise that many researchers have investigated the use of ternary catalysts containing both Ru and Sn along with Pt for the anode of DEFC. Neto *et al.*⁵⁷ investigated the electrooxidation of ethanol on ternary Pt–Sn–Ru/C electrocatalysts with varying Pt : Sn : Ru atomic ratios prepared by a modified polyol process using cyclic voltammetry and chronoamperometry. Their analysis of the XRD patterns revealed differences in the lattice parameters of the catalysts and interactions between Pt, Sn, and Ru. From the chronoamperometric data, it was found that all the ternary Pt–Sn–Ru/C catalysts are more active than the Pt–Ru/C (1 : 1) binary catalyst but less active than the Pt–Sn/C (1 : 1) binary catalyst.

Antolini *et al.*⁷³ studied the effect of Ru addition on the EOR activity of carbon-supported Pt–Sn alloy catalysts prepared by the formic acid method. Two ternary Pt–Sn–Ru/C (1 : 1 : 0.3 and 1 : 1 : 1) catalysts were prepared and their ethanol oxidation activities were benchmarked against the commercial Pt/C and Pt–Ru/C catalysts. In both linear-sweep voltammetry and single-cell measurements, the Pt–Sn–Ru/C (1 : 1 : 0.3) catalyst shows higher activity for the ethanol electrooxidation compared to the binary Pt–Sn/C and Pt–Ru/C and the ternary Pt–Sn–Ru (1 : 1 : 1) catalysts. This enhancement was attributed to the synergistic interaction between Sn oxides and Ru oxides and also the smaller particle size. On the other hand, the Pt–Sn–Ru/C (1 : 1 : 1) catalyst performs poorer than the binary Pt–Sn/C and Pt–Ru/C catalysts, and this was ascribed to the replacement of Pt–SnO₂ interactions by Pt–RuO_x interactions and hence the catalyst is more like the binary Pt–Ru/C. The slightly lower DEFC performance of the Pt–Sn–Ru/C (1 : 1 : 1) catalyst compared to the Pt–Ru/C catalyst was attributed to the decrease in the active surface area due to the presence of SnO₂.

Wu *et al.*⁷⁴ prepared ternary Pt–Sn–Ru/C catalysts with varying atomic ratios (6 : 3 : 1, 6 : 2 : 2, and 6 : 1 : 3) and evaluated their performance in the electrochemical oxidation of ethanol and its various oxidation products. It was found that the Pt₃Sn phase predominates in the Ru-rich Pt–Sn–Ru/C (6 : 1 : 3) catalyst, whereas the PtSn phase and SnO₂ are mainly present in the Sn-rich Pt–Sn–Ru/C (6 : 3 : 1) catalyst. Measurements by cyclic voltammetry indicate that the Ru-rich Pt–Sn–Ru/C (6 : 1 : 3) catalyst has the lowest onset potential for the electrooxidation of adsorbed CO, ethanol, and acetaldehyde, suggesting contributions from Ru and Pt₃Sn alloy to the oxidative removal of the intermediate C₁ and C₂ species from the Pt sites. However, the Sn-rich Pt–Sn–Ru/C (6 : 3 : 1) catalyst is better for the overall oxidation of ethanol, suggesting that the PtSn phase and SnO₂ structure are more favorable for the activation of the C–C bond, thereby generating higher current densities at higher potentials. In addition, the Sn-rich Pt–Sn–Ru/C (6 : 3 : 1) catalyst shows significant improvement in the oxidation of acetic acid to C₁ species, whereas the Ru-rich Pt–Sn–Ru/C (6 : 1 : 3) catalyst is nearly incapable of cleaving the C–C bond to oxidize acetic acid.

Carbon-supported ternary Pt–Sn–Rh (1 : 1 : 0.3 and 1 : 1 : 1) alloy catalysts were prepared upon the reduction of the metal precursors with formic acid by Colmati *et al.*,⁷⁵ and their activities for ethanol electrooxidation were compared with those of binary Pt–Sn/C and Pt–Rh/C catalysts prepared by a similar method. The XRD patterns indicated that both the crystallite size and the lattice parameter of the ternary Pt–Sn–Rh/C alloy catalysts are larger than those of Pt–Rh/C but smaller than those of Pt–Sn/C, signifying the likelihood of the formation of a ternary Pt–Sn–Rh alloy. At potentials higher than 0.45 V versus SHE in linear sweep voltammetry, the ternary Pt–Sn–Rh/C alloy catalysts show higher ethanol electrooxidation activities, whereas at potentials lower than 0.45 V versus SHE, the electrochemical activity of the binary Pt–Sn/C catalyst is higher than those of the ternary catalysts. The authors attributed the activity enhancement in ethanol electrooxidation on the ternary catalysts to the formation of a ternary alloy (which changes the geometric and electronic structures of the Pt–Sn alloy with the introduction of Rh, thus improving the adsorption of ethanol and the breaking of the C–C bond) and to the smaller particle size.

Kowal *et al.* prepared Pt–Rh–SnO₂/C catalysts via the polyol method⁷⁶ and by depositing Pt and Rh atoms on carbon-supported SnO₂ nanoparticles.⁷⁷ Figure 11 shows the potentiodynamic polarization curves of ethanol electrooxidation on these catalysts. The figure shows that the activity of the ternary Pt–Rh–SnO₂/C catalyst is considerably higher than that of Pt–SnO₂/C, despite the fact that the addition of Rh to Pt has no effect on the reaction rate, as can be seen from the almost similar curves for Pt/C and Pt–Rh/C. In the case of the catalyst synthesized by the deposition method, a higher ethanol electrooxidation activity is observed, indicating the need for the ethanol molecule to be in contact with all the active phases of the catalyst in order to be completely

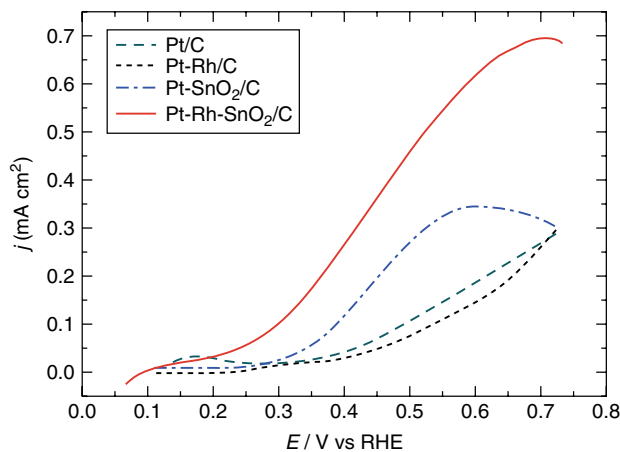


Figure 11 Potentiodynamic polarization curves of EOR recorded in 0.5 M H_2SO_4 + 1 M $\text{C}_2\text{H}_5\text{OH}$ solution. Scan rate 50 mV s⁻¹; temperature 20 °C. (Reproduced from Ref. 76. © Elsevier, 2009.)

oxidized. The authors attributed the improved performance to the three-functional catalyst. SnO_2 , by strongly adsorbing water and interacting with the Pt and Rh deposited on its surface, apparently precludes the Rh and Pt sites from reacting with H_2O to form M–OH, making them available for ethanol oxidation. The SnO_2 with H_2O also provides the OH species to oxidize the dissociated CO at Rh sites. Pt provides the ethanol dehydrogenation function and also modifies the electronic structure of Rh to support moderate bonding to ethanol and its reaction intermediates and products, which is beneficial to C–C bond breaking and, consequently, ethanol oxidation. The density functional theory calculations indicated that the oxidation of ethanol on Pt–Rh/SnO₂ proceeds through an oxametallacyclic conformation that facilitates the direct cleavage of the C–C bond at a reasonable rate.

Neto *et al.*⁷⁸ prepared Pt–Sn/CeO₂–C (Pt:Sn = 1:1) electrocatalysts via an alcohol reduction process using ethylene glycol as the solvent *cum* reducing agent. From chronoamperometric measurements and single-cell tests, the authors found that the best ethanol oxidation activity is from an electrocatalyst with a CeO₂ loading of 15 wt %. Xue *et al.*⁷⁹ investigated the effect of phosphorous content on the electrooxidation of ethanol on Pt–Sn/C (3:1) catalysts by preparing the catalysts via three different methods. The authors observed phosphorous deposition on the carbon surface along with Pt and Sn when sodium hydrophosphite was used as the reducing agent. The phosphorous content could be varied by manipulating the synthesis conditions. From cyclic voltammetry and single-cell tests, they reported the Pt–Sn–P/C (3:1:2) catalyst as the best ternary catalyst for ethanol electrooxidation. The authors attributed this to the size reduction of the Pt–Sn nanoparticles, which improves the catalytic activity through the increase in the electrochemically active surface area.

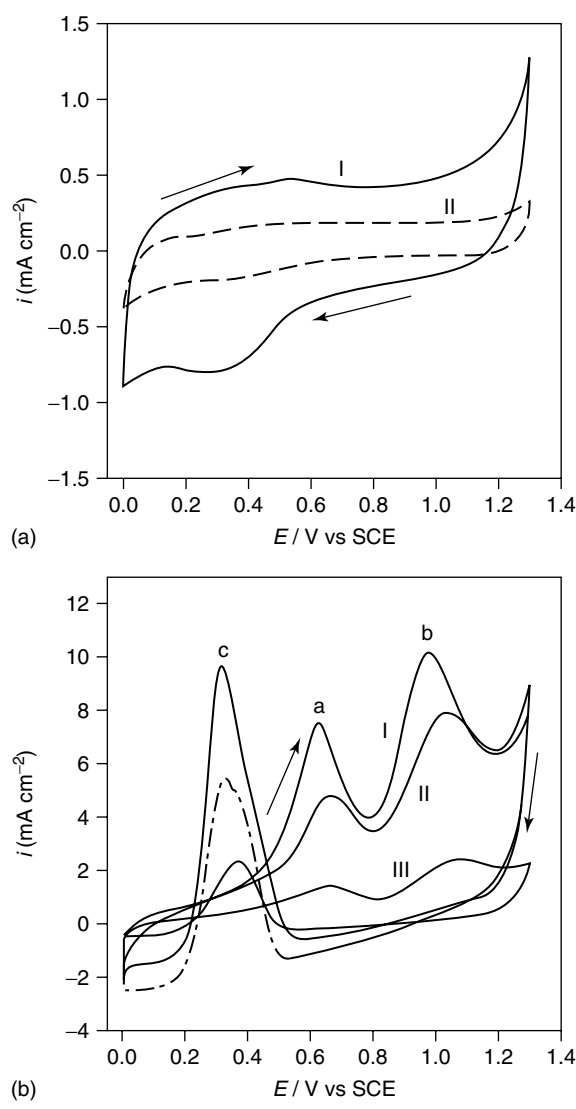


Figure 12 The cyclic voltammograms of various electrodes at 50 mV s⁻¹ in N_2 saturated 0.1 M H_2SO_4 aqueous solutions without (a) and with (b) 1.0 M $\text{CH}_3\text{CH}_2\text{OH}$. (a) CNT/graphite (curve I) and graphite electrodes (curve II); (b) Pt–Ru/CNT/graphite (curve I); Pt/CNT/graphite (curve II) and Pt/graphite (curve III) electrodes. (Reproduced from Ref. 80. © Elsevier, 2004.)

2.3 Promoters/Cocatalysts/Supports

There has also been interest in exploring the effects of catalyst support in EOR. Supports such as Ni,³¹ boron-doped diamond,⁴⁶ carbon nanotubes (CNTs),^{80–83} mesoporous carbon,⁸⁴ and titania nanotubes⁸⁵ have all been examined. Wang *et al.*⁸⁰ investigated the ethanol electrooxidation activities of Pt and Pt–Ru nanoparticles electrodeposited on CNTs. The CNTs were grown directly on a graphite disc by chemical vapor deposition. Figure 12 shows that the electrodes with CNT-supported catalysts outperform the electrode with graphite-supported catalyst. The electrocatalytic activity may be arranged in the following order: Pt–Ru/CNT/Graphite

> Pt/CNT/Graphite > Pt/Graphite. The authors attributed this to three reasons, namely, (i) the three-dimensional structure of CNTs which supports a higher dispersion of Pt nanoparticles and thus a higher available Pt surface area for reactions; (ii) the unique electrical properties of CNTs which increases the conductivity of the electrode for a more effective transfer of electrons during the reactions; and (iii) Pt particles with a thin highly crystalline-faceted structure which are formed upon a strong metal-supported interaction.

Vengatesan *et al.*⁸⁴ investigated the use of mesoporous carbon support for the Pt catalysts in fuel cells. The authors found that the large surface area and the large mesopores present in the mesoporous carbon could support high Pt loadings with good dispersion. The CO stripping and cyclic voltammetric analyses of the mesoporous carbon-supported Pt also show higher mass activities for the electrochemical reactions under fuel cell conditions, and this was attributed to the high dispersion of the Pt particles.

The presence of TiO₂ in the catalyst support^{82,85} also appears to increase the ethanol electrooxidation activity. Song *et al.*⁸⁶ investigated the effect of anatase TiO₂ and TiO₂ nanotubes on the ethanol electrooxidation activity of Pt/C in acidic solutions by cyclic voltammetry, chronoamperometry, and CO stripping voltammetry. The results showed that the addition of the TiO₂ nanotubes could significantly improve the activity of Pt/C catalysts for ethanol electrooxidation, and shifts the onset of CO stripping to lower potentials. Hence CO-electrooxidation is more facile in the presence of TiO₂ nanotubes. The same group also tested the effects of TiO₂ on CNTs⁸² and multiwalled CNTs,⁸⁷ and similar results were obtained. Catalysts with TiO₂ consistently outperform their counterparts without TiO₂ in tests for ethanol electrooxidation activity. The authors attributed this to the presence of TiO₂, which decreases the effect of CO poisoning on the Pt surface.⁸²

2.4 Catalysts for Ethanol Oxidation in Alkaline Solutions

Similar to DMFCs, DEFCs can also be operated under alkaline conditions. In general, current density and maximum power density obtained from alkaline DEFCs are higher than those obtained from acidic DEFCs. However, alkaline DEFCs are not being keenly pursued because of the problem of electrolyte carbonation. In an alkaline DEFC, where an alkaline electrolyte such as KOH is used, the electrolyte can react chemically with the CO₂ in air or CO₂ formed in the oxidation of ethanol to give rise to insoluble carbonates, thereby undermining the electrode performance. If carbonation occurs in the PEM as a result of dissolved CO₂ reacting with the OH groups present in the membrane, the ionic conductivity of the membrane would be substantially reduced. Furthermore there is also the risk of membrane rupture. These concerns, coupled with the fact that the carbonation products are nongaseous, mandate that the fuel cell needs to be purged periodically to prevent the overaccumulation of

the carbonation products. In addition, the use of an alkaline electrolyte in a DEFC requires the use of an anion-exchange membrane, which is not as commonly available as the widely used Nafion cation-exchange membrane.

Pt and Pd are commonly used as the anode electrocatalysts for ethanol electrooxidation in an alkaline environment. Similar to the acidic fuel cells, researchers have tried to modify these catalysts to improve their ethanol oxidation activities. Xu *et al.*⁸⁸ investigated the effect of incorporating Co and Mn into Pt on the ethanol oxidation activity. The Pt–Co and Pt–Mn electrocatalysts were synthesized on Ti by electrodeposition, and the results from cyclic voltammetry indicated that the addition of trace amounts of Co and Mn to Pt (e.g., Pt–Co (1000 : 1) and Pt–Mn (1000 : 1)) could significantly improve the ethanol electrooxidation activity without much change in the electrochemically active area. The Pt–Co (10 000 : 1) and Pt–Mn (10 000 : 1) electrocatalysts show the highest ethanol electrooxidation activities, with the Pt–Co (10 000 : 1) having a slightly better activity and stability than its Mn counterpart. The authors attributed this to the presence of Co and Mn reducing the Pt–CO bond strength substantially and hence enhancing the oxidation of CO to CO₂. Lu *et al.*⁸⁹ similarly prepared nanostructured Pd–Pt bimetallic catalysts supported on Ti via electrodeposition. The authors observed changes in the ethanol electrooxidation onset potential and maximum current density, indicating improvements in kinetics due to the interaction between Pd and Pt in ethanol electrooxidation. They also found that the ethanol oxidation activity is dependent on the Pd to Pt ratio in the Pd–Pt/Ti catalysts and the best performance was delivered by catalysts with a Pd to Pt ratio in the range of 0.5 : 0.5 to 0.8 : 0.2. The Pd–Pt/Ti (0.5 : 0.5) catalyst has the most negative onset potential for ethanol electrooxidation, while the Pd–Pt/Ti (0.8 : 0.2) catalyst has the highest current density. The selective oxidation of ethanol to acetic acid in an alkaline DEFC using Pd–(Ni–Zn)/C as anode was investigated by Bianchini *et al.*⁹⁰ These authors claimed power densities as high as 170 mW cm⁻² at 80 °C, which are higher than any value that has been reported thus far for DEFCs with any electrocatalyst in either alkaline or acidic media.

The effects of the oxide presence on the ethanol oxidation activity of Pd and Pt electrocatalysts under alkaline conditions have also been examined by a few groups. Xu *et al.*⁹¹ studied the effect of the addition of CeO₂ and NiO to the Pt/C and Pd/C electrocatalysts on ethanol oxidation in alkaline solutions using cyclic voltammetry and chronoamperometry. The authors reported higher catalytic activity and better steady-state behavior for ethanol oxidation on the Pd/C electrocatalyst. More importantly, the addition of CeO₂ or NiO was found to improve the activities of both catalysts to a level higher than that of a commercial Pt–Ru/C catalyst. The activities of the various catalysts were found to be in the following order: Pd–NiO/C (6 : 1 by weight) > Pd–CeO₂/C (2 : 1 by weight) > Pt–NiO/C (6 : 1 by weight) > Pt–CeO₂/C (2 : 1 by weight) > commercial Pt–Ru/C (2 : 1 by weight) ≈

Pd/C > Pt/C. The authors attributed the improved performance of the catalysts incorporated with oxides to the bifunctional effect of the oxides, similar to the role of Ru in the Pt–Ru catalysts. The OH_{ads} species can form more easily on the surface of the oxide at lower potentials and can oxidize the CO-like poisoning species on Pt and Pd to CO₂ or other products, releasing the active sites on Pt and Pd for further electrochemical reaction.

3 CATHODE CATALYSTS

An important concern in fuel cells is the poor kinetics of the ORR in acidic media. The activation overpotential for the ORR is of the order of 500 mV at acceptable current densities even with a high loading of expensive noble metal catalysts.⁹² There are three approaches being used to address this inadequacy, namely alloying, the use of nonnoble metal catalysts, and reengineering the electrode. The first two approaches are attempts to enhance the ORR activity of the electrode, whereas the last approach targets the reduction of ohmic and mass transport losses.⁹² However, most nonnoble metal catalysts work under alkaline conditions, and are not useful for the more common acidic fuel cells.

In addition, it is also known that the ethanol fed to the anode compartment of DEFCs can permeate through the polymer electrolyte membrane to the cathode compartment. This is similar to the case of methanol crossover in DMFCs. However, due to both its smaller permeability through the Nafion membrane and its slower electrochemical oxidation kinetics on the Pt/C cathode, ethanol crossover affects the cell performance less severely than methanol crossover.¹¹ Nonetheless, due to the low activity of the ORR on Pt, there is still some interest to look for alternatives to pure Pt for the cathode. A suitable cathode material for the DEFC should therefore have a high tolerance to ethanol as well as improved ORR activity. Thus far, the reports on the development of ethanol-tolerant ORR catalysts are very scarce or nonexistent.

4 CONCLUSIONS

The direct ethanol fuel cells, compared to the direct methanol fuel cells, are still a relatively new technology for mobile power generation. Although plagued with many problems, the potential benefits of using ethanol as a fuel compared to methanol (e.g., the use of a renewable fuel with low toxicity) make it a most promising candidate to succeed methanol in the future. Although the ethanol oxidation activity of pure Pt catalysts is low, the performance of Pt–Sn and Pt–Ru alloys is better. However, contrary to methanol oxidation, the best binary catalyst for ethanol oxidation in acidic media is not Pt–Ru but Pt–Sn. For the Pt–Sn catalysts, there is

still controversy regarding the effect of Sn content on EOR catalysis. The synthesis method for the Pt–Sn catalysts also has a strong bearing on the optimal composition for ethanol electrooxidation. There are also contentious arguments about the effect of the alloying degree of Sn in the Pt fcc structure on the catalytic behavior for ethanol electrooxidation, partly because the intrinsic properties of the catalyst (such as the particle size, distribution, and surface composition) and the measurements conditions (such as the temperature and electrochemical methods) were not standardized.

Analysis of the reaction products showed that addition of Ru and Sn to pure Pt not only increases the activity of the catalyst for ethanol oxidation but also changes the product distribution. However, incomplete oxidation to acetaldehyde and acetic acid still prevails, and hence the performance of current catalysts is mainly limited by their inability to completely cleave the C–C bond. The addition of Rh to Pt results in a more complete oxidation, but the overall ethanol electrooxidation activity of Pt–Rh is still lower than that of Pt–Sn.

For the ternary catalysts, it was found that the fuel cell performance is not significantly affected by adding a third component such as W or Mo to the binary Pt–Ru and Pt–Sn catalysts. Even if the ternary catalysts show an increase in power output relative to Pt–Ru catalysts, they still perform below the level of the Pt–Sn catalysts under the same operating conditions. Currently, the best ternary catalyst appears to be the Pt–Rh–SnO₂ catalysts, with each component performing one of the important steps in ethanol electrooxidation: Pt for the adsorption/dehydrogenation of ethanol, Rh for the C–C bond cleavage, and SnO₂ to provide the OH species to oxidize the dissociated CO at Rh sites. Thus it would appear that future efforts to develop an effective catalyst for the ethanol electrooxidation reaction should focus on these three main aspects.

In conclusion, there have been many arguments as to what is the best catalyst for ethanol electrooxidation—is it the catalyst with the highest activity for the ethanol electrooxidation activity at a certain potential, or is it the catalyst which results in the best CO₂ yield, thus ensuring that most of the ethanol is fully converted into carbon dioxide? It is our opinion that a higher activity is more important than a higher CO₂ yield since the main objective of a DEFC is to provide energy to power devices. However, this also means that a lot of the fuel is only partially converted and the full potential energy of the fuel is not extracted. Therefore, the ultimate aim in catalyst design is still to develop catalysts that can fully oxidize ethanol into carbon dioxide with high activity, but until that is possible, compromises may have to be made. Table 2 provides a brief comparison of the catalysts in use today including their compositions, supports, operating conditions, and methods of preparation, which may help the readers in determining which catalyst is most suitable for their application. Interested readers can then refer to the cited references for more in-depth information.

Table 2 Summary of various anode catalysts and their performance

Catalyst	Composition	Support	Loading	Particle size (nm)	Temperature of measurement (°C)	Onset potential for EtOH oxidation (mV)	Activity		Method of preparation and notes
							CV	CA	
Pt–Ru ⁵³	Atomic ratio 1 : 1	XC-72	20 wt % Pt	1.8	25	~90	~7.5 mA cm ⁻² (@540 mV, 10 mV s ⁻¹)	0.5 M H ₂ SO ₄ , 1.0 M EtOH	• Reduction by EG • OCV of 0.67 V • Max power density of 28.6 mW cm ⁻² @90 °C for single-cell test • Reduction by EG
Pt–Ru ²⁷	Atomic ratio : from 3 : 1 to 1 : 3; best 1 : 3	XC-72	20 wt % Pt	2.5–6.5	25	~11.7 A g ⁻¹ Pt (@800 mV, 10 mV s ⁻¹)	0.5 M H ₂ SO ₄ , 1.0 M EtOH	• Reduction by EG	
Pt–Ru ²⁴	63–85 mol % Pt; Best Pt ₆₃ Rh ₃₇	Gold sheet			25	~30 µA cm ⁻² (@500 mV, 30 min (Pt: ~6 µA cm ⁻²))	0.5 M H ₂ SO ₄ , 1.0 M EtOH	• Electrochemical deposition	
Pt–Ru ⁴⁰	Atomic ratio 1 : 1	XC-72	45 wt % Pt; Best Pt ₆₃ Rh ₃₇	1.6 ± 0.7	25	~27 mA cm ⁻² (@950 mV, 25 mV s ⁻¹)	~16 mA cm ⁻² (@800 mV, 600 s (Pt: ~12 mA cm ⁻²))	0.5 M HClO ₄ , 1.0 M EtOH	
PtSn ⁵	Atomic ratio 9 : 1	XC-72	30 wt % Pt	2.6 ± 1.3	25	130 (Pt:320) ~2.58 mA cm ⁻² (@450 mV, 5 mV s ⁻¹ , 3000 rpm)	0.1 M HClO ₄ , 0.1 M EtOH	• Bonneman method • Max power density of 45 mW cm ⁻² @90 °C for single-cell test	
PtSn ⁵³	Atomic ratio 1 : 1	XC-72	20 wt % Pt	2.4	25	~240 (Pt:~540) ~4.5 mA cm ⁻² (@540 mV, 10 mV s ⁻¹)	0.5 M H ₂ SO ₄ , 1.0 M EtOH	• Reduction by EG • OCV of 0.81 V (Pt:0.55 V) • Max power density of 52 mW cm ⁻² @90 °C for single-cell test (Pt: 10.8 mW cm ⁻²)	

PtSn⁴²	Atomic ratio : From 1:1 to 4:1; Best 3:2	XC-72	20 wt % Pt	2.2–3.0	60	• Reduction by EG • Max power density of ~30 mW cm ⁻² @60 °C for single-cell test
PtSn⁴⁰	Atomic ratio 1 : 1	XC-72	45 wt %	2.7–0.9	25	~29 mA cm ⁻² (@800 mV, 25 mV s ⁻¹) 600 s (Pt: ~12 mA cm ⁻²)
PtSn⁴¹	Atomic ratio 100 : 20	XC-72	30 wt %	20	~100 (Pt: ~300)	0.5 mA cm ⁻² (@400 mV, 5 mV s ⁻¹ , (Pt:~0.1))
PtSn⁹³	Atomic ratio: Pt ₆₄ Sn ₅ O ₃₁ , Pt ₆₀ Sn ₆ O ₃₅ , Pt ₆₆ Sn ₇ O ₂₇ , Pt ₆₈ Sn ₈ O ₂₄ ; Best Pt ₆₄ Sn ₅ O ₃₁	2-mm graphite plates	10 mA cm ⁻² for various durations; 1 mg cm ⁻²	1.9–6.9	25	Lowered by 300 mV compared to Pt
PtSn⁹⁴	1.9–6.2 wt % C Sn; Best 6.2 wt % Sn	C	40 wt % Pt	5.5–6.5	25	100 (Pt:310) ~660 mA cm ⁻² (@450 mV, 10 mV s ⁻¹)
PtSn, PtSnO₂⁴⁸	Atomic ratio 3 : 1	XC-72	40 wt % Pt 1–5	25	105 (PtSnO ₂ , 255 (NaBH ₄)	0.5 M H ₂ SO ₄ , 1.0 M EtOH • PtSnO ₂ /C prepared by successive reduction with EG • PtSn/C prepared by reduction with EG or NaBH ₄ • Max power density of 82 mW cm ⁻² (NaBH ₄) @90 °C for single-cell test

(continued overleaf)

Table 2 (*continued*)

Catalyst	Composition	Support	Loading	Particle size (nm)	Temperature of measurement (°C)	Onset potential for EtOH oxidation (mV)	Activity		Method of preparation and notes
							CV	CA	
Pt–SnO₂⁹⁵	Pt–SnO ₂ —85:15	Boron-doped Diamond		25	350, 610 (Pt)	~6 μA cm ⁻² (@700 mV, 5 mV s ⁻¹ (Pt:~1.5))	0.5 M H ₂ SO ₄ , 0.5 M EtOH	• Catalyst coatings prepared by sol–gel method • Stationary current densities of up to 11 times higher than on Pt/BDD @0.54 V	
Pt–Rh⁶³	35–90 mol % Pt; Best Pt ₇₄ Rh ₂₆	2-mm graphite plates	3 mA cm ⁻² for 60 min	2.7–6.5; 5.2	30	463–525; 479 (Pt:531)	50 mA cm ⁻² (@890 mV, 50 mV s ⁻¹)	~3.75 mA cm ⁻² (@540 mV, 1 h (Pt:~2.2 mA cm ⁻²))	0.5 M H ₂ SO ₄ , 1 M EtOH
Pt–Rh⁶¹	55–90 atomic% Pt	Smooth gold disk (FTIR) /sputtered gold layer (DEMS)	5 min @ 0.2 V				0.1 M HClO ₄ , 0.1 M EtOH	• Potentiostatic deposition • Best CO ₂ yield from Pt ₇₃ Rh ₂₇ , but only Pt ₉₀ Rh ₁₀ provides similar overall reaction current to Pt • Acetaldehyde yield and CO ₂ /CH ₃ CH ₂ O ratio increases as Rh increases	• Best CO ₂ yield from Pt ₇₃ Rh ₂₇ , but only Pt ₉₀ Rh ₁₀ provides similar overall reaction current to Pt • Acetaldehyde yield and CO ₂ /CH ₃ CH ₂ O ratio increases as Rh increases
Pt–Rh⁶⁴	Atomic ratio XC-72 1:1	20 wt % and 40 wt %	1.5–2.3 (FA), 7.3–9.2 (H ₂)	25	300–450 (Pt:300)	0.1 M HClO ₄ , 0.5 M EtOH	• Reduction by H ₂ and Formic acid method • Pt–Rh had slightly higher currents for EOR and higher electrochemical conversion efficiency, effect more prominent in materials with lower crystallite sizes	• Reduction by H ₂ and Formic acid method • Pt–Rh had slightly higher currents for EOR and higher electrochemical conversion efficiency, effect more prominent in materials with lower crystallite sizes	

Pt–Rh⁶²	47–83 atomic% XC-72 Pt: Best Pt ₄₇ Rh ₅₃	25	1.7–2.2	200–550; 500 (Pt:450)	0.1 M DClO ₄ , 0.1 M EtOH	• Reduction by Formic Acid
						• The faradaic current efficiency for the oxidation of EtOH to CO ₂ improved from 0.08 on pure Pt to 0.5 on Pt ₄₇ Rh ₅₃ , but this was not followed by higher current densities
Rh@Pt⁹⁶	1–2 ML Pt shells, Pt–Rh alloy	1 wt % Pt	2.7–3.9 (Rh core), 4.9 (Pt–Rh)	25	200–400; 200 (Pt:400)	~7 μA cm ⁻² (@500 mV, 30 min (Pt:~2 μA cm ⁻²)
						• Reduction by EG with inorganic salts and PVP stabilizers
						• Catalysts tested for PROX and Rh@Pt has best activity with complete CP oxidation at 70 °C and very high PROX selectivity at 40 °C with 50% CO conversion
(Ru/Rh) @Pt⁶⁰	Core-shell; Best Ru @Pt	XC-72	20 wt % Ru or Rh on C	25	200–400; 200 (Pt:400)	~7 μA cm ⁻² (@500 mV, 30 min (Pt:~2 μA cm ⁻²)
						• Reduction by H ₂ followed by galvanic displacement of Pt by UPD Cu monolayer
						• Core-shell catalysts had lower onset potentials, but lower max current density than pure Pt
PtW⁵³	Atomic ratio 1 : 1	XC-72	20 wt % Pt	3.4	25	~390
						~3 mA cm ⁻² (@540 mV, 10 mV s ⁻¹)
						0.5 M H ₂ SO ₄ , 1.0 M EtOH
						• Reduction by EG • OCV of 0.55 V
						• Max power density of 16 mW cm ⁻² @90 °C for single-cell test
PtPd⁵³	Atomic ratio 1 : 1	XC-72	20 wt % Pt	3.0	25	540
						~1 mA cm ⁻² (@540 mV, 10 mV s ⁻¹)
						0.5 M H ₂ SO ₄ , 1.0 M EtOH
						• Reduction by EG • Similar current density–voltage curve as Pt
PtPd⁹⁷	Atomic ratio 1 : 1	XC-72	30 wt %	2.4	25	420
						~2.5 times more than Pt/C
						0.1 M HClO ₄ , 1 M EtOH
						• Polyol method

(continued overleaf)

Table 2 (*continued*)

Catalyst	Composition	Support	Loading	Particle size (nm)	Temperature of measurement (°C)	Onset potential for EtOH oxidation (mV)	Activity		Electrolyte	Method of preparation and notes
							CV	CA		
Pt-Ta ₂ O ₅ ⁹⁵	Pt-Ta ₂ O ₅ –53:47	Boron-doped Diamond		25	390, 610 (Pt)	~6 μA cm ⁻² @700 mV, 5 mV s ⁻¹ (Pt:~1.5)	0.5 M H ₂ SO ₄ , 0.5 M EtOH	• Catalyst coatings prepared by sol–gel method		
PtZrO ₂ ⁹⁸	Mole ratio : From 2:1 to 1:3; Best 1:3	MWCNT Pt	20 wt % 3.6–4.1	25	632 (Pt:772) @692 mV, 50 mV s ⁻¹ (Pt/C: ~14)	~40 mA mg ⁻¹ Pt	1 M HClO ₄ , 1 M EtOH	• Stationary current densities up to 11 times higher than on Pt/BDD @0.54 V		
Pt–RuRh ³⁷	Atomic ratio 1:1 and 1:1:1; Best ternary	XC-72	20 wt % 2.6–7.3	60	100–350; 245 (Pt:350)	~5 μA cm ⁻² @500 mV, 30 min (Pt: ~1 μA cm ⁻²)	0.1 M HClO ₄ , 0.5 M EtOH	• Reduction by H ₂ • Pt–Ru produces a strong decrease in onset potential for CO-oxidation. Pt–Rh presents a better CO ₂ /acetic acid ratio, Pt–RuRh shows a compromise between the two		
Pt(Sn/Ru) _(Ni/Rh) ⁹⁹	Mole ratio: Pt ₃₇ Sn ₄₂ , Pt ₄₇ Sn ₃₀ Rh ₂₃ , Pt ₆₅ Sn ₂₉ Ni ₆ , Pt ₃₆ Ru ₆₂ Ni ₁₂ ; Best PtSnNi	XC-72	~4	60	73.7 μA cm ⁻² @500 mV, 1 h	0.5 M H ₂ SO ₄ , 1 M EtOH	• PVP-polyol-water methodology • At potentials higher than 0.55 V, PtSnRh has higher activity			

PtSnRh⁷⁵	Atomic ratio: Pt ₅₁ Sn ₄₉ , Pt ₄₂ Sn ₄₃ Rh ₁₅ , Pt ₅₀ Sn ₃₇ Rh ₃₃ , Pt ₄₇ Rh ₅₃ ; Best PtSn	XC-72	20 wt % 2.8–6.6 150 (Pt:450) 20 mV s ⁻¹	~6 mA cm ⁻² @450 mV, (Pt:450)	1 M EtOH anode, H ₂ cathode single-cell test	<ul style="list-style-type: none"> • Reduction by Formic Acid • Ternary catalysts provided higher activity for EOR at potentials higher than 0.45 V, whereas binary PtSn was best for potentials lower than 0.45 V
Pt–RhSnO₂⁷³	5 nmol Pt, 5 nmol Rh, 20 nmol SnO ₂	XC-72	1–3	60	~7.5 mA cm ⁻² @300 mV, 50 mV s ⁻¹	<ul style="list-style-type: none"> • Cation -adsorption-reduction-galvanic-displacement synthetic method
Pt–Rh₁₀₀ SnO₂¹⁰⁰	28 mol % Pt–Rh, 72 mol % SnO ₂	XC-72	20 wt % 1–5	30150 (Pt:250)	~1.9 mA cm ⁻² @450 mV, 1 h (Pt:~0.02 mA cm ⁻²)	<ul style="list-style-type: none"> • Polyol method • Catalyst synthesized by cation -adsorption-reduction-galvanic-displacement method⁷⁷ had higher activity for EO probably due to the EtOH molecule needing to be in contact with all phases of catalyst in order to be completely oxidized
PtSnPd¹⁰¹	Atomic ratio: 1 : 1 : 0.3 and 1 : 1 : 1; Best PtSn	XC-72	20 wt %; 1 mg Pt cm ⁻² electrode	25	~22 mA cm ⁻² @800 mV, 1 h	<ul style="list-style-type: none"> • Reduction by Formic Acid • Max power density of ~4.35 mW cm⁻² @60 °C for single-cell test

5 END NOTES

^a The kinetics of ethanol oxidation is indeed slower than that of methanol oxidation. However, further increase in the Pt loading would result in a thick catalyst layer which gives rise to other problems such as high internal cell resistance.

6 RELATED ARTICLES

Enzymes and Microbes for Energy Production by Fuel Cells; Intermediate-Temperature Solid Oxide Fuel Cells; Molecular Catalysis for Fuel Cells; Proton Exchange Membranes for Fuel Cells.

7 ABBREVIATIONS AND ACRONYMS

BDD = boron-doped diamond; CNTs = carbon nanotubes; DEFC = direct ethanol fuel cell; DEMS = differential electrochemical mass spectrometry; DMFC = direct methanol fuel cell; EOR = ethanol oxidation reaction; fcc = face-centered cubic; FTIR = Fourier transform infrared; hcp = hexagonal close-packed; OCV = open-circuit voltage; ORR = oxygen reduction reaction; PEMFCs = polymer electrolyte membrane fuel cells; SHE = standard hydrogen electrode; upd = underpotentially deposited; XRD = X-ray diffraction.

8 REFERENCES

1. K. Joon, *J. Power Sources*, 1998, **71**, 12.
2. C. Lamy, E. M. Belgsir, and J. M. Léger, *J. Appl. Electrochem.*, 2001, **31**, 799.
3. A. Serov and C. Kwak, *Appl. Catal. B: Environ.*, 2009, **90**, 313.
4. W. J. Zhou, B. Zhou, W. Z. Li, Z. H. Zhou, S. Q. Song, G. Q. Sun, Q. Xin, S. Douvartzides, M. Goula, and P. Tsiakaras, *J. Power Sources*, 2004, **126**, 16.
5. C. Lamy, S. Rousseau, E. M. Belgsir, C. Coutanceau, and J. M. Léger, *Electrochim. Acta*, 2004, **49**, 3901.
6. Wikipedia. ‘Energy Density’, 23 August 2009 [cited 25 August 2009]. Available from http://en.wikipedia.org/wiki/Energy_density, 2009.
7. S. D. Minteer, ‘Alcoholic Fuels’, 2006.
8. E. Antolini, *J. Power Sources*, 2007, **170**, 1.
9. G. M. Andreadis, A. K. M. Podias, and P. E. Tsiakaras, *J. Power Sources*, 2009, **194**, 397.
10. G. M. Andreadis, A. K. M. Podias, and P. E. Tsiakaras, *J. Power Sources*, 2008, **181**, 214.
11. S. Song, W. Zhou, Z. Liang, R. Cai, G. Sun, Q. Xin, V. Stergiopoulos, and P. Tsiakaras, *Appl. Catal. B: Environ.*, 2005, **55**, 65.
12. P. Gao, S.-C. Chang, Z. Zhou, and M. J. Weaver, *J. Electroanal. Chem.*, 1989, **272**, 161.
13. G. A. Camara, R. B. de Lima, and T. Iwasita, *J. Electroanal. Chem.*, 2005, **585**, 128.
14. J. Wang, S. Wasmus, and R. F. Savinell, *J. Electrochem. Soc.*, 1995, **142**, 4218.
15. J. P. I. Souza, F. J. Botelho Rabelo, I. R. de Moraes, and F. C. Nart, *J. Electroanal. Chem.*, 1997, **420**, 17.
16. H. Hitmi, E. M. Belgsir, J. M. Léger, C. Lamy, and R. O. Lezna, *Electrochim. Acta*, 1994, **39**, 407.
17. G. A. Camara, T. Iwasita, *J. Electroanal. Chem.*, 2005, **578**, 315.
18. F. Vigier, S. Rousseau, C. Coutanceau, J.-M. Léger, and C. Lamy, *Top. Catal.*, 2006, **40**, 111.
19. S. C. S. Lai and M. T. M. Koper, *Faraday Discuss.*, 2009, **140**, 399.
20. H.-F. Wang and Z.-P. Liu, *J. Am. Chem. Soc.*, 2008, **130**, 10996.
21. S.-B. Han, Y.-J. Song, J.-M. Lee, J.-Y. Kim, and K.-W. Park, *Electrochim. Commun.*, 2008, **10**, 1044.
22. Z. Liu, X. Y. Ling, X. Su, J. Y. Lee, and L. M. Gan, *J. Power Sources*, 2005, **149**, 1.
23. N. Fujiwara, K. A. Friedrich, and U. Stimming, *J. Electroanal. Chem.*, 1999, **472**, 120.
24. G. A. Camara, R. B. de Lima, and T. Iwasita, *Electrochim. Commun.*, 2004, **6**, 812.
25. M. Chatterjee, A. Chatterjee, S. Ghosh, and I. Basumallick, *Electrochim. Acta*, 2009, **54**, 7299.
26. A. O. Neto, M. J. Giz, J. Perez, E. A. Ticianelli, and E. R. Gonzalez, *J. Electrochem. Soc.*, 2002, **149**, A272.
27. E. V. Spinace, A. O. Neto, T. R. R. Vasconcelos, and M. Linardi, *J. Power Sources*, 2004, **137**, 17.
28. F. Colmati, E. Antolini, and E. R. Gonzalez, *J. Power Sources*, 2006, **157**, 98.
29. W. Zhou, Z. Zhou, S. Song, W. Li, G. Sun, P. Tsiakaras, and Q. Xin, *Appl. Catal. B: Environ.*, 2003, **46**, 273.
30. S. Q. Song, W. J. Zhou, Z. H. Zhou, L. H. Jiang, G. Q. Sun, Q. Xin, V. Leontidis, S. Kontou, and P. Tsiakaras, *Int. J. Hydrogen Energy*, 2005, **30**, 995.
31. J. Bagchi and S. K. Bhattacharya, *J. Power Sources*, 2007, **163**, 661.
32. C.-G. Lee, M. Umeda, and I. Uchida, *J. Power Sources*, 2006, **160**, 78.
33. S. Tanaka, M. Umeda, H. Ojima, Y. Usui, O. Kimura, and I. Uchida, *J. Power Sources*, 2005, **152**, 34.
34. M. L. Calegaro, H. B. Suffredini, S. A. S. Machado, and L. A. Avaca, *J. Power Sources*, 2006, **156**, 300.
35. H. B. Suffredini, V. Tricoli, N. Vatistas, and L. A. Avaca, *J. Power Sources*, 2006, **158**, 124.

36. S. Sen Gupta, S. S. Mahapatra, and J. Datta, *J. Power Sources*, 2004, **131**, 169.
37. F. H. B. Lima and E. R. Gonzalez, *Electrochim. Acta*, 2008, **53**, 2963.
38. S. Rousseau, C. Coutanceau, C. Lamy, and J. M. Leger, *J. Power Sources*, 2006, **158**, 18.
39. H. Wang, Z. Jusys, and R. J. Behm, *J. Power Sources*, 2006, **154**, 351.
40. H. Li, G. Sun, L. Cao, L. Jiang, and Q. Xin, *Electrochim. Acta*, 2007, **52**, 6622.
41. F. Vigier, C. Coutanceau, F. Hahn, E. M. Belgsir, and C. Lamy, *J. Electroanal. Chem.*, 2004, **563**, 81.
42. W. J. Zhou, S. Q. Song, W. Z. Li, Z. H. Zhou, G. Q. Sun, Q. Xin, S. Douvartzides, and P. Tsiakaras, *J. Power Sources*, 2005, **140**, 50.
43. P. E. Tsiakaras, *J. Power Sources*, 2007, **171**, 107.
44. J. H. Kim, S. M. Choi, S. H. Nam, M. H. Seo, S. H. Choi, and W. B. Kim, *Appl. Catal. B: Environ.*, 2008, **82**, 89.
45. L. Jiang, H. Zang, G. Sun, and Q. Xin, *Chin. J. Catal.*, 2006, **27**, 15.
46. G. Sine, G. Foti, and C. Comminellis, *J. Electroanal. Chem.*, 2006, **595**, 115.
47. G. R. Salazar-Banda, H. B. Suffredini, L. A. Avaca, and S. A. S. Machado, *Mater. Chem. Phys.*, 2009, **117**, 434.
48. M. Zhu, G. Sun, and Q. Xin, *Electrochim. Acta*, 2009, **54**, 1511.
49. S. Sen Gupta, S. Singh, and J. Datta, *Mater. Chem. Phys.*, 2009, **116**, 223.
50. E. Antolini, F. Colmati, and E. R. Gonzalez, *J. Power Sources*, 2009, **193**, 555.
51. F. Colmati, E. Antolini, and E. R. Gonalez, *J. Electrochem. Soc.*, 2007, **154**, B39.
52. L. H. Jiang, G. Q. Sun, Z. H. Zhou, and Q. Xin, *Catal. Today*, 2004, **93–95**, 665.
53. W. J. Zhou, W. Z. Li, S. Q. Song, Z. H. Zhou, L. H. Jiang, G. Q. Sun, Q. Xin, K. Poulianitis, S. Kontou, and P. Tsiakaras, *J. Power Sources*, 2004, **131**, 217.
54. J. M. Leger, S. Rousseau, C. Coutanceau, F. Hahn, and C. Lamy, *Electrochim. Acta*, 2005, **50**, 5118.
55. F. C. Simoes, D. M. dos Anjos, F. Vigier, J. M. Leger, F. Hahn, C. Coutanceau, E. R. Gonzalez, G. Tremiliosi-Filho, A. R. de Andrade, P. Olivi, and K. B. Kokoh, *J. Power Sources*, 2007, **167**, 1.
56. L. H. Jiang, G. Q. Sun, S. G. Sun, J. G. Liu, S. H. Tang, H. Q. Li, B. Zhou, and Q. Xin, *Electrochim. Acta*, 2005, **50**, 5384.
57. A. O. Neto, R. R. Dias, M. M. Tusi, M. Linardi, and E. V. Spinace, *J. Power Sources*, 2007, **166**, 87.
58. L. Jiang, L. Colmenares, Z. Jusys, G. Q. Sun, and R. J. Behm, *Electrochim. Acta*, 2007, **53**, 377.
59. Z.-B. Wang, G.-P. Yin, and Y.-G. Lin, *J. Power Sources*, 2007, **170**, 242.
60. F. H. B. Lima and E. R. Gonzalez, *Appl. Catal. B: Environ.*, 2008, **79**, 341.
61. J. P. I. de Souza, S. L. Queiroz, K. Bergamaski, E. R. Gonzalez, and F. C. Nart, *J. Biochem. Mol. Biol. Biophys.*, 2002, **106**, 9825.
62. K. Bergamaski, E. R. Gonzalez, and F. C. Nart, *Electrochim. Acta*, 2008, **53**, 4396.
63. S. Sen Gupta and J. Datta, *J. Electroanal. Chem.*, 2006, **594**, 65.
64. F. H. B. Lima, D. Profeti, W. H. Lizcano-Valbuena, E. A. Ticianelli, and E. R. Gonzalez, *J. Electroanal. Chem.*, 2008, **617**, 121.
65. F. Kadırgan, S. Beyhan, and T. Atilan, *Int. J. Hydrogen Energy*, 2009, **34**, 4312.
66. C. W. Xu and P. K. Shen, *J. Power Sources*, 2005, **142**, 27.
67. D. M. Dos Anjos, K. B. Kokoh, J. M. Leger, A. R. De Andrade, P. Olivi, and G. Tremiliosi, *J. Appl. Electrochem.*, 2006, **36**, 1391.
68. N. V. Ageev and V. G. Kuznetsov, *Izvest. Akad. Nauk. SSSR Khim.*, 1937, **6**, 753.
69. E. Antolini, *Mater. Chem. Phys.*, 2003, **78**, 563.
70. Z. Paál, N. Gyorffy, A. Wootsch, L. Tóth, I. Bakos, S. Szabó, U. Wild, and R. Schlägl, *J. Catal.*, 2007, **250**, 254.
71. Z.-B. Wang, G.-P. Yin, J. Zhang, Y.-C. Sun, and P.-F. Shi, *J. Power Sources*, 2006, **160**, 37.
72. E. Ribadeneira and B. A. Hoyos, *J. Power Sources*, 2008, **180**, 238.
73. E. Antolini, F. Colmati, and E. R. Gonzalez, *Electrochem. Commun.*, 2007, **9**, 398.
74. G. Wu, R. Swaidan, and G. Cui, *J. Power Sources*, 2007, **172**, 180.
75. F. Colmati, E. Antolini, and E. R. Gonzalez, *J. Alloys Compd.*, 2008, **456**, 264.
76. A. Kowal, S. L. Gojkovic, K. S. Lee, P. Olszewski, and Y. E. Sung, *Electrochem. Commun.*, 2009, **11**, 724.
77. A. Kowal, M. Li, M. Shao, K. Sasaki, M. B. Vukmirovic, J. Zhang, N. S. Marinkovic, P. Liu, A. I. Frenkel, and R. R. Adzic, *Nat. Mater.*, 2009, **8**, 325.
78. A. O. Neto, L. A. Farias, R. R. Dias, M. Brandalise, M. Linardi, and E. V. Spinacé, *Electrochem. Commun.*, 2008, **10**, 1315.
79. X. Xue, J. Ge, T. Tian, C. Liu, W. Xing, and T. Lu, *J. Power Sources*, 2007, **172**, 560.
80. M. Y. Wang, J. H. Chen, Z. Fan, H. Tang, G. H. Deng, D. L. He, and Y. F. Kuang, *Carbon*, 2004, **42**, 3257.
81. H. T. Zheng, Y. L. Li, S. X. Chen, and P. K. Shen, *J. Power Sources*, 2006, **163**, 371.
82. H. Song, X. Qiu, F. Li, W. Zhu, and L. Chen, *Electrochem. Commun.*, 2007, **9**, 1416.
83. F. Hu, G. Cui, Z. Wei, and P. K. Shen, *Electrochem. Commun.*, 2008, **10**, 1303.

84. S. Vengatesan, H.-J. Kim, S.-K. Kim, I.-H. Oh, S.-Y. Lee, E. Cho, H. Y. Ha, and T.-H. Lim, *Electrochim. Acta*, 2008, **54**, 856.
85. F. P. Hu, F. W. Ding, S. Q. Song, and P. K. Shen, *J. Power Sources*, 2006, **163**, 415.
86. H. Song, X. Qiu, X. Li, F. Li, W. Zhu, and L. Chen, *J. Power Sources*, 2007, **170**, 50.
87. D.-J. Guo, X.-P. Qiu, L.-Q. Chen, and W.-T. Zhu, *Carbon*, 2009, **47**, 1680.
88. C. Xu, Y. Su, L. Tan, Z. Liu, J. Zhang, S. Chen, and S. P. Jiang, *Electrochim. Acta*, 2009, **54**, 6322.
89. J. Lu, S. Lu, D. Wang, M. Yang, Z. Liu, C. Xu, and S. P. Jiang, *Electrochim. Acta*, 2009, **54**, 5486.
90. C. Bianchini, V. Bambagioni, J. Filippi, A. Marchionni, F. Vizza, P. Bert, and A. Tampucci, *Electrochem. Commun.*, 2009, **11**, 1077.
91. C. Xu, Pk. Shen, and Y. Liu, *J. Power Sources*, 2007, **164**, 527.
92. V. K. Ramani, *Electrochem. Soc. Interface*, 2006, **15**, 41.
93. S. Sen Gupta, S. Singh, and J. Datta, *Mater. Chem. Phys.*, 2009, **116**, 223.
94. S. García-Rodríguez, F. Somodi, I. Borbáth, J. L. Margitfalvi, M. A. Peña, J. L. G. Fierro, and S. Rojas, *Appl. Catal. B: Environ.*, 2009, **91**, 83.
95. G. R. Salazar-Banda, H. B. Suffredini, L. A. Avaca, and S. A. S. Machado, *Mater. Chem. Phys.*, 2009, **117**, 434.
96. S. Alayoglu and B. Eichhorn, *J. Am. Chem. Soc.*, 2008, **130**, 17479.
97. F. Kadırgan, S. Beyhan, and T. Atilan, *Int. J. Hydrogen Energy*, 2009, **34**, 4312.
98. H. Song, X. Qiu, and F. Li, *Appl. Catal. A: General*, 2009, **364**, 1.
99. A. Bonesi, G. Garaventa, W. E. Triaca, and A. M. Castro Luna, *Int. J. Hydrogen Energy*, 2008, **33**, 3499.
100. A. Kowal, S. L. Gojkovic, K. S. Lee, P. Olszewski, and Y. E. Sung, *Electrochem. Commun.*, 2009, **11**, 724.
101. E. Antolini, F. Colmati, and E. R. Gonzalez, *J. Power Sources*, 2009, **193**, 555.

Molecular Catalysis for Fuel Cells

Kenichi Oyaizu

Waseda University, Tokyo, Japan

1	Introduction	253
2	Overview of O ₂ Reduction Catalysts	254
3	Diporphyrins and Related Complexes	254
4	Porphyrin Assemblies Based on Intermolecular Interaction	259
5	Multinuclear Complexes as Electron Reservoirs	260
6	Conclusions	260
7	Related Articles	261
8	Abbreviations and Acronyms	261
9	References	261

1 INTRODUCTION

In the fuel cell, the Pt nanoparticle catalyst supported by carbon particles, such as carbon black, is used for the catalyst of the cathode, which reduces O₂ as the cathode-active material. To obtain electric energy from the H₂ fuel supplied to the anode side efficiently, O₂ needs to be reduced with four electrons to H₂O at positive potentials, which requires electrocatalysts.¹ The theoretical electromotive force (emf) of 1.23 V for the fuel cell corresponds to the potential where O₂ is reduced by a one-step four-electron reduction (O₂ + 4e⁻ + 4H⁺ → 2H₂O). It is equivalent to the potential where the maximum oxidation power of O₂ is derived. Actual emf declines to 0.7–1.0 V, because of the changes in the reduction mechanism, in addition to the presence of activation polarization or concentration polarization in the cell. That is, when the reduction of O₂ generates H₂O₂ by the two-electron reduction according to O₂ + 2e⁻ + 2H⁺ → H₂O₂ and then H₂O₂ is reduced to water according to H₂O₂ + 2e⁻ + 2H⁺ → 2H₂O by the two-step mechanism, the overall reaction is identical to that of a one-step mechanism, but the theoretical emf is determined by the potential of the first two-electron reduction. Moreover, H₂O₂ is responsible for the degradation of the fuel cell over time, because it destroys the polymer electrolyte membrane through the attack by peroxide radicals. To suppress such an undesired two-step mechanism, it is necessary to raise the selectivity of the one-step four-electron reduction using a suitable cathode catalyst.

Cytochrome *c* oxidase (CcO) is the enzyme involved in the respiratory system in an aerobic organism and exists in the mitochondrial membrane. CcO catalyzes the four-electron reduction of O₂ taken in by breathing, into H₂O. Since it has two or more hemes and copper atoms per molecule as a prosthetic group, it is believed that their cooperative effects participate in the enzymatic functions. However, the mechanism still has many points in dispute. To reproduce the catalytic function of CcO by an artificial system, a variety of heme derivatives have been synthesized. Interestingly, four-electron reduction of O₂ is difficult with the mononuclear heme derivatives, but becomes feasible using molecular assemblies or polynuclear complexes.² Investigation of the structure of the active site reveals that high activity is derived when O₂ bridges two metal ions to form a μ-peroxo dinuclear complex. Such a metal complex may lead to significant reduction in the amount of the platinum by substituting the platinum-based catalyst currently used in the fuel cell cathodes. Especially, the metal complexes that have macrocyclic ligands, such as porphyrins and phthalocyanines, have been widely investigated including basic studies on the dynamics of O₂ coordination and the structure of the intermediates, which was prompted by the finding that cobalt cofacial porphyrins (Figure 1) show a high catalytic activity for the four-electron reduction of O₂.³ While the highly dispersed adsorption of the metal complexes onto the carbon support as a catalyst carrier and improvement in durability are the important issues for practical application, the metal complex catalysts have advantages over the platinum-based catalysts in terms of flexibility of molecular design. In

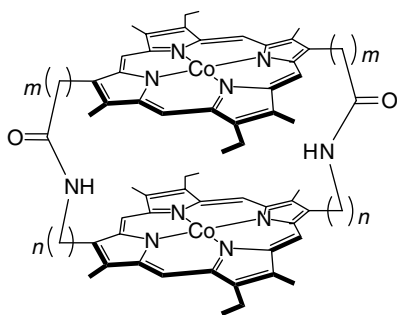


Figure 1 Cobalt cofacial diporphyrin complexes designed for O₂ reduction catalysts

this article, the latest progress in the metal complex cathode catalysts is focused on, aiming at the development of the platinum-free catalyst from unlimited resources.

2 OVERVIEW OF O₂ REDUCTION CATALYSTS

Platinum shows the lowest overpotential of ca 0.3 V and the highest selectivity for the direct reduction of O₂ to H₂O, but it is unfavorable due to the degradation caused by oxidation with O₂ adsorbed on the surface, in addition to the cost and the low abundance. To lower the overall cost of fuel cells through platinum loading reduction, platinum–transition metal alloy catalysts have been investigated, alloying platinum with iron, cobalt, and nickel.^{4,5} Platinum-free catalysts have also been examined, based on the nanoparticles of various transition metals, especially focusing on those of palladium, ruthenium, and gold,^{6–10} and the Ru-based chalcogenide compounds such as Mo₄Ru₂Se₈ and Ru_xSe_y.¹¹ In these catalysts, the catalytically active site is limited to the surface of the metal particles and the bulk phase does not participate in the activity. In the case of a metal complex catalyst, one metal atom can serve as the active site, leading to the more efficient use of metal atoms. The overpotential at the cathode side is influenced by the activation overpotential of the catalyst, the resistance of the catalyst layer, and the amount of O₂ supply. In the case of a metal complex catalyst, the redox potential of the complex also dominates the potential where O₂ is reduced, providing the opportunity to control the emf of the cell.

The performance of a cathode catalyst is evaluated by preparing a membrane electrode assembly (MEA) and measuring the current–voltage characteristics. However, since a large quantity of the catalyst is required in MEA, an alternative screening method is preferred for the metal complex catalyst. For example, one can expect high activity of a catalyst when the peak potential for the O₂ reduction wave obtained by cyclic voltammetry experiments is close to the standard potential for the four-electron reduction of O₂. Comparison of the O₂ reduction potentials for a

number of metal complex catalysts revealed that molecular assemblies and polynuclear complexes show higher catalytic activities than mononuclear analogs. The typical example has been demonstrated by the catalytic activities of a series of cobalt tetraphenylporphyrins that act as two-electron reduction catalysts of O₂ in mononuclear complexes. When the phenyl groups of the meso positions are substituted with pyridine-4-yl group and the ruthenium or osmium ammine complexes are coordinated, the selectivity for the four-electron reduction of oxygen is increased.¹² Studies on the structure of the active site of the catalyst have revealed that four-electron reduction of O₂ becomes feasible when O₂ forms a μ-peroxo complex by bridging two metal centers. Studies on catalysis by the cobalt diporphyrins have revealed that the O=O bond order decreases through the μ-peroxo complex formation and that the O₂ reduction current increases notably with decrease in steric repulsion. Simple and highly convenient methods to prepare the μ-peroxo complexes using μ-(di)oxo complexes have been proposed.¹³

3 DIPORPHYRINS AND RELATED COMPLEXES

3.1 Cobalt Diporphyrins

Mononuclear complexes of cobalt porphyrins ([CoP]) are known to function as two-electron reduction catalysts of O₂.¹⁴ The cofacial diporphyrin complexes, capable of forming μ-peroxo complexes [PCo-O-O-CoP] by sandwiching O₂ with the two metal atoms, show higher selectivity for the four-electron reduction of O₂, because of the decrease in the O=O bond order upon the formation of the μ-peroxo bridge to allow the cleavage of O₂.^{3,15} When rigid pillars such as anthracene (Figure 2(a)) or biphenylene units (Figure 2(b)) are employed to form the diporphyrin on one side of the two porphyrin rings, the steric repulsion between the diporphyrin and O₂ is reduced, resulting in a remarkable increase in the current for the reduction of O₂ (i.e., turnover speed of the catalyst).^{16,17}

Diporphyrin complexes that have a flexible linkage between the two porphyrin rings like a hinge so that the

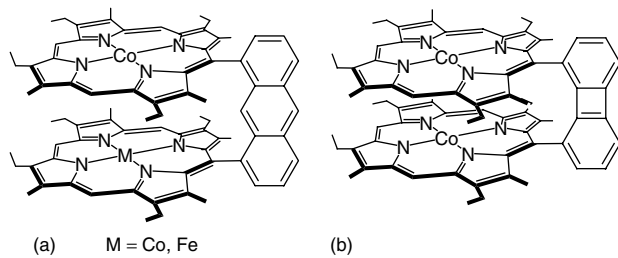


Figure 2 Diporphyrin-type metal complexes pillared by rigid groups to bind the porphyrin rings

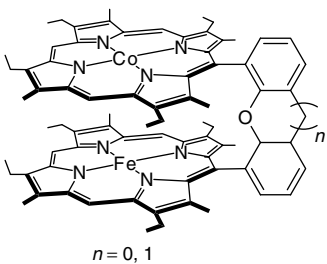


Figure 3 Flexible diporphyrin cobalt–iron complex designed for facile accommodation of oxygen

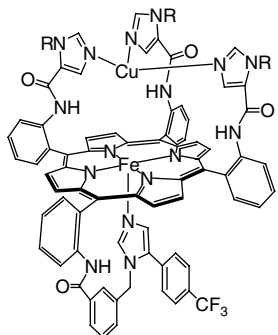


Figure 4 Iron porphyrin designed as the proposed model of the active site of CcO

two porphyrin rings can open and close according to the accommodation of O₂ (Figure 3)^{18–20} are found to catalyze the four-electron reduction of O₂ characterized by faster kinetics.^{21,22} Using ferryl intermediates generated by photoexcitation of the μ -peroxy iron complexes,^{23–25} similar reactions have been applied to highly selective catalytic oxidation of sulfide molecules.²⁶

The dinuclear complex designed as a model of the active site of CcO (Figure 4) functions as a four-electron reduction catalyst of O₂.²⁷ In CcO, there is a large distance between heme a₃ and Cu_B, and O₂ coordinated to heme a₃ is unlikely to reach the Cu_B site, leaving the role of Cu_B undefined. However, the catalysis of the O₂ reduction has demonstrated that the dinuclear complex is mimicry of CcO to act under physiological conditions.

3.2 Modification of Nanocarbon Surface with Metal–N₄ Chelates

3.2.1 Recent Trends in Carbon Modification

Metal complexes with macrocyclic ligands such as porphyrins and phthalocyanines that contain four nitrogen donors (i.e., metal–N₄ chelates) adsorbed on carbon supports are expected to be the alternates to the conventional carbon-supported platinum catalyst in fuel cells. The source

of nitrogen atoms does not necessarily have to be the macrocyclic ligands. Yeager *et al.* found catalytic activity with a heat-treated mixture of transition metal salts, such as cobalt and iron, and nitrogenous polymers such as polyacrylonitrile adsorbed on charcoal.²⁸ Ozaki *et al.* reported that carbonization of cobalt poly(4-vinylpyridine) on carbon black gave rise to O₂ reduction activity.²⁹ Dodelet and coworkers have employed NH₃ and CH₃CN as the precursors of nitrogen atoms and found that, for iron-based catalysts, the nitrogen atoms on the carbon support must be of a pyridine type.^{30–42} It has been reported that heat treatment of carbon supports in NH₃/H₂/argon atmosphere is effective to enrich their surfaces with nitrogen atoms and to provide the pyridine-type coordination site.^{43–46} Activities of the resulting catalysts after adsorbing iron ions are comparable to those of conventional iron complexes with pyridine-type ligands adsorbed on carbon supports.^{47–49} For cobalt-based catalysts, on the other hand, a pyrrole-type nitrogen atom is preferred,⁵⁰ but a convenient method is needed for the development of this type of nitrogen atom to provide a tetrapyrrole-type coordination site on carbons such as those of porphyrins and phthalocyanines.⁵¹

3.2.2 Polypyrrole Metal Complexes

It has been reported that a carbon nanoparticle modified with a cobalt-adsorbed polypyrrole (PPy) film is a good electrocatalyst for the reduction of O₂.^{52–57} Extended X-ray absorption fine structure (EXAFS) spectroscopy and X-ray diffraction (XRD) experiments have revealed that the cobalt ion is coordinated by four nitrogens as the donor atoms, and that the Co–N₄ structure is successfully maintained after heat treatment under an inert atmosphere up to ca 700 °C without deposition of metallic cobalt.⁵²

To accommodate cobalt ions at a coordination site within the PPy layer through a heterogeneous process, the PPy layer has been produced at the surface of a high surface-area carbon nanoparticle by fluid-bed electrolysis. Carbon black with a large BET surface area has been employed for the carbon materials because it is a common support used for the platinum-based catalysts. Obtaining a PPy coating on the carbon black involves the electropolymerization of pyrrole at the surface of the carbon black, which has been accomplished by suspending carbon black into an electrolyte solution of pyrrole and electrolyzing the suspension with the platinum wire as a working electrode with vigorous stirring. Carbon black, upon continuous contact with the platinum electrode, serves as the working electrode during the electrolysis. The resulting PPy/CB particle has been suspended into a solution of transition metal acetates in CH₃OH, which has been then refluxed for a sufficiently long time to allow accommodation of the metal ions at the suitable site (Figure 5).

The pristine CoPPy/CB catalyst (M = Co(II) in MPPy/CB) shows a moderate electrocatalytic activity for the reduction of O₂. To prepare a CoPPy/CB-modified disk

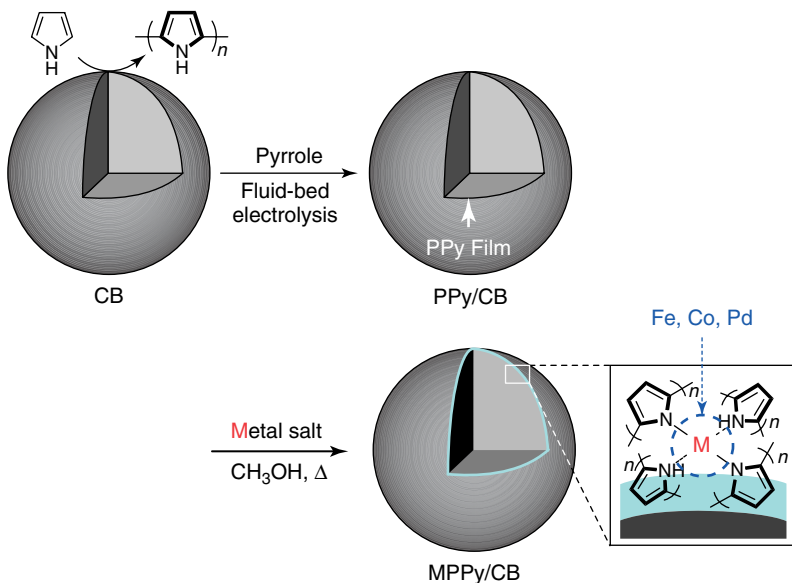


Figure 5 Proposed structure of the active site of the MPPy/CB catalyst

electrode for evaluation of the catalytic activity, an alcoholic suspension of CoPPy/CB containing Nafion has been used as a mother liquor for dip-coating. In the cyclic voltammograms obtained with the electrode modified with CoPPy/CB under O₂, the catalytic current for the reduction of O₂ appears near 0.23 V vs SCE, while the Co(III/II) couple appears at a more positive potential in the absence of O₂ near 0.3 V. The Co(III/II) potential is, however, much more negative than the Co^{3+/2+} potential in aqueous solutions ($E^{\text{f}} = 1.68$ V vs SCE),⁵⁸ which suggests that the cobalt ion is coordinated by donor atoms in PPy, rather than merely adsorbed on the PPy/CB surface.

Added support for coordination of PPy to the cobalt ion has been furnished by EXAFS spectroscopy.⁵² The Fourier-transformed EXAFS function yields an atomic distance of $R_{\text{Co-N}} = 2.07$ Å, which is comparable to the typical coordinate bond lengths in cobalt complexes such as cobalt porphyrins and phthalocyanines. The EXAFS function gives a first-shell cobalt–nitrogen coordination number of 4, which is suggestive of the Co–N₄ structure.

A significant feature of the CoPPy/CB catalyst is a positive shift in the O₂ reduction potential accomplished by heat treatment at elevated temperatures. After heat treatment of the catalyst at 700 °C under vacuum, the catalytic current for the reduction of O₂ appears near 0.38 V vs SCE. Heat treatment of the catalyst not only shifts the half-wave potential to a significantly positive side but also nearly doubles the peak current, while the reduction of O₂ occurs in a single step for both pristine and heat-treated catalysts. No current response is obtained at the electrode under argon, which confirms that these currents are due to the reduction of O₂. Koutecky–Levich plots obtained from the diffusion-limited currents on rotated disk electrodes have revealed

that the heat-treated catalyst reduces O₂ with four electrons ($n_{\text{app}} = 3.7$), while a two-electron reduction is predominant for the pristine catalyst ($n_{\text{app}} = 2.8$). One could speculate that such a difference in the reactivity comes from the presence of two parallel reactions, one involving the bridging of O₂ to two proximate cobalt centers and giving rise to the four-electron reduction of O₂, and the other involving a single cobalt center and yielding the two-electron reduction of O₂. The typical platform to promote the four-electron reduction of O₂ is the covalently linked cofacial metalloporphyrins (Figure 1), allowing both ends of O₂ molecules to interact with the cobalt centers in the transition state. The improved catalytic activity upon heat treatment has been ascribed to the shortening of the cobalt–cobalt distance, allowing O₂ molecules to bridge the two proximate cobalt centers. A maximum in the electrocatalytic activity has been obtained for the CoPPy/CB catalyst by the heat treatment near 700 °C, with a subsequent decrease in the catalytic activity at higher temperatures. XRD experiments have revealed that, at temperatures near 1000 °C, metallic cobalt aggregates are formed and consequently the catalytic activity decreases. XPS measurements have shown that nitrogen atoms are no longer detected after heat treatment around 1000 °C.

The CoPPy/CB catalyst has been synthesized by a multiple modification method for the purpose of modifying Co–N₄ structure in a higher density.⁵⁹ The CoPPy/CB catalyst has been prepared by electropolymerization of pyrrole onto the surface of carbon particles, which is dispersed in the electrolyte solution containing the pyrrole, followed by complexation using cobalt acetates. This modification procedure is then repeated several times to increase the density of the active site at the surface of the carbon particles. The carbon nanoparticles prepared by the multiple modification method is suspended

into Nafion solution, and a pseudo-MEA is fabricated by casting the catalyst onto an edge-plane pyrolytic graphite electrode. The catalyst has been found to reduce O_2 with four electrons ($n_{app} = 3.3$) at a remarkably positive potential ($E_p = 0.31$ V vs SCE). The activity of the catalyst is further improved after the heat treatment ($E_p = 0.42$ V vs SCE, $n_{app} = 3.8$). This type of catalyst has been developed from various analogs containing a variety of metals such as Fe(II) and Pd(II) (Figure 5).⁶⁰

Zelenay *et al.* have reported that a cobalt complex supported on carbon particles, prepared by impregnating an aqueous solution of cobalt nitrate into a composite of polypyrrole and carbon black (Vulcan XC 72), is useful as a cathode catalyst of a polymer electrolyte fuel cell.⁶¹ This catalyst has been coupled with a PtRu anode catalyst, and an MEA has been fabricated for a test cell. The output of 0.15 W cm^{-2} has been obtained for 100 h or more by using H_2 as the fuel. Emphasis is placed on the fact that heat treatment, frequently employed in the studies of the electrode catalyst using metal complexes, is not employed. Instead, pretreatment has been carried out under constant supply of H_2 and O_2 at 80°C by holding the MEA with an applied voltage of 0.40 V for a long time. During the pretreatment, activity improves gradually over 30 h. It has been established by the observation of an XANES and an XAFS spectra that the active site, in which the cobalt(II) center is coordinated to the nitrogen atom of the pyrrole ring, is formed efficiently. The irreversible structural changes in the process of continuous operation as the electrode catalyst have been demonstrated to lead to the formation of the effective O_2 reduction site.

Conductive polymer ligand-coated carbon particles have also been prepared by a fluid-bed electrolysis of 2-(3-pyridyl)thiophene using carbon particles as the working electrode.⁶² The resulting particle has been suspended into a solution of cobalt acetate in DMF. The surface of the carbon particles has been successfully modified with the highly dispersed cobalt complex. The modified carbon particles have been then suspended into an alcoholic solution of Nafion, and a pseudo-MEA has been prepared on an electrode by casting the solution. The electrocatalytic reduction of O_2 has been examined using the modified electrode. When the catalyst is prepared using carbon black with a large surface area and pyrrole is added as a complementary ligand, the catalytic potential for the reduction of O_2 appears at $E_p = 0.37$ V vs SCE. The catalyst reduces O_2 with four electrons ($n_{app} = 3.1$). The improved activity of the catalyst has revealed that the nitrogen atoms of the pyridine-type ligand contribute to accumulate the cobalt ions at the surface of the catalyst. The catalytic activity improves remarkably after the heat treatment of the catalyst under argon. The catalyst has revealed the possibility of a practical cathode catalyst for platinum-free fuel cells.

Polyaniline has also been shown to be an effective ligand to accumulate the cobalt ions, giving rise to the O_2 reduction site.⁶³ A mixture of aniline and pyrrole has

been electropolymerized in the presence of suspended carbon black in an electrolyte solution. The resulting particles have been suspended again in methanol containing cobalt acetate, which is then refluxed for a sufficiently long time to complex with the cobalt ions. The resulting catalyst reduces O_2 with four electrons ($n_{app} = 3.4$) at a relatively positive potential ($E_p = 0.28$ V vs SCE). The catalytic activity of the catalyst improves by the heat treatment under an inert gas atmosphere ($E_p = 0.40$ V vs SCE, $n_{app} = 3.9$).

3.2.3 Cobalt Thienylporphyrins

A long π -conjugated system in which the thienyl groups are connected at 2,5-positions, prepared from a porphyrin complex as a monomer bearing at least one 3-thienyl group linked at the meso position of the porphyrin ring with remaining meso positions substituted with alkyl groups (Figure 6), has been found to be a novel electrocatalyst for the reduction of O_2 . This complex is characterized by the presence of the O_2 bridging site and moderate electric conductivity.^{64,65} The band structure has revealed that the resulting structure is characterized by a band gap equivalent to that of polythiophene ($E_g = \text{ca } 2\text{ eV}$) and a distance between adjacent porphyrin rings that is suitable for accommodation of O_2 as a bridging ligand for the formation of the μ -peroxy complex. The resulting coordination site can be regarded as a structure in which the cofacial multiple porphyrin complexes are bound to the main chain of a conducting polymer as a pendant group.

The corresponding polymer has successfully been synthesized as follows. Considering the steric repulsive effect around the oxygen coordination site, ethyl groups have been employed as the alkyl group as in Figure 6 ($n = 2$). The porphyrin monomer bearing a 3-thienyl group at one of the meso positions and three ethyl groups at the remaining meso positions, 5-(3-thienyl)-10,15,20-triethyl-21*H*,23*H*-porphine ($H_2(\text{tep})$) has been synthesized by the condensation of propionaldehyde and 3-thiophenecarbaldehyde. Difficulties faced in the synthesis of porphyrin rings using aliphatic aldehydes and aromatic aldehydes are that aliphatic aldehydes are generally volatile and their reactivity with a pyrrole ring remarkably differs from that of aromatic aldehydes. That is,

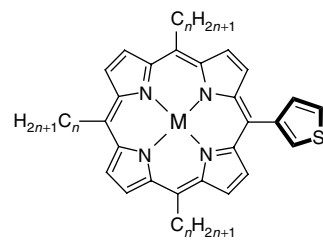


Figure 6 5-(3-Thienyl)-10,15,20-trialkylporphyrin complex [M(tep)]

under conditions for the usual porphyrin ring formation at elevated temperatures, control of an aldehyde ratio is highly difficult because of the volatility of one of the aldehydes. Therefore, it becomes very easy to generate the side products and acyclic oligomers into which two or more thiophene rings are introduced. To solve such a problem, the solution of pyrrole in propionic acid has been preheated to temperatures suitable for the ring-closing reaction, and the mixture of aldehydes with a predetermined ratio has been slowly added to the solution to increase the yield of the desired product, which has been obtained as purple needle crystals. The cobalt complex $[\text{Co}(\text{ttep})]$ has been prepared by dissolving the ligand in dimethylformamide and refluxing in the presence of an excess amount of cobalt acetate. The obtained complex is polymerizable due to the presence of thiényl groups at the meso position and is sufficiently stable due to the ability of alkyl groups to prevent decomposition of the porphyrin ring.

Oxidative polymerization of $\text{H}_2(\text{ttep})$ using FeCl_3 as an oxidant produces the corresponding polymer in a high yield. Because of the steric effect of the bulky porphyrin ring bound to the β -position of the thiophene ring, a high regularity with an HT-HT content of more than 95% has been accomplished by the polymerization at room temperature. In addition, a relatively high conductivity has been confirmed after doping ($\sigma_{\text{RT}} \approx 4 \times 10^{-1} \text{ S cm}^{-1}$). Since the obtained polymer has the HOMO level higher than the unsubstituted polythiophene because of the localization of HOMO on the porphyrin ring, a higher doping level has been accomplished. The structural regularity of the polymer originates from the controlled bond formation between the thiophene rings, which is regulated by the porphyrin ring. The porphyrin rings are arranged cofacially, giving rise to the structure suitable for the accommodation of O_2 to produce the bridged peroxy bond.

Electropolymerization of $[\text{Co}(\text{ttep})]$ has been carried out, and the polymeric thin film has been prepared on the surface of a carbon electrode. Cyclic voltammetry recorded under acidic electrolyte conditions saturated with O_2 has revealed a reduction wave for the catalytic reduction of O_2 at a peak potential of $E_p = 0.38 \text{ V}$. A convenient method to prepare the electropolymerized film of $[\text{Co}(\text{ttep})]_n$ on a carbon particle has been examined, using the electrolysis in the presence of the carbon particles as the working electrode that is dispersed in the electrolyte solution. The catalyst obtained by such a method is denoted as $[\text{Co}(\text{ttep})]_n/\text{CB}$ (Figure 7).

To support the polymer complex $[\text{Co}(\text{ttep})]_n$ on a carbon particle by electrolytic polymerization, a carbon particle with a large surface area (carbon black with a BET surface area of ca $800 \text{ m}^2 \text{ g}^{-1}$) has been employed. The obtained $[\text{Co}(\text{ttep})]_n/\text{CB}$ catalyst has been dispersed in an alcohol solution of Nafion. The modified electrode has been prepared by casting the suspension on the edge-plane pyrolytic graphite electrode. The catalyst activity for O_2 reduction has been investigated using the modified electrode. Cyclic voltammetry under acidic conditions have revealed a reduction peak at $E_p = 0.48 \text{ V}$ vs SCE due to the

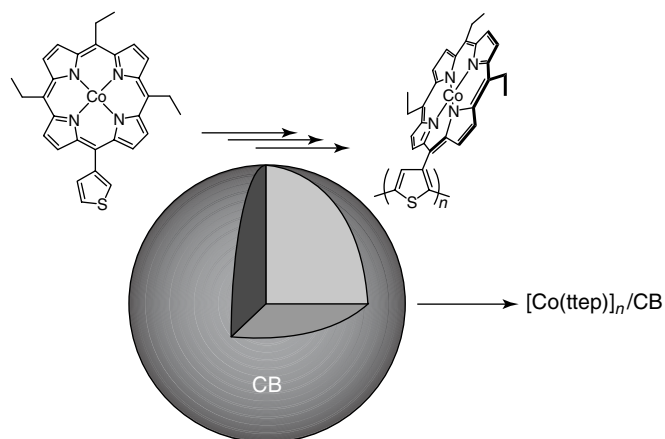


Figure 7 Preparation of a $[\text{Co}(\text{ttep})]_n/\text{CB}$ catalyst using a fluid-bed electrolytic polymerization method

electroreduction of O_2 . This value is remarkably more positive than that obtained for the $[\text{Co}(\text{ttep})]_n$ catalyst produced on the surface of the glassy carbon electrode, and higher activity has been accomplished by using the carbon particles as the support of the catalyst. Diffusion-limited current obtained with a rotating disk electrode (i_L) has been analyzed by using the Koutecky–Levich plots (i_L^{-1} vs $\omega^{-1/2}$). The high selectivity for the four-electron reaction ($n_{\text{app}} = 3.8$) has been accomplished, revealing that the catalytically active center and the electron transfer path are provided by the π -conjugated polymeric structure with the high regioregularity. Furthermore, when the catalyst is heat-treated under an inert atmosphere, the catalytic activity improves to $E_p = 0.51 \text{ V}$. In this case, the rotating disk electrode reduces O_2 at $E_{1/2}(\text{O}_2) = 0.57 \text{ V}$ vs SCE ($= 0.81 \text{ V}$ vs NHE). These results suggest that O_2 reduction proceeds at potentials more positive than that for the two-electron reduction. Further improvement in the catalytic activity is anticipated by optimizing conditions to produce a homogeneous thin film of $[\text{Co}(\text{ttep})]_n$ on a carbon nanoparticle, thereby reducing the resistance overpotential for the reduction of O_2 .

The performance of a complex catalyst is evaluated by preparing an MEA to obtain the $I - V$ curve, but using half-wave potentials of the O_2 reduction obtained at a rotating disk electrode ($E_{1/2}(\text{O}_2)$) is also a simple method for convenient comparison of the catalytic activity. The theoretical emf of the fuel cell is determined by the potential at which O_2 receives electrons. Employing $E_{1/2}(\text{O}_2)$ at low electrode rotation rates (i.e., at low currents), the potentials for the reduction of O_2 catalyzed by various metal complexes have been compared at small resistance overpotentials. It has been revealed that many metal complexes catalyze the O_2 reduction at potentials more negative than the two-electron reduction potential. The heat-treated $[\text{Co}(\text{ttep})]_n/\text{CB}$ catalyst has been characterized by the capability of reducing O_2 at potentials where the four-electron reaction selectively takes place. A test cell has been fabricated with the MEA using the $[\text{Co}(\text{ttep})]_n/\text{CB}$ catalyst. The $I - V$

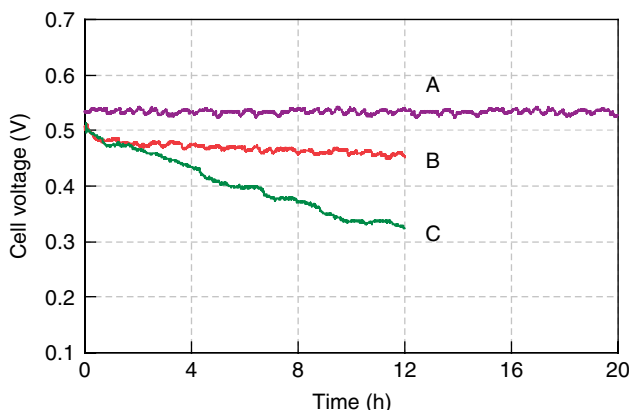


Figure 8 I – V curves obtained for the fuel cells fabricated using the MEA with the $[\text{Co}(\text{ttep})]_n/\text{CB}$ catalyst after (curve A) and before (curve B) the heat treatment. Curve C represents the performance of the cell when cobalt *meso*-tetra(3-thienyl)porphyrin was employed in place of $[\text{Co}(\text{ttep})]$ to prepare the catalyst according to Figure 7. Current density = 0.1 A cm^{-2}

curve at a current density of 0.1 A cm^{-2} revealed the cell voltage of 0.54 V and demonstrated that the catalytic activity persisted without significant degradation for more than 20 h , which supported the high activity and the robustness of the $[\text{Co}(\text{ttep})]_n/\text{CB}$ catalyst (Figure 8).

4 PORPHYRIN ASSEMBLIES BASED ON INTERMOLECULAR INTERACTION

The diporphyrins described in Section 3.1 require the synthetic process with multiple steps. Cofacial porphyrin assemblies suitable for accommodation of O_2 have also been reported. The porphyrin complexes bearing four ionic substituents introduced at the *meso* positions have been found to form ion pairs with the similar complexes bearing opposite charges (Figure 9).^{66–69} The ionic pair that has a composition of $1 : 1$ is prepared by such a simple method, which has been confirmed by using the job plots obtained from the absorption spectra of the solution containing the two complexes with different compositions. Interestingly, the dimeric structure is supposed to be maintained even after adsorption to the surface of an electrode.

Dimeric porphyrins bearing a direct metal–metal bond (Figure 10) have also been reported as the conveniently obtained cofacial dimer.^{70,71} Mononuclear iridium porphyrins adsorbed on the surface of an electrode have been found to form rearranged cofacial dimers upon oxidation ($2[\text{HIrP}] \rightleftharpoons [\text{PIr–IrP}] + 2\text{H}^+ + 2\text{e}^-$; $E^\text{f} = \text{ca } 0.37 \text{ V vs NHE}$). Interestingly, only the dimer has been found to work as a four-electron reduction catalyst of O_2 . Therefore, as the overpotential for the reduction of O_2 becomes sufficiently large

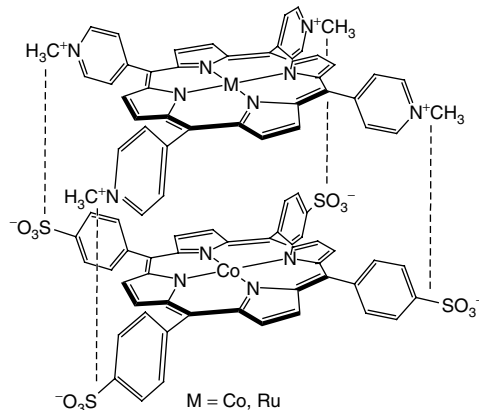


Figure 9 Ion-pair-type diporphyrin metal complexes

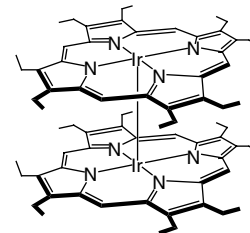


Figure 10 Iridium diporphyrin bearing an Ir–Ir bond

and reaches the reduction potential to form the mononuclear complex (0.37 V), the catalytic reduction current of O_2 is halved rapidly. The structure of the catalytically active site changes with the electrode potential reversibly, and one can use the same electrode surface both for the four-electron reduction of O_2 and the two-electron reduction of O_2 , based on the electrode potential.

Similar structures in which porphyrin complexes are regularly arranged and adsorbed on an electrode with a specific intermolecular distance have been found for cobalt mononuclear porphyrins (Figure 11) adsorbed on the surface of an edge-plane pyrolytic graphite electrode.^{72–74} *meso*-Substituted cobalt porphyrins adsorbed on carbon black have been prepared as the catalysts for the electroreduction of O_2 . The catalyst, which has been prepared by using a homogenizer in mixing cobalt tetraethylporphyrin and carbon black, gives

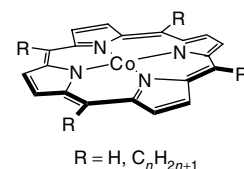


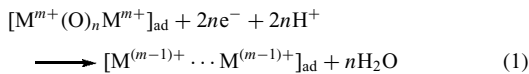
Figure 11 *meso*-Tetraalkylporphyrin cobalt complexes used as the electrocatalyst for oxygen reduction by adsorption onto carbon black

rise to the electroreduction of O_2 at a remarkably positive potential ($E_p = 0.45$ V vs SCE) and shows a high selectivity for the four-electron reduction ($n = 3.8$). Electrochemical study and EXAFS analysis have revealed that the adsorbed face-to-face dimeric aggregates of cobalt porphyrin molecules are highly efficient catalysts for the electroreduction of O_2 .

The degree of the steric repulsion between the almost planar porphyrin molecules is determined by the alkyl substituents bound to the meso position. To maintain the distance between the central cobalt atoms suitable for the accommodation of O_2 , it has been established that the structure of the alkyl chains is an important factor.^{75–79}

A cofacial arrangement of the porphyrin rings has been accomplished in many organized molecular assemblies and supramolecular systems.^{80–82} The reverse micelles of cobalt porphyrins bearing long alkylamidophenyl substituents at the meso positions in alcohols by spontaneous self-organization are the typical examples that have been applied to the catalyst for the electroreduction of O_2 (Figure 12).⁸³ It has been reported that cobalt(II) *meso*-tetrakis(4-hexadecylamidophenyl)porphyrin (CoTAPP) self-assembles in ethanol/1-propanol 2/1 (v/v) to form a rodlike micelle with nanoscale dimensions. Static light scattering (SLS) and spectroscopic experiments reveal that the nanorod is a face-to-face aggregate having a hydrophobic corona around a polar core and is thus characterized as a reverse micelle. The aggregate reduces O_2 with four electrons ($n_{app} = 3.7$), while a two-electron reduction is predominant for the monomeric complex ($n_{app} = 2.0$). The cobalt–cobalt distance in the CoTAPP aggregate is in the range of those for the covalently bound cofacial porphyrin (Figure 1).

μ -(Di)oxo porphyrin complexes adsorbed on the glassy carbon electrodes containing manganese^{84,85} and iron^{86–91} as the central metal atoms and similar complexes containing vanadium^{92–103} produce the O_2 accommodation site by the electrolytic reduction under strongly acidic conditions according to



where $n = 1$ or 2. The resulting $[M^{(m-1)+} \dots M^{(m-1)+}]_{ad}$ is capable of forming the μ -peroxy-bridged complex.^{104,105}

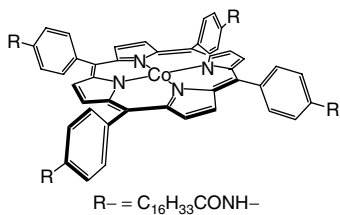


Figure 12 Cobaltporphyrin that forms nanorod-type reversed micelles in alcohols

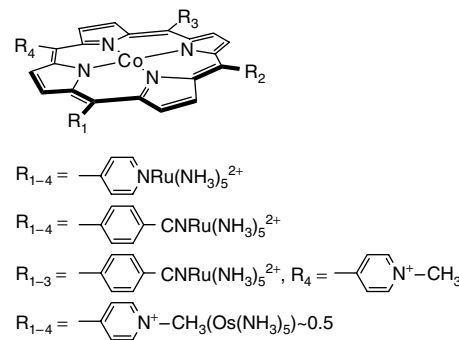


Figure 13 Porphyrin cobalt complexes tetrametalated at the periphery

Four-electron reduction of O_2 occurs highly selectively at the electrode surface, because the electrode acts as the electron reservoir of electrons.

5 MULTINUCLEAR COMPLEXES AS ELECTRON RESERVOIRS

If electrons are delivered toward a central metal core from many sites of the complex periphery, it is considered that many electrons can be taken out from the central metal core at once so that the multiple electrons available for the reduction of O_2 . Such a concept of multiple electron transfer process has been examined by the unique four-electron reduction system of O_2 . When the ammine complex of ruthenium or osmium is coordinated to the pyridyl groups at the meso position of a cobalt porphyrin, these peripheral complexes serve as the electron reservoir to donate electrons into the central core, resulting in the increase in the selectivity for the four-electron reduction of O_2 (Figure 13).^{106–109} The supply of the electron to the catalytically active site is based on the back electron transfer from the ruthenium or osmium centers to the ligand at the meso position of the porphyrin ring.¹¹⁰ The effect of two or less ammine complexes per central cobalt is insufficient, and three or more peripheral complexes are necessary for the four-electron transfer. Four-electron transfer within the short time in which O_2 molecule is coordinated is considered to be the requirement of the selective four-electron reduction, which is accomplished by the presence of the multiple peripheral complexes.

6 CONCLUSIONS

The direct four-electron reduction of O_2 to H_2O is an important issue in developing efficient cathode catalysts for fuel cells. Metalloporphyrins and related metal complexes

have been demonstrated to serve as catalysts for the four-electron reduction of O₂, especially in the forms of cofacial and multinuclear metalloporphyrins. Simple cobaltporphyrins with spontaneous face-to-face aggregation properties are also expected as efficient catalysts. For practical application as fuel cell cathode catalysts, it is necessary to use metal complexes dispersed on the surface of carbon particles with the high surface area. The recent developments of metal-complex-based catalysts and attempts to prepare face-to-face aggregates adsorbed or electrochemically polymerized dispersively on carbon black reveal the prospects of the metal complex catalysts for practical application. The metal complex catalysts give rise to the electroreduction of O₂ at remarkably positive potentials and with a high selectivity for the direct four-electron reduction process.

7 RELATED ARTICLES

Direct Ethanol Fuel Cells; Enzymes and Microbes for Energy Production by Fuel Cells; Intermediate-Temperature Solid Oxide Fuel Cells; Molecular Catalysts for Oxygen Production from Water; Proton Exchange Membranes for Fuel Cells.

8 ABBREVIATIONS AND ACRONYMS

CcO = Cytochrome *c* oxidase; emf = electromotive force; EXAFS = Extended X-ray absorption fine structure; MEA = membrane electrode assembly; PPy = polypyrrole; SLS = Static light scattering; XRD = X-ray diffraction; XRD = X-ray diffraction.

9 REFERENCES

- K. Kinoshita, ‘Electrochemical Oxygen Technology’, John Wiley & Sons, New York, 1992.
- J. P. Collman, R. Boulatov, C. J. Sunderland, and L. Fu, *Chem. Rev.*, 2004, **104**, 561.
- J. P. Collman, P. Denisevich, Y. Konai, M. Marrocco, C. Koval, and F. C. Anson, *J. Am. Chem. Soc.*, 1980, **102**, 6027.
- G. Gupta, D.A. Slanac, P. Kumar, J.D. Wiggins-Camacho, X. Wang, S. Swinnea, K. L. More, S. Dai, K. J. Stevenson, and K. P. Johnston, *Chem. Mater.*, 2009, **21**, 4515.
- J. Yang, J. Y. Lee, Q. Zhang, W. Zhou, and Z. Liu, *J. Electrochem. Soc.*, 2008, **155**, B776.
- C. Bianchini and P. K. Shen, *Chem. Rev.*, 2009, **109**, 4183.
- W. Chen and S. Chen, *Angew. Chem. Int. Ed.*, 2009, **48**, 4386.
- C. Xu, Y. Zhang, L. Wang, L. Xu, X. Bian, H. Ma, and Y. Ding, *Chem. Mater.*, 2009, **21**, 3110.
- Y.-C. Yeh, H. M. Chen, R.-S. Liu, K. Asakura, M.-Y. Lo, Y.-M. Peng, T.-S. Chan, and J.-F. Lee, *Chem. Mater.*, 2009, **21**, 4030.
- S. Barazzouk, M. Lefèvre, and J.-P. Dodelet, *J. Electrochem. Soc.*, 2009, **156**, B1466.
- J.-W. Lee and B. N. Popov, *J. Solid State Electrochem.*, 2007, **11**, 1355.
- C. Shi and F. C. Anson, *J. Am. Chem. Soc.*, 1991, **113**, 9564.
- E. Tsuchida and K. Oyaizu, *Coord. Chem. Rev.*, 2003, **237**, 213.
- R. R. Durand Jr and F. C. Anson, *J. Electroanal. Chem.*, 1982, **134**, 273.
- R. R. Durand Jr, C. S. Bencosme, J. P. Collman, and F. C. Anson, *J. Am. Chem. Soc.*, 1983, **105**, 2710.
- C. K. Chang, H. Y. Liu, and I. Abdalmuhdi, *J. Am. Chem. Soc.*, 1984, **106**, 2725.
- C.-L. Ni, I. Abdalmuhdi, C. K. Chang, and F. C. Anson, *J. Phys. Chem.*, 1987, **91**, 1158.
- C. J. Chang, Y. Deng, A. F. Heyduk, C. K. Chang, and D. G. Nocera, *Inorg. Chem.*, 2000, **39**, 959.
- C. J. Chang, Y. Deng, S.-M. Peng, G.-H. Lee, C.-Y. Yeh, and D. G. Nocera, *Inorg. Chem.*, 2002, **41**, 3008.
- L. L. Chng, C. J. Chang, and D. G. Nocera, *J. Org. Chem.*, 2003, **68**, 4075.
- C. J. Chang, Y. Deng, C. Shi, C. K. Chang, F. C. Anson, D. G. Nocera, *Chem. Commun.*, 2000, 1355.
- S. Fukuzumi, K. Okamoto, C. P. Gros, and R. Guillard, *J. Am. Chem. Soc.*, 2004, **126**, 10441.
- Z.-H. Loh, S. E. Miller, C. J. Chang, S. D. Carpenter, and D. G. Nocera, *J. Phys. Chem. A*, 2002, **106**, 11700.
- C. J. Chang, E. A. Baker, B. J. Pistorio, Y. Deng, Z.-H. Loh, S. E. Miller, S. D. Carpenter, and D. G. Nocera, *Inorg. Chem.*, 2002, **41**, 3102.
- J. M. Hodgkiss, C. J. Chang, B. J. Pistorio, and D. G. Nocera, *Inorg. Chem.*, 2003, **42**, 8270.
- B. J. Pistorio, C. J. Chang, and D. G. Nocera, *J. Am. Chem. Soc.*, 2002, **124**, 7884.
- R. Boulatov, J.P. Collman, I. M. Shiryaeva, and C. J. Sunderland, *J. Am. Chem. Soc.*, 2002, **124**, 11923.
- S. Gupta, D. Tryk, I. Bae, W. Aldred, and E. Yeager, *J. Appl. Electrochem.*, 1989, **19**, 19.
- R. Kobayashi and J. Ozaki, *Chem. Lett.*, 2009, **38**, 396.
- H. Wang, R. Côté, G. Faubert, D. Guay, and J.-P. Dodelet, *J. Phys. Chem. B*, 1999, **103**, 2042.
- M. Lefèvre, J.-P. Dodelet, and P. Bertrand, *J. Phys. Chem. B*, 2002, **106**, 8705.
- M. Lefèvre and J.-P. Dodelet, *Electrochim. Acta*, 2003, **48**, 2749.

33. M. Lefèvre, E. Proietti, F. Jaouen, and J.-P. Dodelet, *Science*, 2009, **324**, 71.
34. M. Lefèvre and J.-P. Dodelet, *Electrochim. Acta*, 2008, **53**, 8269.
35. F. Charreteur, S. Ruggeri, F. Jaouen, and J.-P. Dodelet, *Electrochim. Acta*, 2008, **53**, 6881.
36. E. Proietti, S. Ruggeri, and J.-P. Dodelet, *J. Electrochem. Soc.*, 2008, **155**, B340.
37. F. Charreteur, F. Jaouen, S. Ruggeri, and J.-P. Dodelet, *Electrochim. Acta*, 2008, **53**, 2925.
38. F. Jaouen, M. Lefèvre, J.-P. Dodelet, and M. Cai, *J. Phys. Chem. B*, 2006, **110**, 5553.
39. F. Jaouen and J.-P. Dodelet, *Electrochim. Acta*, 2007, **52**, 5975.
40. S. Ruggeri and J.-P. Dodelet, *J. Electrochem. Soc.*, 2007, **154**, B761.
41. J. Herranz, M. Lefèvre, N. Larouche, B. Stansfield, and J.-P. Dodelet, *J. Phys. Chem. C*, 2007, **111**, 19033.
42. F. Jaouen, A. M. Serventi, M. Lefèvre, J.-P. Dodelet, and P. Bertrand, *J. Phys. Chem. C*, 2007, **111**, 5971.
43. F. Jaouen, S. Marcotte, J.-P. Dodelet, and G. Lindbergh, *J. Phys. Chem. B*, 2003, **107**, 1376.
44. N. P. Subramanian, X. Li, V. Nallathambi, S. P. Kumaraguru, H. Colon-Mercado, G. Wu, J.-W. Lee, and B. N. Popov, *J. Power Sources*, 2009, **188**, 38.
45. V. Nallathambi, J.-W. Lee, S. P. Kumaraguru, G. Wu, and B. N. Popov, *J. Power Sources*, 2008, **183**, 34.
46. Y. Shao, J. Sui, G. Yin, and Y. Gao, *Appl. Catal. B*, 2008, **79**, 89.
47. J. Jiang and A. Kucernak, *Electrochim. Acta*, 2002, **47**, 1967.
48. M. Bron, J. Radnik, M. Fieber-Erdmann, P. Bogdanoff, and S. Fiechter, *J. Electroanal. Chem.*, 2002, **535**, 113.
49. M. Bron, S. Fiechter, M. Hilgendorff, and P. Bogdanoff, *J. Appl. Electrochem.*, 2002, **32**, 211.
50. A. L. Bouwkamp-Wijnoltz, W. Visscher, J. A. R. van Veen, and S. C. Tang, *Electrochim. Acta*, 1999, **45**, 379.
51. C. W. B. Bezerra, L. Zhang, K. Lee, H. Liu, A. L. B. Marques, E. P. Marques, H. Wang, and J. Zhang, *Electrochim. Acta*, 2008, **53**, 4937.
52. M. Yuasa, A. Yamaguchi, H. Itsuki, K. Tanaka, M. Yamamoto, and K. Oyaizu, *Chem. Mater.*, 2005, **17**, 4278.
53. W. Seeliger and A. Hamnett, *Electrochim. Acta*, 1992, **37**, 763.
54. K. Lee, L. Zhang, H. Lui, R. Hui, Z. Shi, and J. Zhang, *Electrochim. Acta*, 2009, **54**, 4704.
55. H. Y. Qin, Z. X. Liu, W. X. Yin, J. K. Zhu, and Z. P. Li, *J. Power Sources*, 2008, **185**, 909.
56. H. Y. Qin, Z. X. Liu, L. Q. Ye, J. K. Zhu, and Z. P. Li, *J. Power Sources*, 2009, **192**, 385.
57. H. Liu, Z. Shi, J. Zhang, L. Zhang, and J. Zhang, *J. Mater. Chem.*, 2009, **19**, 468.
58. A. J. Bard, J. Jordan, and R. Parsons, ‘Standard Potentials in Aqueous Solutions’, Marcel Dekker, New York, 1985.
59. M. Yuasa, K. Oyaizu, H. Murata, K. Tanaka, and M. Yamamoto, *Kobunshi Ronbunshu*, 2006, **63**, 601.
60. M. Yuasa, K. Oyaizu, H. Murata, K. Tanaka, M. Yamamoto, and S. Sasaki, *Electrochemistry*, 2007, **75**, 800.
61. R. Bashyam and P. Zelenay, *Nature*, 2006, **443**, 63.
62. K. Oyaizu, A. Yamaguchi, Y. Iai, K. Tanaka, and M. Yuasa, *Kobunshi Ronbunshu*, 2006, **63**, 189.
63. H. Murata, Y. Iai, T. Otake, K. Oyaizu, K. Kozawa, and M. Yuasa, *Electrochemistry*, 2007, **75**, 964.
64. K. Oyaizu, M. Hoshino, M. Ishikawa, T. Imai, and M. Yuasa, *J. Polym. Sci. A*, 2006, **44**, 5403.
65. M. Yuasa, K. Oyaizu, A. Yamaguchi, T. Imai, and M. Kitao, *Kobunshi Ronbunshu*, 2006, **63**, 182.
66. M. Yuasa, K. Imura, and I. Sekine, *Mater. Technol.*, 2000, **18**, 171.
67. K. Yamamoto, S. Nakazawa, A. Matsufuji, and T. Taguchi, *J. Chem. Soc., Dalton Trans.*, 2001, 251.
68. T. Imaoka, S. Nakazawa, and K. Yamamoto, *Chem. Lett.*, 2001, **30**, 412.
69. T. Imaoka and K. Yamamoto, *Phys. Chem. Chem. Phys.*, 2001, **3**, 4462.
70. J. P. Collman and K. Kim, *J. Am. Chem. Soc.*, 1986, **108**, 7847.
71. J. P. Collman, L. L. Chng, and D. A. Tyvoll, *Inorg. Chem.*, 1995, **34**, 1311.
72. C. Shi, B. Steiger, M. Yuasa, and F. C. Anson, *Inorg. Chem.*, 1997, **36**, 4294.
73. M. Yuasa, R. Nishihara, C. Shi, and F. C. Anson, *Polym. Adv. Technol.*, 2001, **12**, 266.
74. M. Yuasa, K. Oyaizu, M. Kitao, and K. Fujita, *Kobunshi Ronbunshu*, 2006, **63**, 607.
75. K. Oyaizu, Y. Fujito, T. Sato, M. Kitao, A. Yamaguchi, and M. Yuasa, *Polym. Prepr. Jpn.*, 2004, **53**, 2260.
76. M. Kitao, A. Yamaguchi, K. Oyaizu, and M. Yuasa, *Polym. Prepr. Jpn.*, 2004, **53**, 4063.
77. M. Yuasa, K. Oyaizu, H. Itsuki, K. Ikkanda, K. Tanaka, and A. Yamaguchi, *Polym. Prepr. Jpn.*, 2004, **53**, 2261.
78. M. Yuasa, K. Oyaizu, and A. Yamaguchi, *Polym. Prepr. Jpn.*, 2004, **53**, 4760.
79. H. J. Zhang, X. Yuan, W. Wen, D.-Y. Zhang, L. Sun, Q.-Z. Jiang, and Z.-F. Ma, *Electrochim. Commun.*, 2009, **11**, 206.
80. H. Uno, A. Masumoto, and N. Ono, *J. Am. Chem. Soc.*, 2003, **125**, 12082.
81. M. Shirakawa, S. Kawano, N. Fujita, K. Sada, and S. Shinkai, *J. Org. Chem.*, 2003, **68**, 5037.
82. K. Kano, K. Fukuda, H. Wakami, R. Nishiyabu, and R. F. Pasternack, *J. Am. Chem. Soc.*, 2000, **122**, 7494.

83. M. Yuasa, K. Oyaizu, A. Yamaguchi, and M. Kuwakado, *J. Am. Chem. Soc.*, 2004, **126**, 11128.
84. K. Oyaizu, A. Haryono, H. Yonemaru, and E. Tsuchida, *J. Chem. Soc., Faraday Trans.*, 1998, **94**, 3393.
85. K. Oyaizu, T. Nakagawa, and E. Tsuchida, *Inorg. Chim. Acta*, 2000, **305**, 184.
86. K. Oyaizu, A. Haryono, J. Natori, H. Shinoda, and E. Tsuchida, *Bull. Chem. Soc. Jpn.*, 2000, **73**, 1153.
87. K. Oyaizu, A. Haryono, J. Natori, and E. Tsuchida, *J. Chem. Soc., Faraday Trans.*, 1998, **94**, 3737.
88. A. Haryono, K. Oyaizu, K. Yamamoto, J. Natori, and E. Tsuchida, *Chem. Lett.*, 1998, **27**, 233.
89. K. Oyaizu, A. Haryono, Y. Nishimura, K. Yamamoto, and E. Tsuchida, *Bull. Chem. Soc. Jpn.*, 1999, **72**, 1781.
90. K. Oyaizu, E. L. Dewi, and E. Tsuchida, *Inorg. Chim. Acta*, 2001, **321**, 205.
91. K. Oyaizu and E. Tsuchida, *Inorg. Chim. Acta*, 2003, **355**, 414.
92. K. Oyaizu and E. Tsuchida, *J. Am. Chem. Soc.*, 1998, **120**, 237.
93. K. Oyaizu, E. L. Dewi, and E. Tsuchida, *J. Electroanal. Chem.*, 2001, **498**, 136.
94. E. L. Dewi, K. Oyaizu, and E. Tsuchida, *Inorg. Chim. Acta*, 2003, **342**, 316.
95. E. Tsuchida, K. Yamamoto, K. Oyaizu, N. Iwasaki, and F. C. Anson, *Inorg. Chem.*, 1994, **33**, 1056.
96. K. Oyaizu, K. Yamamoto, K. Yoneda, and E. Tsuchida, *Inorg. Chem.*, 1996, **35**, 6634.
97. K. Yamamoto, K. Oyaizu, and E. Tsuchida, *J. Am. Chem. Soc.*, 1996, **118**, 12665.
98. E. Tsuchida, K. Yamamoto, and K. Oyaizu, *J. Electroanal. Chem.*, 1997, **438**, 167.
99. E. Tsuchida, K. Oyaizu, E. L. Dewi, T. Imai, and F. C. Anson, *Inorg. Chem.*, 1999, **38**, 3704.
100. K. Oyaizu, E. L. Dewi, and E. Tsuchida, *Inorg. Chem.*, 2003, **42**, 1070.
101. K. Oyaizu and E. Tsuchida, *J. Am. Chem. Soc.*, 2003, **125**, 5630.
102. K. Oyaizu and E. Tsuchida, *Inorg. Chim. Acta*, 2003, **353**, 332.
103. E. L. Dewi, K. Oyaizu, H. Nishide, and E. Tsuchida, *J. Power Sources*, 2004, **130**, 286.
104. E. Tsuchida, K. Yamamoto, and K. Oyaizu, 'Multi-Electron Transfer Process of a Vanadium Dinuclear Complex for Molecular Conversions', in 'Metal Containing Polymeric Materials', eds. C. U. Pittman, C. E. Carraher, B. M. Culberston, M. Zeldin, and J. E. Sheets, Plenum Press, New York, 1996, p. 139.
105. E. Tsuchida, K. Yamamoto, and K. Oyaizu, 'Multi-Electron Transfer and Catalytic Mechanisms in Oxidative Polymerization', in 'Bioinorganic Catalysis Second Edition, Revised and Expanded', eds. J. Reedijk and E. Bouwman, Marcel Dekker, New York, 1999, p. 535.
106. C. Shi and F. C. Anson, *Inorg. Chem.*, 1992, **31**, 5078.
107. H.-Z. Yu, J. S. Baskin, B. Steiger, F. C. Anson, and A. H. Zewail, *J. Am. Chem. Soc.*, 1999, **121**, 484.
108. B. Steiger and F. C. Anson, *Inorg. Chem.*, 1994, **33**, 5767.
109. C. Shi and F. C. Anson, *Inorg. Chem.*, 1996, **35**, 7928.
110. F. C. Anson, C. Shi, and B. Steiger, *Acc. Chem. Res.*, 1997, **30**, 437.

Recent Advances in Photo-Initiated Electron-Transfer at the Interface between Anatase TiO₂ Nanocrystallites and Transition-Metal Polypyridyl Compounds

Shane Ardo and Gerald J. Meyer

Johns Hopkins University, Baltimore, MD, USA

1	Introduction	265
2	Solar Light Harvesting	267
3	Photoinduced Electron Injection	275
4	Sensitizer Regeneration	280
5	Sensitization at the Power Point	287
6	Conclusions	289
7	Acknowledgments	290
8	End Notes	290
9	Related Articles	290
10	Abbreviations and Acronyms	290
11	Further Reading	290
12	References	290

1 INTRODUCTION

Hoffert and colleagues documented recent energy needs on the terawatt ($TW = 10^{12} W$) scale.^{1,2} They described the pitfalls of a “wait-and-see” approach and recommended immediate action that has now been dubbed the Terawatt Challenge.³ As the worldwide rate of energy expenditure is related to the number of people on Earth, the population growth experienced over the last quarter-century is staggering: a 45% increase which equates to roughly two billion people and 6 TW of energy (~63% increase).⁴ This coupled with the urbanism of third-world and nonindustrialized nations and cities has led to an increase in the demand for fossil fuel.⁴ However, as mentioned by Hoffert, the continued use of fossil fuels is not a long-term solution, and the deleterious environmental consequences of their combustion have become evident. Ice-core data over the past three-quarters-of-a-million years that correlate temperature with greenhouse gas concentration are sobering.^{5,6} The current atmospheric CO₂ levels of >380 ppm⁷ exceed any values attained over this same time period.^{5,8,9} The increased average global temperature and rates of glacial melting measured over the last few decades are telling signs.¹⁰ Regardless, if one thinks that these “signs” are the results

of global climate change, it is very difficult to argue with two key points: our civilization needs to better appreciate the “cost” of energy and begin to implement sustainable renewable power-conversion technologies.

The sun is the one source that *on its own* could supply the world’s projected energy demand in a sustainable fashion.⁷ To put it in perspective, the amount of solar energy reaching the earth *in one day* could power the planet for *an entire year*.^{3,11} More realistically, covering roughly 1/800th of the land on Earth with 10% efficient solar cells would generate enough power to compensate the world’s average power usage,^{3,4} while the land area occupied by the nation’s federally numbered highways would approximately power the United States.³ Remaining is the challenge of harvesting and storing this energy in a cost-effective way.

It has been 19 years since Grätzel, O’Regan, and Anderson first introduced thin films comprised of ~20-nm anatase TiO₂ particles interconnected in a mesoporous 10-micron thick film for applications in regenerative, dye-sensitized solar cells (DSSCs).^{12,13} Global conversion efficiencies greater than 11% have now been confirmed by several certified national laboratories.^{14–19} This efficiency is encouraging as future advancements could assist in solving

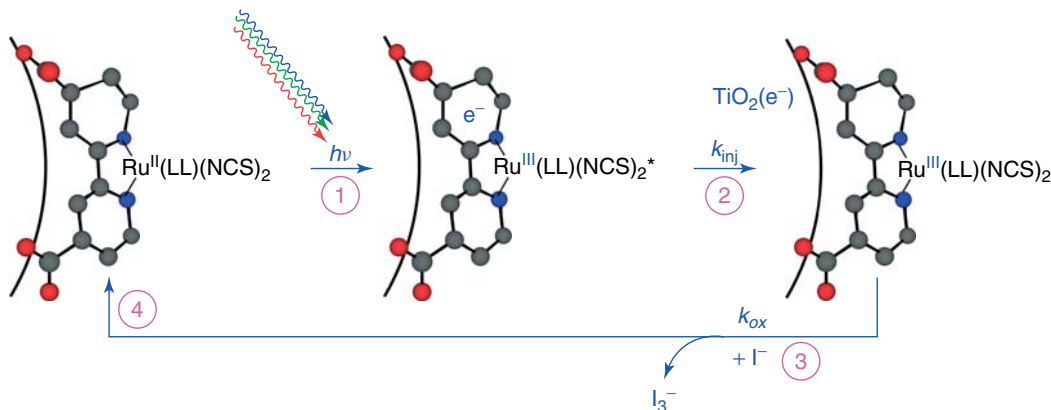
the Terawatt Challenge and allow for the replacement of traditional silicon solar cells, whose purification procedure is highly energy intensive and expensive.³ A solar cell that can be manufactured inexpensively with the use of nontoxic and abundant precursors would undoubtedly enhance the sustainability of our civilization.²⁰

Inorganic chemistry has and will continue to be important for the optimization of DSSCs and for advancement of our fundamental knowledge of photoinduced electron transfer at molecular–semiconductor interfaces. The light-harvesting and redox properties of transition-metal coordination compounds are well understood and continue to be optimized for applications in DSSCs. This is particularly true for $d\pi^6$ transition-metal polypyridyl compounds, such as Ru(II) tris-bipyridine, $\text{Ru}(\text{bpy})_3^{2+}$.^{21–23} Coordination compounds based on Cu, Ir, and Pt have recently received renewed attention as sensitizers. Transition-metal compounds and halide chemistry is also highly relevant to redox mediation in DSSCs. Alkali and alkaline earth cations are known to have large impacts on the solar conversion efficiencies, yet our understanding of this behavior is currently lacking. Also important is the synthesis of new inorganic materials with tailored architectures on the nano- and micrometer length scales. DSSCs, therefore, provide many exciting opportunities for chemists interested in these diverse areas of inorganic chemistry.

In this article, we highlight some of the recent (roughly, publication year from 2004 to present) inorganic advances, techniques, and avenues for further exploration that involve photoinduced electron transfer at anatase TiO_2 nanocrystallites which are often at the heart of current DSSC-related research. The focus is predominantly on those related to the steps comprising the metal-to-ligand charge-transfer (MLCT) “sensitization cycle” Scheme 1, for TiO_2 -based DSSCs, which is described further below. As such, this article

is not exhaustive. A comprehensive review, including historical background, can be found elsewhere;²¹ however as this article expands on certain areas highlighted in the comprehensive review, descriptions of some of the historical studies may be similar. First, a brief overview of the mechanism of DSSC operation and the current–voltage (i – V) curves that characterize the power-conversion efficiencies of solar cells has been presented.

The most practically useful “sensitizers” in DSSCs are polypyridyl compounds of Ru^{II} and, to a lesser extent, Os^{II} .^{21–23} The photophysical properties of MLCT excited states are well characterized in fluid solution,^{24–32} yet identifying their behavior at sensitized TiO_2 interfaces remains an unresolved issue. Ruthenium polypyridyl compounds, such as N3, [*cis*-Ru(dcb)₂(NCS)₂], where dcb is 4,4’-(COOH)₂-2,2’-bipyridine, are generally the optimum sensitizers for this application due to their photochemical and thermal stability and broad spectral light harvesting.^{33,34} In sunlight, such sensitizers bind to TiO_2 rapidly and quantitatively undergo three consecutive charge-transfer reactions^{20,21,35}: (i) MLCT excitation; (ii) excited-state electron injection into TiO_2 ; and (iii) reduction *via* iodide oxidation, at which time the sensitizer is “regenerated” and can repeat the “sensitization cycle” of light absorption, excited-state injection, and iodide oxidation as shown in Scheme 1. Not shown, but necessary to the function of the DSSC, is the transport of the injected electron through the mesoporous thin film to the external circuit with eventual arrival at the counter electrode, where it uses its remaining free energy to reduce tri-iodide. Hence, the solar cell is termed “regenerative” as all oxidation chemistry at the dye-sensitized photoanode is reversed at a dark counter electrode such that no net chemistry occurs. Building on the success of the DSSC and developing low-cost architectures for solar energy conversion and storage is just one of many motivations for understanding the interfacial sensitization cycle in precise molecular detail.



Scheme 1 Light absorption, excited-state injection, and iodide oxidation termed the “sensitization cycle.” In the operational DSSC, under 1 sun, AM1.5 spectral irradiance each sensitizer repeats this sensitization cycle roughly twice per second. (Reproduced from Ref. 36. © American Chemical Society, 2010.)

2 SOLAR LIGHT HARVESTING

2.1 Determination of the Light-Harvesting Efficiency

The fraction of light that is absorbed by a DSSC is wavelength dependent and is often called the *light-harvesting efficiency (LHE)* or *absorptance* (α).³⁸ When light scattering is absent, the absorptance is simply one minus the transmittance.³⁸ The absorptance of a monolayer of sensitizers anchored to a surface is related to the molar extinction coefficient of the sensitizer ($M^{-1} \text{ cm}^{-1}$), ε , and the surface area occupied by the sensitizer on a planar surface in \AA^2 , $A_{\text{sensitizer}}$, *i.e.*, the footprint:

$$\alpha(\lambda) = 1 - \frac{I(\lambda)}{I_0(\lambda)} = 1 - 10^{-\text{Absorbance}(\lambda)}, \quad \text{where} \quad (1)$$

$$\text{Absorbance}(\lambda) = 1000 \cdot \varepsilon(\lambda) \cdot \Gamma = \frac{10^{19} \cdot \varepsilon(\lambda)}{N_A \cdot A_{\text{sensitizer}}} \quad (2)$$

where I_0 is the intensity of the incoming incident light, I is the intensity of the light transmitted through the sample, Γ is the macroscopic surface coverage in moles per square centimeter, and N_A is Avogadro's number. Calculations show that even a monolayer of phthalocyanines or porphyrins, which have among the highest extinction coefficients known, packed within van der Waals distance of one another on planar surfaces, absorbs <10% of light at their maximum absorbance and far less than 1% of the 1 sun, AM1.5 spectrum.³⁹ This underscores the need for high surface-area materials to increase the LHE of a molecular monolayer of sensitizers. It is for this reason that DSSCs typically consist of anatase TiO_2 nanocrystallites ($\sim 20 \text{ nm}$ in diameter) sintered into a transparent, sponge-like network on transparent fluorine- or indium-doped SnO_2 -conductive substrates.²¹

2.2 Evaluation of Solar Cell Performance

The success of a solar cell is quantified by its light-to-electrical power-conversion efficiency, η :

$$\eta = \frac{V_{\text{oc}} \cdot i_{\text{sc}} \cdot \text{FF}}{A_{\text{cell}} \cdot P_0} \quad (3)$$

where V_{oc} is the open-circuit photovoltage, i_{sc} is the short-circuit photocurrent, FF is the fill factor, A_{cell} is the cell's projected area, and P_0 is the incident irradiance.⁴⁰ P_0 is usually fixed to 1 sun (100 mW cm^{-2}) of solar irradiance and an air mass 1.5 (AM1.5) spectral distribution, which is often taken as an average irradiance and spectral distribution of sunlight in the United States. The AM1.5 spectrum can be downloaded from the National Renewable Energy Laboratory (NREL) website.⁴¹ V_{oc} is the maximum Gibbs free energy that one can abstract from a regenerative solar cell while i_{sc} is the maximum rate at which the charge can flow through the external circuit and is ultimately limited by the photon flux.

The theoretical, detailed-balance limit for the light-to-electrical power-conversion efficiency of a solar cell with a single light absorber was elegantly derived by Shockley and Quissar in 1961.⁴² Under 1 sun of AM1.5 irradiance, this efficiency has been deemed to be $\eta = 29\text{--}33\%$.^{42\text{--}47} Similar values have been obtained *via* derivations based on molecular light absorbers and first-principles thermodynamics,^{46,47} indicating that DSSCs would possess a similar upper limit.

What cannot be stressed enough is that the i_{sc} of a solar cell is directly related to its *absorptance*, (α), not its *absorbance*.²¹ In the absence of nonlinear effects, the measured absorptance spectrum can be used to calculate the fraction of AM1.5 solar photons absorbed, which provides an upper limit to the i_{sc} of a DSSC. Likewise, the optimal incident photon-to-current efficiency (IPCE) can be calculated from the absorptance spectrum of the solar cell. When the IPCE is measured as a function of the wavelength of light, the so-called photocurrent action spectrum is obtained. The IPCE is the product of three terms: the absorptance (α), the injection quantum yield (φ_{inj}), and the quantum yield for electron collection (φ_{coll}). In fact, the integral of the IPCE (λ)-weighted solar flux is mathematically *identical* to the i_{sc} . This equality can actually be used to test the validity of the 1-sun, AM1.5-simulated light source used for the power-conversion-efficiency measurements.⁴⁸ Thus, ultimately, the i_{sc} is solely based on the sensitizer's (i) extinction coefficient, (ii) molecular footprint and surface roughness as they relate to the surface coverage, (iii) quantum yield for injection, and (iv) collection efficiency. Recent advances in each are discussed in detail in the sections that follow, as they relate to the aforementioned sensitization cycle.

The FF can be related to i_{sc} and V_{oc} through the corresponding current and voltage at the power point (PP):

$$\text{FF} = \frac{i_{\text{PP}} \cdot V_{\text{PP}}}{i_{\text{sc}} \cdot V_{\text{oc}}} \quad (4)$$

where the PP occurs at the maximum product of the cell output photovoltage and photocurrent obtained along the current–voltage curve, Figure 1(a). While an FF of unity is ideal, such a value cannot be achieved because of various loss mechanisms such as charge recombination. Under short-circuit conditions, the injected electrons in DSSCs are rapidly and quantitatively collected in the external circuit. At open circuit, current does not flow and the concentration of electrons injected into the TiO_2 nanoparticles, $\text{TiO}_2(\text{e}^-)$ s, increases to a steady-state value. At the PP, roughly 10 electrons have been estimated to reside in each TiO_2 nanocrystallite.⁴⁹

Rough estimates of the theoretical ultimate (ideal) values for V_{oc} , i_{sc} , and power-conversion efficiency can be obtained by straightforward analysis of the AM1.5 solar irradiance spectrum (Figure 1b) and the absorptance spectrum of the surface-anchored sensitizers. As described previously,²¹ the long-wavelength absorption edge (the “effective bandgap”) sets a (thermodynamic) limit to the V_{oc} while integration of the 1-sun solar photon flux to this

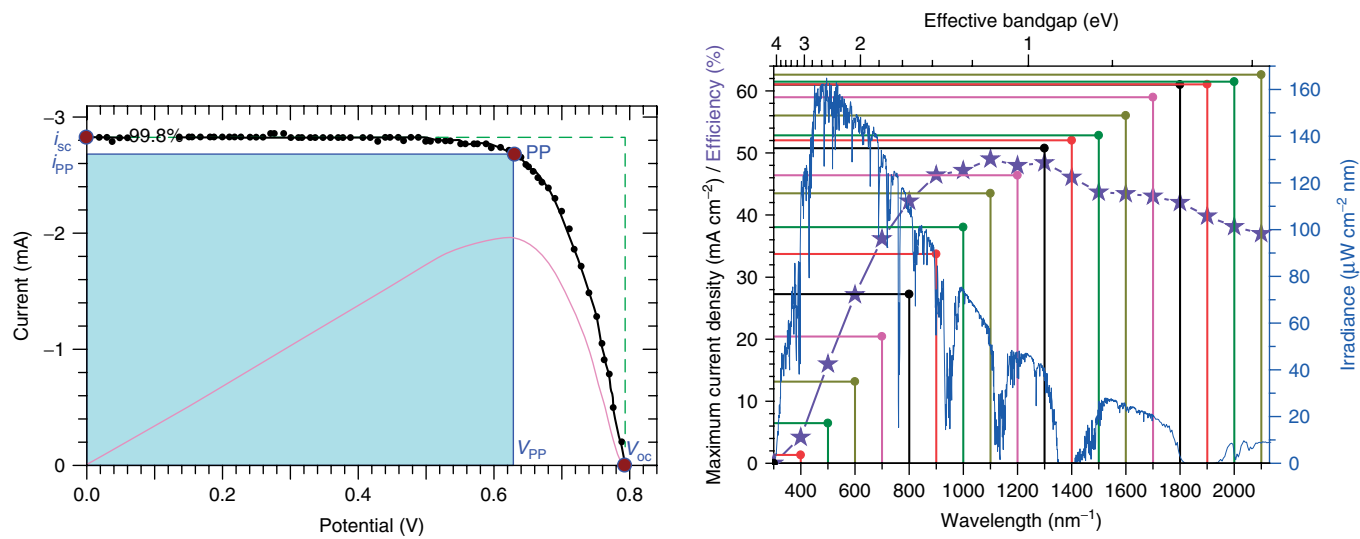


Figure 1 (a) Typical current–voltage curve for a champion DSSC under approximately 1 sun, AM1.5 illumination. Labeled are the short-circuit photocurrent (i_{sc}), open-circuit photovoltage (V_{oc}), and power point (PP) along with its corresponding photovoltage (V_{pp}) and photocurrent (i_{pp}). The fill factor (FF) is the area of the shaded region, which is bounded by the V_{pp} and i_{pp} , divided by the area of the region outlined by the dashed line, which is bounded by the V_{oc} and i_{sc} . The curve in magenta represents the power as a function of voltage in arbitrary units further illustrating that the PP coincides with the condition of maximum power output. (Reproduced from Ref. 52. © Elsevier, 2003.) (b) Circular points represent the maximum current density that can be obtained from a complete light absorber whose “effective bandgap” corresponds to the wavelength or energy indicated on the abscissa axes. Also shown, as stars, are the maximum possible efficiencies obtainable from the said light absorber assuming the unrealistic case where there are neither current nor voltage losses. The spectral irradiance for 1 sun of AM1.5 sunlight is shown in blue and corresponds to the right axis

“effective bandgap,” and conversion to current density, sets a limit to the i_{sc} . Thus, assuming a fill factor of unity, the largest possible efficiency (Figure 1b, purple stars) can be estimated from the absorptance spectrum. For champion DSSCs based on the so-called “black dye” (N749) sensitizer, maximum V_{oc} and i_{sc} values of 0.74 V and 21 mA cm⁻² have been achieved.^{17,50,51} Based on these assumptions, with an absorption edge of 900 nm, this yields theoretical maximum values for V_{oc} and i_{sc} of 1.38 V and 33.7 mA cm⁻² (red), and $\eta = 46.5\%$. This approximate value not only greatly exceeds the actual value obtained, $\eta \approx 11\%$,^{17,51} but is also clearly impossible as it exceeds the Shockley–Qiessar limit described above. The crude analysis fails to account for entropic and resistive voltage and recombination losses at the PP of operational DSSCs, which have thus far proven impossible to prevent.

Theoretical efficiencies estimated in this manner far exceed those obtained in practice. The optimal i_{sc} is within experimental error practically realized in champion DSSCs.³³ However, for V_{oc} , this is not the case and the spectroscopically estimated maximum V_{oc} values are at least a full volt larger than those that have been observed experimentally.²¹ Also, while a fill factor of unity is ideal, in reality such a value cannot be achieved because of various loss mechanisms and overpotential requirements.⁴⁸ Notwithstanding, most of the recent advances in DSSCs are from increases in i_{sc} because of enhancements in extinction coefficient, spectral bandwidth, and charge-separated lifetime; optimizing V_{oc} and FF values

has proven to be a much more difficult undertaking. For these reasons, inorganic advances related to the ultimate enhancement of i_{sc} are predominantly covered throughout this article.

2.3 Tuning Orbitals for Increased Light Harvesting

The MLCT excited states of dπ⁶ coordination compounds have emerged as the most efficient states for solar harvesting and sensitization of wide-bandgap semiconductor materials. As the name implies, light absorption promotes an electron from the metal d orbitals to the ligand π* orbitals, d(π) → π*; where the d(π) nature of the highest occupied molecular orbital (HOMO) is due to mixing of the t_{2g} states of the metal with the π orbitals of the ligands.^{53–55} A number of electric-dipole-allowed charge-transfer transitions are observed, which give rise to intense absorption bands in the visible region with moderate extinction coefficients. There is no formal spin for each excited state due to heavy-atom spin–orbit coupling from the transition-metal center (especially for 4d and 5d metals).^{24,28,56,57} Crosby *et al.* have proposed that the excited state is accurately described solely by the symmetry label of the molecular point group to which it belongs and not the spin and an orbital individually.⁵⁶ Furthermore, the effects of spin–orbit coupling must be introduced in order to rationalize the relative oscillator strengths and absorption spectra of M(bpy)²⁺ (M = Fe^{II}, Ru^{II}, and Os^{II}) compounds, where bpy is 2,2'-bipyridine.

The classical example of a compound with such transitions is $\text{Ru}(\text{bpy})_3^{2+}$, which is arguably the most well-studied coordination compound. The ground state is threefold symmetric and is best described by the symmetry label D_3 . Demas and colleagues have shown that intersystem crossing from the charge-localized, C_2 -symmetrical, $^1\text{MLCT}$ excited state to a manifold of relaxed states occurs with a quantum yield near unity in fluid solution.^{58–60} Although not formally triplet or singlet in nature, the predominantly triplet character of the lowest energy excited state, $1\ \text{E}'$,^{61,62} and singlet character of the initial, Franck–Condon state allow the transition between them to be labeled as intersystem crossing. It is for this reason that these states will be labeled as $^3\text{MLCT}$ and $^1\text{MLCT}$, respectively, throughout this article. Crosby, Hager, and colleagues have shown that photoluminescence arises from three closely spaced electronic states.^{63–67} Rapid thermal equilibrium between this manifold of states, $< kT$ in energy apart, happens such that photoluminescence occurs from what appears to be a single thermally equilibrated, or thexi,^{68,69} state. Yersin, *et al.* discovered evidence for two more highest energy states by temperature-dependent emission polarization experiments and labeled them per the D_3' double symmetry group, which takes into account the spin–orbit coupling.^{61,62} Recently, these transitions have generally been supported by those obtained from computational density functional theory (DFT) calculations.⁷⁰ These calculations also revealed that there was a D_3 and C_2 excited state within a few wavenumbers of one another, thus rationalizing the discrepancies found in the literature for the identity of the symmetry of the initial, Franck–Condon excited state.^{71–76} A dissociative, metal-centered state from a ligand-field (LF) transition ($\text{d} \rightarrow \text{d}$) was also identified, at roughly the same energy, where it was proposed that a four-coordinate species may result.

Recently, Chergui and coworkers have shown by polychromatic femtosecond fluorescence upconversion that intersystem crossing to the $^3\text{MLCT}$ excited state of $\text{Ru}(\text{bpy})_3^{2+*}$ occurs within $15 \pm 10\ \text{fs}$; as this corresponds to the vibrational period of a high-frequency mode, this points to a strongly nonadiabatic process.⁷⁷ Subsequent dissipation of the excess thermal energy within the thexi state manifold in $< 300\ \text{fs}$ is also rather rapid and was suggested to be because of intramolecular vibrational-energy redistribution, where the excess thermal energy in the predominant $1607\ \text{cm}^{-1}$ higher frequency mode was transferred to low-energy metal–ligand modes.⁷⁸

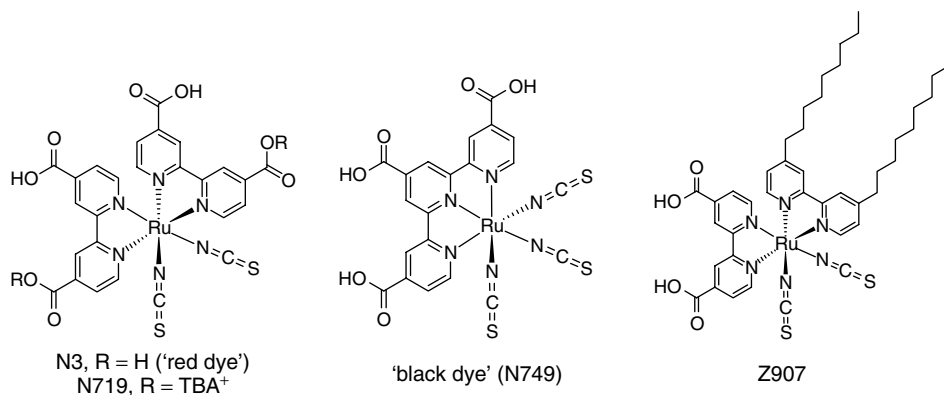
Hammarström and colleagues have shown by transient-absorption anisotropy measurements in acetonitrile that $1\ \text{ps}$ following photoexcitation, the electron has no memory of which bipyridine was initially photoselected.^{71,79} This was also found to be true in ethanol solution and with $\text{Ru}(\text{bpy})_2(\text{mcb})/\text{TiO}_2$ thin films, where mcb is 4-COOH-4'-CH₃-bpy.⁸⁰ These findings are in contrast to older models where electron hopping randomization among ligands was

proposed to explain the time evolution of the spectroscopically isotropic signal.^{81,82}

The excited-state lifetime of $[\text{Ru}^{\text{III}}(\text{bpy})_2(\text{bpy}^-)]^{2+*}$ is $\sim 1\ \mu\text{s}$ in water.⁸³ The radiative rate constant, k_r , is typically about two orders-of-magnitude smaller than the nonradiative rate constant, k_{nr} , and hence the excited-state lifetime is generally controlled by the latter.⁸³ Often Ru^{II}- and Os^{II}-polypyridyl excited states have been shown to follow Jortner's energy gap law, where k_{nr} increases exponentially with decreasing energy gap.^{84–88} For this reason, preparation of compounds that emit in the infrared region and have long-lived excited states has proven difficult. However, small k_{nr} values are not sufficient to realize long-lived excited states. A large ligand-field splitting parameter is also required in this class of excited states as the presence of low-lying, LF states can rapidly deactivate the thexi states. A classical example of this is $\text{Fe}(\text{bpy})_3^{2+}$ that until recently was thought to be completely nonemissive due to rapid and quantitative internal conversion/intersystem crossing through ligand-field states. Notwithstanding, realization of efficient sensitization by Fe^{II} polypyridyl compounds would decrease the cost of DSSCs. However, efficient power-conversion with Fe^{II} sensitizers has not been realized.

Chergui and coworkers provided clear transient femtosecond structural and absorption evidence that the mechanism of relaxation in $\text{Fe}(\text{bpy})_3^{2+*}$ is intersystem crossing from the $^1\text{MLCT}$ to $^3\text{MLCT}$ state followed by direct relaxation to the high-spin $^5\text{T}_2$ state in $\sim 150\ \text{fs}$,^{89–94} termed spin crossover or light-induced excited spin-state trapping (LIESST) when the state is long-lived. The MLCT intersystem crossing was in a strongly non-Born Oppenheimer regime mediated by high-frequency modes of the molecule. Ultimately, thermally activated relaxation to the energy-minimum initial low-spin $^1\text{A}_1$ state completed the cycle. These data were obtained by time-resolved optical-pump experiments, where the probe technique was based on extended X-ray absorption fine spectroscopy (EXAFS), X-ray absorption near-edge structure (XANES), or visible transient-absorption spectroscopy. McCusker and colleagues observed similar behavior with a hexadentate Fe^{II} coordination compound.^{95–97} Evidence for light-induced spin trapping on TiO₂ was obtained in our laboratories with surface-anchored $\text{Fe}(\text{pymbA})_3^{2+}$, where pymbA is 4-(2-pyridin-2-yl-benzimidazol-1-ylmethyl)-benzoic acid.⁹⁸ Although not proven, the rapid spin trapping observed probably accounts for the inefficient excited-state electron injection into TiO₂. An Arrhenius analysis of the high-spin to low-spin re-equilibration revealed a Gaussian distribution of activation energies.⁹⁹

An important aspect of $d\pi^6$ coordination compounds is that their colors can be controlled with synthetic chemistry. The MLCT absorption bands can be tuned in energy by altering the substituents on the bpy ligands or, simplistically, by controlling the extent of σ -donation from the nonchromophoric ligands or $d(\pi)-\pi^*$ back-bonding donation to ligands.²⁸ How these changes affect the photophysical



Scheme 2 The chemical structures of historically the most successful Ru^{II}-polypyridyl sensitizers employed in champion DSSCs

properties of the compounds has been the subject of many investigations affording further insights into the factors that govern radiative and nonradiative excited-state decay.^{24–32,100}

As many of the sensitizers employed in champion DSSCs are of the form *cis*-Ru(LL)₂X₂, where LL is a bpy-like ligand and X is an anionic nonchromophoric ligand, their spectral differences and similarities to Ru(bpy)₃²⁺ are discussed. In terms of DSSC light-to-electrical power-conversion efficiency, N3/N719, where LL = dc^{0/-} and X = SCN⁻,^{33,34} and closely related analogs, until recently, remained unsurpassed, Scheme 2.^a Although slightly solvatochromic, the visible absorption spectrum of N3, and that of its “LL = bpy” derivative, exhibit two well-resolved bands because of its symmetry. The symmetry of the ground state is C₂ whereas that for Ru(bpy)₃²⁺ is D₃. It has been postulated that the spectroscopic signatures are due in part to a shift in the electron density of the HOMO from the Ru^{II} metal center to the isothiocyanate ligands.^{101–103} Roughly, 75% of the HOMO density was calculated to reside on the isothiocyanate ligands, mainly on the sulfur atom. The gain in red absorption over Ru(dc^{0/-})₃²⁺ and subsequent increase in LHE occurs at the expense of the driving force for iodide oxidation and the excited-state lifetime, by the energy gap law. However, the performance of the DSSC is generally not affected by either of these undesirable traits because of the many orders-of-magnitude faster rates of the competing processes (i.e., interfacial charge recombination and excited-state injection, respectively).^{104,105} Also, a recent Raman study has shown that when anchored to TiO₂, the solvent reorganization energy of N3 decreased by a factor of 6.¹⁰⁶

In champion DSSCs, the presence of Li⁺ in the electrolyte is a requirement.²¹ This hard Lewis acidic cation affects all of the steps related to the sensitization cycle.^{21,107,108} In a step toward controlling this chemistry, Grätzel and coworkers recently synthesized a novel N3 analog where one dc^{0/-} ligand was replaced with 4,4'-(triethylene oxide methyl ether)₂-bpy.^{109,110} The 12-crown-4 ether groups on the bipyridine ligand provide a coordination environment for Li⁺. Interestingly, in comparative photoelectrochemical studies,

N3-like sensitizers with these crown ether ligands displayed a significant increase in *i_{sc}* with little-to-no variation in *V_{oc}*. This was unusual as the loss of Li⁺ from the TiO₂ surface was expected to destabilize the TiO₂ acceptor states, presumably resulting in less efficient excited-state injection and hence a lower photocurrent.^{21,107} Similar results have since been observed with a more hydrophobic version of the sensitizer.¹¹¹ Such amphiphilic sensitizers have also recently gained interest as possible sensitizers that are more forgiving toward trace amounts of water and are also often found to be more stable toward temperature stress and light soaking.^{112–121}

Recently, a new motif for Ru^{II} sensitizer chelation was employed using an N3-like compound, where one dc^{0/-} was replaced with two pyridines linked in their 2 positions by the nitrogen atom of an aniline.¹²² The photoelectrochemical properties were all found to be very similar to those of N719.^{122,123} Another novel motif involved replacement of the two isothiocyanate ligands with a single sulfur-donor bidentate ligand.¹²⁴ Although these first-generation sensitizers had lower efficiencies than N719, it was interesting that of these sensitizers, the ones with the most favorable photophysical characteristics did not perform as well. This was proposed to be due to the terminal cyano groups of the sulfur-donor ligands, which may have directly bound to the TiO₂ surface, thus speeding interfacial charge recombination.

2.3.1 Increasing the Extinction Coefficient

Although the excited-state lifetime of Ru^{II}-polypyridyl compounds is sufficiently long-lived for realization of near-quantitative excited-state injection and sensitization, a shortcoming of sensitization by these visible-light MLCT transitions is their relatively low extinction coefficients as compared to intraligand (IL) $\pi \rightarrow \pi^*$ transitions. Ru(bpy)₃²⁺ has a molar extinction coefficient of roughly 15 000 M⁻¹ cm⁻¹ for its MLCT electronic transitions.¹²⁵ In contrast, natural and synthetic organic and porphyrin/phthalocyanine pigments also absorb solar photons,

but with extinction coefficients that are often in excess of $200\,000\text{ M}^{-1}\text{ cm}^{-1}$ for their IL transitions.³⁹ Thus 5–10 μm thick films of nanocrystallite TiO₂, with internal surface areas up to 1000 times larger,^{126–128} are required for efficient solar harvesting with Ru^{II}-polypyridyl coordination compounds.

Fermi's so-called "Second Golden Rule" states that $k_{\text{ET}} = \frac{2\pi}{\hbar} \cdot |\langle \hat{H}_{\text{ab}} \rangle|^2 \cdot \rho_{\text{FCW}}$, where k_{ET} is the rate constant for electron transfer, H_{ab} is the electronic-coupling matrix element between the initial and final states, and ρ_{FCW} is the Franck–Condon weighted density of vibronic states.^{129–132} As electronic transitions follow this rule, both Einstein's *A* and *B* transition probability coefficients relate to the square of the transition dipole moment, under electric dipole-induced conditions. Under the approximation of a two-level system, Einstein's *A* coefficient, which is equal to k_r , is also related to the cube of the average energy gap¹³⁰; as the oscillator strength, absorption cross section, and extinction coefficient all relate to Einstein's *B* coefficient, they too are directly related to the square of the transition dipole moment and to the average energy gap.^{130,133} Taken together, increases in extinction coefficient should most often be accompanied by similar enhancements in k_r . It has long been known that addition of substituents with low-lying π orbitals (such as aromatics, esters, carboxylic acids, or unsaturated organics) to polypyridines can enhance MLCT extinction coefficients relative to unsubstituted polypyridines.^{134–147} However, as described above, it is often k_{nr} , and not k_r , that determines the excited-state lifetime of Ru^{II} polypyridyl compounds. Thus, the question begs, could enhancements in extinction coefficient be coupled to *increases* in the lifetime of the excited state if k_{nr} simultaneously decreased?

Indeed, this has been observed in MLCT compounds employing 4,4'-aryl- or 4,4'-vinyl-disubstituted bpy, 2,2':6',2''-terpyridine (tpy), and 1,10-phenanthroline (phen) ligands.^{134–136,138,139,143–151} As expected, when the transition dipole moment was extended by LUMO π^* delocalization, both the extinction coefficient, or oscillator strength if the band's width was altered, and k_r increased.^{134,139,150} When compared to sensitizers lacking this extended conjugation, k_{nr} decreased because of less electron–vibrational coupling, i.e., smaller Huang–Rhys factors, from the further delocalization of the π^* electron over the entire ligand.¹³⁴ Thus the excited-state lifetimes increased as well!

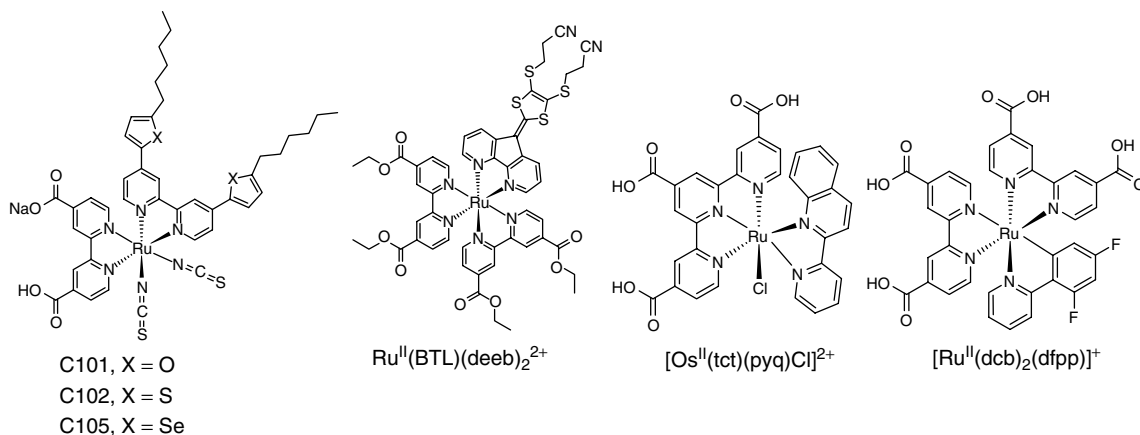
Smaller extinction-coefficient enhancements were observed with 5,5'-aryl-disubstitution,¹³⁹ even though 5,5'-disubstitution increased the conjugation relative to 4,4'-disubstitution. Albeit, 5,5'-aryl-disubstituted ligands did lead to the expected decrease in energy gap and red-shifted MLCT transition because of enhanced conjugation and a lowering of the LUMO energy.¹³⁹ These conflicting findings were rationalized using Mulliken charge-transfer theory,¹³⁹ where the degree of charge transfer is directly proportional to the overlap between the HOMO and LUMO.^{136,152–154} It was determined that the extended intraligand delocalization afforded by the increased conjugation in the 5,5'-disubstituted

ligand actually resulted in *less* electron density on the nitrogen p_z orbital chelated to Ru^{II} as compared to the less-conjugated 4,4'-disubstituted ligand.¹³⁹ Conversely, when delocalization of the ligand π^* orbital was extended in the opposite direction of the MLCT band, e.g., with 6,6'-disubstitution, the magnitude of the transition dipole moment and the extinction coefficient actually decreased.¹³⁶

For these reasons, the preparation of high extinction coefficient, and still rather long-lived, heteroleptic N3 derivatives, where one of the dcb ligands is replaced by a 4,4'-disubstituted bpy, is an extremely active area of research.^{16,115,116,140–142,155–169} This synthetic enhancement, coupled with covalent attachment of thiophene^{16,19,160–163,170–175} or tri-alkyl-/aryl-amine^{156,162,164,167} donor functional groups, has led to great enhancements in extinction coefficient and charge-separated lifetime. The lifetime of the TiO₂(e[−]) and oxidized sensitizer charge-separated state is known to increase when the hole is transferred away from the interface.^{21,176,177} This is not surprising as polythiophenes are often employed as efficient hole conductors in organic and solid-state solar cells.

In a comparative study of N3 analogs containing one chalcogen-substituted, 5-coordinate heteroarene, i.e., selenophene, thiophene, or furan (Scheme 3), it was shown that the extinction coefficient increased with the electropositivity and size of the heteroatom.¹⁷⁸ Calculations revealed that the extent of hole localization on the isothiocyanate ligands decreased as the extinction coefficient increased. The selenophene sensitizer showed great promise in DSSCs as the power-conversion efficiency was superior to that of Z907.

We recently found that employing bpy ligands bridged in the 3,3' positions by dithioline is a viable alternative to the more traditional and widely pursued approach of introducing conjugated groups in the 4 and 4' positions.¹⁶⁵ Substituent effects in this position are not as well documented as they sterically force the two pyridyl rings out of planarity, behavior that can decrease the stability of the compound. This issue is circumvented with bridging ligands but at the expense of opening up the N–Ru–N bite angle, thereby stabilizing LF states and increasing k_{nr} . Nevertheless, it was notable that this first-derivative, MLCT-dithioline compound, [Ru(BTL)(deeb)]²⁺, where BTL is 9'-[4,5-bis-(cyanoethylthio)]-1,3-dithiol-2-ylidene]-4', 5'-diazafluorene and deeb is 4,4'-(CO₂Et)₂-bpy (Scheme 3), had extinction coefficients for their lowest energy transitions that were comparable to the highest ever reported based on Ru^{II}(4,4'-disubstituted-bpy) compounds, $4.4 \times 10^4\text{ M}^{-1}\text{ cm}^{-1}$ at $\lambda_{\text{max}} = 470\text{ nm}$. In a similar absorption region, to the best of our knowledge, only four other efficient sensitizers exceed this value: $4.54 \times 10^4\text{ M}^{-1}\text{ cm}^{-1}$ at $\lambda_{\text{max}} = 471\text{ nm}$ (D16),¹⁵⁶ $7.85 \times 10^4\text{ M}^{-1}\text{ cm}^{-1}$ at $\lambda_{\text{max}} = 449\text{ nm}$ (D6),¹⁵⁶ $7.21 \times 10^4\text{ M}^{-1}\text{ cm}^{-1}$ at $\lambda_{\text{max}} = 442\text{ nm}$ (DCSC13),¹⁷⁹ and $5.43 \times 10^4\text{ M}^{-1}\text{ cm}^{-1}$ at $\lambda_{\text{max}} = 453\text{ nm}$ (C107).¹⁷¹ It should be noted that each of the former three sensitizers contained four phenylene and four vinylene groups on one bpy, while the latter



Scheme 3 The chemical structures of recently developed promising sensitizers with increased extinction coefficients, C101/C102/C105 and $\text{Ru}^{\text{II}}(\text{BTL})(\text{deeb})_2^{2+}$, or enhanced light-harvesting to the red without isothiocyanate ligands, $[\text{Os}^{\text{II}}(\text{tct})(\text{pyq})\text{Cl}]^{2+}$ and $[\text{Ru}^{\text{II}}(\text{dcb})_2(\text{dfpp})]^+$

contained four thiophene groups on one bpy. Part of the success with the dithioline-bpy ligands is that they themselves have IL absorption bands, in addition to the MLCT absorption bands, in the visible region. Regardless, their similar absorption, but with decreased conjugation, relative to the other four highly absorbing sensitizers was quite unexpected and intriguing.

An alternative strategy for increasing the LHE is to use nature's antenna effect, Figure 2.^{180–186} Multiple pigments that are suitably arranged can absorb light and vectorally transfer their energy to a central pigment that can then inject an electron into the semiconductor. If the additional pigments do not increase the footprint of the sensitizer on the semiconductor surface, the LHE could be enhanced. Indeed, the trinuclear Ru^{II} sensitizer utilized in the celebrated 1991 Nature paper¹³ had been previously designed in Italy to function as an antenna.¹⁸³

An issue with the *cis*-Ru(dcb)₂(CN)₂ group used as the energy-transfer acceptor and surface anchor is the *cis* geometry of the ambidentate cyano ligands. This resulted in a larger footprint as the number of Ru^{II} pigments was increased. In this regard, a trans geometry is more preferred, Figure 2.¹⁸⁷ The synthesis of molecules that function as antennae and their use in DSSCs continues to be an active area of research that may one day enable the efficient sensitization of planar semiconductor materials.¹⁸⁵

2.3.2 Broad Spectral Light-Harvesting

Given the usual values for the properties that determine the overall light absorptance of the TiO₂-based DSSCs—i.e., the film thickness = 5–10 μm, roughness = 300–1000, porosity ≈ 50%, and MLCT extinction coefficient ≈ 15 000 M⁻¹ cm⁻¹—already ~90% of the incident light is absorbed at the absorption maximum. Larger extinction coefficients would allow for a more planar film to be employed, i.e., thinner or less roughened, that would most likely manifest itself as an enhancement of V_{oc} . However, the spectral sensitivity of the DSSC would hardly increase. Instead, advancements in LHE can be attained via increasing the region over which the sensitizer absorbs.

Ru(bpy)₃²⁺ and most other tris-heteroleptic d⁶ polypyridyl compounds have redox and optical properties that are fairly insensitive to their environments.^{25,73} This is not the case when ammine or cyano ligands are present in compounds of the type $[\text{M}(\text{bpy}')(\text{X})_4]^{2-/2+}$ or $[\text{cis-M}(\text{bpy}')_2(\text{X})_2]^{0/2+}$, X = NC⁻ or NH₃.²⁵ Outer-sphere interactions with the cyano ligands have a profound influence on $E^{\circ}(\text{Ru}^{\text{III}/\text{II}})$ and hence the color of the compound. For [Fe(bpy)(CN)₄]²⁻ compounds, the excited-state reorganization energy in acetonitrile was found to be significantly larger on TiO₂ than in fluid solution ($\lambda = 0.32$ eV versus 0.10 eV, respectively).¹⁹⁰ This increased reorganization energy may be due to the restricted translational mobility of the semiconductor-bound iron compounds and

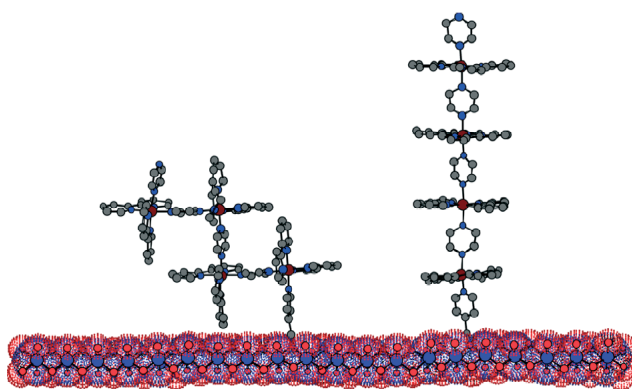


Figure 2 A scheme depicting an array of sensitizers bound to a planar TiO₂ surface consisting of *cis*- and *trans*- $[(\text{Ru}(\text{LL})_2(\text{pz}))_4(\text{ina})]^{8+}$ on the left and right, respectively, where pz is an ambidentate pyrazine ligand and ina is isonicotinic acid. The *trans* orientation enables increased absorptance, α , without changes in the projected footprint of the sensitizer. (Reproduced from Ref. 187. © Elsevier, 2008.)

the ambidentate $\text{Fe}^{\text{II}}\text{--CN--Ti}^{\text{IV}}$ linkages. $[\text{Ru}(\text{dcb})(\text{CN})_4]^{2-}$ is also highly solvatochromic¹⁹¹; the maximum of the lower energy MLCT band of $\text{Ru}(\text{dcb})(\text{CN})_4/\text{TiO}_2$ was observed at $450 \pm 10 \text{ nm}$ in tetrahydrofuran and at $500 \pm 20 \text{ nm}$ in dimethylformamide.¹⁹¹ The color change was due to a shift of $E^\circ(\text{Ru}^{\text{III}/\text{II}})$ with solvent. The compound maintained this solvatochromism upon attachment to mesoporous, nanocrystalline anatase (TiO_2) thin films although the magnitude of the effect decreased. Solvent tuning altered the spectral responses of DSSCs based on these materials in a predictable way and could in theory be used to enhance the LHE of solvatochromic sensitizers.

The position of attachment of the surface-anchoring carboxylic acid groups to bpy has also been examined for N3-like sensitizers of the type *cis*- $\text{Ru}(\text{X},\text{X}'\text{--}(\text{COOH})_2\text{--bpy})_2(\text{NCS})_2$, where $\text{X} = 3, 4$, or 5 . When compared to the 4,4'-disubstituted bpy, 5,5' disubstitution resulted in a gain in red absorbance, because of a more favorable ligand reduction, but also decreased excited-state lifetime; taken together, this resulted in a smaller photocurrent but a similar V_{oc} .¹⁹² The decreased lifetime was rationalized based on the energy gap law,¹⁹² whereas the red enhancement was most likely due to increased conjugation from 5,5' disubstitution.¹³⁹ The lower photocurrent was also later found to be due to inefficient injection from the lower energy thexi state, as photocurrents on lower conduction-band edge SnO_2 were comparable regardless of the substitution position.¹⁹³ Similar decreases in photocurrent were seen for 5,5'-disubstituted N3-like compounds, vs their 4,4'-disubstituted version, containing the related NC^- and Cl^- nonchromophoric ligands.¹⁹² The same 5,5'- vs 4,4'-disubstitution trends in absorbance, ligand reduction, lifetime, and photocurrent were observed with N3-like sensitizers where the carboxylic acid functional groups were replaced with phosphonic acid groups, as well as those containing NC^- and Cl^- nonchromophoric ligands.¹⁹⁴

For 3,3'-disubstituted bpy, the photocurrent and V_{oc} were even worse, behavior attributed in part to lower maximum surface coverages.^{195,196} In addition, the steric hindrance induced by 3,3'-disubstitution led to a less-than-ideal bite angle for Ru^{II} chelation and thus a stabilization of the antibonding ligand-field states.^{28,83,197} This increased the k_{nr} values and results in a faster deactivation of the thexi state back to the ground state. Although difficult to quantify in such short-lived isothiocyanato-based compounds, similar photophysical studies with $\text{Ru}(\text{bpy})_2(\text{dcb})^{2+}$ with 3,3'-vs 4,4'-COOH-disubstitution have shown that the excited-state lifetime and quantum yield for emission decreased for compounds substituted in the 3,3' position,¹⁹⁸ implying that the nonradiative rate constant increased substantially.

A “black dye” that was discovered in the late 1990s is $[\text{Ru}(\text{tct})(\text{NCS})_3]^-$, where tct is 4,4', 4"-tricarboxylic acid-tpy, Scheme 2.⁵⁰ This compound extends the spectral sensitivity of DSSCs significantly toward the red relative to N3. However, the restricted tridentate nature of the terpyridyl ligand results in a far less than octahedral chelation range

that lowers the extinction coefficient throughout the visible region. Quantitative light harvesting at wavelengths near the absorption maximum of the black dye therefore requires thicker TiO_2 films than the 10- μm films typically used. The tradeoff in the effective bandgap and strength of light absorption over the absorbing regions for “black dye” vs N3 results in very similar power-conversion efficiencies in DSSCs.^{17,33,50,51}

Thummel and colleagues recently synthesized a series of N3 derivatives where the dcb ligands were replaced by 1,8-naphthyrid-2-yl ligands functionalized with binding groups.¹⁹⁹ These compounds extended the red-edge absorption beyond 800 nm, which is roughly 100 nm beyond that of N3. Also, Grätzel and colleagues, recently reported the synthesis and characterization of a *trans*- $\text{Ru}^{\text{II}}(\text{NCS})_2$ tetrapyridyl ligand.²⁰⁰ Interestingly, its absorption spectrum extended beyond 800 nm with an MLCT transition maximum near 637 nm. This first-generation sensitizer showed great promise with the proposed feasibility of introducing 4,4', 4'', 4'''-conjugated donor and acceptor groups in order to increase the extinction coefficient and charge-separated state lifetime.

Replacement of Ru^{II} with Os^{II} enhances the electric-dipole allowance of the ground state to ${}^3\text{MLCT}$ absorbance in the near-infrared thereby providing better spectral overlap with the 1 sun, AM1.5 solar irradiance spectrum. Introduction of Os^{II} was calculated to result in up to three times more singlet character in the lower lying excited states,⁵⁷ which would thus make radiative recombination more spin allowed and thus faster.^{201–204} Recently, Bignozzi and coworkers synthesized and investigated Os^{II} -based “black dye” analogs, i.e., each contained a tct ligand, in DSSCs (Scheme 3), where the absorbance was extended out to 1100 nm.¹⁸⁸ Although the photocurrent was ~20% inferior to that measured in champion DSSCs in the mid-visible region, the increased light absorbance in a rather intense region of the AM1.5 solar spectrum highlights promise for future sensitizers. This same group also synthesized $\text{Ru}(\text{dcb})_2\text{LL}$ compounds, where LL is a dioxolene, that can be oxidized to a semiquinone and then a quinone.²⁰⁵ Although reported for use in electrochromic devices, the absorption spectra of the semiquinone forms also extended to 1100 nm because of charge transfer to the semiquinone moiety.

Of note is that none of the sensitizers synthesized by Bignozzi and colleagues contained isothiocyanate ligands. This is desirable as the isothiocyanate ligands are thought to influence the stability of the sensitizer to the greatest extent.⁴⁸ It is for this reason that the newly synthesized and characterized cyclometallated $[\text{Ru}^{\text{II}}(\text{dcb})_2(\text{dfpp})]^+$ sensitizer, where dfpp^- is 2-(2,4-difluorophenyl)pyridine (Scheme 3), with a reported 10.1% light-to-electrical conversion efficiency under simulated 1 sun, AM1.5 conditions, is a significant advancement.¹⁸⁹ Interestingly, the calculated HOMO was almost entirely t_{2g} metal-centered, with a minor contribution from the dfpp^- ligand. Nevertheless, it was proposed that

the anionic nature of the carbon atom bound to the Ru helped to further stabilize the oxidized sensitizer such that the diffuse hole could be transferred away from the Ru toward the solution-based redox mediator. This is in line with the paradigm illustrated above where generally the most efficient sensitizers exhibit partial to entire hole transfer from Ru^{III} to a ligand: isothiocyanate, amine, thiophene, and now difluorophenyl groups.

Lastly, what if instead of tuning the optical properties of the surface-anchored sensitizer for broad solar harvesting, higher energy photons were absorbed by sensitizers in solution followed by efficient energy transfer to the surface-anchored sensitizers? This idea was recently realized by Grätzel and colleagues who dissolved an efficient organic energy relay dye in the solution electrolyte of a DSSC.²⁰⁶ The efficient light harvesting of the organic dye at shorter wavelengths, where surface-anchored Zn-phthalocyanines had a low absorptance, and overlap of its emission spectrum with the Zn-phthalocyanine's absorption spectrum resulted in efficient Förster energy transfer to the surface. This resulted in a 28% increase in i_{sc} and a 26% increase in η . It is interesting to note that energy transfer occurred even in the presence of a redox-active, red-colored electrolyte.

2.4 Sensitization by Pt, Cu, and Ir Polypyridyl Compounds

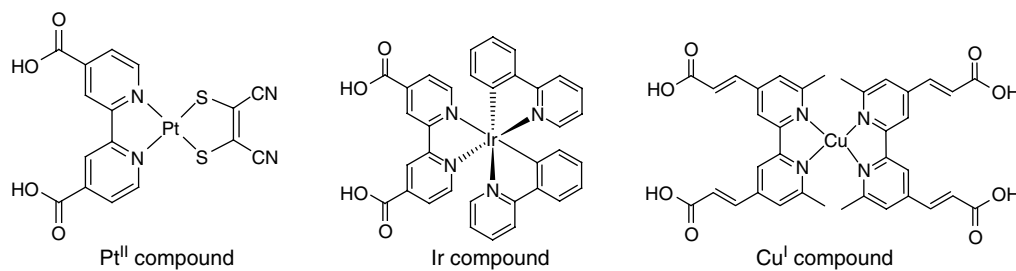
There now exists a large body of literature on the sensitization of TiO₂ by MLCT excited-states of octahedral, dπ⁶ low-spin Fe^{II}-, Ru^{II}-, Os^{II}-,²² and Re^I(CO)₃-polypyridyl compounds.^{138,207–214} There have also been some reports of MLCT sensitization by d¹⁰ Cu^I-polypyridyl compounds^{215–217} and square-planar d⁸ compounds based on Pt^{II}^{218–224} that possesses MLCT-like excited states. A single report on d⁵ Mn^{II}-tpy sensitizers has also appeared.^{225–227}

Durrant, Robertson, and colleagues investigated the effects of 3,3'- and 5,5'- vs 4,4'-(COOR)₂-bipyridine ligands (R = H is dcdb and R = CH₃CH₂ is deeb) on square-planar [Pt^{II}(X,X'-(COOR)₂ bpy)(maleonitriledithiolate)]²⁺ sensitizers. The ground-state possesses partial localization of the highest molecular orbitals on the dithiolate ligand

(Scheme 4).²²³ It was found that disubstitution in the 5,5' or 3,3' position of deeb resulted in a 10–20-nm red-shifted absorption band, respectively, with first ligand reduction potentials being lowered by up to 130 mV. However, contrary to Ru^{II} 4,4'-disubstituted sensitizers, the extinction coefficients were approximately the same (to within 4%) regardless of the disubstitution position. Also of note was that 3,3'-disubstituted sensitized TiO₂ films had a longer lived charge-separated state, i.e., Pt^{III}/TiO₂(e⁻), and larger V_{oc} as compared to the 4,4'-disubstituted sensitized thin films. This was rationalized by EPR results. The 3,3'-disubstituted compound was far from planar²²⁸ and the HOMO was calculated to have much more dithiolate, and less Pt^{II} character. With 5,5'-disubstitution the location of orbital density was reversed.²²⁹

Although fundamentally important, current Ir^{III} sensitizers absorb far less visible light than those based on Ru^{II}, etc. Regardless, it has been shown that TiO₂ can be sensitized to ligand-to-ligand charge-transfer (LLCT) bands using cyclometallated, dcdb- or dcdb-containing, octahedral Ir^{III} sensitizers, where dcdb is 4,4'-(COOH)₂-2,2'-biquinoline.²³¹ The novelty in these is that upon light excitation, a larger charge-separated-state distance is generated whereby the hole immediately resides on a ligand not bound to TiO₂. These first-generation sensitizers resulted in values for V_{oc} and FF that were similar to those for Ru(bpy)₂(dcdb)²⁺. Grätzel and colleagues have since synthesized a cyclometallated Ir^{III} sensitizer with a chelating acac ligand whose i_{sc} is practically twofold larger, V_{oc} is over 150 mV larger, and η of 1.87% is almost three times higher.²³² In addition, Tian and coworkers reported a novel Ir^{III} sensitizer (Scheme 4) with a 2.86% light-to-electrical power-conversion efficiency.²³⁰

Cu^I-polypyridyl sensitizers represent an interesting alternative to the other sensitizers outlined in this article. They differ from other first-row transition-metal analogs, i.e., Fe^{II} and Mn^{II}, in that they possess long-lived MLCT excited states that can be explained by their filled d¹⁰ subshell.²³³ In addition, the rather low cost and high abundance of Cu relative to Re, Ru, Os, Ir, and Pt makes them commercially viable alternatives. Recently a 2.3% efficient DSSC was constructed with a Cu^I sensitizer containing two 4,4'-disubstituted conjugated bpy ligands (Scheme 4) for increased LHE.²¹⁵ The ligands also contained two methyl groups in the 6 and 6' positions to



Scheme 4 The chemical structures of recently developed non-Ru^{II}, Os^{II}, Fe^{II}, or Re^I sensitizers that exhibit significant photovoltaic performance when incorporated into a DSSC, based on Pt^{II}, Ir^{III}, and Cu^I

destabilize the Cu^I state via a Jahn–Teller distortion toward the expected more planar orientation in the excited state. Although η was four times lower than that for N719, the cost to manufacture such a DSSC was determined to be an order-of-magnitude lower. Chen and colleagues have shown by XANES and EXAFS that sterically similar [Cu^I(2,9-(CH₃)₂-phen)₂]⁺ adopts a four-coordinate, tetrahedral ground-state geometry but that the equilibrated excited state is five-coordinate, likely a distorted trigonal bipyramidal geometry.²³⁴

3 PHOTOINDUCED ELECTRON INJECTION

There are three means by which surface-anchored transition-metal sensitizers can achieve interfacial charge separation at anatase TiO₂ nanocrystalline interfaces (Figure 3): (a) metal-to-particle charge transfer (MPCT) sensitization where light absorption promotes an electron from the metal d orbitals directly to TiO₂; (b) excited-state sensitization, where an electronically excited compound transfers an electron to TiO₂; (c) reduced sensitization that results from reductive quenching of the excited state by a donor, followed by electron transfer from the reduced sensitizer to TiO₂. What follows is a discussion of each from a brief historical perspective accompanied by recent advances and techniques to monitor/verify such mechanisms of sensitization.

3.1 Direct Metal-to-Particle Charge Transfer

There is a less well-studied mechanism of photoinduced electron injection that has been observed for metal-cyano compounds anchored to TiO₂ and is termed MPCT.²³⁷ This mechanism is apparent based on the observations that (i) sensitizer–TiO₂ reactions yield a new absorption band that is not a result of Bronsted acid–base chemistry;

and (ii) light excitation into said absorption band results in immediate formation of S⁺/TiO₂(e⁻). A useful feature of this sensitization mechanism is that the injection yield is by definition unity on an absorbed photon basis as electron transfer to TiO₂ is one in the same process. This is in contrast to excited-state injection, whose injection efficiency has been shown to be a function of the pH, ionic strength, excitation wavelength, and temperature.²³⁸ MPCT absorption bands were observed for the first time upon binding M(CN)_x⁴⁻ compounds to TiO₂ nanocrystallites (M = Fe^{II}, Ru^{II}, Os^{II}, Re^{III}, Mo^{IV}, W^{IV}).^{239,240} Some of these adducts extended the visible light photoresponse of TiO₂ beyond 700 nm. Hupp *et al.* discovered that the resonance Raman spectrum of [Fe(CN)₆]⁴⁻/TiO₂ colloids exhibited the coupling of ten vibrational modes to MPCT, three of which were surface modes.^{241,242} Jortner and colleagues have previously described an applicable theoretical model for describing such multimode electron transfer^{129,243–247}; however, the coupling of multiple surface modes to interfacial electron transfer was unprecedented experimentally.

Intervalence charge-transfer (IVCT) absorption bands are known for mixed-valence Fe^{II}–CN–Ti^{IV} cyano compounds and are speculated to be related to MPCT bands in [Fe(CN)₆]⁴⁻/TiO₂.²⁴⁸ From this, an interesting question arises: does light absorption promote an electron from Fe^{II} to an adjacent Ti^{IV} site or to a Ti^{IV} site within the interior of a TiO₂ nanocrystallite? This question was addressed by electroabsorption (Stark) spectroscopy. Previously, Boxer and Oh reported Stark spectra of Ru(diimine)₃²⁺ compounds⁷⁵ and others have since studied related Ru^{II} compounds.^{249–251} Stark spectra are generally obtained in amorphous solid-state media with the application of a unidirectional, oscillating electric field relative to the laboratory frame-of-reference. The electric field induces changes in the extinction coefficient and energetic shifts in absorption and/or photoluminescence maxima.^{252,253} Spectral modeling allows for the assignment

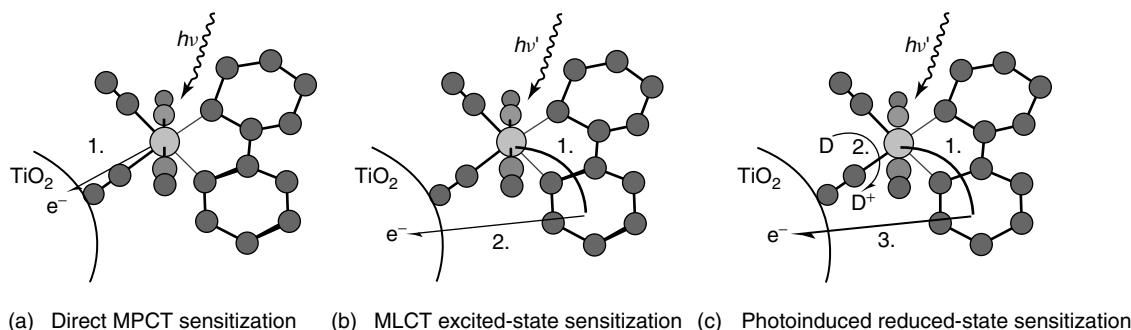


Figure 3 Ball-and-stick models for [Fe(bpy)(CN)₄]²⁻/TiO₂ depicting the three possible mechanisms for photoinduced electron injection into TiO₂: (a) direct, metal-to-particle charge-transfer (MPCT) sensitization; (b) excited-state injection, sensitization by means of a metal-to-ligand charge-transfer (MLCT) excitation followed by excited-state electron injection; (c) reduced-state sensitization, sensitizer injection that results from reductive quenching of the excited state with a donor, D, and then dark electron injection from the reduced sensitizer. To the best of our knowledge, only the former two have been reported in the literature for iron polypyridyl sensitizers. (Reproduced from Ref. 235, and Ref. 236. © American Chemical Society, 2000 and 2003.)

of these shifts as alterations in the transition moment (via the transition polarizability and hyperpolarizability) or peak position (via the difference dipole moment and polarizability), and from these data the charge-transfer dipole moment and distance can be determined via the Liptay treatment.²⁴⁸

For $[\text{Fe}(\text{CN})_6]^{4-}/\text{TiO}_2$, the charge-transfer distance was determined to be 5.3 Å based on the dipole moment change.²⁴⁸ This was within error of the distance from Fe^{II} to Ti^{IV} using molecular modeling on $[(\text{CN})_5\text{Fe}^{\text{II}}-\text{CN}-\text{Ti}^{\text{IV}}(\text{H}_2\text{O})_4\text{O}]^{2-}$, although the distance was slightly larger than empirical values measured for related $\text{Fe}^{\text{II}}-\text{CN}-\text{M}$ compounds. Similar values were found for Ru^{II} -, Mo^{IV} -, and W^{IV} -cyano compounds on TiO_2 and support the hypothesis that MPCT bands represent electronic transitions to an orbital on a Ti^{IV} atom that is in close proximity to the bound cyano nitrogen atom.²⁵⁴ In addition, on the basis of the above calculated distance and the fact that the unbound cyano ligands were even further from the surface than the metal center, identification of the process as MPCT and not ligand-to-metal charge transfer (LMCT), i.e. from a free NC^- to Ti^{IV} , was substantiated.

Some organic molecules are also known to display direct, ligand-to-particle charge-transfer (LPCT) absorption bands when anchored to TiO_2 , the most well known being catechol.^{238,255} Electroabsorption techniques are also useful in these cases; although most studies concluded that the excitation bands are LPCT in nature,^{256,257} excited-state injection was deduced for a select few sensitizers, i.e. eosin Y and alizarin.^{256,258} For this reason, a catechol group was covalently incorporated into tpy^{-226,259} and bpy-based²⁶⁰⁻²⁶² ligands as a strong anchoring group for transition-metal, coordination-compound sensitizers. Two Os^{II} ²⁶⁰ and a *cis*- $\text{Ru}^{\text{II}}(\text{NCS})_2$ -polypyridyl²⁶² compounds with bpy-catechol derivatives for surface attachment were recently reported that extended the visible light absorption to beyond 750 nm. Absorption features assigned as direct catechol → particle LPCT on TiO_2 , ZrO_2 and MLCT were observed. The observation of a direct charge-transfer band in the visible region was unexpected for ZrO_2 due to its large bandgap and the unfavorable reduction of Zr(IV).

3.2 Excited-State Injection

After light absorption, the MLCT excited state of the sensitizer may inject an electron into the anatase nanocrystallite, a process also referred to as interfacial charge separation. For sensitizers like N3, light absorption formally promotes an electron from the Ru^{II} metal center to a dcb ligand that is directly bound to the semiconductor surface. Therefore, excited-state charge separation occurs from the π^* orbitals of the organic ligand to the acceptor states in TiO_2 . There is now an overwhelming body of data that indicates that such charge separation occurs on a femto- to picosecond timescale. Experimentally, ultrafast

spectroscopists have all found that excited-state electron injection into TiO_2 is nonexponential, behavior attributed to the surface heterogeneity of TiO_2 and its density of acceptor states (DOS), distributions of sensitizer binding modes, strengths, and interactions, and multiple ultrafast injection processes occurring from various states in the thermal relaxation pathway, i.e., Franck–Condon singlet injection, internally converted singlet injection, intersystem crossing to the ${}^3\text{MLCT}$ thexi state(s) followed by injection. This has been thoroughly reviewed for both organic and transition-metal coordination compounds bound to semiconductor metal oxides.^{212,263,264} While the explanations given to rationalize the complex kinetics observed for excited-state injection for Ru^{II} sensitizers are often reasonable, satisfactory mechanistic models are still lacking.

It has been suggested that ultrafast, interfacial charge separation, following light absorption, occurs from the Franck–Condon excited state. Evidence for room-temperature injection occurring with a lifetime faster than a molecular vibration, i.e., $k_{\text{B}}T/h = 1.6 \times 10^{-13} \text{ s} = 160 \text{ fs}$,^{265,266} eludes this phenomenon.^{207,208,212,213,263,264,267-278} This would imply that injection occurs before thermal relaxation of the molecular excited state. Willig and coworkers found that excited-state electron injection from N3* into TiO_2 occurred in <25 fs under ultrahigh vacuum conditions.²⁷¹ The process therefore did not involve redistribution of vibrational excitation energy by exchange with phonons in the solid, and thus was entirely different from the weak-electronic-coupling case of Marcus–Levich–Jortner–Gerischer-type electron transfer.²⁷⁹⁻²⁸⁴ The finite reaction time for injection ruled out direct excitation of an electron from the Ru^{II} metal center to the semiconductor, yet the sub-100 fs rise-time implied vibrational wave packet motion-induced electron transfer. A detailed analysis of theoretical and empirical results supporting these conclusions using a perylene sensitizer can be found elsewhere.^{270,285-289} The quantitative, ultrafast excited-state electron injection reported for N3/ TiO_2 under ultrahigh vacuum conditions was not always observed when the sensitized thin films were placed in organic solvents or electrolytes. Under such conditions, injection was nonexponential and occurred on the femtosecond to hundreds-of-picoseconds timescale.

Sundström and colleagues have recently further investigated the ultrafast injection of N3 into TiO_2 by femtosecond transient-absorption anisotropy techniques.²⁹⁰ They reported that for N3, the fast, <100 fs, injection component occurred from the ${}^1\text{MLCT}$ excited state whereas the slower, picosecond injection process proceeded from the ${}^3\text{MLCT}$ excited state. Anisotropy measurements indicated that the slower injection was due to interligand electron transfer from a free nonsurface-anchored dcb ligand to one that was in intimate contact with TiO_2 . This interligand hopping could be altered by chemical modification of the ligands and by solvent environment and was the rate-limiting step for injection from the ${}^3\text{MLCT}$ thexi state. They also

showed that excited-state electron injection is slowed and gradually becomes less efficient as the excitation wavelength moves to the red of the absorption maximum.²⁷⁶ This was proposed to be due to direct ³MLCT population and thermal electron-transfer injection from the differences in population of the thexi states. These same authors also determined that by varying the method of TiO₂ film preparation, both rate constants for the biphasic injection kinetics for N3* into TiO₂ were directly related to the degree of TiO₂ crystallinity.²⁷²

Lian and coworkers found by femtosecond time-resolved infrared (TRIR) spectroscopy that excited-state electron injection into TiO₂ was biphasic for three [cis-Ru(dcb)₂(X)₂]^{0,0,2+} compounds (X = NCS, X = CN, or (X)₂ = dcb).²⁶⁷ The rate of the slower component was directly related to the sensitizer excited-state reduction potential. No noticeable changes were apparent for the fast component within the time resolution of the measurement, i.e., ~200 fs. Later, the same group compared the injection dependence for N3 sensitizers containing carboxylic acid or phosphonic acid linkers.²¹³ The amplitude of the fast component was larger for N3, which suggested stronger electronic coupling between the carboxylate and the TiO₂. However, the slow component for the phosphonated version of N3 was faster, which was assigned to injection from the relaxed ³MLCT thexi state and attributed to the slightly more favorable energetics for injection from the bpy-PO₃H₂ group orbitals. This led to more efficient excited-state injection from the ³MLCT of the phosphonated version of N3.

Durrant and coworkers found that an N3 sensitizer in which two of the carboxylic acid groups were deprotonated, N719, prior to sensitizer surface binding had a 30-fold slower rate of injection than N3*.²⁹¹ In a followup paper, it was determined that the concentration of potential-determining ions, e.g., H⁺ and Li⁺,^{21,107} and factors that influence the TiO₂ DOS resulted in N719's less-efficient excited-state injection.²⁹² After performing multiple washings of the N3/TiO₂ films in neat ethanol, the injection rates were found to be very similar to those of N719/TiO₂ thin films.²⁹¹ It was suggested that the labile protons from the carboxylic-acid binding groups of N3 had lowered the DOS in TiO₂ and promoted more favorable energetics for injection. To control this variable, Lian and coworkers pretreated N3/TiO₂ thin films for one day in aqueous buffer solutions at pH 2, 4, 6, or 8.²⁶⁷ After removing weakly bound and desorbed sensitizers, the biphasic kinetics and injection yields were found to be pH dependent. As the pH was raised from 2 to 8, there was a decrease in the rate of the slower component to injection, the ratio of the slower-to-faster components to injection, and the injection yield. Such behavior is consistent with the expected Nernstian shift of the TiO₂ conduction-band edge toward the vacuum level as the pH is raised.

Grätzel and coworkers reported that the slower picosecond components for excited-state electron injection could be removed with low concentration or sonicated dying solution, or by employing a lower surface-coverage thin

film.^{293,294} Under such conditions, only an ultrafast component (<20 fs) for injection remained. In support of this, Piotrowiak and coworkers found that dialysis of sensitized TiO₂ colloids resulted in much shorter excited-state lifetimes as measured by time-correlated single photon counting.²⁹⁵ However, in this case multiexponential kinetics were required to adequately fit the observed data.

The multiphasic character of the picosecond dynamics of excited-state electron injection into TiO₂ alludes to the consideration that at least some injection is occurring from a thexi state. This state, which can be described by a Boltzmann population, may exhibit behavior typical of nonadiabatic thermal electron transfer and/or electron tunneling. (The latter is clearly evident by temperature- and distance-dependent studies.) At low temperatures, a constant, nonzero rate for injection may persist while the room-temperature injection rate ought to exhibit an exponential dependence on distance, given that the inaccessible LUMOs are of similar energy:

$$A = A_0 \exp[-\beta \cdot x] \quad (5)$$

where β is the dampening factor. A dampening factor, $\beta = 1.0 \text{ \AA}^{-1}$, is often indicative of saturated hydrocarbon, through-bond superexchange tunneling behavior;^{296–299} in general, larger values imply at least partial through-space character, while smaller ones are associated with tunneling through conjugated π systems.²⁹⁹

An early study demonstrated that efficient excited-state electron injection did occur from sensitizers of the general type Ru(dmb)₂(L)²⁺, where dmb is 4,4'-(CH₃)₂-bpy and L contained unconjugated -(CH₂)_x-linkers between the Ru-chelating bpy moiety and one carboxylic acid group.³⁰⁰ In this same study, the acetylacetone (acac) linker was first employed to bind sensitizers to TiO₂. Recently, the acac ligand was again employed for a proposed water oxidation sensitizer–catalyst bound to TiO₂.²²⁵ Acac is known to bind hard Ti^{IV/III} strongly and is very stable toward hydrolysis and oxidation in various aqueous pH conditions and in the presence of strongly oxidizing environments, respectively.²²⁵ For these Mn^{II}(tpy-acac)-based sensitizers, and others with catechol-containing binding groups, ultrafast injection, which was proposed based on theoretical calculations, was confirmed via femtosecond terahertz time-domain (THz-TD) spectroscopy.^{225,226} THz-TD spectroscopy allows one to spectroscopically monitor free conduction-band electrons as they have a large absorption cross section in the THz frequency domain.^{301–303} The novelty of this technique is that electron diffusion and drift can be monitored by a noncontact, nonelectrochemical means. The same research group was also successful in binding a dinuclear Mn^{IV,III}(tpy)-based sensitizer–catalyst through a μ -oxo bridge from the Mn^{IV} to a Ti^{IV} on TiO₂.²²⁷

A more systematic distance-dependent study was later reported using three Re^I(bpy-(CH₂)_{2n}-(COOH)₂)(CO)₃Cl ($n = 0, 1, 3$) sensitizers, where it was shown that ultrafast

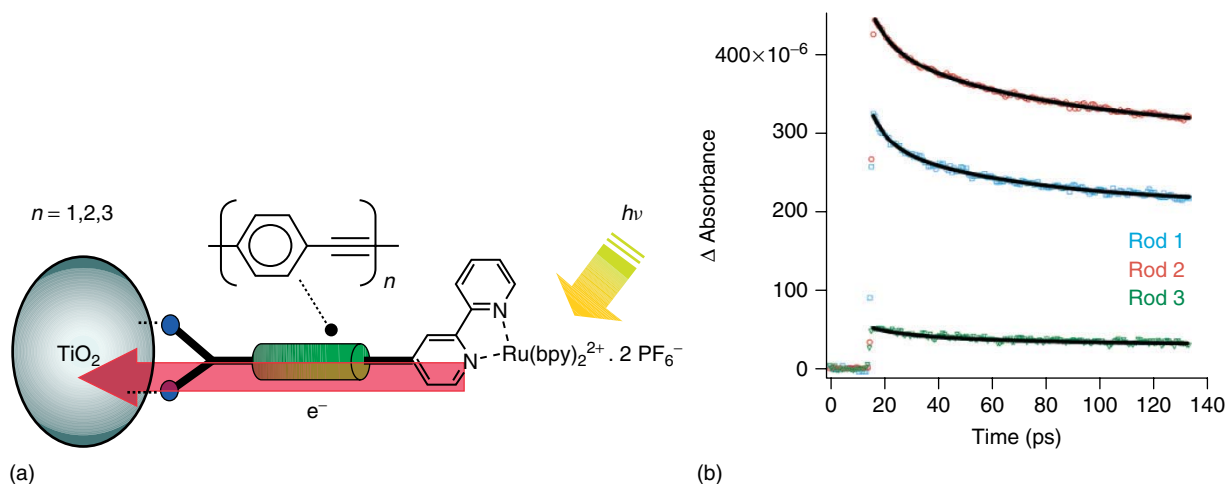


Figure 4 (a) A schematic depicting a rigid-rod, Ru(bpy)₃²⁺-based sensitizer bound to a TiO₂ nanocrystallite under light excitation. (b) Single-wavelength kinetic absorption difference spectra of these TiO₂-bound sensitizers containing rods of oligo(phenylene-ethynylene) linkers ($n = 1, 2, 3$). Although the injection yields were not distance dependent, the rates were inversely related to n . (Reproduced from Ref. 310. © American Chemical Society, 2007.)

injection into TiO₂ did not occur when electronic coupling between the surface-bound ligand and the TiO₂ surface was removed by unconjugated methylene spacers, i.e., when $n = 1$ or 3 .^{207,208} For the same two sensitizers, the slower picosecond injection process could be successfully fit to a stretched exponential and the distance dependence of the injection rate could be qualitatively modeled by equation (5) using $\beta = 1.2$ for each C–C bond, indicative of nonadiabatic electron transfer. The >200-fold increase in injection rate from $n = 1$ to $n = 0$ could not be fit to such a model and was explained as adiabatic electron transfer because of a greatly increased strong electronic coupling from the lack of an unconjugated spacer moiety. Detailed comparison of the $n = 0$ with the $n = 1$ or 3 compounds was complicated by the fact that the $n = 0$ compound had significantly different photophysical and redox properties.

With three phosphonated, “black dye”-like compounds of the form [Ru(4'-PO₃²⁻-(Ph)_n-tpy)(NCS)₃]³⁻ ($n = 0, 1, 2$), the distance dependence of excited-state electron injection through conjugated linkers was studied.³⁰⁴ Femtosecond pump–probe transient absorption measurements revealed that the rate of each phase of an observed biphasic injection process was dependent on distance. The fast picosecond component fit nicely to an exponential distance-dependent model, equation (5), with dampening factor, $\beta = 0.19 \text{ Å}^{-1}$, while the slower component for injection was assumed to be because of injection from loosely bound or aggregated sensitizers. As this dampening factor was much smaller than typical ones obtained for donor–bridge–acceptor systems in solution, it was proposed that nuclear reorganization played a negligible role in injection, a hypothesis supported by theoretical calculations.

Some novel ligand architectures that could be used to study the distance dependence for injection rates/

yields have recently been employed.³⁰⁵ Galoppini and coworkers often employ sensitizers with either a rigid-rod or tripododal linker containing at least one functional group to bind to TiO₂.^{306–309} These have predominantly consisted of oligo(phenylene-ethynylene) linkers (E-Ph) and 1,3,5,7-tetraphenyladamantane (Ad-Tripod), respectively. A comparative excited-state electron-injection study of three rigid-rod, Ru(bpy)₃²⁺-based sensitizer compounds was reported, Figure 4(a).³¹⁰ It was found that a monotonic decrease in injection rate occurred as the number of linkers was increased with a dampening factor, $\beta = 0.04 \text{ Å}^{-1}$, for both a slow and a fast injection component. A similar study on SnO₂ resulted in a value of $\sim 0.8 \text{ Å}^{-1}$ and theoretical values were $> 0.4 \text{ Å}^{-1}$.³¹¹ Although this small distance dependence agrees rather well with the conclusions from the phosphonated compounds, these results were further complicated by the lack of the expected similar trend in injection yields, where the middle-length spacer was found to inject best, Figure 4(b). By linking the ethynylene-bpy group to the meta position of a phenyl ring, it was recently shown that the extinction coefficient was roughly half that of the para isomer.³¹² Nevertheless, the photoinduced injection yields remained independent of the position of covalent attachment, i.e., meta or para. With the use of a phosphonated-tpy ligand with and without an intervening thieryl group chelating Ru^{II}(4'-R-tpy), where R = H or 4-bromo-2,5-dimethylphenyl, as expected the extinction coefficients practically doubled and the band red-shifted with increased conjugation.³¹³ However, contrary to what may be expected, introduction of the thieryl group between a tpy ligand and the surface-anchoring phosphonic acid group led to a faster injection rate and more favorable photoelectrochemical properties when compared to the compounds lacking the thieryl group.

In dichloromethane electrolytes with TBAI/I₂, V_{oc} values were found to be directly related to the number of phenylene-ethynylene spacer groups.^{306,307,314} As ion pairing was previously shown to occur in dichloromethane with [Ru(bpy)₂(deeb)]²⁺ and I⁻ or I₃⁻,^{315–317} it was proposed that recombination may occur with acceptors further from the TiO₂ surface for the longer tripodal sensitizers. The V_{oc} data support this distance-dependent recombination over three decades of irradiance.

The dc_b ligand is structurally the same as two ina, i.e., isonicotinic acid, ligands connected in the 2 and 2' positions. The extra covalent bond in the dc_b ligand increases the overall conjugation and thus lowers its LUMO energy. A comparative study of two heteroleptic Ru^{II} compounds, one with a dc_b ligand and the other with two ina ligands, was undertaken; the distance dependence of injection was comparatively studied by investigating the effect of remote versus adjacent excited-state electron injection.³¹⁸ Both compounds exhibited a similar pH-dependent injection at pH > 2 even though the thexi state of the latter compound contained an electron localized on a ligand that was not bound to the TiO₂ surface. The efficient injection from sensitizers with an ina ligand has been observed for Re(bpy)(CO)₃(ina)⁺ as well.²⁰⁹

The distance dependence of excited-state injection was investigated by yet another means: core–shell architectures,^{319–323} with an insulating Al₂O₃ shell with 0.6–6 nm thickness conformally deposited on 20 nm TiO₂ nanocrystals, Figure 5(a).³⁰⁴ As electron tunneling is a factor of distance and barrier height, this architecture allowed solely the distance to be altered. These studies were somewhat hampered by ultrafast injection thought to occur at pinhole imperfections in the Al₂O₃ shell. Neglecting this ultrafast injection, it was shown that the picosecond biphasic nature of injection resulted in $\beta = 0.11 \text{ Å}^{-1}$ and 0.04 Å^{-1} for the fast and slow components,

respectively, Figure 5(b). As the barrier to the conduction band of bulk, crystalline Al₂O₃ is very large, dampening factors over an order-of-magnitude larger were expected. It was proposed that the electronic structure of thin alumina layers differed from that of bulk Al₂O₃.³²⁴

3.3 Reduced Sensitizer Injection

An alternative mechanism exists for photoinduced electron injection wherein the excited state is reduced prior to interfacial charge separation, Figure 3(c). This results in injection from a nonelectronically excited sensitizer. For this reason, DSSCs operating under this mechanism are appropriately termed *regenerative galvanic cells* as injection is a dark, thermodynamically favorable process.³²⁵ This alternative sensitization method has been called *supersensitization*³²⁶; the donor is termed the *supersensitizer* because of its requirement in achieving effective overall sensitization.³²⁷ A unique aspect of this mechanism is that the oxidized form of the sensitizer is never generated. Therefore, it may be particularly well suited for sensitizers that are unstable in their oxidized forms, like N3,^{117,194,328–330} or Pt^{II} sensitizers. An advantage with MLCT excited states is that the reduced form of the sensitizer is a stronger reductant than the MLCT excited state, typically by 200 to 400 mV.

Kirsch-De Mesmaeker and coworkers first reported compelling evidence for reduced ruthenium sensitizers transferring electrons to SnO₂ electrodes.³²⁷ The coincidence of Stern–Volmer constants measured by analysis of the photocurrent enhancement and photoluminescence quenching with hydroquinone donors left little doubt as to the sensitization mechanism. Additional spectroscopic evidence for photoinduced electron injection by reduced sensitizers was reported for Ru(bpy)₂(dc_b)/TiO₂

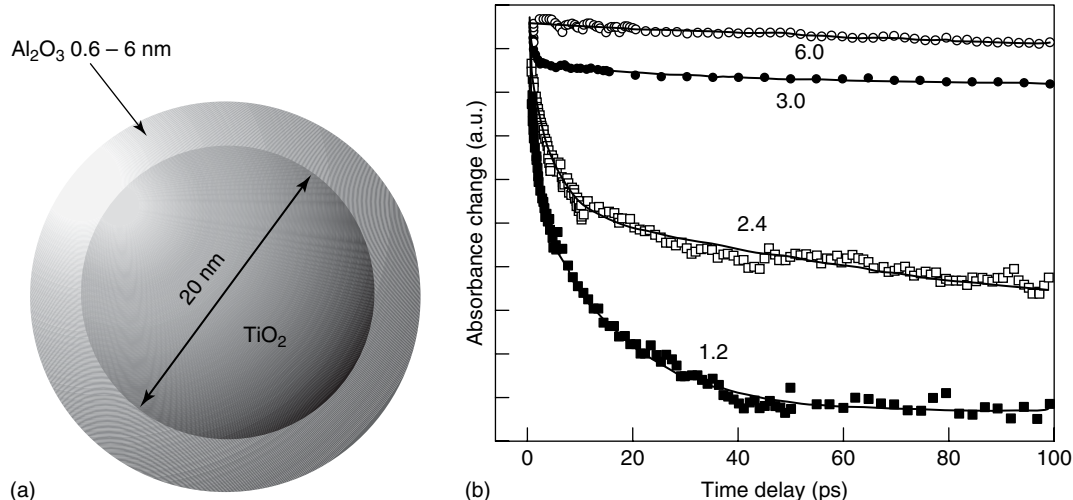


Figure 5 (a) A diagram of a TiO₂/Al₂O₃ core–shell nanoparticle. (b) Single-wavelength kinetic absorption difference spectra for Ru(4'-PO₃²⁻-tpy)(NCS)₃/TiO₂ thin films illustrating that the rate of injection was inversely related to the size of the Al₂O₃ overlayer. The Al₂O₃ overlayers' thickness in nanometers is shown. (Reproduced with permission from Ref. 304. © SPIE, 2006.)

in 0.1 M TBACLO₄ acetonitrile electrolyte with organic phenothiazine (PTZ) electron donors.³³¹ Nanosecond transient absorption data demonstrated the rapid formation of TiO₂(e⁻)/PTZ⁺, while in the absence of PTZ there was little-to-no evidence for injection. Injection was rate limited by diffusional quenching of the MLCT excited state, so the Ru^{II}(dcb⁻) (bpy)₂/TiO₂ intermediate was not directly observed.

An interesting case of reduced-sensitizer electron injection was reported with the bimetallic sensitizer (bpy)₂**Ru^{II}-BL-Rh^{III}**(dcb)₂/TiO₂, BL = 1,2-bis[4-(4'-methyl-bpy)]ethane.³³² About two-thirds of the MLCT excited states of the ruthenium chromophore were quenched by electron transfer to the Rh(dcb)₂ group to form a (bpy)₂**Ru^{III}-BL-Rh^{II}**(dcb)₂/TiO₂ charge-separated state while the remaining directly injected an electron into TiO₂.^b This observed branching ratio was proposed to result from different surface orientations. Approximately 40% of the intramolecular, charge-separated state, (bpy)₂**Ru^{III}-BL-Rh^{II}**(dcb)₂/TiO₂, injected electrons into TiO₂ to form (bpy)₂Ru^{III}-BL-**Rh^{III}**(dcb)₂/TiO₂(e⁻), while the remaining underwent back-electron transfer to form ground-state products. The **Ru^{II*}** injection occurred within the time resolution of the instrument, i.e., <10 ns, while injection from **Rh^{II}** occurred in <100 ns following light excitation.

In order to realize efficient DSSCs that operate by this mechanism, sensitizers that are potent photo-oxidants must be utilized. This stems from that fact that the I₃⁻/I⁻ redox mediator is the only redox mediator that yields high light-to-electrical power-conversion efficiencies and $E^\circ(I^\bullet/I^-)$ is rather positive. Ru^{II} sensitizers that are strong excited-state oxidants can be prepared with ligands such as 2,2'-bipyrazine (bpz).³³³ For example, the $E^\circ(Ru^{2+*/+})$ of [Ru(bpz)₂(deeb)]²⁺ was found to be greater than +1.0 V vs SCE^{334–336} (+1.24 V vs NHE³³⁷). While the excited state of this and related sensitizers were found to be efficiently quenched by iodide or phenothiazine donors, the reduced form of the compound that resulted, Ru^{II}(bpz)(bpz⁻)(deeb)/TiO₂, did not inject electrons into TiO₂.³³⁶ In fact, very similar transient absorption features were observed in solution, on TiO₂, and on insulating ZrO₂. Some improvement was observed when the semiconductor was changed to SnO₂, but the injection yields remained poor.³³⁴

Another interesting case of reductive quenching of an excited state that did not result in electron injection was reported for sensitized films in the presence of a high concentration of 1-propyl-3-methylimidazolium iodide.³³⁸ A new transient spectroscopic feature was discovered that was attributed to the reduced sensitizer, which presumably formed by reductive quenching of the excited state by iodide. The decay of this species was attributed to a back-reaction with I₃⁻ with a half-life of ~1 ms, yet it is not clear why this state did not inject electrons into TiO₂.

4 SENSITIZER REGENERATION

4.1 Intramolecular Regeneration

Considerable effort has been set forth to regenerate the oxidized sensitizer by intramolecular electron transfer. This could be considered a “hole” transfer reaction that translates the oxidizing equivalent away from the Ru^{III} metal center and, ideally, the TiO₂ surface. Very similar mechanisms are well known in the field of supramolecular photochemistry.^{180,186,339,340} To our knowledge, Wrighton and coworkers were the first to extend this photochemistry to a semiconductor electrode.³⁴¹ The ability to control hole-transfer reactions at the molecular level is important for many classes of solar cells. One can envision future-generation DSSCs where multiple hole-transfer steps translate the oxidizing equivalent from the sensitized interface directly to a counter electrode, thereby eliminating the need for the solution-based redox mediators, i.e., I₃⁻/I⁻, that are required today.

In practice, there are at least two ways in which a D⁺-Ru^{II}/TiO₂(e⁻) interfacial charge-separated state can be photocreated. They correspond to the excited-state and reduced-state injection mechanisms described in Sections 3.2 and 3.3, respectively. Since the MLCT excited state is a weaker oxidant than is the oxidized state, it is possible to design dyads with weak donors that only react by the first mechanism, while with potent electron donors the mechanistic pathway is dependent on the relative rate constants for excited-state electron injection and intramolecular charge separation. Since excited-state injection is often found to be ultrafast, the first mechanism probably predominates even though it has not always been unambiguously identified.

It should be pointed out that in some regards N3/TiO₂ is thought to undergo a similar intramolecular, charge-transfer process. As mentioned previously, calculations show considerable hole density on the sulfur atom of the isothiocyanate ligands for N3⁺.^{101–103} It is also known from electrochemical measurements that there are two closely spaced oxidations for N3, the first is predominantly metal based while the second is mainly isothiocyanate based. Therefore, in the charge-separated state, N3⁺/TiO₂(e⁻), there is likely some partial “hole transfer” from the Ru^{III} metal center to the isothiocyanate ligands. In most of the examples discussed below, the electronic coupling between the electron donor and the Ru metal center is much weaker, giving rise to complete hole hopping rather than partial charge transfer.

4.1.1 Organic Donors

Bignozzi and coworkers reported the first time-resolved spectroscopic studies of intramolecular sensitizer regeneration.^{342,343} The dyad was [Ru(4-CH₃,4'-CH₂-PTZ-bpy)(dcb)₂]²⁺, where PTZ was the organic donor phenothiazine, anchored to TiO₂ thin films and immersed in acetonitrile. In fluid methanol solution, visible-light excitation

of this dyad resulted in the creation of the MLCT excited state that was rapidly quenched by electron transfer from the PTZ group. Reductive excited-state quenching was moderately exergonic (<0.25 eV) and occurred with a rate constant of $\sim 2.5 \times 10^8$ s $^{-1}$ in methanol. When the dyad was attached to TiO₂, MLCT excitation resulted in a new charge-separated state with an electron in TiO₂ and an oxidized PTZ group, abbreviated PTZ⁺-Ru^{II}/TiO₂(e⁻). It was not possible to determine the mechanism of charge separation, yet the authors speculated that after excited-state electron injection, electron transfer from PTZ to the Ru^{III} metal center ($-\Delta G \sim 0.36$ eV) produced the charge-separated state, PTZ⁺-Ru^{II}/TiO₂(e⁻). Translation of the “hole” from the Ru^{III} metal center to the pendant PTZ moiety inhibited charge recombination by about three orders of magnitude, and a significant increase in V_{oc} resulted. Since that time, a number of dyads have been attached to TiO₂ and are discussed further below; a commonly utilized electron donor is a triarylamine moiety, NAr₃.^{344–346}

After pulsed-light excitation of similar compounds, some remarkably long-lived charge-separated states were observed possessing half-lives of over half a second, as shown schematically in Figure 6(a).¹⁷⁷ Durrant, Haque, and colleagues increased this lifetime by employing Ru(4,4'-(R)₂-bpy)(dcb)₂/TiO₂ systems, where R contained one triphenylamine group, two triphenylamine groups, or a poly(vinyl-NAr₃) group of about 100 units in length, Figure 6(b).¹⁷⁶ The introduction of about 100 amines increased the half-life of the charge-separated state to over 4 s, as compared to 350 μs and 5 ms for the other two, respectively. The kinetics for excited-state electron injection and subsequent hole transfer from the Ru^{III} metal center to the bound NAr₃ occurred within the instrument response

time, i.e. ~ 10 ns. Durrant and colleagues also studied Ru(4,4'-(R)₂-bpy)(dcb)₂/TiO₂ thin films, where R contained oligo(triphenylamine) groups at varying distances from the Ru^{II} metal center, to determine the distance dependence for back-electron transfer.^{176,177,347–349} Collectively, these data provided strong evidence that back-electron transfer rates displayed an exponential dependence on spatial separation with a dampening factor, $\beta = 0.95 \pm 0.2 \text{ Å}^{-1}$.^{350,351}

N₃ derivatives, *cis*-Ru(4,4'-(R)₂-bpy)(dcb)(NCS)₂, R = triphenylamine or CH₃, bound to TiO₂ thin films were examined in order to study the effects of Ru^{III} hole transfer to a triphenylamine moiety.¹⁶⁴ Unexpectedly, both sensitizers exhibited similar transient features with no spectral evidence for hole transfer to the amine donor. The photoelectrochemical properties of the two sensitized thin-film electrodes differed significantly, and a much larger V_{oc} value was measured for the triphenylamine-containing sensitizer. The authors speculated that the enhanced V_{oc} resulted from a larger dipole that was nascently formed on the sensitizer bearing the triphenylamine moiety. It was proposed that photoinduced electron injection into the TiO₂ acceptor states and *partial* hole delocalization from the Ru^{III} metal center to the triphenylamine moiety occurred in one concerted step.

The compound [Ru(BTL)(deeb)₂]²⁺, where BTL is [9'-[4,5-bis-(cyanoethylthio)-1,3-dithiol-2-ylidene]-4', 5'-diazafluorene, was found to have an extinction coefficient almost three times as large as Ru(bpy)₃²⁺ in the visible region.¹⁶⁵ Interestingly, the transient absorption features in solution and on TiO₂ differed greatly. In solution, a transient state was observed with spectroscopic properties characteristic of an MLCT excited state, with $\tau = 25$ ns at -40°C , whereas when bound to TiO₂ a large positive absorption feature near

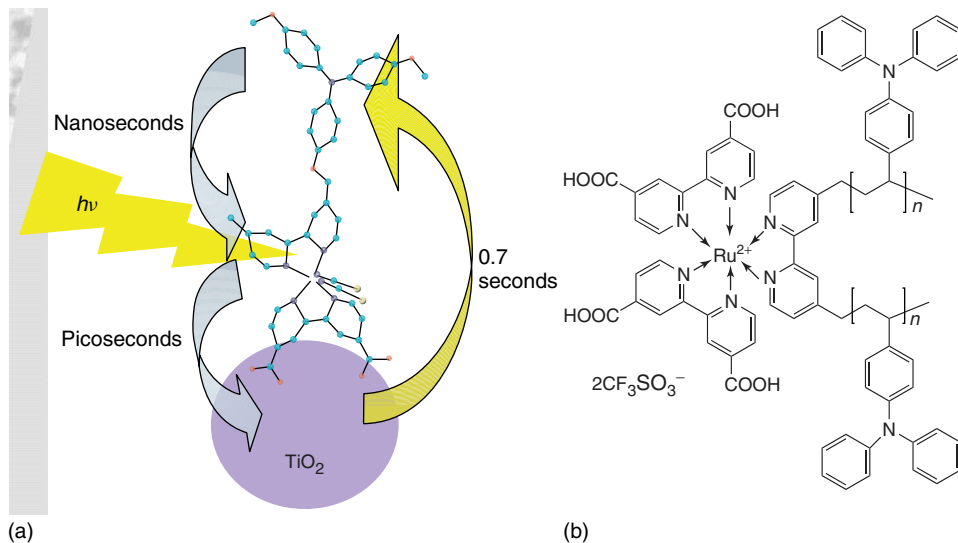


Figure 6 (a) A schematic depicting the *cis*-Ru(dmb-ether-NAr₃)(dcb)(NCS)₂ sensitizer bound to a TiO₂ nanocrystallite and the overall mechanism for photoinduced charge separation and recombination with corresponding timescales. (Taken from cover artwork.¹⁷⁷) (b) The chemical structure of the sensitizer employed to increase the half-life of the S⁺/TiO₂(e⁻) charge-separated state to over 4 s ($n = 100$). (Reproduced from Ref. 176. © Wiley-VCH, 2005.)

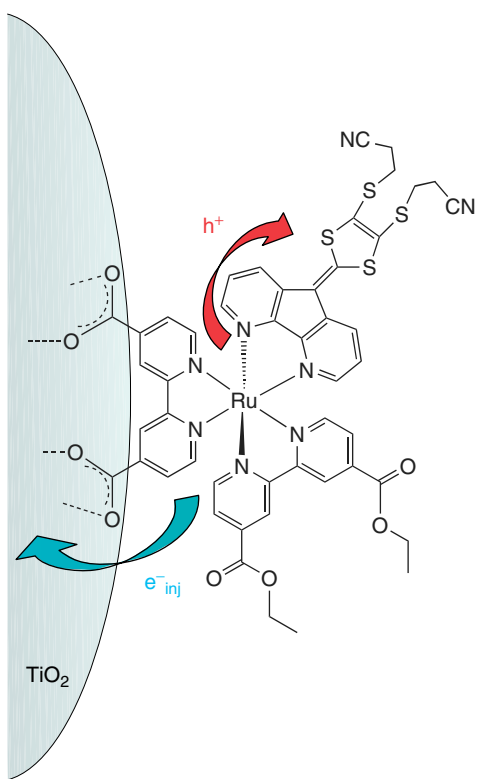


Figure 7 A schematic depicting a novel, high-extinction-coefficient sensitizer bound to a TiO_2 nanocrystallite and photoinduced electron- and hole-transfer mechanisms. This sensitizer is unique in that the extended conjugation on the free ligand is in the 3 and 3' positions. (Reproduced from Ref. 165. © American Chemical Society, 2008.)

520 nm was observed and assigned to the oxidized dithioline ligand. Within 10 ns after light excitation, an electron was injected into TiO_2 and the hole had translated from the Ru^{III} metal center to the dithioline-containing ligand, Figure 7. In fluid solution, the driving force for reductive quenching of the MLCT excited state was unfavorable.

4.1.2 Transition-Metal Donors

An advantage of using transition-metal donors is that the redox potential can be tuned over wide ranges by utilizing different ligands. The bimetallic sensitizer, $[\text{Ru}^{\text{II}}(\text{dcb})_2\text{Cl}-\text{bpa}-\text{Os}^{\text{II}}(\text{bpy})_2\text{Cl}]^{2+}$, abbreviated Ru-bpa-Os, where bpa is 1,2-bis(4-pyridyl)ethane, was anchored to TiO_2 .³⁵² Pulsed 532-nm or 416-nm light excitation of a Os-bpa-Ru/ TiO_2 thin film immersed in 1.0 M LiClO_4 acetonitrile electrolyte resulted in rapid excited-state electron injection ($\text{Ru}^{\text{II}*} \rightarrow \text{TiO}_2$) and intramolecular electron transfer ($\text{Os}^{\text{II}} \rightarrow \text{Ru}^{\text{III}}$) to ultimately form an interfacial charge-separated state with a $\text{TiO}_2(\text{e}^-)$ and an oxidized Os^{III} metal center, $\text{Os}^{\text{III}}\text{-bpa-Ru/TiO}_2(\text{e}^-)$. This same state was also generated after selective ³MLCT excitation of the Os^{II} moiety with 683-nm light. The rates of intramolecular and interfacial electron transfer were fast, $k > 10^8 \text{ s}^{-1}$, while interfacial charge recombination, $\text{Os}^{\text{III}}\text{-bpa-Ru/TiO}_2(\text{e}^-) \rightarrow \text{Os}^{\text{II}}\text{-bpa-Ru/TiO}_2$, required milliseconds for completion.³⁵²

Studies with a solution and surface-bound trinuclear ruthenium complex, $\text{Ru}^{\text{III}}\text{-Ru}^{\text{II}}(\text{L})\text{-amide-(bpy)}\text{Ru}^{\text{II}}(\text{dcb})_2/\text{TiO}_2$, revealed that MLCT excitation of the mononuclear Ru^{II} moiety resulted in a transient absorption spectrum indicative of $\text{Ru}^{\text{III}}\text{-Ru}^{\text{II}}(\text{L})\text{-amide-(bpy)}\text{Ru}^{\text{III}}(\text{dcb})_2/\text{TiO}_2(\text{e}^-)$, Figure 8.³⁵³ This intramolecular charge-separated compound was completely formed in 200 ps, at which time the injection yield was deemed to be <10%. However, at 300 ns, a spectrum consistent with $\text{Ru}^{\text{III}}\text{-Ru}^{\text{III}}(\text{L})\text{-amide-(bpy)}\text{Ru}^{\text{II}}(\text{dcb})_2/\text{TiO}_2(\text{e}^-)$ was observed and was shown to have a half-life of ~1 ms. This illustrates that slow hole transfer can occur over large distances under appropriate conditions.

Coordination compounds of the form $[(\text{LL})(\text{L}'\text{L}')\text{Ru}^{\text{II}}(\text{BL}')\text{Ru}^{\text{II}}(\text{LL})(\text{L}'\text{L}')]^{n+}$ were investigated on TiO_2 , where LL and L'L' are bpy and/or dcbl and BL' is a bridging ligand: either tetrapyrrolo[3,2-*a*:2',3'-*c*:3'',2''-*h*:2''',3'''-*j*]phenazine (tpphz) or 1,4-bis(phen-[5,6-*d*]imidazol-2-yl)benzene (bfimbz), where phen is 1,10-phenanthroline.³⁵⁴

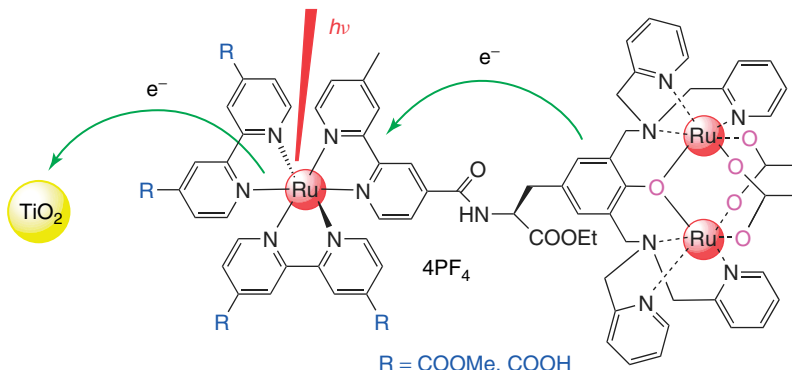


Figure 8 A schematic depicting a sensitizer employed to study intramolecular charge separation on TiO_2 thin films. Interestingly, slow intramolecular charge separation between the mononuclear Ru^{III} and dinuclear $\text{Ru}^{\text{II}}\text{-Ru}^{\text{III}}$ could be observed on the hundreds of nanoseconds timescale. (Reproduced from Ref. 353. © Wiley-VCH, 2005.)

As the BL' ligands are rigid and linear heteroaromatic entities, remote, excited-state electron injection could be examined without unwanted outer-sphere ligand–surface interactions. It was shown that when BL' was tpphz—a ligand possessing π^* energetics below the π^* orbitals of the surface-bound dc_b ligand— injection could be time resolved because of the thexi state being localized on tpphz, away from a surface-bound dc_b ligand and with less reducing power for injection. However, this slow injection was found to be not only distance- and driving force-dependent but orientation-dependent as well. When [(bpy)(dc_b)Ru^{II}(tpphz)Ru^{II}(bpy)(dc_b)]/TiO₂ was employed as the sensitizer, excited-state injection could be time resolved on the nanosecond timescale whereas with [(bpy)₂Ru^{II}(tpphz)Ru^{II}(bpy)(dc_b)]/TiO₂ it could not be, $k_{\text{inj}} > 10^8 \text{ s}^{-1}$. Using geometry optimization software, it was hypothesized that electronic coupling, and not distance from the TiO₂ surface, could explain the differences, Figure 9. The

location of the π^* orbital of the heterobinuclear complex in relation to the TiO₂ surface allowed for better electronic coupling between the sensitizer and the TiO₂ DOS even though the N_{phenazine}–Ti distance was increased by over a factor of two. Photoelectrochemical measurements supported this and indicated that an increased distance for back-electron transfer enhanced the photocurrent.

4.2 Intermolecular Regeneration

In DSSCs, redox mediators are added to the external electrolyte to shuttle charges between the two electrodes. The reduced form of the mediator must regenerate the sensitizer by electron transfer prior to recombination with the injected electron. The oxidized form of the redox mediator must be reduced at the platinum counter electrode, a process not described herein. Ideally, the redox mediators do not absorb

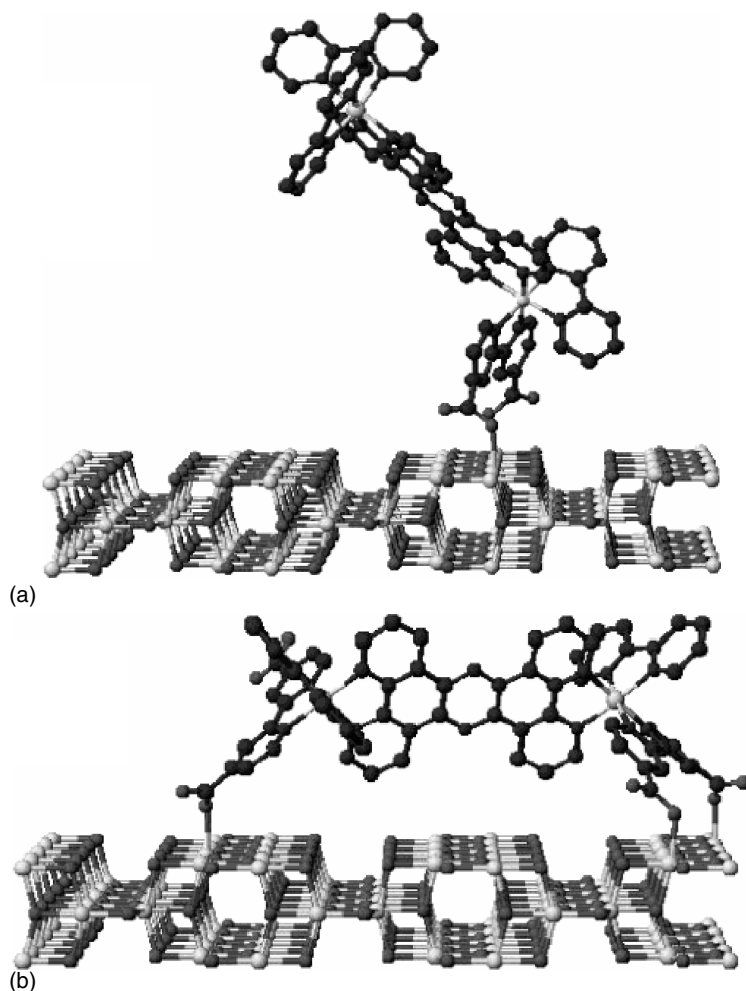


Figure 9 Density functional theory (DFT)-optimized geometry for two bimetallic Ru^{II} compounds. When a distal ligand possessed carboxylic acid functional groups capable of binding to the TiO₂ surface, the geometry of the minimized energy configuration had it binding to the surface as well (b). When the distal ligand was devoid of binding groups, it did not (a). This allowed for better electronic coupling between the sensitizer and the TiO₂ DOS, and resulted in a faster injection rate. (Reproduced from Ref. 354. © American Chemical Society, 2003.)

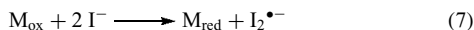
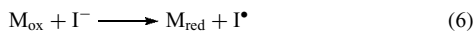
any sunlight. Although ion pairing or surface adsorption with the mediators may occur, for the organization of this article we consider these to be intermolecular electron-transfer reactions.

4.2.1 Regeneration by Iodide

Sensitizers in Solution. By far the most effective donor in DSSCs is iodide.³⁵⁵ All confirmed reports of light-to-electrical power-conversion efficiencies over 10% and state-of-the-art DSSCs require iodide.^{14–19} While many of the details of iodide oxidation at sensitized electrodes are now becoming available, it is important to point out that the aqueous redox chemistry of iodide and homogeneous reactions with transition-metal compounds have long been known.^{356–360}

A Latimer-type diagram for the aqueous redox chemistry of iodide has been previously described.²¹ Additional values and details are available in the review by Stanbury.³⁵⁶ The formal one-electron reduction potential of the iodine atom is very positive, $E^\circ(I^\bullet/I^-) = +1.33$ V vs NHE.³⁵⁶ Therefore, a potent oxidant is required to regenerate iodine atoms. However, another pathway exists, through which two iodides can be directly oxidized to $I_2^{\bullet-}$, $E^\circ(I_2^{\bullet-}/2I^-) = +1.03$ V vs NHE.³⁵⁶ On the basis of potentials alone, it is tempting to conclude that this latter pathway is the only mechanism available to oxidize sensitizers like $N3^+$, since generation of iodine atoms would be thermodynamically unfavorable by close to 250 mV.³³ However, it should be kept in mind that these reduction potentials are for standard-state conditions and that adsorption to the TiO_2 surface may have a significant effect. Walter and Elliott have provided evidence that interactions between iodide and the bpy ring may also activate iodide.³⁶¹ Furthermore, the values reported here are for aqueous electrolytes as few have been reported in acetonitrile solutions.^{362–368} There is good reason to believe that the reduction potentials will vary significantly with solvent, while only two-electron redox processes have been observed at metal electrodes.^{363,369,370}

The transition-metal redox chemistry of iodide has previously been reviewed.^{359,360} Two mechanisms have been observed, based on reactions (6) and (7):



Both are first order in transition-metal compound, M_{ox} ; while reaction (6) is first order in iodide, reaction (7) is second order in iodide. Proposed mechanisms for reaction (7), the overall third-order reaction, include I^- reacting with an $[M_{\text{ox}}, I^-]$ ion pair or M_{ox} with an $[I^-, I^-]$ ion pair. A wide variety of transition-metal compounds have been studied and linear free-energy relations for both reactions now exist. In some cases, with mild oxidants such as $M_{\text{ox}} = Os(\text{bpy})_3^{3+}$, the reverse reactions became significant.^{357–359}

Much less is known about MLCT excited-state oxidation of iodide. The reduced-sensitizer electron-injection process requires excited-state iodide oxidation followed by interfacial electron-transfer chemistry. Early studies with $[\text{Ru}^{\text{III}}(\text{bpy})_2(\text{bpy}^-)]^{2+*}$ revealed very sluggish iodide quenching, i.e., $1 \times 10^6 \text{ M}^{-1} \text{ s}^{-1}$.^{371,372} Interestingly, excited-state quenching of $[\text{Ru}^{\text{III}}(\text{bpy})_2(\text{dcb}^-)]^{2+*}$ anchored to SiO_2 appears to be much more rapid, i.e., $1 \times 10^8 \text{ M}^{-1} \text{ s}^{-1}$.³⁷³ These excited-state electron-transfer reactions have been significantly enhanced through ion pairing.^{315,317} Addition of iodide to a dichloromethane solution of $[\text{Ru}(\text{bpy})_2(\text{deeb})]^{2+}$ resulted in significant changes to the ground-state absorption. A decrease in PLI and excited-state lifetime accompanied the absorption changes consistent with both static- and dynamic-quenching mechanisms, respectively. A Benesi–Hildebrand-type analysis yielded equilibrium constants for ion pairing that were within experimental error the same as those abstracted from photoluminescence quenching data, $K_{\text{eq}} = 59\,700 \text{ M}^{-1}$. Similar behavior was observed in acetonitrile and/or with $\text{Ru}(\text{bpy})_3^{2+}$; however, roughly a two orders-of-magnitude higher iodide concentration was required. Transient absorption measurements clearly showed an electron-transfer mechanism with the appearance of $I_2^{\bullet-}$ and no evidence for iodine atom formation; thus the mechanism appeared to follow reaction (7). The cage escape yields were low, $\varphi = 0.25$, but increased to 0.50 with $\text{Ru}(\text{bpy})_3^{2+}$. Remarkably, the solid-state crystal structure of $[\text{Ru}(\text{bpy})_2(\text{deeb})]\text{I}_2$ showed both iodides associated with the carbonyl oxygens of the ester groups, Figure 10. One might have anticipated that coulombic repulsion would have resulted in a larger interionic distance than the $\sim 6 \text{ \AA}$ observed. If a similar structure exists in solution, the iodides would be well-positioned for a concerted reduction of $[\text{Ru}^{\text{III}}(\text{bpy})_2(\text{deeb}^-)]^{2+*}$ and formation of $I_2^{\bullet-}$. This is

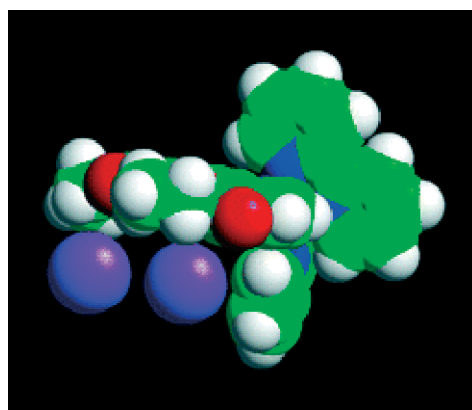


Figure 10 Space-filling representation of a single-crystal structure with two iodides associated with the deeb ligand in $[\text{Ru}(\text{bpy})_2(\text{deeb})]^{2+}$. This geometry would allow for facile reductive quenching of the excited or oxidized forms of the molecule and the proximity of a second iodide could favor $I_2^{\bullet-}$ generation as per equation (7). (Reproduced from Ref. 317. © American Chemical Society, 2006.)

an intriguing possibility as excited-state reactions that form chemical bonds are rare in all of photochemistry.

Also, recent studies in our laboratories highlighted the first evidence for iodine atoms as intermediates in the sensitized oxidation of iodide.^{374,375} In less polar acetonitrile solution containing millimolar concentrations of iodide, careful analyses of the time-resolved absorbance and photoluminescence kinetic data revealed that formation of reduced Ru^{II}(bpz⁻) (bpz)(deeb)⁺ occurred with a second-order rate constant of $(6.6 \pm 0.3) \times 10^{10} \text{ M}^{-1} \text{ s}^{-1}$ while that for the formation of I₂^{•-} was $(2.4 \pm 0.2) \times 10^{10} \text{ M}^{-1} \text{ s}^{-1}$. The lag in I₂^{•-} was due to the slower reaction of I[•], formed via reaction (6), with an I⁻ to form I₂^{•-}. Reaction of the iodine atom with iodide to make an I-I bond lowers the free energy stored in the charge-separated state by 110 mV.^{9,42} Charge recombination to yield ground-state products, Ru⁺ + I₂^{•-} → Ru^{II} + 2I⁻, is highly thermodynamically favored ($-\Delta G^\circ = 1.64 \text{ eV}$) and occurs with a rate constant of $2.1 \times 10^{10} \text{ M}^{-1} \text{ s}^{-1}$, almost ten times larger than the I₂^{•-} disproportionation rate constant. Unwanted charge recombination to I₂^{•-} has previously been proposed to lower the efficiency of DSSCs,⁵ and these data show that it can be a very fast reaction.

Sensitizer/TiO₂ Interfaces. Fitzmaurice and Frei reported the first study of the heterogeneous reduction of Ru^{III}-polypyridyl compounds by iodide.³⁷⁶ Photoinduced electron injection into colloidal TiO₂ from [Ru^{III}(dcb)₂(dcb⁻)]^{2+*} was followed by oxidation of iodide in acidic aqueous solution. From the pseudo-first-order transient kinetics in 0.5 to 100 mM KI, a second-order rate constant for iodide oxidation of $\sim 2.5 \times 10^9 \text{ M}^{-1} \text{ s}^{-1}$ was abstracted. The transient absorption spectra were ascribed to be most consistent with formation of ion pairs.

Since that time, there have been a number of studies aimed at abstracting the rate at which the Ru^{II} form of the sensitizer is regenerated. Such experiments were usually performed by monitoring the recovery of the MLCT absorption after pulsed-laser excitation at wavelengths where the iodide oxidation products did not appreciably absorb light. While this has proven to be a reasonable method, little information regarding the mechanism(s) of iodide oxidation is obtained. Most studies of this type were performed with N3/TiO₂. At low iodide concentrations, the regeneration rate was found to be first order in iodide. At higher iodide concentrations, a static component was often observed. Under the 0.5 M iodide concentration of a DSSC, regeneration is often stated to be complete within 10 ns.^{20,35} The rate constant for regeneration of the oxidized sensitizer, Ru^{III}(bpy)₂(dcb)/SnO₂, by iodide was determined to be $1.2 \times 10^{10} \text{ M}^{-1} \text{ s}^{-1}$. Durrant and coworkers have recently provided evidence that the regeneration rate is dependent on the $E^\circ(\text{Ru}^{\text{III}/\text{II}})$ of the sensitizer. With Ru(dcb)₂(CN)₂/TiO₂ thin films, an intermediate was observed and assigned to a [Ru^{III}, I⁻] ion pair.³⁷⁷ Reaction of this with a second iodide was proposed to yield I₂^{•-}.

The reactivity of iodide with N719^{+/TiO₂(e⁻)}

 increased in the presence of Li⁺ and other cations with large charge-to-radius ratios.³⁷⁸ It was noted that the half-life for sensitizer regeneration abruptly shortened when the concentration of Li⁺ was increased to between 10 and 50 mM. The point of zero ζ -potential (PZZP) was determined to occur at 3 mM Li⁺, a concentration slightly less than that required for the abrupt change in half-life. Also, by titration of iodide to positively charged TiO₂ particles in the presence of Mg²⁺, the experimental data suggested that iodide adsorbed on TiO₂ within the Helmholtz layer even in the presence of sensitizers. It was concluded that the abrupt change in sensitizer regeneration occurred because of ion-pairing of iodide anions with the surface or sensitizer resulting in an increased occurrence of the faster termolecular reaction (7).

4.2.2 Regeneration by Donors Other Than Iodide

Evaluation of the reduction potentials for iodide oxidation reveals the significant problem with the I₃⁻/I⁻ redox mediator required for champion DSSCs. Iodide is oxidized to the iodine atom at +1.33 V vs NHE and I₃⁻ is reduced at +0.04 V. *Thus roughly a volt of free energy is lost with this redox mediator!* While these are aqueous reduction potentials under standard-state conditions, there are reasons to believe that the losses are less significant in acetonitrile electrolytes. Another issue with the I₃⁻/I⁻ redox mediator is that a facile reduction of I₃⁻ at the counter electrode in DSSCs is required so as to minimize the voltage loss. Platinum metal has a large exchange current density and transfer coefficient for this reaction, but it is expensive.³⁷⁹ Electrode materials like graphite do not perform as well, and the corrosive nature of the electrolyte toward less-expensive metals like silver or copper precludes their use.³⁷⁹ In addition, I₂ has an appreciable vapor pressure such that extra care must be taken to ensure a thoroughly and tightly sealed solar cell.³⁸⁰ Therefore, there is ample reason to identify alternative redox mediators for DSSCs.

Historically, one-electron-transfer, outer-sphere donors that have realized limited success in DSSCs include phenothiazine,³⁴³ ferrocene,³⁸⁰ hydroquinone,^{381,382} bromide,³⁸² SeCN⁻, and SCN⁻.³⁸³

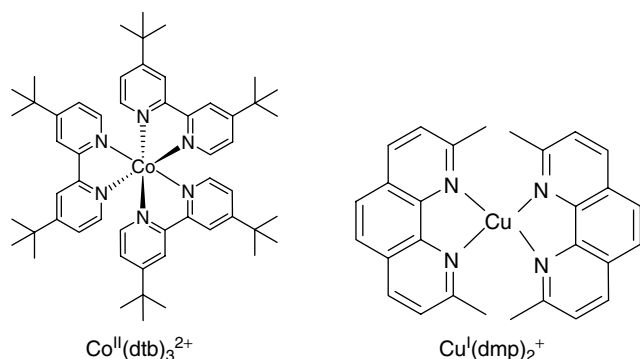
Recently, when SeCN⁻ and SCN⁻-based redox mediators were employed in DSSCs based on mesoporous, nanocrystalline SnO₂ electrodes sensitized with [Ru(deeb)(bpy)]²⁺, the photocurrent was similar to that obtained using the I⁻/I₃⁻ redox mediator.³³⁴ In addition, Wang and Grätzel observed more promising behavior with the (SeCN)₂/SeCN⁻ pseudohalide redox mediator in the 1-ethyl-3-methylimidazolium selenocyanate ionic liquid with added K(SeCN)₃.³⁸⁴ Although this ionic liquid was found to be 35 times less viscous than the more traditional 1-propyl-3-methylimidazolium iodide ionic liquid, it was over 28 times more conductive at room temperature and could solubilize large amounts of (SeCN)₂/SeCN⁻. By transient

absorption spectroscopy, it was shown that SeCN^- and the analogous ionic-liquid-containing SCN^- could rapidly regenerate the sensitizer. It was also shown that the maximum IPCE was close to unity and the power-conversion efficiency was 7.5%. Notwithstanding, the kinetics for iodide oxidation after excited-state injection from $\text{N}_3^*/\text{TiO}_2$ in acetonitrile were found to be more rapid than that for the oxidation of SeCN^- .³⁸³

As for solution-based inorganic donors, octahedral Co^{II} diimine compounds have proven to be effective for sensitizer regeneration. One-electron-transfer, outer-sphere $\text{Co}^{III/II}$ redox mediators have led to promising light-to-electrical power-conversion efficiencies in DSSCs. The $\text{Co}^{III/II}$ self-exchange rate constants are known to be particularly sluggish, behavior that is reasonably understood by the d^6/d^7 electronic configurations that give rise to large inner-sphere reorganization energies.³⁸⁵ It is possible that these same electronic factors are responsible for the slow rates of the $\text{TiO}_2(\text{e}^-) + \text{Co}^{III}$ recombination reaction and the reasonable photocurrent efficiencies that have been reported.

The first studies of cobalt mediators were performed by Grätzel and coworkers.³⁸⁶ A DSSC based on the $[\text{Co}^{III/II}(\text{dbbip})_2]^{3+/2+}$ redox couple, where dbbip is 2,6-bis(1'-butylbenzimidazol-2'-yl)pyridine, resulted in impressive photovoltaic performance and an exchange current density of $7 \times 10^{-6} \text{ A cm}^{-2}$ in an acetonitrile/ethylene carbonate (40 : 60, v/v) electrolyte at a fluorine-doped tin oxide (FTO) electrode.³⁷⁹ With *cis*-Ru(4-methyl-4'-hexadecyl-bpy)(dcb)(NCS)₂/ TiO_2 in an electrolyte with a 1 : 9 stoichiometric ratio of Co^{III} : Co^{II} , a maximum IPCE of >65% was realized, and under reduced light conditions, i.e., <0.1 suns, a power-conversion efficiency of 5.2% was also obtained.³⁸⁶ The use of a neutral sensitizer was found to be necessary in order to attenuate the adsorption of cationic redox species onto TiO_2 . When $\text{Co}^{II}(\text{dbbip})_2^{2+}$ was added above a threshold of 10 mM, the second-order rate constant for regeneration was $2.9 \times 10^6 \text{ M}^{-1} \text{ s}^{-1}$, approximately an order-of-magnitude smaller than values reported for NaI. However, at 100 mM the pseudo-first-order rate constants were similar to those found with the same concentration of iodide.³⁷⁸ In support of previous work, the i_{sc} was found to be dependent on the counterion of the solution $\text{Co}^{III/II}$ redox mediator, where the perchlorate salts resulted in the highest efficiencies.³⁸⁷ Utilizing mediators where the $E^\circ(\text{Co}^{III/II})$ varied over 190 mV, a similar 180-mV variation in V_{oc} was realized. The largest V_{oc} recorded was 660 mV accompanied by a 7.9% power-conversion efficiency, again under illumination conditions of 0.1 sun.

A family of cobalt redox couples employing derivatives of bpy, phen, and tpy ligands were studied in DSSCs.³⁸⁸ The highest efficiencies were reported for the $[\text{Co}^{III/II}(\text{dtb})_3]^{3+/2+}$ perchlorate redox mediator, where dtb is 4,4'-di-*tert*-butyl-bpy (Scheme 5), and were within 80% of that of a comparable I_3^-/I^- -mediated DSSC. However, in contrast to the I_3^-/I^- redox mediator, addition of Li^+ to the cells



Scheme 5 The chemical structures of the reduced versions of the most efficient transition-metal-based redox mediators: $[\text{Co}^{III/II}(\text{dtb})_3]^{3+/2+}$ and $[\text{Cu}^{II/I}(\text{dmp})_2]^{2+/+}$

increased not only the i_{sc} but the V_{oc} as well! This was proposed to be due to a decrease in the recombination rate of $\text{TiO}_2(\text{e}^-)$ s and Co^{III} , most likely from an increase in overpotential for reduction of $[\text{Co}^{III}(\text{dtb})_3]^{3+}$ at the conductive support. Cyclic voltammograms with platinum electrodes revealed sluggish interfacial, $\text{Co}^{III/II}$ electron-transfer kinetics relative to carbon and gold. Although gold was optimal in DSSCs, FTO electrodes coated with graphite nanoparticles initially outperformed those employing platinum; however, the carbon-coated FTO electrodes degraded with time. Nevertheless, the initial response was encouraging and shows promise for replacing platinum with less-expensive, carbon- and/or FTO-based materials.

It has recently been shown that upon introduction of LiClO_4 to DSSCs, the lifetime of the $\text{TiO}_2(\text{e}^-)$ s^{390,391} increased for cobalt-based redox couples, whereas it decreased for the I_3^-/I^- redox mediator. This was rationalized as being due to a cation screening effect, where the local concentration of cationic cobalt-based redox couples decreased near the TiO_2 surface when cationic Li^+ was present.^{390,391}

Although large reorganization energies and slow-electron transfer kinetics for cobalt-based redox couples are advantageous as they attenuate the unwanted, recombination reaction, $\text{TiO}_2(\text{e}^-) + \text{Co}^{III} \rightarrow \text{TiO}_2 + \text{Co}^{II}$, these characteristics are undesirable with respect to sensitizer regeneration, $\text{S}^+/\text{TiO}_2(\text{e}^-) + \text{Co}^{II} \rightarrow \text{S}/\text{TiO}_2(\text{e}^-) + \text{Co}^{III}$. Rapid sensitizer regeneration and sluggish recombination kinetics are traits that make the I_3^-/I^- redox mediator optimal. Use of a second mediator in conjunction with $[\text{Co}^{III/II}(\text{dtb})_3]^{3+/2+}$ was proposed to overcome slow regeneration while maintaining slow recombination.³⁹² Both PTZ and ferrocene were employed in DSSCs because of their small reorganization energies, rapid electron-transfer kinetics, and reduction potentials intermediate between that of $[\text{Co}^{III/II}(\text{dtb})_3]^{3+/2+}$ and the oxidized sensitizer. The oxidized sensitizer was found to recover in the presence of 0.1-M donor in the order ferrocene > PTZ > $\text{Co}(\text{dtb})_3^{2+}$ > no donor. Chronocoulometry of 1 : 2 molar mixtures of PTZ : Co^{II} with FTO electrodes displayed a turnover 45% faster than that for ferrocene/ Co^{II} mixtures. A

maximum IPCE of >80% was achieved. Under illumination conditions of 0.1 sun, the V_{oc} was larger than that for an equivalent DSSC employing the LiI/I₂ redox system (0.3/0.03 M). However, the power-conversion efficiency was smaller due to mass-transport limitations of the bulky cobalt redox mediator that displayed an order-of-magnitude slower diffusion coefficient through a TiO₂ film than did I₃⁻.³⁹³ Ru polypyridyl sensitizers with pendant pyrrole or pyrrolidine groups gave superior photocurrents in the presence of [Co^{III/II}(dtb)₃]^{3+/2+} than in the presence of I⁻/I₃⁻ redox mediator over the entire absorption spectrum.^{169,394} Addition of Fe(dmb)₃²⁺ as a co-mediator resulted in a maximum IPCE of >80% for the best pyrrole-containing sensitizer.¹⁶⁹

The exchange current density for [Co^{III}(dtb)₃]³⁺ reduction was greatly enhanced when *cis*-Os(dcb)₂Cl₂ was anchored to FTO.³⁹⁵ When employed as a counter electrode with N3/TiO₂ in a DSSC, the i_{sc} and V_{oc} were only slightly attenuated relative to a gold counter electrode and, using a three electrode measurement, the potential of the Os(dcb)₂Cl₂/FTO counter electrode was nearly the same under open-circuit conditions.

Cu^I has a d¹⁰ electronic configuration and compounds like Cu(LL)₂⁺ usually adopt a tetrahedral geometry in solution and in the solid state. The Cu^{II} form is subject to a Jahn–Teller distortion that often manifests itself in a geometry with more coplanar diimine ligands, i.e., a flattening, and a fifth ligand from solvent or a counterion axially ligated. It is possible to photoinduce these structural changes, and they have been characterized by time-resolved X-ray techniques.²³⁴ Therefore, like the Co^{III/II} redox mediators, Cu^{II/I} redox chemistry is accompanied by a large inner-sphere reorganization energy change and slow self-exchange rate constants, and has demonstrated some modest success as mediators in DSSCs. For example, Cu^I–diimine compounds have been studied in DSSCs.³⁹⁶ The best-performing mediators produced a maximum IPCE of ~40% and yielded a higher V_{oc} than the I₃⁻/I⁻ redox couple under the same experimental conditions. This was attributed to a decreased dark current due to the large reorganization energy of the Cu^{II/I} redox couple.

Unfortunately, the large reorganization energies for Cu^{II/I} redox mediators suffer the same pitfalls as their Co^{III/II} counterparts, i.e., slow sensitizer regeneration. Thus, a Cu^I compound with a distorted tetrahedral geometry was employed in order to help reduce the large reorganization energy.³⁸⁹ When [Cu^{II/I}(dmp)₂]^{2+/+} (Scheme 5) was employed as the redox mediator, where dmp is 2,9-dimethyl-phen, a light-to-electrical power-conversion efficiency of 2.2% under 0.2-sun illumination was obtained with N719/TiO₂ DSSCs. For a similar reason as for the Cu^I sensitizers, the methyl groups were employed to prevent planarization of the dmp ligands, which manifests itself in a positive shift in $E^\circ(\text{Cu}^{\text{II}/\text{I}})$. Significantly, a higher V_{oc} was realized with the Cu^{II/I} mediator as compared with I₃⁻/I⁻ under the same experimental conditions.

5 SENSITIZATION AT THE POWER POINT

The influence of the TiO₂(e⁻) concentration on the individual steps of the sensitization cycle, shown in Scheme 1, is generally unknown and represents an active area of investigation. Recall that the sensitization cycle consists of (i) light absorption, (ii) excited-state injection, and (iii) sensitizer regeneration/recombination. Recall that at the PP under 1-sun illumination, approximately 10 injected electrons reside in each nanocrystallite. Furthermore, aside from these Faradaic charge-transfer reactions of the sensitization cycle, there exist non-Faradaic processes that are known to accompany interfacial electron transfer. For example, it has been recognized for some time that Li⁺ reversibly intercalates or binds to the surface of reduced anatase TiO₂ nanocrystallites.^{21,378,397–399} Similar, and possibly related, is the cursorily understood phenomenon where prolonged ultraviolet light soaking of an assembled DSSC yields increased power-conversion efficiencies.^{400–402} Recently, it has been shown that even visible-light soaking or forward bias in the absence of Li⁺ induces what are thought to be electron transport levels that enhance DSSC performance.^{403,404} In the presence of Li⁺, intercalation into the TiO₂ lattice may impede this process, and thus it was tacitly presumed that proton intercalation was vital to the behavior.

Recent results from our laboratories suggest new directions for fundamental research and raise the question of what the term “regeneration” actually means. These new results are best understood with an example, [Ru(dt_b)₂(dc_b)](PF₆)₂. Figure 11(a) shows the absorption and photoluminescence spectra of a Ru(dt_b)₂(dc_b)/TiO₂ thin film immersed in 0.1 M LiClO₄ acetonitrile and in neat acetonitrile. In the presence of Li⁺, both maxima red-shifted and their intensity decreased relative to neat acetonitrile. The significant quenching of the photoluminescence intensity results from enhanced excited-state electron injection into TiO₂ as previously described herein.⁴⁰⁵

Pulsed-light excitation of Ru(dt_b)₂(dc_b)/TiO₂ in 0.1/0.5 M LiClO₄/TBAI acetonitrile electrolyte resulted in the microsecond absorption difference spectrum, Figure 11(b). Under such conditions, one would expect to observe a TiO₂(e⁻) and I₃⁻. The absorption features characteristic of I₃⁻ ($\lambda < 420$ nm) and TiO₂(e⁻)s ($\lambda > 560$ nm) were indeed observed. However, the absorption band centered at 460 nm and the bleach at 510 nm could not be assigned to any conceivable electron-transfer products.

Spectral modeling indicated that the absorption features at 460 and 510 nm resulted from [Ru(dt_b)₂(dc_b)]²⁺ sensitizers that were present in an environment significantly different from that which had been initially photoexcited. Spectral modeling indicated that the sensitizers that were initially photoexcited had an absorption spectrum shown in red while immediately after regeneration their spectrum was that shown in black, Figure 11(a). Overlaid on the

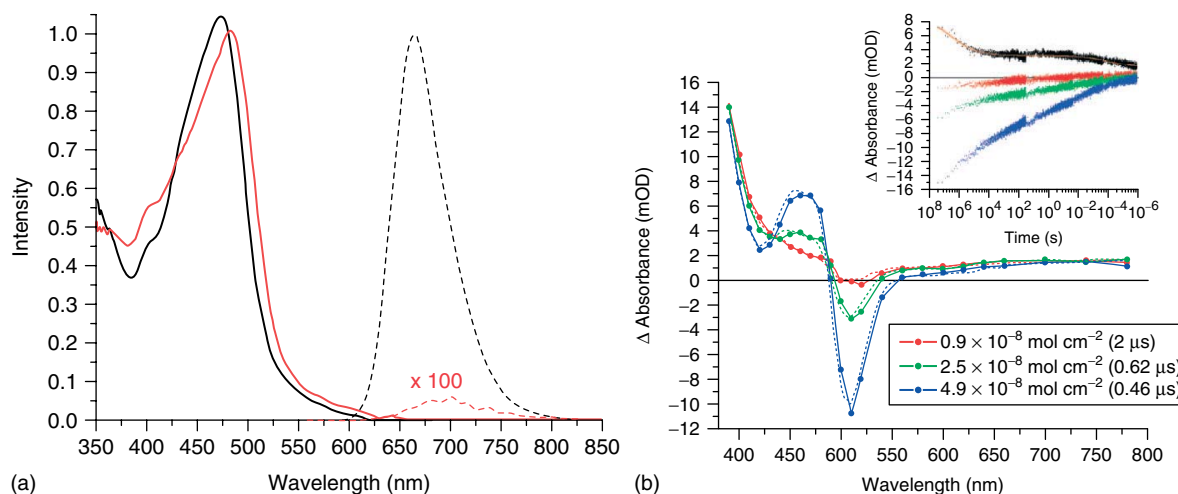


Figure 11 (a) Absorption and photoluminescence spectra of $\text{Ru}(\text{dtBz})_2(\text{dcb})/\text{TiO}_2$ in 0.1 M LiClO_4 acetonitrile electrolyte (—/- -) and in neat acetonitrile after removal of the LiClO_4 by 10 neat acetonitrile washings (—/- -). (b) Transient absorption difference spectra for three $\text{Ru}(\text{dtBz})_2(\text{dcb})/\text{TiO}_2$ thin films at the indicated surface coverages and delay times measured after pulsed 532-nm excitation in 0.1/0.5 M $\text{LiClO}_4/\text{TBAI}$ acetonitrile electrolyte. Overlaid are simulations of the data represented by dashed lines. Inset: Time-resolved, single-wavelength absorption difference spectra measured at 510 nm for each surface coverage—corresponding to cation transfer—and a single difference spectrum measured at 433 nm (—)—corresponding to I_3^- loss—due to $\text{TiO}_2(\text{e}^-) + \text{I}_3^-$ recombination. (Reproduced from Ref. 108. © American Chemical Society, 2008.)

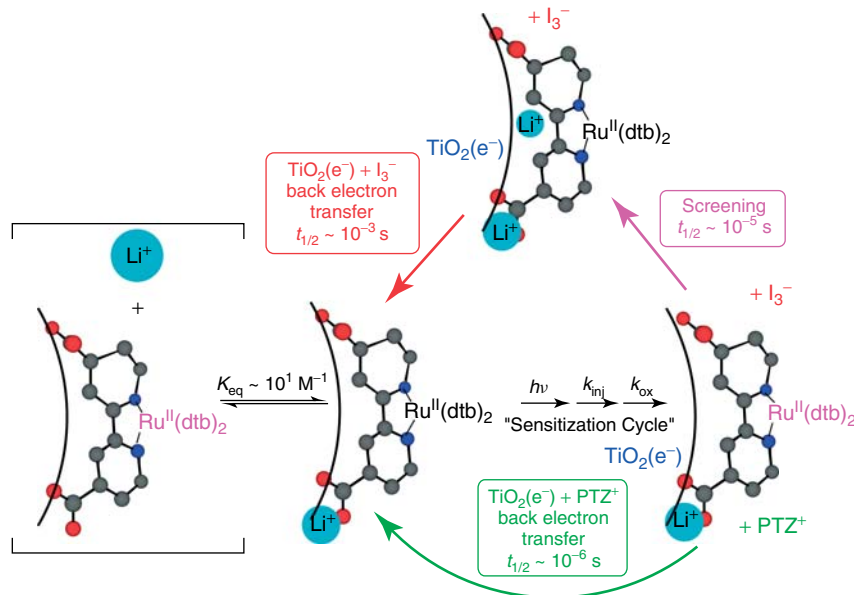
data in Figure 11(b) are simulations based on the weighted addition of (i) the absorption spectrum of I_3^- , (ii) the $\text{TiO}_2(\text{e}^-)$ absorption spectrum, and (iii) the difference in the absorption spectra of $\text{Ru}(\text{dtBz})_2(\text{dcb})/\text{TiO}_2$, in the absence minus the presence of Li^+ . Similar sensitizer absorption features were observed when PTZ was used in the place of iodide. The measured spectral responses are reminiscent of those observed by electroabsorption (Stark) spectroscopy, as described above.^{252,253} While Stark effects have been observed in semiconductor nanocrystallites^{406–408} and Ru^{II} polypyridyl compounds,^{75,249–251} they were not expected in DSSCs because of the high dielectric constant of anatase TiO_2 ($\epsilon = 7–50$)⁴⁰⁹ and acetonitrile ($\epsilon = 37.5$)⁴¹⁰ and the high-ionic-strength electrolytes typically employed.^{12,301,411–425}

Recently, Hagfeldt, Boschloo, and colleagues reported similar Stark-like features in the spectroelectrochemical reduction and photoinduced absorption spectra of perylene-sensitized TiO_2 thin-film electrodes.⁴²⁶ A unique aspect of these perylene sensitizers was that they were neutral compounds that did not contain ionizable functional groups. Therefore, the sensitized thin film was not intentionally exposed to protons or Lewis-acidic cations and the origin of the effect was unlikely solely due to cations.

Results from studies by Staniszewski,¹⁰⁸ Durrant,⁴²⁷ Kamat,³⁷³ and Hagfeldt,⁴²⁶ now clearly indicate that the absorption spectra of surface-anchored molecular sensitizers are influenced by electrons injected into the metal-oxide nanoparticle. After fast excited-state electron injection into TiO_2 and regeneration by iodide, sensitizers were present in an environment distinctly different from that prior to light absorption. Significantly, the newly generated sensitizers

were in an environment that is known to be less favorable for excited-state electron injection.⁴⁰⁵ The sensitization cycle shown in Scheme 1 needs to be modified; the oxidized Ru^{III} sensitizer may be reduced to Ru^{II} on a nanosecond timescale; however, it is not brought back to the environment prior to light absorption, until slow ($\mu\text{s}-\text{ms}$) cation transfer or back-electron transfer via interfacial charge recombination as $\text{TiO}_2(\text{e}^-) + \text{I}_3^-$ has occurred. By further inspection, one realizes that the overall sensitization cycle is merely *redox* regenerative. In other words, the sensitizer does return to its initial formal oxidation state; however, all interfacial-related processes have not reset.

A working hypothesis emerged from the studies, which is consistent with all experimental data. This hypothesis begins with the assertion that electrons injected into TiO_2 immediately produce an electric field. This field extends roughly normal to the semiconductor–sensitizer interface and induces a Stark effect on the sensitizer absorption spectrum. A kinetic competition then exists between ionic reorganization to shield this field, termed screening,^{411,416,423} and interfacial charge recombination, magenta versus green arrows in Scheme 6. With PTZ donors, recombination was fast and screening was not clearly observed. On the other hand, with iodide donors, screening was observed prior to sluggish interfacial charge recombination, i.e. $\text{TiO}_2(\text{e}^-) + \text{I}_3^-$. To our knowledge, this was the first spectroscopic observation¹⁰⁸ and elucidation of an ionic screening process of the electric fields emanating from sensitized TiO_2 nanocrystallites. Although not shown in Scheme 6, the injected electron is found to perturb the absorption spectrum of multiple sensitizers, and not simply the sensitizer that had undergone photoinduced



Scheme 6 Solvated Li^+ in adsorption equilibrium with sensitized TiO_2 nanocrystallites. Pulsed-light excitation in the presence of electron donors results in the sensitization cycle (see Scheme 1) and yields a Ru^{II} sensitizer whose absorption spectrum is perturbed by the injected electron, behavior that is attributed to the Stark effect. With phenothiazine donors, interfacial charge recombination directly yields ground-state products. With iodide donors, charge recombination was slower, and a new dynamic process attributed to ionic reorganization, or “screening,” was observed spectroscopically prior to interfacial electron transfer. (Reproduced from Ref. 36. © American Chemical Society, 2010.)

electron injection. By performing studies employing sensitized TiO_2 in the absence of external donors and on TiO_2 films co-bound with two compounds, one that served as a sensitizer and the other a reporter molecule for the Stark effect, support for the hypothesis that an injected electron influences many sensitizers was garnered.

The Stark effect may influence all of the processes outlined above related to i_{sc} and the sensitization cycle in DSSCs. Photogenerated $\text{TiO}_2(\text{e}^-)$ s that have yet to be collected in the external circuit clearly influence the absorbance spectrum of other sensitizers. The measured blue shifts and decreases of the MLCT absorption are clearly undesirable for solar light harvesting. However, for sensitizers like N3, the effect is quite small and would lead to an insignificant, $<0.001\%$ decrease in LHE at the PP under 1 sun, AM1.5 irradiation. The Stark effect yields a Ru^{II} absorption spectrum that is known to inject poorly when photoexcited.⁴⁰⁵ Excited-state injection yields are also known to decrease with excitation irradiance, yet our understanding of the origin of this behavior is lacking.^{405,428} The observations discussed here suggest that coulombic repulsion by injected electrons may be responsible. Durrant and coworkers have in fact shown that by increasing the $\text{TiO}_2(\text{e}^-)$ concentration, the half-life for recombination to the oxidized sensitizers increased by up to seven orders of magnitude.⁴²⁹ On the other hand, *complete shielding* by the supporting electrolyte would be expected to facilitate longer lived charge-separated states between the $\text{TiO}_2(\text{e}^-)$ s and oxidized sensitizers.

In agreement with previous work, the overall timescales for complete charge recombination of the injected $\text{TiO}_2(\text{e}^-)$ were microseconds to PTZ^+ ,³⁴³ tens of microseconds to milliseconds to the oxidized sensitizer,^{343,405,429} and hundreds of milliseconds to I_3^- .^{377,430,431} The electric field at the TiO_2 interface may also help clarify why recombination to cationic one-electron acceptors, like PTZ^+ or the oxidized sensitizer, is much more rapid than to anionic triiodide. The few orders-of-magnitude slower recombination kinetics seen with anionic triiodide may result from coulombic repulsion between $\text{TiO}_2(\text{e}^-)$ s and I_3^- . Synonymous to increasing the width of the space-charge layer in solid-state p-n junction solar cells, increasing the Debye length for screening should aid in the generation of even further spatially separated and longer lived anionic species, i.e., $\text{TiO}_2(\text{e}^-)$ s and I_3^- . Although speculative, the lethargic pace of this additional screening step may help explain why iodide is far superior to most other donors for redox mediation in DSSCs.

6 CONCLUSIONS

Almost two decades have passed since the celebrated Grätzel and O’Regan paper appeared in Nature. This article demonstrates the tremendous progress that has since been made toward developing a molecular-level understanding of charge-transfer processes at sensitized TiO_2 interfaces. The timescales and dynamics for excited-state electron

injection into TiO₂ have been quantified precisely under many experimental conditions. Regeneration of the photo-oxidized sensitizer by a variety of outer-sphere electron donors, including iodide, has also been quantified in some detail. Much less progress has been made toward our understanding of the unwanted, charge-recombination to the oxidized form of the redox mediators. This is due, at least in part, to the inefficiency of the process which makes characterization difficult. Fundamental data on the identity of the acceptor(s) as well as the reduction mechanism(s) are still lacking. Given the keen interest in these reactions, rapid progress is expected. Understanding the mechanism for charge recombination may ultimately enable the use of alternative redox mediators that are better optimized for light-to-electrical power conversion. In addition, it may prove possible to drive redox reactions to produce useful fuels that can be utilized for power when the sun is down. Inorganic chemistry has played a central role in the development of state-of-the-art, 11+% efficient dye-sensitized solar cells. There exist exciting opportunities for inorganic chemists in the development of future-generation mesoscopic semiconductor thin films, sensitizer coordination chemistry, and redox mediators.

7 ACKNOWLEDGMENTS

This work was funded by the Division of Chemical Sciences, Geosciences, and Biosciences, Office of Basic Energy Sciences of the U.S. Department of Energy through Grant DE-DE-FC02-96ER14662. S. A. acknowledges a Johns Hopkins University Greer graduate student fellowship.

8 END NOTES

^a Analogs where one or more of the carboxylic acid groups have been deprotonated, e.g., the dianion salt of N719 with tetra-*n*-butylammonium (TBA⁺) counterions—N719,³⁴ where three covalently joined 4-carboxylic acid-pyridine substituents were employed,⁵⁰ or where hydrophobic groups were introduced in the 4 and 4' positions of one of the dcbs ligands to increase stability in the presence of water.

^b We emphasize that while the scheme and this abbreviation imply that the reduction is metal based, it may in fact be ligand localized, i.e., on a dcbs.

9 RELATED ARTICLES

Dye-Sensitized Solar Cells: an Overview.

10 ABBREVIATIONS AND ACRONYMS

TBA⁺ = tetra-*n*-butylammonium; bfimbz = 1,4-bis(phen-[5,6-*d*]imidazol-2-yl)benzene; bpz = bipyrazine; DFT = density functional theory; DSSCs = dye-sensitized solar cells; EXAFS = extended X-ray absorption fine spectroscopy; FTO = fluorine-doped tin oxide; HOMO = highest occupied molecular orbital; IPCE = incident photon-to-current efficiency; IVCT = Intervalence charge-transfer; LF = ligand-field; LIESST = light-induced excited spin-state trapping; LLCT = ligand-to-ligand charge-transfer; LMCT = ligand-to-metal charge transfer LPCT = ligand-to-particle charge-transfer MLCT = metal-to-ligand charge-transfer; MPCT = metal-to-particle charge transfer; NREL = National Renewable Energy Laboratory; phen = phenanthroline; PP = power point; PTZ = phenothiazine; PZZP = point of zero ζ -potential; THz-TD = terahertz time-domain; tpphz = tetracyrido [3,2-*a* : 2', 3'-*c* : 3'', 2''-*h* : 2''', 3'''-*j*] phenazine; TRIR = time-resolved infrared; XANES = X-ray absorption near-edge structure *LHE* = light – harvesting efficiency.

11 FURTHER READING

H. Wolpher, S. Sinha, J. Pan, A. Johansson, M. J. Lundqvist, P. Persson, R. Lomoth, J. Bergquist, L. Sun, V. Sundström, B. Åkermark, and T. Polivka, *Inorg. Chem.*, 2007, **46**, 638.

12 REFERENCES

1. M. I. Hoffert, K. Caldeira, A. K. Jain, E. F. Haites, L. D. D. Harvey, S. D. Potter, M. E. Schlesinger, S. H. Schneider, R. G. Watts, T. M. L. Wigley, and D. J. Wuebbles, *Nature*, 1998, **395**, 881.
2. K. Caldeira, A. K. Jain, and M. I. Hoffert, *Science*, 2003, **299**, 2052.
3. United States Department of Energy, Report of the Basic Energy Sciences Workshop on Solar Energy Utilization, in ‘Basic Research Needs for Solar Energy Utilization’, Department of Energy, Washington, DC, 2005.
4. United States Department of Energy Energy Information Administration. <http://www.eia.doe.gov/>. (accessed May 2009).
5. D. Lüthi, M. Le Floch, B. Bereiter, T. Blunier, J.-M. Barnola, U. Siegenthaler, D. Raynaud, J. Jouzel, H. Fischer, K. Kawamura, and T. F. Stocker, *Nature*, 2008, **453**, 379.
6. L. Loulergue, A. Schilt, R. Spahni, V. Masson-Delmotte, T. Blunier, B. Lemieux, J.-M. Barnola, D. Raynaud, T. F. Stocker, and J. Chappellaz, *Nature*, 2008, **453**, 383.
7. N. S. Lewis and D. G. Nocera, *Proc. Natl. Acad. Sci. U. S. A.*, 2006, **103**, 15729.
8. J. R. Petit, J. Jouzel, D. Raynaud, N. I. Barkov, J. M. Barnola, I. Basile, M. Bender, J. Chappellaz, M. Davis, G. Delaygue,

- M. Delmotte, V. M. Kotlyakov, M. Legrand, V. Y. Lipenkov, C. Lorius, L. Pepin, C. Ritz, E. Saltzman, and M. Stievenard, *Nature*, 1999, **399**, 429.
9. U. Siegenthaler, T. F. Stocker, E. Monnin, D. Lüthi, J. Schwander, B. Stauffer, D. Raynaud, J.-M. Barnola, H. Fischer, V. Masson-Delmotte, and J. Jouzel, *Science*, 2005, **310**, 1313.
 10. N. S. Lewis, ‘Powering the Planet - Global Energy Perspective’, <http://nsl.caltech.edu/energy.html>. (accessed May 2009).
 11. United Nations, World Energy Assessment Report: Energy and the Challenge of Sustainability, in ‘United Nations Development Program’, United Nations, New York, 2003.
 12. B. O'Regan, J. Moser, M. Anderson, and M. Grätzel, *J. Phys. Chem.*, 1990, **94**, 8720.
 13. B. O'Regan and M. Grätzel, *Nature*, 1991, **353**, 737.
 14. S. Ito, M. K. Nazeeruddin, P. Liska, P. Comte, R. Charvet, P. Péchy, M. Jirousek, A. Kay, S. M. Zakeeruddin, and M. Grätzel, *Prog. Photovolt. Res. Appl.*, 2006, **14**, 589.
 15. A. G. Martin, E. Keith, H. Yoshihiro, and W. Wilhelm, *Prog. Photovolt. Res. Appl.*, 2009, **17**, 85.
 16. F. Gao, Y. Wang, D. Shi, J. Zhang, M. Wang, X. Jing, R. Humphry-Baker, P. Wang, S. M. Zakeeruddin, and M. Grätzel, *J. Am. Chem. Soc.*, 2008, **130**, 10720.
 17. Y. Chiba, A. Islam, Y. Watanabe, R. Komiya, N. Koide, and L. Han, *Jpn. J. Appl. Phys., Part 2*, 2006, **45**, L638.
 18. J. M. Kroon, N. J. Bakker, H. J. P. Smit, P. Liska, K. R. Thampi, P. Wang, S. M. Zakeeruddin, M. Grätzel, A. Hinsch, S. Hore, U. Würfel, R. Sastrawan, J. R. Durrant, E. Palomares, H. Pettersson, T. Gruszecki, J. Walter, K. Skupien, and G. E. Tulloch, *Prog. Photovolt. Res. Appl.*, 2007, **15**, 1.
 19. Y. Cao, Y. Bai, Q. Yu, Y. Cheng, S. Liu, D. Shi, F. Gao, and P. Wang, *J. Phys. Chem. C*, 2009, **113**, 6290.
 20. A. Hagfeldt and M. Grätzel, *Acc. Chem. Res.*, 2000, **33**, 269.
 21. S. Ardo and G. J. Meyer, *Chem. Soc. Rev.*, 2009, **38**, 115.
 22. G. J. Meyer, *Inorg. Chem.*, 2005, **44**, 6852.
 23. M. Grätzel, *Inorg. Chem.*, 2005, **44**, 6841.
 24. T. J. Meyer, *Pure Appl. Chem.*, 1986, **58**, 1193.
 25. P. Chen and T. J. Meyer, *Chem. Rev.*, 1998, **98**, 1439.
 26. T. J. Meyer, *Prog. Inorg. Chem.*, 1983, **30**, 389.
 27. T. J. Meyer, *Acc. Chem. Res.*, 1989, **22**, 163.
 28. A. Juris, V. Balzani, F. Barigelletti, S. Campagna, P. Belser, and A. von Zelewsky, *Coord. Chem. Rev.*, 1988, **84**, 85.
 29. S. I. Gorelsky, E. S. Dodsworth, A. B. P. Lever, and A. A. Vlcek, *Coord. Chem. Rev.*, 1998, **174**, 469.
 30. A. B. P. Lever, ‘Excited State and Reactive Intermediates’, American Chemical Society, Washington, DC, 1986.
 31. K. Kalyanasundaram and M. Grätzel, ‘Photosensitization and Photocatalysis Using Inorganic and Organometallic Compounds’, Kluwer Academic Publishers, Dordrecht, Netherlands, 1993.
 32. K. Kalyanasundaram, *Coord. Chem. Rev.*, 1982, **46**, 159.
 33. M. K. Nazeeruddin, A. Kay, I. Rodicio, R. Humphry-Baker, E. Mueller, P. Liska, N. Vlachopoulos, and M. Grätzel, *J. Am. Chem. Soc.*, 1993, **115**, 6382.
 34. M. K. Nazeeruddin, S. M. Zakeeruddin, R. Humphry-Baker, M. Jirousek, P. Liska, N. Vlachopoulos, V. Shklover, C. H. Fischer, and M. Grätzel, *Inorg. Chem.*, 1999, **38**, 6298.
 35. A. Hagfeldt and M. Grätzel, *Chem. Rev.*, 1995, **95**, 49.
 36. S. Ardo, Y. Sun, A. Staniszewski, F. N. Castellano and G. J. Meyer, Stark Effects after Excited-State Interfacial Electron Transfer at Sensitized TiO₂ Nanocrystallites, *J. Am. Chem. Soc.*, 2010, **132**, 6696.
 37. M. Grätzel, *Cattech*, 1999, **3**, 4.
 38. K. Laqua, W. H. Melhuish, and M. Zander, *Pure Appl. Chem.*, 1988, **60**, 1449.
 39. G. M. Hasselman, D. F. Watson, J. R. Stromberg, D. F. Bocian, D. Holten, J. S. Lindsey, and G. J. Meyer, *J. Phys. Chem. B*, 2006, **110**, 25430.
 40. G. P. Smestad and M. Grätzel, *J. Chem. Educ.*, 1998, **75**, 752.
 41. National Renewable Energy Laboratory Reference Solar Spectral Irradiance: Air Mass 1.5. <http://rredc.nrel.gov/solar/spectra/am1.5/>. (accessed May 2009).
 42. W. Shockley and H. J. Queisser, *J. Appl. Phys.*, 1961, **32**, 510.
 43. R. T. Ross and A. J. Nozik, *J. Appl. Phys.*, 1982, **53**, 3813.
 44. A. De Vos, *J. Phys. D: Appl. Phys.*, 1980, **13**, 839.
 45. R. T. Ross and J. M. Collins, *J. Appl. Phys.*, 1980, **51**, 4504.
 46. J. R. Bolton, *Science*, 1978, **202**, 705.
 47. R. T. Ross and T.-L. Hsiao, *J. Appl. Phys.*, 1977, **48**, 4783.
 48. M. Grätzel, *Acc. Chem. Res.*, 2009, ASAP **42**(11), 1788.
 49. B. C. O'Regan and J. R. Durrant, *Acc. Chem. Res.*, 2009, ASAP **42**(11), 1799.
 50. M. K. Nazeeruddin, P. Péchy, and M. Grätzel, *Chem. Commun.*, 1997, 1705.
 51. M. K. Nazeeruddin, P. Péchy, T. Renouard, S. M. Zakeeruddin, R. Humphry-Baker, P. Comte, P. Liska, L. Cevey, E. Costa, V. Shklover, L. Spiccia, G. B. Deacon, C. A. Bignozzi, and M. Grätzel, *J. Am. Chem. Soc.*, 2001, **123**, 1613.
 52. M. Grätzel, *J. Photochem. Photobiol. C Photochem. Rev.*, 2003, **4**, 145.
 53. J. P. Paris and W. W. Brandt, *J. Am. Chem. Soc.*, 1959, **81**, 5001.
 54. F. E. Lytle and D. M. Hercules, *J. Am. Chem. Soc.*, 1969, **91**, 253.
 55. F. Felix, J. Ferguson, H. U. Guedel, and A. Ludi, *J. Am. Chem. Soc.*, 1980, **102**, 4096.
 56. G. A. Crosby, K. W. Hipps, and W. H. Elfring, *J. Am. Chem. Soc.*, 1974, **96**, 629.
 57. E. M. Kober and T. J. Meyer, *Inorg. Chem.*, 1982, **21**, 3967.
 58. A. W. Adamson and J. N. Demas, *J. Am. Chem. Soc.*, 1971, **93**, 1800.
 59. G. A. Crosby and J. N. Demas, *J. Am. Chem. Soc.*, 1971, **93**, 2841.

60. J. N. Demas and D. G. Taylor, *Inorg. Chem.*, 1979, **18**, 3177.
61. H. Yersin and E. Gallhuber, *J. Am. Chem. Soc.*, 1984, **106**, 6582.
62. H. Yersin, E. Gallhuber, A. Vogler, and H. Kunkely, *J. Am. Chem. Soc.*, 1983, **105**, 4155.
63. G. D. Hager and G. A. Crosby, *J. Am. Chem. Soc.*, 1975, **97**, 7031.
64. G. D. Hager, R. J. Watts, and G. A. Crosby, *J. Am. Chem. Soc.*, 1975, **97**, 7037.
65. R. W. Harrigan and G. A. Crosby, *J. Chem. Phys.*, 1973, **59**, 3468.
66. R. W. Harrigan, G. D. Hager, and G. A. Crosby, *Chem. Phys. Lett.*, 1973, **21**, 487.
67. K. W. Hipps and G. A. Crosby, *J. Am. Chem. Soc.*, 1975, **97**, 7042.
68. P. D. Fleischauer, A. W. Adamson, and G. Sartori, *Prog. Inorg. Chem.*, 1972, **17**, 1.
69. A. W. Adamson, *J. Chem. Educ.*, 1983, **60**, 797.
70. C. Daul, E. J. Baerends, and P. Vernooij, *J. Am. Chem. Soc.*, 1994, **33**, 3538.
71. S. Wallin, J. Davidsson, J. Modin, and L. Hammarstrom, *J. Phys. Chem. A*, 2005, **109**, 4697.
72. A. T. Yeh, C. V. Shank, and J. K. McCusker, *Science*, 2000, **289**, 935.
73. E. M. Kober, B. P. Sullivan, and T. J. Meyer, *Inorg. Chem.*, 1984, **23**, 2098.
74. R. F. Dallinger and W. H. Woodruff, *J. Am. Chem. Soc.*, 1979, **101**, 4391.
75. D. H. Oh and S. G. Boxer, *J. Am. Chem. Soc.*, 1989, **111**, 1130.
76. M. A. Webb, F. J. Knorr, and J. L. McHale, *J. Raman Spectrosc.*, 2001, **32**, 481.
77. A. Cannizzo, F. van Mourik, W. Gawelda, G. Zgrablic, C. Bressler, and M. Chergui, *Angew. Chem., Int. Ed. Engl.*, 2006, **45**, 3174.
78. H. Yersin, W. Humbs, and J. Strasser, *Coord. Chem. Rev.*, 1997, **159**, 325.
79. S. Wallin, J. Davidsson, J. Modin, and L. Hammarström, *J. Phys. Chem. A*, 2005, **109**, 9378.
80. C. W. Chang, C. K. Chou, I. J. Chang, Y. P. Lee, and E. W. G. Diau, *J. Phys. Chem. C*, 2007, **111**, 13288.
81. R. A. Malone and D. F. Kelley, *J. Chem. Phys.*, 1991, **95**, 8970.
82. L. F. Cooley, P. Bergquist, and D. F. Kelley, *J. Am. Chem. Soc.*, 1990, **112**, 2612.
83. J. Van Houten and R. J. Watts, *J. Am. Chem. Soc.*, 1976, **98**, 4853.
84. W. Siebrand, *J. Chem. Phys.*, 1966, **44**, 4055.
85. R. Englman and J. Jortner, *Mol. Phys.*, 1970, **18**, 145.
86. K. F. Freed and J. Jortner, *J. Chem. Phys.*, 1970, **52**, 6272.
87. M. Bixon and J. Jortner, *J. Chem. Phys.*, 1968, **48**, 715.
88. G. W. Robinson and R. P. Frosch, *J. Chem. Phys.*, 1963, **38**, 1187.
89. W. Gawelda, V.-T. Pham, M. Benfatto, Y. Zaushitsyn, M. Kaiser, D. Grolimund, S. L. Johnson, R. Abela, A. Hauser, C. Bressler, and M. Chergui, *Phys. Rev. Lett.*, 2007, **98**, 057401.
90. C. Cristina, P.-S. Mirabelle, E. Amal, B. Christian, van. M. Frank, C. Andrea, and C. Majed, *Angew. Chem., Int. Ed. Engl.*, 2009, **48**, 7184.
91. W. Gawelda, A. Cannizzo, V.-T. Pham, F. van Mourik, C. Bressler, and M. Chergui, *J. Am. Chem. Soc.*, 2007, **129**, 8199.
92. C. Bressler, C. Milne, V. T. Pham, A. ElNahhas, R. M. van der Veen, W. Gawelda, S. Johnson, P. Beaud, D. Grolimund, M. Kaiser, C. N. Borca, G. Ingold, R. Abela, and M. Chergui, *Science*, 2009, **323**, 489.
93. W. Gawelda, A. Cannizzoa, V.-T. Phama, A. El Nahasa, C. J. Milnea, R. van der Veena, C. Bresslera, and M. Chergui, *Chimia*, 2007, **61**, 179.
94. W. Gawelda, V. T. Pham, R. M. van der Veen, D. Grolimund, R. Abela, M. Chergui, and C. Bressler, *J. Chem. Phys.*, 2009, **130**, 124520.
95. A. L. Smeigh, M. Creelman, R. A. Mathies, and J. K. McCusker, *J. Am. Chem. Soc.*, 2008, **130**, 14105.
96. M. Khalil, M. A. Marcus, A. L. Smeigh, J. K. McCusker, H. H. W. Chong, and R. W. Schoenlein, *J. Phys. Chem. A*, 2006, **110**, 38.
97. N. Huse, M. Khalil, T. K. Kim, A. L. Smeigh, L. Jamula, J. K. McCusker, and R. W. Schoenlein, *J. Phys. Conf. Series*, 2009, **148**, 012043.
98. H.-L. Xia, S. Ardo, A. A. Narducci Sarjeant, S. Huang, and G. J. Meyer, *Langmuir*, 2009, ASAP **25**(23), 13641.
99. A. Hauser, J. Adler, and P. Gütlich, *Chem. Phys. Lett.*, 1988, **152**, 468.
100. J. H. Alstrum-Acevedo, M. K. Brenneman, and T. J. Meyer, *Inorg. Chem.*, 2005, **44**, 6802.
101. P. Persson, R. Bergström, L. Ojamäe, and S. Lunell, Quantum-chemical Studies of Metal Oxides for Photoelectrochemical Applications, in ‘Advances in Quantum Chemistry’, ed. J. Sabin Academic Press, 2002, Vol. 41, p. 203.
102. H. Rensmo, S. Lunell, and H. Siegbahn, *J. Photochem. Photobiol. A Chem.*, 1998, **114**, 117.
103. H. Rensmo, S. Södergren, L. Patthey, K. Westermark, L. Vayssieres, O. Kohle, P. A. Brühwiler, A. Hagfeldt, and H. Siegbahn, *Chem. Phys. Lett.*, 1997, **274**, 51.
104. S. A. Haque, E. Palomares, B. M. Cho, A. N. M. Green, N. Hirata, D. R. Klug, and J. R. Durrant, *J. Am. Chem. Soc.*, 2005, **127**, 3456.
105. J. R. Durrant, S. A. Haque, and E. Palomares, *Coord. Chem. Rev.*, 2004, **248**, 1247.
106. L. C. T. Shoute and G. R. Loppnow, *J. Am. Chem. Soc.*, 2003, **125**, 15636.
107. D. F. Watson and G. J. Meyer, *Coord. Chem. Rev.*, 2004, **248**, 1391.

108. A. Staniszewski, S. Ardo, Y. Sun, F. N. Castellano, and G. J. Meyer, *J. Am. Chem. Soc.*, 2008, **130**, 11586.
109. H. J. Snaith, S. M. Zakeeruddin, L. Schmidt-Mende, C. Klein, and M. Grätzel, *Angew. Chem., Int. Ed. Engl.*, 2005, **44**, 6413.
110. D. Kuang, C. Klein, H. J. Snaith, J.-E. Moser, R. Humphry-Baker, P. Comte, S. M. Zakeeruddin, and M. Grätzel, *Nano Lett.*, 2006, **6**, 769.
111. D. Kuang, C. Klein, H. J. Snaith, R. Humphry-Baker, S. M. Zakeeruddin, and M. Grätzel, *Inorg. Chim. Acta*, 2008, **361**, 699.
112. P. Wang, C. Klein, R. Humphry-Baker, S. M. Zakeeruddin, and M. Grätzel, *Appl. Phys. Lett.*, 2005, **86**, 123508.
113. S. M. Zakeeruddin, M. K. Nazeeruddin, R. Humphry-Baker, P. Péchy, P. Quagliotto, C. Barolo, G. Viscardi, and M. Grätzel, *Langmuir*, 2002, **18**, 952.
114. P. Wang, S. M. Zakeeruddin, J. E. Moser, M. K. Nazeeruddin, T. Sekiguchi, and M. Grätzel, *Nat. Mater.*, 2003, **2**, 402.
115. P. Wang, C. Klein, R. Humphry-Baker, S. M. Zakeeruddin, and M. Grätzel, *J. Am. Chem. Soc.*, 2005, **127**, 808.
116. D. Kuang, S. Ito, B. Wenger, C. Klein, J. E. Moser, R. Humphry-Baker, S. M. Zakeeruddin, and M. Grätzel, *J. Am. Chem. Soc.*, 2006, **128**, 4146.
117. M. K. Nazeeruddin, S. M. Zakeeruddin, J. J. Lagref, P. Liska, P. Comte, C. Barolo, G. Viscardi, K. Schenk, and M. Grätzel, *Coord. Chem. Rev.*, 2004, **248**, 1317.
118. J. E. Kroeze, N. Hirata, S. Koops, M. K. Nazeeruddin, L. Schmidt-Mende, M. Grätzel, and J. R. Durrant, *J. Am. Chem. Soc.*, 2006, **128**, 16376.
119. L. Schmidt-Mende, J. E. Kroeze, J. R. Durrant, M. K. Nazeeruddin, and M. Grätzel, *Nano Lett.*, 2005, **5**, 1315.
120. C. Klein, M. K. Nazeeruddin, D. Di Censo, P. Liska, and M. Grätzel, *Inorg. Chem.*, 2004, **43**, 4216.
121. P. Wang, C. Klein, J.-E. Moser, R. Humphry-Baker, N.-L. Cevey-Ha, R. Charvet, P. Comte, S. M. Zakeeruddin, and M. Grätzel, *J. Phys. Chem. B*, 2004, **108**, 17553.
122. Z. Jin, H. Masuda, N. Yamanaka, M. Minami, T. Nakamura, and Y. Nishikitani, *ChemSusChem*, 2008, **1**, 901.
123. Z. Jin, H. Masuda, N. Yamanaka, M. Minami, T. Nakamura, and Y. Nishikitani, *Chem. Lett.*, 2009, **38**, 44.
124. K. L. McCall, J. R. Jennings, H. Wang, A. Morandeira, L. M. Peter, J. R. Durrant, L. J. Yellowlees, J. D. Woollins, and N. Robertson, *J. Photochem. Photobiol. A Chem.*, 2009, **202**, 196.
125. K. Kalyanasundaram, N. Vlachopoulos, V. Krishnan, A. Monnier, and M. Grätzel, *J. Phys. Chem.*, 1987, **91**, 2342.
126. N. R. de Tacconi, C. R. Chenthamarakshan, G. Yogeeshwaran, A. Watcharenwong, R. S. de Zoysa, N. A. Basit, and K. Rajeshwar, *J. Phys. Chem. B*, 2006, **110**, 25347.
127. M. Paulose, H. E. Prakasam, O. K. Varghese, L. Peng, K. C. Popat, G. K. Mor, T. A. Desai, and C. A. Grimes, *J. Phys. Chem. C*, 2007, **111**, 14992.
128. A. Hagfeldt, N. Vlachopoulos, S. Gilbert, and M. Grätzel, in *Electrochromic Switching with Nanocrystalline TiO₂ Semiconductor Films*, in 'Optical Materials Technology for Energy Efficiency and Solar Energy Conversion XIII', ed. V. Wittwer, C.G. Granqvist, C.M. Lampert, Freiburg, Federal Republic of Germany, SPIE, Freiburg, Federal Republic of Germany, 1994, **2255**, p. 297.
129. N. R. Kestner, J. Logan, and J. Jortner, *J. Phys. Chem.*, 1974, **78**, 2148.
130. P. F. Bernath, 'Spectra of Atoms and Molecules', 2nd edition, Oxford University Press, New York, 2005.
131. P. A. M. Dirac, *Proc. R. Soc. London, A*, 1927, **114**, 243.
132. T. D. Visser, *Am. J. Phys.*, 2009, **77**, 487.
133. J. G. Calvert, J. N. Pitts Jr, 'Photochemistry'. John Wiley & Sons, Inc., New York, 1966.
134. N. H. Damrauer, T. R. Boussie, M. Devenney, and J. K. McCusker, *J. Am. Chem. Soc.*, 1997, **119**, 8253.
135. J. A. Treadway, B. Loeb, R. Lopez, P. A. Anderson, F. R. Keene, and T. J. Meyer, *Inorg. Chem.*, 1996, **35**, 2242.
136. C. C. Phifer and D. R. McMillin, *Inorg. Chem.*, 1986, **25**, 1329.
137. V. Aranyos, J. Hjelm, A. Hagfeldt, and H. Grennberg, *J. Chem. Soc., Dalton Trans.*, 2001, **30**, 1319.
138. K. A. Walters, L. L. Premvardhan, Y. Liu, L. A. Peteanu, and K. S. Schanze, *Chem. Phys. Lett.*, 2001, **339**, 255.
139. Y. Wang, S. Liu, M. R. Pinto, D. M. Dattelbaum, J. R. Schoonover, and K. S. Schanze, *J. Phys. Chem. A*, 2001, **105**, 11118.
140. C. Klein, M. K. Nazeeruddin, P. Liska, D. Di Censo, N. Hirata, E. Palomares, J. R. Durrant, and M. Grätzel, *Inorg. Chem.*, 2004, **44**, 178.
141. P. Wang, C. Klein, R. Humphry-Baker, S. M. Zakeeruddin, and M. Grätzel, *J. Am. Chem. Soc.*, 2004, **127**, 808.
142. P. Wang, S. M. Zakeeruddin, J. E. Moser, R. Humphry-Baker, P. Comte, V. Aranyos, A. Hagfeldt, M. K. Nazeeruddin, and M. Grätzel, *Adv. Mater.*, 2004, **16**, 1806.
143. G. F. Strouse, J. R. Schoonover, R. Duesing, S. Boyde, W. E. Jones, and T. J. Meyer, Jr, *Inorg. Chem.*, 1995, **34**, 473.
144. M. Beley, J.-P. Collin, J.-P. Sauvage, H. Sugihara, F. Heisel, and A. Miehe, *J. Chem. Soc., Dalton Trans.*, 1991, **20**, 3157.
145. R. L. Blakley, M. L. Myrick, R. Pittman, and M. K. De Armond, *J. Phys. Chem.*, 1990, **94**, 4804.
146. L. Hammarström, F. Barigelletti, L. Flamigni, M. T. Indelli, N. Armaroli, G. Calogero, M. Guardigli, A. Sour, J.-P. Collin, and J.-P. Sauvage, *J. Phys. Chem. A*, 1997, **101**, 9061.
147. C. R. Hecker, A. K. I. Gushurst, and D. R. McMillin, *Inorg. Chem.*, 1991, **30**, 538.
148. J. P. Collin, S. Guillerez, J. P. Sauvage, F. Barigelletti, L. De Cola, L. Flamigni, and V. Balzani, *Inorg. Chem.*, 1991, **30**, 4230.
149. J.-P. Collin, S. Guillerez, and J.-P. Sauvage, *J. Chem. Soc., Chem. Commun.*, 1989, **25**, 776.
150. M. Beley, S. Chodorowski, J.-P. Collin, J.-P. Sauvage, L. Flamigni, and F. Barigelletti, *Inorg. Chem.*, 1994, **33**, 2543.

151. F. Barigelli, L. Flamigni, V. Balzani, J.-P. Collin, J.-P. Sauvage, A. Sour, E. C. Constable, and A. M. W. C. Thompson, *J. Am. Chem. Soc.*, 1994, **116**, 7692.
152. R. S. Mulliken, *J. Am. Chem. Soc.*, 1952, **74**, 811.
153. J. N. Murrell, *J. Am. Chem. Soc.*, 1959, **81**, 5037.
154. S. Fukuzumi, C. L. Wong, and J. K. Kochi, *J. Am. Chem. Soc.*, 1980, **102**, 2928.
155. M. K. Nazeeruddin, Q. Wang, L. Cevey, V. Aranyos, P. Liska, E. Figgemeier, C. Klein, N. Hirata, S. Koops, S. A. Haque, J. R. Durrant, A. Hagfeldt, A. B. P. Lever, and M. Grätzel, *Inorg. Chem.*, 2005, **45**, 787.
156. S. R. Jang, C. Lee, H. Choi, J. J. Ko, J. Lee, R. Vittal, and K. J. Kim, *Chem. Mater.*, 2006, **18**, 5604.
157. D. Kuang, C. Klein, S. Ito, J. E. Moser, R. Humphry-Baker, N. Evans, F. Duriaux, C. Grätzel, S. M. Zakeeruddin, and M. Grätzel, *Adv. Mater.*, 2007, **19**, 1133.
158. C. Lee, J.-H. Yum, H. Choi, S. Ook Kang, J. Ko, R. Humphry-Baker, M. Grätzel, and M. K. Nazeeruddin, *Inorg. Chem.*, 2007, **47**, 2267.
159. M. K. Nazeeruddin, T. Bessho, L. Cevey, S. Ito, C. Klein, F. De Angelis, S. Fantacci, P. Comte, P. Liska, H. Imai, and M. Grätzel, *J. Photochem. Photobiol. A Chem.*, 2007, **185**, 331.
160. A. Abbotto, C. Barolo, L. Bellotto, F. D. Angelis, M. Grätzel, N. Manfredi, C. Marinzi, S. Fantacci, J.-H. Yum, and M. K. Nazeeruddin, *Chem. Commun.*, 2008, 5318.
161. A. Abbotto, C. Barolo, J.-H. Yum, L. Bellotto, F. De Angelis, M. Grätzel, C. Marinzi, and M. K. Nazeeruddin, Ruthenium Sensitizers Based on Heteroaromatic Conjugated Bypiridines for Dye-sensitized Solar Cells, in ‘Organic Optoelectronics and Photonics III’, Strasbourg, France, 2008, ed. P. L. Heremans, M. Muccini, E. A. Meulenkamp, SPIE, Strasbourg, France, 2008, **6999**, p. 69990O.
162. H. Choi, C. Baik, S. Kim, M.-S. Kang, X. Xu, H. S. Kang, S. O. Kang, J. Ko, M. K. Nazeeruddin, and M. Grätzel, *New J. Chem.*, 2008, **32**, 2233.
163. F. Gao, Y. Wang, J. Zhang, D. Shi, M. Wang, R. Humphry-Baker, P. Wang, S. M. Zakeeruddin, and M. Grätzel, *Chem. Commun.*, 2008, 2635.
164. H. J. Snaith, C. S. Karthikeyan, A. Petrozza, J. Teuscher, J. E. Moser, M. K. Nazeeruddin, M. Thelakkat, and M. Grätzel, *J. Phys. Chem. C*, 2008, **112**, 7562.
165. A. Staniszewski, W. B. Heuer, and G. J. Meyer, *Inorg. Chem.*, 2008, **47**, 7062.
166. S.-R. Jang, J.-H. Yum, C. Klein, K.-J. Kim, P. Wagner, D. Officer, M. Grätzel, and M. K. Nazeeruddin, *J. Phys. Chem. C*, 2009, **113**, 1998.
167. J.-H. Yum, I. Jung, C. Baik, J. Ko, M. K. Nazeeruddin, and M. Grätzel, *Energy Environ. Sci.*, 2009, **2**, 100.
168. F. Matar, T. H. Ghaddar, K. Walley, T. DosSantos, J. R. Durrant, and B. O'Regan, *J. Mater. Chem.*, 2008, **18**, 4246.
169. D. Martineau, M. Beley, P. C. Gros, S. Cazzanti, S. Caramori, and C. A. Bignozzi, *Inorg. Chem.*, 2007, **46**, 2272.
170. D. Shi, N. Pootrakulchote, R. Li, J. Guo, Y. Wang, S. M. Zakeeruddin, M. Grätzel, and P. Wang, *J. Phys. Chem. C*, 2008, **112**, 17046.
171. Q. Yu, S. Liu, M. Zhang, N. Cai, Y. Wang, and P. Wang, *J. Phys. Chem. C*, 2009, **113**, 14559.
172. C. Y. Chen, H. C. Lu, C. G. Wu, J. G. Chen, and K. C. Ho, *Adv. Func. Mater.*, 2007, **17**, 29.
173. C.-Y. Chen, S.-J. Wu, C.-G. Wu, J.-G. Chen, and K.-C. Ho, *Angew. Chem., Int. Ed. Engl.*, 2006, **45**, 5822.
174. C. Y. Chen, S. J. Wu, J. Y. Li, C. G. Wu, J. G. Chen, and K. C. Ho, *Adv. Mater. (Weinheim, Fed. Repub. Ger.)*, 2007, **19**, 3888.
175. F. Sauvage, M. K. R. Fischer, A. Mishra, S. M. Zakeeruddin, M. K. Nazeeruddin, P. Bäuerle, and M. Grätzel, *ChemSusChem*, 2009, **2**, 761.
176. S. A. Haque, S. Handa, K. Peter, E. Palomares, M. Thelakkat, and J. R. Durrant, *Angew. Chem., Int. Ed. Engl.*, 2005, **44**, 5740.
177. N. Hirata, J.-J. Lagref, E. J. Palomares, J. R. Durrant, M. K. Nazeeruddin, M. Grätzel, and D. Di Censo, *Chem. Eur. J.*, 2004, **10**, 595.
178. F. Gao, Y. Cheng, Q. Yu, S. Liu, D. Shi, Y. Li, and P. Wang, *Inorg. Chem.*, 2009, **48**, 2664.
179. C. Lee, J.-H. Yum, H. Choi, S. Ook Kang, J. Ko, R. Humphry-Baker, M. Grätzel, and M. K. Nazeeruddin, *Inorg. Chem.*, 2008, **47**, 2267.
180. V. Balzani, L. Moggi, and F. Scandola, Towards a Supramolecular Photochemistry: Assembly of Molecular Components to Obtain Photochemical Molecular Devices, in ‘Supramolecular Photochemistry’, ed. V. Balzani, D. Reidel Publishing Co., Dordrecht, Holland, 1987, p. 1.
181. C. A. Bignozzi, R. Argazzi, M. T. Indelli, and F. Scandola, *Sol. Energy Mater.*, 1994, **32**, 229.
182. C. A. Bignozzi, R. Argazzi, F. Scandola, J. R. Schoonover, and G. J. Meyer, *Sol. Energy Mater.*, 1995, **38**, 187.
183. R. Amadelli, R. Argazzi, C. A. Bignozzi, and F. Scandola, *J. Am. Chem. Soc.*, 1990, **112**, 7099.
184. M. K. Nazeeruddin, P. Liska, J. Moser, N. Vlachopoulos, and M. Grätzel, *Helv. Chim. Acta*, 1990, **73**, 1788.
185. D. Holten, D. F. Bocian, and J. S. Lindsey, *Acc. Chem. Res.*, 2002, **35**, 57.
186. R. J. Forster, T. E. Keyes, and J. G. Vos, ‘Interfacial Supramolecular Assemblies’, John Wiley & Sons Ltd., Chichester, 2003, p. 317.
187. F. Gajardo, A. M. Leiva, B. Loeb, A. Delgadillo, J. R. Stromberg, and G. J. Meyer, *Inorg. Chim. Acta*, 2008, **361**, 613.
188. S. Altobello, R. Argazzi, S. Caramori, C. Contado, S. D. Fre, P. Rubino, C. Chone, G. Larramona, and C. A. Bignozzi, *J. Am. Chem. Soc.*, 2005, **127**, 15342.
189. T. Bessho, E. Yoneda, J.-H. Yum, M. Guglielmi, I. Tavernelli, H. Imai, U. Rothlisberger, M. K. Nazeeruddin, and M. Grätzel, *J. Am. Chem. Soc.*, 2009, **131**, 5930.

190. M. Yang, D. W. Thompson, and G. J. Meyer, *Inorg. Chem.*, 2002, **41**, 1254.
191. R. Argazzi, C. A. Bignozzi, M. Yang, G. M. Hasselmann, and G. J. Meyer, *Nano Lett.*, 2002, **2**, 625.
192. R. Argazzi, C. A. Bignozzi, T. A. Heimer, F. N. Castellano, and G. J. Meyer, *Inorg. Chem.*, 1994, **33**, 5741.
193. T. A. Heimer, E. J. Heilweil, C. A. Bignozzi, and G. J. Meyer, *J. Phys. Chem. A*, 2000, **104**, 4256.
194. H. Zabri, I. Gillaizeau, C. A. Bignozzi, S. Caramori, M.-F. Charlot, J. Cano-Boquera, and F. Odobel, *Inorg. Chem.*, 2003, **42**, 6655.
195. Y.-J. Hou, P.-H. Xie, B.-W. Zhang, Y. Cao, X.-R. Xiao, and W.-B. Wang, *Inorg. Chem.*, 1999, **38**, 6320.
196. P.-H. Xie, Y.-J. Hou, T.-X. Wei, B.-W. Zhang, Y. Cao, and C.-H. Huang, *Inorg. Chim. Acta*, 2000, **308**, 73.
197. S. R. L. Fernando, M. Y. Ogawa, *Chem. Commun.*, 1996, 637.
198. P.-H. Xie, Y.-J. Hou, B.-W. Zhang, and Y. Cao, *J. Photochem. Photobiol. A Chem.*, 1999, **122**, 169.
199. A. Kukrek, D. Wang, Y. Hou, R. Zong, and R. Thummel, *Inorg. Chem.*, 2006, **45**, 10131.
200. C. Barolo, M. K. Nazeeruddin, S. Fantacci, D. Di Censo, P. Comte, P. Liska, G. Viscardi, P. Quagliotto, F. De Angelis, S. Ito, and M. Grätzel, *Inorg. Chem.*, 2006, **45**, 4642.
201. E. M. Kober, B. P. Sullivan, W. J. Dressick, J. V. Caspar, and T. J. Meyer, *J. Am. Chem. Soc.*, 1980, **102**, 7383.
202. C. Creutz, M. Chou, T. L. Netzel, M. Okumura, and N. Sutin, *J. Am. Chem. Soc.*, 1980, **102**, 1309.
203. J. V. Caspar, E. M. Kober, B. P. Sullivan, and T. J. Meyer, *J. Am. Chem. Soc.*, 1982, **104**, 630.
204. G. H. Allen, B. P. Sullivan, and T. J. Meyer, *J. Chem. Soc., Chem. Commun.*, 1981, 793.
205. P. F. H. Schwab, S. Diegoli, M. Biancardo, and C. A. Bignozzi, *Inorg. Chem.*, 2003, **42**, 6613.
206. B. E. Hardin, E. T. Hoke, P. B. Armstrong, J.-H. Yum, P. Comte, T. Torres, J. M. J. Frechet, M. K. Nazeeruddin, M. Grätzel, and M. D. McGehee, *Nature Photon.*, 2009, **3**, 406.
207. J. B. Asbury, E. Hao, Y. Wang, H. N. Ghosh, and T. Lian, *J. Phys. Chem. B*, 2001, **105**, 4545.
208. J. B. Asbury, E. Hao, Y. Wang, and T. Lian, *J. Phys. Chem. B*, 2000, **104**, 11957.
209. G. M. Hasselmann and G. J. Meyer, *Z. Phys. Chem. (Munich)*, 1999, **212**, 39.
210. G. M. Hasselmann and G. J. Meyer, *J. Phys. Chem. B*, 1999, **103**, 7671.
211. R. Argazzi, C. A. Bignozzi, T. A. Heimer, and G. J. Meyer, *Inorg. Chem.*, 1997, **36**, 2.
212. N. A. Anderson and T. Lian, *Coord. Chem. Rev.*, 2004, **248**, 1231.
213. C. She, J. Guo, S. Irle, K. Morokuma, D. L. Mohler, H. Zabri, F. Odobel, K. T. Youm, F. Liu, J. T. Hupp, and T. Lian, *J. Phys. Chem. A*, 2007, **111**, 6832.
214. C. She, J. Guo, and T. Lian, *J. Phys. Chem. B*, 2007, **111**, 6903.
215. T. Bessho, E. C. Constable, M. Grätzel, A. H. Redondo, C. E. Housecroft, W. Kylberg, M. K. Nazeeruddin, M. Neuburger, and S. Schaffner, *Chem. Commun.*, 2008, 3717.
216. S. Sakaki, T. Kuroki, and T. Hamada, *J. Chem. Soc., Dalton Trans.*, 2002, **31**, 840.
217. N. Alonso-Vante, J.-F. Nierengarten, and J.-P. Sauvage, *J. Chem. Soc., Dalton Trans.*, 1994, **14**, 1649.
218. S. Chakraborty, T. J. Wadas, H. Hester, R. Schmehl, and R. Eisenberg, *Inorg. Chem.*, 2005, **44**, 6865.
219. P. Du, J. Schneider, F. Li, W. Zhao, U. Patel, F. N. Castellano, and R. Eisenberg, *J. Am. Chem. Soc.*, 2008, **130**, 5056.
220. J. Zhang, P. Du, J. Schneider, P. Jarosz, and R. Eisenberg, *J. Am. Chem. Soc.*, 2007, **129**, 7726.
221. W. Zhao, Y. Sun, and F. N. Castellano, *J. Am. Chem. Soc.*, 2008, **130**, 12566.
222. A. Islam, H. Sugihara, K. Hara, L. P. Singh, R. Katoh, M. Yanagida, Y. Takahashi, S. Murata, and H. Arakawa, *New J. Chem.*, 2000, **24**, 343.
223. E. A. M. Geary, L. J. Yellowlees, L. A. Jack, I. D. H. Oswald, S. Parsons, N. Hirata, J. R. Durrant, and N. Robertson, *Inorg. Chem.*, 2005, **44**, 242.
224. M. Hissler, J. E. McGarrah, W. B. Connick, D. K. Geiger, S. D. Cummings, and R. Eisenberg, *Coord. Chem. Rev.*, 2000, **208**, 115.
225. W. R. McNamara, R. C. Snoeberger, G. Li, J. M. Schleicher, C. W. Cady, M. Poyatos, C. A. Schmuttenmaer, R. H. Crabtree, G. W. Brudvig, and V. S. Batista, *J. Am. Chem. Soc.*, 2008, **130**, 14329.
226. S. G. Abuabara, C. W. Cady, J. B. Baxter, C. A. Schmuttenmaer, R. H. Crabtree, G. W. Brudvig, and V. S. Batista, *J. Phys. Chem. C*, 2007, **111**, 11982.
227. G. Li, E. M. Sproviero, R. C. S. Iii, N. Iguchi, J. D. Blakemore, R. H. Crabtree, G. W. Brudvig, and V. S. Batista, *Energy Environ. Sci.*, 2009, **2**, 230.
228. E. A. M. Geary, K. L. McCall, A. Turner, P. R. Murray, E. J. L. McInnes, L. A. Jack, L. J. Yellowlees, and N. Robertson, *Dalton Trans.*, 2008, **37**, 3701.
229. L. P. Moorcraft, A. Morandeira, J. R. Durrant, J. R. Jennings, L. M. Peter, S. Parsons, A. Turner, L. J. Yellowlees, and N. Robertson, *Dalton Trans.*, 2008, **37**, 6940.
230. Z. Ning, Q. Zhang, W. Wu, and H. Tian, *J. Organomet. Chem.*, 2009, **694**, 2705.
231. E. I. Mayo, K. Kilsa, T. Tirrell, P. I. Djurovich, A. Tamayo, M. E. Thompson, N. S. Lewis, and H. B. Gray, *Photochem. Photobiol. Sci.*, 2006, **5**, 871.
232. E. Baranoff, J.-H. Yum, M. Grätzel, and M. K. Nazeeruddin, *J. Organomet. Chem.*, 2009, **694**, 2661.
233. N. Armaroli, *Chem. Soc. Rev.*, 2001, **30**, 113.
234. L. X. Chen, G. Jennings, T. Liu, D. J. Gosztola, J. P. Hessler, D. V. Scaltrito, and G. J. Meyer, *J. Am. Chem. Soc.*, 2002, **124**, 10861.

235. M. Yang, D. W. Thompson, and G. J. Meyer, *Inorg. Chem.*, 2000, **39**, 3738.
236. B. V. Bergeron and G. J. Meyer, *J. Phys. Chem. B*, 2003, **107**, 245.
237. C. Creutz, B. S. Brunschwig, and N. Sutin, *J. Phys. Chem. B*, 2006, **110**, 25181.
238. F. Liu, M. Yang, and G. J. Meyer, Molecule-to-Particle Charge Transfer in Sol-Gel Materials, in 'Handbook of Sol-Gel Science and Technology: Processing Characterization and Application; Volume II: Characterization of Sol-Gel Materials and Products', ed. R. M. Almeida, Kluwer Academic Publishers, Dordrecht, The Netherlands, 2005, Vol. 2, p. 400.
239. E. Vrachnou, M. Grätzel, and A. J. McEvoy, *J. Electroanal. Chem.*, 1989, **258**, 193.
240. E. Vrachnou, N. Vlachopoulos, and M. Grätzel, *Chem. Commun.*, 1987, 868.
241. R. L. Blackbourn, C. S. Johnson, and J. T. Hupp, *J. Am. Chem. Soc.*, 1991, **113**, 1060.
242. H. Lu, J. N. Prieskorn, and J. T. Hupp, *J. Am. Chem. Soc.*, 1993, **115**, 4927.
243. S. F. Fischer and R. P. Van Duyne, *Chem. Phys.*, 1977, **26**, 9.
244. J. J. Hopfield, *Proc. Natl. Acad. Sci. U. S. A.*, 1974, **71**, 3640.
245. J. Jortner, *J. Chem. Phys.*, 1976, **64**, 4860.
246. J. Ulstrup and J. Jortner, *J. Chem. Phys.*, 1975, **63**, 4358.
247. R. P. Van Duyne and S. F. Fischer, *Chem. Phys.*, 1974, **5**, 183.
248. M. Khoudiakov, A. R. Parise, and B. S. Brunschwig, *J. Am. Chem. Soc.*, 2003, **125**, 4637.
249. L. Karki and J. T. Hupp, *Inorg. Chem.*, 1997, **36**, 3318.
250. F. W. Vance and J. T. Hupp, *J. Am. Chem. Soc.*, 1999, **121**, 4047.
251. S. J. Hug and S. G. Boxer, *Inorg. Chim. Acta*, 1996, **242**, 323.
252. S. G. Boxer, *J. Phys. Chem. B*, 2009, **113**, 2972.
253. G. U. Bublitz and S. G. Boxer, *Annu. Rev. Phys. Chem.*, 1997, **48**, 213.
254. J. A. Harris, K. Trotter, and B. S. Brunschwig, *J. Phys. Chem. B*, 2007, **111**, 6695.
255. J. Moser, S. Punchihewa, P. P. Infelta, and M. Grätzel, *Langmuir*, 1991, **7**, 3012.
256. K. A. Walters, D. A. Gaal, and J. T. Hupp, *J. Phys. Chem. B*, 2002, **106**, 5139.
257. A. Nawrocka, A. Zdyb, and S. Krawczyk, *Chem. Phys. Lett.*, 2009, **475**, 272.
258. A. Nawrocka and S. Krawczyk, *J. Phys. Chem. C*, 2008, **112**, 10233.
259. C. R. Rice, M. D. Ward, M. K. Nazeeruddin, and M. Grätzel, *New J. Chem.*, 2000, **24**, 651.
260. S. Verma, P. Kar, A. Das, D. K. Palit, and H. N. Ghosh, *J. Phys. Chem. C*, 2008, **112**, 2918.
261. G. Ramakrishna, D. A. Jose, D. K. Kumar, A. Das, D. K. Palit, and H. N. Ghosh, *J. Phys. Chem. B*, 2005, **109**, 15445.
262. P. Kar, S. Verma, A. Das, and H. N. Ghosh, *J. Phys. Chem. C*, 2009, **113**, 7970.
263. K. Schwarzburg, R. Ernstorfer, S. Felber, and F. Willig, *Coord. Chem. Rev.*, 2004, **248**, 1259.
264. D. F. Watson and G. J. Meyer, *Annu. Rev. Phys. Chem.*, 2005, **56**, 119.
265. M. G. Evans and M. Polanyi, *Trans. Faraday Soc.*, 1935, **31**, 875.
266. H. Eyring, *J. Chem. Phys.*, 1935, **3**, 107.
267. J. B. Asbury, N. A. Anderson, E. Hao, X. Ai, and T. Lian, *J. Phys. Chem. B*, 2003, **107**, 7376.
268. J. B. Asbury, Y.-Q. Wang, E. Hao, H. N. Ghosh, and T. Lian, *Res. Chem. Intermed.*, 2001, **27**, 393.
269. G. Benkö, J. Kallioinen, J. E. I. Korppi-Tommola, A. P. Yartsev, and V. Sundström, *J. Am. Chem. Soc.*, 2002, **124**, 489.
270. R. Ernstorfer, L. Gundlach, S. Felber, W. Storck, R. Eichberger, and F. Willig, *J. Phys. Chem. B*, 2006, **110**, 25383.
271. T. Hannappel, B. Burfeindt, W. Storck, and F. Willig, *J. Phys. Chem. B*, 1997, **101**, 6799.
272. J. Kallioinen, G. Benkö, P. Myllyperkiö, L. Khriachtchev, B. Skarman, R. Wallenberg, M. Tuomikoski, J. Korppi-Tommola, V. Sundström, and A. P. Yartsev, *J. Phys. Chem. B*, 2004, **108**, 6365.
273. J. Kallioinen, G. Benkö, V. Sundström, J. E. I. Korppi-Tommola, and A. P. Yartsev, *J. Phys. Chem. B*, 2002, **106**, 4396.
274. D. Kuciauskas, J. E. Monat, R. Villahermosa, H. B. Gray, N. S. Lewis, and J. K. McCusker, *J. Phys. Chem. B*, 2002, **106**, 9347.
275. A. Morandeira, G. Boschloo, A. Hagfeldt, and L. Hammarström, *J. Phys. Chem. B*, 2005, **109**, 19403.
276. P. Myllyperkiö, G. Benkö, J. Korppi-Tommola, A. P. Yartsev, and V. Sundström, *Phys. Chem. Chem. Phys.*, 2008, **10**, 996.
277. Y. Tachibana, S. A. Haque, I. P. Mercer, J. R. Durrant, and D. R. Klug, *J. Phys. Chem. B*, 2000, **104**, 1198.
278. Y. Tachibana, J. E. Moser, M. Grätzel, D. R. Klug, and J. R. Durrant, *J. Phys. Chem.*, 1996, **100**, 20056.
279. N. S. Hush, *J. Chem. Phys.*, 1958, **28**, 962.
280. N. S. Hush, *Trans. Faraday Soc.*, 1961, **57**, 557.
281. R. A. Marcus, *Annu. Rev. Phys. Chem.*, 1964, **15**, 155.
282. H. Gerischer, *Surf. Sci.*, 1969, **18**, 97.
283. H. Gerischer, *Photochem. Photobiol.*, 1972, **16**, 243.
284. R. A. Marcus and N. Sutin, *Biochim. Biophys. Rev. Bioenerg.*, 1985, **811**, 265.
285. S. Ramakrishna, F. Willig, V. May, and A. Knorr, *J. Phys. Chem. B*, 2003, **107**, 607.
286. W. Stier and O. V. Prezhdo, *J. Phys. Chem. B*, 2002, **106**, 8047.

287. F. Willig, C. Zimmermann, S. Ramakrishna, and W. Storck, *Electrochim. Acta*, 2000, **45**, 4565.
288. C. Zimmermann, F. Willig, S. Ramakrishna, B. Burfeindt, B. Pettinger, R. Eichberger, and W. Storck, *J. Phys. Chem. B*, 2001, **105**, 9245.
289. M. Thoss, I. Kondov, and H. Wang, *Chem. Phys.*, 2004, **304**, 169.
290. G. Benkö, J. Kallioinen, P. Myllyperkiö, F. Trif, J. E. I. Korppi-Tommola, A. P. Yartsev, and V. Sundström, *J. Phys. Chem. B*, 2004, **108**, 2862.
291. Y. Tachibana, M. K. Nazeeruddin, M. Grätzel, D. R. Klug, and J. R. Durrant, *Chem. Phys.*, 2002, **285**, 127.
292. S. E. Koops, B. C. O'Regan, P. R. F. Barnes, and J. R. Durrant, *J. Am. Chem. Soc.*, 2009, **131**, 4808.
293. B. Wenger, M. Grätzel, and J.-E. Moser, *Chimia*, 2005, **59**, 123.
294. B. Wenger, M. Grätzel, and J. E. Moser, *J. Am. Chem. Soc.*, 2005, **127**, 12150.
295. T. D. M. Bell, C. Pagba, M. Myahkostupov, J. Hofkens, and P. Piotrowiak, *J. Phys. Chem. B*, 2006, **110**, 25314.
296. G. L. Closs and J. R. Miller, *Science*, 1988, **240**, 440.
297. J. F. Smalley, H. O. Finklea, C. E. D. Chidsey, M. R. Linford, S. E. Creager, J. P. Ferraris, K. Chalfant, T. Zawodzinsk, S. W. Feldberg, and M. D. Newton, *J. Am. Chem. Soc.*, 2003, **125**, 2004.
298. J. F. Smalley, S. W. Feldberg, C. E. D. Chidsey, M. R. Linford, M. D. Newton, and Y.-P. Liu, *J. Phys. Chem.*, 1995, **99**, 13141.
299. H. B. Gray and J. R. Winkler, *Proc. Natl. Acad. Sci. U. S. A.*, 2005, **102**, 3534.
300. T. A. Heimer, S. T. D'Arcangelis, F. Farzad, J. M. Stipkala, and G. J. Meyer, *Inorg. Chem.*, 1996, **35**, 5319.
301. E. Hendry, M. Koeberg, B. O'Regan, and M. Bonn, *Nano Lett.*, 2006, **6**, 755.
302. G. M. Turner, M. C. Beard, and C. A. Schmuttenmaer, *J. Phys. Chem. B*, 2002, **106**, 11716.
303. M. C. Beard, G. M. Turner, and C. A. Schmuttenmaer, *J. Phys. Chem. B*, 2002, **106**, 7146.
304. B. Wenger, C. Bauer, M. K. Nazeeruddin, P. Comte, S. M. Zakeeruddin, M. Grätzel, and J.-E. Moser, in Electron Donor-acceptor Distance Dependence of the Dynamics of Light-induced Interfacial Charge Transfer in the Dye-sensitization of Nanocrystalline Oxide Semiconductors, 'Physical Chemistry of Interfaces and Nanomaterials V', San Diego, CA, USA, 2006', SPIE, San Diego, CA, 2006, p. 63250V.
305. K. Kilsa, E. I. Mayo, D. Kuciauskas, R. Villahermosa, N. S. Lewis, J. R. Winkler, and H. B. Gray, *J. Phys. Chem. A*, 2003, **107**, 3379.
306. E. Galoppini, *Coord. Chem. Rev.*, 2004, **248**, 1283.
307. E. Galoppini, W. Guo, P. Qu, and G. J. Meyer, *J. Am. Chem. Soc.*, 2001, **123**, 4342.
308. P. Piotrowiak, E. Galoppini, Q. Wei, G. J. Meyer, and P. Wiewior, *J. Am. Chem. Soc.*, 2003, **125**, 5278.
309. E. Galoppini, W. Guo, W. Zhang, P. G. Hoertz, P. Qu, and G. J. Meyer, *J. Am. Chem. Soc.*, 2002, **124**, 7801.
310. M. Myahkostupov, P. Piotrowiak, D. Wang, and E. Galoppini, *J. Phys. Chem. C*, 2007, **111**, 2827.
311. N. A. Anderson, X. Ai, D. Chen, D. L. Mohler, and T. Lian, *J. Phys. Chem. B*, 2003, **107**, 14231.
312. M. Abrahamsson, O. Taratula, P. Persson, E. Galoppini, and G. J. Meyer, *J. Photochem. Photobiol. A Chem.*, 2009, **206**, 155.
313. C. Houarner-Rassin, F. Chaignon, C. She, D. Stockwell, E. Blart, P. Buvat, T. Lian, and F. Odobel, *J. Photochem. Photobiol. A Chem.*, 2007, **192**, 56.
314. C. C. Clark, G. J. Meyer, Q. Wei, and E. Galoppini, *J. Phys. Chem. B*, 2006, **110**, 11044.
315. C. C. Clark, A. Marton, and G. J. Meyer, *Inorg. Chem.*, 2005, **44**, 3383.
316. C. C. Clark, A. Marton, R. Srinivasan, A. A. Narducci Sarjeant, and G. J. Meyer, *Inorg. Chem.*, 2006, **45**, 4728.
317. A. Marton, C. C. Clark, R. Srinivasan, R. E. Freundlich, A. A. NarducciSarjeant, and G. J. Meyer, *Inorg. Chem.*, 2006, **45**, 362.
318. F. Liu and G. J. Meyer, *Inorg. Chem.*, 2005, **44**, 9305.
319. E. Palomares, J. N. Clifford, S. A. Haque, T. Lutz, and J. R. Durrant, *J. Am. Chem. Soc.*, 2003, **125**, 475.
320. A. R. Kortan, R. Hull, R. L. Opila, M. G. Bawendi, M. L. Steigerwald, P. J. Carroll, and L. E. Brus, *J. Am. Chem. Soc.*, 1990, **112**, 1327.
321. I. Bedja and P. V. Kamat, *J. Phys. Chem.*, 1995, **99**, 9182.
322. Y. Diamant, S. Chappel, S. G. Chen, O. Melamed, and A. Zaban, *Coord. Chem. Rev.*, 2004, **248**, 1271.
323. A. Zaban, S. G. Chen, S. Chappel, and B. A. Gregg, *Chem. Commun.*, 2000, 2231.
324. W. H. Rippard, A. C. Perrella, F. J. Albert, and R. A. Buhrman, *Phys. Rev. Lett.*, 2002, **88**, 046805.
325. P. Qu, G. J. Meyer, Chap. 2: Dye-Sensitized Electrodes, in 'Electon Transfer in Chemistry, Part 2', ed. V. Balzani, 2005, Vol. IV, p. 355.
326. H. Gerischer and F. Willig, *Top. Curr. Chem.*, 1976, **61**, 31.
327. I. Ortmans, C. Moucheron, and A. Kirsch-De Mesmaeker, *Coord. Chem. Rev.*, 1998, **168**, 233.
328. O. Kohle, M. Grätzel, A. F. Meyer, and T. B. Meyer, *Adv. Mater. (Weinheim, Fed. Repub. Ger.)*, 1997, **9**, 904.
329. F. Cecchet, A. M. Gioacchini, M. Marcaccio, F. Paolucci, S. Roffia, M. Alebbi, and C. A. Bignozzi, *J. Phys. Chem. B*, 2002, **106**, 3926.
330. G. Wolfbauer, A. M. Bond, and D. R. MacFarlane, *Inorg. Chem.*, 1999, **38**, 3836.
331. D. W. Thompson, C. A. Kelly, F. Farzad, and G. J. Meyer, *Langmuir*, 1999, **15**, 650.

332. C. J. Kleverlaan, M. T. Indelli, C. A. Bignozzi, L. Pavanin, F. Scandola, G. M. Hasselman, and G. J. Meyer, *J. Am. Chem. Soc.*, 2000, **122**, 2840.
333. S. Ernst and W. Kaim, *Inorg. Chim. Acta*, 1986, **114**, 123.
334. B. V. Bergeron, A. Marton, G. Oskam, and G. J. Meyer, *J. Phys. Chem. B*, 2005, **109**, 937.
335. C. R. Bock, J. A. Connor, A. R. Gutierrez, T. J. Meyer, D. G. Whitten, B. P. Sullivan, and J. K. Nagle, *J. Am. Chem. Soc.*, 1979, **101**, 4815.
336. C. R. Bock, T. J. Meyer, and D. G. Whitten, *J. Am. Chem. Soc.*, 1975, **97**, 2909.
337. A. J. Bard and L. R. Faulkner, 'Electrochemical Methods: Fundamentals and Applications', 2nd edition, John Wiley & Sons, Inc., New York, 2001.
338. P. Wang, B. Wenger, R. Humphry-Baker, J. E. Moser, J. Teuscher, W. Kantlehner, J. Mezger, E. V. Stoyanov, S. M. Zakeeruddin, and M. Grätzel, *J. Am. Chem. Soc.*, 2005, **127**, 6850.
339. D. Gust, T. A. Moore, and A. L. Moore, *J. Photochem. Photobiol. B Biol.*, 2000, **58**, 63.
340. T. A. Moore, A. L. Moore, and D. Gust, *Philos. Trans. R. Soc. London, B*, 2002, **357**, 1481.
341. C. S. Christ, J. Yu, X. Zhao, G. T. R. Palmore, and M. S. Wrighton, *Inorg. Chem.*, 1992, **31**, 4439.
342. R. Argazzi, C. A. Bignozzi, T. A. Heimer, F. N. Castellano, and G. J. Meyer, *J. Am. Chem. Soc.*, 1995, **117**, 11815.
343. R. Argazzi, C. A. Bignozzi, T. A. Heimer, F. N. Castellano, and G. J. Meyer, *J. Phys. Chem. B*, 1997, **101**, 2591.
344. P. Bonhote, J. E. Moser, R. Humphry-Baker, N. Vlachopoulos, S. M. Zakeeruddin, L. Walder, and M. Grätzel, *J. Am. Chem. Soc.*, 1999, **121**, 1324.
345. K. Westermark, S. Tingry, P. Persson, H. Rensmo, S. Lunell, A. Hagfeldt, and H. Siegbahn, *J. Phys. Chem. B*, 2001, **105**, 7182.
346. Z. Ning, and H. Tian, *Chem. Commun.*, 2009, 5483.
347. J. N. Clifford, E. Palomares, M. K. Nazeeruddin, M. Grätzel, J. Nelson, X. Li, N. J. Long, and J. R. Durrant, *J. Am. Chem. Soc.*, 2004, **126**, 5225.
348. S. A. Haque, J. S. Park, M. Srinivasarao, and J. R. Durrant, *Adv. Mater.*, 2004, **16**, 1177.
349. E. Palomares, M. V. Martinez-Diaz, S. A. Haque, T. Torres, and J. R. Durrant, *Chem. Commun.*, 2004, 2112.
350. S. Handa, H. Wietasch, M. Thelakkat, J. R. Durrant, and S. A. Haque, *Chem. Commun.*, 2007, 1725.
351. C. S. Karthikeyan, H. Wietasch, and M. Thelakkat, *Adv. Mater.*, 2007, **19**, 1091.
352. C. Kleverlaan, M. Alebbi, R. Argazzi, C. A. Bignozzi, G. M. Hasselman, and G. J. Meyer, *Inorg. Chem.*, 2000, **39**, 1342.
353. Y. Xu, G. Eilers, M. Borgström, J. Pan, M. Abrahamsson, A. Magnusson, R. Lomoth, J. Bergquist, T. Polivka, L. Sun, V. Sundström, S. Styrling, L. Hammarström, and B. Åkermark, *Chem. Eur. J.*, 2005, **11**, 7305.
354. B. Gholamkhass, K. Koike, N. Negishi, H. Hori, T. Sano, and K. Takeuchi, *Inorg. Chem.*, 2003, **42**, 2919.
355. M. A. Green, K. Emery, Y. Hishikawa, and W. Warta, *Prog. Photovolt. Res. Appl.*, 2008, **16**, 61.
356. D. M. Stanbury, Reduction Potentials Involving Inorganic Free Radicals in Aqueous Solution, in 'Advances in Inorganic Chemistry', ed. A. G. Sykes, Academic Press, 1989, Vol. 33, p. 69.
357. G. Nord, B. Pedersen, and O. Farver, *Inorg. Chem.*, 1978, **17**, 2233.
358. G. Nord, B. Pedersen, L. Floryan, and P. Pagsberg, *Inorg. Chem.*, 1982, **21**, 2327.
359. G. Nord, *Comm. Inorg. Chem.*, 1992, **13**, 221.
360. W. K. Wilmarth, D. M. Stanbury, J. E. Byrd, H. N. Po, and C.-P. Chua, *Coord. Chem. Rev.*, 1983, **51**, 155.
361. B. J. Walter and C. M. Elliott, *Inorg. Chem.*, 2001, **40**, 5924.
362. X. Wang and D. M. Stanbury, *Inorg. Chem.*, 2006, **45**, 3415.
363. I. V. Nelson and R. T. Iwamoto, *J. Electroanal. Chem.*, 1964, **7**, 218.
364. J. Desbarres, *Bull. Soc. Chim. Fr.*, 1961, **28**, 502.
365. A. J. Parker, *J. Chem. Soc. London A*, 1966, 220.
366. R. Alexander, E. C. F. Ko, Y. C. Mac, and A. J. Parker, *J. Am. Chem. Soc.*, 1967, **89**, 3703.
367. F. G. K. Baucke, R. Bertram, and K. Cruse, *J. Electroanal. Chem.*, 1971, **32**, 247.
368. R. Guidelli and G. Piccardi, *Electrochim. Acta*, 1967, **12**, 1085.
369. A. I. Popov and D. H. Geske, *J. Am. Chem. Soc.*, 1958, **80**, 1340.
370. V. A. Macagno, M. C. Giordano, and A. J. Arvíá, *Electrochim. Acta*, 1969, **14**, 335.
371. J. N. Demas and J. W. Addington, *J. Am. Chem. Soc.*, 1976, **98**, 5800.
372. J. N. Demas, J. W. Addington, S. H. Peterson, and E. W. Harris, *J. Phys. Chem.*, 1977, **81**, 1039.
373. C. Nasr, S. Hotchandani, and P. V. Kamat, *J. Phys. Chem. B*, 1998, **102**, 4944.
374. J. M. Gardner, J. M. Giaimuccio, and G. J. Meyer, *J. Am. Chem. Soc.*, 2008, **130**, 17252.
375. J. M. Gardner, M. Abrahamsson, B. Farnum, and G. J. Meyer, *J. Am. Chem. Soc.*, 2009, ASAP **131**(44), 16206.
376. D. J. Fitzmaurice and H. Frei, *Langmuir*, 1991, **7**, 1129.
377. J. N. Clifford, E. Palomares, M. K. Nazeeruddin, M. Grätzel, and J. R. Durrant, *J. Phys. Chem. C*, 2007, **111**, 6561.
378. S. Pelet, J. E. Moser, and M. Grätzel, *J. Phys. Chem. B*, 2000, **104**, 1791.
379. P. J. Cameron, L. M. Peter, S. M. Zakeeruddin, and M. Grätzel, *Coord. Chem. Rev.*, 2004, **248**, 1447.
380. B. A. Gregg, F. Pichot, S. Ferrere, and C. L. Fields, *J. Phys. Chem. B*, 2001, **105**, 1422.
381. J. Desilvestro, M. Grätzel, L. Kavan, J. Moser, and J. Augustynski, *J. Am. Chem. Soc.*, 1985, **107**, 2988.

382. N. Vlachopoulos, P. Liska, J. Augustynski, and M. Grätzel, *J. Am. Chem. Soc.*, 1988, **110**, 1216.
383. G. Oskam, B. V. Bergeron, G. J. Meyer, and P. C. Searson, *J. Phys. Chem. B*, 2001, **105**, 6867.
384. P. Wang, S. M. Zakeeruddin, J. E. Moser, R. Humphry-Baker, and M. Grätzel, *J. Am. Chem. Soc.*, 2004, **126**, 7164.
385. N. Sutin and C. Creutz, *J. Chem. Educ.*, 1983, **60**, 809.
386. H. Nusbaumer, J. E. Moser, S. M. Zakeeruddin, M. K. Nazeeruddin, and M. Grätzel, *J. Phys. Chem. B*, 2001, **105**, 10461.
387. H. Nusbaumer, S. M. Zakeeruddin, J.-E. Moser, and M. Grätzel, *Chem. Eur. J.*, 2003, **9**, 3756.
388. S. A. Sapp, C. M. Elliott, C. Contado, S. Caramori, and C. A. Bignozzi, *J. Am. Chem. Soc.*, 2002, **124**, 11215.
389. S. Hattori, Y. Wada, S. Yanagida, and S. Fukuzumi, *J. Am. Chem. Soc.*, 2005, **127**, 9648.
390. S. Nakade, T. Kanzaki, W. Kubo, T. Kitamura, Y. Wada, and S. Yanagida, *J. Phys. Chem. B*, 2005, **109**, 3480.
391. S. Nakade, Y. Makimoto, W. Kubo, T. Kitamura, Y. Wada, and S. Yanagida, *J. Phys. Chem. B*, 2005, **109**, 3488.
392. S. Cazzanti, S. Caramori, R. Argazzi, C. M. Elliott, and C. A. Bignozzi, *J. Am. Chem. Soc.*, 2006, **128**, 9996.
393. J. J. Nelson, T. J. Amick, and C. M. Elliott, *J. Phys. Chem. C*, 2008, **112**, 18255.
394. A. Grabulosa, M. Beley, P. C. Gros, S. Cazzanti, S. Caramori, and C. A. Bignozzi, *Inorg. Chem.*, 2009, **48**, 8030.
395. M. J. Scott, J. J. Nelson, S. Caramori, C. A. Bignozzi, and C. M. Elliott, *Inorg. Chem.*, 2007, **46**, 10071.
396. M. Brugnati, S. Caramori, S. Cazzanti, L. Marchini, R. Argazzi, and C. A. Bignozzi, *Int. J. Photoenergy*, 2007, **2007**, 80756.
397. B. Enright, G. Redmond, and D. Fitzmaurice, *J. Phys. Chem.*, 1994, **98**, 6195.
398. H. Lindstrom, S. Södergren, A. Solbrand, H. Rensmo, J. Hjelm, A. Hagfeldt, and S. E. Lindquist, *J. Phys. Chem. B*, 1997, **101**, 7710.
399. H. Lindstrom, S. Södergren, A. Solbrand, H. Rensmo, J. Hjelm, A. Hagfeldt, and S. E. Lindquist, *J. Phys. Chem. B*, 1997, **101**, 7717.
400. B. O'Regan and D. T. Schwartz, *Chem. Mater.*, 1998, **10**, 1501.
401. B. A. Gregg, S.-G. Chen, and S. Ferrere, *J. Phys. Chem. B*, 2003, **107**, 3019.
402. S. Ferrere and B. A. Gregg, *J. Phys. Chem. B*, 2001, **105**, 7602.
403. Q. Wang, Z. Zhang, S. M. Zakeeruddin, and M. Grätzel, *J. Phys. Chem. C*, 2008, **112**, 7084.
404. Q. Wang, Z. Zhang, S. M. Zakeeruddin, and M. Grätzel, *J. Phys. Chem. C*, 2008, **112**, 10585.
405. C. A. Kelly, F. Farzad, D. W. Thompson, J. M. Stipkala, and G. J. Meyer, *Langmuir*, 1999, **15**, 7047.
406. E. F. Hilinski, P. A. Lucas, and Y. Wang, *J. Chem. Phys.*, 1988, **89**, 3435.
407. D. J. Norris, A. Sacra, C. B. Murray, and M. G. Bawendi, *Phys. Rev. Lett.*, 1994, **72**, 2612.
408. S. H. Szczepankiewicz, J. A. Moss, and M. R. Hoffmann, *J. Phys. Chem. B*, 2002, **106**, 7654.
409. C. L. Olson, J. Nelson, and M. S. Islam, *J. Phys. Chem. B*, 2006, **110**, 9995.
410. CRC, 'Handbook of Chemistry and Physics'. 73rd edition, CRC Press, Boca Ration, 1992.
411. B. A. Gregg, *Coord. Chem. Rev.*, 2004, **248**, 1215.
412. J. Nelson, *Phys. Rev. B*, 1999, **59**, 15374.
413. G. Schlichthorl, S. Y. Huang, J. Sprague, and A. J. Frank, *J. Phys. Chem. B*, 1997, **101**, 8141.
414. K. Schwarzburg and F. Willig, *J. Phys. Chem. B*, 1999, **103**, 5743.
415. L. Dloczik, O. Ileperuma, I. Lauermann, L. M. Peter, E. A. Ponomarev, G. Redmond, N. J. Shaw, and I. Uhlendorf, *J. Phys. Chem. B*, 1997, **101**, 10281.
416. A. Zaban, A. Meier, and B. A. Gregg, *J. Phys. Chem. B*, 1997, **101**, 7985.
417. A. Zaban, S. Ferrere, and B. A. Gregg, *J. Phys. Chem. B*, 1998, **102**, 452.
418. B. A. Gregg, *J. Phys. Chem. B*, 2003, **107**, 13540.
419. R. Könenkamp, *Phys. Rev. B*, 2000, **61**, 11057.
420. V. Kytin, T. Dittrich, J. Bisquert, E. A. Lebedev, and F. Koch, *Phys. Rev. B*, 2003, **68**, 195308.
421. P. Hoyer and H. Weller, *J. Phys. Chem.*, 2002, **99**, 14096.
422. L. Brus, *Phys. Rev. B*, 1996, **53**, 4649.
423. D. Cahen, G. Hodes, M. Grätzel, J. F. Guillemoles, and I. Riess, *J. Phys. Chem. B*, 2000, **104**, 2053.
424. J. Bisquert, D. Cahen, G. Hodes, S. Ruhle, and A. Zaban, *J. Phys. Chem. B*, 2004, **108**, 8106.
425. C. L. Olson, *J. Phys. Chem. B*, 2006, **110**, 9619.
426. U. B. Cappel, E. A. Gibson, A. Hagfeldt, and G. Boschloo, *J. Phys. Chem. C*, 2009, **113**, 6275.
427. I. Montanari, J. Nelson, and J. R. Durrant, *J. Phys. Chem. B*, 2002, **106**, 12203.
428. A. Kay, R. Humphry-Baker, and M. Grätzel, *J. Phys. Chem.*, 1994, **98**, 952.
429. S. A. Haque, Y. Tachibana, D. R. Klug, and J. R. Durrant, *J. Phys. Chem. B*, 1998, **102**, 1745.
430. C. Bauer, G. Boschloo, E. Mukhtar, and A. Hagfeldt, *J. Phys. Chem. B*, 2002, **106**, 12693.
431. A. N. M. Green, R. E. Chandler, S. A. Haque, J. Nelson, and J. R. Durrant, *J. Phys. Chem. B*, 2005, **109**, 142.

Electrochemical and Photoelectrochemical Conversion of CO₂ to Alcohols

Robert H. Crabtree

Yale University, New Haven, CT, USA

1	Introduction	301
2	Carbon Dioxide	302
3	Catalytic Reduction of Carbon Dioxide	303
4	Conclusions	305
5	Acknowledgments	306
6	Abbreviations and Acronyms	306
7	References	306

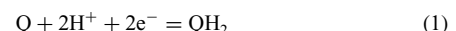
1 INTRODUCTION

In a world increasingly affected by climate change, CO₂ emissions are likely to become more restricted with the implementation of regulations or carbon taxes.¹ The Stern Report calls for a 1.7% per year rise in the rate of CO₂ emissions until 2030, fossil fuel use being the dominant factor.² This, together with processes like cement production and fermentation, will continue for decades to come to provide sources of CO₂-rich effluent gas potentially available for use. Carbon capture and storage (CCS) in geological formations has been suggested as a way to avoid release of this CO₂ but CCS is costly and some regions may well prove not to have suitable geology. Another way of handling some of this CO₂ may be to use it as an energy carrier by recharging it from a nonfossil source such as nuclear energy, solar or wind power. The reduced form of the CO₂, say methane or methanol, could be a fuel for transport applications or a useful carbon source for products in the chemical industry. Most of this reduced CO₂ will no doubt return to the atmosphere on fuel combustion or product disposal but at least the carbon intensity of the combined scheme would be significantly reduced.

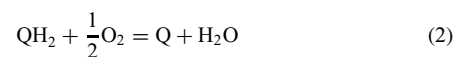
Energy storage needs to be resolved for alternative energy³ to be practical on a global scale because demand is continuous but solar and wind energy supply are intermittent. So far, batteries have not yet proved cheap and efficient enough to be ideal. Present-day batteries also tend to use elements like Li that are not sufficiently abundant to permit economic

use on a global scale. Solar and wind power are also dilute forms of energy, while air and land transportation require a concentrated form of energy, typically in the form of a liquid fuel.

Both of these needs—energy storage and availability of a good transport fuel—can, in principle, be met by combining electrons from the energy source with protons from the medium to electrocatalytically hydrogenate a suitable hydrogen carrier, perhaps, CO₂ to methanol, but, in general, Q to QH₂.



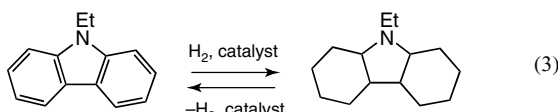
Extraction of the energy thus stored could occur via reversal of equation (1) in a fuel cell with O₂ reduction to water occurring at the cathode to give the overall process shown in equation (2).



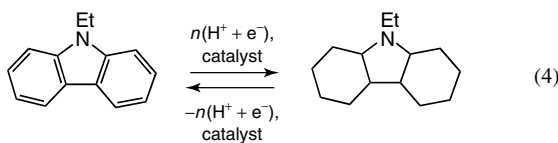
Assuming that Q can be efficiently recycled, this would constitute an energy storage–release cycle with negligible carbon dioxide production. If Q had a sufficiently low molecular weight, this could also provide a concentrated fuel for transport.

Many other suggestions have been made for energy storage. For example, the electric power from alternative energy sources could be converted into H₂ by electrolysis and the H₂ subsequently stored. Hydrogen storage⁴ is a wide field

with numerous competing proposed technologies, but we view storage in nitrogen heterocycles as a particularly attractive possibility; equation (3) shows a liquid carrier successfully tested by Cooper and Pez at Air Products.



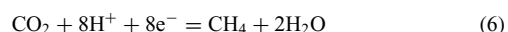
All these schemes rely on the safe handling of free H₂—a difficult problem on a global scale. Since gases like CO₂ and H₂ are hard to handle, we have suggested electrocatalytic reduction of the same types of liquid organic carrier, with partial oxidation back to the arene form in a fuel cell to release the energy content without forming CO₂. Now, the H₂ production and storage steps, usually considered separately, are combined into one, with the reasonable expectation of higher efficiency. Likewise, the H₂ release and H₂ oxidation steps, usually separate, are also combined. We have called this strategy *virtual hydrogen storage* (*VHS*) since no free H₂ is ever involved.⁵



In this article, we consider the claims of CO₂ as a hydrogen carrier. Although present in air (350 ppm), extraction is costly and CO₂-rich effluent from conventional power plants or cement plants is thus preferred. Instead of being released or stored in deep rock formations, some of this CO₂ could be reduced to a fuel such as methane or methanol. Ideally, an economic way would be found to recapture the CO₂ from the second and subsequent energy release steps so that the carbon can be recycled numerous times. Where solar energy is used, the overall scheme is related to photosynthesis because in both cases solar light is converted into a chemical fuel that is a reduced form of CO₂, methanol in one case, sugar in the other.

A potential advantage of CO₂ over the organic carriers mentioned above is that water is lost on reduction of CO₂, leading to reduced weight of the ultimate fuel formed. The separation of the methanol from the water would be energy-intensive and detract from the overall efficiency. However, as a gas, methane might well be a more desirable product. If methanol or methane is the fuel formed from CO₂, we effectively store 6(H⁺ + e⁻) or 8(H⁺ + e⁻). Although only four H atoms appear in the products, the energy of all six or eight is stored. Dehydration of CH₃OH to Me₂O or to gasoline-range hydrocarbons is also possible. In the latter case, gasoline-range hydrocarbons would provide access to conventional fuels that are even more energy-rich than

methanol. Conventional fuels also minimize the need for costly infrastructure changes.



For any of these alternative strategies to be viable, we need to be able to electrocatalytically reduce CO₂ to methanol or a related energy-rich molecule. This cannot yet be done with high efficiency, although important work has been published that shows promise.

2 CARBON DIOXIDE

Carbon dioxide is a key greenhouse gas that has been implicated in global warming and climate change.⁶ The ca 280 ppm preindustrial level in the atmosphere has now reached 390 ppm and is most likely responsible for the estimated warming of ca 0.75 °C since 1850 and the current warming trend of 0.2 °C per decade.⁷ Fears about the possible future course of climate change have made CO₂ chemistry a recent topic of close attention.

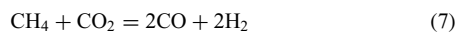
It is hard to imagine that a significant fraction of the CO₂ released over the last century could be removed from the atmosphere by any chemical process, because the amounts in question are so huge—this has even been called the *teraton challenge*.⁸ Nevertheless, chemical conversions could contribute, acting along with other measures, to avoiding additional future injections of CO₂. As pointed out by Sakakura and coworkers, using CO₂ as a feedstock will not lead to a significant net reduction in atmospheric CO₂. The energy requirement for the processes involved will necessarily produce some CO₂. The total amount plausibly usable by the chemical industry is a very small fraction of the excess CO₂ in the atmosphere relative to preindustrial levels. Finally, many of the resulting products will emit CO₂ at the disposal stage.⁹

Several problems arise in trying to bring about the chemical reduction of CO₂. Many reactions of CO₂ are thermodynamically unfeasible because CO₂ itself is so thermodynamically stable. Kinetically, nonpolar CO₂ is also relatively unreactive. As a gaseous molecule, any fixation of an electrode or catalyst carries with it an entropic penalty. It has a relatively high LUMO (lowest unoccupied molecular orbital), thus being a poor candidate for direct electron injection. Once bound to a metal complex it can be easier to reduce, but such binding is not common. It does react easily with bases, particularly with OH⁻ to give bicarbonate, but this product is harder, not easier, to reduce than CO₂ itself. Finally, in any reaction, linear CO₂ has to rehybridize its carbon atom from sp to sp², a step that may contribute to the kinetic barrier in some cases.

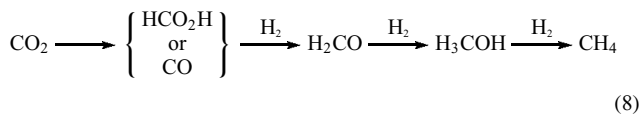
3 CATALYTIC REDUCTION OF CARBON DIOXIDE

3.1 Thermal Processes

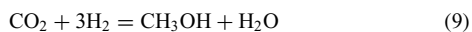
Thermal processes have received much more attention than electrochemical or photochemical ones and help provide an insight into the requirements for CO₂ binding and reduction that must also apply to the electrochemical and photoelectrochemical routes to be discussed below. CH₄ reforming, normally carried out with steam, can alternatively be done with CO₂ to form synthesis gas with Ni, Rh, or Ru catalysts (“dry reforming”).¹⁰ H₂/CO is suitable for conversion to hydrocarbon fuels via the Fischer–Tropsch reaction but not for methanol formation via CO hydrogenation because this needs a 2 : 1 H₂ : CO ratio.



Hydrogenation can, in principle, give a number of products as illustrated in equation (8), of which methanol is perhaps the most desirable as a feedstock or fuel.



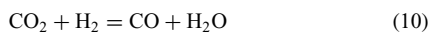
Hydrogenation of CO₂ to methanol with any of a variety of catalysts, homogeneous and heterogeneous, has proved possible by equation (6). ΔG is only +3 kJ mol⁻¹ for equation (6) at 298 K, illustrating the high stability of CO₂.⁸ The preferred commercial catalyst is Cu/ZnO/Al₂O₃, but the mechanism is still under discussion.



The Sabatier process involves the hydrogenation of CO₂ with Ni, Ru, or Rh catalysts to give methane. The high cost of H₂ versus methane is a limitation for practical work, however.⁸

The Carnol process, proposed by workers at Brookhaven National Lab, combines methane pyrolysis to carbon and hydrogen with catalytic CO₂ reduction by the hydrogen produced to give methanol. Solid carbon is considered to be much easier to sequester than CO₂ and the methanol can again be used as a feedstock or fuel.¹¹

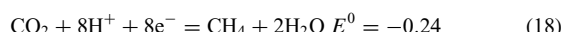
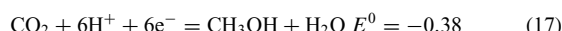
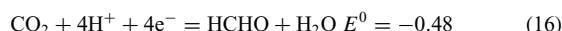
The reverse of the water gas shift (equation 10) has been invoked to explain the fact that both hydroformylation (equation 11) and methanol homologation (equation 12)—reactions that normally go with CO—can also be brought about with H₂/CO₂.¹²



Hydrogenation in supercritical CO₂ as both solvent and substrate, for example, with [RuCl₂(PMe₃)₄] catalyst, has proved very effective for producing formic acid.¹³

3.2 Electrochemical Processes

Multielectron reduction of CO₂ with the assistance of protonation is, in principle, accessible without great difficulty as shown by the appropriate reduction potentials (equations 13–18, E⁰ vs SHE, pH = 1 in H₂O).¹⁴ Catalysts are needed, however, and these tend to show low activity.



Important early work by Eisenberg¹⁵ provided the first efficient electrocatalytic CO₂ reduction with a variety of tetraaza macrocycles of Ni and Co. In addition to CO, H₂ was also produced. Since protons must be present for CO₂ reduction, proton reduction to H₂ is always a possible side reaction. Since H₂/CO mixtures are themselves useful precursors to alcohols and hydrocarbons, however, the production of both materials may not be a problem. Current efficiencies were high but turnover frequencies were only in the range of 1–10 h⁻¹. Sauvage’s¹⁶ Ni cyclam and Savéant’s¹⁷ iron porphyrins improved on the earlier work with turnovers of several hundred per hour. The overpotentials were high in these systems, however. Lehn’s¹⁸ Re(bipy)(CO)₃Cl (bipy = bipyridine) system and Kubiak’s dicopper catalysts fall into the same category. The most extensive series of catalysts for CO production is the phosphine palladium series of Dubois,¹⁹ for example, [Pd(triphos)(solvent)]²⁺. A metalacarboxylic acid, Pd–COOH is proposed as intermediate. Protonation is then thought to form a Pd=C(OH)₂ carbene, from which CO is produced by dehydration.

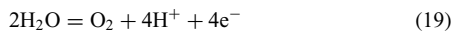
Meyer’s 2,2'-bipyridine complexes such as *cis*-[Rh(bipy)₂Cl₂]⁺ reduce CO₂ to give formate, rather than CO.²⁰

These reductions proceed by transfer of (H⁺ + e⁻) to the CO₂. In this kind of process, a proton-coupled electron transfer (PCET) pathway is often favored. Not only does it minimize charge separation when the H⁺ and e⁻ are transferred in a concerted manner, but the protonation also helps electron transfer. Kubiak and coworkers²¹ note that the 1 e reduction of CO₂ to ·CO₂⁻ without protonation has an E⁰ of −1.9 V, while E⁰s for reactions with protonation are much more accessible, e.g., equations (13–18).

Multielectron transfer is harder than the single electron case because if successive 1 e steps are involved, the

intermediates formed all have to be stable enough to provide a viable pathway. The role of the electrocatalyst is both to stabilize the intermediates by coordination and to undergo a redox process at a suitable E^0 to furnish a species capable of reducing the bound CO₂ and the subsequent intermediates.

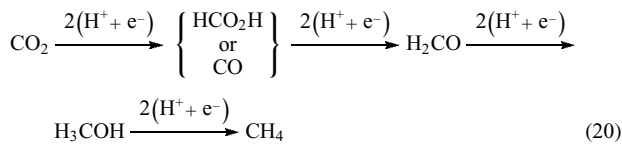
The reduction processes of equations (17, 18) require six to eight (H⁺ + e⁻) per mole of CO₂. If we assume the electrons will come from solar, wind, or nuclear power, we still need to provide the protons. This $n(H^+ + e^-)$ proton requirement for the cathodic reduction side implies that the anodic oxidation side must release protons and electrons in a 1 : 1 ratio. Water oxidation is the most plausible way of doing this on the huge scale required. Equation (19) illustrates the water oxidation side of the process. In a device, the protons released would pass through a proton-permeable membrane to reach the cathode. This emphasizes the central place that water oxidation catalysis holds in alternative energy schemes, just as it does in oxygenic photosynthesis in green plants.



In any electrochemical reduction, a number of intermediate oxidation states are in principle possible as illustrated for CO₂ in equation (20), where each step is separated from the next by 2(H⁺ + e⁻); loss of H₂O is also required in several steps. All the steps need a suitable electrocatalyst, and for a deep reduction to methanol or methane, the catalyst will have to be active for multiple steps in succession. This raises the question of whether a single catalyst can be well adapted to all of the steps or whether we will need to have several catalysts present to obtain high selectivity.

Methanol and methane in equation (7) are plausible fuels but the other reduction products are not sufficiently rich in energy. Of the two, methanol has the advantage of being a liquid and also of transforming into gasoline-range hydrocarbons on treatment with acidic zeolites. Methane is richer in energy but harder to transport.

Formic acid and CO are the products most often seen in practice, so the second step of equation (20) is evidently difficult. Formaldehyde is rare, so its reduction must be relatively easy. Deeper reduction is very rare. Alternative reduction products such as oxalate are seen but these are not on the pathway to methanol.



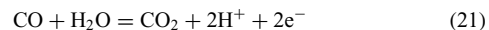
The recent key review by Savéant²² not only outlines the general principles of electrocatalytic reactions but also devotes considerable space to the specific case of CO₂ reduction. We do not attempt to duplicate this information

here, but we can draw some broad conclusions. Co and Ni tetraaza macrocycles have proved to be among the most effective base metal catalysts, and rhenium and ruthenium bipyridyl and related N-donor complexes are effective among the rare metals. The main difficulties so far are the slow rates of catalysis and the tendency to give formate and CO as reduction products; these are of little immediate use as fuels. Deeper reduction to methanol or methane is extremely rare.

The propensity for formation of CO on reduction of CO₂ may be a result of the ease of loss of CO from the electrocatalyst. This suggestion is strengthened by the fact that reduction beyond the CO level has been seen at low temperature where the entropic driving force for CO loss from the electrode is lower. This is the case for [Ru(terpy)(dipy)CO]²⁺ as catalyst.

Electrocatalytic formation of CO could be helpful if accompanied by water reduction to H₂. In principle, such H₂/CO mixtures (syngas) could be converted to conventional liquid hydrocarbon fuels by the Fischer–Tropsch process. Only a very large power source could provide the great quantities of syngas required for an efficient Fischer–Tropsch plant, however, so the viability of this option is unclear.

There is some hope of a biomimetic CO₂ reduction catalyst since Ni and Fe containing CO dehydrogenase (CODH) is a highly efficient catalyst for equation (21) and we have reported a Ni(II) complex as a model catalyst for this process.²³



3.3 Photochemical Processes

The most efficient method of solar-to-fuel conversion with CO₂ as carbon source may eventually prove to be a combination of conventional photovoltaic devices with electrochemical CO₂ reduction. Nevertheless, much current work is aimed at direct solar-to-fuel conversion in a single photoelectrochemical cell. Typically, the plan is for water to be oxidized to O₂ at the anode, thus providing electrons that traverse the external circuit and reduce CO₂ to fuel at the cathode, the whole system being driven by solar light. The well-known Grätzel cell is often taken as the starting point. In this cell, a ruthenium dye attached to the photoanode absorbs light and injects an electron into the anode. The electron traverses the external circuit, doing work, and returns to the cell at the cathode. This electron reduces the triiodide electrolyte to iodide. The iodide migrates to the anode and reduces the oxidized form of the dye that is left after photoinjection of the electron. No net electrochemistry occurs because the last step regenerates the triiodide and the cell produces a photocurrent as sole output.²⁴

Turning a Grätzel cell into a water-splitting cell that produces H₂ and O₂ is a difficult problem because a catalyst for water oxidation is now required at the anode. Few such catalysts are known, perhaps the best being heterogeneous

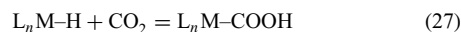
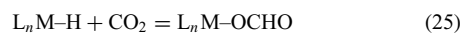
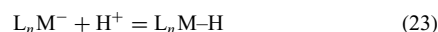
IrO_2 . Mallouk has shown initial progress in constructing such a cell with IrO_2 .²⁵ The H_2 produced constitutes the fuel in this type of cell but H_2 being a noncondensable gas complicates the problem of fuel delivery and storage. Hydrogen storage in various materials has been proposed as a solution but no fully satisfactory option has yet emerged.

Interest has therefore turned to a photoelectrochemical cell in which CO_2 reduction, for example, to methanol, would provide an easily storable fuel. This raises several problems including how methanol is to be separated from the electrolyte. Assuming this problem can be solved, we still need to have an electrocatalyst for selective CO_2 reduction at the cathode. This catalyst could be any one of those discussed in the last section. As we saw previously, the problem that then arises is the low activity of catalysts so far developed and their strong tendency to give 2 e reduction to formic acid or to CO, materials having too low an energy density for fuels, rather than deeper reduction to high energy density fuels like methane and methanol.

In catalyst development for such cells, a simplification is often adopted. Because construction of the full cell requires optimization of two separate catalysts, the problem is often reduced to a one-catalyst level by providing a sacrificial reductant if CO_2 reduction is being studied or a sacrificial oxidant if H_2O oxidation is being studied. The sacrificial reagent avoids the need for a catalyst at the counterelectrode because a much easier substrate than H_2O or CO_2 is used. Progress is at a very early stage in this type of work, however.

Photosynthesis shows that efficient solar-to-fuel conversion is possible in principle and much effort is currently being directed toward various types of "artificial photosynthesis". Apart from the photoelectrochemical cell described above, homogeneous photoreduction has also been investigated. The recent review by Morris, Meyer, and Fujita covers the key points.²⁶ In most such work on the photochemical reduction of CO_2 , separate homogeneous components act as sensitizer, catalyst, and reductant, although the sensitizer and catalyst are sometimes combined. The photoactive $[\text{Ru}(\text{bipy})_3]^{2+}$ complex is the preferred sensitizer because it has a long-lived excited state and good absorption of visible light. Once an electron has been promoted to the π^* level of the bipy ligand the resulting "hole" in the sensitizer can be quenched by the sacrificial electron donor, NEt_3 or triethanolamine, to give a highly reducing Ru species that can transfer 1 e to the catalyst, reducing it and preparing it for substrate reduction. For the catalyst component, the Co and Ni tetraaza complexes, mentioned previously, as well as $[\text{Ru}(\text{CO})_2(\text{bipy})_2]^{2+}$ complexes have proved successful. In such studies, the reducing power does not all come from the solar energy input, it also comes from the triethanolamine or other sacrificial donors. Formate and CO are the two products seen with homogeneous catalysts. With Ru nanoparticles as catalyst, however, reduction to methane can occur.²⁷ Quantum yields are in the range 10^{-4} to 0.4.^{28,29}

The mechanism typically proposed for the catalytic reduction is protonation of the reduced metal complex, denoted L_nM^- , to give the hydride (equations 22, 23). This opens the way to a side reaction, protonation, and further reduction to give H_2 (equation 24). One desired pathway instead calls for CO_2 insertion into the M–H bond to give a formato complex that goes on to give formic acid (equations 25, 26). Another pathway commonly invoked is CO_2 insertion into the M–H bond in the opposite direction to give a metalacarboxylic acid that goes on to give CO by loss of water (equations 27, 28). The quantum yield for CO formation even reached 59% using $\text{Re}(\text{bpy})(\text{CO})_3\text{X}$ catalysts.



In several cases, it has been proved possible to covalently link the sensitizer and catalyst, typically using a short aliphatic tether, with the aim of improving the efficiency of the process.³⁰

The major deficiency relative to true photosynthesis is the absence of a sustainable electron source. In natural oxygenic photosynthesis, this is water. Four solar photons are needed to oxidize the oxygen evolving center's Mn_4OCa active site cluster to its highest oxidation state, plausibly involving a formal Mn(V) oxo unit. This may undergo nucleophilic attack by water to make the needed O–O bond and release O_2 . In spite of much effort, only a very few good synthetic water-oxidizing catalysts are known,³¹ and some of these involve rare metals and so cannot be considered ideal.³² Current work is directed to producing a photoelectrochemical cell in which water oxidation takes place at the anode and water reduction takes place at the cathode. Semiconductors, particularly modified TiO_2 , have also proved active for CO_2 reduction although with low quantum yield.^{33,34}

4 CONCLUSIONS

Carbon dioxide reduction either electrochemically or photochemically may offer advantages for the carbon-neutral production of organic compounds or fuels. In the case of fuels, the CO_2 can be considered to act as a carrier of $(\text{H}^+ + \text{e}^-)$. The main limitations so far are the relatively low activity of the catalysts discovered to date and their tendency to give the $2(\text{H}^+ + \text{e}^-)$ reduction products, CO, and formic acid, rather than the deep reduction products, methanol and methane. This area is likely to come under even more intense study in future.

5 ACKNOWLEDGMENTS

I thank the US Department of Energy catalysis, solar energy, and EFRC (ANSER, CCHF and CETM) programs for support of our work in the area.

6 ABBREVIATIONS AND ACRONYMS

bipy = bipyridine; CCS = carbon capture and storage; LUMO = lowest unoccupied molecular orbital; PCET = proton-coupled electron transfer; SHE = standard hydrogen electrode; VHS = virtual hydrogen storage.

7 REFERENCES

1. A. Rose, ‘The Economics of Climate Change Policy’, CCS, Washington, DC, 2009.
2. N. Stern, ‘The Economics of Climate Change (Stern Report)’, HMSO, London, 2006.
3. N. S. Lewis and D. G. Nocera, *Proc. Nat. Acad. Sci. USA*, 2006, **103**, 15729.
4. A. W. C. van den Berg and C. O. Arean, *Chem. Commun.*, 2008, 668.
5. R. H. Crabtree, *Energy Environ. Sci.*, 2008, **1**, 134.
6. R. K. Pachauri and A. Reisinger, eds, ‘Intergovernmental Panel on Climate Change Assessment Reports’, IPCC, Washington, DC, 2001–2009.
7. B. Dawson and M. Spannagle, ‘Complete Guide to Climate Change’, Routledge, New York, 2009.
8. M. Mikkelsen, M. Jørgensen, and F. C. Krebs, *Energy Environ. Sci.*, 2010, **3**, 43.
9. T. Sakakura, J.-C. Choi, and Hiroyuki Yasuda, *Chem. Rev.*, 2007, **107**, 2365.
10. J. Maa, N. Sun, X. Zhang, N. Zhao, F. Xiao, W. Wei, and Y. Sun, *Catal. Today*, 2009, **148**, 221.
11. M. Steinberg, *Int. J. Hydrogen Energy*, 1999, **24**, 771.
12. K. Tominaga, *Catal. Today*, 2006, **115**, 70.
13. P. G. Jessop, F. Jóo, and C. C. Tai, *Coord. Chem. Rev.*, 2004, **248**, 2425.
14. M. Aresta and A. Dibenedetto, *Dalton Trans.*, 2007, **28**, 2975.
15. B. Fisher and R. Eisenberg, *J. Am. Chem. Soc.*, 1980, **102**, 7361.
16. M. Beley, J. P. Collin, R. Ruppert, and J. P. Sauvage, *J. Am. Chem. Soc.*, 1986, **108**, 7461.
17. I. Bhugun, D. Lexa, and J. M. Savéant, *J. Am. Chem. Soc.*, 1996, **118**, 1769.
18. J. Hawecker, J. M. Lehn, and R. Ziessel, *J. Chem. Soc., Chem. Commun.*, 1984, 328.
19. D. L. DuBois, A. Miedaner, and R. C. Haltiwanger, *J. Am. Chem. Soc.*, 1991, **113**, 8753.
20. C. M. Bolinger, N. Story, B. P. Sullivan, and T. J. Meyer, *Inorg. Chem.*, 1988, **27**, 4582.
21. E. E. Benson, C. P. Kubiak, A. J. Sathrum, and J. M. Smieja, *Chem. Soc. Rev.*, 2009, **38**, 89.
22. J.-M. Savéant, *Chem. Rev.*, 2008, **108**, 2348.
23. Z. Lu and R. H. Crabtree, *J. Am. Chem. Soc.*, 1995, **117**, 3994.
24. M. Grätzel, *Nature*, 2001, **414**, 338.
25. W. J. Youngblood, S. H. A. Lee, K. Maeda, and T. E. Mallouk, *Acct. Chem. Res.*, 2009, **42**, 1966.
26. A. J. Morris, G. J. Meyer, and E. Fujita, *Acct. Chem. Res.*, 2009, **42**, 1983.
27. I. Willner, R. Maidan, D. Mandler, H. Dürr, G. Dörr, and K. Zengerle, *J. Am. Chem. Soc.*, 1987, **109**, 6080.
28. J.-M. Lehn and R. Ziessel, *J. Organomet. Chem.*, 1990, **382**, 157.
29. K. Mochizuki, S. Manaka, I. Takeda, and T. Kondo, *Inorg. Chem.*, 1996, **35**, 5132.
30. B. Gholamkhass, H. Mametsuka, K. Koike, T. Tanabe, M. Furue, and O. Ishitani, *Inorg. Chem.*, 2005, **44**, 2326.
31. N. Kanan, *Science*, 2008, **321**, 1072.
32. J. F. Hull, D. Balcells, J. D. Blakemore, C. D. Incarvito, O. Eisenstein, G. W. Brudvig, and R. H. Crabtree, *J. Am. Chem. Soc.*, 2009, **131**, 8730.
33. M. Anpo, H. Yamashita, K. Ikeue, Y. Fuji, S. G. Zhang, and Y. Ichihashi, *Catal. Today*, 1998, **44**, 327.
34. X.-H. Xia, Z.-J. Jia, Y. Yu, Y. Liang, Z. Wang, and L.-L. Ma, *Carbon*, 2007, **45**, 717.

PART 2

Energy Storage

Hydrogen Economy

Stephen A. Wells

University of Warwick, Coventry, UK

and

Asel Sartbaeva, Vladimir L. Kuznetsov and Peter P. Edwards

University of Oxford, Oxford, UK

1	Introduction: Basic Concepts	309
2	Key Technologies	317
3	Economic, Social, and Political Issues	326
4	Future Prospects for a Hydrogen Energy Economy	327
5	Concluding Remarks	330
6	Acknowledgments	330
7	Related Articles	330
8	Abbreviations and Acronyms	330
9	References	330

1 INTRODUCTION: BASIC CONCEPTS

A future “hydrogen energy economy” is one in which the dominant role currently played by fossil fuels as an energy vector, especially in personal transportation, would instead be fulfilled by hydrogen, almost invariably associated with the extensive use of fuel cells. The term is often associated with a cleaner future energy economy, which increasingly relies more heavily on renewable or sustainable rather than fossil energy sources, and in which hydrogen, as a secondary energy carrier, will be the principal currency for the transfer of chemical potential energy.^{1–5} One can therefore distinguish between a *sustainable hydrogen economy*, in which fossil fuels can play no part, and a *transitional hydrogen economy*, in which hydrogen will almost certainly be generated using fossil fuels (for example, by the steam reforming of methane) while an infrastructure for hydrogen production, distribution, and end utilization, for vehicular transportation especially, is established.

The development of such a future hydrogen energy economy is motivated by a vision to move away from the fossil fuel or carbon economy, because of the finite available reserves of fossil fuel, especially petroleum, and the damaging

environmental consequences of carbon dioxide emissions from fossil fuel combustion, such as anthropogenic climate change and ocean acidification. The vision is assisted by specific properties of hydrogen that make it attractive as a future energy carrier. One of the most attractive of such properties is that hydrogen can be produced from a variety of primary energy sources, for example, by electrolysis using sustainable electricity, and the latent chemical potential energy of molecular hydrogen can be converted back into electricity with very high efficiency in a fuel cell. Hydrogen fuel cell electric vehicles (FCEVs) will be the central transportation technology of any future hydrogen economy and, in principle, offer significant advantages over the internal combustion engine (ICE), namely, higher thermodynamic efficiency and zero emissions except water at the point of use.⁵

The future use of hydrogen is therefore linked to the transportation sector’s embrace of fuel cells. With the assistance of hydrogen technology, sustainable energy can be “harvested” (Figure 1) and channeled to those parts of the transport and power sectors that are currently (exclusively) dependent upon oil. For example, wind, solar, wave, and nuclear power can be used to generate hydrogen, which can subsequently be used in combination with low-temperature

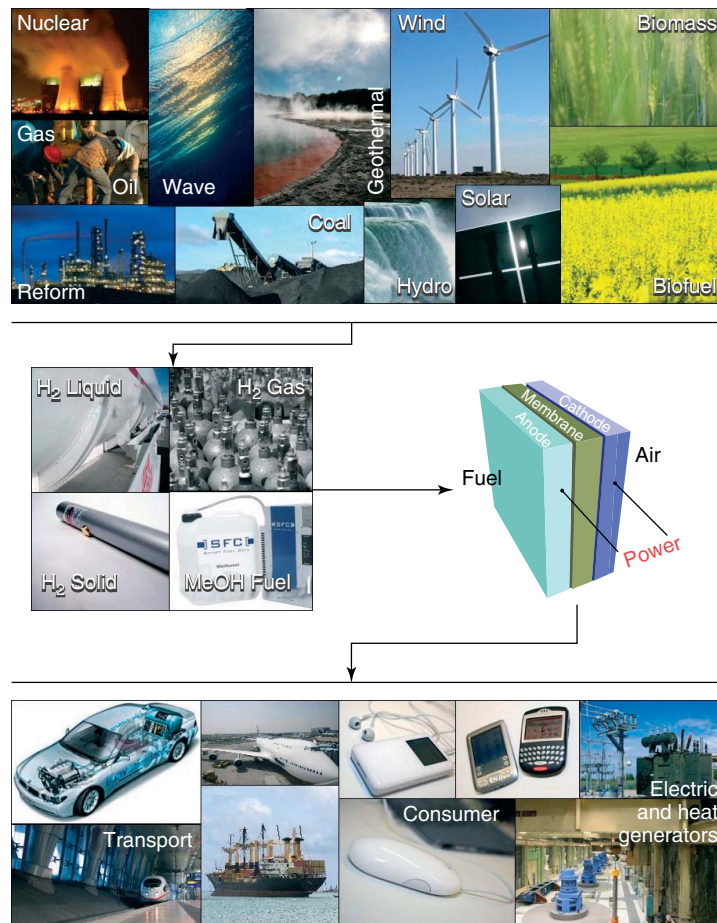


Figure 1 An idealization of a future hydrogen energy economy in which hydrogen, in association with fuel cells, becomes the principal energy vector connecting production to consumption. (Reproduced from Ref. 6. © Elsevier, 2008.)

fuel cells in cars, buses, etc. Similarly, large-scale applications are centered on “combined heat and power” from hydrogen high-temperature fuel cell combinations.⁶

Significant scientific, technological, and socioeconomic challenges must be overcome before any transition to a hydrogen economy becomes feasible, and these include the sustainable, high-efficiency production of hydrogen, the development of a safe and practical on-board hydrogen store for vehicles, and the development of fuel cells with a longer lifespan and much lower unit cost than is currently available. Various roadmaps have been proposed for the development of transitional hydrogen economies in, for example, Japan, the United States, and the European Union, essentially setting out a timeline for the necessary technological and socioeconomic developments to be achieved. The solutions to these challenges represent real opportunities for the physical sciences and engineering and inorganic chemistry in particular. In this work, we briefly examine the principal technologies underpinning the hydrogen energy economy which require such breakthrough solutions—a substantial number of which require significant input from chemistry, in close multidisciplinary collaborations

with our sister disciplines of chemical engineering, materials science, physics, and indeed the social sciences.

The first vision of a hydrogen economy was initially developed during the energy crises of the 1970s to describe a national or international energy infrastructure based on hydrogen produced from nonfossil primary energy sources. It is now widely taken as a term for a future energy economy that relies on renewable rather than fossil energy sources, and in which hydrogen will play a major role as a suitable storage and transmission vector for energy.^{1–5} It is helpful to review the factors that motivate the development of a hydrogen economy; we can divide these into general factors that motivate a move away from fossil fuels and toward renewable or sustainable energy sources and specific factors that make hydrogen an attractive energy vector. It is also necessary to consider factors that militate against a hydrogen economy; these, in turn, can be divided into negative factors regarding the use of hydrogen, constituting difficulties that must be overcome if a hydrogen economy is to be achieved, and positive features of certain alternatives, which could, in principle, make a hydrogen economy unnecessary.

Of course, in a truly sustainable hydrogen economy, the use of fossil fuels would be abandoned entirely; all energy inputs would come from renewable, sustainable sources, and the resulting economy would be viable and self-sustaining. This, however, is clearly a long-term goal. In a short- or medium-term transitional hydrogen economy, it would be expected that hydrogen would be generated from fossil fuel resources (in particular, the steam reforming of methane), ideally with carbon capture and storage to mitigate CO₂ emissions, so that an infrastructure of hydrogen production and distribution, and a large user base for hydrogen consumption can be steadily built up (especially the deployment of hydrogen FCEVs). It is this transitional hydrogen economy that must be the goal of policymakers in the short term.⁷

1.1 Energy from Fossil Fuels: The Carbon Economy

Our global energy economy is at present dominated by fossil fuels—coal, petroleum, and natural gas (methane)—which represent the primary energy sources for industry, transport, heat, and electricity generation (Figure 2).^{7–9} The importance of fossil fuels to our present human society cannot be overstated, but the usage of fossil fuels also comes at a cost.

Fossil fuel reserves represent energy harvested from the sun, stored by living organisms, and deposited in sedimentary strata over geological timescales, and in our current exploitation of these reserves, we are depleting them at roughly a million times their original rate of deposition. Reserves of even the most abundant fossil fuel, coal, will

be exhausted at current usage on a timescale of a few centuries at most. While this may seem like a long time relative to an individual human life or political career, it is short compared to the duration of human civilization (several millennia). Reserves of petroleum, which are especially vital to the modern transport economy, are under even more pressure and face exhaustion on a timescale of decades. The exploitation of unconventional fossil fuel sources, such as tar sands and methane clathrates, can only postpone but not prevent the eventual exhaustion of global fossil fuel reserves.¹² The problem is only exacerbated by the increasing global population (which has more than doubled in the past 50 years, now standing at almost 7 billion, and projected to reach 9 billion by 2040) and by generally rising standards of living, with a concomitant increase in energy usage per person. Even before the actual exhaustion of reserves, the declining availability of dwindling fossil fuel resources will create serious geopolitical problems of energy security and competition for resources. A move to renewable and sustainable resources is therefore vital if modern civilization is to be sustained in a form that supports the global human population and provides a tolerable standard of living.

Apart from the issue of medium- and long-term availability, there is a second serious problem with our ever-increasing demand for fossil fuels, that of “carbon emissions” in the form of carbon dioxide, which are strongly implicated as the main driver of climate change.¹³ The combustion of fossil carbon is putting the global carbon cycle out of balance and increasing the atmospheric concentration of carbon dioxide, which has risen from about 280 ppm to about 380 ppm over the past 150 years; the current rate of increase is about 1–2 ppm

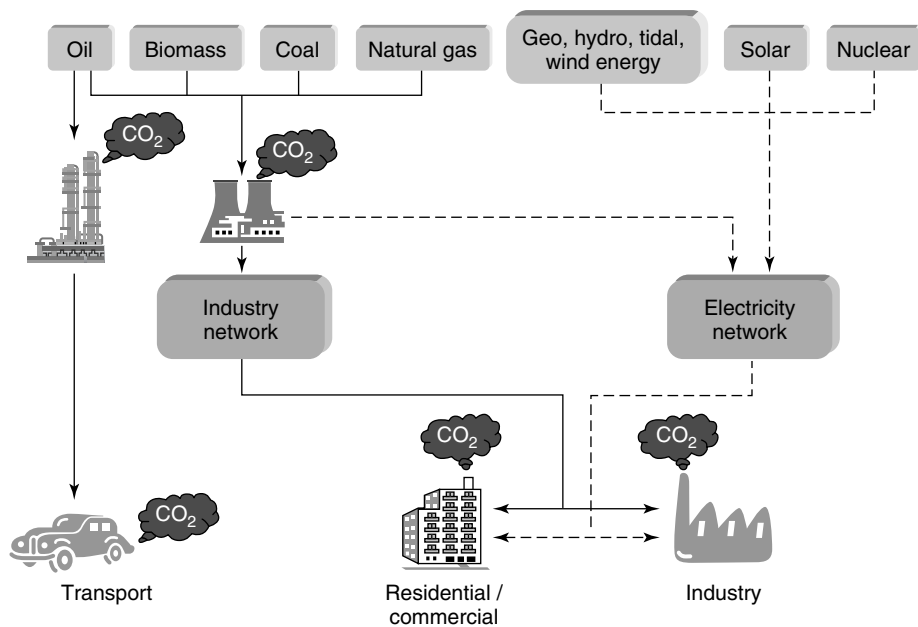


Figure 2 Our current energy infrastructure. The overwhelming majority of our current energy needs are met by the combustion of fossil hydrocarbon fuels. (Adapted from Ref. 10. © Royal Society of Chemistry, 2008, and from Ref. 11. © Elsevier, 2007.)

annually. The proposition that increased atmospheric CO₂ must lead to an overall warming of the globe is scientifically uncontroversial; remarkably, Svante Arrhenius estimated the consequences of a doubling of atmospheric CO₂ in the 1890s.¹⁴ The reports of the Intergovernmental Panel on Climate Change (IPCC) summarize the issue of anthropogenic global warming (AGW) and make it clear that climate change induced by human activity is a serious and urgent issue; AGW is not the only problem caused by our CO₂ emissions.¹⁵ The ocean is the major sink for CO₂, whose dissolution acidifies the ocean and thus affects the formation of calcareous mineral structures, e.g., shells, by corals and marine larvae. Continued CO₂ emissions and increased ocean acidification could have cascading detrimental consequences for the entire oceanic food chain.

These problems with our virtually complete reliance on fossil fuels require that in the long term the global energy economy must surely move away from the use of fossil fuels.^{16–18} In the short term, and during the transition to a hydrogen economy, the development of efficient methods for carbon capture and storage (CCS) is seen as a possibility.^{19,20} In CCS, carbon dioxide is scrubbed from the exhaust gases produced by combustion of carbon compounds and stored, for example, in underground reservoirs such as exhausted oil or natural gas fields.²¹ CCS is far from an accepted, mature commercial technology; significant scientific and technical challenges remain in the development of better solvents, adsorbents, and membranes for the removal of CO₂ from exhaust gas, and equally daunting engineering and socioenvironmental challenges remain in the identification of suitable sites for safe, long-term storage. CCS is likely to be an important factor in the transitional hydrogen economy, especially with regard to the generation of hydrogen by steam reforming of methane. It is advantageous, in terms of both greenhouse gas emissions and thermodynamic efficiency, to generate hydrogen from methane in centralized facilities with CCS and to use the hydrogen in FCEVs rather than to run internal combustion engine vehicles on methane directly.

1.2 The Pivotal Role of Renewable and Sustainable Primary Energy Sources in a Hydrogen Economy

Hydrogen is not a primary energy source, but a secondary energy vector—an energy store. There is no reservoir of “fossil hydrogen” comparable to the fossil carbon reserves that have fueled the global economy since the Industrial Revolution. In a sustainable energy future, energy must be obtained from renewable resources (*see H₂ Production from Renewables*)²²; it can then be stored as chemical potential energy in molecular hydrogen (or hydrogen storage materials) and this energy is liberated by subsequent oxidation, emitting only water as a by-product at the point of use. It is as well to review the renewable sources of energy that are potentially available, including solar, wind, hydroelectric, ocean, geothermal, and biomass.^{23,24}

Solar power generation options include solar photoelectric, in which electrical power is generated using solar panels; solar thermal, where the heat of the sun is concentrated using mirrors and used to run a turbine generator; and solar photochemical, where sunlight incident on a photocatalyst splits water into hydrogen and oxygen directly. The total solar energy flux incident on the earth’s surface exceeds our global energy consumption by a factor of around 10 000; therefore, our civilization’s energy needs could, in theory, be met by intercepting only a small fraction of the incident solar radiation.²⁵ In practice, however, this is a considerable scientific, technological, and socioeconomic challenge. Ambitious plans have been proposed for large-scale solar power projects in well-insolated regions. The design of new functional materials with significantly improved efficiency and reduced cost, which can be used in solar panels or as photocatalysts, is a major research topic for the area of energy chemistry.

The harvesting of wind energy using large turbines is one of the fastest-growing forms of renewable energy generation. Both wind and solar energy generation involve gathering energy over large areas using arrays of relatively small dispersed generating units. Since, moreover, the areas that are ideal for wind and solar generation are often distant from the major population centers where the demand for energy is greatest, we have the concept of “stranded renewables”, where there is a serious difficulty in conveying the energy from where it is generated to where it is needed. The options are either to transmit electrical energy directly via an improved electrical distribution network, or to convert the energy to a chemical form, e.g., hydrogen or other chemical fuels, and then to transport it via pipeline or tanker.

Hydroelectric power, where flowing water is held back by dams and released through turbines so that we obtain electrical power from its gravitational potential energy, is currently the largest renewable energy contribution to electricity generation, though it still amounts to only a small per cent of global energy use. Ocean energy covers the harvesting of energy from the tides or from the waves and is not yet a major player in electricity generation, although pilot plants are in operation. Geothermal energy is in theory available almost anywhere on Earth if deep drilling is possible, but in practice is most accessible in regions of young volcanism where very hot rock lies close to the surface. Iceland in particular, lying on the Mid-Atlantic Rift, has been a pioneer in both geothermal energy and in the introduction of hydrogen vehicles, with a policy aimed at phasing out fossil fuels by 2030.

Biomass as an energy source covers primary production of biomass intended as energy fuel from forestry or agriculture; the use of biomass waste from agriculture, wood processing in industry, and municipal waste or sewage; and new proposals such as large-scale algal culture for the production of biofuels (*see Enzymes and Microbes for Energy Production by Fuel Cells*). Perhaps the greatest advantage of biomass is its higher “controllability” in the

Table 1 Fuel shares, including renewable energy sources (RES) of world total primary energy supply (above) and electricity production (below) in 2004^{23,26}

	Oil	Coal	Nuclear	Gas	Renewables		
					Combustible renewables	Hydro	Other renewables ^(a)
Fuel shares of world total primary energy supply in 2004	34.2%	25.0%	6.5%	20.8%		13.1%	
					10.6%	2.2%	0.5%
Renewable energy sources in electricity production in 2004	6.7%	39.8%	15.7%	19.6%		17.9%	
					1.0%	16.1%	0.8%

^(a) Other renewables include tide, solar, wind, and geothermal sources.

Table 2 Annual global primary technical and theoretical potentials for various renewable energy sources in 2004^{23,27,28}

Resources	Current use (2004) (EJ)	Technical potential (EJ)	Theoretical potential (EJ)
Biomass energy	50.0	250	2900
Geothermal energy	2.0	5000	140 000 000
Hydropower	10.0	50	150
Ocean energy	—	—	7400
Solar energy	0.2	1600	3 900 000
Wind energy	0.2	600	6000
Total	62.4	7500	143 916 450

EJ, Exajoule; 1 EJ = 10^{18} ; 1 TJ = 10^{15} J.

provision of sustainable energy compared to solar, wind, and hydroelectric power generation, which are subject to natural fluctuations. Moreover, hydrogen is produced directly from biogas without the intermediate stages of electricity generation and electrolysis. The comparatively low energy density of biomass does, however, make its transport inefficient—certainly over long distances.

Renewable resources collectively contribute about 13% of world total primary energy supply, whereas coal, oil, and gas collectively contribute about 80%. In electricity production, renewable resources contribute 18% of global production, almost all of which comes from large hydroelectric projects. In Table 1, we summarize the proportional contribution of different energy sources in 2004 to total primary energy supply and to electricity production^{23,26}; Table 2 summarizes the current energy production from renewables, the theoretical potential available, and the potential technically available, given reasonable technology assumptions.^{23,27,28}

A potentially important application for hydrogen as an energy vector, in the context of sustainable energy generation, is in energy load balancing, or buffering, and storage. The process of harvesting energy from the environment is susceptible to variations in the natural environment, both predictable and unpredictable; solar power will not work at night

or under heavy cloud, while wind power cannot be generated during a calm. Some form of load balancing will therefore be necessary in order for renewable energy to deliver reliable, continuous power to the electricity distribution grid. The production of hydrogen from water by electrolysis is a process that copes very well with variations in load. Therefore a potential load-balancing mechanism is to apply the variable or intermittent power obtained from renewables to the production of hydrogen by electrolysis, and either to make use of the hydrogen in vehicles or to reconvert the stored hydrogen to electrical power using fuel cells at a steady rate suitable for delivery to the electricity grid; a third alternative would be the synthesis of chemical fuels in such “stranded locations” and subsequent transportation of the fuel.

Currently, production of hydrogen by electrolysis (using grid electricity) is about three times more expensive than chemical production from methane. In a comprehensive analysis relative to the UK energy scene, Dutton²⁹ finds that, for a scenario in which transport is fueled entirely from hydrogen (i.e., ignoring biofuels), and if that hydrogen is to be supplied solely by renewable electricity, the additional electricity demand is likely to be roughly equivalent to the present conventional electricity demand. He further notes that in the short term, the link between the intermittent nature of renewable electricity generation and the inherent storage

capacity of the hydrogen economy will be best suited for (stranded) remote areas as possible niche application. In the longer term, beyond 2025, a growing hydrogen economy could indeed start to fulfill the role of energy buffering to facilitate a penetration of renewable electricity toward 100%.

Nuclear fission is currently the largest nonfossil fuel contributor to electricity generation, and an expansion of nuclear power is one proposal for meeting the world's growing energy needs without increased combustion of fossil fuels and the attendant emissions of carbon dioxide. The nuclear industry has always had an uneasy relationship with the environmental movement, because of its links with the military production of plutonium, and due to the still unsolved problem of the disposal of "hot" (highly radioactive) nuclear waste from spent reactor fuel, which requires safe storage, sequestered from the environment, over geological timescales. Nevertheless, nuclear power is currently undergoing something of a renaissance, especially in the emerging economies of China and India.^{30,31}

Fission power is not a genuinely sustainable energy source as it relies on the "burning" of uranium, a nonrenewable mineral resource. Indeed, uranium production has been well below demand since around 1990, with the gap being made up from stockpiles and from weapons-grade uranium and plutonium from decommissioned nuclear weapons. It can, however, be sustained at least over several decades and so may be a valuable energy contributor to the transitional hydrogen economy. Current reactor designs are very inefficient in their use of uranium, extracting only around 1% of the theoretically available fission energy. In theory, far more energy could be obtained from both uranium and thorium in "breeder" reactors. Fission power could indeed contribute to the transitional hydrogen economy both through electricity production and, in theory, through thermochemical cycles of water splitting such as the sulfur–iodine process, powered by waste heat from fission; this, however, is still a subject of basic research and development.

The generation of energy from hydrogen fusion is, ironically, not usually considered an aspect of the "hydrogen economy" per se; it involves the energy released during the fusion of hydrogen isotopes, especially deuterium and tritium, whereas the hydrogen economy is based on the chemistry of protium. Despite decades of intensive research,³² practical energy generation from hydrogen fusion is still at least decades away and thus cannot contribute to a transitional hydrogen economy in the near future. In the long term, hydrogen fusion, if achieved, would be a sustainable source of heat and electrical power.

1.3 Why Hydrogen? Specific Properties and Advantages

Clearly, the desire to transform a fossil-fuel economy into a sustainable one does not in itself motivate the development of any future hydrogen energy economy. The

focus on hydrogen is because of properties of the element itself—in particular, its ready availability by dissociation of water, its very high specific energy (the highest of any chemical substance) of 33.3 kWh kg^{-1} , the fact that it oxidizes to form only water, and its ready applicability in fuel cells, which convert its latent chemical energy into electrical energy with very high efficiency.

Hydrogen is the most abundant element in the universe (making up about 75% by mass of all baryonic matter). Although it is not found in free molecular form on Earth in any significant quantity, it is abundant in a myriad of chemical compounds, particularly in water. The electrolytic dissociation of water to form hydrogen and oxygen can be achieved with high thermodynamic efficiency, up to 85% in a conventional alkaline water electrolyzer. Given sufficient electrical power, therefore, hydrogen could be produced in abundance; of course, as noted earlier, such power would have to be produced from sustainable sources in order for hydrogen itself to be correctly labeled as a sustainable or renewable energy carrier.

Other chemical and thermochemical methods for hydrogen production also exist, as discussed in Section 2. At present, the dominant method for commercial hydrogen production is steam reforming of methane.

Hydrogen is, of course, the lightest element in the Periodic Table. The amount of energy produced during hydrogen combustion is higher than that released by any other fuel on a mass basis; hence, molecular hydrogen has the highest energy-to-mass ratio of any chemical fuel. Petrol-fueled car engines can be (and have been) converted to use hydrogen, and sophisticated technology for such combustion engines have been optimized over decades of experience (for example, BMW first carried out research into engines and vehicles operating on liquefied hydrogen since 1978). Far more efficient are combined hydrogen-fuel-cell-electric-motor (Hy-FC-EM) systems, known generally as a *power train*. The automotive industry—or at least part of it—sees fuel cells as its inevitable, desired future.

The hydrogen fuel cell is therefore the primary motivator for the use of hydrogen as an energy vector in transport. It is possible to simply burn hydrogen in an ICE with only slight modifications from the petrol-burning norm—indeed, the first successful ICE of de Rivaz in 1806 was a hydrogen-burning engine. This application, however, does not offer any advantage in efficiency over current ICEs. The efficiency of ICEs is thermodynamically limited by the Carnot cycle, which constrains the theoretical maximum efficiency of any heat engine, and reduced still further by typical driving and traffic conditions; this leaves engines operating for long periods inefficiently at partial load. In the fuel cell, on the other hand, the chemical energy of hydrogen and oxygen is converted directly into electrical energy with very high efficiency. This means that an FCEV could operate at efficiencies of around 45% overall,

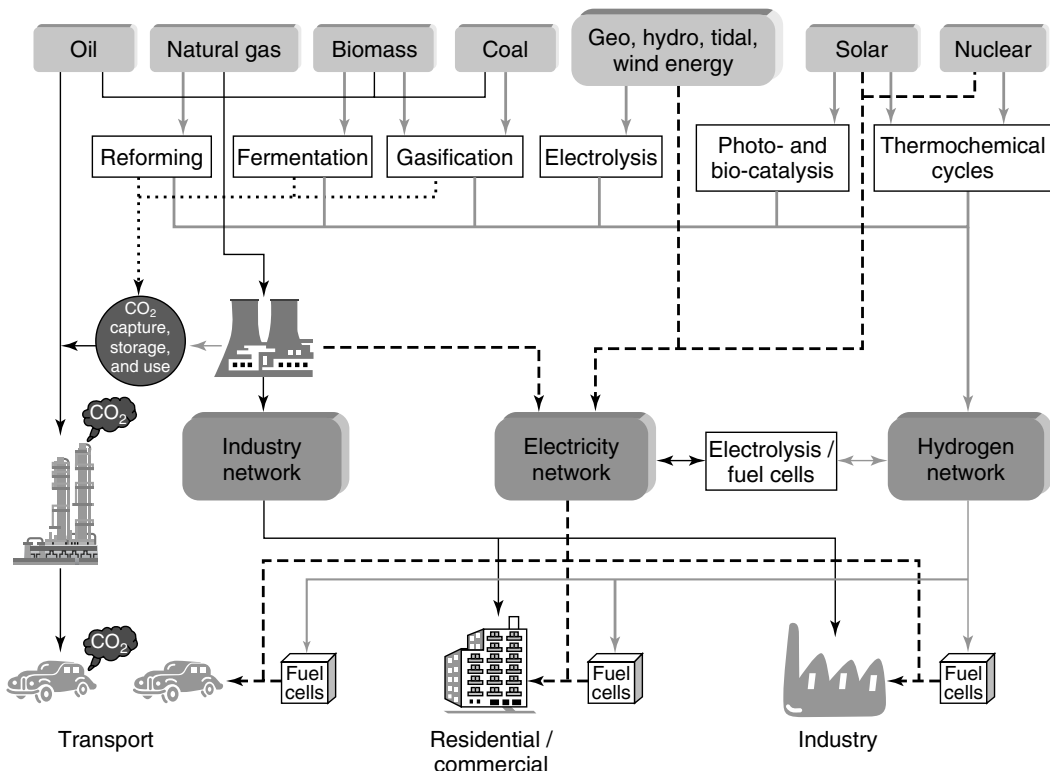


Figure 3 A possible model for a transitional hydrogen energy economy. Note that in this view, renewable energies are considerably intensified and hydrogen fuel cells are employed throughout as critical technologies. (Adapted from Ref. 10. © Royal Society of Chemistry, 2008, and from Ref. 11. © Elsevier, 2007.)

whereas current ICE vehicles typically do no better than 25%.

Multiple types of fuel cells exist for the production of electrical energy from hydrogen or hydrogen-containing fuels—for example, the solid-oxide fuel cell (SOFC), molten carbonate fuel cell (MCFC), phosphoric acid fuel cell (PAFC), alkaline fuel cell (AFC), and “polymer electrolyte membrane” or “proton-exchange membrane” fuel cell (PEMFC) (*see Proton Exchange Membranes for Fuel Cells*). The SOFC and MCFC operate at high temperatures and are more suitable for stationary power generation and heat and power cogeneration; since they take several hours to start up from cold, they are not suitable for road vehicle use. Development of hydrogen FCEVs is focused on the PEMFCs, as these can operate at low temperature (below 100 °C) and offer immediate startup—a vital characteristic for vehicular applications. Of course, it is difficult to predict the world’s long-term energy vision, but one scenario is shown in Figure 3, where we illustrate the concept of a hydrogen economy in which hydrogen generation and its use in fuel cells are a critical, integral part of a future energy economy. Here, oil will not be used as the dominant energy source, but used instead for chemical products. A wide range of primary energy sources contributes to the energy mix.

1.5 Potential Drawbacks with Hydrogen

The advantages of hydrogen might seem so overwhelming that one might wonder why hydrogen FCEV is not already the norm. There are a number of key issues which have so far prevented the widespread use of hydrogen. As noted, hydrogen is not a primary energy source, but an energy carrier, and consequently it will be as clean as the method used in its production. Another chief problem is, of course, that gaseous hydrogen at room temperature and pressure takes up an impractically large amount of space. The currently available technologies of hydrogen storage, as highly compressed gas or as cryogenic liquid, have certain disadvantages for vehicular applications. The weight of a compressed-gas storage system is such that only around a few weight percent hydrogen is achieved, and the work done in compressing or liquefying the hydrogen is a significant fraction of its energy content. Volumetric density is also a significant consideration as there is limited space for fuel storage within a small vehicle. It is widely believed that a really practical hydrogen FCEV will require a different form of hydrogen storage, either by physisorption in a highly porous material or chemisorption in some form of hydride; it must be easily and repeatedly reversible, rapidly taking up hydrogen at a fueling station and

releasing it to the fuel cell when needed, with high enough mass and volumetric densities when fully loaded that the mass and volume of the fuel storage system are practical. The achievement of such a hydrogen store is widely regarded as one of the greatest challenges in the transition to a hydrogen economy, as discussed in Section 2.

Hydrogen storage has distinctive safety issues. Hydrogen gas will burn in air over a wide range of concentrations (4–75% by volume), will detonate over a wide range (18.3–59.0% by volume), and has an extremely low minimum ignition energy of only 0.017 mJ. For comparison, methane has a minimum ignition energy of 0.29 mJ, and methane–air mixtures can be ignited by the spark of a static discharge. New types of ventilation and safety precautions are therefore required for hydrogen vehicles, especially for hydrogen storage facilities and hydrogen filling stations. A gradual loss of hydrogen from storage is inevitable for cryogenic storage of liquid hydrogen, due to evaporation.

The establishment of a hydrogen infrastructure also has its own challenges. Compared to natural gas (for which pipeline distribution over thousands of kilometers is quite practical), hydrogen is more difficult to work with as the small, light molecule diffuses through metals, causing not only loss of hydrogen but also dangerous embrittlement of the pipeline structure. However, pipeline distribution of hydrogen over distances of hundreds of miles has been commonplace in the chemical industry for several decades. Distribution of liquid hydrogen or compressed gas by tanker trailers suffers from the issue of the energy input to achieve liquefaction or high compression, and is only practical over short distances and small amounts, for example, the supply of hydrogen to local filling stations from a centralized production or delivery facility.

Another fundamental barrier to the widespread use of hydrogen, however, is cost. Hydrogen production, storage, distribution, and use have not had the century of large-scale, mass-market investment, and development that has made petroleum so dominant in the transport sector, and hydrogen vehicle technologies are still at the prototype stage and have not yet achieved the economies of scale that are possible with mass-market products. Current PEMFCs rely on precious metal catalysts containing rare and expensive elements, especially platinum in a nanoparticulate form; this raises the cost of the fuel cell and, since the catalysts are very sensitive to poisoning by impurities such as CO, places high demands on the purity of the fuel supply. The unit cost of fuel cells must be reduced dramatically (from \$2000–4000 per kilowatt to below \$100 per kilowatt for PEMFCs) and their lifetimes extended (from below 2000 h to around 5000 h) before they are economically practical for widespread use in personal vehicles. The development of new catalyst and electrolyte materials for fuel cells is another major challenge for chemistry in the development of the hydrogen economy.

1.6 Alternatives and Complements to Hydrogen

The centerpiece of any vision of the hydrogen economy is the transition in the transport sector from ICE vehicles powered by fossil fuels to hydrogen FCEVs. Any other non-fossil-fuel-ICE vehicle technology is therefore an alternative to the hydrogen FCEV and could be viewed as a competitor or (more positively) as a complementary technology. We should note that our discussion applies mostly to the automotive sector—passenger cars and buses, which are responsible for more than 80% of total energy use in the transport sector—rather than to heavy-goods vehicles, where the traditional diesel engine is likely to retain its dominance for the foreseeable future.

Electric vehicles already exist in the form of both battery electric vehicles (BEVs) and hybrid ICE/battery vehicles such as the well-known Toyota Prius. BEVs can be practical for short-range commuter driving, but suffer from limited operational range and long recharging times. Typical hybrids can only operate for a range of around 20 km on batteries alone. The energy density of even a modern Li-ion battery (around 120 Wh kg⁻¹) is only around 1% of the energy density of gasoline, so unreasonable large battery weights (on the order of 1000 kg) would be required to give BEVs the ~500-km range of a typical modern small car. Battery recharging is also very slow compared to the rapid refueling of a gasoline or hydrogen vehicle—typically an overnight process from a household circuit for a plug-in BEV. A proposed method for overcoming these issues is to make the battery pack itself an interchangeable component, which can be replaced at a battery-swapping station equivalent to a filling station. While this system may well be practical for urban driving within a restricted area, it ties vehicles closely to the battery-swapping system and so is unsuitable for long-range or free-roaming driving.

Batteries do possess attractive features for electric vehicles, especially for their energy efficiency; about 90% of a battery's stored energy can be extracted as useful electricity, and electric motors are about 95% efficient, giving BEVs a net efficiency of around 85%. This is three to four times the efficiency of an ICE and at least twice the efficiency of a hydrogen FCEV. In principle, a dramatic improvement in battery technology could make the range, power, and charging/discharging kinetics of an electric vehicle fully competitive with conventional ICEs. In this scenario, the sustainable energy economy would be based on electricity generated from renewable resources, distributed by power lines, and used in fully electric vehicles, making the hydrogen fuel-cell vehicle unnecessary or obsolete. The required improvement in energy density and cost of electric batteries is beyond what currently seems attainable, however, and hydrogen remains the front-runner for an electric vehicle technology that is truly competitive with the conventional ICE car. For some vehicular applications, especially urban buses that travel only short distance between regular stops, supercapacitors (*see Supercapacitors: Electrode Materials*

Aspects) are a potential alternative to either battery or fuel-cell vehicles, as they can be charged rapidly at stops with enough energy to propel the vehicle to the next recharging point.

Another approach is to continue the use of ICEs running on “biofuels” generated from biomass or with synthetic fuels produced by CO₂ conversion. Since the carbon in the fuels has recently been fixed from the atmosphere by vegetation, the use of biofuels is, in principle, carbon-neutral. Bioethanol, from the fermentation of plant sugars, is usable in flex-fuel engines (for example, in E85 blended fuel: 85% ethanol, 15% gasoline) and is currently the most widely used biofuel. Biodiesel, produced by processing of vegetable oils, is a potentially carbon-neutral direct replacement for diesel in ICEs. The environmental benefits of current approaches to biofuels is questionable, however, as their production competes strongly with agricultural food production and planting for biofuels is associated with deforestation. Moreover, any use of fertilizers in crop production carries with it a latent carbon penalty derived from the use of hydrogen in fertilizer production. The continued use of ICEs also lacks the efficiency benefits and reduction in emissions associated with BEVs and FCEVs.

Yet another potential alternative to biodiesel is synthetic fuel (methane, methanol, or diesel) generated by chemical means, e.g., the Fischer–Tropsch process, from water, sustainable hydrogen and carbon dioxide captured in CCS; essentially the reverse of steam reforming (see Section 2.1). The development of efficient and cost-competitive methods of converting CO₂ into fuels could address the issue of both carbon sequestration and sustainable and economic production of carbon-neutral fuels, and may be of use in producing synthetic fuel for gasoline ICEs, ideally without using fossil-fuel resources. Such carbon-neutral or sustainable organic fuels offer the possibility of decarbonizing our transport system without the undoubted paradigm shifts required by conversion to a hydrogen energy economy, or indeed by the electrification of the vehicle fleet. Olah *et al.*³³ have pioneered and advanced the concept, and potential widespread adoption, of the methanol economy, emphasizing the production of CH₃OH (or dimethyl ether) by the chemical recycling of CO₂ (Figure 4). A real attraction of such an approach is that one could envisage the catalytic hydrogenation of CO₂ focused at small, delocalized production sites as an alternative to the current large-scale, localized sites producing methanol by steam reforming of CH₄.

2 KEY TECHNOLOGIES

2.1 Production

Hydrogen is not found in free molecular form in any significant quantity on Earth. However, compounds of hydrogen are plentiful and hydrogen can be produced in large quantities by a variety of chemical and electrochemical

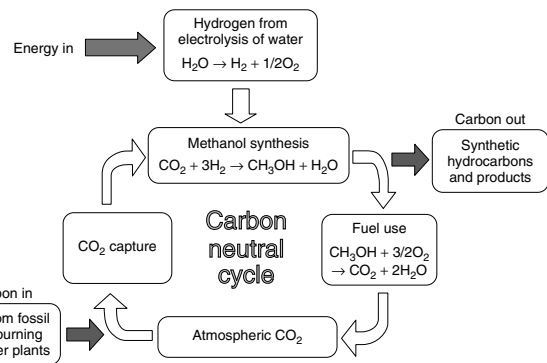


Figure 4 A cycle for sustainable methanol production. (Reproduced from Ref. 33. © American Chemical Society, 2009.)

means.^{34,35} Hydrogen has been utilized in a variety of ways for more than 100 years. Total global hydrogen production is currently around 60 Mt per year, which could be sufficient to fuel at least 600 million fuel cell vehicles, which would be around 80% of the world vehicle fleet. However, such “merchant hydrogen” is presently used almost exclusively as an industrial chemical for a wide variety of processes, including in ammonia production for fertilizers, in refineries for desulfurization and other important processes, in the food industry, and in methanol production. An enormous increase in hydrogen production would be required in order to provide fuel for hydrogen vehicles and realize the hydrogen economy. Hydrogen is generated as a by-product of many industrial processes, for example, the manufacture of chlorine gas by chlorine–alkali electrolysis, and from coke oven gas from steel making. This by-product hydrogen is, in principle, available as a contribution to a transitional hydrogen economy, though the quantities involved are hard to estimate accurately.

At present, the overwhelming majority of hydrogen production, about 96%, comes from fossil fuels. The single largest method of production is the steam reforming of natural gas, producing about 48% of the total. Refinery processes from petroleum, particularly the partial oxidation of heavy hydrocarbons and recovery of by-product hydrogen, contributes about 30%, and the gasification of coal about 18%. Electrolysis, which is assumed to be a dominant production method in a sustainable hydrogen economy, currently accounts for only 4% of total production. Electrolysis is only economically viable where cheap hydroelectric power is available, for example, in Canada or Norway.

2.1.1 Steam Reforming

Steam reforming of methane (or propane) over a catalyst, followed by elimination of trace carbon monoxide and subsequent separation (usually via a membrane) yields high-purity hydrogen. The process requires heat (temperatures of 800–900 °C are typical), pressure (typically 20–40 bars),

and a nickel catalyst. Steam methane reforming has the benefit of high efficiency and the economics favors large installations. The thermal efficiency of a large steam-reforming plant, producing around 100 tons of hydrogen per day, is around 70%. Steam reforming is a fully developed commercial technology and is the most economical method for production of hydrogen, at a cost of around £1 per kg. In order to avoid greenhouse gas emissions, CCS will have to be applied to remove the CO₂ and sequester it. The additional cost of CCS would add a premium of up to 20% to this cost. We should expect that it will continue to be a major method of hydrogen production in the transitional hydrogen economy.

2.1.2 Coal Gasification

Coal gasification generates hydrogen from the reaction of steam and oxygen with pulverized coal. Pyrolysis of the coal produces a raw syngas contaminated by impurities, such as sulfur compounds, and ash particles. Once cleaned and cooled, the syngas can be passed to a shift reactor and to pressure-swing adsorption (PSA), as for steam reforming. Like steam reforming, coal gasification is a well-established commercial technology, in use worldwide, and an economic method of hydrogen production, and we should expect coal gasification with the addition of CCS to be an important method of hydrogen production in the transitional hydrogen economy.

Following Ball *et al.*,³⁴ we distinguish three main groups of coal gasification process based on the flow regime by which the fuel and oxidant pass through the system. “Moving bed” gasifiers operate at the lowest temperatures (370–600 °C) and at pressures of 20–25 bars, using either air or oxygen as the oxidant. The syngas produced has a relatively high methane content and so is less suitable for hydrogen production, and the efficiency of carbon conversion is up to 90%. “Fluidized bed” gasifiers operate at higher temperatures of 800–1000 °C, using oxygen and air, and produce a syngas with lower CH₄ content with a carbon conversion efficiency of up to 95%.

For hydrogen production the ideal process is the “entrained flow” gasifier, which operates at pressures of 20–85 bars and temperatures of 1400–1600 °C using very finely pulverized coal, with grain sizes below 0.1 mm, and oxygen rather than air as the oxidant. This system can achieve carbon conversion in excess of 95% and produces a synthesis gas with low methane content, consisting mostly of hydrogen and carbon monoxide.

It is of historical interest to note that from the 1800s until the 1960s, municipal gas supplies in the United Kingdom typically consisted of gases produced from coal, with a high hydrogen content; “town gas” for street lighting and domestic supply typically consisted of 50% hydrogen with the balance made up of methane and carbon monoxide. Thus, hydrogen gas was a major component in domestic energy supply until

the rise of natural gas in the later twentieth century displaced the older form of gas supply.

2.1.3 Electrolysis

Electrolytic production of hydrogen from water is an efficient, yet costly process due to the comparatively high price of electricity; at present, less than 1% of worldwide hydrogen production originates from electrolysis of water. In simple terms, reverse operation of a PEMFC can be used to generate hydrogen and oxygen from water with an overall efficiency of about 90%. Apart from the PEM cell, all that is required is a source of DC electrical power, which can be supplied either by a conventional grid, or generated on-site from renewable sources such as wind and photovoltaics. In the long term, it is assumed that electrolysis using sustainably generated electricity will supply the needs of the hydrogen economy. At present, however, electrolysis is only a minor player in hydrogen generation, since the associated cost per unit of hydrogen is three to four times higher than in the case of steam reforming; the cost of the electricity supply is the dominant factor. This balance of costs will undoubtedly change in the future, as fossil fuels become increasingly expensive and sustainable electricity generation becomes more widespread, but economic incentives and subsidies will be needed to encourage the development of increased electrolytic hydrogen production capacity in the transitional hydrogen economy.

The alkaline water electrolyzer is the oldest and most widespread form of electrolysis technology. The feedwater is mixed with potassium hydroxide in a 20–40% solution, making a strong alkali. The electrodes are usually nickel or chromium–nickel steel for their corrosion resistance and catalytic properties. Electrolyzers typically operate at temperatures of 70–90 °C with a cell voltage around 2 V, achieving energy efficiencies of around 70% (compared to a theoretical maximum of 85%) and producing hydrogen purities (after drying and deoxidizing of the output hydrogen stream) in excess of 99.8%. They may be operated either at ambient pressure or under pressures of 10–30 bars. The latter case has advantages if the hydrogen is to be distributed by pipeline or stored under compression, but causes difficulties for gas purity as the pressurized gases permeate through the diaphragms separating the cells of the electrolyzer.

High-temperature electrolysis, proceeding at temperatures around 800 °C, is potentially more efficient than low-temperature alkaline electrolysis if the heat required is obtained from the waste heat of some other process. However, this technology is not yet established commercially, although laboratory-scale prototypes have been demonstrated.

Particularly attractive features of electrolyzers are that they are intrinsically modular, so that they can be scaled up by the addition of more cells, and they cope very well with intermittent power supply; the reaction proceeds when current is available and stops when it is not. This is a clear example of linking hydrogen to clean energy production from

renewable, intermittent resources; the electrolytic separation of hydrogen from water can be carried out independently of any fossil energy source.

2.1.4 Innovative Methods

Biomass gasification is proposed as a method for generating hydrogen from solid (woody) biomass, and is strongly analogous to coal gasification. Various demonstration units exist and the method is the subject of ongoing research and development. Since biomass is the fuel, its combustion is, in principle, carbon-neutral, so CCS would not be absolutely necessary. Similar considerations apply to biomass pyrolysis. Hydrogen can be generated by some microorganisms in the course of their metabolic processes. Research into possibilities including photoproduction of hydrogen by algae or bacteria, and hydrogen generation from biomass fermentation is ongoing (see *Enzymes and Microbes for Energy Production by Fuel Cells*). Issues of limited arable land area for biomass crop production and high costs of collection are major concerns with biomass approaches.

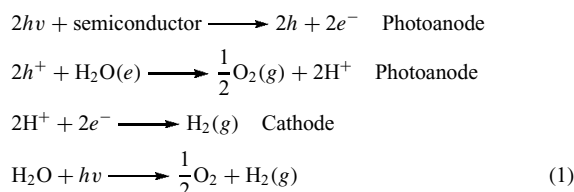
Partial oxidation is a process used in the oil industry to obtain hydrogen from heavy hydrocarbons. Steam reforming is neither usable on long-chain hydrocarbons, as the deposition of soot would rapidly deactivate the catalyst and block the reactor, nor on high-sulfur oils because of catalyst poisoning. Partial oxidation, in which the hydrocarbons are reacted with pure oxygen and steam in an exothermic process, which produces a syngas with a high carbon monoxide content, proceeds at a higher temperature (1300–1500 °C) and pressure (30–100 bars) and does not require a catalyst. This makes the process more tolerant of low-quality feedstock. Autothermal reforming combines partial oxidation with steam reforming to convert both lighter and heavier hydrocarbons.

The Kvaerner process uses a plasma arc to split natural gas directly into hydrogen gas and carbon soot, using about one-third of the electricity required for water electrolysis. This process has recently entered the market and could develop as a potential competitor to steam reforming for the generation of hydrogen from natural gas, and as

such may be a contributor to the transitional hydrogen economy.

Water splits into oxygen and hydrogen through thermal activation at temperatures in excess of 2200 °C, which is too high for the process to be technologically practical. This energy barrier can be reduced significantly using a so-called thermochemical pathway (see *Thermochemical Water-Splitting*). For example, in the sulfur–iodine process, iodine, sulfur dioxide, and water react together at 120 °C, forming hydrogen iodide and sulfuric acid. Both of these molecules thermally dissociate at higher temperatures (300 °C for hydrogen iodide, 850 °C for sulfuric acid), releasing hydrogen and oxygen and regenerating iodine and sulfur dioxide. This would be an efficient way to generate hydrogen from the heat of nuclear reactors or from concentrated solar radiation, and the engineering and materials challenges in handling the highly reactive components of the cycle are currently under active investigation.

Photocatalytic dissociation or splitting of water is a highly attractive mechanism for hydrogen production. In general, water can be cleaved directly by a photocatalyst or by use of a “tandem” cell. Here, light is absorbed in two cells, valence band “holes” oxidize water to oxygen, and conduction band electrons reduce hydronium ions to hydrogen (Figure 5).³⁶ The process of photocatalytic splitting water is summarized as follows:



This reaction is catalyzed by means of inorganic semiconductors. The three important processes are (i) absorption of photons with energy greater than the electronic band gap; (ii) conversion of absorbed photons into electrical charges; and (iii) the utilization of the photo-induced electrical charges for water splitting. In Figure 6, a plot of quantum efficiency (QE) against wavelength of a wide range

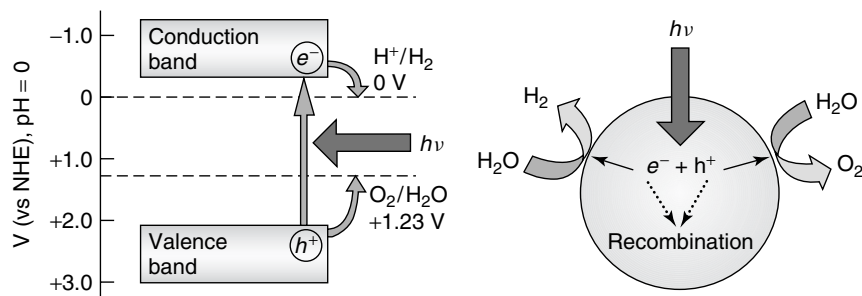


Figure 5 H₂ production via H₂O splitting. (Adapted from Ref. 36. © American Chemical Society, 2008.)

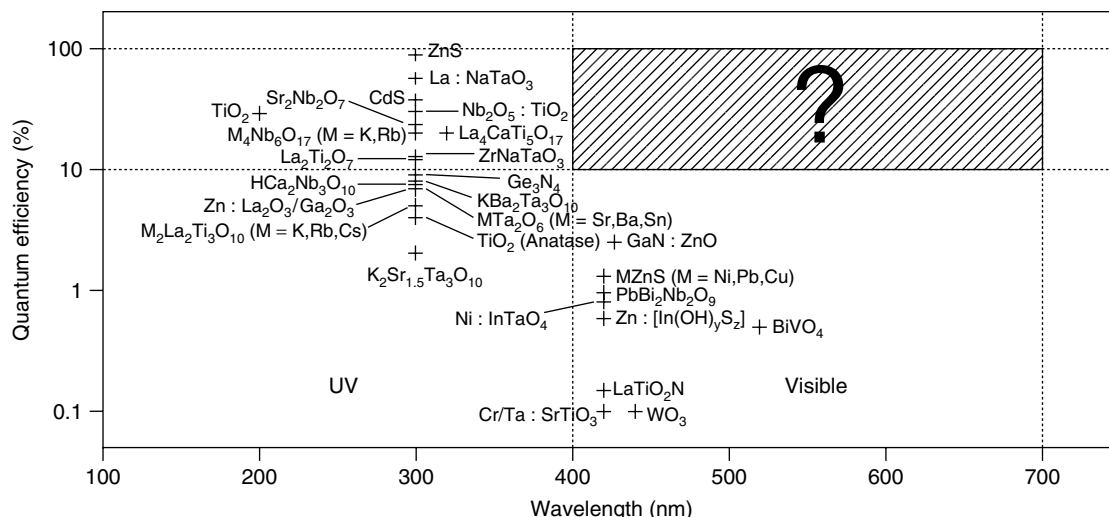


Figure 6 Quantum efficiency of different materials for photocatalytic water splitting in the UV and visible part of spectrum. (Adapted by D. Payne from Ref. 37. © American Chemical Society, 2008.)

of inorganic materials is shown.³⁷ For any prospective photocatalyst to be considered commercially viable, it has to display a QE of >10% in the visible region of the electromagnetic spectrum. To date, no materials have been discovered with that criterion (as seen in the shaded area). Current record holders are ZnS with a QE of ca 90% in UV light with a Pt cocatalyst and for splitting water with visible light GaN : ZnO with a Cr/Rh cocatalyst at 2.5%. Worldwide, research is now actively targeted toward photocatalysts that have an electronic energy band gap that allows the efficient use of the visible spectrum of sunlight. If such materials can be developed with sufficient stability and activity, photocatalytic production of hydrogen and oxygen could be competitive with the generation of solar photoelectricity and subsequent electrolysis.

It is clear that there are a variety of production pathways to hydrogen and these encompass fossil fuels, solar and nuclear energy, as well as a range of renewable sources (Figure 3); similarly, additional strategies for carbon sequestration are integral components for any route to hydrogen. Ewan and Allen³⁸ have carried out an important assessment of four key measures to yield comparative figures of merit for the various routes to large-scale and additional hydrogen production. The measures considered were the level of CO₂ emission reduction, primary energy availability, land use implications, and hydrogen production costs. This important overall comparison of routes shows a clear division between those using renewable energies and those associated with the traditional “high energy density” primary energy sources. These authors also point to desired research advances that would make a significant improvement in the position of hydrogen production routes.

Recent advances in the catalytic production of hydrogen from renewable sources are also highlighted in a special issue of the journal *Catalysis Today*³⁹; here, renewable

sources such as biomass and biomass-derived oxygenates including methanol, ethanol, and glycerol are outlined, as well as the photocatalytic decomposition of water. This direct water dissociation is regarded by many as a potential “showstopper” if conversion efficiencies could be increased by a factor of 2 to 3.

2.2 Hydrogen Distribution

Clearly, current energy supply systems and infrastructure focus on fossil energy sources. It is challenging to plan for the future possibility of an alternative energy source such as hydrogen meeting society’s large-scale energy demands in the future (Figures 1 and 3). What is the most suitable supply and infrastructure model—central or delocalized production and storage?

Current prototype hydrogen FCEVs make use of either liquid hydrogen or highly compressed gas (350 bars or more) for on-board storage of the 4–5 kg of hydrogen required to give a hydrogen FCEV a range comparable to a modern gasoline ICE vehicle.^{11,35} This is workable for technology development but the weights and, more importantly, the volumes of such storage systems are considered excessive for mass-market vehicles. The cost of the fuel system is also a significant factor; gasoline storage tanks represent a negligible fraction of the cost of production of a gasoline ICE vehicle, but hydrogen storage systems are currently far more expensive, and costs must be reduced in order for mass production of hydrogen vehicles to be economically practical. Storage systems based on physisorption or on chemisorption in novel hydride materials are the subject of intensive research.^{40,41}

How could an alternative energy vector such as hydrogen meet society’s large-scale and ever-increasing energy demand in the future? Pipeline transport of compressed

hydrogen under pressures around 20 bars is already common in chemical industries. When hydrogen is produced at such pressures from PSA or from high-pressure electrolysis, this is advantageous for pipeline transport as less work need be done in compressing the hydrogen. The existing natural gas distribution network includes long-distance pipelines, usually made of steel, and local networks of plastic pipes, made from materials such as high-density polyethylene (HDPE) or polyvinyl chloride (PVC), which distribute gas at lower pressures (around 4 bars). There are difficulties in adapting the natural gas network for hydrogen distribution, as the plastic pipes are much too porous to hydrogen, and steel natural gas pipelines are vulnerable to hydrogen embrittlement. The construction of a new pipeline system, using sufficiently nonporous materials such as stainless steel, would be necessary for widespread transportation of hydrogen on the same scale as current natural gas distribution. The scale of pipeline construction is minimized if hydrogen is produced as close to the point of use as possible. For small quantities of hydrogen and transportation over short distances, trailer transport is possible for either compressed gas or liquid hydrogen; transport of liquid hydrogen is more efficient because of its much greater volumetric density. Since the production of liquid hydrogen is uneconomic in small quantities, trailer transport of liquid hydrogen will be the normal method of supplying liquid hydrogen to fueling stations.^{42,43}

Transportation of large quantities of liquid hydrogen by ship, analogous to the current bulk transportation of oil in tanker vessels, is still a theoretical idea at present. If it could be achieved, however, the economy of maritime transport would make it highly competitive with gas pipeline transport and might allow for the transport of hydrogen generated from renewable sources—geothermal energy in Iceland, for example, or solar power in the Sahara or the Middle East—over thousands of miles to European, North American, or Asian energy markets.

The term ‘*hydrogen corridor*’ has been used to describe the ensemble of large-scale production of hydrogen in one region or country and its long-distance transport in bulk by ship or pipeline to consumers in another region or country.

Apart from meeting economic, environmental, and safety criteria, the new hydrogen technology must be usable without undue constraints. Operability, everyday suitability, and acceptance of hydrogen energy technology mandate the testing of systems in actual practice. In fact, there are currently around 300 hydrogen fueling stations in operation worldwide, mostly in the United States, Japan, and Germany, as part of various hydrogen-transport projects.⁴² The first public filling station for liquid hydrogen was taken into service in Munich airport in 1999. A large fueling station needs to provide hydrogen to 300–400 cars per day to be comparable to a conventional petrol station, which, at around 5 kg of hydrogen to fully refuel a car, would require more than a ton of hydrogen per day. Fueling stations may be divided into compressed-gas hydrogen (CGH_2) and liquid hydrogen (LH_2) types.

A CGH_2 station would maintain a store of compressed hydrogen at relatively low pressure, comparable to the 20 bars at which hydrogen can be produced and distributed by pipeline. On-site booster compression is required to dispense hydrogen to vehicles at the pressures of up to 800 bars required to refuel vehicles with on-board 700-bar compressed-gas storage.

An LH_2 station would maintain an underground cryogenic tank of liquid hydrogen, supplied to the site by trailer. This aspect of the design is similar to current gasoline filling stations, although, of course, the handling of cryogenic liquids is more challenging; careful attention must be paid to the venting of excess boil-off gas from such a station to avoid any risk of combustion or detonation. LH_2 stations have the advantage that they can dispense both liquid hydrogen and boil-off gas as CGH_2 . This flexibility will be valuable if both LH_2 and CGH_2 hydrogen FCEVs reach the marketplace.

It is clear that the development of industry standards for the dispensers for LH_2 and CGH_2 to vehicles, and for the vehicle interface to the dispenser, will be vitally necessary for hydrogen FCEVs to become widespread; a situation in which vehicles from a given supplier were physically unable to refuel from fueling stations associated with a competing supplier would not be tolerable to consumers.

2.3 Storage

Storage of hydrogen as a cryogenic liquid or a compressed gas are the best-developed methods at present. Reversible storage in solid or liquid materials is less well developed but is a subject of intense research effort. Figure 7 gives an overview of hydrogen storage methods and materials,⁴⁴ drawing attention to the system’s materials weight percent hydrogen, the operating temperature, and the energy required for hydrogen release.

2.3.1 Liquefied, Cryogenic Hydrogen

Hydrogen has been liquefied on an industrial scale for more than 70 years, and used in a variety of applications. Hydrogen can be transformed from a gas to a liquid by cooling to temperatures below 20 K; the very low temperature required is natural, given the low molecular weight of hydrogen. The phase diagram of hydrogen is such that the liquid phase exists in only a relatively narrow range of temperatures and pressures; there is a critical point at 33 K, above which the liquid phase does not exist, and it also does not exist at pressures above a few bars. This causes difficulty with liquid hydrogen storage; the evaporation of some of the liquid is inevitable as heat is absorbed from the environment, and the evaporated gas cannot be reliquefied by increased pressure. Venting of boil-off gas is therefore vital for safe LH_2 storage and involves a loss on the order of 1% per day of stored hydrogen.

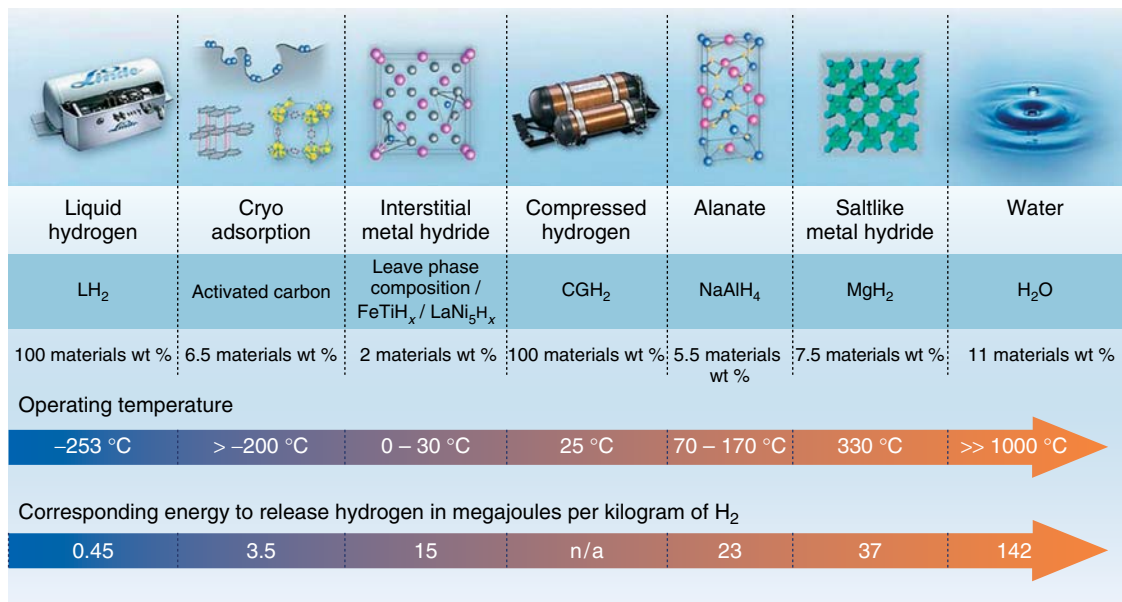


Figure 7 Overview of hydrogen storage methods and materials. (Reproduced from Ref. 44. © Wiley-VCH, 2009.)

The cooling process for hydrogen involves multiple stages, including a step for the catalytic conversion of orthohydrogen to parahydrogen (a transition in the spin states of the nuclei in the molecule), and is energy intensive. The process is more efficient in larger plants, but generally requires energy input on the order of 20–40% of the chemical energy content of the hydrogen. This figure affects the effective energy efficiency of hydrogen applications, and the avoidance of this large energy loss is one of the drivers in the search for reversible solid-state hydrogen storage materials. Liquid hydrogen storage can be effective for stationary applications, such as the LH_2 fueling station, but the weight of the well-insulated tank required to store small amounts of hydrogen safely is a negative feature for on-board vehicular hydrogen storage; such tanks offer a gravimetric hydrogen density of only a few weight percent (up to 10 wt % in some cases), and the venting of boil-off hydrogen from parked cars is a safety issue. Current LH_2 prototype vehicles, for example, cannot be parked in enclosed spaces in case of gas buildup. The cost of on-board cryogenic storage tanks must also be reduced greatly for LH_2 to be commercially practical. Until recently, liquid hydrogen was evaluated as a viable on-board storage option for transportation. However, virtually all of the world's major car manufacturers are concentrating their efforts on compressed-gas storage (which we now focus on) or liquid hydrogen storage in combination with cryoabsorption on tailored sorbents.

2.3.2 Hydrogen Compressed-Gas Storage

A priority development goal is a vehicle fuel tank with maximum energy storage capacity and minimum weight,

volume, and cost. One solution is a pressure vessel made of composite materials in which hydrogen is stored at high pressure. Hydrogen gas compression from ambient pressure to 800 bars—a pressure suitable to refuel a storage system operating at around 700 bars—requires work equivalent to about 15% of the energy content of the hydrogen, and thus is slightly less energetically costly than liquefaction. The energy cost is reduced somewhat if compression begins with gas at a higher pressure, for example, as produced from PSA or high-pressure electrolysis. The weight of a steel tank capable of containing such high pressures safely is considerable. Current 350-bar CGH_2 storage tanks for vehicles achieve about 6 wt % of hydrogen, while 700-bar tanks have slightly poorer gravimetric performance at around 4.5 wt % of hydrogen, though with a gain in volumetric performance. The development of improved high-pressure tanks using lightweight composite materials does improve the gravimetric performance. These generally consist of a thin-walled, seamless aluminum liner, completely enveloped by a high-strength carbon-fiber laminate. The cost of the tank is, if anything, a greater barrier than the weight; current tanks cost thousands of dollars, whereas gasoline tanks cost on the order of \$50 apiece. To achieve the goal of 600 km, the operating pressure will have to be increased to 35–70 MPa: the solution will surely involve composite materials with high-strength metal liners.

2.3.3 Hydrogen Storage in Materials

It is clear that the safe, compact storage of hydrogen is one of the major obstacles to the widespread adoption of hydrogen as a fuel. Hydrogen storage materials (in

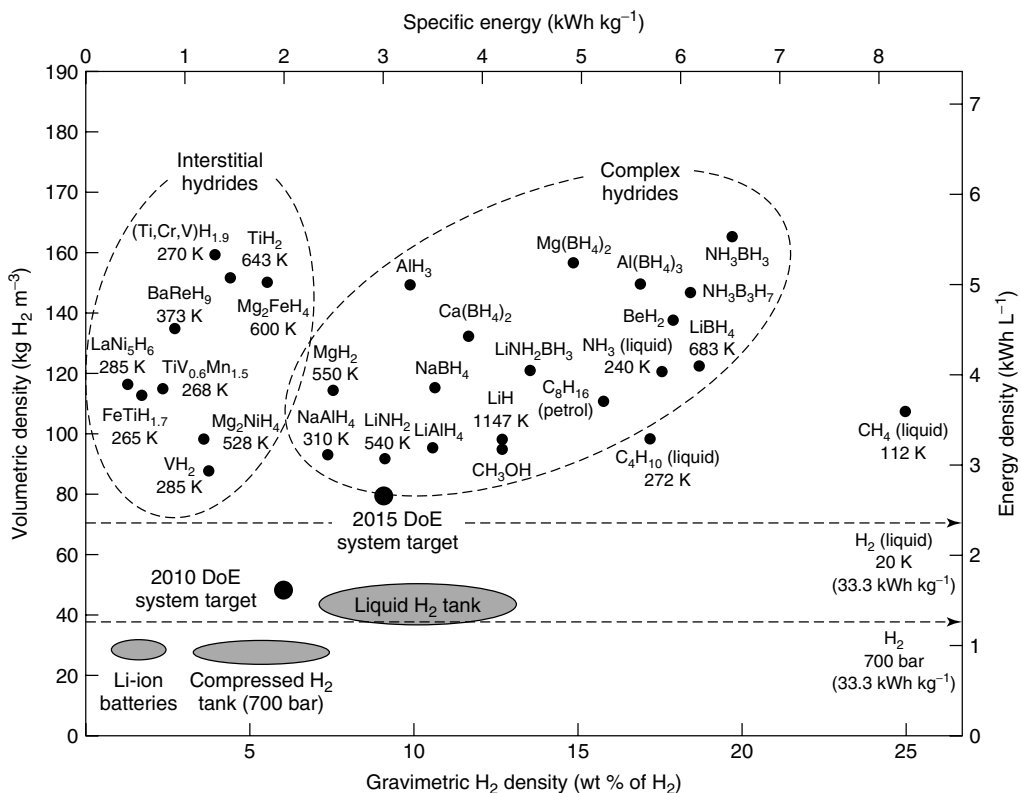


Figure 8 Energy density of various energy storage materials and technologies, illustrating the respective volumetric and gravimetric densities with temperature data for some materials under the composition indicating equilibrium temperature at a hydrogen pressure 1 bar. (Reproduced from Ref. 36. © Wiley-VCH, 2010.)

essence, “solid” hydrogen storage) can provide a high energy density, compact, and low-pressure route to storing hydrogen. However, Figure 8 clearly indicates the storage challenge for hydrogen (and indeed other energy sources, e.g., lithium batteries) when compared with fossil fuels. The latter clearly have exceptional volumetric and gravimetric energy densities. Although liquid hydrogen on its own would massively outperform them on specific energy, current LH₂ and CGH₂ storage systems have much poorer performance because of the weight and volume of the ancillary material required to contain the hydrogen. Research is therefore directed to the area for a storage system that will make on-board hydrogen storage a practical reality. This is now a major focus of significant international activity.

Hydrogen can be bound within a solid material by two mechanisms, physisorption or chemisorption. In physisorption, molecular hydrogen is bound by van der Waals’ type forces to the surfaces of a porous material. As these interactions are very weak (on the order of 5–8 kJ mol^{−1} of H₂), physisorption requires cryogenic temperatures, and research is often directed at systems operating at liquid nitrogen temperature (77 K). However, this is far less challenging than working with liquid hydrogen and avoids the high energy cost of liquefaction. Hydrogen release is,

in turn, achieved by the introduction of a small amount of heat energy. The storage material must offer extremely high internal surface area on which to absorb the hydrogen, so nanostructured materials such as zeolites, metal–organic frameworks (MOFs), and nanocarbons have been investigated. Light weight and stability are also required; the latter is critical as the material must function for thousands of cycles of hydrogen loading and unloading. The intrinsic advantage of hydrogen physisorbed in such materials is their rapid charge/discharge times—here hydrogen maintains its molecular identity at all times. Important strategies are now emerging for the optimization of pore sizes and hydrogen adsorption energy in both MOFs and zeolites and there is a real optimism that significant advances are possible toward achieving the Department of Energy (DOE) targets for on-board hydrogen storage.

In chemisorption, by contrast, the hydrogen molecule is dissociated into atoms which are stored either in chemical compounds or within the lattice of a metallic host material. The advantage of this approach is that it is possible to achieve extremely high volumetric and gravimetric hydrogen densities in some cases, even exceeding that of liquid hydrogen (67.8 kg m^{−3}); for example, the material Mg₂FeH₆ stores 150 kg m^{−3} of H₂, and more complex alloys like (Ti,

$\text{Cr}_x\text{VH}_{1.9}$ store 160 kg m^{-3} of H_2 . Since chemisorption involves the breaking and formation of chemical bonds, the hydrogen-binding energies are much higher than in physisorption. Such materials offer the prospect of a high energy density, compact, and low-pressure means of storing hydrogen. Thermal management of the system is therefore critical. During fueling, heat is released from the reaction of molecular hydrogen with the dehydrogenated storage material. In operation, heat must be introduced to provoke the release of hydrogen from the store. It is therefore desirable that the temperature required for thermal release should not be greater than the temperature of the exhaust gases from the hydrogen fuel cell (less than 100°C for PEMFCs) so that heat energy can be recycled and no additional energy input is required for hydrogen release. Low temperature of dehydrogenation is also required for a quick start of a fuel-cell system. The decomposition temperature for binary metal hydrides (MH_n) is found to correlate strongly with the structural electrode potential, E^0 . In particular, the easier it is to reduce the metal (i.e., a larger reduction potential), the lower the temperature that is required to decompose the solid into the metal and hydrogen gas.

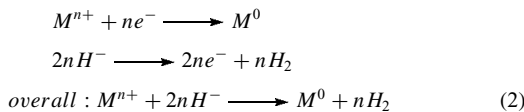


Figure 9 shows the relationship between the reduction potential and decomposition temperature for binary hydrides.³⁶ It also “calibrates” such considerations against the operating temperatures of the various hydrogen fuel cells. Given that only light elements of the periodic table are able to meet the gravimetric weight density, considerable emphasis is now being placed on complex ternary hydrides, NaBH_4 and LiBH_4 . These can achieve impressive gravimetric densities. With respect to materials design, the decomposition temperature of ternary hydrides can also be altered through the choice of metal constituent, and the trends in decomposition temperature can be rationalized by the relative difference in electronegativities of the metal and anion components.

Arguably, the best-developed methods for solid-state hydrogen storage are based on metal alloy or interstitial hydrides.^{40,41,45} Several types of interstitial hydrides exist which operate at different temperatures and pressures from below zero up to 300°C and above (Figure 7). Transition metal hydrides are too heavy for vehicular applications but have potential applications in stationary hydrogen storage (e.g., for hydrogen generated from intermittent sources, as mentioned in Section 1.2) or in maritime applications, where heavy hydrogen storage materials can be used in ballast. Research for vehicular solid-state hydrogen storage is now concentrated on hydrides of light elements such as lithium, boron, sodium, magnesium, and aluminum.² These can achieve impressive gravimetric hydrogen densities (up to 18 wt % in the case of LiBH_4). The bonding in these hydrides is intermediate

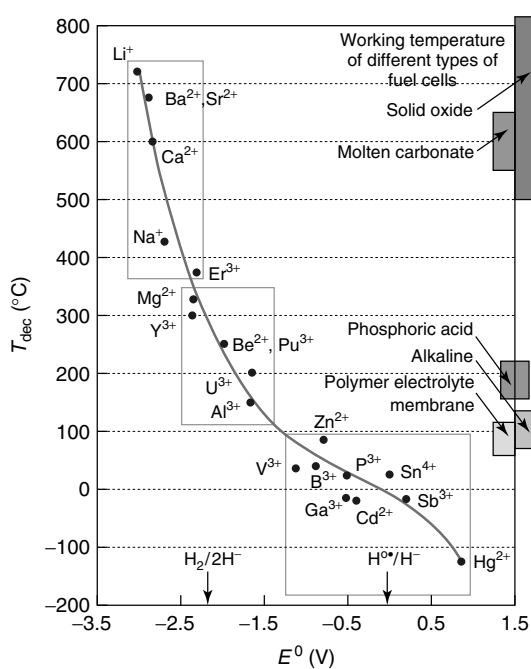


Figure 9 Correlation between temperature, T_{dec} , at which thermal decomposition of binary hydride MH_n to the constituent elements proceeds, and the corresponding redox potential of the redox pair M^{n+}/M^0 in acidic aqueous conditions. (Reproduced from Ref. 36. © Wiley-VCH, 2010.)

between ionic and covalent; reversibility and the kinetics and temperature requirements of hydrogen release and uptake are still major unresolved issues.^{40,41}

It seems likely that CGH_2 and LH_2 systems will continue to play their part in the transitional hydrogen economy. If a breakthrough in hydrogen storage materials were forthcoming, a favorable impetus would then be applied to resolving many of the other challenges facing the hydrogen economy. Solid-state materials do indeed have the potential to outperform other storage technologies; the issue here—as in many new areas—is that of materials discovery.

A possible solution to the reversibility issue is off-board regeneration, where the spent storage material is removed from the vehicle and reprocessed at a chemical facility. This is very similar to the battery-swapping concept for BEVs, but with a much more competitive range between reloads, and allows for hydrogen production on-board by hydrolysis reactions. Attractive, new-generation hybrid storage systems offer a combination of chemisorption and storage under pressure; essentially a pressurized storage tank is filled with an interstitial metal hydride, resulting in a system in which working pressures are lowered considerably.

The storage of hydrogen in liquid-phase organic heterocycles is also a highly promising option for storing hydrogen because of simplicity, safety, scalability, low cost, and easy heat management compared to solid-state hydrogen

storage materials.⁴⁶ The well-known cyclohexane–benzene system has a very high dehydrogenation temperature ($>300^\circ\text{C}$) but nitrogen-containing organic ring compounds (for example, N-ethyl carbazole and related compounds) have demonstrated reversible hydrogen storage capacities of >7 wt % at $150\text{--}200^\circ\text{C}$ due to an optimal heat of dehydrogenation of $10\text{--}13\text{ kcal mol}^{-1}$ of H_2 .⁴⁶ Selective catalysts enable highly reversible catalytic hydrogenation and dehydrogenation of these materials with no significant degradation of the molecules.

Organic liquid hydrogen storage materials have a number of significant engineering advantages since they can be easily pumped during distribution, delivery, and car refueling process. They also have low volatility (b.p. $>300^\circ\text{C}$) and a high flash point, and can employ a simple and light fuel tank that would not require handling high pressures and temperatures. In addition, the dehydrogenation can be done in a small catalytic dehydrogenation chamber, which would require heating only a small amount of liquid material instead of heating the whole hydrogen storage tank. Organic hydrogen storage materials also consist of abundant and cheap elements (carbon, nitrogen) and only require a small amount of precious metal catalyst for dehydrogenation and hydrogenation steps. The remaining issues for introduction of organic hydrogen storage materials include the understanding and optimization of dehydrogenation mechanism against undesired decomposition pathways, improving kinetic facility for the hydrogenation step and decreasing the toxicity.

2.4 Hydrogen Use: The Fuel Cell

Fuel cells are electrochemical converters, transforming chemical energy from a controlled reaction directly into direct-current electrical power.⁴⁷ The important distinction between a battery and a fuel cell is that a battery contains its own reaction substances, which are consumed until the battery is discharged, whereas a fuel cell is provided with a continuous flow of reactants from an external source. The basic layout of a fuel cell involves the provision of a fuel to the anode; the transfer of a mobile ion across an electrolyte barrier separating the anode from the cathode; and the provision of oxygen or air at the cathode. Electrons are liberated at the anode and consumed at the cathode; electrical power is extracted from the device by connecting a load across the terminals allowing electrons to flow from the anode to the cathode. This makes the cathode the positive terminal, as is normal for a galvanic cell supplying current. The electrolyte must permit the passage of the mobile ions but be impermeable to electrons, as electron transfer across the electrolyte would constitute a short circuit in the device. In different forms of fuel cell, the mobile ions may either be negative (oxide, hydroxide, or carbonate) and move from cathode to anode, or positive (protons) moving from anode to cathode. The first fuel cell was reported in 1839 by Sir William Grove, consuming hydrogen and oxygen

with platinum electrodes and a sulfuric acid electrolyte—an electrolyzer operated in reverse.

The theoretical maximum efficiency of a fuel cell is given by the ratio of the free-energy change to the enthalpy change during the reaction; for a hydrogen fuel cell operating at temperatures around 100°C , this efficiency is around 90%. The theoretical voltage of a hydrogen cell is 1.23 V, though in practice cells operate at around 0.7 V, and multiple cells must be stacked together, connected by bipolar plates, to achieve higher voltages. The lower cell voltage and resistance losses in the system reduce the efficiency considerably below the theoretical maximum, but even so a hydrogen FCEV can operate with a net efficiency including the drive train of up to 45%. This greatly exceeds the performance of ICEs, which at partial load (typical of driving conditions) routinely operate at around 20% efficiency; the theoretical maximum efficiency of ICEs is limited by the Carnot cycle. Although the efficiency advantages of fuel cells have been appreciated since the nineteenth century, they have repeatedly failed to break into the mass market, largely due to the materials problems involved in developing effective, durable, and inexpensive materials for the anode and cathode catalysts and for the electrolyte.

We briefly summarize the main types of fuel cells in terms of their operating temperatures and the nature of the electrolyte. The SOFC (ceramic oxide electrolyte) operates in the range of $600\text{--}1000^\circ\text{C}$ and the molten carbonate fuel cell at around 650°C . These types are considered more suitable for stationary electricity generation applications than for transport because of their slow start-up from cold (see *Intermediate-Temperature Solid Oxide Fuel Cells*). We note that at these high temperatures of operation, the cells can be fueled either with hydrogen or with a hydrogen- and CO-rich syngas generated from the reforming of a purified hydrocarbon gas.

Lower temperature fuel cells fueled by hydrogen include the alkaline fuel cell, operating at around 80°C with hydroxide ions as the charge carrier; the phosphoric acid fuel cell, operating at around 200°C with protons mobile in concentrated phosphoric acid; and the PEMFC, operating at around 80°C . The PEMFC is the leading candidate for the power source in hydrogen FCEVs (see *Proton Exchange Membranes for Fuel Cells*) (Table 3). The low-temperature fuel cells are less tolerant of fuel variations than the high-temperature cells, as carbon monoxide is a catalyst poison, and must be provided with high-purity hydrogen as fuel.

A variant of the PEMFC is the direct methanol fuel cell, powered not by hydrogen but by a dilute methanol solution. This cell is proposed as a power supply for portable applications such as laptop computers, where it would offer much longer operating times than batteries can; the ease of handling of the methanol solution makes it more suitable than hydrogen for such small-scale applications. The alkaline fuel cell can also be fueled by ammonia.

Perhaps the biggest challenge facing the utilization of the PEMFC for hydrogen vehicles are lifetime and cost. At present, the electrodes are made with a nanostructured

Table 3 Types of fuel cells, their temperature of operation, electrical efficiency, and applications. Adapted from Ref. 6

Type of cell	Electrolyte	Mobile ion	Temperature of operation	Electrical power range (kW)	Electrical efficiency (%)	Application
Alkaline (AFC)	Liquid KOH	OH ⁻	50–200 °C	0.1–50	50–70	Space vehicles
Phosphoric acid (PAFC)	Liquid phosphoric acid	H ⁺	~220 °C	50–1000	40–45	Stationary applications
Proton exchange membrane (PEM)	Polymeric film	H ⁺	30–100 °C	—	—	Transport applications
Molten carbonate (MCFC)	Molten alkali metal carbonates	CO ₃ ²⁻	~650 °C	200–100 000	50–60	Stationary application
Solid oxides (SOFC)	Ceramic YSZ	O ²⁻	500–1000 °C	0.5–2000	40–72	Stationary applications

platinum catalyst, an expensive material and one which is sensitive to poisoning by carbon monoxide, ammonia, and by sulfur compounds. Materials costs and the costs of manual production of components give a current price of \$2000–\$4000 per kilowatt, and the lifetime of the cell is below 2000 h.⁴⁸ For hydrogen FCEVs to be economically competitive with gasoline vehicles, and thus be an attractive option for consumers in the transitional hydrogen economy, costs must be reduced below \$100 per kilowatt and lifetime must be increased to above 5000 h. While mass production can help in cost reduction, cheaper and more durable catalyst and electrolyte materials are urgently needed—another fascinating challenge for chemistry and materials in the development of the hydrogen economy (*see Molecular Catalysis for Fuel Cells*). A considerable contribution to these challenges is indeed being made by chemists, in association, in multidisciplinary projects, in developing new generation, high-performance catalysts, membranes, electrodes, and materials for the new fuel cell technologies.

Conceptually, and indeed operationally, hydrogen fuel and the hydrogen fuel cell form the “hydrogen nexus,” connecting diverse methods of hydrogen generation and possible applications, as illustrated in Figure 1.¹⁰

very hard, especially if it’s about the future.” Nonetheless, we briefly sketch the likely nature of these changes. As noted recently by Ekins,⁴⁹ “...a technological challenge of the kind envisaged is far more than a change in the physical technologies employed in the energy system, important though this change is.” He further notes that “...change cannot and will not come about unless it is accompanied by parallel changes in the economic and social systems.”

The energy sector may expect an increasing emphasis on renewable energy generation; more solar panel construction and installation; more wind turbines and tidal or wave generators; greatly increased production of biofuels; the construction of a new generation of nuclear fission reactors; and the development of an enhanced electrical grid, incorporating new features such as high-temperature superconducting transmission lines and long-distance high-tension DC transmission. We must also expect increasing emphasis, in all technology sectors and in the construction industry, on energy efficiency; reductions in demand by efficiency gains reduce both our current use of fossil fuels and the load on the developing renewable energy supply.⁵⁰ Geopolitically, the changes required for the development of a hydrogen economy may be perceived as a threat by countries whose economies are heavily dependent on the production of fossil fuels or otherwise heavily invested in the fossil fuel economy.

There are substantial differences worldwide in the cultural expectations that drivers have regarding their vehicles and their use. For example, in the United States, in recent years, there has been a shift toward heavy and inefficient “sports utility vehicles” (SUVs), and there is a long-standing cultural bias toward long-distance free-roaming driving. The development of prototype hydrogen vehicles is biased more toward smaller, lighter vehicles which are suited to short-range urban driving and may be more welcome in the European and Japanese markets.

The transition from gasoline ICEs to hydrogen FCEVs will have fundamental socioeconomic consequences on employment patterns and the skills required of the automotive industry workforce. Essentially, the costs of the drive train of a gasoline ICE include substantial contributions from the mechanical elements of the engine itself and the mechanical transmission system. FCEVs are simpler,

3 ECONOMIC, SOCIAL, AND POLITICAL ISSUES

The desirability of hydrogen relates mainly to the challenges of pollution (most notably, climate change and local air pollution) and energy security that have arisen from the current reliance on fossil fuels as the primary energy source.⁴⁹ However, for the hydrogen economy to ever come about, there will need to be a fundamental transition away from the fossil fuel economy and its associated energy system and all-pervasive infrastructure. The development of a hydrogen economy is not only an engineering and scientific challenge; it will have fundamental consequences on the socioeconomic and geopolitical scales; patterns of employment will shift as the newer technology makes different demands on the workforce and supply chain, and regional and global trade patterns will alter as the sources of energy supply shift from fossil-fuel-rich to renewable-resource-rich areas. It is said that “prediction is

mechanically, as they have far fewer moving parts, and so the production and assembly of the power supply and transmission will constitute a smaller fraction of the cost of the drive train. The contribution of electrical and electronic engineering to vehicle construction, by contrast, will increase because of the increased use of electric motors and complex electronic control systems. Different demands will be made on the chemical industry, as there will be an increased need for the components of the fuel cell system (especially the catalyst electrodes and the electrolyte membrane), and a decreased need for products such as the catalytic convertor—currently a major component of the ICE exhaust system.

The widespread use of hydrogen could potentially have environmental effects due to increased anthropogenic emissions of molecular hydrogen to the atmosphere.⁵¹ Hydrogen participates in stratospheric chemical cycles involving H₂O and various greenhouse gases, and a substantial increase in its concentration might lead to changes in the equilibrium composition of the stratosphere. More accurate modeling of these stratospheric processes and better understanding of other factors such as hydrogen uptake in soil and its effect on microbial communities are required to assess the potential environmental impact of the hydrogen economy. We have 10–20 years, before hydrogen is widely used as an energy carrier, to understand, and take any necessary actions to prevent, any harmful environmental impact. We must avoid a repetition of the mistakes of the past, when the harmful effects of chemicals such as chlorofluorocarbons, lead in petrol, and indeed the use of fossil fuels in general, were understood only after significant damage to the environment had been done. Any potential concern over the use of hydrogen, however, is outweighed by the very real dangers associated with our escalating CO₂ emissions.

The safety of hydrogen production, storage, and use is not only a technological issue but also the major psychological and sociological issue facing the adoption of the hydrogen economy. To be accepted by the public, hydrogen must be considered safe. Consumers will undoubtedly have concerns about the safety and dependability of fuel-cell-powered equipment, new dispensing technology, etc., just as they had about other modern devices when they were introduced. Confidence-building will be necessary for transportation, stationary residential and portable applications where customers will interact directly with hydrogen and fuel-cell technology. An important factor in promoting public confidence will be the development and adoption of internationally accepted codes and standards. Education projects, product exposure, and marketing should be developed in order to facilitate the successful introduction of hydrogen as an alternative fuel.⁵²

Although the investments required for the development of a hydrogen economy are substantial, they must be viewed not as a cost but as a long-term investment with a large expected return. In the next few decades, we must expect that countries and regions that can successfully make the transition

to sustainability, cutting their dependence on fossil fuels and improving their energy security by efficiency gains and diversification of energy supply, will reap substantial economic and political benefits.

4 FUTURE PROSPECTS FOR A HYDROGEN ENERGY ECONOMY

At present, the hydrogen economy is at best embryonic.⁵³ Hydrogen vehicles exist in prototype form, with around 1000 FCEVs in operation worldwide at the end of 2007; typically these development models use 350-bar or 700-bar CGH₂ storage and have ranges of 200–300 km. In the public transport sector, around 100 hydrogen buses are in operation. Around 200 hydrogen fueling stations are active. Hydrogen-transport projects are concentrated in cities, as the prototype vehicles are most suitable for short-range urban driving in the vicinity of hydrogen fueling stations. In terms of global geography, hydrogen transport is concentrated in North America, Europe (especially Germany) and Japan. A small number of hydrogen buses were used as part of transportation service at the 2008 Beijing Olympic Games.

The timescale and evolution of a potential transition are the focus of many “road maps” emanating from the United States, Japan, Canada, the European Union, and many others. The key components of these hydrogen roadmaps relate to hydrogen production, storage, distribution, and utilization, and encompass many of the scientific and technological issues and challenges outlined earlier. In January 2004, the European Commission initiated the European Hydrogen and Fuel Cell Platform (HFP) with the expenditure of €2.8 billion over a period of 10 years, with the aim to prepare and direct an effective strategy for developing and exploiting a hydrogen-oriented economy for the period up to 2050. Key highlights and scenarios challenging European hydrogen vision are summarized in Figure 10.⁵⁴

This long-term vision regarding the potential of hydrogen and fuel cells illustrates the final goal of a hydrogen economy that relies mainly on renewable energy production pathways. A target scenario for 2020 was developed for guiding the transition toward introducing hydrogen and fuel cells to the market. In March 2005, HFP published a Strategic Research Agenda and Deployment Strategy,⁵⁵ followed by an Implementation Plan in January 2007, which combined these two documents into a long-term road map for Europe. The primary objective of this roadmap is to achieve by 2020 EU-wide availability of hydrogen and fuel-cell vehicles with an appropriate coverage of refueling infrastructure. Table 4 summarizes the forecasts of several roadmaps for deployment status and targets for hydrogen technologies and fuel-cell applications.^{55,56}

In 2002, the US DOE, in conjunction with the auto industry, established the US FreedomCAR and Fuel

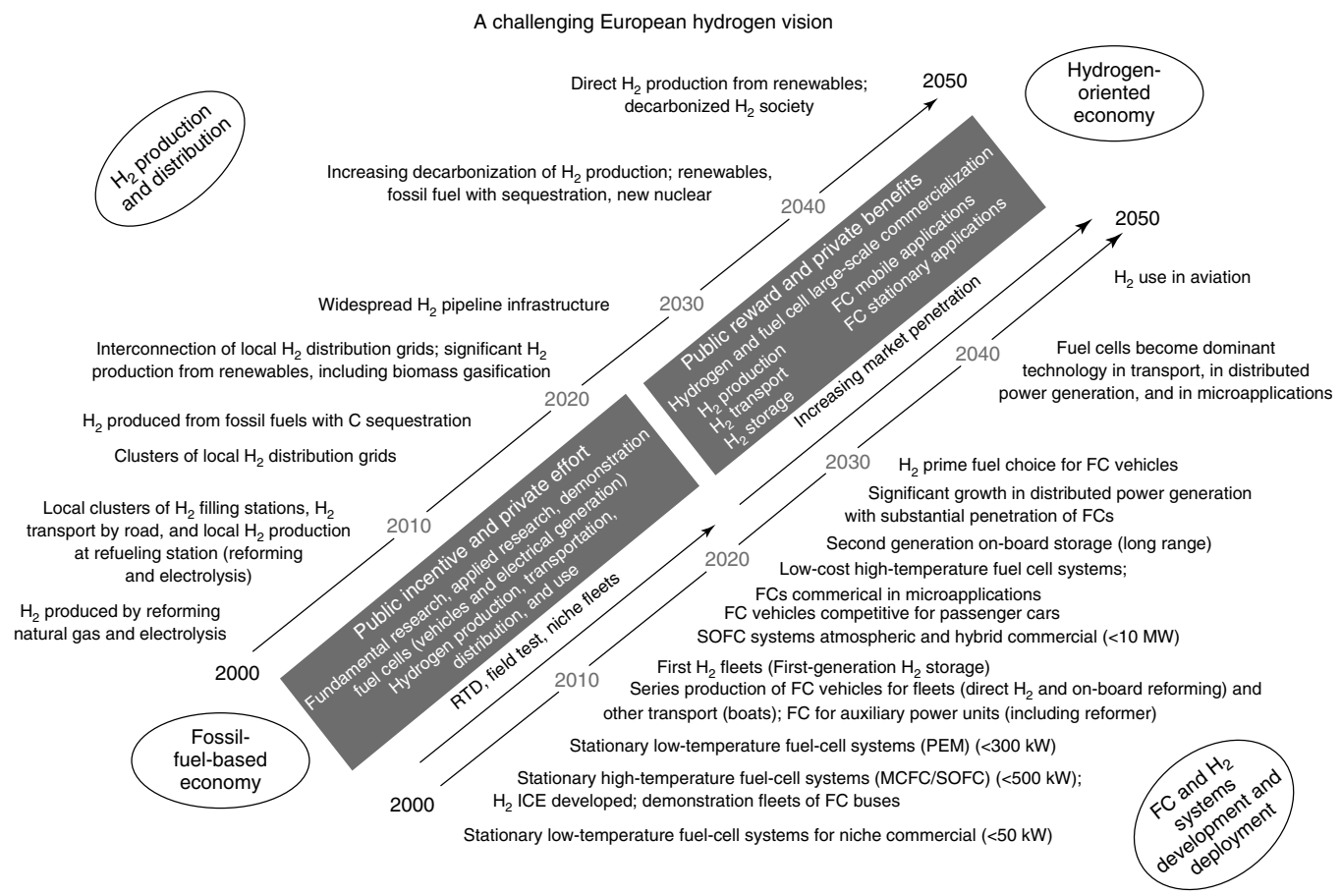


Figure 10 The European hydrogen and fuel-cell road map. (Reproduced with permission from Ref. 54. © European Commission, 2003.)

Table 4 Key assumptions on hydrogen and fuel cell applications. Adapted from Ref. 55, 56

Technology	Today	2020	2050
Hydrogen produced from coal with CCS (€ GJ ⁻¹)	8–10	7–9	3–5
Hydrogen transportation/storage cost (pipeline, 5000 kg h ⁻¹ , 800 km) (€ GJ ⁻¹)	10–15	3	2
PEM fuel-cell cost (€ kW ⁻¹)	6000–8000	400	40
High-temperature fuel-cell cost (€ kW ⁻¹)	8000–10000	800	200
European Union: portable fuel cells, sold per year	n.a.	250 million	n.a.
European Union: fuel-cell vehicles, sold per year	n.a.	0.4–1.8 million	n.a.
European Union: stationary fuel cells (CHP), sold per year	n.a.	100 000–200 000 (2–4 GW)	n.a.
United States: number of fuel-cell vehicles	n.a.	2 million	n.a.
Japan: fuel-cell vehicles, cumulative sale target	n.a.	5 million	n.a.
IEA forecast: global fleet of fuel-cell vehicles	n.a.	n.a.	700 million

CHP, combined heat and power; IEA, International Energy Agency; n.a., not applicable.

Partnership. This partnership set technology goals and demonstration targets for 2015 that were considered sufficient to enable the industry to move toward the commercialization of the hydrogen technologies as illustrated in Figure 11.⁴⁸ Some of the most important R&D goals for hydrogen and fuel cell technology are listed in Table 5.

In 2008, the US National Research Council's Committee concluded that on the basis of the substantial financial commitments and technical progress, the hydrogen production technologies and hydrogen and fuel cell vehicles could be ready for commercialization in the period 2015–2020. It was also estimated that, while fuel cell

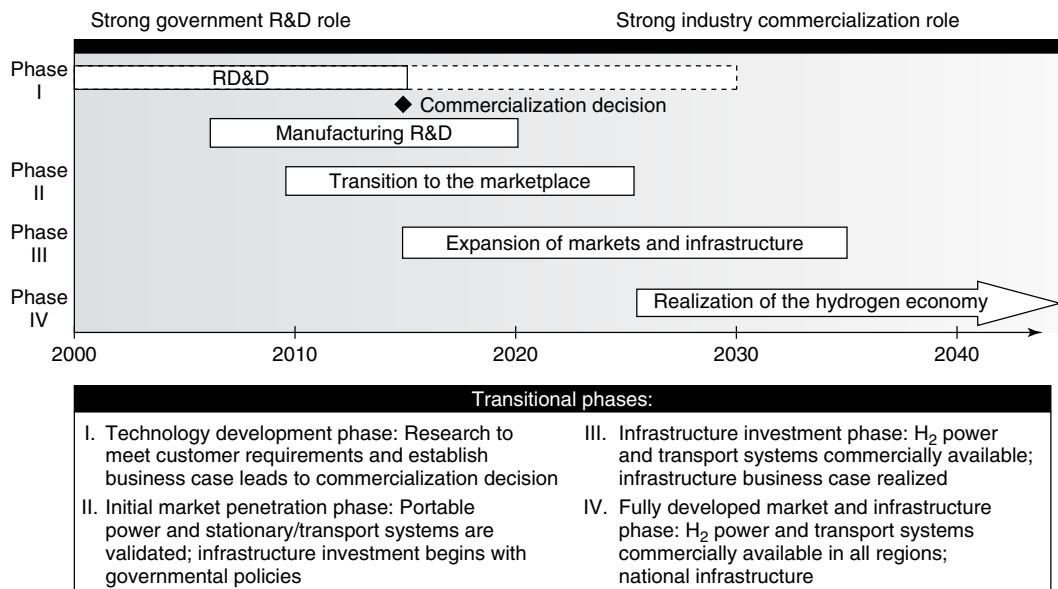


Figure 11 US hydrogen economy timeline with manufacturing R&D shown. (Reproduced from Ref. 48. © U.S. Department of Energy, 2004.)

Table 5 DOE's 2015 goals for hydrogen and fuel-cell technology

Targeted factor	Goal for 2015
Hydrogen production	\$2 per kilogram (by distributed methane reforming)
Hydrogen storage: specific energy density	10.8 MJ kg ⁻¹ (9.0 wt %)
Hydrogen storage: volumetric energy density	9.7 MJ L ⁻¹ (81 g of H ₂ per liter)
Hydrogen storage: system cost	\$0.56 per megajoule (\$66 per kilogram of H ₂ stored)
Hydrogen storage: delivery pressure	2.5 bars
Hydrogen storage: operating temperature	From -40 to +85 °C
Hydrogen storage: cycle life (1/4 tank to full)	1500
Hydrogen storage: refueling rate	2.0 kg of H ₂ per minute
Hydrogen storage: loss of usable H ₂	0.05 g h ⁻¹ per kilogram of H ₂ stored
Fuel-cell cost	\$30 per kilowatt at a volume of 500 000 units per year
Fuel-cell lifetime	5000 h
Fuel-cell efficiency (80 mpg equivalent)	60%
Vehicle driving range	300 miles
Vehicle efficiency	80 miles/gasoline-gallon-equivalent

vehicles would not become competitive with gasoline-powered vehicles by 2020, they could account for more than 80 % of new vehicles entering the fleet by 2050.⁵⁷

These efforts will require considerable resources, especially government and private sector funding. The committee estimated that in addition to the current US government hydrogen R&D expenditures of about \$300 million per year, additional \$55 billion from 2008 to 2023 will be needed to support a transition to hydrogen fuel cell vehicles. This funding includes an extensive R&D program (\$5 billion), support for the production of hydrogen (\$10 billion) and support for the demonstration and deployment of the hydrogen vehicles at the earlier stages of commercialization (\$40 billion). It is also estimated that private industry would need to invest about \$145 billion for R&D, vehicle

manufacturing, and hydrogen infrastructure over the same period.⁵⁷

Across the full range of energy use, hydrogen and fuel cells provide a major opportunity to shift our carbon-based global energy economy ultimately to a clean, renewable and sustainable economy based on hydrogen. To achieve a significant penetration of hydrogen into future energy systems, the methods of hydrogen production, distribution, storage, and utilization must be significantly improved beyond their present performance, reliability, and cost. In addition to technological developments, significant new energy security and environmental policy actions will be also required. To enable competitive and self-sustaining hydrogen and fuel cell systems in the long term, hydrogen-specific policies adopted in the nearer term will be required in order to assure industry

that the necessary long-term investments can be made safely. This will allow for the development of sufficient capacity for hydrogen production, distribution, and use to make a hydrogen economy feasible.

Any assessment of the feasibility of a sustainable hydrogen energy economy will involve an appraisal of the many steps, not only in sciences and technology but also social and economic considerations, which will have to be taken on the road to that future. The “systems approach” of looking at the future of hydrogen energy, outlined in the Hydrogen Strategic Framework for the UK⁵⁸ concludes that there is not one single route to a hydrogen economy, but rather that many factors/variables are involved in determining its direction. It may, therefore, not only be rather difficult—but indeed limiting—to establish one single path to the hydrogen economy at this juncture. A complementary analysis of how a transition to a hydrogen energy economy may enter the UK energy system is the focus of an important new volume by Ekins.⁴⁹

5 CONCLUDING REMARKS

Any transition to a future hydrogen energy economy will derive largely from a desire to reduce the pollution and energy insecurity that are associated with fossil fuels. At present, such pressures do not appear sufficient to drive the transition—any transition—to a hydrogen energy economy, although, of course, it is possible that this could become so.⁴⁹ In the case of hydrogen, one can therefore categorize both the *physical* and *socioeconomic dimensions* for their successful coevolution toward a hydrogen energy economy. The *physical dimension* deals with the physical issues (and attendant scientific and technological breakthroughs) involved in the production/storage/distribution/end use of hydrogen, which have been reviewed here. The socioeconomic dimension deals with interests and drivers that push technical change along; a cursory review of these issues has been outlined here.

For a hydrogen economy, the *physical dimension* encompasses the following⁴⁸:

- *Science of hydrogen production, storage, and utilization*—the physically possible in advances.
- *Technology*—the physical realization of the physically possible.
- *Infrastructure*—the physical and technical support of the realization of the new energy system.

The *socioeconomic dimension* centers on the following:

- *Economics*—competition and distribution.
- *Institutions*—regulatory, financial, and planning.
- *Political drivers*—social perceptions driving political priorities and the planning system.
- *Culture*—social perceptions driving acceptability and demand.

In this article, we have illustrated the scale and extent of the scientific, technical, and socioeconomic challenges for hydrogen energy technologies, in order to try to understand the kind of transformation of our energy system to which they might ultimately give rise.

6 ACKNOWLEDGMENTS

We thank the EPSRC for support. Asel Sartbaeva thanks the Samuel and Violet Glasstone Research Fellowship and Stephen Wells thanks Leverhulme Trust for funding. We thank D. Payne for adapting the figure 6.

7 RELATED ARTICLES

Enzymes and Microbes for Energy Production by Fuel Cells; H₂ Production from Renewables; Intermediate-Temperature Solid Oxide Fuel Cells; Molecular Catalysis for Fuel Cells; Proton Exchange Membranes for Fuel Cells; Supercapacitors: Electrode Materials Aspects; Thermochemical Water-Splitting.

8 ABBREVIATIONS AND ACRONYMS

AGW = anthropogenic global warming; BEV = battery electric vehicle; CCS = carbon capture and storage; CGH₂ = compressed gas hydrogen (storage method); EV = electric vehicle; FC = fuel cell; FCEV = fuel-cell electric vehicle; HDPE = high-density polyethylene; ICE = internal combustion engine; IPCC = intergovernmental panel on climate change; kWh = kilowatt-hour; measure of energy equal to 3.6 million joules; LH₂ = liquid hydrogen (storage method); MOF = metal–organic framework; PHEV = plug-in hybrid electric vehicle; PSA = pressure-swing adsorption (gas purification method); PEMFC = polymer electrode membrane (or proton exchange membrane) fuel cell; ppm = parts per million (gas concentration); PVC = polyvinyl chloride; RD & D = research development and demonstration; SOFC = solid oxide fuel cell; wt % = weight percent (composition).

9 REFERENCES

1. G. W. Crabtree, M. S. Dresselhaus, and M. V. Buchanan, *Phys. Today*, 2004, **57**(12), 39.
2. P. P. Edwards, V. L. Kuznetsov, and W. I. F. David, ‘Sustainable Hydrogen Energy’, in ‘Energy...Beyond Oil’, eds.

- F. Armstrong and K. Blundell, Oxford University Press, Oxford, 2007, p. 156.
3. M. S. Dresselhaus, *Mater. Issues Hydrogen Econ.*, 2009, **3**.
 4. J. Kilner, P. P. Edwards, V. Kuznetsov ‘‘Celling future’’, *Materials World*, 2009, **17**(7), 36.
 5. S. Young, *Nature*, 2001, **414**(6863), 487.
 6. P. P. Edwards, V. L. Kuznetsov, W. I. F. David, and N. P. Brandon, *Energy Policy*, 2008, **36**, 4356.
 7. IEA (International Energy Association), ‘World Energy Outlook’, OECD/IEA, Paris, 2006.
 8. World Energy Council, ‘Survey of Energy Resources’, 2007, www.worldenergy.org/publications.
 9. IEA (International Energy Association), ‘World Energy Outlook’, OECD/IEA, Paris, 2008.
 10. A. Sartbaeva, V. L. Kuznetsov, S. A. Wells, and P. P. Edwards, *Energy Environ. Sci.*, 2008, **1**(1), 79.
 11. G. Marbán and T. Valdés-Solís, *Int. J. Hydrogen Energy*, 2007, **32**(12), 1625.
 12. M. Ball, ‘Non-renewable Energy Resources: Fossil Fuels—Supply and Future Availability’, in ‘The Hydrogen Economy’, eds. M. Ball and M. Wietschel, Cambridge University Press, Cambridge, 2009, p. 46.
 13. IPCC, ‘Climate Change 2007: The Physical Science Basis. Contribution of Working Group I to the Fourth Assessment Report of the Intergovernmental Panel on Climate Change’, Cambridge University Press, Cambridge, 2007.
 14. S. Arrhenius, *Philos. Mag.* 5, 1896, **41**(251), 237.
 15. IPCC, ‘Climate Change 2007: Impacts, Adaptation and Vulnerability. Contribution of Working Group II to the Fourth Assessment Report of the Intergovernmental Panel on Climate Change’, Cambridge University Press, Cambridge, 2007.
 16. N. Stern, ‘The Economics of Climate Change. The Stern Review’, Cambridge University Press, New York, 2006.
 17. N. A. Rokke, ‘CO₂ Capture, Transport and Storage for Coal, Oil and Gas: Technology Overview’, in ‘Future Electricity Technologies and Systems’, eds. T. Jamasb, W. J. Nuttall, and M. G. Pollitt, Cambridge University Press, Cambridge, 2006, p. 179.
 18. D. Vincent, ‘Arresting Carbon Dioxide Emissions: Why and How?’ in ‘Energy...Beyond Oil’, eds. F. Armstrong and K. Blundell, Oxford University Press, Oxford, 2007, p. 9.
 19. IPCC, ‘Special Report on Carbon Dioxide Capture and Storage. Prepared by Working Group III of the Intergovernmental Panel on Climate Change’, Cambridge University Press, Cambridge, 2005.
 20. C. Cremer, ‘Carbon Capture and Storage’, in ‘The Hydrogen Economy’, eds. M. Ball and M. Wietschel, Cambridge University Press, Cambridge, 2009, p. 168.
 21. IEA (International Energy Association), ‘CO₂ Capture and Storage—A Key Carbon Abatement Option’, OECD/IEA, Paris, 2008.
 22. E. Martinot, ‘Renewable Energy Futures’, 2007, www.martinot.info/futures.htm.
 23. IEA (International Energy Association), ‘Renewables in Global Energy Supply’, OECD/IEA, Paris, 2007.
 24. S. Dunn, *Int. J. Hydrogen Energy*, 2002, **27**(3), 235.
 25. K. Zweibel, J. Mason, and V. Fthenakis, *Sci. Am.*, 2008, **298**(1), 64.
 26. IEA (International Energy Association), ‘Renewables Information’, OECD/IEA, Paris, 2006.
 27. T. B. Johansson, H. Kelly, A. K. N. Reddy, and R. H. Williams, ‘A Renewables-intensive Global Energy Scenario (Appendix to Chapter 1)’, in ‘Renewable Energy Sources for Fuels and Electricity’, eds. T. B. Johansson, H. Kelly, A. K. N. Reddy, and R. H. Williams, Island Press, Washington, DC, 1993, p. 1071.
 28. G. Resch, A. Held, F. A. Toro, and M. Ragwitz, ‘Assessment of the Potentials for Renewable Energy Sources’, in ‘The Hydrogen Economy’, eds. M. Ball and M. Wietschel, Cambridge University Press, Cambridge, 2009, p. 135.
 29. A. G. Dutton, *Wind Eng.*, 2003, **27**, 239.
 30. IEA (International Energy Association), ‘Nuclear Power’, OECD/IEA, Paris, 2007.
 31. J. M. Deutch and E. J. Moniz, *Sci. Am.*, 2006, **295**(3), 76.
 32. ITER, www.iter.org, 2007.
 33. G.A. Olah, A. Goeppert, and G.K. Surya Prakash, *J. Org. Chem.*, 2009, **74**, 487.
 34. M. Ball, W. Weindorf, and U. Bunger, ‘Hydrogen Production’, in ‘The Hydrogen Economy’, eds. M. Ball and M. Wietschel, Cambridge University Press, Cambridge, 2009, p. 277.
 35. IEA (International Energy Association), ‘Hydrogen Production and Distribution’, OECD/IEA, Paris, 2007.
 36. V. L. Kuznetsov and P. P. Edwards, *ChemSusChem*, 2010, **3**(1), 44.
 37. F. E. Osterloh, *Chem. Mater.*, 2008, **20**(1), 35.
 38. B. C. R. Ewan and R. W. K. Allen, *Int. J. Hydrogen Energy*, 2005, **30**(8), 809.
 39. V. Subramani, C. Song, M. Anpo, J. M. Anderson eds, ‘Recent Advances in Catalytic Production of Hydrogen from Renewable sources’ in ‘Catalysis Today’, Elsevier Science, 2007, **129**.
 40. S. I. Orimo, Y. Nakamori, J. R. Eliseo, A. Zuttel, and C. M. Jensen, *Chem. Rev.*, 2007, **107**(10), 4111.
 41. W. Grochala and P. P. Edwards, *Chem. Rev.*, 2004, **104**(3), 1283.
 42. M. Ball, W. Weindorf, and U. Bunger, ‘Hydrogen Distribution’, in ‘The Hydrogen Economy’, eds. M. Ball and M. Wietschel, Cambridge University Press, Cambridge, 2009, p. 322.
 43. S. S. Penner, *Energy*, 2006, **31**(1), 33.
 44. U. Eberle, M. Felderhoff, and F. Schuth, *Angew. Chem.-Int. Ed.*, 2009, **48**(36), 6608.
 45. I. R. Harris, D. Book, P. A. Anderson, and P. P. Edwards, *Fuel Cell Rev.*, 2004, **1**(1), 17.
 46. R. H. Crabtree, *Energy Environ. Sci.*, 2008, **1**(1), 134.

47. F. Marscheider-Weidemann, E. Schirrmeister, and A. Roser, 'Key Role of Fuel Cells', in 'The Hydrogen Economy', eds. M. Ball and M. Wietschel, Cambridge University Press, Cambridge, 2009, p. 348.
48. U.S. Department of Energy, 'Hydrogen Posture Plan: an Integrated Research, Development, and Demonstration Plan 2004', 2004, <http://www.hydrogen.energy.gov/>.
49. P. Ekins ed., 'Hydrogen Energy: Economic and Social Challenges', Earthscan Publications Ltd., 2010, p. 1.
50. E. Jochem, 'Energy-efficient Solutions Needed—Paving the Way for Hydrogen', in 'The Hydrogen Economy', eds. M. Ball and M. Wietschel, Cambridge University Press, Cambridge, 2009, p. 599.
51. T. K. Tromp, R. L. Shia, M. Allen, J. M. Eiler, and Y. L. Yung, *Science*, 2003, **300**(5626), 1740.
52. I. Schulte, D. Hart, and R. van der Vorst, *Int. J. Hydrogen Energy*, 2004, **29**(7), 677.
53. M. Wietschel, M. Ball, and P. Seydel, 'Hydrogen Today', in 'The Hydrogen Economy', eds. M. Ball and M. Wietschel, Cambridge University Press, Cambridge, 2009, p. 254.
54. European Commission, 'Hydrogen Energy and Fuel Cells a Vision of Our Future', European Commission, 2003.
55. European Hydrogen & Fuel Cell Technology Platform, 'Deployment Strategy 2005', 2005, <https://www.hfpeurope.org/hfp/keydocs>.
56. International Energy Agency, 'Prospects for Hydrogen and Fuel Cells—2005', 2005, <http://www.iea.org/textbase/nppdf/free/2005/hydrogen2005.pdf>.
57. Transitions to Alternative Transportation, 'Technologies—A Focus on Hydrogen', US National Research Council, National Academy Press, 2008, p. 142.
58. E4tech, 'Element Energy, Eoin Lees Energy, A Strategic Framework for Hydrogen Energy in the UK', Final report to Department of Trade and Industry, UK. 2004.

Thermal Stability of Lithium Ion Battery Electrolytes

Brett L. Lucht, Tippawan Markmaitree and Li Yang

University of Rhode Island, Kingston, RI, USA

1	Introduction	333
2	Thermal Decomposition of LIB Electrolytes	335
3	Thermal Reactions of LIB Electrolytes with the Electrode Surface	337
4	Summary	339
5	Related Articles	339
6	Abbreviations and Acronyms	339
7	References	339

1 INTRODUCTION

While commercial lithium ion batteries (LIBs) perform well for most home electronic applications, currently available LIB technology does not satisfy some of the performance goals for plug-in hybrid electric vehicles (PHEVs). In particular, currently available LIB technology does not meet the 10–15 year calendar life requirement set by the United States Advanced Battery Consortium (USABC).¹ The most extensively used LIB electrolytes are composed of lithium hexafluorophosphate (LiPF_6) dissolved in organic carbonates or esters.² However, LiPF_6 electrolytes have poor thermal stability and the required use of ethylene carbonate (EC) limits low-temperature performance. Significant energy fading occurs after several years at room temperature and over only a few months at moderately elevated temperatures ($>55^\circ\text{C}$).³ While there are several different factors that limit the thermal stability and calendar life of LIBs, the reactions of the electrolyte with the surface of the electrode materials is frequently reported to be the most significant.⁴

The low electrochemical potential and atomic weight of lithium has prompted investigation of rechargeable lithium batteries over the past 30 years. Initial investigations focused on lithium metal batteries. However, growth of lithium dendrites during cycling made lithium metal batteries unsafe due to the potential to short-circuit and initiate a thermal runaway.⁵ The next generation of rechargeable lithium batteries was the LIB. The lithium metal anode was replaced by a graphitic anode. Graphite anodes allow lithium ion intercalation and have electrochemical potential that is relatively close to that

of Li/Li^+ ; they do not form dendritic lithium and provide superior safety.⁶

The LIBs are composed of a cathode, anode, separator, and electrolyte (Figure 1). The cathode material is typically composed of lithiated transition metal oxide or phosphate, such as LiCoO_2 , LiFePO_4 , and LiMn_2O_4 , etc. To date, LiCoO_2 is the most commonly and widely used cathode material in commercial LIBs owing to its high working voltage, structural stability, and long cycle life.⁶ The anode is typically composed of graphitic carbon materials due to their capability to intercalate Li^+ s and the very low electrode potential vs the standard hydrogen electrode (SHE). The separator is typically a porous polyolefin,⁷ single polyethylene, polypropylene layer film, or both, and has a typical thickness of 1 mil (25.4 μm), and pore size of 50 to 100 nm.

1.1 Electrolyte System

Commercial LIBs have a typical working voltage range from 3.0 to 4.2 V and aqueous electrolyte based batteries such as lead acid and Ni–MH batteries cannot be used as 4-V batteries because of the low decomposition voltage of water (~ 1.2 V). The most commonly used electrolyte for LIBs is composed of 1M LiPF_6 in 1 : 1 : 1 (v : v : v) EC : dimethyl carbonate (DMC) : diethyl carbonate (DEC) with/without additives.^{2,8} While EC has the largest dielectric constant and therefore the strongest solvating ability, EC also has a high melting point and high viscosity. Thus DMC and DEC are added as cosolvents to dilute and expand the operational range of the electrolyte.

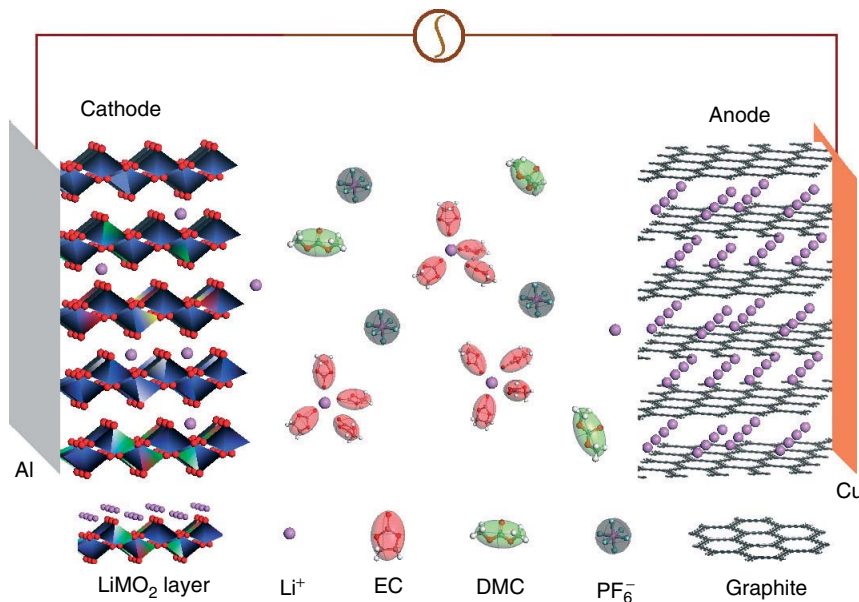


Figure 1 Typical lithium-ion battery

1.2 Working Mechanism

When an LIB is assembled, i.e., the cathode, separator, and anode plates are stacked and inserted into a container, followed by injection of electrolyte; the voltage of the cell is around 0 V. The cathode and anode are at approximately the same voltage (~ 3 V) versus Li/Li^+ . The battery is in its discharged state and not ready for power output. During the first charging, the Li^+ 's leave the cathode (such as LiCoO_2), transport through the electrolyte and intercalate into the graphite lattice. At the same time, the voltage of the Li_xCoO_2 slowly increases to 4.2 V (vs Li/Li^+), while the voltage of graphite decreases and becomes close to Li/Li^+ . The charged battery has a total voltage around 4 V. Discharging an LIB is the opposite process: the Li^+ 's move out from the graphite and into electrolyte and reintercalate into Li_xCoO_2 .

1.3 Solid Electrolyte Interphase (SEI)

During the first charging process of the LIBs, carbonate-based solvents, especially EC, are reduced at a voltage of 1.5 to 0.6 V⁹ vs Li/Li^+ (prior to Li^+ intercalation into the graphite) to form a solid electrolyte interphase (SEI) layer on the surface of the graphite.^{10,11} The SEI functions as an ionic conductor that allows Li^+ conduction but is electrically insulating. This is very important, since without the selective SEI film, the electrolyte is continuously reduced on the surface of the anode, consuming active lithium and generating a thick and resistive surface film (Figure 2).⁹

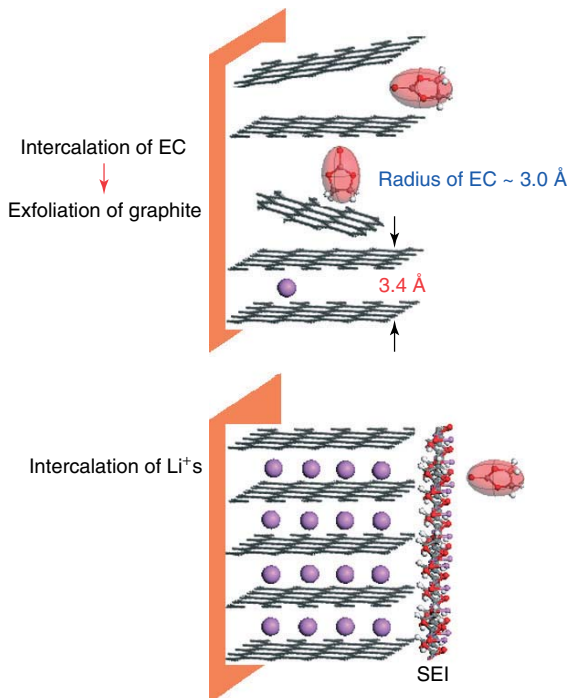
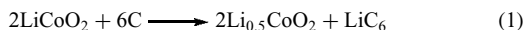


Figure 2 Comparison of Li^+ intercalation into graphite with/without SEI film on graphite

1.4 Reactions Other than the Li^+ Intercalation and Deintercalation

The primary electrochemical reaction of the LIBs is the Li^+ intercalation and deintercalation between the

cathode and anode (equation 1). In an ideal world, the reaction would be 100% reversible and the battery would last forever. However, this is not the case since most chemical processes include side reactions. If the primary electrochemical reaction is 99.9% reversible and battery failure is defined as retention of 75% of the initial capacity, then the total number of cycles for the battery is approximately 300. The gradual loss of capacity is due to the physical and chemical damage of the electrolyte, cathode, and anode materials.^{12,13} This article focuses on one area of capacity fade: the decomposition of the electrolyte and reactions of the electrolyte with the surface of the electrode materials.



The performance loss of LIB upon cell aging, to a large extent, is due to the thermal instability of the electrolyte.^{14,15} The process is usually linked to the thermal dissociation of LiPF₆ (equation 2) followed by reactions of PF₅ with the carbonates composing the solvent. A number of studies, as discussed below, have been performed to support this point of view.



Accelerated aging tests on LIB suggest that the reaction of the electrolyte with the surface of cathode materials is the leading source of power loss for batteries after extended calendar life or accelerated aging tests.^{16,17} A detailed investigation of the reactions of the electrolyte with cathode particles was reported.^{18,19} The products of the simple thermal reactions between cathode particles and the electrolyte, lithium, and phosphorus fluorides and polyethers or polycarbonates, are very similar to the products observed via accelerating aging experiments of full cells. The surface films are generated from decomposed electrolyte and result in a significant increase in the impedance of the cathode reducing the cyclability of the LIB.

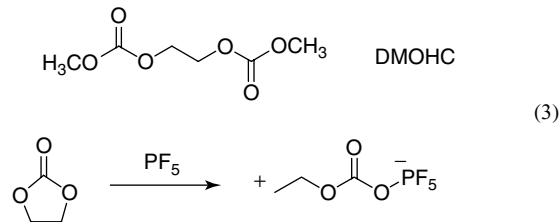
On the anode, the surface of carbon electrode is covered with the products of the electrolyte reduction, which form a protective SEI.^{20–23} The anode SEI is critical for the cyclability of LIBs. However, the anode SEI has poor thermal stability due to the reaction of the SEI with LiPF₆-based electrolytes.²⁴ The loss of capacity and power from LIBs that are stored at elevated temperature has been attributed to the presence of thermal decomposition products of the electrolyte in the anode SEI.²⁵ Methods to stabilize the anode SEI or inhibit the thermal reactions between the anode SEI and LiPF₆ electrolytes will improve the stability of the anode SEI and lead to improvements in calendar life.

2 THERMAL DECOMPOSITION OF LIB ELECTROLYTES

2.1 Thermal Decomposition of LiPF₆ in Ethylene Carbonate/Dialkyl Carbonate Solutions

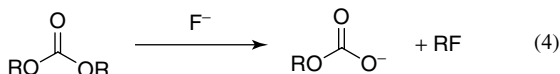
The preferred electrolytes for commercial LIBs are 1.0–1.2 M LiPF₆ in mixtures of carbonate solvents.² EC is typically a required component due to the SEI formation properties. The concentrations of EC typically vary from 25–50% (by volume). The other carbonate components are linear alkyl carbonates consisting of DMC, ethyl methyl carbonate (EMC), and DEC. While the thermal and hydrolytic stability of LiPF₆ electrolytes had been known since the initial usage of LiPF₆/carbonate electrolytes, an understanding of the decomposition mechanisms and products had been lacking.

Initial investigations of the thermal decomposition reactions of LiPF₆/carbonate electrolytes were conducted by Kerr and coworkers.^{14,26} These investigations focused on the reactivity of the strongly Lewis acidic PF₅ (generated during the thermal dissociation of LiPF₆) with EC and dialkyl carbonates. The investigations utilized gas chromatography and size exclusion chromatography and uncovered the presence of the disproportionation products of carbonates. Storage of LiPF₆ in EC/EMC at 60 °C results in the generation of a statistical mixture (1 : 2 : 1) of DMC : EMC : DEC. In addition, the ring-opening reaction of EC occurs as evidenced by the presence of dialkyl-2,5-dioxahexane carboxylate (DAOHC) and the related polyethylene carbonate (PEC). The presence of significant concentrations of CO₂ supports the decarbonylation of the PEC to generate polyethylene oxide (PEO). Similar products were observed upon the addition of PF₅ to EC/EMC mixtures, while no decomposition products of carbonates were observed when LiTFSi was used as the lithium salt. The results support the reactivity of the PF₅ as the source of decomposition since LiTFSi cannot dissociate to generate a Lewis acidic species. This leads to mechanistic proposals based on PF₅-catalyzed cationic ring-opening reactions of EC (equation 3).



While several research groups have utilized accelerating rate calorimetry (ARC) to investigate the thermal stability of LiPF₆/carbonate electrolytes, few have conducted detailed chemical analysis of the products.^{27,28} However, one study by Aubach and coworkers characterized several of the decomposition products by NMR and IR.²⁹ The products of 1 M LiPF₆ in 2 : 1 : 2 EC : DEC : DMC ramped to 240 °C

include HF, HOCH₂CH₂OH, FCH₂CH₂OH, FCH₂CH₂F, PF₅, CO₂, CH₃F, and CH₃CH₂F. The presence of the alkyl fluorides was attributed to the nucleophilic reaction of fluoride anions on carbonates (equation 4) or the reaction of alcohols generated during the degradation of carbonates (equation 5).



A more detailed investigation of LiPF₆/carbonate electrolytes was conducted by Lucht and coworkers.^{30,31} Analysis of the reaction of LiPF₆, PF₅, and OPF₃ with DEC followed by related reactions with a mixture of EC, DMC, and DEC lead to the characterization of many additional decomposition products and a mechanistic understanding of the decomposition reaction. In addition to carbonate disproportionation and polymerization products, several other components were characterized via a combination of GC/MS and multinuclear NMR spectroscopy. The decomposition products of 1 M LiPF₆ in 1 : 1 : 1 EC : DEC : DMC stored at 85 °C for 1–2 weeks include HF, LiF, CO₂, CH₂=CH₂, CH₃F, CH₃CH₂F, (CH₃)₂O, CH₃OCH₂CH₃, (CH₃CH₂)₂O, OPF₂OCH₃, OPF₂OCH₂CH₃, OPF(OCH₃)(OCH₂CH₃), (OPF(OCH₃)₂), (OPF(OCH₂CH₃)₂), and related oligomeric compounds.

The proposed autocatalytic mechanism for the decomposition of LiPF₆ in carbonates is shown in Scheme 1. Trace impurities of water react with LiPF₆/PF₅ to generate phosphorus oxyfluoride (OPF₃). The POF₃ reacts with carbonate to generate OPF₂OR along with CO₂ and RF. Exchange of fluoride for alkoxide generates POF₃ and the

unstable PF₄OR, which undergoes an Arbuzov rearrangement to generate a second equivalent of POF₃ and RF.³² The proposed reaction mechanisms were confirmed via a detailed kinetic analysis of the reaction products. Independent reaction of PF₅ and OPF₃ with pure carbonates and mixtures of carbonates further supported the proposed mechanism.

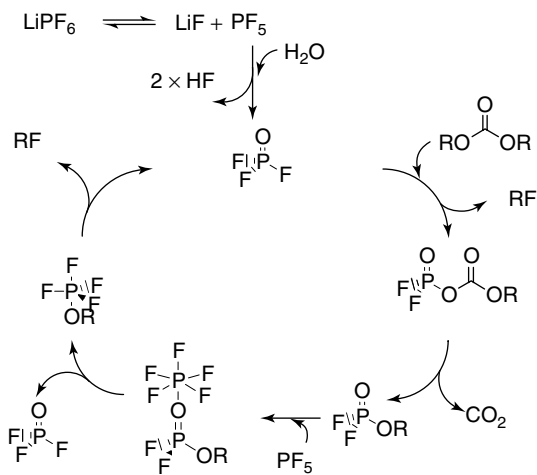
2.2 Inhibition of the Thermal Decomposition of LiPF₆

While the thermal stability of LiPF₆ electrolytes was well known and mechanistic insight was being developed, researchers investigated methods to stabilize LiPF₆/carbonate electrolytes. Since the Lewis acidic PF₅ was frequently suggested as a primary culprit affecting the stability of LiPF₆, various Lewis basic species have been investigated. Zhang and coworkers reported the use of *tris*(2,2,2-trifluoroethyl) phosphite (TTFP) as a thermal stabilizing additive for LiPF₆/carbonate electrolytes.³³ The addition of 0.2 to 5.0% TTFP prevented the discoloration of 1.2 M LiPF₆ 3 : 3 : 4 PC/EC/EMC upon storage at 60 °C for 2 weeks. While the authors attributed the stabilization to the formation of a TTFP–PF₅ complex, which deactivates the Lewis acidity of PF₅, the complexes were not characterized.

Further investigation of Lewis basic species including pyridine, hexamethoxycyclotriphosphazene, hexamethylphosphoramide (HMPA), and dimethyl acetamide (DMAc) were reported.^{34,35} The incorporation of 1–10% Lewis basic species into 1 M LiPF₆ in 1 : 1 : 1 EC : DEC : DMC provides dramatic increase in the thermal stability of the electrolyte as confirmed by NMR spectroscopy and GC/MS. No decomposition products are observed upon storage for 1–52 weeks at 85 °C depending upon the structure of the base. The formation of base–PF₅ complexes was confirmed by the characterization of the HMPA–PF₅ complex by ¹⁹F and ³¹P NMR spectroscopy. The characterization of the base–PF₅ complex and the related inhibition of the decomposition of LiPF₆/carbonate electrolytes suggest that the addition of the Lewis base sequesters the PF₅ generated from the thermal dissociation of LiPF₆. This prevents the generation of the free PF₅ required to initiate the autocatalytic reaction.

Several other additives, including vinylene carbonate (VC) and lithium bis(oxalate)borate (LiBOB), have been reported to improve the stability of LiPF₆/carbonate electrolytes. Most of these additives were designed to generate more stable anode SEIs. However, the effect of these additives on the stability of the bulk electrolyte has been investigated. The addition of 2% VC to 1 M LiPF₆ in 1 : 1 EC : DEC had no effect on the stability of the electrolyte.³⁶ The appearance of decomposition products of the electrolyte with or without VC, as determined by NMR and IR spectroscopy, was very similar. Thus, the addition of VC to LiPF₆/carbonate electrolytes does not alter the thermal stability of the bulk electrolyte.

The addition of low concentrations (1–5%) of LiBOB to LiPF₆/carbonate electrolytes has also been reported to improve the thermal stability of LIB.³⁷ Addition of 5%



Scheme 1

LiBOB to 1 M LiPF₆ in 1 : 1 : 1 EC : DEC : DMC, followed by storage at 85 °C for 4 months, does not result in decomposition of the electrolyte.³⁸ The appearance of EMC from disproportionation reactions is not observed nor are any ethers or alkyl fluorides observed. A low concentration of OPF₂O⁻ is observed initially, but the concentration does not increase with time. The appearance of OPF₂O⁻ is likely related to the presence of trace protic impurities. Disproportionation reactions of the salts, LiPF₆ and LiBOB, occur, resulting in the generation of LiBF₄, LiBF₂(C₂O₄), and LiPF₄(C₂O₄) in a statistical ratio. However, no other decomposition reactions are observed.

3 THERMAL REACTIONS OF LIB ELECTROLYTES WITH THE ELECTRODE SURFACE

3.1 Thermal Reactions with the Carbon Anode

During the initial charging cycles, the electrolyte is reduced on the surface of the anode to generate an anode SEI. The anode SEI is composed of the reduction products of the solvent, salt, and sacrificial additive. The SEI formation mechanisms have been previously reviewed and are not discussed here.^{20–23,39} While the anode SEI protects the electrolyte from further reduction by the anode, the thermal stability of the anode SEI has been reported to be poor. Several research groups have investigated the reaction of LiPF₆/carbonate electrolytes with the surface of the carbon anodes before and after formation of the anode SEI.

Analysis of the thermal reactions between mesocarbon microBead (MCMB) graphite, prior to formation cycling and the generation of an anode SEI, and 1.0 M LiPF₆ in EC/DEC/DMC was reported.³⁵ Storage of MCMB in the presence of LiPF₆ electrolyte at elevated temperatures results in the thermal decomposition of the electrolyte and the deposition of electrolyte decomposition products on the surface of the MCMB. The rate of electrolyte decomposition and product distribution are similar to those previously reported for the thermal decomposition of pure LiPF₆ electrolytes. The primary components on the surface of the MCMB include oligocarbonates, oligoethylene oxide, PEO, fluorophosphates, and lithium fluoride. The appearance of the organic components, oligocarbonates, oligoethylene oxides, and PEO most likely results from ring-opening reactions of EC. These ring-opening reactions can be mediated by Lewis acidic species, such as PF₅, or by reactive surface sites on the MCMB. The presence of lithium fluorophosphates (Li_xPO_yF_z) results from the thermal decomposition of LiPF₆. The concentration of both the organic and inorganic components of the surface films increases as a function of time and temperature. Higher temperatures and longer storage times lead to more decomposition

products and thicker surface films, while the addition of Lewis basic species inhibits decomposition.

The thermal decomposition of LiPF₆ electrolyte in the presence of graphite with a preformed SEI provides different results. The presence of the graphite with SEI inhibits the thermal decomposition reactions of the bulk electrolyte.³⁰ This is presumably due to the presence of Lewis basic species, including LiOCO₂R, Li₂CO₃, and ROLi, in the anode SEI.²⁰ However, while the bulk electrolyte is stabilized in the presence of the graphite with preformed SEI, the anode SEI is destabilized in the presence of LiPF₆/carbonate electrolytes. An elegant study by Wan and coworkers uncovered a strong dependence of the thermal stability of the anode SEI on the lithium salt used in the electrolyte.²⁴ Thermal abuse of lithium ion cells containing LiPF₆ electrolytes results in an oscillating thickness of the anode SEI. The oscillating phenomenon was attributed to an alternating deterioration and re-formation of the anode SEI. Similar investigations were conducted with cells containing LiClO₄ electrolytes, and the results suggested a gradual change in the SEI thickness. The addition of PF₅ to LiPF₆ electrolytes enhanced the rate of SEI thickness oscillation, and this further supports PF₅ as the primary cause of the deterioration of the anode SEI.

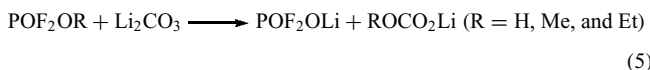
The analysis of the anodes extracted from thermally abused 18 650 lithium ion cells provided complementary results.²⁵ The results of the analysis of cells that had undergone initial formation cycling only, support the previously reported primary SEI components.^{20,21} However, analysis of the cells after thermal abuse, 55 °C for 4–40 weeks at 3.72 V, supports thermal decomposition reactions that largely result from the thermal instability of LiPF₆. The anode SEI is initially composed of solvent-based decomposition products including LiOCO₂R, ROLi, polycarbonates, and polyethers. However, upon aging, the anode SEI becomes thicker and the composition changes. The concentration of LiPF₆ decomposition products, including LiF, Li_xPF_y, and Li_xPF_yO_z, increases significantly upon thermal abuse. The increased concentration of F- and P-containing species results from thermal decomposition reactions occurring on the anode SEI, which are related to the reactions occurring in solution. The presence of high concentrations of LiF, Li_xPF_y, and Li_xPF_yO_z increases the impedance of the electrode and contribute to power fade.

3.2 Thermal Reactions with the Cathode

The analysis of the reaction between LiPF₆/carbonate electrolyte and uncharged metal oxide (LiCoO₂, LiNi_{0.8}Co_{0.2}O₂, or LiMn₂O₄) and metal phosphate (LiFePO₄) cathode particles at elevated temperature (>60 °C) has been reported.^{18,19} The thermal stability of ternary electrolyte is dramatically enhanced in the presence of metal oxide electrode materials. There are two primary methods for the inhibition of thermal decomposition. First, the metal oxide surface, or reaction products, could behave as a Lewis base and reversibly sequester

free PF_5 preventing autocatalysis.³⁰ Second, the metal oxide could irreversibly react with one of the species in the autocatalytic cycle, thus removing a key component of the catalytic cycle and preventing further decomposition. Both mechanisms appear to be in operation for metal oxide cathode materials. The metal phosphate cathode materials are covered with a thin conductive carbon coating, which limits the interaction between the electrolyte and the metal phosphate. The thermal decomposition of the electrolyte is not significantly affected by the presence of the carbon-coated metal phosphate.

The surface of LiCoO_2 is covered with a surface layer of Li_2CO_3 , which is partially responsible for the increased stabilization. Initial reactions of the electrolyte with surface Li_2CO_3 enhance the thermal stability of the electrolyte via generation of low concentrations of the Lewis basic species ROCO_2Li . While the mechanism for formation of ROCO_2Li is unclear, the reaction of POF_2OR with Li_2CO_3 can afford POF_2OLi and ROCO_2Li through an exchange reaction:



Upon consumption of the protective Li_2CO_3 on LiCoO_2 , or in the presence of LiMn_2O_4 which does not contain a Li_2CO_3 coating, the thermal decomposition of the electrolyte results in the deposition of surface films containing LiF , Li_xPF_y , $\text{Li}_x\text{PO}_y\text{F}_z$, PEO, metal fluorides, and other

organic materials (ROLi , ROCO_2Li , polycarbonate, etc.). Higher temperature leads to more deposition of electrolyte decomposition products and higher concentrations of HF and POF_2OR in the liquid electrolyte. Similar reactions occur on the surface of metal oxides upon addition of PF_5 solutions or carbonates. This suggests that PF_5 generation via the thermal dissociation of LiPF_6 is largely responsible for the thermal decomposition reactions on the surface of the cathode particles. Figure 3 provides a graphic depiction of the reactions occurring on the surface of the metal oxide particles.

Similar changes occur at the surface of the carbon-coated metal phosphate materials. However, the limited surface reactions between the electrolyte and the cathode particles result in a loss of thermal stability of the electrolyte. The electrolyte decomposition occurs at a rate comparable to electrolyte in the absence of metal phosphate particles.

Incorporation of Lewis bases into LiPF_6 -containing electrolytes suppresses the corrosion of cathode particles by inhibiting thermal decomposition reactions of the electrolyte. The thermal dissociation of LiPF_6 to generate LiF and PF_5 initiates the thermal decomposition of LiPF_6 -based electrolytes.^{14,30} Lewis bases complex and stabilize PF_5 preventing reaction with the carbonate solvents and the subsequent generation of HF and fluorophosphates ($\text{OP}(\text{OR})\text{F}_2$).^{30,34} Addition of a Lewis base impedes the formation of acid species in the electrolyte, which decreases the surface corrosion of cathode particles.

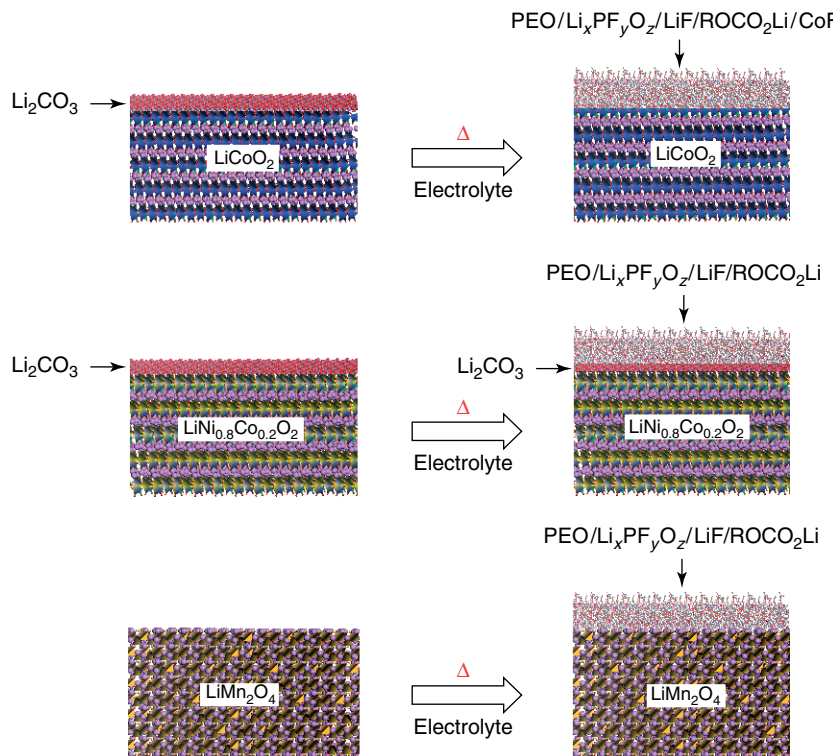


Figure 3 Depiction of the reactions that are occurring on the surface of metal oxide cathode particles

The analysis of $\text{LiNi}_{0.8}\text{Co}_{0.2}\text{O}_2$ cathode materials extracted from full cells after accelerated aging experiments provide similar results.¹⁶ The surface of the cathode particles are covered with polycarbonates, LiF , Li_xPF_y , and $\text{Li}_x\text{PF}_y\text{O}_z$. Depth profiling suggests that the surface layer thickness increases as a function of storage temperature. The presence of the thick surface films on the cathode materials is reported to be responsible for the increased impedance. The generation of the surface films is largely due to the thermal instability of LiPF_6 and the generation of PF_5 and related fluorophosphates.

4 SUMMARY

LIBs have been widely utilized for small electronic devices in the last decade. However, there is significant current interest in the development of LIBs for electric vehicle (EV) applications. One of the limiting factors for the incorporation of LIBs into EV applications is the calendar life of the batteries. Most current LIBs have a calendar life of 3–5 years. EV applications require a 10–15 year calendar life. The thermal instability of the electrolytes commonly used in current LIBs has been reported to be a primary contributor to the poor calendar life.

The current state-of-art electrolyte for LIBs is LiPF_6 in a mixture of carbonate solvents containing EC. The instability of the electrolyte and the reactions of the electrolyte with the surface of the electrode materials are primarily because of the thermal dissociation of LiPF_6 to generate LiF and PF_5 . The strong Lewis acidity of PF_5 initiates decomposition reactions of the electrolyte, degrades the anode SEI, and corrodes the cathode surface. These detrimental reactions limit the calendar life and thermal stability of LIBs. In order to improve the performance of LIBs for EV applications, new electrolytes or electrolyte additives must be developed.

5 RELATED ARTICLES

Lithium Ion Batteries for Transportation and Electrical Energy Storage Applications: Nuclear Magnetic Resonance Studies of Structure and Function.

6 ABBREVIATIONS AND ACRONYMS

ARC = accelerating rate calorimetry; DAOHC = dialkyl-2,5-dioxahexane carboxylate; DEC = diethyl carbonate; DMAc = dimethyl acetamide; DMC = dimethyl carbonate; EC = ethylene carbonate; EMC = ethyl methyl carbonate; EV = electric vehicle; HMPA = hexamethylphos-

phoramide LiBOB = lithium bis(oxalate)borate; LIBs = lithium ion batteries; MCMB = mesocarbon microbead; PEC = polyethylene carbonate; PEO = polyethylene oxide; PHEVs = plug-in hybrid electric vehicles; SEI = solid electrolyte interphase; SHE = standard hydrogen electrode; TTFP = *tris*(2,2,2-trifluoroethyl) phosphite; USABC = United States Advanced Battery Consortium; VC = vinylene carbonate.

7 REFERENCES

1. www.uscar.org, 2010.
2. K. Xu, *Chem. Rev.*, 2004, **104**, 4304.
3. M. Broussely, S. Herreyre, P. Biensan, P. Kasztejna, K. Nechev, and R. J. Staniewicz, *J. Power Sources*, 2001, **97–98**, 13.
4. D. P. Abraham, ed., ‘Diagnostic Examination of Generation 2 Lithium-Ion Cells and Assessment of Performance Degradation Mechanisms’, ‘Advanced Technology Development Program for Lithium Ion Batteries’, U.S. Department of Energy, 2005.
5. J. R. Dahn, A. K. Sleigh, H. Shi, and B. M. Way, in ‘Lithium Batteries-New Materials, Developments and Perspectives’, ed. G. Pistoia, Elsevier, Amsterdam, 1994.
6. R. Fong, U. Von Sacken, and J. R. Dahn, *J. Electrochem. Soc.*, 1990, **137**, 2209.
7. F. G. B. Ooms, E. M. Kelder, J. Schoonman, N. Gerrits, J. Smedinga, and G. Callis, *J. Power Sources*, 2001, **97–98**, 598.
8. M. C. Smart, B. V. Ratnakumar, and S. Surampudi, *J. Electrochem. Soc.*, 1999, **146**, 486.
9. J. O. Besenhard, M. Winter, J. Yang, and W. Biberacher, *J. Power Sources*, 1995, **54**, 228.
10. D. Aurbach, B. Markovsky, A. Schechter, and Y. Ein-Eli, *J. Electrochem. Soc.*, 1996, **143**, 3809.
11. D. Aurbach, Y. Ein-Eli, and A. Zaban, *J. Electrochem. Soc.*, 1994, **141**, L1.
12. W. Li, J. N. Reimers, and J. R. Dahn, *Solid State Ionics*, 1993, **67**, 123.
13. H. Arai, S. Okada, and J. Yanaki, *Solid State Ionics*, 1997, **95**, 275.
14. S. E. Sloop, J. K. Pugh, S. Wang, J. B. Kerr, and K. Kinoshita, *Electrochim. Solid State Lett.*, 2001, **4**, A42.
15. D. Aurbach, *J. Power Sources*, 2003, **119–121**, 497.
16. D. P. Abraham, R. D. Tweten, M. Balasubramanian, J. Kropf, D. Fischer, J. McBreen, I. Petrov, and K. Amine, *J. Electrochem. Soc.*, 2003, **150**, A1450.
17. A. M. Andersson, D. P. Abraham, R. Hasch, S. MacLaren, J. Liu, and K. Amine, *J. Electrochim. Soc.*, 2002, **149**, A1358.
18. W. Li and B. L. Lucht, *J. Electrochim. Soc.*, 2006, **153**, A1617.
19. W. Li and B. L. Lucht, *J. Power Sources*, 2007, **168**, 258.

20. D. Aurbach, Y. Ein-Eli, O. Chusid, Y. Carmeil, M. Babai, and H. Yamin, *J. Electrochem. Soc.*, 1994, **141**, 603.
21. D. Aurbach, B. Markovsky, A. Shechter, Y. Ein-Eli, and H. Cohen, *J. Electrochem. Soc.*, 1996, **143**, 3809.
22. E. Peled, D. Golodnitski, C. Menachem, and D. Bar-Tow, *J. Electrochem. Soc.*, 1998, **145**, 3482.
23. R. Imhof and P. Novak, *J. Electrochem. Soc.*, 1998, **145**, 1081.
24. H. H. Lee, C. C. Wan, and Y. Y. Wang, *J. Electrochem. Soc.*, 2004, **151**, A542.
25. M. Herstedt, D. P. Abraham, J. B. Kerr, and K. Edstrom, *Electrochim. Acta*, 2004, **49**, 5097.
26. S. E. Sloop, J. B. Kerr, and K. Kinoshita, *J. Power Sources*, 2003, **119–121**, 330.
27. H. Maleki, G. Deng, A. Anani, and J. Howard, *J. Electrochem. Soc.*, 1999, **146**, 3224.
28. E. P. Roth, *Proc. Electrochem. Soc.*, 2000, **99-25**, 763.
29. J. S. Gnanaraj, E. Zinigrad, L. Asraf, H. E. Gottlieb, M. Sprecher, M. Schmidt, W. Geissler, and D. Aurbach, *J. Electrochem. Soc.*, 2003, **150**, A1533.
30. C. Campion, W. Li, W. B. Euler, B. L. Lucht, B. Ravdel, J. DiCarlo, R. Gitzendanner, and K. M. Abraham, *Electrochem. Solid State Lett.*, 2004, **7**, A194.
31. C. L. Campion, W. Li, and B. L. Lucht, *J. Electrochem. Soc.*, 2005, **152**, A2327.
32. G. M. Kosolapoff, ‘Organophosphorus Compounds’, John Wiley & Sons, New York, 1950, p. 213.
33. S. S. Zhang, K. Xu, and T. R. Jow, *Electrochem. Solid State Lett.*, 2002, **5**, A206.
34. W. Li, C. Campion, B. L. Lucht, B. Ravdel, and K. M. Abraham, *J. Electrochem. Soc.*, 2005, **152**, A1361.
35. A. Xiao and B. L. Lucht, *J. Power Sources*, 2006, **162**, 1282.
36. H. H. Lee, Y. Y. Wang, M. H. Wan, H. C. Wu, and D. T. Shieh, *J. Appl. Electrochem.*, 2005, **35**, 615.
37. K. Xu, U. Lee, S. Zhang, M. Wood, and T. R. Jow, *Electrochem. Solid-State Lett.*, 2003, **6**, A144.
38. A. Xiao, L. Yang, and B. L. Lucht, *Electrochem. Solid State Lett.*, 2007, **10**, A241.
39. A. Xiao, B. L. Lucht, S.-H. Kang, and D. P. Abraham, *J. Electrochem. Soc.*, 2009, **156**, A318.

Supercapacitors: Electrode Materials Aspects

Li Li Zhang, Zhibin Lei, Jintao Zhang, Xiaoning Tian and Xiu Song Zhao

National University of Singapore, Singapore

1	Introduction	341
2	Principle of Energy Storage in Supercapacitors	342
3	Electrode Materials for Supercapacitors	345
4	Summary and Perspectives	359
5	Acknowledgments	360
6	Abbreviations and Acronyms	360
7	References	360

1 INTRODUCTION

Global warming and limited supply of fossil fuels have been increasingly driving the world toward clean energy alternatives. With the fast-growing market for portable electronic devices and hybrid electric vehicles, there has been an increasing and urgent demand for environmentally friendly high-power energy resources. Supercapacitors, also known as *electrochemical capacitors* or *ultracapacitors*, are gaining increasing attention because of their pulse power supply, long cycle life ($>100\,000$ cycles), simple principle, and high dynamics of charge propagation.^{1–4} With many thousands of times higher power density than lithium-ion batteries and much larger energy density than conventional capacitors, supercapacitors offer a promising approach to meeting the increasing power demands of energy-storage systems. Nowadays, supercapacitors are widely used in consumer electronics, memory back-up systems, regenerative braking applications, and industrial power and energy management.³ They are ideal for applications having a short load cycle and high reliability requirement, such as energy capture sources including load crane, forklifts, and electric vehicles.⁵ A more recent application is the use of supercapacitors in emergency doors of Airbus A380, showing their safe and reliable performance.

While the energy density of supercapacitor is much higher compared to that of the conventional dielectric capacitor, it is still lower than those of batteries and fuel cells. Most of the available commercial supercapacitor products have specific energy densities less than 10 W h kg^{-1} , which is 3 to 15 times smaller than that of batteries (150 W h kg^{-1} is

possible for lithium-ion batteries).⁶ Thus, there is a strong research interest to increase the energy performance of supercapacitors to be close to or even larger than that of batteries.

A supercapacitor stores energy using either ion adsorption (electrical double layer capacitors, EDLCs) or fast and reversible faradic reactions (pseudocapacitors). These two mechanisms can function simultaneously depending on the nature of the electrode material. Progress toward supercapacitor technologies can benefit from the continuous development of nanostructured electrode materials. A number of recent reviews and books have discussed the scientific and technological aspects of supercapacitor devices and electrode materials.^{1,2,7–10} In the development of EDLCs, a proper control over the pore size and specific surface area of the electrode for an appropriate electrolyte solution is crucial to ensure a good performance of the supercapacitor in terms of both power delivery rate and energy-storage capacity.¹¹ To further enhance the specific capacitance of the electrode, the pseudocapacitance that is present because of the presence of foreign electroactive species on the electrode can be coupled with the EDL capacitance. The capacitive performance of various carbon-based electrodes and the most commonly studied pseudocapacitive materials in the literature is shown in Figure 1.¹⁰

Activated carbons (ACs) are the most widely used electrode materials because of their large surface area, low cost, and easy processability.^{12–14} However, as is seen from Figure 1, the limited energy-storage capacity (typically below 200 F g^{-1}) and rate capability restrict their applications only to certain niche markets. Tempered porous

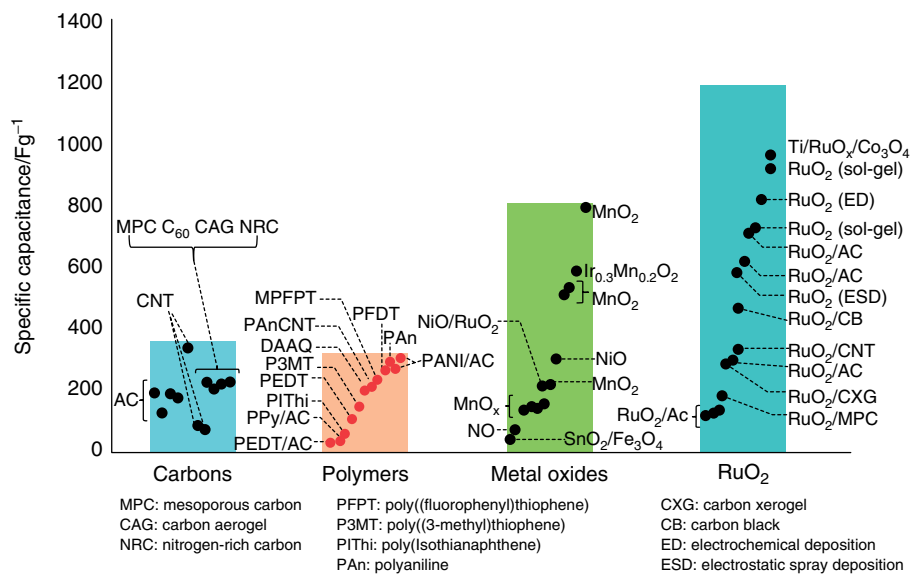


Figure 1 Capacitive performance of carbon and pseudocapacitor electrodes. (Reproduced with permission from Ref. 10. © The Electrochemical Society, 2008.)

carbons of microporous, mesoporous, and macroporous sizes with a tailorabile hierarchical structure hold great promise as supercapacitor electrode materials. Graphene-based materials, including one-dimensional (1D) carbon nanotubes (CNTs) and a new class of two-dimensional (2D) graphene materials, are of particular interest because of their exceptionally excellent electrical and mechanical properties and unique structures.¹⁵ On the other hand, the pseudocapacitive materials including oxygen- and nitrogen-containing surface functional groups, electrically conducting polymers, and transition-metal oxides (e.g., RuO₂, MnO_x, etc.) are promising high-performance electrode candidates if the cost and the stability issues can be tackled.

In this article, we focus on the recent advancements in electrode materials for supercapacitor applications.

performance of the device; these must be considered while designing a supercapacitor device.

Energy storage in a supercapacitor is in principle based on two types of capacitive behaviors: the EDL capacitance from the pure electrostatic charge accumulation at the electrode–electrolyte interface and the pseudocapacitance developed from surface redox processes at characteristic potentials. It is more convenient to discuss the two mechanisms separately though they usually function together in a supercapacitor.

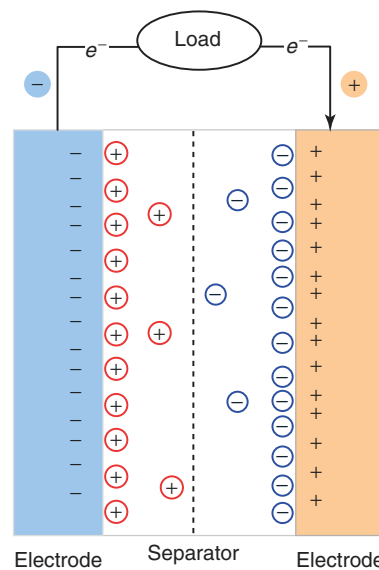


Figure 2 Schematic diagram of a supercapacitor device

2 PRINCIPLE OF ENERGY STORAGE IN SUPERCAPACITORS

2.1 The Mechanisms of Energy Storage in Supercapacitors

Supercapacitors are electrochemical energy-storage devices. The structure of a supercapacitor is similar to that of a battery. It consists of two electrodes in contact with an electrolyte solution, separated by a separator (Figure 2). The supercapacitor is made up of several components, including the electrodes, the separator, the current collector, as well as the electrolyte, all of which have an effect on the overall

2.1.1 The EDL Mechanism

Conventional capacitors store little energy owing to the limited charge-storage areas and geometric constraints related to the separation distance between the two charged plates. However, supercapacitors based on the EDL mechanism can store much more energy because of the large interfacial area and the atomic range of charge separation distances. The concept of the EDL was first described and modeled by von Helmholtz in the nineteenth century when he investigated the distribution of opposite charges at the interface of colloidal particles.¹⁶ The Helmholtz double layer model states that two layers of opposite charges are formed at the electrode–electrolyte interface separated by an atomic distance. The model is similar to that of two-plate conventional capacitors. This simple Helmholtz EDL model was further modified by Gouy and Chapman^{17,18} on the consideration of a continuous distribution of the electrolyte ions (both cations and anions) in the electrolyte solution because of thermal motion, which is referred as a *diffuse layer*. However, the Gouy–Chapman model leads to an overestimation of the EDL capacitance since the capacitance of two separated arrays of charges increases inversely with their separation distance; hence, a very large capacitance value would arise in the case of the point charge ions close to the electrode surface. Later, Stern¹⁹ combined the Helmholtz model with the Gouy–Chapman model to explicitly recognize two regions of ion distribution—the inner region called the *compact layer* or *Stern layer* and the diffuse layer.

A schematic illustration of EDL structure based on Stern model at a positively charged electrode surface without considering the curvature of the pore is shown in Figure 3. In the compact layer, ions (very often hydrated) are strongly adsorbed on the electrode, and hence the name *compact layer*. In addition, the compact layer consists of specifically adsorbed ions (in most cases, they are anions irrespective of the charge nature of the electrode) and nonspecifically adsorbed counterions. The inner Helmholtz plane (IHP) and the outer Helmholtz plane (OHP) are used to distinguish the two types of adsorbed ions. The diffuse layer region is as defined by the Gouy and Chapman model.

The capacitance in the EDL (C_{dl}) can be treated as the combination of the capacitances from two regions—the Stern layer region capacitance (C_H) and the diffusion region capacitance (C_{diff}), as expressed below:

$$\frac{1}{C_{dl}} = \frac{1}{C_H} + \frac{1}{C_{diff}} \quad (1)$$

The parameters that determine the EDL behavior at a planar electrode surface include the electrical field across the electrode, the type of electrolyte, the solvent in which the electrolyte is dissolved, and the chemical affinity between the electrode surface and the electrolyte ion with an opposite charge to the electrode. Because the electrode is usually a porous material with a high specific surface area, the

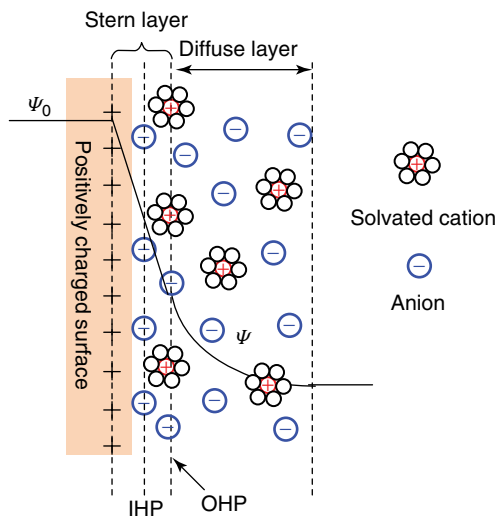


Figure 3 The EDL structure based on Stern model, formed at a positively charged porous electrode surface. The IHP refers to the distance of closest approach of specially adsorbed ions (generally anions) and OHP refers to that of the nonspecifically adsorbed ions. The OHP is also the plane wherefrom the diffuse layer begins

EDL behavior at the pore surface of the porous electrode is more complex than that at an infinitely planar surface as ion transportation in a confined system can be drastically affected by the tortuous mass transfer path, the space constraint inside the pores, ohmic resistance associated with an electrolyte, and the wetting behavior of the pore surface by the electrolyte.

For the EDL type of supercapacitor, the specific capacitance, C , ($F\text{ g}^{-1}$) of each electrode is generally assumed to follow that of a parallel-plate capacitor¹⁴:

$$C = \frac{\varepsilon_r \varepsilon_0}{d} A \quad (2)$$

where ε_r (a dimensionless constant) is the relative permittivity, ε_0 ($F\text{ m}^{-1}$) is the permittivity of vacuum, A ($m^2\text{ g}^{-1}$) is the specific surface area of the electrode accessible to the electrolyte ion, and d (m) is the effective thickness of the EDL (also known as *Debye length*). From equation (2), one can infer that there is a linear relationship between C and A . However, experimental results have shown that this simple linear relationship does not hold in many cases.^{20,21} It is traditionally believed that the submicropores of an electrode do not participate in the formation of EDL owing to the inaccessibility of the submicropore surfaces to large solvated ions. However, according to a recent work of Beguin *et al.*,²² partial desolvation of hydrated ions can occur so that EDL can form in micropores. Gogotsi and coworkers⁹ observed an anomalous increase in capacitance in carbon electrodes with pore sizes less than 1 nm. The authors also observed that the EDL capacitance reached a maximum when the electrode pore size was very close to that of the ion, confirming capacitance

contributions from the pores with sizes smaller than that of the solvated ion.

These new experimental findings, however, cannot be fully interpreted by the EDL theory, because in such confined spaces of micropores, there would be insufficient room to accommodate both the compact layer and the diffuse layer. Huang and coworkers²³ proposed a heuristic approach to describing the capacitive behaviors of nanoporous-carbon-based supercapacitors. In this approach, the pore curvature is taken into account and different capacitive mechanisms are suggested for electrodes with different pore sizes. An electric double-cylinder capacitor (EDCC) model is used to describe mesoporous carbon electrodes, while an electric wire-in-cylinder capacitor (EWCC) model is proposed for modeling microporous carbon electrodes, as schematically illustrated in Figure 4. When the pores are large enough so that the pore curvature is no longer significant, the EDCC model naturally reverts to the traditional planar EDL model given in equation (2). The calculations for the capacitance of the two proposed models, the EDCC model and the EWCC model, are given in equations (3) and (4), respectively:

$$C = \frac{\epsilon_r \epsilon_0}{b \ln[b/(b-d)]} A \quad (3)$$

$$C = \frac{\epsilon_r \epsilon_0}{b \ln(b/a_0)} A \quad (4)$$

where b is the pore radius, d is the distance between approaching ions and the surface of the carbon electrode, and a_0 is the effective size of the counterions (that is, the extent of electron density around the ions).

With these models, the authors were able to fit the mathematical results obtained using equations (3) and (4) well with the experimental data regardless of the types of carbon materials and electrolytes employed. Both the anomalous increase in capacitance for pores below 1 nm and the trend of slightly increasing capacitance with the increase in pore

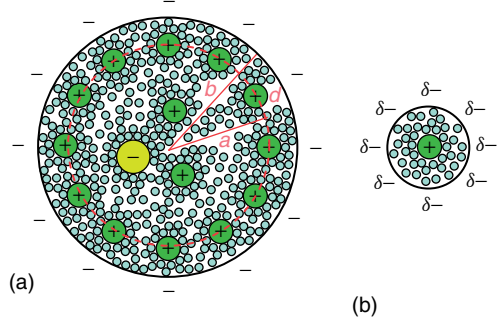


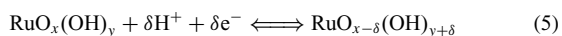
Figure 4 Schematic diagrams (top views) of (a) a negatively charged mesopore with solvated cations approaching the pore wall to form an electric double-cylinder capacitor and (b) a negatively charged micropore of radius b with cations lining up along the pore axis to form electric wire-in-cylinder capacitor. (Reproduced from Ref. 23. © Wiley-VCH, 2008.)

size above 2 nm can be explained by fitting with the proposed EWCC and EDCC models, respectively. In addition, the calculated dielectric constant from the fitting results using equation (4) is close to the value obtained under vacuum, which indicates the desolvation of hydrated ions before entering the micropores.

2.1.2 The Pseudocapacitance Mechanism

Differing from the EDL capacitance, pseudocapacitance arises between the extent of charge acceptance (Δq) and the change of potential (ΔV) because of thermodynamic reasons.⁷ The derivative $C = d(\Delta q)/(d\Delta V)$ corresponds to a capacitance, which is referred to as the pseudocapacitance. The main difference between the pseudocapacitance and the EDL capacitance is that pseudocapacitance is faradic in origin, involving fast and reversible redox reactions between the electrolyte and some electroactive species on the electrode surface. The most commonly known active species are ruthenium oxide,²⁴ manganese oxide,²⁵ vanadium nitride,²⁶ electrically conducting polymers such as polyaniline (PANI),²⁷ and oxygen-/nitrogen-containing surface functional groups.²⁸ While the pseudocapacitance can be higher than EDL capacitance, it suffers from the drawbacks of a low power density (because of the poor electrical conductivity), and lack of stability during cycling.

A good example of a material possessing pseudocapacitive property is ruthenium oxide. Owing to the intrinsic reversibility of various surface redox couples^{7,29} and high conductivity, the electrochemical behavior of both amorphous and crystalline forms of ruthenium oxide has been widely studied in acidic electrolyte solution over the past few decades. It has been shown that amorphous hydrous ruthenium oxide ($\text{RuO}_2 \cdot x\text{H}_2\text{O}$) exhibits a much higher specific capacitance value (720 F g^{-1}) than anhydrous ruthenium oxide.³⁰ This is attributed to the mixed proton–electron conductivity within $\text{RuO}_2 \cdot x\text{H}_2\text{O}$, as the superficial redox transitions of ruthenium oxide involve the proton and electron double injection/expulsion according to the following reaction^{7,24}:



where $\text{RuO}_x(\text{OH})_y$ and $\text{RuO}_{x-\delta}(\text{OH})_{y+\delta}$ represent the interfacial oxyruthenium species at higher and lower oxidation states. In a proton-rich electrolyte (e.g., H_2SO_4), the faradic charges can be reversibly stored and delivered through the redox transitions of the oxyruthenium groups, i.e., $\text{Ru(IV)}/\text{Ru(III)}$ and $\text{Ru(III)}/\text{Ru(II)}$. On the basis of the mean electron transfer numbers, the theoretical specific capacitance of $\text{RuO}_2 \cdot x\text{H}_2\text{O}$ is estimated to range from ca. 1300 to 2200 F g^{-1} .³¹ A very high specific capacitance of 1300 F g^{-1} was reported for a pure bulk nanostructured $\text{RuO}_2 \cdot x\text{H}_2\text{O}$ electrode.²⁴ As implied by equation (5), the reversible redox transitions depend on both proton exchange and electron-hopping processes. In addition, the hydrous nature of

$\text{RuO}_2 \cdot x\text{H}_2\text{O}$ ensures high rate of proton exchange, because the surface of hydrous oxide has been considered as a proton liquid.³² As a result, the designed nanostructure demonstrated to be a promising electrode material for energy storage. However, the cost of the precious metal oxide and difficulty in large-scale production limit its practical applications.

2.2 Performance Requirements

There are fundamental differences between batteries and supercapacitors in terms of energy-storage mechanism and electrode materials. Hence, the characteristic performance of supercapacitors that sets them apart from batteries should be attained while improving the technology.

The performance of supercapacitors is mainly evaluated on the basis of the following criteria: (i) a power density substantially greater than that of batteries; (ii) an acceptably high energy density; (iii) an excellent cyclability (more than 100 times that of batteries); (iv) fast charge/discharge processes that occur within seconds; (v) low self-discharging; (vi) safe operation, and (vii) low cost. The basic operation of a single-cell supercapacitor consisting of two electrodes is illustrated in Figure 5 as a simple representation of an equivalent resistor–capacitor (RC) circuit. Here, C_a and C_c are the capacitances of the anode and the cathode, respectively (the specific capacitance of a single electrode reported in the literature is based on three-electrode cell configuration). R_s is the equivalent series resistance (ESR) of the cell. R_F is the resistance responsible for the self-discharge of a single electrode (R_{Fa} and R_{Fc} refer to R_F for the anode and the cathode, respectively). The total capacitance of the cell (C_T) is calculated according to the following equation:

$$\frac{1}{C_T} = \frac{1}{C_a} + \frac{1}{C_c} \quad (6)$$

In the RC circuit, the time constant expressed as resistance (R) times capacitance (C) gives important information on the characteristic of a capacitor. For example, the time constant for self-discharge for an anode is equal to $R_{Fa}C_a$, and hence a larger value of R_{Fa} is desirable for a smaller leakage of the anode. The maximum energy stored and the power delivered for such a single-cell supercapacitor

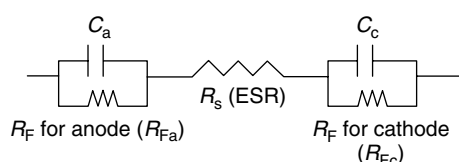


Figure 5 A simple RC equivalent circuit representation illustrates the basic operation of single-cell supercapacitor

are, respectively, given in equations (7) and (8):

$$E = \frac{1}{2}C_T V^2 \quad (7)$$

$$P = \frac{V^2}{4R_s} \quad (8)$$

where V is the cell voltage (in volts), C_T is the total capacitance of the cell (in farads) and R_s is the ESR (in ohms). Each element inside the equivalent circuit is crucial to the final performance of the supercapacitor. The capacitance of the cell depends extensively upon the electrode material. The cell voltage is limited by the thermodynamic stability of the electrolyte solution. ESR comes from various types of resistance associated with the intrinsic electronic properties of the electrode matrix and electrolyte solution, mass transfer resistance of the ions in the matrix, and contact resistance between the current collector and the electrode. Hence, to be a supercapacitor with a good performance, it must simultaneously satisfy the requirements of having large capacitance value, high operating cell voltage, and minimum ESR. It is thus obvious that the advancements in both electrode materials and the electrolyte solutions are made in order to optimize the overall performance of supercapacitors.

With regard to supercapacitor electrodes, high-surface-area carbon materials with a proper pore size distribution and pseudoactive materials with a good stability have been widely studied. In addition, high-density electrode materials with a high volumetric energy density have received growing interest, because such electrode materials are desirable for the design of highly compact energy-storage devices. When electrolytes are considered, nonaqueous electrolytes with a low resistivity are preferred for high-power- and high-energy-density supercapacitors because of the high operating voltages of the nonaqueous electrolytes (up to 4 V). The following section discusses recent advancements in various electrode materials for supercapacitor applications.

3 ELECTRODE MATERIALS FOR SUPERCAPACITORS

3.1 Carbon Materials

3.1.1 Activated Carbon

AC is the most widely used electrode material because of its large surface area, relatively good electrical property, and low cost. AC can be produced using physical activation, chemical activation, or a combination of both, with various carbonaceous precursors (e.g., coal, wood, and nutshells). Physical activation refers to the treatment of a carbon precursor at elevated temperatures (up to 1200 °C) in

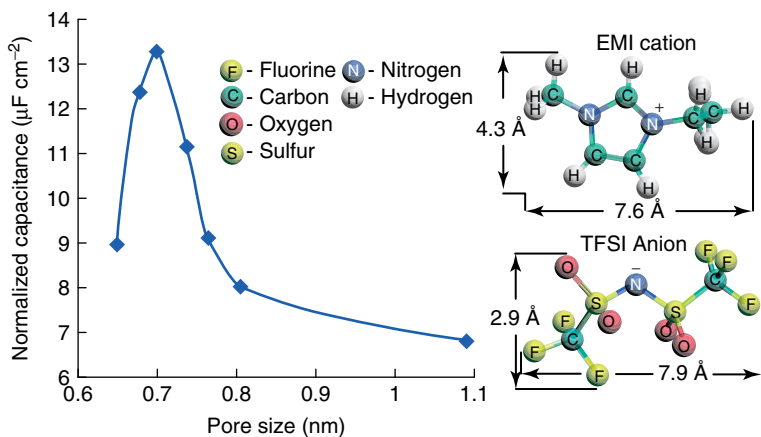


Figure 6 Normalized capacitance as a function of pore size for carbide-derived-carbon (CDC) electrode. Ionic liquid EMI/TFSI was used as the electrolyte and the maximum capacitance is obtained when the size of the pore matches that of the ion. (Reproduced from Ref. 11. © American Chemical Society, 2008.)

the presence of an oxidizing gas, such as steam, CO_2 , and air. Chemical activation is usually carried out at relatively low temperatures (from 400 to 700 °C) with an activating agent like phosphoric acid, potassium hydroxide, sodium hydroxide, and zinc chloride. Depending on the activation methods as well as the carbon precursor used, numerous AC materials with various physicochemical properties have been used as supercapacitor electrodes.^{13,20–22,33–35} As AC materials produced using the activation methods have pores with a wide range of sizes, including micropores (<2 nm), mesopores (2–50 nm), and macropores (>50 nm), disproportion between the capacitance of the AC and the specific surface area has been observed. For instance, AC with a surface area of about 3000 $\text{m}^2 \text{ g}^{-1}$ displayed a relatively small specific capacitance of less than 10 $\mu\text{F cm}^{-2}$, which is smaller than the theoretical EDL capacitance (15–25 $\mu\text{F cm}^{-2}$).⁷ The disproportion indicates that not all pores are effective in charge accumulation.³³ Hence, although specific surface area is an important parameter for evaluating the performance of EDLCs, other aspects of the electrode such as pore size distribution, pore shape and connectivity, electrical conductivity, and surface functionalities may significantly influence the electrochemical performance. Furthermore, excessive activation leads to large pore volume, which results in drawbacks such as low material density and conductivity. These in turn cause a low volumetric energy density and loss of power capability. In addition, high active surface area may increase the risk of decomposition of the electrolyte at the dangling bond positions.³⁵ The presence of acidic functionalities and moisture on the surface of AC is responsible for the aging of the supercapacitor electrode in organic electrolyte.³⁶

The capacitive behaviors of AC electrodes in different electrolytes have been studied. In general, the capacitance of AC is higher in aqueous electrolytes (ranging from 100 F g^{-1} to 300 F g^{-1}) than in organic electrolytes

(less than 150 F g^{-1}). The main reason is believed to be the larger size of the organic electrolyte ion than that of the aqueous electrolyte ion. Pores smaller than the electrolyte ion are inaccessible; thus there is no contribution to the charge stored. The wettability of the carbon surface by the electrolyte may be another reason. Aurbach and coworkers³⁴ concluded that pore sizes above 0.4 nm can be active in EDL charging in aqueous solution. Beguin *et al.*²² suggested that the optimal pore sizes for EDL capacitance are 0.7 nm in aqueous media and 0.8 nm in organic electrolyte, respectively. All these findings have shown the essential role of micropores, which are electrochemically accessible by the electrolyte ions, in improving capacitive performance. Recent studies¹¹ clearly demonstrated the relation between ion size and pore size for an EDLC using carbide-derived carbons (CDCs) and concluded that the maximum EDL capacitance is achieved when the pore size matches the ion size. The pore-size-dependent capacitive behavior is shown in Figure 6.

Besides the porous structure of AC, surface functionalities also play an important role in the capacitive performance as they affect the wettability of carbon surface by the electrolyte and exhibit pseudocapacitance.^{12,28,35} Pandolfo and Hollenkamp¹² reviewed various types of functional groups on AC and pointed out that the presence of some surface oxygen-containing groups would result in instability of the electrode and increase in series resistance. Other studies^{36,37} showed that aging of AC electrodes in organic electrolyte is because of the presence of surface oxygen-containing groups.

By selecting various carbon precursors as well as controlling the preparation conditions, it is possible to prepare AC materials with different functional groups. The most common ones are oxygen- and nitrogen-containing groups. Oxygenated groups can be derived from oxygen-containing carbon precursors or from the treatment of carbon in the air.^{12,38} Depending on the specific preparation procedure, acidic, basic, and neutral oxygenated surface groups can form

on the surface of AC. Acidic groups, such as carboxylic, lactonic, and phenolic functionalities, however, are less stable than basic and neutral groups. In spite of the fact that these acidic groups increase the specific capacitance of the carbon through enhancing the surface wettability, they can potentially increase the rate of self-charge by catalyzing the electrochemical redox reactions of some of the electrolyte components.³⁹

Nitrogen can be incorporated into AC by ammoniation⁴⁰ or carbonization of a nitrogen-containing precursor at high temperatures.^{41,42} Nitrogen can exist in AC in four types as shown in Figure 7. Those nitrogen atoms that replace carbon atoms in graphene and are bonded to other three carbon atoms are indexed as quaternary nitrogen (Q-N). Those that are bonded to two carbon atoms in six-membered rings at the edge of the graphene layer correspond to pyridinic-N (N-6). N-5 represents pyrrolic-N in five-membered rings and pyridonic-N. N-X refers to pyridine N-oxide.

The capacitive behavior of nitrogenated carbon electrode is highly dependent on the nature of the electrolyte. In organic electrolytes, the effect of nitrogen is not evident. However, in aqueous electrolytes especially acidic media, the capacitance was found to increase linearly with the increase in nitrogen content.¹⁴ The enhancement in the capacitive behavior in acidic electrolyte is associated with the pseudocapacitance originating from the interaction between the nitrogen species and protons of the electrolyte.⁴³

Besides oxygenated and nitrogenated groups, phosphorus-containing carbon was also demonstrated to display capacitive behaviors different from that of phosphorus-free carbon.⁴⁴ The specific capacitance of the phosphorus-containing carbon electrode was measured to be 220 F g^{-1} at a current density of 1 A g^{-1} and cell voltage of 1 V in $1 \text{ M H}_2\text{SO}_4$ electrolyte, significantly higher than that of the phosphorous-free carbon (below 64 F g^{-1}). It is interesting to note that the presence of phosphorus groups allowed the

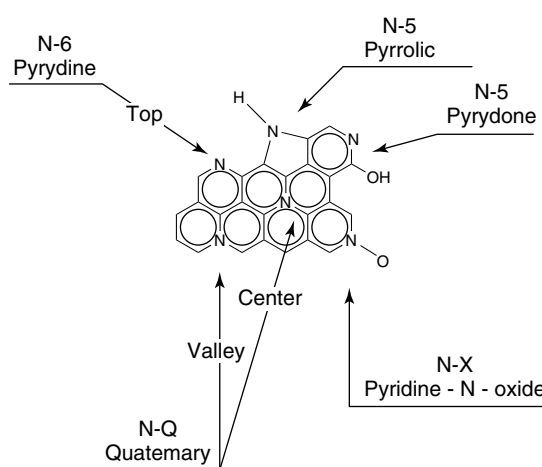


Figure 7 Schematic representation of the nitrogenated groups in the graphene sheet. (Reproduced from Ref. 40. © Elsevier, 2003.)

carbon electrode to be operated at a voltage larger than 1.3 V in H_2SO_4 (see Figure 8a). As can be seen from the data in Figure 8(b), 5000 cycles at a voltage of 1.0 V, followed by 5000 cycles at 1.2 V and 5000 cycles at 1.3 V, with a current load of 5 A g^{-1} confirmed the stable performance of the phosphorous-containing carbon at such harsh conditions. The effect of P atoms on the enhanced capacitance was ascribed to the pseudocapacitance from P functional group as well as the optimized porous structure generated during the H_3PO_4 activation.

3.1.2 Tempered Carbon

The template method offers another effective way of producing nanostructured carbons with well-controlled pore size, large specific surface area, and interconnected

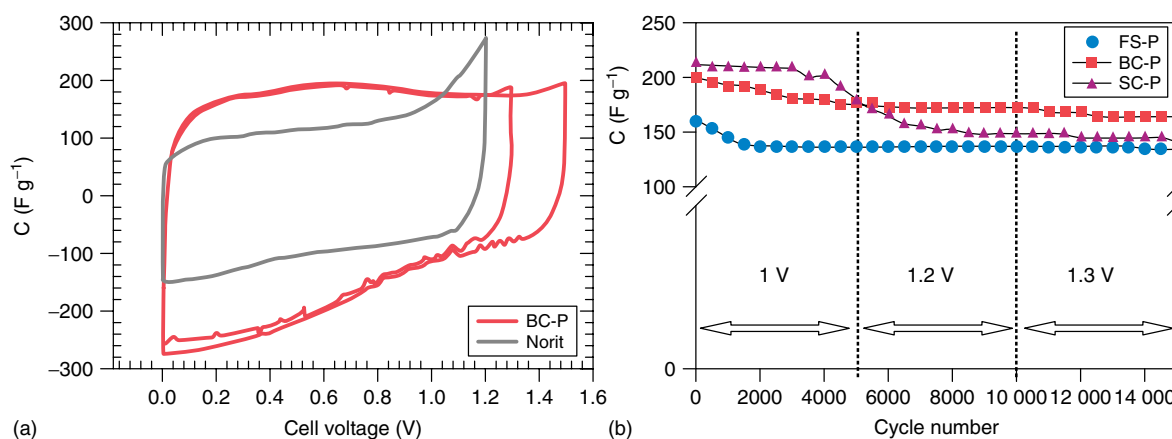
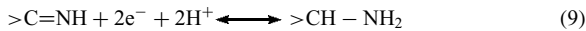


Figure 8 (a) Cyclic voltammograms of H_3PO_4 -activated bismelimidio-diphenylmethane-divinylbenzene copolymer (BC-P) recorded at 5 mV s^{-1} with the cell voltages of 1.3 and 1.5 V compared with Norit at 1.2 V. (b) Galvanostatic cycling at the current load of 5 A g^{-1} and cell voltage of 1, 1.2, and 1.3 V. (Reproduced from Ref. 44. © American Chemical Society, 2009.)

pore network, which makes nanostructured carbons promising candidates as supercapacitor electrode materials. Recently, the synthesis of ordered nanostructured carbons using template methods has advanced very rapidly.^{45,46} The procedure of template synthesis includes infiltration of carbon precursor into the pores of a template, polymerization/carbonization, and finally the removal of the template to leave behind a porous carbon structure.

Many carbon structures with well-controlled pore sizes prepared using different templates and carbon precursors have been studied for supercapacitor applications.^{14,47–49} Since the capacitance based on the EDLC is closely associated with the specific surface area accessible to the electrolyte, microporous carbons replicated from zeolites using acrylonitrile and propylene as carbon precursors⁴⁷ have been found to possess a gravimetric capacitance of as high as 340 F g^{-1} in aqueous electrolytes with a cyclability over 10 000 cycles. Compared to ACs whose micropores are essentially of a broad distribution, the templated microporous carbons with narrow pore size distribution, pore size well adapted to the electrolyte ions, and the ordered straight pore channels are better for use as high-energy-density electrode materials.

Nitrogenated functional groups on carbon surface have been found to contribute significantly to the overall capacitance through the pseudocapacitance.^{43,47,50–52} Hulicova and coworkers^{43,50} described carbon electrode materials prepared using mica template and melamine as carbon precursors. The authors found that nitrogen-containing species were located preferably at the edges of graphene sheets. The maximum gravimetric specific capacitance of the carbon materials in aqueous H_2SO_4 solution was about 204.8 F g^{-1} . The high values of capacitance in acidic aqueous solution are associated with the pseudocapacitance originating from the interaction between the nitrogen species and the protons in the electrolyte, as illustrated in the following equations^{14,52,53}:



Metal–organic frameworks (MOFs) have also been used as templates for preparing microporous carbons as EDLC electrodes.⁵⁴ A nanoporous carbon replicated from MOF-5 exhibited a BET surface area of $2872 \text{ m}^2 \text{ g}^{-1}$, very close to the theoretical surface area of graphene sheets ($2965 \text{ m}^2 \text{ g}^{-1}$).⁵⁵ The specific capacitance of the nanoporous carbon measured using the galvanostatic charge/discharge technique was about 258 F g^{-1} at a current density of 250 mA g^{-1} in an acidic aqueous solution, which is much higher than that of mesoporous carbon replicated from SBA-15 template. The large number of micropores, together with the mesopores created by the reduction of ZnO by carbon, is believed to be responsible for the observed excellent electrochemical performances.

Mesoporous carbon CMK-3⁵⁶ replicated from SBA-15 template possesses 2D hexagonal nanorods consisting

of either amorphous⁵⁶ or graphitic carbon.⁵⁷ By controlling the amount of carbon precursor infiltrating into the pores of SBA-15, the so-called surface-templated carbon CMK-5 can be obtained.⁵⁸ The unique properties of CMK-5 lie in the uniform nanopipes and extremely high specific surface area.^{59–61} It has been reported that mesoporous carbon materials templated from MCM-48 and SBA-15 displayed supercapacitive properties, power output, and high-frequency performance in EDLCs.⁶² The unique mesopore network of the templated carbon materials is favorable for fast ion transport in comparison with microporous carbon.⁶² Upon increasing the sweep rate from 5 mV s^{-1} to 50 mV s^{-1} , mesoporous carbon replicated from SBA-15 can retain about 87% of the initial capacitance. However, only 22% of the initial capacitance can be retained for a commercial carbon, namely, Maxsorb AC.

Recently, direct functionalization of CMK-5 mesoporous carbon was achieved by selecting nitrogen-containing quinoline as the carbon precursor and SBA-15 as the template.⁶³ The carbon sample contained about 6 wt % nitrogen and was observed to not only increase the electrical conductivity but also improve the wettability of the carbon surface by the electrolyte. Mesoporous carbons doped with 0.2–0.6% boron were prepared by coimpregnation and carbonization of sucrose and boric acid confined in the mesopores of SBA-15 template.⁶⁴ X-ray photoelectron spectroscopy (XPS) data revealed that low-level boron doping could catalyze the chemisorption of oxygen, leading to a much higher concentration of oxygen functional groups than that of the boron-free counterpart. By comparing the interfacial capacitance of B-doped and B-free mesoporous carbons, it was found that the enhanced pseudofaradaic capacitance of the B-doped carbon mainly arose from the protonic exchange between quinine and hydroquinine complexes. On the other hand, the low-level doping of boron could also alter the electronic structure of the space charge layer of doped mesoporous carbon. This may be related to the three-valence electronic configuration of boron atom, which results in a hole in the graphene lattice upon replacing a carbon atom with four-valence electron. This substitution could increase the charge density and density of states at the Fermi level, thereby increasing the double layer capacitance of the doped mesoporous carbon.

The presence of mesopores of sizes in the range of 2–8 nm can accelerate the kinetics of ion diffusion in the electrode, thus improving the power performance at large current densities. On the other hand, micropores accessible to electrolyte ions are essential for large energy storage.^{14,23,49} Cheng and coworkers⁴⁹ described a 3D hierarchical porous graphitic carbon (HPGC) material with macroporous cores, mesoporous walls, and micropores for high-rate supercapacitor applications. The hierarchical carbon structure, as illustrated in Figure 9, contains macropores as ion-buffering reservoirs, and mesopores with graphitic carbon walls providing excellent electrical conductivity capable of overcoming the primary kinetic limits of electrochemical

process in porous electrodes. In addition, the presence of micropores can enhance charge storage.

For organic electrolytes, carbon electrodes with large pore sizes are desirable. Three-dimensionally ordered macroporous carbon sphere arrays consisting of mesopores were synthesized by a two-step templating route.⁶⁵ As an electrode material for supercapacitors, this carbon displayed a rectangular CV curve with a capacitance of $14 \mu\text{F cm}^{-2}$ between 0 and 3 V over a wide range of scan rates, and exhibited a good cycling stability with capacitance retention of 93% over 5000 cycles. The good performance was mainly related to its large ordered pore size (10.4 nm) and the continuously connected windows between the spheres which are favorable for the penetration of electrolyte and ion diffusion at high scan rates. A similar 3D ordered macroporous carbon with mesoporous walls was prepared by heat treatment of colloidal-crystal template consisting of polystyrene spheres and colloid silica spheres with varying size (5–50 nm).⁶⁶ The fabricated bimodal pore carbon exhibited capacitance up to 120 F g^{-1} in propylene carbonate solution containing

$1 \text{ mol L}^{-1} (\text{C}_2\text{H}_5)_4\text{NBF}_4$ and displayed excellent rate capacity (109 F g^{-1}) at a current density of 4 A g^{-1} .

Many kinds of conducting polymers (PANI, polypyrrole (Ppy), polythiophene, and their derivatives) have been tested in electrochemical capacitor (EC) application as pseudocapacitive materials and have displayed high gravimetric and volumetric pseudocapacitance. When used as bulk materials, conducting polymers usually suffer from a limited cycle performance because of the degradation from the swelling and shrinkage during the charge/discharge process. Recently, Zhao and his coworkers⁶⁷ reported the preparation of composite electrode materials of macroporous carbon coated with a thin layer of PANI using an electrochemical deposition process (see Figure 10). The ordered, three-dimensionally interconnected macroporous structure and large pores in combination with good electronic conductivity due to the layer of PANI resulted in the composite to exhibit a dramatically enhanced capacitance (250 – 350 F g^{-1}) relative to the pure macroporous carbon (140 F g^{-1}). A specific capacitance of 1490 F g^{-1} was realized for the PANI deposited in the composite electrode. In addition, the composite electrode displayed a good cyclability. At a current density of 1.5 A g^{-1} , greater than 85% capacitance was retained after 1000 cycles. The three-dimensionally ordered macroporous structure favors the diffusion of the electrolyte ions while the capacitive performance of PANI was enhanced by deposition on the surface of carbon.

Yamada and coworkers⁶⁸ synthesized ordered porous carbons containing macro-/meso-/micropores with a large surface area by the colloidal-crystal templating approach. EDL capacitances ranging from 200 to 350 F g^{-1} were achieved in an acidic electrolyte solution. The observations on pore-dependent capacitance properties revealed that micropores

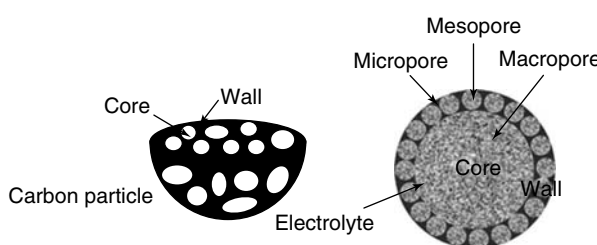


Figure 9 Schematic representation of the 3D HPGC material. (Reproduced from Ref. 49. © Wiley-VCH, 2008.)

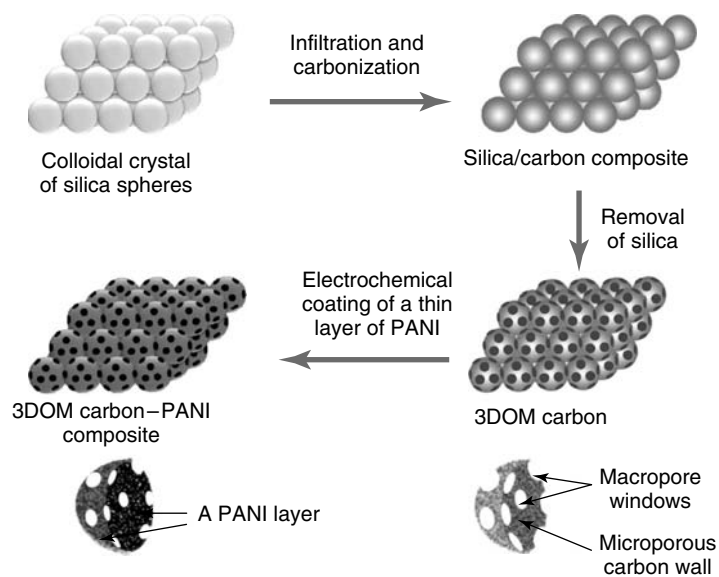


Figure 10 Schematic illustration of the preparation of 3DOM (three-dimensionally ordered macroporous) carbon and the 3DOM carbon–PANI composite. (Reproduced from Ref. 67. © American Chemical Society, 2009.)

adjacent to the opening mouths are effective in charge storage while interconnected larger pores (mesopores and macropores) are important for rapid electrolyte transportation. Hence, carbon materials having a well-controlled hierarchical porous structure would be favorable for designing high-performance EDLC electrodes.

The template method has been shown to be one of the most suitable techniques to control the pore structure of porous materials, especially ordered porous solids.⁴⁵ Through proper selection of template and carbon precursor together with control of carbonization parameters, porous carbons with desirable physical and chemical properties can be obtained. In view of the relatively high cost of production, development of simple, cost-effective, and environmentally benign template routes is advantageous for practical applications. Despite the cost, templated carbons are good materials to study, since they provide valuable information about the effect of pore size, pore shape, channel structures, and other parameters connected with ion diffusion and charge storage in nanoconfined systems.

3.1.3 Carbon Nanotubes (CNTs)

The discovery of CNTs has significantly advanced the science and engineering of carbon materials. With unique physical properties, such as high electrical conductivity and good chemical and mechanical stabilities, CNTs including both single-walled carbon nanotubes (SWCNTs) and multiwalled carbon nanotubes (MWCNTs) have proven themselves as promising electrodes in electrochemical energy conversions and storage.^{6,25,69–74} SWCNTs consist of a single graphene sheet rolled into a cylindrical tube (Figure 11). MWCNTs comprise an array of such nanotubes that are concentrically nested. CNTs are usually regarded as the material of choice for a high-power electrode because of their good electrical conductivity and readily accessed surface area.

Niu *et al.*⁷⁵ reported an MWCNT-based supercapacitor electrode with a high specific capacitance of 102 F g^{-1} and a power density of 8 kW kg^{-1} in an acidic electrolyte. According to An and coworkers,⁷⁶ a SWCNT-based supercapacitor electrode exhibited a maximum specific capacitance of 180 F g^{-1} and a measured power density of 20 kW kg^{-1} at an energy density of 7 W kg^{-1} in KOH electrolyte. A recent study⁷⁷ showed that the electrode fabricated with entangled CNTs was less efficient in facilitating ion transport than the electrode fabricated with aligned CNTs because of the irregular pore structure and high entanglement of the structure of the former. Hence, the use of aligned CNTs is advantageous in terms of high-power supercapacitors. Hata and coworkers⁷¹ described a method to fabricate a densely packed, aligned SWCNT electrode by utilizing the zipping effect of liquids, which allowed the bulk materials to retain their intrinsic properties. The energy density of the aligned SWCNT electrode was about 35 Wh kg^{-1} (normalized to a cell consisting of two

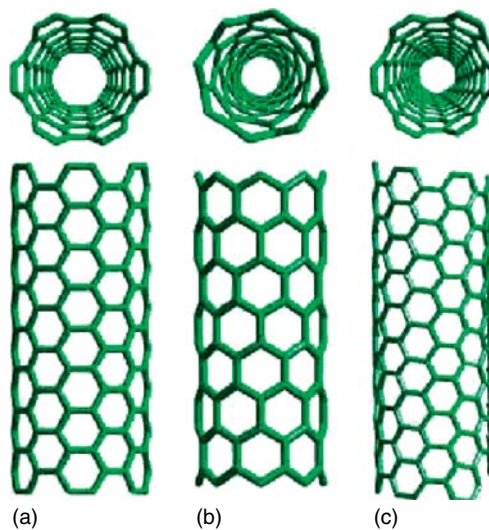


Figure 11 Schematic diagram showing how a graphene sheet is “rolled” to form different atomic structures: (a) armchair, (b) zigzag, and (c) chiral CNTs

identical electrodes) in an organic electrolyte. In addition, the rate capability was observed to be better than that of ACs.

Improvement in the energy density of CNT electrodes through an increase in the specific surface area via KOH activation was described.¹² The porosity and electrical conductivity must be properly balanced in order to achieve both high capacitance and good rate performance. An interesting CNT–aerogel composite material was synthesized recently by uniformly dispersing carbon aerogel (CAG) throughout the CNT host matrix without destroying the integrity or reducing the aspect ratio of the CNT.⁷² The important features of the nanocomposite include large surface area ($1,059 \text{ m}^2 \text{ g}^{-1}$), high mechanical resilience, lightweight matrix with pore spaces on micrometer scale, and binderless electrode. The specific capacitance was measured to be 524 F g^{-1} .

In spite of the superior electrical properties, CNT-based supercapacitors do not meet the expected performance.^{76,78} One of the major issues is the high contact resistance between the electrode and the current collector, greatly limiting the power performance. Compared with binding electrode material to the current collectors indirectly, growing CNTs directly onto a conductive substrate is a promising approach to reducing the contact resistance. A template method for fabricating CNT/Au nanowire hybrid electrode was reported (Figure 12).⁷⁹ Both the electrode (CNT) and current collector (Au nanowire) are integrated into a single nanostructure, thus leading to a largely improved electrochemical performance with a power density as high as 48 kW kg^{-1} .

Another approach to enhancing the specific capacitance is to modify CNTs with active materials to realize pseudocapacitance. Zhang and coworkers²⁵ described the use

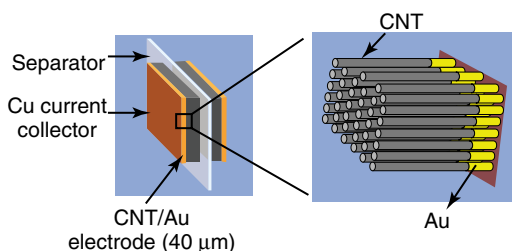


Figure 12 A scheme showing a supercapacitor device with CNT/Au electrodes. (Reproduced from Ref. 79. © Royal Society of Chemistry, 2008.)

of carbon nanotube arrays (CNTAs), which were directly connected with the current collector (a Ta foil) to make composite electrodes with a hierarchical porous structure. Pseudoactive materials such as manganese oxide,²⁵ PANI,^{80,81} and Ppy⁸² were used to prepare composite electrodes to enhance the overall capacitive performance. The manganese oxide/CNTA composite possessed a moderate specific capacitance of about 100 F g^{-1} at a current density of 77 A g^{-1} with good cyclability. The observed electrochemical performances of the composite electrode materials were ascribed to the direct growth of CNTA on the current collector and the pseudocapacitive behavior of the active materials. In addition, the high density of the manganese oxide/CNTA composite material led to a high volumetric capacitance, suitable for compact supercapacitor design.

It is worthy to note that the pseudocapacitance depends strongly on the surface utilization of the active material. Simon and Gogotsi⁹ suggested that one possible strategy to improve both energy and power densities for supercapacitors is to achieve a conformal deposit of pseudocapacitive materials onto highly ordered, high-surface-area CNT and AC electrodes.

3.1.4 Graphene-Based Materials

Graphene, a two-dimensional flat monolayer of sp^2 hybridized carbon bonded in a hexagonal lattice, is a rising star in the field of materials science and physics.⁸³ While theoretical studies on graphene started many years ago,^{84,85} it is only when Geim and coworkers⁸⁶ experimentally

demonstrated the preparation of a single layer of graphite with atomic thickness has it aroused worldwide resurgence. Because of its unique properties, such as tunable band gap, extraordinary electronic transport properties, excellent thermal conductivity, great mechanical strength, and large surface area, graphene has been explored for applications ranging from electronic devices to electrode materials.^{87,88}

Over the past few years, many methods have been reported for the synthesis of graphene materials. These methods include mechanical cleavage of graphite,⁸⁶ unzipping CNTs,⁸⁹ chemical exfoliation of graphite,⁹⁰ solvothermal synthesis,⁹¹ epitaxial growth on SiC surface⁹² and metal surface,⁹³ chemical vapor deposition,⁹⁴ and bottom-up organic synthesis.⁹⁵ Among these preparation methods, mechanical exfoliation produces highest quality graphenes consisting of a few layers, while chemical method is demonstrated to give high throughput. As schematically illustrated in Figure 13, graphite is firstly oxidized to produce graphene oxide (GO) using either the Hummers method⁹⁶ or the modified Hummers method.⁹⁷ Chemically derived graphene is then obtained by the reduction of GO with hydrazine solution or other reducing agents. GO is an excellent precursor in the synthesis of graphene nanosheets.⁹⁸ The larger interlayer distance makes it readily dispersed in solution with a relatively high stability.

Ruoff's group⁹⁹ demonstrated a solution-based process for the production of chemically derived single-layer graphene with an excellent stability. A two-step method was recently reported for nearly complete reduction of surface functionalities of GO by deoxygenation with NaBH_4 and dehydration with concentrated sulfuric acid.¹⁰⁰ However, the harsh oxidation and reduction reactions may deteriorate graphene structure and decrease the performance of graphene-based devices. Ang *et al.*¹⁰¹ proposed a straightforward one-step intercalation and exfoliation method to produce large-sized, conductive graphene sheets without the use of surfactants. The method (Figure 14) is based on the rich intercalation chemistry of GO aggregates. The large-sized GO aggregates consist of multilayer graphene flakes, which are highly oxidized on the outer layer. The inner layer, on the other hand, consists of mildly oxidized graphene sheets. Intercalation of GO aggregates by tetrabutylammonium (TBA) cations via electrostatic attraction and cation–Pi interaction followed by exfoliation in DMF (*N,N*-dimethylformamide) yields large-sized conductive graphene sheets with a high yield (>90%).

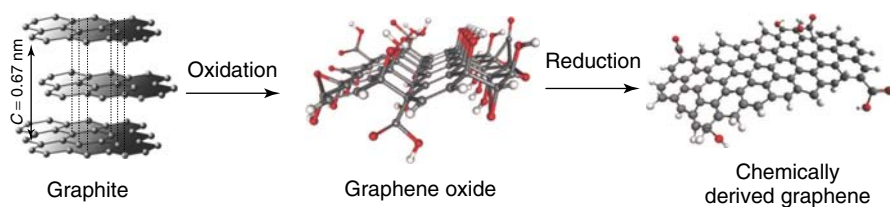


Figure 13 Scheme of chemical route to the synthesis of chemically derived graphene. (Reproduced from Ref. 90. © Nature Publishing Group, 2009.)

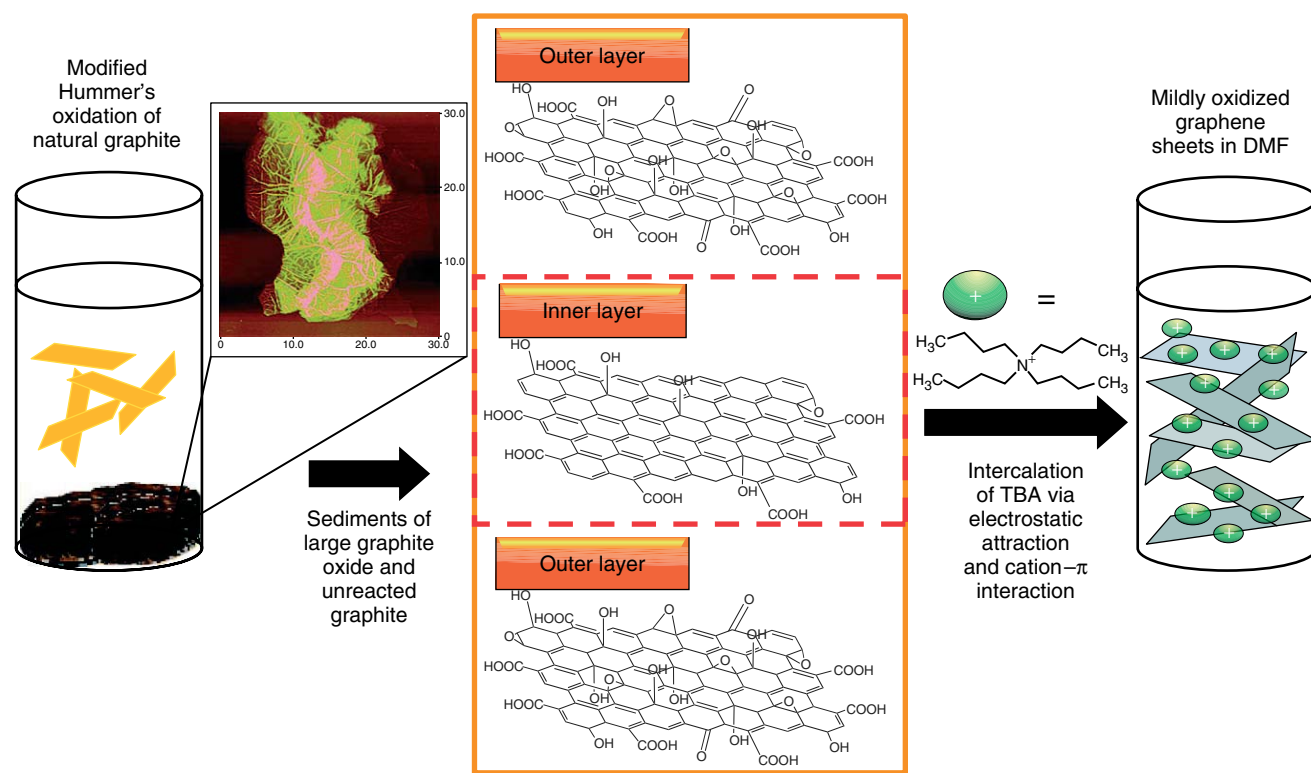


Figure 14 Schematic representation of intercalation of tetrabutylammonium ions into large graphite oxide sediments and unreacted graphite particles to obtain mildly oxidized graphene single sheets in DMF. (Reproduced from Ref. 101. © American Chemical Society, 2009.)

Thin films are useful structures in many technological applications, particularly as electrodes in supercapacitors and batteries, fuel cells, and electronic devices. A flow-directed assembly method was recently described to produce GO paper-like materials.¹⁰² The chemical functional groups on the surface of the GO provide opportunities for tailoring the physical and chemical properties of the material. The preparation of macroscopic free-standing GO membranes with controlled thickness and area at a liquid/air interface was demonstrated.¹⁰³ Very recently, Yang and coworkers⁹⁵ reported a chemical growth method for the synthesis of 2D graphene nanoribbons with lengths up to 12 nm, and the synthesis scheme is shown in Figure 15.

Graphene films have been used as stretchable electrodes.⁹⁴ Chemically modified graphene (CMG) sheets can physically adjust themselves to be accessible to different types of electrolyte ions, free from the use of conductive fillers and binders. Besides, CMG's flexibility facilitates an easy fabrication of supercapacitor devices. Research on the fundamental chemistry of CMG materials has been carried out by research groups of Ruoff from UT-Austin, Kaner from UCLA, and Kern from the Max Planck Institute.¹⁰⁴

Studies^{105,106} have shown that the specific capacitances of graphene can reach 135 F g^{-1} , 99 F g^{-1} , and 75 F g^{-1} in aqueous, organic, and ionic liquid electrolytes, respectively. Despite the intense interests and continuously growing number

of publications, practical applications of graphene have not yet been realized. This is mainly because of the difficulty in the reliable production of high-quality graphene through a scalable approach.^{107,108} While mechanical exfoliation produces graphene with the highest quality, the method produces neither high throughput nor high yield. Zhao *et al.*¹⁰⁹ employed the chemical vapor deposition method to synthesize carbon nanosheets composed of graphene layers on conventional carbon fibers and carbon papers. It was found that such carbon nanosheets possess a capacitance value of 0.076 F cm^{-2} based on the geometric testing area in a H_2SO_4 solution. Hence, the total capacitance was estimated to be $1.49 \times 10^4 \text{ F}$ based on a virtual supercapacitor device rolled in a sandwich pad with the given dimensions.

The experimentally observed capacitances are mainly limited by the agglomeration of graphene sheets and do not reflect the intrinsic capacitance of an individual graphene sheet. Very recently, an experimental determination of EDL capacitance ($\sim 21 \mu\text{F cm}^{-2}$) and quantum capacitances of single-layer and double-layer graphenes was reported.¹¹⁰ In order to harness the unique properties of graphene, graphene- and GO-based composite materials have been explored.^{99,111} Ruoff *et al.*⁹⁹ reported a general approach to preparing graphene-polymer composites via exfoliation of graphite and molecular-level dispersion of CMG sheets within polymers. A polystyrene-graphene composite was

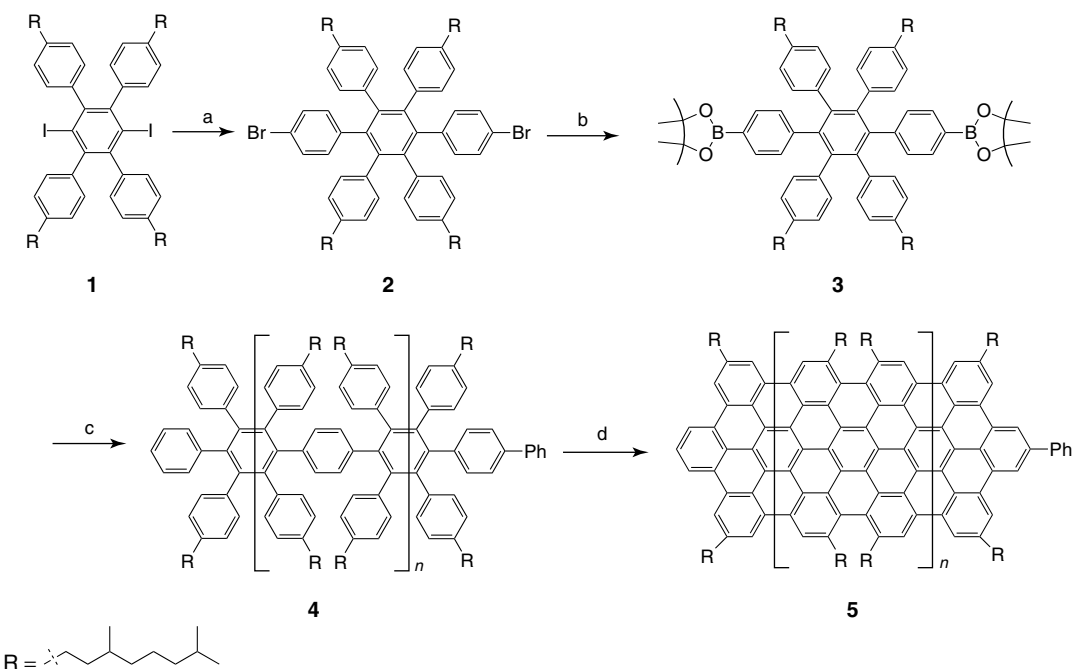


Figure 15 Synthesis of linear two-dimensional graphene nanoribbons. (Reproduced from Ref. 95. © American Chemical Society, 2008.)

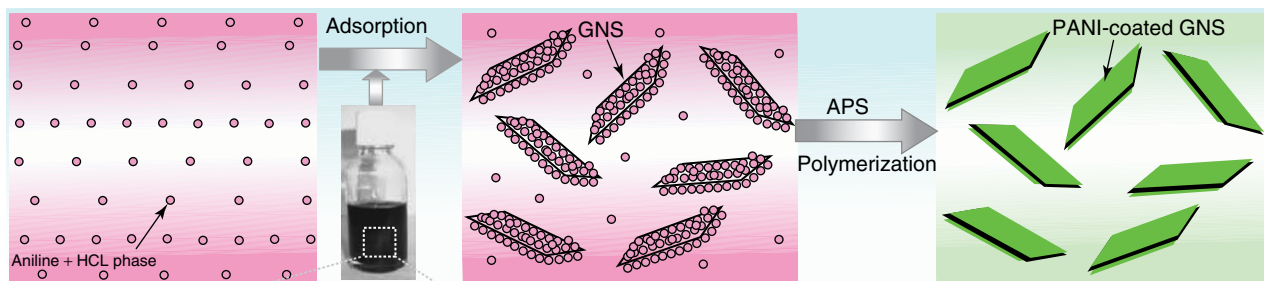


Figure 16 A scheme illustrating the synthesis of GNS/PANI composite. (Reproduced from Ref. 114. © Elsevier, 2010.)

found to exhibit a percolation threshold of around 0.1 vol % for room-temperature conductivity, the lowest reported value for any carbon-based composite and almost the same as that of an SWNT–polymer composite. At 1 vol %, the composite displayed a conductivity of 0.1 S m^{-1} , which is sufficient for many applications.

Graphene-conducting-polymer composites have received the greatest interest.^{112–115} Cheng and coworkers¹¹² prepared a graphene/polyaniline composite paper (GPCP) by *in situ* anodic electropolymerization of aniline monomer as a PANI film on graphene paper. The obtained composite paper had a combination of flexibility, conductivity, and electrochemical activity, and exhibited a gravimetric capacitance of 233 F g^{-1} and a volumetric capacitance of 135 F cm^{-3} . Graphene nanosheet/polyaniline (GNS/PANI) composite was also synthesized using the polymerization method (see Figure 16).¹¹⁴ Graphene (about 15 wt %) was

homogeneously coated on the surface of PANI nanoparticles. A specific capacitance of 1046 F g^{-1} was observed at a low scan rate. The energy density of the composite could reach 39 Wh kg^{-1} at a power density of 70 kW kg^{-1} .

Although graphene nanosheets are excellent electrode materials, the use of highly toxic reducing agents such as hydrazine and dimethylhydrazine remains a serious issue for large-scale production. Murugan and coworkers¹¹³ demonstrated a microwave-assisted solvothermal process to produce graphene nanosheets without the need for highly toxic chemicals. The authors investigated the energy-storage properties of graphene nanosheets thus prepared and associated PANI composites. The graphene/PANI composite with 50 wt % graphene displayed both EDL capacitance and pseudocapacitance with an overall specific capacitance of 408 F g^{-1} .

Very recently, we prepared a series of CMG and PANI nanofiber composites using the *in situ* polymerization

method.¹¹⁶ PANI fibers were observed to adsorb on the graphene surface and/or filled between the graphene sheets. The composite displayed a specific capacitance as high as 480 F g⁻¹ at a current density of 0.1 A g⁻¹. The results showed that good capacitive performance can be obtained by doping either graphene with a small amount of PANI or bulky PANI with a small amount of graphene.

3.1.5 Other Carbon Structures

Other carbon structures such as activated carbon fibers (ACFs), CAGs, carbon onions, and fullerenes have also been studied for supercapacitor applications. ACFs, which are usually produced by the carbonization of preformed fibrous carbon precursors followed by activation, possess a high specific surface area (can be as high as 3000 m² g⁻¹) but with a poor control over the pore size.¹¹⁷ In addition, ACFs are mechanically unstable, and the manufacture cost is relatively high.⁹ Therefore, ACs are not a good candidate for supercapacitor electrodes.

CAGs are the other interesting carbon materials that are suitable for supercapacitors. They are ultralight, highly porous, and can even be used without a binder. CAGs are typically prepared using the solgel method, with a subsequent pyrolysis process. The pores of CAG are formed because of the interconnections between colloid-like carbon nanoparticles. Owing to the dominance of mesopores, the EDL capacitance is not so effective in CAG-based electrode materials. Hence, an additional activation process was employed to further increase the specific surface area by introducing micropores. Despite a large increase in the total surface area (from 592 to 2371 m² g⁻¹), the improvement in the charge-storage capacity was relatively small, especially at a high discharge rate,¹¹⁸ which is primarily due to the inaccessibility of the micropores produced during postactivation and the relatively high internal resistance of the CAG matrix.

Carbon onions consisting of concentric graphene spherical shells are high-surface-area (from 350 to 520 m² g⁻¹) graphitic carbon materials with little subnanometer pores. The completely accessible surface of carbon onions to electrolyte ions manifests them as a good candidate for high-power supercapacitor applications. A study¹¹⁹ on high current charge–discharge performance revealed a decrease in specific capacitance because of diamond particle graphitization and defect formation on particle surfaces. The carbon onion could deliver the stored energy under a high current density, since its capacitance is less dependent on current density. Capacitances of onion-like carbon materials ranging between 20 and 40 F g⁻¹ in an acidic electrolytic solution (1 M H₂SO₄), and between 70 and 100 F g⁻¹ in an alkaline electrolytic solution (6 M KOH) have been reported.^{120,121}

Fullerenes and their derivatives are another family of carbon materials that have been exploited for supercapacitor applications.^{122,123} The discovery of C₆₀ in 1985¹²⁴ led to the award of Nobel prize in Chemistry to Smalley, Curl,

Table 1 Physical properties of fullerenes. (Reproduced from Ref. 123. © Springer, 2009.)

Fullerene geometry	Volume (Å ³)	Surface area (Å ²)	Specific surface area (m ² g ⁻¹)
C ₆₀ (sphere)	186.5	157.8	1364
C ₇₀ (prolate spheroid)	205.2	166.5	1234
C ₈₂ (C _{2v} , prolate spheroid)	239.8	186.8	1182

and Kroto in 1996.¹²⁵ Theoretical predictions indicated that the lowest unoccupied molecular orbital (LUMO) of C₆₀ is capable of accepting at least six electrons upon reduction. In addition to having high reversible redox charge capability, being chemically stable, and having uniformity in size and shapes, fullerenes and their derivatives have a large specific surface area (Table 1).¹²³ The electrochemical properties of pure fullerenes and endohedral metallofullerenes are strongly dependent upon solute–solvent interactions.^{122,125}

Tran and coworkers¹²³ examined the dependence of size, shape, and metal species (La) on the redox properties of C₆₀, C₇₀, and La@C₈₂ in an ammonia solution containing 0.1 M potassium triflate (KCF₃SO₃). The relative magnitude of transfer coefficients that represent a measure of the symmetry of the energy barrier for the oxidation and reduction of the monoanionic species of the fullerenes suggested that the availability of the surface area, which permits delocalization of π electrons, is a determining factor of their reduction potentials. The lower reduction potential of La@C₈₂ (about -0.72 V) compared to those of pure fullerenes C₆₀ and C₇₀ (about -0.96 V and -0.94 V, respectively) indicated that the former is a stronger electron acceptor. The rehybridization of C₈₂ by the three electrons donated by the La atom makes it easier for La@C₈₂ than other fullerenes to accept an electron.

3.2 Transition-Metal Oxides

3.2.1 Ruthenium Oxides

Transition-metal oxides are excellent pseudocapacitive electrode materials.¹²⁶ The most active structure is that of hydrous ruthenium oxide because of its intrinsic reversibility for various surface redox couples and high conductivity. The specific capacitance for hydrous ruthenium oxide ranges from 600 to 800 F g⁻¹, depending on the nature of structure. Amorphous hydrous ruthenium oxide synthesized by the solgel method exhibits a specific capacitance of 720 F g⁻¹, which is about threefold greater than that of anhydrous ruthenium dioxide. Ruthenium oxide electrodes with specifically designed structure, crystalline phase, particle size, and morphology have been shown to display excellent capacitive properties.^{9,24} In addition, the nanotubular structure provides a higher surface area and a shorter pathway for ion transport, addressing the problem of laggard charge transfer.^{9,127–129}

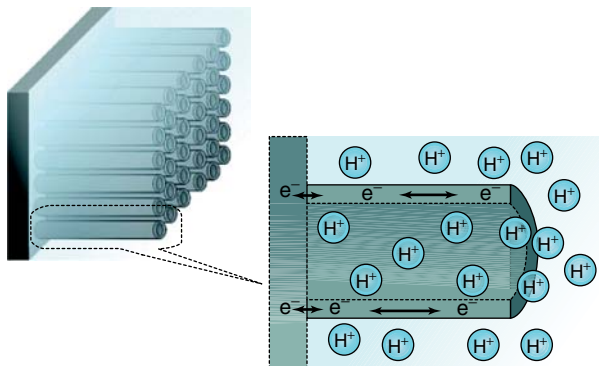


Figure 17 A scheme showing a supercapacitor electrode with hydrous ruthenium oxide nanotubular arrays. (Reproduced from Ref. 24. © American Chemical Society, 2006.)

Hu *et al.*²⁴ designed an ideal ruthenium oxide electrode structure, as illustrated in Figure 17. As a model supercapacitor electrode, such a nanotubular arrayed $\text{RuO}_2 \cdot x\text{H}_2\text{O}$ electrode fabricated by means of the anodic deposition method exhibits a specific capacitance as high as 1300 F g^{-1} . The superior electrochemical performance is related to its tailored nanotubular arrayed porous architecture as well as the hydrous nature. The nanotubular structure allows one to easily control the capacity and rate of charge/discharge by controlling the length and thickness of the nanotube wall. In addition, the nanotubular structure provides a higher surface area and short pathway for ion transport, which can address the problem of laggard charge transfer.⁹

The electrical and capacitive properties of ruthenium oxides are closely related to the amount of water in the materials.^{130–132} Hydrothermal or heat treatment is usually employed to regulate water content in ruthenium oxides. Results have showed that hydrous ruthenium oxides not only lower proton diffusion resistance but also enhance the electronic conductivity for the redox transitions of active species. This is because the hydrous regions allow facile proton permeation through the materials.^{32,133} Recently, mesoporous RuO_2 thin films were found to exhibit a specific capacitance of about 1000 F g^{-1} at a scan rate of 10 mV s^{-1} . The high capacitance originates from the intrinsic nature of hydrous ruthenium oxide and high mesoporosity. Mesoporous ruthenium oxide films with excellent capacitive properties have also been prepared via the evaporation-induced self-assembled (EISA) method.¹³⁴

Another structure of hydrous ruthenium oxide with interesting capacitive properties is the lamellar ruthenic acid hydrate ($\text{H}_{0.2}\text{RuO}_{2.2} \cdot n\text{H}_2\text{O}$). The electronic conductivity of the layered ruthenic acid is accomplished via a crystalline ruthenium oxide layer interleaved with layers of water, which account for the protonic conduction.¹³⁵ The specific capacitance of the lamellar ruthenic acid hydrate was found to be 390 F g^{-1} in a H_2SO_4 solution. After 10 000 consecutive cycles, the capacitance loss was negligible. The protonic

and electronic conducting behavior of a series of ruthenium oxide nanoparticles with different water contents and layered ruthenic acid hydrate was investigated by electrochemical impedance spectroscopy.¹³⁶ The impedance data indicated that the charge-transfer resistance through the film is not significantly affected by the water content, and that the capacitor frequency response is dominated by the protonic conduction. The results demonstrated the importance of hydrous regions (either interparticle or interlayer) in allowing appreciable protonic conduction for high energy and high power electrochemical capacitors.

The high cost of noble metals is a great issue for practical applications. Two solutions have been put forward to address this problem. One is to use a supporting material for the noble metal.¹³⁷ Ruthenium oxide dispersed on CNT was reported.¹³⁸ Hydrous ruthenium oxide nanodots were dispersed on the surface of MWCNTs functionalized with poly(sodium 4-styrene sulfonate). A maximum specific capacitance of 1474 F g^{-1} and electrochemical utilization of 71% for the Ru species were obtained on the composite electrode with 10 wt % hydrous ruthenium oxide. The other solution is to use non-noble metals, such as manganese oxides, nickel oxides, cobalt oxides, and vanadium nitrides.

3.2.2 Manganese Oxides

Manganese oxides (MnO_x) have attracted much attention due to their low cost, environmental friendliness, natural abundance, and high energy density.^{139,140} The theoretical specific capacitance value of manganese dioxide (MnO_2) can be as high as 1370 F g^{-1} .¹⁴⁰ Various manganese oxide materials with different crystalline structures, morphologies, and particle sizes have been prepared and examined. The structure effect on charge-storage properties of MnO_2 -based electrodes was investigated by Ghodbane and coworkers.¹⁴¹ Structures including 1D tunnels, 2D layers, and 3D interconnected channels were prepared (Figure 18). The results showed that the specific capacitance values increase in the following order: pyrolusite < Ni-todorokite < ramsdellite < cryptomelane < OMS-5 < birnessite < spinel, hence 1D < 2D < 3D, indicating that increase in the cavity size and connectivity improves the electrochemical performance.

MnO_2 samples with different crystallographic structures were investigated as electrode materials for electrochemical capacitors in aqueous $0.1 \text{ M Na}_2\text{SO}_4$ solution. The specific capacitance values were observed to decrease in the order of $\alpha(\text{m}) > \alpha = \delta > \gamma > \lambda > \beta$.¹⁴² Hu *et al.*¹⁴³ studied the capacitive properties of single crystalline Mn_3O_4 and MnOOH . The results showed that Mn_3O_4 is electrochemically active but MnOOH is not, in a $1 \text{ M Na}_2\text{SO}_4$ electrolyte.

Anodic electrodeposition of macroporous manganese oxide thin films with the assistance of polystyrene sphere template was used to produce high specific capacitance electrodes.¹⁴⁴ It was found that the specific capacitance dramatically dropped when the MnO_2 thickness increased,

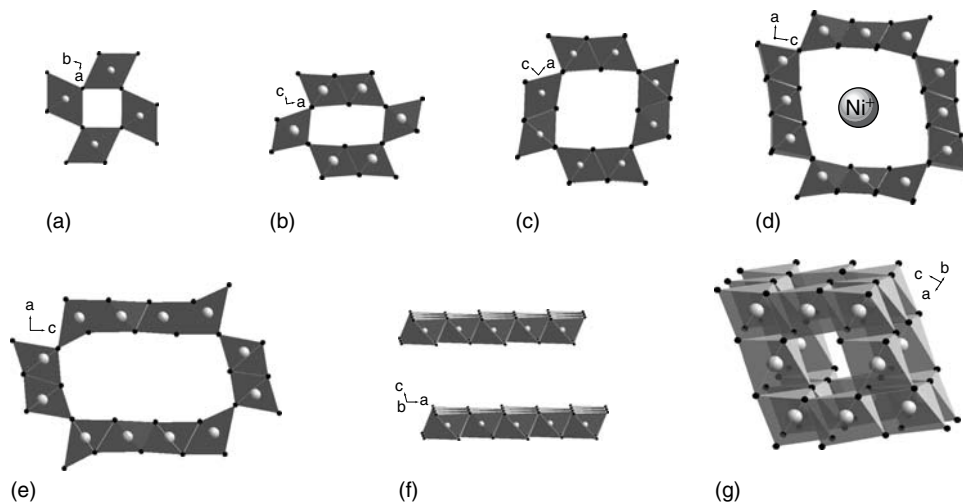


Figure 18 Crystallographic structures of MnO_2 pyrolusite (a), ramsdellite (b), cryptomelane (c), Ni-todorokite (d), OMS-5 (e), birnessite (f), and spinel (g). (Reproduced from Ref. 141. © American Chemical Society, 2009.)

indicating that capacitance strongly depends on the morphology and surface area of the film electrode.

Nanostructured and porous MnO_2 materials have received a great deal of research interest.¹⁴⁵ Hollow α - MnO_2 spheres and urchin-like structure were synthesized via hydrothermal process without using a template.¹⁴⁶ Samples consisting of thin plates and nanowires exhibited an enhanced rate capacity and cyclability in comparison with bulk α - MnO_2 . Porous MnO_2 with a crystalline framework was synthesized using mesoporous silica SBA-15 as the template.¹⁴⁷ The MnO_2 materials showed a specific capacitance of 258 F g^{-1} and a good reversibility because of the macro–mesoporous hierarchical nanostructure with a high surface area of $142 \text{ m}^2 \text{ g}^{-1}$. An organic–aqueous interfacial method was developed to synthesize porous MnO_2 .¹⁴⁸ The pore size distribution and surface area of the MnO_2 were tailored by adjusting the dosage of surfactant and the reaction time. The porous MnO_2 exhibited a good cycle stability with 97% of its initial capacity over 1300 cycles, reaching a coulomb efficiency of approximately 100%.

However, the poor conductivity of manganese oxides is a great hindrance. This perhaps interprets why the experimentally observed specific capacitance values of MnO_x electrodes are far below the theoretical value. MnO_x -based composite materials with a good electrically conductive component (e.g., carbon materials and conducting polymers) can significantly improve the electrochemical performance. Deposition of birnessite ribbons and amorphous MnO_2 on porous carbon structures was carried out by a self-limiting electroless reaction between carbon nanofoams and aqueous permanganate.¹⁴⁹ The coated MnO_2 improved the capacitance of the carbon nanofoam while maintaining the favorable high-rate electrochemical performance. Such a three-dimensional design exploits the benefits of a nanoscopic MnO_2 –carbon interface to produce an exceptionally high

area-normalized capacitance of 1.5 F cm^{-2} , as well as a high volumetric capacitance (90 F cm^{-3}). $\text{MnO}_2/\text{PEDOT}$ (poly(3,4-ethylenedioxythiophene)) coaxial nanowires fabricated using a one-step electrodeposition method were found to be promising electrochemical energy-storage materials.¹⁵⁰ The core MnO_2 provides high energy-storage capacity, while the highly conductive, porous, and flexible PEDOT shell facilitates the electron transport and ion diffusion into the core MnO_2 and protects it from significant structural collapses. The coaxial nanowires preserved 85% of its specific capacitance (from 210 to 185 F g^{-1}) as the current density was increased from 5 to 25 mA cm^{-2} . These specific capacitance values are comparable to those of electrodeposited MnO_2 films, which, however, decreased significantly with increasing current density (e.g., from 210 to 40 F g^{-1} when current density was increased from 1 to 10 mA cm^{-2}). A free-standing, flexible electrode was fabricated by electrodeposition of MnO_2 nanowires on CNT paper.¹⁴⁵ The flexible electrode displayed a specific capacitance of 168 F g^{-1} at a current density of 77 mA g^{-1} . After 3000 cycles, the composite paper retained over 88% of its initial capacitance, showing a good cyclability. Manganese oxide nanoflower/CNTA composite electrodes with a hierarchical porous structure, large surface area, and superior conductivity were prepared.²⁵ Such binder-free manganese oxide/CNTA electrodes displayed an excellent rate capability (50.8% capacity retention at 77 A g^{-1}), high capacitance (305 F cm^{-3}), and long cycle life (3% capacity loss after 20 000 charge/discharge cycles). Zhang *et al.*¹⁵¹ demonstrated the preparation of Mn_2O_3 –carbon composite materials with nanosized Mn_2O_3 particles, homogeneously dispersed in the carbon matrix. A specific capacitance of over 600 F g^{-1} was realized for manganese oxide in the composite electrode. The greatly enhanced energy storage and high rate capability are attributed to the homogeneous dispersion of

the nanosized transition-metal oxide together with the tailored carbon nanostructure.

3.2.3 Nickel Oxides

Nanoporous nickel hydroxide films were electrodeposited on titanium substrate by using Brij 56 (polyoxyethylene cetyl ether) as the template.^{152,153} A maximum specific capacitance of 578 F g^{-1} was realized. A loss of only 4.5% in capacitance after 400 cycles indicates that the charge–discharge process did not induce noticeable degradation of the microstructure. Porous NiO microspheres with a specific capacitance of 710 F g^{-1} at 1 A g^{-1} and a capacitance retention of 98% after 2000 continuous charge–discharge cycles were reported.¹⁵⁴ Loosely packed NiO nanoflakes were prepared using a chemical precipitation method.¹⁵⁵ The material exhibited a maximum specific capacitance of 942 F g^{-1} , which is so far the highest observed on NiO electrodes.

3.2.4 Cobalt Oxides

Cobalt oxides are cost-effective transition-metal oxide electrodes for supercapacitors.^{156–158} Mesoporous Co_3O_4 nanocrystals with well-controlled shapes were prepared using the solvothermal method.¹⁵⁸ The specific capacitance was measured to be about 85 F g^{-1} at a current density of mA cm^{-2} . Cobalt oxide aerogels were synthesized with propylene oxide as an additive and used as supercapacitor electrodes. A high specific capacitance of 623 F g^{-1} and good cycle stability were observed.¹⁵⁷ The specific capacitance of cobalt oxide aerogels is much higher than that of loosely packed cobalt oxide nanocrystals and xerogels.¹⁵⁹ The electrodeposition technique was also employed to fabricate thin films of ordered mesoporous cobalt hydroxide using nonionic surfactant, polyoxyethylene cetyl ether (Brij 56), as the template.¹⁶⁰ A maximum specific capacitance of 1084 F g^{-1} was realized in a 2 M KOH electrolyte solution at a charge–discharge current density of 4 A g^{-1} . The remarkable performance is attributed to the regular mesoporous structure. Microporous nickel–manganese oxide and cobalt–manganese oxide prepared using the potentiodynamic method exhibited specific capacitance values of 685 and 560 F g^{-1} , respectively, at a current density of 2 mA cm^{-2} .¹⁶¹ These values are much higher than that of most pure manganese oxides.

3.2.5 Iron Oxides

One of the iron oxides, magnetite (Fe_3O_4), possesses interesting pseudocapacitance properties in alkali sulfite and sulfate electrolytes. Wu and coworkers^{162,163} investigated the capacitance mechanisms of Fe_3O_4 in aqueous electrolytes, Na_2SO_4 , KOH, and Na_2SO_3 . The work showed that electrolyte greatly influences the capacitive behavior. In Na_2SO_4

solution, a capacitance of 25 F g^{-1} was found entirely to be the result of EDLC. In electrolyte KOH, a very low capacitance was observed because of surface oxidation of magnetite. Electrolyte Na_2SO_3 gave the highest capacitance of 170 F g^{-1} , which originated from the combination of EDLC and pseudocapacitance because of successive reduction of specifically adsorbed sulfite anions. The results suggest a different capacitance mechanism from those of RuO_2 and MnO_2 electrodes.

3.2.6 Other Metal Oxides

Other metal oxides, such as In_2O_3 , V_2O_5 , and TiO_2 , have also been used as supercapacitor electrodes.^{164–167} Experimental results showed that In_2O_3 nanorods displayed a better capacitive performance than In_2O_3 nanospheres.¹⁶⁴ A layered structure of V_2O_5 prepared using solgel method exhibited the highest specific capacitance of 214 F g^{-1} in 2 M KCl electrolyte than in NaCl and LiCl electrolytes.¹⁶⁵ Vanadium pentoxide (V_2O_5) powders prepared by coprecipitation and calcination at low temperatures showed a maximum specific capacitance of 262 F g^{-1} .¹⁶⁶ Recently, Brezesinski *et al.*¹⁶⁷ reported porous TiO_2 films as electrochemical capacitor electrodes. The experimental results suggested that both the mesoporous structure and the crystallinity of the TiO_2 matrix are important with regard to the rational development of metal-oxide-based supercapacitors.

3.3 Polymer Electrode Materials

In general, the energy density of redox capacitors consisting of conducting polymers is higher than that of double-layer capacitors composed of carbon materials, because conducting polymers can store charge not just in the EDL but also through the rapid faradic charge transfer called *pseudocapacitance*. It is therefore not unexpected that a large number of recent publications have been reported on the synthesis and electrochemical properties of electrically conducting polymers and their derivatives.¹⁶⁸

PANI nanofibers synthesized in the presence of a cationic surfactant exhibited a specific capacitance of 298 F g^{-1} .¹⁶⁹ Xu and coworkers¹⁷⁰ fabricated PANI thin films on a stainless steel substrate and evaluated the film as a supercapacitor electrode. A relatively high specific capacitance (431 F g^{-1}) and good charge–discharge behavior were observed. *In situ* polymerization of aniline was conducted to coat PANI on the surface of PPy nanotubes. The specific capacitances of the PPy/PANI composite were measured to be 416 F g^{-1} in 1 M H_2SO_4 electrolyte and 291 F g^{-1} in 1 M KCl electrolyte, respectively.¹⁶⁸ Polythiophene and polyparafluorophenylthiophene were also tested as supercapacitor electrodes with energy-storage capacities of 260 F g^{-1} for polythiophene and 110 F g^{-1} for polyparafluorophenylthiophene, respectively.¹⁷¹

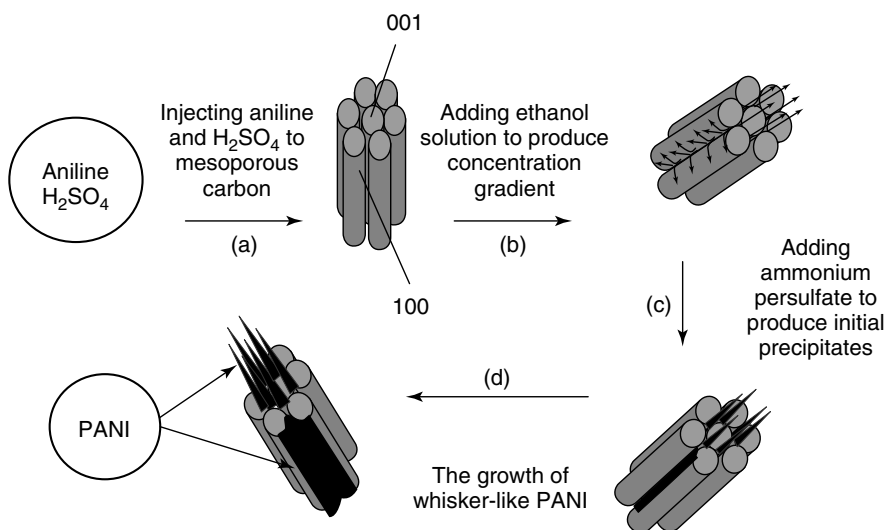


Figure 19 Scheme showing the preparation of whisker-like PANI on the surface of mesoporous carbon. (Reproduced from Ref. 175. © Wiley-VCH, 2006.)

Conducting polymers present a significant disadvantage of lower cycle life than that of carbon electrodes, because the redox sites in the polymer backbone are not sufficiently stable for many repeated redox processes. Variation in the polymer structure can affect the penetration of electrolyte into pores, as well as the ion mobility within the conducting polymer. Design of the electrode structure is the key to obtain a stable conducting polymer electrode. Therefore, the idea of making composite structures with conducting polymers supported on porous rigid materials (e.g., carbon monoliths, porous carbon, CNTs, and porous silica) has been explored.

Hierarchically, porous carbon monoliths were used as a support to prepare carbon/PANI composite electrodes using the electrodeposition method.²⁷ A capacitance of about 300 F g⁻¹ for the composite and a very high capacitance (>1000 F g⁻¹) for pure PANI were realized. The porous carbon monolith served as an effective support for electrodeposition of pseudoactive materials, leading to not only enhanced capacitance with high rate capability but also good cyclability. Fan and Maier¹⁷² reported a highly active Ppy electrode for redox supercapacitors prepared by using electrodeposition of pyrrole on Ti foil via cyclic voltammetry (CV) at a scan rate of 200 mV s⁻¹ in oxalic acid. Ppy/SWCNT composites prepared by in situ polymerization of pyrrole showed a higher specific capacitance than pure PPy and SWCNT electrodes.¹⁷³ PANI^{80,81} and Ppy⁸² were employed as the pseudoactive materials to prepare PANI/CNTA and Ppy/MWCNT composites, respectively. The electrochemical results showed a very high specific capacitance of about 1000 F g⁻¹ for the PANI/CNTA composite with an excellent rate capability (95% capacity retention at 118 A g⁻¹) and a good stability (up to 5000 cycles).

PANI–silica composites synthesized by electrochemical, reactive insertion using the potentiodynamic and potentiostatic methods displayed a capacitance of

606 F g⁻¹.¹⁷⁴ To further increase the electrochemical performance of PANI, Wang and coworkers¹⁷⁵ prepared ordered whisker-like PANI on the surface of mesoporous carbon by a novel synthesis process, as schematically illustrated in Figure 19. The nanosized PANI thorns and the V-shaped nanopores thus formed resulted in a capacitance of 900 F g⁻¹ at a current density of 0.5 A g⁻¹.

Ppy/phosphomolybdate composite films were synthesized in tetrahydrofuran in the presence of sodium sulfate, which acted as a porogen.¹⁷⁶ The hybrid material displayed a peak specific capacitance of around 700 F g⁻¹ and an excellent reversibility and cyclability. The retained phosphomolybdate provides fast and reversible redox behavior, adding to a significant amount of extra pseudocapacitance to the polymer electrode. Increasing the porosity increases the rate at which the hybrid material can be charged and discharged by increasing the ionic conductivity and in turn lowering the RC time constant of the electrode. The ionic conductivity of the resultant porous structure can be increased by an order of magnitude more than that observed for the standard conducting polymer films.

While the mass specific capacitance of poly (3,4-ethylene-dioxythiophene) (PEDOT) is typically lower than those of other conjugated polymers, such as PANI and Ppy, its high stability with respect to repeated cycling makes it a very suitable supercapacitor electrode. Since the charging and discharging of PEDOT involves the mass transport of counterions into and out of the polymer, the rate of ion diffusion is one of the limiting factors in the efficiency of PEDOT-based supercapacitors (Figure 20).¹⁷⁷ Therefore, preparing structured electrodes and limiting the distance of ion diffusion should improve the overall performance.

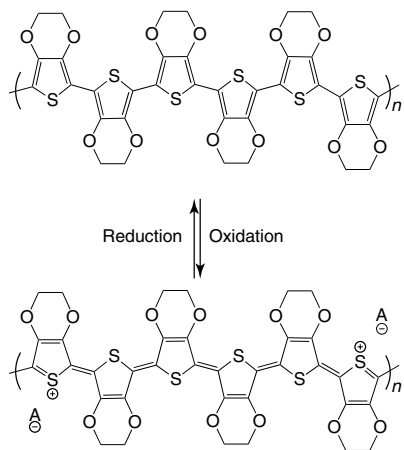


Figure 20 Charging (oxidation) and discharging (reduction) of PEDOT (anions are denoted as A^-). (Reproduced from Ref. 177. © American Chemical Society, 2009.)

Porous PEDOT electrode was prepared by using mesoporous silica spheres as the template.¹⁷⁸ The porous PEDOT showed a specific capacitance of 115 F g^{-1} , which is higher than that of the nonporous counterpart. A PEDOT–carbon structure was prepared using microporous carbon as the template and was observed to exhibit a similar specific capacitance to that of porous PEDOT (Figure 21).¹⁷⁷ The incorporation of PEDOT into the pores of the carbon template did not significantly change the capacitance, because the additional charge-storage capacity provided by the polymer was offset by the elimination of the microporosity of the composite. A new class of dendritic conducting polymers poly(tri(4-(thiophen-2-yl)phenyl)amine) (pTTPA) was electrochemically deposited on highly porous films and templated nanotubular structures.¹⁷⁹ A remarkably high peak capacitance of 950 F g^{-1} was obtained in organic electrolytes.

4 SUMMARY AND PERSPECTIVES

Since the first commercialization of porous-carbon-based supercapacitors in 1957, this energy-storage device has

found application in a wide range of products as a supplement or replacement for batteries: consumer electronics devices, lighting systems, power tools, UPSs, windmills, hybrid electric vehicles, buses, trains, airplanes, telecommunication systems, and industrial equipments. The rapid growth of the supercapacitor market depends critically upon the development of novel electrode materials.

Recent research on electrode materials for supercapacitors has advanced rapidly. Various materials with designed physicochemical and morphological properties have been demonstrated to be tomorrow's high-energy supercapacitor electrodes. Important properties of supercapacitor electrodes, such as surface area, porous structure, pore size, electrical conductivity, and pseudo-properties, are the crucial parameters that must be considered for the design and development of high-performance supercapacitor devices. With the continuous advancement in nanotechnology and emergence of new concepts in electrode design, synthesis of new materials with robust architectures and favorable properties for advanced electrodes will be one of the foremost areas of interest among the scientific and industrial communities.

Improvement in energy-storage capacity can be achieved by designing electrode materials with both EDL capacitance and pseudocapacitance. A good example is carbon-conducting–polymer composite materials. Graphene with a large specific surface area and exceptionally high electronic quality has proven to be a potential supercapacitor electrode. With the theoretical demonstration of pillared graphene for hydrogen storage¹⁸⁰ and experimental results on porous graphene for gas separation,¹⁸¹ research breakthroughs are likely to be made in the near future with regard to nanoporous graphene electrodes. Pillaring graphene sheets with conducting polymers or transition-metal oxides is perhaps a good research direction toward utilizing the unique properties of graphene for supercapacitors.

Electrolytes that are stable at high operating voltages is an area of growing research interest for the design and fabrication of high-power and high-energy supercapacitor devices. New ionic liquids with high electrochemical stability windows are also of increasing research interest. Hybrid supercapacitor systems that can be operated with different potentials for the cathode and anode so as to widen the

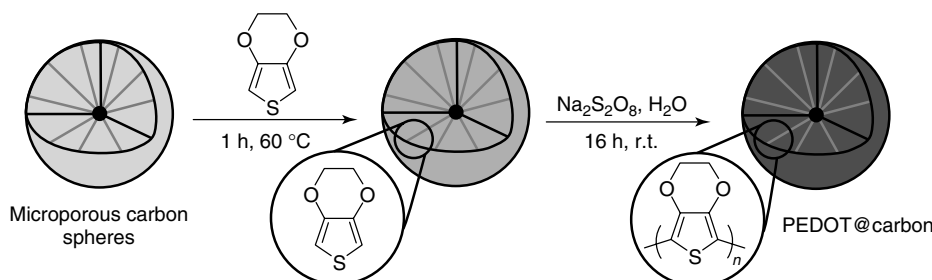


Figure 21 Synthesis of the PEDOT–carbon composite by infiltration of the monomer EDOT followed by subsequent oxidative polymerization. (Reproduced from Ref. 177. © American Chemical Society, 2009.)

overall cell voltage deserve a higher level of research and development.

Development of supercapacitors is also underway to reduce cell size and cost. These two issues, particularly the latter, are considered critical to the continued migration of supercapacitors into new applications. As cost per Farad drops over time, supercapacitor applications will tend to multiply.

With the rapidly growing demand for sustainable energy, it is envisioned that the market for supercapacitors will grow exponentially and they will make inroads into a wider range of technological applications.

5 ACKNOWLEDGMENTS

Financial support from the Ministry of Education under grant number MOE2008-T2-1-004 is appreciated.

6 ABBREVIATIONS AND ACRONYMS

ACFs = activated carbon fibers; ACs = activated carbons; CAG = carbon aerogel; CDCs = carbide-derived carbons; CMG = chemically modified graphene; CNTAs = carbon nanotube arrays; CNTs = carbon nanotubes; CV = cyclic voltammetry; DMF = N,N-dimethylformamide; EC = electrochemical capacitor; EDCC = electric double-cylinder capacitor; EDLCs = electrical double layer capacitors; EISA = evaporation-induced self-assembled; ESR = equivalent series resistance; EWCC = electric wire-in-cylinder capacitor; GNS/PANI = graphene nanosheet/polyaniline; GO = graphene oxide; GPCP = graphene/polyaniline composite paper; HPGC = hierarchical porous graphitic carbon; IHP = inner Helmholtz plane; LUMO = lowest unoccupied molecular orbital; MOFs = Metal–organic frameworks; MWCNTs = multiwalled carbon nanotubes; OHP = outer Helmholtz plane; PANI = polyaniline; Ppy = polypyrrole; pTTPA = poly(tri(4-(thiophen-2-yl)phenyl)amine); RC = resistor–capacitor; SWCNTs = single-walled carbon nanotubes; TBA = tetrabutylammonium; XPS = X-ray photoelectron spectroscopy; 3DOM = three-dimensionally ordered macroporous.

7 REFERENCES

1. M. Winter and R. J. Brodd, *Chem. Rev.*, 2004, **104**, 4245.
2. A. Burke, *J. Power Sources*, 2000, **91**, 37.
3. J. R. Miller and P. Simon, *Science*, 2008, **321**, 651.
4. L. L. Zhang and X. S. Zhao, *Chem. Soc. Rev.*, 2009, **38**, 2520.
5. J. R. Miller and A. F. Burke, *Electrochem. Soc. Interf. Spring*, 2008, **17**, 53.
6. V. V. N. Obreja, *Physica E*, 2008, **40**, 2596.
7. B. E. Conway, ‘Electrochemical Supercapacitors: Scientific Fundamentals and Technological Applications’, Kluwer Academic/Plenum Publisher, New York, 1999.
8. A. S. Arico, P. Bruce, B. Scrosati, J.-M. Tarascon, and W. van Schalkwijk, *Nat. Mater.*, 2005, **4**, 366.
9. P. Simon and Y. Gogotsi, *Nat. Mater.*, 2008, **7**, 845.
10. K. Naoi and P. Simon, *Electrochim. Soc. Interf. Spring*, 2008, **17**, 34.
11. C. Largeot, C. Portet, J. Chmiola, P. L. Taberna, Y. Gogotsi, and P. Simon, *J. Am. Chem. Soc.*, 2008, **130**, 2730.
12. A. G. Pandolfo and A. F. Hollenkamp, *J. Power Sources*, 2006, **157**, 11.
13. O. Barbieri, M. Hahn, A. Herzog, and R. Kotz, *Carbon*, 2005, **43**, 1303.
14. E. Frackowiak, *Phys. Chem. Chem. Phys.*, 2007, **9**, 1774.
15. A. K. Geim and K. S. Novoselov, *Nat. Mater.*, 2007, **6**, 183.
16. Hv. Helmholtz, *Ann. Phys., Leipzig*, 1853, **89**, 21.
17. G. Gouy, *J. Phys. Chem. B*, 1910, **4**, 457.
18. D. L. Chapman, *Phil. Mag.*, 1913, **6**, 475.
19. O. Stern, *Z. Electrochem.*, 1924, **30**, 508.
20. D. Qu and H. Shi, *J. Power Sources*, 1998, **74**, 99.
21. M. Endo, T. Maeda, T. Takeda, Y. J. Kim, K. Koshiba, H. Hara, and M. S. Dresselhaus, *J. Electrochim. Soc.*, 2001, **148**, A910.
22. E. Raymundo-Pinero, K. Kierzek, J. Machnikowski, and F. Beguin, *Carbon*, 2006, **44**, 2498.
23. J. Huang, B. G. Sumpter, and V. Meunier, *Chem. -Euro. J.*, 2008, **14**, 6614.
24. C. C. Hu, K. H. Chang, M. C. Lin, and Y. T. Wu, *Nano Lett.*, 2006, **6**, 2690.
25. H. Zhang, G. Cao, Z. Wang, Y. Yang, Z. Shi, and Z. Gu, *Nano Lett.*, 2008, **8**, 2664.
26. D. Choi, G. E. Blomgren, and P. N. Kumta, *Adv. Mater.*, 2006, **18**, 1178.
27. L. Z. Fan, Y. S. Hu, J. Maier, P. Adelhelm, B. Smarsly, and M. Antonietti, *Adv. Funct. Mater.*, 2007, **17**, 3083.
28. M. Seredych, D. Hulicova-Jurcakova, G. Q. Lu, and T. J. Bandosz, *Carbon*, 2008, **46**, 1475.
29. T.-C. Wen and C.-C. Hu, *J. Electrochim. Soc.*, 1992, **139**, 2158.
30. J. P. Zheng, P. J. Cygan, and T. R. Jow, *J. Electrochim. Soc.*, 1995, **142**, 2699.
31. C. C. Hu, W. C. Chen, and K. H. Chang, *J. Electrochim. Soc.*, 2004, **151**, A281.
32. J. W. Long, K. E. Swider, C. I. Merzbacher, and D. R. Rolison, *Langmuir*, 1999, **15**, 780.
33. K. Kierzek, E. Frackowiak, G. Lota, G. Gryglewicz, and J. Machnikowski, *Electrochim. Acta*, 2004, **49**, 515.
34. G. Salitra, A. Soffer, L. Eliad, Y. Cohen, and D. Aurbach, *J. Electrochim. Soc.*, 2000, **147**, 2486.

35. E. Raymundo-Pinero, F. Leroux, and F. Beguin, *Adv. Mater.*, 2006, **18**, 1877.
36. P. Azais, L. Duclaux, P. Florian, D. Massiot, M.-A. Lillo-Rodenas, A. Linares-Solano, J.-P. Peres, C. Jehoulet, and F. Beguin, *J. Power Sources*, 2007, **171**, 1046.
37. M. Zhu, C. J. Weber, Y. Yang, M. Konuma, U. Starke, K. Kern, and A. M. Bittner, *Carbon*, 2008, **46**, 1826.
38. P. E. Fanning and M. A. Vannice, *Carbon*, 1993, **31**, 721.
39. C. T. Hsieh and H. Teng, *Carbon*, 2002, **40**, 667.
40. K. Jurewicz, K. Babel, A. Ziolkowski, and H. Wachowska, *Electrochim. Acta*, 2003, **48**, 1491.
41. Z. B. Lei, M. Y. Zhao, L. Q. Dang, L. Z. An, M. Lu, A. Y. Lo, N. Y. Yu, and S. B. Liu, *J. Mater. Chem.*, 2009, **19**, 5985.
42. F. B. Su, Z. Q. Tian, C. K. Poh, Z. Wang, S. H. Lim, Z. L. Liu, and J. Y. Lin, *Chem. Mater.*, 2010, **22**, 832.
43. D. Hulicova, M. Kodama, and H. Hatori, *Chem. Mater.*, 2006, **18**, 2318.
44. D. Hulicova-Jurcakova, A. M. Puziy, O. I. Poddubnaya, F. Suarez-Garcia, J. M. D. Tascon, and G. Q. Lu, *J. Am. Chem. Soc.*, 2009, **131**, 5026.
45. X. S. Zhao, F. Su, Q. Yan, W. Guo, X. Y. Bao, L. Lv, and Z. Zhou, *J. Mater. Chem.*, 2006, **16**, 637.
46. C. D. Liang, Z. J. Li, and S. Dai, *Angew. Chem. Int. Ed.*, 2008, **47**, 3696.
47. C. O. Ania, V. Khomenko, E. Raymundo-Pinero, J. B. Parra, and F. Beguin, *Adv. Funct. Mater.*, 2007, **17**, 1828.
48. W. Li, D. Chen, Z. Li, Y. Shi, Y. Wan, G. Wang, Z. Jiang, and D. Zhao, *Carbon*, 2007, **45**, 1757.
49. D. Wang, F. Li, M. Liu, G. Q. Lu, and H.-M. Cheng, *Angew. Chem. Int. Ed.*, 2008, **47**, 373.
50. D. Hulicova, J. Yamashita, Y. Soneda, H. Hatori, and M. Kodama, *Chem. Mater.*, 2005, **17**, 1241.
51. G. Lota, B. Grzyb, H. Machnikowska, J. Machnikowski, and E. Frackowiak, *Chem. Phys. Lett.*, 2005, **404**, 53.
52. W. R. Li, D. H. Chen, Z. Li, Y. F. Shi, Y. Wan, J. J. Huang, J. J. Yang, D. Y. Zhao, and Z. Y. Jiang, *Electrochem. Commun.*, 2007, **9**, 569.
53. F. Beguin, K. Szostak, G. Lota, and E. Frackowiak, *Adv. Mater.*, 2005, **17**, 2380.
54. B. Liu, H. Shioyama, T. Akita, and Q. Xu, *J. Am. Chem. Soc.*, 2008, **130**, 5390.
55. H. K. Chae, D. Y. Siberio-Perez, J. Kim, Y. Go, M. Eddaoudi, A. J. Matzger, M. O'Keeffe, and O. M. Yaghi, *Nature*, 2004, **427**, 523.
56. S. Jun, S. H. Joo, R. Ryoo, M. Kruk, M. Jaroniec, Z. Liu, T. Ohsuna, and O. Terasaki, *J. Am. Chem. Soc.*, 2000, **122**, 10712.
57. T. W. Kim, I. S. Park, and R. Ryoo, *Angew. Chem. Int. Ed.*, 2003, **42**, 4375.
58. S. H. Joo, S. J. Choi, I. Oh, J. Kwak, Z. Liu, O. Terasaki, and R. Ryoo, *Nature*, 2001, **412**, 169.
59. Z. B. Lei, S. Y. Bai, Y. Xiao, L. Q. Dang, L. Z. An, G. N. Zhang, and Q. Xu, *J. Phys. Chem. C*, 2008, **112**, 722.
60. H. Darmstadt, C. Roy, S. Kaliaguine, T. W. Kim, and R. Ryoo, *Chem. Mater.*, 2003, **15**, 3300.
61. M. Kruk, M. Jaroniec, T. W. Kim, and R. Ryoo, *Chem. Mater.*, 2003, **15**, 2815.
62. W. Xing, S. Z. Qiao, R. G. Ding, F. Li, G. Q. Lu, Z. F. Yan, and H. M. Cheng, *Carbon*, 2006, **44**, 216.
63. W. Kim, J. B. Joo, N. Kim, S. Oh, P. Kim, and J. Yi, *Carbon*, 2009, **47**, 1407.
64. D. W. Wang, F. Li, Z. G. Chen, G. Q. Lu, and H. M. Cheng, *Chem. Mater.*, 2008, **20**, 7195.
65. H. J. Liu, W. J. Cui, L. H. Jin, C. X. Wang, and Y. Y. Xia, *J. Mater. Chem.*, 2009, **19**, 3661.
66. S. W. Woo, K. Dokko, H. Nakano, and K. Kanamura, *J. Mater. Chem.*, 2008, **18**, 1674.
67. L. L. Zhang, S. Li, J. T. Zhang, P. Z. Guo, J. T. Zheng, and X. S. Zhao, *Chem. Mater.*, 2010, **22**, 1195.
68. H. Yamada, H. Nakamura, F. Nakahara, I. Moriguchi, and T. Kudo, *J. Phys. Chem. C*, 2007, **111**, 227.
69. M. Pumera, *Chem. Euro. J.*, 2009, **15**, 4970.
70. R. H. Baughman, A. A. Zakhidov, and W. A. de Heer, *Science*, 2002, **297**, 787.
71. D. N. Futaba, K. Hata, T. Yamada, T. Hiraoka, Y. Hayamizu, Y. Kakudate, O. Tanaike, H. Hatori, M. Yumura, and S. Iijima, *Nat. Mater.*, 2006, **5**, 987.
72. T. Bordjiba and L. H. D. M. Mohamedi, *Adv. Mater.*, 2008, **20**, 815.
73. J. Chen, A. I. Minett, Y. Liu, C. Lynam, P. Sherrell, C. Wang, and G. G. Wallace, *Adv. Mater.*, 2008, **20**, 566.
74. J. Yan, H. Zhou, P. Yu, L. Su, and L. Mao, *Adv. Mater.*, 2008, **20**, 2899.
75. C. Niu, E. K. Sichel, R. Hoch, D. Moy, and H. Tennent, *Appl. Phys. Lett.*, 1997, **70**, 1480.
76. K. H. An, W. S. Kim, Y. S. Park, J.-M. Moon, D. J. Bae, S. C. Lim, Y. S. Lee, and Y. H. Lee, *Adv. Funct. Mater.*, 2001, **11**, 387.
77. H. Zhang, G. Cao, Y. Yang, and Z. Gu, *J. Electrochem. Soc.*, 2008, **155**, k19.
78. C. Portet, P. L. Taberna, P. Simon, and E. Flahaut, *J. Electrochem. Soc.*, 2006, **153**, A649.
79. M. M. Shaijumon, F. S. Ou, L. Ci and P. M. Ajayan, *Chem. Commun.*, 2008, 2373.
80. H. Zhang, G. Cao, Z. Wang, Y. Yang, Z. Shi, and Z. Gu, *Electrochem. Commun.*, 2008, **10**, 1056.
81. C. Meng, C. Liu, and S. Fan, *Electrochem. Commun.*, 2009, **11**, 186.
82. M. Hughes, M. S. P. Shaffer, A. C. Renouf, C. Singh, G. Z. Chen, D. J. Fray, and A. H. Windle, *Adv. Mater.*, 2002, **14**, 382.
83. A. K. Geim, *Science*, 2009, **324**, 1530.

84. P. R. Wallace, *Phys. Rev.*, 1947, **71**, 622.
85. J. W. McClure, *Phys. Rev.*, 1956, **104**, 666.
86. K. S. Novoselov, A. K. Geim, S. V. Morozov, D. Jiang, Y. Zhang, S. V. Dubonos, I. V. Grigorieva, and A. A. Firsov, *Science*, 2004, **306**, 666.
87. X. Wang, L. J. Zhi, and K. Mullen, *Nano Lett.*, 2008, **8**, 323.
88. T. Yumura, K. Kimura, H. Kobayashi, R. Tanaka, N. Okumura, and T. Yamabe, *Phys. Chem. Chem. Phys.*, 2009, **11**, 8275.
89. D. V. Kosynkin, A. L. Higginbotham, A. Sinitskii, J. R. Lomeda, A. Dimiev, B. K. Price, and J. M. Tour, *Nature*, 2009, **458**, 872.
90. V. C. Tung, M. J. Allen, Y. Yang, and R. B. Kaner, *Nat. Nanotechnol.*, 2009, **4**, 25.
91. M. Chouair, P. Thordarson, and J. A. Stride, *Nat. Nanotechnol.*, 2009, **4**, 30.
92. K. V. Emtsev, A. Bostwick, K. Horn, J. Jobst, G. L. Kellogg, L. Ley, J. L. McChesney, T. Ohta, S. A. Reshanov, J. Rohrl, E. Rotenberg, A. K. Schmid, D. Waldmann, H. B. Weber, and T. Seyller, *Nat. Mater.*, 2009, **8**, 203.
93. P. W. Sutter, J.-I. Flege, and E. A. Sutter, *Nat. Mater.*, 2008, **7**, 406.
94. K. S. Kim, Y. Zhao, H. Jang, S. Y. Lee, J. M. Kim, J. H. Ahn, P. Kim, J. Y. Choi, and B. H. Hong, *Nature*, 2009, **457**, 706.
95. X. Yang, X. Dou, A. Rouhanipour, L. Zhi, H. J. Rader, and K. Mullen, *J. Am. Chem. Soc.*, 2008, **130**, 4216.
96. W. S. Hummers and R. E. Offeman, *J. Am. Chem. Soc.*, 1958, **80**, 1339.
97. N. I. Kovtyukhova, P. J. Ollivier, B. R. Martin, T. E. Mallouk, S. A. Chizik, E. V. Buzaneva, and A. D. Gorchinskiy, *Chem. Mater.*, 1999, **11**, 771.
98. D. Li, M. B. Muller, S. Gilje, R. B. Kaner, and G. G. Wallace, *Nat. Nanotechnol.*, 2008, **3**, 101.
99. S. Stankovich, D. A. Dikin, G. H. B. Dommett, K. M. Kohlhaas, E. J. Zimney, E. A. Stach, R. D. Piner, S. T. Nguyen, and R. S. Ruoff, *Nature*, 2006, **442**, 282.
100. W. Gao, L. B. Alemany, L. J. Ci, and P. M. Ajayan, *Nat. Chem.*, 2009, **1**, 403.
101. P. K. Ang, S. A. Wang, Q. L. Bao, J. T. L. Thong, and K. P. Loh, *ACS Nano*, 2009, **3**, 3587.
102. D. A. Dikin, S. Stankovich, E. J. Zimney, R. D. Piner, G. H. B. Dommett, G. Evmenenko, S. T. Nguyen, and R. S. Ruoff, *Nature*, 2007, **448**, 457.
103. C. Chen, Q.-H. Yang, Y. Yang, W. Lv, Y. Wen, P.-X. Hou, M. Wang, and H.-M. Cheng, *Adv. Mater.*, 2009, **21**, 3007.
104. R. Ruoff, *Nat. Nanotechnol.*, 2008, **3**, 10.
105. M. D. Stoller, S. Park, Y. Zhu, J. An, and R. S. Ruoff, *Nano Lett.*, 2008, **8**, 3498.
106. S. R. C. Vivekchand, C. S. Rout, K. S. Subrahmanyam, A. Govindaraj, and C. N. R. Rao, *J. Chem. Sci.*, 2008, **120**, 9.
107. C. N. R. Rao, A. K. Sood, K. S. Subrahmanyam, and A. Govindaraj, *Angew. Chem. Int. Ed.*, 2009, **48**, 7752.
108. M. J. Allen, V. C. Tung, and R. B. Kaner, *Chem. Rev.*, 2010, **110**, 132.
109. X. Zhao, H. Tian, M. Zhu, K. Tian, J. J. Wang, F. Kang, and R. A. Outlaw, *J. Power Sources*, 2009, **194**, 1208.
110. J. Xia, F. Chen, J. Li, and N. Tao, *Nat. Nano*, 2009, **4**, 505.
111. L. J. Cote, R. Cruz-Silva, and J. Huang, *J. Am. Chem. Soc.*, 2009, **131**, 11027.
112. D. W. Wang, F. Li, J. Zhao, W. Ren, Z. G. Chen, J. Tan, Z. S. Wu, I. Gentle, G. Q. Lu, and H. M. Cheng, *ACS Nano*, 2009, **3**, 1745.
113. A. V. Murugan, T. Muraliganth, and A. Manthiram, *Chem. Mater.*, 2009, **21**, 5004.
114. J. Yan, T. Wei, B. Shao, Z. Fan, W. Qian, M. Zhang, and F. Wei, *Carbon*, 2010, **48**, 487.
115. Y. Zhang, H. Li, L. Pan, T. Lu, and Z. Sun, *J. Electroanal. Chem.*, 2009, **634**, 68.
116. K. Zhang, L. L. Zhang, J. Wu, and X. S. Zhao, *Chem. Mater.*, 2010, **22**, 1392.
117. B. Xu, F. Wu, R. Chen, G. Cao, S. Chen, Z. Zhou, and Y. Yang, *Electrochem. Commun.*, 2008, **10**, 795.
118. B. Fang and L. Binder, *J. Power Sources*, 2006, **163**, 616.
119. C. Portet, J. Chmiola, Y. Gogotsi, S. Park, and K. Lian, *Electrochim. Acta*, 2008, **53**, 7675.
120. E. G. Bushueva, P. S. Galkin, A. V. Okotrub, L. G. Bulusheva, N. N. Gavrilov, V. L. Kuznetsov, and S. I. Moiseevkov, *Phys. Status Solidi B*, 2008, **245**, 2296.
121. C. Portet, G. Yushin, and Y. Gogotsi, *Carbon*, 2007, **45**, 2511.
122. F. Zhou, C. Jehoulet, and A. J. Bard, *J. Am. Chem. Soc.*, 2002, **114**, 11004.
123. N. E. Tran, S. G. Lambrakos, and J. J. Lagowski, *J. Mater. Eng. Perform.*, 2009, **18**, 95.
124. H. W. Kroto, J. R. Heath, S. C. O'Brien, R. F. Curl, and R. E. Smalley, *Nature*, 1985, **318**, 162.
125. L. Echegoyen and L. E. Echegoyen, *Acc. Chem. Res.*, 1998, **31**, 593.
126. Y. Zhang, H. Feng, X. Wu, L. Wang, A. Zhang, T. Xia, H. Dong, X. Li, and L. Zhang, *Int. J. Hydrogen Energy*, 2009, **34**, 4889.
127. S. I. Cho and S. B. Lee, *Acc. Chem. Res.*, 2008, **41**, 699.
128. J. W. Long, B. Dunn, D. R. Rolison, and H. S. White, *Chem. Rev.*, 2004, **104**, 4463.
129. J. Baxter, Z. Bian, G. Chen, D. Danielson, M. S. Dresselhaus, A. G. Fedorov, T. S. Fisher, C. W. Jones, E. Maginn, U. Kortshagen, A. Manthiram, A. Nozik, D. R. Rolison, T. Sands, L. Shi, D. Sholl, and Y. Wu, *Energy Environ. Sci.*, 2009, **2**, 559.
130. D. A. McKeown, P. L. Hagans, L. P. L. Carette, A. E. Russell, K. E. Swider, and D. R. Rolison, *J. Phys. Chem. B*, 1999, **103**, 4825.
131. K.-H. Chang, C.-C. Hu, and C.-Y. Chou, *Electrochim. Acta*, 2009, **54**, 978.

132. K.-H. Chang, C.-C. Hu, and C.-Y. Chou, *Chem. Mater.*, 2007, **19**, 2112.
133. D. R. Rolison, J. W. Long, J. C. Lytle, A. E. Fischer, C. P. Rhodes, T. M. McEvoy, M. E. Bourg, and A. M. Lubers, *Chem. Soc. Rev.*, 2009, **38**, 226.
134. K.-M. Lin, K.-H. Chang, C.-C. Hu, and Y.-Y. Li, *Electrochim. Acta*, 2009, **54**, 4574.
135. S. Wataru, I. Hideki, Y. Yutaka, M. Yasushi, and T. Yoshio, *Angew. Chem. Int. Ed.*, 2003, **42**, 4092.
136. W. Sugimoto, H. Iwata, K. Yokoshima, Y. Murakami, and Y. Takasu, *J. Phys. Chem. B*, 2005, **109**, 7330.
137. G. Bo, Z. Xiaogang, Y. Changzhou, L. Juan, and Y. Long, *Electrochim. Acta*, 2006, **52**, 1028.
138. C. Yuan, L. Chen, B. Gao, L. Su, and X. Zhang, *J. Mater. Chem.*, 2009, **19**, 246.
139. M. Toupin, T. Brousse, and D. Belanger, *Chem. Mater.*, 2002, **14**, 3946.
140. M. Toupin, T. Brousse, and D. Belanger, *Chem. Mater.*, 2004, **16**, 3184.
141. O. Ghodbane, J.-L. Pascal, and F. Favier, *ACS Appl. Mater. Interf.*, 2009, **1**, 1130.
142. S. Devaraj and N. Munichandraiah, *J. Phys. Chem. C*, 2008, **112**, 4406.
143. C.-C. Hu, Y.-T. Wu, and K.-H. Chang, *Chem. Mater.*, 2008, **20**, 2890.
144. M. Nakayama, T. Kanaya, and R. Inoue, *Electrochem. Commun.*, 2007, **9**, 1154.
145. S.-L. Chou, J.-Z. Wang, S.-Y. Chew, H.-K. Liu, and S.-X. Dou, *Electrochem. Commun.*, 2008, **10**, 1724.
146. M. Xu, L. Kong, W. Zhou, and H. Li, *J. Phys. Chem. C*, 2007, **111**, 19141.
147. H. Chen, X. Dong, J. Shi, J. Zhao, Z. Hua, J. Gao, M. Ruan, and D. Yan, *J. Mater. Chem.*, 2007, **17**, 855.
148. X.-H. Yang, Y.-G. Wang, H.-M. Xiong, and Y.-Y. Xia, *Electrochim. Acta*, 2007, **53**, 752.
149. A. E. Fischer, K. A. Pettigrew, D. R. Rolison, R. M. Stroud, and J. W. Long, *Nano Lett.*, 2007, **7**, 281.
150. R. Liu and S. B. Lee, *J. Am. Chem. Soc.*, 2008, **130**, 2942.
151. L. L. Zhang, T. Wei, W. Wang, and X. S. Zhao, *Micropor. Mesopor. Mater.*, 2009, **123**, 260.
152. D. D. Zhao, W. J. Zhou, and H. L. Li, *Chem. Mater.*, 2007, **19**, 3882.
153. D.-D. Zhao, S.-J. Bao, W.-J. Zhou, and H.-L. Li, *Electrochem. Commun.*, 2007, **9**, 869.
154. C. Yuan, X. Zhang, L. Su, B. Gao, and L. Shen, *J. Mater. Chem.*, 2009, **19**, 5772.
155. L.-B. Kong, J.-W. Lang, M. Liu, Y.-C. Luo, and L. Kang, *J. Power Sources*, 2009, **194**, 1194.
156. M.-B. Zheng, J. Cao, S.-T. Liao, J.-S. Liu, H.-Q. Chen, Y. Zhao, W.-J. Dai, G.-B. Ji, J.-M. Cao, and J. Tao, *J. Phys. Chem. C*, 2009, **113**, 3887.
157. T.-Y. Wei, C.-H. Chen, K.-H. Chang, S.-Y. Lu, and C.-C. Hu, *Chem. Mater.*, 2009, **21**, 3228.
158. S. Xiong, C. Yuan, X. Zhang, B. Xi, and Y. Qian, *Chem. Euro. J.*, 2009, **15**, 5320.
159. C. Lin, L. Mei, and L. Hu-Lin, *J. Electrochem. Soc.*, 2005, **152**, A871.
160. W.-J. Zhou, J. Zhang, T. Xue, D.-D. Zhao, and H.-L. Li, *J. Mater. Chem.*, 2008, **18**, 905.
161. K. Rajendra Prasad and N. Miura, *Electrochem. Commun.*, 2004, **6**, 1004.
162. S.-Y. Wang, K.-C. Ho, S.-L. Kuo, and N.-L. Wu, *J. Electrochem. Soc.*, 2006, **153**, A75.
163. N. L. Wu, W. Y. Wang, C. Y. Han, D. S. Wu, and L. R. Shiue, *J. Power Sources*, 2003, **113**, 173.
164. J. Chang, W. Lee, R. S. Mane, B. W. Cho, and S.-H. Han, *Electrochem. Solid-State Lett.*, 2008, **11**, A9.
165. R. N. Reddy and R. G. Reddy, *J. Power Sources*, 2006, **156**, 700.
166. Z. J. Lao, K. Konstantinov, Y. Tournaire, S. H. Ng, G. X. Wang, and H. K. Liu, *J. Power Sources*, 2006, **162**, 1451.
167. T. Brezesinski, J. Wang, J. Polleux, B. Dunn, and S. H. Tolbert, *J. Am. Chem. Soc.*, 2009, **131**, 1802.
168. H. Y. Mi, X. G. Zhang, X. G. Ye, and S. D. Yang, *J. Power Sources*, 2008, **176**, 403.
169. A. Subramania and S. L. Devi, *Poly. Adv. Technol.*, 2008, **19**, 725.
170. G. C. Xu, W. Wang, X. F. Qu, Y. S. Yin, L. Chu, B. L. He, H. K. Wu, J. R. Fang, Y. S. Bao, and L. Liang, *Eur. Poly. J.*, 2009, **45**, 2701.
171. A. Laforgue, P. Simon, C. Sarrazin, and J. F. Fauvarque, *J. Power Sources*, 1999, **80**, 142.
172. L. Z. Fan and J. Maier, *Electrochem. Commun.*, 2006, **8**, 937.
173. K. H. An, K. K. Jeon, J. K. Heo, S. C. Lim, D. J. Bae, and Y. H. Lee, *J. Electrochem. Soc.*, 2002, **149**, A1058.
174. F. Montilla, M. A. Cotarelo, and E. Morallón, *J. Mater. Chem.*, 2009, **19**, 305.
175. Y.-G. Wang, H.-Q. Li, and Y.-Y. Xia, *Adv. Mater.*, 2006, **18**, 2619.
176. G. M. Suppes, B. A. Deore, and M. S. Freund, *Langmuir*, 2008, **24**, 1064.
177. T. L. Kelly, K. Yano, and M. O. Wolf, *ACS Appl. Mater. Interf.*, 2009, **1**, 2536.
178. T. L. Kelly, Y. Yamada, S. P. Y. Che, K. Yano, and M. O. Wolf, *Adv. Mater.*, 2008, **20**, 2616.
179. M. E. Roberts, D. R. Wheeler, B. B. McKenzie, and B. C. Bunker, *J. Mater. Chem.*, 2009, **19**, 6977.
180. G. K. Dimitrakakis, E. Tylianakis, and G. E. Froudakis, *Nano Lett.*, 2008, **8**, 3166.
181. D.-E. Jiang, V. R. Cooper, and S. Dai, *Nano Lett.*, 2009, **9**, 4019.

Thermochemical Water-Splitting

Ali T-Raissi

University of Central Florida, Orlando, FL, USA

1	Introduction	365
2	Hydrogen Production Technologies	365
3	Water-Splitting Cycles for Hydrogen Production	366
4	Two-Step Water-Splitting Cycles	366
5	Multistep Water-Splitting Cycles	367
6	Related Articles	371
7	Abbreviations and Acronyms	371
8	References	371

1 INTRODUCTION

A large and growing hydrogen (H_2) market already exists in the United States and elsewhere. Hydrogen production worldwide amounts to about 50 million tons per year, valued at \$280 billion (2006), growing at a rate of approximately 10%, annually.¹ Presently, most of the hydrogen is in captive use, i.e., hydrogen is produced at the site of usage. Only a small fraction of the total production is sold as merchant hydrogen. Worldwide, the amount of captive hydrogen is about seven times that of merchant hydrogen, which consists of both gaseous and liquid H_2 .¹

In 2003, the United States consumed a total of 7.74 million tons of hydrogen, of which 53% was used in oil refining, 34% for ammonia production, and 5% for methanol synthesis,² while worldwide, ammonia production, oil refining, and methanol synthesis accounted for 57, 27, and 10% of the total hydrogen demand, respectively.³

According to Energy Information Administration (EIA) estimates, the US share of the 53 million tons of hydrogen produced globally (2004) was 17%.⁴ Therefore, there is already a fairly large-scale hydrogen economy in existence today in the United States and elsewhere. However, the perceived transition to a full-fledged “Hydrogen Economy (see **Hydrogen Economy**)” will require significant boost in the H_2 production. For example, serving all the US transportation energy needs with hydrogen would multiply the current demand by a factor of at least 18. To provide for all nonelectric US energy needs would require about a 40-fold increase over the current hydrogen production levels.

2 HYDROGEN PRODUCTION TECHNOLOGIES

Today, by and large, fossil fuels are used to produce hydrogen. At present, 48, 30, 18, and 4% of the hydrogen produced worldwide employ, respectively, natural gas, petroleum, coal, and water (via electrolysis) as feedstock.³ By far, the largest amounts of H_2 produced are captive hydrogen used for methanol and ammonia syntheses and in refineries for the hydro-treatment of heavy crude, production of reformulated gasoline, and the hydro-desulfurization of middle distillate diesel fuel.¹

The technology options for hydrogen production include partial oxidation or gasification of fossil fuels, in general, and steam reformation of natural gas, in particular. In situations where low-cost or excess electricity is available, water electrolysis has been employed for generating hydrogen. In general, hydrogen production via renewable energy resources is not yet economically viable. Currently, with the exception of hydroelectric power, less than 1% of the electricity generated in the United States is produced by renewable energy. As for the hydropower, the electricity produced by large hydroelectric power plants costs about \$0.0085 per kilowatt-hour (kWh), considerably less than that generated by nuclear, coal, or natural gas powered plants.⁵

Currently, production of renewable hydrogen is an area of great interest and focus of worldwide research and development (see **H_2 Production from Renewables**). Production of hydrogen using renewable power such as wind, geothermal, ocean, biomass, and solar energy is beginning to become cost competitive with the conventional

production techniques, especially in niche markets.^{6,7} Also, there are other advanced technologies that are being developed for generating hydrogen from renewable resources (*see Photocatalytic Hydrogen Production from Water*).⁸ One such technology is to use a high-temperature energy source to power a thermochemical water-splitting cycle (TCWSC) for the production of hydrogen (H_2) and oxygen (O_2). TCWSCs are discussed in this article.

3 WATER-SPLITTING CYCLES FOR HYDROGEN PRODUCTION

Since the introduction of the concept in the early 1960s,^{9,10} hydrogen generation by splitting water has become the focus of extensive research and development, worldwide. Consequently, now there are more than 350¹¹ thermochemical cycles conceived for splitting water, of which only less than a dozen or so are still being researched intensely. Examples include sulfur–iodine (SI) cycle, hybrid sulfur (HyS) cycle, copper–chlorine (CuCl) cycle, calcium–bromine–iron (UT-3) cycle, zinc–zinc oxide (Zn/ZnO) cycle, iron oxide cycle, and cerium(IV) oxide–cerium(III) oxide cycle.¹² Figure 1 shows the number of references resulting from literature search by year through 2009. The total is well over 1000. The number of annual publications has surged recently, showing accelerated increase in interest beginning in 2000. There are several excellent reports and reviews available on the subject.^{13–38}

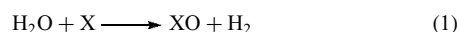
The objective of hydrogen production via TCWSC is finding more efficient processes that utilize mostly heat (rather than electricity as in the case of water electrolysis) for splitting water. Thermochemical water-splitting can be

accomplished by direct heating of H_2O to very high temperatures (above 4330 K, at which the Gibbs free energy, ΔG° , becomes zero)³⁷ followed by separation of hydrogen from the equilibrium $H_2O/H_2/O_2$ mixture. Furthermore, the costs of high-temperature materials of construction as well as the separation issues make direct water decomposition challenging. The property changes for water decomposition at 298 K and 1 atm are $\Delta H^\circ = 68.3 \text{ kcal g}^{-1} \text{ mol}$; $\Delta G^\circ = 56.69 \text{ kcal g}^{-1} \text{ mol}$; and $\Delta S^\circ = 0.039 \text{ kcal g}^{-1} \text{ mol K}$. Since ΔS° (which is the negative of the temperature derivative of the ΔG°) is too small, direct decomposition of water is simply not yet feasible. The thermochemical cycles for hydrogen production discussed here are those for which water is the only consumable and hydrogen and oxygen are the only products of the process.

4 TWO-STEP WATER-SPLITTING CYCLES

Two-step TCWSCs take one of the following three forms of redox reaction couples.^{31,37,39}

Oxide type:



Hydride type:

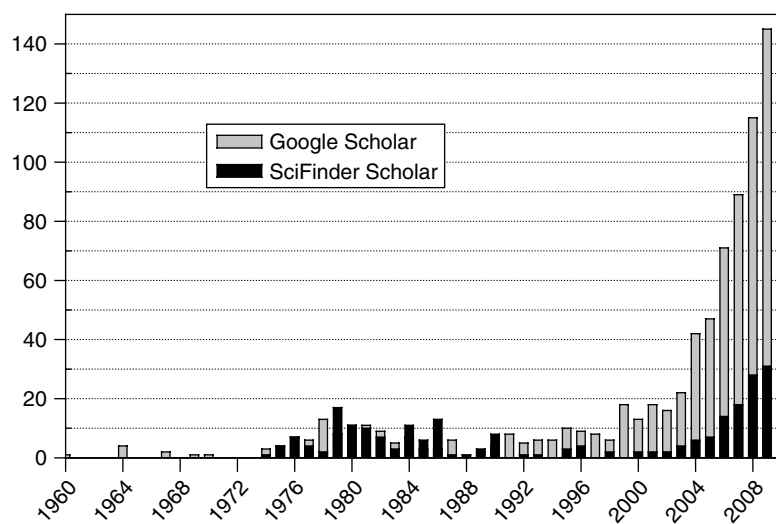
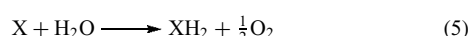
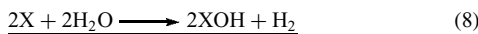
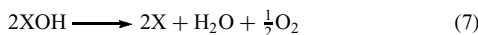


Figure 1 The number of citations resulting from Google Scholar (articles and patents) and SciFinder Scholar (only journal articles) search of “thermochemical cycles” for “splitting water”

Hydroxide type:



Thermodynamic analysis for the entropy change of two-step water-splitting cycles shown above indicates that the minimum number of required reaction steps for cycles operating between 298 and 1000 K is three.⁴⁰ In practice, temperatures well above 2000 K are needed for splitting water via two-step TCWSCs. Most TCWSCs proposed to date, require more than two chemical reactions to operate.

One of the most extensively studied metal-oxide-type redox couple as a two-step cycle is Zn/ZnO, wherein X ≡ Zn in reactions (1) and (2).^{41–44} Hydrogen is produced from water by reaction (1), the exothermic hydrolysis of Zn_(l) at 700 K to form H₂ and ZnO_(s), and reaction (2), the endothermic thermal dissociation of ZnO_(s) into Zn_(g) and O₂ at 2300 K using process heat derived from concentrated solar energy. The net reaction is H₂O → H₂ + 1/2O₂, but since H₂ and O₂ are formed in different processes, there is no need for the high-temperature gas separation that would be otherwise necessary. Techniques for recovering the latent heat of products from reaction (2) include condensation of zinc vapor by fractional crystallization and in situ electrothermal separation of Zn_(g) and O₂ at high temperatures.^{45,46}

One of the very first two-step cycles investigated is the redox pair Fe₃O₄/FeO.⁴⁷ The high-temperature step of the Fe₃O₄/FeO cycle is the thermal dissociation of magnetite to wustite at temperatures above 2500 K. To prevent back reaction, it is necessary to quench the products of Fe₃O₄ decomposition reaction. But, quenching hot reaction products containing O₂ and FeO introduces a large energy penalty. Furthermore, Fe₃O₄ does not readily reduce water by itself. Combining Fe₃O₄ with an added metal such as zinc results in H₂O decomposition at 873 K and formation of hydrogen and ZnFe₂O₄ (zinc ferrite).⁴⁸ At 1900 K, ZnFe₂O₄ decomposes into Zn, ZnO, and Fe₃O₄ via the following reaction: 3ZnFe₂O₄ → 3Zn + 2Fe₃O₄ + 2O₂, generating oxygen and magnetite, and closing the cycle.⁴⁹

The TiO₂/TiO_x (with x < 2) is another redox couple that has been studied for thermochemical hydrogen production.⁵⁰ It was found that TiO₂ liquid dissociates in argon atmosphere to oxides of the form TiO_x where, the lowest values of x at 2300, 2500, and 2700 K are 1.905, 1.856, and 1.825, respectively. The value of x also depends on the O₂ partial pressure. A reoxidation reaction occurs between the liquid oxide and oxygen as the temperature of the oxide is reduced to 298 K—forming a mixture of Magneli phases that reacts with ZnO to produce Zn and TiO₂. Thermal reduction of TiO₂, in argon atmosphere and temperatures in the range of 2300–2700 K, resulted in Ti_nO_{2n-1} with n in the range of 4–1. Furthermore, the decomposition reaction was found to be limited by the rate at which oxygen diffuses from the liquid–gas interface.

A new two-step TCWSC for hydrogen production based on CeO₂/Ce₂O₃ redox couple has been demonstrated recently.⁵¹ Reduction and hydrolysis reaction steps of the cycle are 2CeO₂ → Ce₂O₃ + 1/2O₂ and Ce₂O₃ + H₂O → 2CeO₂ + H₂, respectively. The thermal reduction of Ce⁺⁴ to Ce⁺³ (endothermic step) is conducted inside a solar reactor under inert atmosphere at 2273 K and pressures ranging from 100 to 200 mbar. The H₂ generation step occurs in a fixed-bed reactor in the temperature range of 673–873 K.

Finally, there are a number of other redox pairs that have been proposed as two-step TCWSC for hydrogen production. Examples include: cycles based on Mn₃O₄/MnO, Co₃O₄/CoO, Nb₂O₅/NbO₂, CdO/Cd, In₂O₃/In, WO₃/W, and SnO₂/Sn.^{37,52,53} However, for these cycles, either the yield of H₂ via reaction (1) is too low to make them viable or other shortcomings such as use of toxic materials, etc. render them undesirable.

5 MULTISTEP WATER-SPLITTING CYCLES

Many thermochemical cycles have been conceived in the past 50 years or so, employing many elements such as Fe, Cl, Br, Ca, S, I, N, Li, Ba, Ni, Sb, Cd, etc. in many different compounds. Table 1 presents several examples of multistep TCWSC for hydrogen generation. Earlier, multistep (i.e., more than two) TCWSCs had peak temperatures below about 1200 K that made them inherently less efficient, due, in part, to heat-transfer limitations and product-separation issues.³¹

Presently, the high-temperature heat sources suitable for running TCWSC are limited to concentrated solar

Table 1 Summary of multistep TCWSC for hydrogen generation. (Reproduced from Ref. 31. © Elsevier.)

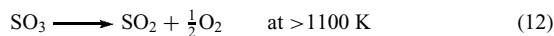
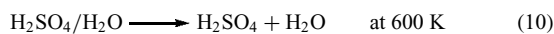
Elements in cycle	Maximum cycle temperature (K)	Number of cycle reaction steps
Hg, Ca, Br	1050	4
Hg, Ca, Br	1050	4
Cu, Ca, Br	1070	4
Hg, Sr, Br	1070	3
Mn, Na, (K)	1070	3
Mn, Na, (K), C	1120	4
V, Cl	1070	4
Fe, Cl, S	1070	4
Hg, Ca, Br, C	1120	5
Cr, Cl, Fe, (V)	1070	4
Cr, Cl, Fe, (V) Cu	1070	5
Fe, Cl	920–1120	3–5
Mn, Cl	1120	3
I, S, N	1120	6
S (hybrid)	1120	2
I, S, N, Zn	1120	4
Br, S (hybrid)	1120	3
S, I	1120	3

thermal and nuclear (provided by the high-temperature gas-cooled reactor, HTGR) power. In particular, large-scale solar thermal power towers⁵⁴ capable of delivering high-temperature heat to TCWSC plants are being considered with renewed interest.⁵⁵ TCWSC efficiencies (first law) for heat-to-hydrogen energy conversion as high as 50% have been projected.⁵⁶ TCWSCs have been demonstrated in several laboratories.^{25,57–65} However, no large-scale TCWSC plant has been fielded, to date.

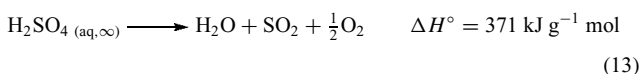
Among the most developed TCWSCs are Westinghouse HyS cycle, four-step CuCl cycle, General Atomics (GA) three-step SI cycle, and the four-step UT3 cycle. A brief review of the HyS, SI, and UT3 multistep water-splitting cycles capable of operation below 1200 K is presented in the following sections.

5.1 Sulfur Family Cycles

The main reaction of the sulfur family cycles is the decomposition of sulfuric acid. The cycle reactions are as follows³⁷:



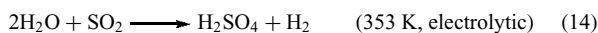
Reaction (10) involves concentration and vaporization of sulfuric acid. Reaction (11) is the decomposition of H_2SO_4 to form SO_3 and H_2O at temperatures ranging from 600 to 1000 K. At temperatures above 1100 K and in the presence of a catalyst, SO_3 decomposes to SO_2 and O_2 . Reactions (10–12) are all endothermic reactions. The overall reaction for decomposition of sulfuric acid can be written as follows:



where subscript “aq,∞” refers to an aqueous solution of infinite dilution.³⁷

5.1.1 Westinghouse (Hybrid Sulfur) Cycle

The Westinghouse (HyS) cycle combines the sulfuric acid decomposition reaction (13) with electrochemical oxidation of SO_2 as follows^{66–71}:



This is not a pure thermochemical but a hybrid electrochemical–thermochemical (i.e., “heat plus work”) cycle. In theory, electrolysis of aqueous sulfur dioxide can be conducted at a potential ($E^\circ = -0.17 \text{ V}$) that is lower than direct water electrolysis ($E^\circ = -1.23 \text{ V}$). Therefore, the electrical power required should be much less. However, in

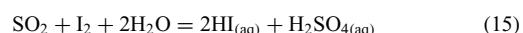
practice, overpotential and cell losses are significant. The major factor affecting efficiency of the Westinghouse cycle is the electrode overpotential.

Reductions in the electrolytic cell overpotential may be possible through electrode material improvements and better cell design. This cycle has been experimentally demonstrated and its electrochemical step operated (pressures as high as 15 bar and cell temperature of 353 K) at a cell voltage of 0.6 V at 100 mA cm⁻² and 0.8 V at 200 mA cm⁻². The aforementioned cell potentials were reduced by 0.05 and 0.1 V, respectively, by using an improved tungsten–carbide-coated cathode.⁷⁰ For the Westinghouse cycle, the trade-off is between sulfuric acid concentration and minimum cell voltage achieved.

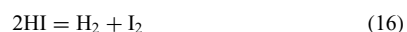
Reaction (13) of the Westinghouse cycle is high-temperature thermal decomposition of sulfuric acid which is common to most sulfur family cycles—requiring advanced reactor materials of construction in order to mitigate corrosion and fatigue.²⁵ Researchers at the Sandia National Laboratories (SNL) have developed a bayonet-type heat exchanger having SiC components as an all-in-one system. In the SNL design, the acid boiler and decomposer is combined into a single SiC-based unit, which also provides heat recuperation between the reactor effluent and incoming liquid sulfuric acid stream.^{72,73}

5.1.2 General Atomics (Sulfur–Iodine) Cycle

The SI cycle is a three-step cycle whose net reactant is water and the only products are hydrogen and oxygen. All other chemicals are recycled. The SI process requires a high-temperature heat source. SI cycle combines the sulfuric acid decomposition reaction (13) with Bunsen reaction involving iodine as follows:



plus thermal decomposition of hydroiodic acid (HI):



This cycle, proposed by Norman, is the basis of the GA and JRC-Mark 16 cycles.³¹ The sulfur–iodine cycle is an all-liquid/gas process. If reactants in the Bunsen reaction are used in a stoichiometric ratio, the yield is very poor. To improve the kinetics and facilitate separation of the reaction products into two liquid phases, the reaction must be carried out using a large amount of excess water and I_2 . Excess water causes the physical separation and thermal decomposition of HI to be very energy intensive. A major breakthrough at GA was the determination of conditions under which the products of the Bunsen reaction of water, iodine, and sulfur dioxide form two phases, one rich in HI and the other rich in H_2SO_4 .⁶⁵

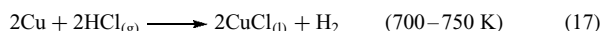
The advantages of the SI cycle are that (i) it is an all-fluid continuous process, and chemicals are all recycled and there are no effluents; (ii) reactions all have

been demonstrated; and (iii) it offers one of the highest efficiencies quoted for any water-splitting process, i.e., 47%. The challenges still remaining are (i) the high peak temperature requirement close to 1100 K; (ii) lack of a large-scale plant operating in an integrated closed loop cycle; and (iii) unknown process cost and economics.

Work on improvements to the SI cycle continues at various locations, worldwide. In addition to GA, this cycle has been studied by the JRC Ispra, Rheinisch Westfälische Technische Hochschule (RWTH) in Aachen, le Commissariat à l'Energie Atomique (CEA) in France, and the Japanese Atomic Energy Agency (JAEA), among others.^{65,74–77}

5.2 Copper–Chlorine Cycle

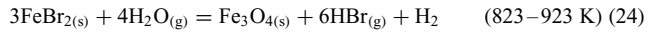
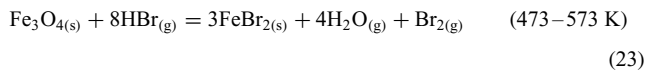
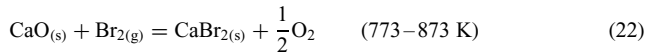
The Cu–Cl cycle, originally proposed in the 1970s, has recently been demonstrated in the laboratory.⁷⁸ The Cu–Cl cycle is a four-step TCWSC, whose net reaction is the splitting of water into hydrogen and oxygen. The CuCl cycle is a hybrid process that employs both thermochemical and electrolysis steps. The four reactions in the CuCl cycle are^{79–83}



The Atomic Energy of Canada Ltd has been able to combine reaction steps (17) and (20) by demonstrating the operation of a CuCl electrolyzer that generates H₂ at the cathode while Cu⁺ is oxidized to Cu²⁺ at the anode.⁸³ The copper–chlorine cycle has lower peak temperature and as such can utilize a broader range of low-quality and waste-heat sources. Furthermore, due to the lower operating temperatures of this cycle, there are no serious materials issues for its implementation. The electrolytic step (20) requires a relatively low voltage (0.6–1.0 V).⁸⁴ The overall efficiency of the CuCl cycle has been projected to be about 43%.^{85–87} A key challenge for the CuCl cycle is effective catalysis of the low-temperature reactions.

5.3 UT-3 Cycle

The UT-3 cycle, developed at the University of Tokyo, is a purely thermochemical cycle composed of the following four gas–solid reactions^{58–61,88–90}:



The cycle is operated in a cyclic manner in which the solids remain in their reaction vessels and the flow of gases is switched when the desired extent of reaction is reached. The two pairs of hydrolysis (endothermic) and bromination (exothermic) reactions occur in four reactors arranged in series. In the process, only solid and gas reactants/products are used and the maximum temperature achieved is 1033 K.

The UT-3 cycle is one of the most studied thermochemical hydrogen production cycles in the world. It is noted that the UT-3 cycle had been envisioned originally for coupling to the advanced nuclear power reactors, i.e., HTGRs. The reported cycle efficiency is in the range of 40–50%. UT-3 cycle operates by only changing the direction of the flow of reactant gas while the solid reactants remain fixed in the reactors. Others including the so-called sulfur family cycles do not possess this superb operational advantage. However, in order to maintain the solid reactants in fixed-bed reactors, the process gases have to flow, intermittently, in opposite directions. One reactor has to perform an endothermic hydrolysis reaction for about 2 h and then switch and allow an exothermic reaction involving bromine to take place—for the next 2 h while the direction of flow changes.

The requirement of reversing the gas flow and reactant compositions (with an intermediate purge) makes the process relatively inflexible and possibly difficult to control. The reaction (21) of the UT-3 cycle has been the slowest, kinetically, of the four reactions involved, thus being the rate-limiting step for the entire cycle. Since it is necessary, for the continuous operation of the cycle, that all of the reactions proceed at the same rate, the slow rate of calcium bromide hydrolysis adversely affects the overall process efficiency. The following summarizes some of the more specific issues that require further development and optimization.

1. Reactions (21) and (24) are endothermic hydrolytic reactions that require input heat. In contrast, reactions (22) and (23) are exothermic processes requiring heat removal from the reactors. Conducting both endothermic and exothermic reactions in one reactor is complex as two sets of heat exchangers are required, one for cooling and the other for heating reactants and products.
2. The transient periods may occur as a result of cycling that can lead to lower overall efficiency for the process. Complicated heating and cooling is then necessary to minimize the transient effects, resulting in higher operational and capital costs.
3. Steam is used in excess as heat-transfer fluid and sweep gas for the reaction products in the fixed-bed reactors. Because the high-temperature steam carries high heat duties, cooling the steam can result in excessive energy loss. To prevent this, hydrogen and oxygen are not separated from steam. Instead, membrane separation has been suggested.
4. The longevity of the UT-3 reactants/catalysts is an issue of concern.

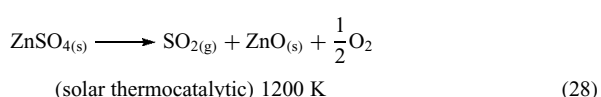
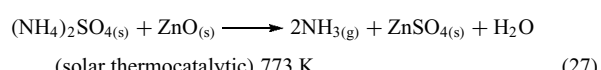
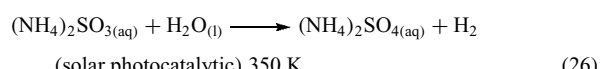
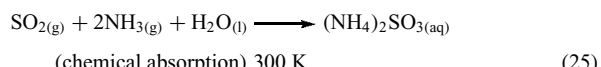
5. Hydrogen and oxygen are produced at subatmospheric pressures and require compression during the process.
6. The potential for the cycle efficiency improvement is limited by the melting point of CaBr_2 .

Finally, the original UT-3 cycle was developed for coupling with HTGR. Later, a new version (i.e., adiabatic UT-3) was conceived for interfacing with a solar heat source.^{60,91} In the new cycle, all four reactions are carried out, continuously, in adiabatic equipment where steam (or steam + nitrogen) is used as a vector. The adiabatic UT-3 cycle is conceptually simple. During sunshine hours, the energy is supplied to the process directly from the solar receiver. During dark periods, it is supplied from a thermal storage reservoir where the high-temperature heat is stored during sunshine hours. The reported overall thermal and exergetic efficiencies of the solar/UT-3 cycle were projected to be about 49.5 and 52.9%, respectively.

5.4 Sulfur–Ammonia (SA) Cycle

A limitation of most solar thermochemical cycles proposed for water splitting is that they do not take advantage of the unique characteristics of the solar resource. For example, the spectrum of sunlight contains ultraviolet and visible photons that are very energetic and able to trigger photocatalytic reactions (*also see Photocatalytic Hydrogen Production from Water; Recent Advances in Photo-Initiated Electron-Transfer at the Interface between Anatase TiO_2 Nanocrystallites and Transition-Metal Polypyridyl Compounds; Some Computational Challenges in Energy Research*). Most solar thermochemical cycles ignore the potential of these photons and use their energy only as heat to drive thermochemical reactions.

In the photocatalytic sulfur–ammonia (SA) cycle, depicted in Figure 2, the photonic portion of solar spectrum is used directly to accomplish the hydrogen evolution step of the cycle. This means that less exergy is needed in the high-temperature oxygen production part of the cycle, leading to comparatively lower operating temperatures and reduced requirements on the heliostat field and its associated costs. Reactions involved in the photocatalytic SA cycle are⁹²



The photocatalytic step (26) occurs at near ambient temperatures under one sun irradiation. Therefore, photoreactors can be inexpensive and made from low-cost materials. The oxygen production step (28) provides facile separation of O_2 from SO_2 and water vapor. Reactions (27) and (28) form a subcycle by which ZnO is reacted with ammonium sulfate, in the low-temperature reactor, to form zinc sulfate that is fed to the high-temperature reactor wherein it is decomposed to SO_2 , O_2 , and ZnO . Zinc oxide is returned to the low-temperature reactor—closing the subcycle. The net cycle reaction, represented by reactions (25–28), is splitting of water to form hydrogen and oxygen. All of the reaction steps described above have been demonstrated in the laboratory and shown to occur without undesirable side reactions.

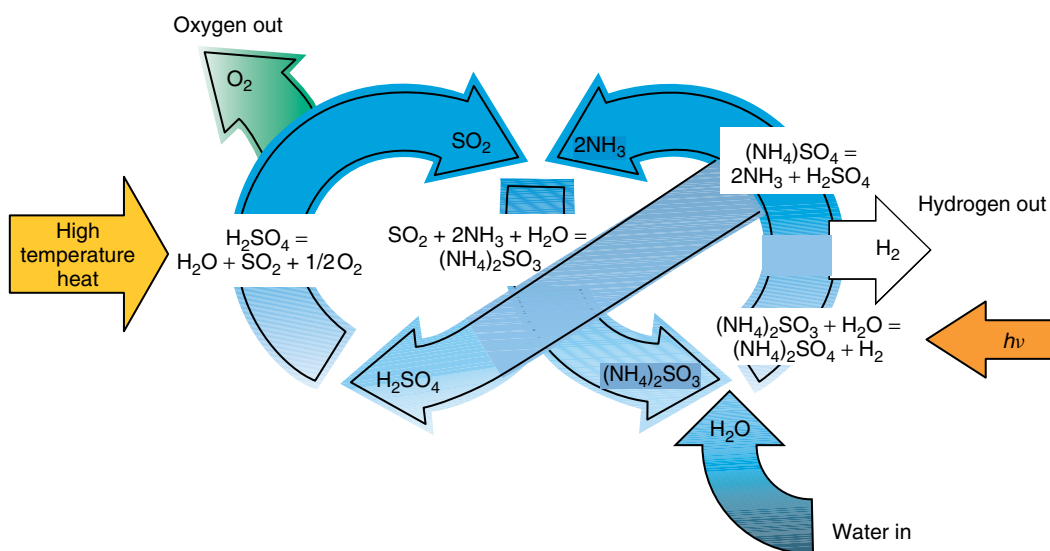


Figure 2 A schematic diagram of sulfur–ammonia cycle

This new cycle has the potential to achieve high overall efficiency utilizing only nontoxic and inexpensive chemicals. Solar energy is applied as a heat source and promotes the photocatalytic redox reaction.

6 RELATED ARTICLES

H₂ Production from Renewables; Hydrogen Economy; Photocatalytic Hydrogen Production from Water; Recent Advances in Photo-Initiated Electron-Transfer at the Interface between Anatase TiO₂ Nanocrystallites and Transition-Metal Polypyridyl Compounds; Some Computational Challenges in Energy Research.

7 ABBREVIATIONS AND ACRONYMS

HTGR = high-temperature gas-cooled reactor; CEA = Commissariat à l'Energie Atomique; CuCl = copper –chlorine; EIA = Energy Information Administration; GA = General Atomics; HI = hydroiodic acid; HyS = hybrid sulfur; JAEA = Japanese Atomic Energy Agency; RWTH = Rheinisch Westfälische Technische Hochschule; SA = sulfur –ammonia; SI = sulfur–iodine; SNL = Sandia National Laboratories; TCWSC = thermochemical water-splitting cycle; Zn/ZnO = zinc–zinc oxide.

8 REFERENCES

1. C.-J. Winter, *Int. J. Hydrogen Energy*, 2009, **34**, S1.
2. B. Yildiz, G. Conzelmann, M. C. Petri, and C. Forsberg, ‘Configuration and Technology Implications of Potential Nuclear Hydrogen System Applications’, Argonne National Laboratory Report: ANL-05/30, July 31, 2005.
3. B. Suresh, M. Yoneyama, and S. Schlag, ‘CEH Marketing Research Report Abstract: HYDROGEN’, Chemical Industries Newsletter, SRI Consulting, Menlo Park, CA, October 2007.
4. U.S. Department of Energy, ‘The Impact of Increased Use of Hydrogen on Petroleum Consumption and Carbon Dioxide Emissions, Energy Information Administration (EIA) Report: SR/OIAF-CNEAF/2008-04’, Office of Integrated Analysis and Forecasting, Office of Coal, Nuclear, Electric and Alternate Fuels, U.S. Department of Energy, August 2008.
5. National Hydrogen Association, ‘Renewable Hydrogen Production Using Electrolysis’, National Hydrogen Association Fact Sheet, 2010, <http://www.hpath.org/resources/Factsheet-Renew.pdf>.
6. A. Contreras, F. Posso, and T. N. Veziroglu, *Int. J. Hydrogen Energy*, 2007, **32**(9), 1219.
7. M. C. Rodrigues Halmeman, S. N. Melegari de Souza, and P. T. Oyama, *Int. J. Hydrogen Energy*, 2008, **33**(23), 6858.
8. US Department of Energy, ‘Hydrogen Production R&D Activities, Energy Efficiency and Renewable Energy’, US Department of Energy, 2010, website at: http://www1.eere.energy.gov/hydrogenandfuelcells/production/doe_activities.html.
9. J. E. Funk and R. M. Reinstrom, ‘System Study of Hydrogen Generation by Thermal Energy’, Report No. TID-20441(Vol. 2), Allison Division of General Motors Corp., 1964.
10. J. E. Funk and R. M. Reinstrom, *Ind. Eng. Chem. Process Design Dev.*, 1966, **5**(3), 336.
11. A. Weimer, ‘Development of Solar-powered Thermochemical Production of Hydrogen from Water’, ‘Solar Thermochemical Hydrogen (STCH) Team Progress, DOE Annual Merit Review Meeting’, Arlington, Virginia, 17 May 2006, available at <http://www.hydrogen.energy.gov/>.
12. A. Weimer, ‘Development of Solar-powered Thermochemical Production of Hydrogen from Water’, ‘Solar Thermochemical Hydrogen (STCH) Team Progress, DOE Annual Merit Review Meeting’, Arlington, Virginia, 25 May 2005, available at <http://www.hydrogen.energy.gov/>.
13. J. L. Russell Jr and J. T. Porter, ‘Hydrogen Economy. Miami Energy Conference’, Miami, 1974.
14. J. O. M. Bockris, ‘Energy. The Solar-hydrogen Alternative’, Wiley, Australia, 1975.
15. J. E. Funk, *Int. J. Hydrogen Energy*, 1976, **1**(1), 33.
16. J. R. Schuster and J. L. Russell Jr, ‘Proceedings of ERDA Contractors Review Meeting, Chemical Energy Storage Hydrogen Energy Systems’, (CONF-761134), 1976, 106.
17. J. L. Russell Jr, K. H. McCorkle, J. H. Norman, J. R. Schuster, and P. W. Trester, ‘Development of Thermochemical Water Splitting for Hydrogen Production at General Atomic Company’, Report GA-A-14050, 1976.
18. M. S. Casper ed., ‘Hydrogen Manufacture by Electrolysis, Thermal Decomposition, and Unusual Techniques’, Noyes Data Corp, Park Ridge, 1978.
19. C. E. Bamberger, *Cryogenics*, 1978, **18**(3), 170.
20. T. Ohta, ‘Solar-hydrogen Energy Systems’, Pergamon Press, Oxford, 1979.
21. L. Williams, ‘Hydrogen Power’, Pergamon Press, New York, 1980.
22. R. H. Carty, M. M. Mazumder, J. D. Schreider, and J. B. Panborn, ‘Thermochemical Hydrogen Production’, GRI-80/0023, Gas Research Institute for the Institute of Gas Technology, Chicago, 1981, Vol. 1-4.
23. G. E. Beghi, ‘Nucl. Heat Appl., Proc. Tech. Comm. Meet. Workshop’, Krakow, Poland, 1984, Meeting Date 1983, p. 315.
24. J. Gretz, ‘Solar Energy ’85’, 1985, 115.
25. G. E. Beghi, *Int. J. Hydrogen Energy*, 1986, **11**(12), 761.
26. C. W. Pretzel and J. E. Funk, ‘The Development Status of Solar Thermochemical Hydrogen Production’, Sandia Report 86-8056, 1987.
27. S. Yalcin, *Int. J. Hydrogen Energy*, 1989, **14**(8), 551.

28. T. Ohta, *NATO ASI Series, Series E: Appl. Sci.*, 1995, **295**, 69. (Hydrogen Energy System).
29. M. Momirlan and T. N. Veziroglu, *Renew. Sus. Energy Rev.*, 1999, **3**, 219.
30. T. Kodama, *Prog. Energy Combustion Sci.*, 2003, **29**(6), 567.
31. J. E. Funk, *Int. J. Hydrogen Energy*, 2001, **26**, 185.
32. K. Onuki, H. Nakajima, S. Kubo, M. Futakawa, S. Higashi, G.-J. Hwang, T. Masaki, K. Ikenoya, S. Ishiyama, N. Akino, and S. Shimizu, 'Hydrogen Planet, World Hydrogen Energy Conference, 14th', Montreal, QC, Canada, June 9-13, 2002, 2003.
33. S. Kubo, H. Nakajima, S. Kasahara, S. Higashi, T. Masaki, H. Abe, and K. Onuki, *Nucl. Eng. Design*, 2004, **233**(1-3), 347.
34. B. W. McQuillan, L. C. Brown, G. E. Besenbruch, R. Tolman, T. Cramer, and B. E. Russ, 'High Efficiency Generation of Hydrogen Fuels Using Solar-thermochemical Splitting of Water: Annual Report', GA-A24972, San Diego, CA, 2005.
35. S. Abanades, P. Charvin, G. Flamant, and P. Neveu, *Energy*, 2006, **31**(14), 2805.
36. K. Verfondern, *Schriften Forschungszentrums Juelich, Energy Technol.*, 2007, **58**(i-ii), 1.
37. T. Kodama and N. Gokon, *Chem. Rev.*, 2007, **107**(10), 4048.
38. R. R. Sadhankar, *Int. J. Energy Res.*, 2007, **31**(12), 1131.
39. T. Nakamura, *Solar Energy*, 1977, **19**, 467.
40. B. M. Abraham and F. Schreiner, *Ind. Eng. Chem. Fundam.*, 1974, **13**(4), 305.
41. R. Palumbo, J. Lede, O. Boutin, E. Elorza Ricart, A. Steinfeld, S. Moeller, A. Weidenkaff, E. A. Fletcher, and J. Bielicki, *Chem. Eng. Sci.*, 1998, **53**, 2503.
42. A. Weidenkaff, A. Reller, A. Wokaun, and A. Steinfeld, *Thermochim. Acta*, 2000, **359**, 69.
43. A. Weidenkaff, A. Reller, F. Sibieude, A. Wokaun, and A. Steinfeld, *Chem. Mater.*, 2000, **12**, 2175.
44. A. Steinfeld, *Solar Energy*, 2005, **78**, 603.
45. A. Weidenkaff, A. Wuillemin, A. Steinfeld, A. Wokaun, B. Eichler, and A. Reller, *Solar Energy*, 1999, **65**, 59.
46. E. A. Fletcher, *Ind. Eng. Chem. Res.*, 1999, **38**(6), 2275.
47. T. Nakamura, *Solar Energy*, 1977, **19**, 467.
48. H. Kaneko, N. Gokon, N. Hasegawa, and Y. Tamaura, *Energy*, 2005, **30**, 2171.
49. Y. Tamaura and H. Kaneko, *Solar Energy*, 2005, **78**(5), 616.
50. R. D. Palumbo, A. Rouanet, and G. Pichelin, *Energy -Int. J.*, 1995, **20**, 857.
51. S. Abanades and G. Flamant, *Energy*, 2006, **80**(12), 1611.
52. F. Sibieude, M. Ducarroir, A. Tofighi, and J. Ambriz, *Int. J. Hydrogen Energy*, 1982, **7**, 79.
53. M. Lundberg, *Int. J. Hydrogen Energy*, 1993, **18**, 369.
54. Wikipedia, 'Concentrating Solar Power', from Wikipedia—the free encyclopedia; 2010, available at: http://en.wikipedia.org/wiki/Comparisation_of_CSP_plants.
55. R. Garland, *Preprints of Symp.—Am. Chem. Soc., Div. Fuel Chem.*, 2007, **52**(2), 231.
56. C. W. Forsberg, *Int. J. Hydrogen Energy*, 2003, **28**(10), 1073.
57. T. Nakayama, H. Yoshioka, H. Furutani, H. Kameyama, and K. Yoshida, *Int. J. Hydrogen Energy*, 1984, **9**(3), 187.
58. M. Sakurai, M. Aihara, N. Miyake, A. Tsutsumi, and K. Yoshida, *Int. J. Hydrogen Energy*, 1992, **17**(8), 587.
59. M. Sakurai, A. Tsutsumi, and K. Yoshida, *Int. J. Hydrogen Energy*, 1995, **20**(4), 297.
60. M. Sakurai, E. Bilgen, A. Tsutsumi, and K. Yoshida, *Int. J. Hydrogen Energy*, 1996, **21**(10), 865.
61. Y. Tadokoro, T. Kajiyama, N. Sakai, H. Kameyama, and K. Yoshida, *Int. J. Hydrogen Energy*, 1997, **22**(1), 49.
62. X. Wu and K. Onuki, *Tsinghua Sci. Technol.*, 2005, **10**(2), 270.
63. S. Kubo, H. Nakajima, S. Kasahara, S. Higashi, T. Masaki, H. Abe, and K. Onuki, *Nucl. Eng. Des.*, 2004, **233**, 347.
64. M. Yamawaki, T. Nishihara, Y. Inagaki, K. Minato, H. Oigawa, K. Onuki, R. Hino, and M. Ogawa, *Int. J. Hydrogen Energy*, 2007, **32**(14), 2719–2725.
65. D. R. O'Keefe, C. L. Allen, G. E., Besenbruch, L. C. Brown, J. H. Norman, R. Sharp, and K. McCorkle, *Int. J. Hydrogen Energy*, 1982, **7**, 381.
66. R. H. Carty and W. L. Conger, *Int. J. Hydrogen Energy*, 1980, **5**(1), 7.
67. P. W. T. Lu, *Int. J. Hydrogen Energy*, 1983, **8**(10), 773.
68. W. Weirich, K. F. Knoche, F. Behr, and H. Barnert, *Nucl. Eng. Des.*, 1984, **78**(2), 285.
69. E. Bilgen, *Solar Energy*, 1988, **41**(2), 199.
70. Y. H. Jeong, M. S. Kazimi, K. J. Hohnholt, and B. Yildiz, 'Optimization of the Hybrid Sulfur Cycle for Hydrogen Generation', Massachusetts Institute of Technology Center for Advanced Nuclear Energy Systems, Cambridge, MA, 2005, available at <http://web.mit.edu/canes/pdfs/reports/nes-004.pdf>.
71. C. Bilgen, A. Broggi, and E. Bilgen, *Solar Energy*, 1986, **36**(3), 267.
72. M. B. Gorensen and T. B. Edwards, *Ind. Eng. Chem. Res.*, 2009, **48**(15), 7232.
73. R. Moore, E. Parma, P. Pickard, B. Russ, W. Sweet, L. C. Brown, M., Helie, and P. Carles, 'Sulfur-iodine Thermochemical Cycle', DOE Hydrogen Program FY, 2008, available online at: www.hydrogen.energy.gov/pdfs/progress08/ii_h_1_pickard.pdf.
74. K. Onuki, S. Shimizu, H. Nakajima, S. Fujita, Y. Ikezoe, S. Sato, and S. Machi, 'Proceedings of the 8th World Hydrogen Energy Conference', Hawaii, 1990, Vol. 2, 547.
75. H. Engels and K. F. Knoche, *Int. J. Hydrogen Energy*, 1986, **11**, 703.
76. S. Sato, S. Shimizu, H. Nakajima, and Y. Ikezoe, *Int. J. Hydrogen Energy*, 1983, **8**, 15.
77. J. H. Norman, G. E. Besenbruch, L. C. Brown, D. R. O'Keefe, and C. L. Allen, 'General Atomics Report', GA-A 16713, 1982.

78. M. Tolga Baltaa, I. Dincer, and A. Hepbaslia, *Int. J. Hydrogen Energy*, 2009, **34**(7), 2925.
79. M. A. Rosen, G. F. Naterer, R. Sadhankar, and S. Suppiah, 'Canadian Hydrogen Association Workshop', Quebec, October 2006.
80. M. A. Lewis, M. S. Ferrandona, D. F. Tattersonb, and P. Mathias, *Int. J. Hydrogen Energy*, 2009, **34**(9), 4136.
81. M. S. Ferrandon, M. A. Lewis, D. F. Tatterson, A. Gross, D. Doizi, L. Croizé, V. Dauvois, J. L. Roujou, Y. Zanella, and P. Carles, *Int. J. Hydrogen Energy*, 2010, **35**(3), 992.
82. M. S. Ferrandon, M. A. Lewis, F. Alvarez, and E. Shafirovich, *Int. J. Hydrogen Energy*, 2010, **35**(5), 1895.
83. G. F. Naterer, S. Suppiah, M. A. Lewis, K. Gabriel, I. Dincer, M. A. Rosen, M. Fowler, G. Rizvi, E. B. Easton, B. M. Ikeda, M. H. Kaye, L. Lu, I. Pioro, P. Spekkens, P. Tremaine, J. Mostaghimi, A. Avsec, and J. Jiang, *Int. J. Hydrogen Energy*, 2009, **34**(7), 2901.
84. M. Dokya and Y. Kotera, *Int. J. Hydrogen Energy*, 1976, **1**, 117.
85. C. Chukwu, G. F. Naterer, and M. A. Rosen, 'Process Simulation of Nuclear-produced Hydrogen with a Cu-Cl Cycle', '29th Conference of the Canadian Nuclear Society', Toronto, Ontario, Canada, June 1-4, 2008.
86. M. F. Orhan, I. Dincer, and M. A. Rosen, *Int. J. Hydrogen Energy*, 2008, **33**(22), 6456.
87. M. A. Rosen, *Energy*, 2010, **35**(2), 1068.
88. A. Aochi, T. Tadokoro, K. Yoshida, H. Kameyama, M. Nobue, and T. Yamaguchi, *Int. J. Hydrogen Energy*, 1989, **14**(7), 421.
89. K. Yoshida, H. Kameyama, T. Aochi, M. Nobue, M. Aihara, R. Amir, H. Kondo, T. Sato, T. Tadokoro, T. Yamaguchi, and N. Sakai, *Int. J. Hydrogen Energy*, 1990, **15**(3), 171.
90. M. Sakurai, Y. Miyake, A. Tsutsumi, and K. Yoshida, *Int. J. Hydrogen Energy*, 1996, **21**(10), 871.
91. M. Sakurai, E. Bilgen, A. Tsutsumi, and K. Yoshida, *Solar Energy*, 1996, **57**(1), 51.
92. A. T-Raissi, N. Z. Muradov, C. Huang, and O. Adebisi, *J. Solar Energy Eng.*, 2007, **129**, 2.

Lithium Ion Batteries for Transportation and Electrical Energy Storage Applications: Nuclear Magnetic Resonance Studies of Structure and Function

Jordi Cabana

Lawrence Berkeley National Laboratory, Berkeley, CA, USA

and

Clare P. Grey

Stony Brook University, Stony Brook, NY, USA and University of Cambridge, Cambridge, UK

1	Introduction	375
2	NMR Studies of Lithium Ion Battery Electrode Materials: Background	377
3	Lithium Ion Electrode Chemistries	378
4	Concluding Remarks	389
5	Acknowledgments	389
6	Related Articles	389
7	Abbreviations and Acronyms	389
8	References	389

1 INTRODUCTION

Current concern about limited energy resources, coupled with the need to decrease greenhouse gas emissions, has motivated a push to move beyond an oil-based economy by making use of renewable energies on a much larger scale. The widespread implementation of hybrid and electric vehicles forms part of this strategy, since it both increases the efficiency of fuel use and allows for fuel diversification (since multiple fuels can be used to produce the electricity). However, the intermittent and/or diffuse nature of renewable sources requires efficient means with which to store electrical energy, which is clearly also a key requirement for electrical means of transportation. Among the various conversion/storage systems proposed over the two last centuries, electrochemical storage and, more specifically, batteries seem to be very well positioned to satisfy many of these needs. In particular, Li ion batteries offer the highest energy density among the currently available technologies, with ever-improving power

capabilities. Lithium ion batteries, however, currently fall short of some of the goals established for the end-use applications. For instance, for electric drive vehicles,¹ energy density, safety, and cost are all concerns. Therefore, mature as the technology may appear, both fundamental research and development are still needed to enable technological breakthroughs and market penetration of lithium ion batteries, to provide solutions to some of these energy challenges.²

Lithium ion batteries were first commercialized by Sony Corporation in 1990,³ making use of the discoveries and extensive knowledge in intercalation chemistry accumulated by inorganic and solid state chemists in the 1970s and, in particular, the work of John Goodenough and coworkers on LiCoO₂.^{4–6} The first generation of such batteries allowed more than twice the energy to be stored than nickel or lead batteries of the same size and mass, and did not suffer from problems such as the “memory effect.” These batteries consisted of LiCoO₂ and graphitic carbon at the positive (cathode) and negative (anode) electrode, respectively, both electrodes operating via a redox reaction involving Li intercalation into

the host material. Thus, the field of intercalation chemistry has contributed significantly to the development of lithium ion technology, to date, primarily for use in portable electronics such as laptops and mobile phones. In the almost 20 years of life of the lithium ion battery, we have witnessed a continuous progress in the discovery and optimization of new intercalation materials for this application,^{7,8} and alternatives to LiCoO₂ have reached the market at different levels, bringing about incremental improvements in performance. A ubiquitous approach has consisted in the partial substitution of Co in the octahedral sites of the layered, α -NaFeO₂-type framework by other metals such as Mn, Ni, and/or Al, leading to a vast array of candidates with different compositions and, in some cases, enhanced storage capacity (energy) and cycle life. Examples that have received a great deal of attention are LiNi_{0.8}Co_{0.2}O₂⁹ and LiNi_{1/3}Co_{1/3}Mn_{1/3}O₂, since these electrode materials show higher rate (power) performances and capacity, respectively.^{10,11} Another family of materials with the same basic layered structure, Li[Ni_xLi_(1/3-2x/3)Mn_(2/3-x/3)]O₂,^{12,13} is also receiving considerable attention, because its complex mechanism of lithium extraction, which involves significant structural rearrangements in the 1st cycle, leads to noticeably higher capacities than LiCoO₂.

The search for new materials was revolutionized by the discovery in 1999 that the application of a thin carbon-coating on the particle surface enabled the extraction of essentially all of the Li ions from LiFePO₄.¹⁴ This phospho-olivine was first proposed for use as a positive electrode by Padhi *et al.*,¹⁵ but in this initial work, only 0.6 Li could be extracted, largely because of the low electronic conductivity of this phase. It has now been shown that careful tailoring at the nanoscale can lead to outstanding performance.^{16–19} As a consequence, LiFePO₄ is a strong candidate to be the positive electrode of choice in the next generation of batteries designed for transportation, because of the low cost of the raw materials, low toxicity, and excellent thermal stability.²⁰ Furthermore, the voltage at which this material operates (3.5 V) means that it is considered to be a “safe” material, since it is well below the decomposition potential of the electrolyte (approximately 4.3–4.5 V, vs Li),²¹ as opposed to the larger operation windows, extending to above 4.3 V, required for LiMO₂-type phases. The success achieved with this compound has led to an increased interest in other lithium transition metal phosphate phases as possible electrode materials,²² with two structural types, olivine^{15,23} and NASICON,^{24,25} gaining the most attention.

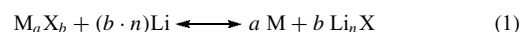
Despite these critical advances, many of the materials that follow intercalation mechanisms upon lithium extraction/insertion have intrinsic limitations in terms of capacity and rate, which are derived from their redox mechanism of operation and structural aspects. Indeed, the ability to reversibly intercalate lithium ions is mostly limited by the changes a crystal structure is able to withstand, in the presence of Li vacancies and changes of the oxidation state (and thus size and coordination preference) of the

metal ion.²¹ Most materials are synthesized in their fully lithiated state, and the fully and partially delithiated phases are generally metastable with respect to different crystal type(s) or toward decomposition and oxygen loss. Thus, the kinetics associated with the transformation of the metastable phases is crucial, and has been studied in much detail.^{26,27} The quest to identify improved materials that are stable in the charged and discharged states has never been so intense.²⁸

Increasing the capacity of both the anode and cathode requires that processes or redox reactions are found that involve multiple changes in (formal) oxidation state of the redox active element, which are (i) reversible, (ii) occur in the appropriate voltage windows, (iii) involve minimal changes in volume, and (iv) minimal changes in the host structure. Ideally, the materials should also be good electronic and ionic conductors. Since it is difficult, in practice, to identify materials that simultaneously fulfill all these criteria, much research has focused on materials that meet many of these criteria, to design strategies to overcome or minimize some of their inherent problems.

The first example of this strategy, which brings about substantial increases in storage capacity, is the use of metals and semimetals that can electrochemically and reversibly form alloys with lithium.²⁹ The capacities that can be achieved from these alloying reactions can reach extremely high values, both by weight and by volume (e.g., 8322 mA h cm⁻³ and 3572 mA h g⁻¹ for silicon compared to 975 mA h cm⁻³ and 372 mA h g⁻¹ for graphite, where the volumetric capacity has been calculated on the basis of the original volume of graphite and silicon) because phases with a large lithium content (e.g., Li_{3.75}Si and Li_{4.4}Sn) are stable. However, the practical utilization of these reactions has been severely handicapped by the huge volume changes associated to the (de)alloying process, which introduce large strains in the particles of active material, leading to pulverization and, subsequently, to capacity loss.³⁰ The strategies used to circumvent these issues involve (i) the dilution of the active material in an inert matrix that can absorb the stresses, (ii) limiting the range over which the materials are cycled, and (iii) the development of new binders.³¹ The efforts in this direction have proved successful, and have resulted in press releases announcing the commercialization of batteries that contain Sn- or Si-based negative electrodes.

A second advance in the field came with the discovery of materials that operate via what is now referred to as a *conversion reaction*. This concept was first demonstrated by Idota *et al.* in 1997, where a tin-based amorphous oxide was used as the anode material in a Li ion battery, the reaction mechanism relying on the formation of metal particle surrounded by an oxide phase.³² The reaction can be generalized as follows:



where M is the metal, X is the anion, and n is the formal oxidation state of X. A subsequent report that several simple

transition metal oxides can reversibly deliver huge stable capacities,³³ largely because of the nanometric character of the composite structure formed on cycling, has led to extensive research in this area. As a result, conversion reactions have now been reported for binary M–X compounds with X = O, N, F, S, P, and even H. While most of these compounds react at low voltages, in principle, making them suitable alternatives for the negative electrode, some of the more ionic fluoride phases were shown to be active at potentials above 2 V. Therefore, in contrast to alloy-based electrodes, the use of materials that react through conversion reactions could potentially result in a whole new array of candidates for the positive electrode with very high energy densities.^{34,35} Given that the positive electrode is currently the component that limits the energy of lithium ion batteries, this solution could constitute a significant advance. However, several issues remain that hinder the commercial realization of conversion-based electrodes: (i) unsatisfactory cycling performance; (ii) an unacceptably large, in terms of energy loss, voltage hysteresis between discharge and charge; (iii) the virtually ubiquitous large columbic inefficiency observed in the first cycle. While efforts have been directed to solve the first problem, basically employing electrode design strategies similar to those used for alloy electrodes, the origins for the other two are largely unresolved. While the reaction appears to be rather simple on paper, the details of the mechanism of reaction upon conversion and reformation are yet to be fully unraveled, with some studies hinting at differences that could be behind the observed hysteresis.³⁶ It is thus clear that more fundamental knowledge needs to be acquired before technological solutions to these three barriers can be proposed.

In general, the research advances in this field have been huge and have involved contributions from multiple research groups worldwide; this review cannot cover all of them. We hope, however, to touch on some of the key areas and highlight how nuclear magnetic resonance (NMR) spectroscopy has played an important role in some of these discoveries and advances.

2 NMR STUDIES OF LITHIUM ION BATTERY ELECTRODE MATERIALS: BACKGROUND

Understanding the processes that are at the origin of both successful and unsatisfactory electrochemical behavior of electrode materials is of the utmost importance so as to allow a rational design of new alternatives that outperform the current candidates. The implementation of new technology cannot come with a penalty in terms of cycle life of the device. Hence, the mechanisms by which the electrodes react with lithium need to be well understood in order to locate possible sources of failure. While long-range structural information is typically available from diffraction methods, solid state magic angle spinning (MAS) NMR is an extremely useful tool

for characterizing local structure in these materials, even in highly disordered systems. The lithium nuclei (⁷Li and ⁶Li) are typically (but by no means exclusively) used as probes because it is the lithium ions that are directly involved in the electrochemical processes. The NMR spectra are strongly influenced by the electronic structure of the materials, and it is often possible to distinguish between insulators and conductors, and between diamagnets and paramagnets. The method is quantitative and can be used to determine which species are removed on charging the battery and how the local structures change on extended cycling. NMR is also sensitive to dynamics that occur on the NMR timescale. When experiments at different temperatures are combined with two-dimensional (2D) exchange NMR, additional information regarding the diffusion of lithium and/or electron hopping can also be obtained.^{37–40} The use of NMR to characterize electrode material structure was extensively reviewed by one of us a few years ago.^{41–43} This review, therefore, focuses on some of the newer applications of NMR subsequent to those publications. The earlier reviews discussed, in considerable detail, the interactions that govern the NMR signals and outlined how these interactions could be used to extract structural, electronic, and magnetic information from these materials. While a brief summary of the various interactions is now presented, we refer the reader to the aforementioned articles for a more detailed analysis of NMR shift mechanisms. A wide range of other nuclei have been used to complement the Li NMR studies, and these are reviewed where appropriate throughout the text.

The NMR studies of materials in this field have been dominated by the use of ⁶Li and ⁷Li NMR. Both Li nuclei are quadrupolar (⁶Li, spin, $I = 1$; ⁷Li, $I = 3/2$), and the quadrupole interaction—the interaction between the quadrupole moment and the electric field gradient at the nucleus—due to the surrounding electrons and nuclei can be used to probe distortions in the local environment and the dynamics of the Li⁺ ions. The chemical shift range for lithium NMR spectra is very small and it is not always possible to resolve resonances due to different local environments in the NMR spectra of diamagnetic materials, based solely on the chemical shift interaction. Many of the electrode materials are, however, either paramagnetic or metallic and the interactions with the unpaired localized or conduction electrodes result in interactions that dominate the spectra, particularly at high fields. The interactions can be divided into two categories, those that occur through-space, namely, the dipolar interactions between the local fields caused by the nuclear and electronic magnetic moments, and the through-bond (hyperfine) interactions that are transmitted via the bonds between atoms. The hyperfine interaction (in paramagnetic solids) is a measure of the unpaired electron spin density that is transferred from the paramagnet to the s-orbital of the nucleus under investigation. In paramagnetic materials, this interaction gives rise to a “Fermi-contact” shift, which depends on both the values of the thermally averaged magnetic

moments of the nearby paramagnets and a hyperfine coupling constant, A. The latter is a measure of the extent and nature of the overlap between the Li s-orbital and the (metal, M) orbitals that contain the unpaired electrons, and in the case of the transferred hyperfine interaction, the intervening, atoms (generally, anions, X). Both interactions have been used to extract structural and electronic information from these solids. In particular, we and others^{41–43} have analyzed the shifts produced in a variety of lithium-containing paramagnetic solids, and have extracted rules and correlations that link the observed shift with the number and bond angles of the Li–X–M connectivities that characterize the Li local environment. These correlations work well in many systems, because the bond angles dictate which d-orbitals (in the case of transition metal ions) overlap with the nearby anion p-orbitals. For example, a so-called 90° interaction (i.e., a Li–X–M bond angle of 90°) allows for maximum overlap of the t_{2g} metal orbitals with the X orbitals, while a 180° interaction maximizes the overlap involving the e_{2g} orbitals, where t_{2g} and e_g labels refer to the d-orbital splittings for octahedral symmetry. Since the thermally averaged values of the magnetic moments are proportional to the susceptibility, the sizes of the shifts will be affected by any residual magnetic interactions (anti- or ferromagnetic) that exist between the ions, even in the paramagnetic state. An investigation of the temperature dependence of the shift, $\delta(T)$, can be used to investigate these interactions. For Curie paramagnets showing a clear $1/\delta(T)$ dependence on temperature, T, the extrapolation of $1/\delta(T)$ to zero gives an estimate of the Weiss constant.

Although NMR spectroscopy has been used to obtain detailed local structural information from battery materials, it has not been widely used to study batteries under realistic

operating conditions. The first in situ NMR experiments of batteries were performed using an NMR toroid cavity,⁴⁴ but poor signal-to-noise ratio was obtained and the toroid design was difficult to combine with a standard lithium ion battery. More recent experiments were performed by Letellier *et al.* to examine the insertion reaction of lithium in disordered carbon and graphitic anodes by ^7Li NMR spectroscopy employing a cell design based on the Bellcore plastic technology.^{45,46} This design is advantageous because the battery is flexible and does not require external pressure to maintain contact between the cathode, electrolyte, and anode. All in situ experiments performed to date were done in static mode, i.e., without MAS. The Bellcore design was also used in recent studies, as described in more detail below, and attempts are being made to expand the application of this in situ technique to other systems and even to design setups that enable the use of MAS.

3 LITHIUM ION ELECTRODE CHEMISTRIES

3.1 Layered Lithium Transition Metal Oxides

LiCoO_2 currently represents the most widely used positive electrode in commercial rechargeable lithium batteries. It has a layered framework corresponding to the $\alpha\text{-NaFeO}_2$ structure (space group $\text{R}\bar{3}\text{m}$, No. 166) with a close-packed oxygen ion array, and the transition metal (TM) and lithium ions occupying the octahedral sites in alternating layers (Figure 1). Unfortunately, the safety issues associated with LiCoO_2 , its poor rate performance, and the toxicity of

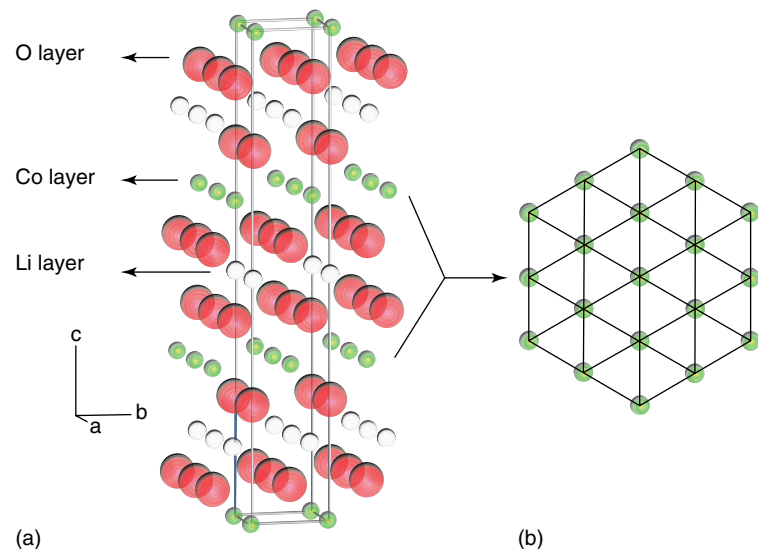


Figure 1 (a) The structure of the layered material LiCoO_2 , used in the first commercial lithium ion rechargeable battery. (b) The material adopts the $\alpha\text{-NaFeO}_2$ -type structure; the trigonal lattice of the transition metal layer (Co in this case) is shown. (Reproduced with permission from Ref. 57. © American Chemical Society, 2007.)

cobalt limit its use in applications where large batteries are required. This has motivated the study of a wide variety of other layered compounds that contain less or no cobalt at all, such as LiNiO_2 ,^{47,48} $\text{LiNi}_{1-y}\text{Co}_y\text{O}_2$,⁴⁹ LiMnO_2 ,⁵⁰ $\text{LiNi}_{1-y}\text{Mn}_y\text{O}_2$,^{51,52} and $\text{LiNi}_{1-y-z}\text{Mn}_y\text{Co}_z\text{O}_2$.^{13,53} NMR spectroscopy, as discussed in our earlier review article,⁴³ has played a key role in understanding the metal to insulator phase transformation in Li_xCoO_2 and the effect of metal substitution on the electronic structures of these phases.^{54–56}

Among the layered compounds, members of the compositional series $\text{Li}[\text{Ni}_x\text{Mn}_x\text{Co}_{1-2x}]\text{O}_2$, and $\text{Li}[\text{Ni}_x\text{Mn}_{(2-x)/3}\text{Li}_{(1-2x)/3}]\text{O}_2$, first synthesized independently by Ohzuku and Makimura⁵⁸ and Lu *et al.*,⁵⁹ show excellent electrochemical behavior and, consequently, have triggered a large amount of research. In particular, $\text{Li}[\text{Ni}_{1/3}\text{Mn}_{1/3}\text{Co}_{1/3}]\text{O}_2$, and $\text{Li}[\text{Ni}_{0.5}\text{Mn}_{0.5}]\text{O}_2$ show stable capacities of around 150 mA h g⁻¹ in the voltage window 3.5–4.2 V and a capacity of over 180 mA h g⁻¹ on cycling to 5.0 V.⁵⁸ ⁶*Li* MAS NMR spectroscopy has been extensively used to probe the local environments of the different ions and the changes in the electronic structure of the compounds upon charging. In particular, ⁶*Li* NMR spectroscopy has led to a detailed understanding of the cation local ordering in the $\text{Li}[\text{Ni}_x\text{Mn}_{(2-x)/3}\text{Li}_{(1-2x)/3}]\text{O}_2$ phases. Two distinct series of Li resonances were observed in the pristine materials, one due to the Li ions in the predominantly Li-containing layers, and a second due to Li in the TM layers. The second series of resonances, expected in the so-called Li excess materials ($x < 0.5$) but not in the end member composition $\text{Li}[\text{Ni}_{0.5}\text{Mn}_{0.5}]\text{O}_2$, could be used to quantify the number of Li ions in the TM layers and provided clear evidence for significant Li–metal (Ni²⁺) exchange between the layers, with the extent increasing as x increased. On the basis of the hyperfine shift observed for these resonances, Li was shown to occupy local environments in the TM layers surrounded by either six Mn⁴⁺ or five Mn⁴⁺ and one Ni²⁺ ion in its first cation coordination shell, in arrangements similar to that found in the [Mn⁴⁺_{2/3}Li⁺_{1/3}] layers of Li_2MnO_3 . Studies of these materials following charging and discharging showed that both the Li in the Li layers and in the TM layers participate in the electrochemistry.^{60–62} Even the Li in the Ni/Mn layers can be cycled reversibly, at least in the first few cycles, if the material is not charged to above 4.5 V. However, extended cycling to 4.6 V, or charging only once to 5.0 V, results in the complete removal of the lithium ions from this site, and reorganization of the cations within the TM layers.⁶²

More recent work by the authors and coworker (Zeng) has focused on the cobalt-containing family of compounds $\text{Li}[\text{Ni}_x\text{Mn}_x\text{Co}_{(1-2x)}]\text{O}_2$ ($0.01 \leq x \leq 1/3$).^{57,63} The local environment and short-range ordering were investigated using a combination of ⁶*Li* MAS NMR spectroscopy and neutron pair distribution function (PDF) analysis, associated with reverse Monte Carlo (RMC) calculations.⁵⁷ Several well-resolved resonances were observed in the compounds with low Ni/Mn contents ($x \leq 0.10$). These could be assigned on the basis

of predictions for Mn⁴⁺ and Ni²⁺ ions in the first and second coordination shells, confirming the oxidation state of the TM ions in these compounds (Figure 2). An analysis of the intensities of the resonances seen in a very dilute sample, ${}^6\text{Li}[\text{Ni}_{0.02}\text{Mn}_{0.02}\text{Co}_{0.96}]\text{O}_2$, indicated the formation of “Ni²⁺/Mn⁴⁺ clusters” in the TM layers, even at these low doping levels. A few isolated Ni³⁺ ions were observed in the TM layers, their concentrations depending on the synthesis method. The presence of Ni²⁺–Mn⁴⁺ clustering in materials with higher Ni and Mn contents was confirmed by PDF analysis of neutron diffraction data. $\text{Li}[\text{Ni}_{1/3}\text{Mn}_{1/3}\text{Co}_{1/3}]\text{O}_2$ contained a nonrandom distribution of Ni and Mn cations in the TM layers, with more Ni and Mn contacts in the first coordination shell, while the Co ions were distributed randomly. The disappearance of local environments for lithium containing only Co³⁺ ions in the first and second coordination shells, with increasing Ni/Mn content, with the disappearance of the well-resolved electrochemical signature of a metal–insulator transition. A more recent study has focused on the structural changes seen in $\text{Li}[\text{Ni}_{0.05}\text{Mn}_{0.05}\text{Co}_{0.90}]\text{O}_2$ upon electrochemical lithium deintercalation.⁶³ Li NMR showed that the ions in the first cation coordination shell of Mn⁴⁺ were extracted first, although Ni acts as the redox center. Since Ni and Mn cluster, these Li ions are still near Ni. Further deintercalation (an additional 0.2 mol of Li) induces an insulator to metal transition that is similar to that reported for LiCoO_2 . However, this reaction follows a solid solution mechanism even for this low level of substitution, rather than the two-phase reaction reported for the Ni,Mn-free oxide. The NMR results for deintercalation of more than 50% Li were compared to those for Li_xCoO_2 at similar stages of charge, and indicate that the behavior of these two phases at these potentials is very similar. NMR results for $\text{Li}[\text{Co}_{1/3}\text{Ni}_{1/3}\text{Mn}_{1/3}]\text{O}_2$ have also been performed as a function of state of charge, and reveal that some Li is found in the TM layers of this phase, the amount varying depending on the mode of synthesis.^{64,65}

3.2 Lithium Transition Metal Phosphates

3.2.1 Olivine Structures

The crystal structure of LiMPO_4 (M = Mn, Fe, Co, Ni) is formed by a hexagonal close-packed framework of oxygen ions, in which phosphorus ions occupy tetrahedral cavities, the lithium and iron ions being located in two different types of octahedral sites, commonly referred to as M1 and M2, respectively. This structural arrangement leads to linear and staggered chains of edge-sharing (M1) O_6 and corner-sharing (M2) O_6 octahedra, respectively, aligned parallel to the *b* direction. The existence of only one local environment for the lithium cations produces a single resonance, accompanied by an envelope of spinning sidebands, in the Li MAS NMR spectra of LiMPO_4 .^{66–70} The range of isotropic shifts was reported to span from 68 ppm for M = Mn to –86 ppm

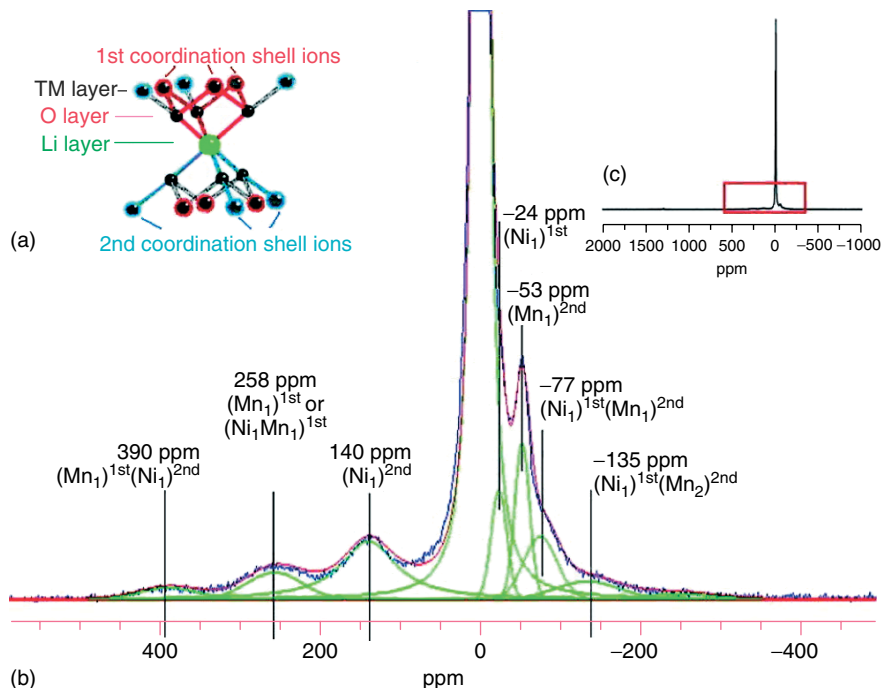


Figure 2 A ⁶Li MAS NMR spectrum of Li[Co_{0.96}Ni_{0.02}Mn_{0.02}]O₂, acquired by using a spinning speed of 38 kHz. The full spectrum (c) is dominated by the resonance due to the local environment Li(OCO₆)^{1st}(OCO₆)^{2nd}, i.e., the environment containing Co³⁺ ions only in the first and second coordination shells formed by the cations in the transition metal layers, above and below the Li layers. An enlargement of the region highlighted by the red box reveals a series of resonances, shifted from the spectral region expected for Li in environments nearby diamagnetic ions. A deconvolution of the spectrum (b) is shown (green peaks and red line (sum)) along with the signal assignments. The assignments are proposed on the basis of a consideration of how the unpaired electrons in the Ni²⁺ and Mn⁴⁺ d-orbitals overlap with the nearby oxygen p-orbitals, and thus transfer electron density from the paramagnetic ions to the Li s-orbitals. Scheme (a) depicts the arrangement of the 12 neighboring atoms around a central lithium. (Ni_{x1}Mn_{y1})^{1st}(Ni_{x2}Mn_{y2})^{2nd} represents the composition of the two coordination shells for each lithium, where x and y, along with the subscripts 1 (for the first coordination shell) and 2 (for the second coordination shell), indicate the Ni²⁺ and Mn⁴⁺ contents, respectively. The other neighboring cations are all Co³⁺ (and Li⁺) and are omitted for clarity. (Reproduced with permission from Ref. 57. © American Chemical Society, 2007.)

for M = Co^{66,67} (Figure 3). The smaller magnitude of the hyperfine shift as compared to lithium TM oxides (*vide supra*) has been ascribed to the increase in the ionic character of the Li–O and M–O bonds as a result of the presence of covalent (PO₄) units, thereby weakening the hyperfine transfer of spin from the metal to the lithium ion. Indeed, the hyperfine coupling constant (A/h) for the Li–O–M interaction has been shown to be around an order of magnitude larger in spinel-type oxides⁷¹ than in olivine phosphates.⁷² The hyperfine constants for the P–O–M interaction in LiMPO₄ (M = Mn, Fe, Co, Ni) phases were systematically found to be around two orders of magnitude larger than the Li–O–M constants *in the same material* and huge shifts are observed in the ³¹P MAS NMR spectra of these materials, which range from 7296 ppm for M = Mn to 1706 ppm for M = Ni⁷² (Figure 3).

The causes of the Li shifts in LiMPO₄ are not fully understood yet and *simple* analyses of the bond angles of the different Li–O–M pathways (Table 1), which have been successfully employed to predict the sizes of the shifts in more symmetric solids based on cubic close-packed arrays, fail to predict their values. A striking example is the wide

range of Li shifts that have been observed for nominally stoichiometric LiFePO₄, which appear to depend strongly on its synthesis and processing conditions. Hamelet *et al.* report isotropic shifts of –14 and –30 ppm for two different samples prepared following a modified Pechini route and by direct precipitation in water under reflux conditions, respectively,⁶⁹ suggesting that the synthetic method has a notable effect. However, different shifts have been observed even for samples obtained using the same method, as in the case of LiFePO₄ synthesized hydrothermally from mixtures of FeSO₄ · xH₂O, LiOH, and H₃PO₄. While Tucker *et al.*^{66,67} and Recham *et al.*⁶⁸ report very similar values of –8 and –3 ppm for samples prepared at 120 and 180 °C, respectively, a shift of –56 ppm was observed by Cabana *et al.* for materials prepared by hydrothermal treatment at 220 °C.⁷⁰ Given the sensitivity of NMR to small distortions in the environment of the observed nucleus, it would be tempting to ascribe these differences to slight changes in the coordination sphere of lithium (see Table 1), especially if the shift mechanisms were dominated by Fermi contacts. However, no obvious correlation can be drawn between the geometric data for each

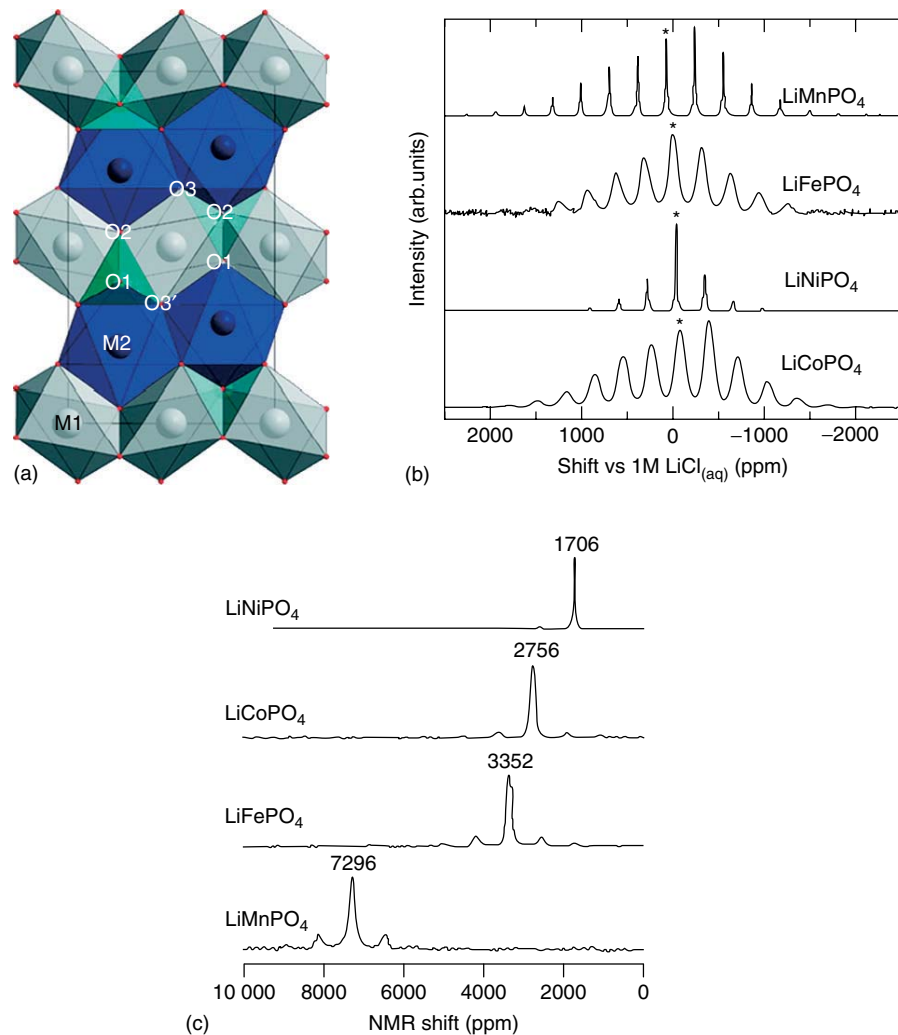


Figure 3 (a) Crystal structure (*ab* plane) (Reproduced with permission from Ref. 68. © American Chemical Society, 2008), (b) ⁷Li (Reproduced with permission from Ref. 67. © American Chemical Society, 2002), and (c) ³¹P MAS NMR spectra of different LiMPO₄ phases. (Reproduced with permission from Ref. 72. © Springer, 2007.)

Table 1 Local coordination environments of the M1 and M2 sites in the LiFePO₄ ideal olivine-type structure. Geometric data were obtained from a refinement of a sample synthesized hydrothermally at 220 °C⁷⁵

Site	Number of nearby cations	Number of Li–O–M interactions	Angle (°)	Distance (Å)
M1	2 in M1	2	88	3.0
		2	91	3.0
M2	6 in M2	2	94	3.3
		2	97	3.3
		2	112	3.6
		2	121	3.7
		4 in M2	94	3.3
		2	97	3.3
		2	112	3.6
		2	121	3.7
		4	127	3.9

of the measured samples and the corresponding observed shift (see Table 2), which adds to the evidence that the hyperfine couplings are not the sole contributor to these resonances. The most compelling example of this lack of correlation comes, from a comparison of the extremes in the shift dispersion, which correspond to LiFePO₄ prepared hydrothermally at 180 (−3 ppm) and 220 °C (−56 ppm); the corresponding crystal structures are almost identical (see Table 2). Another effect associated with changes in synthetic methods and conditions are the likely changes in micro and nanostructure (i.e., particle size and shape, degree of agglomeration, or aggregation) of the resulting powdered samples. Single-crystal measurements for LiFePO₄ have revealed that this material has a significant anisotropic contribution to the magnetic moment.⁷³ This observation suggests that the pseudocontact shift, i.e., the contribution to the isotropic shift due to the dipolar coupling between the Li nucleus and an anisotropic magnetic moment,

Table 2 Unit cell parameters of LiFePO₄ (space group: *Pnma*) synthesized using different synthetic conditions

Method	T (°C)	<i>a</i> (Å)	<i>b</i> (Å)	<i>c</i> (Å)	<i>V</i> (Å ³)	δ (ppm)	Reference
Hydrothermal	120	10.381	6.013	4.716	294.37	-8	(a) 66,67
	180	10.331	6.001	4.700	291.38	-3	68
	220	10.334	6.001	4.695	291.16	-56	70
Pechini	650	10.345	6.004	4.699	291.86	-14	69
Precipitation	100	10.314	5.993	4.695	290.21	-30	69

(a) Crystallographic data originally reported by Yang *et al.*⁷⁶ using the same conditions.

may be significant in this system.⁷⁴ Furthermore, since the overall shifts in this system are small, the relative contribution from a pseudocontact shift is likely to be larger. Calculations are underway to explore this proposal in greater detail.⁷⁴

NMR has been used to probe the defects in LiFePO₄, for example, the presence of lithium ions in both the M1 and M2 sites in the olivine structure. M2 Li occupancy can be related to the occurrence of intersite Fe/Li exchange⁷⁷ observed, for instance, in samples prepared by low-temperature synthetic routes,^{69,78,79} or to element substitution.^{68,80} In theory, the local environments of the M1 and M2 sites are different (see Table 1), so their corresponding resonances are expected to appear at different frequencies, especially if, as it is normally the case, the amount of defects is small and most iron ions stay in the M2 site. For instance, if we consider a Li on a M1 site, and then replace one of the nearby Fe²⁺ cations on a M2 site connected via a 110°–120° interaction by a Li ion, and move the Fe²⁺ ion moves onto a M1 site (associated with two Li–O–M interactions), then the total number of Li–O–Fe interactions will increase, resulting in a new environment with a large isotropic shift. In practice, other factors also affect the actual experimental values. Hamelet *et al.* report a small signal at +44 ppm that has been ascribed to the presence of lithium in the M2 site of a sample prepared by direct precipitation, in addition to the larger peak at -30 ppm assigned to the M1 site.⁶⁹ Given that the Fe²⁺–O–Li interactions in olivine-type phases systematically lead to negative shifts, the appearance of the resonance at large positive shifts was explained by the existence of either Fe³⁺ ions or clusters around the lithium defect in the M2 site. This conclusion was supported both by the observation of Fe³⁺ signals in the ⁵⁷Fe Mössbauer spectra, and by the large and positive ⁷Li NMR shifts reported for oxides⁸¹ and phosphates⁸² that exclusively contain this ion (vide infra). In a different example, Recham *et al.* have used Li MAS NMR to follow cationic site disorder in several members of the olivine-type Li_{1-x}Fe_{1+x}P_{1-x}Si_xO₄ system.⁶⁸ Li–Fe site disorder is induced as increasing amounts of iron and silicon are introduced in the structure, so that the lithium ions are no longer exclusively located in the M1 site. This mixing has several experimental consequences in the ⁷Li MAS NMR spectra. First, a new signal located at -110 ppm can be detected for x = 0.15, and is assigned to the creation of Li defects in (i.e., substitution on) the M2 site. Second, the

resonance due to the normal M1 site slightly shifts from -3 to -8 ppm with respect to the x = 0.0 spectrum. Both signals continue to shift to lower frequencies as the samples contain more iron and silicon, down to -26 and -125 ppm for the M1 and M2 sites, respectively, for x = 0.75. The increase in the absolute value of the ⁷Li NMR shift of the both the M1 and M2 resonances is likely due to the presence of an increasing number of paramagnetic Fe²⁺ ions in the M1 and M2 environments as a result of an increasing proportion of the Fe²⁺ later in the different phases. However, this argument does not satisfactorily explain why the shift for the M2 is larger than that for the M1 site. As shown in Table 2, a lithium ion in an M1 and M2 site have eight and four Li–O–M2 contacts at different angles, respectively, so, given that M2 is predominantly occupied by Fe, a larger shift would be expected for Li(M1). While this deviation may simply reflect the lack of understanding of the mechanisms that control the shift mechanisms in LiFePO₄ as discussed above, another possible explanation for the higher shift of Li(M2) is that the Fe²⁺ present in the M1 site tends to be clustered near the lithium defects in the M2 site, thereby increasing the amount of TM ions in the coordination sphere of these lithium ions. Using the quantitative character of NMR, the ⁷Li data was used in conjunction with ⁵⁷Fe Mössbauer spectroscopy to track the degree of Li–Fe disorder in Li_{1-x}Fe_{1+x}P_{1-x}Si_xO₄ as a function of Si-doping (x) (Figure 4).

Lithium can be electrochemically extracted from LiFePO₄ through a two-phase reaction that has FePO₄ as the final product. Such reaction can be easily followed by ³¹P NMR, as the initial signal at 3600 ppm due to the lithiated phase slowly decreases in intensity concomitant with the onset and growth of a new one at 5500 ppm, assigned to the delithiated phase. However, lithium miscibility has been reported in some cases for both end members before the onset of the actual first-order transition, leading to Li_αFePO₄ and Li_{1-β}FePO₄ intermediates with different values of α and β.⁸³ Such miscibility has been shown to depend on the temperature^{84,85} and the size and shape of the particles involved.^{80,86} Li_xFePO₄ (with, e.g., x = 0.6 or 0.34) solid solutions have also been successfully stabilized at room temperature by slow cooling or quenching of samples that were heated above the temperature of miscibility, and, especially in the case of Li_{0.6}FePO₄, subsequently characterized.^{75,84,85,87–91} While slow cooling produces multiphase samples that also

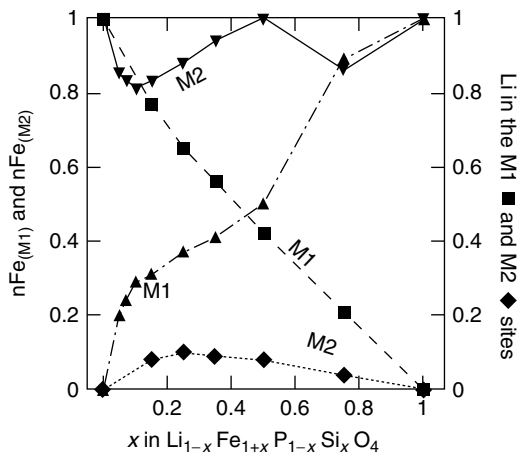


Figure 4 Cationic occupation of the M1 and M2 sites in the $\text{Li}_{1-x}\text{Fe}_{1+x}\text{P}_{1-x}\text{Si}_x\text{O}_4$ phases, as calculated from ^{57}Fe Mössbauer and ^7Li MAS NMR data. (Reproduced with permission from Ref. 68. © American Chemical Society, 2008.)

contain different proportions of the end members, quenching generally leads to single-phase samples. Neutron diffraction experiments indicate that $\text{Li}_{0.6}\text{FePO}_4$ shows long-range lithium/vacancy disorder,⁸⁷ but the possibility of short-range $\text{Li}^+-\text{Fe}^{2+}$ clustering so as to maintain charge neutrality along the framework cannot be ruled out. In turn, the ^{57}Fe Mössbauer signals of both Fe^{2+} and Fe^{3+} could be resolved at room temperature, pointing to the existence of electron localization and absence of hopping at the timescale of this spectroscopic technique (in the order of megahertz).^{89,91} Electron hopping was subsequently observed upon heating, thereby raising the question as to whether some slow-motional process already takes place even at room temperature. All these questions can potentially be resolved by using the short-range sensitivity and longer timescale of the NMR experiment. In particular, the coalescence of different resonances can sometimes be observed if the timescale of any motion that involves exchange between the different environments that give rise to these resonances is of the order of the frequency separation between them. Motion is also visible via the averaging of anisotropic interactions, such as the quadrupolar and dipolar interactions. Given that the frequency separations and anisotropic interactions are typically associated with frequencies or sizes of hundreds of hertz to many kilohertz, these result in sensitivity of the NMR experiment to motion in the 0.1–10 ms timescale.

Evidence of both Li–electron (i.e., Fe^{2+}) correlation and electron hopping, albeit with different degrees, was found for both the $\text{Li}_{0.6}\text{FePO}_4$ and $\text{Li}_{0.34}\text{FePO}_4$ phases that coexist in multiphase crystals (with LiFePO_4 and/or FePO_4 as the other components). These multiphase crystals result from the partial delithiation and heat treatment of LiFePO_4 grown hydrothermally at 220 °C, which shows single ^7Li and ^{31}P resonances at –56 and 3600 ppm, respectively. $\text{Li}_{0.6}\text{FePO}_4$

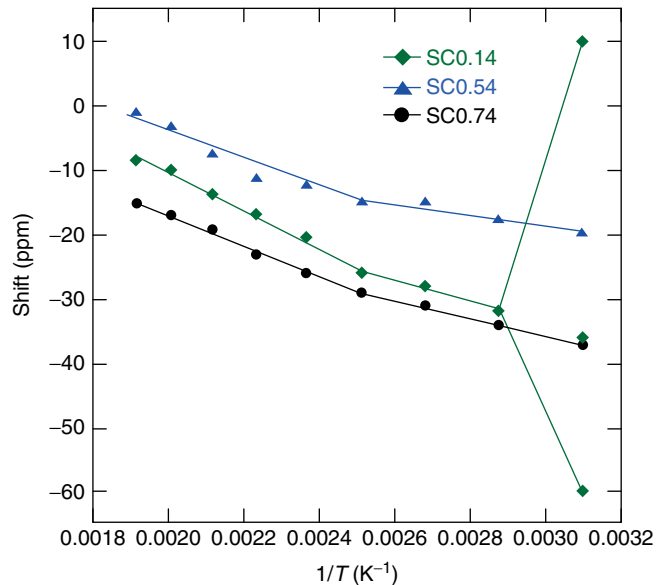


Figure 5 Evolution of the ^7Li MAS NMR shifts with $1/T$ for samples containing a mixture of FePO_4 and $\text{Li}_{0.34}\text{FePO}_4$ (SC0.14), LiFePO_4 and $\text{Li}_{0.6}\text{FePO}_4$ (SC0.54), and FePO_4 and $\text{Li}_{0.6}\text{FePO}_4$ (SC0.74). (Reproduced with permission from Ref. 70. © American Chemical Society, 2010.)

shows a single ^7Li MAS NMR resonance at –26 ppm at room temperature, and at least two environments were detected at –1 and –63 ppm for $\text{Li}_{0.34}\text{FePO}_4$. The existence of an intense resonance at a very similar position as that of LiFePO_4 was taken as a clear indication of the existence of $\text{Li}-\text{Fe}^{2+}$ clustering in a phase that only contains 0.34 Li per Fe. In turn, the existence of a single resonance for $\text{Li}_{0.6}\text{FePO}_4$ suggests that a degree of electronic hopping/lithium motion, and, therefore, signal averaging, may occur for this phase even at room temperature, whereas the resolution of (at least) two signals for $\text{Li}_{0.34}\text{FePO}_4$ indicates that the hopping/motion is slow enough on the timescale of ^7Li NMR, so that the coalescence of the resonances is not observed. The ^{31}P MAS NMR spectra of both compounds are composed of series of resonances at different shift positions, covering a range that extends from ca. 3000 to 5800 ppm, consistent with the existence of a complex distribution of Fe^{3+} and Fe^{2+} within these phases. Motion was significantly enhanced for both solid solution phases on heating up to 250 °C. In the case of $\text{Li}_{0.6}\text{FePO}_4$, a change in the slope of a plot of shift ($\text{Figure } 5$) versus $1/T$, (which is expected to be linear due to the temperature dependence of the magnetic susceptibility of the compound (vide supra)) was observed above 100 °C, for all samples containing this phase. This was ascribed to a change in mechanism and/or extent of electronic/ionic hopping above this temperature: At this temperature, both the Li^+ ions and electrons start to hop independently, entropy effects dominating over the weak lithium–electron (Fe^{2+}) interaction. This indicates that this interaction, although weaker than for

$\text{Li}_{0.34}\text{FePO}_4$, also exists in $\text{Li}_{0.6}\text{FePO}_4$ at room temperature. The generation around 50–75 °C of a new coalesced signal for $\text{Li}_{0.34}\text{FePO}_4$, with a shift corresponding to the weighted average of the resonances at room temperature, indicates that lithium and electron mobility within this compound are highly concerted at these temperatures. A change in the temperature dependence of the shift was again observed above 100 °C (Figure 5) and was similarly assigned to the disruption of the lithium–electron correlation and the consequent induction of independent lithium motion and electron hopping. These results offered very valuable insight into the structural and transport features of the two-phase LiFePO_4 – FePO_4 system, thereby providing a clear example of how powerful a technique NMR can be for the characterization of inorganic solids with application to lithium ion batteries.

A striking change in the chemical properties of LiFePO_4 toward oxidation was unraveled when comparing the thermal behavior of samples composed of particles with noticeably different particle sizes.⁶⁹ Micrometric particles are stable up to 300 °C before they decompose into $\text{Li}_3\text{Fe}_2(\text{PO}_4)_3$ and Fe_2O_3 , as shown by X-ray diffraction (XRD). In contrast, progressive oxidation of iron was observed between 180 and 240 °C for a nanometric sample, inducing a progressive shift of the XRD peaks to higher angles while the overall collection of reflections due to an olivine structure is retained. Such oxidation was confirmed by MAS NMR; once again, the presence of Fe^{3+} in samples that were heat-treated at 170–240 °C resulted in new ${}^7\text{Li}$ signals at positive shifts, as opposed to the negative shift at –30 ppm of the dominant resonance for the pristine sample, along with the appearance of a FePO_4 -like ${}^{31}\text{P}$ signal at 5560 ppm. The large proportion of intensity found under the peaks generated by Fe^{3+} -rich environments and their position is an indication of the considerable degree of oxidation that the phase undergoes without either losing the olivine framework or suffering severe lithium loss, thereby creating a novel compound that was tentatively formulated as $\text{Li}_{0.97}\text{Fe}_{0.74}\text{PO}_4$ following the refinement of neutron diffraction data.

3.2.2 NASICON-Type Structures

Although LiFePO_4 is, by far, the most commercially viable phosphate-based lithium battery electrode material studied by NMR, other phases with interesting properties, such as $\text{Li}_3\text{M}_2(\text{PO}_4)_3$ with M = Fe, V, have also been widely investigated. Complete lithium extraction from $\text{Li}_3\text{V}_2(\text{PO}_4)_3$, with subsequent oxidation of V from 3+ to 5+ would result in a very attractive theoretical capacity of 197 mA h g^{−1}. However, in practice, only 2/3 of this value has been obtained after extended cycling.⁹² Two polytypes have been described for $\text{Li}_3\text{M}_2(\text{PO}_4)_3$, one with a monoclinic distortion (also referred to as *polytype (A)*) and another one with a NASICON-type framework (B).^{92–94} The monoclinic unit cell of $\text{A-Li}_3\text{M}_2(\text{PO}_4)_3$ contains three crystallographic sites with equal occupancies of lithium, consistent with the observation

of three resolvable Li NMR resonances of the same intensity. For M = V, they appear at 17, 52, and 103 ppm,^{40,95–97} whereas for M = Fe, the observed shifts were at 45, 102, and 216 ppm.⁸² The larger values for the latter are explained by the existence of more unpaired electron density in Fe^{3+} (high spin d^5 configuration) than in V^{3+} (d^2). Assignment of the resonances to the different sites was made on the basis of the predicted strength of the Fermi contact between the TM ions and Li^+ in each environment.^{40,82} This prediction was achieved by assuming that the delocalization mechanism for electron density transfer dominates in these compounds, due to the existence of unpaired electrons in t_{2g} orbitals and close-to-90° Li–O–M interactions. In contrast, only one lithium resonance at 85 ppm was resolved for $\text{B-Li}_3\text{V}_2(\text{PO}_4)_3$, in agreement with the single crystallographic site in the NASICON framework.⁹⁴

Detailed studies of the mobility of lithium between the three crystallographic sites in $\text{A-Li}_3\text{M}_2(\text{PO}_4)_3$ have been performed by combining 1D data collected at different temperatures with 2D exchange NMR spectroscopy.^{40,82} Lithium exchange occurred even at room temperature between the three sites in the monoclinic structure and low degrees of thermal activation were sufficient to produce signal averaging. The activation energies for a hop to take place, calculated from 2D data acquired at different temperatures, range from 0.6 to 0.8 eV and vary depending on the actual path. The variations in activation energy were successfully correlated with the distance between exchange sites and the size of the bottleneck for diffusion, as defined by the area created by O vertices of PO_4 and FeO_6 polyhedra; short distances and large O–O spacings were shown to favor Li–Li exchanges. The facile motion of lithium within the structure of $\text{A-Li}_3\text{V}_2(\text{PO}_4)_3$ is thought to be, at least in part, at the origin of the good performance toward lithium extraction reported for this compound.⁹² Additional information regarding the motion of the alkali ions within their sites in this phase was later obtained from ${}^6\text{Li}({}^{31}\text{P})$ rotational-echo, double-resonance (REDOR) NMR.⁹⁷ Such motion could be detected for all three sites by comparing the relative attenuation of dipolar couplings at each site with respect to simulations of a hypothetical case in the absence of motion. The magnitude of the attenuation was shown to correlate well with the size of the actual crystallographic void, taken as the shortest Li–O distance. The work on $\text{A-Li}_3\text{V}_2(\text{PO}_4)_3$ clearly highlights a powerful characteristic of solid state NMR; i.e., the capability of probing mobility within a crystal framework.

The structural changes upon lithium (de)intercalation from $\text{A-Li}_3\text{V}_2(\text{PO}_4)_3$ were followed by using a combination of diffraction techniques and Li MAS NMR spectroscopy. A series of complex line phases, namely, $\text{Li}_{2.5}\text{V}_2(\text{PO}_4)_3$, $\text{Li}_2\text{V}_2(\text{PO}_4)_3$, and $\text{LiV}_2(\text{PO}_4)_3$, were formed upon extraction,^{95,96,98} which, in turn, gave rise to a series of discrete resonances for the compounds, with the total number of resonances decreasing from 5 (at 189, 122, 51, 28, and –9 ppm) to 2 (143 and 77 ppm) and, finally, 1 (at 138 ppm),

respectively. The existence of well-resolved peaks indicates a high degree of ordering. Combined with diffraction, these results indicate that lithium is first extracted from the Li_1 site (appearing at the lowest frequency, 17 ppm), leading to a structure with V^{3+} and V^{4+} ordering. While the nature of this ordering has not been fully elucidated for $\text{Li}_{2.5}\text{V}_2(\text{PO}_4)_3$,⁹⁸ in $\text{Li}_2\text{V}_2(\text{PO}_4)_3$, the charges were shown to arrange in columns running along the b axis, generating two crystallographic sites for vanadium. Lithium ions in Li_1 and Li_2 only have contacts with one type of TM ion, consistent with the presence of only two resonances.^{95,96} $\text{LiV}_2(\text{PO}_4)_3$ only contains lithium in one site (related to the original Li_2 , at 103 ppm) and V^{4+} , and, therefore, one peak is to be expected. The transitions between the intermediate phases upon lithium deintercalation are all first order. Although full understanding of the mechanisms that lead to the shift values in all phases has not been achieved, Li MAS NMR still offered valuable insight into the charge ordering differences produced by the electrochemical extraction from and reinsertion into the framework of A- $\text{Li}_3\text{V}_2(\text{PO}_4)_3$.

Strikingly, the mechanism for reintercalation was quite different: $\text{V}_2(\text{PO}_4)_3$ is lithiated to form $\text{Li}_2\text{V}_2(\text{PO}_4)_3$ via a solid solution $\text{Li}_x\text{V}_2(\text{PO}_4)_3$ and $\text{LiV}_2(\text{PO}_4)_3$ is no longer formed as an intermediate line phase.⁹⁶ A fingerprint of this hysteresis is the generation of ${}^7\text{Li}$ MAS NMR spectra with a larger degree of complexity; the peaks are now notably broader and, for $\text{Li}_x\text{V}_2(\text{PO}_4)_3$ with $0 \leq x \leq 1$, new weaker peaks exist at 182, 166, 92, and 32 ppm, suggesting that $\text{V}^{4+}/\text{Li}^+$ ordering is not complete. The hysteresis is ascribed to the absence of charge ordering in $\text{V}_2(\text{PO}_4)_3$ and thus the lack of a driving force to order the lithium and vacancies, as occurs in $\text{Li}_2\text{V}_2(\text{PO}_4)_3$. As a consequence, contrary to what happens upon extraction, the Li_1 and Li_2 sites are filled simultaneously. This reinsertion mechanism explains why two discrete resonances, at 77 and 134 ppm, dominate the spectra for $x \geq 0.75$, in contrast with the single resonance at 138 ppm observed for the line phase $\text{LiV}_2(\text{PO}_4)_3$ upon extraction. The similarity of these shifts to those of $\text{Li}_2\text{V}_2(\text{PO}_4)_3$ is taken as further confirmation of the simultaneous filling of Li_1 and Li_2 (Figure 6). Despite

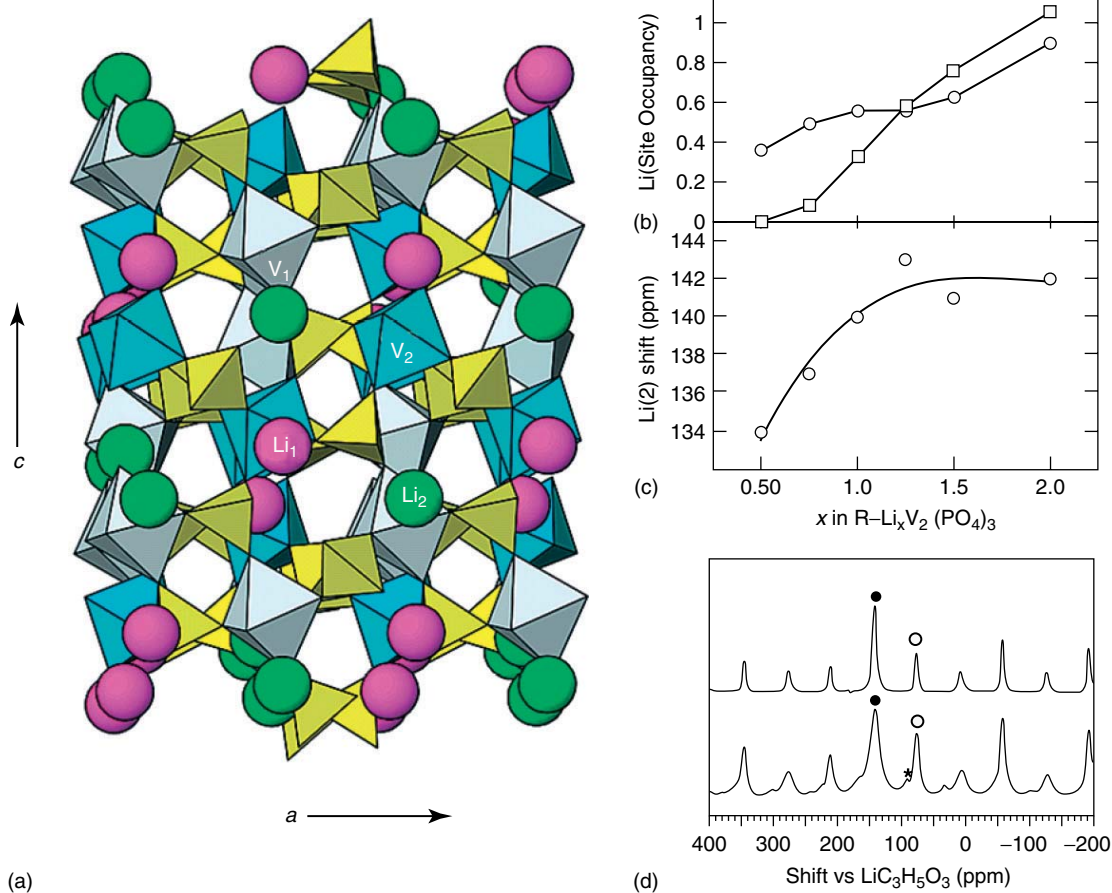


Figure 6 (a) Representation of the unit cell of A- $\text{LiV}_2(\text{PO}_4)_3$; (b) site occupancy; (c) evolution of the shift value with the Li content in $\text{Li}_x\text{V}_2(\text{PO}_4)_3$ (squares: Li_1 ; circles: Li_2); (d) comparison of the ${}^7\text{Li}$ MAS NMR spectra for $\text{Li}_2\text{V}_2(\text{PO}_4)_3$ obtained upon lithium deintercalation (top) and re-intercalation (bottom). (Reproduced with permission from Ref. 96. © American Chemical Society, 2003.) Closed and open circles indicate isotropic resonances

this structural disorder, still no filling of the Li_3 site occurs, possibly due to the same mechanisms (i.e., size of the bottleneck to access the site, *vide supra*) that render lithium exchange difficult between this site and Li_1/Li_2 . The $\text{Li}_2\text{V}_2(\text{PO}_4)_3$ phases formed both upon lithium deintercalation and reintercalation show similar ^{7}Li MAS NMR spectra (Figure 6). The newly generated $\text{V}^{3+}/\text{V}^{4+}$ ordering induces a two-phase transition upon further lithium intercalation to form $\text{Li}_3\text{V}_2(\text{PO}_4)_3$ again.

A NASICON-like structure is also produced upon lithiation of $\text{LiTi}_2(\text{PO}_4)_3$ to form $\text{Li}_3\text{Ti}_2(\text{PO}_4)_3$,^{99,100} and good reversibility was observed.¹⁰¹ This process entails a displacement of the lithium ions already in the structure into a new site within a larger cavity, where the newly inserted ions are also located. Two crystallographic positions for lithium ions are generated in the cavity after the intercalation is complete. The short Li–Li distance created by this arrangement is thought to be at the origin of the partial occupancies found for these sites after Rietveld refinement. This complex arrangement results in a subsequently complex ^{7}Li MAS NMR spectrum, with a set of, at least, seven resonances that range from 0 to 75 ppm, in contrast to the single resonance at ca. –4 ppm observed for $\text{LiTi}_2(\text{PO}_4)_3$.¹⁰⁰ The difference in shift magnitude is due to the creation of unpaired electron spin density as Ti^{4+} is reduced to Ti^{3+} . The presence of lithium or a vacancy in either of the two sites available was shown to create a distortion of the neighboring (TiO_6) octahedra, which are, in turn, connected to other lithium sites. This distortion must affect the efficiency of the Fermi contact between Ti and Li, through O, and it is expected to produce slight changes in shift. Since a given lithium site is connected to three (TiO_6) octahedra, a large number of environments are possible with the different lithium sites subsequently connected to these neighboring octahedra being empty or full. As a consequence, a variety of environments with slight differences in $\text{Li}^+-\text{O}-\text{Ti}^{3+}$ angles and distances are possible, thereby generating a complex spectrum with a large number of resonances.

3.2.3 Other Phosphate-Containing Phases

The six different lithium environments in $\text{Li}_5\text{V}(\text{PO}_4)_2\text{F}_2$, a compound with a 2D layered structure, have been resolved by NMR.¹⁰² Initial assignment to the crystallographic sites was carried out based on the correlation of site multiplicities and resonance intensity and the rationalization of the strength of the Li–O/F–V interaction from their proximity to ideal 90° geometry for a delocalization mechanism. Some of the ambiguities were resolved by analyzing the 2D exchange NMR spectra and postulating that exchange predominates between sites in close geometric proximity. Following the same hypothesis, the data also revealed that Li ions can exchange as long as their environments share a face. Mobility is more prominent along channels in the *a*-direction but is impeded through the lithium layers that lie in the (100) plane. However, the timescale for this mobility was found to be much

longer than for $\text{Li}_3\text{V}_2(\text{PO}_4)_3$, which may partially explain the poorer electrochemical performance toward lithium extraction of this phase.

3.3 Novel Negative Electrodes Based on Non-oxidic and Mixed Anion Phases

The quest for alternatives to graphite as the negative electrode has benefited from the extensive developments that have occurred during the past 20 years in the field of inorganic chemistry of oxide-free or mixed anion phases. Indeed, several lithium TM nitrides were proposed as high-energy density, long-cycle life candidates in the 1990s.^{103–105} Among them, Li_7MnN_4 , from which lithium can be topotactically deintercalated, shows very stable capacities of ca. 300 mA h g^{−1}, mostly at voltages above 1 V,^{39,103} which makes it a safe material vis-à-vis the reactivity against the electrolyte.²¹ Nevertheless, its considerable sensitivity to contact with air or moisture constitutes a severe handicap toward its practical application. More recently, in an effort to find novel phases with enhanced stability and good electrochemical properties, several lithium TM oxynitrides with similar reactivity as electrodes were evaluated, with those containing Mn showing the most attractive performance.^{106–109} In addition to capacities above 300 mA h g^{−1} that can be sustained over tens of cycles, $\text{Li}_{7.9}\text{MnN}_{3.2}\text{O}_{1.6}$ and Li_7MnN_4 have been recently shown to have excellent high rate capabilities (Figure 7), especially when compared to a state-of-the-art material such as $\text{Li}_4\text{Ti}_5\text{O}_{12}$.¹¹⁰ The origin of such promising performance lies not only on the small volume changes undergone by the phases during lithium (de)intercalation but also on the 3D antifluorite framework and, in the case of the oxynitride, the presence of cationic vacancies that enable fast lithium diffusion. ^{6}Li MAS NMR was a key technique in identifying motional processes in these phases. Facile mobility of lithium within the pristine compound was identified by performing experiments at several temperatures; while distinct resonances, corresponding to nonequivalent lithium environments, can be resolved at room temperature, progressive coalescence into a single resonance was observed upon heating^{39,108} (Figure 7). The fact that full coalescence is observed at lower temperatures in $\text{Li}_{7.9}\text{MnN}_{3.2}\text{O}_{1.6}$ than in Li_7MnN_4 indicates that presence of vacancies in the former is beneficial for the mobility of lithium. Nonetheless, the existence of chemical exchange between certain lithium environments in Li_7MnN_4 was demonstrated even at room temperature by using 2D exchange ^{6}Li MAS NMR,³⁹ further proving that these antifluorite-type phases are excellent lithium conductors. Conduction of lithium at room temperature becomes even faster as Li is removed from the structure; the ^{6}Li MAS NMR spectra of samples, when as little as 0.5 mol Li is extracted, comprise single very broad peaks that become narrower upon further oxidation,^{39,108} an unequivocal sign that extensive lithium motion is occurring at these stages. Indeed, this enhanced motion upon lithium removal seems to be at the origin of a peculiar behavior of these materials. While

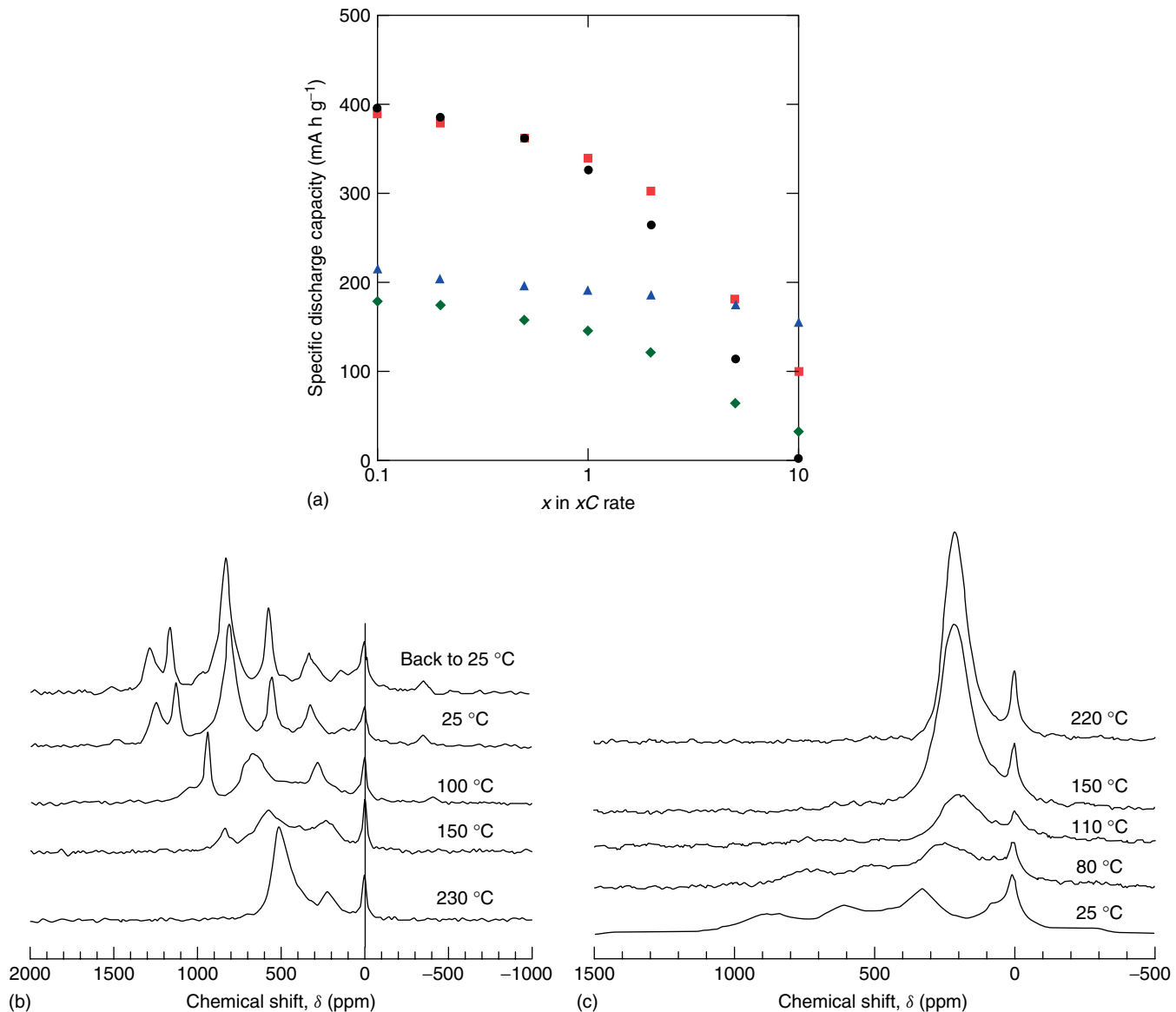


Figure 7 (a) Rate capability of $\text{Li}_{7.9}\text{MnN}_3.2\text{O}_{1.6}$ (red squares) and Li_7MnN_4 (black circles) as electrodes in lithium batteries, compared to two samples of $\text{Li}_4\text{Ti}_5\text{O}_{12}$, one made in the laboratory (green diamonds) and the second, commercially available (blue triangles). (Reproduced with permission from Ref. 110. © Elsevier, 2010). Variable temperature ^{29}Si MAS-NMR spectra of (b) Li_7MnN_4 (Reproduced with permission from Ref. 39. © The Electrochemical Society, 2005) and (c) $\text{Li}_{7.9}\text{MnN}_3.2\text{O}_{1.6}$. (Reproduced with permission from Ref. 108. © Elsevier, 2005.)

good capacities and cycle life were observed at fairly fast rates, excellent performance was reported at current densities as high as 5C when a first preconditioning charge at moderate rates ($C/10$) is performed compared to a cycling regime without this step.¹¹⁰ Owing to the thorough NMR characterization of the materials, it can be hypothesized that since more lithium can be removed during a slow initial charge, a larger amount of lithium vacancies are created that enhance mobility and rate capability upon subsequent cycling.

Another family of mixed anion compounds with interesting properties as electrodes in lithium batteries is that of $\text{Sr}_2\text{MnO}_2\text{Cu}_{2m-0.5}\text{S}_{m+1}$ ($m = 1-3$).¹¹¹ They consist

of alternating perovskite-type Sr_2MnO_2 layers and copper sulfide antifluorite-type layers of different thickness (as defined by m). Copper can be extruded in the form of metal particles as lithium is inserted electrochemically, in an extrusion reaction that proved to be very reversible, leading to capacities of 100–200 mA h g^{-1} . It was observed that a correlation exists between m and the electrochemical performance; while the capacity increases with m , the cycle life worsens. This correlation was related to the structural integrity that is provided by the inactive perovskite block, which does not undergo any changes during the copper extrusion, thereby enabling the conservation of the framework

during the reaction.¹¹² ^{6,7}Li MAS NMR was used to show that lithium substitutes for copper in the antifluorite layers and is coordinated by sulfide ions. The reaction of copper extrusion and lithium insertion follows a complex mechanism that appears to involve intermediate sites and partial reduction of Mn.¹¹³ Moreover, variable temperature experiments have also shown that the mobility of lithium in the structure increases with *m*,¹¹¹ which is thought to facilitate lithium transport in and out of the phases.

3.4 Conversion Reactions

NMR spectroscopy has been used to follow the structural transformations that occur in conversion reactions. To date, the technique has been used to probe four different phenomena. First, NMR is extremely sensitive to the formation of any intercalation compounds before the conversion reaction starts. Second, the method is sometimes sensitive to the sizes of the metal nanoparticles that are formed during the reaction. Third, and most importantly, because these conversion reactions generally involve the formation of nanoparticles, the structures of these materials are extremely difficult to follow using conventional probes for long-range structures; thus, NMR spectroscopy can be used to identify the formation of products that could not be seen by diffraction because they are too small. Finally, NMR can be used to test hypotheses concerning the nature of the metal–salt interfaces, for example, those formed on reducing RuO₂ to Li₂O and ruthenium nanoparticles.¹¹⁴

For the conversion reaction involving the cathode material FeF₃, ⁶Li, and ⁷Li NMR spectroscopy was used to show that an insertion reaction into the ReO₃-type structure occurs via two steps: a two-phase reaction between Li = 0 and 0.5 occurs first—the Li_{0.5}FeF₃ phase formed gives rise to a Li NMR resonance due to Li⁺ near both Fe³⁺ and Fe²⁺ ions.¹¹⁵ Second, a single-phase intercalation reaction occurs between Li = 0.5 and 1.0, the Li NMR indicating a progressive increase in the concentration of Fe²⁺ ions. In the second region (the conversion reaction), nanosized Fe metal (\sim 3 nm) is formed, as seen by XRD. LiF can be detected by NMR even when its concentration is too low to be detected by diffraction. The observation of the LiF signal, albeit with very large spinning manifolds ascribed to the dipolar interactions between Li ions and the unpaired electrons in Fe⁰, indicates that the Fe⁰ particles are superparamagnetic and not ferromagnetic, consistent with the sizes of these particles estimated by XRD. The charge process involves the formation of a series of intercalation phases with increasing Fe oxidation state, as detected by Li NMR. An NMR and XRD study was performed on the rutile compound FeF₂, and by comparing the results from both these systems, the reconversion reaction of FeF₃ was shown to occur directly via the formation of a lithiated rutile phase, not a ReO₃ phase, the lithium incorporation and iron oxidation state increasing with state of charge. The final material obtained on charging to 4.0 V, contains both Fe²⁺ and

Fe³⁺ and has a composition close to Li_{0.5}FeF₃ consistent with the capacity estimated from the electrochemical curve and with theoretical predictions that rationalized the formation of this phase. A rutile lattice had been observed in earlier transmission electron microscope (TEM) results,¹¹⁶ but it was unclear as to how to account for the electrochemical results that were not consistent with the formation of a FeF₂ lattice with an iron oxidation state of 2+. The NMR results provided clear evidence that this rutile phase is lithiated, at least below 4 V, and that it contained both Fe²⁺ and Fe³⁺.

The conversion reaction mechanisms of CuS, CuF₂, and CuO following electrochemical reaction with Li were studied by solid state ⁶³Cu, ¹⁹F, ⁷Li NMR, and XRD.¹¹⁷ For CuS, NMR spectroscopy provided clear evidence for a two-step reaction, which was associated with an insertion reaction involving, first, limited incorporation of Li into CuS, and then, a two-phase reaction to form a material with approximate composition of LiCuS. This is followed by a conversion reaction to form Li₂S and Cu, with Cu_{1.96}S being formed as a sideproduct of the decomposition of LiCuS. In contrast, a direct conversion reaction to form LiF and Cu is seen for CuF₂, while the ⁷Li NMR results indicated that CuO could tolerate a small amount of Li substitution before reacting to form Li₂O and Cu. Both the diffraction and NMR results indicated that the size of the Cu particles formed on discharge is much larger in the CuS system, which is thought to result from the higher Cu¹⁺ mobilities in the intermediate intercalation compounds Li_xCuS.

3.5 Silicon

The crystalline-to-amorphous phase transition that occurs in crystalline silicon electrodes on electrochemical Li insertion during the first discharge to form Li_xSi hinders attempts to link the structure in these systems with electrochemical performance. A combination of static, in situ and magic angle spinning, ex situ ⁷Li NMR studies were applied to investigate the changes in local structure that occur in an actual working lithium battery.¹¹⁸ A series of crystalline lithium silicides were first synthesized to develop an understanding of the factors that control the lithium chemical shifts seen in this system. For the diamagnetic (semiconducting) phases, Li₁₂Si₇, Li₇Si₃, Li₁₃Si₄, and Li₁₅Si₄, clear chemical shift ranges for Li were detected. Lithium ions near the rings, small clusters, and [Si=Si]⁴⁻ pairs found in the phases with lower lithium contents resonated close to 18 ppm, while lithium ions near isolated silicon anions, with formal charge Si⁴⁻, resonated near 6 ppm. In contrast, the metallic phase Li₂₁Si₅ showed distinct Knight-shifted (due to the interaction of Li with the conduction electrons) resonances 60–80 ppm.

Similar shifts were observed for the samples of Li_xSi prepared electrochemically to those found for the semiconducting phase, allowing the structural evolution to be monitored. The first discharge occurs via the formation of isolated Si ions and smaller Si–Si clusters embedded in

a Li matrix; the latter are broken apart at the end of the discharge forming isolated Si ions. A spontaneous reaction of the lithium silicide with the electrolyte is directly observed in the in situ NMR experiments; this mechanism results in self-discharge, and, potentially, capacity loss. This reaction was particularly pronounced for the crystalline phase $\text{Li}_{15}\text{Si}_4$ formed right at the end of discharge. Furthermore, new lithium resonance was observed for this phase (at approximately -10 ppm) that differed from that observed in the ex situ experiments ($+6\text{ ppm}$). This difference was ascribed to the nonstoichiometry of the $\text{Li}_{15}\text{Si}_4$ phase and the formation of phases with excess lithium via the electrochemical reaction with lithium. These highly lithiated phases are extremely reactive, and could not be detected in the ex situ NMR experiments unless the phases were very quickly removed from a discharged battery. This study provides a clear advantage of the in situ approach to capture metastable and short-lived phases. From a practical standpoint, the rate of this self-discharge process could be slowed down noticeable when the binder CMC (carboxymethylcellulose) was used to coat the particles.

4 CONCLUDING REMARKS

The development of NMR methods to investigate lithium ion battery electrode materials over the last few years has been impressive. The method has led to new insight into the structure, dynamics, and electronic properties, and has, without doubt, contributed to our understanding of how these classes of materials function. We hope that the work described in this review article, which has by no means been comprehensive, attests the role that NMR has played in this field. The considerable societal importance of lithium ion batteries, the impact that they will make in energy-related technologies, in addition to their already widespread use in portable technologies, and the tremendous increase in research in this field, ensures that NMR spectroscopy will continue to make ever-increasing contributions to this area.

5 ACKNOWLEDGMENTS

This work was supported by the Assistant Secretary for Energy Efficiency and Renewable Energy, Office of Vehicle Technologies of the US Department of Energy under Contract No. DE-AC02-05CH11231 via subcontract No. 6517749 with the Lawrence Berkeley National Laboratory. Clare P. Grey thanks all of her coworkers, students, postdoctoral workers, and collaborators, who have greatly contributed to the work described in this article over the last few years.

6 RELATED ARTICLES

Thermal Stability of Lithium Ion Battery Electrolytes.

7 ABBREVIATIONS AND ACRONYMS

2D = two-dimensional; CMC = carboxymethylcellulose; MAS = magic angle spinning; NMR = nuclear magnetic resonance; PDF = pair distribution function; REDOR = rotational-echo, double-resonance; RMC = reverse Monte Carlo; TEM = transmission electron microscope; TM = transition metal; XRD = X-ray diffraction.

8 REFERENCES

- U.S.A.B.C. ‘Energy Storage System Goals’. http://www.uscar.org/guest/article_view.php?articles_id=85 (accessed February 2010).
- M. Armand and J. M. Tarascon, *Nature*, 2008, **451**, 652.
- Y. Nishi, *Chem. Rec.*, 2001, **1**, 406.
- D. Guerard and A. Herold, *Carbon*, 1975, **13**, 337.
- M. S. Whittingham, *Prog. Solid State Chem.*, 1978, **12**, 41.
- K. Mizushima, P. C. Jones, P. J. Wiseman, and J. B. Goodenough, *Mater. Res. Bull.*, 1980, **15**, 783.
- M. S. Whittingham, *Chem. Rev.*, 2004, **104**, 4271.
- B. L. Ellis, K. T. Lee, and L. F. Nazar, *Chem. Mater.*, 2010, **22**, 691.
- C. Delmas, I. Saadoune, and A. Rougier, *J. Power Sources*, 1993, **44**, 595.
- Z. H. Lu, D. D. MacNeil, and J. R. Dahn, *Electrochim. Solid State Lett.*, 2001, **4**, A200.
- T. Ohzuku and Y. Makimura, *Chem. Lett.*, 2001, **7**, 642.
- Z. Lu, D. D. MacNeil, and J. R. Dahn, *Electrochim. Solid State Lett.*, 2001, **4**, A191.
- M. M. Thackeray, C. S. Johnson, J. T. Vaughey, N. Li, and S. A. Hackney, *J. Mater. Chem.*, 2005, **15**, 2257.
- N. Ravet, J. B. Goodenough, S. Besner, M. Simoneau, P. Hovington, and M. Armand, Abstract #127, *196th ECS Meeting*, Honolulu, October 17–22, 1999.
- A. K. Padhi, K. S. Nanjundaswamy, and J. B. Goodenough, *J. Electrochem. Soc.*, 1997, **144**, 1188.
- S. Y. Chung, J. T. Bloking, and Y. M. Chiang, *Nat. Mater.*, 2002, **1**, 123.
- P. S. Herle, B. Ellis, N. Coombs, and L. F. Nazar, *Nat. Mater.*, 2004, **3**, 147.
- C. Delacourt, P. Poizot, S. Levasseur, and C. Masquelier, *Electrochim. Solid State Lett.*, 2006, **9**, A352.
- B. Kang and G. Ceder, *Nature*, 2009, **458**, 190.
- D. D. MacNeil, Z. H. Lu, Z. H. Chen, and J. R. Dahn, *J. Power Sources*, 2002, **108**, 8.

21. J. B. Goodenough and Y. Kim, *Chem. Mater.*, 2010, **22**, 587.
22. M. S. Whittingham, Y. N. Song, S. Lutta, P. Y. Zavalij, and N. A. Chernova, *J. Mater. Chem.*, 2005, **15**, 3362.
23. S. Okada, S. Sawa, M. Egashira, J. Yamaki, M. Tabuchi, H. Kageyama, T. Konishi, and A. Yoshino, *J. Power Sources*, 2001, **97–98**, 430.
24. A. K. Padhi, K. S. Nanjundaswamy, C. Masquelier, and J. B. Goodenough, *J. Electrochem. Soc.*, 1997, **144**, 2581.
25. K. S. Nanjundaswamy, A. K. Padhi, J. B. Goodenough, S. Okada, H. Ohtsuka, H. Arai, and J. Yamaki, *Solid State Ionics*, 1996, **92**, 1.
26. A. R. Armstrong, N. Dupré, A. J. Paterson, C. P. Grey, and P. G. Bruce, *Chem. Mater.*, 2004, **16**, 3106.
27. J. Reed and G. Ceder, *Chem. Rev.*, 2004, **104**, 4513.
28. M. R. Palacin, *Chem. Soc. Rev.*, 2009, **38**, 2565.
29. A. N. Dey, *J. Electrochem. Soc.*, 1971, **118**, 1547.
30. A. Timmons and J. R. Dahn, *J. Electrochem. Soc.*, 2006, **153**, A1206.
31. D. Larcher, S. Beattie, M. Morcrette, K. Edstroem, J. C. Jumas, and J. M. Tarascon, *J. Mater. Chem.*, 2007, **17**, 3759.
32. Y. Idota, T. Kubota, A. Matsufuji, Y. Maekawa, and T. Miyasaka, *Science*, 1997, **276**, 1395.
33. P. Poizot, S. Laruelle, S. Grignon, L. Dupont, and J. M. Tarascon, *Nature*, 2000, **407**, 496.
34. F. Badway, F. Cosandey, N. Pereira, and G. G. Amatucci, *J. Electrochem. Soc.*, 2003, **150**, A1318.
35. M. Bervas, F. Badway, L. C. Klein, and G. G. Amatucci, *Electrochem. Solid-State Lett.*, 2005, **8**, A179.
36. R. E. Doe, K. A. Persson, Y. S. Meng, and G. Ceder, *Chem. Mater.*, 2008, **20**, 5274.
37. V. W. J. Verhoeven, I. M. de Schepper, G. Nachtegaal, A. P. M. Kentgens, E. M. Kelder, J. Schoonman, and F. M. Mulder, *Phys. Rev. Lett.*, 2001, **86**, 4314.
38. M. Wagemaker, A. P. M. Kentgens, and F. M. Mulder, *Nature*, 2002, **418**, 397.
39. J. Cabana, N. Dupré, G. Rousse, C. P. Grey, and M. R. Palacín, *Solid State Ionics*, 2005, **176**, 2205.
40. L. S. Cahill, R. P. Chapman, J. F. Britten, and G. R. Goward, *J. Phys. Chem. B*, 2006, **110**, 7171.
41. C. P. Grey and S. G. Greenbaum, *MRS Bull.*, 2002, **27**, 613.
42. C. P. Grey and Y. J. Lee, *Solid State Sci.*, 2003, **5**, 883.
43. C. P. Grey and N. Dupré, *Chem. Rev.*, 2004, **104**, 4493.
44. R. E. Gerald, R. J. Klingler, G. Sandi, C. S. Johnson, L. G. Scanlon, and J. W. Rathke, *J. Power Sources*, 2000, **89**, 237.
45. F. Chevallier, M. Letellier, M. Morcrette, J. M. Tarascon, E. Frackowiak, J. N. Rouzaud, and F. Beguin, *Electrochem. Solid State Lett.*, 2003, **6**, A225.
46. M. Letellier, F. Chevallier, and M. Morcrette, *Carbon*, 2007, **45**, 1025.
47. J. R. Dahn, U. von Sacken, and C. A. Michal, *Solid State Ionics*, 1990, **44**, 87.
48. A. D. Robertson and P. G. Bruce, *Chem. Mater.*, 2003, **15**, 1984.
49. Y. Paik, C. P. Grey, C. S. Johnson, J. S. Kim, and M. M. Thackeray, *Chem. Mater.*, 2002, **14**, 5109.
50. P. Mustarelli, V. Massarotti, M. Bini, and D. Capsoni, *Phys. Rev. B*, 1997, **55**, 12018.
51. W. P. Tang, H. F. Kanoh, X. J. Yang, and K. Ooi, *Chem. Mater.*, 2000, **12**, 3271.
52. M. H. Rossouw, D. C. Liles, and M. M. Thackeray, *J. Solid State Chem.*, 1993, **104**, 464.
53. C. S. Johnson, J. S. Kim, C. Lefief, N. Li, J. T. Vaughney, and M. M. Thackeray, *Electrochem. Commun.*, 2004, **6**, 1085.
54. D. Carlier, M. Ménétrier, and C. Delmas, *J. Mater. Chem.*, 2001, **11**, 594.
55. S. Levasseur, M. Menetrier, and C. Delmas, *J. Electrochem. Soc.*, 2002, **149**, A1533.
56. S. Levasseur, M. Menetrier, and C. Delmas, *J. Power Sources*, 2002, **112**, 419.
57. D. Zeng, J. Cabana, J. Bréger, W. S. Yoon, and C. P. Grey, *Chem. Mater.*, 2007, **19**, 6277.
58. A. D. Robertson, A. R. Armstrong, and P. G. Bruce, *Chem. Commun.*, 2000, 1997.
59. H. Kobayashi, Y. Arachi, H. Kageyama, and K. Tatsumi, *J. Mater. Chem.*, 2004, **14**, 40.
60. W. S. Yoon, N. Kim, X. Q. Yang, J. McBreen, and C. P. Grey, *J. Power Sources*, 2003, **119–121**, 649.
61. C. P. Grey, W. S. Yoon, J. Reed, and G. Ceder, *Electrochem. Solid State Lett.*, 2004, **7**, A290.
62. M. Jiang, B. Key, Y. S. Meng, and C. P. Grey, *Chem. Mater.*, 2009, **21**, 2733.
63. D. Zeng, J. Cabana, W. S. Yoon, and C. P. Grey, *Chem. Mater.*, 2010, **22**, 1209.
64. W. S. Yoon, C. P. Grey, M. Balasubramanian, X. Q. Yang, D. A. Fischer, and J. McBreen, *Electrochem. Solid State Lett.*, 2004, **7**, A53.
65. L. S. Cahill, S. C. Yin, A. Samoson, I. Heinmaa, L. F. Nazar, and G. R. Goward, *Chem. Mater.*, 2005, **17**, 6560.
66. M. C. Tucker, M. M. Doeff, T. J. Richardson, R. Fiñones, J. A. Reimer, and E. J. Cairns, *Electrochem. Solid State Lett.*, 2002, **5**, A95.
67. M. C. Tucker, M. M. Doeff, T. J. Richardson, R. Fiñones, E. J. Cairns, and J. A. Reimer, *J. Am. Chem. Soc.*, 2002, **124**, 3832.
68. N. Recham, M. Casas-Cabanas, J. Cabana, C. P. Grey, J. C. Jumas, L. Dupont, M. Armand, and J. M. Tarascon, *Chem. Mater.*, 2008, **20**, 6798.
69. S. Hamelet, P. Gibot, M. Casas-Cabanas, D. Bonnin, C. P. Grey, J. Cabana, J.-B. Leriche, J. Rodriguez-Carvajal, M. Courty, S. Levasseur, P. Carlach, M. Van Thourout, J. M. Tarascon, and C. Masquelier, *J. Mater. Chem.*, 2009, **19**, 3979.
70. J. Cabana, J. Shirakawa, G. Chen, T. J. Richardson, and C. P. Grey, *Chem. Mater.*, 2010, **22**, 1249.

71. M. C. Tucker, L. Kroek, J. A. Reimer, and E. J. Cairns, *J. Electrochem. Soc.*, 2002, **149**, A1409.
72. S. L. Wilcke, Y. J. Lee, E. J. Cairns, and J. A. Reimer, *Appl. Magn. Reson.*, 2007, **32**, 547.
73. G. Liang, K. Park, J. Y. Li, R. E. Benson, D. Vaknin, J. T. Markert, and M. C. Croft, *Phys. Rev. B*, 2008, **77**, 064414.
74. B. Zhou, D. Middlemiss, J. Cabana, and C. P. Grey (Unpublished).
75. G. Chen, X. Y. Song, and T. J. Richardson, *J. Electrochem. Soc.*, 2007, **154**, A627.
76. S. F. Yang, P. Y. Zavalij, and M. S. Whittingham, *Electrochem. Commun.*, 2001, **3**, 505.
77. M. S. Islam, D. J. Driscoll, C. A. J. Fisher, and P. R. Slater, *Chem. Mater.*, 2005, **17**, 5085.
78. S. F. Yang, Y. N. Song, P. Y. Zavalij, and M. S. Whittingham, *Electrochem. Commun.*, 2002, **4**, 239.
79. P. Gibot, M. Casas-Cabanas, L. Laffont, S. Levasseur, P. Carlach, S. Hamelet, J. M. Tarascon, and C. Masquelier, *Nat. Mater.*, 2008, **7**, 741.
80. M. Wagemaker, B. L. Ellis, D. Luetzenkirchen-Hecht, F. M. Mulder, and L. F. Nazar, *Chem. Mater.*, 2008, **20**, 6313.
81. J. Kim, U. G. Nielsen, and C. P. Grey, *J. Am. Chem. Soc.*, 2008, **130**, 1285.
82. L. J. M. Davis, I. Heinmaa, and G. R. Goward, *Chem. Mater.*, 2010, **22**, 769.
83. A. Yamada, H. Koizumi, S. I. Nishimura, N. Sonoyama, R. Kanno, M. Yonemura, T. Nakamura, and Y. Kobayashi, *Nat. Mater.*, 2006, **5**, 357.
84. C. Delacourt, P. Poizot, J. M. Tarascon, and C. Masquelier, *Nat. Mater.*, 2005, **4**, 254.
85. J. L. Dodd, R. Yazami, and B. Fultz, *Electrochem. Solid State Lett.*, 2006, **9**, A151.
86. N. Meethong, H. Y. S. Huang, W. C. Carter, and Y. M. Chiang, *Electrochem. Solid State Lett.*, 2007, **10**, A134.
87. C. Delacourt, J. Rodriguez-Carvajal, B. Schmitt, J. M. Tarascon, and C. Masquelier, *Solid State Sci.*, 2005, **7**, 1506.
88. R. Stevens, J. L. Dodd, M. G. Kresch, R. Yazami, B. Fultz, B. Ellis, and L. F. Nazar, *J. Phys. Chem. B*, 2006, **110**, 22732.
89. J. L. Dodd, I. Halevy, and B. Fultz, *J. Phys. Chem. C*, 2007, **111**, 1563.
90. S. Miao, M. Kocher, P. Rez, B. Fultz, R. Yazami, and C. C. Ahn, *J. Phys. Chem. A*, 2007, **111**, 4242.
91. H. J. Tan, J. L. Dodd, and B. Fultz, *J. Phys. Chem. C*, 2009, **113**, 2526.
92. H. Huang, S. C. Yin, T. Kerr, N. Taylor, and L. F. Nazar, *Adv. Mater.*, 2002, **14**, 1525.
93. F. D'Yvoire, M. Pintard-Scrépel, E. Bretey, and M. de la Rochère, *Solid State Ionics*, 1983, **9–10**, 851.
94. J. Gaubicher, C. Wurm, G. Goward, C. Masquelier, and L. Nazar, *Chem. Mater.*, 2000, **12**, 3240.
95. S. C. Yin, H. Grondby, P. Strobel, H. Huang, and L. F. Nazar, *J. Am. Chem. Soc.*, 2003, **125**, 326.
96. S. C. Yin, H. Grondby, P. Strobel, M. Anne, and L. F. Nazar, *J. Am. Chem. Soc.*, 2003, **125**, 10402.
97. L. S. Cahill, C. W. Kirby, and G. R. Goward, *J. Phys. Chem. C*, 2008, **112**, 2215.
98. S. C. Yin, P. S. Strobel, H. Grondby, and L. F. Nazar, *Chem. Mater.*, 2004, **16**, 1456.
99. C. Delmas, A. Nadiri, and J. L. Soubeyroux, *Solid State Ionics*, 1988, **28**, 419.
100. A. Aatiq, M. Menetrier, L. Croguennec, E. Suard, and C. Delmas, *J. Mater. Chem.*, 2002, **12**, 2971.
101. J. Y. Luo, L. J. Chen, Y. J. Zhao, P. He, and Y. Y. Xia, *J. Power Sources*, 2009, **194**, 1075.
102. Y. Makimura, L. S. Cahill, Y. Iriyama, G. R. Goward, and L. F. Nazar, *Chem. Mater.*, 2008, **20**, 4240.
103. M. Nishijima, N. Takodoro, Y. Takeda, N. Imanishi, and O. Yamamoto, *J. Electrochem. Soc.*, 1994, **141**, 2966.
104. T. Shodai, S. Okada, S. Tobishima, and J. Yamaki, *Solid State Ionics*, 1996, **86–88**, 785.
105. M. Nishijima, T. Kagokashi, Y. Takeda, M. Imanishi, and O. Yamamoto, *J. Power Sources*, 1997, **68**, 510.
106. J. Cabana, G. Rousse, A. Fuertes, and M. R. Palacin, *J. Mater. Chem.*, 2003, **13**, 2402.
107. J. Cabana, C. D. Ling, J. Oro-Sole, D. Gautier, G. Tobias, S. Adams, E. Canadell, and M. R. Palacin, *Inorg. Chem.*, 2004, **43**, 7050.
108. J. Cabana, N. Dupré, C. P. Grey, G. Subias, M. T. Caldes, A. M. Marie, and M. R. Palacín, *J. Electrochem. Soc.*, 2005, **152**, A2246.
109. J. Cabana, N. Dupré, F. Gillot, A. V. Chadwick, C. P. Grey, and M. R. Palacín, *Inorg. Chem.*, 2009, **48**, 5141.
110. J. Cabana, C. M. Ionica-Bousquet, C. P. Grey, and M. R. Palacín, *Electrochem. Commun.*, 2010, **12**, 315.
111. S. Indris, J. Cabana, O. J. Rutt, S. J. Clarke, and C. P. Grey, *J. Am. Chem. Soc.*, 2006, **128**, 13354.
112. O. J. Rutt, G. R. Williams, and S. J. Clarke, *Chem. Commun.*, 2006, 2869.
113. D. Zeng, S. Indris, J. Cabana, O. J. Rutt, C. F. Smura, S. J. Clarke, and C. P. Grey (In preparation).
114. E. Bekaert, P. Balaya, S. Murugavel, J. Maier, and M. Menetrier, *Chem. Mater.*, 2009, **21**, 856.
115. N. Yamakawa, M. Jiang, B. Key, and C. P. Grey, *J. Am. Chem. Soc.*, 2009, **131**, 10525.
116. F. Badway, N. Pereira, F. Cosandey, and G. G. Amatucci, *J. Electrochem. Soc.*, 2003, **150**, A1209.
117. N. Yamakawa, M. Jiang, and C. P. Grey, *Chem. Mater.*, 2009, **21**, 3162.
118. B. Key, R. Bhattacharyya, M. Morcrette, V. Seznec, J. M. Tarascon, and C. P. Grey, *J. Am. Chem. Soc.*, 2009, **131**, 9239.

Index

- 2 + 2 mechanism, O–O bond formation, 29
- Acetic acid (HOAc), methane functionalization, 103, 116–118, 131–133, 135
- Activated carbons (ACs), 341–342, 345–347, 354
- Aging, lithium ion batteries, 333–339
- AGW *see* anthropogenic global warming
- Air-regenerable systems, methane functionalization, 102, 104, 113–129, 133–135
- Alcohols
- carbon dioxide reduction, 301–306
 - direct ethanol fuel cells, 229–252
 - methane functionalization, 101–105, 111–112
- Algae, photobiological water splitting, 146
- Alkaline solutions, ethanol oxidation, 242–243
- Alkanes, methane to higher alkane conversion, 101, 103
- Anaerobic anodes, microbial fuel cells, 81
- Anatase TiO₂ nanocrystalites
- dye-sensitized solar cells, 56, 62
 - photo-initiated electron transfer, 265–299
 - properties, 56
- Anhydrous proton exchange membranes, 98
- Anodes
- catalysts, direct ethanol fuel cells, 230–249
 - cermet materials, 182–183
 - enzymatic biocatalysts, fuel cells, 75–76
 - materials, lithium ion batteries, 375–376, 386–388
 - microbial biocatalysts, fuel cells, 82
 - solid-oxide fuel cells, 180–183
 - surface reaction with electrolytes, lithium ion batteries, 337
- Anodophiles, microbial fuel cells, 81
- Anthracene-bridged dinuclear Ru complexes, 45–46
- Anthropogenic global warming (AGW), 199, 265, 302, 309, 312
- Apatite-type electrolytes, 179
- Aqueous phase reforming (APR), 7–9
- Aromatic hydrocarbons, proton exchange membranes, 96–98
- Artificial photosynthesis, 199–227
- carbon dioxide reduction, 302, 305
 - computational challenges, 191–197
 - electron transfer reactions, 208–217
 - iron-based supramolecular complexes, 152–154
 - proton reduction systems, 218–225
 - ruthenium(II) polypyridyl photosensitizers, 202–208
 - supramolecular approach, 201
 - water oxidation, 35–37
- Associated gas conversion, 101, 135–136
- Autocatalytic mechanisms, thermal decomposition, 336
- Autothermal partial oxidation of bioethanol, 7
- Autothermal reforming of bio-oils, 5
- Azadithiolate-bridged Fe₂ complexes, 219–221
- Bacteria
- cyanobacteria, 146
 - microbial fuel cells, 80–82
- Ballard Advanced Materials 3rd Generation (BAM3G) membranes, 97–99
- Barium strontium cobalt ferrite (BSCF), 184
- Battery electric vehicles (BEVs), 316, 333, 339, 375
- Binary catalyst anodes, direct ethanol fuel cells, 232–239, 244–247
- Biocatalysts *see* enzymes; microorganisms
- Biocompatibility, biological fuel cells, 74
- Bioethanol
- hydrogen production, 6–7, 16
 - internal combustion engines, 317
- Biofuel cells, 74–80
- anodic biocatalysts, 75–76
 - applications, 80
 - cathodic biocatalysts, 76–79
 - inorganic perspective, 79–80
 - performance, 80, 83
- Biofuels, environmental issues, 317
- Biological fuel cells, 73–87
- enzymatic catalysts, 73–80, 85–86
 - microbial catalysts, 73–74, 80–86
 - transformation and production roles of enzymes and microbes, 84–85
- Biological systems
- photosynthesis, 21–33, 35, 199–201
 - respiration, 253
- see also* living organisms
- “The biological way”, solar energy conversion, 37
- Biomass
- derivatives, 5–9
 - aqueous phase reforming, 7–9
 - bioethanol reforming, 6–7
 - bio-oils reforming, 5–6
 - partial oxidation, 7
 - steam reforming, 5–7
 - sugar reforming, 8–9
 - fast pyrolysis, 5
 - gasification, 4–5
 - hydrogen production, 3–9, 16, 312, 319
- Biomimetic systems *see* artificial photosynthesis
- Bio-oils, hydrogen production, 5–6
- Bipolar plates (interconnects), solid-oxide fuel cells, 185–186
- 2,2'-bipyridine (bpy), ruthenium complexes, 202
- dye-sensitized solar cells, 266, 268–269
 - Grätzel cell, 35–36
 - multicomponent molecular-based photocatalysis, 147–149
- 3,5-bis(2-pyridyl)pyrazolate (bpp), polynuclear ruthenium complexes, 43–45

- Bistridentate rutheniumII complexes, 202–208
 bite angle increase, 205–208
 chromophore–quencher assemblies, 204–205, 208
 classical, 202–205
 first generation, 205–206
 second generation, 206–208
BLS *see* bridging ligands
 Blue copper oxidases, biofuel cells, 76, 78
 Blue dimer/analogs, polynuclear ruthenium complexes, 39–43
 Bonded seals, solid-oxide fuel cells, 186
 Boundary conditions, dye-sensitized solar cell modeling, 68–69
Bpp *see* 3,5-bis(2-pyridyl)pyrazolate
 BPSH copolymers, proton exchange membranes, 97–98
Bpy *see* 2,2'-bipyridine
 Bridging ligands (BLs)
 biomimetic photocatalytic water splitting, 149, 157, 159–162
 ruthenium complexes, 39
 Bridging motifs, Fe₂ complex biomimetic catalysts, 219–222
 Broad spectral light harvesting, 272–274
BSCF *see* barium strontium cobalt ferrite
 Butterfly mechanism, O–O bond formation, 29
- CAG** *see* carbon aerogel
 Calcium peroxide, methane functionalization, 134
 Calendar life, lithium ion batteries, 333, 339
 Carbide-derived carbons (CDCs), supercapacitors, 346
 Carbohydrate formation, 22–24
 Carbon aerogel (CAG), 354
 Carbon anodes, lithium ion batteries, 337
 Carbon black catalyst supports, 253, 255–257
 Carbon capture and storage (CCS), 301, 311–312, 317
 Carbon dioxide, 301–302
 catalytic reduction methods, 303–305
 climate change, 301–302
 conversion to synthetic fuels, 301–305, 317
 electrochemical reduction, 303–304
 fixation, photosynthesis, 21–24
 fossil fuel emissions, 309, 311–312
 methane functionalization, 134–135
 photochemical reduction, 304–305
 reduction, 301–306
 sequestration, 3, 317, 320, 328
 thermal reduction, 303
 Carbon economy, 309, 311–312
 Carbon fibers, 354
 Carbon formation, solid-oxide fuel cells, 180–181
 Carbon materials, supercapacitors, 341–342, 345–354
 Carbon monoxide, methane functionalization, 131–135
 Carbon nanoparticles, catalyst adsorption, 255–257
 Carbon nanotubes (CNTs)
 direct ethanol fuel cells, 241–242
 photobiological water splitting, 146
 supercapacitors, 342, 350–351
 Carbon onions, 354
 Carbon-supported metal catalysts, 233, 238, 253, 255–259
 Carboxylation, methane functionalization, 111, 132–133
 Carotenoids, 24
- Catalysts**
 aqueous phase reforming, 8
 direct ethanol fuel cells
 anodes, 230–249
 cathodes, 243
 promoters/cocatalysts/supports, 241–242
 ethanol oxidation
 acidic conditions, 230–242
 alkaline solutions, 242–243
 [FeFe] hydrogenases active site mimicry, 218–223
 fuel cells, 253–263
 platinum-free cathodes, 253–263
 oxygen production from water, 35–52
 photocatalytic cells, 191–197
 steam reforming of ethanol, 6–7
 Catalytic cracking of bio-oils, 5–6
 Catalytic membrane reactors, 4, 16
 Catalytic partial oxidation of bioethanol, 7
 Catalytic reactions, methane functionalization, 102–103
 Catalytic reduction of carbon dioxide, 303–305
Cathodes
 fuel cell catalysts, 75–76, 82, 183–185, 243, 253–261
 lithium ion batteries, 337–339, 375–376, 378–386
CcO *see* cytochrome oxidase
CCS *see* carbon capture and storage
CDCs *see* carbide-derived carbons
 Ceramic anodes, 183
 Ceramic interconnects, 185
 Cerium catalysts, 121
 Cermet anodes, 182–183
CEs *see* counterelectrodes
CGH₂ *see* compressed-gas hydrogen
 Ch activation by coordination catalysts, 102–109
 Chain reactions
 methane functionalization, 102–104, 120–121, 129–135
 air-regenerable systems, 133–135
 direct use of dioxygen, 130
 non-air-regenerable systems, 130–133
 Charge accumulation, artificial photosynthesis, 208–217
 Charge compensation reactions, photosystem II mimicry, 208–209
 Charge distribution, interfacial electron transfer, 194
 Charge separation
 artificial photosynthesis, 150–152, 204–205, 214
 photosynthesis, 24–25, 199–200
 Charge transfer (CT)
 dye-sensitized solar cells, 266
 ruthenium(II) polypyridyl complexes, 202–208
 supramolecular complexes, 149
 Chemically modified graphene (CMG) sheets, 352
 Chemisorption, hydrogen storage, 323–324
 Chlorination, methane functionalization, 105–106, 110
 Chlorophylls, 24
 Chloroplasts, 21
CHP *see* combined heat and power
 Chromium interconnects, solid-oxide fuel cells, 185–186
 Chromophore–quencher assemblies, 204–205, 208, 210–215
 Climate change, carbon technology, 199, 302, 309, 311–312
CMG *see* chemically modified graphene
Cnts *see* carbon nanotubes

- Coal gasification, 318
Cobalt-based supramolecular photocatalysts, 154–157
Cobalt catalysts
 methane functionalization, 114
 oxygen production from water, 49–50
Cobalt complexes, lithium ion batteries, 376, 378–379
Cobalt diporphyrins, cathode catalysts, fuel cells, 254–255
Cobalt oxides
 oxygen production from water, 50
 supercapacitors, 357
Cobalt polypyrrole (CoPPy), fuel cells, 255–257
Cobalt porphyrin assemblies, fuel cells, 259–260
Cobalt thiencylporphyrins, fuel cells, 257–259
Cocatalysts, direct ethanol fuel cells, 241–242
Cofactors, photosynthesis, 26, 31
Combined heat and power (CHP), 176, 310, 328
Composite cathodes, solid-oxide fuel cells, 184–185
Composite membranes, perfluorinated sulfonic acid, 95–96, 99
Compressed-gas hydrogen (CGH₂), 321–322
Compressive seals, solid-oxide fuel cells, 186
Computational challenges, photocatalytic cells, 191–198
Computational studies, photosynthesis, 29–30
Conformational changes, oxygen-evolving complex, 28–29
Contaminants, solid-oxide fuel cells, 182
Continuity equation, semiconductors, 66–67
Conversion reactions, lithium ion batteries, 376–377, 388
Coordination catalysts
 methane functionalization, 102–129
 air-regenerable systems, 113–129
 CH activation, 104–109
 oxidant activation, 109–113
Coordination environment, oxygen-evolving complex, 28
Copolymers, proton exchange membranes, 97–98
Copper complexes, biofuel cells, 76
Copper polypyridyl compounds, dye-sensitized solar cells, 274–275
Copper–chlorine cycle, 369
CoPPy *see* cobalt polypyrrole
Costs
 hydrogen economy, 313, 316, 325–327
 photocatalytic cells, 191
 polymer electrolyte membrane fuel cells, 91, 99
Counterelectrodes (CEs), dye-sensitized solar cells, 53–54, 58, 64
Covalent bond energy storage, photosynthesis, 22–23
Cryogenics, hydrogen storage, 321–323
CT *see* charge transfer
Cyanobacteria, 146
Cytochrome *b*₆*f*, 31
Cytochrome oxidase (CcO), 253, 255
- Dπ⁶ coordination compounds, dye-sensitized solar cells, 266, 269–270
“Dark” reactions, photosynthesis, 21–24
DEC *see* diethyl carbonate
DEFCS *see* direct ethanol fuel cells
Degradation
 proton exchange membranes, 98–99
 solid-oxide fuel cells, 187
- Deintercalation, lithium ion batteries, 334
Density functional theory (DFT), 283
Depolymerization, proton exchange membranes, 99
Diethyl carbonate (DEC), lithium ion batteries, 333, 335–336
Dimethyl carbonate (DMC), lithium ion batteries, 333, 335–336
Dioxygen
 cathodic enzymatic biocatalysts, fuel cells, 76
 co-reactant, methane functionalization, 102, 113–118, 130, 134–135
 four electron reduction, 253
 production from water, 35–52
Diporphyrin cathode catalysts, fuel cells, 254–259
2,6-di(quinolin-8-yl)pyridine, bistridentate rutheniumII complexes, 206–208
Direct ethanol fuel cells (DEFCS), 229–252
Direct metal-to-particle charge transfer, 275–276
Direct methanol fuel cells (DMFCs), 229, 242–243, 325
Direct reaction with dioxygen, methane functionalization, 114–115, 130
Direct semiconductor excitation, 146–147
DMC *see* dimethyl carbonate
DMFCs *see* direct methanol fuel cells
Double-layer capacitance, electrochemical impedance spectroscopy, 60–61
Double perovskite structures, 184
DSCs *see* dye-sensitized solar cells
DSSCs *see* dye-sensitized solar cells
Durability
 proton exchange membranes, 95, 99
 solid-oxide fuel cells, 186–187
Dye-sensitized solar cells (DSCs/DSSCs), 53–72, 147, 265–290
 anatase TiO₂ nanocrystalites, 265–290
 boundary conditions, 68–69
 counterelectrode, 53–54, 58, 64
 developments, 70
 dye types, 53, 57
 electrochemical impedance spectroscopy, 58–64
 electrolytes, 54, 57–58, 67–68, 70
 experimental/simulation results, 69–70
 light harvesting, 266–275
 materials, 56–58
 phenomenological modeling, 64–70
 photoinduced electron injection, 275–280
 principles, 53–56
 semiconductors, 53–57, 65–68, 147, 192
 sensitization at the power point, 287–289
 sensitizer regeneration, 53–54, 57, 266, 280–287
- EAs *see* electron acceptors
EC *see* ethylene carbonate
Economic issues
 hydrogen economy, 326–327
 see also costs
EDL *see* electrical double layer
EDLCs *see* electrical double layer capacitors
EDs *see* electron donors

- EIS *see* electrochemical impedance spectroscopy
- Electrical analogs, dye-sensitized solar cells, 60–64
- Electrical double layer capacitors (EDLCs), 341, 346, 348
- Electrical double layer (EDL) mechanisms, 341, 343–344
- Electric vehicles (EVs) *see* battery electric vehicles; fuel cell electric vehicles
- Electrocatalysts, direct ethanol fuel cells, 230–249
- Electrochemical capacitors (supercapacitors), 341–363
- Electrochemical impedance spectroscopy (EIS), 58–64
- Electrochemical reactions
- carbon dioxide reduction, 301–305
 - photoelectrochemical water splitting, 12–13, 146–147
- Electrodes
- dye-sensitized solar cells, 53–54
 - materials
 - lithium ion batteries, 375–389
 - supercapacitors, 341–342, 345–359
 - polymer electrolyte membrane fuel cells, 89–90
 - surface reaction with electrolytes, lithium ion batteries, 337–339
- Electrolysis, hydrogen production, 313, 318–319
- Electrolytes
- dye-sensitized solar cells, 54, 57–58, 67–68, 70
 - lithium ion batteries, 333–339
 - solid-oxide fuel cells, 177–180
- Electromotive force (emf), fuel cells, 253
- Electron acceptors (EAs)
- photocatalytic water splitting, 144, 148, 151, 157
 - photosynthesis, 201
- Electron collectors, photocatalytic water splitting, 157
- Electron distribution, semiconductors, 65–66
- Electron donors (EDs), photocatalytic water splitting, 144, 147–148, 151, 157
- Electron donors side, photosystem II mimicry, 208–217
- Electronically conducting/ionically conducting composites
- materials, 185
- Electron injection, dye-sensitized solar cells, 275–280
- Electron relays (ERs), photocatalytic water splitting, 146–147
- Electron reservoirs, multinuclear complexes, 260
- Electrons, dye-sensitized solar cell modeling, 68
- Electron transfer (ET)
- Grätzel cell, 36
 - interfacial, photocatalytic cells, 192–196
 - photo-initiated, anatase TiO₂ nanocrystallites, 265–299
 - photosynthesis, 22, 24–31
 - preventing quenching, artificial photosynthesis, 209
 - rates, Marcus theory, 210
- Electroosmotic drag, 92
- Electrooxidation, ethanol, 229–252
- Emf *see* electromotive force
- Energy band structure, semiconductors, 65
- Energy conversion, photosynthesis, 21–33
- Energy efficiency
- hydrogen economy, 314–315
 - solar energy conversion, 24–25, 265–267
- Energy storage
- carbon dioxide reduction, 301–306
 - hydrogen carriers, 301–302
 - hydrogen economy, 309–332
- lithium ion batteries, 333–339, 375–391
- photosynthesis, 22–24
- supercapacitors, 341–363
- Energy transmission vector, hydrogen economy, 309–310, 313
- Energy use, USA, 90
- Enzymes
- active site mimicry, 218–223
 - fuel cells, 73–80, 84–85
 - hydrogen production, 146, 201
 - photosynthesis, 21–22
 - proton-coupled electron transfer, 37
 - respiration, 253
- EOR *see* ethanol oxidation reaction
- ERS *see* electron relays
- ET *see* electron transfer
- Ethanol
- fuel cells, 229–252
 - steam reforming, 6–7, 16
- Ethanol oxidation reaction (EOR), 231
- Ethylene carbonate (EC), lithium ion batteries, 333–336
- Ethylene glycol, aqueous phase reforming, 8
- Europe, hydrogen economy, 326–327
- EVs (electric vehicles) *see* battery electric vehicles; fuel cell electric vehicles
- Excited-state electron injection, 266, 275–279
- Experimental results, dye-sensitized solar cells, 69–70
- Extinction coefficient, 270–272
- Fast pyrolysis of biomass, 5
- FCEV *see* fuel cell electric vehicles
- [Fefe] hydrogenases, 201, 218–223
- Fermentation, 5, 6, 229, 315, 317
- Ferredoxin:NAPDP⁺ oxidoreductase, 31
- Ferredoxin, 31
- Ferritic interconnects, solid-oxide fuel cells, 186
- Fluorite-based electrolytes, 178
- Fossil fuels
- carbon/hydrogen transition economy, 309, 311–312
 - dependence, 89–90
- Four electron reduction, dioxygen, 253
- Fuel cell electric vehicles (FCEVs)
- hydrogen economy, 309, 311–312
 - advantages, 314–315
 - alternatives, 316–317
 - drawbacks, 315–316
 - fuel cells, 309, 314–316
 - importance, 309, 311
 - socioeconomic issues, 326–327
 - present status, 327
- Fuel cells
- biological, 73–87
 - direct ethanol, 229–252
 - hydrogen economy, 309–310, 314–315, 325–326
 - molecular catalysts, 253–263
 - operating temperatures, 174–175
 - processes, 173–174
 - proton exchange membranes, 89–100
 - solid-oxide cells, 173–189

- theory, 73
types, 173–175, 325–326
- Fuel contaminants, solid-oxide fuel cells, 182
- Fuel formation
carbon dioxide conversion, 301–305, 317
methane functionalization, 101–141
photocatalytic cells, 196–197
- Fuelling stations for hydrogen vehicles, 315–316, 321, 327
- Fuel shares, world energy sources, 313
- Fullerenes, 354
- Functionalization of methane, 101–141
chain reactions, 102–104, 129–135
coordination catalysts, 102–129
high-temperature syngas-based MTL processes, 101–102
- Functionalization of semiconductors, 192–194
- Fungal enzymes, 76, 78
- Gas diffusion layer (GDL), polymer electrolyte membrane fuel cells, 90
- Gasification of biomass, 4–5
- Gaskets, solid-oxide fuel cells, 186
- GDL *see* gas diffusion layer
- General Atomics (sulfur–iodine) cycle, 368–369
- Geometry optimization, dye-sensitized solar cells, 283
- Glass seals, solid-oxide fuel cells, 186
- Global warming, 199, 265, 302, 309, 312
- Glucose oxidase, 74–76, 79
- Gold catalysts, methane functionalization, 125–126
- Graphene materials, supercapacitors, 342, 351–354
- Grätzel cells, 35–37, 147, 304–305
- Greenhouse gases
carbon dioxide, 301–302
hydrogen economy, 312, 318, 327
hydrogen production methods, 3
see also global warming
- H₂ases *see* hydrogenases
- H-cluster, [FeFe] hydrogenases, 201
- High-temperature fuel cells, 175–176, 185
- High-temperature gas cooled reactors (HTGRs), 368, 370
- High-temperature methane functionalization, 101–102
- High-temperature solid-oxide fuel cells (HT-SOFCs), 175–176, 185
- High-temperature syngas-based MTL processes, 101–102
- HOAc *see* acetic acid
- Homogenous methane functionalization systems, 102
- Homogenous water oxidation, 215–217
- HTGRs *see* high-temperature gas cooled reactors
- HT-SOFCs *see* high-temperature solid-oxide fuel cells
- Hybrid sulfur cycle, 368
- “The hybrid way”, solar energy conversion, 37
- Hydration, Nafion® membranes, 92–95
- Hydrocarbons
hydrogen production, 3, 319
proton exchange membranes, 96–98
solid-oxide fuel cells, 180–182
see also methane
- Hydroelectric power, 312
- Hydrogen
atmospheric pollution, 327
polymer electrolyte membrane fuel cells, 89–90
safety issues, 327
- Hydrogenases (H₂ases)
biocatalysts, 201, 218
photobiological water splitting, 146
synthetic active site mimicry, 218–223
- Hydrogen-bonded tyrosine, 210–212
- Hydrogen carriers *see* hydrogen storage
- ‘Hydrogen corridor’ concept, 321
- Hydrogen distribution, 316, 320–321
- Hydrogen economy, 89, 187, 309–332, 365
advantages, 314–315
alternatives/complements, 316–317
drawbacks, 315–316
economic/social/political issues, 310, 326–327
future prospects, 327–330
key technologies, 317–326
sustainable, 309, 311–314, 316–317, 329–330
transition, 309, 311–312, 315
US hydrogen use, 365
- Hydrogen fuel cells
hydrogen economy, 187, 309–310, 314–315, 324–326
indirect fuel cells, 229
oxygen reduction at cathode, 253
theory, 73–74
- Hydrogen peroxide
methane functionalization, 106
oxygen reduction at fuel cell cathode, 253
- Hydrogen production
biological systems, 201
biomass, 3–9, 16
derivative reforming, 5–9
fast pyrolysis, 5
gasification, 4–5
biomimetics, 201, 218–225
costs, 313
fossil fuels, 365
key technologies, 317–320
molecular catalysts for water splitting, 35–36
natural gas, 3
photocatalytic water splitting, 143–171
cobalt-based photocatalysts, 154–157
iron-based biomimetic supramolecular systems, 152–154
mixed-valence systems, multielectron photochemistry, 157–159
multicomponent molecular-based photocatalysis, 147–149
osmium/rhodium-based supramolecular photocatalysts, 163
photobiological water splitting, 146
photoinitiated charge separation/molecular design, 150–152
photoinitiated electron collectors/functioning systems, 157
platinum/palladium supramolecular photocatalysts, 163–166

- Hydrogen production (*continued*)
 rhodium-based supramolecular photocatalysts, 159–163
 supramolecular charge-transfer complexes, 149
 renewable energy sources, 3–20, 312–314, 365–366
 ruthenium complexes, 37–38
 solar energy, 4, 9–17
 thermochemical water splitting cycles, 366–371
- Hydrogen storage, 301–302
 carbon dioxide reduction, 301–306
 nitrogen heterocycle carriers, 302
 technologies, 321–325
 vehicles, 315–316, 320–321
- Hydroxylation of methane, 111, 113
- ICEs *see* internal combustion engines
 IET *see* interfacial electron transfer
 ILs *see* ionic liquids
 Impedance spectra *see* electrochemical impedance spectroscopy
 Initial photoinduced charge separation, 199
- Inorganic chemistry
 enzymatic biofuel cells, 78–80
 microbial biofuel cells, 82–83
 photo-initiated electron transfer, 266
 solid-oxide fuel cells, 176
- Intercalation
 lithium ion batteries, 333–334, 375–376, 379, 384–386, 388
 supercapacitors, 351–352
- Interconnects (bipolar plates), solid-oxide fuel cells, 185–186
- Interfacial electron transfer (IET), 192–196
- Intermediate-temperature fuel cells, 175
- Intermediate-temperature solid-oxide fuel cells (IT-SOFCs), 173, 175–187
 advantages over high-temperature, 175
 anodes, 180–183
 applications, 176
 cathodes, 183–185
 electrolytes, 177–180
 interconnects, 185–186
 materials, 176–186
 performance durability, 186–187
 seals, 186
 support architectures, 175–176
- Intermolecular sensitizer regeneration, 283–287
- Internal combustion engines (ICEs)
 advantages of fuel cells, 3, 173, 309, 312
 alternatives to fossil fuels, 301–305, 314–315, 317
- Intramolecular charge separation, chromophore–quencher assemblies, 204–205
- Intramolecular sensitizer regeneration, 280–283
- Iodide/triiodide ions, dye-sensitized solar cells, 53–55, 57–58, 67, 69, 284–285
- Iodine catalysts, methane functionalization, 124–125
- Ion absorption, supercapacitors, 341
- Ionic liquids (ILs), Nafion® membrane impregnation, 96, 99
- Iridium catalysts, methane functionalization, 108
- Iridium complexes, oxygen production from water, 49
- Iridium polypyridyl compounds, TiO₂ sensitization, 274
- Iron-based biomimetic supramolecular systems, 152–154
- Iron complexes
 biomimetic catalysts, 218–225
 [FeFe] hydrogenases, 201, 218
 ruthenium–[FeFe] systems, 223–225
- Iron diporphyrin cathode catalysts, fuel cells, 255
- Iron oxides
 photoelectrodes active under visible light, 12–13
 supercapacitor electrodes, 357
- Iron polypyridyl compounds, dye-sensitized solar cells, 268, 272, 274–275
- Iron/steel, solid-oxide fuel cells, 186
- IT-SOFCs *see* intermediate-temperature solid-oxide fuel cells
- Japan, University of Tokyo (UT-3) cycle, 369–370
- Kinetics, S-state transitions, 26–28
- Kvaerner process, 319
- La₂Mo₂O₉-based electrolytes, 179
- Laccase, dioxygen reduction, 76, 78
- LAs *see* light absorbers
- Layered lithium transition metal oxide electrodes, 378–379
- LH₂ *see* liquid hydrogen
- Li₃V₂(PO₄)₃, 384–386
- LIBs *see* lithium ion batteries
- LiCoO₂ cathodes, 375–376, 378–379
- LiFePO₄, 376, 380–384
- Ligand-based electron collectors, 157
- Ligand-to-metal charge transfer (LMCT), 276
- Light absorbers (LAs), photocatalytic water splitting, 144–145
- Light-driven proton reduction, [FeFe] hydrogenase models, 218–225
- Light energy *see* photo...; solar energy
- Light harvesting
 dye-sensitized solar cells, 266–275
 efficiency, 267
 performance evaluation, 267–268
 tuning orbitals, 268–274
- hydrogen production, 144–145
- photosynthesis, 24–25
- “Light” reactions, photosynthesis, 21–23
- LiMPO₄, 379–384
- LiPF₆ *see* lithium hexafluorophosphate
- Liquid fuels
 alternatives, 317
 carbon dioxide conversion, 301–305, 317
 methane functionalization, 101–141
- Liquid hydrogen (LH₂), 321–322
- Liquid phase organic heterocycles, hydrogen storage, 324–325
- Lithium hexafluorophosphate (LiPF₆), 333–339
- Lithium ion batteries (LIBs), 333–339, 375–391
 electrode materials, 375–389
 conversion reactions, 376–377, 388
 development history, 375–377
 NASICON-type structures, 376, 384–386

- NMR studies, 377–389
 olivines, 376, 379–384
- electrolytes, 333–339
 composition, 333
 electrode surface reactions, 337–339
 solid electrolyte interphase, 334
 thermal decomposition, 335–337
 working mechanism, 334
- Living organisms
 photobiological water splitting, 146
 transformation/production role in fuel cells, 84–85
see also bacteria; fermentation; microbial.; microorganisms
- LMCT *see* ligand-to-metal charge transfer
- $\text{Ln}_1(\text{XO}_4)_6\text{O}_{2\pm y}$ systems, 179
- Low pressure membrane distillation (LPMD), 123
- Low-temperature fuel cells, 174–175
- Low temperature methane functionalization, 101–137
- Magic angle spinning (MAS) NMR, 377–380, 386
- Manganese/calcium cluster (Mn_4Ca), oxygen-evolving complex, 200–201
- Manganese catalysts
 methane functionalization, 114
 titanium dioxide semiconductor functionalization, 192–194
- Manganese cluster, oxygen-evolving complex, 21, 25–30
- Manganese complexes
 artificial photosynthesis, 210, 215–217
 oxygen production from water, 49–50
- $\text{Mn}_2^{\text{II,II}}\text{--Ru}^{\text{II}}\text{--NDI}$ triad, 214–215
- Manganese oxides
 lithium ion batteries, 379
 supercapacitors, 355–357
- Marcus theory, 210
- MAS *see* magic angle spinning
- Mass transport, electrochemical impedance spectroscopy, 61
- “The materials science way”, solar energy conversion, 37
- Membrane electrode assembly (MEA), fuel cells, 90–91, 254
- Membranes
 biological fuel cells, 73–76, 81–84
 catalytic membrane reactors, 4, 16
 low pressure membrane distillation, 123
 novel proton exchange membranes, 96–98
 perfluorinated sulfonic acid, 91–96
 photosynthesis, 21–27
 proton exchange membranes, 35, 89–100, 315
- Mercury catalysts, methane functionalization, 119–121, 133
- Metal..., *see also* individual metals; transition metal...
- Metal-based electron collectors, 157
- Metal complex cathode catalysts, 253–254
- Metallic interconnects, solid-oxide fuel cells, 185–186
- Metallic seals, solid-oxide fuel cells, 186
- Metalloenzymes
 biofuel cells, 76–79
 photosynthesis, 21
see also oxygen-evolving complex
- Metal-N₄ chelate cathode catalysts, 255–259
- Metal oxides
 cathode surface reactions with electrolytes, 337–339
- photoelectrodes active under visible light, 12
 redox pairs, 10–11, 367
- Metal-to-ligand charge transfer (MLCT)
 photocatalytic water splitting, 144–145, 148–149, 152, 155
 ruthenium(II) polypyridyl complexes, 202, 204
 sensitization cycle, 266
- Metal-to-metal charge transfer (MMCT), 160–162, 167–168
- Metal-to-particle charge transfer (MPCT), 275–276
- Metal–ceramic composites (cermets), 182–183
- Metal–metal-to-ligand charge transfer (MMLCT), 165
- Methane
 carbon dioxide reduction, 301–302, 305
 functionalization, 101–141
 chain reactions, 102–104, 129–135
 coordination catalysts, 102–129
 high-temperature syngas-based MTL processes, 101–102
 solid-oxide fuel cells, 180–182
 steam reforming, 3, 16, 309, 317–319, 365
- Methanesulfonic acid (MSA), methane functionalization, 103, 130–131
- Methane-to-liquid (MTL) technology, 101–102
- Methane-to-methanol conversion, 101–105, 111–112, 114, 135
- Methanol
 carbon dioxide reduction, 301–306
 fuel cells, 229, 242–243
 methane functionalization, 101–105, 111–112
- Methylformate, methane functionalization, 112
- Methyl hydroperoxide, methane functionalization, 112–113
- Microbial fuel cells, 73–74, 80–84
 anodic biocatalysts, 82
 applications, 83
 cathodic biocatalysts, 82
 inorganic perspectives, 82–83
 performance, 83
- Micro-CHP (small-scale combined heat and power), 176
- Microorganisms
 photobiological water splitting, 146
 transformation/production role, 84–85
- Mixed anion/non-oxide phase anodes, lithium ion batteries, 386–388
- Mixed conducting composite cathodes, solid-oxide fuel cells, 184–185
- Mixed-valence systems, multielectron photochemistry, 157–159
- MLCT *see* metal-to-ligand charge transfer
- MMCT *see* metal-to-metal charge transfer
- MMLCT *see* metal–metal-to-ligand charge transfer
- Modeling
 dye-sensitized solar cells, 60, 64–70
 [FeFe] hydrogenases, light-driven proton reduction, 218–225
 interfacial electron transfer, photocatalytic cells, 193
- Molecular design, photoinitiated charge separation, 150–152
- Molecular oxygen *see* dioxygen
- Molecular–semiconductor interfaces, 266, 285
- Mononuclear ruthenium complexes
 oxygen production, 47–49
 $\text{N}_4\text{O}_2\text{Ru}$ type, 48
 $\text{N}_5\text{Ru-OH}_2$ type, 47–48
 N_6Ru type, 48
 pincer type, 48–49

- MPCT *see* metal-to-particle charge transfer
- MSA *see* methanesulfonic acid
- MTL *see* methane-to-liquid technology
- Multicomponent molecular-based photocatalysis, 147–149
- Multielectron photochemistry mixed-valence systems, 157–159
- M multinuclear complex electron reservoirs, 260
- Multi-step thermochemical water splitting cycles, 367–371
-
- N_4O_2 mononuclear ruthenium complexes, 48
- $\text{N}_5\text{Ru}-\text{OH}_2$ type mononuclear ruthenium complexes, 47–48
- N_6Ru mononuclear ruthenium complexes, 48
- Nafion®
- degradation, 98–99
 - membranes, 91–96, 99
 - characteristics, 91–92
 - composite, 95–96
 - molecular transport, 92–94
 - morphology, 92–94
 - short side-chain membrane comparison, 94–95
 - water dependence, 91–92
- Nanostructures
- carbon cathode catalysts, fuel cells, 255–259
 - carbon supported platinum catalysts, fuel cells, 253
 - cermet anodes, solid-oxide fuel cells, 183
 - electrolytes, solid-oxide fuel cells, 180
 - semiconductors, dye-sensitized solar cells, 53, 56–57, 62, 70
 - TiO_2 , dye-sensitized solar cells, 56, 62, 265–290
 - transition metal catalysts, fuel cells, 254
- Naphthalenediimide (NDI), electron acceptor, 204, 214–215
- NASICON-type electrodes, 376, 384–386
- Natural gas
- distribution network, 321
 - hydrogen production, 3, 317, 319, 365
 - solid-oxide fuel cells, 176, 180–182
 - see also* methane
- NDI *see* naphthalenediimide
- Negative electrodes *see* anodes
- Nickel, lithium ion batteries, 379
- Nickel oxide electrodes, supercapacitors, 357
- Nitration, methane functionalization, 110–111
- Nitrogen-ligated platinum catalysts, 122–123
- NMR *see* nuclear magnetic resonance
- Non-air-regenerable systems, methane functionalization, 102, 104–113, 130–133
- Non-catalytic reactions, methane functionalization, 102–103
- Non-iodide intermolecular sensitizer regeneration, 285–287
- Non-oxide/mixed anion phase anodes, lithium ion batteries, 386–388
- Nuclear energy
- hydrogen economy, 314
 - thermochemical water splitting cycles, 368, 370
- Nuclear magnetic resonance (NMR), 377–389
-
- O_2 *see* dioxygen
- Ocean acidification, carbon dioxide, 309, 312
- Oec *see* oxygen-evolving complex
- Ohmic resistance, electrochemical impedance spectroscopy, 60
- Oil drilling, associated gas, 101, 135, 136
- Olivine electrodes, lithium ion batteries, 376, 379–384
- One-step oxygen reduction, fuel cells, 253
- Operating temperatures, solid-oxide fuel cells, 174–175, 181–182, 187
- Organic donors, intramolecular sensitizer regeneration, 280–282
- Organic liquids, hydrogen storage, 324–325
- Organometallic complex catalysts, oxygen production from water, 35–50
- Osmium complexes, biofuel cells, 75–77
- Osmium polypyridyl compounds, 266, 268, 274
- Osmium/rhodium supramolecular photocatalysts, 163
- Oxidant activation, methane functionalization, 102–103, 109–113
- Oxidation
- ethanol, direct ethanol fuel cells, 230–243
 - methane
 - catalytic mechanism, 123–124
 - high temperature technology, 101–102
 - low temperature technology, 101–137
 - water, photosynthesis, 21, 25–30
- Oxidation state changes, oxygen-evolving complex, 28–29
- Oxide ion conduction in electrolytes, 177–178
- Oxo-manganese complexes, titanium dioxide semiconductor functionalization, 192–193
- Oxygen
- production from water, molecular catalysts, 35–52
 - reductions, fuel cell cathodes, 243, 253–261
 - see also* dioxygen
- Oxygen-evolving complex (OEC), 23, 25–30, 200
- Oxygen–oxygen ($\text{O}-\text{O}$) bond formation, 29, 38–39
-
- Palladium-based supramolecular photocatalysts, 163–165
- Palladium-carbene complexes, methane functionalization, 106–108
- Palladium catalysts, methane functionalization, 106, 114–115, 117–118, 127–129
- PANI *see* polyaniline
- Partial oxidation of ethanol (POE), 6, 7
- Partial oxidation of hydrocarbons, 319
- Particulate photocatalysts, visible light, 13–16
- PCET *see* proton-coupled electron transfer
- PEC *see* photoinitiated electron collection
- PEDOT *see* poly (3,4-ethylenedioxythiophene)
- PEEK *see* poly(ether ether ketone)
- PEMFCs *see* polymer electrolyte membrane fuel cells
- PEMs *see* proton exchange membranes
- Perfluorinated sulfonic acid (PFSA)
- proton exchange membranes, 91–96
 - composite, 95–96
 - degradation, 98–99
 - short side-chain modifications, 94–95
 - see also* Nafion®
- Performance, biofuel cells, 80, 83
- Performance durability, solid-oxide fuel cells, 186–187
- Performance evaluation, light harvesting, dye-sensitized solar cells, 267–268
- Performance requirement, supercapacitors, 345
- Perovskites, 178–179, 184
- Peroxides, methane functionalization, 106, 134

- Petroleum drilling, associated gas, 101, 135–136
PFSA *see* perfluorinated sulfonic acid
Phenomenological modeling, dye-sensitized solar cells, 64–70
PHEVs *see* plug-in hybrid electric vehicles
Phosphates, lithium ion batteries, 376, 379–386
Photobiological water splitting, 146
see also artificial photosynthesis
Photocatalytic cells
computational challenges, 191–197
fuel formation, 196–197
interfacial electron transfer, 193–196
proton-coupled electron transfer, 194–195
semiconductor surface functionalization, 192–194
Photocatalytic water splitting
hydrogen production, 11–16, 143–171, 319–320
iron-based biomimetic supramolecular systems, 152–154
light absorption, 144–145
molecular design, photoinitiated charge separation, 150–152
multicomponent molecular-based systems, 147–149
sulfur–ammonia cycle, 370–371
thermodynamics, 144–145
see also artificial photosynthesis; photosynthesis
Photochemical reduction, carbon dioxide, 304–305
Photoelectrochemical cells, 12–13, 305
Photoelectrochemical water splitting, 12–13, 146–147
Photoelectrodes
visible light, 12–13
see also semiconductors
Photoinduced charge separation, photosynthesis, 199–200
Photoinduced electron injection, dye-sensitized solar cells, 275–280
Photoinitiated charge separation, molecular design, 150–152
Photoinitiated electron collection (PEC), 144, 151, 157
Photoinitiated electron transfer, anatase TiO₂ nanocrystalites, 265–299
Photolysis, methane, 133
Photonic energy capture, photosynthesis, 22, 24–25
Photophysics, supramolecular photocatalysts, 155, 160–161
Photosensitizers, ruthenium(II) polypyridyl, 202–208
Photosynthesis, 21–33
artificial carbon dioxide reduction comparison, 302, 305
cofactors, 26, 31
cytochrome *b*₆*f*, 31
“dark” reactions, 21–24
energy storage/carbon fixation, 22–24
lessons for synthetic energy systems, 21
“light” reactions, 21–23
molecular processes, 199–201
photonic energy capture, 22, 24–25
photosystem I, 22, 24–25, 30–31
photosystem II, 21–30
water oxidation, 24–31, 35, 37
see also artificial photosynthesis
Photosystem II (PSII)
mimicry, electron transfer reactions, 208–209
oxygen production from water, 35, 199–200
photosynthesis, 21–30
Photosystem I (PSI), photosynthesis, 22, 24–25, 30–31
Photovoltaics (PV), 53
see also dye-sensitized solar cells
Physisorption, hydrogen storage, 323
Pigments
dye-sensitized solar cells, 53, 57
photosynthesis, 24
Pincer type mononuclear ruthenium complexes, 48–49
Plants
fuel cells, 84–85
see also photosynthesis
Plastocyanin, 31
Platinum-based supramolecular photocatalysts, 163–166
Platinum catalysts
dioxygen reduction, fuel cells, 78–79
direct ethanol fuel cells, 230–249
alkaline conditions, 242–243
binary catalysts, 232–239, 244–247
promoters/cocatalysts/supports, 241–242
ternary catalysts, 239–241, 248–249
dye-sensitized solar cells, 58, 68–69
hydrogen fuel cells, 253–254
methane functionalization, 104–106, 115, 118, 121–124
Platinum-free catalysts, fuel cells, 254–261
Platinum nanoparticles, proton exchange membranes, 95, 99
Platinum polypyridyl compounds, TiO₂ sensitization, 274
Plug-in hybrid electric vehicles (PHEVs), 333
POE *see* partial oxidation of ethanol
Political issues, hydrogen economy, 326–327
Polyaniline (PANI), supercapacitors, 344, 353–354, 357–358
Poly(ether ether ketone) (PEEK), proton exchange membranes, 96–97
Poly(3,4-ethylen-dioxythiophene) (PEDOT), supercapacitors, 358–359
Polymer backbone enzymatic catalysts, biofuel cells, 76
Polymer electrode materials, supercapacitors, 357–359
Polymer electrolyte membrane fuel cells (PEMFCs), 89–100
degradation, 98–99
design, 89–91
direct ethanol fuel cell comparison, 230
hydrogen economy, 315–316, 325–326
membrane types, 91–98
water problems, 92, 98
see also proton exchange membranes
Polynuclear ruthenium complexes, oxygen production, 39–47
anthracene-bridged, 45–46
blue dimer/analogs, 39–43
POM-bridged, 46–47
pyridazine-bridged, 45
Ru–Hbpp/analogs, 43–45
Polyoxometalate (POM) ligands, 46–47
Polypyridyl compounds, *see also* ruthenium(II) polypyridyl; transition metal polypyridyl compounds
Polystyrene sulfonic acid (PSSA), proton exchange membranes, 96
POM *see* polyoxometalate
POM-bridged tetranuclear Ru complexes, 46–47
Porphyrins, fuel cell cathode catalysts, 254–260
Positive electrodes *see* cathodes
Potassium peroxide, methane functionalization, 134
Power point sensitization, 287–289
Promoters, direct ethanol fuel cells, 241–242

- Proton-conducting electrolytes, solid-oxide fuel cells, 179–180
- Proton-coupled electron transfer (PCET)
hydrogen-bonded tyrosine, 210–212
natural systems, 37
photocatalytic cells, 194–195
- Proton exchange membranes (PEMs), 89–100
anhydrous, 98
aromatic hydrocarbons, 96–98
characteristics, 90–92
composite, 95–96
degradation, 98–99
hydrocarbons, 96–98
modeling, 92–93
Nafion®, 91–96
novel, 96–98
perfluorinated sulfonic acid membranes, 91–96
polystyrene sulfonic acid, 96
see also polymer electrolyte membrane fuel cells
- Proton hopping, water, 91
- Proton reduction, light-driven reactions, 218–223
- Pseudocapacitance mechanisms, 341, 344–345, 354
- PSI *see* photosystem I
- PSII *see* photosystem II
- PSSA *see* polystyrene sulfonic acid
- PV *see* photovoltaics
- Pyridazine-bridged dinuclear Ru complexes, oxygen production, 45
- Pyrolysis of biomass, 5
- P–n junction solar cells, 53–54
- Quenching prevention in electron transfer pathways, 209
- Rectification, interfacial electron transfer, 195–196
- Redox-active cofactor Y_z , 25–26
- Redox couples, thermochemical water splitting cycles, 10–11, 367
- Redox enzymes, biological fuel cells, 74–80
- Redox mediators, biofuel cells, 79
- Redox potentials, water oxidation, 38
- Redox properties, supramolecular photocatalysts, 154–155, 159–160
- Reduced sensitizer electron injection, 275, 279–280
- Regeneration
dye-sensitized solar cells, 53–54, 57, 266, 280–287
methane functionalization, 102, 104
- Renewable energy sources
hydrogen production, 3–20, 312–314
share of world energy, 313
technical and theoretical potentials, 313
thermochemical water splitting cycles, 365–373
see also solar energy
- Respiration, 253
- Rhodium-based supramolecular photocatalysts, 159–163
hydrogen production, 161–163
photophysics, 160–161
redox properties, 159–160
spectroscopic properties, 160
- Rhodium catalysts, methane functionalization, 116–117
- Rhodium–platinum catalysts, direct ethanol fuel cells, 237–238, 246–249
- Roadmap to hydrogen economy, 310, 327, 328
- Ru–Hbpp/analogs, polynuclear ruthenium complexes, 43–45
- Ru–OH₂/Ru=O system, 37–38
- Ruthenium catalysts, methane functionalization, 114
- Ruthenium complexes
oxygen production from water
mononuclear complexes, 47–49
O–O bond formation, 38–39
polynuclear complexes, 39–47
water oxidation process, 35–38
- photocatalytic water splitting, iron-based biomimetic supramolecular systems, 152–153
- Ruthenium(II) polypyridyl complexes
artificial photosynthesis, 202–208
chromophore–quencher assemblies, 204–205, 208
classical complexes, 202–205
first generation complexes, 205–206
increasing bite angle, 205–208
intramolecular charge separation, 204–205
photosensitizers, 202
second generation complexes, 206–208
stereochemical synthetic outcomes, 203–204
structure and properties, 202–203
synthesis strategies, 203
- dye-sensitized solar cells, 266, 268–274, 278–287
multicomponent molecular-based photocatalysis, 147–149
oxygen production from water, 35–36
- Ruthenium oxide electrodes, supercapacitors, 354–355
- Ruthenium polyazine chromophores, light absorption, 145–146
- Ruthenium–[FeFe] systems, photochemical hydrogen production, 223–225
- Ruthenium–palladium-based supramolecular photocatalysts, 164
- Ruthenium–platinum-based supramolecular photocatalysts, 163–166
- Ruthenium–platinum catalysts, direct ethanol fuel cells, 232–233, 239–240, 244, 248
- Rutile TiO₂ properties, 56
- SA *see* sulfur–ammonia cycle
- Sacrificial reagents, water splitting, 14–15
- Safety issues
cobalt in lithium ion batteries, 378–379
hydrogen economy, 316, 322, 327
- Scandium catalysts, methane functionalization, 108–109
- SCWG *see* supercritical water gasification
- Seals, solid-oxide fuel cells, 186
- SEI *see* solid electrolyte interphase
- Semiconductors
dye-sensitized solar cells, 53–57, 65–68, 265–290
photocatalytic cells, 192–194
photoelectrochemical water splitting, 146–147
- Sensitization at the power point, 287–289
- Sensitizers
dye-sensitized solar cells, 53–55, 57, 70
regeneration, 53–54, 57, 266, 280–287

- Short side-chains (SSCs), perfluorinated sulfonic acid membranes, 94–95
- SI *see* sulfur–iodine cycle
- Silicon, lithium ion batteries, 388–389
- Simulations
- dye-sensitized solar cells, 69–70
 - interfacial electron transfer, photocatalytic cells, 193
 - $\gamma\text{-SiW}_{10}\text{O}_{36}^{8-}$ polyoxometalate ligand, 46–47
- Small scale combined heat and power (micro-CHP), 176
- Socioeconomic challenges, hydrogen economy, 310, 326–327
- SOFCs *see* solid-oxide fuel cells
- Solar energy
- artificial photosynthesis, 199–227
 - carbon dioxide reduction, 302, 304–305
 - conversion efficiency, 24–25, 265–267
 - conversion methods, “the materials science way”/“the hybrid way”/“the biological way”, 37
 - dye-sensitized solar cells, 53–72, 191–197
 - Grätzel cells, 35–37
 - growth in capacity, 53
 - hydrogen economy, 312
 - hydrogen production, 4, 9–17, 143–171
 - importance, 199
 - light absorption, 144–145, 266–275
 - photocatalytic water splitting, hydrogen production, 143–171
 - photochemical water splitting, 11–16
 - thermochemical water splitting, 9–11, 367–368, 370–371
 - utilization methods, 199
 - see also* photosynthesis
- Solid electrolyte interphase (SEI), lithium ion batteries, 334
- Solid-oxide fuel cells (SOFCs), 173–189
- high temperature, 175
 - hydrogen economy, 325
 - intermediate-temperature, 173, 175–187
 - operation, 173–174
- Solid state hydrogen storage, 322–324
- Solvent water nucleophilic attack, 38–39
- Spectroscopic properties, rhodium-based supramolecular photocatalysts, 160
- SPEEK *see* sulfonated poly(ether ether ketone)
- SSCs *see* short side-chains
- S-state transitions, 26–28
- Stability, dye-sensitized solar cells, 70
- Stationary power generation, hydrogen economy, 315
- Steam addition, solid-oxide fuel cells, 181
- Steam reforming, 3, 5–6, 180
- ethanol, 6–7, 16
 - methane, 3, 16, 309, 317–319, 365
- Storage materials for hydrogen, 322–325
- Substrate water exchange/binding, photosynthesis, 28
- Sugars
- aqueous phase reforming, 8–9, 16
 - biomass conversion, 4–5
 - fermentation to bioethanol, 229, 317
 - photosynthesis, 22, 302
- Sulfonated poly(ether ether ketone) (SPEEK), proton exchange membranes, 97
- Sulfonation, methane functionalization, 130–131
- Sulfur family cycles, thermochemical water splitting, 368–369
- Sulfur trioxide/sulfuric acid, methane functionalization, 118–129
- Sulfur–ammonia (SA) cycle, thermochemical water splitting, 370–371
- Sulfur–iodine (SI) cycle, thermochemical water splitting, 368–369
- Superacid catalysts, methane functionalization, 109–111
- Supercapacitors, 341–363
- electrode materials, 341–342, 345–359
 - energy storage mechanisms, 341–345
 - performance requirement, 345
 - vehicle applications, 316–317
- Supercritical water gasification (SCWG), biomass, 5
- Supported catalysts, fuel cells, 233, 238, 241–242, 253, 255–259
- Supramolecular complexes
- photocatalytic water splitting, 143
 - cobalt-based photocatalysts, 154–157
 - evaluation of properties, 145–146
 - iron-based biomimetic systems, 152–154
 - osmium/rhodium photocatalysts, 163
 - platinum/palladium photocatalysts, 163–166
 - properties, 149–151
- Surface catalysts, photocatalytic cells, 192–193
- Surface reactions of electrodes with electrolytes, 337–339
- Sustainable hydrogen economy, 309, 311–314, 316–317, 329–330
- Swedish Consortium for Artificial Photosynthesis, 199–227
- Syngas chemistry, 101–102
- Synthetic fuels, 101–141, 301–305, 317
- TCO *see* transparent conducting oxide
- TCWSCs *see* thermochemical water splitting cycles
- Technological challenges, hydrogen economy, 310
- Temperature
- fuel cell operation, 174–175, 181–182, 187
 - lithium ion batteries, 333–339
- Templated carbon, supercapacitors, 347–350
- Terawatt Challenge, 265–266
- Ternary catalysts, direct ethanol fuel cells, 239–241, 245–246, 248–249
- Thermal reduction, carbon dioxide, 303
- Thermal stability of electrolytes, 333–339
- Thermochemical water splitting, 9–11, 319, 365–373
- Thermochemical water splitting cycles (TCWSCs), 366–371
- Thermodynamics
- photocatalytic water splitting, 144–145
 - S-state transitions, 26–28
- Thin-film photovoltaics, 53
- see also* dye-sensitized solar cells
- Tin–platinum catalysts, direct ethanol fuel cells, 233–237, 240–241, 244–246, 248–249
- TiO₂/Al₂O₃ nanoparticles, 279
- Titanium dioxide (TiO₂)
- functionalization, 192–193
 - nanocrystalites, 56, 62, 265–299
 - photoelectrodes active under visible light, 12–13

- Titanium dioxide (TiO_2) (*continued*)
 photo-initiated electron transfer, 265
 rutile/anatase properties, 56
 semiconductors, 56–57, 62–64
- Town gas, 318
- TPB *see* triple phase boundary
- Trametes versicolor*, 76, 78
- Transitional hydrogen economy, 309, 311–312, 315
- Transition metal catalysts
 oxygen production from water
 cobalt species, 49–50
 iridium complexes, 49
 manganese complexes, 49–50
 O–O bond formation, 38–39
 ruthenium complexes, 35–49
- Transition metal donors, intramolecular sensitizer regeneration, 282–283
- Transition metal oxide electrodes
 lithium ion batteries, 376–379
 supercapacitors, 344, 354–357
- Transition metal oxide redox pairs, thermochemical splitting of water, 10–11, 367
- Transition metal phosphate electrodes, lithium ion batteries, 379–386
- Transition metal polypyridyl compounds
 dye-sensitized solar cells, 266, 268–269
 fuel cell cathode catalysts, 255–257
- Transmission line model, electrochemical impedance spectroscopy, 61–64
- Transparent conducting oxide (TCO), 58, 62, 64, 68–69
- Transport *see* vehicle energy sources
- Triple phase boundary (TPB), fuel cells, 174
- Trisbidentate rutheniumII complexes, 202–205
- Tuning orbitals, light harvesting, 268–274
- Two dimensional graphene materials, supercapacitors, 342, 351
- Two-step thermochemical water splitting cycles, 366–367
- Tyrosine, proton-coupled electron transfer, 210–212
- Tyrosine Z, oxygen-evolving complex, 25–26
- Ultracapacitors *see* supercapacitors
- United states advanced battery consortium (USABC), 333
- United States of America
 energy use, 90
 hydrogen economy, 326–329
- University of Tokyo (UT-3) cycle, 369–370
- Unzipping mechanism, proton exchange membranes, 99
- Urea peroxide, methane functionalization, 134
- USABC *see* united states advanced battery consortium
- UT-3 cycle, thermochemical water splitting, 369–370
- Vehicle energy sources
 alternatives, 316–317
- battery electric vehicles, 316, 333, 339, 375
 hydrogen economy, 309, 311–312, 314–317, 320–321, 326–327
 synthetic fuels, 101–141, 301–305, 317
- Virtual hydrogen storage (VHS), 302
- Visible light, water splitting, 12–16
- Water
 Nafion® membranes, 91–94
 proton hopping, 91
- Water-free proton exchange membranes, 98
- Water nucleophilic attack (WNA), 38–39
- Water splitting
 artificial photosynthesis, 21, 199–202, 208
 direct thermal decomposition, 366
 Grätzel cells, 35–37, 147, 304–305
 hydrogen production
 photobiological, 146
 photocatalytic, 143–171
 photochemical, 11–16
 photoelectrochemical, 146–147
 thermochemical, 9–11
 molecular mechanisms, 37–38
 oxygen production
 molecular catalysts, 35–52
 other transition metal catalysts, 49–50
 ruthenium catalysts, 35–49
 photobiological, 146
 photocatalysis, 143–171, 191–197
 photochemical, 11–16
 photoelectrochemical, 146–147
 photosynthesis, 21, 25–30, 200
 redox potentials, 38
 solar fuel production, 199
 synthetic manganese complexes, 215–217
 thermochemical cycles, 9–11, 365–373
- WE *see* working electrode
- Westinghouse (hybrid sulfur) cycle, 368
- Wind energy, 312
- WNA *see* water nucleophilic attack
- Working electrode (WE)
 dye-sensitized solar cells, 53
see also semiconductors
- World energy sources, 313
- Yeast, 80–81
- Zinc tetraphenylporphyrin (ZnTPP), 152–154
 “Z-scheme”, photosynthesis, 22–23
- Zundel ions, 91

Abbreviations and Acronyms used in this Volume

1-mim	1-Methylimidazolium	DMAc	Dimethyl Acetamide
2-ph-py	2-Phenyl-Pyridine	DMC	Dimethyl Carbonate
2D	Two-dimensional	DMF	N,N-Dimethylformamide
3DOM	Three-dimensionally Ordered Macroporous	DMFC	Direct Methanol Fuel Cell
4-pic	4-Methylpyridine	DOE	United States Department of Energy
ABTS	2,2'-Azino-bis(3-Ethylbenzo-Thiazoline-6-Sulfonic Acid) Diammonium Salt	DS	Degree of Sulfonation
acac	Acetylacetato	DSC	Dye-Sensitized Solar Cells
AC	Activated Carbons	EA	Electron Acceptor
ACF	Activated Carbon Fibers	EC	Electrochemical Capacitor
AFC	Alkaline Fuel Cells	EC	Ethylene Carbonate
AGW	Anthropogenic Global Warming	EDCC	Electron Donor
ANF	Alumina Nanofiber	EDLC	Electric Double-Cylinder Capacitor
APR	Aqueous Phase Reforming	EIA	Electrical Double Layer Capacitor
APU	Auxiliary Power Unit	EIS	Energy Information Administration
ARC	Accelerating Rate Calorimetry	EISA	Electrochemical Impedance Spectroscopy
ASR	Area-specific Resistance	EMC	Evaporation-Induced Self-Assembled
ATP	Adenosine Triphosphate	emf	Ethyl Methyl Carbonate
ATR-SEIRAS	Attenuated Total Reflection Surface Enhanced Infrared Absorption Spectroscopy	EOR	Electromotive Force
BAM3G	Ballard Advanced Materials 3 rd Generation	EPR	Ethanol Oxidation Reaction
bdc ²⁻	2,2'-Bipyridine-6,6'-Dicarboxylato Anion	EPT	Electron Paramagnetic Resonance
BDD	Boron-doped Diamond	ER	Concerted Proton-Coupled Electron Transfer
BDE	Bond Disassociation Energy	ESD	Electron Relay
BEV	Battery Electric Vehicle	ESI	Electrostatic Spray Deposition
bfimbz	1,4-bis(phen-[5,6-d]imidazol-2-yl)Benzene	ESR	Electrospray Ionisation
binapypyrr	3,6-bis[6'-(1',8''-naphthyrid-2''-yl)-pyrid-2'yl]Pyridazine	ET	Equivalent Series Resistance
Bipy	Bipyridine	et-bpy ₂	Electron Transfer
BL	Bridging Ligand	ETPT	Ethyl-bis-bpy
BoP	Balance-of-Plant	EV	Electron Transfer Followed by Proton Transfer
bpc	3,6-bis(6'-Carboxypyrid-2'-yl)-Pyridazine	EW	Electric Vehicle
bpm	2,2'-Bipyrimidine	EWCC	Equivalent Weight
bpy	2,2'-Bipyridine	EXAFS	Electric Wire-in-Cylinder Capacitor
bpym	Bipyrimidine	FAD	Extended X-ray Absorption Fine Structure
bpz	2,2'-Bipyrazine	FADH ₂	
btpyan	1,8-bis(2,2':2'',2'''-Terpyridine)Anthracene	FC	Flavin Adenosine Dinucleotide
BtU	British Thermal Unit	fcc	Flavin Adenine Dinucleotide (reduced, by two electrons and two protons)
CAG	Carbon Aerogel	FCEV	Fuel Cell
CASPT2	Complete Active Space with Second-order Perturbation Theory	FD	Face-Centred Cubic
CB	Conduction Band	FF	Fuel-Cell Electric Vehicle
CcO	Cytochrome c Oxidase	FNR	Ferredoxin
CCS	Carbon Capture and Storage	FTIR	Fill Factor
CDCs	Carbide-derived Carbons	FTO	Ferrodoxin:NADP ⁺ Oxidoreductase
CE	Counterelectrode	GA	Fourier Transform Infrared
CEA	Commissariata l'Engergie Atomique	GDL	Fluorine-Doped Tin Oxide
CEP	Concerted Electron-Proton	GHG	
CGH ₂	Compressed Gas Hydrogen (storage method)	GNS/PANI	Graphene Nanosheet/Polyaniline
Chl	Chlorophyll	GO	Graphene Oxide
CHP	Combined Heat and Power	GPCP	Graphene/Polyaniline Composite Paper
CMC	Carboxymethylcellulose	Hbpp	3,5-bis(2-pyridyl)Pyrazole
CMG	Chemically Modified Graphene	hcp	Hexagonal Close-Packed
CNT	Carbon Nanotube	HDPE	High-Density Polyethylene
CNTA	Carbon Nanotube Arrays	hfacac	1,1,1,5,5-Hexafluoropentane-2,4-Dione
Cp [*]	Pentamethylcyclopentadienyl Anion	HI	Hydroiodic Acid
CPE	Constant Phase Element	His	Histidine
CS	Charge Separated	HMPA	Hexamethylphosphoramide
CuCl	Copper(I) Chloride	HOAc	Acetic Acid
CV	Cyclic Voltammetry	HOMO	Highest Occupied Molecular Orbital
Cyt	Cytochrome	HPGC	Hierarchical Porous Graphitic Carbon
Cyt-P ₄₅₀	Cytochromes P ₄₅₀	HT-SOFC	High-Temperature Solid Oxide Fuel Cell
		HTFA	Trifluoroacetic Acid
DAOHC	Dialkyl-2,5-Dioxahexane Carboxylate	HTGR	High-Temperature Gas-Cooled Reactor
DEC	Diethyl Carbonate	HyPr-RING	Hydrogen Production by Reaction-Integrated Novel Gasification
DEFc	Direct Ethanol Fuel Cell	HyS	Hybrid Sulfur
dema-TfOH	Diethylmethyl Amine-Trifluoromethane Sulfonic Acid	I2M	Interaction of Two M-O Entities
DEMS	Differential Electrochemical Mass Spectrometry	ICE	Internal Combustion Engine
DFAFC	Direct Formic Acid Fuel Cell	IET	Interfacial Electron Transfer
DFT	Density Functional Theory		
DMA	N, N-Dimethylaniline		

IHP	Inner Helmholtz Plane	P	Photosensitizer
ILs	Ionic Liquids	PAFC	Phosphoric Acid Fuel Cells
im	Imidazolium	PANI	Polyaniline
IPCC	Intergovernmental Panel on Climate Change	PBI	Poly(Benzimidazole)
IPCE	Incident Photon-to-Current Conversion Efficiency	PC	Plastocyanin
IR	Infrared	PCA	Pyrazine-2-Carboxylic Acid
IT	Intermediate-Temperature	PCET	Proton-Coupled Electron Transfer
ITO	Indium Tin Oxide	PDF	Pair Distribution Function
IVCT	Intervalence Charge-Transfer	PEC	Photoinitiated Electron Collection
JAEA	Japanese Atomic Energy Agency	PEC	Polyethylene Carbonate
KIE	Kinetic Isotope Effect	PEDOT	Poly 3,4-Ethylenedioxythiophene
kWh	Kilowatt-Hour Measure of Energy Equal to 36 Million Joules	PEEK	Poly(Ether Ether Ketone)
LC	Ligand-Centered	PEFC	Polymer Electrolyte Fuel Cells
LF	Ligand-Field	PEM	Proton Exchange Membrane
LH ₂	Liquid Hydrogen (storage method)	PEMFC	Polymer Electrode Membrane (or Proton Exchange Membrane) Fuel Cell
LHE	Light-Harvesting Efficiency	PEMFC	Polymer Electrolyte Membrane Fuel Cell
LiBOB	Lithium bis(oxalate)Borate	PEN	Positive-Electrolyte-Negative
LIBs	Lithium Ion Batteries	PEO	Polyethylene Oxide
LIESST	Light-Induced Excited Spin-State Trapping	PES	Polyether Sulfone
LLCT	Ligand-to-Ligand Charge-Transfer	PFSA	Perfluorinated Sulfonic Acid
LMCT	Ligand-to-Metal Charge Transfer	Ph-SPEEKDK	Phenylated Sulfonated Polyether Ether Ketone Diphenyl Ketone
LPCT	Ligand-to-Particle Charge-Transfer	phen	Phenanthroline
LUMO	Lowest Unoccupied Molecular Orbital	Pheo	Pheophytin a
MAS	Magic Angle Spinning	PHEVs	Plug-in Hybrid Electric Vehicles
MBS	Methyl Bisulfate	PI	Pyromellitimide
MC	Metal Centered	PIL	Protic Ion Liquid
MCCE	Multi Conformer Continuum Electrostatics	PMD	Photochemical Molecular Device
MCMB	Mesocarbon Microbead	PNN	2-(di- <i>Tert</i> -Butylphosphino-Methyl)-6-Diethylaminomethyl)Pyridine
MD	Molecular Dynamics	POE	Partial Oxidation of Ethanol
MEA	Membrane Electrode Assembly	POM	Polyoxometalate, e.g., $\gamma\text{-SiW}_{10}\text{O}_{36}^{8-}$
MeCN	Acetonitrile	PP	Power Point
MeTFA	Methyl Trifluoroacetate	ppm	Parts Per Million
MIEC	Mixed Ionic-Electronic Conduction/Conductor/Conducting	Ppy	Polypprole
MLCT	Metal-to-Ligand Charge Transfer	PQ	Plastoquinone
MMCT	Metal-to-Metal Charge Transfer	PSA	Pressure Swing Adsorption
MOF	Metal-Organic Framework	PSI	Photosystem I
MPCT	Metal-to-Particle Charge Transfer	PSII	Photosystem II
MPP	Maximum-Power Point	PSSA	Polystyrene Sulfonic Acid
MS-EPT	Multiple Site Concerted Proton-Coupled Electron Transfer	PT	Proton Transfer
MSA	Methanesulfonic Acid	PTET	Proton Transfer Followed by Electron Transfer
MTL	Methanol to Liquids	PTFE	Poly Tetra Fluoro Ethylene
MWCNTs	Multiwalled Carbon Nanotubes	pTTPA	Poly(Tri(4-(Thiophen-2-yl)Phenyl)Amine)
NAD ⁺	Nicotinamide Adenine Dinucleotide (Oxidized)	PTZ	Phenothiazine
NADH	Nicotinamide Adenine Dinucleotide (reduced, by two electrons and one proton)	PV	Photovoltaics
NADP ⁺	Oxidized Nicotinamide Adenine Dinucleotide Phosphate	PVC	Polyvinyl Chloride
NADPH	Reduced Nicotinamide Adenine Dinucleotide Phosphate	PVDF	Polyvinylidene Fluoride
NCS	Thiocyanate	PVI	Polyvinylimidazole
NDI	Naphthalenediimide	PVP	Polyvinylpyridine
NEGF	Nonequilibrium Green's Function	py	Pyridine
NHC	N-Heterocyclic Carbene	PZZP	Point of Zero ζ -Potential
NHE	Normal Hydrogen Electrode	Q	Quinone
NIR	Near Infrared	Q _A	Plastoquinone
NMR	Nuclear Magnetic Resonance	QM/MM	Combined Quantum Mechanics/Molecular Mechanics
NNC	6-Phenyl-2,2'-Bipyridine	RC	Resistor-Capacitor
NP	Nanoparticle	RDS	Rate-Determining Step
NREL	National Renewable Energy Laboratory	REDOR	Rotational-Echo, Double-Resonance
OAc	Acetate	RH	Relative Humidity
OCV	Open Circuit voltage	RMCA	Reverse Monte Carlo
OEC	Oxygen-Evolving Complex	RT	Room Temperature
OEC-PSII	Oxygen Evolving Complex of Photosystem II	Rubisco	Ribulose 1,5-Bisphosphate Carboxylase/Oxygenase
OHP	Outer Helmholtz Plane	RWTH	Rheinisch Westfälische Technische Hochschule
ORR	Oxygen Reduction Reaction	SA	Sulfur-Ammonia
OSET	Outer Sphere Electron Transfer	SANS	Small-Angle Neutron Scattering
Ox	Electron Acceptor	SAXS	Small-Angle X-Ray Scattering
		SCWG	Gasified Under Supercritical Water
		SEI	Solid Electrolyte Interphase
		SHE	Standard Hydrogen Electrode

SI	Sulfur–Iodine	TPB	Triple Phase Boundary
SLS	Static Light Scattering	tpphz	Tetrapyrido[3,2-a:2',3'-c:3'',2''-h:2'',3'''-j]Phenazine
SNL	Sandia National Laboratories	TRIR	Time-Resolved Infrared
SOFC	Solid Oxide Fuel Cell	trpy-pyr	4'-(<i>para</i> -Pyrrolylmethyl-Phenyl)-2,2':6',2'-Terpyridine
SPEKs	Sulfonated Polyether Ketones	trpy	2,2':6',2''-Terpyridine
SPFC	Solid Proton Fuel Cell	TTFP	Tris(2,2,2-Trifluoroethyl) Phosphite
SRE	Steam Reforming of Ethanol	Tyr	Tyrosine
SSC	Short Side-Chain		
SSCE	Sodium-Saturated Calomel Electrode	upd	Underpotentially Deposited
SSZ	Scandia-Stabilized Zirconia	USABC	United States Advanced Battery Consortium
STY	Space–Time Yield (mol/cc/s)	UV	Ultraviolet
SWCNTs	Single-Walled Carbon Nanotubes		
TBA ⁺	Tetra- <i>n</i> -Butylammonium	VB	Valence Band
TBHP	<i>Tert</i> -Butyl Hydroperoxide	VC	Vinylene Carbonate
TBP	<i>Tert</i> -Butylpyridine	VHS	Virtual Hydrogen Storage
TCO	Transparent Conducting Oxide	VK ₃	2-Methyl-1,4-Naphthoquinone, Vitamin K ₃
TCWSC	Thermochemical Water-Splitting Cycle	WE	Working Electrode
TEA	Triethylamine	WGS	Water Gas Shift
TEC	Thermal Expansion Coefficient	WNA	Solvent Water Nucleophilic Attack
TEM	Transmission Electron Microscope	wt%	Weight Percent (Composition)
TEOA	Triethanolamine		
TFA	Trifluoroacetate	XANES	X-ray Absorption Near-Edge Structure
TFAA	Trifluoroacetic Anhydride	XPS	X-ray Photoelectron Spectroscopy
TFAPA	Trifluoroacetic Propylamine	XRD	X-ray Diffraction
THz-TD	Terahertz Time-Domain		
TL	Terminal Ligand	YCZ	Yttria-Stabilized Cubic Zirconia
TM	Transition Metal	YO	O-Atom Donor
TMTACN	1,4,7-Trimethyl-1,4,7-Triazacyclononane	YSZ	Yttria-Stabilized Zirconia
TN	Turnover Number	Zn/ZnO	Zinc–Zinc Oxide
TOF	Turnover Frequency		
TON	Turnover Number		

Periodic Table of the Elements

Group	1	2	3	4	5	6	7	8	9	10	11	12	13	14	15	16	17	18
Period	1	H																
Atomic number	1	1.0079																
Atomic weight	2	Li	Be															
	3	Na	Mg															
	19	20	21	Sc	Ti	V	Cr	Mn	Fe	Co	Ni	Cu	Zn	Ga	Ge	As	F	² He
	39.0983	40.078	44.9559	47.867	50.9415	51.996	54.0380	55.845	58.933	58.693	58.546	58.409	63.723	72.64	74.9216	78.96	18.9984	4.0026
	4	K	Ca															
	37	38	39	40	41	42	43	44	45	46	47	48	49	50	51	52	53	Xe
	85.4678	87.62	88.9059	91.224	92.9064	95.94	98.9062	101.07	102.9055	106.42	107.8682	112.41	114.818	118.710	121.760	127.60	126.9045	131.29
	5	Rb	Sr	Y	Zr	Nb	Mo	Tc	Ru	Rh	Pd	Ag	Cd	In	Sn	Sb	Te	I
	55	56	57	*	72	73	74	75	76	77	78	79	80	81	82	83	84	85
	132.9054	137.327	138.9055	178.49	180.9479	183.84	186.207	190.2	192.22	195.08	196.9665	200.59	204.3833	207.2	208.9804	(209)	(210)	Rn (222)
	6	Cs	Ba	La	Hf	Ta	W	Re	Os	Ir	Pt	Au	Hg	Tl	Pb	Bi	Po	At
	87	88	89	**	104	105	106	107	108	109	110	111	112	113	114	115	116	
	7	Fr	Ra	Ac	Rf	Db	Sg	Bh	Hs	Mt	Ds	Rg	(272)					

*	58	59	60	61	62	63	64	65	66	67	68	69	70	71			
	Ce	Pr	Nd	Pm	Sm	Eu	Gd	Tb	Dy	Ho	Er	Tm	Yb	Lu			
	140.12	140.9077	144.24	(147)	150.36	151.96	157.25	158.9254	162.50	164.9304	167.26	168.9342	173.04	174.967			

**

ACTINIDES	90	91	92	93	94	95	96	97	98	99	100	101	102	103			
	Th	Pa	U	Np	Pu	Am	Cm	Bk	Cf	Es	Fm	Md	No	Lr	(259)	(260)	(262)

Based on information from IUPAC, the International Union of Pure and Applied Chemistry (version dated 1st November 2004).
For updates to this table, see http://www.iupac.org/reports/periodic_table.